

Micro/Nano Technologies
Series Editors: Zheng You · Xiaohao Wang

SPRINGER
REFERENCE

Jiwang Yan *Editor*

Micro and Nano Fabrication Technology

 Springer

Micro/Nano Technologies

Series Editors

Zheng You

Department of Precision Instrument

Tsinghua University

Beijing, China

Xiaohao Wang

Department of Precision Instrument

Tsinghua University

Beijing, China

The series consists of five volumes: *Micro and nano fabrication technology*, *MEMS*, *Nanomaterial*, *Nanomedicine* and *Applications of micro-/nanotechnologies* in IT. Experienced researchers and experts are invited to contribute in each of these areas. The series is published under Springer Major Reference works, which allows continuous online update and publication. These features allow newcomers and other readers to keep in touch with the most up-to-date information in micro-/nanotechnologies. It presents an overview of the knowledge base, as well as selected topics and provides comprehensive and authoritative information on the field for researchers, engineers, scientists and graduate students who are involved in different aspects of micro-/nanotechnologies. This publication will provide inspiration for innovative research and application ideas for continued growth of the field. Micro-/nanotechnologies are techniques to fabricate and build systems with dimensions ranging from nanometers to microns. Advances in these technologies have created many interdisciplinary research opportunities and have been applied in various areas from nanomedicine to space systems. After several decades of development, a knowledge base of micro-/nanotechnologies covering all areas of research has now been created. It includes design and simulation, fabrication and manufacturing, packaging and assembly, device and system technologies, and application in different areas.

More information about this series at <http://www.springer.com/series/13903>

Jiwang Yan
Editor

Micro and Nano Fabrication Technology

With 817 Figures and 72 Tables

 Springer

Editor
Jiwan Yan
Department of Mechanical Engineering
Keio University
Yokohama, Japan

ISBN 978-981-13-0097-4 ISBN 978-981-13-0098-1 (eBook)
ISBN 978-981-13-0099-8 (print and electronic bundle)
<https://doi.org/10.1007/978-981-13-0098-1>

Library of Congress Control Number: 2018942026

© Springer Nature Singapore Pte Ltd. 2018

This work is subject to copyright. All rights are reserved by the Publisher, whether the whole or part of the material is concerned, specifically the rights of translation, reprinting, reuse of illustrations, recitation, broadcasting, reproduction on microfilms or in any other physical way, and transmission or information storage and retrieval, electronic adaptation, computer software, or by similar or dissimilar methodology now known or hereafter developed.

The use of general descriptive names, registered names, trademarks, service marks, etc. in this publication does not imply, even in the absence of a specific statement, that such names are exempt from the relevant protective laws and regulations and therefore free for general use.

The publisher, the authors and the editors are safe to assume that the advice and information in this book are believed to be true and accurate at the date of publication. Neither the publisher nor the authors or the editors give a warranty, express or implied, with respect to the material contained herein or for any errors or omissions that may have been made. The publisher remains neutral with regard to jurisdictional claims in published maps and institutional affiliations.

Printed on acid-free paper

This Springer imprint is published by Springer Nature
The registered company is Springer Nature Singapore Pte Ltd.
The registered company address is: 152 Beach Road, #21-01/04 Gateway East, Singapore 189721, Singapore

Series Preface

Micro/nano technologies are those techniques to fabricate and build systems with dimensions ranging from nanometer to micron. The advancement of these technologies has been creating many interdisciplinary research opportunities and has been applied in various areas from nano-medicine to space systems. After several decades of development, a knowledge base of micro/nano technologies forms. It comes from every achievement of research and consists of design and simulation, fabrication and manufacturing, packaging and assembly, device and system technologies, and application in different areas.

Main structure of the knowledge base and selected topics are shown in this series of books. This work provides a comprehensive and authoritative knowledge of the field for researchers, engineers, scientists, and graduate students who are engaged in different aspects of micro/nano technologies. The series consists of five books, which are Micro and nano fabrication, MEMS, Nanomaterial, Nanomedicine, and Applications of Micro/nano technologies in IT/IoT. In the books, the latest researches of micro-nano technology are summarized and the history and roadmap of related techniques, devices, and applications are discussed. The authors invited come from China, Japan, USA, Germany, Great Britain, Austria, etc. Their research activities in this area are remarkable and prospective. The readership is not merely specialists in this field but also a broad range of students and researchers from other related disciplines.

The Chinese Society of Micro/Nano Technology (CSMNT) has organized the Micro/Nano Technologies series in cooperation with Springer. This series would be the first systematic series of books in Micro/Nano Technologies and provides a comprehensive and authoritative knowledge system. The series is published under Springer Major Reference, which allows continuous online update and publication. These features allow the new comers and other content users to keep in touch with the most updated information in micro/nano

technologies. It is expected that this publication will provide a new window to sparkle innovative research and application ideas for the continuous growth of the field.

December, 2017
Tsinghua University, Beijing, China
President of the Chinese Society of
Micro/Nano Technology

Zheng You

Tsinghua University, Beijing, China
Secretary-general of the Chinese Society of
Micro/Nano Technology

Xiaohao Wang

Volume Preface

Smaller is better. Small things can save space, reduce weight and material/energy consumption, and improve portability and ease of system integration. For a long time, researchers and engineers have been attempting to make things as small as possible. Today, new fabrication technologies have already enabled the generation of 2D and 3D structures and devices on the micrometer, submicrometer, and even down to nanometer ranges. This represents a triumph for modern science and technology. Despite various revolutionary changes in the past decades that significantly advanced micro/nanofabrication technology, we still face new problems and new tasks to create new products with higher precision and quality. Thus, understanding the fundamentals and mastering the status of micro/nanofabrication technology has become crucial for engineers and researchers working in this area. This volume focuses on the state-of-the-art micro and nano fabrication technologies for creating miniature structures with high precision. These multidisciplinary technologies include mechanical, electrical, optical, physical, and chemical methods, as well as hybrid processes, covering subtractive and additive material manufacturing, as well as net-shape manufacturing. The materials the volume deals with include metals, alloys, semiconductors, polymers, crystals, glass, ceramics, composites, and nanomaterials. The targeted products include micro/nanomachines, sensors, optics, electromechanical systems, fluidics, biomedical parts, and energy storage devices.

The volume is composed of 30 chapters, which are grouped into five parts. Part 1 is focused on cutting technology, which is the most popular method for generating micro/nanostructures on metal materials. The topics include microchiseling, micro-milling, microturning, nanogrooving, elliptical vibration-assisted cutting, roller machining, and tool servo-driven diamond turning. Part 2 presents abrasive/tip-based machining technologies, such as ultrasonic vibration-assisted grinding, micro-structure grinding, micro-fluid-jet polishing, bonnet polishing, chemical mechanical polishing, and scanning probe lithography. Part 3 deals with high-energy-beam machining technologies, such as femtosecond laser direct writing, laser patterning, ion beam machining, electron beam machining, and laser lithography combined with ion etching. Part 4 covers molding, forming, and self-organization technologies. The chapters in this part describe microinjection molding, nanoimprinting, press molding, anisotropic gelation, metal film dewetting/patterning, and self-assembly of fine particles. The subject of Part 5 is physical and chemical machining, where

microelectrical discharge machining, microelectrochemical machining, tip-based localized catalytic etching, photocatalytic reaction, deep reactive ion etching, and local wettability modification by laser irradiation are presented.

The chapters in this volume were mostly contributed by authors from the Asia-Pacific region, which is a rapidly growing region with research activities that are attracting attention in the area of micro/nanofabrication. Engaging with the latest research in the field, these chapters provide important perspectives on key topics, from process developments at the shop level to scientific investigations at the academic level, offering both experimental work and theoretical analysis. Moreover, the content of this volume is highly interdisciplinary in nature, with insights from not only manufacturing technology but also mechanical/material science, optics, physics, chemistry, and more. I hope this volume can deliver a timely integration of the latest achievements and advances in this area. It is intended to serve as a “toolbox” for manufacturing engineers, enabling them to identify suitable “tools” easily for the cost-effective production of different types of products. Furthermore, it is expected to stimulate more research interest in this area and help orient young researchers, particularly graduate students, to new research directions in future. Finally, as the volume’s editor, I would like to thank all the chapter authors for the time and energy they spent in preparing and revising their manuscripts. It is their generous dedication that made the on-schedule publication of the volume possible.

Yokohama, Japan

Jiawang Yan

Contents

Part I Cutting Technology	1
1 Micro Chiseling of Retroreflective Arrays	3
Lars Schönemann and Ekkard Brinksmeier	
2 Micro Milling for Functional Surface	33
Takashi Matsumura	
3 Micro Cylindrical Turning of Calcium Fluoride	67
Yasuhiro Kakinuma and Yuta Mizumoto	
4 Nano-grooving by Using Multi-tip Diamond Tools	97
Xichun Luo and Zhen Tong	
5 Elliptical Vibration Cutting for Difficult-to-Cut Materials	139
Hongjin Jung, Takehiro Hayasaka, and Eiji Shamoto	
6 Micromachining of Roller Mold for Roll-to-Roll Manufacturing	183
Rui Huang, XinQuan Zhang, and Kui Liu	
7 Tool-Servo Driven Diamond Turning for Structured Surface	215
Mao Mukaida and Jiwang Yan	
Part II Abrasive/Tip-Based Machining Technology	245
8 Micro-/Nano-texturing by Ultrasonic-Assisted Grinding	247
Masayoshi Mizutani, Shaolin Xu, Keita Shimada, and Tsunemoto Kuriyagawa	
9 Precision Grinding for Functional Microstructured Surface	301
Jin Xie	
10 Micro Fluid Jet Polishing	333
Anthony T. Beaucamp	
11 Bonnet Polishing of Microstructured Surface	371
Lingbao Kong, Zhongchen Cao, and Laiting Ho	

12	Soft-Brittle Semiconductors Polishing with Environment-Friendly Slurries	421
	Zhenyu Zhang, Bo Wang, and Dongming Guo	
13	Three-Dimensional Fabrication of Micro-/Nanostructure Using Scanning Probe Lithography	445
	Yanquan Geng and Yongda Yan	
Part III	High-Energy Beam Machining Technology	479
14	Femtosecond Laser Direct Writing	481
	Mitsuhiro Terakawa	
15	Laser Patterning of Metallic Glass	499
	Hu Huang and Jiwang Yan	
16	Ion Beam Machining	529
	Noritaka Kawasegi	
17	Electron-Beam Machining	555
	Jun Taniguchi	
18	Microfabrication by Laser Lithography Combined with Ion Etching	577
	Zhiyu Zhang, Ruoqiu Wang, and Donglin Xue	
Part IV	Molding/Forming/Self-Organization Technology	605
19	Replication of Micro-/Nanostructures	607
	Paritat Muanchan and Hiroshi Ito	
20	Precision Molding of Microstructures on Chalcogenide Glass for Infrared Optics	635
	Tianfeng Zhou	
21	Press Molding of Hybrid Fresnel Lenses for Infrared Applications	661
	Ahmad Rosli Abdul Manaf and Jiwang Yan	
22	Microspring Fabrication by Anisotropic Gelation	691
	Hiroaki Onoe and Koki Yoshida	
23	Fabrication of Metallic Nanodot Arrays	711
	Masahiko Yoshino and Motoki Terano	
24	Surface Micro-/Nanostructuring Using Self-Assembly of Fine Particles	745
	Arata Kaneko	

Part V Physical/Chemical Machining Technology	773
25 Micro-electrical Discharge Machining of Hard Brittle Materials	775
Pay Jun Liew and Jiwang Yan	
26 Micro Electrochemical Machining	807
Wataru Natsu	
27 Catalytic AFM-Based Nanofabrication	857
Takayuki Shibata, Junji Sasano, and Moeto Nagai	
28 3D Microfabrication Using Photocatalytic Reaction	881
Satoru Takahashi	
29 Silicon Etching for Multiple-Height Microstructures	903
Minoru Sasaki	
30 Local Wettability Modification and Its Micro-Fluidic System Application	925
Yuko Aono and Atsushi Hirata	

About Series Editors



Zheng You is currently a Professor in the Department of Precision Instrument in Tsinghua University, Beijing, China. He is also serving as the Director of Micro-Nano Technology Research Center at Tsinghua University, the Director of State Key Laboratory of Precision Measurement Technology and Instruments, and Vice President of National Institute for Nano-Technology and Engineering. He has been elected as an Academician of Chinese Academy of Engineering since 2013 and President of Chinese Society of Micro-Nano Technology (CSMNT).

Prof. Zheng You's main research interests fall in micro-nano technology, MEMS, satellite technology, and measurement and instruments.

Prof. You has published 322 papers and 32 research reports, holds 12 Chinese invention patents, among which over 114 papers are retrieved and embodied by the SCI or EI journals. He developed the first microsatellite in China and rewarded with numerous awards including the Second-class National Scientific and Technical Advance Awards, the First-class Scientific and Technical Awards of China Instrument and Control Society, the First-class and the Second-class Scientific and Technical Advance Awards of the Education Ministry, the First-class and Second-class Scientific and Technical Advance Award of the Beijing Municipality, and Second-class Science Technology and Industry Awards for National Defense.



Xiaohao Wang is currently a Professor in the Department of Precision Instrument, Tsinghua University. He also serves as Associate Dean of Education and Director of the Division of Advanced Manufacturing, Graduate School at Shenzhen, Tsinghua University, and executive secretary general of the Chinese Society of Micro-Nano Technology (CSMNT).

Prof. Xiaohao Wang received both a bachelor degree and a Ph.D. from Tsinghua University in 1994 and 1999, respectively. During 1998 to 2001, he joined the Department of Precision Instrument in Tsinghua University as an Assistant Professor and was promoted to Associate Professor in 2001. During 2007 to 2008, he was a visiting scholar at Technische Universitaet, Berlin. In 2010, he became a Professor of the Department of Precision Instrument in Tsinghua University.

Prof. Xiaohao Wang's research interests cover MEMS-based sensors, actuators, ionizing sources and portable mass spectrometer, ion mobility spectrometer, and high-field asymmetric waveform ion mobility spectrometer. He has published over 200 technical papers and applied tens of patents in the area of MEMS and the portable instrumentation.

About the Editor



Jiwang Yan is currently a Professor of Mechanical Engineering at Keio University, Japan, leading the Laboratory for Precision Machining and Nano Processing (PMNP). His research areas include ultraprecision machining, micro/nanomanufacturing, material processing, and nanomechanics. He has led the implementation of several dozens of research projects supported by governments and industry to develop key fabrication processes for optics, molds, cutting/grinding tools, semiconductor substrates, batteries, and biomechanical components. He has published over 200 journal papers, 300 conference papers, 17 book chapters, and applied for 20 patents. He has received over 30 awards from academic societies and scientific foundations for his contributions in research. He is now a member of the Japan Society of Mechanical Engineers (JSME), Japan Society for Precision Engineering (JSPE), Japan Society for Abrasive Technology (JSAT), Japan Society for Applied Physics (JSAP), American Society for Precision Engineering (ASPE), European Society for Precision Engineering and Nanotechnology (euspen), and the International Academy for Production Engineering (CIRP). He also serves on the editorial boards of 10 academic journals, such as the *International Journal of Machine Tools and Manufacture* (IJMTM).

Contributors

Ahmad Rosli Abdul Manaf Faculty of Manufacturing Engineering, Universiti Malaysia Pahang, Pekan, Pahang, Malaysia

Yuko Aono Department of Mechanical Engineering, Tokyo Institute of Technology, Tokyo, Japan

Anthony T. Beaucamp Department of Micro-Engineering, Kyoto University, Kyoto, Japan

Ekkard Brinksmeier Laboratory for Precision Machining LFM, Leibniz Institute for Materials Engineering IWT, Bremen, Germany

MAPEX Center for Materials and Processes, University of Bremen, Bremen, Germany

Zhongchen Cao Key Laboratory of Advanced Ceramics and Machining Technology, Ministry of Education, Tianjin University, Tianjin, China

Yanquan Geng Center for Precision Engineering, Harbin Institute of Technology, Harbin, Heilongjiang, China

Dongming Guo Key Laboratory for Precision and Non-Traditional Machining Technology of Ministry of Education, Dalian University of Technology, Dalian, China

Takehiro Hayasaka Graduate School of Engineering, Nagoya University, Nagoya, Aichi, Japan

Atsushi Hirata Department of Mechanical Engineering, Tokyo Institute of Technology, Tokyo, Japan

Laiting Ho Partner State Key Laboratory of Ultra-Precision Machining Technology, The Hong Kong Polytechnic University, Hung Hom, Hong Kong

Hu Huang School of Mechanical Science and Engineering, Jilin University, Changchun, Jilin, China

Department of Mechanical Engineering, Faculty of Science and Technology, Keio University, Yokohama, Japan

Rui Huang Machining Technology Group, Singapore Institute of Manufacturing Technology, Singapore, Singapore

Hiroshi Ito Department of Organic Materials Science, Yamagata University, Graduate School of Organic Materials Science, Yamagata, Japan

Hongjin Jung Graduate School of Engineering, Nagoya University, Nagoya, Aichi, Japan

Yasuhiro Kakinuma Department of System Design Engineering, Keio University, Yokohama, Japan

Arata Kaneko Faculty of System Design, Tokyo Metropolitan University, Tokyo, Japan

Noritaka Kawasegi Toyama Industrial Technology Center, Takaoka-shi/Toyama, Japan

Lingbao Kong Shanghai Engineering Research Center of Ultra-Precision Optical Manufacturing, Fudan University, Shanghai, China

Tsunemoto Kuriyagawa Tohoku University, Sendai, Japan

Pay Jun Liew Manufacturing Process Department, Faculty of Manufacturing Engineering, Universiti Teknikal Malaysia Melaka, Hang Tuah Jaya, Melaka, Malaysia

Kui Liu Machining Technology Group, Singapore Institute of Manufacturing Technology, Singapore, Singapore

Xichun Luo Centre for Precision Manufacturing, Department of Design, Manufacture and Engineering Management, University of Strathclyde, Glasgow, UK

Takashi Matsumura Department of Mechanical Engineering, Tokyo Denki University, Tokyo, Japan

Yuta Mizumoto Department of System Design Engineering, Keio University, Yokohama, Japan

Masayoshi Mizutani Tohoku University, Sendai, Japan
Department of Mechanical Systems Engineering, Graduate School of Engineering, Tohoku University, Sendai, Japan

Paritat Muanchan Department of Organic Materials Science, Yamagata University, Graduate School of Organic Materials Science, Yamagata, Japan

Mao Mukaida Department of Mechanical Engineering, Faculty of Science and Technology, Keio University, Yokohama, Japan

Moeto Nagai Department of Mechanical Engineering, Toyohashi University of Technology, Toyohashi, Japan

Wataru Natsu Tokyo University of Agriculture and Technology, Koganei City, Tokyo, Japan

Hiroaki Onoe Department of Mechanical Engineering, Faculty of Science and Technology, Keio University, Kanagawa, Japan

Minoru Sasaki Toyota Technological Institute, Nagoya, Japan

Junji Sasano Department of Mechanical Engineering, Toyohashi University of Technology, Toyohashi, Japan

Lars Schönemann Laboratory for Precision Machining LFM, Leibniz Institute for Materials Engineering IWT, Bremen, Germany

MAPEX Center for Materials and Processes, University of Bremen, Bremen, Germany

Eiji Shamoto Graduate School of Engineering, Nagoya University, Nagoya, Aichi, Japan

Takayuki Shibata Department of Mechanical Engineering, Toyohashi University of Technology, Toyohashi, Japan

Keita Shimada Tohoku University, Sendai, Japan

Satoru Takahashi Research Center for Advanced Science and Technology (RCAST), The University of Tokyo, Tokyo, Japan

Jun Taniguchi Faculty of Industrial Science and Technology, Department of Applied Electronics, Tokyo University of Science, Tokyo, Japan

Mitsuhiro Terakawa Department of Electronics and Electrical Engineering, Keio University, Yokohama, Japan

Motoki Terano Department of Mechanical Systems Engineering, Okayama University of Science, Okayama, Japan

Zhen Tong Centre for Precision Manufacturing, Department of Design, Manufacture and Engineering Management, University of Strathclyde, Glasgow, UK

Centre for Precision Technologies, University of Huddersfield, Huddersfield, UK

Bo Wang Key Laboratory for Precision and Non-Traditional Machining Technology of Ministry of Education, Dalian University of Technology, Dalian, China

Ruoqiu Wang Changchun Institute of Optics, Fine Mechanics and Physics, Chinese Academy of Sciences, Changchun, Jilin, China

Jin Xie School of Mechanical and Automotive Engineering, South China University of Technology, Guangzhou, China

Shaolin Xu Southern University of Science and Technology, Shenzhen, Guangdong, China

Donglin Xue Changchun Institute of Optics, Fine Mechanics and Physics, Chinese Academy of Sciences, Changchun, Jilin, China

Jiawang Yan Department of Mechanical Engineering, Keio University, Yokohama, Japan

Yongda Yan Center for Precision Engineering, Harbin Institute of Technology, Harbin, Heilongjiang, China

Koki Yoshida Department of Mechanical Engineering, Faculty of Science and Technology, Keio University, Kanagawa, Japan

Masahiko Yoshino Department of Mechanical Engineering, Tokyo Institute of Technology, Tokyo, Japan

XinQuan Zhang Machining Technology Group, Singapore Institute of Manufacturing Technology, Singapore, Singapore

Zhenyu Zhang Key Laboratory for Precision and Non-Traditional Machining Technology of Ministry of Education, Dalian University of Technology, Dalian, China

Zhiyu Zhang Changchun Institute of Optics, Fine Mechanics and Physics, Chinese Academy of Sciences, Changchun, Jilin, China

Tianfeng Zhou Key Laboratory of Fundamental Science for Advanced Machining, Beijing Institute of Technology, Beijing, China

Part I

Cutting Technology



Micro Chiseling of Retroreflective Arrays

1

Lars Schönemann and Ekkard Brinksmeier

Contents

1.1	Introduction to Retroreflectors	4
1.2	Machining Processes for Generating Retroreflective Surfaces	5
1.3	Principles of Diamond Micro Chiseling	6
1.3.1	DMC Process Kinematics	7
1.3.2	Diamond Tools for DMC	8
1.3.3	Requirements on Machine Tool	9
1.3.4	Evaluation of Process Performance	10
1.4	Diamond Micro Chiseling of Miniaturized Retroreflectors	18
1.4.1	General Principle	18
1.4.2	Assessment of Required Machining Time	19
1.4.3	Optimization Strategies	22
1.5	DMC on Curved Surfaces	26
1.6	Summary and Outlook	29
	References	29

Abstract

Diamond Micro Chiseling (DMC) has been established as a machining process for generating miniaturized retroreflective arrays with structure sizes in the micrometer range. This chapter focuses on a comprehensive overview on principles, process performance, and optimizations of DMC for generating micro full-cube retroreflectors on planar surfaces. Furthermore, considerations and initial results for transferring DMC to the machining of curved and freeform surfaces will be shown.

L. Schönemann (✉) · E. Brinksmeier
Laboratory for Precision Machining LFM, Leibniz Institute for Materials Engineering IWT,
Bremen, Germany

MAPEX Center for Materials and Processes, University of Bremen, Bremen, Germany
e-mail: schoenemann@lfm.uni-bremen.de; brinksmeier@iwt.uni-bremen.de

Keywords

Precision Machining · Retroreflector · Diamond Micro Chiseling · Micro Structure · Functional Surface

1.1 Introduction to Retroreflectors

Retroreflectors are a special type of optical components that allows for a light ray to be reflected back to its source, regardless of its incident direction. A prominent example in everyday life is the safety reflectors of bicycles and car lights, which, for instance, reflect the front light of a car back to its driver, as described by Luoma et al. (1996). Other applications can be found in optical communication as shown by Rabinovich et al. (2003), laser trackers as shown by Estler et al. (2002), distance metrology as shown by Ren et al. (2007), or object detection via light barriers as shown by Hering and Martin (2006).

As an optical component, retroreflectors can be realized as a combination of mirror and lens (Luneburg lens or “cat’s eye”-reflector) or in the shape of three perpendicular reflecting facets (“corner reflector”); see Liepmann (1994). As described by Seward and Cort (1999), the former are mainly used in safety applications, due to their larger acceptance angle and tolerance to errors (only the distance between mirror and lens determines its functionality). Hence, Beer and Marjaniemi (1966) stated that they are easy to produce and thus comparably cheap products.

The second type of retroreflectors, corner reflectors, is based on an idea of the Swiss astrophysicist Alexander Beck dating back to the year 1887 and makes use of three mutually perpendicular facets (cf. Beck 1887). The reflective functionality can either be achieved by direct reflection on a mirror surface or by total internal reflection (TIR) within a prism. With less light being lost due to scattering, these are the preferred reflectors to be used in metrology systems; see Seward and Cort (1999). In most applications, multiple structures are arranged into an array to generate a retroreflective surface. The shape of the reflecting facets determines the footprint of the retroreflective elements and has a major impact on their optical performance. The two basic shapes are triangular facets, forming a pyramid-shaped retroreflective structure, and square facets forming a cube-shaped element (“corner cubes” or “full-cube retroreflectors”). Pyramidal retroreflectors can easily be generated, for example, as triple mirrors by fly-cutting processes but, according to Eckard (1971), are only capable of retroreflecting 67% of the incident light (Fig. 1). In contrast, cube-shaped retroreflectors may theoretically reflect up to 100% of the incident light.

Full-cube mirror-based retroreflectors, however, are difficult to machine, especially at very small scales. Thus, several types of geometries have been invented in order to bridge the gap between pyramidal and full-cube retroreflectors, providing a performance superior to that of pyramidal retroreflectors. Gubela (1994), for example, invented a machining process which allows for nearly cube-shaped retroreflectors to be machined in a two-step process. Kim and Lee (2007) have shown that a complex prism shape achieves 100% efficiency as a single element and may be

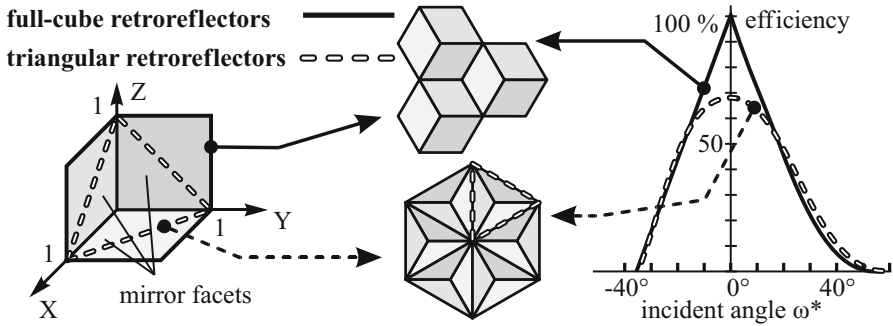


Fig. 1 Theoretical efficiency of triangular and full-cube corner reflectors

closely packed in a hexagonal pattern. However, being a purely theoretical work, they show no feasible process for generating such elements, and the pattern of the elements is irregular which would affect the overall performance.

Many industrial applications require the applied structures to be as small as possible. This allows for the production of sensors with reduced footprint, which, for example, are applied by Gubela for laser sensors (patent of 1997), or for the detection of small objects via light barriers (patent of 2012). Furthermore, small structures may be placed on curved substrates or sheets without affecting their functionality, as, for example, disclosed in the respective patents by Benson et al. (1997) and Huang et al. (1999).

In summary, the machining of miniaturized full-cube retroreflectors is the ultimate aim for generating high-performance retroreflective surfaces.

1.2 Machining Processes for Generating Retroreflective Surfaces

Optical parts with retroreflective structures in the millimeter range are typically generated by pin building or sheet laminating techniques. The optical facets are ground or cut at the top of several millimeter-long hexagonal pins or on thin sheets which are then assembled in the desired pattern. For instance, a patent for such techniques was issued nearly 100 years ago to Stimson (1926). Normally, the model is then replicated several times to obtain a mold for replication by glass pressing or injection molding. As described by Elsner-Dörge et al. (2014), the multiple replication steps make these molds susceptible to wear which requires to overhaul the molds, e.g., by corrective polishing.

For miniaturized retroreflectors, the aforementioned approaches are not feasible as the pins or sheets become too small. Thus, the respective pattern has to be directly machined on a metal substrate. Consequently, the machinable geometry is very much dependent on the kinematics of the applied process, as, for example, described by Brinksmeier et al. (2012b). While arrays of pyramidal retroreflectors in the

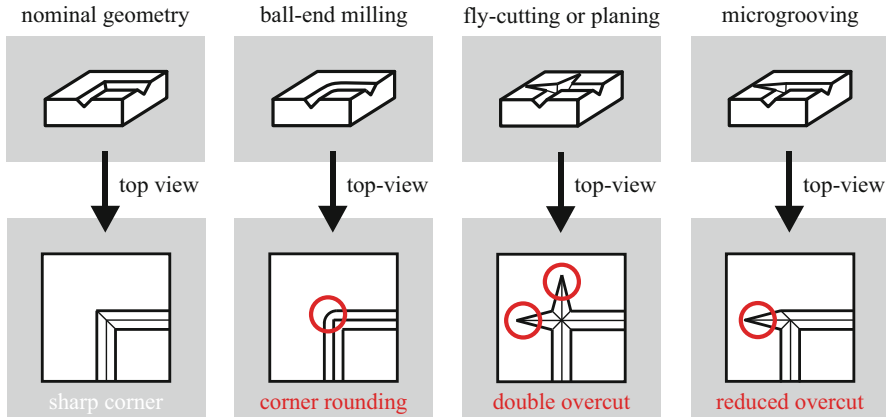


Fig. 2 Capability of different machining processes for generating sharp-edged corners

submillimeter regime can easily be machined by diamond fly-cutting, the discontinuous pattern of full-cube retroreflective arrays is particularly challenging (Fig. 2). Especially processes based on tool (milling) or workpiece (turning) rotation cannot be applied. Also, planing processes, such as described by Brecher et al. (2007), cannot be applied, because the generated structures do not feature defined start and endpoints and thus no appropriate toolpath for discontinuous structures may be generated. The microgrooving process presented by Takeuchi et al. (2003) and later extended by Moriya et al. (2010) is capable of machining V-grooves with geometrically defined endpoints, but not prismatic structures as required for retroreflectors. Recently, Tauhiduzzaman et al. (2017) have presented a novel process for machining triple-mirror retroreflectors at a small scale, which they call “inverted diamond cutting.” However, this process is not capable of generating true full-cube retroreflectors.

1.3 Principles of Diamond Micro Chiseling

Due to the aforementioned limitations of typical ultraprecision machining processes, a new process for generating prismatic microstructures of less than 500 μm wrench size, the so-called Diamond Micro Chiseling (DMC), has been developed at the Laboratory for Precision Machining (LFM). It was first presented by Flucke et al. at the 2006 euspen conference. The general idea of this process is to generate the prismatic structure by plunge-cutting each facet individually using a V-shaped diamond tool, similar to chip carving techniques used in the shaping of wood; see Barton (1984). The transfer of this idea to a usable and efficient machining process has been subject of the dissertations of Flucke (2011) and Schönemann (2014) which are only available in German. There are several publications on this matter in English, for example, by Flucke et al. (2008) in the Production Engineering journal, by Brinksmeier et al. (2012a) in Precision Engineering, and by Brinksmeier and

Schönemann (2014) in the CIRP Annals. Most recently, the process was adopted by Gurganus et al. (2017a, b), as the first international group to implement DMC. All these works, however, only show a fraction of the current state of the process. Thus, this contribution will focus on an extensive presentation of the current state of the art in Diamond Micro Chiseling.

1.3.1 DMC Process Kinematics

For each facet of the microstructure to be machined by DMC, a sequence of cuts is generated; each facet requires at least one cut, but as the structures usually are divided into multiple layers, the number of cuts is equivalent to the number of layers. In each cut, the diamond tool, which has a defined inclination angle to the workpiece surface χ_t , is moved along a toolpath consisting of usually three discrete points (Fig. 3). A fourth point may be added to extend a prismatic cavity to a groove-type structure. The first point is located at the corner of the structure on the workpiece surface. From there, the tool is moved in $[+X+Y-Z]$ direction toward the second point, the apex of the structure. Now the tool may be moved in $[+Y]$ to generate a groove-type structure. The last part of the toolpath always performs the retraction of the tool in $[-X+Y+Z]$ direction to the subsequent corner of the structure at the workpiece surface. The result of this cut is a triangular or trapezoid facet in optical quality that has an inclination angle χ_s equivalent to that of the diamond tool χ_t .

After cutting one facet, the tool is retraced, the workpiece is rotated by a defined angle (e.g., 120° in case of a three-sided cavity), and the tool is repositioned to the endpoint of the previous cut. This is repeated according to the number of facets of the structure, usually until the starting corner point of the cavity is reached again.

Because the cutting forces generally rise with increasing area of the undeformed chip, larger cavities are subdivided into discrete layers with a thickness equivalent to the desired undeformed chip thickness (Fig. 4). Thus, the size of the cavity is subsequently increasing with each cut, until the nominal size is reached.

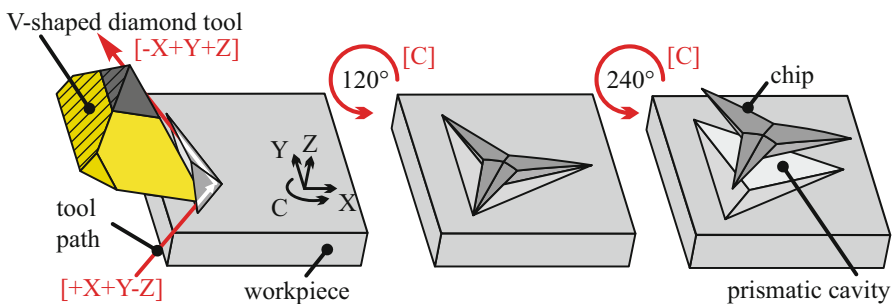


Fig. 3 Process kinematics for Diamond Micro Chiseling

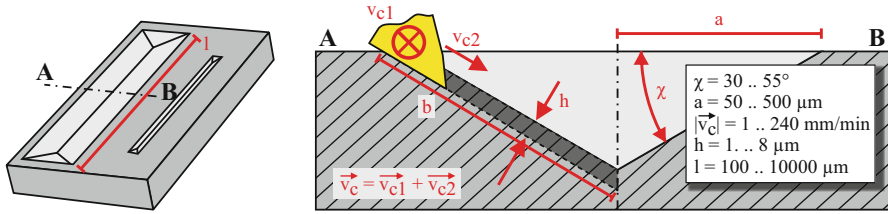


Fig. 4 Separation of structure into discrete layers and typical process parameters for DMC

3. generation DMC tool

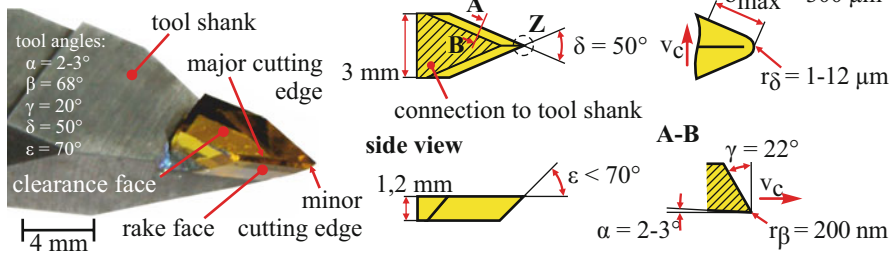


Fig. 5 Three-generation DMC tool and schematics of tool geometry

1.3.2 Diamond Tools for DMC

Diamond Micro Chiseling relies on dedicated monocrystalline diamond tools with a complex V-shaped geometry (Fig. 5). At first sight, these tools look similar to conventional diamond turning or milling tools, but the major cutting direction is orthogonal to the main axis of the tool shank. This means that the rake face of conventional tools becomes the clearance face in DMC and one of the clearance faces becomes the rake face of the tool.

The DMC rake face is oriented in a way that the tool features an intrinsic rake angle γ . Values from $\gamma = 18^\circ$ to 22° have been tested in previous studies, and it has been found that larger rake angles have a positive impact on the chip-forming mechanism, although it makes the tool tip more fragile and thus susceptible to fracture (cf. Brinksmeier et al. 2012a).

In the initial tool design, the clearance angle was set by simply rotating the tool shank around its main axis. This, however, inevitably leads to a change of the rake angle and thereby causes deviating cutting conditions. As a result, subsequent developments included an intrinsic clearance angle of $\alpha = 2-3^\circ$, i.e., a tilt of the rake face along the major cutting edge. This allows for a more precise tool setting via reference planes on the tool shank.

The overall shape of the diamond tool is of importance to the achievable geometric spectrum of the machined microstructures. The opening angle of the clearance face δ limits the minimum opening angle of the facets and thus the number

of facets that may be machined without distortion. A value of $\delta = 50^\circ$ has been proven to be a good compromise between tool stability and geometric versatility, i.e., cavities with up to six sides may be machined securely.

The effective wedge angle ε_{eff} is a result of the intersection between rake and secondary clearance face and thus directly dependent on δ and γ . This angle limits the achievable aspect ratio of the structures and has to be smaller than 180° two times the nominal structure angle χ , or otherwise the secondary cutting edge would destroy the opposite structure faces in subsequent cuts. For the machining of full-cube retroreflectors, the effective wedge angle needs to be $\varepsilon_{\text{eff}} \leq 180^\circ - 2 \cdot 54.7356^\circ = 70.5266^\circ$.

In theory, a sharp tool tip is required for machining truly prismatic cavities. The actual tools, however, feature a rounded nose with a radius $r_\delta = 1\text{--}15\ \mu\text{m}$ to increase their durability. Additionally, the cutting edge may be slightly blunted to a radius of $r_\beta = 200\text{--}300\ \text{nm}$.

1.3.3 Requirements on Machine Tool

DMC may be applied on any ultraprecision machine tool that provides at least linear movements in all orthogonal directions [XYZ] plus a rotary axis for aligning the tool or workpiece in the respective direction of cut. For machining structures on curved surfaces, a fifth axis for in-process setting of the tool inclination angle is necessary. On planar surfaces this axis is not required, although it facilitates the tool setting considerably.

In the past, DMC has been established on two ultraprecision machine tools, the 350FG and the 500FG (Fig. 6), from Moore Nanotechnology, both featuring five

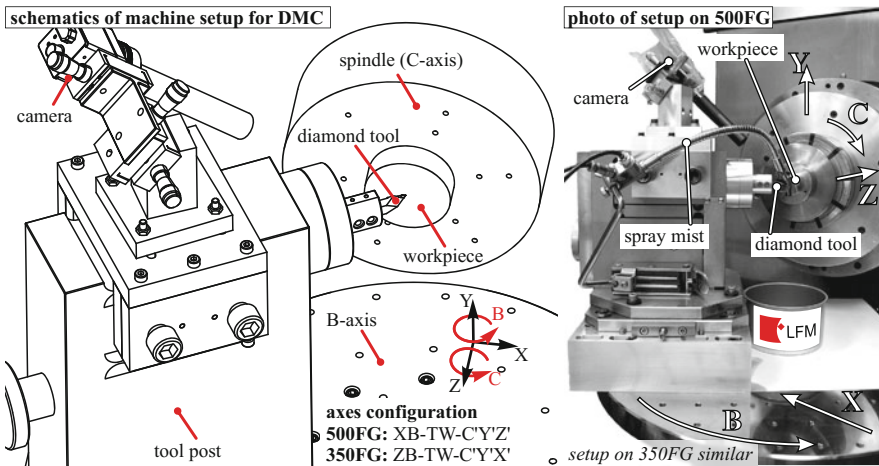


Fig. 6 Schematics of machine setup for DMC and photo of exemplary setup on the Moore Nanotechnology 500FG

numerically controlled axes (three linear and two rotational). Both machines feature three oil hydrostatic linear slides X, Y, and Z, an air bearing spindle C, and a hydrostatic rotary B-table. From the kinematics point of view, the main difference between both machines is the configuration of the axes. The 500FG carries the B-table and the tool post on the X-slide (XB-TCP-C'Y'Z'), whereas the 350FG carries both these items on the Z-slide (ZB-TCP-C'Y'X'). As all basic toolpath calculations remain the same, this difference can be compensated by applying a simple coordinate transformation.

A precise tool setting is a basic prerequisite for Diamond Micro Chiseling. The tool tip typically has to be referenced with a precision of $<1 \mu\text{m}$ in all linear directions. For this, dedicated alignment procedures have been established in which test structures are cut and evaluated by high-resolution microscopic images. Furthermore, the orientation of the diamond tool has to be known in order to guarantee that the set tool inclination angle χ_t corresponds with the nominal structure angle χ_s . Deviations between χ_t and χ_s ultimately lead to a distortion of the machined structure which affects its optical performance. For high-precision retroreflective arrays, the tool inclination angle has to be set with a precision of $\Delta\chi_t < 0.1^\circ$.

1.3.4 Evaluation of Process Performance

1.3.4.1 Structure Quality

The structure quality of DMC machined structures is affected by various influences from the workpiece material, the tool setting, and the process kinematics. Even with extensive care on tool setting, a residual deviation of the tool position cannot be prevented. As long as there is no additional tool setting during the process and no significant wear occurs, this deviation remains constant for the whole cutting procedure.

A tool displacement in X and Y causes the structure edges either to be over- or undercut (Fig. 7, top right). Additionally, due to the nose radius of the tool, the apex of the cavity cannot be cut completely, leading to residual material left at the bottom of the structure (Fig. 7, top center). Furthermore, choosing large values for the undeformed chip thickness (i.e., layer thickness) causes material to be piled up when the tool enters or exits the substrate (Fig. 7, top left). All these deviations ultimately have an impact of the smallest machinable structure size.

In order to assess the typical geometric deviations, microstructures were cut with selected parameters, varying structure size a , and structure angle χ . Then, the form deviation was evaluated on the basis of SEM images, by calculating the ratio between defective and functional structure parts. Because the deviation is set in relation to the nominal structure size, values of $>100\%$ are possible. A representative evaluation of structures cut into N37 is depicted in the bottom part of Fig. 7.

By setting a threshold for the tolerable defects (here, 5%), a minimum structure size can be calculated. The experiments have shown that this minimum structure size is dependent on the structure angle. For 30° structures a size of $a = 15 \mu\text{m}$ was calculated, while at 54° structure angle, the minimum size settles between $a = 50 \mu\text{m}$

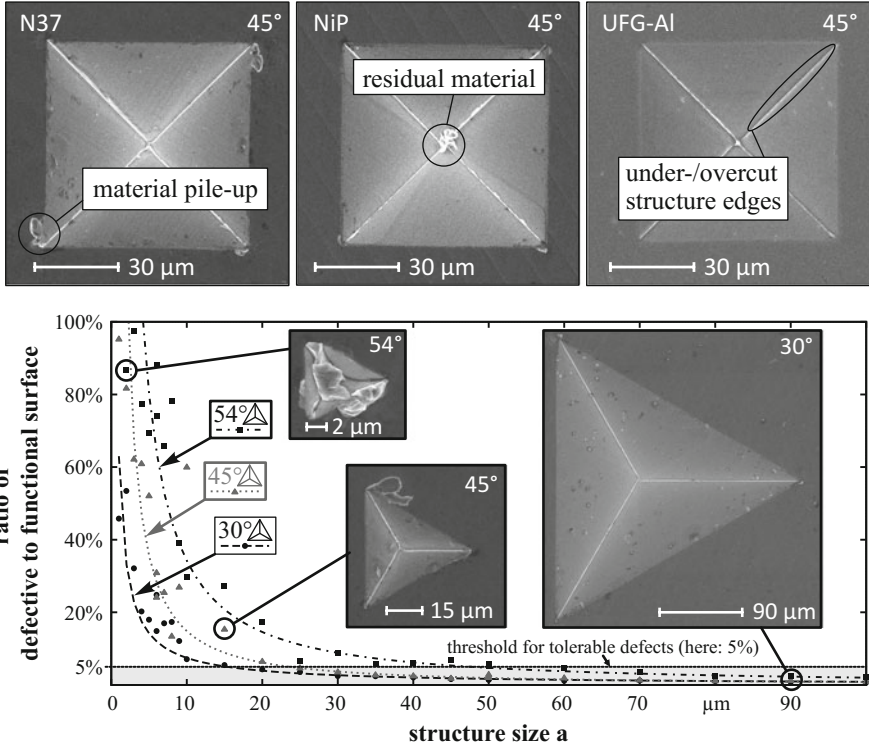


Fig. 7 Typical defects of DMC machined structures (top) and ratio of defective to functional surface for machining N37 with selected structure sizes and angles (bottom)

and 60 μm. The minimum structure size also increases with rising number of structure facets, as more residual material is left at the bottom of the cavity.

Not only the adherence to a nominal structure geometry is important for DMC but also achieving an optical surface finish on the structure facets. In DMC, the cutting edge geometry is directly copied on the facets of the structure, according to the given toolpath. Thus, no feed marks are generated. The main parameters influencing the surface quality are the cutting speed v_c and the undeformed chip thickness h , while the structure size a has no significant impact. Figure 8 shows the measured surface roughness (arithmetic mean height S_a) for continuous and discontinuous 30° structures in N37. On the left side, the undeformed chip thickness was varied between $h = 1 \mu\text{m}$ and $h = 8 \mu\text{m}$ at a constant cutting speed of $v_c = 1 \text{ mm/min}$. The right side shows the variation of the cutting speed ($v_c = 1\text{--}240 \text{ mm/min}$) for a constant undeformed chip thickness ($h = 1 \mu\text{m}$).

While the values obtained for a constant cutting speed follow a similar trend, an increase of cutting speed causes a significant deviation of the measured surface roughness. Further investigations have shown that this is mainly caused by the vibration of the machine tool as a result of the abrupt changes in the direction of

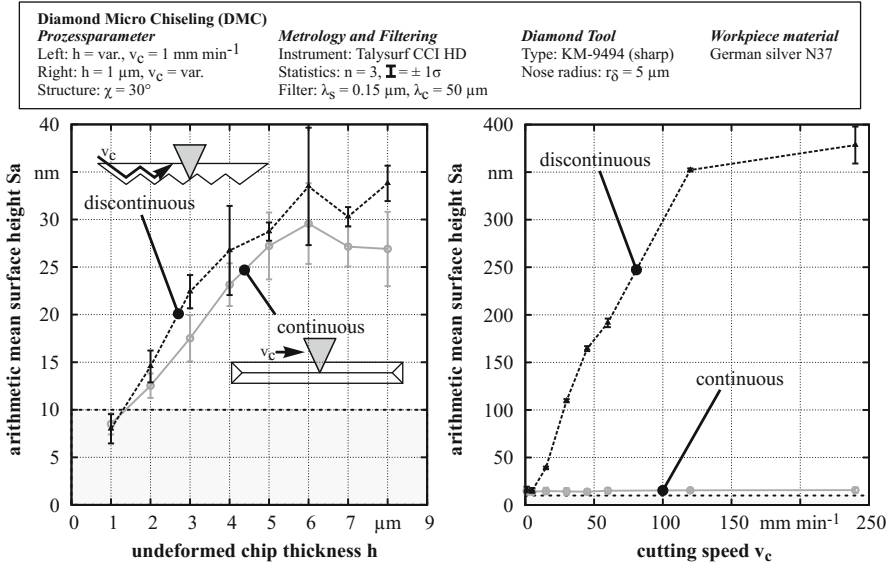


Fig. 8 Surface roughness S_a of DMC machined structure with varied undeformed chip thickness (left) and cutting speed (right)

cut (Fig. 9). In theory, the maximum cutting speed of 240 mm/min is reached after only a few micrometers ($\approx 4 \text{ }\mu\text{m}$) of the cutting path. The real acceleration of the machine tool is, however, much smaller, which means that in a typical cavity with $s \geq 100 \text{ }\mu\text{m}$ path length, a maximum speed of roughly $v_c = 120 \text{ mm/min}$ is achieved. At such “high” cutting speeds, the abrupt change of directions results in a significant jerk, causing the machine tool to oscillate. This vibration is transferred to the machined surface via the tool and is largest at the corner points of the facet.

The temporal development of the vibration can be assessed when machining V-grooves. According to the respective length and cutting speed, a time constant of 100 ms was calculated for the vibrations. For machining discontinuous structures, this time/path is too long for the vibration to settle before reaching the next corner point. Hence, additional vibrations occur and interfere with the previous ones. Examples for this are shown in the right part of Fig. 9.

Consequently, without changing the machines’ control system, the only measure to avoid these vibrations is limiting the cutting speed and introducing a settling time (dwell time t_{dw}) after each movement. Initial estimations for the dwell time were done according to in-process video recordings ($t_{dw} = 2300 \text{ ms}$). After further analysis of the process, this could be reduced to $t_{dw} = 1000 \text{ ms}$.

1.3.4.2 Process Forces

Knowledge of the acting process forces is important in Diamond Micro Chiseling, because the filigree diamond tools are prone to tool chipping when exposed to too high mechanical loads. Thus, the cutting forces limit the undeformed chip thickness

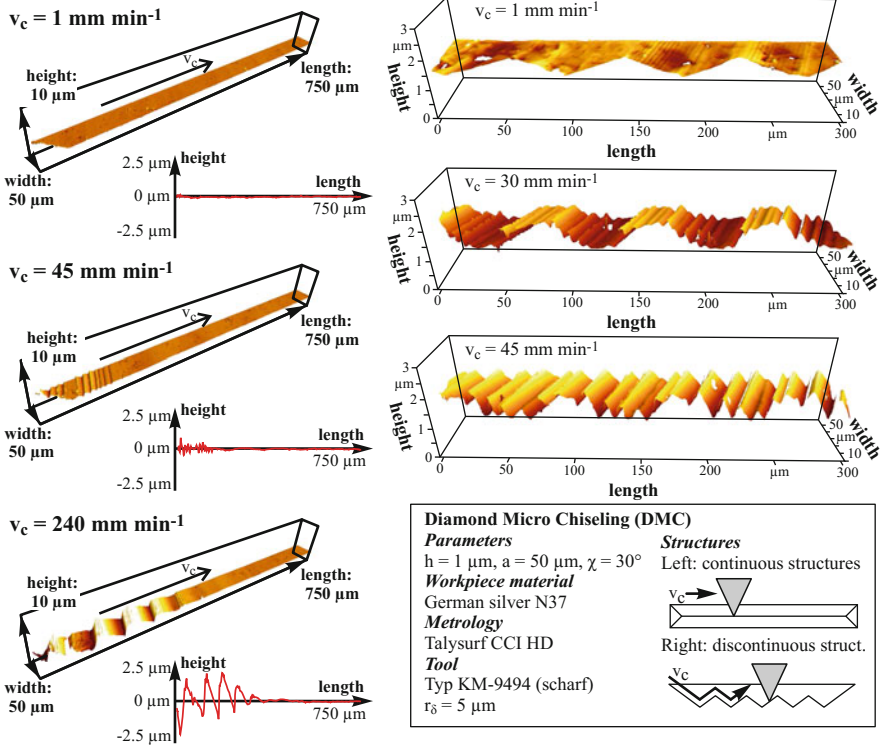


Fig. 9 Effect of machine vibration on surface generation at higher cutting speeds

and also the maximum structure size. In DMC the three force components are the cutting force opposed to the direction of cut ($F_c = F_y$), the thrust force along the shank axis (F_z), and the second thrust force orthogonal to the facet plane (F_x). The latter two are usually combined into a common force value $F_p = \sqrt{F_x^2 + F_z^2}$.

Depending on the type of structure (continuous, discontinuous), different force progressions are observed (Fig. 10). In both cases, the cutting and thrust forces increase linearly, while the tool descends into the workpiece. For continuous structures, cutting the linear part of the grooves causes a stepwise increase of the forces. While the thrust force returns to its previous value after a short time, the cutting force remains at a higher level throughout the cut. For discontinuous structures, the retraction of the tool causes a reduction of both force components, the cutting force linearly to a lower level and the thrust force abruptly down to slightly above 0 N.

Therefore, the following charts only concentrate on the forces obtained for V-grooves, as they are expected to be higher and are easier to evaluate.

For standard DMC parameters ($h_f = 4 \mu\text{m}$; $v_c = 45 \text{ mm/min}$; Iso-paraffin spray mist) the measured forces show a mainly linear trend (Fig. 11). Increasing the

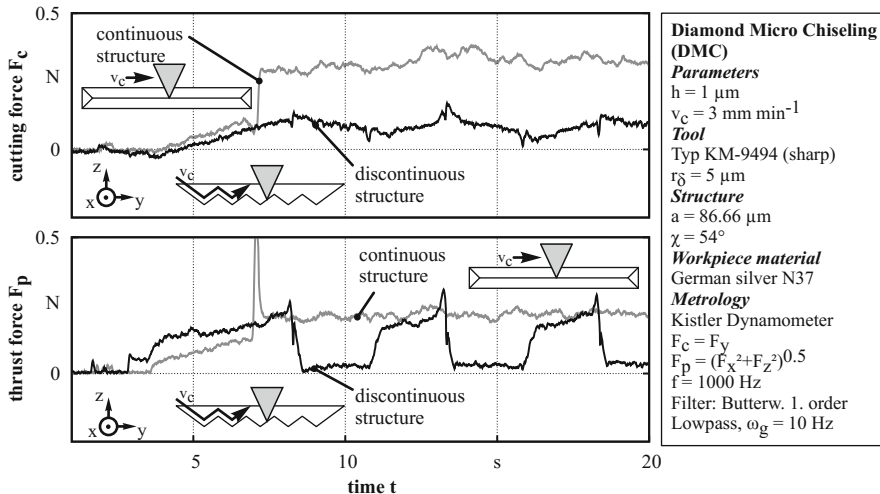


Fig. 10 Exemplary force progression for cutting cavities and V-grooves by DMC

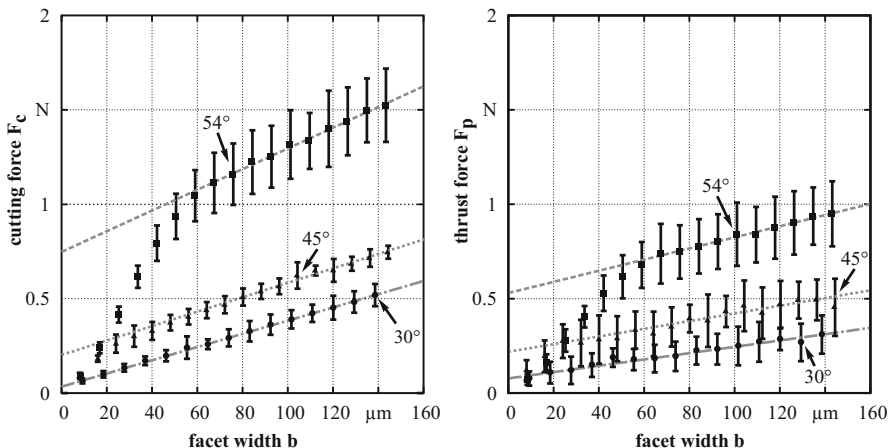
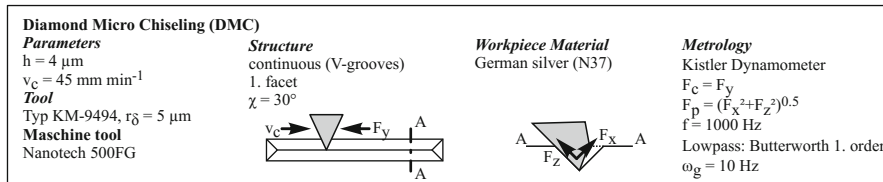


Fig. 11 Cutting and thrust force for generating V-grooves of selected structure angles in N37 by DMC

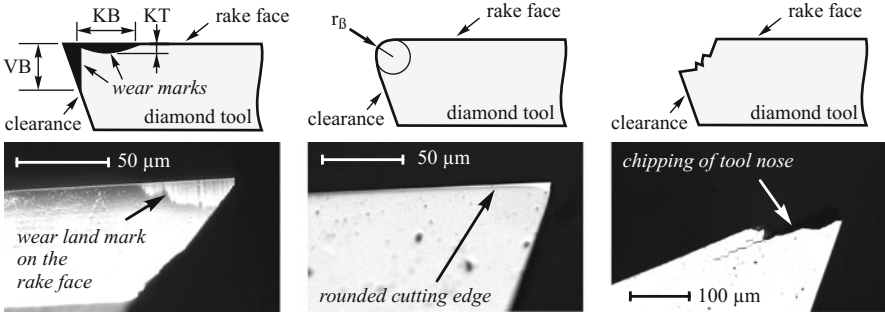


Fig. 12 Common wear phenomena of diamond tools used for DMC

structure angle to steeper values also increases the maximum cutting and thrust forces. For the steepest structure angle of 54° , a significant deviation from this trend is observed at small facet widths. This is explained by the difference in chip cross section. At steep angles, the minor cutting edge also removes material of the opposite structure half and thus causes a deviation from the linear force progression. With increasing depth, this proportion decreases, and from $b = 60 \mu\text{m}$ onward, the forces follow a linear trend.

1.3.4.3 Tool Wear

Tool wear becomes important when machining a large number of structures, such as retroreflective arrays, and manifests as wear land, rounding of the cutting edge or simply by chipping of the tool nose due to brittle fracture (Fig. 12).

To assess the resulting wear in DMC, $l = 1\text{-mm}$ -long V-grooves with a half-width of $a = 15 \mu\text{m}$ and $\chi = 30^\circ$ were cut in German silver N37 specimens. In different experiments, these grooves were cut with $h = 7.5 \mu\text{m}$ (i.e., in one layer) and with $h = 3.75 \mu\text{m}$ (two layers) to simulate different cutting conditions. The total length of cut was $s = 43.5 \text{ m}$ for both parameters, respectively. Cutting forces were recorded using a Kistler “MiniDyn 9256C” dynamometer, and the surface roughness was measured at different intervals of s . Additionally, the diamond tool geometry was measured before and after the experiments using a high-resolution video microscope (status of rake and clearance face) as well as an atomic force microscope (cutting edge radius).

Figure 13 shows the measured surface quality and process forces for an undeformed chip thickness of $h = 3.75 \mu\text{m}$. The roughness R_a shows an increase from $R_a = 7.7 \text{ nm}$ at the beginning of the cutting procedure to $R_a = 9.6 \text{ nm}$ at the end, which is larger than the standard uncertainty $\sigma = 1.4 \text{ nm}$ of the measurements and therefore significant. The waviness shows no clearly distinguishable trend. Nonetheless, all measurements remain $R_a < 10 \text{ nm}$, i.e., an optical surface finish was achieved throughout. The process forces follow the trend of the surface roughness and increase from $F_c = 0.09 \text{ N}$ to 0.1 N (+10%) and from $F_p = 0.05 \text{ N}$ to 0.06 N (+20%).

Diamond Micro Chiseling (DMC)			
Parameters	Metrology (R_a, W_a)	Metrology (F_c, F_p)	Workpiece
$h = 3.75 \mu\text{m}$	Tencor P15 Profilometer	Kistler Dynamometer	German silver (N37)
$v_c = 15 \text{ mm min}^{-1}$	$n = 10$, $\mathbf{I} = \pm 1\sigma$	$f = 1000 \text{ Hz}$, $\omega_g = 10 \text{ Hz}$	Structure
Tool	Cut-off: $\lambda_c = 80 \mu\text{m}$	Filter: Butterworth LP	V-groove, $\chi = 30^\circ$
$r_\delta = 5 \mu\text{m}$		1. ord., $n = 10$, $\mathbf{I} = \pm 1\sigma$	1. facet

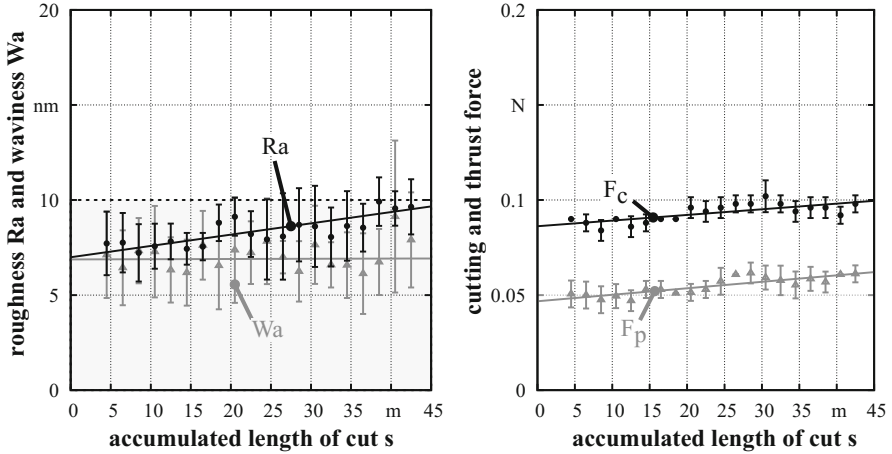


Fig. 13 Development of surface quality (left) and process force (right) according to the accumulated length of cut for German silver N37

For determining the wear of the diamond tool, the cutting edge radius was measured at discrete locations, directly at the tool tip and with a distance of $7.5 \mu\text{m}$, $15 \mu\text{m}$, and $30 \mu\text{m}$ using an AFM. Figure 14 shows the mean of five measurements for the experiments with $h = 3.75 \mu\text{m}$ and $h = 7.5 \mu\text{m}$. At the first three locations, a moderate increase from $r_\beta \approx 50 \text{ nm}$ to $r_\beta \approx 70 \text{ nm}$ was determined. The radius at the fourth location remained unchanged, which was expected, because at this structure size, the width of the facet $b = 17.6 \mu\text{m}$ is smaller than the distance to the tool tip, i.e., this part of the tool was not engaged in cutting.

A possible explanation for the increasing surface roughness and process forces can be found in the evaluation of the cutting edge radius. As the cutting edge gets blunter, the primary deformation zone in which the shearing of the chip takes place is enlarged. Thus, a bigger force is required to induce the required load into workpiece. In addition, the chip-forming mechanism changes and leads to a rougher surface.

The machining of German silver N37 shows no significant wear when generating large structure arrays. After cutting V-grooves with a path length of $l_c = 40 \text{ m}$, no visible tool wear could be observed (Fig. 15, bottom center). By using atomic force microscopy, an increase in cutting edge radius of $10\text{--}25 \text{ nm}$ was measured, but no deterioration of the surface roughness could be observed. Another experiment only showed noticeable tool wear after completely machining two retroreflective arrays with $A = 7.5 \times 7.5 \text{ mm}^2$ at $CC_R = 150 \mu\text{m}$ structure size and $A = 10 \times 10 \text{ mm}^2$ at

Diamond Micro Chiseling (DMC)		Tool	Metrology	Structure	Workpiece
<i>Process parameters</i>	<i>h</i> = varied	Type KM-9494	AFM: Nanoscope III	V-groove, $\chi = 30^\circ$	German silver (N37)
$v_c = 15 \text{ mm min}^{-1}$		$r_\delta = 5 \text{ }\mu\text{m}$	$n = 5, \mathbf{I} = \pm 1\sigma$	1. facet	

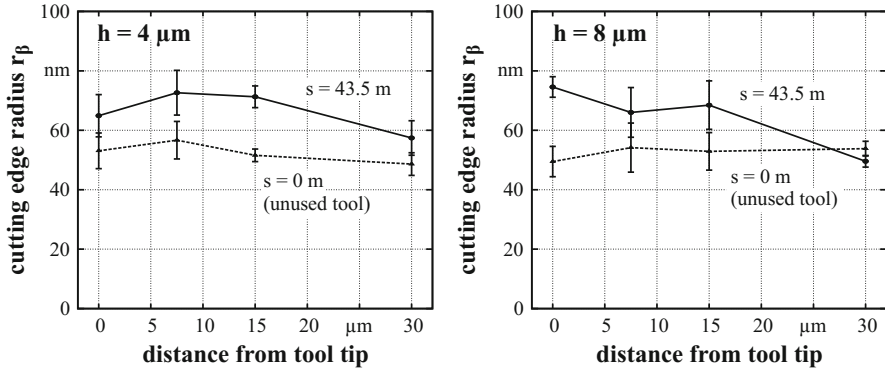


Fig. 14 Cutting edge radius before and after machining V-grooves in German silver N37

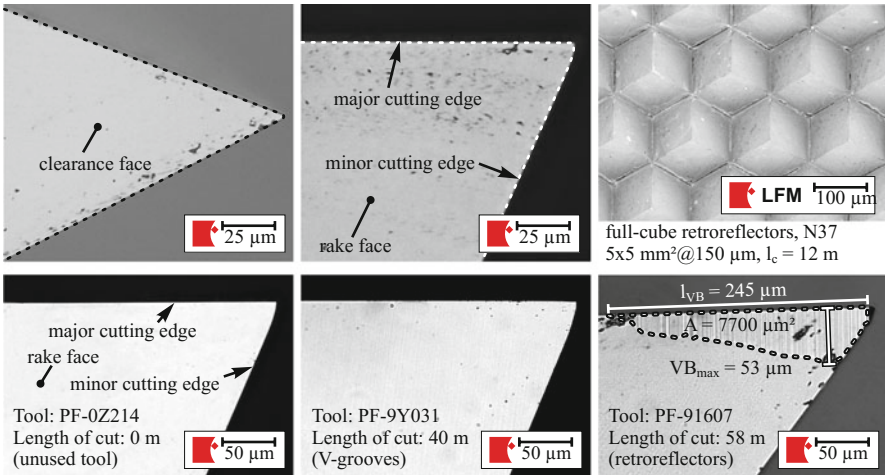


Fig. 15 Rake and clearance face of a DMC tool as well as generated structure with a cutting distance of 12 m in German silver N37 (top) and rake face wear of unused tool, after cutting $l_c = 40 \text{ m}$ of V-grooves and after cutting $l_c = 58 \text{ m}$ of retroreflectors with visible wear mark (bottom)

$CC_R = 200 \text{ }\mu\text{m}$, i.e., after a length of cut of 58 m. Here, a distinct wear mark is visible, as shown on the right in Fig. 15. The maximum wear land with is $VB = 53 \text{ }\mu\text{m}$. With increasing distance to the tool tip, up to $l_{VB} \approx 245 \text{ }\mu\text{m}$, this width decreases. This can be explained by the cutting kinematics which causes the tool tip to be engaged in all layers of the structure, while the rest of the tool only gradually comes into contact with the workpiece.

1.4 Diamond Micro Chiseling of Miniaturized Retroreflectors

1.4.1 General Principle

The machining of retroreflective arrays by DMC is, in principle, simply the manufacture of overlapping three-sided cavities in a specific hexagonal pattern (Fig. 16).

The spacing of the columns (dy) and rows (dx) of this matrix can be calculated according to the following equations, depending on the characteristic structure size of the cavities a (see Eqs. 1 and 2). For obtaining a hexagonal pattern, every second column of the matrix has to be shifted by $dy/2$ in positive Y-direction.

$$dy = \sqrt{3} \cdot a \quad (1)$$

$$dx = 3/2 \cdot a \quad (2)$$

The structure size of the retroreflectors is usually given as the circumcircle, i.e., wrench size, of the resulting triple-mirror CC_R . The necessary characteristic dimension of the underlying three-sided cavities is calculated according to Eq. 3.

$$CC_R = a \cdot \sqrt{3} \quad (3)$$

From the spacing of the matrix and the characteristic structure size, the number of individual elements n_{total} for structuring a specific area ($A = x_{\text{target}}y_{\text{target}}$) may be calculated:

$$n_{\text{total}} = n_x \cdot n_y \quad (4)$$

$$n_x = \left[\left(2/3 \cdot \frac{x_{\text{target}}}{a} \right) + 1 \right] \quad (5)$$

$$n_y = \left[\frac{y_{\text{target}}}{a \cdot \sqrt{3}} + 1/2 \right] \quad (6)$$

The structured area is scaling linearly in both directions, with the number of columns n_x increasing faster than the number of rows n_y .

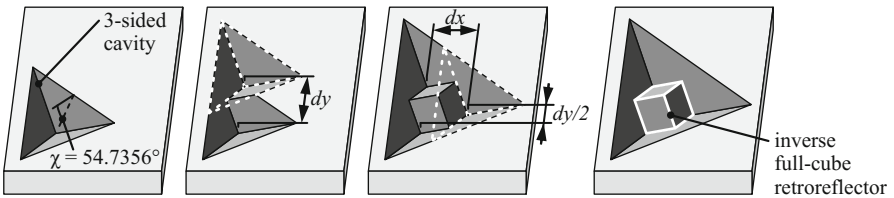


Fig. 16 Generation of full-cube retroreflectors by DMC

Example: For machining a retroreflective array on an area of $A = 10 \times 10 \text{ mm}^2$, with a circumcircle of the retroreflective elements of $CC_R = 150 \text{ }\mu\text{m}$, $78 \times 68 = 5304$ three-sided cavities have to be machined. Considering that each structure is machined from three different orientations and divided into discrete layers of constant chip thickness (e.g., $h_{coarse} = 4 \text{ }\mu\text{m}$, $h_{fine} = 1 \text{ }\mu\text{m}$, i.e., 19 layers), this means that a total of $19 \cdot 3 \cdot 78 \cdot 68 = 302,328$ individual cuts have to be made. Additionally, each cut requires a dedicated positioning of the tool and a rotary alignment of the workpiece in cutting direction.

1.4.2 Assessment of Required Machining Time

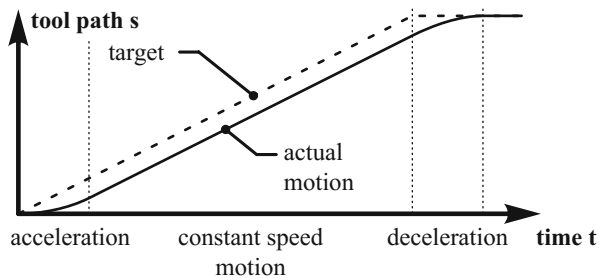
The previous example shows that a manual assessment of the required machining time is not practical. The high number of cuts requires an automated evaluation of the NC-scripts to generate a reliable estimation. The easiest way to calculate the cutting time is by implementing a respective function into the CAD/CAM software for DMC which records the length of a cut $|\mathbf{l}_s|$ and calculates the required time according to the set value of the cutting velocity v_c :

$$t = \sum_{s=1}^n (|\mathbf{l}_s| \cdot v_c^{-1}) \quad (7)$$

For longer cuts in which a constant chip thickness is held (e.g., V-grooves), this method has an uncertainty of about 10%, according to Flucke (2011). However, for a multitude of short cuts (e.g., for retroreflective arrays), this uncertainty increases to $>30\%$, because the acceleration or deceleration of the axes becomes more and more relevant. Thus, the actual machining time is longer than the predicted one. To compensate for this issue, a novel approach for calculating the machining time was implemented, which considers both, the proportion $|\mathbf{l}_a|$ of the cut with acceleration until $v_{max} = v_c$ and the proportion $|\mathbf{l}_s|$ of constant speed; see Fig. 17 and Eq. 8).

$$t = \sum_{s=1}^n \left(\underbrace{(|\mathbf{l}_s| - 2 \cdot |\mathbf{l}_a|) \cdot v_c^{-1}}_{\text{uniformspeed}} + \underbrace{2 \cdot v_c \cdot a^{-1}}_{\text{acceleratedmotion}} \right) \quad (8)$$

Fig. 17 Cut with proportions of accelerated motion and constant speed



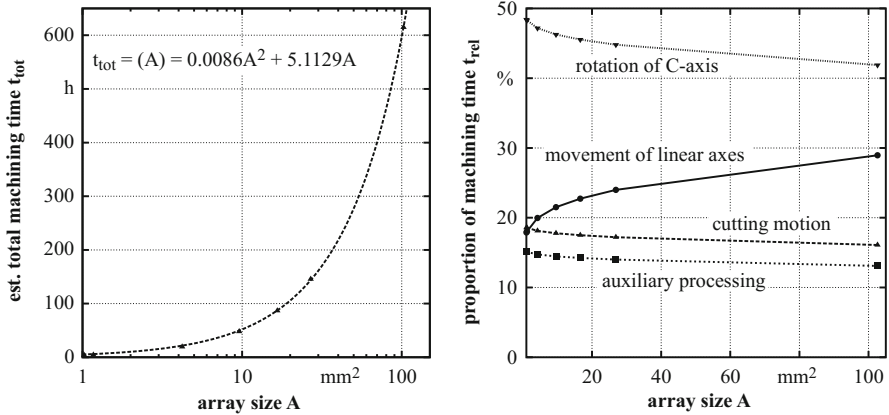


Fig. 18 Assessment of total machining time (left) and its components (right) against array dimension for machining retroreflective arrays with constant structure size

With an experimentally determined value for the acceleration, this method results in a more precise estimation of the machining time, especially for discontinuous patterns, such as retroreflective arrays. As there are still some influencing factors, e. g., varying acceleration values for different axes, the time calculated by this method still deviates from the actual machining time, but the uncertainty was reduced to $<6\%$.

In addition to the more precise consideration of the cutting time, the overall calculation for the machining time was implemented in a way that different aspects of the machining procedure could be separated, i.e., positioning time of the linear axes, time for rotating the workpiece, and auxiliary processing time (e.g., dwell time for reducing parasitic vibrations or a spray mist burst to clean the tool).

1.4.2.1 Influence of Structure and Array Size

This section will show estimations of the total machining time for retroreflective arrays with constant structure size and varied array dimensions as well as with varied structure size and constant array dimensions. The process parameters were set to identical values for all calculations:

- On the first $n - 2$ structure layers
 - A constant undeformed chip thickness $h_{coarse} = 4 \mu\text{m}$
 - A cutting velocity $v_{c,fast} = 45 \text{ mm/min}$
- On the final two structure layers
 - A constant undeformed chip thickness $h_{fine} = 1 \mu\text{m}$
 - A cutting velocity $v_{c,slow} = 3 \text{ mm/min}$
- For all layers
 - A constant feed velocity $v_{f,l} = 400 \text{ mm/min}$ for positioning the tool
 - A rotation speed of $v_{f,r} = 3000 \text{ }^\circ \text{ min}^{-1}$ for aligning the workpiece

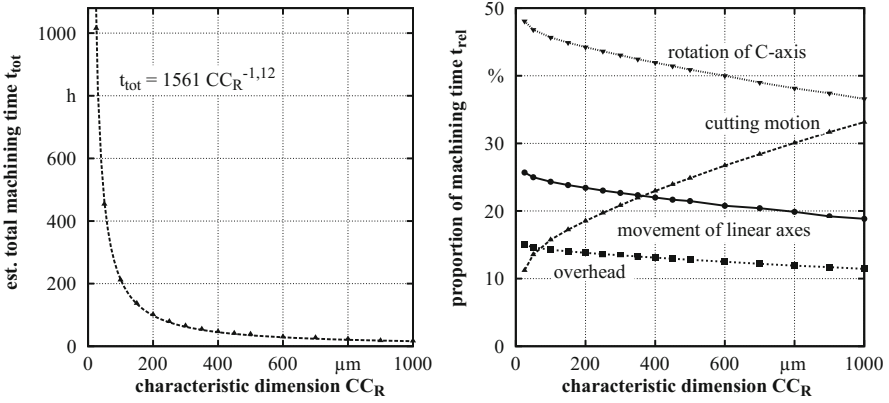


Fig. 19 Assessment of total machining time (left) and its components (right) against characteristic structure dimension for machining retroreflective arrays of constant dimensions

No optimization was applied to the NC-program, i.e., all cavities were machined individually and only after finishing a complete cavity the procedure was advanced to the next cavity of the array. For minimizing positioning movements, the array has been placed at the center of the machine coordinate system.

Figure 18 shows the total machining time for retroreflective arrays with constant structure size $CC_R = 150 \mu\text{m}$ and varied array dimensions.

The estimated total machining time and the array size are linked by a quadratic relation. This means that small arrays may be produced faster ($1 \text{ h}/\text{mm}^2$) than large arrays (up to $6 \text{ h}/\text{mm}^2$). Nevertheless, the machining time even for small array sizes of 20 mm^2 exceed a duration of 100 h. Hence, such arrays can only be generated economically by optimizing the process kinematics.

From the proportions of the contributing factors (Fig. 18, right), it can be seen that between 40% and 50% of the estimated machining time is attributed to the rotation of the C-axis and another 20% to 30% is required for (re-)positioning the tool. Furthermore, a significant portion of the machining time ($\approx 15\%$) is attributed to auxiliary processing time. In contrast, the cutting itself only consumes 15–20% of the total time.

Figure 19 shows the estimated machining time for a constant array size of $A = 5 \times 5 \text{ mm}^2$ and varied characteristic dimension between $CC_R = 25 \mu\text{m}$ and $1000 \mu\text{m}$.

This estimation shows, as expected, a relation between characteristic structure size and machining time according to a power function, because the number of structures scales linearly for both dimensions. For increased structure size, the actual cutting becomes predominant.

1.4.2.2 Influence of Undeformed Chip Thickness and Cutting Velocity

In addition to the variation of structure and array size, the influence of the two important process parameters, undeformed chip thickness h and cutting velocity v_c , was evaluated (Fig. 20).

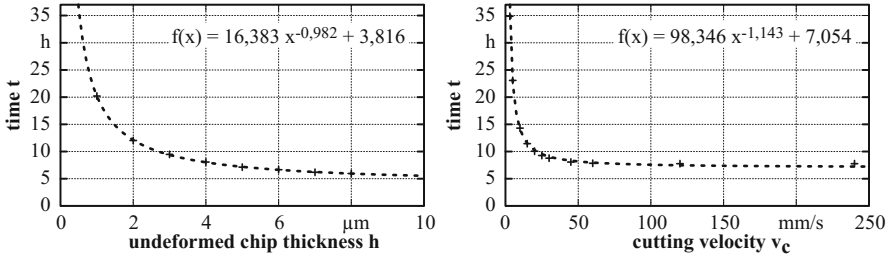


Fig. 20 Estimated machining time of a $3 \times 3 \text{ mm}^2$ retroreflective array with $150 \text{ }\mu\text{m}$ structure size for varied undeformed chip thickness h and cutting velocity v_c

This estimation shows that the undeformed chip thickness and the cutting speed are related to the machining time with a power function. Hence, increasing these parameters would lead to a significant reduction of machining time. However, the structure quality deteriorates, for instance, due to machine vibrations, pile-up material, or edge rounding effects (interpolation of the machine motion by the CNC).

Therefore, an increase of h and v_c is only applicable for pre-machining the $n - x$ initial layers of the structure, whereas the final layer(s) need to be machined at low speed and small undeformed chip thickness to maintain a high structure quality. Furthermore, the fragility of diamond tools sets a limit to the increase of h , which could be counteracted by using different tools for pre-machining (with a large nose radius) and finish machining (small tool nose for improve structure accuracy).

1.4.3 Optimization Strategies

In the previous sections, it was shown that the tool life for machining German silver N37 is sufficient for large-scale retroreflective arrays. The required machining time, however, acts as a limiting factor, as even small areas of $A \geq 10 \times 10 \text{ mm}^2$ require more than 100 h of machining time. Hence, this section concentrates on new strategies to reduce the machining time by optimizing the underlying process kinematics.

As even with an optimized kinematic approach, long machining times are to be expected, and additional measures had to be found to detect and compensate for tool wear. Two approaches will be presented here, a procedure for in situ tool change and a new tool geometry dedicated to the machining of retroreflectors.

1.4.3.1 Improved Cutting Kinematics

A reduction of machining time for DMC can be achieved by different approaches, such as increasing the cutting speed or the undeformed chip thickness. The estimations in the previous section, however, have shown that a lot of time may be saved by optimizing the process kinematics first. All following examples for a reduction of machining time have been estimated with the aforementioned approach for a retroreflective array of $A = 5 \times 5 \text{ mm}^2$ and $CC_R = 150 \text{ }\mu\text{m}$ structure size. The process

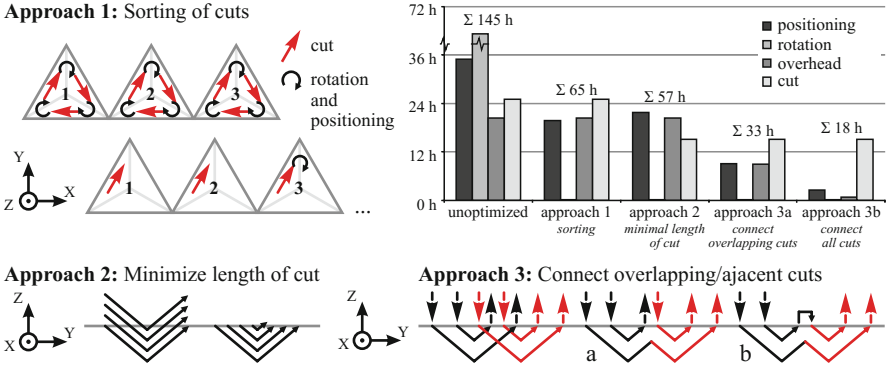


Fig. 21 Approaches for optimized DMC-kinematics and impact on resulting machining time for a $5 \times 5 \text{ mm}^2$ retroreflective array with $150 \mu\text{m}$ structure size

parameters were set to fixed values of $h_g = 4 \mu\text{m}$, $v_{c,fast} = 60 \text{ mm/min}$ for the first $n-2$ layers, $h_f = 1 \mu\text{m}$ and $v_{c,slow} = 3 \text{ mm/min}$ for the last two layers, and a dwell time of $t_{dw} = 1000 \text{ ms}$ for reducing parasitic vibrations of the machine tool. For the unoptimized kinematics, the total machining time with these values sums up to $t_{tot} = 145 \text{ h}$.

As a first approach, all cuts should be arranged in a way that equally oriented cuts are conducted in a row, such as proposed by Flucke (2011). In this case, unnecessary rotation of the workpiece and repositioning of the tool are avoided (approach 1 in Fig. 21). In the CAD/CAM software, this is done by sorting all cuts in ascending order according to their layer, orientation, and XY-position in the machine coordinate system. This alone allows for a reduction of machining time up to 55% to $t_{tot} = 65 \text{ h}$ for the considered array.

The largest proportion of the remaining machining time is attributed to the cutting motion. This may be directly diminished by increasing the cutting speed; however, this measure also has an influence on the achievable surface quality. Thus, a purely geometric optimization will be introduced first: as full-cube retroreflectors are an overlay of multiple triangular cavities, which are gradually “sunk” layer by layer into the substrate, a multitude of “air cuts” occur. During these, the tool moves above the workpiece surface or in regions in which material has already been removed by a previous cut. To avoid these air cuts, now an optimally sized cavity is utilized for each layer (approach 2). Furthermore, all intersections between overlapping cavities are calculated in advance and used as start end endpoints of the respective cuts to minimize the cutting motion to a geometric optimum (approach 3a). Without an adaption the complete cutting procedure, this change has little effect, because the tool is still moved out of contact with the workpiece, repositioned, cleaned by a spray mist burst, and engaged once again. This results in a lot of time wasted in auxiliary processing (settling time, spray mist burst).

By combining those cuts without disengaging the tool (“approach 3b”), a significant amount of machining time is saved. Several experiments have also proven that

a spray mist burst after each cut is not necessary to ensure an undistorted cut. It is sufficient to do this after reaching the edges of the whole array. In general, this optimization is not limited to overlapping cuts, but may be applied to all cuts with a similar orientation. With all optimizations applied, the estimated machining time of the test array could be reduced to $t_{\text{tot}} \approx 18$ h.

1.4.3.2 In Situ Tool Change

DMC could be significantly sped up by using two different tools with dedicated parameters, e.g., a large nose radius $r_e = 12 \mu\text{m}$ for rough and a small nose tool $r_e = 1 \mu\text{m}$ for finish cutting. Nevertheless, the application of more than one tool requires an in situ tool change which exhibits a huge challenge, as the second tool needs to be exactly aligned to the position of the first one. With the DMC tool alignment procedure presented in subsection “Requirements on Machine Tool,” the tool is always aligned to the C-axis of the machine tool, with a precision of $<1 \mu\text{m}$ in all linear directions, and is thus independent of the previously machined structures. Therefore, the cutting may theoretically be continued, if a second tool is aligned in the same way. In this case, it has to be guaranteed that the inclination angle of both tools χ_t does not cause a deviation larger than the undeformed chip thickness (cf. Fig. 22). The maximum tolerable angular deviation may be estimated according to Eq. 9.

$$\Delta\alpha_\chi = \frac{b_n}{\sin\left(180^\circ - \max(\chi_n, \chi_t)\right)} \cdot \sin(|\chi_n - \chi_t|) \quad (9)$$

Choosing typical values for structure size and undeformed chip thickness for the last layer, e.g., $CC_R = 150 \mu\text{m}$, $h_f = 1 \mu\text{m}$, the maximum tolerable angular deviation is calculated to approximately $\Delta\chi_t = 0.15^\circ$. Because this value is larger than the typical angular precision of the alignment procedures, this poses no problem for machining the respective retroreflective array. In all cases, it has to be ensured that the workpiece is not dismounted in between two cutting passes. As there is no workpiece alignment procedure, apart from a manual centering of the workpiece with an accuracy of a few micrometers, this would lead to a deviation in the position of the array which cannot be compensated by cutting the last one to

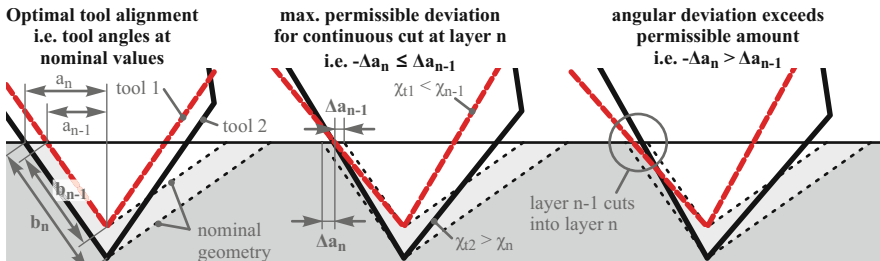


Fig. 22 Result of angular deviation on structure geometry

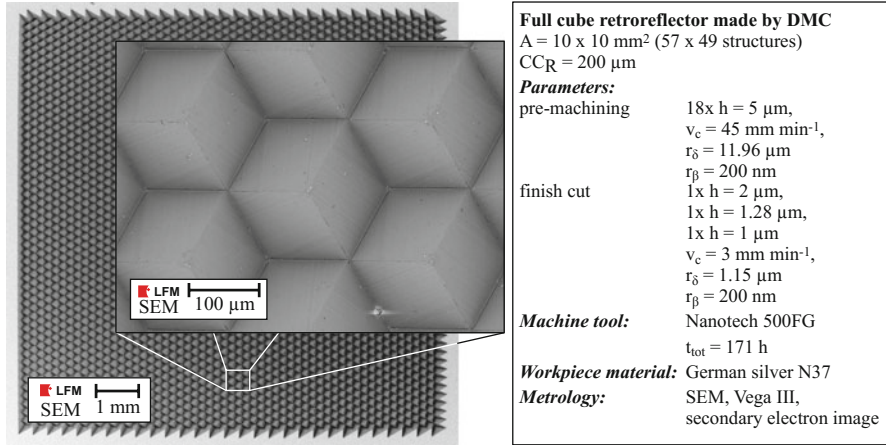


Fig. 23 DMC retroreflector array machined with in situ tool change

two layers with a layer thickness of $h_f = 1 \mu\text{m}$. An example of an array machined with two tools is shown in Fig. 23.

1.4.3.3 Novel Tool Geometries for Retroreflectors

For retroreflective arrays in particular, a completely new tool design has the potential to help in reducing the overall machining time. By aligning the rake and clearance face in a dedicated way, the 90° angle of the retroreflector can be made intrinsic to the tool. As long as this angle features a sufficient precision, three-sided structures may be cut in only two passes with such tools. In the initial cut, the first and second facets are directly generated in optical quality by the major and minor cutting edge, respectively. Then, the third facet is generated in the subsequent and final cut.

To test the applicability of this method, a new tool design was devised featuring a sharp secondary cutting edge and an intrinsic secondary clearance angle of $\alpha_2 = 3^\circ$ (Fig. 24). In addition, the resistance of the tool to wear or chipping was increased by using an asymmetrically shaped diamond ($\delta_1 = 25^\circ$, $\delta_2 = 42^\circ \rightarrow \delta = \delta_1 + \delta_2 = 67^\circ$). The rake angle was decreased to $\gamma = 16^\circ$, which is a bit lower than for universally applicable DMC tools.

The orientation of rake face, major and minor clearance face, and structure angle of ψ is made intrinsic to the tool. At $\psi = 90^\circ$, retroreflectors can be machined in two passes, and if this angle is smaller than 90° , the machining of retroreflective structures may be done in three passes, as usual. However, at $\psi > 90^\circ$, the tools are not applicable to retroreflective arrays, because too much material is removed from the cavities.

The manufacture of these tools within the required precision is extremely challenging. Of three tools ordered, one featured an angle $>90^\circ$ and was therefore unusable for machining retroreflectors. The other two featured an angle $<90^\circ$ and therefore could only be utilized for generating cavities in three cuts. Nevertheless, it was shown that the surface and structure quality generated by these tools is

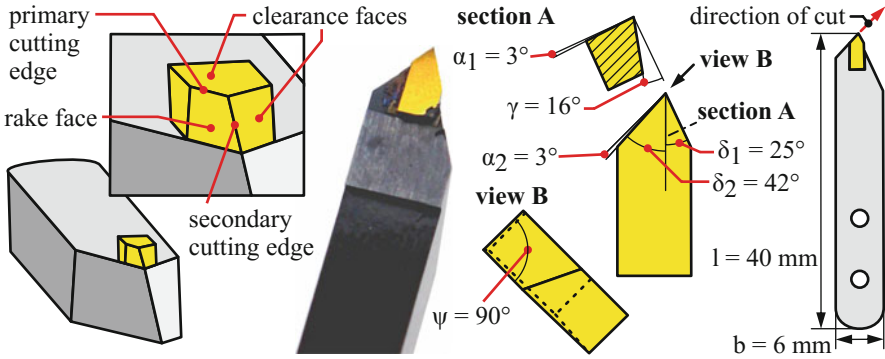


Fig. 24 Geometry of an asymmetric diamond tool for Diamond Micro Chiseling (fourth-generation tool)

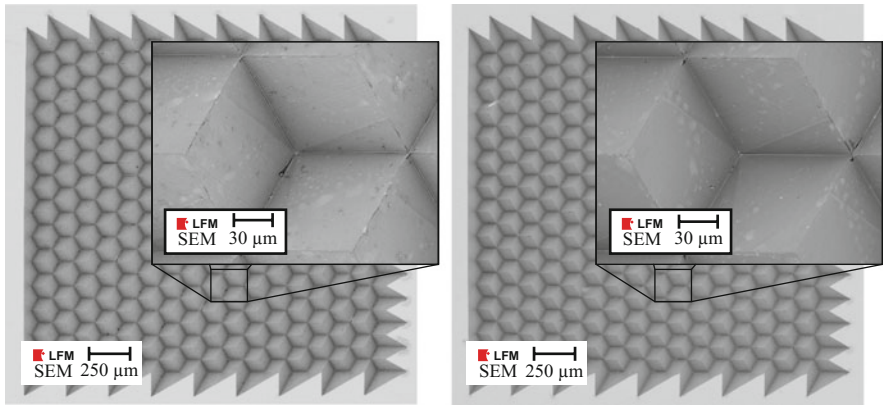


Fig. 25 SEM images of retroreflectors made with standard DMC tools (left) and asymmetric DMC tools with intrinsic 90° angle (right)

equivalent to standard DMC tools (Fig. 25). The quality of the concave structure edges was even slightly increased, because of the sharp tool nose. Thus, the tools could be aligned with greater precision and especially without the need for software-based radius compensation.

1.5 DMC on Curved Surfaces

For specific applications, the machining of retroreflective arrays on curved or freeform surfaces is necessary. The applicability of DMC for such purposes is closely connected to the available machine axes and the tool design. Whether a structure is or is not machinable with a given setup can be determined by applying a

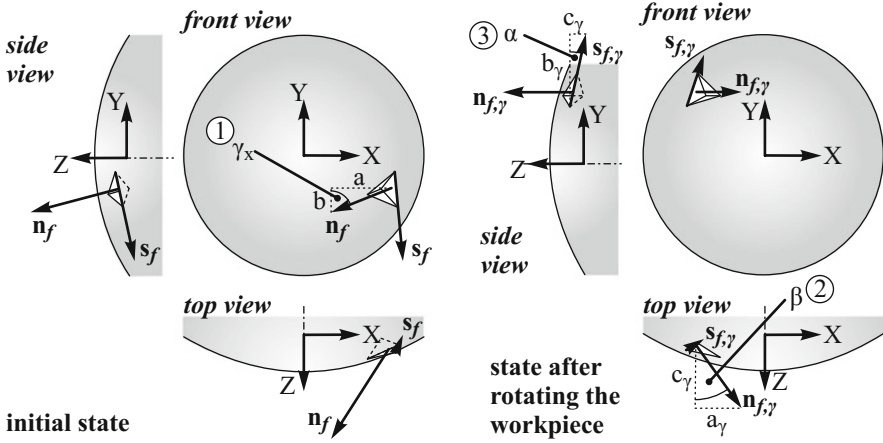


Fig. 26 Alignment of tool and structure for DMC on curved surfaces

series of theoretical calculations. The basic prerequisite for a structure to be machined is that the tool must be aligned to each facet of the structure by using the given rotary axes. In addition, the V-shaped diamond has to fit into the facet without overcutting on either side. In the following calculations, \mathbf{n}_t will be used as the normal vector of the tool plane, as the direction of cut and rotary matrices will be used for representing the tool rotation around the B-axis ($R_y(\beta)$ for setting the structure angle) and around a possible A-axis ($R_x(\alpha)$, for changing the orientation of the diamond tool). Although the latter is not available in current setups, it may be necessary to machine structures on curved surfaces. In the structure/workpiece side, \mathbf{n}_f is the normal vector of the facet, \mathbf{s}_f the intended direction of cut, and $R_z(\gamma)$ the rotation of the workpiece around the C-axis. Thus, for a facet to be machinable, the following correlation needs to be fulfilled (Eq. 10).

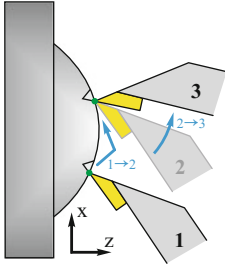
$$R_y(\beta) \cdot \mathbf{n}_s = R_z(\gamma) \cdot \mathbf{n}_f \wedge R_y(\beta) \cdot \mathbf{s}_t = R_z(\gamma) \cdot \mathbf{s}_f \quad (10)$$

A solution for this equation is found in a stepwise calculation of the necessary workpiece alignment angle γ , and the tool inclination angle χ_t is performed (cf. Fig. 26). The angle γ_x between a given facet plane $\mathbf{n}_f = (a \ b \ c)^T$ and the X-axis is calculated according to Eqs. 11 and 12. Adding 90° to this yields the angle γ' for aligning the facet parallel to the Y-axis (Eq. 13).

$$R_z(\gamma_x) \cdot \mathbf{n}_f = \begin{pmatrix} a \cdot \cos(\gamma_x) - b \cdot \sin(\gamma_x) \\ a \cdot \sin(\gamma_x) - b \cdot \cos(\gamma_x) \\ c \end{pmatrix} = \begin{pmatrix} 0 \\ b_x \\ c_x \end{pmatrix} \quad (11)$$

$$\arctan\left(\frac{a}{b}\right) = \gamma_x \quad (12)$$

ideal case: tool tip perfectly aligned with B-axis



- 1 original orientation
 - 2 repositioning to start of second cavity
 - 3 rotation of tool to new structure angle
- B-axis center

real case: tool tip decentration to B-axis

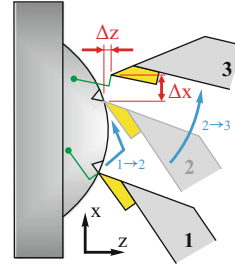


Fig. 27 Parasitic movement due to decentration of tool tip on B-axis

$$\arctan\left(\frac{a}{b}\right) + 90^\circ = \gamma' \quad (13)$$

As the calculated angle γ' is the minimal angle for parallel alignment, it has to be checked whether the intended direction of cut is still maintained after the rotation or if the workpiece alignment angle γ has to be corrected by 180° (Eq. 14).

$$|R_z(\gamma') \cdot \mathbf{s}_f + \mathbf{s}_t| \begin{cases} \leq |\mathbf{s}_t| \Rightarrow \gamma = \gamma' + 180^\circ \\ > |\mathbf{s}_t| \Rightarrow \gamma = \gamma' \end{cases} \quad (14)$$

After rotating the workpiece by γ , the facet is aligned parallel to the cutting direction \mathbf{s}_t . Now, the tool plane can be aligned to the facet by rotating the B-axis (Eq. 16).

$$R_z(\gamma) \cdot \mathbf{n}_f = (a_\gamma b_\gamma b_\gamma)^T \quad (15)$$

$$\beta = 90^\circ - \arctan\left(\frac{c_\gamma}{a_\gamma}\right) \quad (16)$$

Depending on the tool geometry, an additional rotation of the tool around the X-axis may be necessary. Assuming that this rotational axis is put on the B-axis, the required angle is calculated by Eq. 17.

$$\alpha = \arctan\left(\frac{c_\gamma}{b_\gamma}\right) \quad (17)$$

As long as α is smaller than the difference between the opening angle of the tool δ and the opening angle of the facet ξ_γ , no additional A-axis is necessary.

Due to the inevitable mechanical deviations of the setup, the tool tip is never perfectly aligned with the center of rotation of the B-axis (Fig. 27). Thus, an in-process change of the tool inclinations angle is not trivial; rather, additional tool alignment steps have to be performed in order to compensate for the parasitic tool

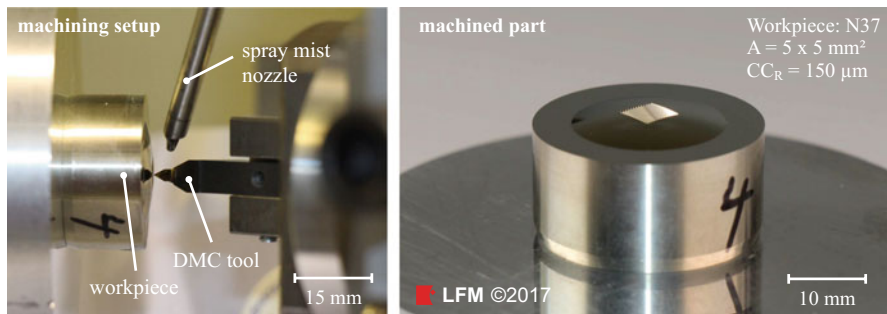


Fig. 28 Retroreflective array on curved substrate machined by DMC

movement. With an offset between the B-axis and the tool tip, it is assumed that the latter moves on a circular path. By evaluating the tool tip position at different orientations of the B-axis, this movement can be tracked and used for correcting the final position of the tool tip.

In recent studies of Dörgeloh et al. (2017), a circle interpolation was used to calculate the center coordinates as well as the radius of the corresponding tool rotation circle. Thereby, the position of the tool tip can be interpolated for every tool angle of the retroreflective array. Dörgeloh et al. furthermore discuss the impact of tool alignment errors on the structure quality for machining structures on a curved substrate. After optimizing the alignment procedure to minimize deviations, a $5 \times 5 \text{ mm}^2$ array with a structure size of $CC_R = 150 \text{ }\mu\text{m}$ was machined successfully (Fig. 28).

1.6 Summary and Outlook

Diamond Micro Chiseling (DMC) has been established to directly machine retroreflective arrays with a structure size in the micrometer range and is still the only process available to fulfill that task. In this publication, a comprehensive overview on the process kinematics, their optimization, and possible extension to curved surfaces is presented. It is shown that miniature retroreflective arrays can be machined on planar as well on curved substrates. However, despite recent optimizations of the process kinematics, DMC is still limited to machining only small array sizes. Thus, future work will concentrate on novel approaches to further increase the pattern size.

References

- Barton W (1984) Chip carving: techniques and patterns. Sterling Publishing Company, New York
 Beck A (1887) Ueber einige neue Anwendungen ebener Spiegel. Zeitschrift für Instrumentenkunde
 7: 380–389

- Beer R, Marjaniemi D (1966) Wavefronts and construction tolerances for a cat's-eye retroreflector. *Appl Opt* 5(7):1191–1197
- Benson O Jr, Frey CM, Shusta JM, Nestegard SK, Lightle VL, Smith KL, Bacon Jr, Chester A (1997) Ultra-flexible retroreflective cube corner composite sheetings and methods of manufacture. US 5,691,846
- Brecher C, Baum C, Winterschladen M, Wenzel C (2007) Dynamic long axis for ultra-precision machining of optical linear structures. *Prod Eng Res Dev* 1(3):315–319. <https://doi.org/10.1007/s11740-007-0050-8>
- Brinksmeier E, Schönemann L (2014) Generation of discontinuous microstructures by diamond micro chiseling. *CIRP Ann Manuf Technol* 63(1):49–52. <https://doi.org/10.1016/j.cirp.2014.03.066>
- Brinksmeier E, Gläbe R, Schönemann L (2012a) Diamond micro chiseling of large-scale retroreflective arrays. *Precis Eng* 36(4):650–657. <https://doi.org/10.1016/j.precisioneng.2012.06.001>
- Brinksmeier E, Gläbe R, Schönemann L (2012b) Review on diamond-machining processes for the generation of functional surface structures. *CIRP J Manuf Sci Technol* 5(1):1–7. <https://doi.org/10.1016/j.cirpj.2011.10.003>
- Dörgeloh T, Schönemann L, Riemer O, Brinksmeier E (2017) Diamond micro chiseling of retroreflective arrays on curved surfaces. In: 17th euspen International Conference & Exhibition, pp 125–126
- Eckard HD (1971) Simple model of corner reflector phenomena. *Appl Opt* 10(7):1559–1566. <https://doi.org/10.1364/AO.10.001559>
- Elsner-Dörge F, Riemer O, Brinksmeier E (2014) Robot-assisted vibration polishing of nico retroreflector moulds. *Adv Mater Res* 1018:175–181. <https://doi.org/10.4028/www.scientific.net/AMR.1018.175>
- Estler WT, Edmundson KL, Peggs GN, Parker DH (2002) Large-scale metrology – an update. *CIRP Ann Manuf Technol* 51(2):587–609. [https://doi.org/10.1016/s0007-8506\(07\)61702-8](https://doi.org/10.1016/s0007-8506(07)61702-8)
- Flucke C (2011) Strukturierung optischer Oberflächen durch Diamant-Mikroschneiden, Forschungsberichte aus der Stiftung Institut für Werkstofftechnik, vol 55. Shaker, Aachen
- Flucke C, Gläbe R, Brinksmeier E (2006) Diamond micro chiselling of micro structured moulds. In: 6th euspen international conference, vol 2, pp 437–440
- Flucke C, Gläbe R, Brinksmeier E (2008) Diamond micro chiselling of molding inserts for optical micro structures. In: 23th ASPE Annual Meeting and 12th ICPE, vol 44, pp 92–95
- Gubela HE (1994) Manufacturing method for triple reflectors and their tools – has strips formed by grinding in different directions, following direction of strip extension during process. DE 42 36 799 C2
- Gubela HE (1997) Lasersensorik mit Mikrotripelrückstrahler. DE 197 27 527 A1
- Gubela HE (2012) Reflektor mit einer Trapez-Reflexion und Verfahren für die Licht-Feinabstastung zur Erkennung eines Gegenstandes. DE 10 2007 006 405B4
- Gurganus DK, Sizemore NE, Owen JD, Davies MA (2017a) Force measurement in diamond micro-chiseling. In: 32nd ASPE Annual Meeting, pp 558–561
- Gurganus DK, Sizemore NE, Owen JD, Davies MA (2017b) Force measurement of diamond micro-chiseling. In: ASPEN/ASPE 2017 Spring Topical Meeting, pp 36–39
- Hering E, Martin R (2006) *Photonik Grundlagen, Technologie und Anwendung*. Springer, Berlin
- Huang TLJ, Smith KL, Coderre JC (1999) Flexible cube-corner retroreflective sheeting. US 5,988,820
- Kim H, Lee B (2007) Optimal design of retroreflection corner-cube sheets by geometric optics analysis. *Opt Eng* 46(9):094,002–1–14. <https://doi.org/10.1117/1.2779030>
- Liepmann TW (1994) How retroreflectors bring the light back. *Laser Focus World* 30(10):129
- Luoma J, Schumann J, Traube EC (1996) Effects of retroreflector positioning on nighttime recognition of pedestrians. *Accid Anal Prev* 28(3):377–383. [https://doi.org/10.1016/0001-4575\(96\)00004-8](https://doi.org/10.1016/0001-4575(96)00004-8)
- Moriya T, Nakamoto K, Ishida T, Takeuchi Y (2010) Creation of v-shaped microgrooves with flat-ends by 6-axis control ultraprecision machining. *CIRP Ann Manuf Technol* 59(1):61–66

- Rabinovich WS, Mahon R, Goetz PG, Waluschka E, Katzer DS, Binari SC, Gilbreath GC (2003) A cat's eye multiple quantum-well modulating retro-reflector. *Photon Technol Lett IEEE* 15 (3):461–463
- Ren D, Lawton KM, Miller JA (2007) Application of cat's-eye retroreflector in micro-displacement measurement. *Precis Eng* 31(1):68–71. <https://doi.org/10.1016/j.precisioneng.2006.02.002>
- Schönemann L (2014) Potenziale und Grenzen des Mikroschneidens zur Herstellung optischer Funktionsflächen, Forschungsberichte aus der Stiftung Institut für Werkstofftechnik, vol 62. Shaker, Aachen
- Seward GH, Cort PS (1999) Measurement and characterization of angular reflectance for cube-corners and microspheres. *Opt Eng* 38(1):164–169
- Stimson JC (1926) Process and apparatus for making central triple reflectors. US 1,591,572 A
- Takeuchi Y, Murota M, Kawai T, Sawada K (2003) Creation of flat-end v-shaped microgrooves by non-rotational cutting tools. *CIRP Ann Manuf Technol* 52(1):41–44
- Tauhiduzzaman M, Milliken N, Tutunea-Fatan OR, Bordatchev EV (2017) Inverted diamond cutting of right triangular retroreflectors: surface quality and cutting forces. In: 32nd ASPE Annual Meeting, pp 647–650



Micro Milling for Functional Surface

2

Takashi Matsumura

Contents

2.1	Introduction	34
2.2	Microscale Cutting: Difference with Conventional Milling	36
2.2.1	Micro End Mill	36
2.2.2	Cutter Runout	38
2.2.3	Cutting Process	40
2.3	Milling of Fine-Grained Steel	46
2.3.1	Crystal Grains in Materials	46
2.3.2	Micro Cutting Processes	47
2.3.3	Surface Integrities in Micro Milling	50
2.4	Micro Dimple Milling for Functional Surfaces	54
2.4.1	Machining Principle	54
2.4.2	Mechanistic Model in Micro Dimple Milling	55
2.4.3	Surface Functions	60
2.5	Conclusions	64
	References	64

Abstract

Micro manufacturing has recently increased in the several fields that include optics, electronics, medicine, biotechnology, and communications. Then, drastic progresses have been seen in the micro milling with the technologies in micro/nano-scale measurement, control, and tooling. This chapter describes the micro milling for manufacturing of the functional surfaces, which control material behavior with the surface topography. In the introduction, the current technical status in the functional surfaces is reviewed with the micro fabrication processes, and some issues in the micro milling are described to achieve high qualities of the micro elements and structures on the surfaces. Then, the typical micro milling

T. Matsumura (✉)

Department of Mechanical Engineering, Tokyo Denki University, Tokyo, Japan

e-mail: tmatsumu@cck.dendai.ac.jp

© Springer Nature Singapore Pte Ltd. 2018

J. Yan (ed.), *Micro and Nano Fabrication Technology*, Micro/Nano Technologies,

https://doi.org/10.1007/978-981-13-0098-1_2

33

process is discussed in terms of the operations and the removal process. Regarding material behavior, the effect of crystal grain size and orientation on the removal process becomes relatively large. When the grain size reduces, the dynamic components in the cutting force, burr formation, and affected layer can be controlled in micro cutting. Micro milling is applied to manufacture the functional surfaces with the micro dimples at high machining rates. The micro dimples are machined in milling with the inclined spindle at 45° . The milling with the cutter axis inclination is also applied to machine the micro dimples on the cylinder surfaces. A mechanistic model is applied to control the dimple shape for the cutting parameters, the feed direction, and the tool geometry. The surfaces with the micro dimples are applied to control the surface functions such as optical reflection and wettability.

Keywords

Surface function · Micro milling · Mechanistic model · Fine grained steel · Micro dimple · Optical control · Wettability

2.1 Introduction

The demands of functional surfaces, which control physical and/or chemical properties at interface between substances, have recently increased in many industries. Generally, many surface functions are controlled by the material properties of thin layers coated on surfaces. The surface functions can also be controlled by the surface structures manufactured artificially for industrial uses (Bruzzone et al. 2008). As an application of the functional surfaces, the tribological properties have been associated with the surface topography. Friction coefficient was reduced by micro dimples machined by an abrasive jet or an excimer laser beam (Wakuda et al. 2003). In order to improve tribological properties, the micro dimples have also been used to maintain a lubricant at the interface, as micro reservoirs of solid lubricants (Basnyat et al. 2008; Voevodin and Zabinski 2006).

The surface structures have been manufactured in various processes. In etching, the machining area is controlled by printing masks in photolithography and subsurface in the exposed area is removed by the chemical reaction. Nanoscale structures were fabricated on surfaces by plasma etching (Krupenkin et al. 2004; Sommers and Jacobi 2006). Wet chemical etching was applied to fabrication of nanoclusters on silicon wafers (Kim et al. 2009). The surface structures were also fabricated in electro-chemical machining using the mask, which consisted of a conductive metal layer and an insulation layer (Zhu et al. 2009). The micro dimples were machined by reactive ion etching in mixed Ar/CF₄ plasma (Basnyat et al. 2008).

Regarding laser beam processes for the functional surfaces, the micro dimples were fabricated in laser coating-texturing (Wan et al. 2008). CO₂ laser beam modulation was also applied to fabrication of the micro dimples on the roll surfaces with a rotating polygon (Luo et al. 2011). The micro dimples were fabricated on the surface of hard TiCN coatings by a focused UV laser beam (Voevodin and Zabinski 2006).

Although etching and energy beam processes have been applied to fabrication of the surface structures, some issues have been left on the environmental impact, flexibility, the cost, and the production rate. In addition, the processes have been limited to basically 2 or 2.5 dimensional manufacturing. Therefore, alternative processes have been required for controls of three-dimensional parts. As an alternative process, mechanical processes such as cutting and forming have been economically applied to manufacturing of three-dimensional shapes at high production rates. Furthermore, they are flexible enough to manufacture diversified shapes of the micro parts with numerical control systems. Downsizing technologies of the mechanical processes have recently developed with miniaturized tools and micro/nano-scale motion controls. Therefore, these mechanical processes have been expected to expand the applications of the micro fabrication at high production rates and low costs.

An interesting work was done to form the micro dimples mechanically in pellet-pressing and improved tribological properties (Wang et al. 2009). The micro dimples were also machined in cutting with a ball end mill (Kogusu et al. 2007) and applied to control the optical properties on the plates (Matsumura and Takahashi 2011). The micro dimple milling was also used for the cylinder surfaces (Matsumura and Takahashi 2012).

In micro cutting, some issues, which have been ignored in macroscale cutting, are prevailed to control the removal performance including the surface quality. When the milling tool is miniaturized, the material removal volume should be reduced to prevent tool breakage and vibration. Then, the edge radius of the tool has an influence on the removal mechanism. When the uncut chip thickness is of the same order or less than the edge radius of the tool, the effective rake angle becomes highly negative which, in turn, causes ploughing and associated elastic-plastic deformation of the workpiece material to become much more dominant factors in the process. Then, a chip may not be formed during each tooth passing. In milling, where the uncut chip thickness varies during a single engagement of a tooth in the cut, the cutting mechanism may change from ploughing-dominated to shearing-dominated and back to ploughing-dominated again within a single excursion of a tooth through the cut.

In conventional removal processes of polycrystalline materials, workpieces have been regarded as isotropic materials. Meanwhile, in microscale cuttings, the crystal grain sizes become relatively large compared to the removal volumes. The removal processes depend on the sizes, the shapes, and the orientations of the crystal grains. Therefore, the influence of the crystal grains in materials should be considered in micro milling.

This chapter focuses on the micro milling for manufacturing the functional surface. In the first section, the micro milling is reviewed to understand the micro-scale mechanical removal process in terms of the cutting operations and the material behavior. The second section describes the micro cutting of fine-grained materials, in which the crystal grain sizes are reduced to submicroscale. The third section takes a micro fabrication of the functional surfaces in milling. In general, the micro mechanical fabrications require long processing times for finishing large-scale machining areas. The machining rate should be improved for implementation of the micro

mechanical processes to practical manufacturings. In the last section, the micro millings are performed to fabricate micro dimples on the surfaces at high machining rates. Then, the surfaces with the micro dimples are applied to change the functionalities, as examples of micro millings.

2.2 Microscale Cutting: Difference with Conventional Milling

2.2.1 Micro End Mill

Micro milling has been progressed with miniaturizing the end mills. The micro milling requires machining accuracy in the order of submicrometer and surface roughness in the order of nanometer. Therefore, in manufacturing of the micro end mills, not only the accuracy of the edge shape but also the edge roughness should be considered in grinding, coating, and measurement.

Figure 1 shows examples of micro square and ball end mills, where the diameters of these tools are 0.03 mm, 0.015 mm, and 0.1 mm, respectively. The recent tool manufacturing technology has achieved reduction of end mill diameter, which is

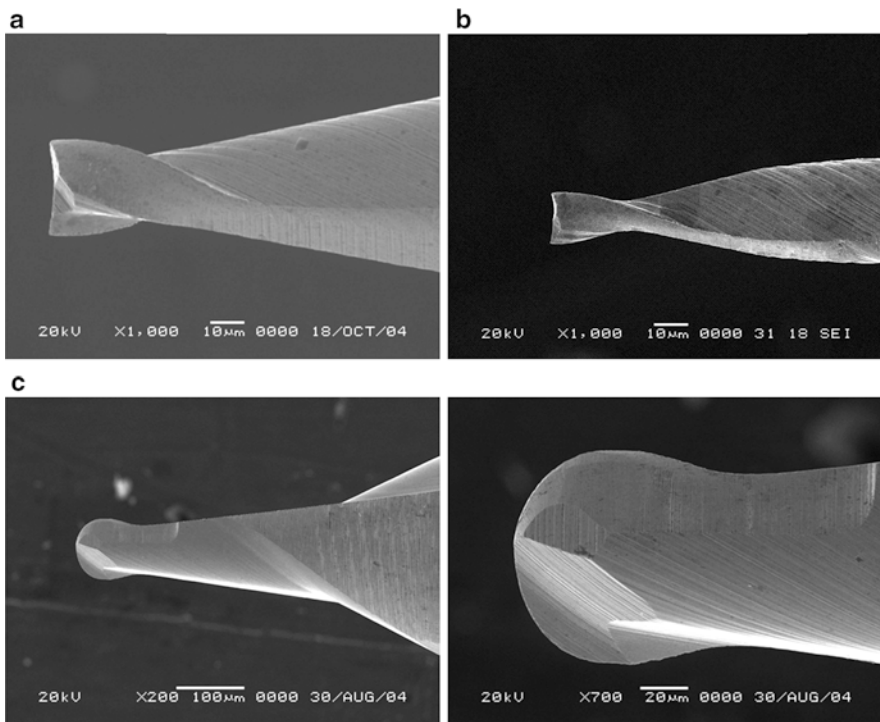


Fig. 1 Micro end mill: (a) square end mill, diameter 0.03 mm; (b) square end mill, diameter 0.015 mm; (c) ball end mill, diameter 0.1 mm. (Mitsubishi Hitachi Tool Engineering, Ltd.)

Fig. 2 Actual rake angle in micro cutting

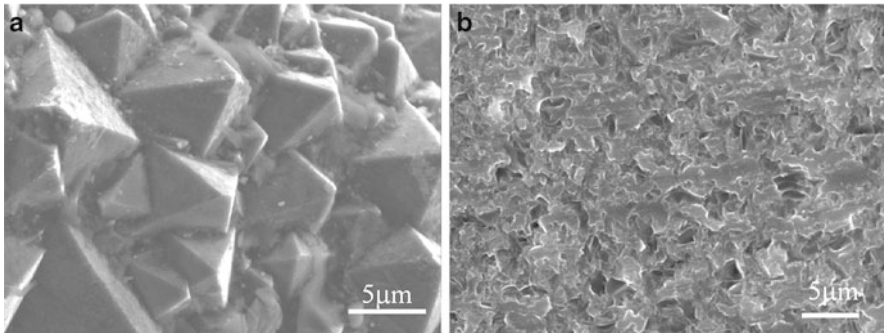
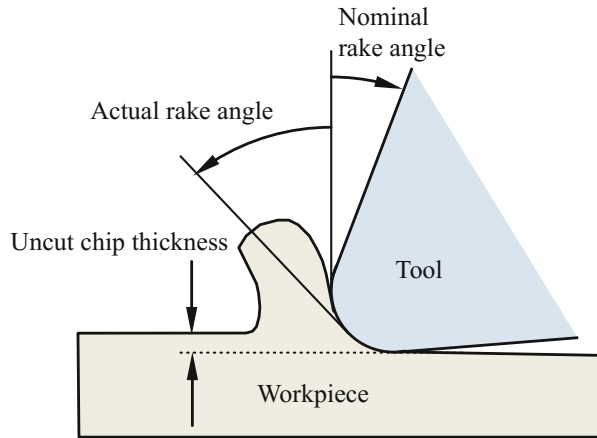


Fig. 3 Glass milling with diamond coated end mill: (a) diamond coating; (b) surface finish. A micro groove is machined by a 0.4 mm diameter ball end mill inclined at 45° in feed direction. Cutting conditions: spindle speed, 15,000 rpm; depth of cut, 0.02 mm; feed rate, 0.24 mm/min; and lubrication, water

much smaller than human hair. Because the miniature end mill is easy to be broken, the grinding force in the edge finishing should be controlled to keep small with sharpness of the grains. The edge sharpness is associated with chip formation in micro cutting. Because the material removal volume reduces to the same size or less than the edge radius, the actual rake angle becomes highly negative, as shown in Fig. 2. Then, the material cannot be removed under a critical uncut chip thickness, and ploughing occurs with elastic deformation. Because the critical uncut chip thickness is associated with the edge radius, the grinding of the edge on the end mill has to be considered how sharp can be finished.

The edge roughness has also an influence on the surface finish in micro milling. Especially in milling of brittle materials, the edge roughness induces brittle fracture in micro milling. The diamond coating has recently developed for machining of nonmetallic materials. When the coating grains are diversified, as shown in Fig. 3a, brittle

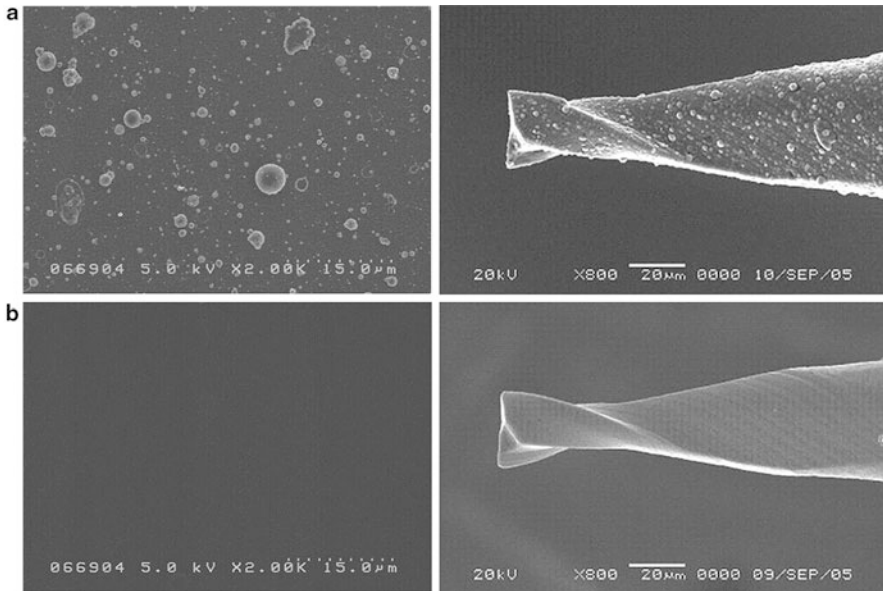
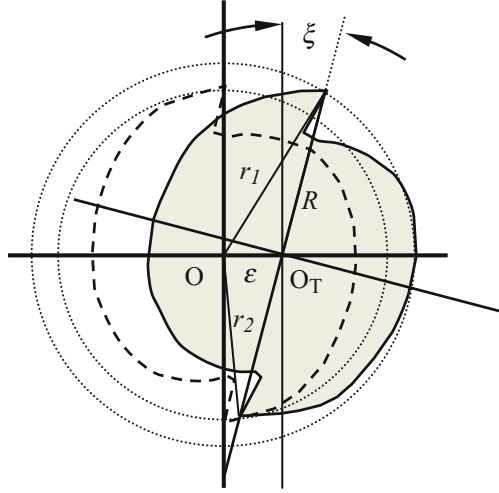


Fig. 4 Comparison between nanocoated and conventional-coated end mills: (a) conventional coated end mill; (b) nanocoated end mill. (Mitsubishi Hitachi Tool Engineering, Ltd.)

fracture cannot be controlled any more in glass cutting, as shown in Fig. 3b. Coating materials and processing on the micro end mill should be controlled to finish fine surfaces, because the uncut chip thickness is nearly the same order as the coating grains in micro milling. Figure 4 compares a nanometer-scale coated end mill with the conventional coated one. The grain sizes are much smaller than those of the conventional end mill. It is known that the wear resistance and the delamination of the coated layers depend on the material properties and the grain sizes. The reduction of coating grain sizes has also an effect on surface finish. The micro milling requires downsizing of not only the end mill size but also the coating grain sizes.

2.2.2 Cutter Runout

Cutter runout is usually accompanied with clamping of the tool even though the precisely finished end mill is used for the micro milling operation. The cutter runout in micro milling becomes relatively large compared to the material removal size. The cutter runout is induced by eccentricity and axial inclination of the tool-spindle system. The shank runout is due to alignment error, and tool runout depends on the tool manufacturing accuracy. Although the detail analysis is discussed (Jun et al. 2006; Filiz and Ozdoganlar 2008), a simple model is shown to understand the effect

Fig. 5 Cutter runout model

of the cutter runout here. At a height of cutter, the center of the tool (O_T) is located at a distance of ε from the rotation center of the spindle (O), as shown in Fig. 5. Then, an edge is orientated at an angle ξ when the tool is clamped. Because O_T rotates around O in the radius ε at a spindle speed, the rotating radii r_1 and r_2 of edges are:

$$\left. \begin{aligned} r_1 &= \sqrt{\varepsilon^2 + R^2 - 2\varepsilon R \cos(\pi/2 + \xi)} = \sqrt{\varepsilon^2 + R^2 + 2\varepsilon R \sin(\xi)} \\ r_2 &= \sqrt{\varepsilon^2 + R^2 - 2\varepsilon R \cos(\pi/2 - \xi)} = \sqrt{\varepsilon^2 + R^2 - 2\varepsilon R \sin(\xi)} \end{aligned} \right\} \quad (1)$$

where R is the radius of the tool. Therefore, the difference between r_1 and r_2 results in the cutter runout. Because the feed per tooth should be small to prevent the tool breakage and improve the machining accuracy, the cutter runout has a relatively large influence on the chip formation. When milling is performed with the cutter runout, the different cutting forces are loaded on the edges with the cutting thicknesses. Because the tool wear also depends on the cutting force, different wear progress is observed on the edges.

In micro milling, the cutter runout should be reduced to the order of micrometer or submicrometer for high machining accuracy. However, it is not so easy to measure the cutter runout directly during rotation. Because the cutter runout is associated with the cutting force, the tool clamping may be adjusted with measuring the cutting force. Figure 6 shows measurement of the force at contacts of the tool with the workpiece, which is measured with a piezoelectric dynamometer. Figure 6b shows an example of Z (vertical) component in the contact force onto a glass plate. Different peaks in the contact force are induced by the cutter runout. As described above, the cutter runout may be controlled by the tool orientation angle ξ . Therefore, the tool clamping such as the tool orientation and the position may be adjusted in the clamping device (collet chuck) so that the same maximum contact forces are loaded on each cutting edge.

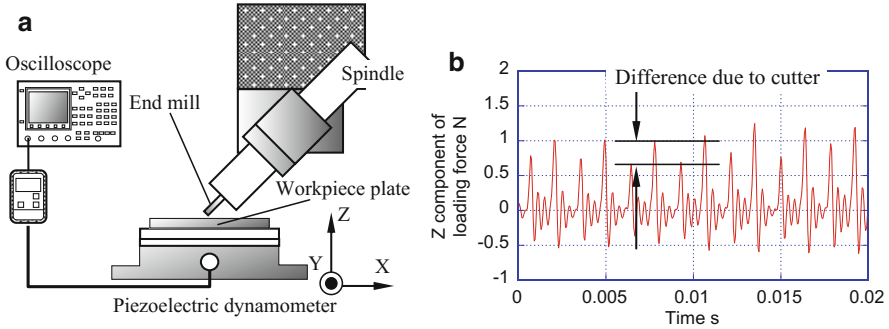


Fig. 6 Adjustment of cutter runout: (a) measurement of contact force; (b) difference of Z component in loading force due to cutter runout

2.2.3 Cutting Process

2.2.3.1 Chip Formation in Micro Cutting

Chip formation is generally associated with the uncut chip thickness in micro milling (Chae et al. 2006). The typical material behavior modes in micro cutting are illustrated in Fig. 7. When the uncut chip thickness, h , is less than a critical minimum chip thickness, h_m , as shown in Fig. 7a, elastic deformation occurs and the edge does not remove material. As the uncut chip thickness approaches the minimum chip thickness, chips are formed in shearing though elastic deformation occurs, as illustrated in Fig. 7b. The removal depth results in less than the specified depth. When the uncut chip thickness increases beyond the minimum chip thickness, elastic deformation decreases significantly and the entire specified depth of material is removed as a chip, as shown in Fig. 7c.

In conventional cutting, the rake angle is defined as the inclination angle of the rake face. Chip formation is controlled by the rake angle in a large uncut chip thickness. However, when the uncut chip thickness reduces to micrometer scales, the material is removed around the edge corner, and the actual or effective rake angle is controlled by the edge radius. Therefore, cutting is performed at large negative rake angles, which affects the magnitude of the ploughing and shearing forces. The minimum chip thickness is also associated with the edge radius and the material. Figure 8 shows the change in the chip load/cutting force with the uncut chip thickness (Liu et al. 2004). A sudden drop in thrust component occurs at a transition from ploughing/sliding to shearing dominant mode. According to this example, the minimum chip thickness of steel is estimated to be 0.2 and 0.3 times the edge radius for pearlite and ferrite, respectively.

2.2.3.2 Force in Micro Milling

The uncut chip thickness changes with the cutter height in helical end mills during a rotation of the tool. Therefore, the cutting forces are estimated with dividing the flutes into discrete small elements. The cutting force is induced by the ploughing

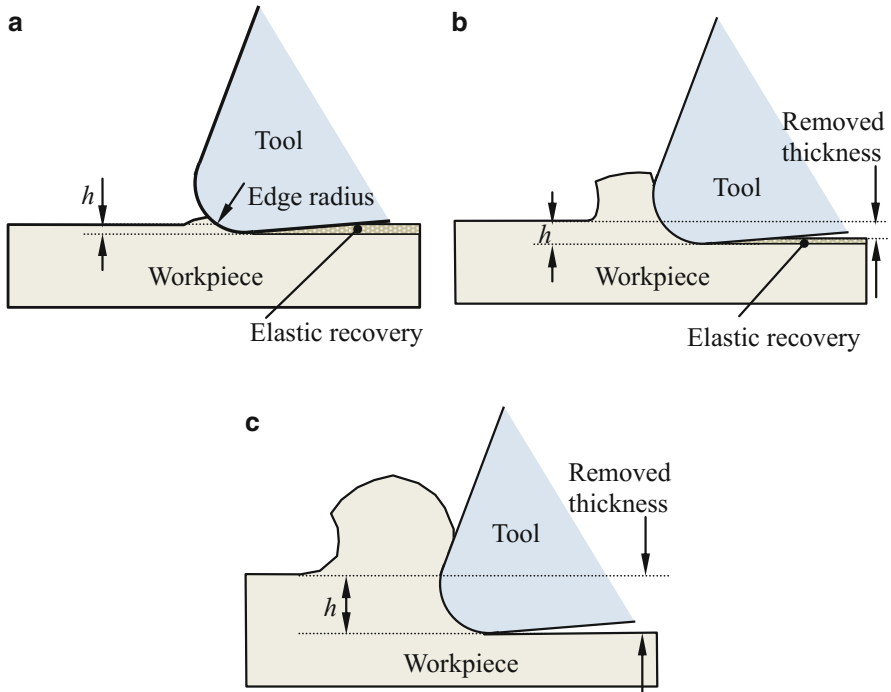


Fig. 7 Chip formation in micro cutting: (a) uncut chip thickness $h < \text{minimum chip thickness } h_m$; (b) $h \approx h_m$; (c) $h > h_m$. (Chae et al. 2006)

Fig. 8 Change in chip load/ cutting force with cutting thickness. (Liu et al. 2004)

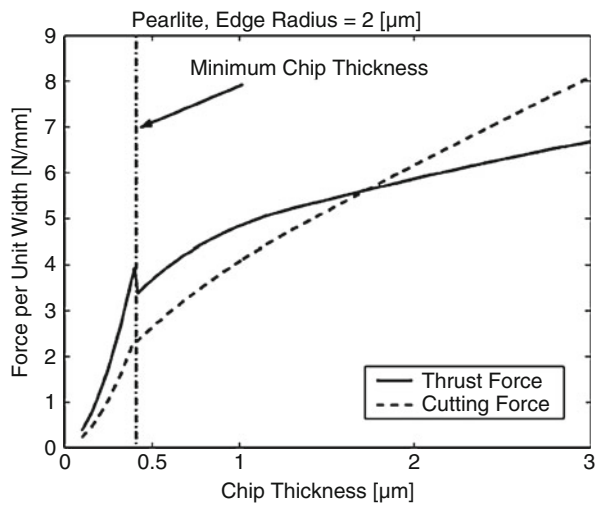
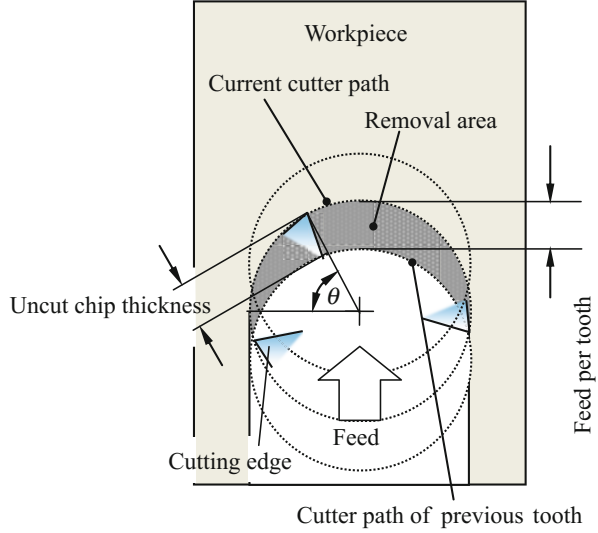


Fig. 9 Uncut chip thickness in milling



force around the edge radius and the shearing force for chip formation. When an edge element locates at an instantaneous angle, θ , the cutting force loaded on the element, $dF(\theta)$, is estimated as:

$$dF(\theta) = k_e dz + k_c h(\theta) dz \quad (2)$$

where k_e and k_c are the ploughing and the shearing force coefficients, respectively (Perez et al. 2007). $h(\theta)$ is the uncut chip thickness associated with the instantaneous rotation angle θ . Being loaded on the edge, the ploughing force depends on the edge length as the first terms in Eq. (2). The second term is associated with the shearing force controlled by the cutting area. Figure 9 shows the geometrical removal area during a rotation of the cutter in milling, where the noncutting due to ploughing is not considered. When the edge engages the workpiece, $h(\theta)$ is too small to form the chip. Because only ploughing force is loaded on the tool, Eq. (2) may be expressed as:

$$dF(\theta) = k_e dz \quad (3)$$

After rotating at a certain large angle, $h(\theta)$ becomes large enough to form the chip and the cutting force is estimated in Eq. (2). However, the first term in Eq. (2) is relatively large compared to the second term when the uncut chip thickness is small. In micro milling, the feed rate is generally low to prevent the tool deflection and the tool breakage. Because the uncut chip thickness is small, the ploughing effect becomes large in estimation of the cutting force. Considering the noncutting due to ploughing in the uncut chip thickness of less than the minimum chip thickness, a sawtooth-like surface profile may be finished, as shown in Fig. 10 (Weule et al. 2001).

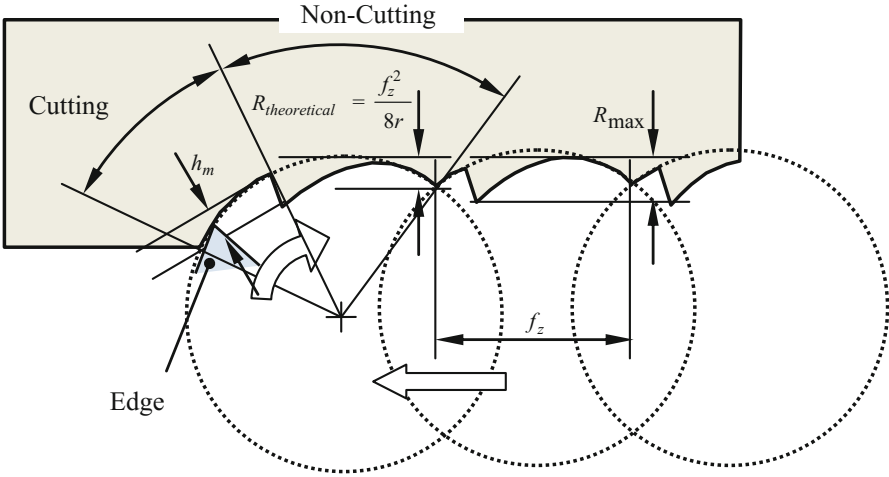


Fig. 10 Surface profile in micro milling. (Weule et al. 2001)

2.2.3.3 Intermittent Chip Formation

If the feed per tooth is small compared to the cutting edge radius, a chip may not form with each pass of the tool. As a result, intermittent chip formation occurs. The intermittency in the chip formation process is caused by the lack of material removal when the uncut chip thickness is smaller than the minimum chip thickness. Deflection of the end mill due to small stiffness is another factor to control the chip formation. A model of chip formation is discussed with accounting for the above effects of the tool deflection and the noncutting process (Kim et al. 2004).

Figure 11a illustrates the model of milling with tool deflection due to the forces acting on the cutting edge viewed from the top of the tool. The tool will deflect away from the workpiece due to the cutting forces, which can be decomposed into radial thrust force F_T and tangential cutting force F_C . The figure describes the relative displacement of the cutting edge with respect to the center of rotation. Although the milling tool actually deflects in both directions, the displacement in the tangential direction is neglected here. The tool deflection, therefore, is modeled as one-dimensional displacement of a rigid cutting edge with respect to a stationary point representing the center of rotation, utilizing a Hookean spring with spring constant equated to the milling tool stiffness in the radial direction k .

If the machine tool system and the milling tool are completely rigid, the cutting edge follows the paths denoted with the dashed arcs in Fig. 11 as the tool rotates. The bottom and top dashed arcs represent the path of the tool tip for the previous and current tooth pass, respectively. At a specific position angle θ_0 , the theoretical uncut chip thickness, $h(\theta_0)$, is associated with ωt , where ω and t are the angular velocity and time, respectively. In the real process, the tool usually deflects away from the workpiece in the radial direction due to the cutting forces. No chip formation may

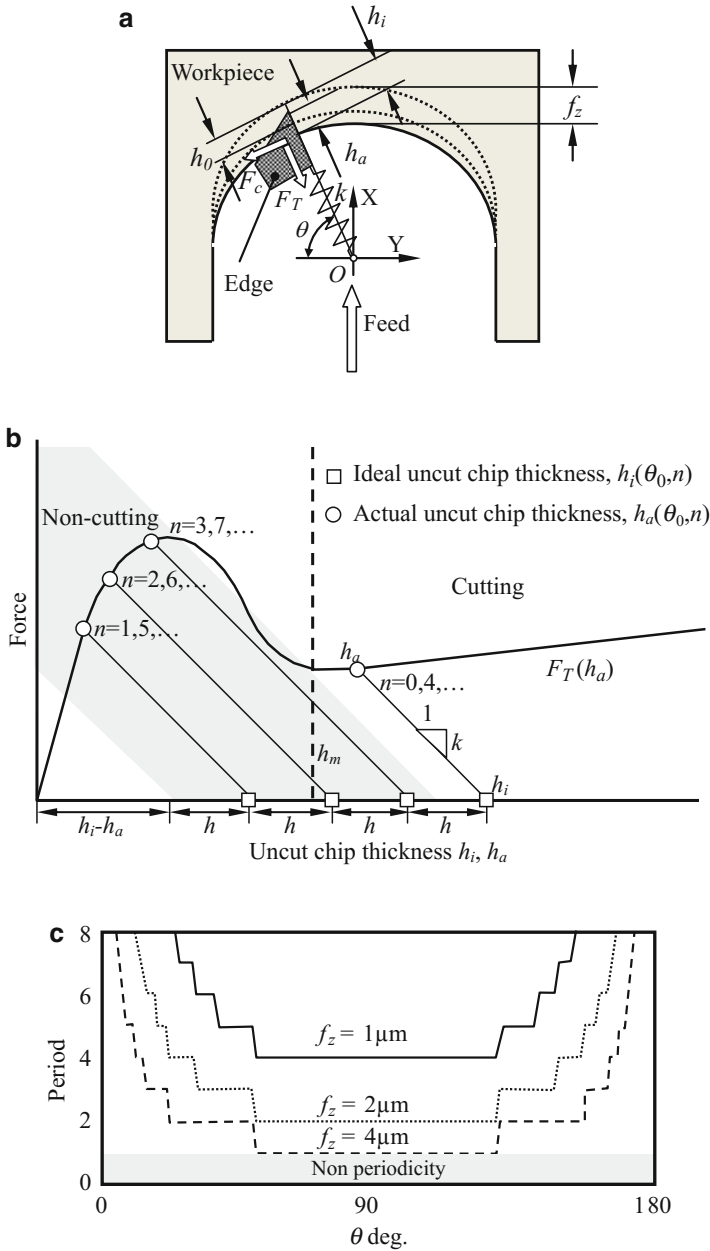


Fig. 11 Intermittent chip formation: (a) model in milling (top view); (b) change in force with uncut chip thickness; (c) examples of periods with position angle. (Kim et al. 2004)

also occur when the uncut chip thickness is smaller than the minimum chip thickness. In n -th tool pass, therefore, the ideal uncut chip thickness, $h_i(\theta_0, n)$, is given by adding the noncutting thickness in the previous tooth passes. Therefore, the actual uncut chip thickness, $h_a(\theta_0, n)$, is given by the magnitude of the deflection of the tool in the radial direction during the current tooth pass. For a given $h_i(\theta_0, n)$, $h_a(\theta_0, n)$ is achieved when the restoring force in the tool due to deflection, $k\{h_i(\theta_0, n) - h_a(\theta_0, n)\}$, is balanced with the radial thrust force F_T :

$$F_T = k\{h_i(\theta_0, n) - h_a(\theta_0, n)\} \quad (4)$$

The thrust force varies depending on material properties of the workpiece, tool geometry, the actual uncut chip thickness, and the axial depth of cut. The force is illustrated schematically in Fig. 11b. For a specified $h_i(\theta_0, n)$, $h_a(\theta_0, n)$ is given in Eq. (4) with obtaining F_T in Fig. 11b.

After the milling process settles into a steady state, the magnitude of tool deflection will be constant, and thus, the actual uncut chip thickness $h_a(\theta_0, n)$ will be the same as the projected feed per tooth. When $h_a(\theta_0, n)$ is greater than the minimum chip thickness h_m , the tooth pass produces a chip and the process continues in a steady cutting regime:

$$h_a(\theta_0, n) = h(\theta_0) \quad h(\theta_0) > h_m \quad (5)$$

If $h(\theta_0)$ is smaller than h_m , the formation of a chip at a specific position angle depends on whether $h_a(\theta_0, n)$ is greater than h_m or not. Therefore, the ideal uncut chip thickness in the following tooth pass, $h_i(\theta_0, n + 1)$, is given by adding the material as thick as the amount of tool deflection:

$$\left. \begin{array}{l} h_i(\theta_0, n + 1) = [h_i(\theta_0, n) - h_a(\theta_0, n)] + h(\theta_0) \\ h(\theta_0) < h_m \quad h_a(\theta_0, n) > h_m \end{array} \right\} \quad (6)$$

When no material is removed on the noncutting tooth passes, $h_i(\theta_0, n + 1)$ on the following tooth pass is:

$$\left. \begin{array}{l} h_i(\theta_0, n + 1) = h_i(\theta_0, n) + h(\theta_0) \\ h(\theta_0) < h_m \quad h_a(\theta_0, n) < h_m \end{array} \right\} \quad (7)$$

This equation is valid for any noncutting tooth pass for which $h_a(\theta_0, n)$ is smaller than h_m . In the illustrative example presented in Fig. 11b, the ideal uncut chip thickness for $n = 2, 3$, and 4 can be obtained using Eq. (7). On the cutting tooth pass $n = 4$, which is identical with the initial cutting tooth pass $n = 0$, the material accumulated during previous three noncutting tooth passes will be removed as a chip, and afterward, this series of tooth passes – three noncutting and one cutting – will continuously repeat. Consequently, the actual uncut chip thickness and the corresponding cutting and thrust forces vary with respect to the number of tooth passes, with a period of 4 in this particular example. Figure 11c shows examples of variations of periodicity as a function of position angle at feeds per tooth.

2.3 Milling of Fine-Grained Steel

2.3.1 Crystal Grains in Materials

The size of crystal grain is generally ranged from 100 nm to 100 μm in engineering materials. Polycrystalline materials have certain distributions in the crystal grain sizes with random crystal orientations. Figure 12a shows microstructure of 0.45% carbon steel, which is widely used for the mechanical structures. The grain size is distributed from 10 to 20 μm . The shapes of the crystal grains are not uniform, and then, anisotropy may appear in material behavior.

The material technologies have recently progressed to improve the mechanical strengths and their uniformities of the materials with reducing the crystal grain sizes. The crystal grain size of 0.15% carbon steel was reduced in forming at large strains (Murty et al. 2005). Then, multiple deformations were applied to form fine-grained structures in austenitic stainless steels (Belyakov et al. 2000). The changes in mechanical properties with microstructures were studied to associate the material strength with Hall–Petch relationship in the fine-grained steels (Takaki et al. 2001). Hall–Petch relation was also discussed for fine-grained stainless steel (Rajasekhara et al. 2007). Mechanical property distribution was also measured in fine-grained steels by nanoindentation (Choi et al. 2001). A nanocrystalline structure was formed in a large plastic deformation (Umemoto 2000). Figure 12b shows microstructure of a fine-grained 0.45% carbon steel. The grains are much smaller than those of the standard steel. Then, the workpiece to be cut may be regarded as a uniform material.

In terms of material-related issues in micro cutting, when the uncut chip thickness is less than the grain size, the material is not regarded as isotropic any more (Chae et al. 2005). The cutting process depends on each crystal grain size and orientation and becomes unstable with vibration. Furthermore, the size and the orientation of the crystal grains in the material have an influence on not only the surface finish but also the affected layer in subsurface. Therefore, in micro cutting, the grain size in the material to be cut is a critical factor to control the surface quality.

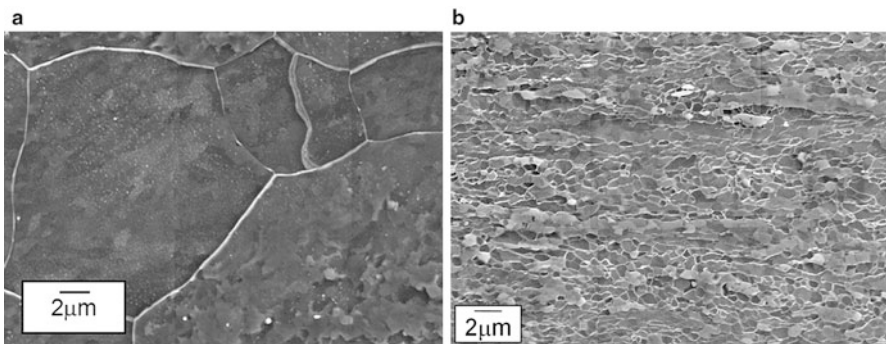


Fig. 12 Crystal grains of carbon steels: (a) normal steel (conventional material); (b) fine-grained steel

2.3.2 Micro Cutting Processes

In order to understand the effect of the grain size on machining process, the micro planing and milling processes of a fine-grained stainless steel is compared with those of standard one. The standard stainless steel was formed to reduce the plate thickness from 3 mm to 0.2 mm in rolling with heat treatment, where the average size is 9.10 μm . The fine-grained steel was formed to be 1.52 μm with repeating plastic deformation and reverse phase transformation (Nagayama et al. 2008). Tables 1 and 2 show the chemical compositions the mechanical properties of the materials employed in the cutting tests. Although the grain sizes in the materials were different, the tensile stresses of the materials were adjusted to be around 900 MPa.

Figure 13 compares the microstructure of the materials which is observed by electron back scatter diffraction (EBSD), where red, green, and blue color shows [001], [101], and [111] planes in the crystal, respectively. Because all crystal planes are observed in Fig. 13a, b, the materials are regarded as isotropic in a large-scale area. However, in a view of 10 μm square area, which is the same grain size in Fig. 13a, the standard steel is not regarded as an isotropic material any more. The anisotropic properties are, therefore, induced by the crystal orientation. Meanwhile, isotropic material behavior is expected in the fine-grained steel. Figure 14 shows the grain size distributions of the materials. The scattering of the grain sizes in the standard steel is much larger than that of the fine-grained steel. The scattering induces the unstable process with vibration in cutting.

The planing operations are conducted with the single-point tools made of single crystal diamond, as shown in Fig. 15a. The tools are controlled to remove the materials, where the cutting depth gradually increases to the specified cutting depth with the cutting travel, as shown in Fig. 15b. Figure 16 compares the cutting

Table 1 Chemical composition

	Composition %
Carbon (C)	0.06
Silicone (Si)	0.4
Manganese (Mg)	1.09
Phosphorus (P)	0.03
Sulfur (S)	0.004
Nickel (Ni)	8.03
Chromium (Cr)	18.02

Table 2 Mechanical properties

		Standard	Fine grained
Vickers hardness (HV)		260	260
Tensile strength (MPa)	RD	870	919
	ND	858	880
Elongation (%)	RD	51.1	42.5
	ND	57.5	46.4
Ave. grain size (μm)		9.10	1.52

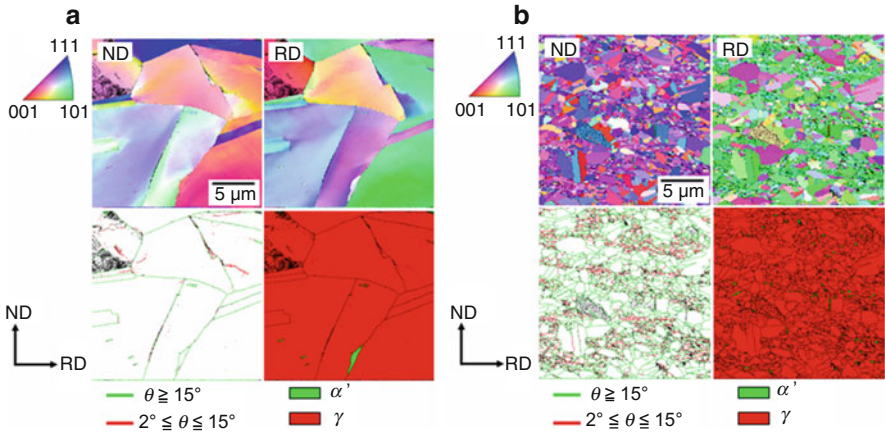


Fig. 13 Microstructures of stainless steels observed by EBSD: (a) standard steel; (b) fine-grained steel. RD and ND show the microstructure in the rolling and the perpendicular directions, respectively

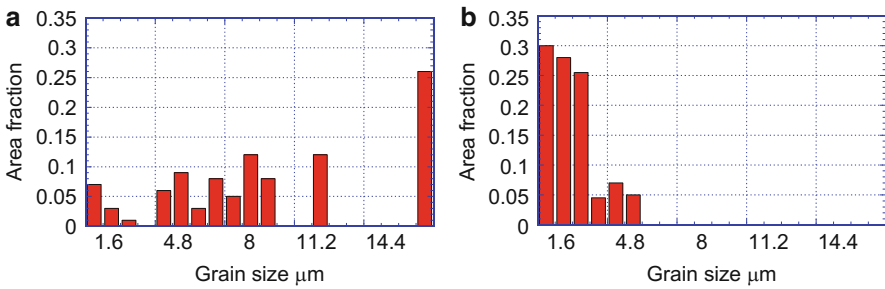


Fig. 14 Grain size distributions: (a) standard steel; (b) fine-grained steel

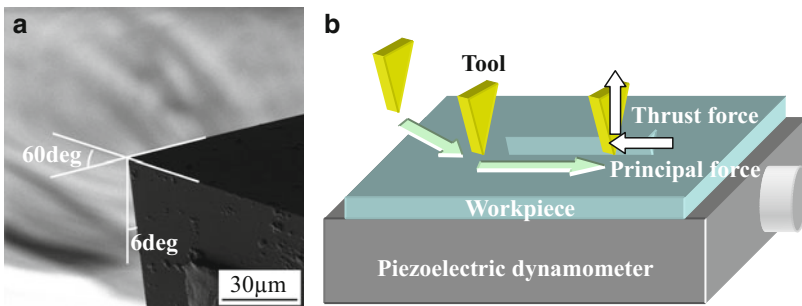


Fig. 15 Micro planing experiment: (a) single-crystal diamond tool; (b) tool path and cutting force components

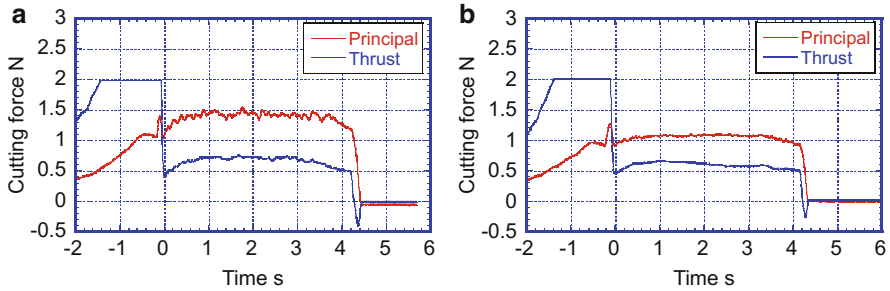
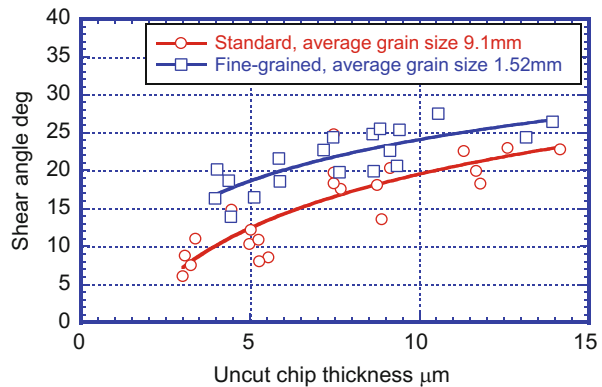


Fig. 16 Cutting forces of stainless steels: (a) standard steel (average grain size $9.1 \mu\text{m}$); (b) fine-grained steel (average grain size $1.52 \mu\text{m}$). Cutting conditions: depth of cut, $14 \mu\text{m}$ and cutting speed, 0.5 mm/sec

Fig. 17 Shear angles: (a) standard steel (average grain size $9.1 \mu\text{m}$); (b) fine-grained steel (average grain size $1.52 \mu\text{m}$). Cutting conditions are the same as those in Fig. 16



forces of the standard and the fine-grained steels (Because the slope angle is larger than the clearance angle of the tool, the flank face contacts workpiece during penetration of the edge. Therefore, the vertical force before the time 0 is larger than the principal force. The cutting force in the steady process is performed after time 0.). The cutting force of the fine-grained steel is smaller than that of the standard steel with the vibration component. Figure 17 shows the shear angles with changing the cutting depth. The shear angles of the fine-grained steel are larger than those of the standard one. The reduction of the cutting force is owing to the increase of the shear angle (Komatsu et al. 2011).

The milling tests were conducted to machine grooves with measuring the cutting forces and the surface profiles, as shown in Fig. 18a. Figure 18b shows 0.8 mm diameter ball end mill used in the cutting experiments. The tool material is tungsten carbide coated by TiAlN thin layer. The ball end mill is inclined at an angle of 45° in the feed direction to finish good surfaces at high cutting speeds in the stable cutting process.

Figure 19 shows the cutting forces of the standard and the fine-grained steels in milling with the inclined end mill at an angle of 45° . The force components in the

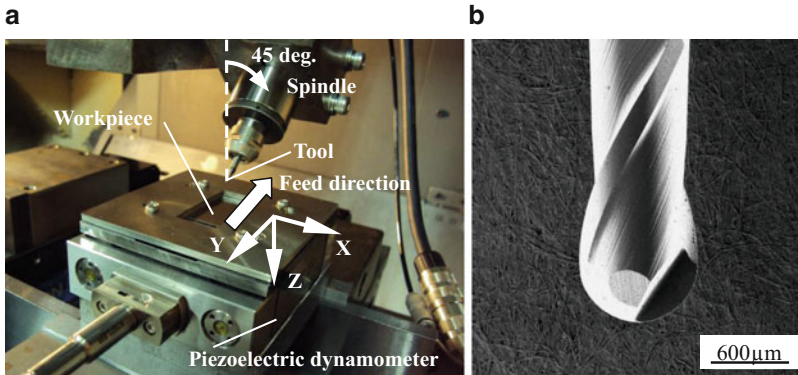


Fig. 18 Micro milling experiment: (a) setup; (b) ball end mill

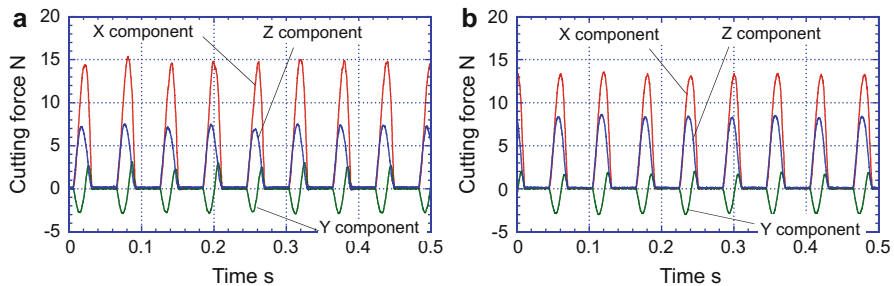


Fig. 19 Cutting forces in millings: (a) standard steel (average grain size $9.1\ \mu\text{m}$); (b) fine-grained steel (average grain size $1.52\ \mu\text{m}$). Cutting conditions: depth of cut, $42\ \mu\text{m}$; spindle speed, 500 rpm; feed rate, 50 mm/min ($0.05\ \text{mm/tooth}$); and lubrication, dry. Tool: material, carbide coated by TiAlN; and diameter, 0.8 mm

cutting force are designated in Fig. 18a. X component of the fine-grained steel is smaller than that of the standard steel. Meanwhile, Z component becomes large compare to that of the standard steel. Because the helix angle of the ball end mill is more or less 14° and the depth of cut is much less than the tool radius, X and Z components are regarded as the tangential and radial forces, respectively. According to Figs. 16 and 17, when the fine-grained steel is machined, the principal component reduces with increasing the shear angle. The reduction of the tangential force is associated with the change in the shear angle.

2.3.3 Surface Integrities in Micro Milling

In terms of the surface qualities, burr formation and affected layer should be discussed for the practical applications such as implant parts. Figure 20 compares

the surface finishes observed with a laser confocal microscope. Because the end mills were fed from the bottom to the top in the pictures, the cutting edges penetrated into the workpiece at the left hand of the groove and exited from the workpiece at the right hand. The cutter marks are observed on the surfaces in the grooves. Figure 21 compares the surface finishes R_a of the standard and the fine-grained steels, where the surface finishes are measured in three areas for each workpiece. The average R_a and R_z of the standard steel are $0.090 \mu\text{m}$ and $1.94 \mu\text{m}$, respectively and those of the fine-grained steels are $0.076 \mu\text{m}$ and $1.63 \mu\text{m}$, respectively. The surface finishes of the fine-grained steel are better than those of the standard steel. A remarkable difference of the surface finishes is observed at the right edges of the grooves, as shown in Fig. 22. Large burrs were formed along the edge of the groove of the standard steel. In order to analyze the distributions of the burr shapes, the surface profiles were measured with an increment of $7 \mu\text{m}$ in the feed direction. The height and width of burr were defined, as shown in Fig. 22a. Figures 23 and 24 compare the distributions of the height and the width, respectively. The burr shapes and their scattering in milling of the standard steel are larger than those of the fine-grained steel.

Figures 25 and 26 show the microstructures of the noncutting and the cutting areas in the cross section perpendicular to the feed direction, where the materials are

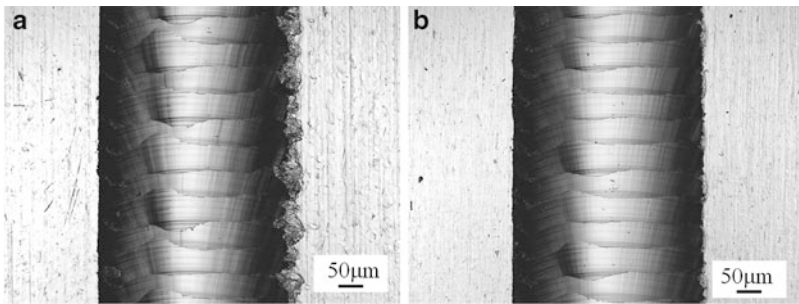
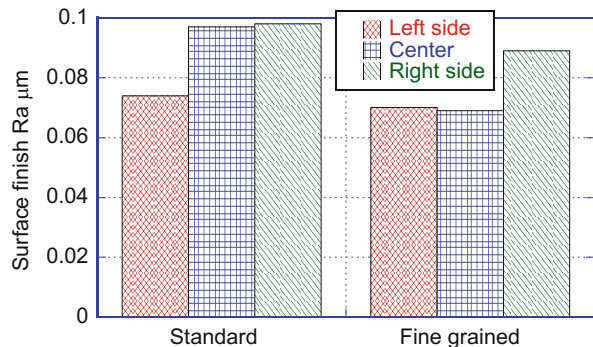


Fig. 20 Surface finishes in millings: (a) standard steel (average grain size $9.1 \mu\text{m}$); (b) fine-grained steel (average grain size $1.52 \mu\text{m}$). Cutting conditions are the same as those in Fig. 19

Fig. 21 Change in surface finish of removed area; cutting conditions are the same as those in Fig. 19



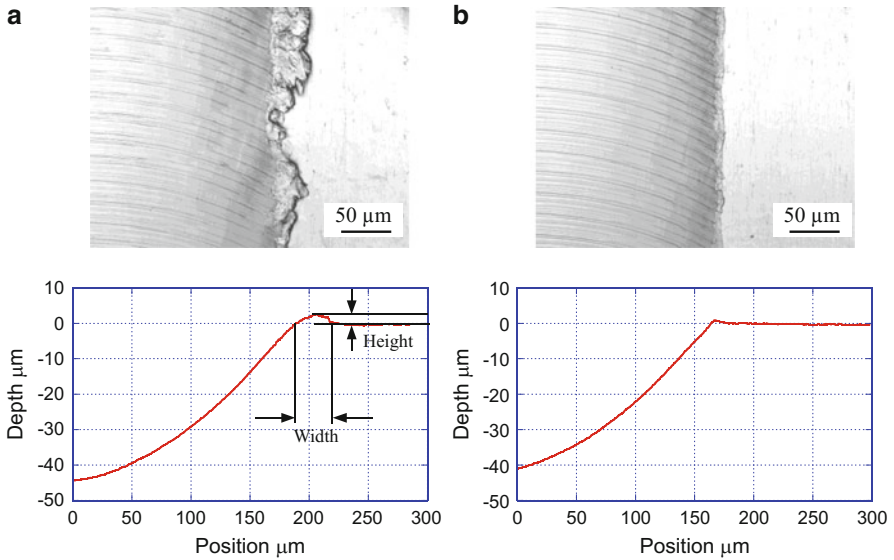


Fig. 22 Burrs on edges of grooves: (a) standard steel (average grain size 9.1 μm); (b) fine-grained steel (average grain size 1.52 μm). Cutting conditions are the same as those in Fig. 19

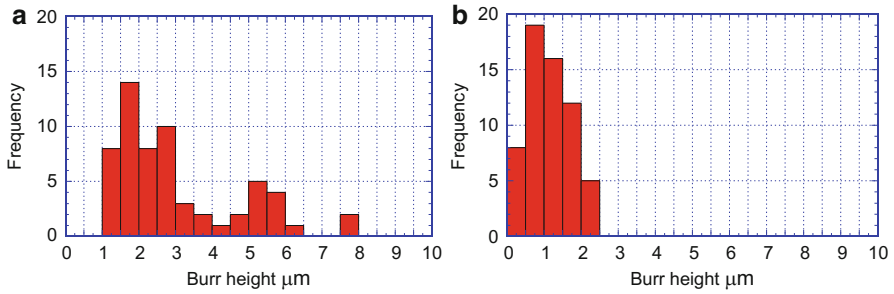


Fig. 23 Distributions in heights of burrs: (a) standard steel (average grain size 9.1 μm); (b) fine-grained steel (average grain size 1.52 μm). Cutting conditions are the same as those in Fig. 19

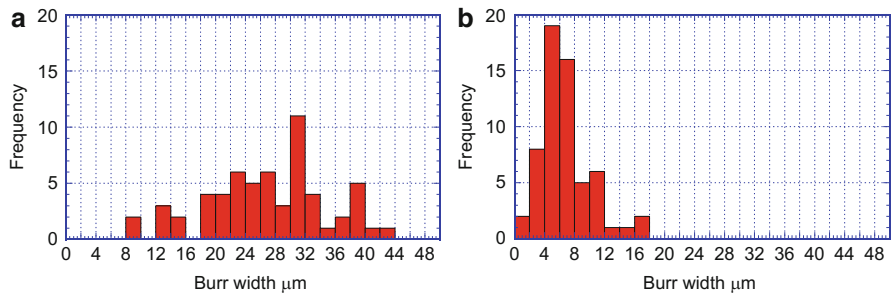


Fig. 24 Distributions in widths of burrs: (a) standard steel (average grain size 9.1 μm); (b) fine-grained steel (average grain size 1.52 μm). Cutting conditions are the same as those in Fig. 19

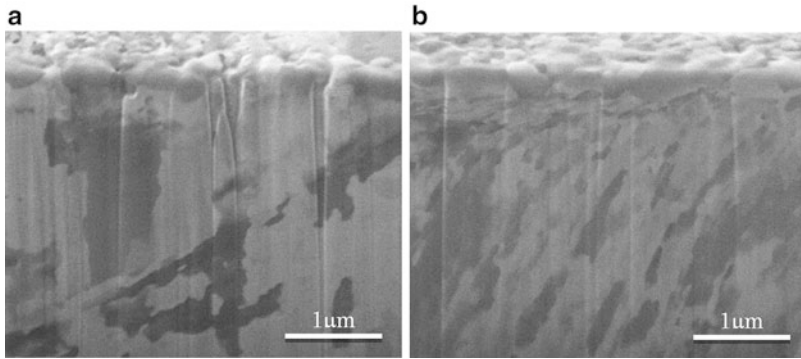


Fig. 25 Microstructures in subsurfaces of standard steel: (a) original; (b) machined. Cutting conditions are the same as those in Fig. 19

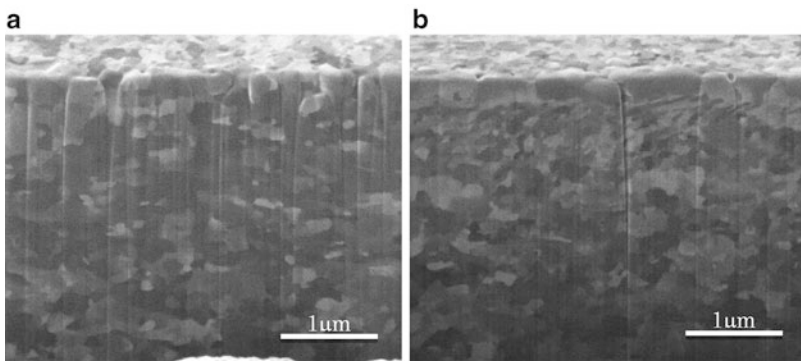


Fig. 26 Microstructures in subsurfaces of fine grained steel: (a) original; (b) machined. Cutting conditions are the same as those in Fig. 19

cut in sputtering by focused ion beam. Figures 25a and 26a are subsurfaces in the noncutting areas of the standard and the fine-grained steels. Different grain sizes are also confirmed as well as EBSD analysis shown in Fig. 13. Figures 25b and 26b are subsurfaces in the cutting area. Because the cutting edge moved from the left to the right hand, subsurface undergoes a certain force enough to large to deform in the cutting direction. The crystal grains of the standard steel deform largely into the inclined long shape. When the depths of the changed shapes of the crystal grains are measured, the deformation zone is estimated as more than $3\ \mu\text{m}$ in the standard steel; meanwhile, deformation occurs in depths of less than $1\ \mu\text{m}$ in milling of the fine-grained steel. The thickness of the affected layer largely depends on the grain size. According to the results in Fig. 19, the tangential component (X) in the cutting force of the fine-grained steel is less than that of the standard steel. The force reduction also suppresses deformation in subsurface as well as the effect of the grain size.

2.4 Micro Dimple Milling for Functional Surfaces

2.4.1 Machining Principle

This section shows the micro dimple milling with an inclined ball end mill and associates the surface structures with functionality, as an application of the micro milling. Here, the micro dimples are fabricated on the surfaces with a 2 flutes ball end mill. When the cutter axis is inclined and the depth of cut of less than the radius of a ball end mill, as shown in Fig. 27a, noncutting time, during which neither of the two cutting edges contacts the workpiece, appears in a rotation of the cutter. Figure 27b shows an example of the cutting force in milling of a groove on a glass surface with a ball end mill inclined at 45° . The noncutting process is confirmed when the cutting force is 0 during a rotation. If the feed rate of the milling tool is high enough that the removal areas of all edges are not overlapped each other, the concave dimples are machined periodically in each rotation of the cutter, as shown in Fig. 28.

The advantage in this process is high machining rates compared to the other fabrication processes. For instance, when a 2 flutes end mill rotates at a spindle speed of 20,000 rpm, 40,000 dimples are machined in a minute. Furthermore, the micro dimples are machined on a large surface in a short time, because the feed rate is higher than those of the conventional milling operations. Because the micro dimple milling is performed in depths of cut much less than the tool radius, the air cutting time is longer than the actual cutting during a rotation of the cutter. Therefore, the tool wear is suppressed by cooling in the air cutting. The milling manner also machines the dimples on the sculptured surfaces with controlling the depth of dimples by the numerical control (NC). In terms of the manufacturing process, the dimple milling is conducted as a surface fabrication after machining the product shape without material handling on a machine tool. Therefore, machining error induced by the material handling is excluded and the manufacturing time reduces with the nonproduction time.

Based on the milling process with the cutter axis inclination, the micro dimples are, in turn, machined on the cylinder surface, as shown in Fig. 29. In order to incline

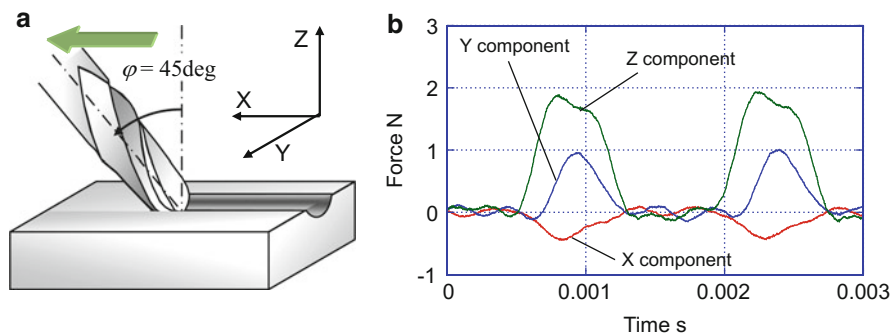


Fig. 27 Milling process with cutter axis inclination: (a) cutting with inclined ball end mill; (b) an example of cutting force. Cutting conditions: depth of cut, $20\ \mu\text{m}$; spindle speed, 2000 rpm; feed rate, $0.48\ \text{mm}/\text{min}$; and lubrication, water. Tool: material, carbide coated by TiAlN; and diameter, $0.4\ \text{mm}$

Fig. 28 Micro dimple milling with inclined ball end mill

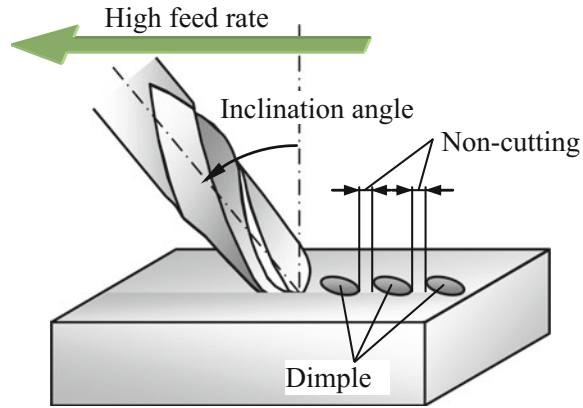
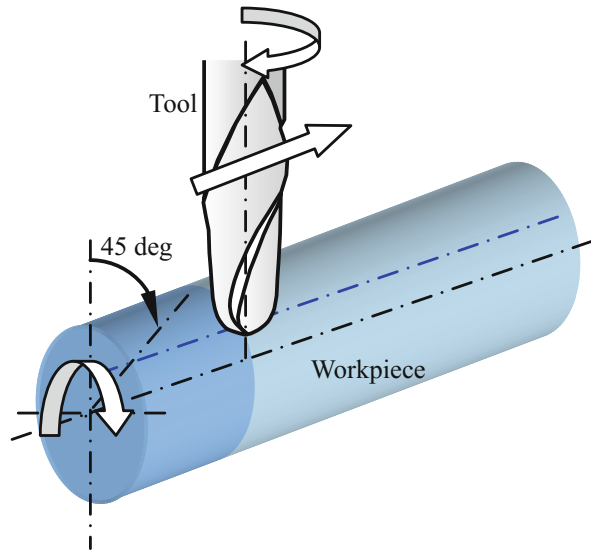


Fig. 29 Micro dimple milling on cylinder surface



the tool with respect to the tangential direction on the workpiece surface, the tool is located at a position oriented at 45° from the top of the workpiece. When the revolution rate of the workpiece and the feed rate of the tool are high enough that the removal areas are not overlapped each other, the micro dimples are machined independently.

2.4.2 Mechanistic Model in Micro Dimple Milling

2.4.2.1 Micro Dimple Milling on Flat Surface

The shape and the alignment of the micro dimples are controlled by the tool geometry and the cutting parameters. The edge on the ball end mill is defined in the coordinate system U-V-W, as shown in Fig. 30a, where ρ is the nose radius of the

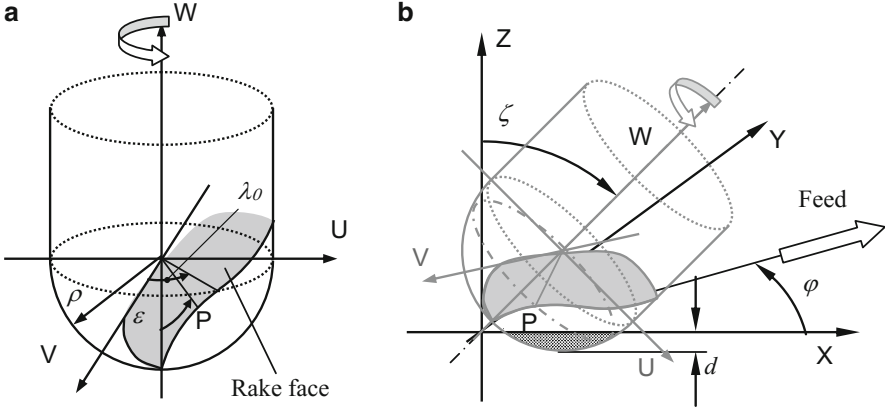


Fig. 30 Mechanistic model in micro dimple milling: (a) tool model; (b) removal model

tool and the origin in the coordinate system is located at the center of the nose radius. A Point P on an edge is given by angles ε and λ_0 . ε is the circumferential angle from the bottom of the tool, and the points on the ball nose edge are given in the range of $[0, 90]$ degrees. λ_0 is the delay angle at the end of the nose ($\varepsilon = 90^\circ$) with respect to the bottom edge. The delay angle of P on the i -th edge, γ , is given by:

$$\gamma = (i - 1) \frac{2\pi}{n} + \lambda_0 \cdot (1 - \cos \varepsilon) \quad (8)$$

When the tool rotates at an angular velocity ω_t , the coordinates (u, v, w) at P are given at time t :

$$\left. \begin{aligned} u &= \rho \sin \varepsilon \cos (\omega_t t + \gamma) \\ v &= \rho \sin \varepsilon \sin (\omega_t t + \gamma) \\ w &= -\rho \cos \varepsilon \end{aligned} \right\} \quad (9)$$

Figure 30b shows milling of the micro dimples with a ball end mill inclined at an angle ζ toward X direction in a feed direction of cutter φ with respect to X-axis. The dimples are machined in a depth d at a feed rate f . The coordinates (x, y, z) at P is given at time t :

$$\left. \begin{aligned} x &= \rho \sin \varepsilon \cos (\omega_t t + \gamma) \cos \zeta + \left(\frac{\rho - d}{\cos \zeta} - \rho \cos \varepsilon \right) \sin \zeta + f t \cos \varphi \\ y &= \rho \sin \varepsilon \sin (\omega_t t + \gamma) + f t \sin \varphi \\ z &= -\rho \sin \varepsilon \cos (\omega_t t + \gamma) \sin \zeta + \left(\frac{\rho - d}{\cos \zeta} - \rho \cos \varepsilon \right) \cos \zeta \end{aligned} \right\} \quad (10)$$

The removal shape is determined to satisfy $z < 0$ with changing t and ε .

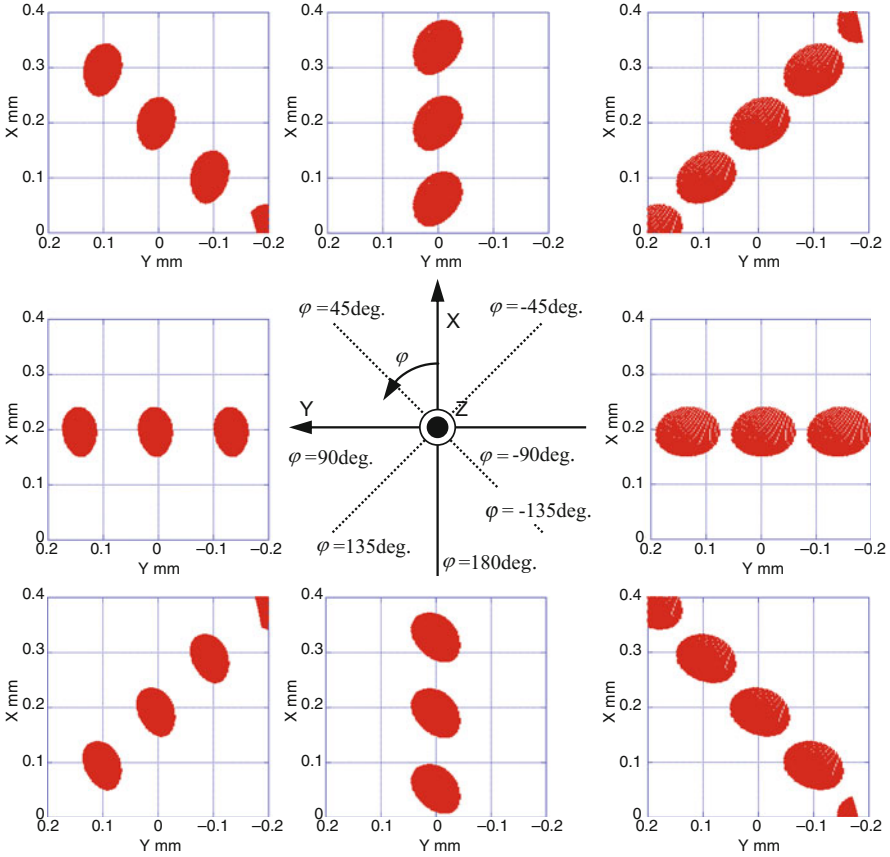


Fig. 31 Simulation of micro dimples machined

Figure 31 shows simulations of the dimples machined by a ball end mill inclined at 45° in the +X direction, where the figure views from +Z axis to X-Y plane. The feed direction changes with an increment of 45° , where φ in Fig. 30b is taken in the counterclockwise sense in this figure. The ball nose radius ρ is 0.2 mm, and the delay angle λ_0 is 20° . The feed rate, the depth of cut, and the spindle speed are 3300 mm/min, 5 μm , and 12,000 rpm, respectively. Because the dimples are machined by the rotation of the cutting edge and the feed of the end mill, the ellipsoidal dimples are shaped. The dimple shape and the apse line of the ellipse change with the feed direction. The edges engage the workpiece at the left side and exit at the right side of the dimple. Therefore, the width of the dimple becomes large when the end mill is fed in the negative Y direction.

The micro dimples are actually machined on an aluminum plate with a 0.4 mm diameter ball end mill at an inclination angle of 45° on a machining center. The cutter runout should be adjusted to fabricate the uniform dimples before the operations, as described in the Sect. 2.2. Figure 32a shows the dimples when the tool is fed at a feed rate of 3300 mm/min in the direction of X-axis ($\varphi = 0$ in Fig. 31). The depth of cut and the

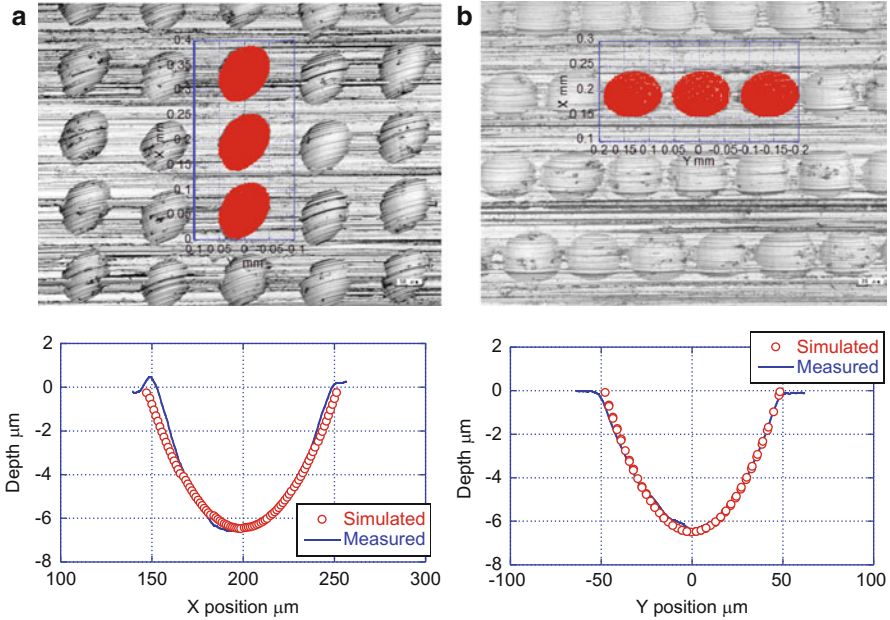


Fig. 32 Dimple profiles on aluminum plates: (a) end mill is fed from bottom to top ($\varphi = 0$ in Fig. 31); (b) end mill is fed from left to right ($\varphi = -90$ in Fig. 31)

spindle speed are $6.7 \mu\text{m}$ and $12,000 \text{ rpm}$, respectively. Figure 32b shows the dimples when the tool is fed at a feed rate of 2900 mm/min in the negative direction of Y-axis ($\varphi = -90$ in Fig. 31). The depth of cut and the spindle speed are $5 \mu\text{m}$ and $12,000 \text{ rpm}$, respectively. The simulation results are overlapped on the pictures in both results. The profiles of the dimples may also be simulated by the mechanistic model well.

2.4.2.2 Micro Dimple Milling on Cylinder Surface

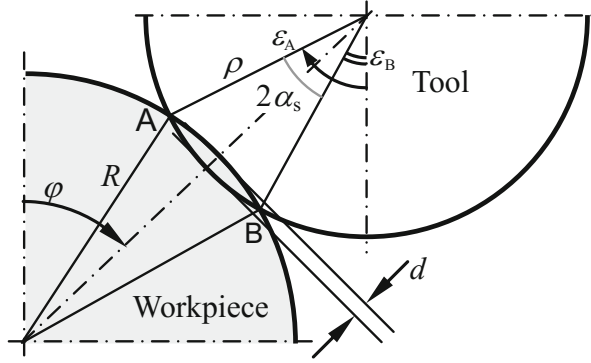
The edge on the ball end mill is defined in the coordinate system U-V-W, as shown in Fig. 30a, where ρ is the nose radius of the tool and the origin in the coordinate system is located at the center of the nose radius. When the tool rotates at an angular velocity of ω_t , the coordinates (u, v, w) of Point P are:

$$\left. \begin{aligned} u &= \rho \sin \varepsilon \cos (\omega_t t + \gamma) \\ v &= \rho \sin \varepsilon \sin (\omega_t t + \gamma) \\ w &= -\rho \cos \varepsilon \end{aligned} \right\} \quad (11)$$

When the rake face is defined with respect to the direction of rotation, as shown in Fig. 30a, ω_t is negative in U-V-W.

Figure 33 shows the contact area of an edge with the workpiece when the depth of cut is d . Points A and B are the highest and the lowest positions in the cutting area on

Fig. 33 Contact area of tool with workpiece



the edge, respectively. When the tool position is oriented at an angle φ from the top of the workpiece, positions A and B are associated with the angles ε_A and ε_B :

$$\left. \begin{aligned} \varepsilon_A &= \varphi + \alpha_s \\ \varepsilon_B &= \varphi - \alpha_s \end{aligned} \right\} \quad (12)$$

where α_s is a half of the contact angle with the workpiece:

$$\alpha_s = \cos^{-1} \left\{ \frac{\rho^2 + (R + \rho - d)^2 - R^2}{2\rho(R + \rho - d)} \right\} \quad (13)$$

The workpiece rotates at an angular velocity ω_w in the actual cutting operation. Meanwhile, in the analytical model, the tool is assumed to rotate around the workpiece at an angular velocity ω_w , as shown in Fig. 34a. Because the cutter axis is inclined at an angle φ with respect to the tangential direction on the workpiece surface, the tool is inclined at an angle of $\varphi - \omega_w t$. Thus, the coordinates of Point P on the edge in U-V-W are:

$$\left. \begin{aligned} u &= \rho \sin \varepsilon \cos (\omega_t t + \gamma) \cos (\varphi - \omega_w t) - \rho \cos \varepsilon \sin (\varphi - \omega_w t) \\ v &= \rho \sin \varepsilon \sin (\omega_t t + \gamma) \\ w &= -\rho \sin \varepsilon \cos (\omega_t t + \gamma) \sin (\varphi - \omega_w t) - \rho \cos \varepsilon \cos (\varphi - \omega_w t) \end{aligned} \right\} \quad (14)$$

When the tool moves in the axial direction at a feed rate f and the material is removed in a depth of cut d , as shown in Fig. 34b, the coordinates (x, y, z) of Point P in X-Y-Z at a time t are given as follows:

$$\left. \begin{aligned} x &= \rho \sin \varepsilon \cos (\omega_t t + \gamma) \cos (\varphi - \omega_w t) - \rho \cos \varepsilon \sin (\varphi - \omega_w t) + (R + \rho - d) \cos \omega_w t \\ y &= \rho \sin \varepsilon \sin (\omega_t t + \gamma) + ft \\ z &= -\rho \sin \varepsilon \cos (\omega_t t + \gamma) \sin (\varphi - \omega_w t) - \rho \cos \varepsilon \cos (\varphi - \omega_w t) + (R + \rho - d) \sin \omega_w t \end{aligned} \right\} \quad (15)$$

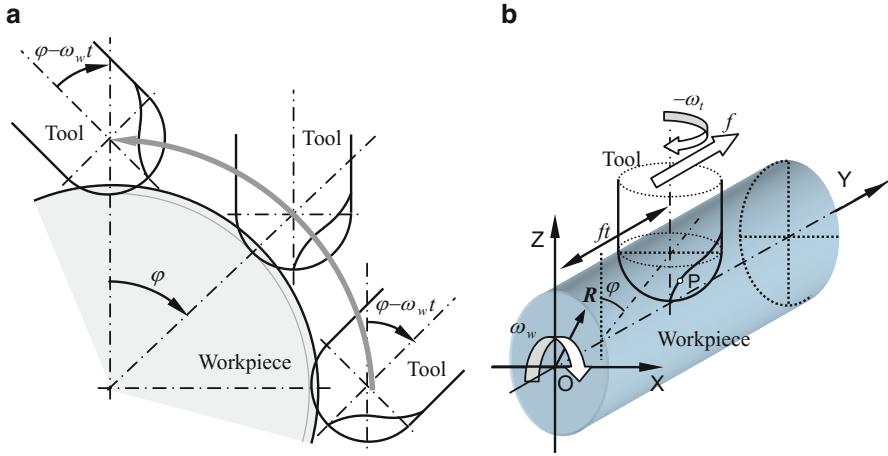


Fig. 34 Analytical model: (a) tool rotation around workpiece; (b) tool feeding along workpiece axis

The removal shape is determined to satisfy the following equation with changing t and ε :

$$\sqrt{x^2 + z^2} < R \quad (16)$$

The micro dimples were machined on an aluminum alloy cylinder with a ball end mill on a machine tool shown in Fig. 35. The diameter of the 2 flutes ball end mill was 0.4 mm and that of workpiece was 6 mm. The position of the tool is oriented at 45° from the top of the workpiece. Because the cutting operation requires high cylindricity of the workpiece, the workpiece was finished in longitudinal turning and polishing before the cutting tests. The cutter runout was also adjusted before the operation, as described in Sect. 2.2.

Figure 36 shows the micro dimples in a part of machining area and a surface profile of a dimple, where the simulated dimples and the profile are overlapped in both of figures. The analytical model works well to control the dimple shape. As may be seen from the edge of the dimple, no burr is observed. However, burr formation should be considered when the cutting parameters and the tool geometry are changed.

2.4.3 Surface Functions

2.4.3.1 Optical Function

The surfaces with the micro dimples may control the optical reflection. The optical reflection light can be observed in a booth filled with smoke, as shown in Fig. 37. Figure 38 shows the incident and the reflection lights on the flat and the dimpled surfaces, where the wavelength of the laser light was 532 nm. The light path reflected on the flat surface is observed clearly, as shown in Fig. 38a. On the other hand, the

Fig. 35 Machine tool for micro dimple milling on cylinder surface

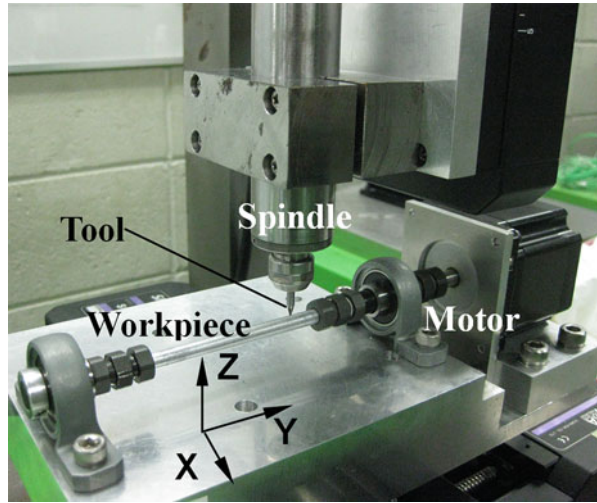
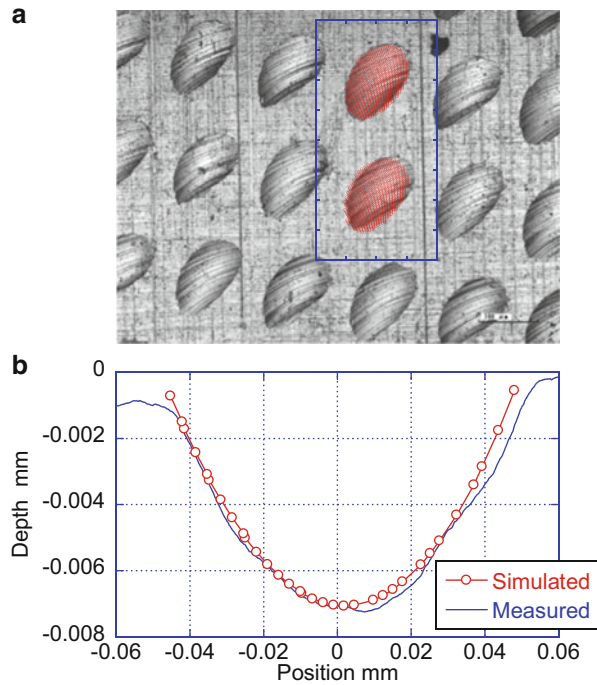


Fig. 36 Dimple profile on cylinder surface: (a) dimple shape; (b) surface profile



reflection is scattered on the dimpled surface in Fig. 38b. Although the light scattering is induced by the surface roughness in the dimples, the reflection range depends on the shape of the dimples. The profile of the dimples can be approximated as a circular arc

Fig. 37 Optical reflection test

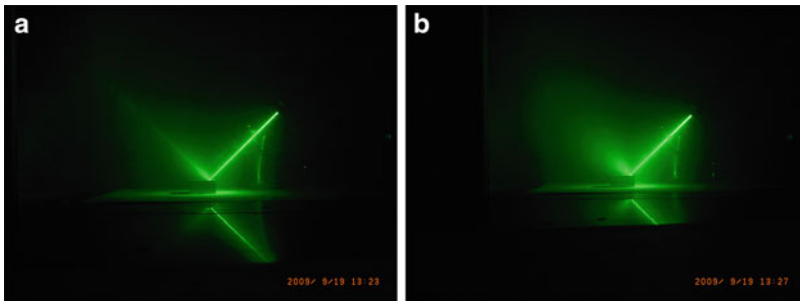
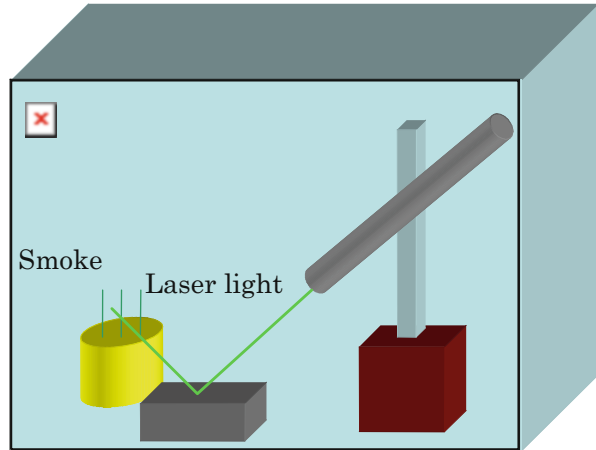


Fig. 38 Optical reflections on surfaces: (a) flat surface; (b) surface with micro dimples

connecting the edges around the dimple, as shown in Fig. 39. When the inclination angle of the tangent on the dimple surface is ξ , the light inclined at an incidence angle θ is reflected at $\theta - 2\xi$. Therefore, the maximum and the minimum reflection angle are given by the angles at the edge of the dimples.

2.4.3.2 Wettability

Wettability is measured by the dynamic contact angles of the liquid droplets onto the surface with the micro dimples, as shown in Fig. 40. Figure 41 compares the changes in the contact angles on a flat surface and a dimpled surface when the water volume increases from 0.5 to 1.5 μl at a rate of 0.075 $\mu\text{l/s}$. The water droplet on the flat surface expands continuously and thus nearly constant contact angle continues. Meanwhile, the contact angle on the dimpled surface increases when the water reaches the edge of the dimples at A in Fig. 41, and the angle becomes larger than 90° , which is regarded as a hydrophobic surface. Then, the contact angle decreases abruptly when the water is supplied over the critical volume at B. The discrete

Fig. 39 Reflection on micro dimple

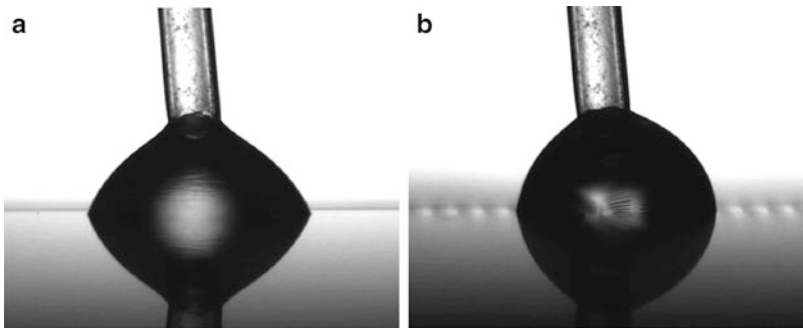
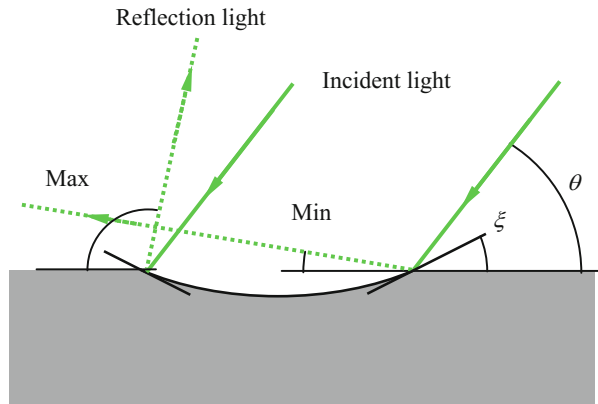
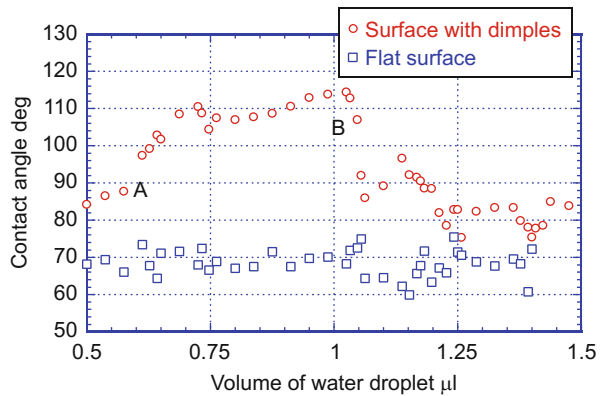


Fig. 40 Water droplets: (a) flat surface; (b) surface with micro dimples

Fig. 41 Change in dynamic contact angle



change in the contact angle is induced by the pinning effect at the edge of the dimples. The structured surface with the micro dimples changes the dynamic contact angles.

2.5 Conclusions

This chapter has been described the micro milling for manufacturing of the functional surfaces. The cutting process has many advantages in terms of control of three-dimensional shapes, flexibility on the operation, lower investment of the facilities than the other process, and lower energy consumption per unit material removal volume. The recent progresses in the high precision positioning and the miniaturized tool have realized the micro fabrications in mechanical manners. Then, the technical status in the mechanical removal process has achieved to control the surface structures for the functional surfaces.

In micro cutting, material behavior becomes critical in deformation of the crystal size. With the progress in the material science and technology, the grain sizes have been reduced to improve the physical and the chemical properties. The reduction of the grain sizes in material, then, brings high technical achievements in micro machining in terms of their accuracy and affected layer. The edge radius cannot be ignored to estimate the minimum chip thickness, which has an influence on the machining accuracy and the quality of the microscale structures on the surfaces. Burr formation should be controlled in the micro cutting as well as the conventional machining size. Especially, in micro cutting, the burr size is relatively large compared to the micro elements of the microstructured designed. Therefore, burr control is more critical issue in the micro cutting. The reduction of the crystal grain sizes also suppresses burr formation in this section.

The macro fabrication for the functional surfaces requires high production rates for large surface areas. A micro milling is shown to fabricate the micro dimples on the large surfaces at high production rates. In milling with inclination of the tool, the noncutting occurs during a rotation of the cutter. Then, the micro dimples are left on the surface at high feed rates so that the machining areas of all cutting edges are not overlapped each other. The principal may be extended to fabrication of the micro dimples on the cylinder surfaces. The mechanistic model controls the dimple shapes with the cutting parameters, the feed direction, and the tool geometry. Some examples have been shown to control the surface functions with the surface structures. Although the examples are simple, optical reflection and wettability may be controlled by the dimples on the surfaces.

Some applications of the functional surfaces will appear more according to the industrial demands in the future. In terms of implementation to manufacturing plants, the critical issues of the micro fabrication are high efficiency, controllability of the microstructures, flexibility for specified operation, and low running cost and initial investments.

References

- Basnyat P, Luster B, Muratore C, Voevodin AA, Haasch R, Zakeri R, Kohli P, Aouadi SM (2008) Surface texturing for adaptive solid lubrication. *Surf Coat Technol* 203:73–79

- Belyakov A, Sakai T, Miura H (2000) Fine-grained structure formation in austenitic stainless steel under multiple deformation at 0.5Tm. *Mater Trans Jpn Inst Met Mater* 41:476
- Bruzzone AAG, Costa HL, Lonardo PM, Lucca DA (2008) Advances in engineered surfaces for functional performance. *CIRP Ann Manuf Technol* 57:750–769
- Chae J, Park SS, Freiheit T (2005) Investigation of micro-cutting operations. *Int J Mach Tool Manuf* 46:313–332
- Chae J, Park SS, Freiheit T (2006) Investigation of micro-cutting operations. *Int J Mach Tools Manuf* 46:313–332
- Choi Y, Choo WY, Kwon D (2001) Analysis of mechanical property distribution in multiphase ultra-fine-grained steels by nanoindentation. *Scr Mater* 45:1401–1406
- Filiz S, Ozdoganlar OB (2008) Microendmill dynamics including the actual fluted geometry and setup errors – part I: model development and numerical solution. *J Manuf Sci E T ASME* 130:031119-1–031119-10
- Jun MBG, Liu X, Devor RE, Kapoor SG (2006) Investigation of the dynamics of microend milling – part I: model development. *J Manuf Sci E T ASME* 128:893–900
- Kim CJ, Mayor JR, Ni J (2004) A static model of chip formation in microscale milling. *J Manuf Sci E T ASME* 126:710–718
- Kim TI, Dongha T, Hong HL (2009) Wettability-controllable super water- and moderately oil-repellent surface fabricated by wet chemical etching. *Langmuir* 25:6576–6579
- Kogusu S, Ishimatsu T, Ougiya Y (2007) Rapid generation of surface dimples using end milling. *Int J Autom Technol* 1:45–51
- Komatsu T, Matsumura T, Torizuka S (2011) Effect of grain size in stainless steel on cutting performance in micro-scale cutting. *Int J Autom Technol* 5:334–341
- Krupenkin NT, Taylor JA, Schneider MT, Yang S (2004) From rolling ball to complete wetting: the dynamic tuning of liquids on nanostructured surfaces. *Langmuir* 20:3824–3827
- Liu X, DeVor RE, Kapoor SG, Ehmann KF (2004) The mechanics of machining at the microscale: assessment of the current state of the science. *J Manuf Sci E T ASME* 126:666–678
- Luo X, Wang Y, Chen P, Zhou L (2011) Investigation of CO₂ laser beam modulation by rotating polygon. *Opt Lasers Eng* 49:132–136
- Matsumura T, Takahashi S (2011) Machining of micro dimples in milling for functional surfaces. *AIP Conf Proc* 1353:567–572
- Matsumura T, Takahashi S (2012) Micro dimple milling on cylinder surfaces. *J Manuf Process* 14:135–140
- Murty SVSN, Torizuka S, Nagai K (2005) Microstructural and micro-textural evolution during single pass high Z-large strain deformation of a 0.15%C steel. *Iron Steel Inst Jpn Int* 45:1651–1657
- Nagayama S, Torizuka S, Komatsu T (2008) Test production for ultra fine grain SUS 304 stainless steel with cold rolling and clad rolling. The Proceedings of the 2008 Japanese spring conference for the technology of plasticity: 341
- Perez H, Vizan A, Hernandez JC, Guzman M (2007) Estimation of cutting forces in micromilling through the determination of specific cutting pressures. *J Mater Process Technol* 190:18–22
- Rajasekhara S, Ferreira PJ, Karjalainen LP, Kyröläinen A (2007) Hall–Petch behavior in ultra-fine-grained AISI 301LN stainless steel. *Metall Mater Trans A* 38:1202–1210
- Sommers AD, Jacobi AM (2006) Creating micro-scale surface topology to achieve anisotropic wettability on an aluminum surface. *J Micromech Microeng* 16:1571–1578
- Takaki S, Kawasaki K, Kimura Y (2001) Mechanical properties of ultra fine grained steels. *J Mater Process Technol* 117:359–363
- Umamoto M (2000) Formation of nanocrystalline structure by severe plastic deformation. *Feram* 781
- Voevodin AA, Zabinski JS (2006) Laser surface texturing for adaptive solid lubrication. *Wear* 261:1285–1292
- Wakuda M, Yamauchi Y, Kanzaki S, Yasuda Y (2003) Effect of surface texturing on friction reduction between ceramic and steel materials under lubricated sliding contact. *Wear* 254:356–363

-
- Wan DP, Chen BK, Shao YM, Wanga SL, Hu DJ (2008) Microstructure and mechanical characteristics of laser coating–texturing alloying dimples. *Appl Surf Sci* 255:3251–3256
- Wang YQ, Wu GF, Han QG, Fang L, Ge SR (2009) Tribological properties of surface dimple-textured by pellet-pressing. *Procedia Earth Planet Sci* 1:1513–1518
- Weule H, Huntrup V, Tritschle H (2001) Micro-cutting of steel to meet new requirements in miniaturization. *Ann CIRP* 50:61–64
- Zhu D, Qu NS, Li HS, Zeng YB, Li DL, Qian SQ (2009) Electrochemical micromachining of microstructures of micro hole and dimple array. *CIRP Ann Manuf Technol* 58:177–180



Micro Cylindrical Turning of Calcium Fluoride

3

Yasuhiro Kakinuma and Yuta Mizumoto

Contents

3.1	Introduction	68
3.2	Basics for Ultra-Precision Turning of CaF ₂	69
3.2.1	Brittle–Ductile Transition	69
3.2.2	Subsurface Damage	70
3.3	Experimental Setup of Cylindrical Turning	71
3.4	Evaluation of Surface Morphology and Surface Roughness	73
3.4.1	Process Parameter	73
3.4.2	Crystal Anisotropy	75
3.4.3	Tool Geometry	82
3.5	Evaluation of Subsurface Damage	84
3.5.1	Process Parameter	85
3.5.2	Crystal Anisotropy	87
3.6	Summary and Outlook	92
	References	94

Abstract

Single-crystalline CaF₂ is one of the key materials for next-generation micro-optical devices, such as optical microcavities, because of its excellent performance in a wide range of wavelength regimes. Nevertheless, typical chemical processes such as etching are not applicable to the fabrication process in this case, because the material has crystal anisotropy and a complex shape is required. The most feasible and promising approach is ultra-precision cutting. Here, the machinability of CaF₂ in micro cylindrical turning and its influence on surface integrity are described based on detailed experimental results. It is clarified that the machined surface integrity varies in dependency with cutting crystalline

Y. Kakinuma (✉) · Y. Mizumoto
Department of System Design Engineering, Keio University, Yokohama, Japan
e-mail: kakinuma@sd.keio.ac.jp

planes and directions, and the surface morphology, surface roughness, and critical depth of cut change according to its crystalline structure.

Keywords

Single-crystalline CaF₂ · Ultra-precision cutting · Cylindrical turning · Crystal anisotropy · Subsurface damage

3.1 Introduction

Single-crystalline CaF₂ shows excellent characteristics in a wide range of wavelength regimes, such as high permeability and anomalous dispersion. The crystal structure is categorized as a cubic fluorite structure, which consists of the Ca²⁺ ions arranged in a face-centered cubic lattice and F⁻ ions in a cubic lattice. The lattice constant is given as 0.54603 nm, so CaF₂ belongs to the space group Fm3m (Bezuidenhout 1997). The cubic fluorite structure shows a Mohs hardness of 4 (Knoop hardness value of 158.3 N/mm²). Although CaF₂ is a relatively soft material in minerals, it is a brittle material which originated from cleavage (Janicki et al. 2016). CaF₂ has an excellent transparency in the range of 125 nm to 10 μm wavelength, i.e., from the deep ultraviolet spectral regime to the infrared light regime, and its reflection rate between two planes is 5.6%, which is much lower than for other optical crystalline materials. Moreover, it shows anomalous dispersion and cancels out the effect of aberrations in the optic system. Additionally, CaF₂ is less deliquescent than other crystalline materials (Yoshizawa 2009); therefore, one can use CaF₂ in a physically and chemically stable condition. The material properties of CaF₂ are listed in Table 1. Because of its excellent optical property, CaF₂ is widely used in the industry, e.g., in spectroscopic mirrors (Schick et al. 2004), 157 nm lithography systems (Lieberman et al. 1999), and optical windows (Reichling et al. 1996). However, CaF₂ is characterized by brittleness and crystal anisotropy, and the optical devices prohibit the existence of cracks. To achieve a fine surface quality, a polishing process needs to be employed after the cutting or grinding process. However, polishing a complicated geometry part (e.g., aspherical lenses, diffraction gratings, and microcavities) is still challenging and inevitably deteriorates the form accuracy. From the viewpoint of both surface quality and form accuracy, the ultra-precision machining process is a promising approach for fabrication of complicated shapes (Chen et al. 2017a).

Research on ultra-precision cutting of CaF₂ has been conducted for decades. Furukawa compared the machinabilities of single-crystalline materials, polycrystalline materials, and amorphous materials on an ultra-precision scale. CaF₂ was selected as one of the materials, and the anisotropy on the machined surface was found in which cleavage took a key role (Furukawa and Moronuki 1988). Yan investigated the cutting mechanisms of CaF₂ in more detail and discussed the influence of negative rake angle, lubricant, and crystallographic effects in the face-turning process (Yan et al. 2004a, b). Referring to the achievement of Yan's research,

Table 1 Material properties of CaF₂

Parameter	Value	Ref.
Permeable wavelength [μm]	0.125–12	Technical Document
Reflection loss [%]	5.6 (4 μm wavelength)	Technical Document
Knoop hardness [kg/mm^2]	158.3	Technical Document
Young's modulus [GPa]	75 (25 °C)	Yan et al. 2004b
Thermal conductivity [$\text{cal}/\text{cm s}^\circ\text{C}$]	2.32×10^{-2}	Technical Document
Coefficient of thermal expansion [$1/^\circ\text{C}$]	24×10^{-6} (20–60 °C)	Technical Document
Melting point [$^\circ\text{C}$]	1360	Technical Document
Specific heat [$\text{cal}/\text{g}^\circ\text{C}$]	0.204 (0 °C)	Technical Document
Fracture toughness [$\text{MPa}\cdot\text{m}^{1/2}$]	0.4–0.6	Chen et al. 2017b

Grudinin succeeded in manufacturing whispering gallery mode (WGM) CaF₂ cavities (Grudinin et al. [2006](#)). Meanwhile, the similar anisotropic behavior for surface integrity was observed in the grinding process by Namba (Namba et al. [2005](#)). Namba also conducted ultra-precision float polishing on the CaF₂ ground surface whose crystalline structures were regularly aligned, i.e., a strain-free surface was achieved (Namba et al. [2004](#)). Recently, Wang noticed that asymmetric crystal anisotropy existed in a single groove in plunge-cut tests (cracks were observed on one side of the single groove). Wang used a crystal plasticity finite-element method (FEM) that assimilates slip rate to analyze the mechanism (Wang et al. [2016](#)). For quantitative analysis of crystal anisotropy, the fracture toughness parameter was recently employed by Chen (Chen et al. [2017b](#)).

3.2 Basics for Ultra-Precision Turning of CaF₂

3.2.1 Brittle–Ductile Transition

Brittleness has been one of the challenges in the cutting of CaF₂, as well as ceramics. Unlike for metals, the deformation mechanism of brittle materials is not governed by ductility. Therefore, it is well known that cracking initiates in conventional cutting or grinding. This indicates that brittle materials show ductility in some regions, and Bifano (Bifano et al. [1989](#)) first proposed that there is a ductile regime in the machining of brittle materials. It was found that fused silica can be cut in a ductile regime when uncut chip thickness is set as less than the critical value, by analogy with metal cutting, i.e., a brittle–ductile transition (BDT) existed. Consequently, interest in ductile-regime machining of brittle material expanded worldwide. A classical cutting model for brittle materials was first proposed by Blake and Scattergood for the turning of germanium and silicon (Blake and Scattergood [1990](#)). As shown in Fig. 1, when feeding a cutting tool constantly, its uncut chip thickness differs from the cutting points, and critical uncut chip thickness t_c is defined as the point where the first crack occurs. A side view of the model shows a

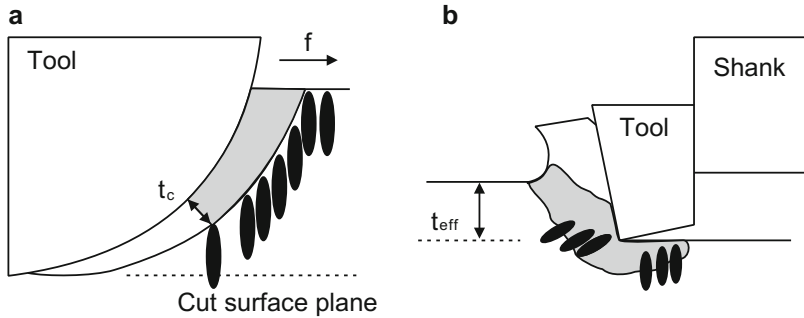


Fig. 1 Model for ductile-regime machining with nose round tool: (a) front view of the model; (b) side view of the model. (Blake PN, Scattergood RO. Ductile-Regime Machining of Germanium and Silicon. *J Am Ceram Soc* 1990;73(4):949–57. Reprinted with permission from John Wiley & Sons) (Blake and Scattergood 1990).

quasi-orthogonal cutting model, and cracking occurs when the depth of cut exceeds a critical uncut chip thickness. It is essential to identify the critical uncut chip thickness of each brittle material in this procedure.

Blake and Scattergood also noticed that a negative rake angle of the cutting tool could enhance the ductility of brittle materials and increase the critical uncut chip thickness. It was assumed that the compression stress in front of the cutting edge increased and suppressed the formation of brittle fractures. The discussion is supported by various works to clarify that hydrostatic pressure stress fields are formed by a negative rake angle tool and the field promoted plastic deformation in the cutting of brittle materials (Yan et al. 2004a, b; Fang and Chen 2000; Nakasuji et al. 1990; Yan et al. 2000, 2002, 2009, 2012).

Investigation of slip and cleavage is necessary for the cutting of brittle materials. As shown in Fig. 2, on the one hand, slip promotes the ductile fracture of materials, i.e., plastic deformation; on the other hand, cleavage is a trigger for brittle fracture. In ultra-precision cutting, the activated deformation based on dislocation at an atomic level must be considered, because it strongly affects the surface integrity. The phenomenon is known as “crystal anisotropy,” and the surface quality greatly depends on the crystal planes or crystal directions during cutting. There has been much work regarding the influence of crystal anisotropy on surface quality in the machining of CaF_2 (Chen et al. 2017a; Yan et al. 2004b; Wang et al. 2016; Marsh et al. 2005).

3.2.2 Subsurface Damage

While surface roughness indicates the geometrical evaluation of the surface quality, subsurface damage means a change of the inner structure of the material, which affects fatigue strength, residual stress, or optical performance. This is caused by the

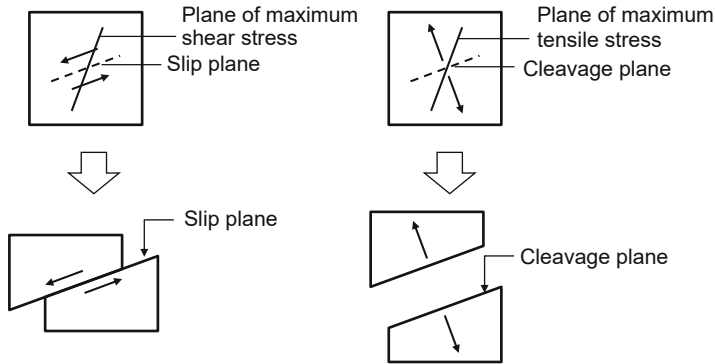


Fig. 2 Model for the deformation mechanism related to the cutting process: (a) slip; (b) cleavage. (Nakasuji T, Kodera S, Hara S, Matsunaga H, Ikawa N, Shimada S. *Diamond Turning of Brittle Materials for Optical Components*. CIRP Ann-Manuf Techn 1990;39(1):89–92. Reprinted with permission from Elsevier B.V.)

extensive plastic flow under high temperature and high pressure in the cutting process. Then, the subsurface damage indicates the layer that shows a different material property from the base material. The layer causes the variation in the crystal structure, hardness, or residual stress. In general, the subsurface layer can be suppressed by increasing the shear angle, setting a cutting condition to decrease the stress concentration region, or supplying lubricant. However, the mechanism of subsurface generation strongly depends on the material property of the workpiece or machining process; therefore, subsurface damage has been discussed in the machining field and the material science field, including measurement methods and repairing (relaxing) methods (Jawahir et al. 2011; Lucca et al. 1998; Inasaki 2009). Various types of measurement or methods for analysis of subsurface damage caused by ultra-precision machining have been proposed, e.g., transmission electron microscopy (TEM) observation (Namba et al. 2004; Wang et al. 2016; Yan et al. 2012), Raman spectroscopy (Yan et al. 2008; Wermelinger et al. 2007), and stress releasing by etching (Namba et al. 2005; Gu et al. 2011). TEM observation makes it possible to observe the crystalline lattice arrangement in the subsurface layer directly; therefore, this technique is well utilized for the analysis of crystalline materials.

3.3 Experimental Setup of Cylindrical Turning

Ultra-precision cylindrical turning (UPCT) of CaF_2 was conducted using an ultra-precision aspheric surface machine tool (ULG-100E, Toshiba Machine Ltd.). A CaF_2 cylinder workpiece with 35 mm length and 6 mm diameter was prepared. The CaF_2 was fixed in a brass jig by wax and then clamped by a collet chuck (Fig. 3). The collet chuck was mounted onto a vacuum chuck. The crystal orientation of the

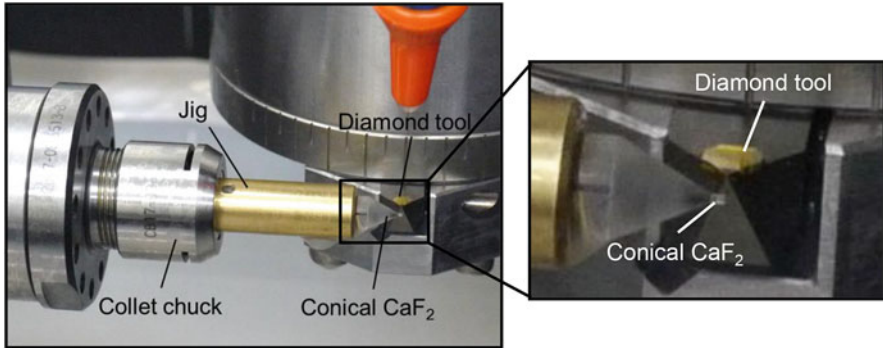


Fig. 3 Experimental setup of UPCT. (Azami S, Kudo H, Mizumoto Y, Tanabe T, Yan J, Kakinuma Y. Experimental study of crystal anisotropy based on ultra-precision cylindrical turning of single-crystal calcium fluoride. *Precis Eng* 2015;40:172–81. Reprinted with permission from Elsevier B.V.)

end face was set as (100), (110), or (111). First, a workpiece was turned in the brittle regime (rough cutting) to form a CaF_2 cone with 1 mm diameter under the following cutting conditions: 1000 min^{-1} rotational speed, $20 \mu\text{m/rev}$ feed per revolution, and $2 \mu\text{m}$ depth of cut. After rough cutting, prefinish cutting was conducted to eliminate the large cracks under the following cutting conditions: 1000 min^{-1} rotational speed, $3.0 \mu\text{m/rev}$ feed per revolution, 100 nm depth of cut, and $5 \mu\text{m}$ total removal depth. Finally, the surface was finished by ductile-regime cutting with $1 \mu\text{m}$ total removal depth.

Variation in the conditions of finish cutting is listed in Table 2. Single-crystal-line diamond (SCD) tools with different geometries were used. The specification of the tools is listed in Table 3. The depth of cut a_p in a radial direction is set to 50 nm . It was assumed that it was possible to obtain the entire surface without cracks according to the quasi-turning model (Blake and Scattergood 1990) (see Fig. 1). The machined surface quality of CaF_2 depends on crystalline planes and directions because of the anisotropy. Because of the cutting of crystalline planes and directions simultaneously and continuous change in cylindrical turning, the whole cylindrical surface needed to be evaluated. The entire surface was divided into 24 points along the circumference, and the surface morphologies and surface roughness S_a at each point were observed by optical microscope (VHX-600 and VHX-5000, Keyence) and the white light interferometer (WLI) (New View 6200, Zygo). Each observation point was named in the order of the Roman alphabet (Fig. 4), and the observation point (a) was determined to be 0° (starting point). For each end face, the observation point (a) was identified by $[010]$ for (100), $[\bar{1}\bar{1}1]$ for (110), and $[01\bar{1}]$ for (111) (see Fig. 4). The machined surface was characterized by some symmetry based on the crystal structure, so the observation points for evaluation of surface morphologies were cut down, depending on the crystal orientation of the end face. For example, six observation points were set in the case of the (100) plane – see Fig. 4a.

Table 2 Variation in process parameters of the UPCT tests

Parameter	Value
Cutting speed V_f [m/min]	0.94, 2.20, 3.14, 4.71
Rotational speed T [min^{-1}]	300, 700, 1000, 1500
Feed per revolution f [$\mu\text{m}/\text{rev}$]	0.1, 0.3, 0.7, 1, 3, 5, 7
Depth of cut a_p [nm]	50
Orientation of end face of workpiece	(100), (110), (111)
Lubricant	Water-soluble oil (diluted by 1:100 ratio)

Table 3 Specification of the tools used in UPCT tests

Specification	Tool #1	Tool #2	Tool #3
Nose radius R [mm]	0.2	0.05	0.01
Rake angle α [$^\circ$]	-20	0	0
Open angle [$^\circ$]	90	40	40
Orientation of rake face	(100)	(100)	(100)

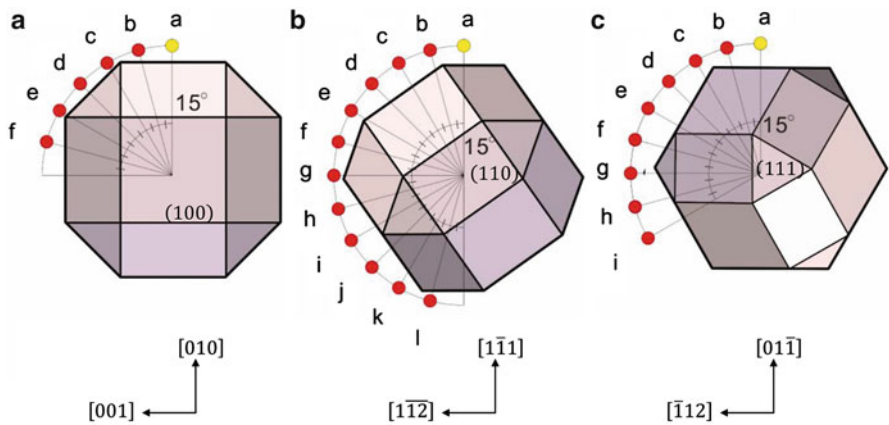
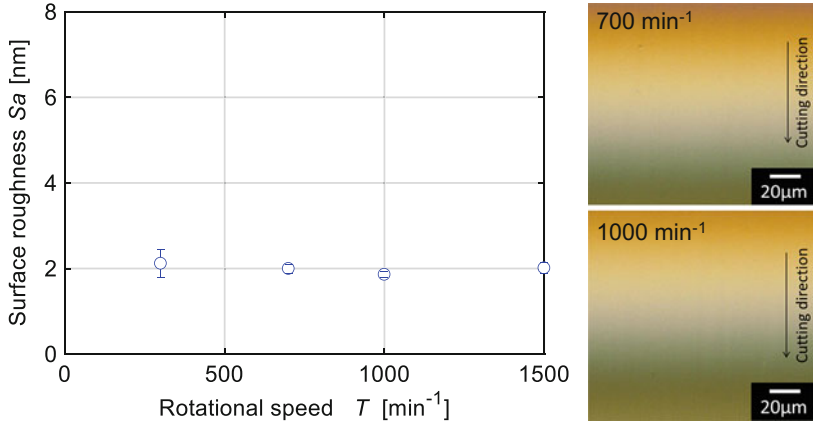


Fig. 4 Crystallographic diagrams of the observation points, which are viewed from the end face: (a) (100), (b) (110), and (c) (111) planes. (Azami S, Kudo H, Mizumoto Y, Tanabe T, Yan J, Kakinuma Y. Experimental study of crystal anisotropy based on ultra-precision cylindrical turning of single-crystal calcium fluoride. *Precis Eng* 2015;40:172–81. Reprinted with permission from Elsevier B.V.)

3.4 Evaluation of Surface Morphology and Surface Roughness

3.4.1 Process Parameter

For each test, the crystal orientation of the end face of CaF_2 was set to (100). The surface roughness Sa values at 24 measured points were averaged. Variation in the surface roughness Sa depending on rotational speed T and feed per revolution f is



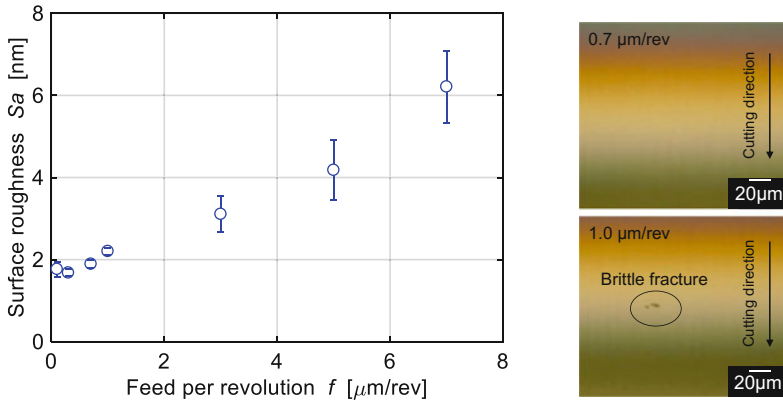
Workpiece:	Cutting tool:	Process parameter:
Material: CaF_2	Type: SCD	Rotational speed T [min^{-1}]: Variable
Orientation of end face: (100)	Rake angle α [$^\circ$]: -20	Feed per revolution f [$\mu\text{m}/\text{rev}$]: 1.0
	Nose radius R [mm]: 0.2	Depth of cut a_p [nm]: 50

Fig. 5 Variation in surface roughness S_a in accordance with rotational speed T .

shown in Figs. 5 and 6, respectively. The surface roughness was not affected by rotational speed (cutting speed). The maximal rotational speed of the work spindle was 1500 min^{-1} , and, because the diameter of the workpiece did not exceed 1 mm, it was not necessary to investigate deeply the influence of cutting speed in this study. Determining that a 1000 min^{-1} rotational speed T was optimal in this test, the following tests were performed. Compared to the cutting speed, a feed per revolution affected the surface quality more. Although the surface was smooth in the low-feed regime ($f = 0.1\text{--}0.7 \mu\text{m}/\text{rev}$), the brittle fracture began to exhibit more than a $1.0 \mu\text{m}/\text{rev}$ feed per revolution (see Fig. 6), and the S_a value increased. In turning, the critical uncut chip thickness was determined by combination of a_p and feed per revolution (Blake and Scattergood 1990, 1991). Even if the a_p was smaller than the critical depth of cut (CDC) value, the feed per tooth was too large, and the cutting mode turns into brittle regime. The maximal uncut chip thickness d_{max} is given as follows (Liu et al. 2009):

$$d_{max} = R - \sqrt{R^2 + f^2 - 2f\sqrt{2Ra_p - a_p^2}} \quad (1)$$

For $1 \mu\text{m}/\text{rev}$ feed per revolution f , the d_{max} can be calculated as approximately 20 nm. This value is much lower than the minimal value of the CDC in the plunge-cut tests (approximately 50 nm) (Azami et al. 2015). One of the reasons might be the size of the workpiece. Because the size of the workpiece is very small (cylinder of 1 mm diameter and 1–2 mm length), the ratio of a_p to the diameter of the workpiece increases, and the cylindrical workpiece becomes easily deflected by the cutting



<u>Workpiece:</u>	<u>Cutting tool:</u>	<u>Process parameter:</u>
Material: CaF_2	Type: SCD	Cutting speed T [min^{-1}]: 1000
Orientation of end face: (100)	Rake angle α [$^\circ$]: -20	Feed per revolution f [$\mu\text{m}/\text{rev}$]: Variable
	Nose radius R [mm]: 0.2	Depth of cut a_p [nm]: 50

Fig. 6 Variation in surface roughness S_a in accordance with feed per revolution f

force. Therefore, the cutting process can be much more unstable owing to the thrust force between the tool and the workpiece compared with face turning or plunge-cut. In addition, the surface quality can be influenced by edge geometry, i.e., the size effect. It is assumed that plowing could be conducted due to the influence of the edge radius. Nevertheless, the surface quality is enhanced in a low-feed regime. It can be said that the cutting edge is extremely sharp, e.g., less than 10 nm, as shown by Sumiya (Sumiya et al. 2012).

3.4.2 Crystal Anisotropy

The machined surface strongly relates to the cutting crystalline planes and directions in UPCT, as well as the results of the plunge-cut. The S_a values and surface morphologies are characterized by threefold symmetry when the end face is set as (111), as shown in Figs. 7 and 8. The surface morphologies at observation points (a) and (e) are smooth, and their crystalline planes and cutting directions correspond to (110) planes and 90° directions in the plunge-cut tests where the CDC values were high (Mizumoto and Kakinuma 2018). When one cuts at observation points (b)–(d) and (f)–(g), some cracks appear with some directions, e.g., the microtorn fracture runs along the cleavage planes (Fig. 9).

A strong dependence on the crystal anisotropy is seen in the case of the end face (110) plane (see Figs. 10 and 11). The surface morphologies and CDC values exhibit twofold symmetry, i.e., the symmetric cycle appears at every 180° . Analogous to the case of the (111) end face, a qualitative discussion can be done. Although the cutting

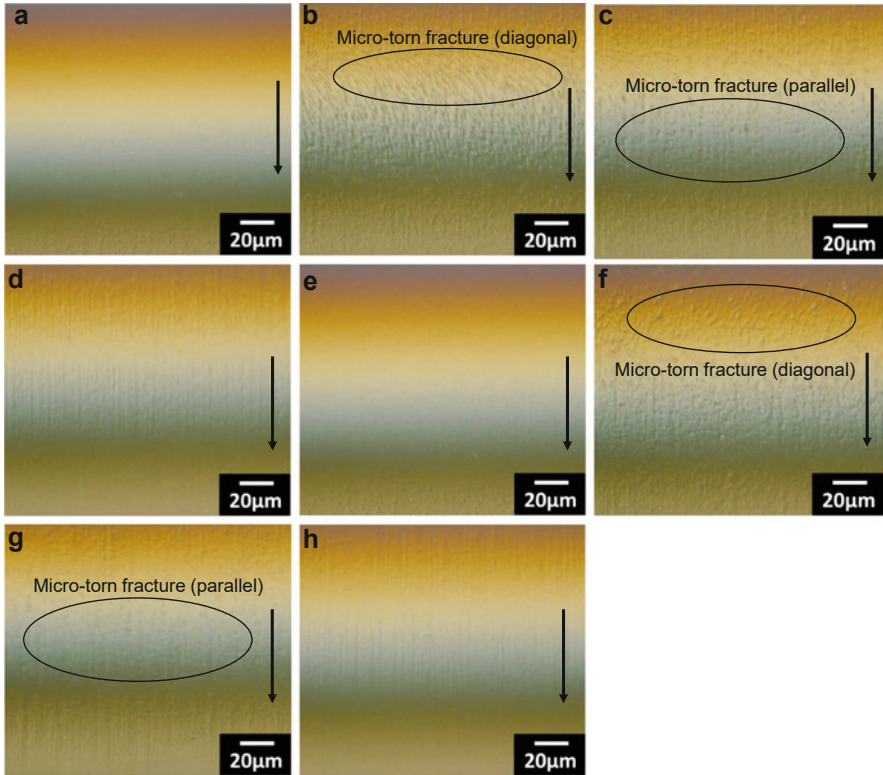


Fig. 7 Surface morphologies of the machined cylindrical surface with end face (111): each point corresponds to the observation points of Fig. 4c; a black arrow indicates a cutting direction. (Azami S, Kudo H, Mizumoto Y, Tanabe T, Yan J, Kakinuma Y. Experimental study of crystal anisotropy based on ultra-precision cylindrical turning of single-crystal calcium fluoride. *Precis Eng* 2015;40:172–81. Reprinted with permission from Elsevier B.V.)

crystalline plane is the same at observation points (a) and (f), the machined surface is rough at (a), whereas a smooth surface was obtained at (f). However, the CDC value is high in the direction of 90° , i.e., at (e). A microtorn fracture that runs parallel to the cutting direction at observation point (d) and the sculpted fracture at observation point (e) were seen, both of which are assumed to be induced by $\{110\}$ cleavages (see Fig. 12).

A pyramidal fracture was seen at observation point (g). It is a well-known fracture induced by $\{111\}$ cleavage. The surface quality at observation points (h) through (k) is apt to be smooth. Considering the crystallographic diagrams at (i), (j), the cutting crystalline plane and cutting directions relatively correspond to the (100) plane and the [011] directions.

The CDC value was high in the case of the (100) plane and 0° , 90° , 180° , and 270° cutting directions; thus, near the cutting (100) plane and [011] directions, the ductility is high, and the corresponding machined surface can be smoother. It should

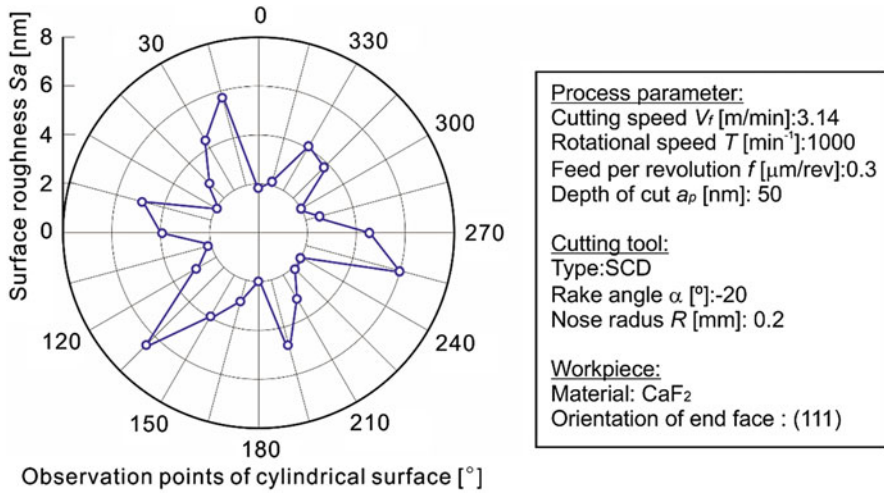


Fig. 8 Variation in surface roughness S_a in accordance with crystal anisotropy, (111) end face. (Azami S, Kudo H, Mizumoto Y, Tanabe T, Yan J, Kakinuma Y. Experimental study of crystal anisotropy based on ultra-precision cylindrical turning of single-crystal calcium fluoride. *Precis Eng* 2015;40:172–81. Reprinted with permission from Elsevier B.V.)

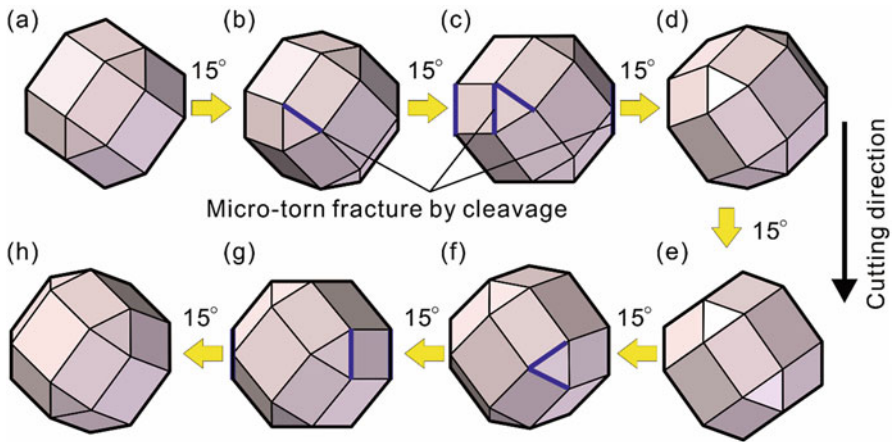


Fig. 9 Variation in geometrical relation of the crystal model with end face (111); each point corresponds to the observation points of Fig. 4c. (Azami S, Kudo H, Mizumoto Y, Tanabe T, Yan J, Kakinuma Y. Experimental study of crystal anisotropy based on ultra-precision cylindrical turning of single-crystal calcium fluoride. *Precis Eng* 2015;40:172–81. Reprinted with permission from Elsevier B.V.)

be mentioned that the surface morphology at (i) is slightly worse near the (100) plane and [011] cutting direction. That can be a remaining crack originated from crack formation in rough cutting or some cleavage phenomena; however, the reason was unclear from observation. A triangular crack was observed in the images of point (g).

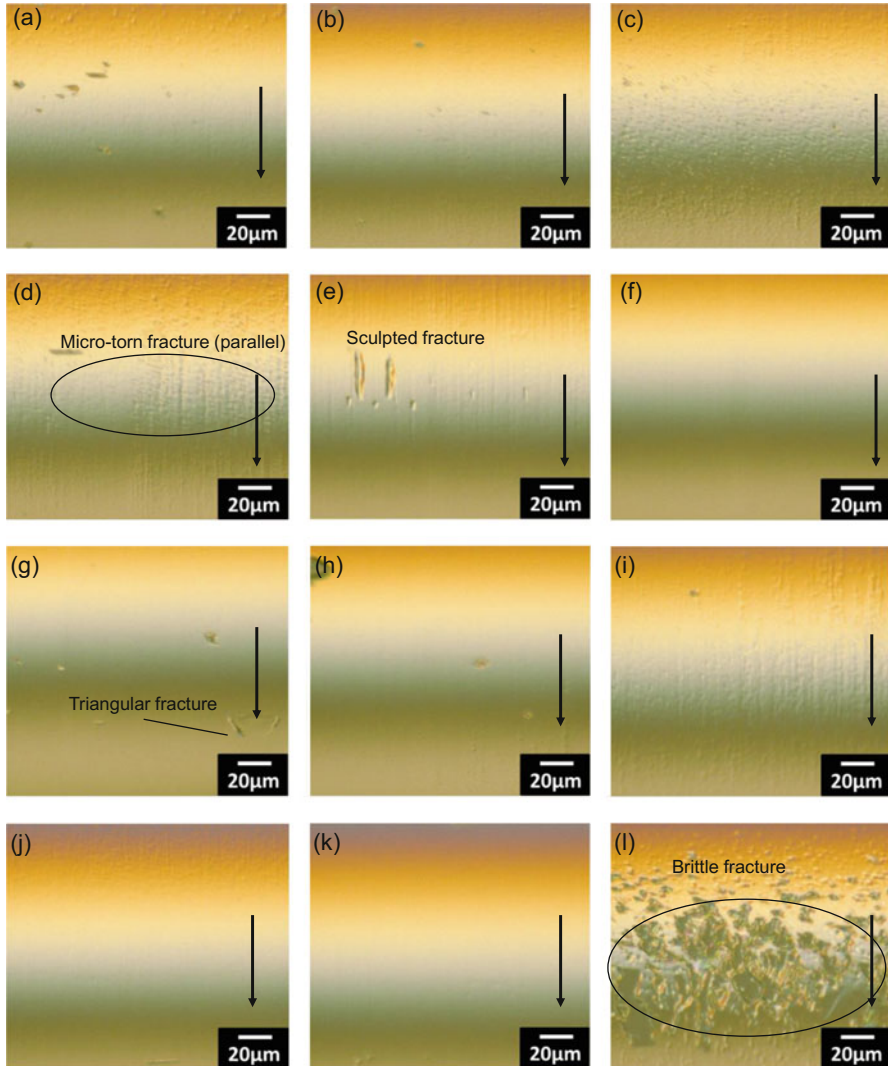


Fig. 10 Surface morphologies of the machined cylindrical surface with end face (110): each point corresponds to the observation points of Fig. 4b; a black arrow indicates a cutting direction. (Azami S, Kudo H, Mizumoto Y, Tanabe T, Yan J, Kakinuma Y. Experimental study of crystal anisotropy based on ultra-precision cylindrical turning of single-crystal calcium fluoride. *Precis Eng* 2015;40:172–81. Reprinted with permission from Elsevier B.V.)

The triangular crack was well-reported in other work (Yan et al. 2004a; Wang et al. 2016), and it corresponds to the $\{111\}$ cleavage families. It is evident that the brittle fracture dominates the machine surface at (l). The brittle fracture that takes place in the rough-cutting process can remain, even in the ductile-regime cutting.

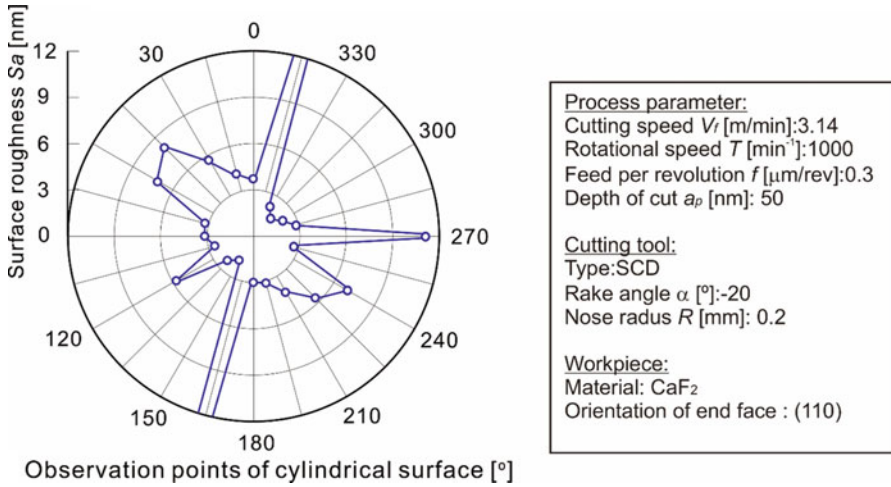


Fig. 11 Variation in surface roughness S_a in accordance with crystal anisotropy, (110) end face. (Azami S, Kudo H, Mizumoto Y, Tanabe T, Yan J, Kakinuma Y. Experimental study of crystal anisotropy based on ultra-precision cylindrical turning of single-crystal calcium fluoride. *Precis Eng* 2015;40:172–81. Reprinted with permission from Elsevier B.V.)

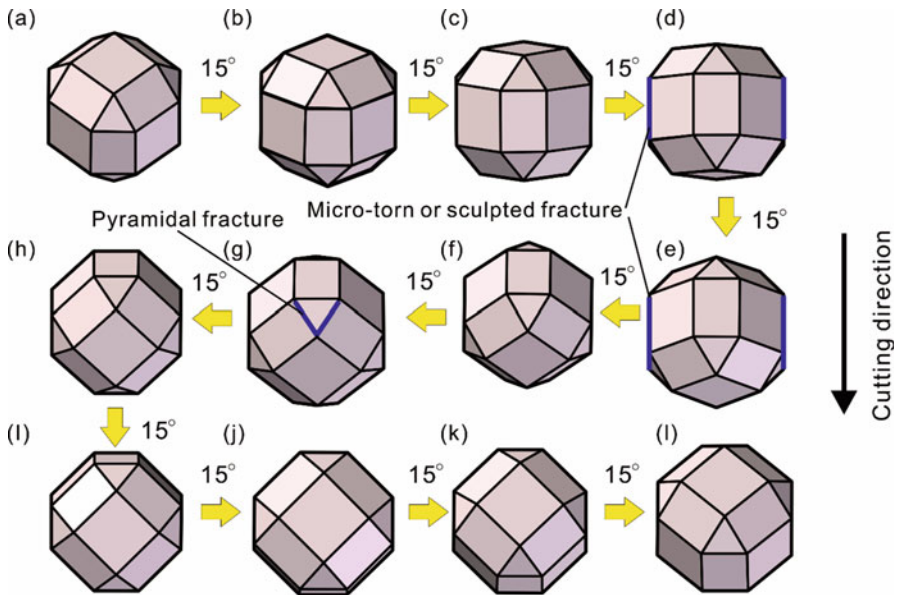


Fig. 12 Variation in geometrical relation of crystal model with end face (110): each point corresponds to the observation points of Fig. 4b. (Azami S, Kudo H, Mizumoto Y, Tanabe T, Yan J, Kakinuma Y. Experimental study of crystal anisotropy based on ultra-precision cylindrical turning of single-crystal calcium fluoride. *Precis Eng* 2015;40:172–81. Reprinted with permission from Elsevier B.V.)

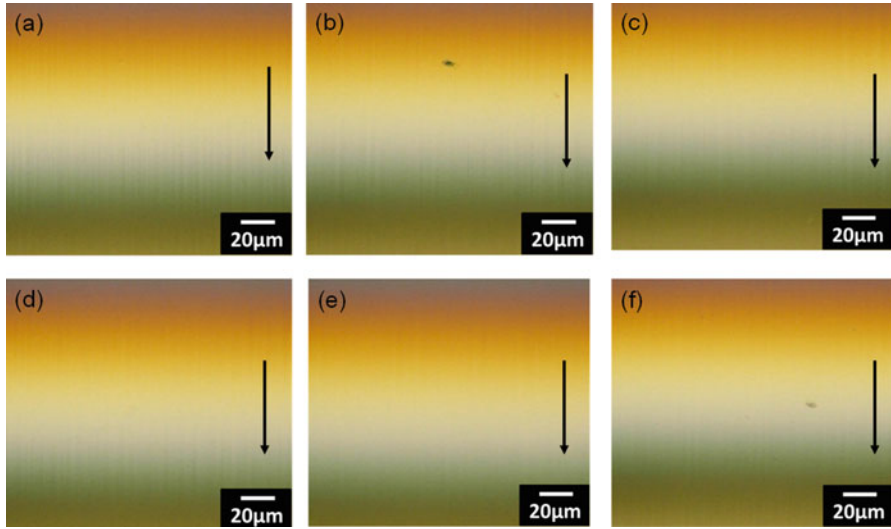


Fig. 13 Surface morphologies of the machined cylindrical surface with end face (100): each point corresponds to the observation points of Fig. 4a; a black arrow indicates a cutting direction. (Azami S, Kudo H, Mizumoto Y, Tanabe T, Yan J, Kakinuma Y. Experimental study of crystal anisotropy based on ultra-precision cylindrical turning of single-crystal calcium fluoride. *Precis Eng* 2015;40:172–81. Reprinted with permission from Elsevier B.V.)

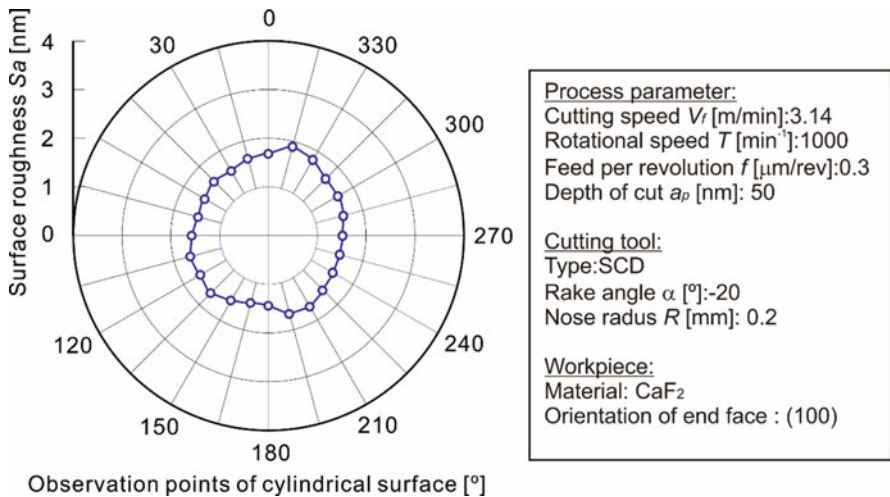


Fig. 14 Variation in surface roughness S_a in accordance with crystal anisotropy, (100) end face. (Azami S, Kudo H, Mizumoto Y, Tanabe T, Yan J, Kakinuma Y. Experimental study of crystal anisotropy based on ultra-precision cylindrical turning of single-crystal calcium fluoride. *Precis Eng* 2015;40:172–81. Reprinted with permission from Elsevier B.V.)

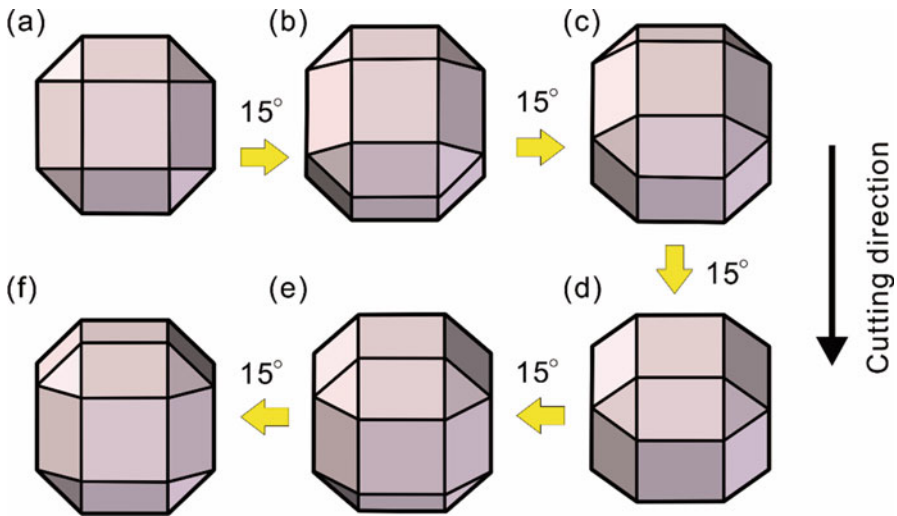


Fig. 15 Variation in geometrical relation of crystal model with end face (100): each point corresponds to the observation points of Fig. 4a. (Azami S, Kudo H, Mizumoto Y, Tanabe T, Yan J, Kakinuma Y. Experimental study of crystal anisotropy based on ultra-precision cylindrical turning of single-crystal calcium fluoride. *Precis Eng* 2015;40:172–81. Reprinted with permission from Elsevier B.V.)

Contrary to the results for end faces (111) and (110), a homogeneous surface was obtained at all observation points in the case of (100) (Figs. 13 and 14), although fourfold symmetry was expected, considering the crystal symmetry, as shown in Fig. 4a. At the entire cylindrical surface, the surface roughness Sa was below 1.7 nm, and few visible cracks were observed. The machined surface at (d) in Fig. 13 could be deteriorated, since the point corresponds to the results of plunge-cut tests of the (110) plane at 150° directions where the CDC was quite low (Mizumoto and Kakinuma 2018). In the UPCT, a cutting model is different because feed force also acts; therefore, the applied force vector should also be different from the plunge-cut process. It is assumed that the force vector can act on the directions that always activate the slip systems or prohibit the occurrence of cleavage (Fig. 15). Although questions about the obtained surface quality remain, it is concluded that the cylindrical surface with the end face of the (100) plane is most suitable. It is noted that the surface quality sometimes changes, even if the cutting condition is the same. One problem is that a chatter-like vibration was observed in the tests, as shown in Fig. 16. The chatter frequency $f_{chatter}$ is calculated to be 4.85 kHz. Because the diameter of the workpiece is quite small and the acting force can fluctuate due to the crystal anisotropy of the resolved stresses (Nakasuji et al. 1990), the cutting process can be unstable. To suppress the instability, the thrust force should be reduced. The thrust force can be reduced using a smaller nose radius, as reported by Nath (Nath et al. 2009). In addition, the negative rake angle is favorable for ductile cutting; however, the negative rake causes an increase in thrust force (Matsubara et al. 1984). Therefore, tool geometry also must be considered.

Fig. 16 Deterioration of the machined surface caused by chatter vibration. (Kakinuma Y, Azami S, Tanabe T. Evaluation of subsurface damage caused by ultra-precision turning in fabrication of CaF_2 optical micro resonator. CIRP Ann-Manuf Techn 2015;64(1):117–20. Reprinted with permission from Elsevier B.V.)

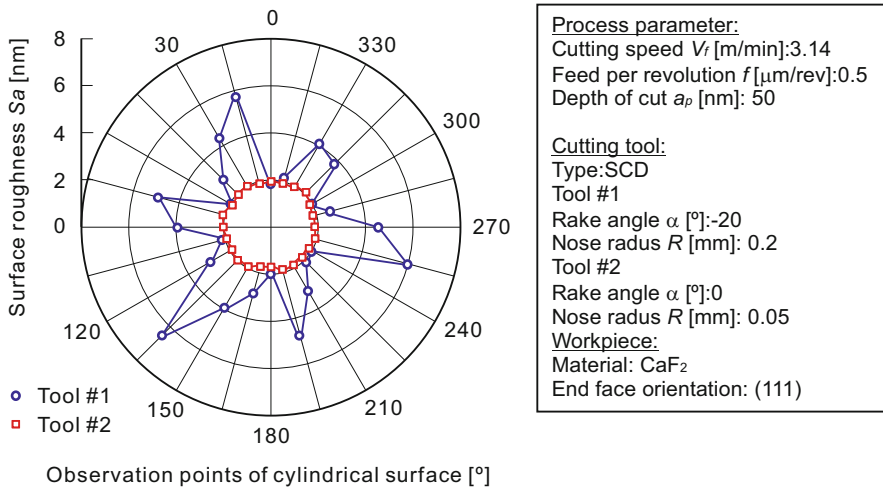
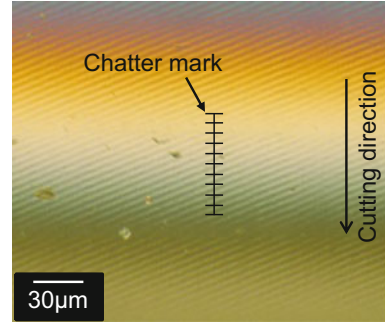


Fig. 17 Influence of tool geometry on surface roughness of CaF_2 cylinder with end face (111). (Kakinuma Y, Azami S, Tanabe T. Evaluation of subsurface damage caused by ultra-precision turning in fabrication of CaF_2 optical micro resonator. CIRP Ann-Manuf Techn 2015;64(1):117–20. Reprinted with permission from Elsevier B.V.)

3.4.3 Tool Geometry

To reduce the thrust force, a smaller nose radius tool (0.05 mm nose radius and 0° rake angle) was introduced (see the specification of Tool 2 in Table 3). The S_a values were investigated on each CaF_2 with end faces (100), (110), and (111). For all crystalline planes, a homogeneous surface was obtained, and a fluctuated surface induced by chatter vibration was not seen (Figs. 17, 18, and 19). One of the reasons can be the rake angle, i.e., the thrust force was reduced by using a 0° rake angle tool. Normally, the negative rake angle enhances the ductility of brittle materials because of the induced hydrostatic pressure formed by the compressive stress region. However, the reduction of the compressive stress region can lead to reduction of the thrust

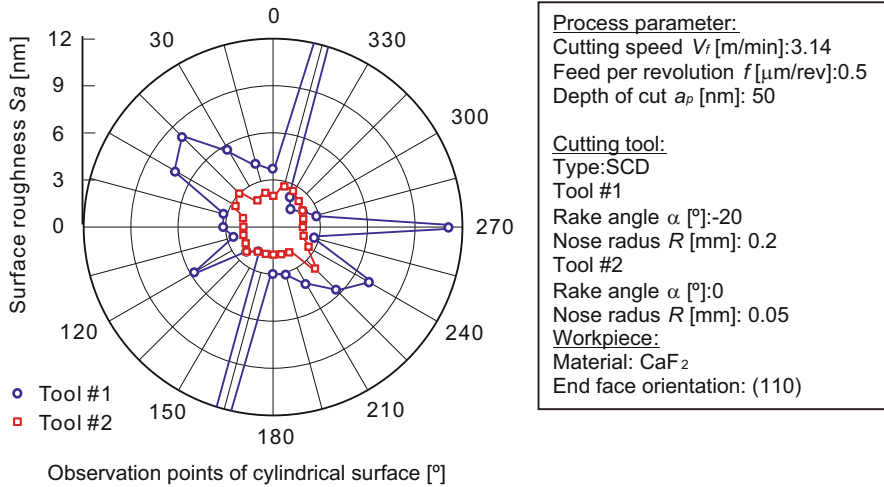


Fig. 18 Influence of tool geometry on surface roughness of CaF₂ cylinder with end face (110). (Kakinuma Y, Azami S, Tanabe T. Evaluation of subsurface damage caused by ultra-precision turning in fabrication of CaF₂ optical micro resonator. CIRP Ann-Manuf Techn 2015;64(1):117–20. Reprinted with permission from Elsevier B.V.)

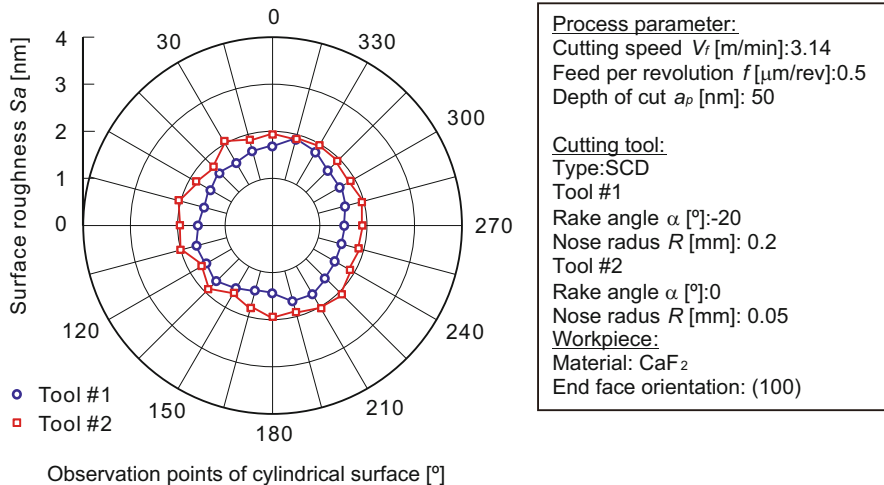


Fig. 19 Influence of tool geometry on surface roughness of CaF₂ cylinder with end face (100). (Kakinuma Y, Azami S, Tanabe T. Evaluation of subsurface damage caused by ultra-precision turning in fabrication of CaF₂ optical micro resonator. CIRP Ann-Manuf Techn 2015;64(1):117–20. Reprinted with permission from Elsevier B.V.)

force, which causes instability of the UPCT process. Nose radius could also contribute to the stabilization of the UPCT process. When changing the nose radius, the contact area between the tool and the workpiece also changes. The contact length l can be calculated from the geometrical relationship shown in Fig. 20.

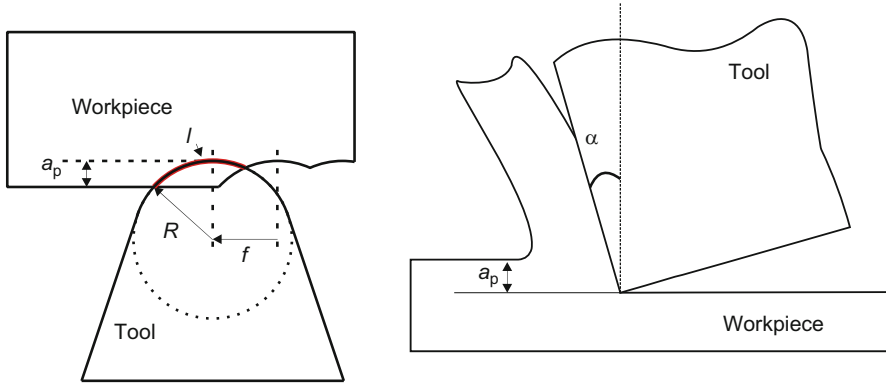


Fig. 20 Characterization of tool contact length in cylindrical turning

The tool contact lengths were calculated as 4.8 μm and 2.5 μm for Tools 1 and 2, respectively. Although the difference is on a micrometric scale, this can be crucial for the UPCT of the small workpiece. In UPCT, the material flow is strongly related to the contact area of the tool (process force), because the plastic flow area is assumed to be relatively small.

Overall, the surface quality strongly depends on the selection of an appropriate tool and crystal orientation. Although the surface quality was investigated, subsurface damage (SSD) is also very essential for the optical devices. The process parameter and crystal anisotropy can affect the SSD formation. The subsurface quality will be investigated.

3.5 Evaluation of Subsurface Damage

SSD has been widely studied in the manufacturing, material science, and optics fields (Jawahir et al. 2011; Lucca et al. 1998). SSD can be induced by various mechanisms, and the subsurface crystalline structure is changed by crystal shear and rotation, as in Fig. 21a (Panin et al. 2001). The valid measurement methods – e.g., X-ray diffraction (XRD), electron backscatter diffraction (EBSD), Raman spectroscopy, TEM, and releasing residual stress by etching – are selected depending on the material, size of specimen, or purpose. In this study, TEM was chosen to elucidate the variation in crystalline lattice arrangement induced by the ultra-precision cutting process. A field emission TEM (FE-TEM, Tecnai TM G2 F20 S-Twin) was used. Before the measurement, a focused ion beam (FIB) process was used to slice the TEM specimen to approximately 50 nm (Quanta 200 3 Di). SSD of the cylindrical surface was viewed from the end face, as shown in Fig. 21b. The obtained TEM images were rotated to adjust the cutting plane to the horizontal direction.

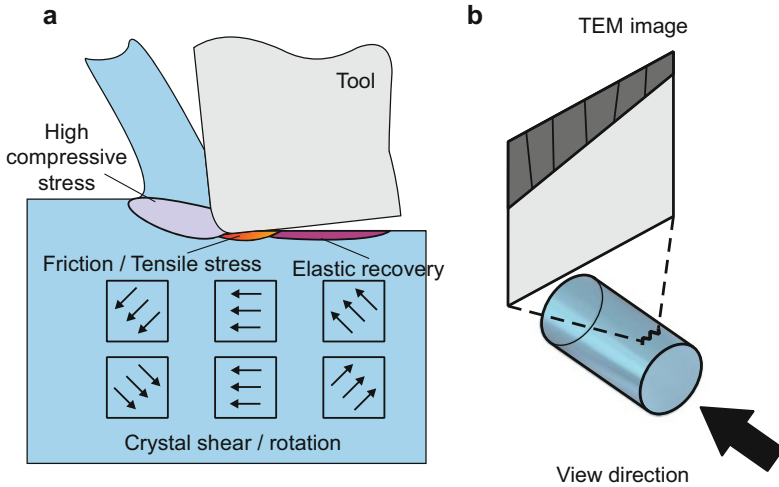


Fig. 21 Schematic illustration of the related mechanisms to SSD and its observation: (a) plausible material flow under cutting process and (b) observation procedure by TEM (Panin et al. 2001; Goel et al. 2015)

3.5.1 Process Parameter

Following the previous results, the influence of process parameters (a_p and tool geometry) on SSD was investigated. For the TEM observation, the cylindrical surface with end face (100) was selected. First, the influence of tool geometry on SSD was investigated and compared (Fig. 22). The machined surface at observation point (a) with the (100) end face, shown in Fig. 4a, was chosen for the investigation of the influence of process parameters. To focus on the nose radius, Tools 2 and 3 were used, and results were compared. To evaluate the SSD under the same surface roughness, the feed per revolution f was determined as $0.1 \mu\text{m}/\text{rev}$ for Tool 3 (0.01 mm nose radius). Although the Sa values are similar for each machined surface (approximately Sa 2 nm), the SSD depth tends to decrease in dependency with reduction of nose radius. As discussed in Section 4, nose radius has a great influence on the surface quality, e.g., a small nose radius contributes to obtaining a smooth and homogeneous surface (Fig. 17). This indicates that the tool geometry affects SSD more than surface roughness, because SSD changes with a few tens nanometric order. A decrease in the contact length between the tool and workpiece is assumed to result in reduction of the process force, which influences surface quality. In addition, plastic flow in severe stress zones is also affected by the tool contact length, i.e., nose radius. The tool contact lengths are calculated as 2.5 and $1.0 \mu\text{m}$ for Tools 2 and 3, respectively. Thus, the difference of the tool contact length also contributes to the reduction of the SSD.

Since a_p determines the surface quality, the influence of a_p was also investigated. Tool 2 (0.05 mm nose radius) was used for the tests, and a_p was set as 20, 50, and 100 nm. It should be noted that smooth surfaces with an Sa of approximately 2 nm were

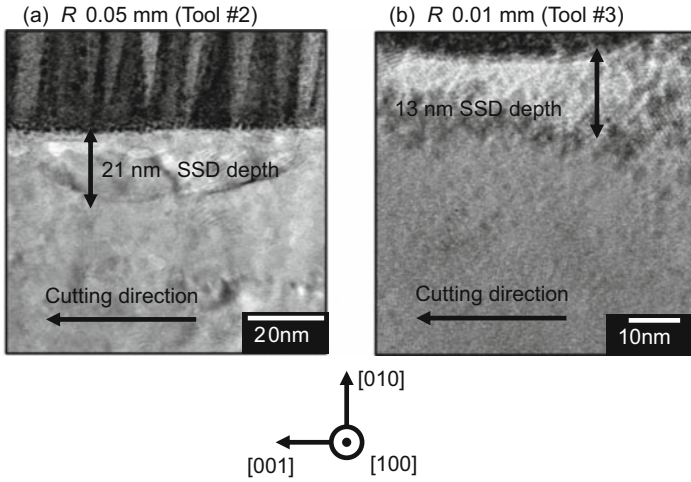


Fig. 22 TEM images of machined surface (010) plane machined with a tool of (a) R 0.05 mm and (b) R 0.01 mm

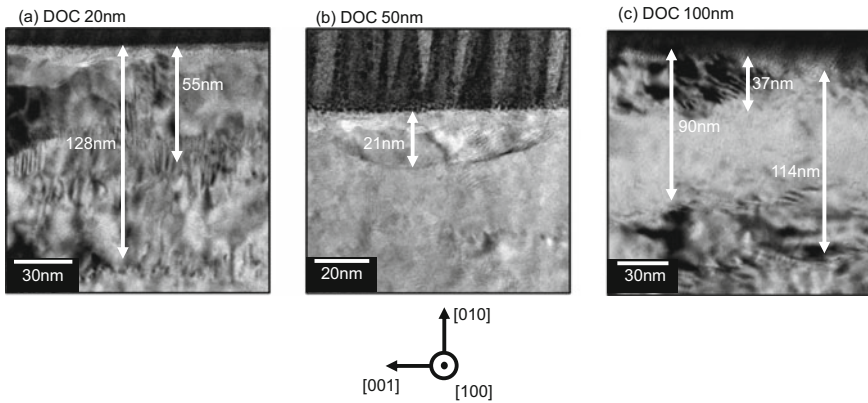


Fig. 23 TEM images of machined surface at the cutting direction of [001] with depth of cut (DOC) a_p of (a) 20 nm, (b) 50 nm, and (c) 100 nm

obtained for each surface. It was assumed that the deeper a_p is, the more SSD depth increases (Fig. 23). The deeper a_p leads to the increase in cutting volume and the plastic deformation zone; therefore, the subsurface layer is more severely affected. Although one boundary line was observed in Fig. 23b, there are some boundary lines when a_p is higher, shown in Fig. 23c, which is assumed to be formed by a larger amount of dislocations compared to a small a_p . However, when a_p was set at 20 nm, the SSD depth was higher compared to the case of the 50 nm a_p . The edge radius was confirmed to be in the range of 10 nm to 50 nm. Hence, it is thought that plowing was

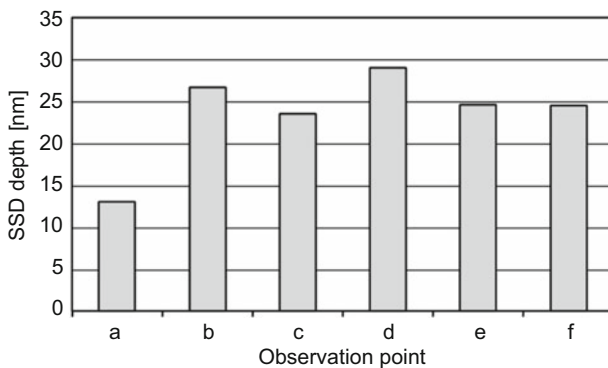
performed, because of the size effect and the higher compressive stress in front of the cutting tools caused the deeper SSD.

Even if the plowing occurs, the workpiece can be cut, because the UPCT process is repeated (i.e., repetition of cutting and plowing); however, the residual compressive stress induced by plowing causes the machinability to deteriorate; thus, the SSD depth is higher. It is concluded that a_p can affect SSD, and the SSD depth was smallest when a_p was 50 nm in the experiments.

3.5.2 Crystal Anisotropy

Whereas the Sa values are almost the same, the subsurface quality changes according to the process parameter or tool geometry. This is indicative of the influence of crystal anisotropy. For the investigation of the anisotropic deformation behavior of SSD in UPCT, the workpiece with end face (100) was chosen because the surface roughness did not vary depending on the tool geometry and because it is easy to obtain the smooth surface experimentally. Considering the symmetry of crystalline structure, six observation points, (a) to (f), were investigated – see the corresponding observation points in Fig. 4a.

Variation in the SSD depth according to the observation points is shown in Fig. 24, and it is obvious that the SSD depth significantly differs. Especially, the SSD depth is the lowest at point (a). To analyze the crystalline lattice arrangement, fast Fourier transform (FFT) and inverse fast Fourier transfer (IFFT) analyses were employed to show clearly the crystalline structure in a real space. Because the raw



Workpiece:

Material: CaF₂

Orientation of end face: (100)

Cutting direction: Variable

Cutting tool:

Rake angle α [°]: 0

Nose radius R [mm]: 0.01

Process parameter:

Cutting speed V_f [m/min]: 3.14

Feed per revolution f [μ m/rev]: 0.1

Depth of cut a_p [nm]: 50

Fig. 24 Variation in SSD depth depending on observation points. (Crystal anisotropy. Mizumoto Y, Kangawa H, Itobe H, Tanabe T, Kakinuma Y. Influence of crystal anisotropy on subsurface damage in ultra-precision cylindrical turning of CaF₂. *Precis Eng* 2017;49:104–14. Reprinted with permission from Elsevier B.V.)

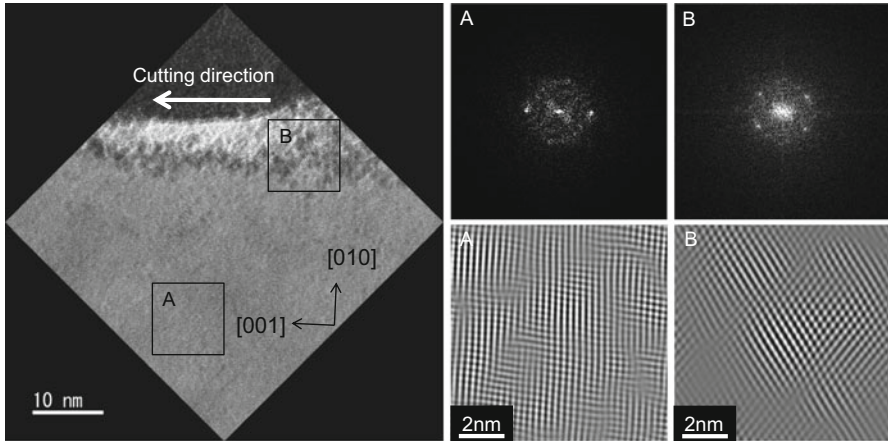


Fig. 25 TEM image at point (a) with end face (100): Regions A (nondeformed region) and B (deformed region) are analyzed by FFT and IFFT. (Mizumoto Y, Kangawa H, Itobe H, Tanabe T, Kakinuma Y. Influence of crystal anisotropy on subsurface damage in ultra-precision cylindrical turning of CaF_2 . *Precis Eng* 2017;49:104–14. Reprinted with permission from Elsevier B.V.)

TEM image includes both diffraction spots and appearance of the specimen, it is difficult to observe the crystalline lattice arrangement clearly. Once the TEM image was processed by FFT, only diffraction spots were chosen to analyze the crystalline lattice information by IFFT processing. The TEM image of SSD at point (a) is shown in Fig. 25, closing up the nondeformed layer (Region A) and deformed layer (Region B) through FFT and IFFT analyses. Comparing the FFT and IFFT images, the crystalline lattice changes from a nondeformed layer (Fig. 25, Region A) to a deformed layer (Fig. 25, Region B). On the one hand, it is observed that the crystalline lattice is arranged regularly with its original crystalline structure – the diffraction spots construct the cubic structure, i.e., the view from the (100) plane. On the other hand, although the crystalline lattice in Region B is also regularly arranged, its arrangement differs from the original crystalline structure. This indicates that the original nondeformed layer is deformed by a slip glide induced by the cutting process, which leads to the occurrence of the deformed layer (Region B).

In Fig. 26, variation in the crystalline lattice arrangement is illustrated. Because the crystalline lattice arrangement changes from (a) before the deformation state to (b) after the deformation state, it is thought that a slip glide takes place along the slip system $(010)[\bar{1}01]$ and $(010)[101]$, where the slip plane corresponds to the cutting plane. The slip direction viewed from the (100) plane is identical to the cutting direction, so the nondeformed layer is deformed along the cutting plane.

Figure 27 shows a TEM image of SSD at point (b). Although the crystalline lattice arrangement changes along the slip direction at the boundary line (Region B), the crystalline lattice rotates counterclockwise beneath the surface. Because the crystal

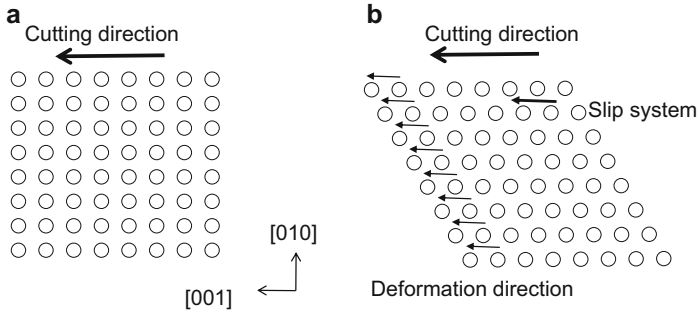


Fig. 26 Schematic illustration of the variation in crystalline structure in UPCT at point (a) with end face (100), (a) before deformation and (b) after deformation

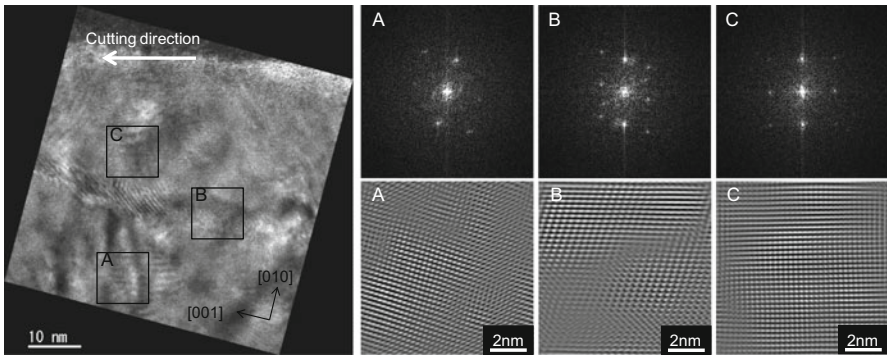


Fig. 27 TEM image at point (b) with end face (100): Regions A (nondeformed region), B (boundary region), and C (rotational region) are analyzed by FFT and IFFT. (Mizumoto Y, Kangawa H, Itohe H, Tanabe T, Kakinuma Y. Influence of crystal anisotropy on subsurface damage in ultraprecision cylindrical turning of CaF_2 . *Precis Eng* 2017;49:104–14. Reprinted with permission from Elsevier B.V.)

rotation is induced by slip glides under tensile loading (Mittermeijer 2010), the crystal shear in Region B can be a trigger for the crystalline rotation, as shown in Fig. 28.

Figure 29 shows a TEM image of SSD at point (c). The nondeformed (Region A) and deformed (Region B) layers are clearly identified from the image. The slip system $(010)[1\bar{1}0]$ and $(010)[\bar{1}\bar{1}0]$ contribute to the deformation, as illustrated in Fig. 30. A similar tendency for the SSD formation is seen at point (d), as shown in Figs. 31 and 32. The same deformation mechanism is observed at points (e) and (f), i.e., SSD induced by slips is seen along the slip direction; therefore, the detailed schematic illustration is omitted (Figs. 33 and 34).

Overall, the SSD depth changes depending on the observation points. In other words, crystal anisotropy can influence the SSD formation compared with surface

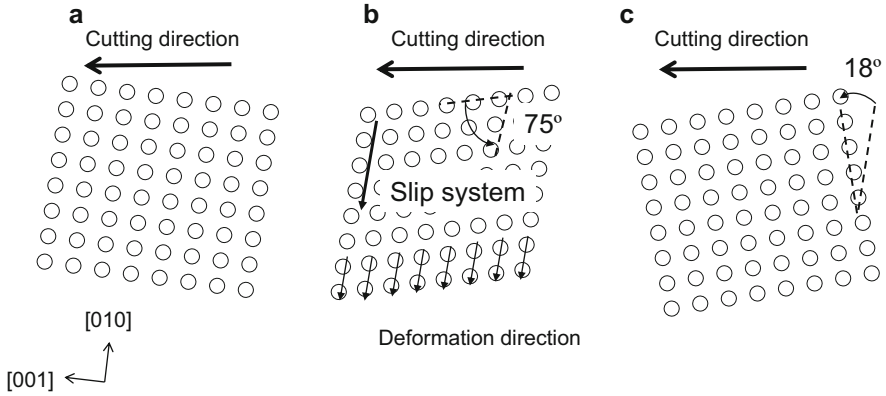


Fig. 28 Schematic illustration of the variation in crystalline structure in UPCT at point (b) with end face (100), (a) before deformation, (b) after deformation, and (c) after rotation

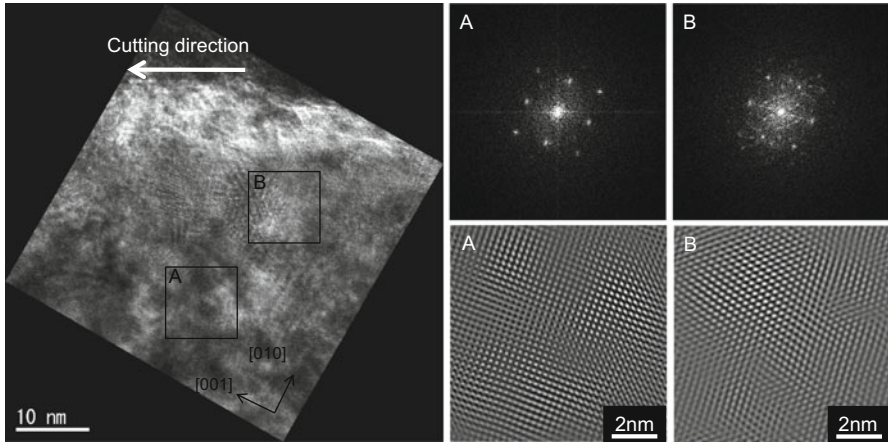


Fig. 29 TEM image at point (c) with end face (100): Regions A (nondeformed region) and B (deformed region) are analyzed by FFT and IFFT. (Mizumoto Y, Kangawa H, Itobe H, Tanabe T, Kakinuma Y. Influence of crystal anisotropy on subsurface damage in ultra-precision cylindrical turning of CaF_2 . *Precis Eng* 2017;49:104–14. Reprinted with permission from Elsevier B.V.)

roughness, and the SSD depth is shallow, especially at point (a). This is because the cutting crystalline plane (010) is a slip plane, and the slip occurs parallel to the cutting direction. The subsurface layer is pulled in the parallel direction by the slip, and the SSD depth becomes shallow. Notably, analysis of the depth direction in the TEM image is omitted, because the FIB is destructive; therefore, it is impossible to see the same specimen from a different view. Additionally, from the front view of the TEM image (viewing from the parallel direction to the cutting direction), activation

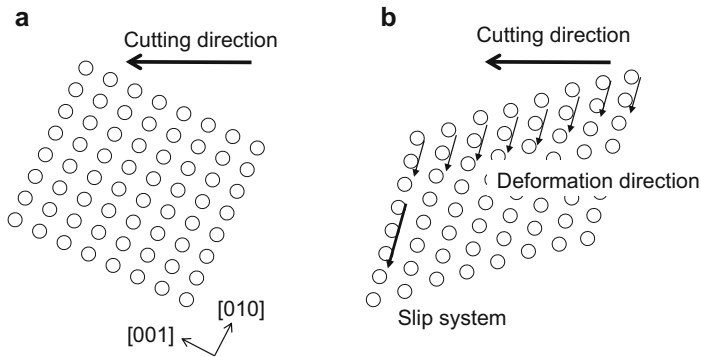


Fig. 30 Schematic illustration of the variation in crystalline structure in UPCT at point (c) with end face (100), (a) before deformation and (b) after deformation

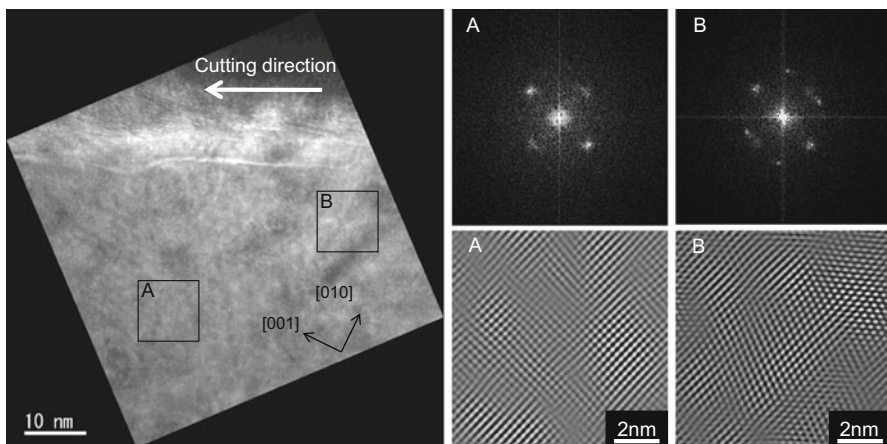


Fig. 31 TEM image at point (d): Regions A (nondeformed region) and B (deformed region) are analyzed by FFT and IFFT. (Mizumoto Y, Kangawa H, Itobe H, Tanabe T, Kakinuma Y. Influence of crystal anisotropy on subsurface damage in ultra-precision cylindrical turning of CaF₂. *Precis Eng* 2017;49:104-14. Reprinted with permission from Elsevier B.V.)

of the slip system is hard to identify because all of the slip system exists in a depth direction. For the cylindrical surface machined by Tool 2 (0.05 mm nose radius), points (a), (d), and (e) were also observed. The SSD depths in their dependency on nose radius are shown in Fig. 35. At every observation point, Tool 3 reduced the SSD depth. As noted in Section 4, the deviation between the contact areas that is determined by tool geometry could contribute to the increments of SSD depth. It is concluded that, although the surface roughness value does not vary depending on the tool geometry and crystal anisotropy, limited to the case of end face (100), the SSD depth significantly changes.

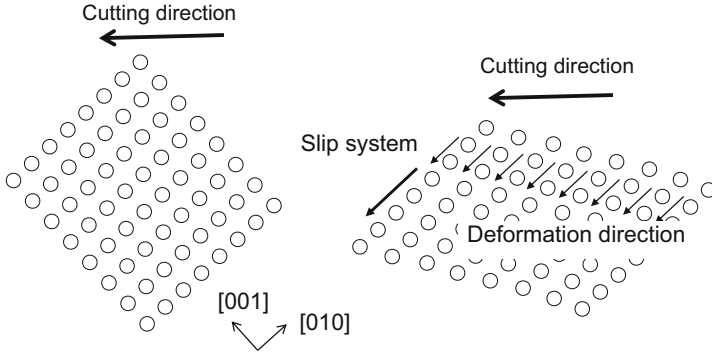


Fig. 32 Schematic illustration of the variation in crystalline structure in UPCT at point (d) with end face (100), (a) before deformation and (b) after deformation

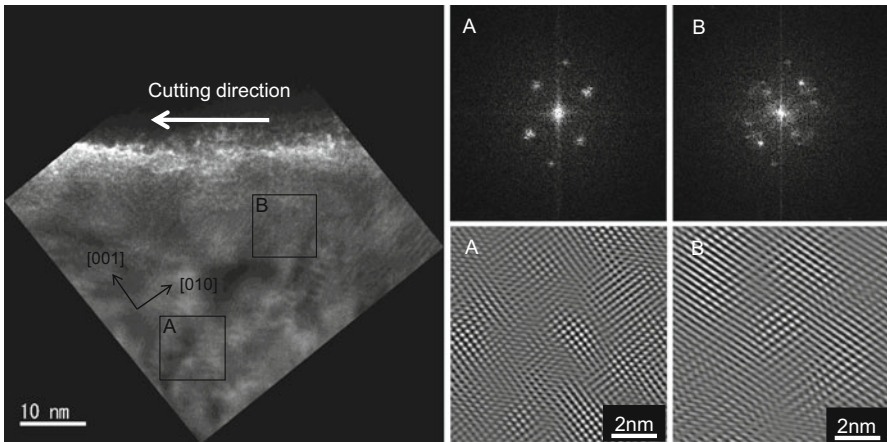


Fig. 33 TEM image at point (e): Regions A (nondeformed region) and B (deformed region) are analyzed by FFT and IFFT. (Mizumoto Y, Kangawa H, Itobe H, Tanabe T, Kakinuma Y. Influence of crystal anisotropy on subsurface damage in ultra-precision cylindrical turning of CaF_2 . *Precis Eng* 2017;49:104–14. Reprinted with permission from Elsevier B.V.)

3.6 Summary and Outlook

The machinability of single-crystalline CaF_2 in ultra-precision cylindrical turning is described. Specifically, the anisotropic behavior of the machined surface and SSD formation are discussed. The contents are summarized as follows.

1. Even though the radial a_p and uncut chip thickness were set below CDC values obtained by plunge-cut tests, the surface quality strongly depends on the

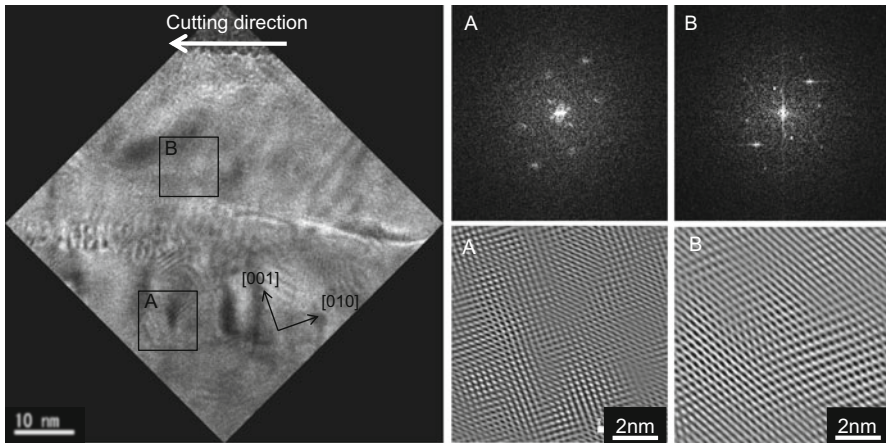


Fig. 34 TEM image at point (f): Regions A (nondeformed region) and B (deformed region) are analyzed by FFT and IFFT. (Mizumoto Y, Kangawa H, Itobe H, Tanabe T, Kakinuma Y. Influence of crystal anisotropy on subsurface damage in ultra-precision cylindrical turning of CaF_2 . *Precis Eng* 2017;49:104–14. Reprinted with permission from Elsevier B.V.)

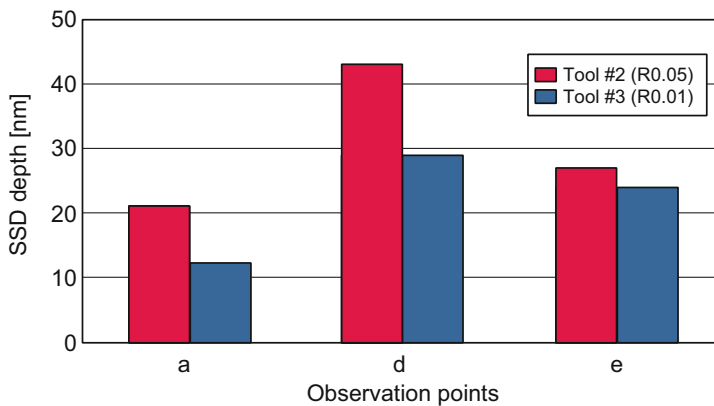


Fig. 35 Comparison of SSD depth depending on crystalline direction and nose radius. (Mizumoto Y, Kangawa H, Itobe H, Tanabe T, Kakinuma Y. Influence of crystal anisotropy on subsurface damage in ultra-precision cylindrical turning of CaF_2 . *Precis Eng* 2017;49:104–14. Reprinted with permission from Elsevier B.V.)

corresponding cutting crystalline planes and directions. To suppress the thrust force, the smaller nose radius and 0° rake angle were used, and homogeneous surfaces were obtained regardless of the crystalline structure. In terms of the relation between machinability and setting crystal orientation, end face (100) remarkably enhances the surface quality compared with end faces (111) and (110).

- The subsurface quality was investigated on the cylindrical surface via TEM observation. Even if the surface roughness is uniform, the SSD depth varies

depending on process parameters, tool geometry, or crystal anisotropy from 10 to 100 nm in scale. For the process parameters, the lower process force is assumed to be required to decrease the SSD depth. The geometrical relation between slip systems and cutting planes caused the deviation in SSD depth.

Single-crystalline CaF₂ is expected to be applicable to next-generation optical devices having a complicated shape such as optical microcavity. While micro cylindrical turning is the most promising fabrication approach, further researches to enhance the productivity and to remove SSD maintaining the form accuracy are required. Vibration or laser-assisted techniques and functional diamond tools such as nano-polycrystalline diamond may drastically improve the performance of micro cylindrical turning.

References

- Azami S, Kudo H, Mizumoto Y, Tanabe T, Yan J, Kakinuma Y (2015) Experimental study of crystal anisotropy based on ultra-precision cylindrical turning of single-crystal calcium fluoride. *Precis Eng* 40:172–181
- Bezuidenhout DF (1997) Handbook of optical constants of solids. Academic Press, London
- Bifano GT, Dow TA, Scattergood RO (1989) Ductile-regime grinding of brittle materials: experimental results and the development of a model. 32nd Annual Technical Symposium, International Society for Optics and Photonics, pp 108–115
- Blackley WS, Scattergood RO (1991) Ductile-regime machining model for diamond turning of brittle materials. *Precis Eng* 13(2):95–103
- Blake PN, Scattergood RO (1990) Ductile-regime machining of germanium and silicon. *J Am Ceram Soc* 73(4):949–957
- Chen L, Hu LC, Xiao C, Qi YQ, Yu BJ, Qian LM (2017a) Effect of crystallographic orientation on mechanical removal of CaF₂. *Wear* 376:409–416
- Chen X, Xu J, Fang H, Tian R (2017b) Influence of cutting parameters on the ductile-brittle transition of single-crystal calcium fluoride during ultra-precision cutting. *Int J Adv Manuf Tech* 89:219–225
- Fang FZ, Chen LJ (2000) Ultra-precision cutting for ZKN7 glass. *CIRP Ann-Manuf Techn* 49(1):17–20
- Furukawa Y, Moronuki N (1988) Effect of material properties on ultra precise cutting processes. *CIRP Ann-Manuf Techn* 37(1):113–116
- Goel S, Luo XC, Agrawal A, Reuben RL (2015) Diamond machining of silicon: a review of advances in molecular dynamics simulation. *Int J Mach Tool Manu* 88:131–164
- Grudinin IS, Matsko AB, Savchenkov AA, Strelakov D, Ilchenko VS, Maleki L (2006) Ultra high Q crystalline microcavities. *Opt Commun* 265(1):33–38
- Gu W, Yao Z, Li H (2011) Investigation of grinding modes in horizontal surface grinding of optical glass BK7. *J Mater Process Tech* 211(10):1629–1636
- Inasaki I (2009) Machining system. Tokyo, Yokendo. (in Japanese)
- Janicki MJ, Drzymala J, Kowalczyk PB (2016) Structure and surface energy of both fluorite halves after cleaving along selected crystallographic planes. *Physicochem Probl Mi* 52(1):451–458
- Jawahir IS, Brinksmeier E, M'Saoubi R, Aspinwall DK, Outeiro JC, Meyer D et al (2011) Surface integrity in material removal processes: recent advances. *CIRP Ann-Manuf Techn* 60(2):603–626
- Liberman V, Bloomstein TM, Rothschild M, Sedlacek JHC, Uttaro RS, Bates AK et al (1999) Materials issues for optical components and photomasks in 157 nm lithography. *J Vac Sci Technol B: Microelectron Nanometer Struct* 17(6):3273

- Liu K, Zuo DW, Li XP, Rahman M (2009) Nanometric ductile cutting characteristics of silicon wafer using single crystal diamond tools. *J Vac Sci Technol B* 27(3):1361–1366
- Lucca DA, Brinksmeier E, Goch G (1998) Progress in assessing surface and subsurface integrity. *CIRP Ann-Manuf Techn* 47(2):669–693
- Marsh ER, John BP, Couey JA, Wang J, Grejda RD, Vallance RR (2005) Predicting surface figure in diamond turned calcium fluoride using in-process force measurement. *J Vac Sci Technol B* 23(1):84–89
- Matsubara T, Yamamoto H, Mizumoto H (1984) Study on regenerative chatter vibration with dynamic cutting force. *Japan journal of. Precis Eng* 50(7):11–15. (in Japanese)
- Mittemeijer EJ (2010) Fundamentals of materials science: the microstructure-property relationship using metals as model systems. Springer, Berlin
- Mizumoto Y, Kakinuma Y (2018) Revisit of the anisotropic deformation behavior of single-crystal CaF₂ in orthogonal cutting. *Precis Eng* (accepted for publication).
- Nakasuji T, Kodera S, Hara S, Matsunaga H, Ikawa N, Shimada S (1990) Diamond turning of brittle materials for optical components. *CIRP Ann-Manuf Techn* 39(1):89–92
- Namba Y, Ohnishi N, Yoshida S, Harada K, Yoshida K, Matsuo T (2004) Ultra-precision float polishing of calcium fluoride single crystals for deep ultra violet applications. *CIRP Ann-Manuf Techn* 53(1):459–462
- Namba Y, Yoshida T, Yoshida S, Yoshida K (2005) Surfaces of calcium fluoride single crystals ground with an ultra-precision surface grinder. *CIRP Ann-Manuf Techn* 54(1):503–506
- Nath C, Rahman M, Neo KS (2009) A study on the effect of tool nose radius in ultrasonic elliptical vibration cutting of tungsten carbide. *J Mater Process Tech* 209(17):5830–5836
- Panin V, Kolubaev A, Tarasov S, Popov V (2001) Subsurface layer formation during sliding friction. *Wear* 249(10–11):860–867
- Reichling M, Wilson RM, Bennewitz R, Williams RT, Gogoll S, Stenzel E et al (1996) Surface colloid evolution during low-energy electron irradiation of CaF₂(111). *Surf Sci* 366(3):531–544
- Schick M, Dabringhaus H, Wandelt K (2004) Macrosteps on CaF₂(111). *J Phys Condens Matter* 16(6):33–37
- Sumiya H, Harano K, Murakami H (2012) Application of Nano-polycrystalline diamond o cutting tools. *SEI TECHNICAL REVIEW* 75:18–23
- Technical Document of OKEN Co. Ltd.
- Wang H, Riemer O, Rickens K, Brinksmeier E (2016) On the mechanism of asymmetric ductile–brittle transition in microcutting of (111) CaF₂ single crystals. *Scr Mater* 114:21–26
- Wermelinger T, Borgia C, Solenthaler C, Spolenak R (2007) 3-D Raman spectroscopy measurements of the symmetry of residual stress fields in plastically deformed sapphire crystals. *Acta Mater* 55(14):4657–4665
- Yan J, Syoji K, K T (2000) Ductile–brittle transition at large negative tool rake angles. *Japan Journal of Precision Engineering* 66(1):1130–1134
- Yan J, Syoji K, Kuriyagawa T, Suzuki H (2002) Ductile regime turning at large tool feed. *J Mater Process Tech* 121(2–3):363–372
- Yan J, Syoji K, Tamaki J (2004a) Crystallographic effects in micro/nanomachining of single-crystal calcium fluoride. *J Vac Sci Technol B: Microelectron Nanometer Struct* 22(1):46–51
- Yan J, Tamaki J, Syoji K, Kuriyagawa T (2004b) Single-point diamond turning of CaF₂ for nanometric surface. *Int J Adv Manuf Tech* 24(9–10):640–646
- Yan J, Asami T, Kuriyagawa T (2008) Nondestructive measurement of machining-induced amorphous layers in single-crystal silicon by laser micro-Raman spectroscopy. *Precis Eng* 32(3):186–195
- Yan J, Asami T, Harada H, Kuriyagawa T (2009) Fundamental investigation of subsurface damage in single crystalline silicon caused by diamond machining. *Precis Eng* 33(4):378–386
- Yan J, Asami T, Harada H, Kuriyagawa T (2012) Crystallographic effect on subsurface damage formation in silicon microcutting. *CIRP Ann-Manuf Techn* 61(1):131–134
- Yoshizawa T (2009) Handbook of optical metrology: principles and applications. CRC Press, Boca Raton



Nano-grooving by Using Multi-tip Diamond Tools

4

Xichun Luo and Zhen Tong

Contents

4.1	Introduction	98
4.2	Brief History	99
4.3	Machining Mechanism	103
4.3.1	MD Nanometric Cutting Model	103
4.3.2	MD Simulation Setup	105
4.3.3	The Post-processing Methods	107
4.3.4	Nanostructure Generation Process	109
4.3.5	Cutting Force	111
4.3.6	Temperature Distribution	113
4.3.7	Thermal Annealing at Machined Surface	115
4.3.8	Summary	116
4.4	Influence of Processing Parameters	117
4.4.1	Experimental Setup	119
4.4.2	MD Simulation Setup	120
4.4.3	Nanostructures Formed Under Different Cutting Conditions	121
4.4.4	Effects of Depth of Cut	123
4.4.5	Effects of Cutting Speed	125
4.4.6	Summary	129
4.5	Tool Wear	130
4.6	Concluding Remarks	133
	References	135

X. Luo (✉)

Centre for Precision Manufacturing, Department of Design, Manufacture and Engineering Management, University of Strathclyde, Glasgow, UK

e-mail: Xichun.luo@strath.ac.uk

Z. Tong

Centre for Precision Manufacturing, Department of Design, Manufacture and Engineering Management, University of Strathclyde, Glasgow, UK

Centre for Precision Technologies, University of Huddersfield, Huddersfield, UK

e-mail: Z.Tong@hud.ac.uk

© Springer Nature Singapore Pte Ltd. 2018

J. Yan (ed.), *Micro and Nano Fabrication Technology*, Micro/Nano Technologies,

https://doi.org/10.1007/978-981-13-0098-1_4

97

Abstract

This chapter introduces nano-grooving approach by using multi-tip diamond tools to generate nanostructures such as nano-gratings/nano-grooves on large substrates. It starts by briefing the work principle and history of this nano-fabrication approach. It then introduces the machining mechanism, influences of processing parameters, and tool wear on the machined nanostructures. It concludes with a summary of research challenges, current research achievements, and future research directions to systematically establish this nanofabrication approach.

Keywords

Nano-grooving · Multi-tip diamond tool · MD simulation · Tool wear · Surface integrity · Structural defect

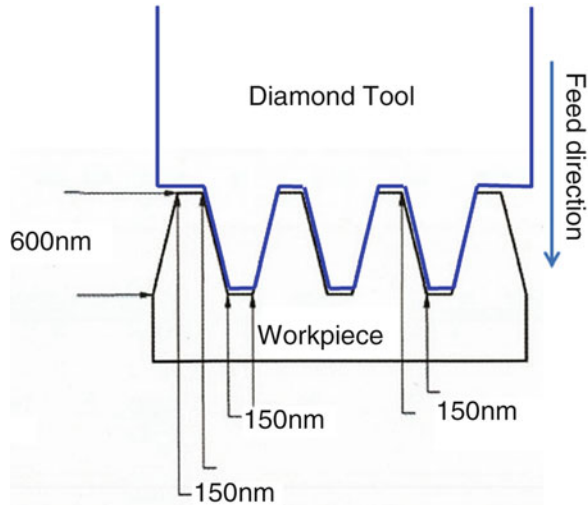
4.1 Introduction

Fabrication of periodic micro- and nanostructures over a large area has attracted great interest in recent years due to growing applications of such functional structures in optics, automotive, aerospace, biomedical, and power generation devices (Holmberg et al. 2014; Bartolo et al. 2012; Berman and Krim 2013; Kaur and Singh 2014). For example, periodic nano-grating is a typical nanostructure for the excitation of surface plasmon resonance (Atwater and Polman 2010; Liu et al. 2005). It is the basis of many resonance-coupling-based plasmonic devices such as the plasmonic solar cell (Mokkapati et al. 2009; Akimov and Koh 2010) and the surface-enhanced Raman spectroscopy (SERS) for the massively enhancing adsorption of signal onto planar metal surfaces (Clark and Cooper 2011).

Several nanofabrication techniques are currently used to obtain nanostructured surfaces, such as focused ion beam (FIB) machining, laser machining, optical lithography (EUV, UV, and X-ray lithography, etc.), electron beam lithography, nanoimprint lithography (NIL), and scanning probe lithography. Apart from these techniques, ultra-precision diamond turning is another promising approach to obtain nanostructures in a repeatable and cost-effective manner while maintaining high precision. The work principle of this new nano-grooving approach is illustrated in Fig. 1. It can be seen that the nano-gratings/nano-grooves are generated on the workpiece surface by plunging cut using a diamond tool with prefabricated nano-grating structures on its tip. By this method many gratings/grooves can be generated in one single cutting pass.

The crystalline structure of diamond permits the fabrication of cutting tools with very sharp cutting edges which result in nanometer-level surface finish for these nanostructures after a single cutting pass. Varieties of tool geometries, such as single-tipped and dual-tipped tools having rectangular-, triangular-, and other complex-shaped face designs, have been produced to generate functional structured surfaces through ultra-precision diamond turning process (Picard et al. 2003; Ding et al.

Fig. 1 Work principle of nano-grooving by using multi-tip diamond tool



2008; Xu et al. 2010). Moreover, ultra-precision diamond turning technique also offers an opportunity to create 3D structures on nonplanar surfaces (Davies et al. 2003). This approach, therefore, fully utilizes the fine process capability of the physical sputtering actions of the FIB and the high productivity of diamond turning. This chapter will introduce the history of nano-grooving approach, machining mechanism, and influences of processing parameters and tool wear on the generated nanostructures.

4.2 Brief History

Nano-grooving by using a multi-tip diamond tool is inspired by the pioneering work of Friedrich and Vasile et al. for the fabrication of microstructures (Friedrich and Vasile 1996; Vasile et al. 1996, 1999; Friedrich et al. 1997). They used FIB milling to produce nominal 25 μm diameter micro tools used on an ultra-precision machining center. Because of the Gaussian ion beam intensity profile, the cutting edge near the ion beam is rounded off and other edges away from the beam become sharper (Friedrich and Vasile 1996; Vasile et al. 1996).

Picard et al. (2003) from Sandia National Laboratories (SNL) presented the method of FIB shaping micro-scale tools (with dimensions in a range of 15–100 μm) analogous to a cutting tool used in lathes. They proposed a procedure for shaping a two-tip micro cutting tool (as shown in Fig. 2). The cutting tools having rectangular, triangular, and trapezoid shapes were successfully fabricated by FIB. Among the tested tool materials, diamond and tungsten carbide materials are easier to form a sharp cutting edge than high-speed steel. These tools were further applied for ultra-precision machining of microgrooves, microcoils, and curvilinear structures (as shown in Fig. 3).

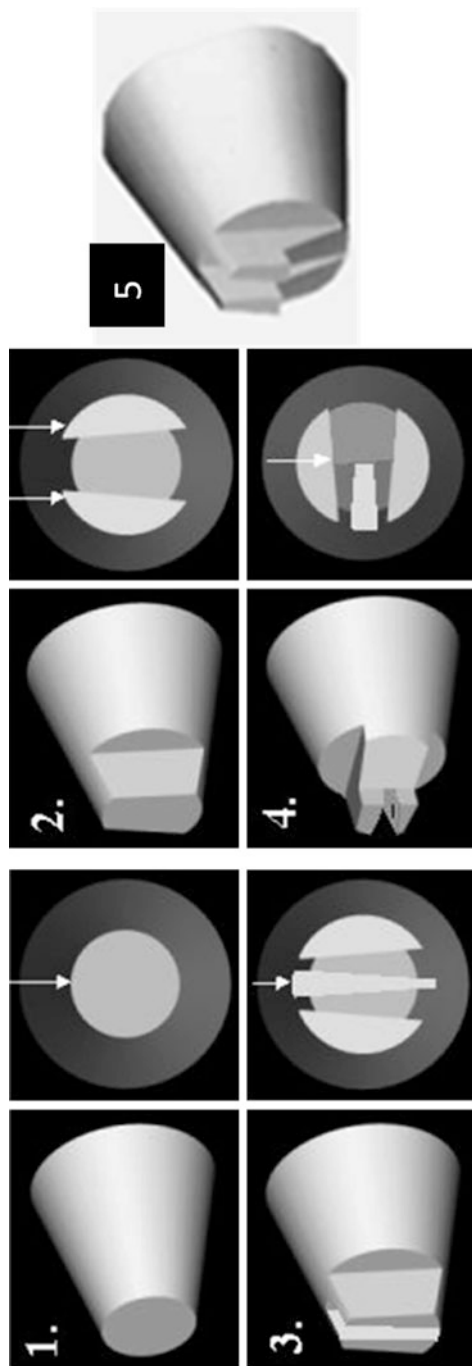


Fig. 2 The procedures for FIB milling a micro-threading tool. For all sputter steps, a tool is fixed, and the arrows indicate the direction of the ion beam (Picard et al. 2003)

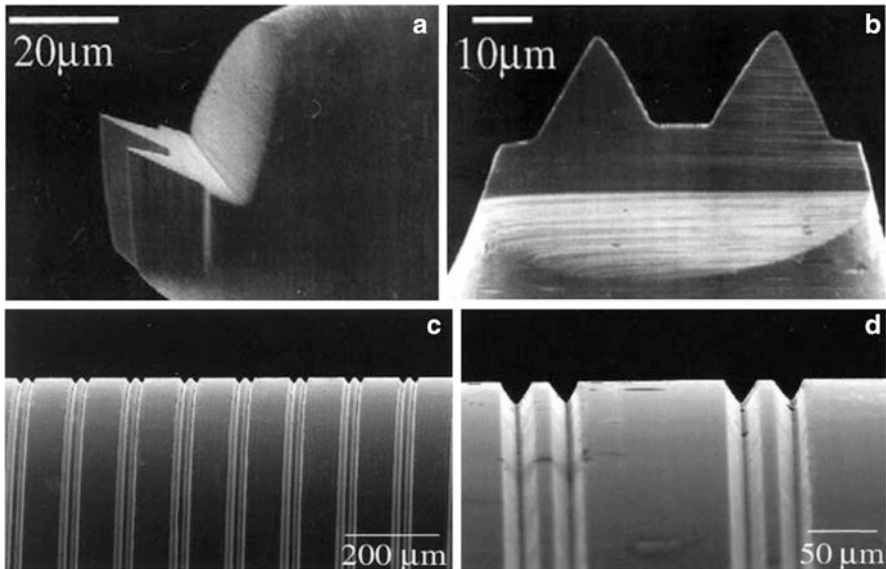


Fig. 3 FIB-shaped two-tip micro tool having triangular cutting faces and the machined micro-grooves. (a) and (b) show the tool tips; (c) and (d) show the machined grooves on PEEK workpiece surface by the two-tip tool (Picard et al. 2003)

Ding et al. (2008, 2012) evaluated the dependence of machining removal rate and surface morphology of FIB-sputtered diamond on FIB processing parameters such as the beam current and the ion incident angle. Their results indicate that a single crystal diamond tool fabricated by FIB under lower beam current of 4.6 nA offers a smoother cutting edge and a better tool surface quality as compared to that generated at a current of 20 nA (Ding et al. 2008).

Xu, Zhang, and their co-workers (2010; Zhang et al. 2009) developed semicircular micro tools and diffractive optical elements (DOE)-shaped micro tools to fabricate micro-DOE (MDOE) which are widely used in solar condense lenses, infrared sensors, laser beam shaping, and high-performance optical imaging systems. The measured radius of cutting edges of the micro tool was approximately 25 nm (Xu et al. 2010). The DOE-shaped micro tool and the machined MDOE are shown in Fig. 4 in which nanoscale surface finish was obtained.

Most recently, nano-gratings with the pitch as small as hundreds of nanometres has been generated by using nanoscale multi-tip diamond tools (with tool tip width of 150 nm) by Sun et al. (2012; Sun and Luo 2014). They proposed a divergence compensation method to facilitate FIB machining of nanoscale 3D structures. Through adjusting key fabrication parameters such as dwell time distribution, scanning passes, scanning pitch, and scanning strategy, they successfully fabricated a nanoscale diamond cutting tool with nanoscale periodical chisel structures on the tool tip as shown in Fig. 5. Initial results of using the nanoscale multi-tip diamond tool in the scratching of nano-grating arrays on an electroless nickel substrate show a

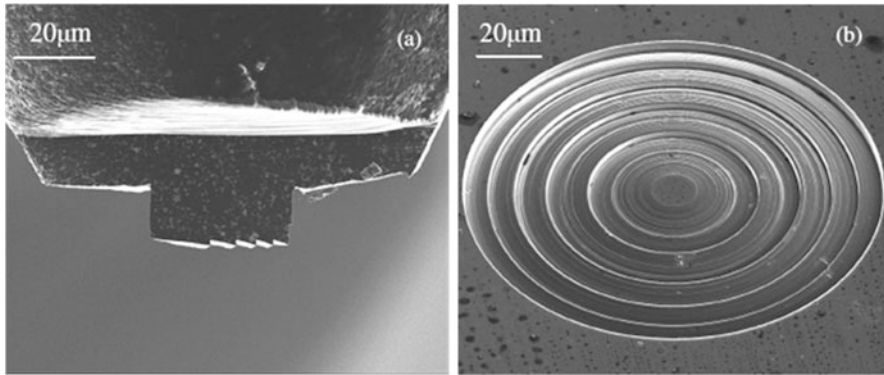


Fig. 4 SEM images of MDOE fabricated by a DOE-shaped micro tool. (a) DOE-shaped micro tool by FIB, (b) MDOE machined by the DOE-shaped micro tool (Xu et al. 2010)

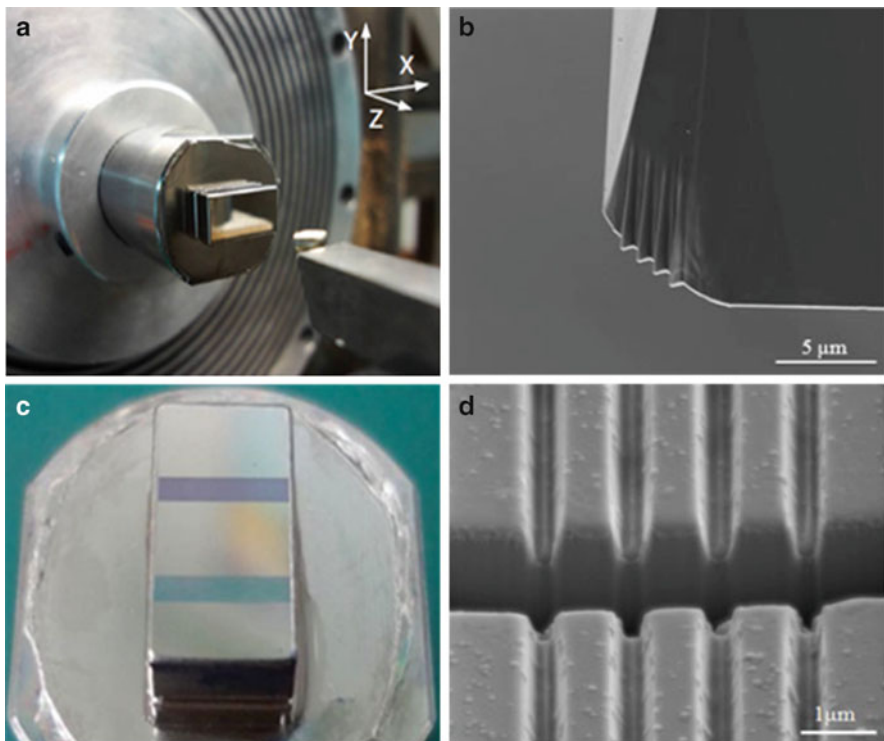


Fig. 5 Diamond machining of nano-grating arrays using a nanoscale multi-tip diamond tool. (a) Experimental setup of the ultra-precision diamond turning test; (b) SEM image of the nanoscale multi-tip diamond tool; (c) nano-grating arrays fabricated in two regions on the Nickel sample surface; and (d) the cross-sectional view of the machined nano-grating arrays (Sun et al. 2012)

high machining efficiency. The material removal rate was proved to be 30,000 times higher than purely FIB machining with ion current of 1 nA when machining these nanostructures (Sun et al. 2012). Since then, nano-grooving technique has been extensively studied by researchers to explore its manufacturing capability (Tong et al. 2014a, b, 2015a; Luo et al. 2014). The following session will introduce these studies from the aspects of machining mechanism, influence of processing parameters, and tool wear on the generated nanostructures.

4.3 Machining Mechanism

While using a nanoscale multi-tip cutting tool, the nanostructures are synchronously generated through a single cutting pass. The material removal process in a nanoscale multi-tip tool cutting will be different from that of using a single-tip cutting tool. In-depth understanding of the nanostructure formation process during multi-tip tool cutting is a necessity to further improve the nanomanufacturing capacity of this technique. To overcome the limitation in real-time experimental observation molecular dynamics (MD), simulations are often used by researchers to reveal the machining mechanism and obtain valuable feedback and guidance for further development of this new technique. In this session, the nanostructure generation processes, when using a single-tip and a multi-tip diamond tool, are modelled by MD simulation method. In order to benchmark the advantages and disadvantages of diamond turning using nanoscale multi-tip diamond tools, a comparison between using single-tip and multi-tip nanoscale tools in nanometric cutting is made from the viewpoint of nanostructure generation, cutting forces, and cutting temperature.

4.3.1 MD Nanometric Cutting Model

Geometric model for MD simulation: The geometry of the cutting tools is shown in Figs. 6a and 6b. Both the single-tip and the multi-tip diamond tool models are created based on the perfect diamond crystal structure. The tool-tip width is $W_a = 15a_1$ ($a_1 = 3.567 \text{ \AA}$) with the tool rake angle α being 0° and the tool clearance angle β being 12° . To save the computational time, a nanoscale double-tip diamond tool with a pitch of $L = 10a_1$ is employed in current research to represent the nanoscale multi-tip diamond tool. Since the radius of the cutting edge of the diamond tool is usually larger than the minimum depth of cut in nanometric cutting, in present large-scale MD simulations, all the tool models are built with a round cutting edge with the edge radius of $r = 5a_1$ instead of sharp cutting edges.

The workpiece has a dimension of $50a_2 \times 80a_2 \times 40a_2$ ($a_2 = 3.615 \text{ \AA}$ is the lattice constant of copper) and consists of a boundary layer and a thermostat layer with thicknesses of $2a_2$ and $3a_2$, respectively (as shown in Fig. 6c and d). The three orientations of the workpiece are $[1\ 0\ 0]$, $[0\ 1\ 0]$, and $[0\ 0\ 1]$ in the X , Y , and Z directions. Free boundary conditions are applied in all directions. Both the nanosized workpiece and the diamond cutting tool were modelled as deformable bodies.

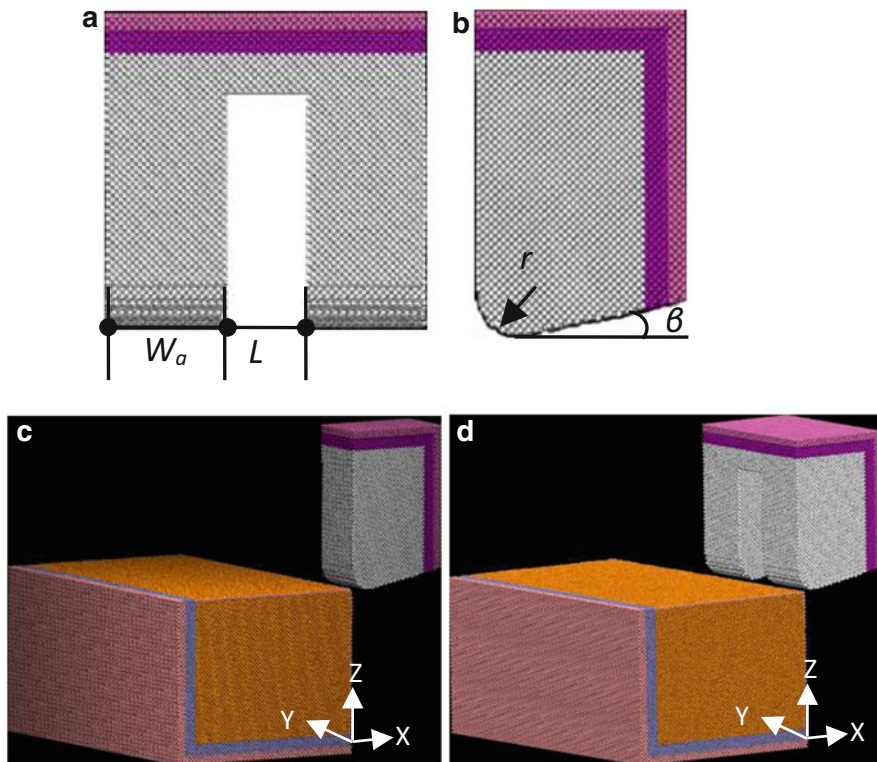


Fig. 6 Models of MD nanometric cutting simulation. (a) Front view of the multi-tip tool model; (b) right-hand end elevation of the tool tip model; (c) single-tip tool cutting model; and (d) multi-tip tool cutting model (Tong et al. 2014a)

During nanometric cutting, the bottom and outer sides of the substrate (atoms in pink color) are fixed as it has been suggested to be an appropriate configuration to simulate the nanometric cutting process (Lin and Huang 2008; Zhu et al. 2010).

Potential functions: In nanometric cutting, hybrid potential functions can be used to describe the interactions between the tool and the workpiece as well as the quantum interactions between electron shells and represent the physical properties of each atom type being simulated, such as elastic constants and lattice parameters. Balamane et al. (1992) and Smith et al. (2004) have presented a comprehensive review of the potential energy functions that have been used in recent decades.

In nanometric cutting of copper, there are three different atomic interactions in the MD simulation: (1) the interaction between copper atoms (Cu–Cu) of the workpiece, (2) the interaction between diamond atoms (C–C) of the tool, and (3) the interaction between workpiece and tool (Cu–C). For the Cu–Cu interaction, the embedded atom method (EAM) potential proposed by Foiles et al. (Daw et al. 1993) is used since it has been widely used in description of metallic materials (Ye et al. 2003; Pei et al. 2009; Pelaz et al. 2004). As it is shown in Eq. 1, the total energy E_{eam} of the atomistic

system comprises summation over the atomistic aggregate of the individual embedding energy F^i of atom i and pair potential ϕ_{ij} between atom i and its neighboring atom j , which can be expressed as:

$$E_{eam} = \sum_i F^i \left(\sum_{j \neq i}^n \rho^i(r^{ij}) \right) + \frac{1}{2} \sum_{ij, i \neq j} \phi_{ij}(r^{ij}) \quad (1)$$

where the E_{eam} is the total energy of the atomistic system which comprises summation over the atomistic aggregate of the individual embedding energy F^i of atom i and the pair potential ϕ_{ij} between atom i and its neighboring atom j . The lower case Latin superscripts i and j refer to the different atoms, r^{ij} is the distance between the atoms i and j , and $\rho^i(r^{ij})$ is the electron density of the atom i contributed by atom j .

For C–C atoms, we adopt the Tersoff potential (Tersoff 1989) computed as follows:

$$V_{ij} = f_C(r_{ij}) [f_R(r_{ij}) + b_{ij}f_A(r_{ij})] \quad (2)$$

where V_{ij} is the bond energy, i and j label the atoms of the system, r_{ij} is the length of the ij bond, b_{ij} is the bond order term, f_R is a two-body term, f_A includes three-body interactions, and f_C represents a smooth cutoff function to limit the range of the potential.

The Morse potential function (Ikawa et al. 1991a) was used to describe the interaction between Cu and C, and the total energy E_{tot} is expressed as:

$$E_{tot} = \sum_{ij} D_0 \left[e^{-2\alpha(r-r_p)} - 2e^{-\alpha(r-r_p)} \right] \quad (3)$$

where r is the instantaneous distance between atoms i and j . The cohesion energy D_0 , the elastic modulus α , and the equilibrium bond distance r_p are 0.087 eV, 5.14 \AA^{-1} , and 2.05 \AA , respectively (Ikawa et al. 1991a).

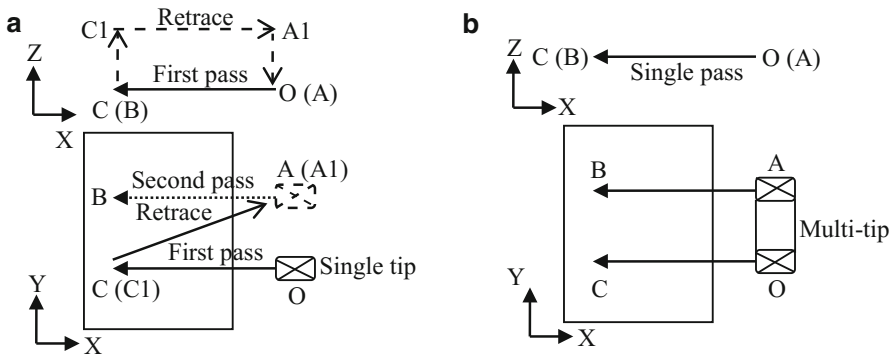
4.3.2 MD Simulation Setup

All of the cutting tools are applied along the $[-1 \ 0 \ 0]$ direction on the $(0 \ 0 \ 1)$ surface of the copper at a constant cutting speed of 200 m/s. Of course, the simulation may have its own limitations including the need to run at very high cutting speeds, but this may not be a serious limitation as long as we are interested in the general nature of the process without consideration of the speed effects (Komanduri et al. 2001). The main computational parameters used in the MD simulations are summarized in Table 1 for reference.

The equations of atom motion were integrated using velocity Verlet algorithm with a time step of 1 fs. Moreover, 85,000 time steps were carried out as the relaxation process to adjust the system to 293 K before cutting. During cutting and the thermal annealing processes, the systems were controlled by NVE ensemble, and the thermostat atoms were kept at a constant temperature of 293 K through a velocity

Table 1 MD simulation parameters for nanometric cutting of copper (Tong et al. 2014a)

	Single-tip with multi-pass	Multi-tip with single pass
Workpiece material	Copper	Copper
Workpiece dimension	$50a_2 \times 80a_2 \times 40a_2$ ($a_2 = 3.615 \text{ \AA}$)	$50a_2 \times 80a_2 \times 40a_2$ ($a_2 = 3.615 \text{ \AA}$)
Number of atoms	760, 355	894, 870
Tool tip width	$15a_1$ ($a_1 = 3.567 \text{ \AA}$)	$15a_1$ ($a_1 = 3.567 \text{ \AA}$)
Tool rake angle	0°	0°
Tool clearance angle	12°	12°
Time step	1 fs	1 fs
Initial temperature	293 K	293 K
Depth of cut	1 nm	1 nm
Cutting speed	200 m/s	200 m/s

**Fig. 7** (a) Single-tip cutting with two passes; (b) multi-tip cutting with single pass (Tong et al. 2014a)

scaling method to perform the heat dissipation (Yan et al. 2007). The velocity scaling method controls the temperature by rescaling the thermal atoms velocities to 293 K if the temperature departs more than 5 K from the specified temperature at a certain time step. Thus, this algorithm allows the heat transferring from shear region to the bulk of the workpiece which conforms to experimental observation.

Figure 7 shows the simulation procedure of nanometric cutting and traces of the tool. For a single-tip tool, it scratched the surface in X-Y plane along the OC direction for the first cutting pass (as shown in Fig. 7a). Then the tool followed trace (C-C1) in the Y-Z plane. The tool moved along line C1A1 and moved down to point A. At last, the tool scratched the second groove along the line AB with same depth of cut (as the dotted line shows). For multi-tip tool, only single pass was taken with the same cutting distance as shown in Fig. 7b. All the simulations were performed by a high-performance computing cluster (HPC) using 24 cores.

4.3.3 The Post-processing Methods

Calculation of the stresses and cutting forces: In LAMMPS, the stress for each atom is attributed to its interaction with all other atoms in the simulation, and the stress tensor for an atom i can be calculated from Eq. 4.

$$S_{ab} = \left[\begin{aligned} &mv_a v_b + \frac{1}{2} \sum_{n=1}^{N_p} (r_{1a} F_{1b} + r_{2a} F_{2b}) + \frac{1}{2} \sum_{n=1}^{N_b} (r_{1a} F_{1b} + r_{2a} F_{2b}) \\ &- \left[\begin{aligned} &+ \frac{1}{3} \sum_{n=1}^{N_a} (r_{1a} F_{1b} + r_{2a} F_{2b} + r_{3a} F_{3b}) + \frac{1}{4} \sum_{n=1}^{N_d} (r_{1a} F_{1b} + r_{2a} F_{2b} + r_{3a} F_{3b} + r_{4a} F_{4b}) \\ &+ \frac{1}{4} \sum_{n=1}^{N_i} (r_{1a} F_{1b} + r_{2a} F_{2b} + r_{3a} F_{3b} + r_{4a} F_{4b}) + \text{Kspace}(r_{ia}, F_{ib}) \end{aligned} \right] \end{aligned} \right] \quad (4)$$

where a and b denote x, y, z to generate six components of the symmetric stress tensor. The first term of the equation is a contribution due to the kinetic energy of atom i . The second term is a pair-wise energy contribution where n loops over the N_p neighbors of atom i and r_1 and r_2 are the positions of the two atoms in the pair-wise interaction. F_{1b} and F_{2b} are the forces on the two atoms resulting from the pair-wise interactions. The third term is a bond contribution over the N_b bonds of atom i . There are similar terms for N_a angle, N_d dihedral, and N_i improper interactions. Kspace term represents long-range Coulombic interactions.

The tensor for each atom has six components and is stored as a six-element vector in the following order: $\sigma_{xx}, \sigma_{yy}, \sigma_{zz}, \tau_{xy}, \tau_{xz}, \tau_{yz}$. However, it is noted that the per-atom stress is really a stress-volume formulation. In order to generate continuous matter, it would need to be divided by a per-atom volume to have units of stress. The hydrostatic stress (σ_{hydro}) and von Mises stress (σ_{von}) can be further computed using the following equations:

$$\sigma_{\text{hydro}} = \frac{\sigma_{xx} + \sigma_{yy} + \sigma_{zz}}{3} \quad (5)$$

$$\sigma_{\text{von}} = \sqrt{\frac{(\sigma_{xx} - \sigma_{yy})^2 + (\sigma_{xx} - \sigma_{zz})^2 + (\sigma_{yy} - \sigma_{zz})^2 + 6(\tau_{xy}^2 + \tau_{yz}^2 + \tau_{xz}^2)}{2}} \quad (6)$$

For cutting forces, action and reaction are opposite and equal. Since it is quite difficult to accurately measure the volume of the workpiece in cutting zone, the cutting forces were obtained by summing the forces of tool atoms. In LAMMPS, this can be done using “stress/atom” command followed by a “reduce sum” command. A schematic diagram of the forces directions is shown in Fig. 8b.

Calculation of the cutting temperature: Cutting heat has been regarded as one of the key factors to influence the quality of the generated nanostructures as well as the tool life in nanometric cutting process. According to the law of equipartition of

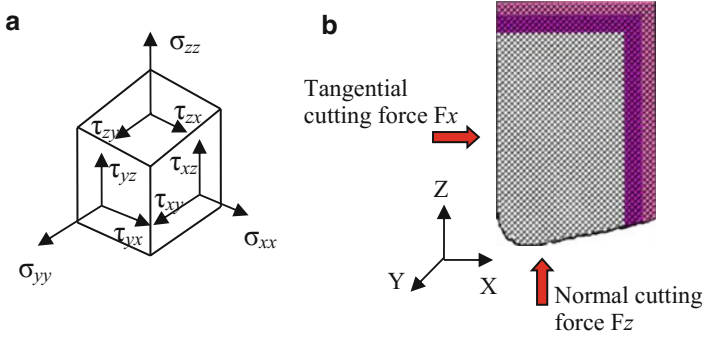


Fig. 8 Schematic diagrams of the stresses and cutting forces. (a) Stress directions and (b) the direction of cutting forces (Tong et al. 2014a)

energy, the representative temperature of a group of atoms can be calculated from the total atomic kinetic energies of the group. As the nature of the temperature is statistical, the instantaneous kinetic energy of each atom during nanometric cutting differs significantly from the temperature of the bulk. Therefore, the measurement of cutting temperature is not straight forward.

In order to more accurately characterize the variation of temperature during the cutting process, we employed the concept of atomistic equivalent temperature T_i (Tong et al. 2014b) to analyze the cutting temperature. A cutoff distance $r_0 = 4a_0$ was used to select atoms as it can reflect the thermal feature of the short-range structure of copper lattice during nanometric cutting processes. It is noted that only the thermal velocities of atoms are used to compute the temperature. The kinetic energy contributed by the advection movement of the tool should be subtracted beforehand.

CSP: Dislocations play a crucial role in governing the plastic response of ductile materials. The thermal vibration of atoms at finite temperatures makes it difficult to observe dislocations in a thermal-sensitive environment. The widely used methods for tracing such dislocations and other lattice defects are coordinate number analysis, slip vector, and centro-symmetry parameter (CSP). It has been reported that centro-symmetry parameter (CSP) is less sensitive to the temperature increase compared with other methods such as atomic coordinate number and the slip vector (Zong et al. 2010). The CSP method proposed by Kelchner et al. (1998) quantifies local deviations from centro-symmetry in a given centro-symmetric structure such as FCC and BCC (body-centered cubic). The centro-symmetry parameter P_i is defined as follows:

$$P_i = \sum_{i=1}^6 \left| \bar{R}_i + \bar{R}_{i+6} \right|^2 \quad (7)$$

where \bar{R}_i and \bar{R}_{i+6} are the position vectors corresponding to the six pairs of opposite nearest atoms. The parameter P_i increases from 0 for perfect FCC lattice to positive

Table 2 The default value of atomic structural defects in CSP (Tong et al. 2014a)

CSP value P	Lattice structure	Represent atom color
$P < 3$	Ideal FCC structure	Yellow
$3 < P < 5$	Partial dislocation	Cyan
$5 < P < 8$	Stacking fault	Blue
$8 < P < 21.5$	Surface atoms	Orange
$P > 21.5$	Surface atomic step atoms	Pink

values for defects and for atoms close to free surfaces. In the case of the single crystal copper, the default value of P_i corresponding to those atomic defect structures and its representing color are indicated in Table 2.

4.3.4 Nanostructure Generation Process

We first simulated the generation process of nanostructures on the copper surface using the single-tip tool with two cutting passes. The nanostructure in this chapter means a nano-groove machined on the copper surface. It should be noted that the distance between two cutting passes is specified as $10a_1$ ($a_1 = 3.567 \text{ \AA}$) according to the pitch of the multi-tip tool. Figure 9 shows the snapshots of nanometric cutting process as well as the atomistic dislocation evolutions in the workpiece when using the single-tip tool under a depth of cut of 1.0 nm. Every workpiece atom was colored by its CSP value. It should be pointed out that the isolated atoms with a green color inside the workpiece are not lattice defects. Those atoms with CSP above three are caused by thermal vibration at a finite temperature. Moreover, the defect-free atoms were removed from the visualizations.

At initial cutting stage, with the penetration of the tool, the lattice of workpiece deformed as buckled, and the outer kinetic energy of tool transmitted onto the workpiece and converted into potential energy stored in the deformed lattice. When the energy or shear stress of copper atoms exceeds a specific level, the atoms tend to rearrange into lower-energy lattice to relax lattice strain through dislocation nucleation (as shown in Fig. 9a). As the tool advances, more dislocations initiate and propagate in preferred (1 1 1) crystal slip planes systems. The pile-ups of atoms in front of the tool rake face lead to the formation of cutting chip (as shown in Fig. 9b). At the same time, dislocations that penetrated the workpiece migrate out toward the machined surface and create atomic sized steps (atoms in pink color) on the machined surface, which represents the best surface roughness possible.

The second cutting pass was taken along line AB with the same processing parameters (as shown in Fig. 7a). After two consecutive cutting passes, two nano-grooves were machined by the single-tip tool (as shown in Fig. 9c). However, it is found that at the end of the second pass, there were some disordered atoms moved into the first nano-groove. This resulted in the reshaping of the right side of the first machined groove due to the lack of support on that side. This phenomenon is recognized as the feed rate effect in the nanometric cutting. When the distance

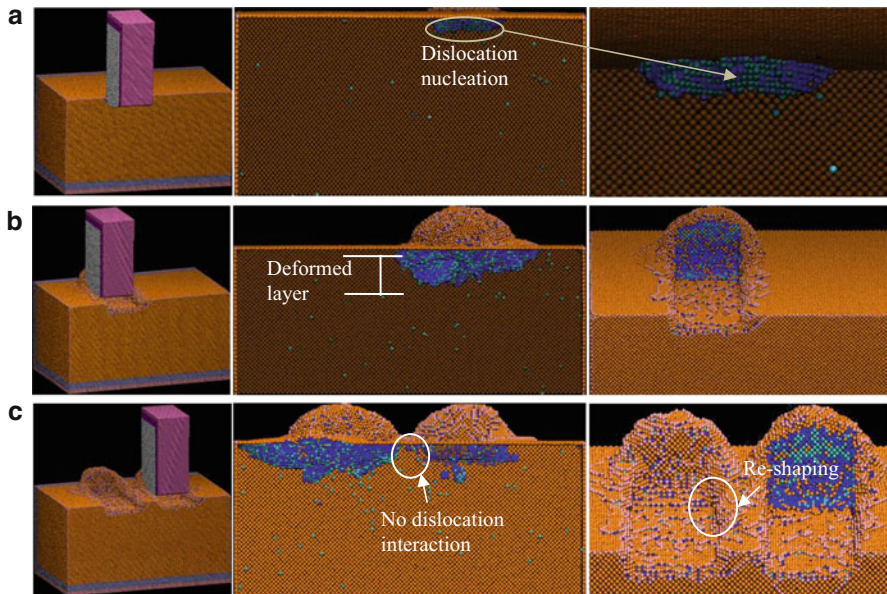


Fig. 9 Snapshots of cutting process and dislocation evolution of workpiece using a single-tip tool with multi-tip passes. (a) Dislocation nucleation; (b) first cutting pass; and (c) the second cutting pass (Tong et al. 2014a)

between two passes is less than a critical value, there is a strong possibility that the material plastic side flow (in terms of dislocation movements) created in the second pass will extend to the machined surface of the first cutting and thus reshape the first nano-groove. It is noted that this critical value is not fixed as the dislocation nucleation and movements are affected by the tool geometry, depth of cut, cutting speed, and local cutting temperature (Zhu et al. 2010).

A similar phenomenon has been reported by Yan et al. (Pei et al. 2009) in their MD study of the AFM scratching of copper. The tool model was built with a rounded regular three-sided pyramid with a hemisphere at the end (radius of the tool cutting edge of 1 nm). Their investigation showed that the cross-sectional shape of the first scratch was very close to that of the second one when the feed reached 3.62 nm (Pei et al. 2009). Fang et al. (2002) qualitatively compared the feed effect behavior predicted by the MD simulations with the AFM experiments (a diamond AFM tip with radius of 10 nm). Our results agree with their conclusions and further confirm that the feed rate effect also occurs in the rectangular shape tool-tip cutting.

For multi-tip tool cutting, it can be seen from Figs. 10a and 10b that the initial cutting stage was almost the same as that of single-tip tool cutting. The dislocations initiated under the tool-workpiece contact surface due to the compressive stress induced by the initial impact of the tool tips and then propagated along the (1 1 1) crystal slip planes. The atoms accumulated and piled up in front of the multi-tip tool, resulting in the formation of two independent initial chips. The increasing of the chip

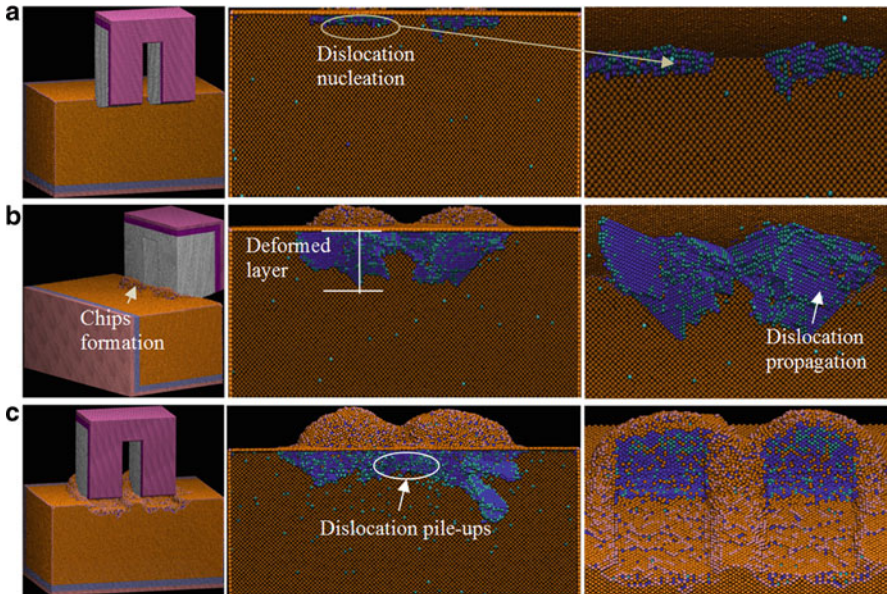


Fig. 10 Snapshots of cutting process and dislocation evolution in workpiece when using the multi-tip tool at cutting distances of (a) 2.55 nm, (b) 3.95 nm, and (c) 15.45 nm (Tong et al. 2014a)

volume indicated that the material deformation states for all cutting conditions were dominated by cutting and accompanied by plough.

However, unlike the single-tip tool cutting, where the nano-grooves were formed through two cutting passes separately, interactions between the dislocations around tool tips were observed when using the multi-tip tool (as shown by Figs. 10b and 10c). Because two nano-grooves were synchronously generated through a single cutting pass, the effect of feed rate observed in single-tip tool cutting can be completely eliminated when using the multi-tip tool. Compared with the nano-groove machined by the single-tip tool cutting, the nano-grooves generated by the multi-tip tool are closer to ideal center line symmetry (Fig. 10c).

4.3.5 Cutting Force

The variations of cutting forces during the steady cutting process were summarized in Fig. 11. The comparison was made between the first and the second cutting pass of the single-tip tool cutting and the multi-tip tool cutting. The results show that the tangential cutting force F_x and normal cutting force F_z in all simulations are fluctuating around an approximately constant value at the steady cutting stage. The dynamic equilibrium of the tool-workpiece contact area and the activities of dislocations accompanying the material removal process are responsible for the fluctuations. Both the normal and tangential cutting forces of the multi-tip tool cutting were

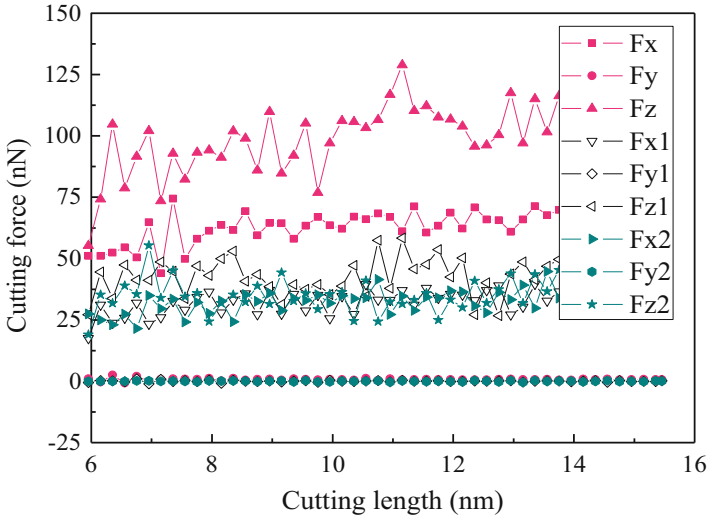


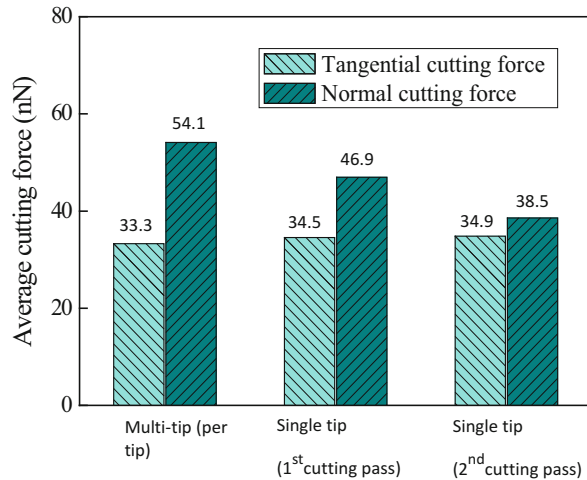
Fig. 11 The force-displacement curves under a depth of cut of 1.0 nm. F_x , F_y , and F_z represent the cutting forces of using the multi-tip tool; F_{x1} , F_{y1} , and F_{z1} and F_{x2} , F_{y2} , and F_{z2} represent the forces for the first and second passes when using the single-tip tool, respectively (Tong et al. 2014a)

larger than those of the single-tip tool cutting (for the first and the second cutting pass). However, the cutting forces in the Y direction were found to have an average value near zero because of the balanced forces contributing from each side.

In order to further quantify the difference of cutting forces between using the single-tip and the multi-tip tool, the average tangential cutting forces and normal cutting forces at the steady cutting state were calculated (as shown in Fig. 12). It was found that the tangential cutting forces of the first and the second cutting passes when using the single-tip tool were nearly the same, but the normal cutting force of the second pass was smaller than that of the first pass. The drop of the normal cutting force resulted from the feed rate effect which appeared at the end of the second cutting pass (as shown in Fig. 9c). The material side flows in terms of the dislocation extension released the extra stress during the second pass and thus lead to a drop of the normal cutting force. For multi-tip tool cutting, while the tangential cutting force per tip has a value of 33.3 nN which is slightly smaller than that of using a single-tip tool, the normal cutting force per tip of 54.1 nN is much larger than those observed when using the single-tip tool (46.9 nN for the first pass, 38.5 nN for the second pass). The significant dislocation pile-ups beneath the tool tips resulted in a local strengthening of the material in the normal direction during the multi-tip cutting process.

Moreover, the ratio of tangential cutting force to normal cutting force ($\mu = F_x/F_z$) is used to assess the alteration of local physical property during the nanometric cutting process. From the average forces at the steady stage, we obtain $\mu \approx 0.61$ for multi-tip cutting and a larger average value of 0.82 for the single-tip tool cutting. Lin et al. have measured the cutting forces in their scratching copper test and found that

Fig. 12 The average cutting forces for the single-tip tool and multi-tip tool cutting (Tong et al. 2014a)



the actual tangential cutting force F_x is 2,780.2 nN and the normal cutting force F_z is 5,686.2 nN (Lin and Huang 2008). The ratio of tangential cutting force to normal cutting force from their experimental data is 0.49. It is noted that our calculated ratio of F_x/F_z is larger than the experimental result because the value also depends on the tool rake angle and surface smoothness and the crystal structure of materials used. Komanduri et al. (2000) have investigated the atomic-scale friction at extremely fine scratch depths (from 0.8 nm to almost zero) and pointed out that for tool built with zero rake angle, the force ratio of F_x/F_z can be as large as 1.170.

Recently, Luan and Robbins have argued that the atomic-scale surface roughness produced by discrete atoms had significant effect on the coefficient of friction, and the contact areas and stresses may be changed with the local alteration of friction and lateral contact stiffness in an order of magnitude (Luan and Robbins 2005). Thus, the difference of the ratio of F_x/F_z observed in the nanometric cuttings between using the single-tip tool and the multi-tip tool may also be attributed to the different local tool-workpiece contact status.

4.3.6 Temperature Distribution

Figure 13 shows the cross-sectional view of the atomistic equivalent temperature distribution for the single-tip tool and the multi-tip tool cuttings. Atoms are colored according to their atomistic equivalent temperature. For better visualization, the white dotted lines are used as the boundaries between the low- and high-temperature zones (>550 K). It was found that in all simulations, the temperature in shear zone was around 650 K. The range of high-temperature region (>550 K) when using the multi-tip tool was apparently larger than that of using the single-tip tool. The highest-temperature regions were found at the tool-chip interface slightly toward the workpiece side.

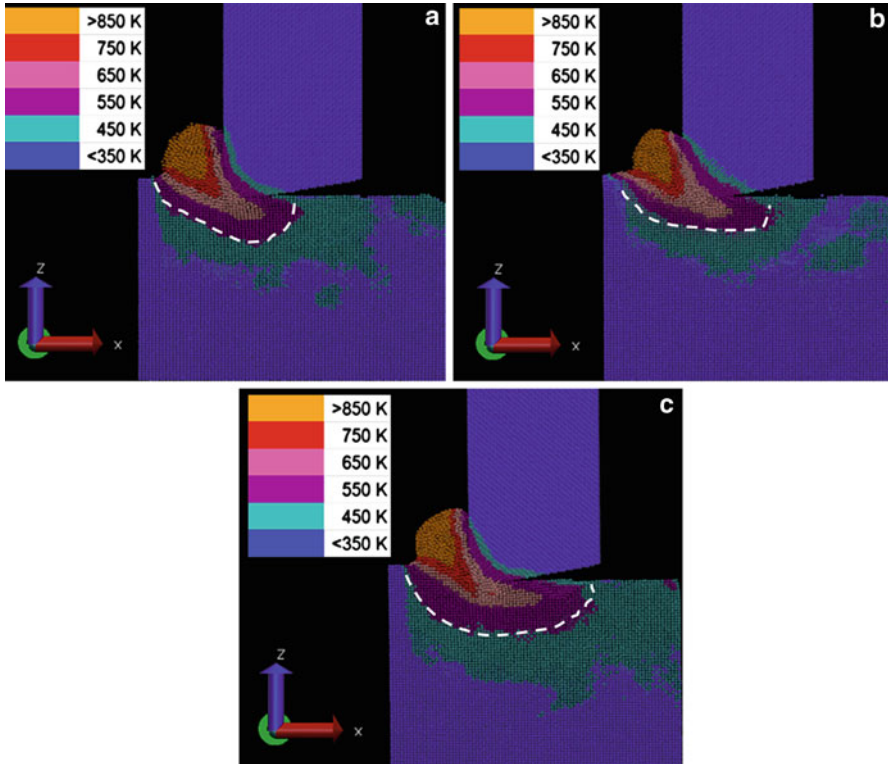


Fig. 13 The cross-sectional views of the temperature distribution at a depth of cut of 17 nm. (a) Single-tip cutting (first pass), (b) single-tip cutting (second pass), and (c) multi-tip cutting with single pass (Tong et al. 2014a)

Unlike traditional metal cutting, in this study the diamond tool material is significantly harder than the workpiece material, i.e., copper. It is a common knowledge that when the cutting tool material is significantly harder than the substrate, the plastic deformation of the softer work material will be the main heat source (Norouzifard and Hamed 2014). In our MD model, the energy transfer between copper and diamond is described by the selected potential functions. At the interface of the diamond tool and copper substrate, there is an atomic layer (with a thickness of several atoms) which transmits the energy between C and Cu atoms. Copper and the diamond materials both have high thermal conductivity. However, the thermal conductivity of the natural diamond is about $22 \text{ W}/(\text{cm}\cdot\text{K})$ which is five times more than that for copper. As a result, a large temperature gradient toward the cutting tool was observed in Fig. 13. Moreover, the large diamond cutting tool model built in the present study also helped to release the cutting heat at the tool cutting edge. Therefore, the diamond cutting tool would have lower temperature than the copper substrate, and the highest temperature regions were found at the tool-chip interface slightly toward the workpiece.

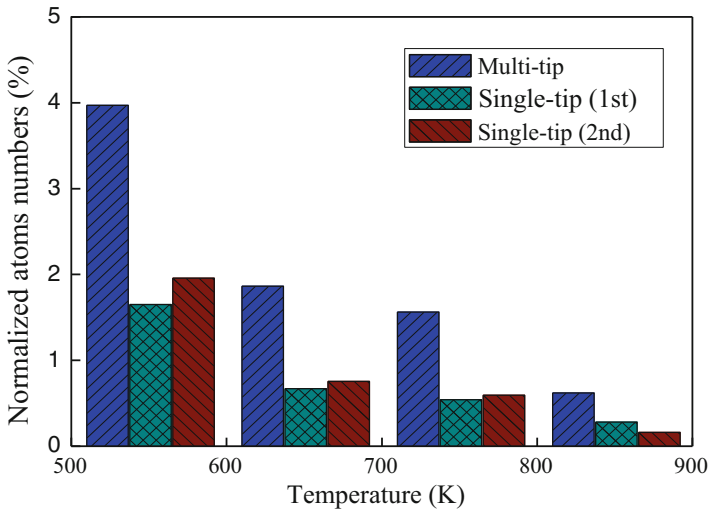


Fig. 14 The normalized atom numbers in different temperature ranges (Tong et al. 2014b)

In order to further quantify the difference in cutting heat when using different kinds of tools, detailed analysis has been done by comparing the number of atoms in different temperature ranges. For a better comparison, only the workpiece atoms within the cutting zone (z coordinate larger than $20a_2$) were taken into account, and the numbers of atoms in different temperature ranges were normalized by the total number of atoms selected (as shown in Fig. 14). It was found that the proportion of atoms with atomistic equivalent temperature larger than 500 K in the multi-tip tool cutting was 8.01% which was apparently larger than that of the single-tip tool cutting (being 3.3%). This result quantitatively demonstrated that the cutting heat generated while using the multi-tip tool was much higher than that of the single-tip tool cutting.

In addition, the higher cutting temperature observed in the multi-tip cutting also explained the feature of cutting forces discussed in the above section. Although the normal cutting force per tip of the multi-tip cutting was larger than that of using the single-tip tool, the tangential cutting force per tip is slightly lower than that of using the single-tip tool. This is mainly due to the fact that the much higher local temperature generated during the multi-tip cutting process would result in local weakening of the Cu-Cu bond force and thus lead to a lower tangential cutting force per tip.

4.3.7 Thermal Annealing at Machined Surface

It has been widely accepted that recrystallization happens during local annealing process, not only in ductile metallic materials but also in brittle materials such as silicon and diamond. In macro machining practice, after the tool has left the machined region, there is a macroscopic time (\sim ms) for the machined surface to relax (Ye et al. 2003). And by that time, the subsurface atomic defects might be able to get annealed

partly. In a nanometric cutting, the thermal effects happen in such a short timescale that to accurately detect and measure the temperature distribution, it requires a thermal measurement system with extremely short response time and high resolution. However, the spectral wavelength of sensors used in most current commercial infrared thermography are ranging from 0.8 to 14 μm with the response time ranging from 2 to 120 ms. It is therefore very difficult to detect and monitor the nanometric cutting heat accurately by those temperature measurement systems. MD simulation provides an alternative way to solve this problem by allowing the atomistic insight into the material thermal behavior during nanometric cutting processes.

In present work, in order to investigate the thermal effects when different kinds of tools were used, time relaxations of the machined work material were further performed for both the single-tip and multi-tip tool cuttings. It was found through trial simulations that a period of 50 ps relaxation process was enough for the present system to cool down to 293 K. The CSP and the RDF were used to identify the changes in the lattice structure during the relaxation process.

Figure 15 shows the cross-sectional views of the defect zones at 0 and 50 ps. It can be seen that before the relaxation, there are large numbers of dislocations and atomic defects beneath the tool tip (Fig. 15a and c). The thickness of the atomic defect layer formed in the multi-tip tool cutting is about ~ 6 nm which is nearly twice the thickness created by the single-tip tool cutting (being ~ 3.5 nm). However, as shown in Fig. 15b, most of atomic defects and dislocations in the machined area were annealed after 50 ps for the single-tip tool cutting. For multi-tip tool cutting, the atomic defects and dislocations were also remarkably annealed after the relaxation process (as shown in Fig. 15d), leaving behind an almost dislocation-free machined workpiece.

In order to further identify the lattice integrity of the machined structure, the RDFs of the machined nano-grooves were calculated. Compared with the single-tip cutting, before relaxation a slightly smaller RDF peak value was found for the nano-grooves machined by the multi-tip tool (Fig. 16a), which indicates that the atoms are in a higher short-range disorder in the multi-tip tool cutting. However, after the relaxation process, there is an increase of the first peak value of RDF for both the single-tip and the multi-tip tool cutting, and the two RDF curves have nearly the same shape (as shown in Fig. 16b). This result is in good agreement with the CSP result as discussed above and indicates that local recrystallization takes place on the machined surface during the relaxation process.

Nevertheless, it is noted that the local recrystallization observed in the multi-tip tool cutting is more noticeable than the single-tip tool cutting. Although the thickness of the atomic defect layer before relaxation when using the multi-tip tool was much larger than that of using the single-tip tool, most of the defects were annealed and left almost an ideal FCC lattice structure after the relaxation process. As evident from Figs. 15b and 15d, the thickness of the residual atomic defect layers are 3.0 and 3.9 nm for the single-tip and the multi-tip tool cuttings, respectively.

4.3.8 Summary

This session was dedicated to provide a detailed understanding on the nanostructure generation processes when using a single-tip and a multi-tip diamond tool through

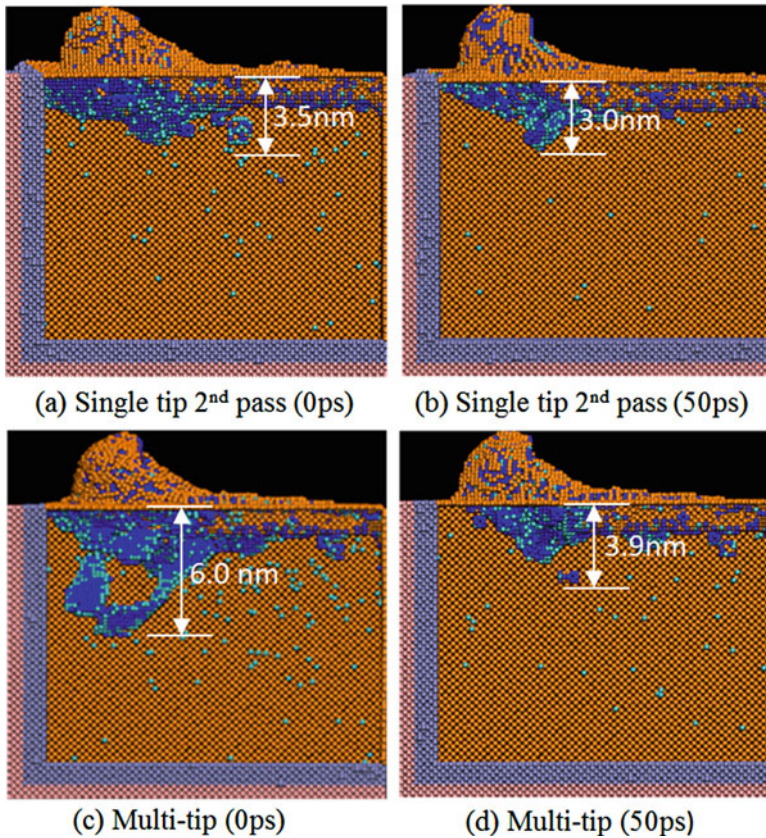


Fig. 15 The cross-sectional views of the defect zones after 0 and 50 ps relaxation process. Cyan and blue atoms represent particle dislocation and stacking fault, respectively (Tong et al. 2014b)

MD simulation studies. Compared with the single-tip cutting, the new features of multi-tip tool cutting such as the improved center line symmetry of machined nanostructures, the high cutting temperature, and the high normal cutting force per tip have been identified. The simulation results indicate that, in addition to the high machining efficiency, the effect of feed rate and the alignment issues on machining accuracy associated with the use of separate single-tip tool can be completely eliminated when using nanoscale multi-tip tools.

4.4 Influence of Processing Parameters

In diamond turning using nanoscale multi-tip diamond tools, as the tools and the machined structures are in a range of submicron or even dozens of nanometers, even tiny (nanometer-level) machining defects can degrade the form accuracy and the integrity of machined nanostructures. In-depth understanding of the machining process, especially knowing the nanomanufacturing capability under different cutting

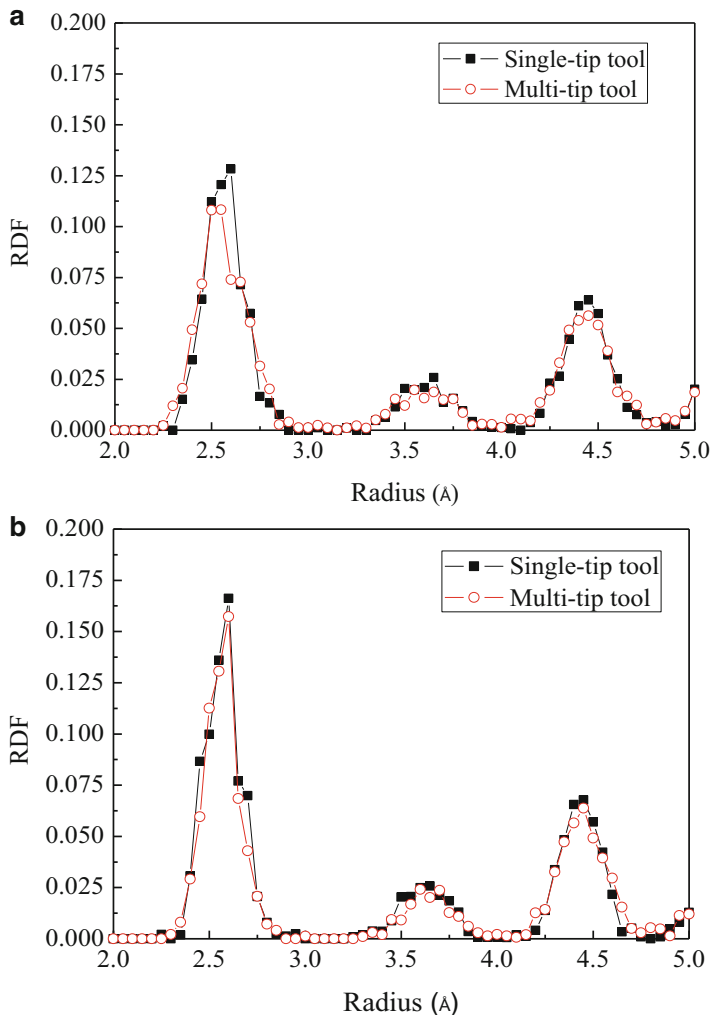
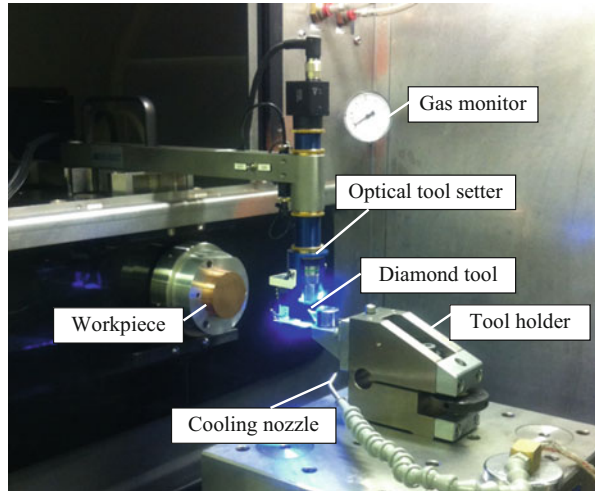


Fig. 16 RDF of machined nano-grooves. (a) Before the relaxation and (b) after 50 ps relaxation (Tong et al. 2014b)

conditions, is of great significance to the full exploration of the advancement of this technique. In this session, the focus will be on the influence of processing parameters on the accuracy and the integrity of machined nanostructures. A series of nanometric cutting trials (under 15 different cutting conditions) on copper substrates are carried out using the nanoscale multi-tip diamond tool fabricated with L/W_f of 1.54, which has been approved to possess the best shape transformability from the tool to the workpiece surface (Luo et al. 2014). In order to reveal the underlying mechanism for machining defects observed in experiments, MD simulations are also carried out to gain atomistic insight into the work material behavior during the nanometric cutting process.

Fig. 17 Experimental configuration and tooling setup (Tong et al. 2015a)



4.4.1 Experimental Setup

The nanometric face cutting trials using a nanoscale multi-tip diamond tool were carried out on a diamond turning machine (Precitech Nanoform 250). The configuration of the cutting trials is shown in Fig. 17. The cutting tools were mounted on a tool holder. An optical tool setter with a 20x long working distance objective lens was used to set the tools.

Nanometric machining was conducted on an oxygen-free copper (OFC) wafer. It had a diameter of 50 mm and the following properties: hardness 89HV50, density 8.94 g/cm^3 , shear modulus 44.0 GPa, Poisson's ratio 0.31, and annealing temperature $37\text{--}650 \text{ }^\circ\text{C}$

Three-diamond cutting tools were used in the experiment. Before the multi-tip diamond tool cutting, a flat copper substrate surface was prepared by face diamond turning using two normal diamond tools. One conventional roughing tool was used for rough cutting of the copper surface. After the rough cutting, a controlled waviness diamond tool was used to generate the surface with mirror finish. The cutting fluid (CLAIRSOL 330 special kerosene) was applied in these steps. Then, the multi-tip diamond tool was used to generate nano-grooves on the flat copper surface. The multi-tip tool had a tip height of 589.8 nm, a tip width of 152.9 nm, and a tip base width of 458.5 nm with the tip distance being 706 nm. The geometrical features of the cutting tools are listed in Table 3.

Three spindle speeds tested were 12 rpm (low), 60 rpm (medium), and 120 rpm (high). For each spindle speed, the value of depth of cut was set at five different levels, from 100 nm to 500 nm with an increment of 100 nm. The parameters are list in Table 4.

The multi-tip diamond tool is fabricated by using a dual-beam FIB facility (FEI Quanta3D FEG). After the machining trials, the machined surface roughness and the nanostructure pattern were measured by using a white light interferometer (Form TalySurf CCI 3000) and a scanning electron microscope within the FEI Quanta3D FEG, respectively.

Table 3 Geometric features of the cutting tools used in the cutting trials (Tong et al. 2015a)

	Tool nose radius (mm)	Rake angle (°)	Clearance angle (°)	Cutting edge radius
Roughing tool	0.5	0	10	Standard
Controlled waviness tool	0.5	0	10	Standard
Nanoscale Multi-tip tool	–	0	10	40 nm

Table 4 Operational variables and their levels in face turning trials (Tong et al. 2015a)

Face cutting	No. of cut	Depth of cut (nm)	Spindle speed (rpm)	Radius of start point (mm)	Cutting speed (m/s)	Feed rate (μm/re)
Group A	1st	100	12	23.0	0.02890	9
	2nd	200	12	22.5	0.02827	9
	3rd	300	12	22.0	0.02765	9
	4th	400	12	21.5	0.02702	9
	5th	500	12	21.0	0.02639	9
Group B	6th	100	60	19.0	0.11938	9
	7th	200	60	18.5	0.11624	9
	8th	300	60	18.0	0.11310	9
	9th	400	60	17.5	0.10996	9
	10th	500	60	17.0	0.10681	9
Group C	11th	100	120	15.0	0.18850	9
	12th	200	120	14.5	0.18221	9
	13th	300	120	14.0	0.17593	9
	14th	400	120	13.5	0.16965	9
	15th	500	120	13.0	0.16336	9

4.4.2 MD Simulation Setup

The MD nanometric cutting model was developed as shown in Fig. 18 (Tong et al. 2015a). The geometrical parameters of the tool were built according to the shape of the multi-tip tool tips fabricated by FIB. The tool had a tip width W_a of $3a_1$ ($a_1 = 3.567 \text{ \AA}$), a tip base width W_f of $9a_1$, a tool rake angle α of 0° , a tool clearance angle β of 10° , a tip angle θ of 14° , and a cutting edge radius r of $5a_1$. To save the computational time, a double-tip nanoscale diamond tool with the tool tip distance L of $14a_1$ was employed in present work to represent the nanoscale multi-tip diamond tool (as shown in Fig. 18a). The systems were controlled by NVE ensemble, and the thermostat atoms were kept at a constant temperature of 293 K through a velocity scaling method to perform the heat dissipation. The other computational parameters used in the MD simulations are summarized in Table 5 for reference.

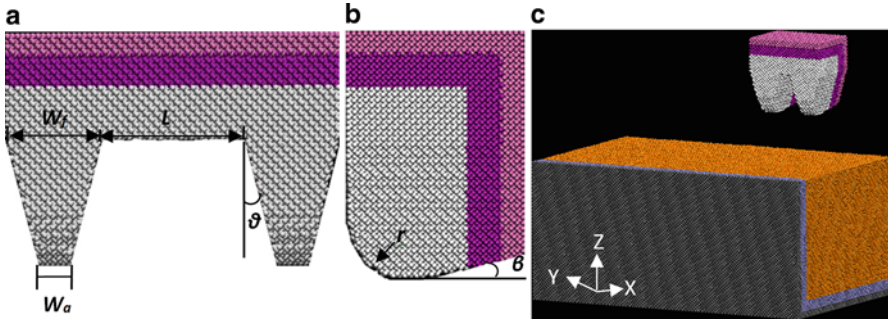


Fig. 18 Molecular dynamics simulation model: (a) Front view of the multi-tip tool model; (b) right-hand end elevation of the multi-tip tool model; and (c) nanometric cutting model (Tong et al. 2015a)

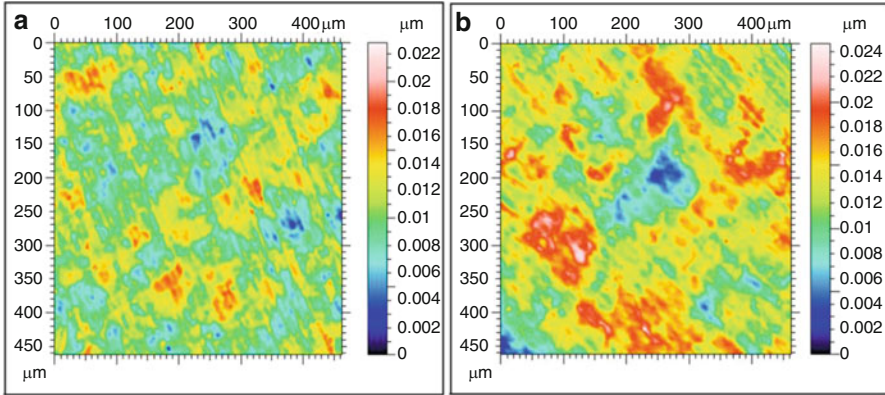
Table 5 Simulation parameters of MD nanometric cutting model (Tong et al. 2015a)

Workpiece materials	Copper
Workpiece dimensions	$50a_2 \times 80a_2 \times 40a_2$ ($a_2 = 3.615 \text{ \AA}$)
number of atoms	714,707
Time step	1 fs
Initial temperature	293 K
Depth of cut (cutting speed = 200 m/s)	2.0 nm, 2.5 nm, 3.0 nm, 3.5 nm, 4.0 nm
Cutting speed (depth of cut = 2.0 nm)	10 m/s, 50 m/s, 100 m/s, 160 m/s, 200 m/s, 250 m/s

4.4.3 Nanostructures Formed Under Different Cutting Conditions

As shown in Fig. 19a (Tong et al. 2015a), the surface roughness S_a of the copper substrate was 1.85 nm prepared by the face diamond turning. The surface was then machined by the nanoscale multi-tip diamond tool with a depth of cut of 100 nm (a cutting speed of 0.03 m/s, a feed rate of 9 $\mu\text{m}/\text{rev}$).

The SEM images of several machined grooves using different depths of cut are shown in Fig. 20 (Tong et al. 2015a). In general, the periodic nanostructures on the diamond tool tip were successfully replicated on the surface of the copper substrate when the depths of cut of 100 and 200 nm were used. As shown in Fig. 20a, the measured bottom widths of the nano-grooves generated under the depth of cut 100 nm ranged from 142.3 to 150.2 nm, which are slightly less than the tool tip width of 152.9 nm. The deviation is mainly due to the elastic recovery of the work material after the tool tip released from the surface. Moreover, the surface roughness S_a of the region between each cutting pass was found to be slightly increased to 2.50 nm (as shown in Fig. 19b), which is mainly caused by the material squeezed from the adjacent cutting passes.



Parameters calculated on the surface before cutting (form removed, polynomial of order 2)

Amplitude Parameters:

$$S_a = 0.0018541 \mu\text{m}; S_q = 0.0023312 \mu\text{m}$$

$$S_z = 0.019278 \mu\text{m}$$

Parameters calculated on the surface after cutting (form removed, polynomial of order 2)

Amplitude Parameters:

$$S_a = 0.0025008 \mu\text{m}; S_q = 0.0031812 \mu\text{m}$$

$$S_z = 0.019631 \mu\text{m}$$

Fig. 19 The surface roughness of workpiece (a) before nanoscale multi-tip tool cutting and (b) after nanoscale multi-tip tool cutting (the lens was focused on the surface region between each cutting pass) (Tong et al. 2015a)

However, the form accuracy and integrity of the machined nano-grooves were found to be degraded with the increase of depth of cut. Lots of side burrs were observed when the depth of cut was equal or larger than 300 nm (Fig. 20c). Structure damage was found when a depth of cut of 400 nm was used (Fig. 20d). The results indicate that there exists an upper limit of depth of cut when machining nano-grooves using nanoscale multi-tip diamond tools.

The SEM images of nanostructures machined at different cutting speeds are shown in Fig. 21 (depth of cut = 100 nm). The results show that the form accuracy of the machined nano-grooves degrades with the increase of the cutting speed. No visible defect was found in the case of cutting speed being 0.03 and 0.12 m/s. However, side burrs were observed when the cutting speed increased to 0.18 m/s. A similar cutting speed effect was observed when a depth of cut of 200 nm was used (Fig. 22) (Tong et al. 2015a). However, under a large depth of cut of 300 nm (Fig. 23) (Tong et al. 2015a), the increase of high cutting speed finally resulted in a seriously structure damage.

Therefore, it can be concluded that the burr and the structure damage are the two major types of machining defects when improper processing parameters are used in the nanoscale multi-tip tool cutting. The atomistic insight into the work material behavior responsible for the formation of the machining defects will be discussed in the next section.

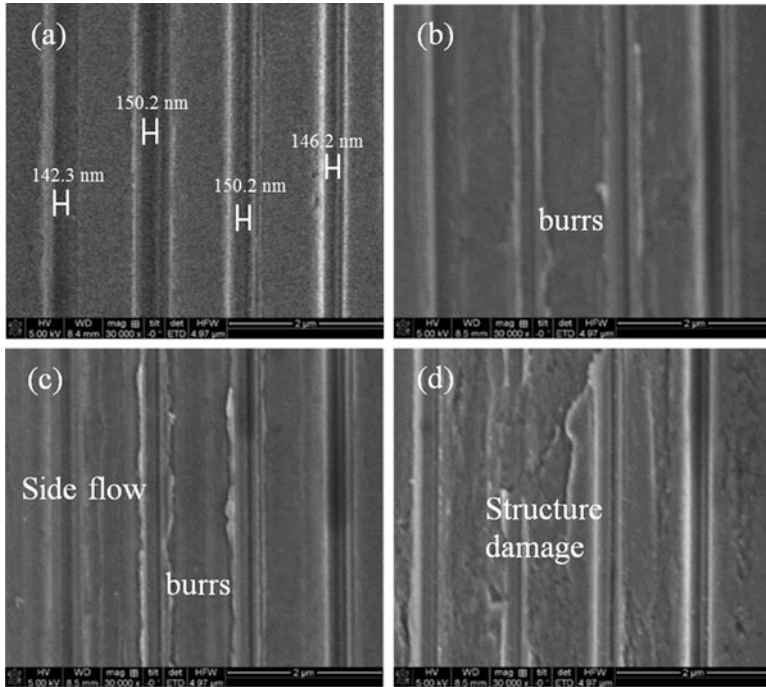


Fig. 20 SEM images of nano-grooves machined using different depths of cut (a) 100 nm, (b) 200 nm, (c) 300 nm (d) 400 nm (cutting speed = 0.03 m/s, feed rate = 9 $\mu\text{m}/\text{rev}$) (Tong et al. 2015a)

4.4.4 Effects of Depth of Cut

In order to reveal the underlying mechanism for machining defects, an MD nano-metric cutting model was built to simulate the nanometric cutting process when using a nanoscale multi-tip diamond tool. For better comparison, a ratio of depth of cut to tip height (d/h) was employed when comparing the simulation results with the experimental results. The quality of the machined nanostructures was characterized by both the form accuracy of the machined nanostructures achieved in depth direction and the thickness of the deformed layers. The form error was calculated by the deviation of the depth of machined nano-groove to the design dimension.

The simulation results of machined nanostructures under different depths of cut are shown in Fig. 24 (Tong et al. 2015a). Two nano-grooves were successfully generated when a depth of cut of 2.0 nm ($d/h = 0.46$) was applied (Fig. 24a). However, as evident from Fig. 24b–e, the form accuracy is degraded with the further increase of the depth of cut. Apparent side burrs were observed on both edges of the machined nano-grooves. The form error of nano-grooves in the depth direction is 4.0% when a depth of cut of 2.5 nm was used. It increased to 20% when cutting under the depth of cut of 4.0 nm.

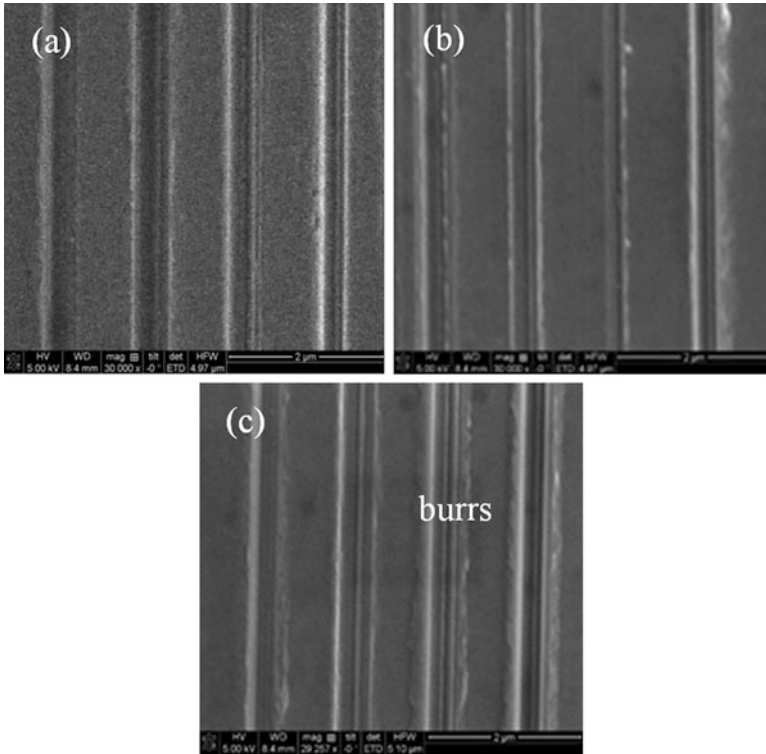


Fig. 21 SEM images of nano-grooves machined under different cutting speeds (a) 0.03 m/s, (b) 0.12 m/s, (c) 0.18 m/s (depth of cut = 100 nm, feed rate = 9 $\mu\text{m}/\text{rev}$) (Tong et al. 2015a)

Moreover, the wedge of cutting tool resulted in material pileups around tool tips. Visible material bulge between the machined nano-grooves was found when a depth of cut of 2.5 nm was used (Fig. 24b), mainly due to the overlap effect of the multi-tip tool cutting. However, with further increase of the depth of cut, the height of bulge reduced, and it disappeared when a depth of cut of 3.5 nm ($d/h = 0.81$) was applied (Fig. 24d). Apparently structure damage was found when a depth of cut of 4.0 nm ($d/h = 0.93$) was used (Fig. 24e).

The thicknesses of the deformed layer when using different depths of cut are shown in the middle column of Fig. 24. Significant dislocation pile-ups were observed beneath the tool tips. The larger the depth of cut, the larger the range of the deformed layer and the dislocations pile-ups were observed. The dislocation pile-ups would result in local strengthening of the work material in the normal direction. The resistance force makes work materials in front of each tip and between the tips flow up. This trend resulted in the built-up volume of each cutting tip merging into one big chip as shown in Fig. 24c–e. Due to the chip merging, the volume of chip and the height of the tool-chip separation point significantly increased. When the static friction force between the inner side of the tool tip and the workpiece is large enough, adhesion slip takes place and results in burrs and structure damage between the tool tips.

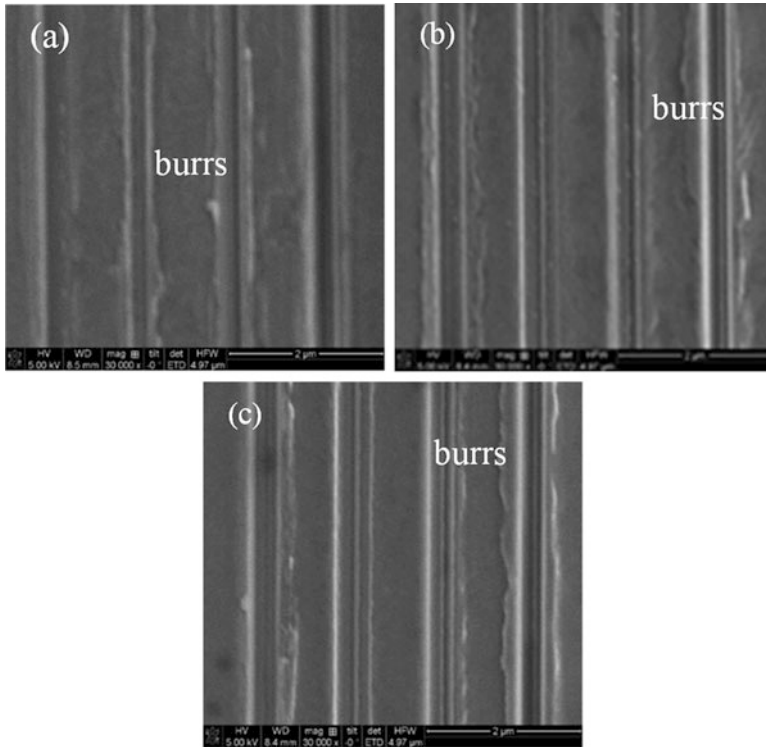


Fig. 22 SEM images of nano-grooves machined under different cutting speeds (a) 0.03 m/s, (b) 0.12 m/s, (c) 0.18 m/s (depth of cut = 200 nm, feed rate = 9 $\mu\text{m}/\text{rev}$) (Tong et al. 2015a)

In the experimental work (Fig. 20), the visible machining defects are observed when the depth of cut is equal and larger than 300 nm ($d/h = 0.51$). In the MD simulation, the critical value of d/h for the onset of visible form errors (larger than 13.3%) is 0.70. The ratio predicted by simulation is larger than the experimental result which is mainly due to the ideally perfect single crystal structure of copper material and the cutting tool assumed in the MD simulation model. In practice, a small depth of cut is usually a necessary condition of improving the machining precision (Neugebauer et al. 2012). The current experimental and simulation results indicate that this rule also works for the nanoscale multi-tip diamond tool cutting.

4.4.5 Effects of Cutting Speed

In order to obtain in-depth understanding of the effect of cutting speed observed in the experiments, simulations of a nanometric cutting process using a multi-tip tool were performed over a wide range of cutting speeds (10–250 m/s) using the same depth of cut of 2.0 nm.

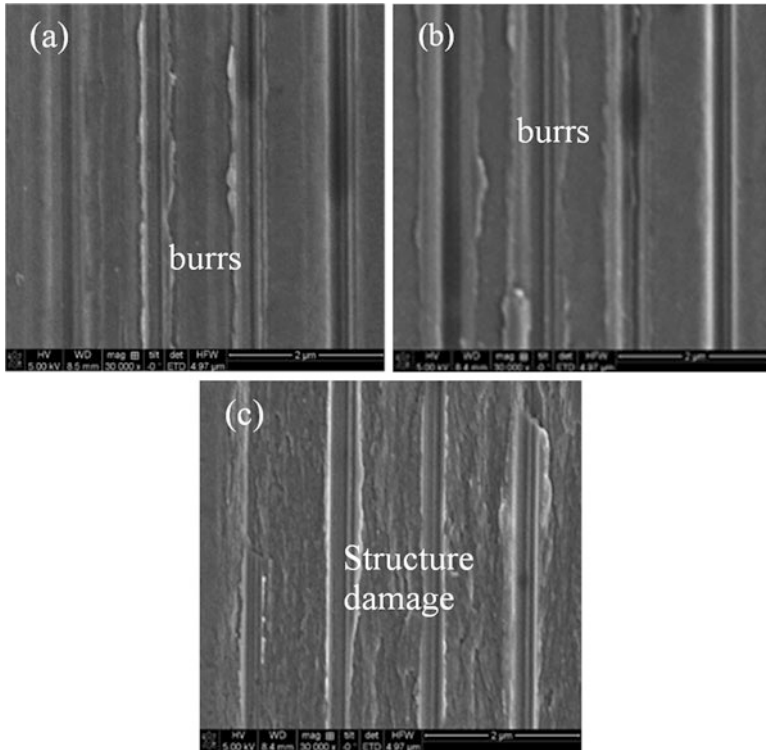


Fig. 23 SEM images of nano-grooves machined under different cutting speeds (a) 0.03 m/s, (b) 0.12 m/s, (c) 0.18 m/s (depth of cut = 300 nm, feed rate = 9 $\mu\text{m}/\text{rev}$) (Tong et al. 2015a)

As shown in Fig. 25 (Tong et al. 2015a), nano-grooves were indicated when the cutting speed was lower than 160 m/s. With the wedge of the cutting tool, each tip created a built-up volume around the tool tip. Although the tiny bulge of materials was observed when the cutting speed increased to 100 m/s, visible side burrs were found when the cutting speed was equal or higher than 200 m/s (Fig. 25e). Moreover, dislocation pile-ups were found when the cutting speed increased to 160 m/s (right column of Fig. 25). This phenomenon indicates that the overlap effect took place when a high cutting speed was used.

Figure 26 (Tong et al. 2015a) summarizes the distributions of local cutting temperatures under different cutting speeds. As expected, the range of the high-temperature region (>450 K) significantly increases with the cutting speed. The high cutting temperature would soften the work material at the cutting zone and extend the range of material plastic deformation zone, finally resulting in the overlap effect between the tool tips and the formation of the side burr. Although the range of the cutting speed used in simulations is still higher than the cutting speed used in experiment, the trend of the cutting speed effect obtained from simulations agreed with the experimental results qualitatively. The form accuracy of the machined nano-grooves degraded with the increase of cutting speed due to the formation of side burrs.

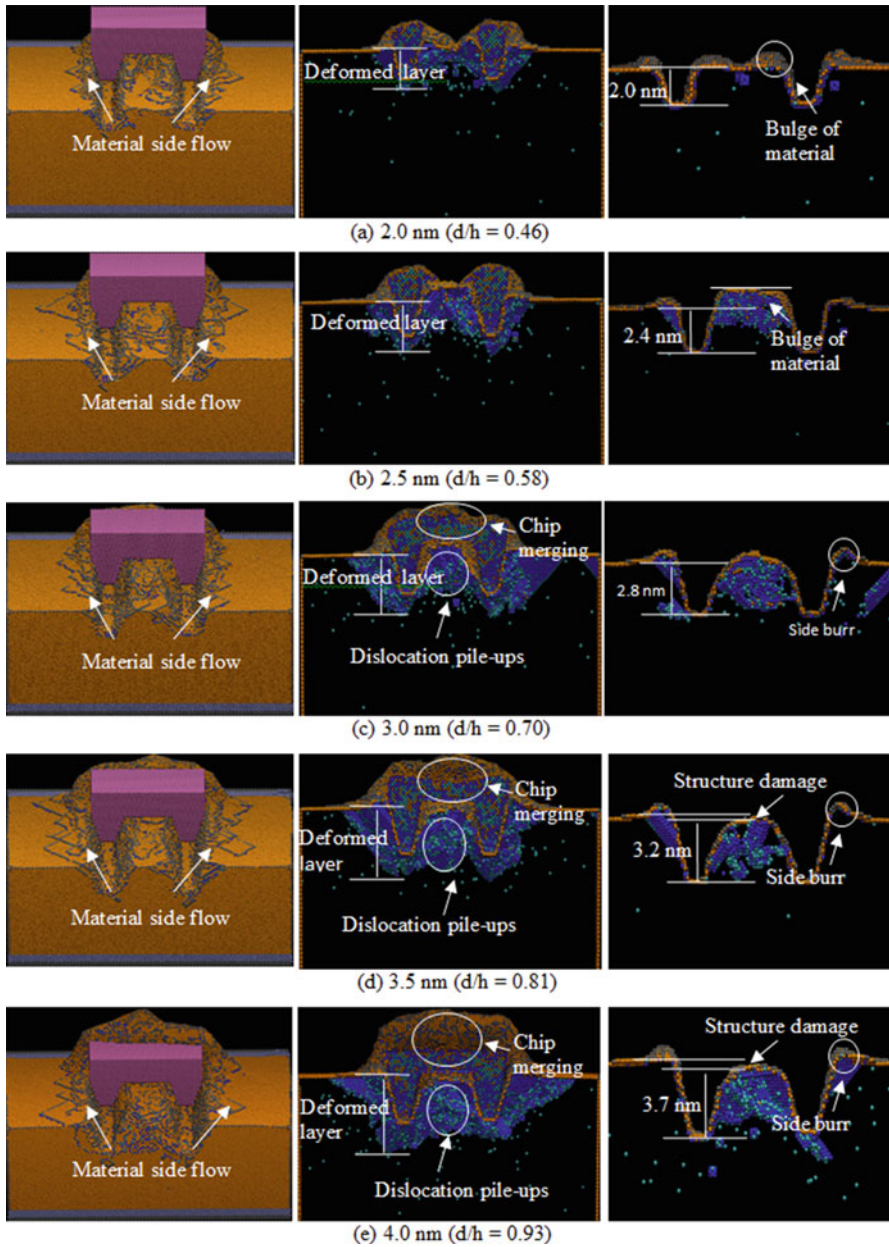


Fig. 24 MD simulation results of machined nanostructures (left), the cross-sectional views of deformed layers (middle), and the cross-sectional views of machined nano-grooves (right) using different depths of cut: (a) 2.0 nm, (b) 2.5 nm, (c) 3.0 nm, (d) 3.5 nm, (e) 4.0 nm (Tong et al. 2015a)

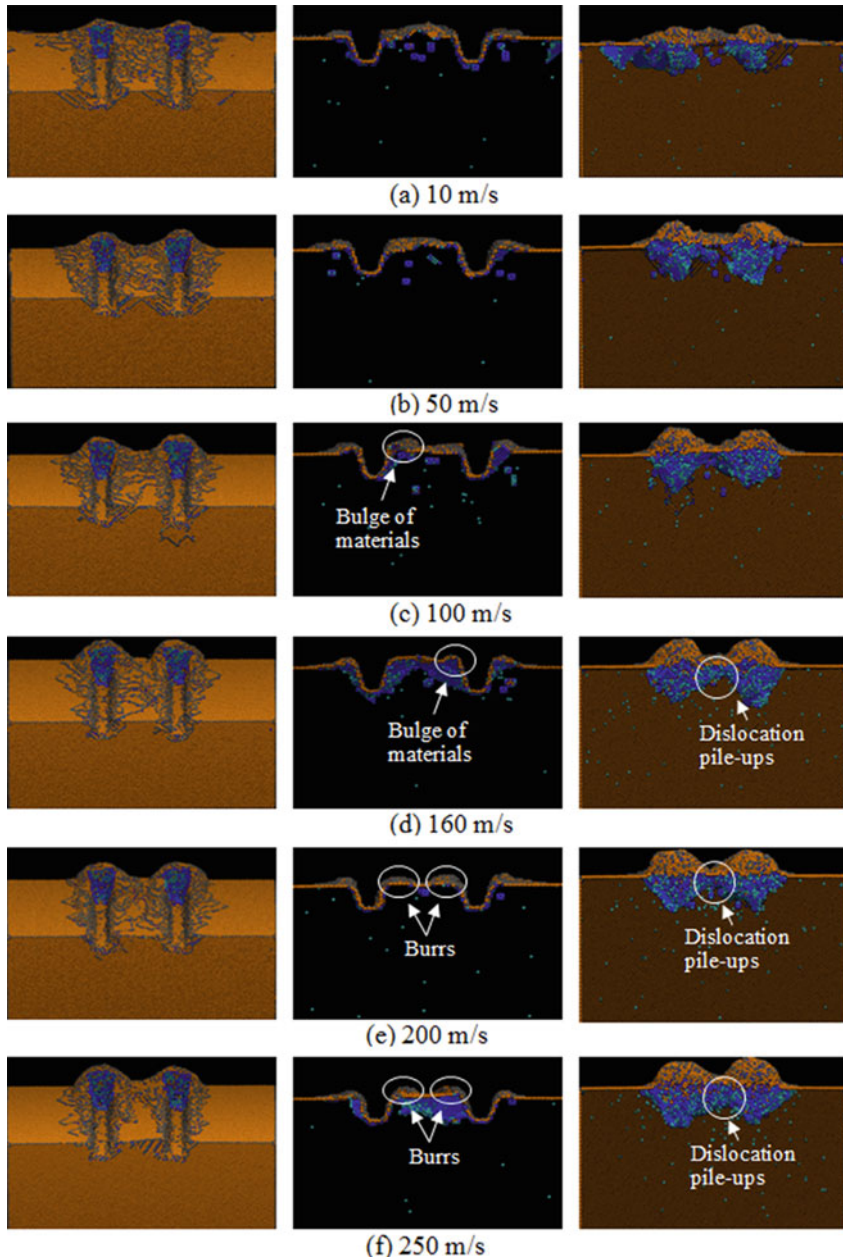


Fig. 25 The MD simulation results of nanostructures formed using the cutting speed of (a) 10 m/s, (b) 50 m/s, (c) 100 m/s, (d) 160 m/s, (e) 200 m/s, and (f) 250 m/s. The left column shows the surface of machined nanostructures; the middle column shows the cross-sectional view of formed nanostructures; the right column shows the inside view of the dislocation distribution under the cutting tool tips (Tong et al. 2015a)

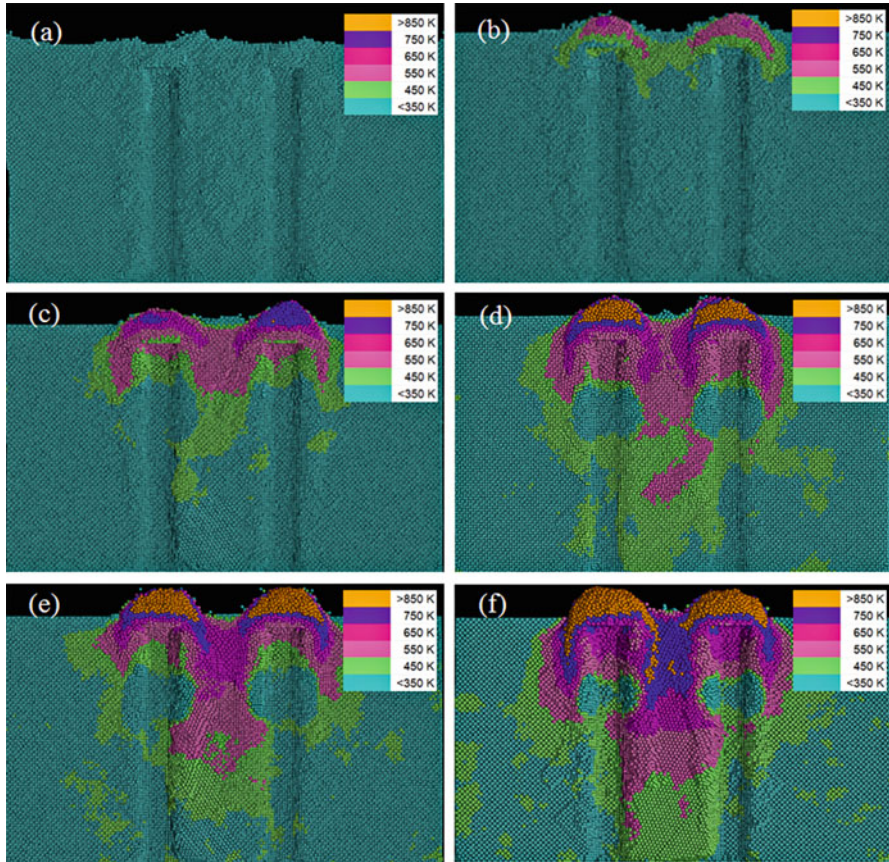


Fig. 26 Temperature distribution under different cutting speeds (a) 10 m/s, (b) 50 m/s, (c) 100 m/s, (d) 160 m/s, (e) 200 m/s, (f) 250 m/s (Tong et al. 2015a)

Nevertheless, it is noted that the form errors of the machined nanostructures in depth direction are all less than 5% for the cutting speed applied. Visible side burrs were observed only when the dislocation pile-ups took place. Thus it is predicted that, in nanoscale multi-tip tool cutting, there is a critical cutting speed below which the overlap effect can be ignored in machining nanostructures under a certain acceptable accuracy. More nanometric cutting experiments need to be carried out in the future for a fully quantitative validation.

4.4.6 Summary

In this session both nanometric cutting experiments and MD simulations have been carried out to study the processing capability of diamond turning using a nanoscale multi-tip diamond tool. It found that the operational parameters significantly affect

the quality of the machined nanostructures. The high-precision nanostructures were successfully produced by diamond face cutting under a depth of cut of 100 nm and a cutting speed of 0.03 m/s. Under the studied cutting conditions, the burr and structure damage are the two major types of machining defects. The formation of machining defects has been emulated by MD simulations. The investigation showed that with the increase of the depth of cut and the cutting speed, the increasing overlap effect between the tool tips is responsible for the formation of side burr and structural damage.

4.5 Tool Wear

As in other ultra-precision diamond turning processes, tool wear is also a big concern when using nanoscale multi-tip diamond tool for nano-grooving. The SEM images of the nanoscale multi-tip diamond tool before and after the cutting trials are shown in Fig. 27 (Tong et al. 2015a). Unlike the conventional single-tip diamond tool cutting where the initial tool wear was mostly found at the clearance face near the tool cutting edges, the tool wear in the multi-tip tool cutting was found on both the

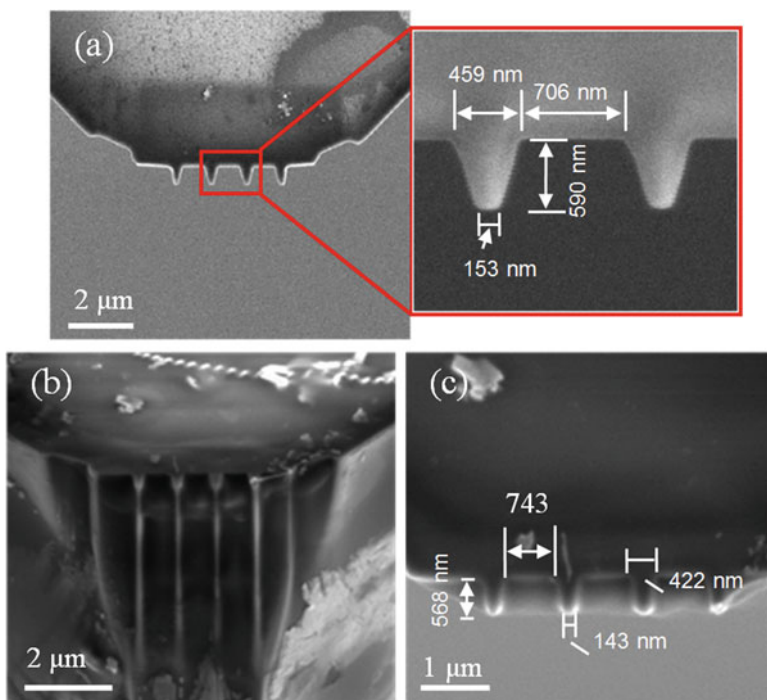


Fig. 27 SEM images of the nanoscale multi-tip diamond tool. (a) SEM image of the tool before cutting, (b) SEM image of the tool cutting edges after cutting, and (c) a close-up view of the shape of tool tips after cutting (Tong et al. 2015a)

clearance face and the sides of the tool tips after a cutting distance of 2.5 μm . No visible wear marks were observed at the rake face of the tool tips. The measured tip distance enlarged from 706 to 743 nm because of the wear on the sides of the tool tips. The main reason of tool wear is that for multi-tip tool cutting, the nanostructures are formed synchronously within a single cutting pass. The sides of the tool tips are involved in the formation of nanostructures. The compressive stress produced at the sides of the tool tips results in the friction between the tool tip and workpiece and thus results in the initiation of tool wear in this region.

Moreover, the tool wear is closely related to the local cutting temperature. Many research works have emphasized the significance of thermal effects on tool wear and suggested that an important way to control the tool wear is to reduce the cutting temperature in the cutting zone (Tong et al. 2014b; Ikawa et al. 1991b; Cheng et al. 2003). Figure 28a–c (Tong et al. 2015a) suggests the temperature distributions of tool tips for different depths of cut obtained by MD simulations. It is found that the temperature was uniformly distributed at the tool tip when a small depth of cut of 2.0 nm was used. However, when cutting under a depth of cut of 3.0 nm, a high local temperature (>620 K) was generated both at the cutting edges and the side edges of the tool tips. Similar results were observed when the depth of cut increased to 4.0 nm. This high local temperature would soften the C–C bonds and accelerate the tool wear process in these regions.

In addition, it has been shown that a high cutting speed will apparently increase the cutting temperature at the cutting zone. It is anticipated that the tool wear rate will increase with the cutting speed as well.

Usually, the progressive thermochemical wear of a diamond tool is mainly attributed to the oxidation, graphitization, diffusion, and carbide formation during the long-term cutting process. For FIB-shaped diamond tools, the ion irradiation-induced doping and defects will also degrade the property of cutting tools. A previous study by Tong et al. on ion-induced damaged layer during tool fabrication process has shown that the energetic ion collision can result in an amorphous carbon layer around the tool tips (Tong et al. 2015b). This damaged layer would increase the adhesion between tool and work materials (Kawasegi et al. 2014a). As schematically shown in Fig. 29, during the nanometric cutting process, the FIB-induced damaged layer was expected to worn away firstly because of its non-diamond phase. Most recently, a similar phenomenon has been reported in micro-machining of NiP using a FIB-irradiated single-tip diamond tool (Kawasegi et al. 2014a, b). The present study, for the first time, provides significant information about the initial tool wear in the nanometric cutting of copper using a nanoscale multi-tip diamond tool. More research work needs to be carried out in the future to obtain a sufficient data for building a rigorous tool-life management and prediction program.

To sum up, due to the limitation of current computational power, performing MD simulation on nanometric cutting with the same physical size and small cutting speed used in experiments remains a big challenge, especially for the large-scale MD model built in present work. However, this does not affect our analysis of the general nature of machining. Although it is not possible to have quantitative comparison to

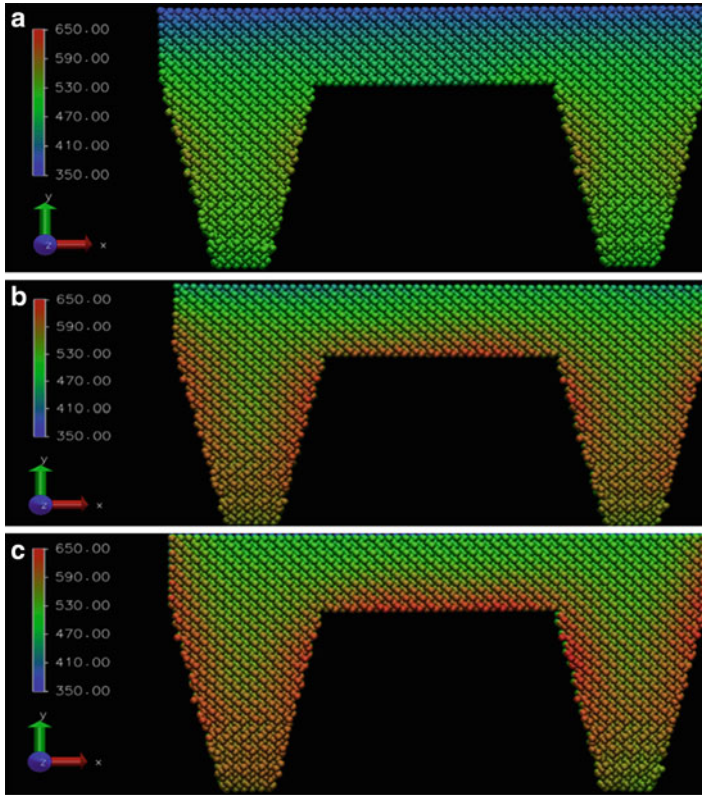


Fig. 28 MD simulation results of the temperature distributions on the nanoscale multi-tip diamond tools for different depths of cut. (a) 2 nm, (b) 3.0 nm, and (c) 4.0 nm (Tong et al. 2015a)

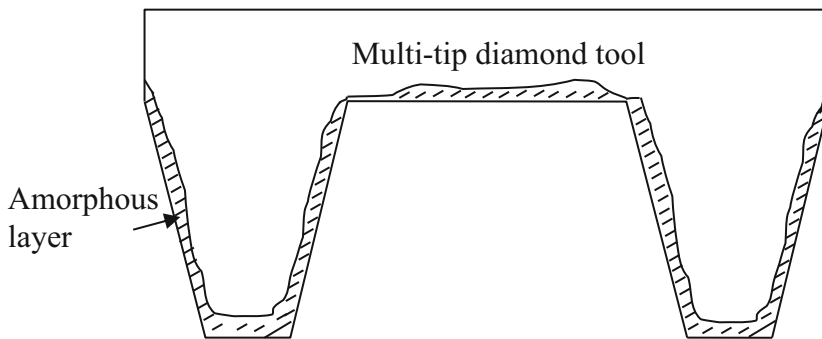


Fig. 29 Schematic illustration of the early tool wear region of a multi-tip diamond tool resulting from FIB-induced damage (Tong et al. 2015a)

the experimental measurement, the MD nanometric cutting model allows the atomistic insight into the work material behavior and reveals the underlying mechanisms for the machining defects as well as the tool wear during nanometric cutting process. The research findings obtained from MD simulations can help interpret the experimental data. The present analysis will be valuable to any nanomanufacturing practice where a nanoscale multi-tip diamond tool is used. Therefore, if the full advantages of nanometric cutting using multi-tip diamond tool predicated by the MD simulations are to be realized, selection of parameters used in tool fabrication, optimal design of tool geometry, and optimization of processing parameters used in nanometric cutting practice are critical to provide high-performance and efficient machining when using nanoscale multi-tip diamond tools. The FIB-induced damaged layer, the cutting speed, and the depth of cut have significant effects on the tool wear. Based on the obtained results, it is reasonable to anticipate that, in nanoscale multi-tip tool cutting, high-precision nanostructures can be achieved under an optimal cutting condition where the overlap effect can be ignored in the nanostructure generation process.

4.6 Concluding Remarks

Currently, it is still quite difficult to compare MD simulations with experimental results in the same spatial and time scale. From the MD simulation side, the difficulties lie in developing a super high-performance computing system for solving a highly inhomogeneous multibody problem having the same spatial and time scales as experiments, as well as an effective visualization technique for analyzing the large-scale MD simulation results. The difficulties from the experimental side have been the limitation of using FIB to fabricate multi-tip diamond tool with tool tips in several nanometers, and the time resolution that is needed for a detection equipment to capture the transient process of defect formation which evolve on time scales of some nanoseconds.

However, current MD simulation results show that the mechanisms of nanostructure formation by using single-tip tools and multi-tip tools are different. Compared with the single-tip tool cutting, a higher cutting temperature and a higher average normal cutting force per tip were found in the multi-tip tool cutting. Since the nanostructures are synchronously formed by a single cutting pass, the effects of feed rate and the alignment issues associated with the use of single-tip tools can be completely eliminated when using nanoscale multi-tip tools. This unique feature makes the multi-tip tool cutting more practicable and applicable than the single-tip cutting for scale-up fabrication of periodic nanostructures. Owing to the unprecedented merits of high throughput, one-step, and highly flexible precision capabilities, this technique has led to the hope for breaking the technical bottleneck for the scale-up manufacturing nanostructures.

The operational parameters significantly affect the quality of the machined nanostructures. The high-precision nanostructures were successfully produced by diamond face cutting under a depth of cut of 100 nm and a cutting speed of 0.03 m/s.

An optimization of the cutting conditions, by which the overlap effect can be ignored in the nanostructure generation process, is recommended in the future work to obtain high-precision nanostructures when using nanoscale multi-tip diamond tools.

The tool wear is initially found at both the clearance cutting edge and the side edges of tool tips after a cutting distance of 2.5 km. The FIB-induced damaged layer (Tong et al. 2015b) and the friction produced at each side of the tool tip are responsible for the tool wear.

To systematically establish this nano-grooving approach, the following work is thought to be performed in the near future:

1. Developing an Effective Post-processing Method for Tool Fabrication

The study carried out by Tong and co-workers (Tong et al. 2015b) on FIB-induced damage in diamond has demonstrated that the energetic ion collision can result in a damaged zone (a mixture phase of sp^2 and sp^3 hybridization and the implanted gallium), which is much larger than the defined ion irradiated area, even under the low-beam energy of 8 kV. Most recently, it has been reported that the doping of gallium ions at tool rake face would result in a rapid diamond tool wear due to the increase of the adhesion of work materials to the tool surface (Kawasegi et al. 2014b). Thus, the ion irradiation-induced doping and defects will unavoidably degrade the cutting performance of the micro- and nanoscale diamond tools fabricated by FIB. An effective post-processing method which is able to remove/minimize the damaged layers after FIB machining is in high demand. The minimization of the FIB-induced damaged layer will become more important when the dimensions of a multi-tip diamond tool are approaching their ultimate values.

2. Optimization of the Design of Multi-tip Diamond Tools

It is widely known in conventional cutting that the tool geometrical parameters such as the rake angle, clearance angle, and the cutting edge radius can influence the material removal process. The research work done by Tong et al. indicates that, the unique tool geometrical parameters of a multi-tip tool including the tool-tip distance, tip angle, and tip configuration can play an important role in achieving high the accuracy of the machined nanostructures (Luo et al. 2014). It seems to be a complex interplay of all these variables in order to obtain a deterministic fabrication of high-quality nanostructures. Therefore, an optimization of the tool design by considering all these parameters can further improve the shape transferability of multi-tip diamond tools in an SPDT operation.

3. Setting up a Processing Database of the Multi-tip Tool Cutting

The processing parameters such as depth of cut and cutting speed significantly affect the attainable integrity of machined nanostructures as well as the tool life. Due to the limitations of time and the high research cost of using relevant equipment, the experimental results obtained in the present study were not sufficient to set up a processing database for the nanometric cutting of copper using nanoscale multi-tip diamond tools. Currently, the processing parameters such as the maximum feed rate, depth of cut, and cutting speed for a specialized workpiece material have not yet been established. For the commercialization of

this technique in industry, more research work needs to be carried out in the future to obtain sufficient database for building a rigorous tool-life management and predication program and eventually an expert system for intelligently selecting optimal processing parameters for the cost-effective scale-up manufacturing of nanostructures.

References

- Akimov YA, Koh W (2010) Resonant and nonresonant plasmonic nanoparticle enhancement for thin-film silicon solar cells. *Nanotechnology* 21:235201
- Atwater HA, Polman A (2010) Plasmonics for improved photovoltaic devices. *Nat Mater* 9:205–213
- Balamane H, Halicioglu T, Tiller W (1992) Comparative study of silicon empirical interatomic potentials. *Phys Rev B* 46:2250
- Bartolo P, Kruth JP, Silva J, Levy G, Malshe A, Rajurkar K et al (2012) Biomedical production of implants by additive electro-chemical and physical processes. *CIRP Ann Manuf Technol* 61:635–655
- Berman D, Krim J (2013) Surface science, MEMS and NEMS: Progress and opportunities for surface science research performed on, or by, microdevices. *Prog Surf Sci* 88:171–211
- Cheng K, Luo X, Ward R, Holt R (2003) Modeling and simulation of the tool wear in nanometric cutting. *Wear* 255:1427–1432
- Clark AW, Cooper JM (2011) Nanogap ring antennae as plasmonically coupled SERRS substrates. *Small* 7:119–125
- Davies MA, Evans CJ, Vohra RR, Bergener, BC, Patterson SR (2003) Application of precision diamond machining to the manufacture of microphotonics components. In: *Proceedings of SPIE*, 2003
- Daw MS, Foiles SM, Baskes MI (1993) The embedded-atom method: a review of theory and applications. *Mater Sci Rep* 9:251–310
- Ding X, Lim G, Cheng C, Butler DL, Shaw K, Liu K et al (2008) Fabrication of a micro-size diamond tool using a focused ion beam. *J Micromech Microeng* 18:075017
- Ding X, Jarfors A, Lim G, Shaw K, Liu K, Tang L (2012) A study of the cutting performance of poly-crystalline oxygen free copper with single crystalline diamond micro-tools. *Precis Eng* 36:141–152
- Fang TH, Weng CI, Chang JG (2002) Molecular dynamics simulation of nano-lithography process using atomic force microscopy. *Surf Sci* 501:138–147
- Friedrich CR, Vasile MJ (1996) Development of the micromilling process for high-aspect-ratio microstructures. *J Microelectromech Syst* 5:33–38
- Friedrich C, Coane P, Vasile MJ (1997) Micromilling development and applications for micro-fabrication. *Microelectron Eng* 35:367–372
- Holmberg S, Perebikovskiy A, Kulinsky L, Madou M (2014) 3-D Micro and nano technologies for improvements in electrochemical power devices. *Micromachines* 5:171–203
- Ikawa N, Shimada S, Tanaka H, Ohmori G (1991a) An atomistic analysis of nanometric chip removal as affected by tool-work interaction in diamond turning. *CIRP Ann Manuf Technol* 40:551–554
- Ikawa N, Donaldson R, Komanduri R, König W, McKeown P, Moriwaki T et al (1991b) Ultra-precision metal cutting – the past, the present and the future. *CIRP Ann Manuf Technol* 40:587–594
- Kaur IP, Singh H (2014) Nanostructured drug delivery for better management of tuberculosis. *J Control Release* 184:36–50
- Kawasegi N, Niwata T, Morita N, Nishimura K, Sasaoka H (2014a) Improving machining performance of single-crystal diamond tools irradiated by a focused ion beam. *Precis Eng* 38:174–182

- Kawasegi N, Ozaki K, Morita N, Nishimura K, Sasaoka H (2014b) Single-crystal diamond tools formed using a focused ion beam: tool life enhancement via heat treatment. *Diam Relat Mater* 49:14–18
- Kelchner CL, Plimpton S, Hamilton J (1998) Dislocation nucleation and defect structure during surface indentation. *Phys Rev B* 58:11085
- Komanduri R, Chandrasekaran N, Raff L (2000) Molecular dynamics simulation of atomic-scale friction. *Phys Rev B* 61:14007
- Komanduri R, Chandrasekaran N, Raff L (2001) Molecular dynamics simulation of the nanometric cutting of silicon. *Philos Mag B* 81:1989–2019
- Lin Z, Huang J (2008) A study of the estimation method of the cutting force for a conical tool under nanoscale depth of cut by molecular dynamics. *Nanotechnology* 19:115701
- Liu Z, Steele JM, Srituravanich W, Pikus Y, Sun C, Zhang X (2005) Focusing surface plasmons with a plasmonic lens. *Nano Lett* 5:1726–1729
- Luan B, Robbins MO (2005) The breakdown of continuum models for mechanical contacts. *Nature* 435:929–932
- Luo X, Tong Z, Liang Y (2014) Investigation of the shape transferability of nanoscale multi-tip diamond tools in the diamond turning of nanostructures. *Appl Surf Sci* 321:495–502
- Mokkapati S, Beck F, Polman A, Catchpole K (2009) Designing periodic arrays of metal nanoparticles for light-trapping applications in solar cells. *Appl Phys Lett* 95:053115
- Neugebauer R, Drossel W, Wertheim R, Hochmuth C, Dix M (2012) Resource and energy efficiency in machining using high-performance and hybrid processes. *Procedia CIRP* 1:3–16
- Norouzfard V, Hamed M (2014) Experimental determination of the tool–chip thermal contact conductance in machining process. *Int J Mach Tools Manuf* 84:45–57
- Pei Q, Lu C, Lee H, Zhang Y (2009) Study of materials deformation in nanometric cutting by large-scale molecular dynamics simulations. *Nanoscale Res Lett* 4:444–451
- Pelaz L, Marqués LA, Barbolla J (2004) Ion-beam-induced amorphization and recrystallization in silicon. *J Appl Phys* 96:5947–5976
- Picard YN, Adams D, Vasile M, Ritchey M (2003) Focused ion beam-shaped microtools for ultra-precision machining of cylindrical components. *Precis Eng* 27:59–69
- Smith R, Kenny SD, Ramasawmy D (2004) Molecular dynamics simulations of sputtering. *Philos Trans R Soc London, Ser A* 362:157–176
- Sun J, Luo X (2014) Chapter 7: deterministic fabrication of micro- and nanostructures by focused ion beam. In: Wang ZM (ed) *Lecture notes in nanoscale science and technology*. Springer, New York, pp 161–204
- Sun J, Luo X, Chang W, Ritchie J, Chien J, Lee A (2012) Fabrication of periodic nanostructures by single-point diamond turning with focused ion beam built tool tips. *J Micromech Microeng* 22:115014
- Tersoff J (1989) Modeling solid-state chemistry: interatomic potentials for multicomponent systems. *Phys Rev B* 39:5566
- Tong Z, Liang Y, Jiang X, Luo X (2014a) An atomistic investigation on the mechanism of machining nanostructures when using single tip and multi-tip diamond tools. *Appl Surf Sci* 290:458–465
- Tong Z, Liang Y, Yang X, Luo X (2014b) Investigation on the thermal effects during nanometric cutting process while using nanoscale diamond tools. *Int J Adv Manuf Technol* 74:1709–1718
- Tong Z, Luo X, Sun J (2015a) Investigation of a scale-up manufacturing approach for nanostructures by using a nanoscale multi-tip diamond tool. *Int J Adv Manuf Technol* 80(1–4): 699–710
- Tong Z, Xu Z, Wu W, Luo X (2015b) Molecular dynamics simulation of low-energy FIB radiation induced damage in diamond. *Nucl Inst Methods Phys Res B* 358:38–44
- Vasile MJ, Friedrich CR, Kikkeri B, McElhannon R (1996) Micrometer-scale machining: tool fabrication and initial results. *Precis Eng* 19:180–186
- Vasile MJ, Nassar R, Xie J, Guo H (1999) Microfabrication techniques using focused ion beams and emergent applications. *Micron* 30:235–244

- Xu Z, Fang F, Zhang S, Zhang X, Hu X, Fu Y et al (2010) Fabrication of micro DOE using micro tools shaped with focused ion beam. *Opt Express* 18:8025–8032
- Yan Y, Sun T, Dong S, Liang Y (2007) Study on effects of the feed on AFM-based nano-scratching process using MD simulation. *Comput Mater Sci* 40:1–5
- Ye Y, Biswas R, Morris J, Bastawros A, Chandra A (2003) Molecular dynamics simulation of nanoscale machining of copper. *Nanotechnology* 14:390
- Zhang S, Fang F, Xu Z, Hu X (2009) Controlled morphology of microtools shaped using focused ion beam milling technique. *J Vac Sci Technol B* 27:1304–1309
- Zhu PZ, Hu YZ, Ma TB, Wang H (2010) Study of AFM-based nanometric cutting process using molecular dynamics. *Appl Surf Sci* 256:7160–7165
- Zong W, Li Z, Sun T, Cheng K, Li D, Dong S (2010) The basic issues in design and fabrication of diamond-cutting tools for ultra-precision and nanometric machining. *Int J Mach Tools Manuf* 50:411–419



Elliptical Vibration Cutting for Difficult-to-Cut Materials

5

Hongjin Jung, Takehiro Hayasaka, and Eiji Shamoto

Contents

5.1	Introduction	140
5.2	Proposal of Elliptical Vibration Cutting and Fundamental Experiments	141
5.3	Development of Ultrasonic Elliptical Vibration Cutting Device and Practical Use for Machining of Difficult-to-Cut Materials	144
5.3.1	Ultrasonic Elliptical Vibration Cutting Device	144
5.3.2	Mirror Surface Finishing of Hardened Die Steel	146
5.4	Ultraprecision Ductile Machining of Tungsten Carbide	152
5.4.1	Study on Ductile Machining of Tungsten Carbide	153
5.4.2	Study on Tool Life for Practical Applications	159
5.4.3	Preferable Conditions and Micro-/Nano-Sculpturing of Tungsten Carbide	164
5.5	High-Efficiency Machining with High-Power Ultrasonic Vibration Device	165
5.5.1	Development of High-Power Ultrasonic Device	166
5.5.2	High-Efficiency Machining with High-Power Vibration Device	167
5.6	Mirror Surface Finishing of High-Alloy Steels	168
5.7	Summary	180
	References	180

Abstract

Recent researches/developments of elliptical vibration cutting and related topics are introduced in this chapter. The elliptical vibration is applied to the tool together with the cutting motion so that the cutting process becomes intermittent, and the tool can pull up the chip. This unique cutting process leads to many superior machining performances such as low cutting force, high machining accuracy, and long tool life compared to conventional vibration cutting as well as ordinary cutting. For ultraprecision machining of difficult-to-cut materials,

H. Jung (✉) · T. Hayasaka · E. Shamoto
Graduate School of Engineering, Nagoya University, Nagoya, Aichi, Japan
e-mail: jung@upr.mech.nagoya-u.ac.jp; takehiro.hayasaka@mae.nagoya-u.ac.jp;
shamoto@nagoya-u.jp

follow-up studies and developments have been carried out to demonstrate its performances, to expand its applications, and to clarify its mechanics. For example, it is verified that the elliptical vibration cutting can realize mirror surface finishing of difficult-to-cut materials, e.g., hardened steel, with a very small tool wear. Ductile mode machining of brittle materials, e.g., tungsten carbide, can be realized by the elliptical vibration cutting for not only plane surfaces but also textured surfaces which is difficult to be obtained from other cutting methods. High-efficiency mirror surface finishing of hardened die steel is also realized with the developed high-power vibration device. Ultraprecision machining of high-hardness steel, i.e., Rockwell C hardness exceeds 60 HRC, can also be realized, and the alloy elements that affect the tool wear and micro-chipping are investigated to further understand about the mechanism.

Keywords

Elliptical vibration cutting · Difficult-to-cut materials · Precision cutting

5.1 Introduction

Manufacturing of dies and molds is an essential area in the industry because it affects the feasibility and economics of producing tremendous number of assembly products. Especially, dies and molds for information equipment and devices, such as front/back light panels for LCD, holographic optical elements, and optical waveguides, require ultraprecision machining technologies for their superior dimensional and surface qualities. Meanwhile, ultraprecision diamond cutting is superior to produce ultraprecision and sophisticated structures for the reason of its high geometrical accuracy, good surface quality, and high machining efficiency. On the other hand, difficult-to-cut materials such as hardened steel and tungsten carbide are used for ultraprecision dies and molds which are the main concern of this research. However, conventional ultraprecision diamond cutting of ferrous material could not be applied in die steel machining because of the excessive tool wear. This results from the high chemical activity between the carbon of the tool and iron of the workpiece.

Many researches were carried out in order to solve the problem of the rapid tool wear of diamond tools. Casstevens (1983) investigated the feasibility of diamond turning of steel under carbon-saturated gaseous atmospheres, e.g., carbon dioxide and methane, as a way of decreasing diamond tool wear and improving the roughness of the finished surface. As a result, significant tool wear reduction could be achieved in the methane atmosphere compared to the air and carbon dioxide atmospheres. However, the tool wear suppression was still not sufficient to be used as a precision diamond cutting technology. Brinksmeier et al. (2006) applied a nitriding process of steel to avoid the excessive chemical tool wear in diamond cutting of steel alloys. The applied thermochemical process modifies the chemical composition of the steel alloys. Modified layers in the workpiece subsurface resulting from the thermochemical process help preventing the diffusion of carbon

atoms from diamond tool to the steel alloys because the layers are already saturated with nitrogen. Although significant reduction of tool wear as well as mirror-quality surface can be obtained by using this process, micro-chipping is further induced as a negative effect of the cutting process because of significant difference between hardness of matrix and carbides due to the nitriding process. Namely, the carbides cannot be machined by the diamond tool, but move and roll under the flank faces of cutting edges and cause the micro-chipping. Kumabe (1979) applied ultrasonic vibration to the diamond tool for machining of steel, and an optical surface quality was obtained. It is clarified that when the ultrasonic vibration is applied to the cutting edge in the principal direction, the intermittent cutting process due to the high speed of the vibration leads to long life of the diamond tool and suppresses the diffusion of carbon atoms from diamond tool to the steel alloys. However, the small vibration in the thrust direction causes a rough-jagged surface finish or chipping of the tool due to the large interference between the flank face of the tool and cut surface. This becomes a crucial problem in practical applications.

Shamoto and Moriwaki (1994, 1999) proposed the elliptical vibration cutting method in which two-directional vibrations are applied to the cutting edge with the cutting motion and demonstrated the mirror-quality surface finishing of hardened steel with a diamond tool by the ultrasonic elliptical vibration cutting. As a result, it is clarified that the ultrasonic elliptical vibration cutting method significantly improves diamond tool life and does not require the practically difficult adjustment between the vibration and cutting directions which is different from the conventional ultrasonic vibration cutting method. After that, follow-up studies and developments have been carried out to demonstrate its performances, to expand its applications, and to clarify its mechanics. The elliptical vibration cutting technology has been successfully utilized in the industry for mirror surface finishing of hardened dies and molds steel without the polishing process but with a diamond tool. In this chapter, the elliptical vibration cutting for difficult-to-cut materials is described from its proposal to related recent researches.

5.2 Proposal of Elliptical Vibration Cutting and Fundamental Experiments

Figure 1 shows a schematic illustration of one cycle of the proposed elliptical vibration cutting. The elliptical vibration is applied to the cutting edge with the cutting motion as shown in Fig. 1. As the maximum vibration speed is set to be higher than the cutting speed, the tool is separated from the chip in each cycle of the vibration. The cutting takes place after the reentrance of the cutting edge into the workpiece, and the chip is mainly pulled up and formed while the tool moves upward in the chip flow direction. The tool moves down without cutting while it is separated from the chip. The details are explained as follows. Figure 1a shows the instant when the tool is located at the rightward end without cutting. The dashed line shows the locus of the cutting edge. At the second moment shown in Fig. 1b, the tool starts to cut. After the tool moves up and cuts the workpiece as shown in Fig. 1c, the cycle of

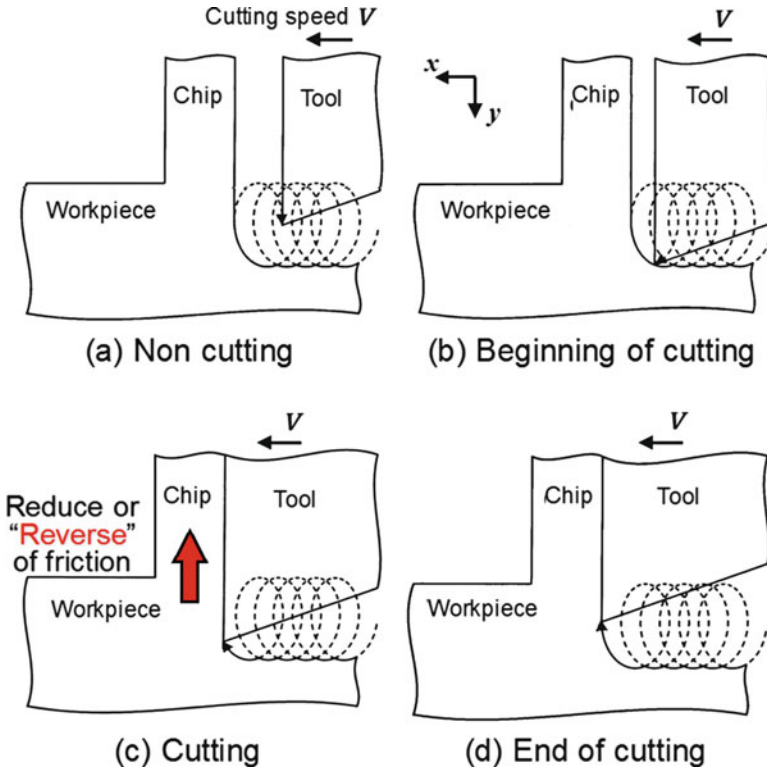


Fig. 1 Elliptical vibration cutting process

cutting ends when the vibration speed in the vertical direction to the rake face is zero (Fig. 1d), and the tool separates from the chip again. At the beginning of the cutting period, the vibration speed in the horizontal direction to the rake face is lower than the chip flow speed. Thus, the chip is pushed down by friction on the rake face in the same way as the conventional cutting methods. On the other hand, the chip is pulled up by the friction after the vibration speed in the horizontal direction to the rake face exceeds the chip flow speed. This reversed friction can cause the average frictional force to be less than zero virtually. Such reduction of frictional force cannot be obtained by the conventional cutting method even if rotary tools are utilized or sufficient lubricant is applied to the cutting zone. The virtual lubrication effect of the elliptical vibration cutting increases the shear angle significantly and hence reduces the cutting force.

Orthogonal cutting experiments of copper are carried out within a scanning electron microscope (SEM) in order to observe the cutting process directly and to measure the dynamic cutting force in each cycle of the vibration. The basic effects of the elliptical vibration conditions on the cutting performance are also clarified by the series of experiments. Figure 2 shows sketches of the setup for the fundamental experiment and the elliptical vibration device. The cutting device is installed within a

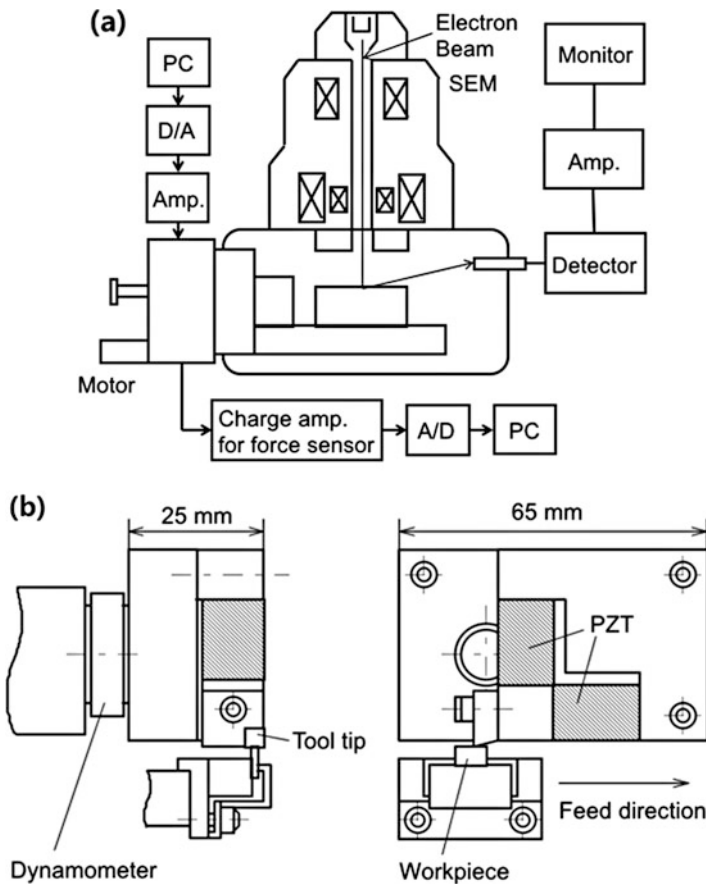


Fig. 2 Setup for fundamental experiment of elliptical vibration cutting. (a) Setup of SEM for elliptical vibration cutting experiment (b) Compact elliptical vibration cutting device installed within SEM

SEM in order to observe the cutting process. The tool is vibrated by two piezoelectric actuators (PZTs) arranged at a right angle, and the cutting force is measured with a piezoelectric-type dynamometer. The workpiece material is oxygen-free copper with a thickness of 0.25 mm. The depth of cut is 10 μm , and the nominal cutting speed, which is equal to the feeding speed of the workpiece in the cutting direction, is 260 mm/min. These conditions are kept constant, but vibration conditions are changed to distinguish conventional cutting, conventional vibration cutting, and elliptical vibration cutting.

Figure 3 shows SEM photographs of the chips obtained in the three different cutting processes and their corresponding principal and thrust force components of the measured cutting forces. As shown in Fig. 3a, the chip is relatively thick, and the cutting forces are high and almost constant in the ordinary cutting. Figure 3b shows results obtained by the conventional vibration cutting. The average cutting force is

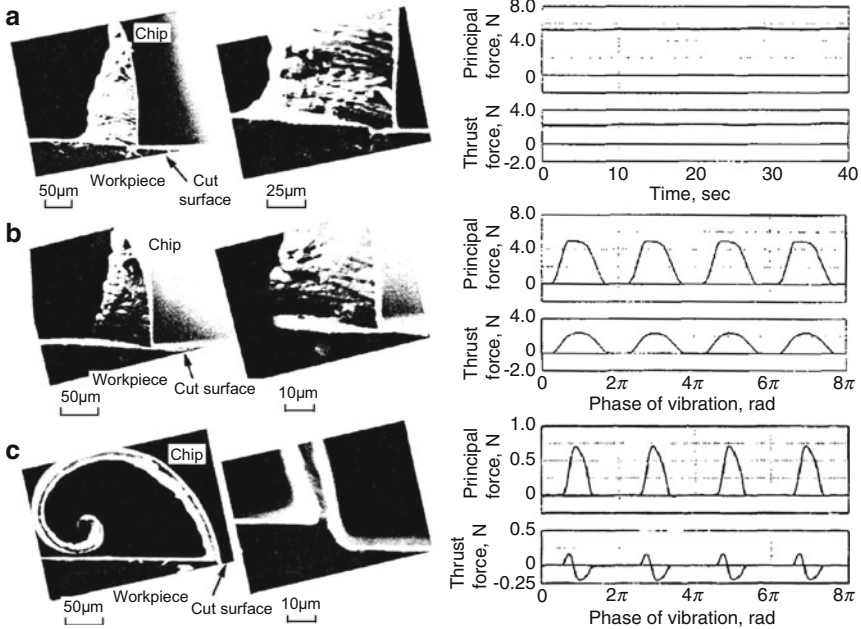


Fig. 3 SEM photographs of chips (left) and principal and thrust components of cutting force measured (right). (a) Ordinary cutting (b) Conventional vibration cutting (c) Elliptical vibration cutting

reduced as compared to the ordinary cutting due to the intermittent cutting. However, the force measured during cutting and the chip thickness are as large as those obtained by the ordinary cutting. On the other hand, the chip thickness becomes extremely small in the case of the elliptical vibration cutting as shown in Fig. 3c. Although the chip is pushed down at the beginning of cutting in each elliptical vibration cycle, there exists a period when the chip is pulled up by the tool moving upward. The negative thrust force shown in Fig. 3c proves the existence of such phenomenon, and this negative thrust force causes reduction in the chip thickness and hence the reduction in the principal force.

5.3 Development of Ultrasonic Elliptical Vibration Cutting Device and Practical Use for Machining of Difficult-to-Cut Materials

5.3.1 Ultrasonic Elliptical Vibration Cutting Device

Figure 4 shows a schematic illustration of an ultrasonic elliptical vibration cutting device whose resonant frequency is approximately 39 kHz (Suzuki et al. 2007). Some PZT actuators are sandwiched with metal blocks, and it is resonated in the

Fig. 4 Schematic illustration of ultrasonic elliptical vibration cutting device

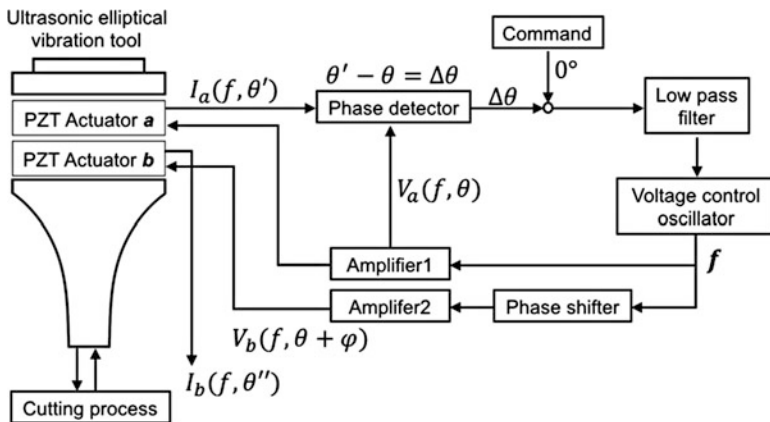
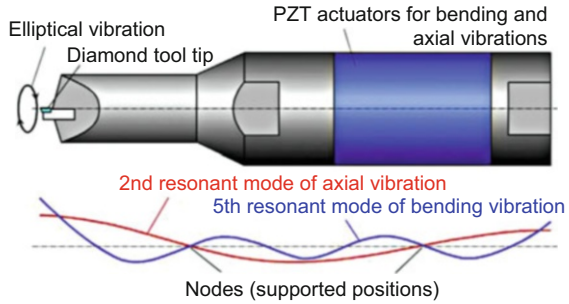
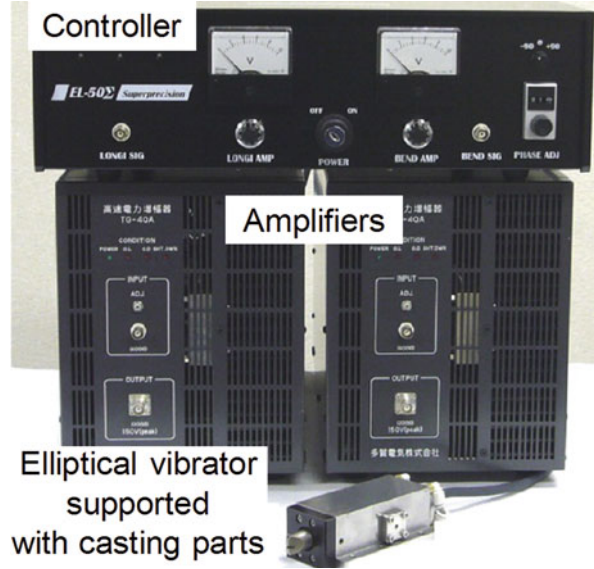


Fig. 5 Block diagram of ultrasonic elliptical vibration control system

second resonant mode of axial vibration and the fifth resonant mode of bending vibration by applying exciting voltages to the actuators. A diamond tool tip is set at the end of the vibrator and vibrated elliptically by combining the two resonant vibrations with some phase shift. In order to attain large elliptical vibration, the vibrator geometry needs to be designed to make a good agreement not only in resonant frequencies but also in node positions for mechanical supports.

Moreover, in order to keep large vibration amplitudes during the machining, a constant alternating voltage having the same frequency as the resonant frequency of the axial mode (or bending mode) in the device should be applied to the PZT actuators. However, according to the conditions of cutting load or tool wear, the resonant frequencies of vibration modes are changed slightly. Therefore, automatic tracking of the resonant frequency is also implemented by applying feedback control in the system called phase lock loop (PLL); see Fig. 5. Two different voltages, which have a phase difference between them, are applied to the two piezoelectric actuators, and the actuators excite the axial and bending vibration modes. The piezoelectric actuator *a* excites the axial mode, while the actuator *b* excites the bending mode. When cutting the material with this vibration tool, the energy (dynamic) state of the vibration tool will be changed because of the cutting forces. According to the states

Fig. 6 Elliptical vibration control system



of the vibration tool, the amplitudes or phases of the electric currents (shown by I_a , I_b , θ' , θ'' in Fig. 5) will change. Especially, as the vibration is in the resonant mode, which means that the frequency of the excited voltage is the same with the resonant frequency, the phase difference $\Delta\theta$ between the excited voltage and electric current is zero. Therefore, to chase the resonant frequency of the axial mode, the PLL is configured in order to make the phase difference $\Delta\theta$ between the excited voltage and electric current flowing in the piezoelectric actuator for the excitation of the axial mode to be zero continuously. The vibration locus is, therefore, controlled in an ultraprecision manner.

Figure 6 shows the vibrator and its control system developed in a collaborative research between Taga Electric Co., Ltd. Figure 7 shows an example of the vibration locus at the cutting edge measured by laser Doppler vibrometers.

5.3.2 Mirror Surface Finishing of Hardened Die Steel

Comparison between conventional cutting and elliptical vibration cutting.

Ultraprecision diamond cutting experiments were carried out with the developed vibration cutting system. Figure 8 shows the setup for the ultraprecision elliptical vibration planing experiments, where the X-axis is utilized for the cutting feed. The elliptical vibration tool is attached to the upper index table, and the workpiece is fixed to the lower index table of the ultraprecision planing machine. For comparison, the ordinary cutting without vibration was applied to planing of hardened steel with hardness of HRC 42.

Fig. 7 Measured elliptical vibration locus

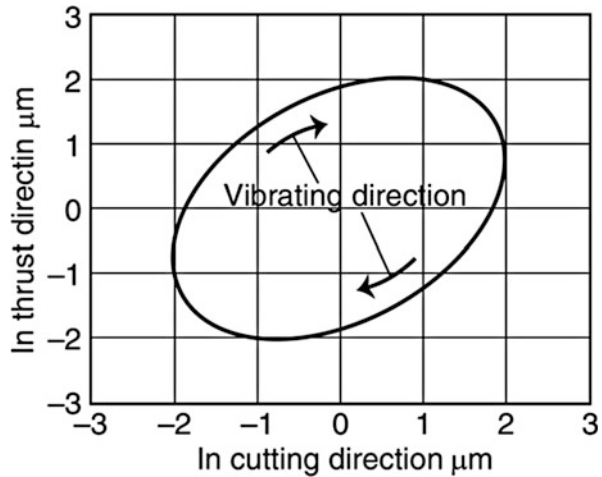


Fig. 8 Experimental setup for planing

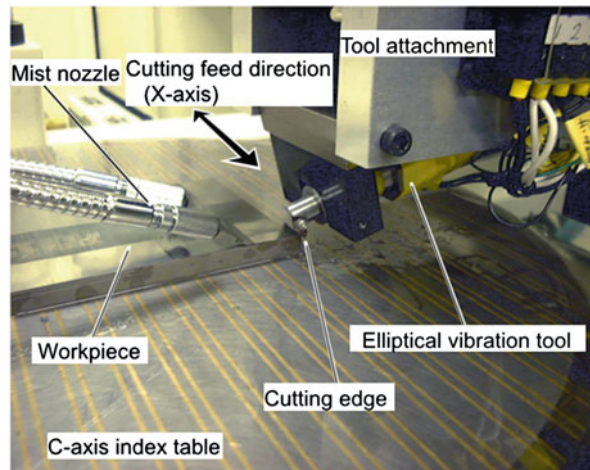


Figure 9a shows the surface finished by the ordinary cutting, and it indicates that the diamond cutting edge was worn out after cutting of a small area of the workpiece. Figure 10a shows the surface profile measured in the feed direction, which indicates that the diamond cutting edge was worn out after cutting of 18 m in the total cutting distance of 70 m. The workpiece material was removed only at the beginning and rubbed during the rest of the cutting period. SEM photographs of the cutting edge before and after the cutting experiment are shown in Fig. 11a. The cutting edge was worn out completely by 3.5 μm , which corresponds to the depth of cut. It is confirmed that the hardened die steel cannot be finished by the ordinary diamond cutting in practice due to the excessive tool wear. This results from the high chemical activity between the carbon of the tool and iron of the workpiece.

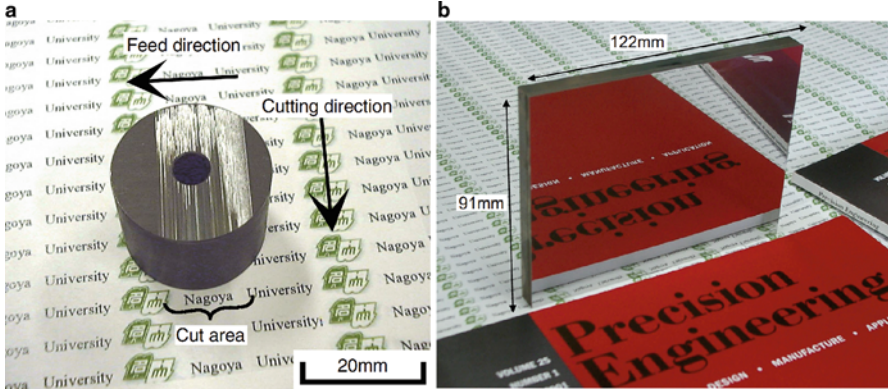


Fig. 9 Photographs of surface finished by (a) ordinary cutting and (b) mirror surface finished by elliptical vibration cutting. (Conditions (a)) workpiece: hardened die steel (JIS – SUS420J2, HRC42), cutting speed, 1.0 m/min; depth of cut, 3.5 μm (set value); pick feed, 5 μm ; diamond tool, R 1 mm; rake angle, 0 deg. (Conditions (b)) workpiece: hardened die steel (JIS – SUS420J2, HRC53), cutting speed, 0.7 m/min; depth of cut, 5 μm ; pick feed, 10 μm ; diamond tool, R 1 mm; rake angle, 0 deg.; vibration, circular; amplitude, 3 μm_{0-p} ; frequency, 19.6 kHz

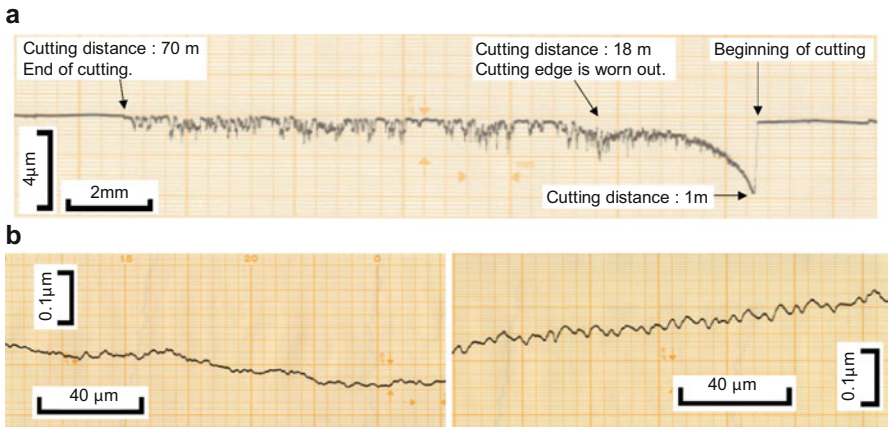


Fig. 10 Measured of surface profiles. (a) Results of finished by ordinary cutting and measured over whole cut area in feed direction (b) Results of finished by elliptical vibration cutting and measured at cutting distance of 1065 m in cutting direction (left) and in feed direction (right)

An optical quality mirror surface finish was realized over the whole area of the large finished surface with the developed elliptical vibration cutting system as shown in Fig. 9b. The measured surface roughness is less than 0.04 μm Ry even at the cutting distance of 1065 m, as shown in Fig. 10b. The optical quality surface was obtained up to the long cutting distance even though the diamond cutting edge was worn to some extent as shown in Fig. 11b. The chippings observed in the photograph occurred in another experiment, so they are not related to the present cutting

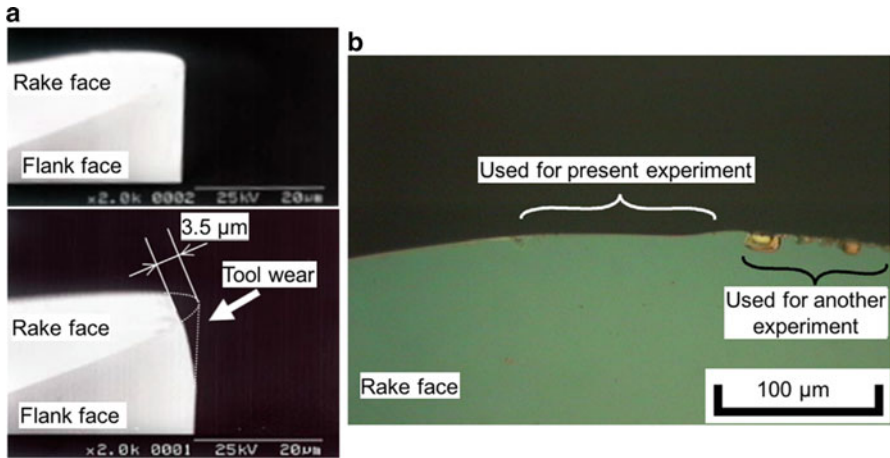


Fig. 11 Tool wear. (a) SEM photographs of cutting edge before and after ordinary cutting experiment (upper, before cutting; lower, after cutting) (b) Microphotograph of cutting edge after elliptical vibration cutting of 1110 m

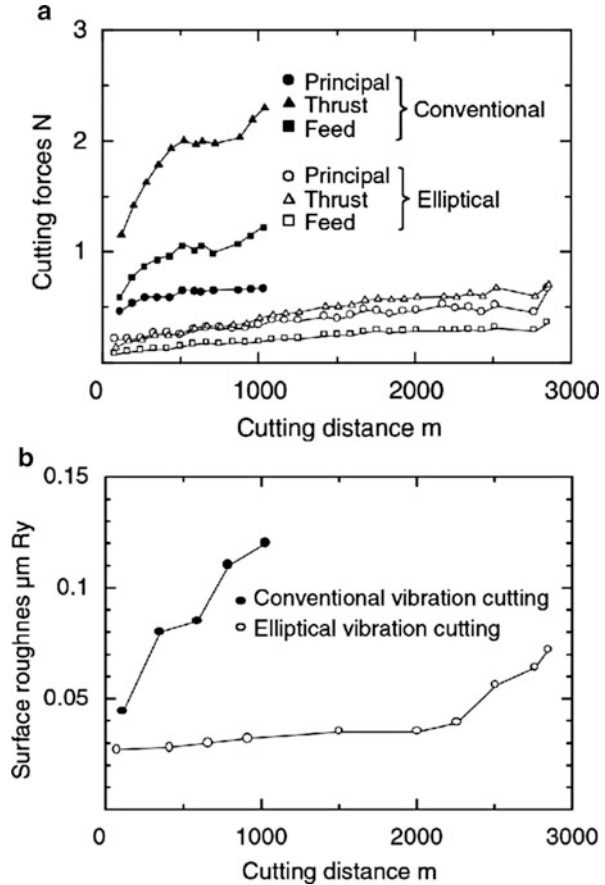
experiment. It is clarified that the tool wear is restrained drastically by intermittent cutting process of the elliptical vibration cutting and that the diamond cutting edge can be used over a long cutting distance of 1110 m.

There are several researches about the reduction of tool wear during the intermittent cutting process. Song et al. (2009) clarified that the reduction of the contact time between the diamond tool and the steel is crucial to reduce tool wear. In continuous cutting, the cutting temperature rises rapidly at the start of the cut and quickly reaches a steady-state temperature that is too high for cutting steel, so excessive chemical reaction between the tool and workpiece occurs. In the case of intermittent cutting, however, the cutting temperature is changed cyclically with the material-cut and air-cut phases, and the temperature of the tool is moderated by cooling during the air-cut time when there is no contact between the tool and the workpiece. This means that the chemical reaction between the diamond and steel is also reduced. Mizutani et al. (2016) also investigated the reduction of tool wear by adopting adsorption films on newly formed ferrous surfaces to protect the diamond tools from diffusion wear during the intermittent cutting process. The ultrasonic vibration cutting in a vacuum chamber was carried out, and it was clarified that the diamond tool edge was rapidly worn out even during the intermittent process at the high vacuum which makes the generation of adsorption films difficult. In other words, air in the cutting atmosphere reacts with the newly formed ferrous surface before it reacts with carbon in the diamond tool so that the tool wear can be suppressed during the intermittent process.

As a result, the practical ultraprecision machining of a large area of hardened steel with a single crystal diamond tool, which is practically impossible by the ordinary cutting, can be attained by applying the ultrasonic elliptical vibration cutting system.

Comparison between conventional linear vibration cutting and elliptical vibration cutting. A turning experiment was also carried out to compare between

Fig. 12 Life of diamond tools. (a) Cutting forces vs. cutting distances (b) Surface roughness versus cutting distances (Conditions) workpiece: hardened die steel (JIS – SUS430J2, HRC39), feed rate, 10 $\mu\text{m}/\text{rev}$; depth of cut, 10 μm ; cutting speed, 2.5 m/min; diamond tool, R 1 mm; rake angle, 0 deg.; flank angle, 15 deg.; vibration, circular or linear; amplitude, 3.5 μm_{0-p} ; frequency, 20.4 kHz



the elliptical vibration cutting and conventional linear vibration cutting. As mentioned above, the crucial problem in diamond cutting of steel is wear of the diamond tool. In addition, the linear vibration cutting requires precise adjustment of the vibration direction in order to reduce the flank-workpiece interference for avoidance of chipping. Thus, the tool life in elliptical vibration cutting is examined in comparison with conventional vibration cutting, where linear vibration is applied mainly in the nominal cutting direction. Figure 12 summarized the cutting forces and the surface roughness measured at various cutting distances. The cutting forces and the surface roughness increase as the cutting distance increases. The cutting forces, especially the thrust force, measured in the elliptical vibration cutting are much lower than those in the conventional vibration cutting throughout the experiments. Optical quality surface with a maximum roughness of less than 0.05 $\mu\text{m Rz}$ can be obtained up to a cutting distance of 2250 m in the elliptical vibration cutting, while the surface roughness obtained by the conventional vibration cutting increases rapidly at a cutting distance of about 300 m. The reason is considered to be the chipping of the diamond cutting edge. Figure 13 shows the cutting edges after the

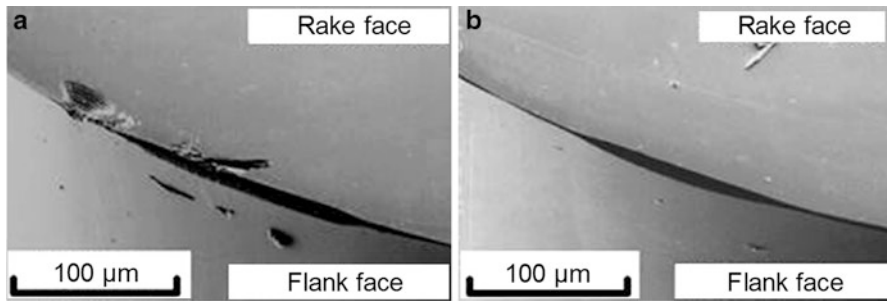


Fig. 13 SEM photographs of cutting edges of worn-out tools. (a) After conventional linear vibration cutting of 1000 m (b) After elliptical vibration cutting of 2800 m

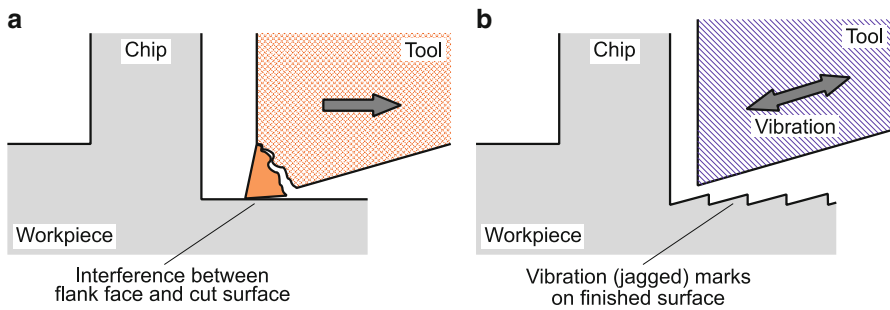


Fig. 14 (a) Chipping problem and (b) vibration mark problem in conventional linear vibration cutting

above experiments. The tool used in the elliptical vibration cutting is worn without chipping, while the one used in the conventional vibration cutting is chipped.

The conventional linear vibration cutting requires careful adjustment of the vibration locus; i.e., the linear vibration should be inclined slightly from the normal cutting direction toward the depth of cut direction so that the flank face does not interfere with the cut surface during the return motion of the tool (see Fig. 14a). If the vibration locus is not exactly linear, i.e., slightly elliptical, the vibration should be clockwise in the case shown in Fig. 1. Otherwise, the sharp and brittle cutting edge is easily chipped due to tensile stress on the flank face. On the other hand, the conventional vibration cutting essentially produces vibration marks (see Fig. 14b) on the finished surface in the cutting direction if the tool edge is not vibrated exactly in the cutting direction to avoid the chipping. This roughness can be large on an ultraprecision level, and hence the vibration direction needs to be aligned precisely with the cutting direction to reduce the jagged marks. This requirement conflicts with the abovementioned requirement to avoid the chipping, and a compromise adjustment between these two requirements is necessary which becomes a crucial problem in practical applications. In the present experiment, the vibration was set with a right inclination, but it might be slightly elliptical and counterclockwise. This is

considered to cause the chipping shown in Fig. 13a. Although the conventional vibration cutting can also realize ultraprecision turning of hardened steel, the same or better surface finish can be obtained by the elliptical vibration cutting without such careful adjustment.

5.4 Ultraprecision Ductile Machining of Tungsten Carbide

In order to realize mass production of optical precision parts, tungsten carbide is heavily used in molding because of its unique mechanical, thermal, and chemical properties. However, since tungsten carbide is a typically hard and brittle material, its ductile machining is extremely difficult by the ordinary ultraprecision cutting technology due to generations of brittle fracture in the workpiece and excessive tool damage. In this section, the ultraprecision ductile machining of tungsten carbide is introduced in terms of verifying the effect of elliptical vibration cutting to ductile machining, clarifying the restrictions in machining conditions for ductile machining of tungsten carbide, and increasing the tool life for practical applications (Suzuki et al. 2007; Zhang et al. 2014).

Eight kinds of workpieces with different binder materials and grain size are prepared for experimental investigations. The material properties including catalog values of hardness and elastic modulus are listed in Table 1. The tool used in these experiments is a single crystalline diamond (SCD) tool with a nose radius of 1 mm, a flank angle of 10° , and a negative rake angle of -20° . The crystal orientation of the flank face is set to be (100), while that of the rake face is set to be (100) or (110). These combinations are denoted as $R(100)F(100)$ and $R(110)F(100)$ in this chapter, where “ R ” and “ F ” represent the rake face and the flank face, respectively.

All experiments are performed on an ultraprecision machine tool, whose position resolution is 1 nm. Figure 15 shows the experimental setup. In order to investigate the influence of the depth of cut on the machined surface quality, the cutting feed is

Table 1 Types of tungsten carbide materials used in cutting experiments

No.	Average grain size [μm]	Binder phase	Hardness [GPa]	Elastic modulus [GPa]
BL1	0.3	Binderless, Co (≤ 0.2 wt%)	25.48	675
BL2	0.5	Binderless, Co (≤ 0.2 wt%)	23.52	680
BL3	1.3–1.5	Binderless, Co (≤ 0.2 wt%)	19.60	650
BL4	0.3	Binderless, Co (≤ 0.1 wt%)	25.98	680
Co1	0.5	Co(≤ 10 wt%)	19.60	560
Co2	1.3–1.5	Co(≤ 10 wt%)	13.72	560
CO3	0.5	Co(12 wt%)	17.30	580
Ni1	0.5	Ni(≤ 10 wt%)	16.66	510

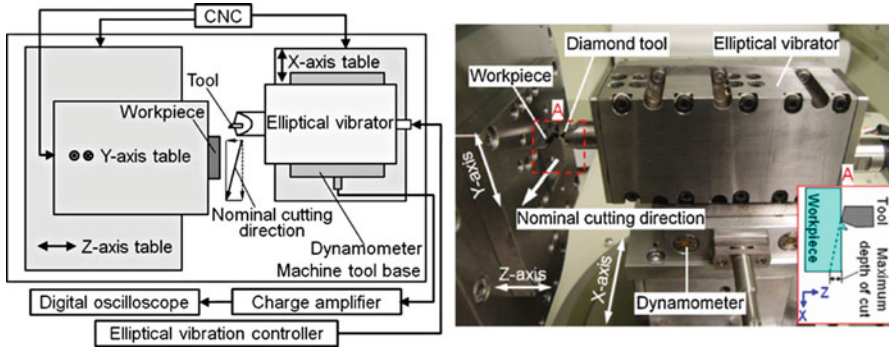


Fig. 15 Illustration and picture of experimental setup. (Conditions) elliptical vibration frequency [kHz], 36.2; amplitude in nominal cutting direction [μm_{p-p}], 2–4; amplitude in depth of cut direction [μm_{p-p}], 1–4; depth of cut [μm], 2; nominal cutting speed [mm/min], 137.5–1100; cutting fluid, oil mist (Bluebe LB-10); cutting tool, single crystalline diamond tool; nose radius [mm], 1; flank angle [deg], 10; rake angle [deg], -20

controlled by the synchronized motion of the X-axis table and the Z-axis table. The depth of cut was linearly increased in grooving and planing, as illustrated in Fig. 15.

5.4.1 Study on Ductile Machining of Tungsten Carbide

Effect of elliptical vibration cutting on ductile machining. At first, comparison between the elliptical vibration cutting and ordinary cutting was carried out. Workpieces of BL4 and Co1 were grooved by the ordinary cutting and the elliptical vibration cutting.

Figure 16a shows the scanning electron microscope (SEM) images of the grooved surface on BL4 at a depth of cut of $0.2 \mu\text{m}$. The groove formed by the ordinary cutting is filled with numerous brittle defects (left). In contrast, a smooth surface can be obtained by the elliptical vibration cutting (right). As no brittle crack and asperity can be observed on the surface in the elliptical vibration cutting, ductile mode machining was attained successfully. From this fact, it can be expected that the inside of tungsten carbide grains existing at the topmost layer of the remained surface was cut without fracture generation on the surface or pullout of the grains, which are observed in the ordinary cutting.

Figure 16b shows the cutting edges after grooving of the binder-containing workpiece of Co1. Considerable adhesion of the workpiece material can be observed on the rake face of the tool used in ordinary cutting (left), which may result in adhesion wear and/or considerable thermochemical reaction. The same phenomenon was observed in the ordinary cutting of other binder-containing materials. On the other hand, no adhesion was observed in the elliptical vibration cutting (right). This fact indicates that the elliptical vibration cutting is effective to suppress tool wear progress and to attain better surface quality in machining of binder-containing tungsten carbide.

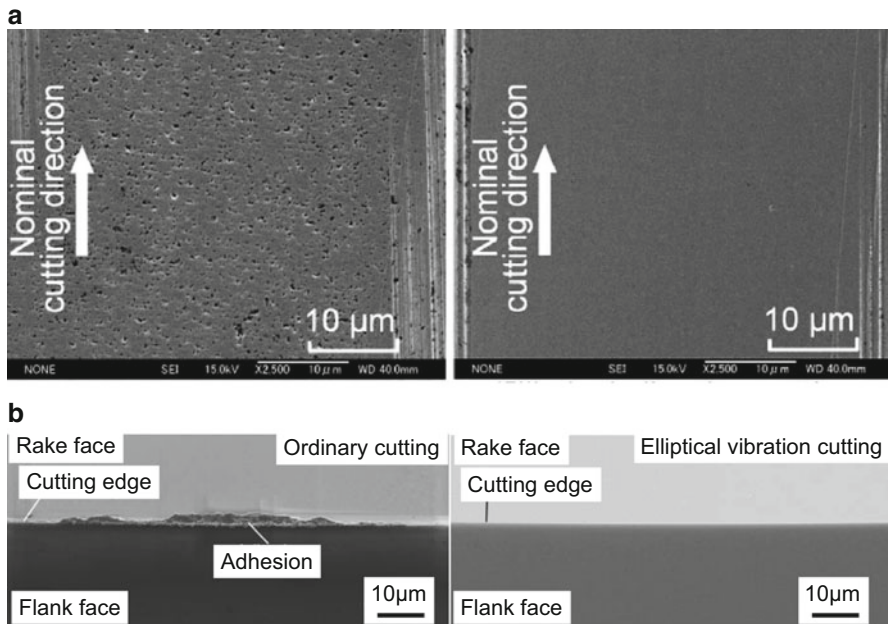


Fig. 16 Comparison of elliptical vibration cutting (right) with ordinary cutting (left). **(a)** SEM images of grooved surface (workpiece, BL4: depth of cut [μm], 0.2; nominal cutting speed [mm/min], 150) **(b)** Cutting edges after grooving (workpiece, Co1)

Mechanism of the ductile mode machining is considered as follows. In elliptical vibration cutting, the tool cuts the surface that is finished in the previous vibration cycle. Thus, the actual uncut chip, i.e., instantaneous uncut chip thickness, becomes extremely thin. Note that this uncut chip thickness becomes generally smaller as compared with the nominal depth of cut. The instantaneous uncut chip thickness in each vibration cycle becomes significantly small especially when the tool cuts the finished surface around the bottom of the elliptical vibration. Because of this process, the actual depth of cut becomes smaller than the critical value for ductile machining due to the size effect in fracture toughness, resulting in significant improvement of the nominal critical depth of cut for ductile machining of tungsten carbide.

Influence of cutting parameters on surface quality. Figure 17a demonstrates the surface quality of microgrooves machined on Co1 where the nominal cutting speed and vibration amplitudes in the nominal cutting and depth of cut directions, A_c and A_d , are changed. The speed ratio, i.e., the ratio of the maximum vibration speeds in the nominal cutting direction to the nominal cutting speed, is kept to be a constant value of 25. The grooved surfaces at the vibration amplitudes A_c-A_d of 4-4 and 2-2 $\mu\text{m}_{\text{p-p}}$ are filled with micrometer-scale brittle defects, as shown in Fig. 17a. The defect size is several times larger than the single grain size of 0.5 μm . Thus, these defects are considered to be made by the pullout of agglomerated tungsten carbide

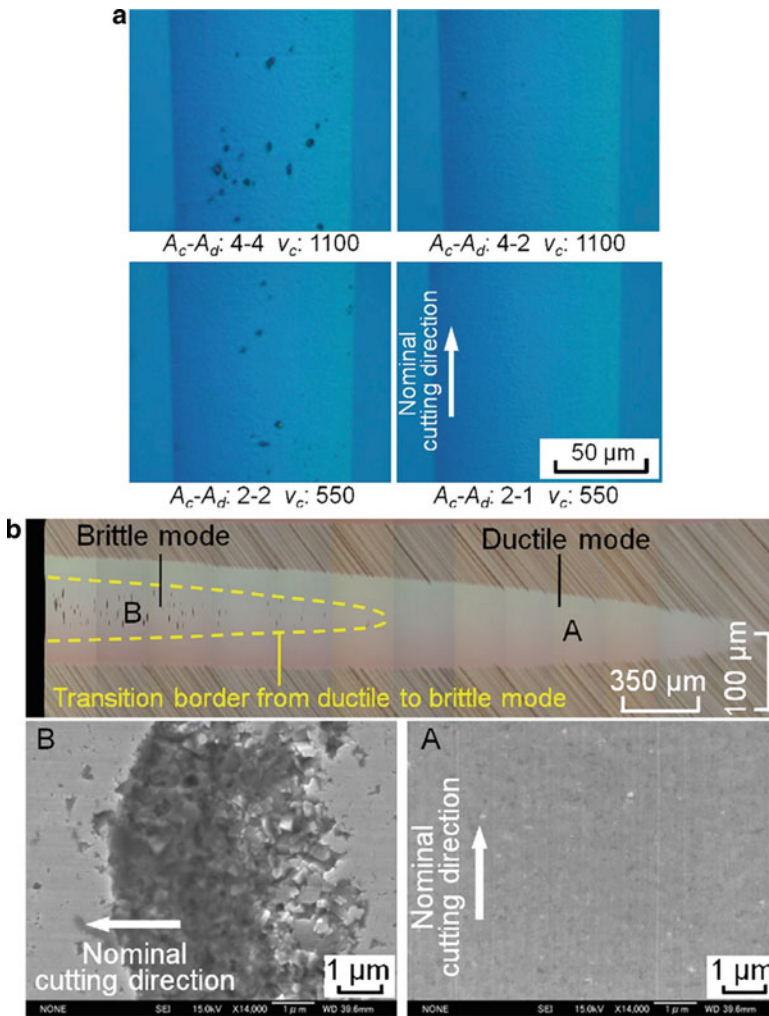


Fig. 17 Influence of cutting parameters on surface quality. (a) Influence of vibration amplitude (Conditions) workpiece, Co1: depth of cut [μm], 0.9; amplitudes in nominal cutting and depth of cut directions [μm_{p-p}], A_c-A_d ; nominal cutting speed [mm/min], v_c (b) Influence of depth of cut (Conditions) workpiece, BL4: amplitudes $A_c - A_d$ [μm_{p-p}], 2-2; nominal cutting speed [mm/min], 150

grains from the workpiece surface. On the other hand, similar large defects do not generate at vibration amplitudes of 4-2 and 2-1 μm_{p-p} . Similar experimental results were also observed in the cases of other binder-containing and binderless materials, and hence it can be concluded that the influence of vibration amplitudes on ductile machining is not negligible.

The influence of the depth of cut on the surface quality was also investigated. Figure 17b demonstrates a groove surface of BL4, which was machined with a

circular vibration ($2 \mu\text{m}_{p-p}$) at a nominal cutting speed of 150 mm/min. The depth of cut is gradually increased from $0 \mu\text{m}$ to $2 \mu\text{m}$. Surface quality changes depending on the depth of cut, where brittle cracks generate at a large depth of cut even in the elliptical vibration cutting. Transition border from ductile to brittle modes are observed at the depth of cut of about $1.5 \mu\text{m}$. Agglomerated grains seem to be pulled out at one time from the surface, and this feature of the defects is the same as that shown in Fig. 17a. This kind of defect characterized by their size is defined as “multi-grain-size defect” here. Note that similar surface deterioration with a large defect is not observed in ordinary cutting. Hence, this is considered to be a specific problem in elliptical vibration cutting.

These amplitude and depth of cut dependencies are considered to be related to the chip pulling-up motion in the elliptical vibration cutting. Figure 18 shows schematic illustrations of the elliptical vibration cutting process. When the vibration amplitude is larger in the depth of cut direction, chip pulling-up distance in this direction becomes longer. In addition, the chip pulling-up distance increases up to about half the amplitude when the depth of cut is large. Sintered materials are not tough against tensile stress. Because of this nature, massive grains may be pulled out from the workpiece surface by the pulling-up motion especially when upward motion distance in the depth of cut direction is longer than the grain size. When the ratio of amplitude in the depth of cut direction to that in nominal cutting direction is large, the slope of the cutting edge trajectory becomes steep while pulling up the chip. This steep trajectory is also considered to enhance the abovementioned pullout phenomena. Hence, the vibration amplitudes and the depth of cut need to be selected properly to avoid the “multi-grain-size defect” occurrence due to the pullout of massive grains.

The influence of the nominal cutting speed on the surface quality was also examined. SEM images of the machined surfaces of BL1 at a depth of cut of $0.5 \mu\text{m}$ are shown in Fig. 19. It is confirmed that higher-quality surfaces in the ductile mode can be attained at lower nominal cutting speeds. The defect size is less than several hundred nanometers, which is almost identical to the grain size. To

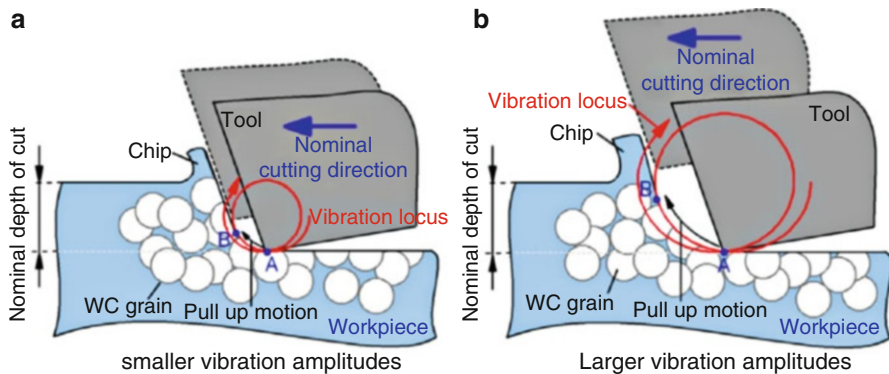


Fig. 18 Pull-up motion with different vibration amplitudes

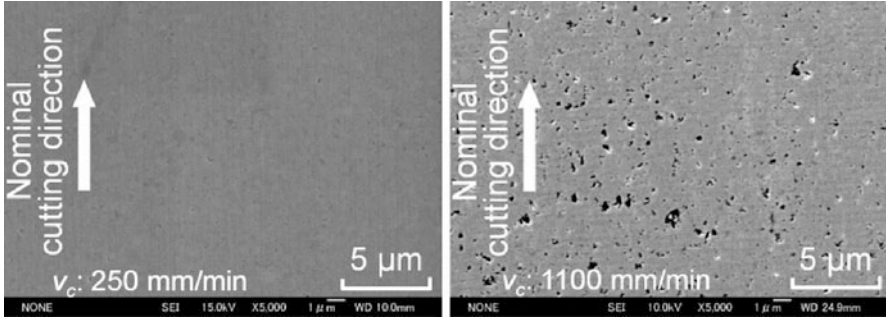


Fig. 19 Effect of nominal cutting speed on surface quality (workpiece: BL1, amplitudes $A_c - A_d$ [μm_{p-p}], 4–2; depth of cut [μm], 0.5)

differentiate it from the “multi-grain-size defect,” this kind of defect is defined as a “single-grain-size defect” here. This cutting-speed dependency of surface quality is considered to be associated with the cut volume in each vibration cycle. It should be noted that the instantaneous uncut chip thickness is almost proportional to the nominal cutting speed. Thus, the cutting forces decrease, and the strain energy at the deformed zone is reduced when the nominal cutting speed decreases. Small force and strain energy are beneficial to suppress crack propagations while machining. Hence, the selection of the cutting-speed condition is significantly important to suppress “single-grain-size defect” occurrence.

Influence of material properties on ductile machining. SEM images of grooved surface of BL1, Co1, BL2, BL3, and Co2 are shown in Fig. 20. As noted in Fig. 20a, brittle cracks are not observed from the machined surfaces. This also indicates that ductile mode machining is realized at a large depth of cut of 0.9 μm . However, ductile machining was not realized by the same cutting conditions in BL2, BL3, and Co2 even when the depth of cut is small (see Fig. 20b). Their surfaces are filled with the single-grain-size defects due to brittle fracture. Comparing the grooving results of BL1, BL2, and BL3, the difference in surface integrity indicates that smaller grain size is advantageous to attain ductile mode machining. It is known that sintered materials consisting of smaller particles generally have better toughness due to smaller initial defect size inside the material (Fang and Eason 1995). Because of this nature, finer grain is advantageous not only to increase the toughness of the material but also to realize ductile mode machining. Comparing the results of Co1 and BL2, it is apparent that the binder phase is also advantageous to suppress the generation of brittle fracture. The defect size is, therefore, smaller in Co2 than that in BL3, where the grain sizes are the same.

Through the grooving experiments, it is found that single-grain-size defects can be generated much more easily as compared to multi-grain-size defects. In order to evaluate the relative difference in surface deterioration due to single-grain-size defects, the machined surface quality was classified into nine levels and a scale from 0 to 8 are provided by the authors based on an optical microscope observation. 0 represents the best surface with minimal defects and 8 represents the worst surface

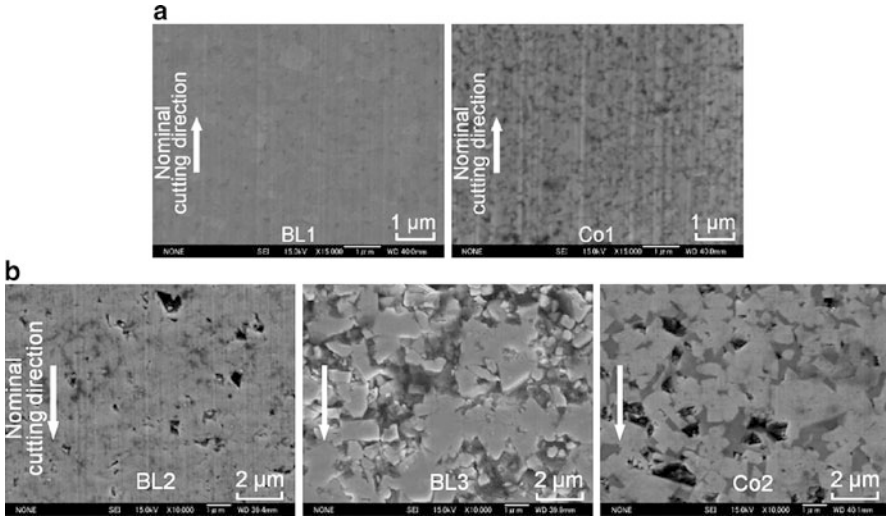


Fig. 20 SEM micrographs of machined groove surfaces. (a) Ductile mode machining results (depth of cut [μm], 0.9; vibration amplitudes [μm_{p-p}], 2–1; nominal cutting speed [mm/min], 137.5) (b) Brittle fractures are observed (depth of cut [μm], 0.2; vibration amplitudes [μm_{p-p}], 2–1; nominal cutting speed [mm/min], 137.5)

finish. By counting the total number of defects with the data processing software, the scores of the machined surfaces are evaluated. For instance, high-quality surfaces of BL1 and Co1 shown in Fig. 20a are indexed as 0 and 1 where no single-grain-size defect is observed. Scores of the machined surfaces of BL2, BL3, and Co2 in Fig. 20b are evaluated as 5, 8, and 6 due to the single-grain-size defect. This quantification process might be influenced by the threshold in data processing, but relative difference in the evaluation results seems to be mostly reliable.

Analysis of fundamental grooving experiments. As mentioned above, surface deterioration due to single-grain-size defects may depend on the instantaneous uncut chip thickness in the elliptical vibration cutting process. In particular, the maximum instantaneous uncut chip thickness while cutting the finished surface is considered to be directly associated with surface deterioration. Figure 21 illustrates the tool trajectory around the bottom of the vibration cycle and the theoretical maximum instantaneous uncut chip thickness at the i -th cycle. By considering the kinematic model of elliptical vibration cutting, the values of the maximum instantaneous uncut chip thickness in the grooving experiment can be calculated according to the cutting velocity and the vibration amplitudes of elliptical vibration.

Figure 22 indicates relations of the surface quality scores and maximum instantaneous uncut chip thicknesses for all evaluated materials in grooving. The values of surface quality index increase with an increase of maximum instantaneous uncut chip thickness regardless of the workpiece material. Hence, the maximum instantaneous uncut chip thickness needs to be decreased to achieve better surface quality. High-quality surfaces in ductile mode, whose score is 0 or 1, are obtained when the maximum

Fig. 21 Maximum instantaneous uncut chip thickness while cutting finished surface

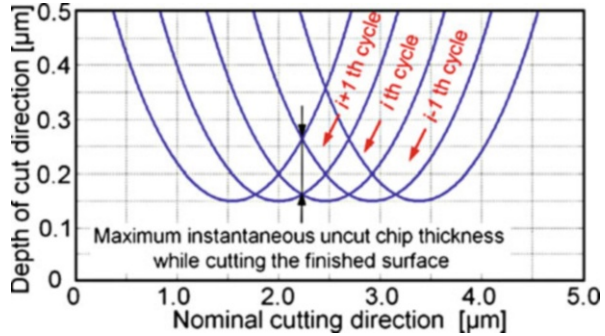
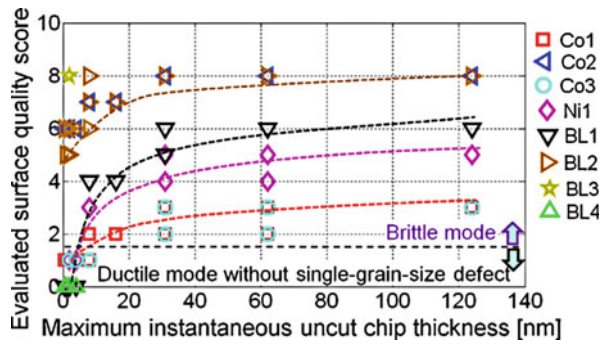


Fig. 22 Influence of maximum instantaneous uncut chip thickness on surface quality (evaluated at a depth of cut about 1 μm)



instantaneous uncut chip thickness is less than or equal to 4 nm and the workpieces are BL1, BL4, Co1, Co3, and Ni1. In other words, ductile machining cannot be attained for Co2, BL2, and BL3 under all evaluated conditions. These facts indicate that appropriate vibration amplitude and cutting-speed conditions need to be selected to satisfy a small maximum instantaneous uncut chip thickness, which is less than or equal to 4 nm. The grain size also needs to be less than or equal to 0.5 μm and binder material is helpful to attain ductile mode machining. The feature of multi-grain-size defect occurrence is almost the same as that of the single-grain-size defect occurrence.

5.4.2 Study on Tool Life for Practical Applications

Influence of cumulative cutting distance on tool life. Figure 23a shows the variation of measured specific cutting forces at the depth of cut of 1 μm with the increase of nominal cutting distance. The specific cutting force increases rapidly at lower cutting speeds, while there is no explicit change of the cutting force in the ordinary cutting within the nominal cutting distance of 4.3 m. Note that the cutting force in the elliptical vibration cutting generally becomes small especially at a low nominal cutting speed due to thinner instantaneous uncut chip thickness in each elliptical vibration cycle. Comparing the results at the same nominal cutting speed of 250 mm/min, the thrust force in the elliptical vibration cutting becomes surprisingly

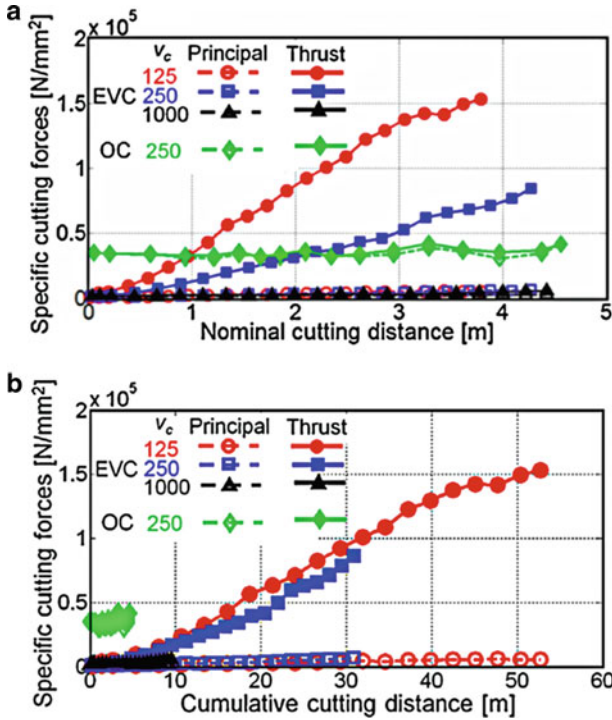


Fig. 23 Influence of (a) nominal cutting distance and (b) cumulative cutting distance on cutting forces. (Conditions) workpiece: BL1, depth of cut [μm], 0–1.2; amplitude [μm_{p-p}], 4–2; nominal cutting speed [mm/min], v_c ; OC, ordinary cutting; EVC, elliptical vibration cutting

larger than that in the ordinary cutting at the nominal cutting distance of larger than 2.4 m. The experimental results indicate that the tool damage is larger in the elliptical vibration cutting especially at low nominal cutting speeds. However, it is generally considered that the nominal cutting speed does not affect the tool life at such low speed conditions in the case of the ordinary cutting of tungsten carbide.

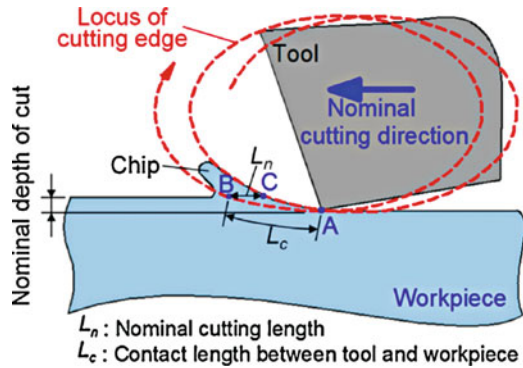
This interesting phenomenon is considered to be related to the characteristics of the elliptical vibration cutting process. In elliptical vibration cutting, the actual cutting distance in one vibration cycle L_c becomes much longer than the tool feed distance in one vibration cycle L_n , as illustrated in Fig. 24. The nominal cutting distance S_{nd} and cumulative cutting distance S_{cd} can be formulated as following:

$$S_{nd} = L_n f t = v_c t \tag{1}$$

$$S_{cd} = L_c f t = L_c f \frac{S_{nd}}{v_c} \tag{2}$$

where f is the vibration frequency, v_c is the nominal cutting speed, and t is the cutting time.

Fig. 24 Nominal cutting length and contact length in one vibration cycle



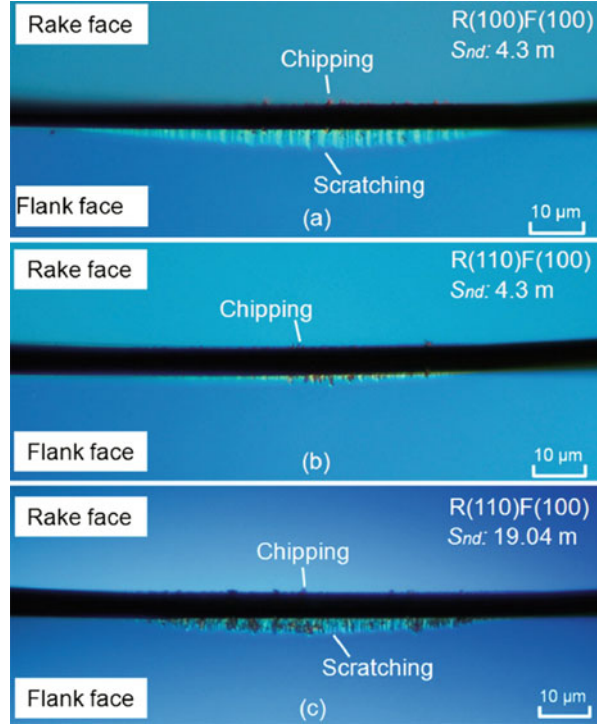
Equation 2 indicates that the cumulative cutting distance is inversely proportional to the nominal cutting speed, namely, the cumulative cutting distance S_{cd} at a certain nominal cutting length S_{nd} becomes longer at a lower nominal cutting speed v_c and vice versa. The tool damage is related to this cumulative cutting distance rather than the nominal cutting distance in the elliptical vibration cutting.

The cumulative cutting distance in the elliptical vibration cutting is calculated for each experiment. The relationship between the specific cutting forces and the cumulative cutting distance is shown in Fig. 23b. The cumulative cutting distance becomes longer in the elliptical vibration cutting especially at lower nominal cutting speed even though the nominal cutting distances are almost identical. The experimental results of force variations with respect to the cumulative cutting distances show similarity in the elliptical vibration cutting. This fact indicates that the cumulative cutting distance has the dominant contribution on the tool damage. Hence, higher nominal cutting speed leads to longer tool life in the elliptical vibration cutting.

Influence of crystal orientation of diamond tool on tool life. In order to investigate the influence of the tool crystal orientation on the tool life, planing experiments of BL1 were carried out by use of tools with crystal orientations of $R(100)F(100)$ and $R(110)F(100)$. Note that diamond is an anisotropic material; thus, the tensile strength of C–C bond on the topmost layer of the cutting edge varies depending on the crystal orientation. The tool damages in the planing experiments are compared in Fig. 25. By changing the crystal orientation from $R(100)F(100)$ to $R(110)F(100)$, flank wear decreases drastically while slightly larger chipping occurs on the flank face at the same nominal cutting distance of 4.3 m. This fact indicates that $R(110)F(100)$ is good at suppressing scratching damage on the flank face but poor in fracture toughness. When the nominal cutting distance in $R(110)F(100)$ is 19.04 m, the maximum flank wear becomes identical with that of $R(100)F(100)$, i.e., the tool life is about 5 times long.

Figure 26a shows variations of the measured specific cutting forces at the depth of cut of 1 μm in the elliptical vibration cutting. Cutting force constants increase considerably slowly when using $R(110)F(100)$. This fact indicates that the reduction of flank wear by use of a tool with $R(110)F(100)$ is significantly

Fig. 25 Microphotographs of cutting edges with crystal orientations of (a) $R(100)F(100)$ and (b), (c) $R(110)F(100)$. (Conditions) amplitude in nominal cutting direction [μm_{p-p}], 4; amplitude in depth of cut direction [μm_{p-p}], 2; nominal cutting speed [mm/min], 250; pick feed [μm], 5; depth of cut [μm], 0–1.2; total nominal cutting distances [m], 4.3 and 19.4



advantageous to decrease the cutting force, which may result in better machining accuracy. Figure 26b shows the measured surface roughness along the pick feed direction. The surface roughness is not distinctively different at the same cutting distance, and the surface roughness is less than 35 nm Rz within the nominal cutting distance of 4.3 m. Considering the nature of the less tool damage in $R(110)F(100)$, crystal orientation of $R(110)F(100)$ is better to attain longer tool life in practical use. With the increase of the nominal cutting distance to 19.04 m, the roughness increases almost linearly, though the maximum roughness is still less than 100 nm Rz.

Prediction model of tool wear. Tool wear causes the cutting force to increase and thus the surface quality deteriorates. Hence, it is important to evaluate features of tool wear. Influence of material properties and cutting conditions on tool wear progress is analyzed. The tool wear amount is represented by the maximum value of the observed flank wear width VB_{max} . Tool wear resistance A_e is an evaluation factor representing the strength of the cutting edge, which is defined and quantified in Zong et al. (2010). High tool wear resistance is considered to be effective to suppress tool wear progress.

As mentioned earlier, tool damage is directly related to the cumulative cutting distance (S_{cd}) rather than the nominal cutting distance. Higher hardness (H_m) and

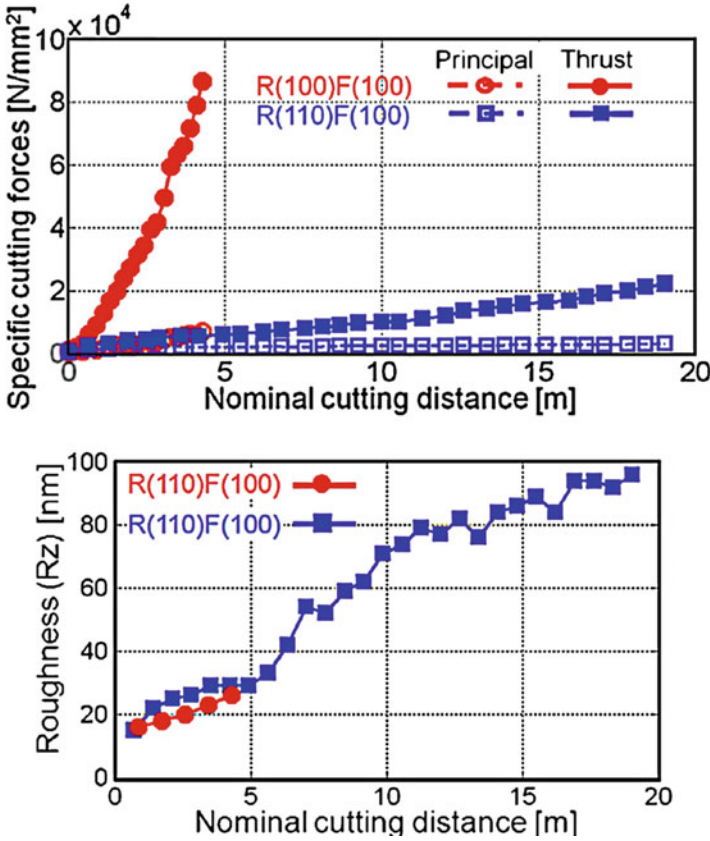


Fig. 26 Influence of crystal orientation on (a) specific cutting force increase and (b) surface roughness Rz variation with increase of nominal cutting distance. (Conditions) workpiece, BL1; amplitude in nominal cutting direction [μm_{p-p}], 4; amplitude in depth of cut direction [μm_{p-p}], 2; nominal cutting speed [mm/min], 250; pick feed [μm], 5; depth of cut [μm], 0–1.2; total nominal cutting distances [m], 4.3 and 19.4

lower tool wear resistance (A_e) are also considered to accelerate flank wear progress. Hence, the relationship between VB_{max} and $S_{cd} \cdot H_m/A_e$ is investigated from the experimental results. Figure 27 shows the plot of VB_{max} against $S_{cd} \cdot H_m/A_e$ and its regression line. From this fact, tool wear can be predicted roughly by the following equation.

$$VB_{max} = a_1 \left(\frac{S_{cd} \cdot H_m}{A_e} \right) + a_0 \tag{3}$$

where $a_1 = 1.33e - 8$ and $a_0 = 1.29e - 6$ [m].

Fig. 27 Tendency of tool wear progression

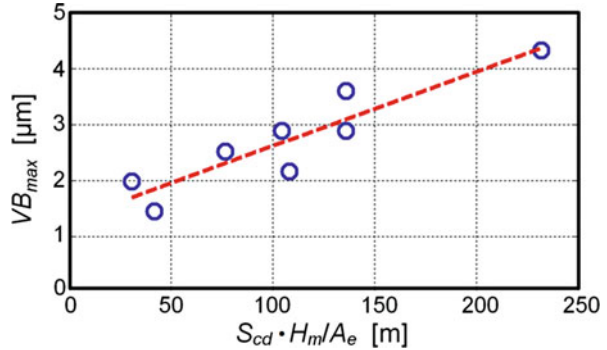


Table 2 Preferable conditions for tungsten carbide machining

Workpiece	Binderless with grain size of less than $0.3 \mu\text{m}$ Binder-containing with grain size of less than $0.5 \mu\text{m}$
Cutting conditions	Nominal cutting speed: About 250 mm/min Maximum depth of cut: At most $1.2 \mu\text{m}$
Vibration conditions	Vibration amplitudes in nominal cutting and depth of cut directions: $4\text{--}2 \mu\text{m}_{p-p}$
Tool	Crystal orientation: $R(110)F(100)$

5.4.3 Preferable Conditions and Micro-/Nano-Sculpturing of Tungsten Carbide

Through fundamental grooving and planing experiments, an interesting nature of tungsten carbide machining is clarified. Ductile mode machining can be attained by means of elliptical vibration cutting, while “single-grain-size defect” and/or “multi-grain-size defect” may generate with inappropriate experimental conditions. In order to suppress the generation of brittle fracture completely, it is necessary to set a small maximum instantaneous uncut chip thickness while cutting the finished surface. In addition, smaller grain size and presence of the binder phase are advantageous to prevent generation of brittle fracture. However, these conditions are inversely disadvantageous to realize longer tool life. Tool damage progress in elliptical vibration cutting also has a strong relation with the cumulative cutting distance and crystal orientation of the tool. Thus, appropriate conditions need to be selected to make a good balance in the surface quality and the tool life. The conditions, which are considered to be comprehensively preferable for practical machining of tungsten carbide in ductile mode, are summarized in Table 2.

Figure 28 shows the photograph of dimple sculptures and measured profiles. In this machining, the amplitude in the depth of cut direction is controlled by a sinusoidal wave pattern, which is changed from $1 \mu\text{m}_{p-p}$ to $2 \mu\text{m}_{p-p}$. The maximum depth of cut is, however, set to be about $0.2 \mu\text{m}$, which is less than half the amplitude variation of $0.5 \mu\text{m}$. By controlling the amplitude in the depth of cut direction

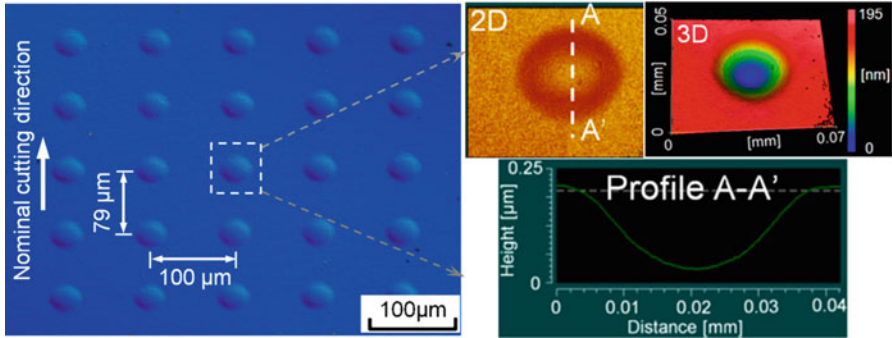


Fig. 28 Microphotographs of sculptured dimples. (Conditions) material, tungsten carbide Co₃; nominal cutting speed [mm/min], 284; pick feed [μm], 100; maximum depth of cut [μm], 0.2; frequency of elliptical vibration [kHz], 36.2; frequency of amplitude oscillation [Hz], 60; amplitude in depth of cut direction [μm_{p-p}], 1–2; amplitude in nominal cutting direction [μm_{p-p}], 4; cutting tool, SCD tool; crystal orientation, $R(100)F(100)$; nose radius [mm], 1.0; rake angle [deg], –20; flank angle [deg], 10

precisely at high speed, ultraprecision sculpturing of difficult-to-cut materials can be achieved efficiently without using the conventional fast tool servo technology (Suzuki et al. 2011). Consequently, independent concave dimples with a maximum depth of about 0.2 μm were machined successfully in ductile mode on tungsten carbide. Note that this nano-sculpturing cannot be attained by ordinary machining methods.

5.5 High-Efficiency Machining with High-Power Ultrasonic Vibration Device

Recently, the elliptical vibration cutting technology has been utilized in practice to produce steel dies and molds mainly for optical parts. However, the application of the elliptical vibration cutting technology has been limited to high-cost ultraprecision machining because of the power limitation of the commercially available elliptical vibration device. Typically, the depth of cut is set in a range from a few micrometers to several tens of micrometers when hardened die steel is machined. Hence, expensive machining facilities such as an ultraprecision machine tool and a temperature-controlled room are required to maintain the small depth of cut. On the other hand, there are much greater industrial needs for low-cost mirror surface finishing of dies and molds with ordinary machining accuracy than the high-cost ultraprecision machining. In the ordinary machining environment, machining error is often greater than 100 micrometers mainly due to thermal deformation of machine tools. Because the available depth of cut of the device is smaller than the machining error, some part of workpiece will not be machined, which is not allowed in mirror surface finishing of dies and molds. In such a case, the whole process needs to be carried out again. This is so much time consuming, and it will be a big loss for

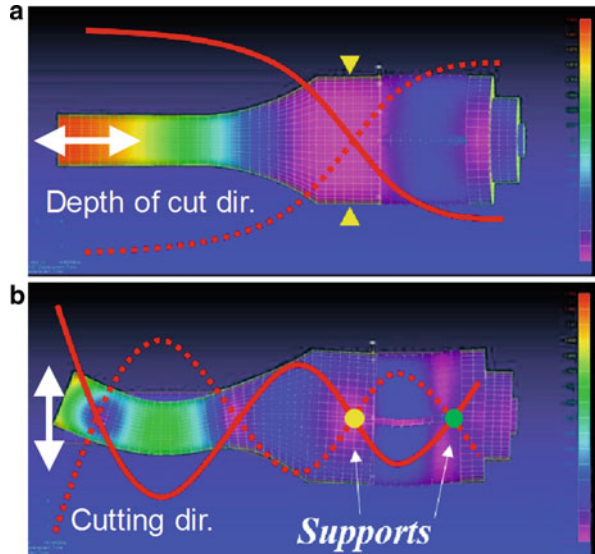
manufacturers. In order to realize the low-cost mirror surface finishing of free-form surfaces of dies and molds, a high-power elliptical vibration device was developed in this research (Jung et al. 2016). This high-power elliptical vibration device can resist more than several hundreds of micrometers. The newly developed high-power elliptical vibration device was applied to the elliptical vibration cutting of hardened die steel with SCD tools and clarified that the device has sufficient capabilities even in the high-efficiency cutting conditions through a series of experiments. Its performance was examined at large depths of cut in terms of surface quality, cutting forces, and tool wear.

5.5.1 Development of High-Power Ultrasonic Device

An elliptical vibration device generally needs to have very unique features, e.g., it must generate high-accuracy large-amplitude ultrasonic elliptical vibration against machining load, and it needs to be rigid enough to suppress other vibrations and static displacement. The elliptical vibration is generated by combining two-directional vibrations. Hence, the vibrator is designed to have the vibration modes in the two directions whose resonant frequencies and nodal positions are almost the same. Then, the two resonant vibration modes are excited while the vibrator is supported rigidly at the nodal positions. In this research, there is an additional requirement of high power. The power of ultrasonic vibration devices generally increases as volumes of the piezoelectric elements increase which can load more electric charge. Thus, larger piezoelectric elements were utilized in this study, which lead to low resonant frequency of about 16.9 kHz. It is considered that this frequency is the lower limit in practice since the elliptical vibration becomes too noisy for operators at further lower frequencies. Meanwhile, a large device is not useful as a cutting tool, and thus the half-wavelength mode of axial vibration was utilized to reduce the size as follows.

A high-power elliptical vibration device was designed based on the finite element analysis. Figure 29 shows results of the finite element analysis after some trials and errors. Figure 29a shows the half-wavelength mode of axial vibration. The 3rd mode of bending vibration is combined as shown in Fig. 29b. One of the challenges of this design is that the half-wavelength mode has only one vibration node, though the vibrator should be supported at plural nodal positions rigidly. Therefore, the vibrator was designed so that the resonant frequencies and the nodal positions (shown by yellow in Fig. 29a) are close to each other. The supports were designed so that the adjusted node of the two modes (shown by yellow) is supported rigidly in every direction and another node of the bending mode (shown by green) is supported flexibly in the axial direction but rigidly in the lateral directions. As a result, it is possible to develop a compact and high-power vibration tool. Its length is only 172.4 mm, and it generates high-precision and high-power elliptical vibration in both directions, which means that it can resist more chip load.

Fig. 29 Results of finite element analysis for high-power ultrasonic elliptical vibration device. (a) Half-wavelength mode of axial vibration (b) 3rd mode of bending vibration



5.5.2 High-Efficiency Machining with High-Power Vibration Device

The developed high-power vibration device was applied to high-efficiency machining experiments. Figure 30 shows an experimental setup and a schematic illustration of the cutting process. The high-power elliptical vibration device was equipped on a precision machine tool (Nagase Integrex Co. Ltd., NIC-300). Typical hardened die steel (ISO: 4028-420-00-I, Stavax) was used as workpiece. A SCD tool with a nose radius R of 1.0 mm was used to obtain mirror surfaces. Oil mist was supplied to the cutting point during the machining. A large depth of cut d was set in a range from 0.1 mm to 0.4 mm to not leave unfinished surface, while the pick feed p was set in a range from 0.005 mm to 0.02 mm to obtain mirror surfaces with a theoretical roughness of less than 0.05 μm .

The cutting forces and the specific cutting forces measured during machining are plotted against cross-sectional area of the uncut chip in Fig. 31a. It shows that the specific cutting forces, especially the thrust force, decrease as the cross-sectional area of the uncut chip is increased. This indicates that roundness of the cutting edge causes a size effect due to the edge force components even though the SCD tool has a very sharp cutting edge. Considering high strength of the hardened die steel, the specific cutting forces are very small especially at the large cross-sectional areas, and this implies that the developed elliptical vibration device works well against the large machining load at the large cross-sectional areas or the large depths of cut. Figure 31b shows the surface roughness measured in the pick feed direction with a stylus type surface roughness measuring instrument (Kosaka Laboratory Ltd., ET4000A) at various depths of cut and pick feeds. As shown in the figure, roughness of the mirror surface obtained at a large depth of cut d of 0.4 mm and a pick feed p of

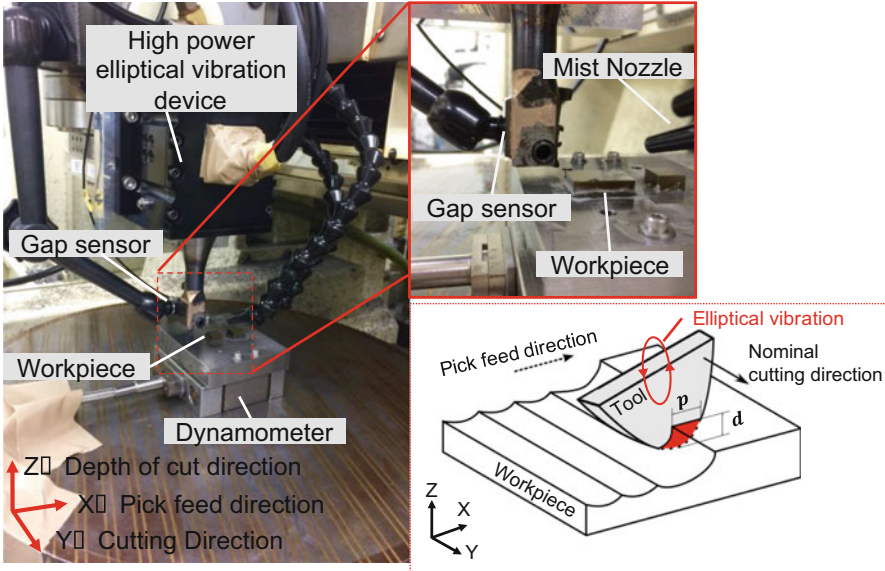


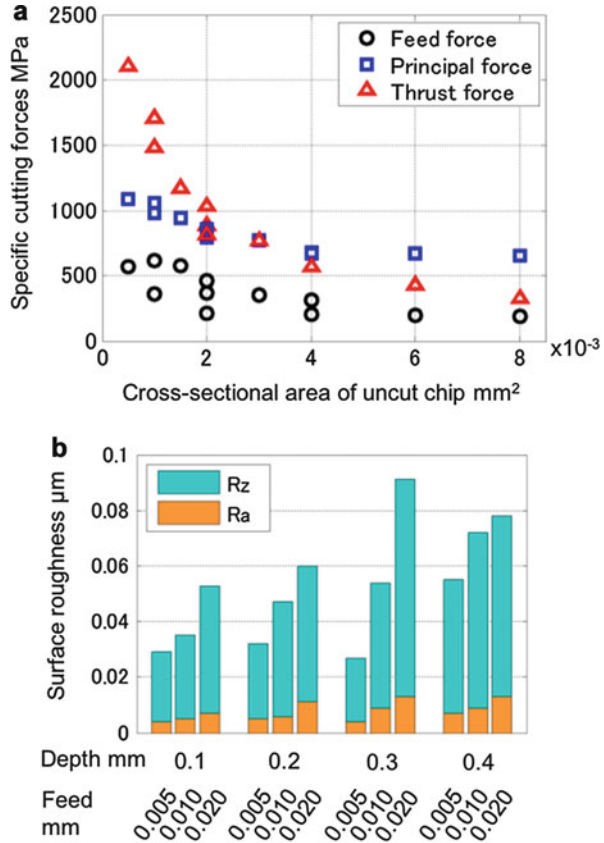
Fig. 30 Photograph of experimental setup (left) and schematic illustration of cutting process (lower right)

0.02 mm is 0.078 μm R_z or 0.013 μm R_a . It also shows that the surface roughness has positive correlation with the pick feed and the depth of cut. The effect of the pick feed can be understood by the theoretical roughness $R_{th} = f^2/(8R)$, i.e., $R_{th}=0.003$, 0.013, and 0.05 μm , when the pick feed p is 0.005, 0.01, and 0.02 mm, respectively, though R_z is always larger than R_{th} especially at low pick feeds. It can be considered that this discrepancy and the effect of depth of cut are caused mainly by undesirable vibrations of the mechanical structures. These results imply that the surface quality may be further improved if the undesirable machine vibrations are reduced by using a better machine tool or developing a better high-power vibration device with higher accuracy and rigidity. Figure 32 shows a photograph of the machined surfaces. As shown, mirror-quality surfaces can be obtained successfully even at large depths of cut d up to 0.4 mm.

5.6 Mirror Surface Finishing of High-Alloy Steels

Recently, industrial demands for mirror surface machining of high-hardness steels such as cold work die steels or high-speed tool steels (hereinafter called “high-alloy steels”) are increasing. The high-alloy steels, whose Rockwell C hardness exceeds 60 HRC, are used in forging processes as well as injection molding processes. However, a long tool life as in the results in hardened stainless steels cannot be obtained even though the elliptical vibration cutting is applied. The hardness of high-alloy steels is higher than that of hardened stainless steels, but their hardness

Fig. 31 Specific cutting forces and surface roughness. (a) Measured specific cutting forces against cross-sectional area of uncut chip (b) Surface roughness measured at various depths of cut and pick feeds



difference should be small considering hardness of the SCD. Reasons for the short tool lives can be the thermochemical wear and micro-chippings caused by the large amount of alloy elements and their carbides, but it has not been clarified yet. In this section, therefore, an experimental study on high-alloy steels using elliptical vibration cutting is carried out to clarify the alloy elements that affect the diamond tool wear and micro-chipping. (Saito et al. 2017)

Methods for experiments and evaluations. The experimental setup for the planing experiments is shown in Fig. 33. An ultraprecision machine tool (Fujikoshi, NANO ASPHER ASP01UPX) was equipped with an elliptical vibration cutting device (Taga Electric, EL-50Σ). A SCD tool whose nose radius is 1 mm was fixed on the vibration device, and vibration at a frequency of approximately 40 kHz and an amplitude of 4 μm_{p-p} was applied. Six kinds of high-alloy steels (Table 3) as well as the four kinds of pure metals (Table 4) were prepared as workpieces.

Among the high-alloy steels, DC53 is a cold work die steel made by Daido Steel, which corresponds to AISI D2 modified. It contains a large amount of chrome, i.e., 8.23 mass%, among the workpieces, and does not contain tungsten. The other five workpieces were chosen from high-speed tool steels. Various amounts of chrome,

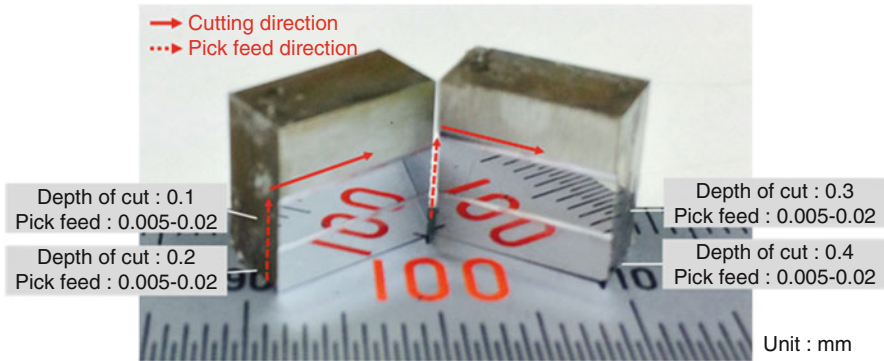
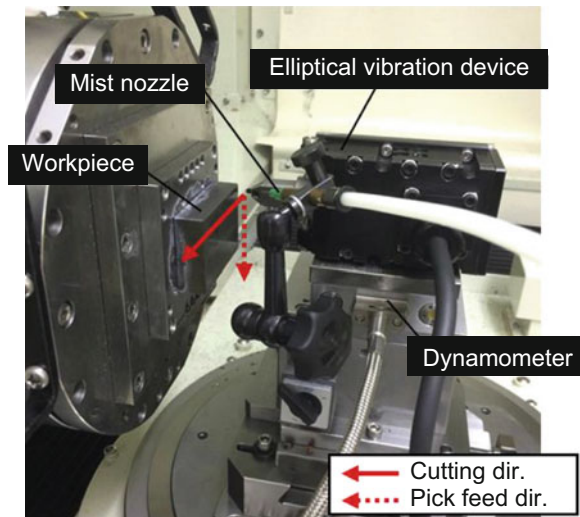


Fig. 32 Photograph of machined mirror surfaces

Fig. 33 Experimental setup for elliptical vibration cutting experiments. (Conditions) cutting tool, SCD tool; nose radius [mm], 1.0; depth of cut [μm], 10; pick feed [μm], 10; cutting speed [mm/min], 1000; coolant, oil mist (Bluebe LB-10); elliptical vibration frequency [kHz], about 40; amplitudes [μm_{p-p}], 4; phase shift [deg], 90 (circular locus)



vanadium, molybdenum, tungsten, and cobalt are added as alloy elements. Out of the workpieces, only ASP23 is a powder metallurgical high-speed tool steel made by Uddeholm, whose composition of alloy elements is similar to AISI M2. The hardness of the carbides as well as the matrix were measured by using the micro Vickers hardness tester to clarify the influence of the carbides on the micro-chipping. Since ASP23 is produced by the powder metallurgy process, the sizes of carbides are too small to measure their hardness. Hence the hardness tests are conducted on the five kinds of high-alloy steels except ASP23. In addition to the hardness tests, the size and the number of the carbide particles were also analyzed based on the metallographic photographs (see Fig. 34) as follows. Binary image processing was performed on the metallographic photographs to extract the carbides. Subsequently, the size of each carbide was calculated by using image processing software, and the

Table 3 Measured hardness of high-alloy steel workpiece and alloy elements

High-alloy steels			Alloy element, mass%						
Manufacturer's code	AISI code	Rockwell hardness, HRC	C	Mn	Cr	V	Mo	W	Co
DC53 (Daido steel)	D2 modified	62.2	0.98	0.52	8.23	0.22	1.99	–	0.01
YXR7 (Hitachi metals)	–	62.7	0.77	0.57	5.00	1.15	5.66	1.18	0.18
–	M2	63.9	0.89	0.34	4.39	2.00	5.08	6.02	0.23
ASP23 (Uddeholm)	M3-ii	63.1	1.27	0.30	4.29	3.13	5.15	6.13	0.38
–	T1	62.1	0.80	0.36	4.24	1.06	0.23	17.59	0.09
–	T5	65.2	0.80	0.23	4.06	1.03	0.61	18.47	10.88

Table 4 Pure metal workpieces and their hardness

Workpiece material	Hardness, HV
Cr (electroplating)	708
Mo (pure metal plate)	276
W (pure metal plate)	530
V (pure metal plate)	136

number of carbide particles was counted up. Moreover, mean particle sizes and particle-size distributions of the carbides in high-alloy steels were analyzed.

Four kinds of pure metals, i.e., chrome, molybdenum, tungsten, and vanadium, were machined. Hardness of the pure metals are summarized in Table 4. Cutting forces, surface roughness, and amounts of tool wear in machining of the pure metals are compared with those in machining of the high-alloy steels, and effects of the alloy elements on the diamond tool wear are discussed.

Figure 35a shows a SEM photograph of the cutting tool which machined the high-alloy steel of ASP23. Micro-chipping and wear can be observed on the cutting edge. There is a tendency that the micro-chipping mostly occurs on the top of the cutting edge where the finished surface is generated, while the wear mainly occurs in the feed directional side where the uncut chip thickness is large. Each type of tool damage was evaluated as follows. First, the micro-chipping was quantitatively evaluated by the binary image processing same as explained above (see Fig. 35b). Then, the total micro-chipping area was calculated by summing each micro-chipping area extracted from the binary image of the cutting edge. Next, the amount of wear was quantitatively evaluated by measuring the cross section perpendicular to the worn cutting edge. The cross section was measured by an optical surface profiler. Figure 35c shows a measured cross section of cutting edge, whose measurement point is indicated in Fig. 35a by a solid line. The solid line and the dashed line in Fig. 35c represent the measured cross section and the initial cross section estimated by the nominal rake angle and flank angle, respectively. The amount of tool wear is defined here by the hatched area surrounded by the solid line and the dashed line.

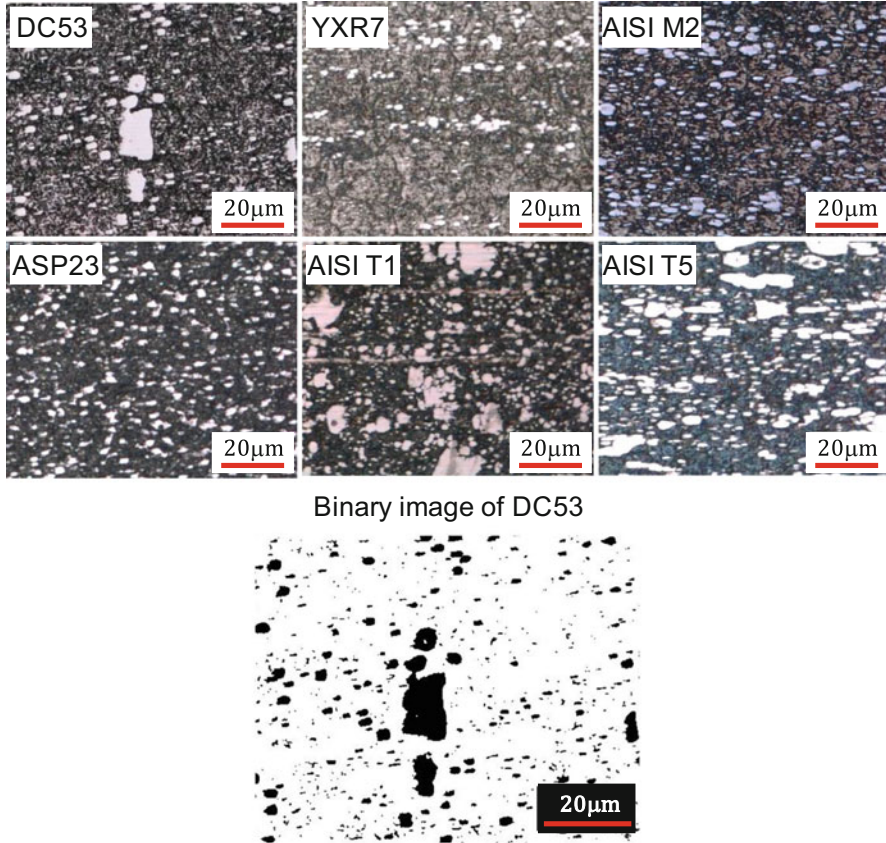


Fig. 34 Metallographic microscope images of high-alloy steels after Nital etching and binary image of metallographic photograph of DC53 (since particles are thought to be compounds, they remain as un-etched and appear white under the microscope)

Results and discussions. Figures 36a and b show the specific cutting forces measured during the planing experiments of the high-alloy steels. The specific cutting forces are calculated by dividing the measured cutting forces by the nominal pick feed and the actual depth of cut which is identified as follows. The planing was conducted on the middle area of each flat workpiece surface, and either end of the flat surface was left uncut. Then, profiles of the cut and uncut surfaces were measured in the feed direction, and the actual depth of cut is identified as step heights between the cut and uncut surfaces. This procedure can consider the decreased actual depth of cut because of the tool wear during the machining process, and it is possible to conduct precise comparison among the experimental results. As shown in Fig. 36b, the thrust forces on AISI T1, T5, and M2 were significantly increase which mainly corresponds to the progress of the tool wear. Figure 36c and d shows the specific cutting forces on the pure metals. Both force components acting on the vanadium were

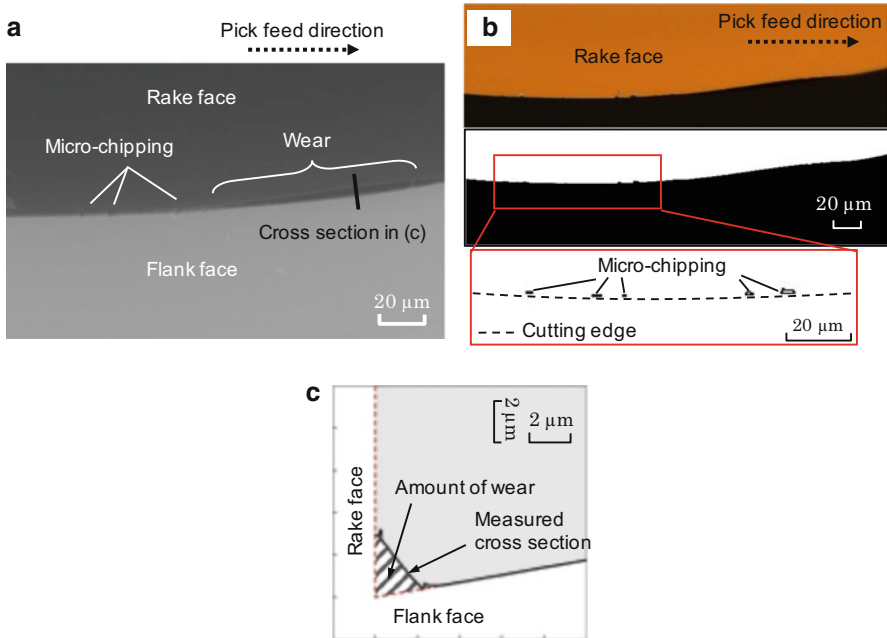


Fig. 35 Evaluation of tool damage. (a) SEM photograph of cutting edge after elliptical vibration cutting of ASP23 (b) Micro-chipping on cutting edge: (top) photomicrograph of cutting edge, (middle) binary image of photomicrograph, (bottom) extracted micro-chipping area (c) Definition of amount of wear based on measured

significantly increased to around 182,000 MPa. This corresponds to the largest cutting edge recession observed on the cutting tool which machined vanadium (see Fig. 39b). Because of the excessive tool wear, it is estimated that the rubbing or plowing process on the workpiece surface became dominant at the end. The increase in the cutting forces on the tungsten is the next largest to the vanadium.

Figure 37 shows the measured surface roughness R_t of the finished surfaces. The bar graph represents averages of 11 parts, and the error bars represent their maximum and minimum values. The surface roughness of high-alloy steels shown by the solid bars vary from 0.04 μm to 0.08 μm. The surface roughness of DC53 is the smallest, which corresponds to the small increase of less than 1100 MPa in the thrust force shown in Fig. 36b. The surface roughness of the pure metals are shown by hatched bars in Fig. 37. The surface roughness of the vanadium and the tungsten are excessively large, which corresponds to the large amounts of tool wear.

Figure 38a shows the Vickers hardness of carbides and matrices. The results indicate that the mean hardness value of carbides exceed 1260 HV, while that of the matrix ranges from 780 to 1050 HV. On the other hand, SCD is considered to have enough hardness to machine the hard carbides. However, their large difference in hardness is considered to cause the micro-chipping on the cutting edges, e.g., micro hard carbide particles existing in soft matrices can move and roll under the flank faces of cutting

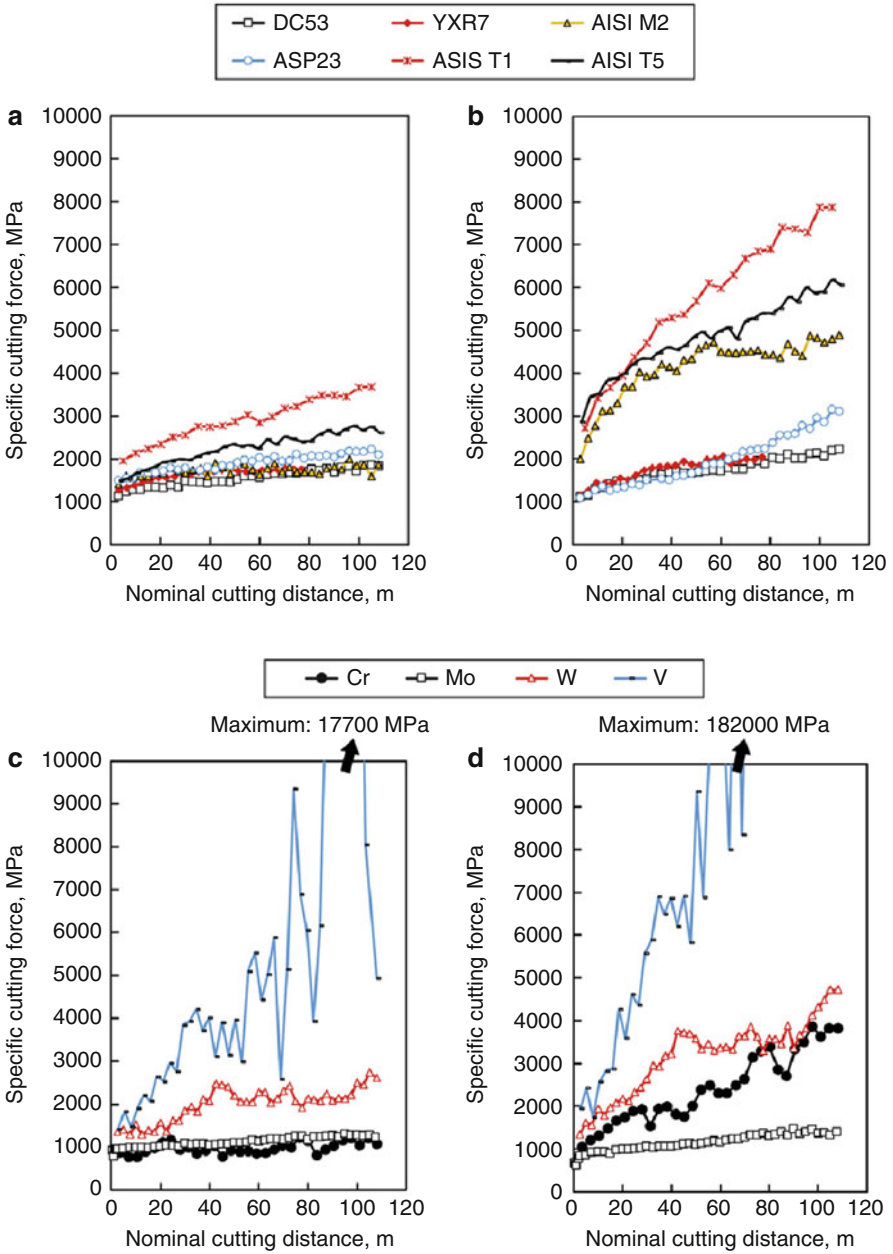


Fig. 36 Measured specific cutting forces. (a) Principal cutting forces of high-alloy steels (b) Thrust cutting forces of high-alloy steels (c) Principal cutting forces of pure metals (d) Thrust cutting forces of pure metals

Fig. 37 Surface roughness Rt of high-alloy steels (solid bars) and pure metals (hatched bars)

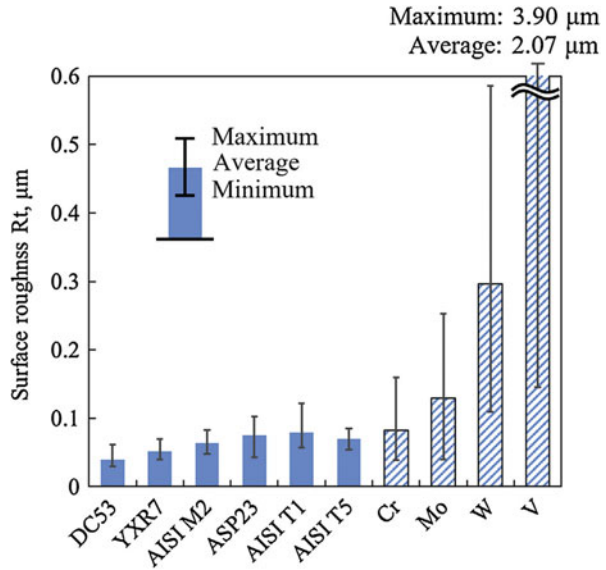


Fig. 38 Important factors which affect the micro-chipping. (a) Vickers hardness of carbides and matrices (b) Particle-size distributions of carbides in high-alloy steels

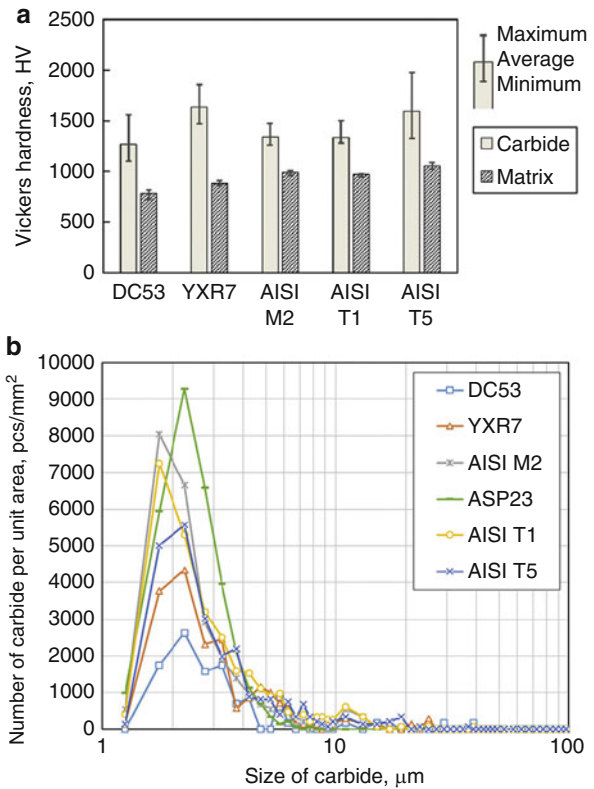
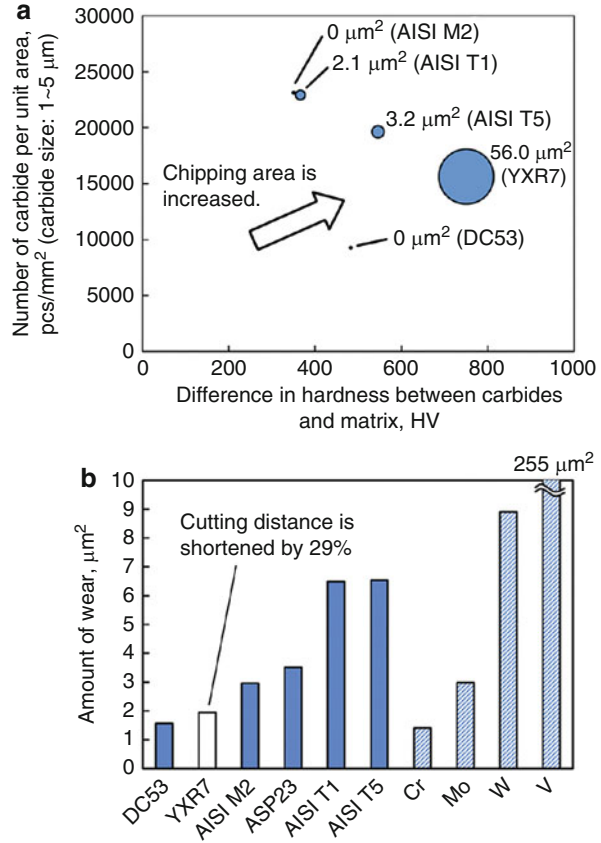


Fig. 39 Analysis and measurement results of tool damages **(a)** Amounts of chipping on cutting edge drawn in bubble chart **(b)** Amounts of wear after elliptical vibration cutting (solid bars, high-alloy steels; hatched bars, pure metals)



edges causing the micro-chipping. Thus, it is considered that the number of the micro hard carbide particles is also an important factor to decrease the micro-chipping. Figure 38b shows the particle-size distributions of the carbides. It is found from the particle-size distribution that the most frequent carbide particle size is around 2 μm in every high-alloy steel. The number of carbides becomes small with the increase of carbide size over 2 μm and finally less than 1000 pcs/mm² when the carbide size exceeds 5 μm .

The total micro-chipping areas calculated from the binarized images are plotted in Fig. 39a against the difference in hardness between carbides and matrices with the number of micro carbides ranging from 1 to 5 μm in length. The micro-chipping area is represented by the bubble size. As indicated in Fig. 39a by a white arrow, the micro-chipping is likely to occur as the number of micro carbides and the difference in hardness increase.

The amount of wear is shown in Fig. 39b. DC53 yields the smallest wear of 1.6 μm^2 among the high-alloy steels, while AISI T1 and T5 produce the largest wear of about 6.5 μm^2 . Among the pure metals, the chrome and the molybdenum yield small wear of less than 3 μm^2 , while the tungsten and the vanadium produce large

wear of 8.9 and 255 μm^2 , respectively. This indicates that tungsten and especially vanadium have a property to cause rapid wear of diamond tool.

The relationship between the amount of wear and each alloy element is shown in Fig. 40. The types of alloy elements are represented by atomic symbols. The result of tungsten is fitted by the least square method and shown by the dotted line, which indicates that the alloy element of tungsten has a high correlation with the diamond tool wear. A similar high correlation can be seen when the amount of tungsten is combined with that of vanadium, which is represented by "W + V." These results suggest that the alloy elements of tungsten as well as vanadium affect the amount of wear, which corresponds to the large increase in the specific cutting force in Fig. 36 and large surface roughness in Fig. 37.

Figure 41 shows X-ray diffraction patterns of high-alloy steels. The common peaks of $\text{Cr}_{0.03}\text{Fe}_{0.97}$ are detected in all steels, and five types of carbides, i.e., Cr_7C_3 , VC, MoC , Mo_2C , and $\text{Fe}_3\text{W}_3\text{C-Fe}_4\text{W}_2\text{C}$, are characterized. Cr_7C_3 is detected only in DC53 which contains 8.23 mass% of chrome and does not contain tungsten (the amounts of alloy elements are listed in Table 3). In contrast, the peaks of $\text{Fe}_3\text{W}_3\text{C-Fe}_4\text{W}_2\text{C}$ are detected in the high-alloy steels which contain tungsten. The peaks of MoC or Mo_2C appear in the high-alloy steels which contain more than 1 mass% of molybdenum. In the same manner, the peaks of VC appear when the alloy element of vanadium added to the steels is more than approximately 1.1 mass%. In the cases of AISI T1 and T5, they contain slightly lower vanadium of 1.06 and 1.03 mass%, respectively, and the peaks of VC were not detected.

Since much of the alloy elements are precipitated as carbides, it is considered that some of them exist in the matrix as alloys of iron, as Sato et al. (1959) reported. The alloy elements of tungsten and vanadium existing in matrices cause the rapid wear of diamond tools because of thermochemical interaction with diamond. For example, 18-4-1 high-speed tool steel (18% tungsten, 4% chrome, 1% vanadium), whose chemical composition is roughly the same as AISI T1 and T5, contains 6.2% of tungsten, 3.8% of chrome, and 0.8% of vanadium in the matrix, and 5-4-3 high-speed tool steel, whose chemical composition is roughly the same as AISI M2 and ASP23, contains 3.5% of tungsten, 3.5% of chrome, and 1.1% of vanadium in the matrix. The amount of tungsten in the matrix of 18-4-1 high-speed tool steel is nearly twice as much as that of 5-4-3 high-speed tool steel. The amount of wear in machining of AISI T1 and T5 is approximately twice as much as those in machining of AISI M2 and ASP23 (see Fig. 39b), which accords with the aforementioned amounts of tungsten in matrices. This accordance suggests that the alloy elements of tungsten and vanadium in the matrices of high-alloy steels have strong thermochemical interaction with diamond tools and thus causes the rapid tool wear.

The results obtained here are applied to practical mirror surface machining of high-alloy steel as a demonstration. DC53 with a hardness of 62.2 HRC is chosen as the workpiece material, since it has the best machinability in the tested high-alloy steels in terms of tool damage and finished surface. This is because DC53 contains smaller number of micro carbides, no tungsten, and a small amount of vanadium. Figure 42 shows the machined mirror surface whose roughness is Rt 0.05 μm . Widespread use of this cutting technology in die and mold industry is expected.

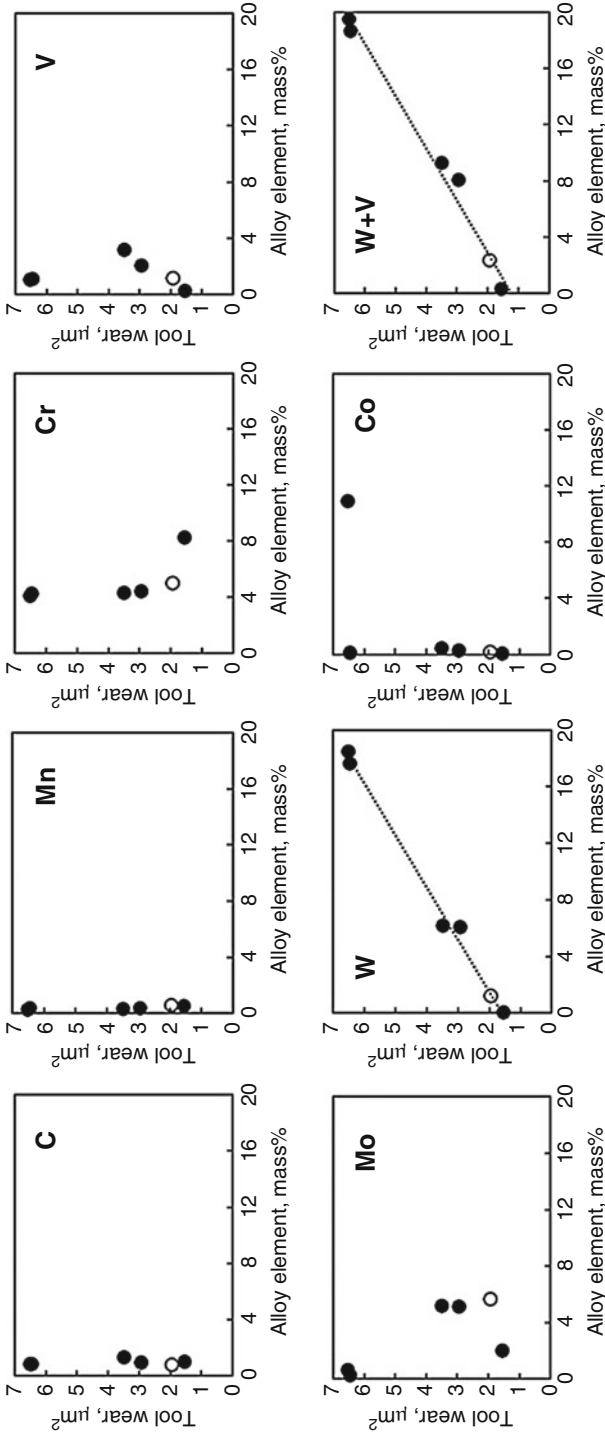


Fig. 40 Amounts of wear plotted against alloy elements. (The symbol “O” represents the results of YXR7, whose cutting distance is shorter by 29% than the standard cutting distance of 108 m)

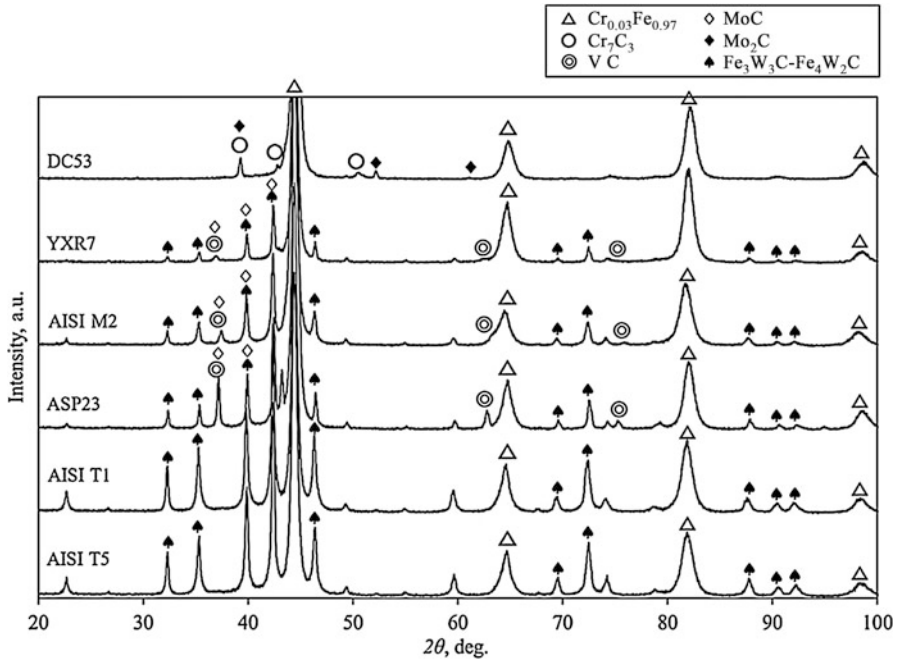
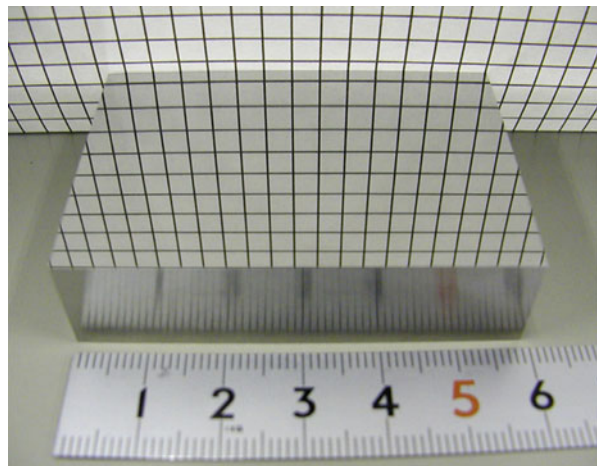


Fig. 41 X-ray diffraction patterns of high-alloy steels (X-ray diffraction analyses were performed by $\theta/2\theta$ method with a scan angle from 20 to 140 deg. However, obvious peaks are mainly observed at the angle less than 100 deg.; the results of the diffraction patterns are plotted against the angle from 20 to 100 deg. The symbols on the top of the peaks represent detected compounds whose chemical formulae are shown in the upper right)

Fig. 42 Photographs of mirror surface of DC53 finished by elliptical vibration cutting with single crystalline diamond tool



5.7 Summary

The elliptical vibration cutting is attracting more and more attention because of its superior machining performances, especially the advantageous in the ultraprecision machining of difficult-to-cut materials. This chapter described the elliptical vibration cutting from its proposal to recent researches and developments regarding the ultraprecision machining of difficult-to-cut materials. The principal mechanism of the elliptical vibration cutting, i.e., intermittent cutting process and chip pulling-up effect, was identified through the fundamental experiments as described in Sect. 2. The superior machining performances, i.e., long tool life, better surface roughness, low cutting force, etc., were also demonstrated through comparisons of the elliptical vibration cutting with the ordinary diamond cutting and conventional vibration cutting especially when the hardened steel is machined. To clarify the mechanics of the elliptical vibration cutting of difficult-to-cut materials, to expand its applications, and to demonstrate its performances, several follow-up studies were carried out as described in Sects. 4, 5, and 6.

Ductile mode machining of tungsten carbide was examined. Then, the machinability of tungsten carbide with the elliptical vibration cutting was also investigated to summarize appropriate conditions, e.g., cutting parameters, material parameters, etc., to efficiently apply the elliptical vibration cutting to tungsten carbide machining for good surface quality and long tool life. Moreover, based on the fundamental experiments, nanoscale sculpturing of a dimple pattern was successfully realized which cannot be obtained from other cutting methods.

To achieve the low-cost mirror surface finishing of hardened steel, the high-power elliptical vibration device was developed to realize the high-efficiency mirror surface finishing. Performance of the high-power elliptical vibration cutting was evaluated in terms of specific cutting force and finished surface quality. As a result, it was found that mirror-quality surfaces with roughness of $0.013 \mu\text{m Ra}$ or less can be obtained even at a relatively large depth of cut of 0.4 mm.

An experimental study on the elliptical vibration cutting of high-alloy steels whose Rockwell C hardness exceeds 60 HRC was carried out. The mechanism of the tool damage, i.e., tool wear and micro-chippings on cutting edge, was demonstrated from the mechanical and chemical viewpoints. As a result, appropriate composition of alloy elements for the high-alloy steel can be suggested in terms of tool damage and finished surface.

It is expected that the elliptical vibration cutting of difficult-to-cut materials summarized in this chapter will contribute to the improvement of machining accuracy and surface quality for various difficult-to-cut materials and realization of new products that require difficult machining processes.

References

- Brinksmeier E, Glabe R, Osmer J (2006) Ultra-precision diamond cutting of steel molds. *Ann CIRP* 55(1):551–554
- Casstevens JM (1983) Diamond turning of steel in carbon-saturated atmospheres. *Precis Eng* 5(1): 9–15

- Fang ZG, Eason JW (1995) Study of nanostructured WC–Co composites. *Int J Refract Met Hard Mater* 13:297–303
- Jung H, Shamoto E, Ueyama T, Hamada S, Xu L (2016) Mirror surface finishing of hardened die steel by high-power ultrasonic elliptical vibration cutting. *J Mach Eng* 16(1):5–14
- Kumabe J (1979) *Vibration cutting* (in Japanese). Jikkyou Publishing, Tokyo
- Mizutani Y, Itoigawa F, Shamoto E, Nakamura T (2016) Experimental investigation into suppression mechanism of diamond tool wear in ultrasonic vibration cutting of steel (in Japanese). Paper presented at 2016 JSPE autumn meeting, Ibaraki University, Ibarakai, 6–8 Sep 2016
- Saito H, Jung H, Shamoto E, Wu TC, Chien JT (2017) Mirror surface machining of high-alloy steels by elliptical vibration cutting with single-crystalline diamond tools: Influence of alloy elements on diamond tool damage. *Precis Eng* 49:200–210
- Sato T, Nishizawa T, Murai K (1959) On carbides in high-C high-V high speed steels (in Japanese). *Testu to Hagane* 45(5):511–516
- Shamoto E, Moriwaki T (1994) Study on elliptical vibration cutting. *Ann CIRP* 43(1):35–38
- Shamoto E, Moriwaki T (1999) Ultraprecision diamond cutting of hardened steel by applying elliptical vibration cutting. *Ann CIRP* 48(1):441–444
- Song YC, Nezu K, Park CH, Moriwaki T (2009) Tool wear control in single-crystal diamond cutting of steel by using the ultra-intermittent cutting method. *Int J Mach Tools Manuf* 49:339–343
- Suzuki N, Haritani M, Yang J, Hino R, Shamoto E (2007) Elliptical vibration cutting of tungsten alloy molds for optical glass parts. *Ann CIRP* 56(1):127–130
- Suzuki N, Yokoi H, Shamoto E (2011) Micro/nano sculpturing of hardened steel by controlling vibration amplitude in elliptical vibration cutting. *Precis Eng* 35:44–50
- Zhang J, Suzuki N, Wang Y, Shamoto E (2014) Fundamental investigation of ultra-precision ductile machining of tungsten carbide by applying elliptical vibration cutting with single crystal diamond. *J Mater Process Technol* 214:2644–2659
- Zong WJ, Li ZQ, Sun T, Li D, Cheng K (2010) Analysis for the wear resistance anisotropy of diamond cutting tools in theory and experiment. *J Mater Process Technol* 210:858–867



Micromachining of Roller Mold for Roll-to-Roll Manufacturing

6

Rui Huang, XinQuan Zhang, and Kui Liu

Contents

6.1	Introduction: Background	184
6.2	Micromachining of Gravure Roller Mold	186
6.2.1	R2R Gravure Printing of Flexible Electronics	186
6.2.2	Chemical Etching	188
6.2.3	Electromechanical Engraving	188
6.2.4	Laser Engraving	190
6.2.5	Diamond Micro-engraving	191
6.2.6	Scaling Down of Printed Line Width	192
6.3	Micromachining of Embossing Roller Mold	195
6.3.1	R2R Embossing of Functional Optical Film	195
6.3.2	Conventional Diamond Turning of Rotational Symmetric Feature	198
6.3.3	Rotating-Tool Diamond Turning of Non-rotational Symmetric Feature	199
6.3.4	Measurement of Micromachined Roller Mold	204
6.3.5	Characterization of R2R Embossed Optical Film	207
6.3.6	Performance Evaluation and Functionality Test	210
6.4	Summary and Outlook	212
	References	212

Abstract

The advent of roll-to-roll (R2R) manufacturing is a significant breakthrough as a high-throughput and low-cost technology for continuous fabrication of functional substrate film for various applications, especially for mass production of printed electronics and functional optical film. Structured roller mold utilized in R2R manufacturing is the essential component, which transfers the micro-feature or pattern from the mold onto the polymer film. It requires high-profile accuracy,

R. Huang · X. Zhang (✉) · K. Liu
Machining Technology Group, Singapore Institute of Manufacturing Technology,
Singapore, Singapore
e-mail: zhangxq@SIMTech.a-star.edu.sg

excellent surface quality, and consistent feature uniformity; hence it is usually fabricated by micromachining technologies. This chapter emphasizes on micromachining of roller mold for R2R manufacturing process, and fabrication technology of two major types of roller mold are mainly discussed: gravure roller mold and embossing roller mold. Recent advances in micromachining of these two types of roller mold is addressed, particularly on novel machining process invented for enhanced film performance and complex micro-features generation. Measurement and characterization of both the machined roller and R2R manufactured film are also discussed in detail.

Keywords

Micromachining · Roll-to-roll manufacturing · Diamond tool · Printing electronics · Functional optical film

6.1 Introduction: Background

Roll-to-roll (R2R) manufacturing has been proven to be a high-throughput and low-cost technology for continuous fabrication of functional substrate film for various applications. In particular, as a large area processing technology, R2R manufacturing has attracted a lot of attention in recent years, because it is able to print or create functional electronic devices or optical features on a roll of flexible plastic film or metal foil. Today, R2R manufacturing has already been applied in many industrial areas for production of flexible electronics, optical film, flexible solar panels, printed thin-film lighting, and printed thin-film battery. Among all the applications of R2R manufacturing, printed electronics and functional optical film can be categorized as the two most important industry fields which have the largest market.

Printing electronics has received significant attention because of its low manufacturing cost per unit area, light weight, and high flexibility compared to conventional silicon-based semiconductor electronics. It provides a better alternative to realize a wide range of flexible and costless electronic systems, such as radio-frequency identification tags, electronics labels, sensors, and transparent conductive films. Functional optical film includes brightness enhancement film for LCD display, hologram film for anti-counterfeiting and decoration, Fresnel lens film for concentrator photovoltaics, and micro-lens array film for naked-eye 3D display. Their application is becoming wider and wider, because it is technically difficult to use conventional injection molding technology to produce large-area optics with affordable cost.

To print fine-line circuits on flexible electronics or replicate high-accuracy optical features on thin film, both these two applications of R2R manufacturing usually require high-precision structured roller molds. To form the specified circuit or optical pattern on the film, the reversed pattern, which is usually in micro- or even nanoscale, has to be generated on the roller mold. Although

some technology like inline laser ablation is also able to create electronic circuits without using a patterned roller mold, its manufacturing efficiency in printing electronics is much less compared to others like R2R gravure printing. Most of the optical films are fabricated using a roller mold patterned with micro-optical features, except the hologram film which is comprised of nano-scale features. As it is difficult to directly generate such features on the periphery roller surface, a flexible metallic shim is patterned by replicating the nano-features from an original Si mold which is fabricated using lithography, and such plate is then wrapped onto a non-patterned roller to be used in R2R manufacturing process.

Micromachining refers to a machining process which removes microscopic volume of material from the workpiece, in order to achieve specified features with high geometrical accuracy. As the amount of material removed is small and the removal rate is slow, micromachining is mostly used to fabricate microstructures or micro-components. When the amount of material removed becomes even smaller and reaches nanoscale, nanomachining, particularly lithography or ion beam machining, has to be applied to realize the material removal process. Micromachining can be classified into physical, chemical, and mechanical processes (Brinksmeier and Preuss 2012). Different process has its own advantages and disadvantages, depending on the targeted engineering materials as well as the specified requirements on machining accuracy, quality, and efficiency. Generally speaking, physical micromachining process is dominated by laser beam machining; chemical process is dominated by electrochemical etching; and mechanical process is dominated by diamond cutting, micro-milling, and precision grinding.

Structured roller mold utilized in R2R manufacturing is usually comprised of an array of pattern like micro-gravure cells, prismatic elements, Fresnel lens, or micro-lens array. These microstructures are usually preferred to be directly machined on the roller mold, because the roller mold has less runout and better geometrical accuracy than the patterned metal sheet mold, leading to superior printing or embossing performance in terms of circuit consistency, mold life, and feature accuracy. Nowadays, most of the structured roller molds are fabricated by micromachining technologies, in order to realize deterministic material removal to generate the specified micro-features on the roller periphery surface.

This chapter aims to provide an insight on micromachining of roller mold used in R2R manufacturing process. Targeting two most important application fields, printed electronics and functional optical film, two types of roller mold fabrication technology are mainly discussed in this chapter: gravure roller mold and embossing roller mold. Several aspects are discussed, spanning from micromachining methods selection, machine tools, feature types, roller mold measurement, and functionality test. This chapter could help to justify the practical significance of the modern micromachining technology in the application of roller mold fabrication, through the understanding of its capability and limitation, working principles, as well as its extended abilities for complex feature generation.

6.2 Micromachining of Gravure Roller Mold

6.2.1 R2R Gravure Printing of Flexible Electronics

R2R gravure printing has been widely used in high-quality graphic printing (e.g., fine art, bank notes, magazines, postage stamps, and photography reproduction) due to its remarkable density range since the late of the nineteenth century. Color intensities of the printed feature are directly determined by the amount of ink transferred onto the substrates. Typically, the size of printed features of gravure printing is larger than 50 μm . Gravure printing of electronics employs a high-precision gravure roller mold to transfer conductive nanoparticle ink onto flexible substrates using engraved gravure cells on the roller, and the ink volume transferred onto the substrate is directly determined by the volume of engraved cells (Fig. 1). A doctor blade is tightly pressed on the gravure roller to wipe off excessive ink from non-patterned areas of the roller surface before they contact with the substrate. Depending on its cell volume, each cell will carry the particular amount of ink and place individual drops on the substrate after the gravure cell area contact with the impression roller. After the pattern is replicated from the gravure roller by transferring the liquid ink onto the film substrate, the ink is then dried and cured by heat to evaporate the solvent and exsiccate the patterned film. During this curing process, the conductive particles are bound together and tightly stick to the film substrate. Finally, the patterned film substrate is received by another motorized roller at the reeler. Compared to other technologies for printing of flexible electronics (screen printing, offset printing, and inject printing), gravure printing has the advantages of excellent pattern fidelity, homogeneous thickness of printed layer, high throughput due to high printing speed, and high printing resolution.

R2R gravure printing technique was firstly applied in 2005 to transfer conductive inks onto flexible substrates to form conductive lines on paper and plastic films (Pudas et al. 2005). Then, researchers have used R2R gravure printing to realize scale down the printed conductive line width (Sung et al. 2010) and also successfully applied gravure printing of electronics on different substrate materials like glass, which is more common but rigid (Hrehorova et al. 2011). Although miniaturization of cell size is not necessary in paper printing industry because it will exceed the capability of human vision with naked eyes, for printing of high-performance electronics, it has found that scaling down of the printed features is essential because smaller printed features will provide higher circuit density, higher transition frequency of transistors, and lower operating voltages (Kang et al. 2012). It has also been found that the printed line width is about 2–3 times larger than the gravure cell width, and scaling down of the gravure cell size is the most straightforward way to reduce the size of printed features. This will require a high-precision gravure cylinder with smaller cell size and consistent cell structure.

Gravure roller mold patterned with millions of gravure cells is the critical component of the entire R2R gravure printing process. When the printing parameters

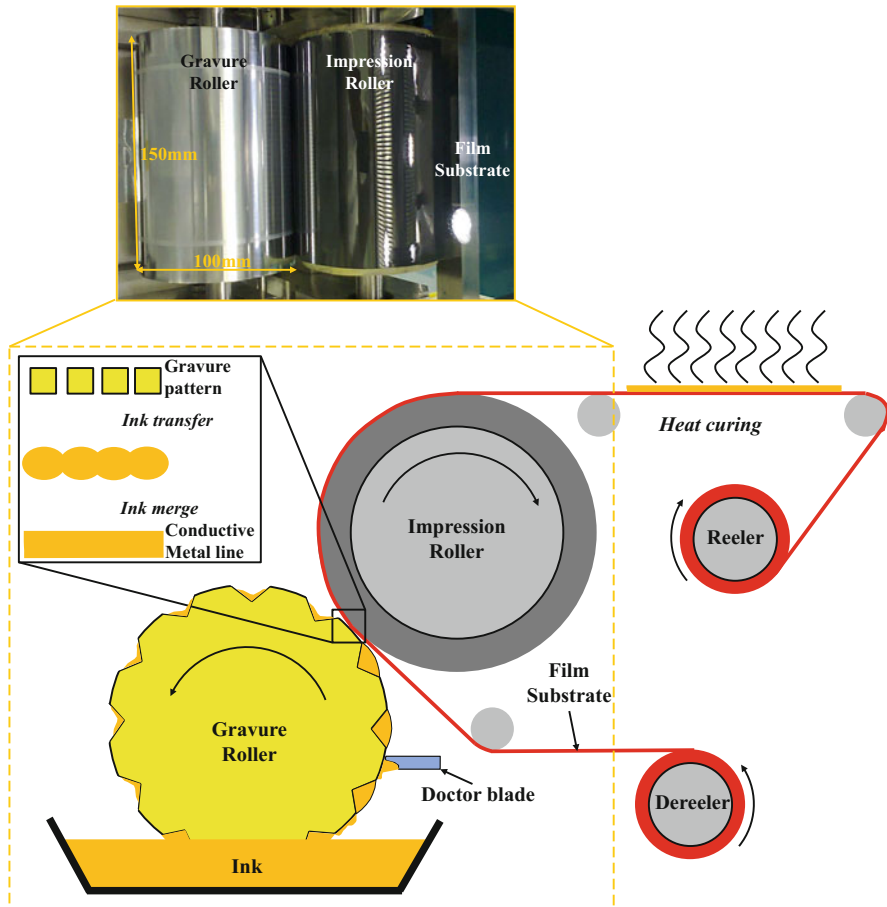


Fig. 1 Schematic process for gravure printing of electronics (Zhang et al. 2015)

are kept constant, the quality of the printed surface is mainly determined by the cells' dimensional accuracy and the surface quality. There are three major machining technologies that have been used in fabricating the gravure roller mold: (1) chemical etching, (2) electromechanical engraving, and (3) direct laser engraving. Each engraving method can produce various shapes and dimensions of gravure cells with different scales (Hrehorova and Kattumenu 2007). Among these three processes, chemical etching also applies laser ablation, but it has not been widely used in fabrication of high-precision gravure roller for printing electronics due to its relatively lower resolution and uncontrolled cell dimensions; electromechanical engraving realizes high level of repeatability and consistency of the cell sizes, while the laser engraving utilizes digital modulation which makes it much more convenient to fabricate cells with varying sizes.

6.2.2 Chemical Etching

Chemical etching has been a popular technique to fabricate gravure cylinders since late last century. The cylinder is first electroplated with copper before it is chemically etched. The roller is usually coated with chrome to enhance its robustness and lifespan after the etching process.

In a typical chemical etching process to prepare the gravure cylinder, a thin layer of photoresist is first coated on the surface of the cylinder, and then the mask containing small cells is positioned on the photoresist coating in direct contact. The masks can be prepared by crafting, electromechanical engraving, or electron beam lithography, depending on the sizes and accuracy requirement of the cells. The cylinder is put under light exposure coupled with ultraviolet light. The cylinder then is cleaned with water or water-based chemical; the unexposed material is rinsed away, leaving just a rigid, hard-edged resist. The cells after cleaning leave exposed inner metal where the resist is removed. After removing the photoresist, the cylinder is ready for the wet chemical etching process to remove the undesired metallic layer to form the featured roller, the type of etchant is mainly dependent on the work material, and mostly acidic or alkaline chemicals are used as the etchant in such processes. Lastly, the gravure cylinder is coated with chrome to improve its lifespan. Unfortunately, most metals are more or less isotopically etched (Lahti et al. 1999), resulting in difficulty of achieving size reduction and cell uniformity; this issue shall be taken into consideration at the beginning in the design phase.

Nevertheless, chemical etching process also has its advantage over electromechanically engraving that it is capable of making cells with larger aspect ratio. Sung et al. compared the electromechanically engraved cells to that made through chemical etching (Sung et al. 2010). It was found that later releases much more ink than chemically etched ones. In that study, though the cell width and printed dot width follow the same linear relationship, they have much larger thickness. This result is expected since the chemically etched cells have a larger aspect ratio, i.e., with comparable cell width, the depth of the cell is higher for chemically etched cylinder compared to the electromechanically engraved one, which results in a larger portion of ink being carried over with each cell. This technique is slowly being replaced nowadays by other techniques like laser or electromechanical engraving, due to various reasons like fabrication efficiency and cell dimension accuracy.

6.2.3 Electromechanical Engraving

Electromechanical engraving is the mostly widely utilized engraving method for fabricating gravure roller, because of its low processing cost and high product quality. This cutting process is conducted on a metal lathe, which is specially designed to shape holes into a cylindrical mold in a highly repeatable and accurate manner. When the cylinder rotates, an engraving diamond needle or stylus is driven to move back and forth at a very high frequency to form engraving cells with inverted pyramid shape. The tip is driven by electromagnetic oscillation,

characterized by a variety of parameters. This is the result of combining both extremely precise bearings and stable oscillation induction mechanism on the bed of the engraving head. The stability and robustness of entire engraving system guarantee the manufacturing of such cells on cylinders with large sizes and heavy weight. The engraving speed can reach up to 8000–20,000 cell per second. The vibration of the cutting stylus is coupled with a uniform rotational motion of the cylindrical mold to fabricate evenly distributed gravure cells. The cell width, depth, and volume are changed by applying different oscillation amplitudes and tool geometries.

The engraved cell eventually becomes a small inverted pyramid, which is very different from a chemically etched or laser machined cell, as shown in Fig. 2. Due to the absolute hardness difference between the stylus which is made of diamond or ceramics and the machined roller mold (brass in most cases), the surface quality and dimensional accuracy of the cells are usually better than those made by etching, which experiences etching rate with random directionality and results in non-uniformity. In addition, by varying the electromechanical engraver, it is capable of realizing a wide range of cell dimensions. The engraving depth can range from 10 μm to 50 μm , or even larger, creating engraved cells with width from 25 μm to 120 μm . Such cell size is smaller than conventional graphic art gravure printing cells, which ranges from 50 μm to 200 μm wide. The fabrication time for such rollers can range from minutes to days depending on the density of the cell sizes as well as the effective machined area on the roller periphery. Although it is technically possible for electromechanical engraving to create smaller engraved cells, it is difficult to make the small cells consistent and precise in geometrical dimensions.

The cell width engraved by electromechanical engraving refers to the side length of a square base of the pyramid, the aspect ratio, i.e., the ratio of cell depth to width is defined by the geometry of the engraving stylus. The transferred ink volume from one gravure cell machined using electromechanical engraving decreased drastically the size of the cells reduce. According to a study conducted by Kang et al., it shows

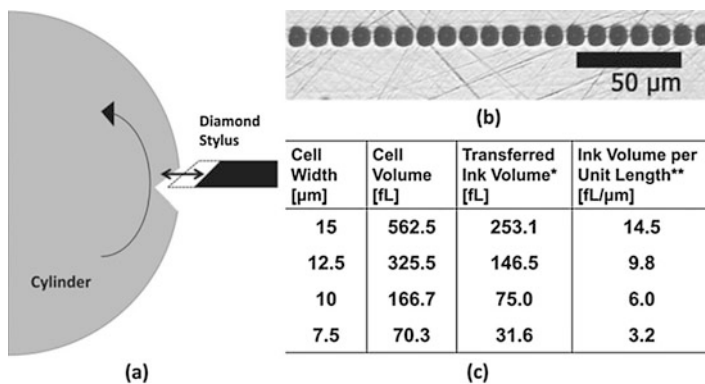


Fig. 2 (a) Section view of electromechanical engraving process, (b) cells machined, (c) calculated cell volume and transferred ink volume (Kang et al. 2012)

that such inverted pyramidal cells transfer higher ink volume as compared to that of the inkjet-printed droplet. As a result, this technique enables the gravure roller to vary the feature sizes drastically of printed features while maintaining high printing speed.

6.2.4 Laser Engraving

In laser engraving process, a laser beam is focused onto the gravure cylinder surface coated with a zinc layer to create cells. Each laser pulse creates one cell, and its cell width, depth, and volume are determined by beam size and energy of the pulse. The gravure roller mold is usually a steel cylinder electroplated with a homogeneous and even layer of copper or zinc. The pattern of gravure cell distribution together with the cell volume information is input to the control system of the laser engraving machine, and the machine will control the laser pulse according to varying rotational position of the cylinder. Figure 3 shows the schematic view of a laser engraving machine for fabrication of gravure roller mold.

Laser engraving is quite efficient due to the elimination of mechanical movement of cutting tool, and the laser beam pulse rate for engraving can reach 70 kHz or even higher, meaning that 70,000 cells can be produced in 1 s. The energy of the laser beam directly determines the volume of the engraved gravure cell, and the mean power during engraving could be 500 W or even higher. The interaction between laser and the copper or zinc material is a thermal-optical local ablation process caused by the laser pulse. The intensity profile and energy distribution of the laser beam will define the formed cell shape. Through applying Gaussian beam or top-hat laser beam, gravure cells with varying or constant diameter can be generated

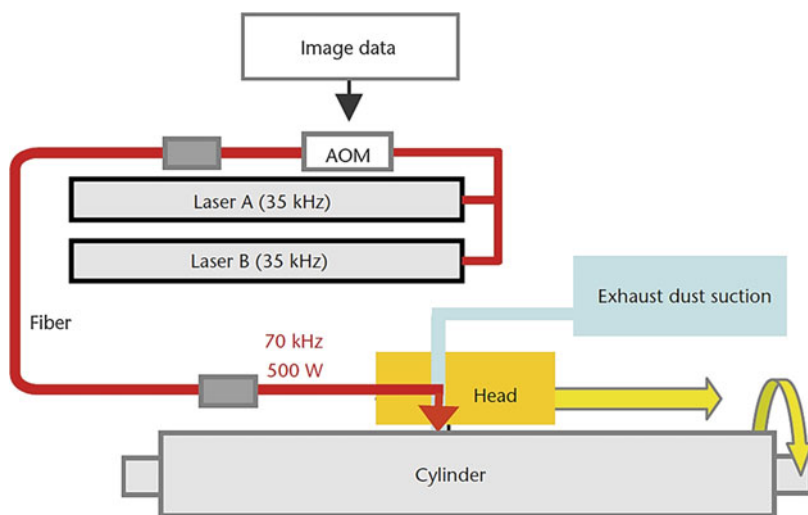


Fig. 3 Direct laser system for fabrication of gravure roller mold (Hennig et al. 2008)

accordingly for different applications. As the material is basically evaporated by the high-power laser beam, there will be a small area of heat affecting zone (2–3 μm) around each cell.

Compared to electromechanical engraving, laser engraving is a noncontact engraving process without using a geometrically defined cutting tool. There is no tool wear and minimum drifting of relative tool cylinder position, which lead to high uniformity of the engraved gravure pattern. The cell depth can range from 0 to 45 μm , but the smallest cell diameter starts from 25 μm and can reach 150 μm , due to the limitation of the smallest laser spot size. Figure 4 shows microscopic images of some laser engraved cells on a roller mold. A relatively large synthesized cell can be formed by overlapping several small cells to hold more ink. Moreover, the engraving efficiency of laser beam can be several times faster than electromechanical engraving, due to the much higher limit of pulse rate that laser can achieve. The electro-mechanical engraving rate is limited by the natural frequency of its corresponding mechanical structure, which is usually much lower than the laser pulse frequency.

6.2.5 Diamond Micro-engraving

A common limitation of the conventional three conventional engraving techniques is that the engraved cell size is usually larger or imprecise, due to the large spot size of laser beam, the inaccurate engraving machine system, and the material removing mechanism. More importantly, conventional engraving methods also suffer from nonuniform gravure pattern due to the lack of environmental temperature control, low positioning and repositioning accuracy, external and internal vibration, inconsistent etching rate, etc. Although this resulted micron-level inaccuracy of cell/pattern does not affect the performance in gravure printing of decorative papers or films, it could pose detrimental effects on the high-resolution electronics printing. For example, an abnormally large cell size may cause transferred ink spreading away and result in short circuit; and an unusually small cell size may cause unconnected electronic lines and result in open circuit. Although researchers (Kitsomboonloha et al. 2012) have recently applied photolithography to generate micro-gravure cells on a small area with the cell size down to 1 μm , it is not possible to apply such technique

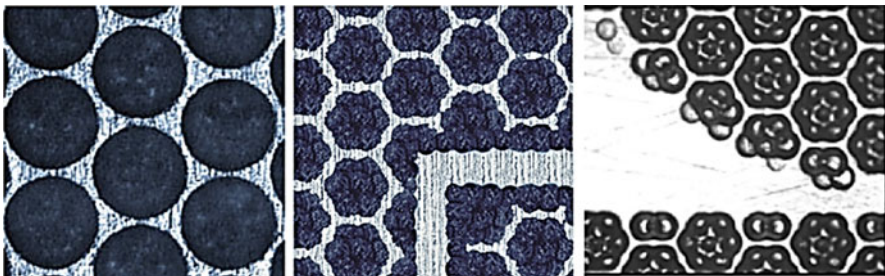


Fig. 4 Laser engraved gravure cells on roller mold (Hennig et al. 2008)

to generate a large-area gravure pattern on rollers because it is very costly and time consuming.

Ultraprecision machining is an advanced material removal technology, which was introduced for machining various optics-related components in the late of 1950s. In 1983, Donaldson and Patterson (1983) reported the completion of the world's most precise machining system, Large Optics Diamond Turning Machine (LODTM), which is constructed by Lawrence Livermore National Laboratory. An ultraprecision machining system could provide high axis motion accuracy, minimum drifting of tool-workpiece position, nanometer movement resolution, and accurate control of tool path and instantaneous tool position. Ultraprecision diamond machining has been widely used in generation of mirror-quality surface and submicron profile accuracy of workpieces made of many engineering materials through conventional machining processes such as turning, milling, or fly cutting. But machining of microstructures with discontinuous concave structure is not possible with such conventional processes, as they usually rely on rotation for generating the required cutting motion.

Relying on the ultraprecision machining technology, another method, Diamond Micro Engraving (DME), is developed to realize miniaturization of gravure cells on high-precision gravure roller molds for R2R printing of fine-line electronics. This process is realized using a V-shape sharp diamond tool with customized geometrical shape to continuously generate concave inverted pyramid structures on the roller surface using an ultraprecision machining system. Continuous engraving of the cell pattern is realized by rotating the roller to the required angular position with C -axis and positioning the tool with the linear axes of X and Z (see Fig. 5). The concave cell structure is designed to have a square-shape top surface with an equal cell width of w and a structure height of h . For obtaining such a structure, the bisecting line of the V-shape diamond tool should be set to be perpendicular to Z -axis, which is achieved by adjusting the B -axis assisted with an optical inspection system. Precise control of interactive movement of the tool and the roller using the slow slide servo technique ensures the structural consistency and the dimensional accuracy of the consecutive gravure cells.

By employing DME process, it is relatively easier to realize cell size miniaturization than the other conventional engraving techniques. Efforts were spent in miniaturizing the engraved gravure cells by reducing the engraving depth and meanwhile maintaining the consistence of cell structure and avoiding the burr formation. Figure 6 shows a series of gravure cells ranging from 32 μm to 3 μm which are machined by DME. It can be seen that the smallest gravure cells (3 μm cell width) are fabricated using Fast Tool Servo (FTS) system, due to the relatively higher tool motion speed and material removal rate. In contrast, the smallest cell size achieved by market-available laser engraved gravure rollers is 25 μm .

6.2.6 Scaling Down of Printed Line Width

One of the applications of R2R gravure printing of electronics is printing of metal mesh film. In recent years, due to the rapid growth of smartphones, tablets, and other electrical devices with touch panels, touch screen modules are obtaining wider and

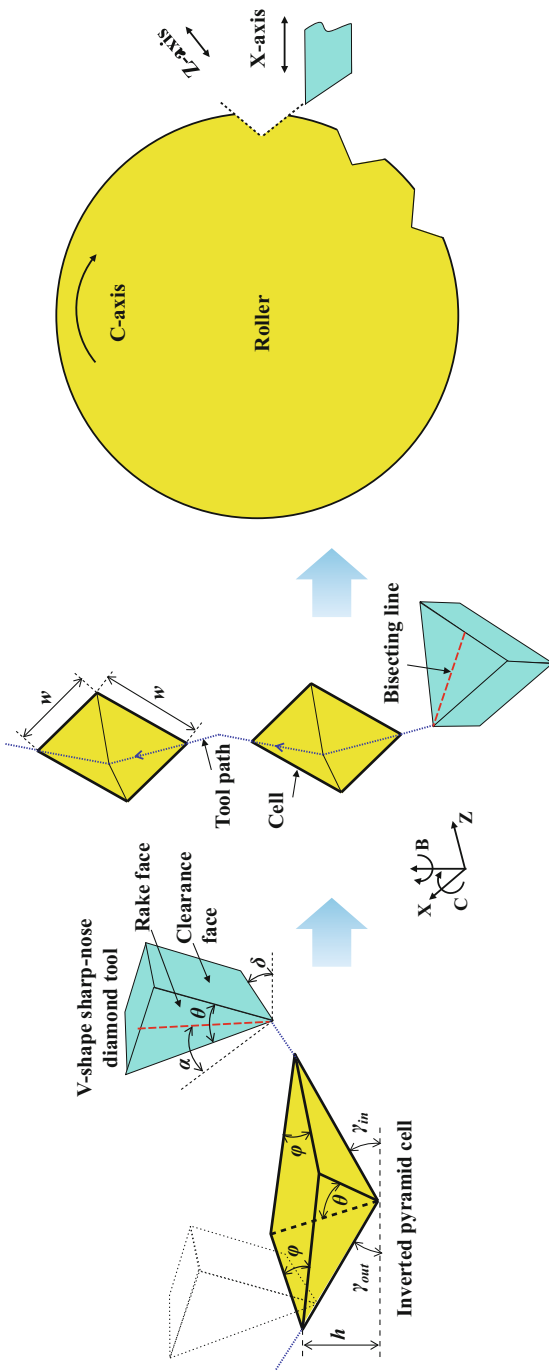


Fig. 5 DME process kinematics and relevant parameters for cutting concave inverted pyramid cells on a gravure roller mold (Zhang et al. 2015)

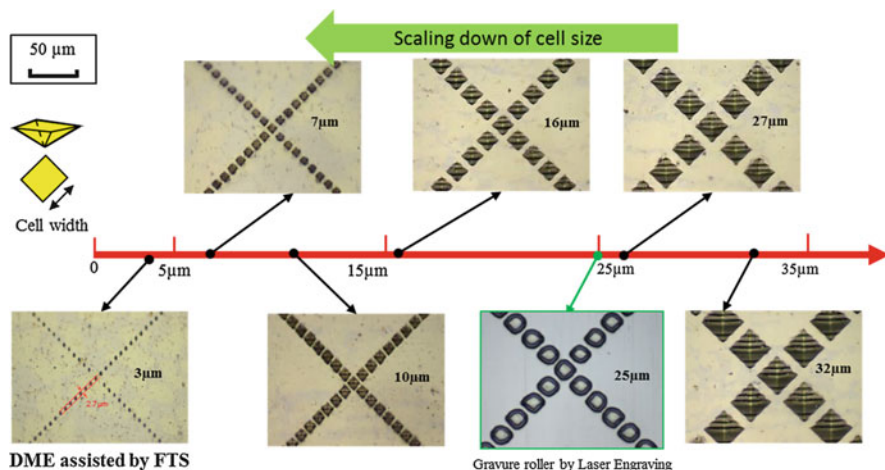


Fig. 6 Miniaturization of gravure cell size by DME (Zhang et al. 2015)

wider application around the world. Transparent conductive film (TCF) is a critical component in the touch screen modules, and until now, classic indium-tin-oxide (ITO) film is still the most widely used TCF in the industry. However, indium, as the film's primary metal, is a rare-earth material with limited reserves, and its price is getting higher and higher due to high market demand; researchers are continuously looking for the alternatives of ITO, such as transparent organic conductors, silver nanowire, carbon nanotube, grapheme, and metal mesh. But each of these alternatives has their own limitation which is difficult to overcome, and none of them has found successful practical industry application until now.

Metal mesh is a promising alternative which has high potential to replace ITO, as it provides sufficient transparency and low sheet resistance. To generate metal mesh on the flexible film, R2R gravure printing works as an effective, low-cost, and high-throughput technique to transfer the nanoparticle conductive ink onto the film and form conductive metal lines after the ink merges.

The gravure cell pattern will directly affect the ink volume transfer on to the printed electronic film. Cell spacing is a key parameter which determines the average ink volume transferred onto the film substrate per unit length and hence the quality of the printed metal lines. If too much ink is transferred on the film, the excess ink will overflow to the non-patterned area and cause smearing and stain on the film, which could not only reduce the transmittance of the printed film, but may also induce short circuit between adjacent metal lines. If too little ink is transferred, the continuous metal lines cannot be formed, and a large number of pinholes will be found on the printed lines. This could significantly increase resistance of the printed electronics and even produce open circuits. An optimized value of cell spacing should realize moderate amount of ink transfer, which spreads and connects properly to form uniform and continuous metal lines. Figure 7 shows a comparison between printed metal mesh with non-optimized and optimized cell spacing.

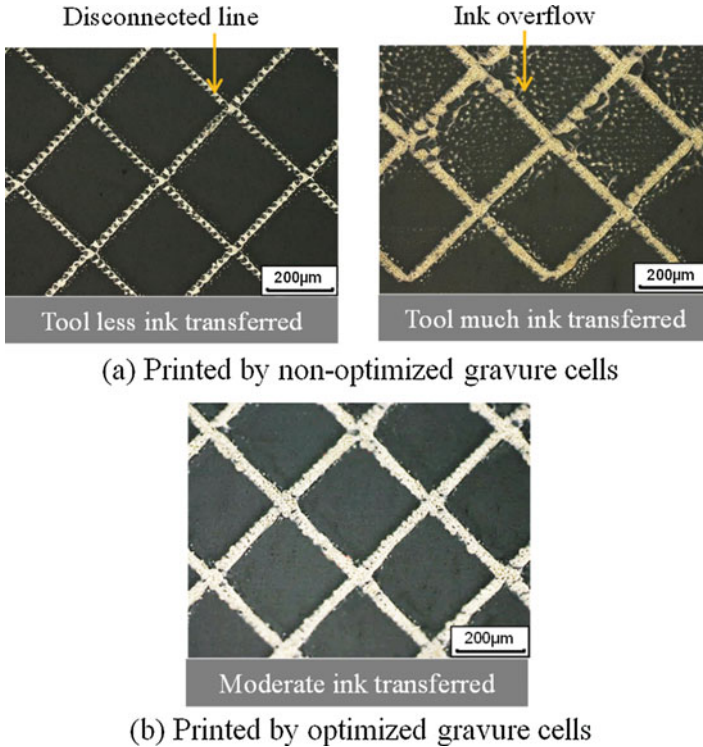


Fig. 7 Printed metal mesh by (a) non-optimized and (b) optimized gravure cell spacing (Zhang et al. 2015)

By reducing the grave cell size, the printed line width can be consistently reduced, as shown in Fig. 8a. Transmittance with respect to visible light is an important feature of transparent conductive film used in touch screen modules. Figure 8b has shown that the average transmittance of printed metal mesh film in the visible light region (390–700 nm) is increased from 65.2% to 80.4%, which is comparable to the transmittance of ITO transparent conductive film (typically $\geq 80\%$).

6.3 Micromachining of Embossing Roller Mold

6.3.1 R2R Embossing of Functional Optical Film

R2R embossing applies the continuous replication process in order to drastically increase the patterning speed and thus the throughput, and it provides an advanced solution for continuous manufacturing of various optical films. Hologram film was the first optical product of R2R embossing process, invented and developed by Stephen Benton and Michael Foster in 1974, and later found its first application in

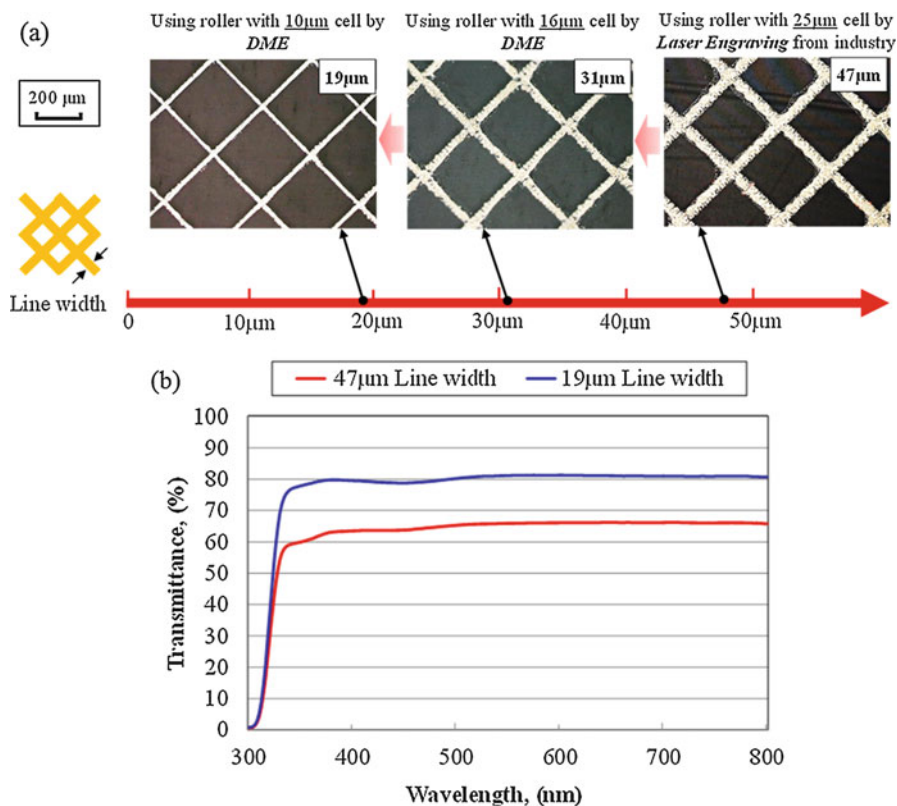


Fig. 8 (a) Scaling down of printed line width using gravure rollers machined by DME. (b) Improved transmittance of metal mesh films printed (Zhang et al. 2015)

bank card security at MasterCard International Inc (Watts and Solutions 2007). In 1997, 3 M filed a patent on the brightness enhancement film manufactured by R2R embossing, which has eventually grown into a market with a few billions US dollars (Allen et al. 2000). There are two types of R2R embossing process: (1) R2R hot embossing which directly structures 3D micropattern on the polymer film and (2) R2R ultraviolet (UV) embossing which structures the liquid resin coated on the film and then cures or solidifies it.

Figure 9 shows a R2R UV embossing system developed at Singapore Institute of Manufacturing Technology. The system is constituted of two main modules: a coating and embossing module and a web handling module. The coating and embossing module is located at the center of the machine and contains all the components required for the coating, embossing, and curing of photosensitive resin on the flexible film substrate through UV light exposure. The key components include a slot die coater, an embossing roller, and a UV lamp. The coating width of the slot die is 200 mm. The web handling module is located at two ends of the embossing system, to drive the flexible film substrate, control the web speed, and

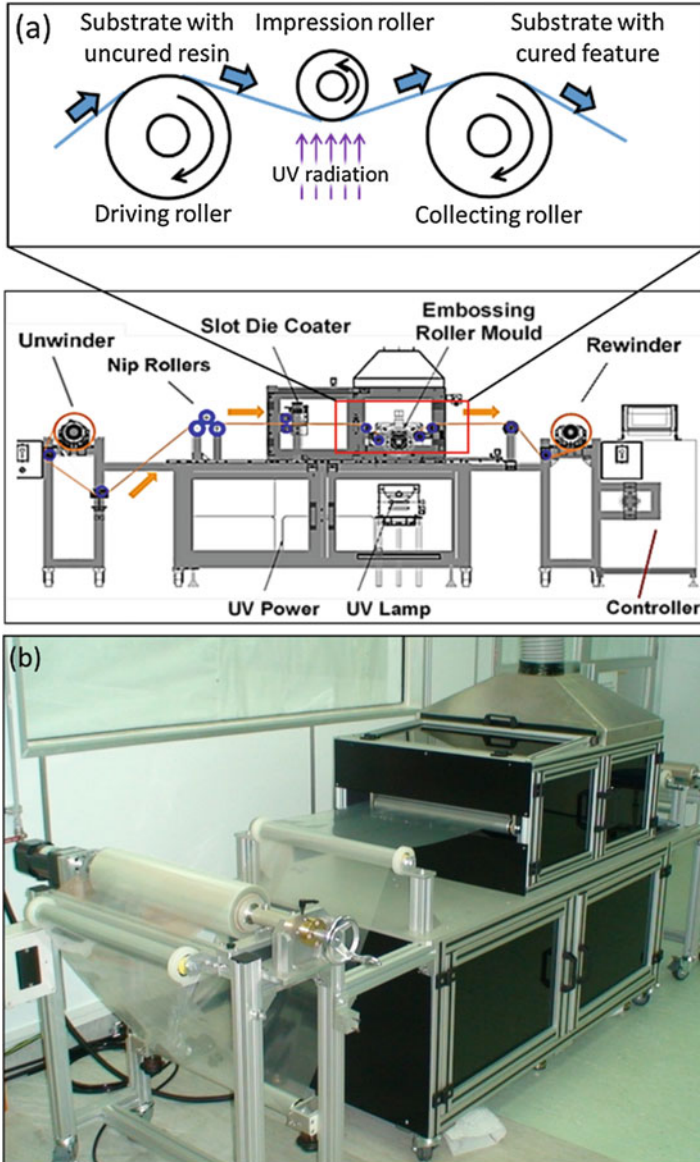


Fig. 9 Schematic and physical views of a roll-to-roll UV embossing system (Zhang et al. 2018)

provide tension to the film substrate in the coating and embossing processes. A raw polymer film roll is installed on a motorized roller at the de-reeler station, which feeds the film substrate into the coating and embossing module. Then the film substrate is evenly coated with a certain thickness of uncured resin using a slot die coater. After the coating, embossing, and curing processes, the film substrate consisting of

embossed micro-features is received by another motorized roller at the rewinder station.

The rotation speed of the embossing roller mold is set at 5 rev/min with the film feeding and the rewinding speed matched at 1.5 m/min. By employing the micro-machined roller mold, it can be calculated that R2R UV embossing (continuous manufacturing) can produce more than $15\times$ times optical lenses than injection molding, because the injection molding is a noncontinuous part-by-part manufacturing process, and a complete molding cycle is composed of filling, packing, cooling, ejection, and resting (typically ≥ 30 s production cycle time). In R2R embossing process, UV curing of the plastic lenses occurs simultaneously with the pattern replication, which hence enables continuous production with extremely high throughput. Due to the inexistence of complex filling and cooling modules in R2R process, it is also considered easier and more cost-effective to realize large-area embossing than multi-cavity injection molding. Hence, it can be derived that the production efficiency for R2R embossing is considered much higher than plastic injection molding in terms of Fresnel lens manufacturing, which could significantly save machine investment and production cost for industry.

Generally speaking, the roller molds applied in R2R embossing of optical films should be prepared by ultraprecision diamond machining. As the functional micro-structures on the optical films are directly replicated from the roller, the high-precision roller mold is required with strict profile accuracy control and optical surface quality which needs experience and know how to be fabricated in terms of tool trajectory optimization and tool-workpiece setting. There are mainly two types of optical features on the roller mold: (1) rotational symmetric feature, like prism pattern for embossing brightness enhancement film, linear Fresnel lens pattern, and micro-lens array pattern and (2) non-rotational symmetric feature, like radial Fresnel lens. Different micromachining technology needs to be employed for such two types of optical pattern on the roller mold, and they are discussed in the following two sections.

6.3.2 Conventional Diamond Turning of Rotational Symmetric Feature

Diamond turning is used primarily in the manufacturing of precision parts for advanced applications that call for high level of form accuracy and surface finishing. Such applications can be found in a number of industry sectors including aerospace, defense, electronics, semiconductor, and biomedical. It is well employed to machine symmetric features (spherical and aspheric feature) and nonsymmetric features (free form and lens array) on mold inserts for injection molding of polymer optical lens or directly on polymer lens for prototyping. On the other hand, diamond turning is also used to produce high-precision roller molds for R2R embossing of functional optical film. Figure 10 shows a drum roll being manufactured by an ultraprecision CNC horizontal drum lathe which is made by Moore Nanotechnology Systems.



Fig. 10 A roller mold installed on an ultraprecision CNC horizontal drum lathe (Zhang et al. 2014)

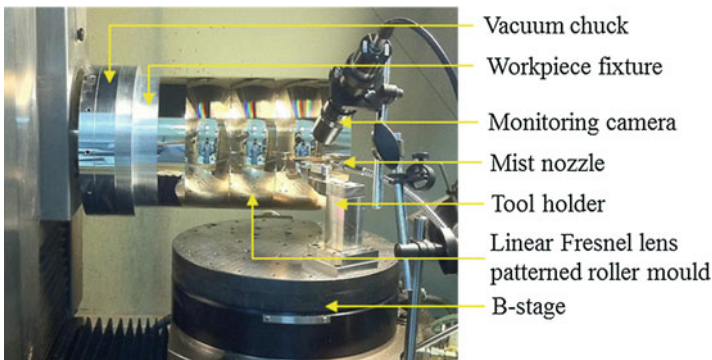


Fig. 11 Machined brass roller mold held on an ultraprecision machining system

Figure 11 shows a brass roller mold held on a five-axis ultraprecision machine system (Moore Nanotech 350FG) to generate the whole Fresnel lens profile on the roller mold. In machining of the linear Fresnel lenses on roller mold, the integral lens profile cannot be generated by one-off setting of the diamond tool, and hence the lens profile was divided into two sectional profiles.

6.3.3 Rotating-Tool Diamond Turning of Non-rotational Symmetric Feature

Compared to linear Fresnel lens, radial Fresnel lens is a more important optical component, with wider application in various fields, such as smartphone flash systems, LED lighting systems, and solar concentration systems. It has the advantages of being lighter, thinner, and easier to fit into complex and miniaturized optical

systems, compared to conventional spherical lenses. These are made possible due to its unique compact structure, where the conventional spherical profile is converted to a functionally equivalent series of concentric rings. It is able to realize similar optical function of conventional spherical and aspherical lenses such as light collimators and concentrators.

In particular, radial Fresnel lens is an essential optical component in concentrated photovoltaic (CPV) systems. Conventional solar power system still suffers the low efficiency due to the utilization of low-cost silicon-based solar cells. Multi-junction solar cells have much higher conversion efficiency (>40%) compared to conventional ones (<20%), but it also suffers from high unit area cost, which significantly limits its wide application for civil use. To overcome the drawback of such high-efficiency cells, concentrated photovoltaic (CPV) systems use polymer Fresnel lens array to collect the sunlight and focus the light onto multi-junction cells, which have a much smaller receiving area compared with that of Fresnel lenses (Xie et al. 2011). By applying the CPV systems, electric energy can be produced more economically and efficiently than conventional solar power systems with the enhanced energy conversion efficiency of solar cells. In the modern industry, the mostly widely utilized approach to mass produce optical Fresnel lenses is still injection molding. Although the unit piece cost for injection molding is already considered small, its unit area cost is still considered high, particularly when it is applied in large-size solar panels. A typical solar plant usually has an area of several square kilometers, which will require tens of billions Fresnel lenses to cover the same area for solar concentration. Hence, the cost of installed optical Fresnel lens components would play a significant portion in the entire CPV system. R2R embossing is an advanced continuous manufacturing method which is able to produce large-area high-quality micro-/nano-surface structures on flexible polymer film substrate at significantly lower cost and higher throughput compared to traditional molding processes, but it requires a high-precision metal roller mold patterned with functional microstructures.

Conventional diamond turning is good at micromachining of rotational symmetric optical features on the roller mold, but it cannot machine some non-rotational symmetric feature, like radial Fresnel lens, on the roller peripheral surface, due to its incapability to cut steep circular grooves on the outer cylindrical surface using conventional approach caused by the fixed tool orientation relative to the roller, as shown in Fig. 12a. To apply R2R embossing in mass production of radial Fresnel lens film, the industry has adopted an alternative method by replicating the radial Fresnel lens structures from a flat mold plate onto a flexible electroplated metal sheet, which is then wrapped onto the outer cylindrical surface to form a structured roller mold. However, such plating and wrapping processes will introduce additional replication and assembly errors and deteriorate the profile accuracy as well as the surface finish. This will eventually affect optical performance of the embossed Fresnel film and significantly limit its industry application.

Rotating-tool diamond turning (RDT) was developed to solve the problem above (Huang et al. 2015). A four-axis synchronized tool-workpiece motion is designed to realize precise machining of the optical feature containing steep circular grooves on

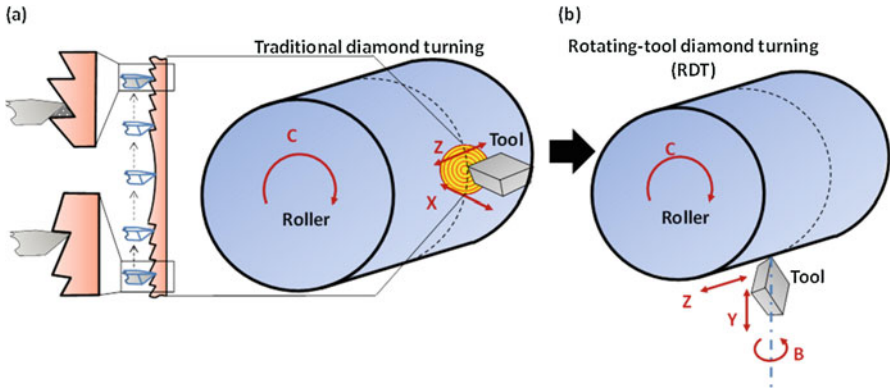


Fig. 12 (a) Incapability to machine radial Fresnel lens on a roller using traditional diamond turning method. (b) RDT method enables the continuous and synchronized variation of the tool orientation (Huang et al. 2017)

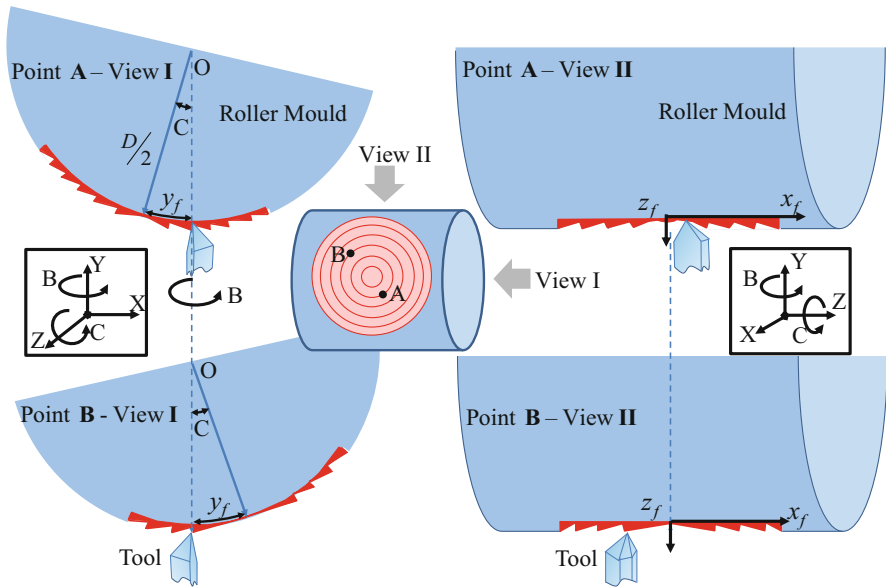


Fig. 13 Schematic illustration of tool-workpiece relative positions at two typical cutting points (Huang et al. 2015)

the outer cylindrical surface, as shown in Fig. 12b. A turning motion is imitated by this RDT process to cut the circular grooves on the outer cylindrical surface without causing any tool-workpiece interference during machining.

The tool path for RDT can be expressed in terms of the machine coordinates, as shown in Eq. 1. Figure 13 illustrates the geometrical relationship of the tool-workpiece relative positions at two arbitrary points during the RDT process. In the machining

process, C- and Z-axes are programmed to perform a resultant rotary motion between the roller surface and the tool tip, thus to enable the imitated turning operation. Continuous B-axis rotation is synchronized to the swing motion of the roller (C-axis) to ensure a constant cutting angle between the tool and the roller surface. Lastly, the depth of cut in the machining process is realized by the Y-axis movement.

$$\begin{cases} X = 0 \\ Y = -f(r_f) \\ Z = r_f \cdot \cos \theta_f \\ B = \theta_f \\ C = \frac{360^\circ \cdot r_f \cdot \sin \theta_f}{\pi \cdot D} \end{cases} \quad (1)$$

where X , Y , and Z represent the machine's three linear coordinate positions and C and B represent coordinate positions of the two rotary axes, where the roller and the tool are held, respectively. Y is a function of r_f , that is dependent on the cross-sectional profile of the Fresnel lens, where r_f is the radius of the radial Fresnel lens, D is the roller diameter, and θ_f is the angular displacement of the corresponding r_f . The tool path can therefore be generated with given lens and mold specifications using the coordinates derived from Eq. 1.

The feasibility of RDT process was firstly demonstrated using a small Fresnel lens ($\Phi 10$ mm) machined on a roller, and the surface quality and profile accuracy have been found acceptable for R2R embossing of optical film. But this process is a very slow machining process, because it needs to synchronize the four-axis tool-workpiece motion: (1) linear motion of Y-axis, (2) sinusoidal linear motion of Z-axis, (3) continuous rotation of B-axis, and (4) sinusoidal swing motion of C-axis. Such complex multiaxis movement makes the imitated turning motion speed of RDT (<90 RPM) much smaller than the spindle rotational speed in conventional diamond turning (a few thousand RPM).

To speed up the RDT process, the machining parameters including arc length and lens radius have been further investigated to get the optimized machining conditions to balance the surface quality and machining efficiency. Figure 14 shows the surface quality results under different machining conditions (arc length and ring radius). Trapezium-shape ring groove shape, instead of the entire Fresnel lens, is designed and machined on the roller periphery surface to investigate the surface quality of rings, to minimize the machining time for investigating the effect of various cutting parameters. From Fig. 14d, a significant increase of surface roughness can be observed on the 90° direction when the arc length is increased to $16 \mu\text{m}$. This could be caused by the increased synchronization error due to the sparse controlling points in SSS-driven tool path, when the arc length is too large. From Fig. 14e, surface roughness at all the three directions becomes significantly larger when the radius of ring groove reaches 20 mm, which could be caused by chattering and increased synchronization errors at a larger ring diameter. It can also be seen, for all the cutting conditions, the surface roughness at 0° direction is consistently less than the other two directions (45° and 90°), which can be caused by the more

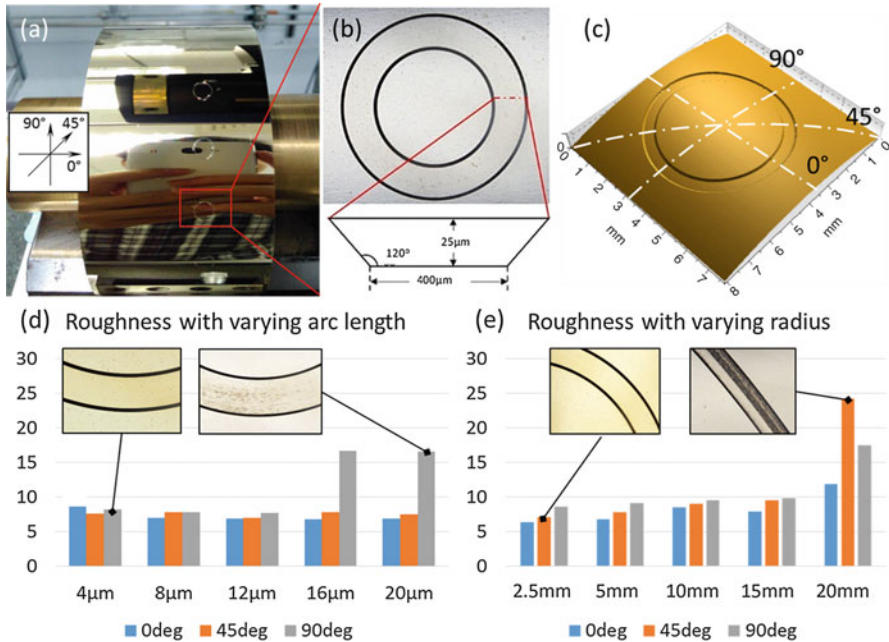


Fig. 14 (a) Ring grooves machined on roller mold, (b) specifications of the ring groove, (c) 3D profile measured by a stylus profilometer, (d) plot of roughness with varying arc length (10 mm ring diameter), (e) plot of roughness with varying radius (12 μm arc length) (Zhang et al. 2018)

involvement of acceleration and deceleration of C-axis when the relative tool cutting motion reaches 45° and 90° positions.

After identifying the maximum allowable arc length and lens diameter by testing with simplified ring grooves to balance surface quality and machining efficiency, the feasibility for fabricating a roller mold patterned with Fresnel lens arrays is studied for the utilization in practical R2R embossing. A set of linear (2×) and radial (6×) Fresnel lens arrays is designed to be directly machined on the roller periphery surface. The radial Fresnel lens array is to be machined utilizing the RDT process, and for comparison, the linear Fresnel lens array with the identical lens geometry is designed and machined using conventional diamond turning process. The six radial lenses are positioned in even distribution with an angular displacement of 60° to each other, and both types of lenses have identical section profiles with the same designed focal distance. Figure 15a and b shows the different machining setup for the radial and linear Fresnel lens array on roller mold, respectively. Figure 15c shows the Fresnel lens surfaces before and after the diamond-like carbon (DLC) coating, which clearly reflects the “SIMTech” logo from a paper. The protective DLC coating is conducted in a physical vapor deposition (PVD) system with a thickness of 300 nm, in order to increase the surface hardness and extend the mold lifespan without affecting the accuracy of the Fresnel lens profile. The DLC coating will also reduce the friction coefficient of the roller surface, which will further improve the

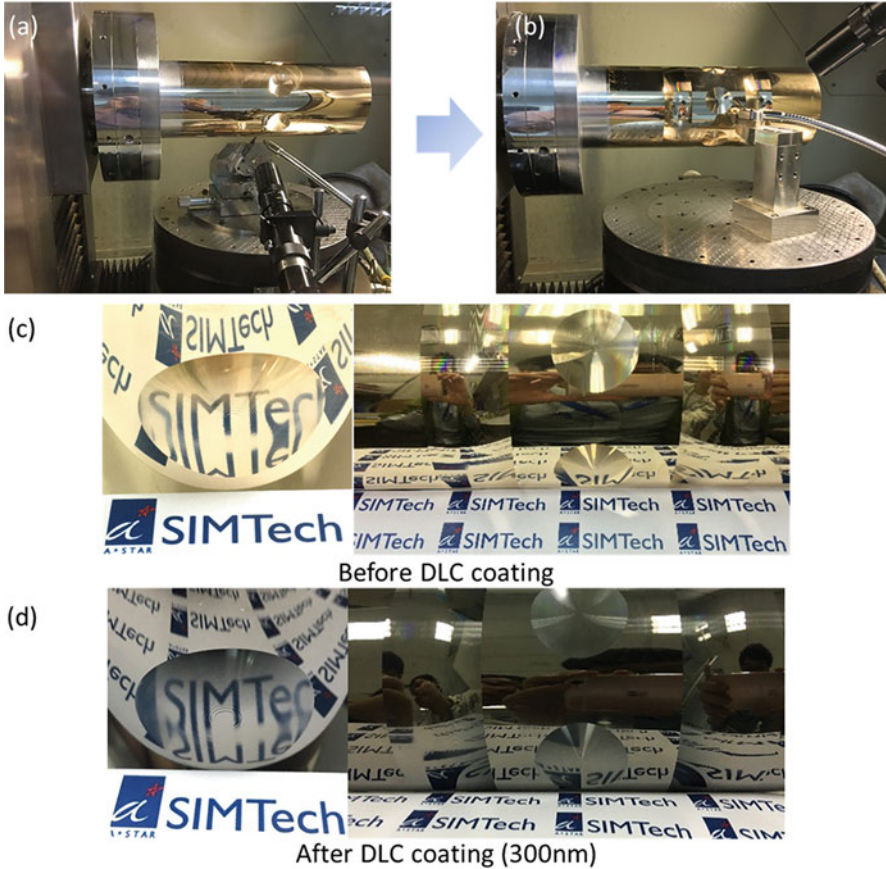


Fig. 15 (a) Machined radial Fresnel lens, (b) machined linear Fresnel lens, (c) roller mold before and (d) after DLC coating (Zhang et al. 2018)

resins' demolding capability to avoid the stagnation of resin at the micro-corners of the Fresnel lens rings during R2R embossing process.

6.3.4 Measurement of Micromachined Roller Mold

For the rotational symmetric feature generated on the roller mold, it is easy to measure the section profile and evaluate its profile accuracy by using a stylus profilometer, and the profile can be compared with the designed one point-to-point precisely. Figure 16 shows the measurement setup and results for the machined linear Fresnel lenses on the metal roller mold (see Fig. 11) using a stylus profilometer. The roller mold was located on a linear and rotary stage, which can realize fine adjustment of the roller position using micrometer. Pre-alignment was conducted to ensure that the roller axis is parallel with the horizontal movement of the stylus head, and the stylus was located at the highest

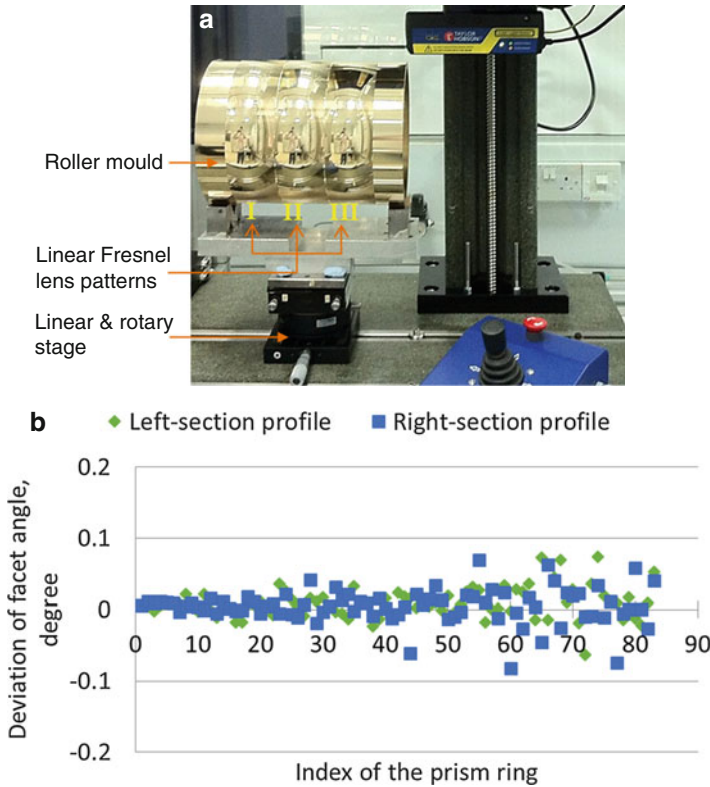


Fig. 16 (a) Close view of the measurement setup. (b) Deviation of measured facet angles on the roller mold from the designed ones

position of the roller. Facet angles play a critical role in the profile of a Fresnel lens, and its angular accuracy for the machined roller mold will directly determine the quality of R2R embossed linear Fresnel lens film and accordingly the capability of light concentration and optical efficiency. By filtering the incorrect profile data caused when measuring the draft faces, the deviation of measured facet angles from the designed ones for each prism ring can be calculated, as shown in Fig. 16b. It can be observed that 93% of the deviation errors fall in the limit of $\pm 0.05^\circ$, and it can also be observed that the deviation error becomes relatively larger when the index of prism ring increases. Such increased deviation should be caused by the more significant arcing motion that occurs when the profilometer stylus vertically swings more sharply during scanning a steeper profile and the decreased ring width which leads to less data points calculated.

For the non-rotational symmetric features, like radial Fresnel lens, there is a lack of existing method to evaluate the quality of machined 3D lens profile in terms of form accuracy. Traditional free-form lens profile on a flat mold is usually evaluated by on-machine measurement methods followed by a feature-matching algorithm, to minimize the inevitable missing of reference coordinates during the off-machine measurement. Unfortunately, on-machine measurement cannot be used due to the

feature of deep circular grooves as discussed in the first section. Therefore, a compensation and comparison algorithm is essential to analyze the machined feature from both the measured 3D profile and its spatial orientation during the measurement to compensate for the alignment errors.

There are inevitable sources of errors present during the off-machine measurement of non-rotational symmetric optical feature on roller mold using the stylus profilometer. For instance, as the stylus tip usually has a tip radius and an included angle which cannot be neglected, it is difficult to precisely measure the steep sites and the very deep end of sharp corners due to the physical constrain. Moreover, misalignment between the workpiece and the measurement coordinates is a major source of errors when evaluating complex optical features with submicron-level accuracy. In particular, optical feature on cylindrical periphery is more difficult to be aligned with the measurement system because of the non-flat base substrate and the inclusion of two additional rotary axes. As no market-available measurement software has the capability to identify the error source and conduct the compensation of the optical features curled on the roller mold, a small alignment error may result in a large deviation when evaluating the form accuracy of the machined feature. Figure 17 shows the three rotational alignment errors R_x , R_y , and R_z errors of the roller mold around the X-, Y-, and Z- axis, respectively. All the three sources of error are represented as an angular displacement from its reference axis. R_x and R_y are defined as the angular differences between the roller axis from the XZ plane and YZ plane of the profilometer stage, respectively, while R_z describes the angular difference of the vector from the roller axis to the center of the radial Fresnel lens feature against the Y-direction of the profilometer stage.

The developed conversion and comparison algorithm is used to evaluate a directly machined radial Fresnel lens on a roller mold, which cannot be precisely evaluated by existing technique. A radial Fresnel lens ($\Phi 10$ mm) is first measured using a stylus profilometer with a scanning area of 12×12 mm². A linear resolution of 10 μ m along both X and Z direction is selected to be the resolution of the lens profile; smaller resolution will improve the characterization accuracy at the cost of long measurement time. Manual alignment of the roller against the profilometer was conducted by an experienced metrologist using a rotary and linear stage, in an attempt to minimize the misalignment errors. By analyzing the obtained data points

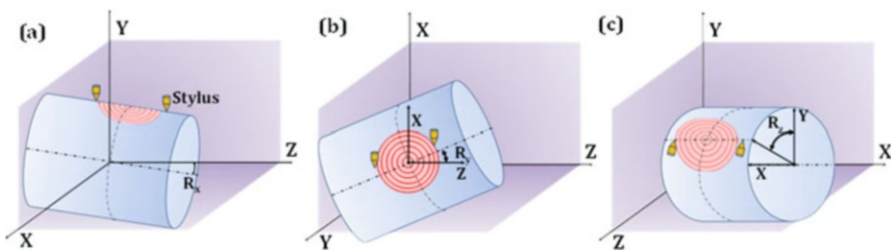


Fig. 17 Rotational misalignment errors in measuring radial Fresnel lens feature on roller mold using a stylus profilometer (a) R_x , (b) R_y , and (c) R_z (Huang et al. 2017)

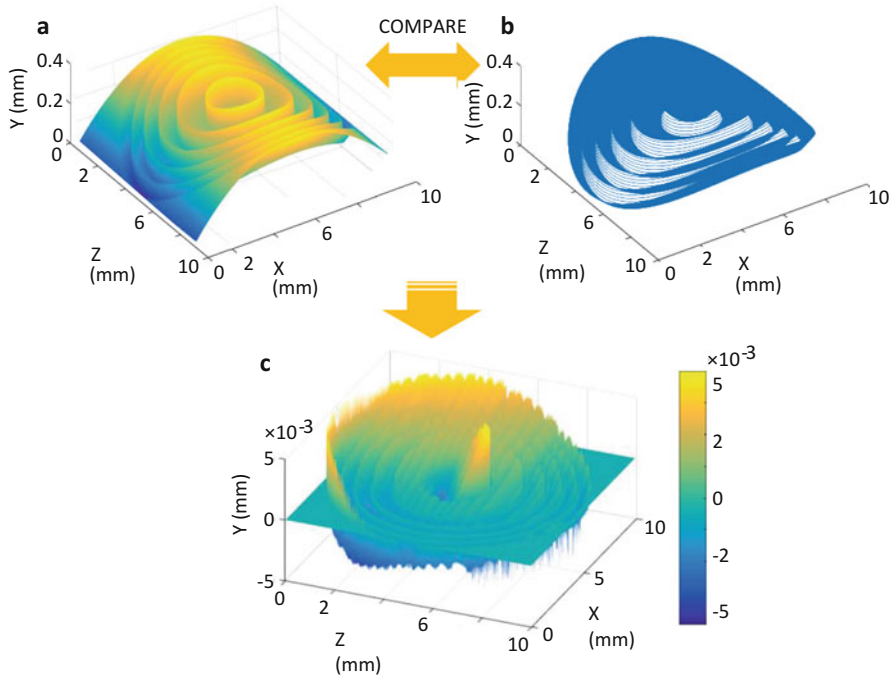


Fig. 18 (a) Measured profile with R_x and R_y compensated. (b) Theoretical profile with R_z introduced. (c) Error distribution profile of the Fresnel lens (Huang et al. 2017)

cloud from the 3D measurement, the three rotational misalignment errors, R_x , R_y , and R_z are identified sequentially, which should not be neglected during precise evaluation of 3D optical profile. By applying the compensation algorithm, the measured profile are restored with R_x and R_y compensated, while the modified theoretical profile is obtained by introducing the rotational error R_z . Lastly, by superimposing the restored profile and the modified theoretical profile, the error distribution profile is obtained from the contraction of the corresponding feature height of each point, as shown in Fig. 18. With the aid of the resultant matrix plotted, it can be observed that the profile error is found to be within $\pm 5 \mu\text{m}$ across the entire Fresnel lens. A clear trend of the error can be observed along the Z direction on the plot, which is the roller axial direction; this error can be caused by the natural deflection of the roller mold, due to its long shape from the hinged point at the vacuum chuck and also the heavy weight of the roller mold itself.

6.3.5 Characterization of R2R Embossed Optical Film

It is necessary to evaluate the quality of R2R embossed optical film based on the measurement results. However, it is difficult to obtain accurate surface profile data of

the embossed optical Fresnel lens films, because they are flexible, transparent, and of high surface finish quality. Optical measurement methods may not work properly because very few light rays shined on the lens surface are reflected back to the lens module and captured by the sensor. Stylus profilometer is generally utilized to measure various surface profiles with high accuracy, but it is challenging to maintain levelness of the flexible film in a large area without warping and deflection. Hence, a high-flatness porous vacuum chuck was used to hold the optical film evenly. 2D and 3D measurement was conducted using the stylus profilometer with the assistance of an additional positioning stage, which is perpendicular to the traverse direction of the profilometer, as shown in Fig. 19.

It can be seen that the linear Fresnel lens pattern is well replicated from the embossing roller mold onto the film substrate, and no pores or defects were observed. The deviation of measured facet angles from the designed ones for each prism ring. 93% of the deviation errors fall in the limit of $\pm 0.5^\circ$, and the maximum deviation was found to be -0.957° . Such $10\times$ higher angular deviations than the mold (see Fig. 16) are expected, because R2R embossing will introduce larger mounting and replication errors compared to conventional plastic injection molding due to the large size of roller mold and its unique continuous replication and curing processes.

For the radial Fresnel lens patterned film embossed by R2R manufacturing, the measurement setup for optical film evaluation is shown in Fig. 20a, while the 3D measurement results for radial Fresnel lenses are shown in Fig. 20b. The film is flattened on a plate to minimize the deflection. From the 3D measurement result of

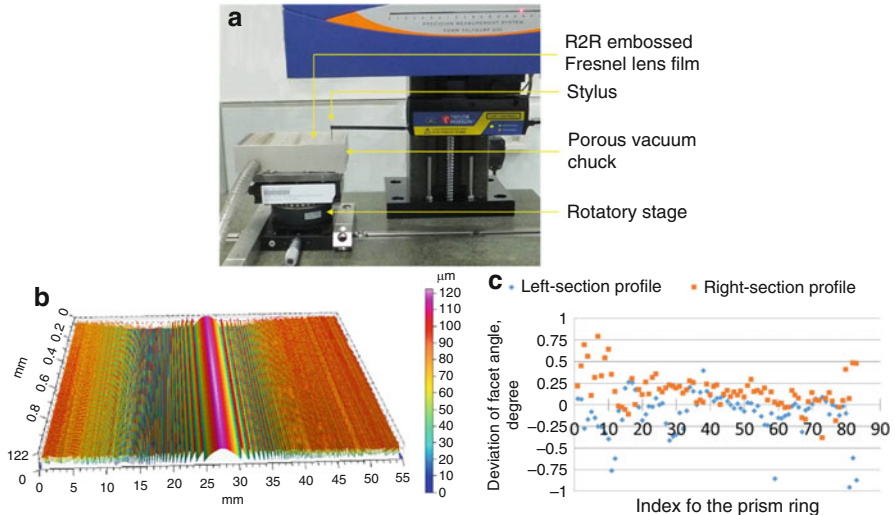


Fig. 19 (a) Measurement of R2R embossed linear Fresnel lens film using a stylus profilometer. (b) Measured 3D profile of one linear Fresnel lens pattern. (c) Deviation of measured facet angles on the Fresnel lens film from the designed ones

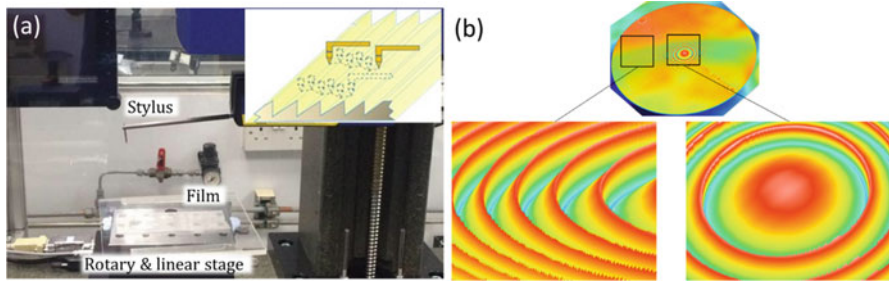


Fig. 20 (a) Physical and schematic views of the film measurement using a stylus profilometer, (b) 3D view of the measured radial Fresnel lens (Zhang et al. 2018)

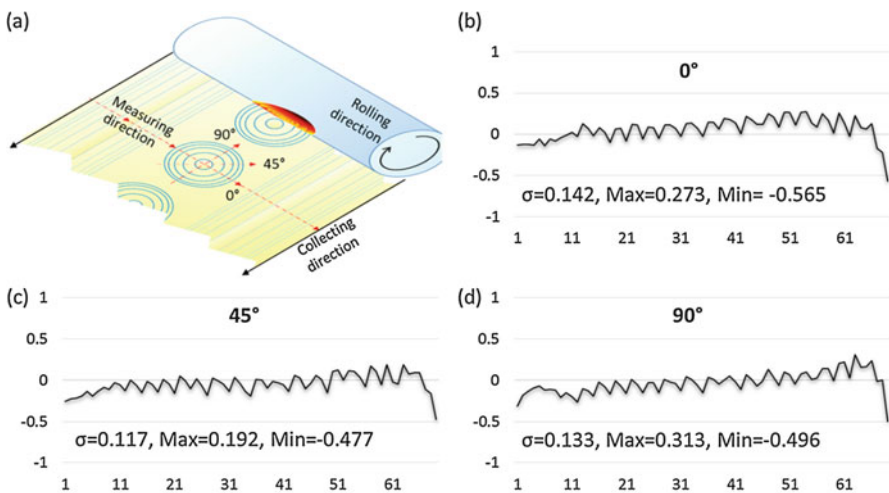


Fig. 21 (a) Schematic view of the measuring directions in R2R process, (b–d) deviation of facet angles the embossed radial lens from design at 0°, 45°, and 90° (Zhang et al. 2018)

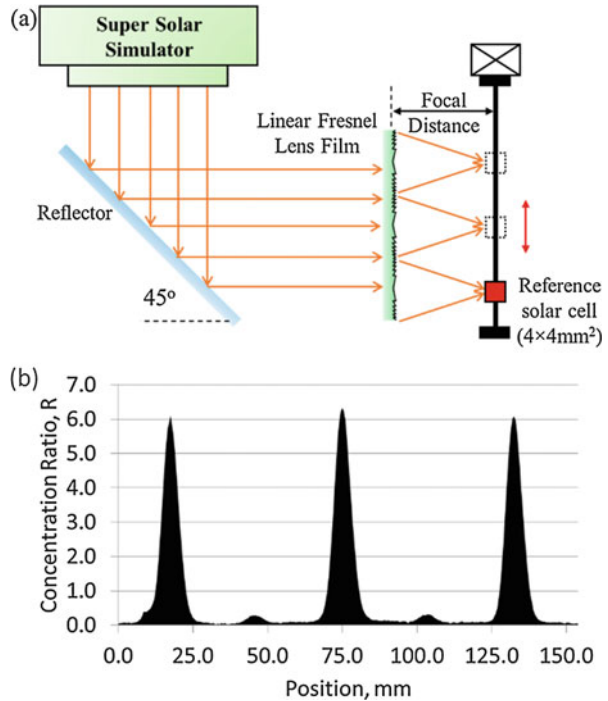
radial Fresnel lens shown, the Fresnel lens feature is well replicated with integrated form, and no significant defects are found on the embossed lens.

Figure 21a shows the schematic view of R2R embossing process with the measurement directions for the radial lens indicated. From Fig. 21b–d, it can be found that the deviations of facet angles at 45° and 90° directions are not significantly larger than 0° direction, which means that the feature replication performance during R2R embossing does not heavily rely on the orientation of microstructures. It can also be observed that the angular deviation increases with the increment of facet index. Particularly, the last facet angles (index #69) deviates heavily from its designed values. This is considered to be caused by the difficulty of the liquid resin to fill the groove feature at this linking portion where large non-patterned surface with no groove features is beside.

6.3.6 Performance Evaluation and Functionality Test

Before the eventual utilization of the fabricated optical film in optical systems, it is necessary to conduct functionality test for the R2R embossed film to evaluate its performance on light manipulation. For the optical linear Fresnel lens, Fig. 22a shows the measurement setup for the light concentration test. The measurement was carried out using a reference solar cell with an aperture ($4\text{ mm} \times 4\text{ mm}$), a computer-controlled linear stage, and a Wacom super solar simulator. The known short-circuit current of the reference solar cell at 123.9 mA was used to calibrate the super solar simulator with a beam divergence angle of $<2.5^\circ$ to obtain a solar irradiance of 1000 W/m^2 . The linear Fresnel lens film was pasted on a transparent plastic plate made of PC, which was then mounted vertically and aligned to the direction of measurement. The Fresnel lens film was irradiated normally by the super solar simulator, and the reference solar cell was vertically mounted on the linear stage and positioned at the focal distance. The reference solar cell was scanned along horizontal axis with an interval of 0.5 mm , and the readings of voltage V_f were taken at each point and recorded in the computer. Then the linear Fresnel lens film was removed, and the voltage reading was recorded as V_0 , and the voltage reading with the solar simulator turned off was recorded as V_d . Hence, the light concentration ratio, R , can be calculated as follows:

Fig. 22 (a) Measurement setup for light concentration test of linear Fresnel lens film. (b) Measured concentration ratio with respect to the position of the referenced solar cell



$$R = \frac{V_f - V_d}{V_0 - V_d} \quad (2)$$

Figure 22b shows the measured relative irradiance distribution on the focal plane of the Fresnel lens film. The concentration ratio was measured to be 6.33 for the receiver area of 16 mm². As R2R embossing usually leads to larger lens profile errors compared to the lenses manufactured by injection molding, the embossed Fresnel lenses may have slightly smaller concentration ratio with the same lens design.

For the radial Fresnel lens fabricated using R2R UV embossing, Fig. 23a and b illustrates the optical film, as well as a preliminary demo setup to show the effect of light concentration using the film. It can be observed that even the nonparallel room light can be effectively concentrated at the focal plane, which demonstrates the high quality and high performance of the film produced by R2R UV embossing process. The same measurement setup for linear Fresnel lens measurement is also used in measuring the radial Fresnel lens film, and the results are shown in Fig. 23c. It can be observed that linear Fresnel lens is able to achieve 4.1× times of light concentration ratio compared to the light level without passing the Fresnel lens, while the radial Fresnel lens can achieve 15.9× times of light concentration ratio, which is almost square of the value of the linear one, demonstrating the strong concentration capability of radial Fresnel lens as designed.

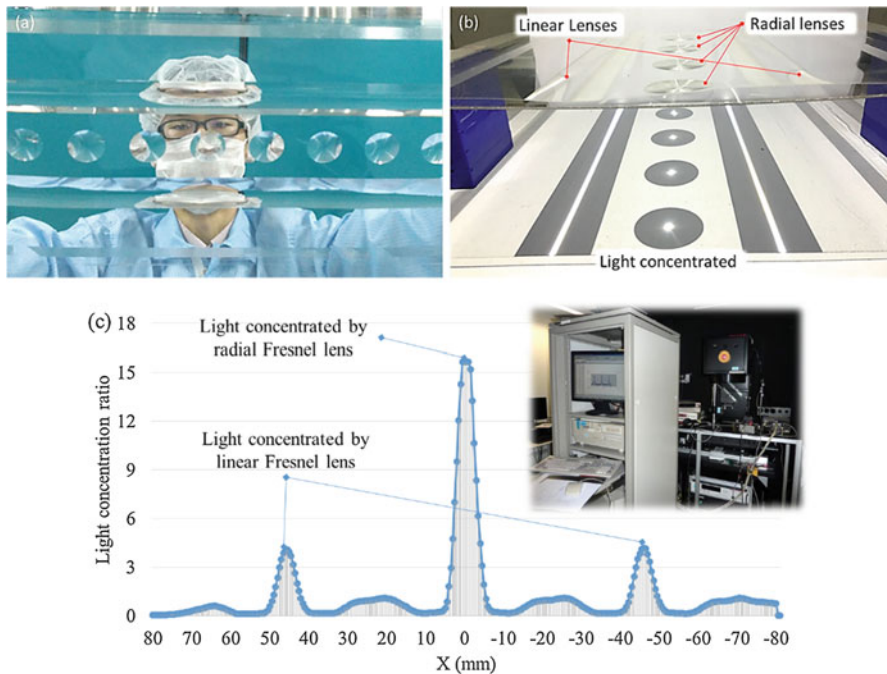


Fig. 23 (a) R2R embossed Fresnel lens film, (b) indoor light concentrated by the optical film, and (c) light concentration ratio calculated from the measurement results (Zhang et al. 2018)

6.4 Summary and Outlook

This chapter attempts to provide a review on micromachining of roller mold for roll-to-roll manufacturing, an advanced continuous manufacturing technology for fabrication of functional films, particularly for printed electronics and optical film. With the joint effort around the world, substantial progress in several key areas has been successfully made including machine tool development, novel tool path planning, process control, parameter optimization, and the fundamental research in cutting mechanics. Despite the growing industry adoption of micromachining of roller mold, the following five areas are in demand for further research and development:

- Machining efficiency enhancement for micro-features generation on large areas
- Machining of submicron pattern and complex features using customized diamond cutters
- New process innovation to enable machining of micro-features on roll mold made of difficult-to-machine materials for R2R manufacturing of patterned glass
- Quality improvement in form accuracy, surface finishing, burr reduction, and subsurface damage control
- Affordable machine tools for small- and medium-sized roller mold fabrication with comparable levels of accuracy

References

- Allen RC et al (2000) Brightness enhancement film. US Patent
- Brinksmeier E, Preuss W (2012) Micro-machining. *Phil Trans R Soc A* 370(1973):3973–3992. <https://doi.org/10.1098/rsta.2011.0056>
- Donaldson R, Patterson S (1983) Design and construction of a large, vertical axis diamond turning machine. In: 27th annual technical symposium, 1983. International Society for Optics and Photonics, pp 62–67
- Hennig G, Selbmann KH, Brüning S (2008) Large scale laser microstructuring in the printing industry. *Laser Technik J* 5:52–56
- Hrehorova E, Kattumenu R-C (2007) Evaluation of gravure print forms for printed electronics. *Gravurezine*
- Hrehorova E, Rebros M, Pekarovicova A, Bazuin B, Ranganathan A, Garner S, Merz G, Tosch J, Boudreau R (2011) Gravure printing of conductive inks on glass substrates for applications in printed electronics. *Display Technol J* 7:318–324
- Huang R, Zhang X, Rahman M, Kumar AS, Liu K (2015) Ultra-precision machining of radial Fresnel lens on roller moulds. *CIRP Ann* 64:121–124. <https://doi.org/10.1016/j.cirp.2015.04.062>
- Huang R, Zhang X, Kumar AS, Liu K, Rahman M (2017) Profile evaluation of radial Fresnel lens directly machined on roller molds by rotating-tool diamond turning. *Precis Eng* 50:44–52. <https://doi.org/10.1016/j.precisioneng.2017.04.012>
- Kang H, Kitsomboonloha R, Jang J, Subramanian V (2012) High-performance printed transistors realized using Femtoliter gravure-printed Sub-10 μm metallic nanoparticle patterns and highly uniform polymer dielectric and semiconductor layers. *Adv Mater* 24:3065–3069
- Kitsomboonloha R, Morris S, Rong X, Subramanian V (2012) Femtoliter-scale patterning by high-speed, highly scaled inverse gravure printing. *Langmuir* 28:16711–16723

- Lahti M, Leppävuori S, Lantto V (1999) Gravure-offset-printing technique for the fabrication of solid films. *Appl Surf Sci* 142:367–370. [https://doi.org/10.1016/S0169-4332\(98\)00676-X](https://doi.org/10.1016/S0169-4332(98)00676-X)
- Pudas M, Halonen N, Granat P, Vähäkangas J (2005) Gravure printing of conductive particulate polymer inks on flexible substrates. *Prog Org Coat* 54:310–316. <https://doi.org/10.1016/j.porgcoat.2005.07.008>
- Sung D, Vornbrock AF, Subramanian V (2010) Scaling and optimization of gravure-printed silver nanoparticle lines for printed electronics components and packaging technologies. *IEEE Trans Compon Packag Technol* 33:105–114. <https://doi.org/10.1109/TCAPT.2009.2021464>
- Watts MP, Solutions I (2007) Advances in roll to roll processing. Impattern solutions. Austin. <http://www.impattern.com/Download/RollToRollProcessing.pdf>
- Xie W, Dai Y, Wang R, Sumathy K (2011) Concentrated solar energy applications using Fresnel lenses: a review. *Renew Sust Energ Rev* 15:2588–2606
- Zhang XQ, Woon KS, Rahman M (2014) Diamond turning. In: Hashmi S, Batalha GF, Tyne CJV, Yilbas B (eds) *Comprehensive materials processing*, vol 11. Elsevier, Oxford, pp 201–220. <https://doi.org/10.1016/B978-0-08-096532-1.01110-9>
- Zhang X, Liu K, Sunappan V, Shan X (2015) Diamond micro engraving of gravure roller mould for roll-to-roll printing of fine line electronics. *J Mater Process Technol* 225:337–346. <https://doi.org/10.1016/j.jmatprotec.2015.05.032>
- Zhang X, Huang R, Liu K, Kumar AS, Shan X (2018) Rotating-tool diamond turning of Fresnel lenses on a roller mold for manufacturing of functional optical film. *Precis Eng* 51:445–457. <https://doi.org/10.1016/j.precisioneng.2017.09.016>



Tool-Servo Driven Diamond Turning for Structured Surface

7

Mao Mukaida and Jiwang Yan

Contents

7.1	Introduction	216
7.2	STS Turning of Silicon for Circular Microlens Arrays	217
7.2.1	Ductile-Brittle Transition	218
7.2.2	Surface Topographical Error	220
7.2.3	Material Phase Transformation	220
7.2.4	Chip Formation	222
7.2.5	Cutting Force Characteristics	223
7.2.6	Tool Wear Characteristics	227
7.3	Segment Turning for Hexagonal Microlens Arrays	227
7.3.1	Mechanism of Segment Turning	228
7.3.2	Effectiveness Verification of Segment Turning	229
7.3.3	Fabrication of Hexagonal Microlens Array on Silicon	238
7.4	Summary and Outlook	242
	References	243

Abstract

Structured surfaces are increasingly demanded in many fields. Ultraprecision cutting is an effective method for machining structured surfaces with high form accuracy, surface quality, and flexibility of geometry. In recent years, tool-servo driven diamond turning has been focused, because it can greatly reduce the machining time for structured surfaces compared to other methods. However, unlike in conventional diamond turning, the tool posture and cutting behavior in tool-servo driven diamond turning change significantly with time. Thus, the machining mechanism becomes

M. Mukaida

Department of Mechanical Engineering, Faculty of Science and Technology, Keio University, Yokohama, Japan

J. Yan (✉)

Department of Mechanical Engineering, Keio University, Yokohama, Japan

e-mail: yan@mech.keio.ac.jp

very complicated, especially for brittle materials. In this chapter, after the recent advances in tool-servo driven diamond turning technology have been overviewed, the fabrication process of microlens arrays on single-crystal silicon by slow tool servo (STS) driven diamond turning will be introduced. The fundamental machining mechanisms including the brittle fracture and phase transformation of silicon will be discussed, and the feasibility of ductile mode cutting will be demonstrated. In STS, machining of microlens arrays with sharp edges, the follow-up error of the machine tool is a potential problem. To reduce the follow-up error, a new method named segment turning method was proposed. From the results of both cutting tests and theoretical analysis, the effectiveness of the proposed method will be examined. Hexagonal microlens arrays of silicon have been successfully machined with a form error less than 300 nmPV and surface roughness less than 5 nmSa.

Keywords

Tool servo · Micro cutting · Diamond turning · Structured surface · Lens array

7.1 Introduction

Structured surfaces are increasingly demanded in the manufacturing of optical and mechanical products. For example, some special optical properties can be realized by microlens arrays (Stevens and Miyashita 2010; Jeong et al. 2006; Arase et al. 2014), prism arrays (Brinksmeier et al. 2008), antireflective surface (Lalanne and Morris 1997), and so on. Another use of structured surfaces is to control the surface wettability, which produces hydrophilicity/hydrophobicity to materials (Asakura and Yan 2015). Reduction of friction and fluid flow resistance is also possible by using a properly designed structured surface (Kim and Kim 2002). High form accuracy is required for structured surface to offer the designed function. Lithographic processes can be used for manufacturing structured surfaces, but the degree of freedom of workpiece geometry is very limited, and it is difficult to ensure surface quality and form accuracy (Ow et al. 2010; Bitterli et al. 2010). Laser processing offers a high machining efficiency, but normally heat affected zones will remain on the workpiece surface (Deng et al. 2015). In contrast, mechanical machining technologies, such as ultraprecision cutting and milling, have advantages of high freedom of geometry, high form accuracy and low surface roughness (Weck et al. 2001). Raster micro-milling and fly cutting are typical methods for machining structured surfaces on metals. However, these machining processes are very time-consuming, especially when the workpiece surface area is large (Scheiding et al. 2011).

In recent years, tool-servo driven diamond turning has enabled machining freeform and structured surfaces by synchronizing the tool movement with the spindle rotation, as shown in Fig. 1. Typically, there are two kinds of tool servos: a slow tool servo (STS) driven by a table of the machine tool, and a fast tool servo (FTS) driven by a piezoelectric actuator in addition to the machine tool itself (Fang et al. 2008; Davis et al. 2009). Compared with other cutting methods, such as micro-milling and fly cutting,

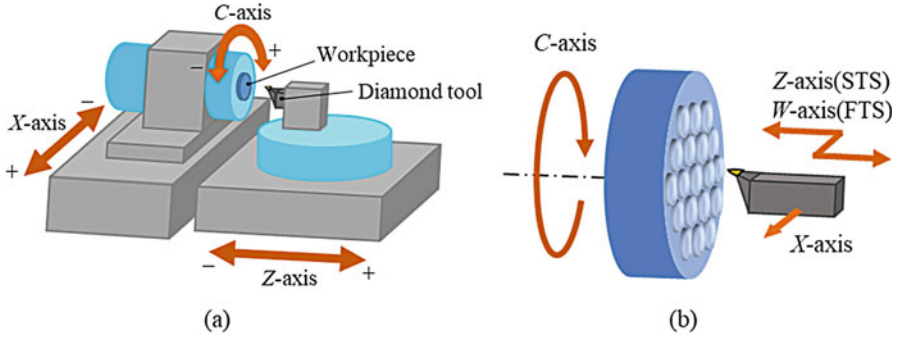


Fig. 1 Schematic of tool-servo driven diamond turning: (a) lathe configuration; and (b) machining of structured surface

tool-servo driven diamond turning can reduce machining time. The main difference between an STS and an FTS is the tool servo stroke and reciprocating frequency. Only the tool is oscillated by a piezoelectric actuator in an FTS system, thus it enables to drive the tool at a very high frequency. Therefore, an FTS is suitable for generating small-amplitude microstructures with a high spatial frequency. On the other hand, an STS enables machining large amplitude surface structures and high aspect ratio freeform surfaces. Also, STS systems are preferable for economic reasons because no extra machine add-ons are necessary for tool drive apart from the machine tool, unlike the FTS (Chen et al. 2013).

Tool-servo driven diamond turning has been researched from various points of view, such as improvement of FTS units, control system of machine tools, and generation of tool paths (Fang et al. 2008; Patterson and Magrab 1985; Rakuff and Cuttino 2009; Wang and Yang 2013; Sze-Wei et al. 2007; Yu et al. 2012; Neo et al. 2014). However, there is very little literature on tool-servo driven diamond turning of brittle materials (Yu et al. 2011a). Unlike in conventional diamond turning, the tool posture and cutting point of the tool, as well as the depth of cut change with time in tool-servo driven diamond turning. Thus, the machining mechanism becomes very complicated, which can affect material removal behavior, especially for a highly brittle material. In this chapter, the fabrication process of microlens arrays on single-crystal silicon, which is a typical hard brittle material, by STS-driven diamond turning will be introduced, and the fundamental machining mechanisms will be discussed.

7.2 STS Turning of Silicon for Circular Microlens Arrays

Microlens arrays are used in advanced high-integration and high-performance optical systems, enabling many kinds of functions such as focusing and homogenizing (Onozawa et al. 2008). Generating micro lens dimples on a silicon substrate enable fabrication of concave microlens arrays for the infrared (IR) light (Mukaida and Yan 2017a). Another possible use of micro dimple arrays on silicon is as a mold substrate for molding convex microlens arrays on polymer and glass (Chang et al. 2006;

Albero et al. 2009; Oliveira et al. 2014; He et al. 2014). The understanding of fundamental machining mechanisms for cutting micro dimples on silicon is very important for fabricating freeform and microstructured optical surface on brittle materials.

Mukaida and Yan conducted STS turning experiments of a single crystal silicon (001) wafer to fabricate spherical micro lens dimples (Mukaida and Yan 2017a). In their experiment, each dimple has a designed diameter of 320 μm and a curvature radius (R_d) of 2.563 mm, thus the depth of the dimple (D) is 5 μm . The dimples are located 1 mm away from the workpiece center, at an angular pitch of 45°. The cutting directions for the dimples located at $C = 0^\circ, 90^\circ, 180^\circ, 270^\circ$ are $\langle 110 \rangle$ directions, while those at $C = 45^\circ, 135^\circ, 225^\circ, 315^\circ$ are $\langle 100 \rangle$ directions.

A four-axis ($XZBC$) simultaneous control ultraprecision lathe Nanoform X (AMETEK Precitech Inc.) having an STS system was used in the experiments. A single crystal diamond tool with a nose radius (R_t) of 1 mm, a rake angle of -30° , and a relief angle of 36° was used. Cutting experiments were conducted under various feed rates f to investigate the effect of undeformed chip thickness.

7.2.1 Ductile-Brittle Transition

Figure 2 shows a photograph of microlens arrays machined on a single-crystal silicon wafer through ductile mode cutting (Mukaida and Yan 2017a). However, brittle fractures occurred under inappropriate conditions. Figure 3 shows microscope images of dimples located at $C = 0^\circ$ and 45° , respectively, at different feed rates. When the cutting direction is along the $\langle 110 \rangle$ direction ($C = 0^\circ$), brittle fractures (black dots) are found in the dimples at a feed rate over 5 $\mu\text{m}/\text{rev}$. The results of dimples located at $C = 90^\circ, 180^\circ, 270^\circ$ were similar to those at $C = 0^\circ$ due to the crystalline symmetry. In contrast, brittle fractures are not observed in dimples located at $C = 45^\circ, 135^\circ, 225^\circ, 315^\circ$ which had the cutting direction of $\langle 100 \rangle$ direction. This agrees with the previous results that the critical chip thickness of $\langle 110 \rangle$ direction is smaller than that of $\langle 100 \rangle$ direction when cutting single-crystal silicon (001) (Yan et al. 2012). That is to say, the $\langle 100 \rangle$ direction is easier for ductile cutting than the $\langle 110 \rangle$ direction.

In addition, it is seen in Fig. 3 that brittle fractures occurred preferentially at the left side (the exit side of tool feed) of the dimples, while the right side is less damaged. In microlens array cutting, depth of cut constantly changes with time and location, leading to the change of undeformed chip thickness. As the depth of cut decreases at the exit side of tool feed, cracks are remained on finished surface.

Fig. 2 Photograph of ductile-cut microlens arrays on a silicon wafer



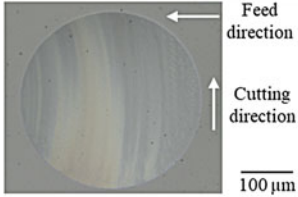
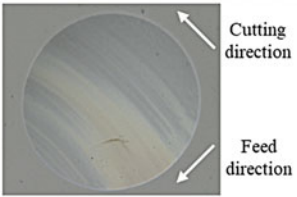
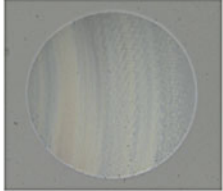
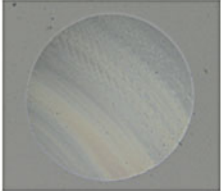
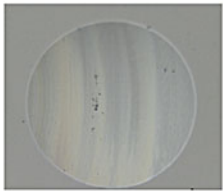

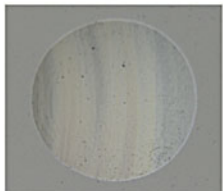
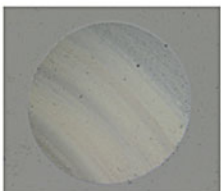
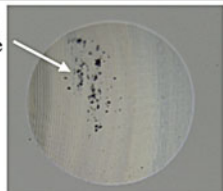
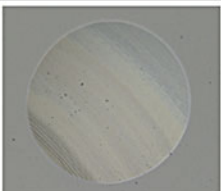
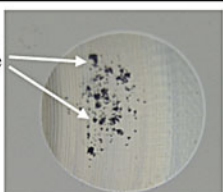
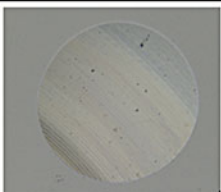
f ($\mu\text{m}/\text{rev}$)	$C = 0^\circ$ Cutting direction $\langle 110 \rangle$	$C = 45^\circ$ Cutting direction $\langle 100 \rangle$
1		
2		
3		
4		
5		
6		

Fig. 3 Microscopic images of silicon dimples machined at various tool feed rates along different cutting directions

7.2.2 Surface Topographical Error

Figure 4 shows the three-dimensional topographies of the dimples machined at $C = 0^\circ$ and $f = 1$ and $5 \mu\text{m}/\text{rev}$. The deviation of a dimple surface from the ideal sphere ($R_d = 2.563 \text{ mm}$) was calculated and shown in the same figure. From the deviation results, form error and surface roughness were further analyzed. High-precision dimples with a form error of $\sim 300 \text{ nm}$ and surface roughness of $\sim 6 \text{ nmSa}$ were successfully obtained when a small tool feed rate ($< 2 \mu\text{m}/\text{rev}$) was used. The present result has satisfied the form accuracy requirement over the entire infrared region for silicon (Ottevaere et al. 2006; Harvey et al. 2012). As the feed rate increased, the form errors of the dimples increased slightly. Surface roughness increased with the feed rate due to the occurrence of brittle fractures at high feed rates.

7.2.3 Material Phase Transformation

To investigate possible material structural changes of the machined dimples, laser micro-Raman spectroscopy was performed on the dimple surfaces. As known from

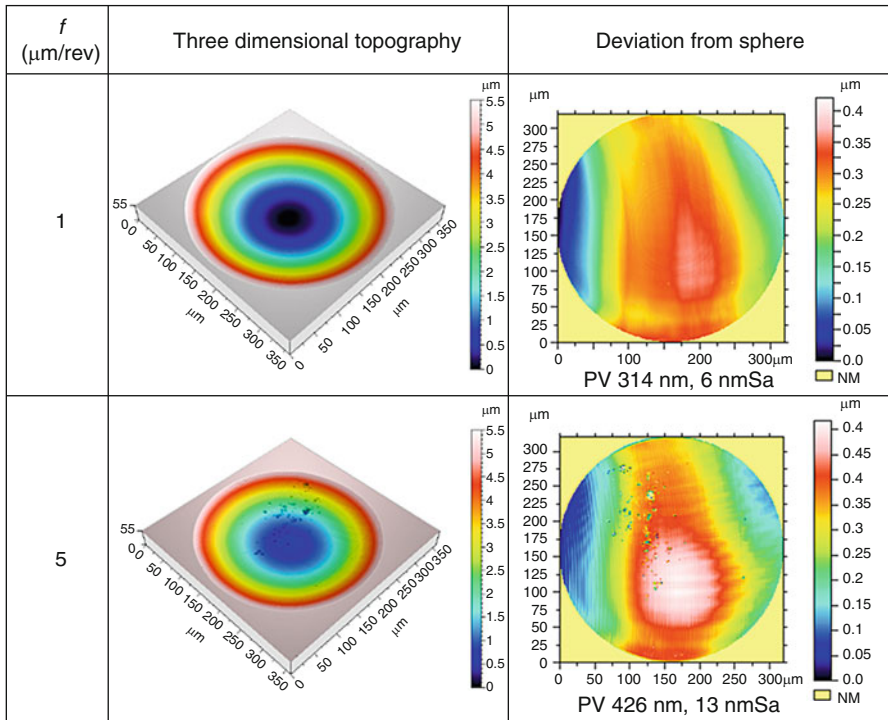


Fig. 4 Three-dimensional topographies of dimples located at $C = 0^\circ$, and their deviations from an ideal spherical surface

previous studies, ductile mode cutting of single crystal silicon is associated with phase transformation into amorphous silicon caused by high pressure (Yan et al. 2009). The resulting amorphous silicon may affect the IR optical performances, such as refractive index, if it is very thick. For this reason, it is important to know how amorphous silicon is distributed within the micro dimples.

Figure 5 shows mapping results of the peak heights for amorphous silicon for dimples machined under various conditions. It was found that the peak height of amorphous silicon increased as the feed rate increased. In addition, a higher amorphous peak seems to be located at the left side of the dimples. It should be pointed out that in Fig. 5, the tool feed direction is from the right to the left. Thus, amorphization of single crystal silicon occurred preferentially at the exit side of tool feed of the lens dimple.

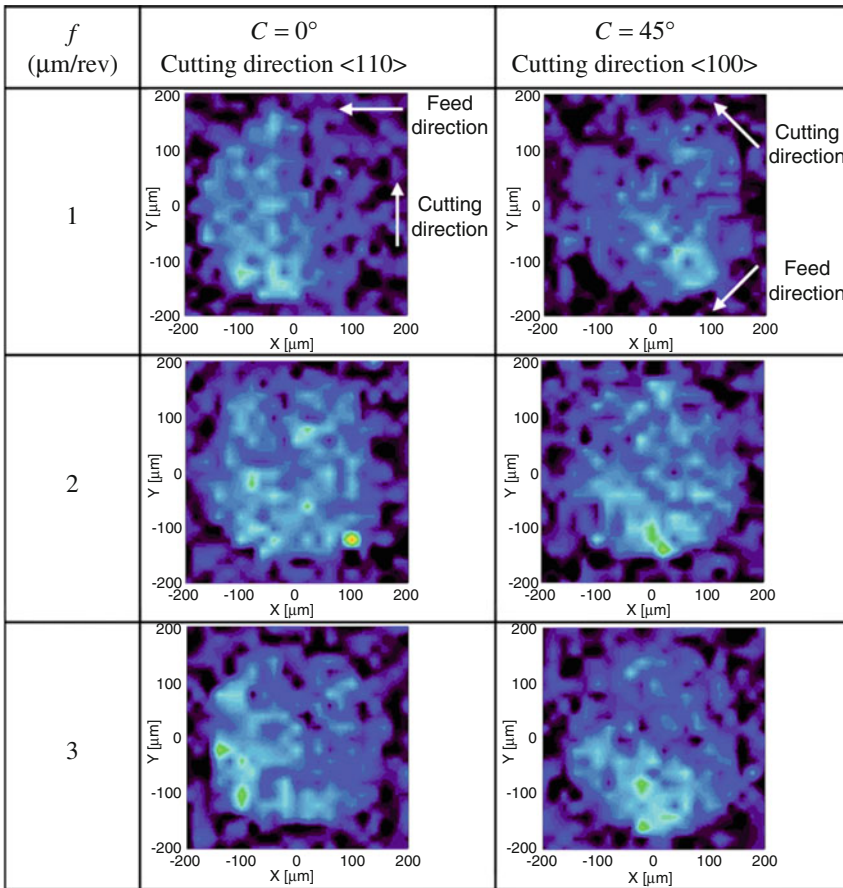


Fig. 5 (continued)

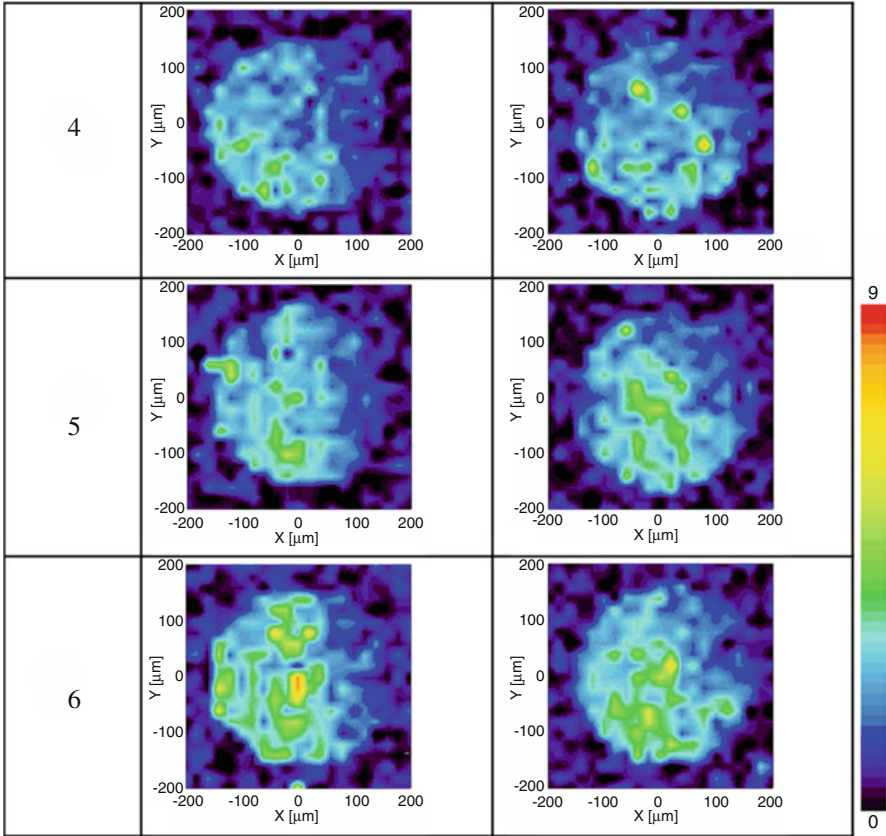


Fig. 5 Mapping results of peak height of amorphous silicon measured using a laser micro-Raman spectrometer

7.2.4 Chip Formation

Figure 6 shows SEM images of cutting chips obtained under different conditions. Continuous chips, which indicate ductile cutting mode, were generated at $f = 1 \mu\text{m}/\text{rev}$ (Fig. 6a) for a $5 \mu\text{m}$ -deep lens dimple. The chips are not very long, because cutting was interrupted by separated dimples. On the other hand, a mixture of powder chips and a few continuous chips were found at $f = 6 \mu\text{m}/\text{rev}$ (Fig. 6b). This means that both brittle and ductile cutting modes existed under this condition, which agrees with the surface observation results in Fig. 3. Figure 6c is an SEM image of cutting chips obtained at $f = 1 \mu\text{m}/\text{rev}$ when cutting a shallower lens array (lens depth $D = 2 \mu\text{m}$). In this case, the chips look much thinner and longer than those in Fig. 6a where the lens depth is $5 \mu\text{m}$, and some chips are even partially transparent. When the lens depth is $2 \mu\text{m}$, the maximum undeformed chip thickness is extremely small (68 nm), enabling this kind of extremely thin chip formation.

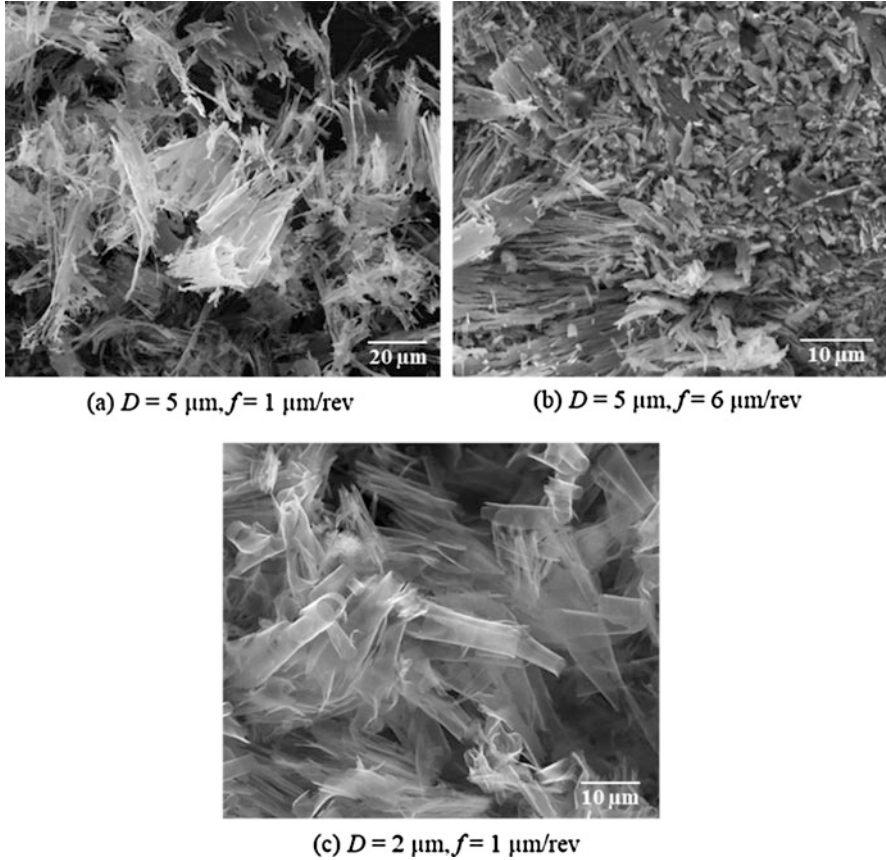


Fig. 6 SEM images of chips obtained when cutting lens dimples with different depths at different tool feed rates

Laser micro-Raman spectroscopy was also performed to detect the microstructure of cutting chips. Figure 11 shows the Raman spectrum of chips obtained at $f = 1$ and $6 \mu\text{m/rev}$. In case of $f = 1 \mu\text{m/rev}$, some areas of chips only showed the peak of amorphous silicon (Fig. 7a), and other areas showed a mixture of amorphous silicon and polycrystalline silicon (Fig. 7b). This fact agrees with previous results where amorphous and polycrystalline chips are generated in ductile cutting (Yan et al. 2009). On the other hand, in case of $f = 6 \mu\text{m/rev}$ only peak of polycrystalline silicon was detected (Fig. 7c). This indicates that in brittle cutting mode, phase transformation to amorphous silicon did not occur.

7.2.5 Cutting Force Characteristics

Cutting force was measured during lens array cutting. Figure 8 shows the force waviness of principal force F_c and thrust force F_t in case of $f = 1$ and $5 \mu\text{m/rev}$,

Fig. 7 Raman spectra of cutting chips showing different significance for amorphous and polycrystalline phases

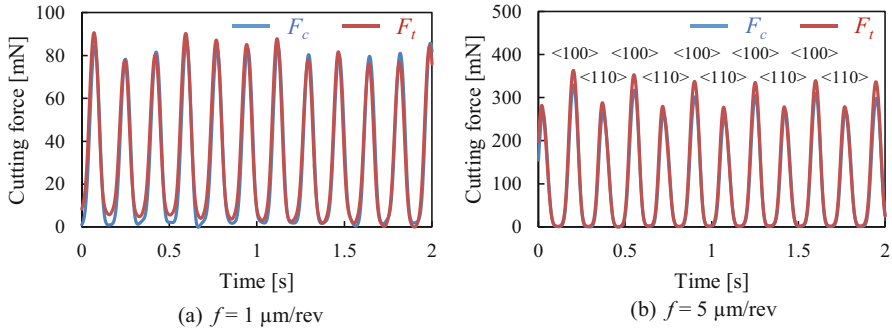
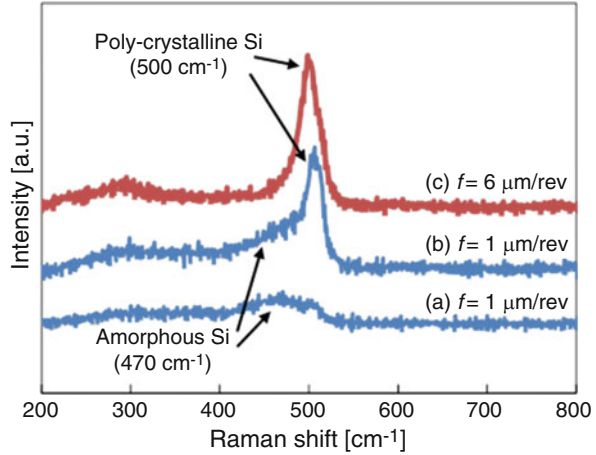


Fig. 8 Variations of cutting forces at different tool feed rates. A strong dependence of peak force on crystal orientation is seen at high tool feed rates

respectively, where the force waviness was recorded when the tool passed the center of dimples. Both F_c and F_t change periodically because the depth of cut changes during cutting dimples. It was found that the peak value of cutting force was almost the same for various crystal orientations at $f = 1 \mu\text{m/rev}$ (Fig. 8a), while it changed greatly depending on crystal orientation at $f = 5 \mu\text{m/rev}$ (Fig. 8b). A smaller peak force corresponds to the $\langle 110 \rangle$ direction where brittle fractures occur, while a larger peak force corresponds to the $\langle 100 \rangle$ direction where ductile cutting is dominant, as shown in Fig. 3.

The average peak values of cutting forces at various feed rates are plotted in Fig. 9. In case of $f = 5, 6 \mu\text{m/rev}$, the average values of low peaks and high peaks were plotted separately with respect to crystal orientations. It is found that cutting forces increase as the feed rate increases when $f < 5 \mu\text{m/rev}$, and decrease when $f > 5 \mu\text{m/rev}$. This drop of force corresponds to the occurrence of brittle fractures as shown in Fig. 3.

Fig. 9 Relationship between cutting forces and tool feed rate

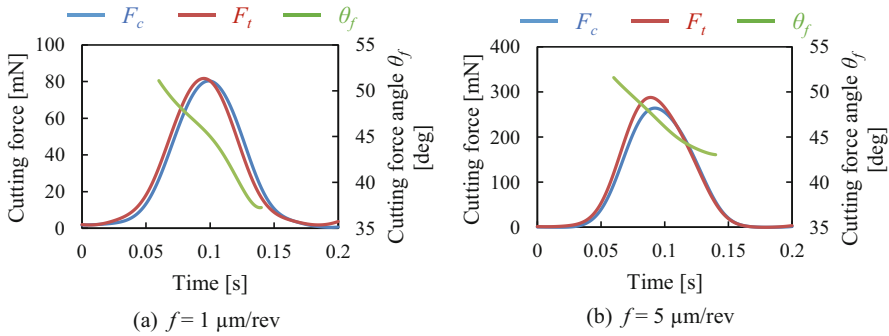
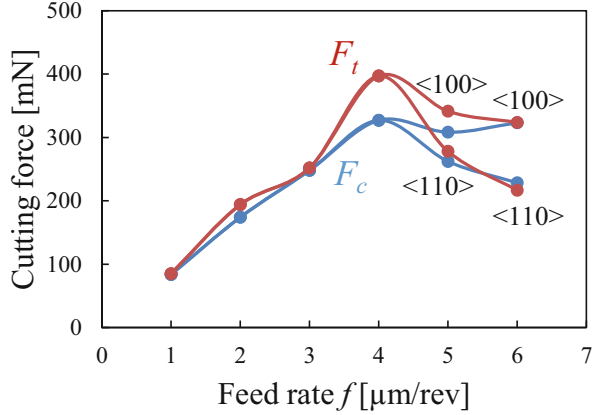


Fig. 10 Variation of cutting force and cutting force angle during cutting a single dimple

It was also found that during cutting a single dimple, F_t reached its maximum earlier than F_c , as shown in Fig. 10. This phenomenon was also observed in previous research on dimple cutting by elliptical vibration texturing on a ductile material (Kurniawan et al. 2016). Now cutting force angle θ_f is defined in Fig. 11, which can be calculated by the following equation:

$$\theta_f = \tan^{-1} \frac{F_t}{F_c} \tag{1}$$

The changes of cutting force angle θ_f are additionally plotted in Fig. 10. It is clear that in Fig. 10a and 10b, θ_f decreases during the cutting of a single dimple.

Figure 11 shows schematically the decomposition of a cutting force at different stages when cutting a single dimple. When start cutting a dimple, the tool moves into the workpiece inducing a positive cutting direction angle θ_w , as shown in Fig. 11a. As the tool reaches the deepest point of a dimple, θ_w decreases to zero (Fig. 11b), and then

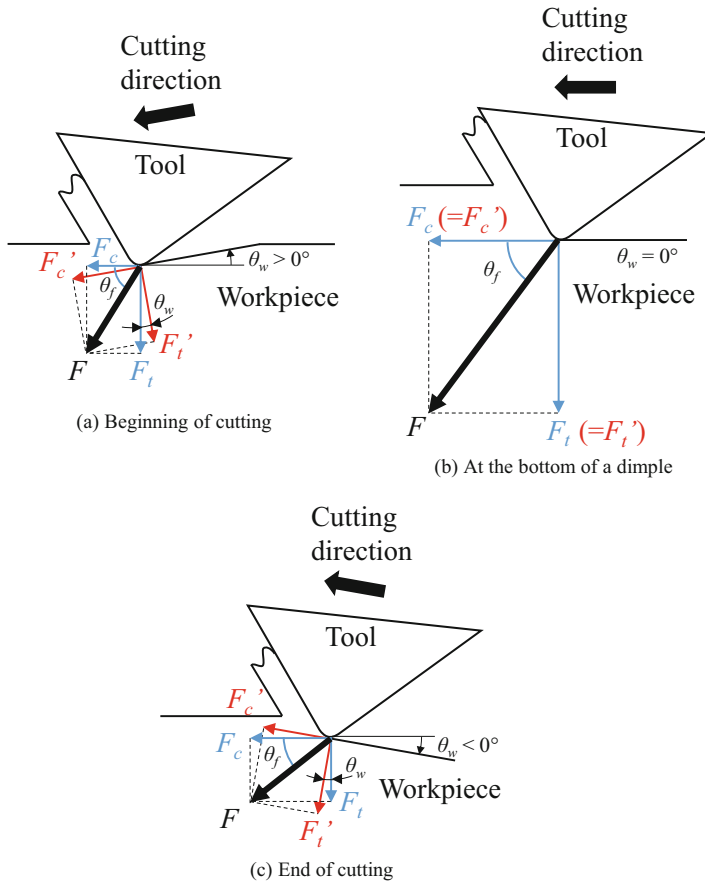


Fig. 11 Change in cutting force angle when cutting a single dimple

θ_w becomes negative as the tool moves away from the workpiece (Fig. 11c). In the present study, the dynamometer measures the force components parallel (F_c) and vertical (F_t) to the flat surface of the workpiece. However, the actual principal force F_c' and thrust force F_t' are parallel and vertical to the cutting direction, as described in Fig. 11. Then the cutting force angle θ_f can be calculated as follows:

$$\theta_f = \theta_w + \tan^{-1} \frac{F_t'}{F_c'} \quad (2)$$

Therefore, θ_f changes with θ_w . In the present experiment, θ_w changed from 3.58° to -3.58° , thus θ_f should be decreased by about 7° during cutting a single dimple. This result agrees very well with the experimental results in Fig. 10.

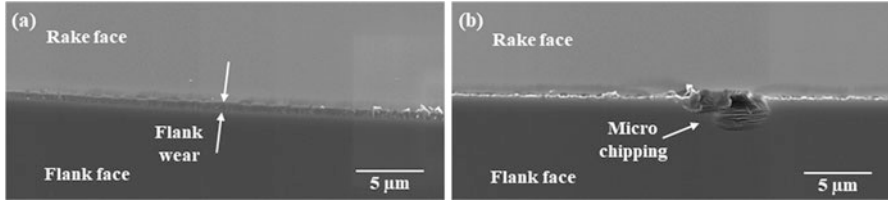


Fig. 12 SEM images of tool edge after dimple cutting on single-crystal silicon, showing two kinds of wear patterns: (a) flank wear and (b) micro chipping

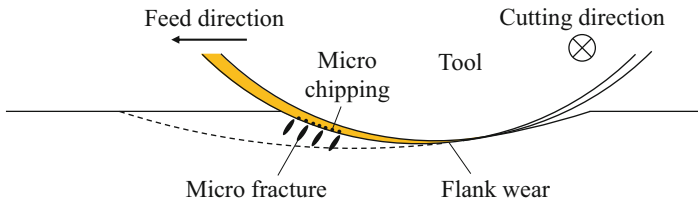


Fig. 13 Schematic diagram for two kinds of tool wear patterns in dimple cutting

7.2.6 Tool Wear Characteristics

The diamond tool was observed using SEM after cutting dimples with a total cutting distance of 500 mm. Figure 12 shows SEM images of the tool edge. Two kinds of tool wear patterns were identified: one is flank wear (wear land width ~ 700 nm) near the tool apex (Fig. 12a); the other is micro chippings near the region contacting with the uncut surface (Fig. 12b). As shown in Fig. 13, undeformed chip thickness is extremely small and approaches zero near the tool apex, where intensive friction between the tool and the workpiece causes flank wear. Near the region contacting with the uncut surface, however, undeformed chip thickness is very large, thus brittle mode cutting leads to micro impacts to the tool, causing micro chippings to happen (Yan et al. 2003).

7.3 Segment Turning for Hexagonal Microlens Arrays

Hexagonal microlens arrays offer a fill factor of 100% and achieve higher light efficiency than circular lens arrays (Chou et al. 2005). However, hexagonal microlens arrays have many sharp edges at the boundaries among the lenslets, which makes the tool-servo driven diamond turning very difficult, especially in case of

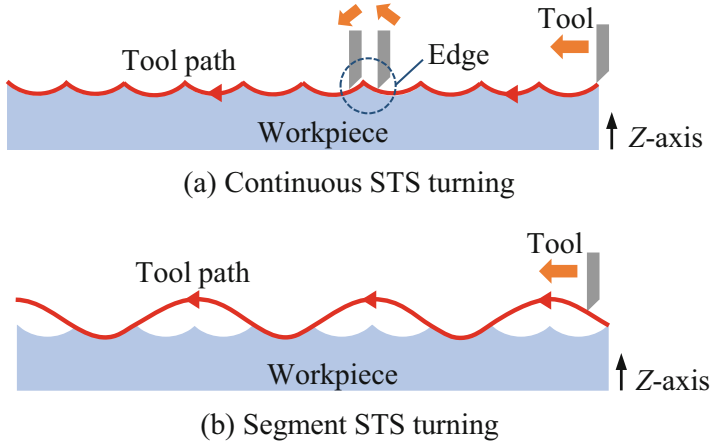


Fig. 14 Schematics of tool paths for two STS turning methods to generate a microlens array

using an STS, because there is a significant dynamic error caused by the excessive acceleration of machine tables (Yu et al. 2012). A few researchers reported the machining of microlens arrays using an STS (Yi and Li 2005; Zhang et al. 2013), but no consideration was given to the edge-induced form error.

A new STS diamond turning method, namely, segment turning method, for machining gapless hexagonal microlens arrays was proposed by Mukaida and Yan to improve lens form accuracy and edge generation (Mukaida and Yan 2017b). In this section, first the effectiveness of the segment turning method will be evaluated by comparing with the conventional STS turning method in cutting hexagonal microlens arrays, and then ductile machining of hexagonal microlens arrays will be attempted on single crystal silicon.

7.3.1 Mechanism of Segment Turning

Conventionally, when machining concave microlens arrays, all lenslets are continuously machined in a single turning cycle, as shown in Fig. 14a. Continuous STS turning leads to excessive Z -axis acceleration at the sharp-edge boundaries among the lenslets, and this causes dynamic errors of the machine tool. In segment STS turning, however, as shown in Fig. 14b, the lenslets are divided into multiple groups where the lenslets in each group are separated from each other and each group of lenslets is machined in a single turning cycle. In this way, the sudden change in direction of the tool path is avoided, which reduces the Z -axis acceleration. This method improves the motion accuracy of the machine tool, and in turn, the resulting lens accuracy.

7.3.2 Effectiveness Verification of Segment Turning

To investigate the effectiveness of segment turning method, hexagonal microlens arrays, which consist of sharp edges among lenslets, were machined by continuous STS turning and segment STS turning, respectively, and the results were compared. To avoid the effects of tool wear, an aluminum alloy A5056 workpiece was used for this comparison experiments. The workpiece was 10 mm in diameter and each lenslet had a concave spherical surface with a radius of 25 mm and a hexagonal shape with a side length of 500 μm . The lenslet sag was 5 μm . An ultraprecision lathe Nanoform X (AMETEK Precitech Inc.) having an STS system was used in the experiments. A single-crystal diamond tool with a nose radius of 0.1 mm, a rake angle of 0° and a relief angle of 6° was used. Oil mist was used for lubrication and cooling during cutting. In order to compare the two methods in terms of cutting speed and machining time, the spindle rotation rate (N) of continuous turning was set to two levels: one is the same as that of segment turning (45 rpm) and the other is one third of that of segment turning (15 rpm), respectively.

Figure 15a shows the distribution of divided lenslet groups in segment turning. In the present test cut, the whole lens array was divided into three groups which were cut sequentially. In a single turning cycle, circular lenslets were cut as shown in Fig. 15b and then hexagonal shape was formed by overlapping the circular lenslets as shown in Fig. 15c. In addition, the outer region of each lenslet had an approach zone for the tool as described by the dashed circle in Fig. 15b and the dashed line in Fig. 15d. The approach zone was designed to make the tool path smooth without sharp turning points. In both continuous turning and segment turning, control points (a control point is a member of a set of points used to determine the shape of a spline curve) were calculated at a constant angular step (2°) on the spiral tool path trajectory around the spindle axis. Linear interpolation was adopted among adjacent control points.

7.3.2.1 Lens Topographical Error

Figure 16 shows a photograph of a microlens array sample machined by segment STS turning at $N = 45$ rpm, which has a mirror finish. The sample surface was then observed using a differential interference contrast microscope. Figure 17 shows microscope images of lenslets machined by continuous turning at different spindle rotation rates, as well as by segment turning. Two groups of images are shown: the lenslets around the workpiece center and those located at an outer region around $x = 0$ mm and $y = 3.0$ mm. From these images, it is clear that the lens edges got blunt and disordered in continuous turning as the distance from the workpiece center increased. In contrast, very sharp edges were generated across the workpiece surface machined by segment turning.

Figure 18 shows three-dimensional topographies of lenslets the center of which are located at $x = 0$ mm, $y = 1.5$ mm, and cross-sectional profiles of lenslets measured along x -axis through the lenslet centers as indicated by the red

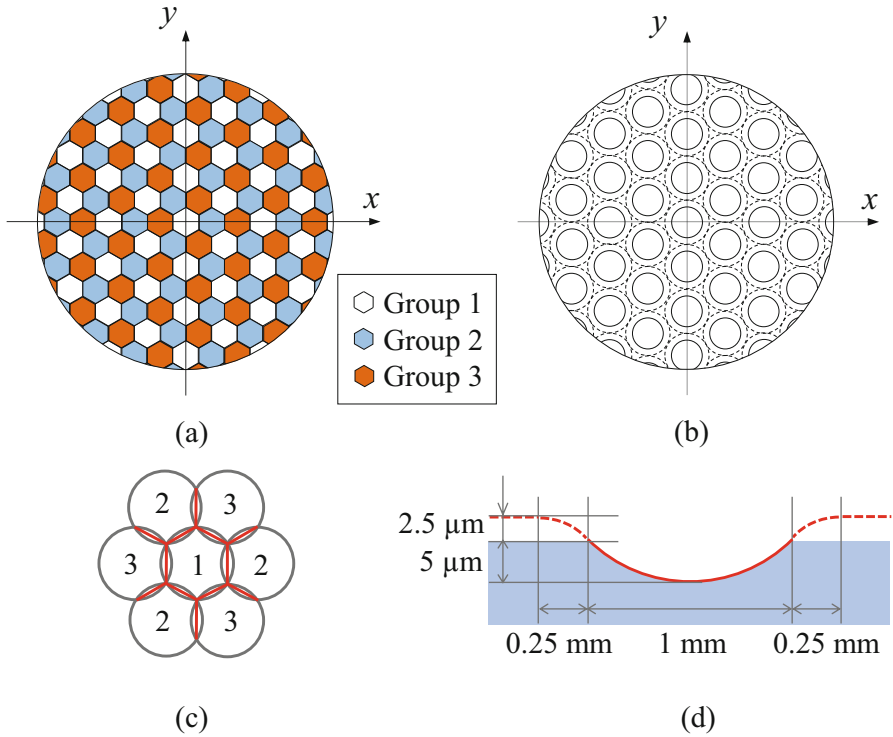


Fig. 15 Tool path generation for segment turning: (a) schematic of segments, (b) dimples generated in a single cycle, (c) generation of hexagonal shape, and (d) tool path for each lenslet

Fig. 16 Photograph of a hexagonal microlens array on aluminum alloy machined by segment STS turning at $N = 45\ \text{rpm}$



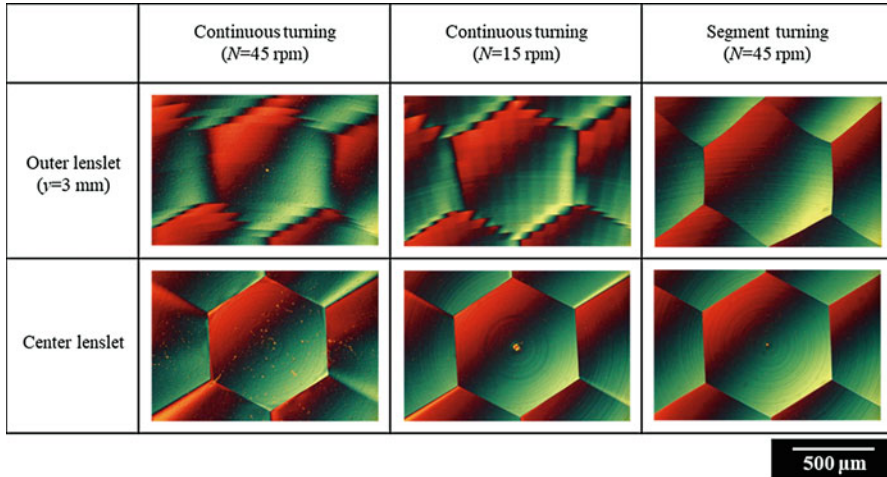


Fig. 17 Differential interference contrast microscope images of lenslets machined by continuous turning at different spindle rotation rates, as well as by segment turning

dashed lines in the three-dimensional topographies. By comparing the theoretical profiles and the measured profiles, form error distributions were obtained and plotted in Fig. 18. The results show that the peak-to-valley (P-V) value of the cross-sectional form error in segment turning was $0.35 \mu\text{m}$, 24% of that in continuous turning ($1.44 \mu\text{m}$) at the same spindle rotation rate ($N = 45$ rpm), and 76% of that in continuous turning ($0.46 \mu\text{m}$) for the same machining time but at a lower spindle rotation rate ($N = 15$ rpm). This means that segment turning offers higher productivity than continuous turning. In addition, a large form error was found in the right side of the plots. Since the cutting direction was in the x -axis negative direction, the form error increased just after passing lenslet edges. Thus, it can be said that lenslet edges induced significant form errors and these form errors can be effectively reduced in segment turning.

7.3.2.2 Measurement of Machine Tool Dynamic Error

To investigate the dynamic errors of the machine tool, the Z -axis position was measured by using the real-time process monitoring system equipped in the machine tool itself and compared with command position. Then, the Z -axis position error was calculated from the difference between the command position and the actual position, and the Z -axis acceleration was calculated from the change of the actual position, respectively. Figure 19 shows the plots of command positions, actual positions, and accelerations in the left-side graphs and the plots of position errors in the right-side graphs. In the figure, the measurements were performed during a period of 0.75 s after the tool passes the point $X = 1.5$ mm in order to compare with the profile error shown in Fig. 18.

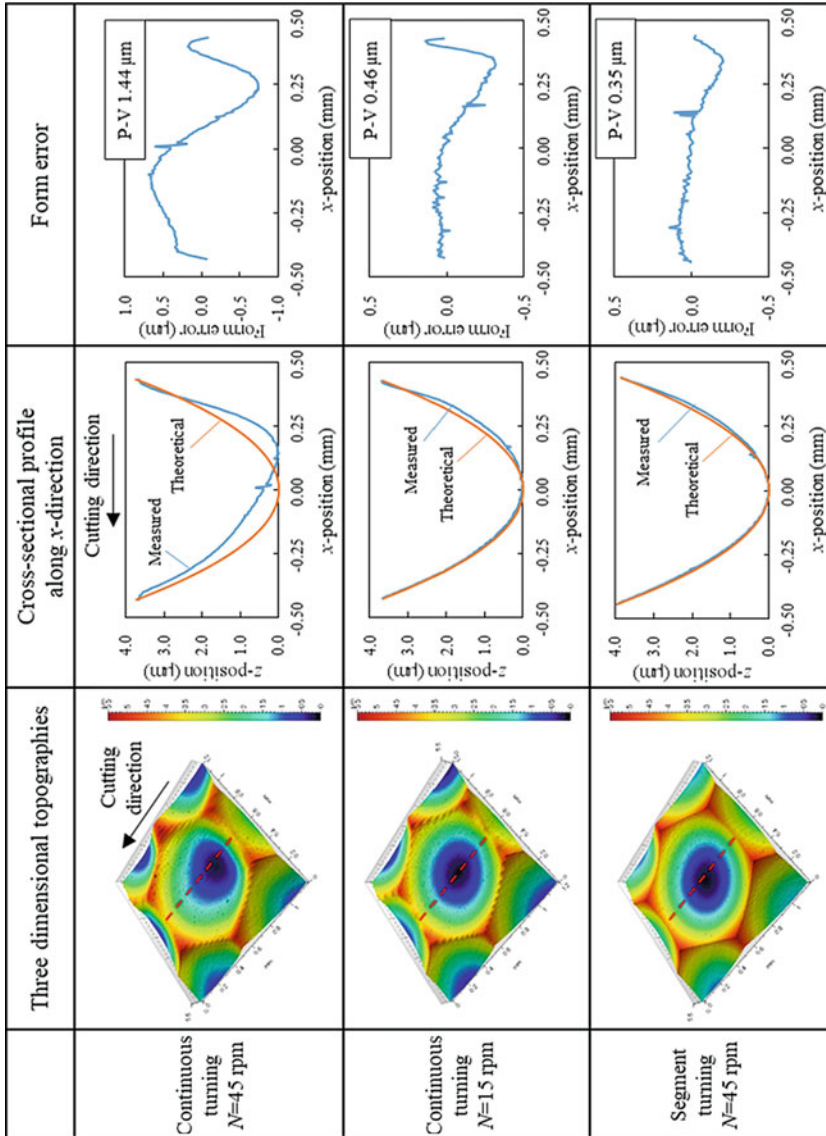


Fig. 18 Three-dimensional topographies and cross-sectional profiles of lenslets the centers of which are located at $x = 0$ mm, $y = 1.5$ mm

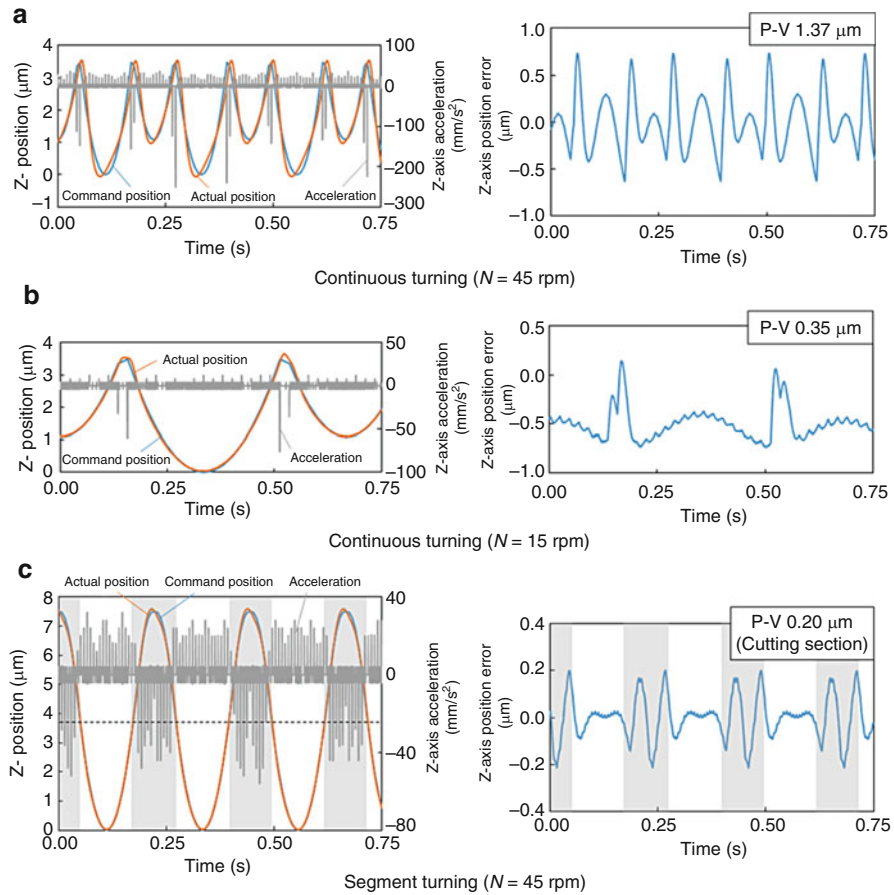


Fig. 19 Plots of command positions, actual positions, and accelerations (*left-side graphs*), as well as position errors (*right-side graphs*) for continuous turning and segment turning

In continuous turning at $N = 45 \text{ rpm}$, the absolute value of acceleration at the lenslet edges was so large that it led to a significant delay in the Z-axis motion of the machine table ($1.37 \mu\text{m}$ P-V). When the spindle rotation rate is decreased to $N = 15 \text{ rpm}$, the acceleration decreased too, causing a decrease in the Z-axis position error to $0.35 \mu\text{m}$ P-V. However, in segment turning at $N = 45 \text{ rpm}$, the acceleration was reduced by a factor of five compared to that in continuous turning at the same spindle rotation rate, which accordingly reduced position error of cutting section ($Z \leq 3.75 \mu\text{m}$) to $0.20 \mu\text{m}$ P-V. The trend of Z-axis position error was almost the same as that of the lens form error shown in Fig. 18, which means the lens form error was mainly caused by the dynamic error of the machine tool. Figure 19 demonstrates strongly that even if the Z-axis acceleration can be reduced by decreasing the spindle rotation rate in continuous turning, it is still significantly higher than that in segment turning.

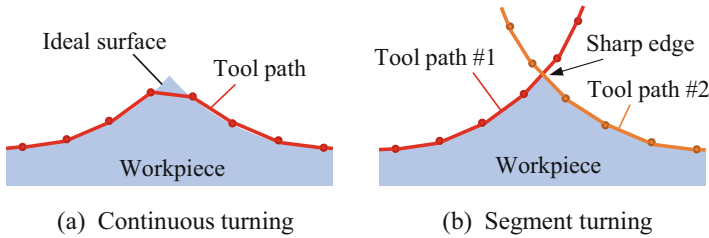


Fig. 20 Effect of linear interpolation on lens edge formation for (a) continuous turning and (b) segment turning

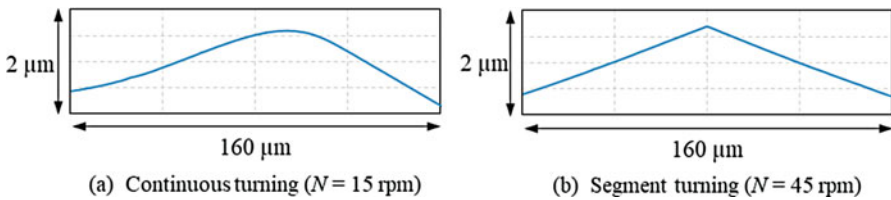


Fig. 21 Magnified cross-sectional profiles of lens edges measured using a white light interferometer, showing a blunt edge for (a) continuous turning and a sharp edge for (b) segment turning

An important factor affecting lens edge formation is interpolation. In STS turning, a freeform surface is generated by calculating coordinates of a finite number of control points on the objective surface and interpolating between these points. Linear interpolation and spline interpolation are two major methods for interpolation. Spline interpolation is suitable for making a smooth tool path, but cannot be used to generate sharp edges. To generate a sharp edge by continuous STS turning, linear interpolation is necessary. However, as shown in Fig. 20a, a sharp edge cannot be formed in continuous turning when the number of control points is not adequate to envelope the edge through linear interpolation. In segment turning, however, the tool path is not affected by interpolation method, as shown in Fig. 20b. This greatly improves the edge accuracy. The differences in tool paths at lenslet edges between continuous turning and segment turning can be confirmed in the left-side graphs of Fig. 19a–c. In addition, Fig. 21 shows magnified cross-sectional profiles of lens edges at $y = 0.75$ mm measured using a white light interferometer. In continuous turning (Fig. 21a), the edge is very dull, with a radius of several hundred microns. In segment turning (Fig. 21b), however, the edge becomes so sharp that the radius of which is hard to identify even at the available magnification of the white light interferometer used in this study.

7.3.2.3 Modelling of Machine Tool Dynamic Error

In order to predict the dynamic errors caused by an STS system in freeform surface generation, it is important to establish a theoretical model for the control system. The

Fig. 22 Block diagram of the feedback control system model for an STS system

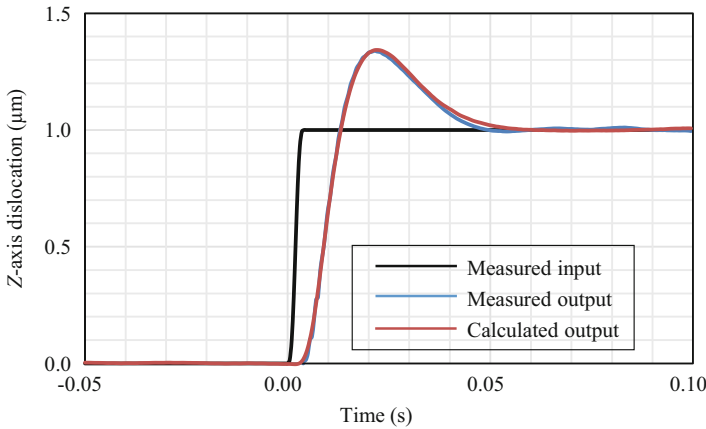
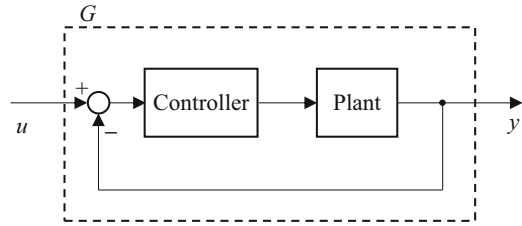


Fig. 23 Measured and calculated step responses of the STS system

actual control system of the STS machine tool might be very complex with a complicated transfer function (Yu et al. 2011b). In this chapter, for simplicity, the STS system was modeled as an open-loop system described by transfer function G according to the direct approach (Hjalmarsson 2005), as shown in Fig. 22.

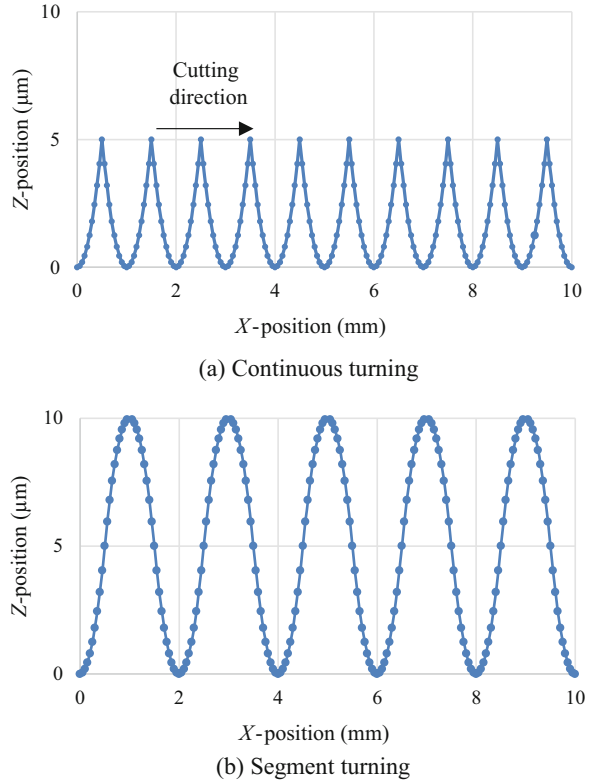
To identify the transfer function G , the actual step response of the STS system was experimentally measured. A Z-axis displacement of $1\ \mu\text{m}$ at a velocity of $1\ \text{mm/s}$ was input to the machine tool as a step input and the output was measured by the real-time process monitoring system of the machine. The results are shown in Fig. 23. Then, the transfer function G is assumed to be an ARX model as follows (Hjalmarsson 2005):

$$A(q) = 1 + a_1q^{-1} + \dots + a_{n_a}q^{-n_a} \tag{3}$$

$$B(q) = b_1q^{-1} + \dots + b_{n_b}q^{-n_b} \tag{4}$$

$$y(k) = \frac{q^{-d}B(q)}{A(q)}u(k) + e(k) = G(q)u(k) + e(k) \tag{5}$$

Fig. 24 Input tool paths for calculating machine tool position errors when cutting concave spherical lenslets



where $u(k)$ is input and $y(k)$ is output at time k , q is shift operator and $e(k)$ is disturbance at time k . Thus, the transfer function G can be determined by n_a , n_b , d and $a_1 \dots a_{na}$, $b_1 \dots b_{nb}$. These parameters were identified by least squares method fitting using the MATLAB System Identification Toolbox as step response of the identified transfer function meets the step response experimentally measured. The calculated step response with these parameters is also shown in Fig. 23 and it is confirmed that the calculated result matches well with the experiments.

Then, the model was used to calculate dynamic errors of various tool paths for microlens array machining. Two typical input tool paths as shown in Fig. 24 were used to generate lenslets having concave spherical surfaces with a depth of $5 \mu\text{m}$ and a pitch of 1 mm . Control points were set at an interval of $50 \mu\text{m}$ along X -direction and linear interpolation was used. The tool path of segment turning included noncutting sections between lenslets, the shape of which was the reversed lenslet shape. Cutting speed was set to 7 mm/s and 2.3 mm/s on the assumption of turning at spindle rotation rates $N = 45 \text{ rpm}$ and $N = 15 \text{ rpm}$ by a distance of 1.5 mm from the spindle rotation center. These conditions correspond to those of position error measurement shown in Fig. 19.

Figure 25 shows results of calculated Z -axis positions and position errors. In continuous turning, very large position errors occur at sharp edges even if the cutting speed is low. In segment turning, however, the P-V value of the position error is

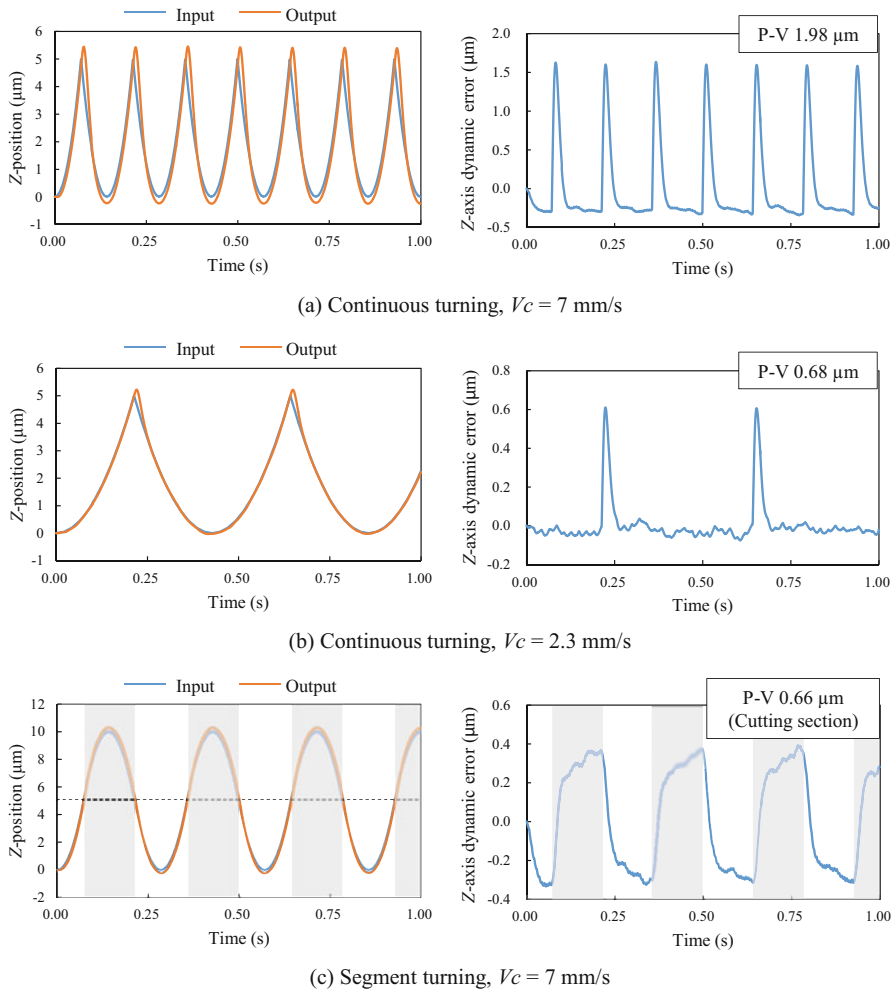


Fig. 25 Calculated Z-axis positions (left-side graphs) and position errors (right-side graphs) for continuous turning and segment turning using an STS system

smaller than that in continuous turning; 33% of that in continuous turning at the same cutting speed ($V_c = 7$ mm/s) and 97% of that at the one-third cutting speed ($V_c = 2.3$ mm/s). Under the same conditions, the measured P-V value of position error of segment turning was 15% and 57%, respectively, of that in continuous turning. Larger dynamic errors in the calculated models might be due to the control system simplification. In addition, the ultraprecision machine tool we used in this study had an STS control system involving adaptive control, where the control system was continuously optimized during machining, and thus the dynamic errors were suppressed effectively.

The distribution of the calculated position error had similar tendency as that of the measured results. From these facts, it might be said that the calculated results are

comparable to the measured results and machine tool position errors can be approximately estimated by the prediction model used in this study. This model can help to generate tool path and decide machining parameters for nonrotationally symmetric surfaces.

Thus, by using the segment turning method, a machine tool equipped with an STS system can be directly used for fabricating high-precision freeform and structured surfaces having sharp edges, without need for introducing machine add-ons such as FTS and so on. This will greatly extend the application fields of the STS-driven ultraprecision machine tools in advanced manufacturing industries for optics, optoelectronics, and micromechanical elements.

7.3.3 Fabrication of Hexagonal Microlens Array on Silicon

Hexagonal microlens arrays were machined on a single crystal silicon (001) wafer using the segment STS turning method. Each lenslet has a concave spherical surface with a curvature radius of 2.563 mm and a hexagonal shape with a side length of 160 μm . The lenslet sag is 5 μm . The whole lens array was divided into three groups of lenslets in the same way as described in Fig. 15. A single crystal diamond tool with a nose radius of 1 mm, a rake angle of -30° , and a flank angle of 36° was used. Feed rate f was determined based on the results of dimple cutting experiments as reported in Sect. 2. In this experiment, control points were calculated at a constant angular step of 1° on the spiral tool path trajectory around the spindle axis, and spline interpolation was adopted among adjacent control points to describe the ideal lenslet surface more precisely.

7.3.3.1 Lens Form Accuracy

Figure 26 shows a photograph of a hexagonal microlens array having 58 lenslets machined on a single crystal silicon wafer (001) plane. It took about 2 h for machining. Figure 27 shows a differential interference contrast microscope image of the hexagonal microlens array. No cracks were found on the machined lenslet surfaces, which means

Fig. 26 Photograph of a hexagonal microlens array machined on a single crystal silicon wafer

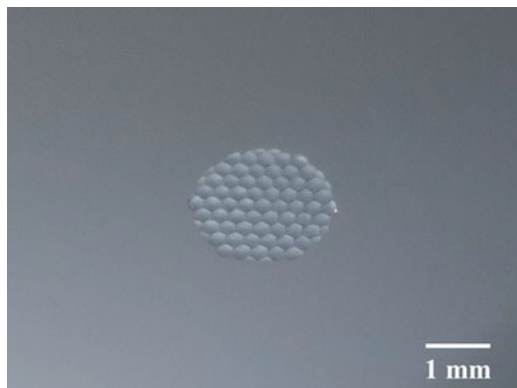


Fig. 27 Differential interference contrast microscope image of the hexagonal microlens array

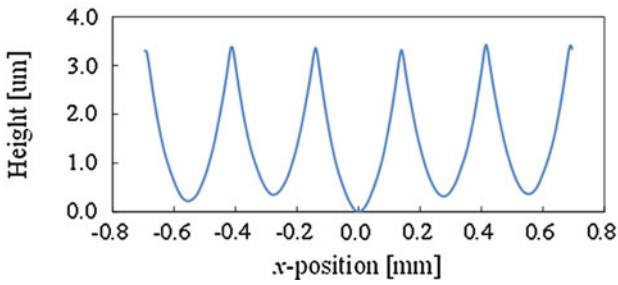
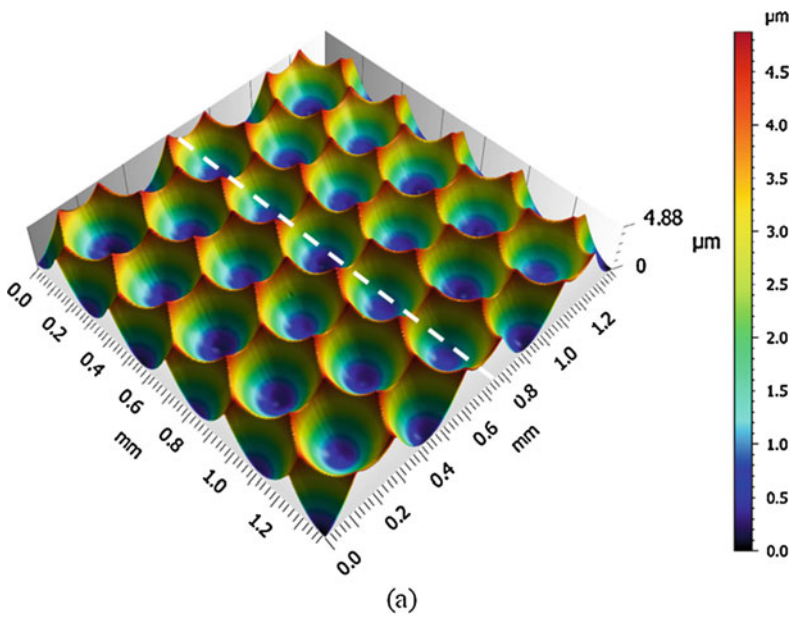
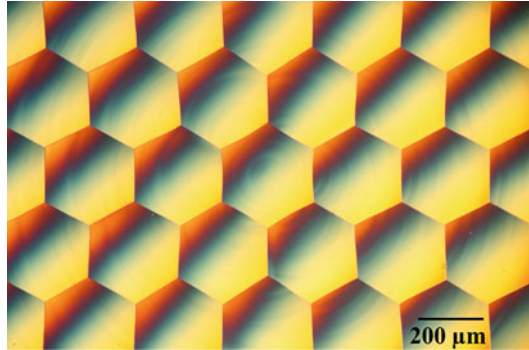


Fig. 28 Lens shape measurement results: (a) three-dimensional topography of a hexagonal microlens array and (b) cross-sectional profile measured along the white dashed line shown in (a)

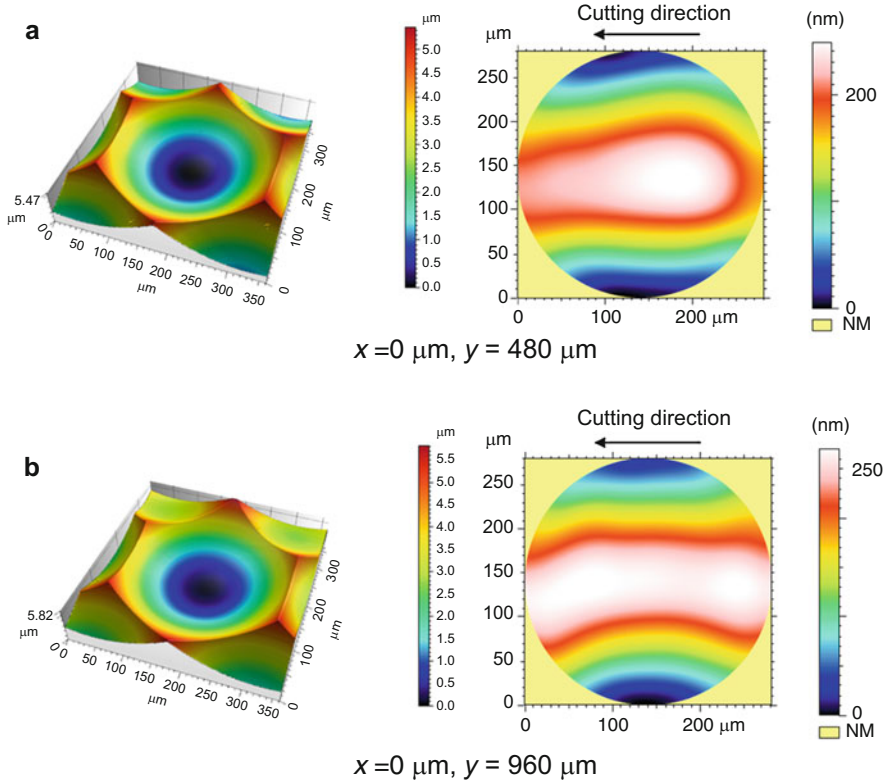


Fig. 29 Three-dimensional topographies of lenslets at different locations and their form error distributions

the microlens arrays were successfully machined in a ductile mode. In addition, sharp edges among the lenslets were precisely generated by the segment turning method.

Figure 28 shows a three-dimensional topography and cross-sectional profile along the white dashed line shown in Fig. 28a. It was confirmed that the lenslets have almost the same depth in the whole lens area. Figure 29 shows three-dimensional topographies and form error distributions of lenslets the center of which is located at $(x, y) = (0 \mu\text{m}, 480 \mu\text{m})$ and $(0 \mu\text{m}, 960 \mu\text{m})$. The P-V value of the form error measured was 270 nm (Fig. 29a) and 249 nm (Fig. 29b). The lenslet surface roughness was 4.8 nmSa (Fig. 29a) and 4.9 nmSa (Fig. 29b). The surface roughness was measured in a round area (diameter $300 \mu\text{m}$) in lenslet centers and calculated by removing the lens curvature and tilt. These results meet the requirement of infrared optical systems.

7.3.3.2 Evaluation of Subsurface Damage

To confirm subsurface damage containing amorphous silicon, laser micro-Raman spectroscopy (Yan et al. 2009) was performed to evaluate the degree of silicon amorphization on the machined lenslet surface. Raman mapping measurements

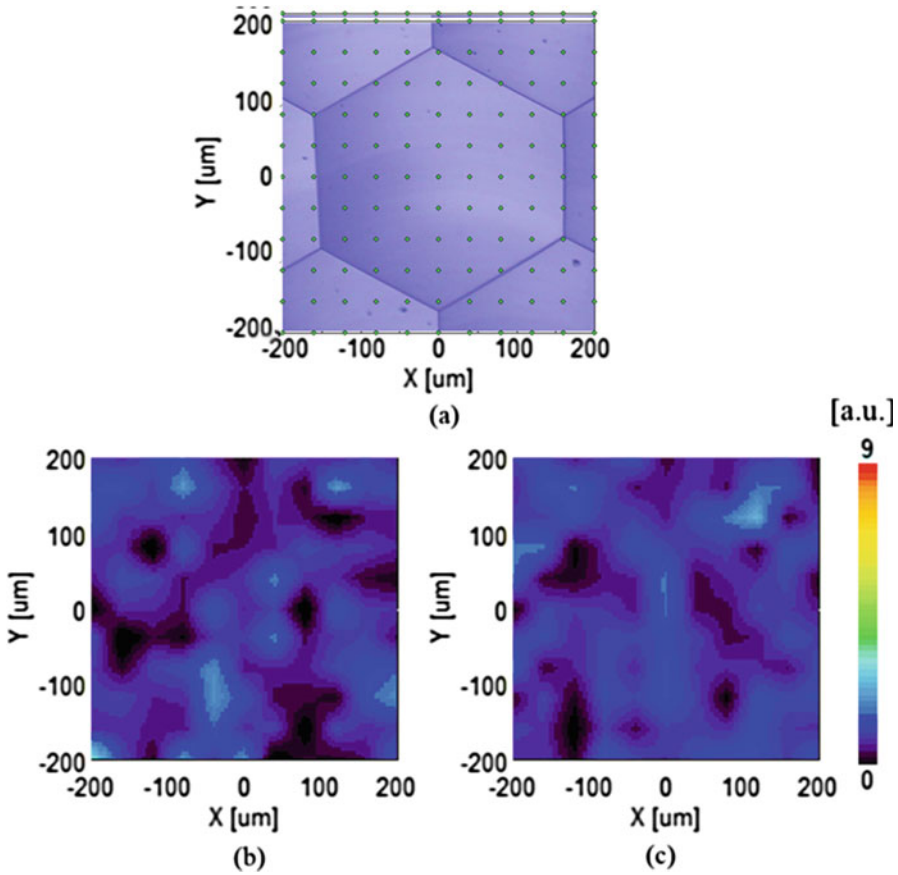


Fig. 30 Mapping measurement of peak intensity of amorphous silicon using a laser micro-Raman spectrometer: (a) distribution of measurement points; (b) mapping result for the lenslet located at $x = 0 \mu\text{m}$, $y = 480 \mu\text{m}$, and (c) $y = 960 \mu\text{m}$

were performed as shown by the dots in Fig. 30a. Figure 30b, c show mapping results of the peak intensity for amorphous silicon (470 cm^{-1}) for a lenslet located at $y = 480 \mu\text{m}$ and $960 \mu\text{m}$. Compared with the mapping result for a circular dimple machined at a higher feed rate shown in Fig. 5, less amorphous silicon was detected. It is thought that the cutting force induced at a small feed rate was so small that it did not cause significant phase transformation of silicon. Thus, the machined microlens arrays in this study have negligible subsurface damage and maybe used in infrared optical systems without any subsequent processing like polishing.

7.3.3.3 Tool Observation

The diamond tool was observed using a scanning electron microscope (SEM) after cutting hexagonal microlens arrays for a total cutting distance of 7.88 m. Figure 31 shows microscopic images and an SEM image of the tool edge. Material adhesion

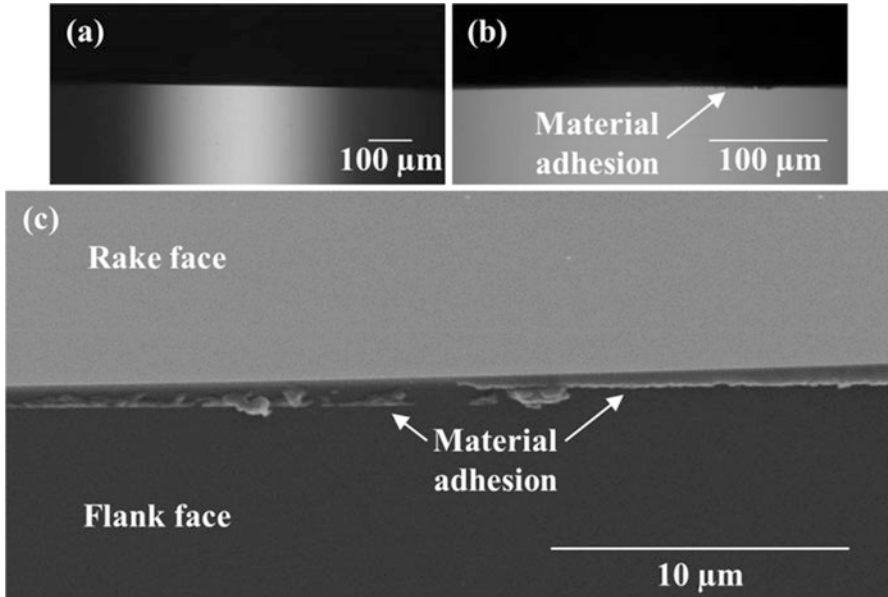


Fig. 31 Tool observation results: (a) microscope image of tool edge before cutting; (b) microscope image, and (c) Scanning electron microscope (SEM) image of the tool edge after cutting hexagonal microlens arrays on silicon

was found on the flank face. This maybe caused by the decrease of effective relief angle when the tool cuts into a lenslet. An extremely small relief angle leads to squeeze and adhesion of workpiece material onto the tool flank face. It is noteworthy that in Fig. 31, no obvious tool wear was observed. This demonstrated that tool wear was insignificant for such a short cutting distance. Especially, in the segment turning method, the tool/workpiece contact is intermittent, which enables the tool to be lubricated and cooled effectively. As a result, tool wear is significantly reduced compared to that in continuous turning (Yan et al. 2003).

7.4 Summary and Outlook

Microlens arrays of single crystal silicon was machined by STS diamond turning for advanced IR optics, and the machining mechanism was investigated by evaluating form error, surface topography, material phase transformation, cutting force characteristics, and tool wear. As a result, low-damage ductile mode cutting was achieved. Moreover, a tool-servo driven segment turning method was proposed for machining structured surfaces with sharp edges, such as hexagonal microlens arrays. This method can reduce the dynamic error of the machine tool induced by lenslet edges. From the results of both cutting experiments and theoretical analysis, it was demonstrated that the segment turning method reduced significantly the dynamic

errors and led to high form accuracy. Finally, sharp edges among the lenslets were generated precisely and microlens arrays with a form error of ~ 300 nm peak-to-valley and surface roughness of ~ 5 nmSa, which meets the requirements of infrared optical systems, were successfully fabricated.

Tool-servo driven diamond turning is a cost-effective method for the manufacturing of structured surface. It can be used for machining not only ductile metal materials, but also for hard and brittle materials such as optical crystals and glasses, ceramics, and so on. Two key factors should be considered in this process: one is the reduction of surface roughness and subsurface damage by optimizing the ductile mode cutting conditions, the other is the reduction of machine tool follow-up errors to improve the form accuracy. This technology will enable the manufacturing of functional surfaces for future high value-added products.

References

- Albero J, Nieradko L, Gorecki C, Ottevaere H, Gomez V, Thienpont H, Pietarinen J, Päivänranta B, Passilly N (2009) Fabrication of spherical microlenses by a combination of isotropic wet etching of silicon and molding techniques. *Opt Express* 17(8):6283–6292
- Arase H, Matsushita A, Itou A, Asano T, Hayashi N, Inoue D, Futakuchi R, Inoue K, Nakagawa T, Yamamoto M, Fujii E, Anda Y, Ishida H, Ueda T, Fidaner O, Wiemer M, Ueda D (2014) A novel thin concentrator photovoltaic with microsolar cells directly attached to a lens array. *IEEE J Photovoltaics* 4(2):709–712
- Asakura K, Yan J (2015) Water repellency control of oxygen-free copper surface by diamond-cut micro grooves. *Int J Autom Technol* 9(4):396–402
- Bitterli R, Scharf T, Herzig HP, Noell W, Rooij N, Bich A, Roth S, Weible KJ, Voelkel R, Zimmermann M, Schmidt M (2010) Fabrication and characterization of linear diffusers based on concave micro lens arrays. *Opt Express* 18(13):14251–14261
- Brinksmeier E, Gläbe R, Flucke C (2008) Manufacturing of molds for replication of micro cuve corner retroreflectors. *Prod Eng* 2:33–38
- Chang CY, Yang SY, Huang LS, Chang JH (2006) Fabrication of plastic microlens array using gas-assisted micro-hot-embossing with a silicon mold. *Infra Phys Technol* 48:163–173
- Chen CC, Huang CY, Peng WJ, Cheng YC, Yu ZR, Hsu WY (2013) Freeform surface machining error compensation method for ultra-precision slow tool servo diamond turning. In: *Proceedings of SPIE* 8838; 88380Y-1-8
- Chou MC, Pan CT, Shen SC, Chen MF, Lin KL, Wu ST (2005) A novel method to fabricate gapless hexagonal micro-lens array. *Sens Actuators A* 118:298–306
- Davis GE, Roblee JW, Hedges AR (2009) Comparison of freeform manufacturing techniques in the production of monolithic lens arrays. In: *Proceedings of SPIE* 7426, 742605–1-8
- Deng Z, Yang Q, Chen F, Meng X, Bian H, Yong J, Shan C, Hou X (2015) Fabrication of large-area concave microlens array on silicon by femtosecond laser micromachining. *Opt Lett* 40(9):1928–1931
- Fang FZ, Zhang XD, Hu XT (2008) Cylindrical coordinate machining of optical freeform surfaces. *Opt Express* 16(10):7323–7329
- Harvey JE, Schröder S, Choi N, Duparré A (2012) Total integrated scatter from surfaces with arbitrary roughness, correlation widths, and incident angles. *Opt Eng* 51(1):013402-1-11
- He P, Li L, Li H, Yu J, James Lee L, Yi AY (2014) Compression molding of glass freeform optics using diamond machined silicon mold. *Manuf Lett* 2:17–20
- Hjalmarsson H (2005) From experiment design to closed-loop control. *Automatica* 41:393–438
- Jeong KH, Kim J, Lee LP (2006) Biologically inspired artificial compound eyes. *Science* 312:557–561

- Kim J, Kim CJ (2002) Nanostructured surfaces for dramatic reduction of flow resistance in droplet-based microfluidics. In: The fifteenth IEEE international conference on micro electro mechanical systems, pp 479–482
- Kurniawan R, Kiswanto G, Ko TJ (2016) Micro-dimple pattern process and orthogonal cutting force analysis of elliptical vibration texturing. *Int J Mach Tools Manuf* 106:127–140
- Lalanne P, Morris GM (1997) Antireflection behavior of silicon subwavelength periodic structures for visible light. *Nanotechnology* 8:53–55
- Mukaida M, Yan J (2017a) Ductile machining of single-crystal silicon for microlens arrays by ultraprecision diamond turning using a slow tool servo. *Int J Mach Tools Manuf* 115:2–14
- Mukaida M, Yan J (2017b) Fabrication of hexagonal microlens arrays on single-crystal silicon using the tool-servo driven segment turning method. *Micromachines* 8:323
- Neo DWK, Kumar AS, Rahman M (2014) A novel surface analytical model for cutting linearization error in fast tool/slow slide servo diamond turning. *Precis Eng* 38:849–860
- Oliveira OG, Lima Monteiro DW, Costa RFO (2014) Optimized microlens-array geometry for Hartmann-shack wavefront sensor. *Opt Lasers Eng* 55:155–161
- Onozawa K, Tshikiyo K, Yogo T, Ishii M, Yamanaka K, Matsuno T, Ueda D (2008) A MOS image sensor with a digital-microlens. *IEEE Trans Electron Devices* 55(4):986–991
- Ottevaere H, Cox R, Herzig HP, Miyashita T, Naessens K, Taghizadeh M, Völkel R, Woo HJ, Thienpont H (2006) Comparing glass and plastic refractive microlenses fabricated with different technologies. *J Opt A Pure Appl Opt* 8:S407–S429
- Ow YS, Breese MBH, Azimi S (2010) Fabrication of concave silicon micro-mirrors. *Opt Express* 18(14):14511–14518
- Patterson SR, Magrab EB (1985) Design and testing of a fast tool servo for diamond turning. *Precis Eng* 7(3):123–128
- Rakuff S, Cuttino JF (2009) Design and testing of a long-range, precision fast tool servo system for diamond turning. *Precis Eng* 33:18–25
- Scheidung S, Yi AY, Gebhardt A, Loose R, Li L, Risse S, Eberhardt R, Tünnermann A (2011) Diamond milling or turning for the fabrication of micro lens arrays: comparing different diamond machining technologies. In: *Proceedings of SPIE 7927, 79270N-1-11*
- Stevens R, Miyashita T (2010) Review of standards for microlenses and microlens arrays. *The Imaging Sci J* 58(4):202–212
- Sze-Wei G, Han-Seok L, Rahman M, Watt F (2007) A fine tool servo system for global position error compensation for a miniature ultra-precision lathe. *Int J Mach Tools Manuf* 47:1302–1310
- Wang H, Yang S (2013) Design and control of a fast tool servo used in noncircular piston turning process. *Mech Syst Signal Process* 36:87–94
- Weck M, Hennig J, Hilbing R (2001) Precision cutting processes for manufacturing of optical components. *Proc SPIE 4440:145–151*
- Yan J, Syoji K, Tamaki J (2003) Some observations on the wear of diamond tools in ultra-precision cutting of single-crystal silicon. *Wear* 255:1380–1387
- Yan J, Asami T, Harada H, Kuriyagawa T (2009) Fundamental investigation of subsurface damage in single crystalline silicon caused by diamond machining. *Precis Eng* 33:378–386
- Yan J, Asami T, Harada H, Kuriyagawa T (2012) Crystallographic effect on subsurface damage formation in silicon microcutting. *CIRP Ann* 61:131–134
- Yi AY, Li L (2005) Design and fabrication of a microlens array by use of a slow tool servo. *Opt Lett* 30(13):1707–1709
- Yu DP, Wong YS, Hong GS (2011a) Ultraprecision machining of micro-structured functional surfaces on brittle materials. *J Micromech Microeng* 21(9):11
- Yu DP, Hong GS, Wong YS (2011b) Integral sliding mode control for fast tool servo diamond turning of micro-structured surfaces. *Int J Autom Technol* 5:4–10
- Yu DP, Hong GS, Wong YS (2012) Profile error compensation in fast tool servo diamond turning of micro-structured surfaces. *Int J Mach Tools Manuf* 52:13–23
- Zhang X, Fang F, Yu LH, Jiang L, Guo Y (2013) Slow slide servo turning of compound eye lens. *Opt Eng* 52(2):023401-1-7

Part II

Abrasive/Tip-Based Machining Technology



Micro-/Nano-texturing by Ultrasonic-Assisted Grinding

8

Masayoshi Mizutani, Shaolin Xu, Keita Shimada, and
Tsunemoto Kuriyagawa

Contents

8.1	Introduction	248
8.1.1	Micro-/Nano-texturing Technologies	248
8.1.2	Rotary Ultrasonic Texturing	249
8.2	Development of Equipment for Rotary Ultrasonic Texturing	250
8.3	Proposed UASG Method	254
8.3.1	The Calculation of the Cutting Loci	256
8.3.2	Conventional Grinding and Slant-Feed Grinding	258
8.3.3	Surface Texturing Mechanisms	260
8.4	Experimental Verification and Discussion	262
8.4.1	Experimental Conditions	262
8.4.2	Experimental Results	262
8.4.3	Limitations of the UASG Technique	266
8.5	Rotary Ultrasonic Texturing Using One-Point Diamond Tools	268
8.5.1	Theories of Texturing Mechanisms	268
8.5.2	Texturing Procedures and Corresponding Cutting Loci	274
8.5.3	Design of Geometrically Defined One-Point Diamond Tools	275
8.5.4	Modeling of the Surface Generation Process	278
8.5.5	Fabrication of Micro-/Nano-textures	286
8.5.6	Discussion	297
8.6	Summary and Outlook	298
	References	298

M. Mizutani (✉)

Tohoku University, Sendai, Japan

Department of Mechanical Systems Engineering, Graduate School of Engineering, Tohoku University, Sendai, Japan

e-mail: mizutani@m.tohoku.ac.jp

S. Xu

Southern University of Science and Technology, Shenzhen, Guangdong, China

K. Shimada · T. Kuriyagawa

Tohoku University, Sendai, Japan

© Springer Nature Singapore Pte Ltd. 2018

J. Yan (ed.), *Micro and Nano Fabrication Technology*, Micro/Nano Technologies,

https://doi.org/10.1007/978-981-13-0098-1_8

247

Abstract

In this chapter, a novel ultrasonic-assisted micro-/nano-texturing method was proposed and developed. A new 3D ultrasonic vibration spindle was developed for carrying out the proposed processes. The texturing mechanisms were analyzed by mathematically calculating the cutting loci and establishing the surface generation modeling processes. Finally, the tool design principles were proposed and experimentally verified. The experimental results and theoretical analysis proved that the proposed method can rapidly and precisely fabricate tailored surface textures at micrometer and nanometer scales.

Keywords

Micro-/nano-texturing · Ultrasonic assisted grinding · Textured surface · Functional surface

8.1 Introduction

8.1.1 Micro-/Nano-texturing Technologies

Methods for fabricating textured surfaces comprising micro-/nanostructures have been exploited in many industries (Masuzawa 2000).

Conventional diamond machining processes, including turning, cutting, milling, microgrinding, and fly cutting, produce surface textures by removing the material using mechanical forces. These methods are capable of machining ultraprecise microstructures (Brinksmeier et al. 2012; Denkena et al. 2010), which are usually fabricated on mold inserts when replicating structures on polymer or glass materials or are directly fabricated on engineering components. There are no specific material requirements for the machining objects because diamond has the highest hardness in nature. On the other hand, tool wear can be an issue, especially when machining ferrous metals. The reason for this is that the high machining temperature usually results in graphitization of the diamond by the ferrous metals (Shimada et al. 2004), which greatly accelerates tool wear and deteriorates surface quality. Surface textures at the submicrometer scale are also difficult to obtain using conventional diamond machining because the radius of the cutting edge is limited and cutting burrs on the edges of the microstructures are usually difficult to prevent or remove (Yan et al. 2009).

Besides using mechanical energy, optical energy and electrical energy are popularly utilized in the current industry, for example, laser beam machining (LBM) (Dubey and Yadava 2008) and electrical discharge machining (EDM) (Ho and Newman 2003; Abbas et al. 2007). Both methods provide optical or electrical energy to the work material, which is locally removed via melting and evaporation. Laser beam or electrical discharge can easily provide heat that exceeds the boiling point of any material. However, in practice, certain materials with low optical absorbance or low electrical conductivity cannot be processed by such methods; therefore, it is very difficult to obtain highly precise structures and surfaces using these methods. The heat-affected zone on the machined surface is also an inevitable problem. However,

with the development of the excimer laser and femtosecond laser, ultrashort laser pulses can be used to remove the material by vaporization; this mitigates the melting phase, which can help in obtaining high dimensional accuracy and fewer heat defects (Liu et al. 1997; Cheng et al. 2013). On the other hand, the machining efficiency is usually lower than that of LBM or EDM.

The micro-fabrication methods used in the microelectromechanical system (MEMS) field, including lithography, chemical etching, plasma etching, electron (or ion) beam etching, and oxidation, are capable of the fabrication of very complex structures at the micrometer and nanometer scales (Lyshevski 2002); these are widely used in the semiconductor industry. However, these methods do exhibit certain problems, such as the limitations of the machinable materials, complicated fabrication processes, and costly equipment. In addition, the fabrication processes are usually carried out in a direction perpendicular to the workpiece surfaces, which also restricts the machinable structures.

Replication processes (Hansen et al. 2011), including molding and embossing (or imprinting), can be used to fabricate microstructures at a relatively low cost and high efficiency. The textural patterns are directly reproduced from those of a die or a mold. However, the materials used for the dies must possess high-temperature strength, thus limiting the range of potential materials. A molding process is typically used when fabricating textures on glass, polymeric, or metal materials, which are melted and then solidified into a mold to replicate the structure. Only metals that exhibit good ductility and are softer than the die/mold materials can be used for the embossing process. A major problem with replication processes is the loss of shape accuracy.

Self-assembling methods like chemical vapor deposition (CVD) and physical vapor deposition (PVD) can be used for producing structures at micrometer and nanometer scales (e.g., nanotubes and nanowire) (Stupp et al. 1997; Shimomura and Sawadaishi 2001). However, these methods are limited to specific materials and are usually time-consuming and costly.

For the generation of geometrically defined surface textures, diamond machining methods have strong merits, including high form accuracy, high flexibility, and high productivity (Denkena et al. 2010). In recent decades, hybrid diamond machining processes, such as laser-assisted machining and ultrasonic-assisted machining, have been developed for improving diamond machining performance. For example, the laser-assisted turning process has been proved to have a higher material removal rate (Rozzi et al. 2000a, b) and to potentially suppress the generation of cutting burrs. The elliptical vibration-assisted cutting process has been proved applicable to machine brittle materials in the ductile regime, helping to decrease tool wear and improve surface quality (Shamoto and Moriwaki 1994; Moriwaki and Shamoto 1995).

8.1.2 Rotary Ultrasonic Texturing

Rotary ultrasonic machining has been widely used in grinding, drilling, and milling operations to fabricate flat surfaces, holes, and various surface structures (Brehl and Dow 2008). To study the effect of ultrasonic vibration on improvements in surface

quality in the 1D ultrasonic-assisted grinding process, K. Shimada (2012) established a theoretical calculation model for predicting the grinding forces and roughness of finished surfaces and found that some micro- and nanostructures could be fabricated using the ultrasonic-assisted slant-feed grinding (UASG) method.

The combination of ultrasonic vibration, tool rotation, and workpiece feed motion can lead to a high-frequency periodic change of the cutting locus of every cutting edge on the grinding wheel. The texturing principle is to fabricate surface textures at the micrometer/nanometer scale by intentionally controlling the cutting locus; the periodic features of the cutting locus can be of micrometer or submicrometer dimensions under appropriate experimental conditions. Until now, only one paper has reported the fabrication of micro-textures using 1D rotary ultrasonic machining with the principle mentioned above – D. Xing (2013) (Xing et al. 2013) studied the kinematics of cutting edges in a 1D ultrasonic-assisted milling process and fabricated a micrometer-scale scaly textured surface on aluminum alloy by controlling the high-frequency periodic change of the cutting locus. There has been no report on the fabrication of surface textures using a 3D rotary ultrasonic machining process, except for the previous work reported by the authors of the present dissertation (Xu et al. 2013, 2014).

In this chapter, a novel ultrasonic-assisted micro-/nano-texturing method that uses diamond grinding wheels or one-point diamond tools, referred to as the rotary ultrasonic texturing (RUT) method, is proposed and developed. A new 3D ultrasonic vibration spindle was firstly developed for carrying out the RUT processes. The surface generation processes were analyzed by mathematically calculating the cutting loci under different vibration modes. The material removal mechanisms were studied by analyzing the relationship between the geometry of the cutting edges and the related textural features. Then, the geometrically defined diamond tools were designed and manufactured for the RUT process, and surface generation models for the use of these tools were established for predicting the 3D surface textures.

8.2 Development of Equipment for Rotary Ultrasonic Texturing

The vibration mode depends on the structure of the ultrasonic vibrator. There are typically two types of ultrasonic vibrator, magnetostrictive and piezoelectric (Thoe et al. 1998). The resonant piezoelectric vibrator was selected for manufacturing the 3D ultrasonic vibration spindle in the present study. The vibrator is resonated by exciting several combined piezoelectric plates, which are sandwiched between metal cylindrical horns, with high-frequency electrical signals; this system is generally referred to as a bolt-clamped Langevin-type transducer (BLT) (Kurosawa et al. 1998). The high-frequency electrical energy is converted into mechanical vibration via the resonant piezoelectric transducer (PZT). The horn/tool assembly is used to amplify the vibration amplitude of the tool because the oscillation amplitude at the face of the piezoelectric transducer is too small to achieve a reasonable cutting rate.

Figure 1 shows two types of PZT system for generating the two basic ultrasonic vibration modes, the longitudinal vibration (LV) mode and the bending vibration (BV)

mode. In the LV mode, the tool vibrates along the axial (Z) direction, whereas in the BV mode, the tool vibrates in the transverse (XY) plane perpendicular to the axis. To produce the LV mode, the PZT comprises only one round piezoelectric plate, as shown in Fig. 1a. When a sinusoidal voltage is applied to the transducer, the piezoelectric plate expands and contracts so that the vibrator is resonated and the tool tip attached to the end of the horn vibrates in the LV mode along the Z axis. The vibration amplitude depends on the applied voltage, the material properties of the PZT, and the spindle structure. The vibration amplitude is magnified by the horns and is maximized at the tool tip. The 1D ultrasonic vibration spindle is widely used in the rotary ultrasonic processes. In Fig. 1b, if two half-round piezoelectric plates are placed on the PZT and two sinusoidal voltages with a 180-degree phase difference are applied to the piezoelectric plates, the two piezoelectric plates will expand and contract alternately. Ultimately, the tool attached to the end of the horn vibrates with the bending mode in the XY plane.

Various ultrasonic vibrators can be developed by combining the two basic PZT systems mentioned above. Figure 2 shows a type of ultrasonic vibrator that is capable of generating 2D vibration in the transverse (XY) plane. Four piezoelectric plates with the same resonant frequency are placed on the ultrasonic actuator. Thus, the specific shape of the vibration locus depends on the vibration amplitudes and phase difference of the applied sinusoidal voltages. If sinusoidal voltages with a 180-degree phase difference are applied to each pair of opposite piezoelectric plates, two BV modes can be generated simultaneously. With a certain phase difference of the two BVs, an elliptical or circular vibration mode can be generated in the transverse (XY) plane. For instance, by applying 0-, 90-, 180-, and 270-degree phase-shifted sinusoidal signals with the same amplitude in the clockwise direction on the four piezoelectric plates, a circular vibration (CV) can be generated.

In the present work, the PZT systems shown in Figs. 1a and 2 were further combined into one ultrasonic vibrator, as shown in Fig. 3, and a new 3D hybrid ultrasonic vibrator was designed and manufactured. The circular vibration was tuned

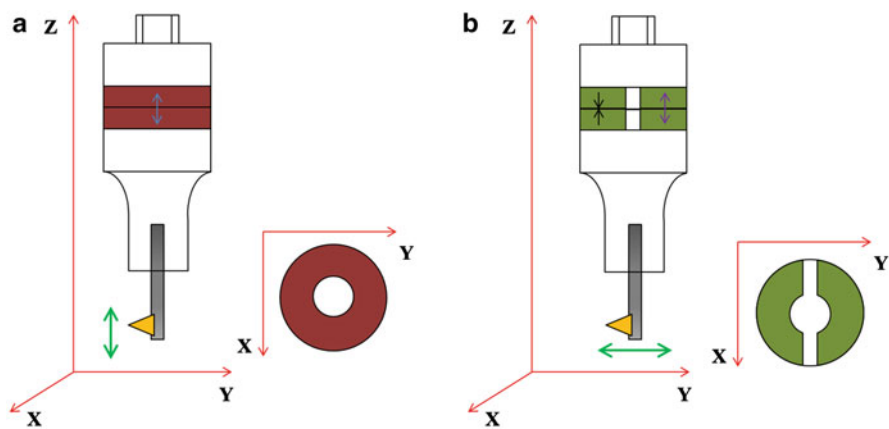


Fig. 1 Two types of PZT system for generating the two basic ultrasonic vibration modes: (a) LV mode and (b) BV mode (Xu et al. 2017)

Fig. 2 PZT systems for generating elliptical or circular vibration in the transverse plane (Xu et al. 2017)

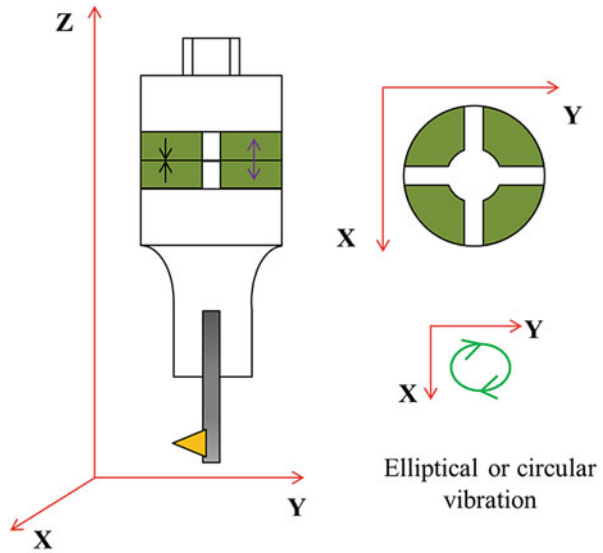
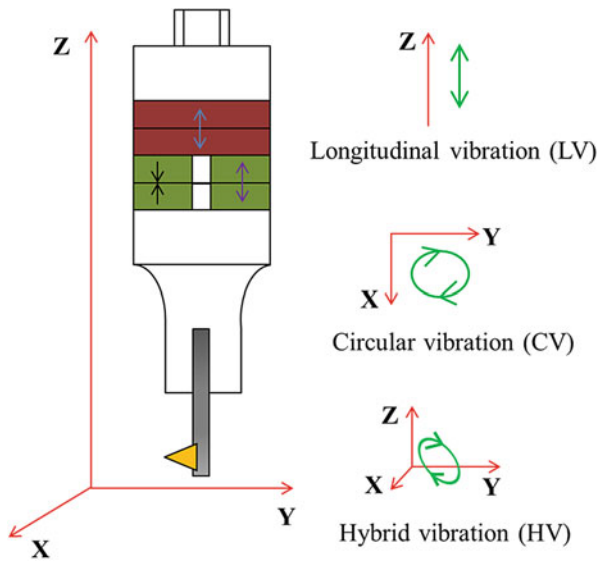


Fig. 3 PZT system used for manufacturing the 3D rotary ultrasonic spindle (Xu et al. 2017)



by modulating the parameters mentioned above for this vibrator. Therefore, by implementing the LV and CV modes simultaneously, the 3D ultrasonic vibrator can generate the LV mode along the axis (Z direction) of the spindle, the CV mode on the transverse (XY) plane, and 3D hybrid vibration (HV) in the 3D space. Figure 4 schematically shows the construction of the ultrasonic vibration spindle. As such, the main spindle is rotationally driven by a motor, the resonant

ultrasonic vibrator controlled by an ultrasonic oscillator is arranged coaxially to the spindle, step horns are integrally connected to the ultrasonic vibrator, and then, a tool (such as a grinding wheel or cutting tool) is mounted at the tip end of the horn.

On the basis of the proposed design principle described above, a 3D ultrasonic vibration spindle (SC-450SP-H24) was successfully manufactured by Taga Electric Co., Ltd. The rotary ultrasonic texturing processes were carried out using this spindle. Picture showing the 3D ultrasonic vibration spindle is shown in Fig. 5. Two types of tool, with the specifications shown in Fig. 6, were used. The specific parameters of the 3D ultrasonic spindle using the two types of tool are presented in Table 1.

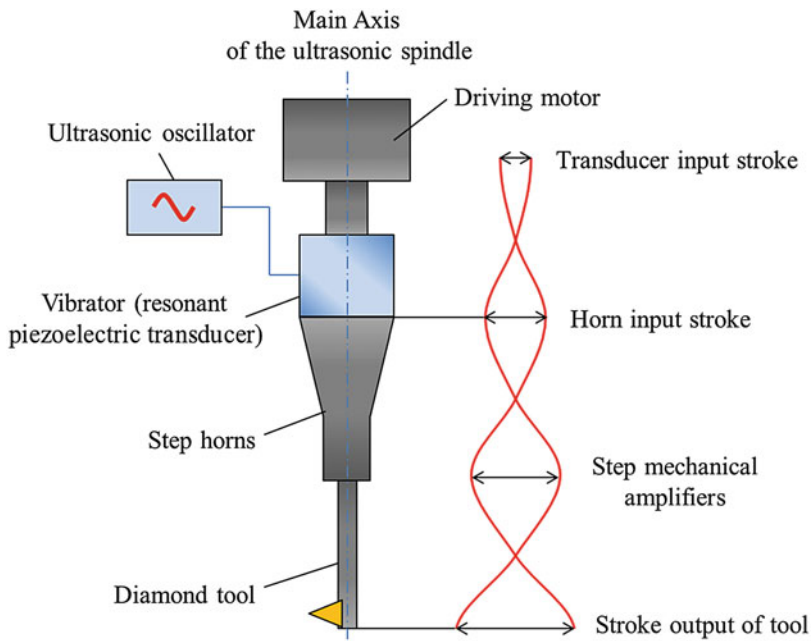


Fig. 4 Schematic of the construction of the 3D rotary ultrasonic spindle (Xu et al. 2017)

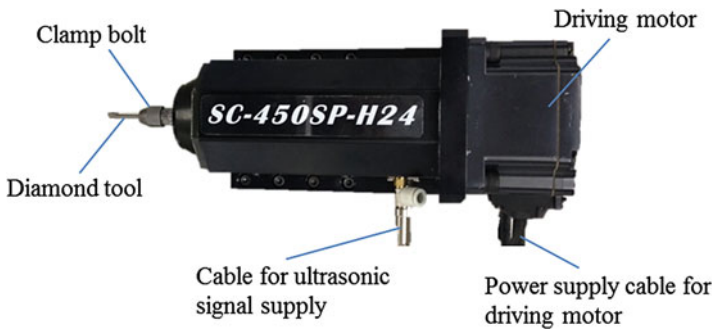


Fig. 5 3D ultrasonic vibration spindle

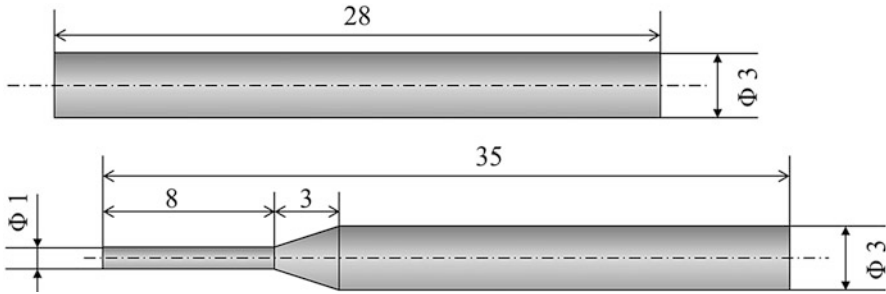


Fig. 6 Specifications of the two types of tool used in the work described in this chapter

Table 1 Specifications of the 3D ultrasonic vibration spindle

3D ultrasonic vibration spindle (SC-450SP-H24)	
Rotation speed	0–4000 rpm (stable at 0–3000 rpm)
Vibrator type	Bolt-clamped Langevin-type transducer (BLT)
Synchronizing system	Microcomputer-controlled phased-locked loop-type automatic synchronization system
Protruding length of tools/total tool length	15/35 mm 12/28 mm
Clamping torque of bolt	12.5 Nm
Vibration frequency (LV mode)	25.0 ± 3.0 kHz
Vibration frequency (CV mode)	19.0 ± 2.0 kHz
Vibration amplitude (LV mode)	1.5 μm (L) 3 μm (H)
Vibration amplitude (CV mode)	$10 \times 10 \mu\text{m}^2$ (L) $15 \times 15 \mu\text{m}^2$ (H)

A four-axis (XYZC) computer numerical control (CNC) precision machine tool (TRIDER-X) produced by the NEXSYS Corporation (as shown in Fig. 7) was used. The 3D ultrasonic vibration spindle is mounted to this machine tool to carry out the RUT process.

8.3 Proposed UASG Method

In the UASG method, the combination of ultrasonic vibration, rotation, and feed motion can lead to a high-frequency periodic cutting locus of each diamond abrasive on the grinding wheel. The cutting loci have periodic features at the micrometer/nanometer scales; these can be actively controlled for micro-/nano-texturing. However, the traditional UASG process does not possess such features, as will be explained in the next section. Therefore, the UASG method shown in Fig. 8 was proposed. Here the diamond grinding wheel rotates and vibrates at an ultrasonic frequency, with the feed direction slanted with respect to the horizontal direction (Y axis).

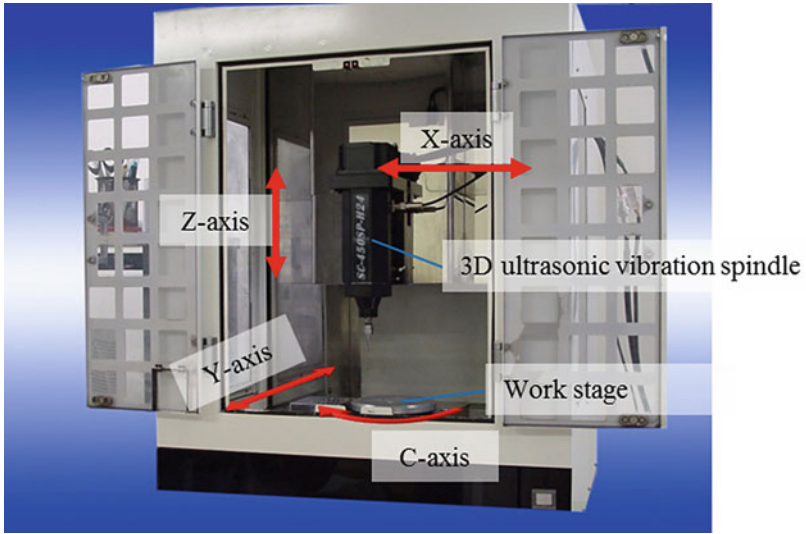


Fig. 7 Equipment used for the RUT process: an ultrasonic vibration spindle mounted on a CNC machine

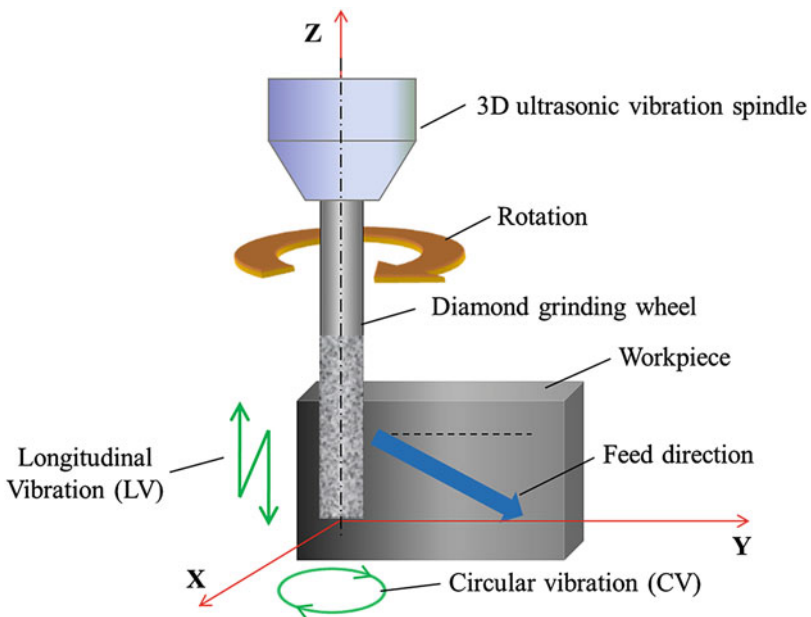


Fig. 8 Schematic of the UASG process (Xu et al. 2017)

8.3.1 The Calculation of the Cutting Loci

To determine the texturing mechanisms of the UASG technique, the kinematic motion of the diamond cutting abrasives should first be analyzed. The vibration loci in the LV, CV, and HV modes can be calculated by Eqs. (1), (2), and (3), respectively, as follows.

$$z(t) = A_l \sin(2\pi f_l t + \varphi_l) \quad (1)$$

$$\begin{cases} x(t) = A_c \sin(2\pi f_c t + \varphi_c) \\ y(t) = A_c \cos(2\pi f_c t + \varphi_c) \end{cases} \quad (2)$$

$$\begin{cases} x(t) = A_c \sin(2\pi f_c t + \varphi_c) \\ y(t) = A_c \cos(2\pi f_c t + \varphi_c) \\ z(t) = A_l \sin(2\pi f_l t + \varphi_l) \end{cases} \quad (3)$$

where subscripts l and c represent the LV and CV modes, respectively, and A , f , and φ are the amplitude, frequency, and initial phase angle of vibration, respectively. If the initial phase angles are assumed to be 0, the vibration loci in the LV, CV, and HV modes can be drawn as shown in Figs. 9, 10, and 11, respectively. The two-bending vibration pair in Fig. 10 has a 90-degree phase difference; therefore, a circular vibration locus is generated, as explained in Sect. 8.2. The vibration frequencies of the LV and CV modes are different; therefore, no periodic features can be observed in the vibration locus of the HV mode, as shown in Fig. 11.

In the tool-in-hand coordinate system shown in Fig. 8, the cutting locus of every diamond abrasive in the UASG process can be mathematically calculated using Eqs.

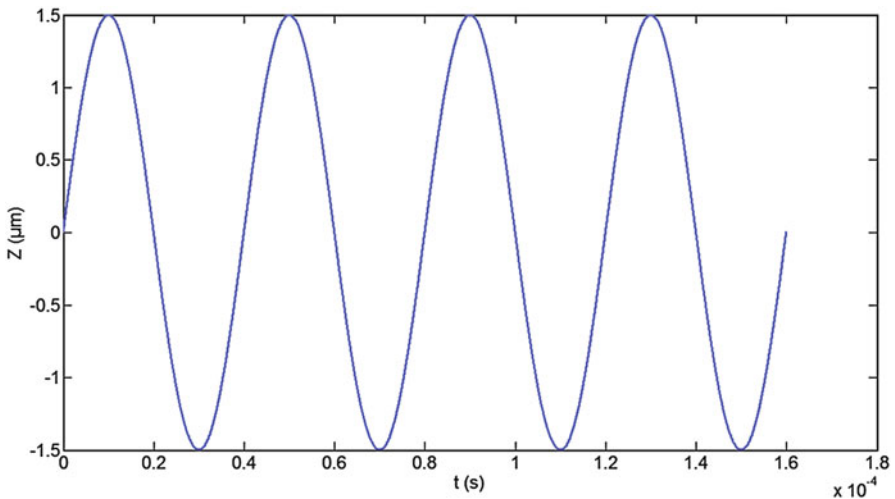


Fig. 9 Vibration locus of the LV mode ($f_l = 25$ kHz and $A_l = 3$ μm)

Fig. 10 Vibration locus of the CV mode ($f_c = 19$ kHz and $A_c = 10 \times 10 \mu\text{m}^2$)

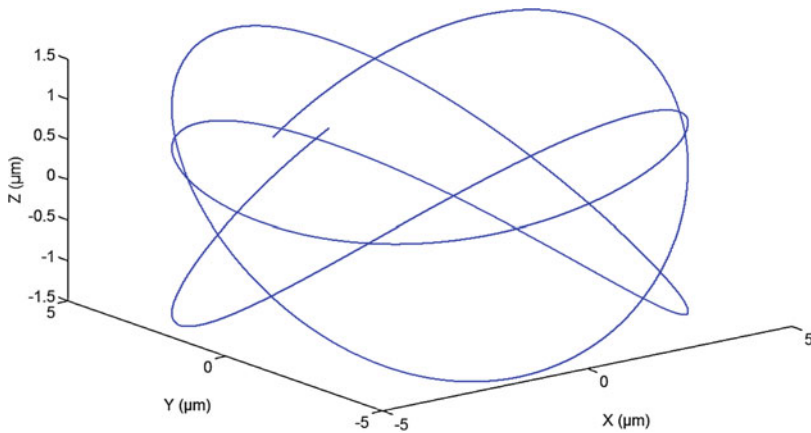
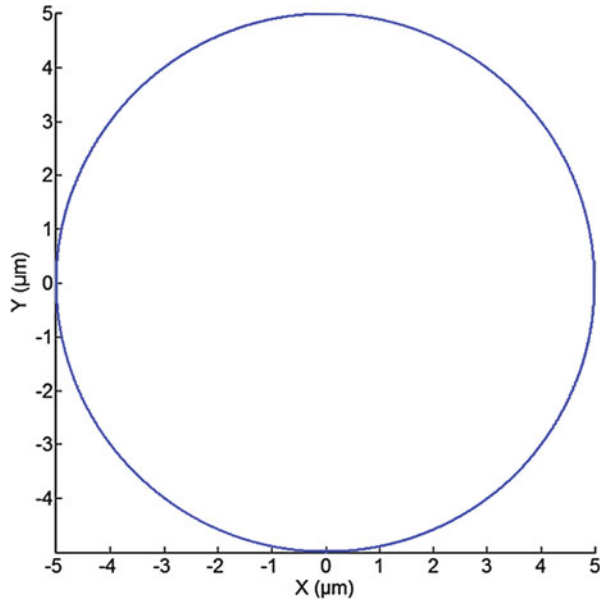


Fig. 11 Vibration locus of the HV mode during four LV periods ($f_l = 25$ kHz, $A_l = 3 \mu\text{m}$, $f_c = 19$ kHz, and $A_c = 10 \times 10 \mu\text{m}^2$)

(4), (5), and (6) in the LV, CV, and HV modes, respectively, where v_{fy} and v_{fz} are the feed speeds in the y and z directions, D is the tool diameter, h_p is the protrusion height of the diamond cutting abrasive, n_t is the rotational frequency of the diamond tool, and φ_r is the initial phase of the rotational motion.

$$\begin{cases} x = \left(\frac{D}{2} + h_p\right) \sin\left(\frac{2\pi n_t t}{60} + \varphi_r\right) \\ y = \left(\frac{D}{2} + h_p\right) \cos\left(\frac{2\pi n_t t}{60} + \varphi_r\right) + v_{fy} t \\ z = A_l \sin(2\pi f_l t + \varphi_l) + v_{fz} t \end{cases} \quad (4)$$

$$\begin{cases} x = \left(\frac{D}{2} + h_p\right) \sin\left(\frac{2\pi n_t t}{60} + \varphi_r\right) + A_c \sin(2\pi f_c t + \varphi_c) \\ y = \left(\frac{D}{2} + h_p\right) \cos\left(\frac{2\pi n_t t}{60} + \varphi_r\right) + A_c \sin(2\pi f_c t + \varphi_c) + v_{fy} t \\ z = v_{fz} t \end{cases} \quad (5)$$

$$\begin{cases} x = \left(\frac{D}{2} + h_p\right) \sin\left(\frac{2\pi n_t t}{60} + \varphi_r\right) + A_c \sin(2\pi f_c t + \varphi_c) \\ y = \left(\frac{D}{2} + h_p\right) \cos\left(\frac{2\pi n_t t}{60} + \varphi_r\right) + A_c \sin(2\pi f_c t + \varphi_c) + v_{fy} t \\ z = A_l \sin(2\pi f_l t + \varphi_l) + v_{fz} t \end{cases} \quad (6)$$

8.3.2 Conventional Grinding and Slant-Feed Grinding

Figure 12 schematically shows the difference between the conventional grinding (CG) and slant-feed grinding (SG) processes. In the SG process, the feed direction is slanted with respect to the Y axis, whereas in the CG process, the feed direction is horizontal along the Y axis.

The diamond abrasives on the grinding wheels are generally randomly distributed. The protrusion height of each abrasive on the surface of a grinding wheel determines its participation in the material removal process. Each abrasive removing material from the workpiece will create a cut track on the workpiece during the

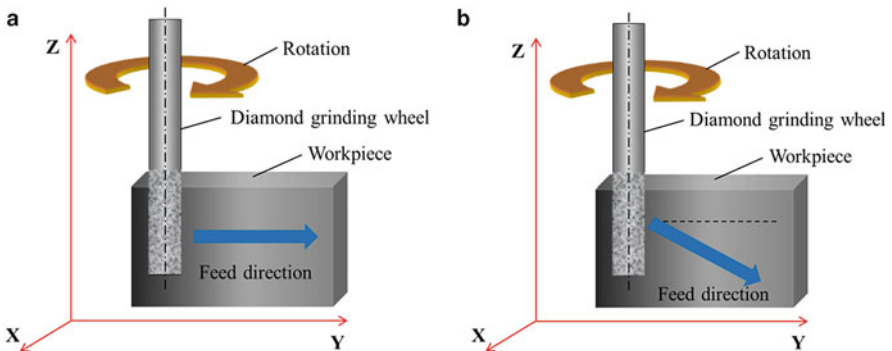


Fig. 12 Schematics of the (a) CG process and (b) SG process (Xu et al. 2017)

grinding process. To explain the differences between the CG and SG procedures, the term “effective cut track” is defined as the cut tracks remaining on the finished surface. The rotation speed of the tool during the grinding process is usually very high; therefore, it is reasonable to assume that only diamond abrasives with the maximum protrusion height on the cross section of a grinding wheel, e.g., the red diamond abrasive shown in Fig. 13a, will leave an effective cut track on the finished surface. Each diamond abrasive shown in Fig. 13b is assumed to be the highest in the cross section and able to produce effective cut tracks on the finished surface when using the CG process. Each diamond abrasive is fed linearly along the horizontal feed direction. Therefore, the cut tracks produced during each wheel rotation period are partially overlapped by the following cut tracks; as such, linear grooves along the horizontal feed direction can be generated, as shown in Fig. 13c.

In contrast, during the SG process, the cut track produced during each rotation period is individually duplicated on the surface of the workpiece with no (or minimal) overlap along the slanted feed direction. Only diamond abrasives with a larger protrusion height than that of adjacent diamond abrasives (e.g., the diamond abrasives labeled 1, 2, 3, and 4 in Fig. 13b) will leave obvious effective cut tracks on the finished surface. Therefore, the surface textures shown in Fig. 13d were generated using the SG process

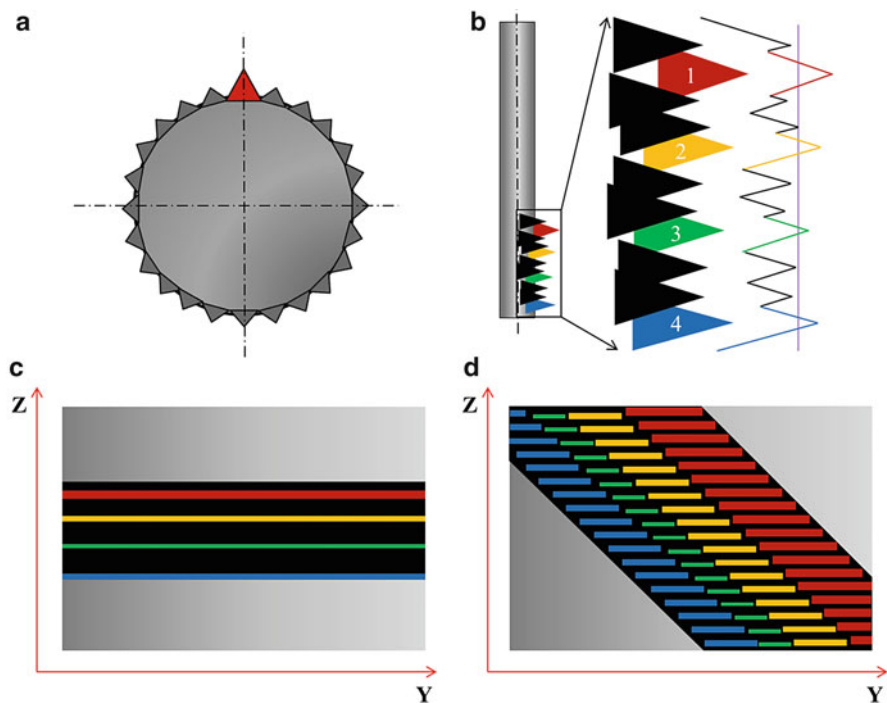


Fig. 13 Schematics of (a) a cross section of a diamond grinding wheel, (b) diamond abrasives for fabricating effective cut tracks, (c) surface textures fabricated by the CG process, and (d) surface textures fabricated by the SG process (Xu et al. 2013)

method. The length of each cut track along the slant feed direction is determined by the protrusion height and distribution of the diamond cutting abrasives.

8.3.3 Surface Texturing Mechanisms

Without consideration of the radial motion of the tool, all of the cut tracks shown in Fig. 13c, d are assumed to be linear grooves on the YZ plane. When the LV mode is used, the linear grooves will be transformed to sinusoidal grooves. Figure 14 shows the cutting loci of one diamond abrasive during three rotation periods of the CG and SG processes in the LV mode. In the CG process, the sinusoidal loci overlap one by one along the horizontal feed direction. In contrast, the sinusoidal loci are distributed along the slant feed direction in the SG process, and the distance between two adjacent sinusoidal loci can be controlled by adjusting the machining conditions. This sinusoidal cutting locus can be actively controlled for fabricating surface micro-/nano-textures.

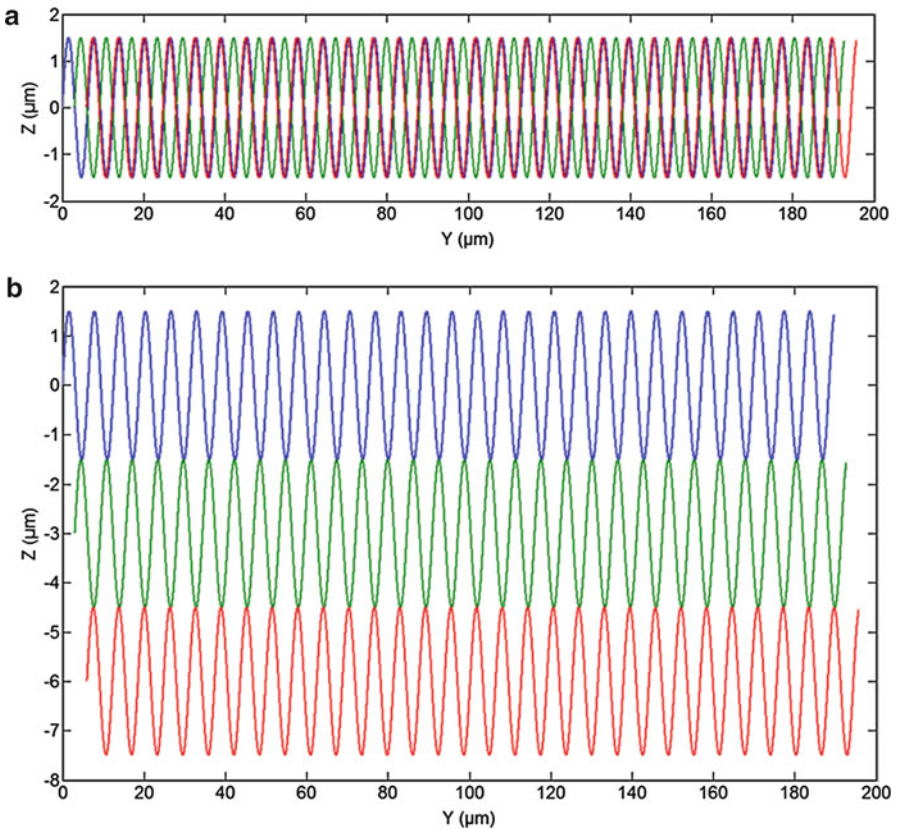


Fig. 14 Cutting loci of one diamond abrasive during three rotation periods of (a) the CG process ($v_{fy} = 3$ mm/min) and (b) the SG process ($v_{fy} = v_{fz} = 3$ mm/min) in the LV mode (Xu et al. 2017)

When the CV mode is used, the linear grooves are transformed to continuous 2D curves in the XY plane, as shown in Fig. 15. The same transformations of the cutting loci can be observed, i.e., the 2D curves for the three rotation periods overlap one by one in the CG process, whereas they distribute along the slant feed direction without any overlap in the SG process. With this 2D cutting locus, the cutting abrasive intermittently comes into contact with the workpiece; thus, micro-concave textures can be fabricated on the surface of the workpiece.

When the HV mode is used, much more complicated cutting loci are generated. Figure 16 shows the cutting loci for three rotation periods of the SG process in the

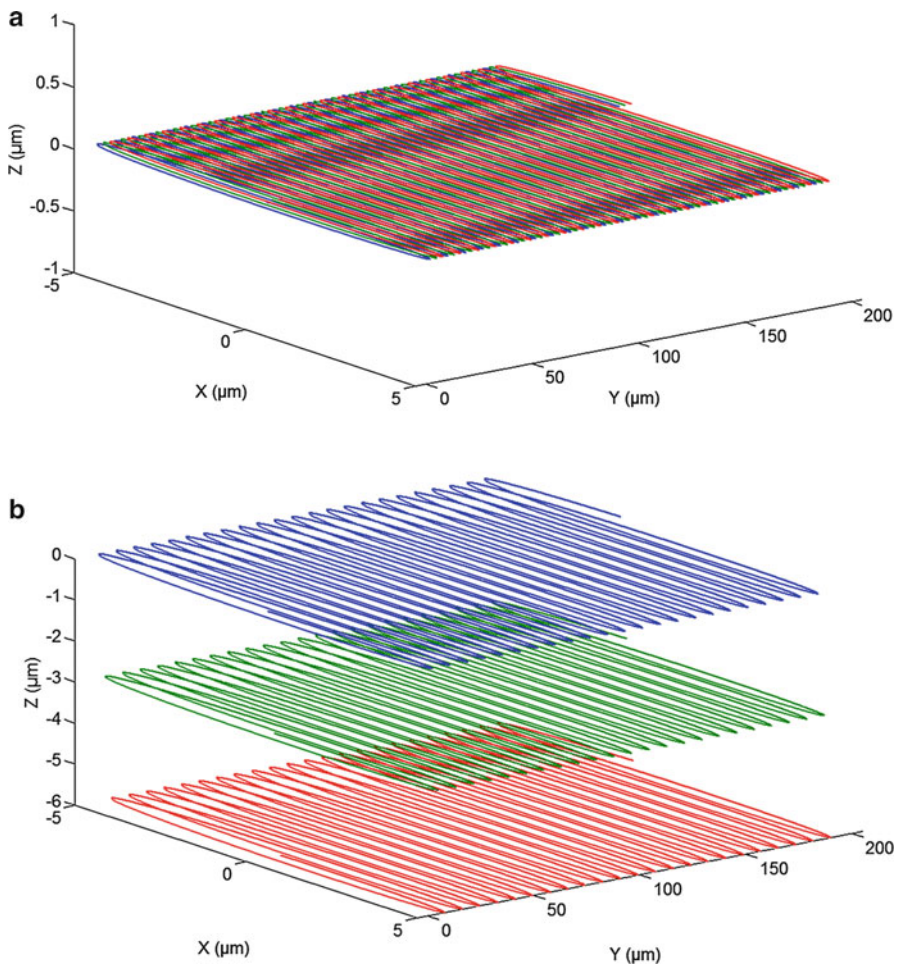


Fig. 15 Cutting loci of a diamond abrasive during three rotation periods in (a) the CG process ($v_{fy} = 3$ mm/min) and (b) the SG process ($v_{fy} = v_{fz} = 3$ mm/min) in the CV mode

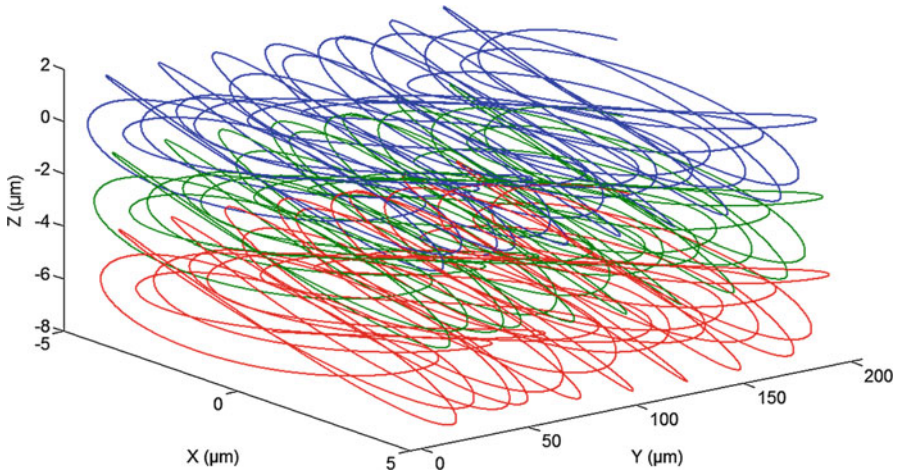


Fig. 16 Cutting loci of one diamond abrasive during three rotation periods of the SG process ($v_{Ry} = v_{Rz} = 3$ mm/min) in the HV mode (Xu et al. 2017)

HV mode. Because the vibration frequencies of the LV and CV modes are different, no periodic features can be observed in these cutting loci. In the HV mode, the UASG process is expected to fabricate random-like surfaces.

8.4 Experimental Verification and Discussion

8.4.1 Experimental Conditions

Electroplated diamond grinding wheels were used to carry out the ultrasonic-assisted grinding processes. Figure 17 shows the surface topography of a 600-mesh-size diamond grinding wheel. It can be observed that the diamond abrasives are randomly distributed on the surface of the grinding wheel and that the shapes of the diamond abrasives are irregular. All samples were pre-machined on a precision machine by successive use of 1000- and 3000-mesh-size diamond grinding wheels. Subsequently, the UASG processes were carried out. Table 2 shows the experimental conditions.

8.4.2 Experimental Results

The surface profiles were measured using a white light interferometer (Zygo, NewView 5000), and the surface textures were examined under scanning electron microscopy (Hitachi, SU1510). Surface textures fabricated using the CG and SG processes without the ultrasonic vibration motion were compared. Figure 18 shows the results when the 600-mesh-size diamond grinding wheel was used. The

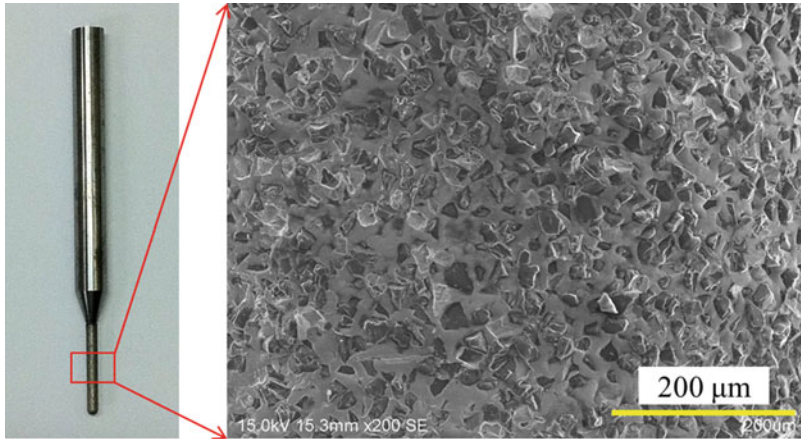


Fig. 17 Surface topography of a 600-mesh-size diamond grinding wheel

Table 2 Experimental conditions

Diamond wheel	Shank materials	Cemented carbide
	Diameter of grinding wheel (mm)	1, 3
	Diamond grit mesh	#600, #1000, #3000
Workpiece	ZrO ₂ ceramics (13 × 14 × 17 mm ³)	
Grinding conditions	Rotation frequency (rpm)	500–2000
	Feed speed along Y axis (mm/min)	0–5
	Feed speed along Z axis (mm/min)	0–5
	Grinding depth (μm)	About 3–20
	Coolant	Solution type
Vibration conditions	Vibration frequency (LV) (kHz)	25
	Vibration frequency (CV) (kHz)	19
	Vibration amplitude (LV) (peak-to-peak) (μm)	3
	Vibration amplitude (CV) (peak-to-peak) μm ²	10 × 10

experimental results coincide well with the theoretical predictions shown in Fig. 13. The surface textures generated by the CG process were composed of continuous linear grooves along the horizontal feed direction. The depth of the linear grooves is determined by the maximum protrusion height of the diamond abrasives along each cross section of the diamond grinding wheel. In contrast, short linear grooves were fabricated one by one along the slant feed direction in the SG process. The same linear grooves along the slant feed direction were generated by the same cutting abrasive with a greater protrusion height, as described in Sect. 8.3.2. If ultrasonic vibration motion was applied, the short linear grooves would be transformed into finer structures.

Figure 19 shows the surface profiles and surface textures fabricated using the UASG method in the LV, CV, and HV modes. The surface profiles agree well with

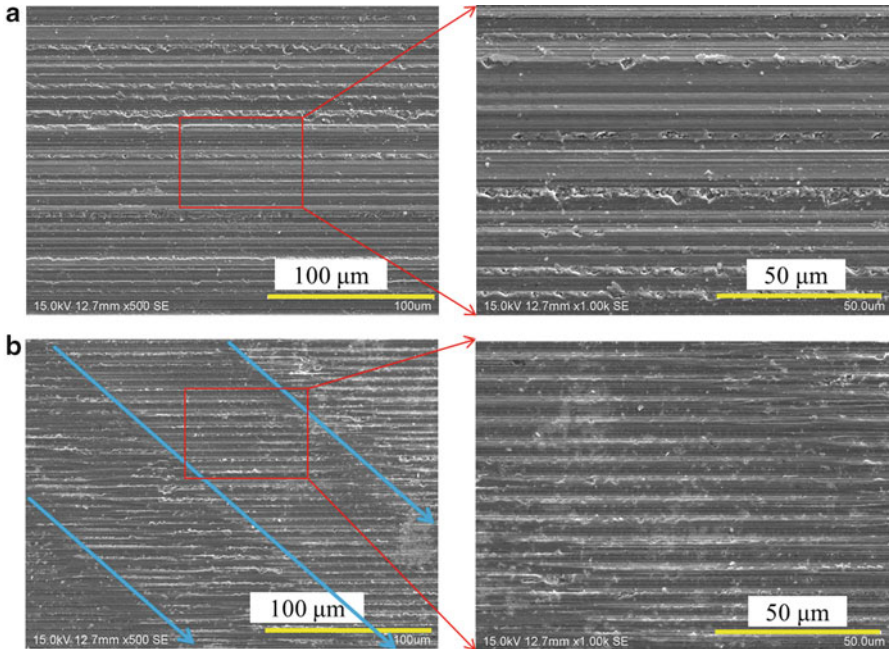


Fig. 18 Surfaces fabricated using the (a) CG process ($\#600$, $D = 3$ mm, $n_t = 500$ rpm, and $v_{fy} = 3$ mm/min) and (b) SG process ($\#600$, $D = 3$ mm, $n_t = 500$ rpm, and $v_{fy} = v_{fz} = 3$ mm/min) (Xu et al. 2013)

the surface generation model, as shown in Fig. 13d. The differences in the protrusion heights of the diamond abrasives on the grinding wheel also result in differences in the depth and width of the short linear grooves along the slant feed direction. The short linear grooves were changed to much finer structures, which coincide well with the cutting loci shown in Figs. 14, 15, and 16. The micro-sinusoidal grooves shown in Fig. 19a were fabricated using the LV mode. The micro-concave textures (e.g., micro-holes) shown in Fig. 19a were fabricated using the CV mode. When the HV mode was employed, a random-like rough surface was successfully fabricated.

Figure 20 shows the experimental results when a 1000-mesh-size diamond grinding wheel was used. The CG and SG processes with and without ultrasonic vibration were compared. It can be observed that no obvious surface micro-/nano-textures were fabricated with the CG process even when ultrasonic vibration was used, as shown in Fig. 20a–e. The reason for this is that the cutting loci overlap one by one along the horizontal feed direction, as shown in Figs. 14a and 15a. Different surface micro-/nano-textures were successfully fabricated along the slant feed direction when using the UASG processes. It can be observed that the surface micro-/nano-textures on the various surface areas along the slant feed direction differ owing to the different shapes of the diamond cutting abrasives. Figures 21 and 22 show different micro-/nano-textural patterns fabricated with the LV and CV modes.

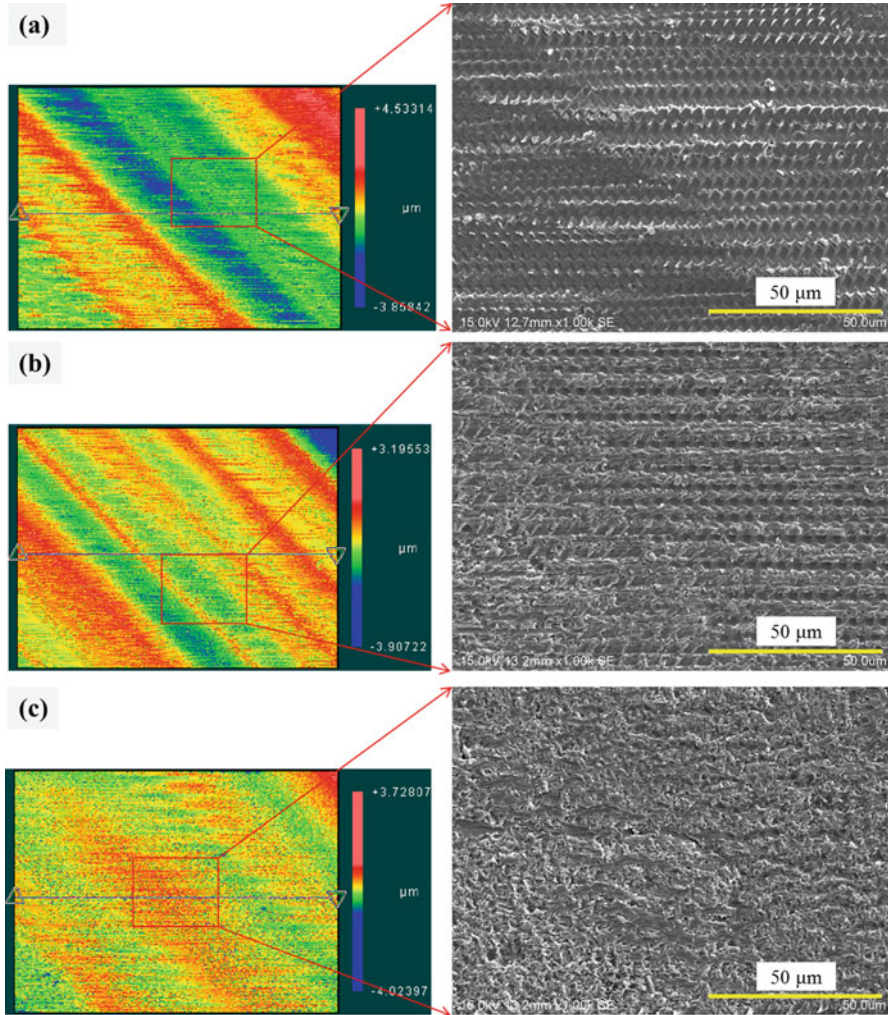


Fig. 19 Surface profiles and textures fabricated using the UASG process ($\#600$, $D = 3$ mm, $n_t = 500$ rpm, and $v_{fy} = v_{fz} = 3$ mm/min) in the (a) LV mode, (b) CV mode, and (c) HV mode

When the LV mode is used, the sinusoidal feature can be clearly observed on the textured surfaces; however, the textural patterns differ even when fabricated under the same experimental conditions. The reason for this is that the shapes of the diamond cutting abrasives also have a significant influence on the surface textural features. The diamond cutting abrasive intermittently contacts with the workpiece under the CV mode; therefore, the material is intermittently removed, and periodic micro-/nanostructures are generated. Owing to the different shapes of the diamond cutting abrasives, different textural patterns are also observed on the finished surfaces.

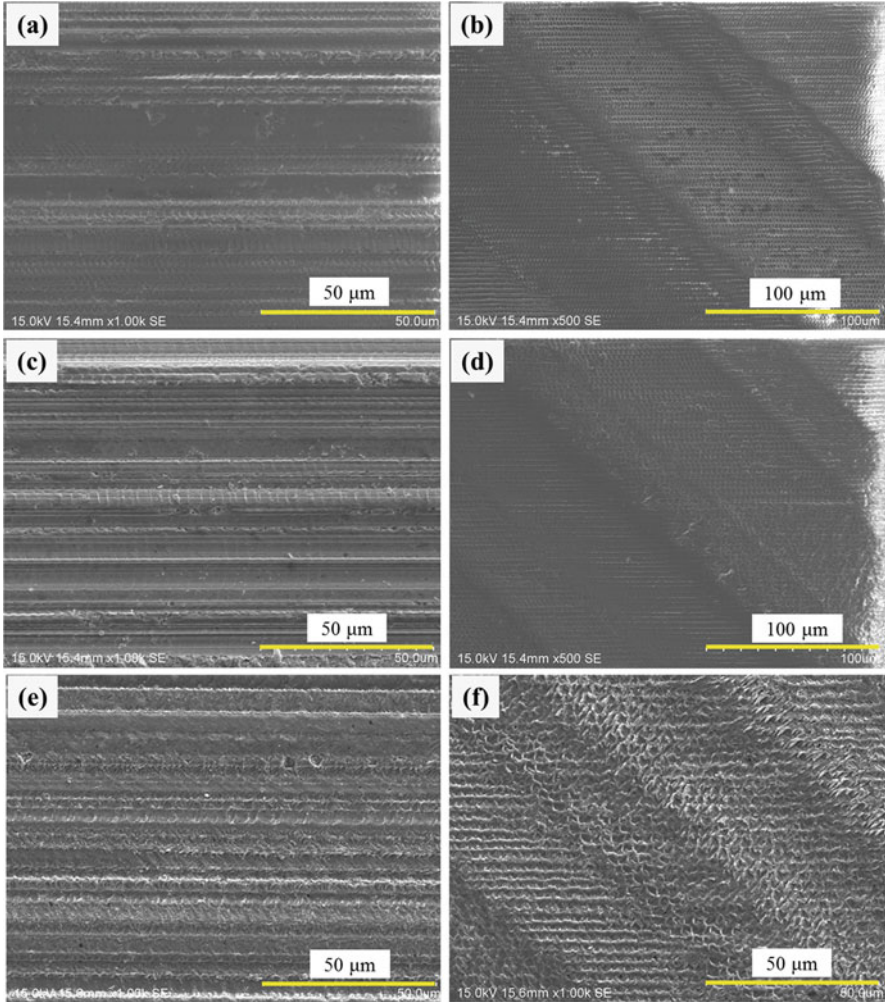


Fig. 20 Surface textures fabricated using the (a) CG process in the LV mode, (b) SG process in the LV mode, (c) CG process in the CV mode, (d) SG process in the CV mode, (e) CG process in the HV mode, and (f) SG process in the HV mode ($\#1000$, $D = 1$ mm, $n_t = 1000$ rpm, $v_{fy} = 3$ mm/min, and $v_{fz} = 3$ mm/min (only for SG))

8.4.3 Limitations of the UASG Technique

The experimental results reveal that the UASG method can be used for fabricating different periodic micro-/nano-textures in the LV and CV modes or random-like surfaces in the HV mode. The irregular shapes of the diamond cutting abrasives also provided various machined structures in the UASG method. If the textural pattern must be controlled, the shapes and distribution of the

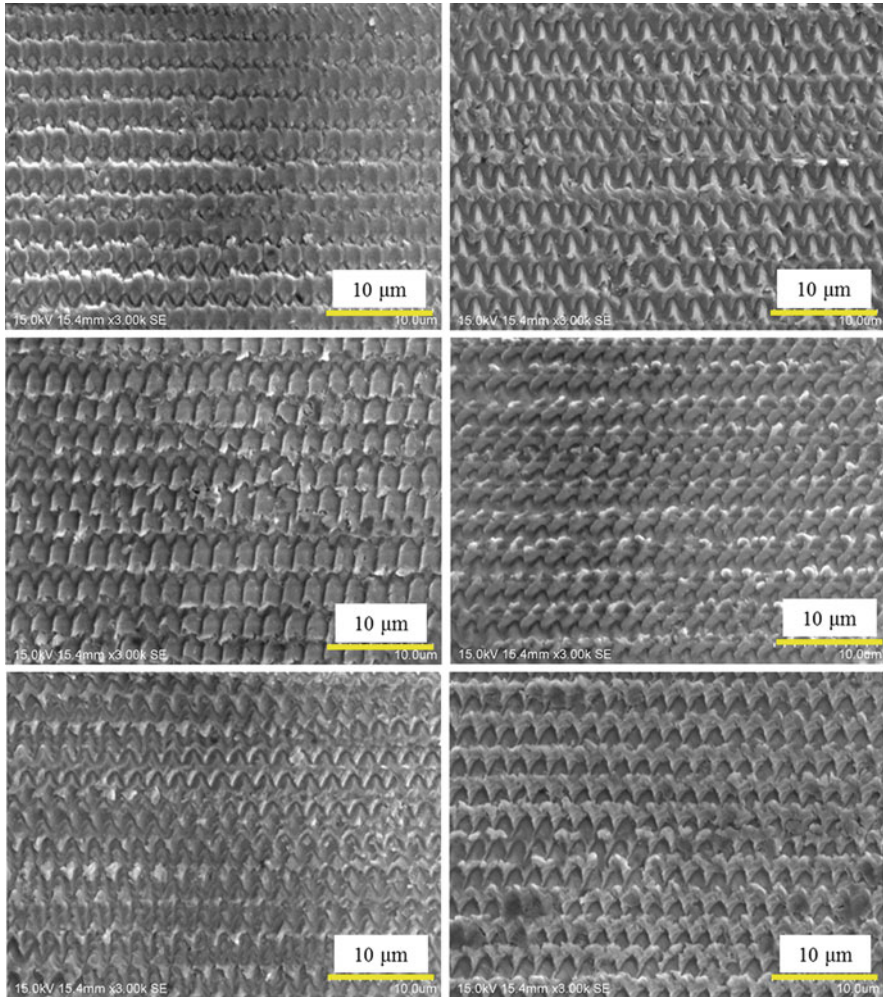


Fig. 21 Various surface micro-/nano-textures on the different areas along the slant feed direction as fabricated using UASG in the LV mode

diamond abrasives must be tailored. In addition, it is virtually impossible to determine the relationship between the shapes of the diamond cutting abrasives and the textural features. Therefore, it is preferable to use another tool to determine the mechanisms of material removal during the micro-/nano-texturing process. To fully control the texturing process, the cutting edges should be geometrically designed and regularly distributed on the surface of the tool. As such, the next section describes the design and manufacture of diamond tools with only one cutting tip. These are referred to as one-point diamond tools, and these were produced using electroplating in the RUT process.

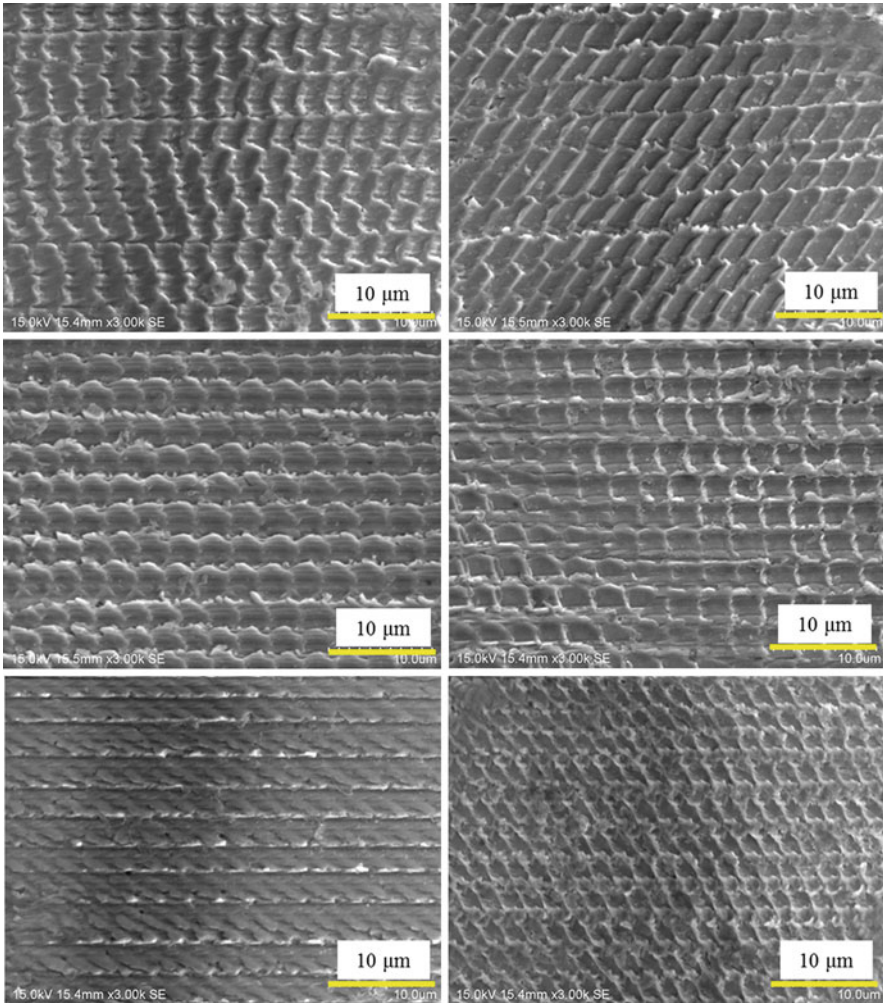


Fig. 22 Various surface micro-/nano-textures on the different areas along the slant feed direction as fabricated using UASG in the CV mode

8.5 Rotary Ultrasonic Texturing Using One-Point Diamond Tools

8.5.1 Theories of Texturing Mechanisms

A cutting tip usually comprises three parts: the cutting corner, the cutting edge, and the cutting face (Boothroyd and Knight 2006). In this section, only the effects of the cutting corner and the cutting edge in the RUT process are discussed. Two types of cutting tip,

one with a conical shape (cutting tip 1) and the other with a triangular prism shape (cutting tip 2), as shown in Fig. 23, were used to analyze the texturing mechanisms of the RUT process in the LV and CV modes. The conical cutting tip is assumed to have a cutting corner that is sharp enough to fabricate grooves of any width. The triangular prism cutting tip is assumed to have a cutting edge of a length that is much larger than the vibration amplitude of the tool in the RUT process. A simple texturing procedure, as shown in Fig. 24, was used to study the technical requirements of the RUT methods. With rotational motion of an ultrasonic vibration spindle, a one-point diamond tool is fed along the negative Z-axis direction on the flat surface of a workpiece. Thus, (1) the diamond cutting tip moves along a helical path, (2) the cutting tip removes the work material to a certain cutting depth (only in the labeled machined area), and (3) the

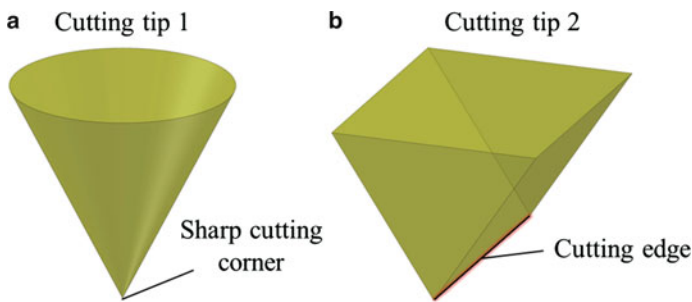


Fig. 23 Two types of cutting tip: (a) a conical shape and (b) triangular prism shape

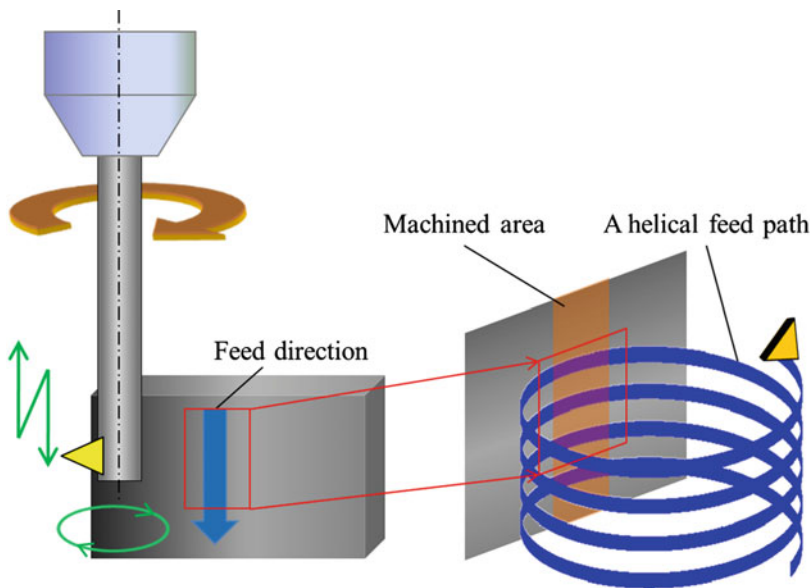


Fig. 24 Texturing procedure used for the RUT process (Xu et al. 2017)

diamond tool vibrates in the LV mode or CV mode simultaneously. To analyze the texturing mechanisms, several assumptions are made: (1) the radial motion of the cutting tip on the tool is ignored when removing the material, and the cutting depth in the machined area is assumed to be constant, (2) the cutting direction in each rotation period is assumed to be along the Y axis, (3) the cutting speed along the Y axis is assumed to be equal to the peripheral velocity of the tool, and (4) the work material is assumed to be completely removed during the material removal process.

8.5.1.1 Surface Generation Mechanisms in the LV Mode

On the basis of the assumptions described above, if diamond cutting tip 1 is used, linear grooves will be generated on the machined area (as shown in Fig. 25a) in the absence of ultrasonic vibration. When the LV mode is employed, the linear grooves become sinusoidal grooves, as shown in Fig. 25b. The width of the sinusoidal grooves (w_s), the axial height of the sinusoidal grooves (A_s), the wavelength of the sinusoidal grooves (l_s), and the distance between two adjacent sinusoidal grooves along the Z axis (l_z) can be calculated by Eqs. (7), (8), (9), and (10), respectively, where α_c is the cone angle of the conical cutting tip. Figure 25c shows the changes in the textural patterns with changes in the texturing parameters, from which it can be seen that different textural patterns can potentially be fabricated by modulating the cutting locus in the texturing process. When the triangular prism cutting tip is used, as shown in Fig. 26a, at an angle oblique to the surface of the workpiece, the cutting edge will remove the material, and the cutting corner will produce textures on the surface generated by the cutting edge, as depicted in Fig. 26b.

$$w_s = 2a_p \tan \frac{\alpha_c}{2} \quad (7)$$

$$A_s = A_l + w_s + \frac{v_{fz}}{120f_l} \quad (8)$$

$$l_s = \frac{\pi D n_t}{60} \times \frac{1}{f_l} \quad (9)$$

$$l_z = \frac{v_{fz}}{n_t} \quad (10)$$

8.5.1.2 Surface Generation Mechanisms in the CV Mode

The same assumptions were used to analyze the texturing process in the CV mode. The CV mode provides the cutting tip with the vibration of the circular locus on the XY plane, as shown in Fig. 27a. The instantaneous speed of the cutting tip (v_c) generated only by the circular vibration can be calculated by Eq. (11), where A_c is the diameter of the circular vibration. The peripheral velocity of the tool (v_p) can be calculated by Eq. (12) when the tool rotates along the spindle axis. The combination of v_c with v_p finally determines the shape of the whole cutting locus. For a certain vibration condition, Fig. 27b shows two typical cutting loci. Two parameters, h_c^* and

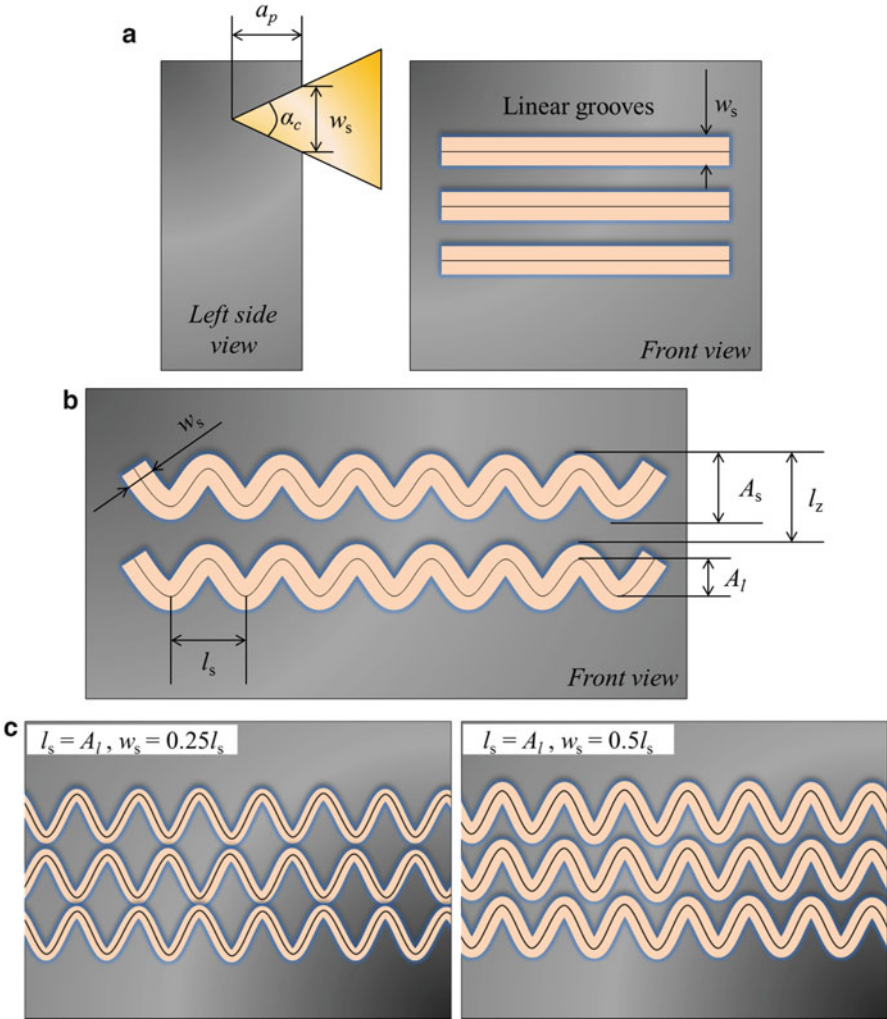
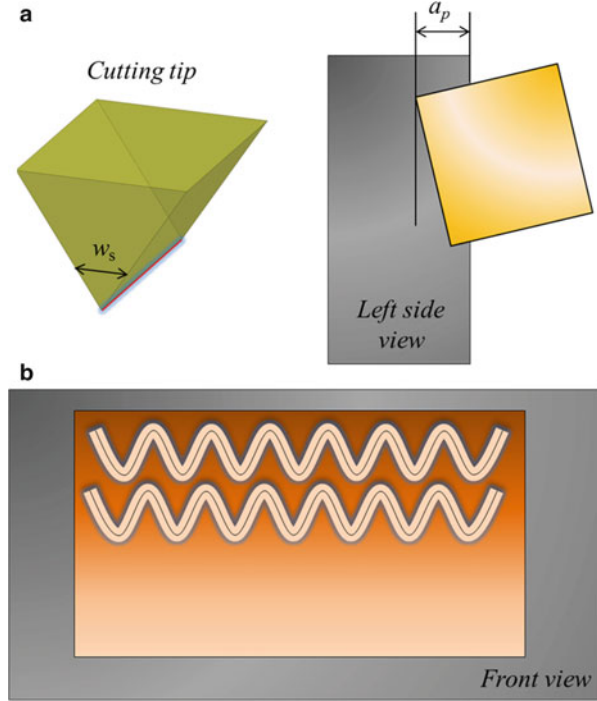


Fig. 25 Schematics of surface textures fabricated by the conical cutting tip under the LV mode: (a) linear grooves, (b) sinusoidal grooves, and (c) textured surfaces fabricated under different texturing parameters

w_c^* , as shown in Fig. 27b, must be considered for the RUT process in the CV mode. The term w_c^* can be calculated using Eq. (13), and h_c^* is given by Eq. (14); τ is the solution of Eq. (15).

If $0 < a_p < h_c^*$, the depth of the textured patterns (h_c) is equal to a_p , and the width of the textured patterns (w_c) is smaller than w_c^* ; thus, discontinuous textured patterns will be generated. If $a_p \geq h_c^*$, the depth of the textured patterns (h_c) is equal to h_c^* , and the width of the textured patterns (w_c) is equal to w_c^* ; thus, continuous textured patterns will be fabricated.

Fig. 26 Schematics of (a) a triangular prism cutting tip and (b) surface textures fabricated by the triangular prism cutting tip in the LV mode



Therefore, by controlling the cutting depth and shape of the cutting loci, different surface textures can be fabricated. For example, continuous micro-dimples and microgrooves (as shown in Fig. 27c) can be fabricated when a_p is bigger than h_c^* using diamond cutting tips 1 and 2, respectively. In the case of the continuous microgrooves, the aspect ratio (the width and depth of the textured grooves) can be plotted against the ratio of v_p to v_c , as shown in Fig. 28. Under a certain vibration condition, v_c is constant according to Eq. (11). Therefore, v_p/v_c increases when n_t is increased. It can be found that the maximum depth of the machinable textured groove is determined by the vibration amplitude of the circular vibration; the largest aspect ratio (approximately 0.32) of the textured groove can be obtained when v_p is equal to v_c . Continuous grooves of several micrometers in depth and from several micrometers to several tens of micrometers in width can be fabricated if the work material is efficiently removed during the RUT process.

$$v_c = \pi A_c f_c \quad (11)$$

$$v_p = \pi D n_t \quad (12)$$

$$w_c^* = \frac{v_p}{f_c} \quad (13)$$

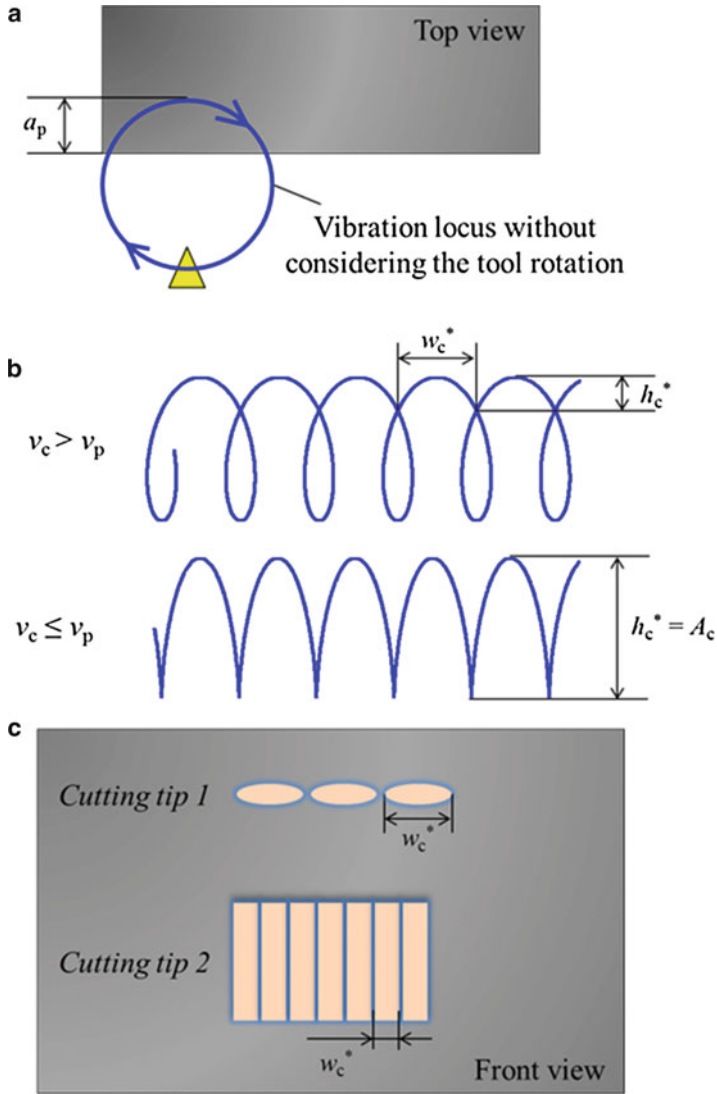


Fig. 27 Schematics of (a) circular vibration locus, (b) two types of cutting loci, and (c) textural patterns fabricated using cutting tips 1 and 2 (Xu et al. 2017)

$$h_c^* = \begin{cases} \frac{A_c}{2} [1 - \cos(2\pi f_c \tau)] & v_c > v_p \\ A_c & v_c \leq v_p \end{cases} \quad (14)$$

$$v_p \tau + \frac{A_c}{2} \sin(2\pi f_c \tau) = \frac{v_p}{2f_c} \quad v_c > v_p \quad (15)$$

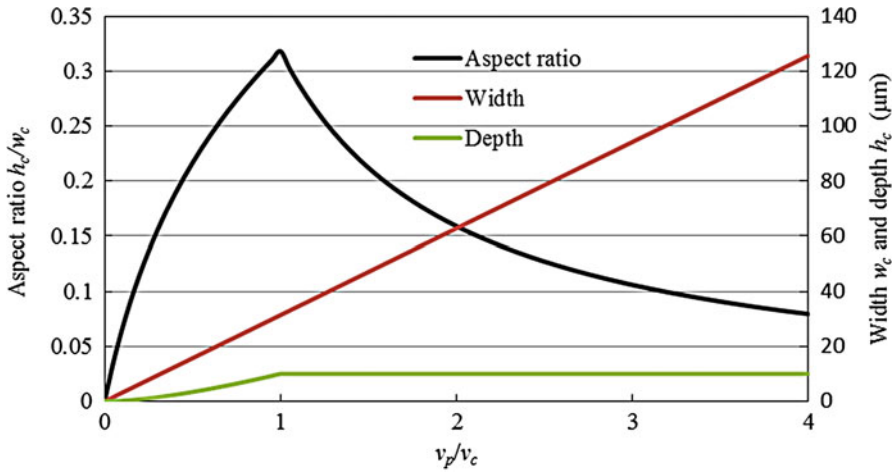


Fig. 28 Aspect ratio h_c/w_c (black line) of the continuous textured grooves as a function of v_p/v_c non-conditionally. Width and depth (red and green lines) of the continuous textured grooves as a function of v_p/v_c when $D = 3$ mm, $A_c = 10$ μm , and $f_c = 19$ kHz (Xu et al. 2017)

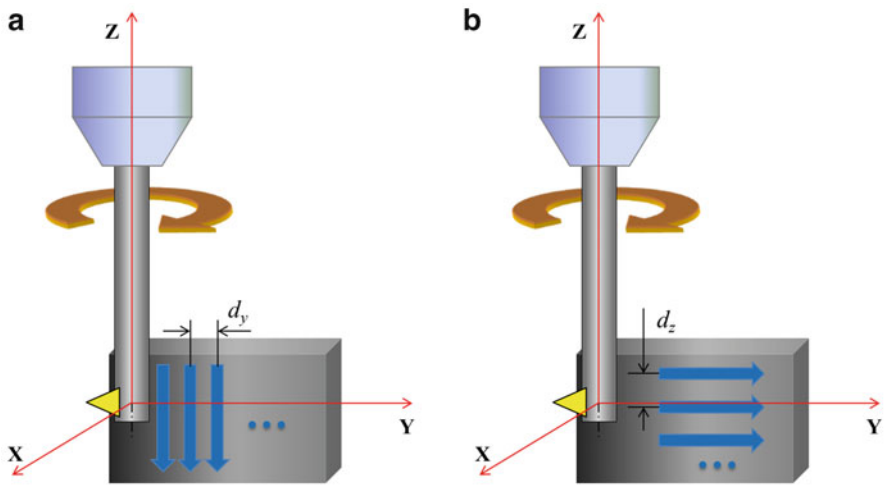


Fig. 29 Schematics of two RUT procedures

8.5.2 Texturing Procedures and Corresponding Cutting Loci

To control the texturing process for specific textural patterns in the machined surface, the cutting loci should first be calculated and intentionally controlled (based on the analysis in the above section). Figure 29 shows the two texturing procedures used in this chapter for the RUT process. In Fig. 29a, the diamond tool is firstly fed along the axial (negative Z) direction, and then, the cutting process is repeated with an

intermittent feed distance (d_y) along the horizontal (Y) direction. In Fig. 29b, the tool is firstly fed along the Y axis, and then, the cutting process is repeated with an intermittent feed distance (d_z) along the axial (Z) direction. The center point of the tool shank's cross section, where the diamond cutting tip is located, is assumed to be the original point in the tool-in-hand coordinate system, as shown in Fig. 29. Therefore, the cutting loci in the LV and CV modes can be calculated in a similar manner to that described in Sect. 8.3.1.

It is necessary to analyze the kinematics of the cutting tip during the RUT process. Figures 30 and 31 describe the feed paths and the cutting loci of the texturing procedures under certain experimental conditions, as shown in Figs. 29a, b, respectively.

In Fig. 30a, the parameter (w_g), the width of a machined area at a certain cutting depth (a_p) in one rotation period, has to be considered; this can be calculated using Eq. (16). If w_g is smaller than d_y , each machined surface along the Y axis will be disconnected. In contrast, if w_g is bigger than d_y , the machined surface areas along the Y axis will be connected. In the LV mode, sinusoidal cutting loci (as shown in Fig. 30b) can be generated, whereas in the CV mode, 2D cutting loci (as shown in Fig. 30c) can be generated.

In Fig. 31a, the parameters l_y and h_g must be considered. The term l_y can be calculated using Eq. (17), and h_g is given by Eq. (18); δ is the solution of Eq. (19). It can be found that the rotational speed and the feed speed along the Y axis determine l_y and h_g . If a_p is smaller than h_g , each machined surface area along the Y axis will be disconnected. In contrast, if a_p is no smaller than h_g , the machined surface areas along the Y axis will be connected. The specific shapes of the cutting loci depend on the tool parameters and experimental conditions. The radial motion of the tool changes the cutting depth from 0 to the maximum value (a_p) and then back to 0 during each rotation period; this must be considered in the RUT process.

$$w_g = 2\sqrt{\left(\frac{D}{2}\right)^2 - \left(\frac{D}{2} - a_p\right)^2} \quad (16)$$

$$l_y = \frac{v_{fy}}{n_t} \quad (17)$$

$$h_g = \frac{D}{2} \left[1 - \cos\left(2\pi \frac{n_t}{60} \delta\right) \right] \quad (18)$$

$$v_{fy} \delta + \frac{D}{2} \sin\left(2\pi \frac{n_t}{60} \delta\right) = \frac{60v_{fy}}{2n_t} \quad (19)$$

8.5.3 Design of Geometrically Defined One-Point Diamond Tools

When fabricating textures on flat surfaces using the RUT method, the radial motion of the diamond cutting tip makes the instantaneous cutting depth change periodically

from 0 to the maximum and then back to 0 during each tool rotation period. Therefore, a design for an advance cutting edge is required to maintain the instantaneous cutting depth at a fixed value. The sinusoidal cutting locus under the LV mode makes the two-rake-face design essential for efficiently removing the work material. When designing tools for the RUT method under the CV mode, the

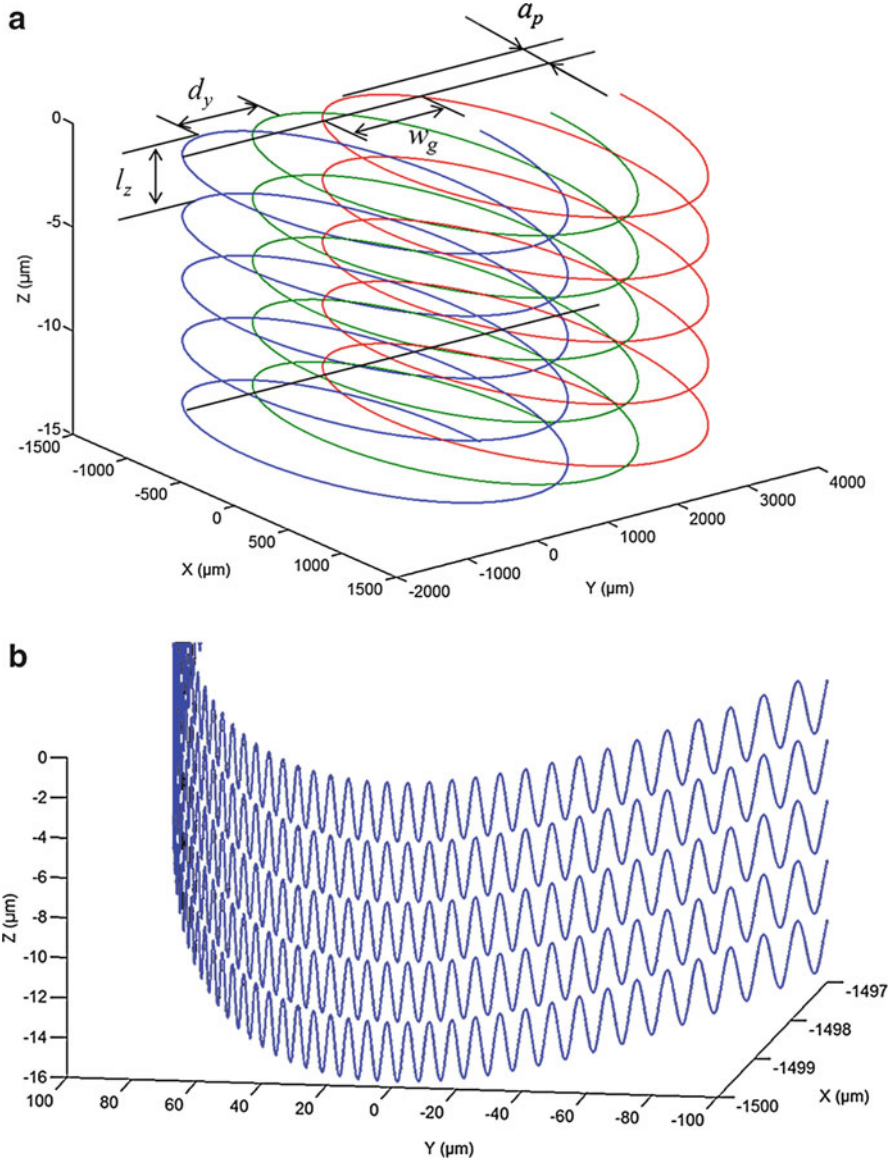


Fig. 30 (continued)

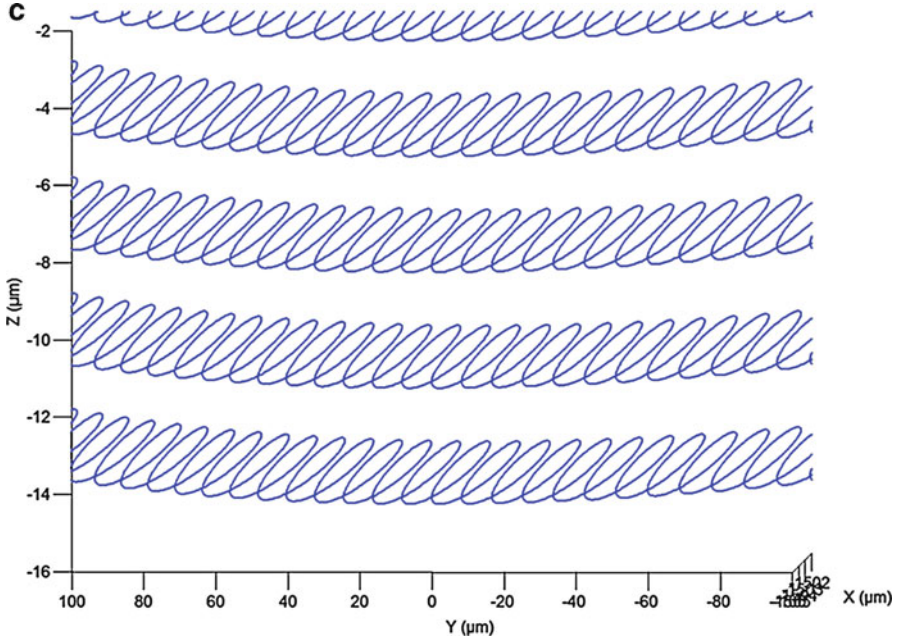


Fig. 30 Feed path and cutting loci of the texturing procedure in Fig. 29a ($n_t = 1000$ rpm, $v_{fz} = 3$ mm/min, $d_y = 1000$ μm , and $a_p = 3$ μm): (a) the feed path, (b) the cutting loci along the Z axis in the LV mode, and (c) the cutting loci along the Z axis in the CV mode

relationship between the tool clearance angle and the curvature of the cutting locus also needs to be considered. Figures 32, 33, and 34 show three types of geometrically defined one-point diamond tool designed for the RUT process. A diamond cutting tip of a certain geometrical shape is cemented to the tool shank. The specifications and SEM images of these diamond cutting tips are given.

The diamond cutting tip shown in Fig. 32 was used for preliminary testing of the RUT process in the LV and CV modes. A square pyramid cutting tip is fixed at the bottom of the tool shank. The included angle of two opposite faces (e.g., face ABE and face CDE) is about 70.5° , and the nose radius is approximately 200 nm.

Figure 33 shows the diamond tool with a triangular pyramid cutting tip, which was used for micro-/nano-texturing in the LV mode. The cutting edge AD (or BD) acts as the advance cutting edge when the tool feeds along the negative (or positive) Z axis. The faces ACD and BCD are the two rake faces when the tool vibrates downward and upward, respectively. The cutting corner D has a radius of approximately 200 nm.

Figure 34 shows the one-point diamond tool designed for the RUT process in the CV mode. The turning diameter is 3.6 mm. A two-level flank face was designed with clearance angles of 15° and 30° to ensure the strength of the cutting edge and reduce the interference between the rake face and workpiece. The major cutting edge has an included angle of 5° to the Z axis, and the minor cutting edge has an included angle of 10° to the Y axis. The nose radius is approximately 20 μm .

8.5.4 Modeling of the Surface Generation Process

The final research objective of the work described in this chapter was to fabricate different surface micro-/nano-textures using the RUT method. Therefore, before conducting practical experiments, it was necessary to predict the machinable structures based on the cutting locus and the diamond cutting tip's geometry, which can

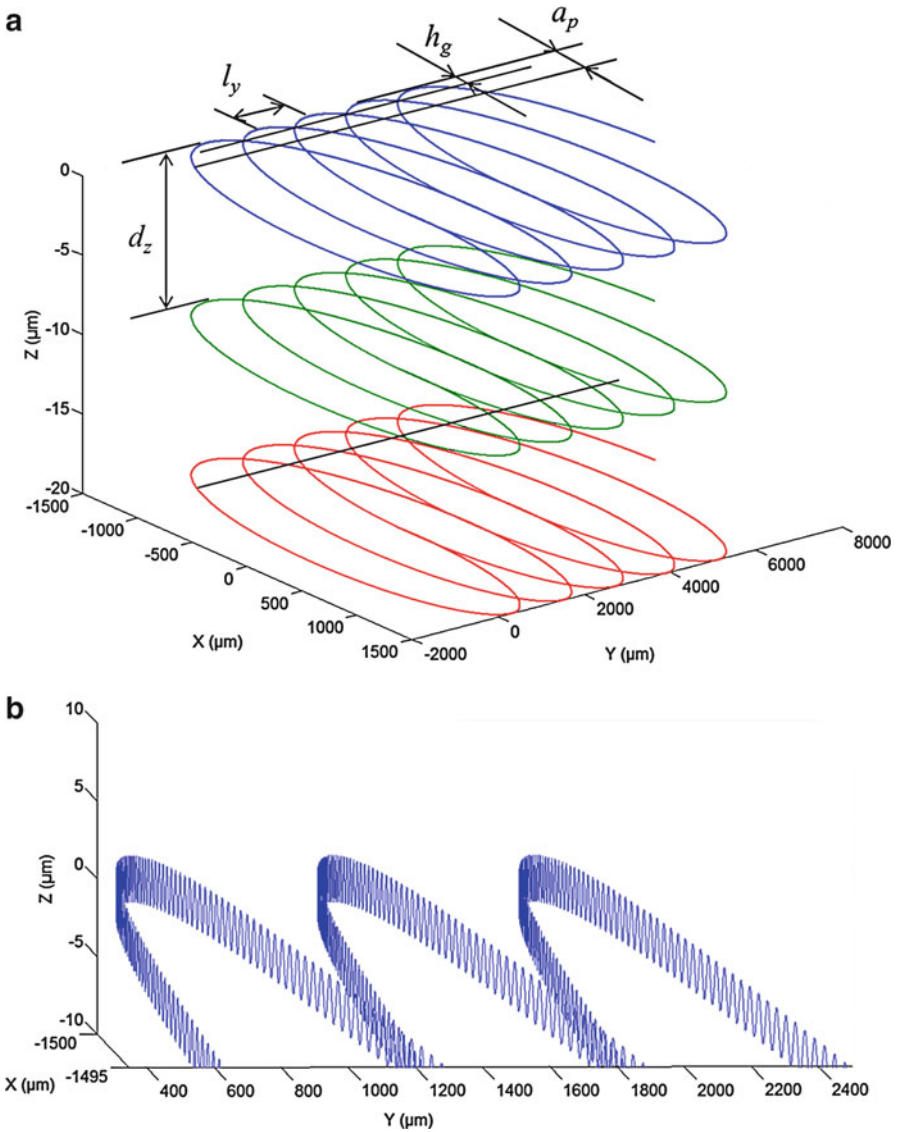


Fig. 31 (continued)

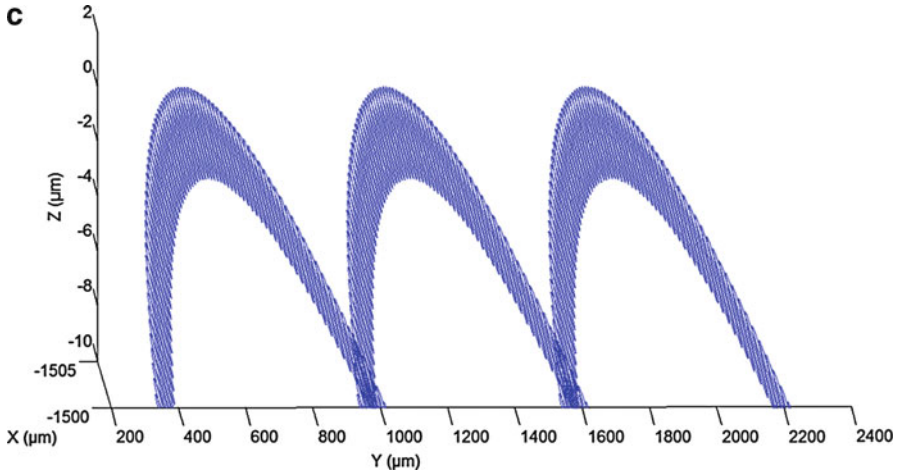


Fig. 31 Feed path and cutting loci of the texturing procedure in Fig. 29b ($n_t = 500$ rpm, $v_{fy} = 600$ mm/min, $d_z = 10$ μm , and $a_p = 5$ μm): (a) the feed path, (b) the cutting loci along the Z axis in the LV mode, and (c) the cutting loci along the Z axis in the CV mode

also be used to guide the design of cutting tip geometries and texturing parameters. There have been many approaches reported (Ehmann and Hong 1994; Lin and Chang 1998; Lee and Cheung 2001; Kim et al. 2002) for predicting surface topography in the diamond machining processes. However, most of these studies only report the resultant surface profiles, and they focus on changes in surface roughness. In this chapter, the textural features of the finished surface at the micrometer/nanometer scale are of greater interest. The material removal process during each vibration period must also be visualized in order to determine the material removal mechanisms. Therefore, a new modeling method applicable to surface generation in the RUT process is proposed. This method can be used to simulate the 3D surface profiles of finished surfaces and visualize the cutting process in each vibration period.

8.5.4.1 Assumptions in the Modeling Process

In the RUT process, each tool rotation fabricates a cut track on the surface of the workpiece at a certain cutting depth. The feed rate along the Z axis is usually set at 0 or a value much lower than the peripheral velocity of the rotating tool. Thus, the included angle between each cutting path on the machined area and the Y axis is maintained at 0 or a very small value, which can be ignored. Therefore, in the modeling process, the direction of each cutting path along the workpiece should be horizontal along the Y axis. The instantaneous cutting depth is also assumed to be constant along each cutting path and equal to the cutting depth. Mechanical deformation of the workpiece is not considered, and the workpiece material is assumed to be fully removed when the rake face contacts the workpiece. The interference between the flank face and workpiece is taken into account.

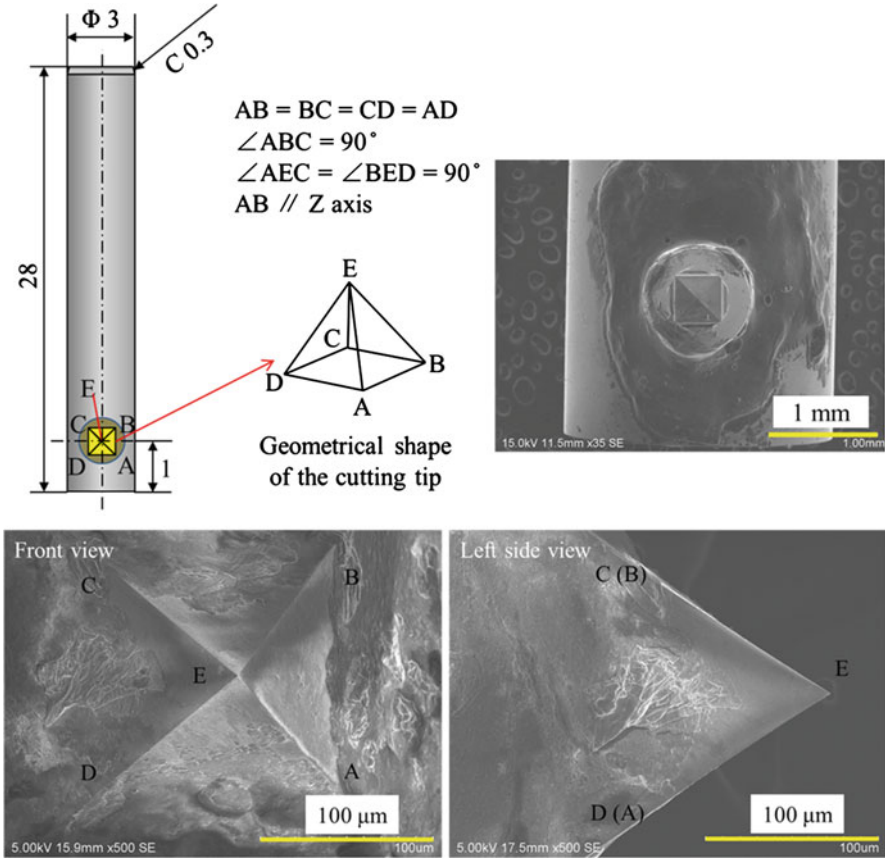


Fig. 32 The geometrically defined one-point diamond tool with a square pyramid cutting tip (Xu et al. 2016)

8.5.4.2 Surface Generation Model Under the LV Mode

On the basis of the above assumptions, the modeling process of surface generation using the triangular pyramid cutting tip is described in Fig. 35. The cutting edge AD acts as an advance cutting edge when the feed direction is along the negative Z axis. The faces ACD and BCD alternately act as the rake face during the texturing process. When the cutting tip vibrates upward from a lower peak point to an upper peak point along the sinusoidal locus, the rake face BCD acts as the rake face and removes the material from the workpiece, as shown in Fig. 35c, e; when the cutting tip vibrates downward, the rake face ACD acts as the rake face and removes the material from the workpiece, as shown in Fig. 35d. The material removal process is carried out along the sinusoidal cutting locus, as shown in Fig. 35b; thus, a surface texture, such as that shown in Fig. 35f, will be generated. The sinusoidal groove is generated by cutting corner D, and the oblique parallel grooves above and under the sinusoidal groove are generated by cutting edges BD and AD, respectively.

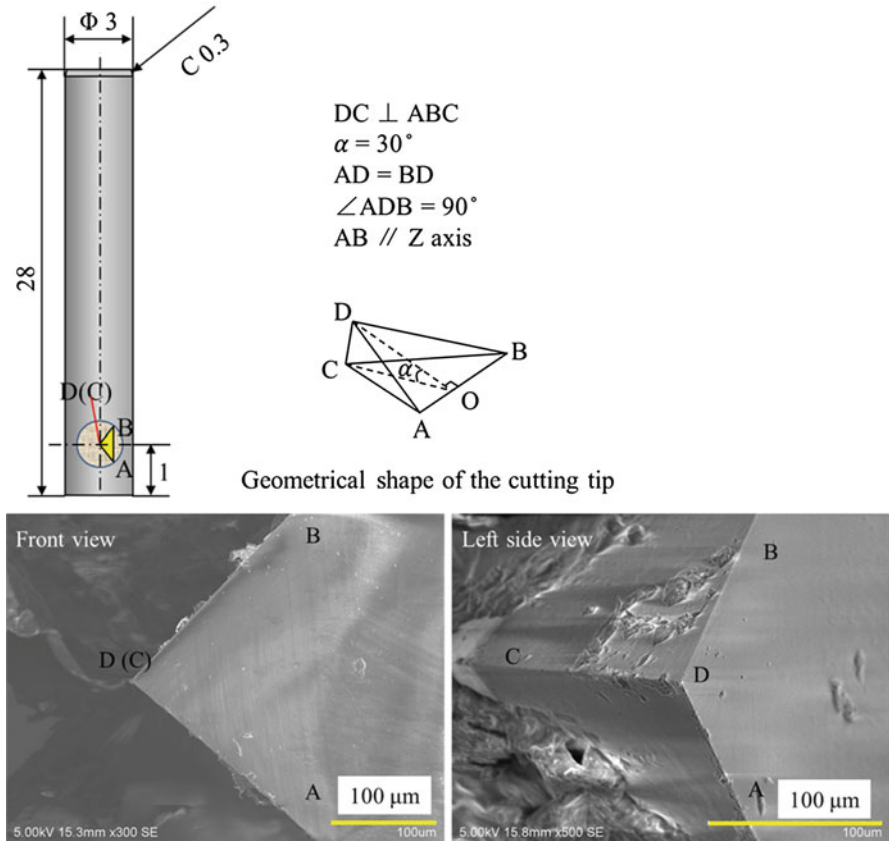


Fig. 33 The geometrically defined one-point diamond tool with a triangular pyramid cutting tip for the RUT process in the LV mode (Xu et al. 2016)

The relationship between the geometries of the cutting tips and the shapes of the cutting loci also requires attention, as shown in Fig. 36. The reason for this is that, when one rake face (e.g., face BCD) removes the material from the workpiece, the interface volume between the other rake face (ACD) and the workpiece must also be considered. The included angle (β^*) of the line segment (between the two adjacent lowest and highest points at the cutting locus) in the horizontal direction (as shown in Fig. 36a) is a critical value and must be considered as follows: if β^* is equal or greater than $\beta/2$ (as shown as shown in Fig. 36b), the rake face BCD removes the material along the sinusoidal cutting locus when the tool vibrates upward. The interference volume between the face ACD and the workpiece is relatively small under these conditions, which are assumed to be only just capable of generating elastic deformation and so are ignored in the present modeling process. The same assumption is used when the tool vibrates downward. However, if β^* is smaller than $\beta/2$ (as shown in Fig. 36c) when the tool vibrates upward (or downward), the interference volume

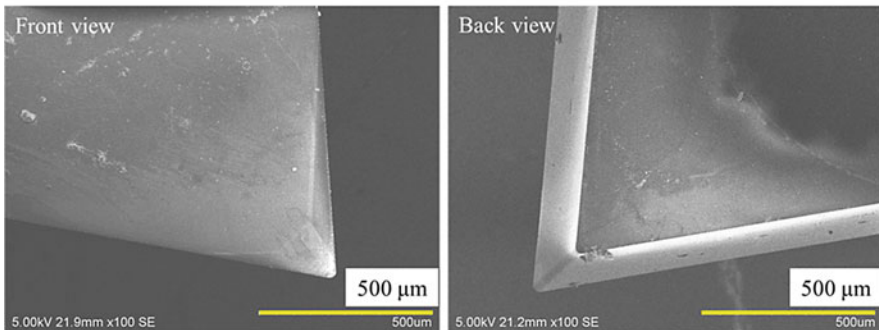
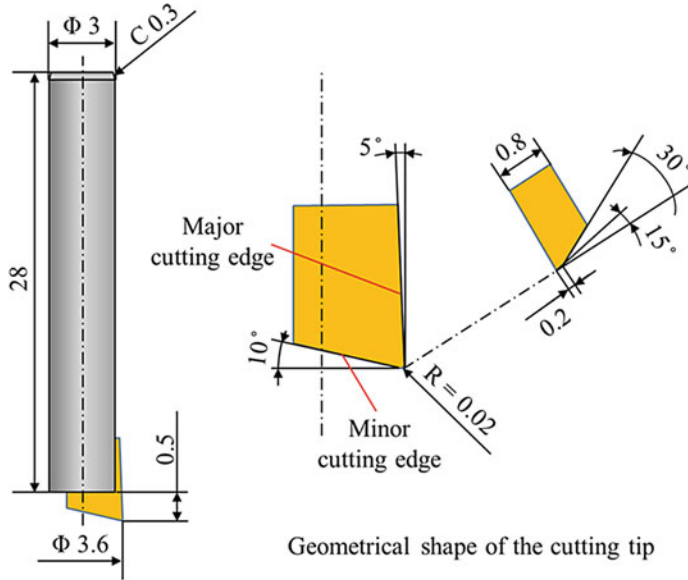


Fig. 34 The geometrically defined one-point diamond tool for the RUT process in the CV mode (Xu et al. 2017)

between face ACD (or face BCD) and the workpiece can be large enough to generate plastic deformation or material removal, which cannot be ignored. Therefore, in the modeling process, the two rake faces are assumed to simultaneously remove the material when β^* is smaller than $\beta^*/2$.

The overall surface textures depend not only on the geometry of the diamond cutting tip but also on the shapes and combinations of the sinusoidal cutting loci along the Z axis. The shape of the sinusoidal cutting locus is determined by (1) the resultant motion of the ultrasonic vibration, (2) the rotation, and (3) the feed motion, which can be fully controlled during the texturing process. Figure 37 shows two types of textured surface when the phase difference of every two adjacent sinusoidal loci along the Z axis is 90° . Figure 38 shows another combination of sinusoidal cutting loci (0-degree phase difference) and the corresponding textured surfaces. It

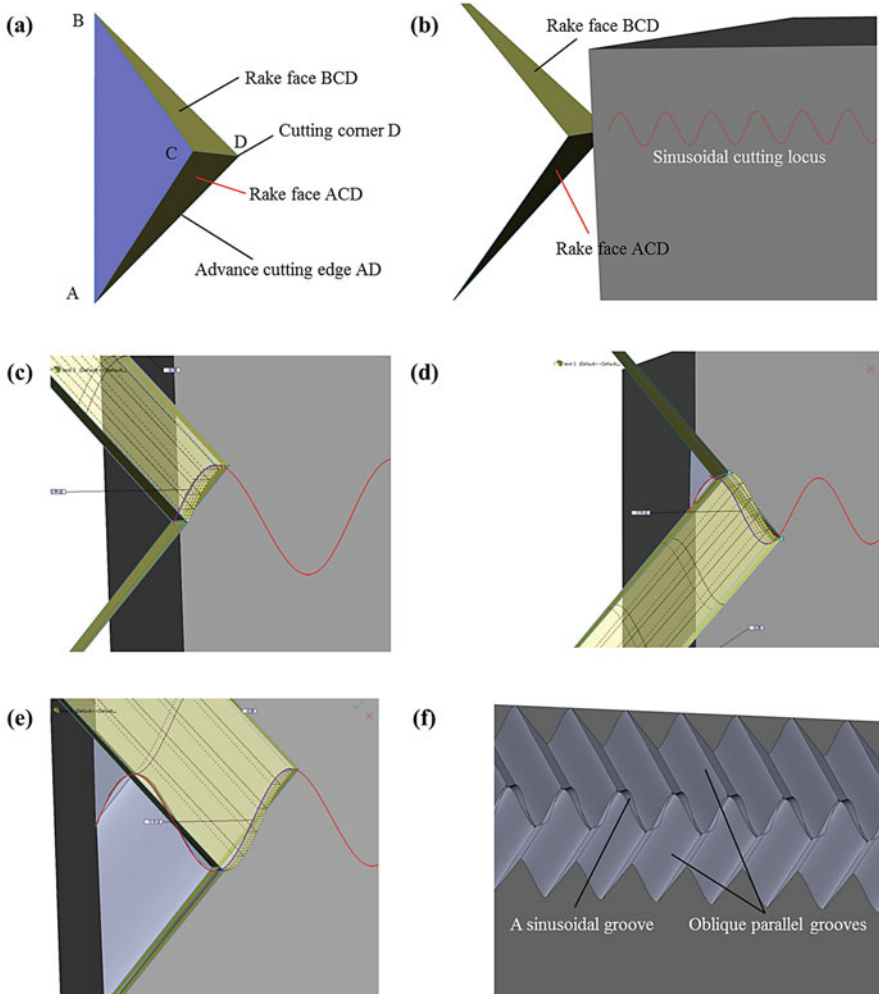


Fig. 35 Illustration of the surface generation model of the RUT process in the LV mode: (a) the triangular pyramid cutting tip, (b) the sinusoidal cutting locus along the workpiece, (c–e) the material removal processes, and (f) a textured surface

can be seen that different 3D textural patterns can be generated by combining various parameters in the RUT process. All of the textural features of these 3D shapes can be mathematically calculated in the present modeling process. For instance, as shown in Fig. 37b, if the surface height of the sinusoidal groove is assumed to be 0, then the surface heights (h_1 and h_2) of the two representative points H_1 (with the maximum surface height) and H_2 can be described by Eqs. (20) and (21), respectively. The length of the oblique parallel grooves (l_o) can be calculated by Eq. (22). Therefore, it can be concluded that the present modeling process can be used to predict and control the textural patterns of the finished surfaces in the LV mode.

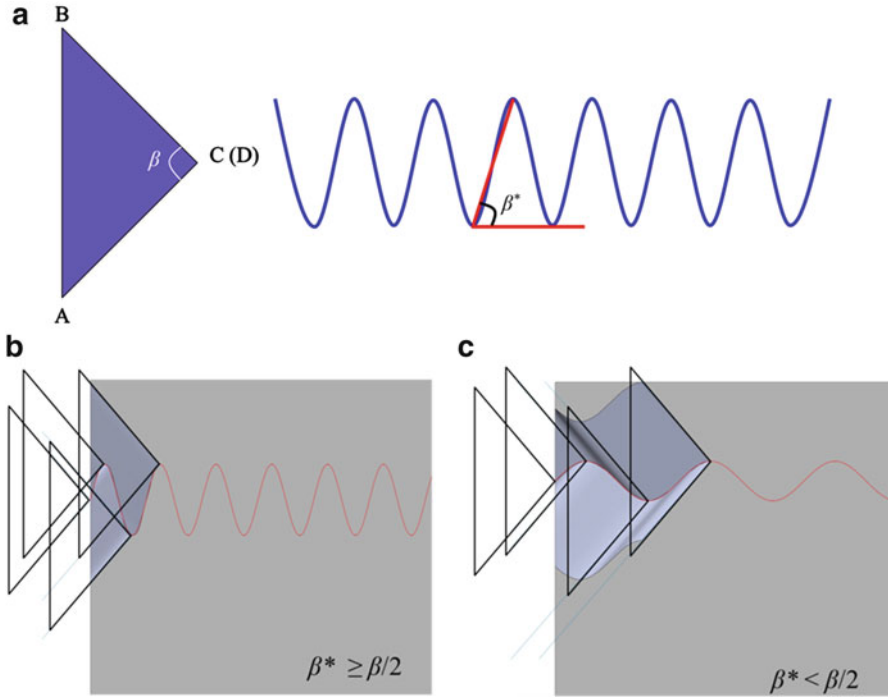


Fig. 36 (a) Relationship between the geometries of the cutting tips and the shapes of the cutting loci, (b) the material removal process ($\beta^* \geq \beta/2$), and (c) the material removal process ($\beta^* < \beta/2$)

$$h_1 = \frac{l_z + A_l}{2} \times \tan \angle BAC \times \tan \alpha = \frac{l_z + A_l}{4} \quad (20)$$

$$h_2 = \frac{l_z - A_l}{2} \times \tan \angle BAC \times \tan \alpha = \frac{l_z - A_l}{4} \quad (21)$$

$$l_o = \frac{l_z - A_l}{2} \times \frac{1}{\cos \angle BAC} \times \frac{1}{\cos \angle DAC} = \frac{l_z - A_l}{\sqrt{2}} \quad (22)$$

8.5.4.3 Surface Generation Model for the CV Mode

Figure 39 describes a surface generation process of the RUT method in the CV mode ($v_c > v_p, a_p > h_c^*$). The diamond tip has one rake face and one flank face, as shown in Fig. 39a. The clearance angle is 15° , and the major cutting edge has an included angle of 5° to the Z axis. The interference volume between the flank face and workpiece is very small and not considered in this modeling process. Figure 39c, d depicts the material removal process when using the rake face and the textured pattern after one tool rotation period, respectively. Along the cutting locus (as shown

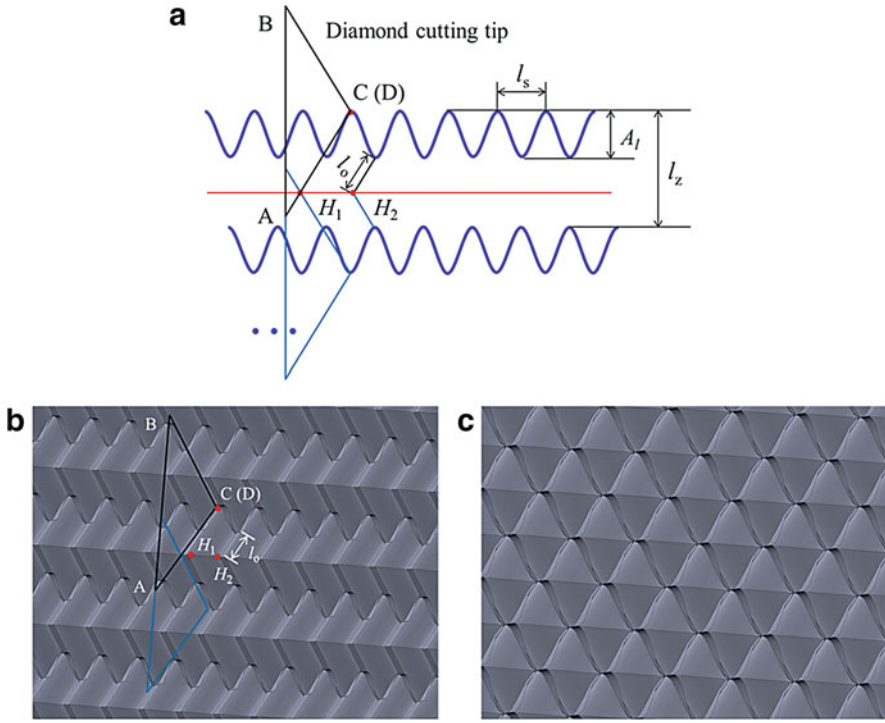


Fig. 37 (a) Two adjacent sinusoidal cutting loci with 90-degree phase difference, (b) generated surface topography when $l_z = 3A_l$, and (c) generated surface topography when $l_z = A_l$

in Fig. 39b), the rake face will intermittently remove the work material to generate surface textures, as shown in Fig. 39e.

Figure 40 shows the textured surfaces when $v_c = 5v_p$. It can be found from Fig. 40c that discontinuous textured patterns can be fabricated when the cutting depth is smaller than the critical value (h_c^*). With an increase in the cutting depth, continuous linear grooves can be generated. The width and depth of the linear grooves (as shown in Fig. 40e) are equal to w_c^* and h_c^* , respectively.

Figure 41 shows the textured surfaces when $v_c = v_p$. It can be found from Fig. 41a that only when the cutting depth is greater than the vibration amplitude ($10 \mu\text{m}$) of the CV mode can the continuous linear grooves be fabricated. However, the volume of the material removed during each period of vibration is very large, and the interference volume between the flank face and the workpiece is also very large; therefore, severe wear of the diamond tools may result. Figure 41b, c shows discontinuous textured patterns when the cutting depth is smaller than the critical value (h_c^* , without considering the interference between the flank face and workpiece). All of the textural features can be directly obtained for the results of the modeling processes.

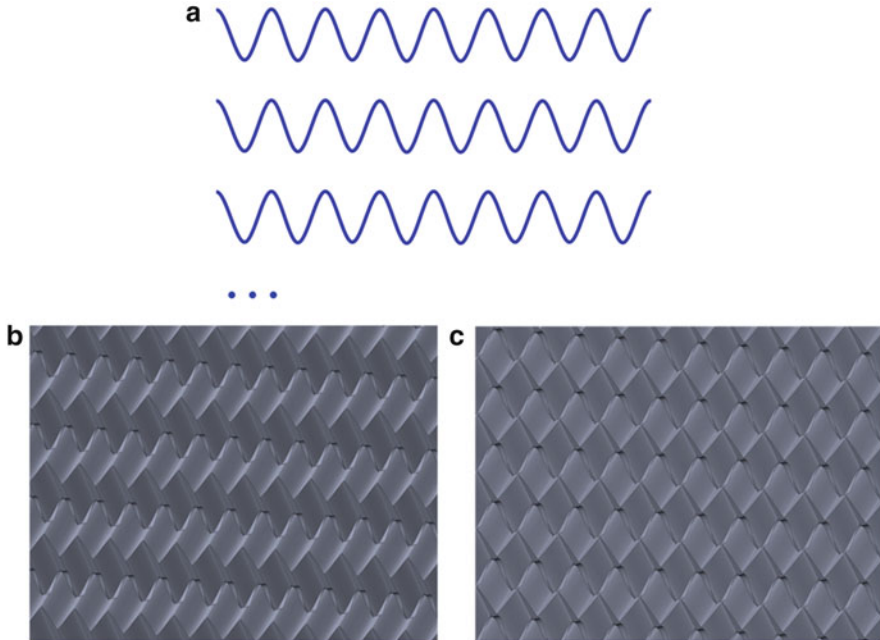


Fig. 38 (a) Sinusoidal cutting loci with 0-degree phase difference, (b) generated surface topography when $l_z = 3A_t$, and (c) generated surface topography when $l_z = 2A_t$

8.5.5 Fabrication of Micro-/Nano-textures

8.5.5.1 Micro-/Nano-texturing in the LV Mode

The diamond cutting tools shown in Figs. 32 and 33 were used successively for texturing experiments in the LV mode. The experimental conditions are listed in Table 3. The 3D textured surfaces were measured using SEM and a white light interferometer (Taylor Hobson, Talysurf CCI – lite noncontact 3D profiler).

Figure 42 shows the SEM images of surfaces fabricated using the tool with the square pyramid cutting tip. To evaluate the texturing performance in the RUT process, the cutting depth was increased gradually along the negative Z axis with an inclined workpiece surface. Owing to the radial motion of the cutting tip, from left to right on the workpiece, the instantaneous cutting depth of the cutting corner E increases from 0 to the maximum and then back to 0, as shown in Fig. 42a. The volume of the work material removed by the cutting tip between every two neighboring peak points at the sinusoidal locus increased when the cutting depth was increased. It can be observed that this kind of tool cannot efficiently remove the cutting chips. Only at a very small cutting depth were the cutting chips removed from the workpiece and the sinusoidal grooves successfully fabricated, as shown in Fig. 42a. However, it is very difficult to control the cutting depth at such a small value in the actual texturing process. The machining efficiency also has to be considered. With an increase in cutting depth, the cutting chips occupy the machined area, and no obvious surface textures are observed, as shown in Fig. 42b. The

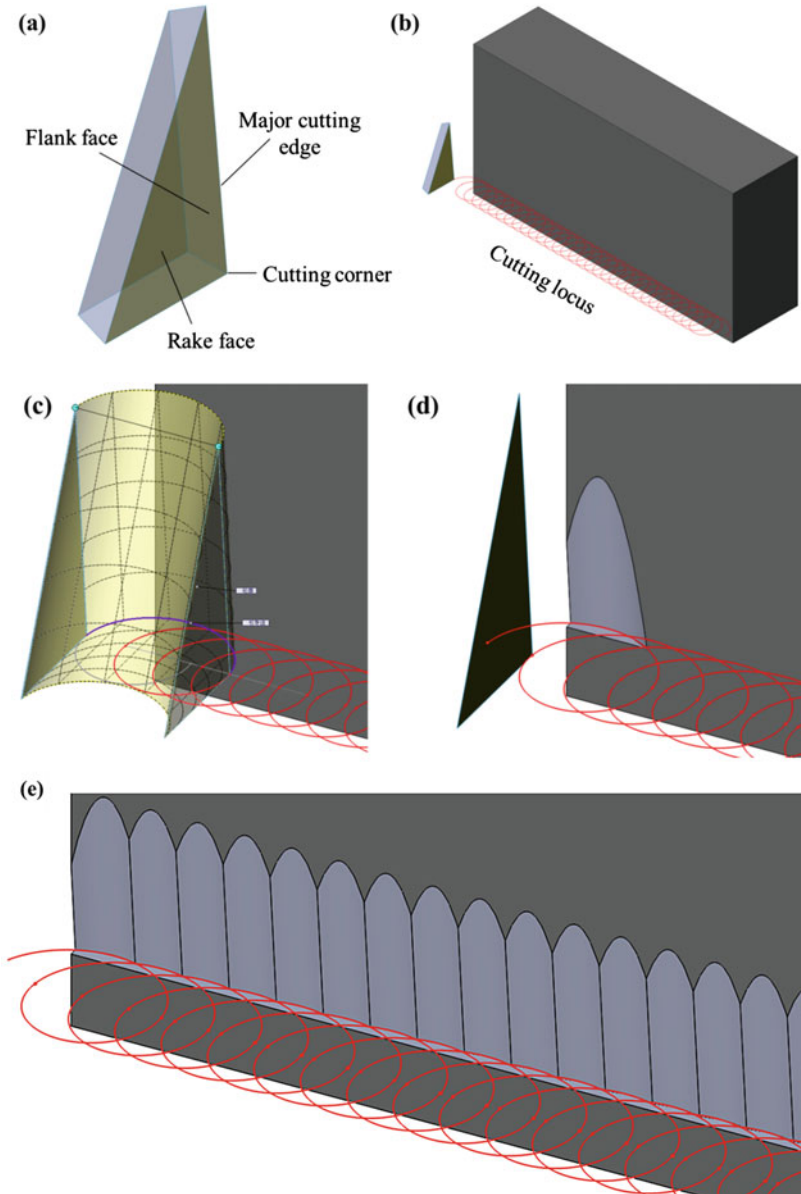


Fig. 39 Illustration of the surface generation model of the RUT process in the CV mode: (a) the diamond cutting tip, (b) the cutting locus along the workpiece, (c) the material removal process, and (d, e) surface textures generated along the cutting locus

experimental results reveal that micro-/nano-fabrication cannot be achieved if the volume of the work material removed by the cutting tip between every two neighboring peak points cannot be controlled. The generation of cutting chips along the sinusoidal locus in an ultrasonic periodical manner also has to be considered in

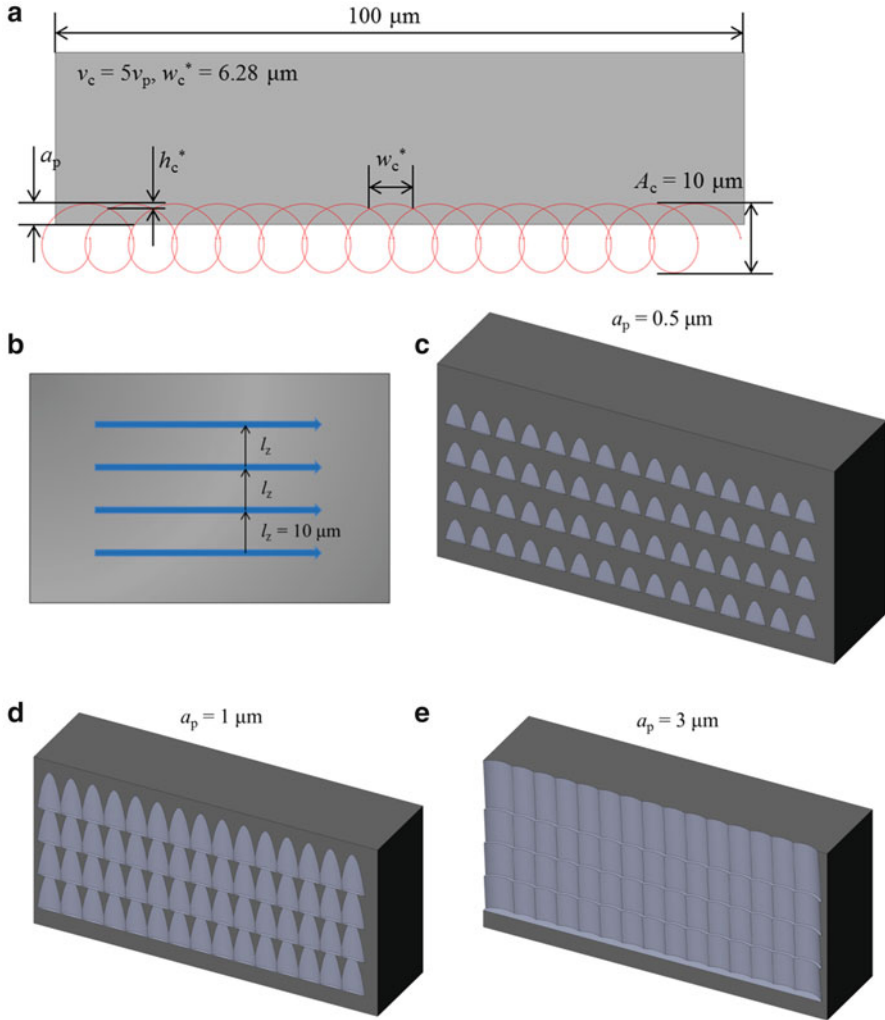


Fig. 40 (a, b) Texturing parameters ($v_c = 5v_p$), (c) textured surface when $a_p = 0.5 \mu\text{m}$, (d) textured surface when $a_p = 1 \mu\text{m}$, and (e) textured surface when $a_p = 3 \mu\text{m}$

relation to the design of a new tool. Therefore, the triangular pyramid cutting tip, with an advance cutting edge and two rake faces, was proposed for controlling the generation and removal of cutting chips in the RUT process.

Figure 43 shows the textured surfaces fabricated using the tool with the triangular pyramid cutting tip. It can be observed that all of the cutting chips have been removed from the workpiece and that the textured surfaces are successfully fabricated in all of the machined areas, as shown in Fig. 43a, b. The textural features are clearly depicted in Fig. 43c, d, which show a larger magnification image and the 3D profile, respectively. It can be seen that the experimental results coincide well with

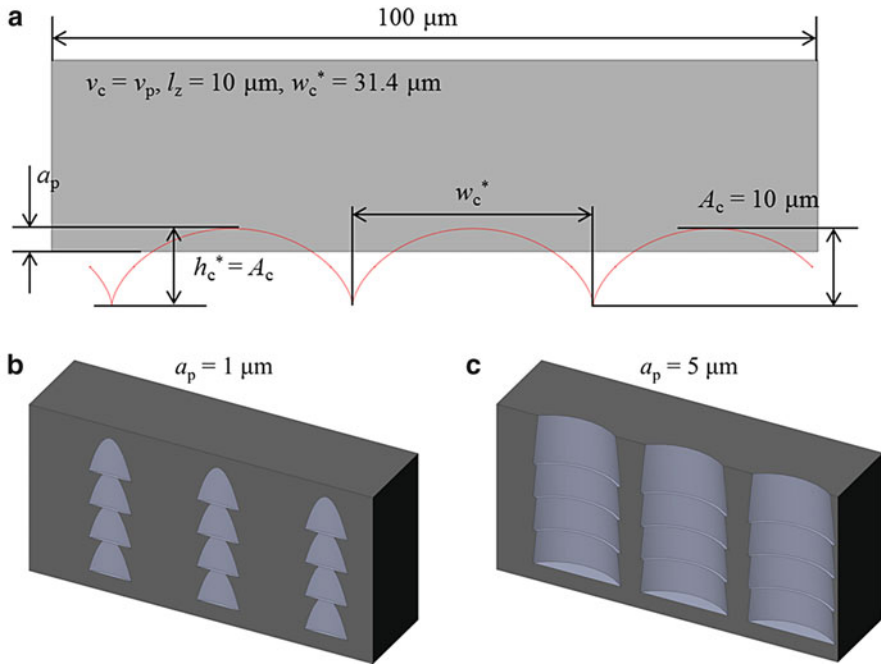


Fig. 41 (a) Texturing parameters ($v_c = v_p$), (b) textured surface when $a_p = 1 \mu\text{m}$, and (c) textured surface when $a_p = 5 \mu\text{m}$

Table 3 Experimental conditions

Workpiece (Ni-P plating)	Phosphorous content	10 wt.%
Machining conditions	Rotational frequency (rpm)	250–1000
	Feed speed along Z axis (mm/min)	1–6
	Cutting depth (μm)	0–10
Ultrasonic vibration spindle (SD-100)	Vibration frequency (kHz)	62
	Vibration amplitude (peak to peak) (μm)	2
Ultrasonic vibration spindle (SC-450SP-H24)	Vibration frequency (kHz)	25
	Vibration amplitude (peak to peak) (μm)	3

the results of the modeling processes, as illustrated in Sect. 8.5.4.2. As such, the sinusoidal grooves with maximum depth are fabricated by cutting corner D; the oblique parallel grooves above and under the sinusoidal grooves are fabricated by cutting edges BD and AD, respectively; the periodic 3D shapes with features similar to those shown in Fig. 37b are successfully fabricated; and the textural features can be calculated using equations in Sect. 8.5.4.2. i.e., $h_1 = 2 \mu\text{m}$, $h_2 = 1 \mu\text{m}$, and $l_o \approx 2.83 \mu\text{m}$. Note that no device for synchronizing the rotation, vibration, and feed motion was employed in the present study. The phase differences between every two

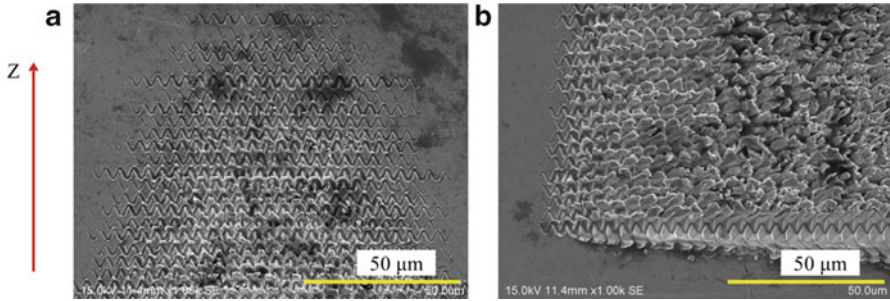


Fig. 42 Textured surfaces fabricated by the tool with the square pyramid cutting tip (SC-450SP-H24; $n_t = 500$ rpm and $v_f = 2$ mm/min): (a) top area and (b) bottom left area (Xu et al. 2016)

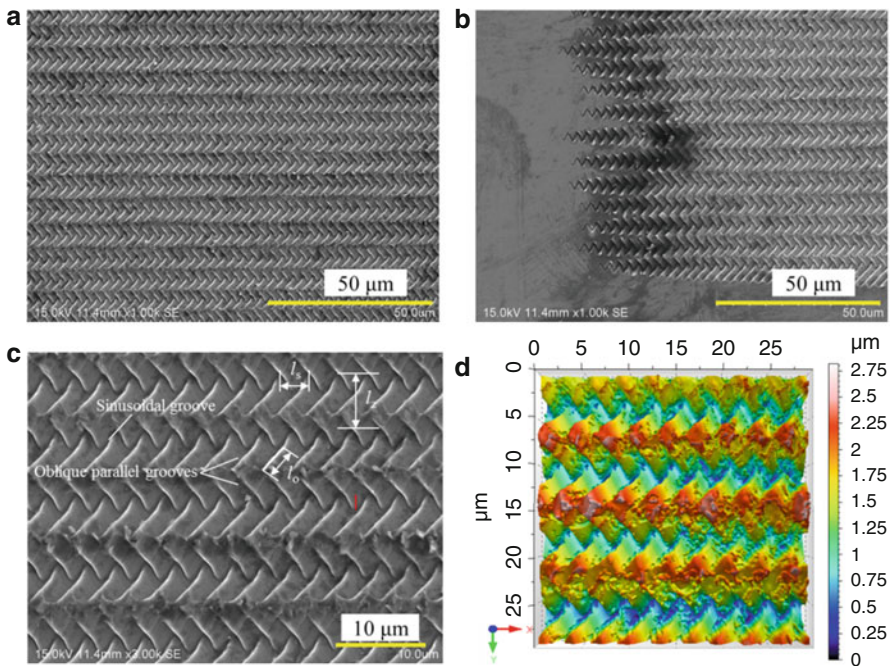


Fig. 43 Textured surfaces fabricated by the tool with the triangular pyramid cutting tip (SD-100; $n_t = 1000$ rpm and $v_f = 6$ mm/min): (a) the middle part, (b) the bottom left area, (c) greater magnification, and (d) the 3D surface profile (Xu et al. 2016)

adjacent sinusoidal grooves along the Z axis are not constant. Therefore, the surface heights of the representative points H_1 and H_2 (as shown in Fig. 43b) are not strictly the same as those shown in Fig. 43d.

Figure 44 shows the 3D surface profiles of a hybrid linear groove with micro-/nanostructures on its inner surface. This was fabricated with the triangular pyramid

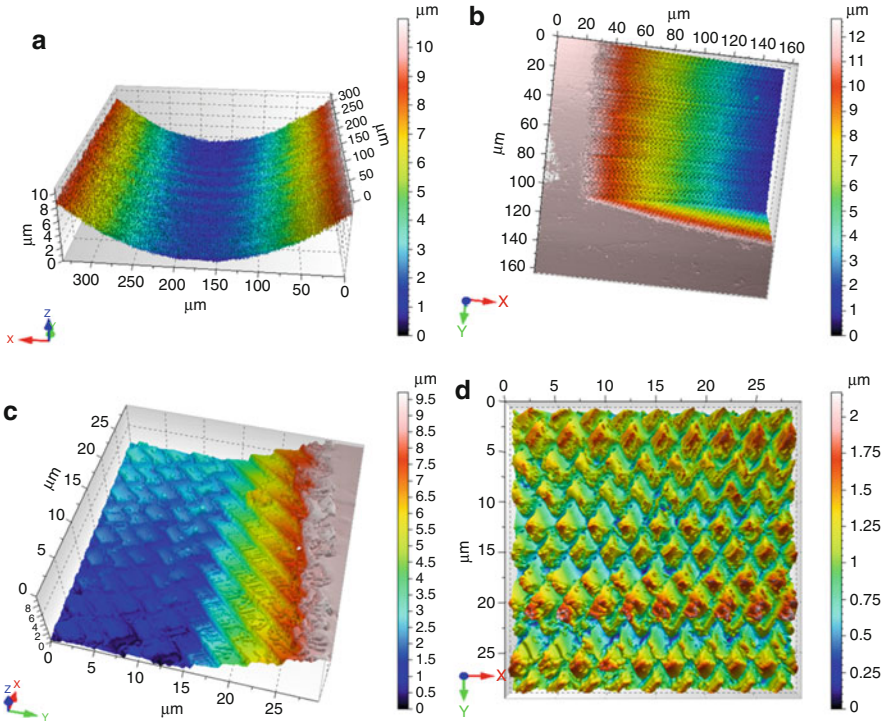


Fig. 44 3D surface topographies of a hybrid groove along the Z axis, as fabricated by the tool with a triangular pyramid cutting tip (SD-100; $n_t = 1000$ rpm and $v_f = 2$ mm/min): (a) linear groove along the Z axis, (b) bottom left of the textured area, (c) middle bottom of the textured area, and (d) textures on the groove's inner surface (Xu et al. 2016, 2017)

cutting tip after one feed path along the Z axis. The following are observed: (1) the linear groove is approximately $10\ \mu\text{m}$ in depth and $340\ \mu\text{m}$ in width; (2) the change in the cutting depth of the cutting corner with radial motion of the cutting tip can be observed in Fig. 44b; (3) the advance cutting edge AD removes most of the work material and fabricates oblique parallel grooves in advance, as shown in Fig. 44c; and (4) various 3D shapes are seen in Fig. 44d owing to the change in phase differences between every two adjacent sinusoidal grooves along the Z axis, which also suggests that different structures could be fabricated if the rotation, vibration, and feed motion can be synchronized in the RUT process. SEM images and 3D surface profiles of three other types of textured surfaces with a bigger magnification are presented in Fig. 45. The results clearly show that various periodic sinusoidal grooves and 3D shapes with dimensions of several micrometers and even several hundred nanometers are successfully fabricated. The value of l_z remains the same in all of the three images, whereas l_s doubles as n_t doubles. The highest points of the 3D shapes, which can be clearly observed in Fig. 45c, agree well with the results of the modeling processes described in Sect. 8.5.4.2.

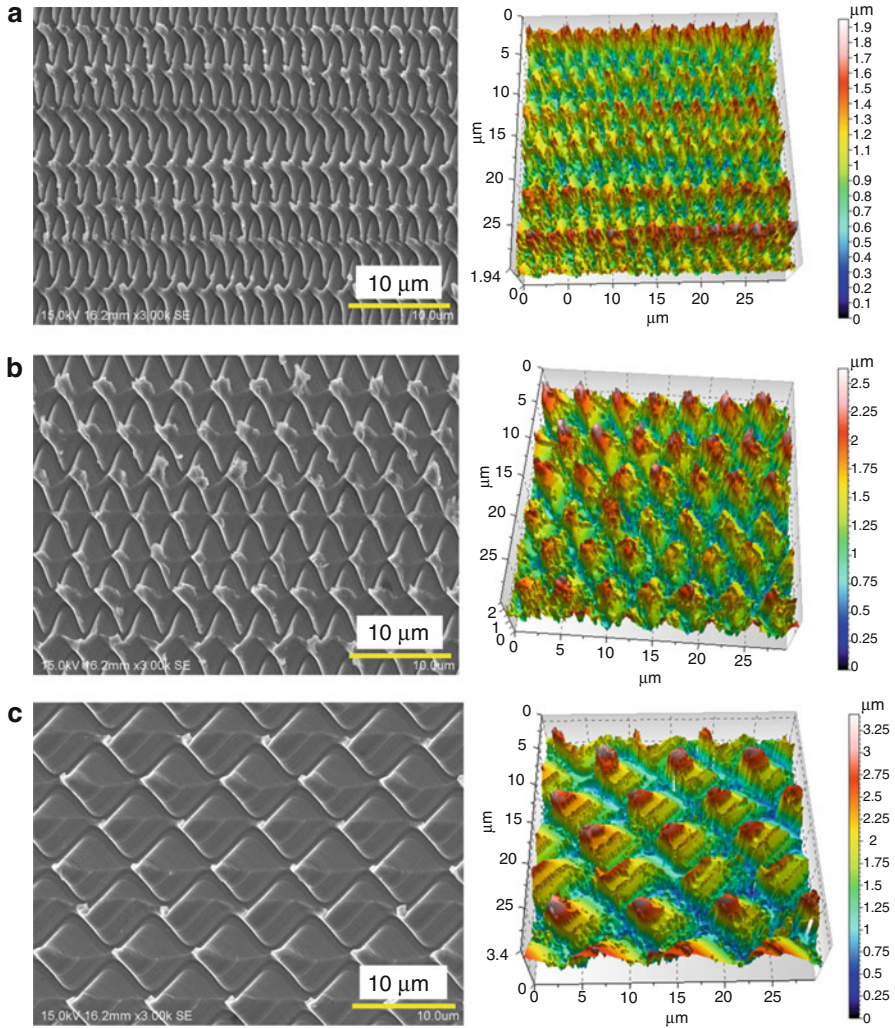


Fig. 45 Three other textured surfaces fabricated using the tool with a triangular pyramid cutting tip (SC-450SP-H24): (a) $n_t = 250$ rpm and $v_f = 1$ mm/min, (b) $n_t = 500$ rpm and $v_f = 2$ mm/min, and (c) $n_t = 1000$ rpm and $v_f = 4$ mm/min (Xu et al. 2016, 2017)

8.5.5.2 Micro-/Nano-texturing in the CV Mode

The diamond cutting tools shown in Figs. 32 and 34 were successively used for surface texturing experiments in the CV mode. The experimental conditions are listed in Table 4. A 3D ultrasonic vibration spindle (SC-450SP-H24) was utilized to generate circular vibration in the experiments. All workpiece samples were pre-machined using a single-point diamond tool for generating flat surfaces with roughness of less than $0.01 \mu\text{m}$.

Table 4 Experimental conditions in the CV mode

Workpiece	Pure aluminum	99.9 wt.%
	Ni-P plating	Phosphorous content: 10 wt.%
Machining conditions	Rotational frequency (rpm)	500, 1000, 3000
	Feed speed along Z axis (mm/min)	2, 4, 40, 120
	Cutting depth (μm)	0–10
Ultrasonic vibration spindle (SC-450SP-H24)	Vibration frequency (kHz)	19
	Vibration amplitude (peak to peak) (μm^2)	10×10

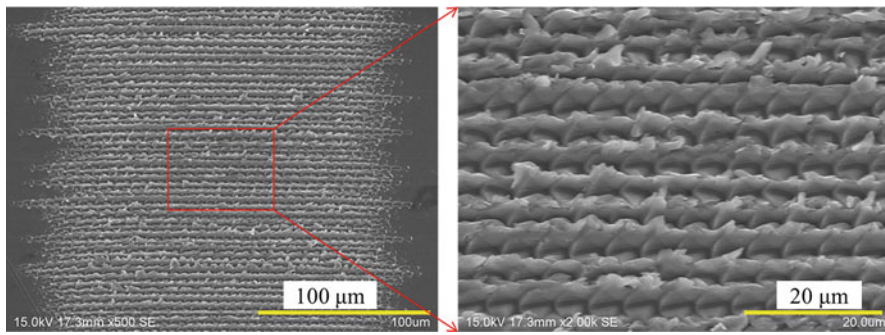
**Fig. 46** Textured surfaces fabricated using the tool with a square pyramid cutting tip ($n_t = 500$ rpm and $v_{tz} = 2$ mm/min)

Figure 46 shows SEM images of the textured surfaces fabricated on an aluminum sample using the tool with a square pyramid cutting tip (as shown in Fig. 32). It can be seen that the cutting tip was sufficiently sharp to scratch cut tracks on the finished surface. However, the material was not efficiently removed from the workpiece; rather, it gathered on both sides of the cut tracks. The reason for this is that the instantaneous rake angle in the texturing process was around -35° (the negative value of half of the included angle); therefore, the ductile material, pure aluminum, was extruded and flowed to both sides of the cut tracks with plastic deformation. The experimental results indicate that the negative rake angle may result in the gathering of cutting debris on the textured surface; this requires further attention.

Figures 47, 48, and 49 show SEM images and surface profiles of the textured surfaces fabricated on the Ni-P plating samples using the tool shown in Fig. 34. In Fig. 47, l_z can be calculated as $4 \mu\text{m}$, which is too small to generate obvious linear grooves along the Z axis. With an increase in feed speed along the Z axis while keeping the rotation speed constant at 1000 rpm, the continuous linear grooves shown in Fig. 48 were successfully fabricated. The experimental results coincide well with the results of the modeling processes, as depicted in Fig. 40e. The cutting debris was efficiently removed from the workpiece, and textured surfaces with few

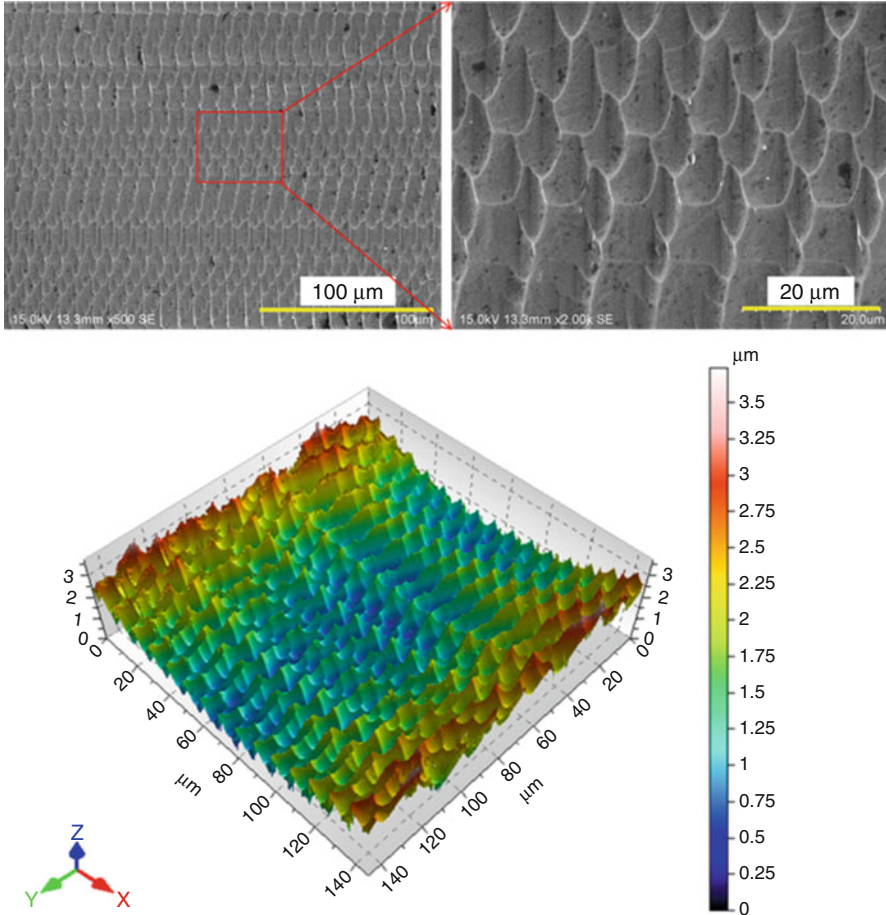


Fig. 47 Surface structures and profiles of the textured surfaces fabricated using the tool shown in Fig. 34 ($n_t = 1000$ rpm and $v_{tz} = 4$ mm/min) (Xu et al. 2017)

burrs were fabricated. Again, since no device for synchronizing rotation, vibration, and feed motion was employed (as explained in Sect. 8.5.5.1), the phase differences of every two adjacent cutting loci along the Z axis were not controlled during the texturing process. Therefore, phase shifts of the linear grooves along the Z axis were observed. The 2D surface profile along the axial direction (as shown in Fig. 48) is caused by the included angle (5°) between the major cutting edge and the Z axis. Therefore, the continuous linear grooves were fabricated on inclined surfaces. The surface profile along the horizontal direction (as shown in Fig. 48) shows that the width of the linear grooves is approximately $9 \mu\text{m}$, which agrees with the result ($8.2 \mu\text{m}$) calculated using Eq. (13). When the rotation speed increased further, linear grooves with larger depth and width can be generated, as described in the modeling process. Figure 49 shows the structures and profile of a textured surface fabricated at the maximum rotation speed of the 3D ultrasonic vibration spindle. Continuous

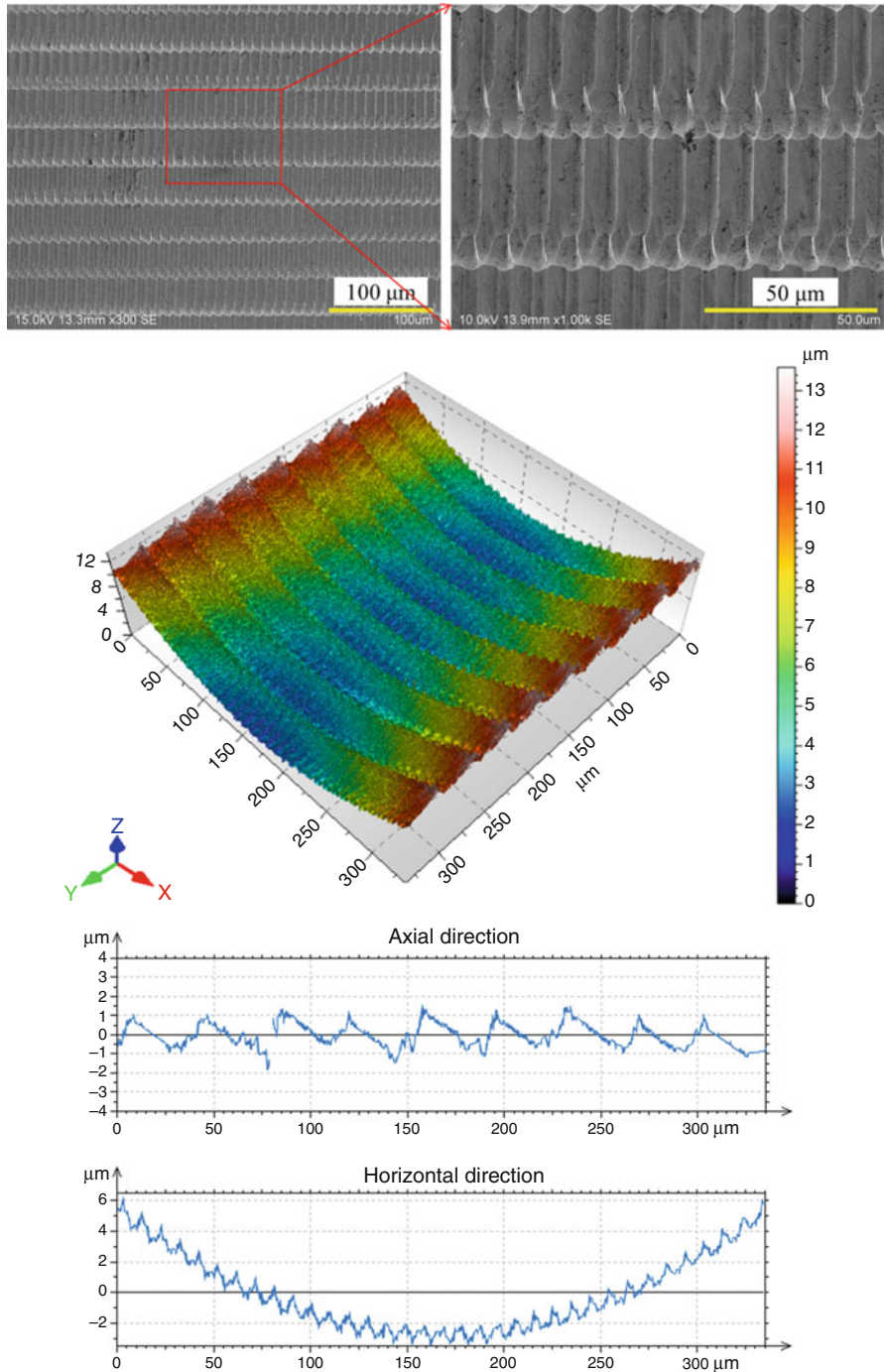


Fig. 48 Surface structures and profiles of the textured surfaces fabricated using the tool shown in Fig. 34 ($n_t = 1000$ rpm and $v_{tz} = 40$ mm/min) (Xu et al. 2017)

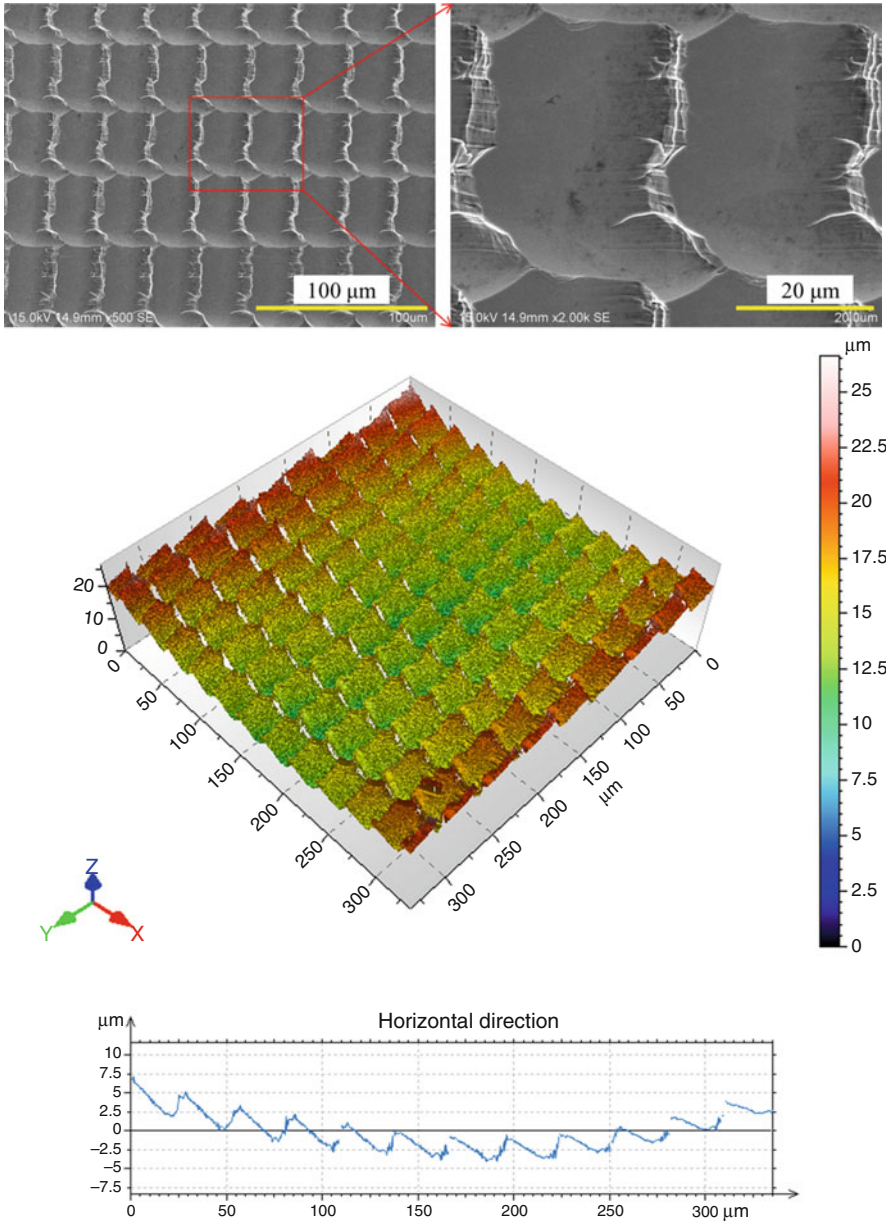


Fig. 49 Surface structures and profiles of the textured surfaces fabricated using the tool shown in Fig. 34 ($n_t = 3000$ rpm and $v_{tz} = 120$ mm/min) (Xu et al. 2017)

linear grooves with a depth of approximately 4 μm and a width of approximately 25 μm were successfully fabricated. However, cutting burrs were observed on the conjunct areas of every two adjacent linear grooves. The interference between the flank face and the workpiece may partly result in the cutting burrs. Another reason is that the instantaneous rake face may maintain a very large negative value when (1) the cutting depth is larger than the vibration amplitude and (2) the rotation speed is greater than the critical value, as described in the modeling process.

8.5.6 Discussion

8.5.6.1 Effect of Cutting Loci Shape

The surface condition that occurs in most machining operations is a result of the cutting edge exiting the workpiece (Boothroyd and Knight 2006). The ultrasonic vibration makes the tool periodically vibrate at a very high frequency; thus, the cutting edge contacts and exits the workpiece at the same frequency along the cutting locus. Specifically, the sinusoidal cutting locus in the LV mode in the RUT process makes the cutting edge remove the material and exit the workpiece at each peak point of the sinusoidal locus, which results in the formation of cutting debris and the generation of burrs around the peak points on the textured surfaces. The cutting loci in the CV mode, as described in the modeling process, make the cutting edge intermittently or continuously remove the material. The relationship between the shape of the cutting edge and the shape of the cutting loci determines the interference between the flank face and the workpiece. It also determines the instantaneous rake angle, which results in different material removal mechanisms. The large interference volume and large negative rake angle could be prevented by an improved design of the shape of the cutting loci. The work material is sheared and removed in an ultrasonic periodical manner, which is fundamentally different from that of the conventional cutting process. Therefore, the geometry of the tool cutting tip should be carefully designed to control the generation and removal of cutting chips along the cutting loci, thus allowing for efficient chip removal and the fabrication of surfaces with fewer cutting burrs.

8.5.6.2 Effect of Cutting Edge Geometry

The geometry of the cutting edges should be designed to more efficiently remove cutting chips and decrease cutting burrs on the edges of textural patterns. This would increase the stability and capability of the micro-/nano-texturing technique.

The radial motion of the diamond cutting tip makes the instantaneous cutting depth change periodically when fabricating textures on flat surfaces. The advance cutting edge could be designed to control the instantaneous cutting depth along the feed direction, i.e., by modulating the amount of the work material removed by the cutting tip in each vibration period, thus making the texturing process more stable.

When the LV mode is employed, the design of the triangular pyramid cutting tip can be used to efficiently remove the cutting chips. As shown in Fig. 36b, the cutting chips and cutting burrs generated in one vibration period can be removed by the cutting process in the next vibration period along the sinusoidal cutting locus. In the

case shown in Fig. 36c, the cutting chips and cutting burrs generated by the upper rake face or lower rake face in a half vibration period can be immediately removed by the same rake face in the next half vibration period. Therefore, the adverse effect of the high-frequency tool-exit-workpiece motion can be largely eliminated. Ultimately, the micro-/nano-textures were successfully fabricated.

When the CV mode is employed, the large interference volume between the flank face and workpiece should be avoided. Continuous textural patterns are required to eliminate the adverse effect of the high-frequency tool-exit-workpiece motion. Therefore, the tool flank angle should be designed based on a consideration of the shapes of the applied cutting loci.

8.6 Summary and Outlook

The newly proposed ultrasonic-assisted texturing method provides designers with additional freedom to fabricate precisely controlled micro-/nano-textured surfaces at relatively high speed. The geometrically defined one-point diamond tools enrich tool design principles in the diamond machining field, and they also enlarge the range of machinable structures possible using diamond machining techniques. Theoretically, various surface textures other than those discussed in the present dissertation can be fabricated using the RUT method if the diamond tools are designed with cutting edges of appropriate geometry. To further develop the RUT technique, diamond tools should be designed and optimized so as to be capable of fabricating the textural patterns required in practical application fields.

In a future work, a more robust and flexible ultrasonic-assisted texturing method should be developed based on the rotary ultrasonic spindle. Moreover, the scientific principles applicable to the design of textural patterns for functional performance should be given greater attention.

References

- Abbas NM, Solomon DG, Bahari MF (2007) A review on current research trends in electrical discharge machining (EDM). *Int J Mach Tools Manuf* 47(7–8):1214–1228
- Boothroyd G, Knight WA (2006) *Fundamentals of machining and machine tools*. Taylor and Francis, UK
- Brehl DE, Dow TA (2008) Review of vibration-assisted machining. *Precis Eng* 32(3):153–172
- Brinksmeier E, Gläbe R, Schönemann L (2012) Review on diamond-machining processes for the generation of functional surface structures. *CIRP J Manuf Sci Technol* 5(1):1–7
- Cheng J, Liu C, Shang S, Liu D, Perrie W (2013) A review of ultrafast laser materials micro-machining. *Opt Laser Technol* 46:88–102
- Denkena B, Kästner J, Wang B (2010) Advanced microstructures and its production through cutting and grinding. *CIRP Ann Manuf Technol* 59(1):67–72
- Dubey AK, Yadava V (2008) Laser beam machining – a review. *Int J Mach Tools Manuf* 48(6):609–628
- Ehmann KF, Hong MS (1994) A generalized model of the surface generation process in metal cutting. *CIRP Ann Manuf Technol* 43(1):483–486

- Hansen HN, Hocken RJ, Tosello G (2011) Replication of micro and nano surface geometries. *CIRP Ann Manuf Technol* 60(2):695–714
- Ho KH, Newman ST (2003) State of the art electrical discharge machining (EDM). *Int J Mach Tools Manuf* 43(13):1287–1300
- Kim DS, Chang IC, Kim SW (2002) Microscopic topographical analysis of tool vibration effects on diamond turned optical surfaces. *Precis Eng* 26(2):168–174
- Kurosawa M, Kodaira O, Tsuchitoi Y, Higuchi T (1998) Transducer for high speed and large thrust ultrasonic linear motor using two sandwich-type vibrators. *IEEE Trans Ultrason Ferroelectr Freq Control* 45(5):1188–1195
- Lee WB, Cheung CF (2001) A dynamic surface topography model for the prediction of nano-surface generation in ultra-precision machining. *Int J Mech Sci* 43(4):961–991
- Lin SC, Chang MF (1998) A study on the effects of vibrations on the surface finish using a surface topography simulation model for turning. *Int J Mach Tools Manuf* 38(7):763–782
- Liu X, Du D, Mourou G (1997) Laser ablation and micromachining with ultrashort laser pulses. *IEEE J Quantum Electron* 33(10):1706–1716
- Lyshevski SE (2002) MEMS and NEMS: systems, devices, and structures. Taylor & Francis, UK
- Masuzawa T (2000) State of the art of micromachining. *CIRP Ann Manuf Technol* 49(2):473–488
- Moriwaki T, Shamoto E (1995) Ultrasonic elliptical vibration cutting. *CIRP Ann Manuf Technol* 44(1):31–34
- Rozzi JC, Pfeifferkorn FE, Incropera FP, Shin YC (2000a) Transient, three-dimensional heat transfer model for the laser assisted machining of silicon nitride: I. Comparison of predictions with measured surface temperature histories. *Int J Heat Mass Transf* 43(3):1409–1424
- Rozzi JC, Pfeifferkorn FE, Shin YC (2000b) Transient, three-dimensional heat transfer model for the laser assisted machining of silicon nitride: II. Assessment of parametric effects. *Int J Heat Mass Transf* 43(8):1425–1437
- Shamoto E, Moriwaki T (1994) Study on elliptical vibration cutting. *CIRP Ann Manuf Technol* 43(1):35–38
- Shimada K (2012) Study on vibration grinding. Doctoral thesis
- Shimada S, Tanaka H, Higuchi M, Yamaguchi T, Honda S, Obata K (2004) Thermo-chemical wear mechanism of diamond tool in machining of ferrous metals. *CIRP Ann Manuf Technol* 53(1):57–60
- Shimomura M, Sawadaishi T (2001) Bottom-up strategy of materials fabrication: a new trend in nanotechnology of soft materials. *Curr Opin Colloid Interface Sci* 6(1):11–16
- Stupp SI, LeBonheur V, Walker K, Li LS, Huggins KE (1997) Supramolecular materials: self-organized nanostructures. *Science* 276(5311):384–389
- Thoe TB, Aspinwall DK, Wise MLH (1998) Review on ultrasonic machining. *Int J Mach Tools Manuf* 38(4):239–255
- Xing D, Zhang J, Shen X, Zhao Y, Wang T (2013) Tribological properties of ultrasonic vibration assisted milling aluminium alloy surfaces. *Procedia CIRP* 6:539–544
- Xu S, Nishikawa C, Shimada K, Mizutani M, Kuriyagawa T (2013) Surface textures fabrication on zirconia ceramics by 3D ultrasonic vibration assisted slant feed grinding. *Adv Mater Res* 797:326–331
- Xu S, Shimada K, Mizutani M, Kuriyagawa T (2014) Fabrication of hybrid micro/nano-textured surfaces using rotary ultrasonic machining with one-point diamond tool. *Int J Mach Tools Manuf* 86:12–17
- Xu S, Shimada K, Mizutani M, Kuriyagawa T (2016) Analysis of machinable structures and their wettability of rotary ultrasonic texturing method. *Chinese J Mechanical Eng* 29 (6):1187–1192
- Xu S, Shimada K, Mizutani M, Kuriyagawa T (2017) Development of a novel 2D rotary ultrasonic texturing technique for fabricating tailored structures. *Int J Adv Manuf Tech* 89 (1–4):1161–1172
- Xu S, Shimada K, Mizutani M, Kuriyagawa T (2017) Recent advances in ultrasonic-assisted machining for the fabrication of micro/nano-textured surfaces. *Front Mech Eng* 12(1):33–45
- Yan J, Oowada T, Zhou T, Kuriyagawa T (2009) Precision machining of microstructures on electroless-plated NiP surface for molding glass components. *J Mater Process Technol* 209(10):4802–4808



Precision Grinding for Functional Microstructured Surface

9

Jin Xie

Contents

9.1	Introduction	302
9.2	Precision Dressing and Truing of Diamond Wheel Micro-Tip	303
9.2.1	Mechanical Mutual-Wear Truing	303
9.2.2	Electro-Contact Discharge (ECD) Ting	305
9.2.3	Micro-Grinding Mechanism	309
9.3	Micro-Grinding Optic Glass for Solar Electricity	310
9.3.1	Precision Grinding of Microlens Array	310
9.3.2	The Micro-Grinding Substrates for Electricity Generation	315
9.4	Micro-Grinding Silicon for Wetting	318
9.4.1	Micro Grinding of Gradient Array Micro-V-Microgrooved Silicon Surface	319
9.4.2	The Wetting of Accurate Microgroove Array	320
9.5	Micro-Grinding Quartz Glass for Microfluidic Chip	322
9.5.1	Micro-Grinding of Microchannel on Microfluidic Chip	322
9.5.2	The Form Accuracy of Ground Microchannel	324
9.5.3	The Flowing Speed on Microfluidic Chip	325
9.6	Summary	329
	References	330

Abstract

The microstructure surface can produce new functions and features compared to smooth surface in industry. Accordingly, the accurate and smooth microstructures may display predominant surface function on high-performance materials such as silicon, optical glass, ceramics, and so on. However, it is difficult to control the

J. Xie (✉)

School of Mechanical and Automotive Engineering, South China University of Technology, Guangzhou, China

e-mail: jinxie@scut.edu.cn

© Springer Nature Singapore Pte Ltd. 2018

J. Yan (ed.), *Micro and Nano Fabrication Technology*, Micro/Nano Technologies,

https://doi.org/10.1007/978-981-13-0098-1_9

301

micron-scale structured profiles in micro-machining of these difficult-to-cut materials. Hence, the micro-grinding with a superhard diamond wheel micro-tip is proposed to fabricate the microgroove array on silicon and glass. In order to assure the profile accuracy of diamond wheel micro-tip, the mechanical truing and the electro-contact discharge (ECD) truing were developed to control the form accuracy and the micro grain protrusions of diamond wheel micro-tip on machine, respectively. ECD truing can improve the truing efficiency by about 59 times against mechanical truing. Then, the on-machine micro truing was employed in micro-grinding of microgroove array on optic glass, silicon, and quartz glass, respectively. In the micro-grinding, the accurate and smooth microstructured array may be achieved through on-machine dressing and ductile-mode grinding. The micro-ground form error, surface roughness, and micro-tip radius may reach 0.7–6%, 40–60 nm, and 4–8 μm , respectively. When the microlens array were ground on macro curved optical glass, it may increase the electricity generation by 260–419% against traditional plane surface and by 119–106% against general microlens array, respectively. Through micro-grinding, the accurate microgroove array on silicon may enhance the contact angle by 106% against the irregular microgrooved surface. In micro-grinding of accurate microchannels on microfluidic chip of quartz glass, large microchannel gradient, small microchannel angle, and small surface roughness may increase the microfluidic flowing speed. Moreover, the glass microchannel with nano-scale cracks may improve the flowing speed by about 40 times against the polymer one without any cracks.

Keywords

Micro-grinding · Diamond wheel · Microstructure · Surface function

9.1 Introduction

A microstructured surface can produce predominant features and functions compared with smooth surface in high value-added industrial fields such as optical, solar engineering, and biomedical. For example, the microstructured silicon surface may lead to heat transfer enhancement of evaporative spray cooling (Hsieh and Yao 2006). As the increasingly wider application of difficult-to-cut materials such as silicon and glass, researchers have focused on eco-effective micro-machining of these materials. The fabrication of micron-scale structured surface mainly depends on photolithography, etching, and laser techniques, but it is difficult for them to control the form accuracy and surface quality. Moreover, they require extensive capital investment, process time, and pollute liquid. For example, a YAG laser-turning was employed to machine the microgrooves on ceramic cylinder (Dhupal et al. 2008), but the microgrooved surface was rough and its shape was also irregular. In addition, a micro pyramid-structure surface may be patterned on silicon surface by using special sequences of wet-chemical oxidation and etching steps (Hsieh and Yao 2006), but their

pyramid arrays were much randomly distributed on micron-scale spatial surface. As for mechanical fabrication method, micro end mill with the diameter of 254 μm has been developed with an axial depth of cut in 30 μm to conduct micro-machining (Filiz et al. 2007), but it is too difficult to plan complex tool curve path for machining micron-scale solid arrays due to the limitation of tool form and machine accuracies.

In this chapter, a superhard diamond wheel micro-tip is proposed to perform the micro-grinding along with on-machined truing and dressing of the micro-tip. The objective is to fabricate accurate and smooth microstructured surface for high-performance surface functions. First, the mechanical truing and the electro-contact discharge (ECD) truing were developed to maintain the accuracy and dressing of diamond wheel micro-tip on machine; then, the diamond wheel micro-tip was employed to perform the precision micro-grinding of microgroove array on difficult-to-cut silicon and glass; finally, then, the accurate and smooth microstructured surfaces were applied to solar electricity, wetting, and microfluidic chip.

9.2 Precision Dressing and Truing of Diamond Wheel Micro-Tip

Nowadays, many hard and brittle materials, such as silicon (Hsieh and Yao 2006), ceramics (Clinard 1979), and glass (Namba et al. 1993) have been widely applied to various high value-added industrial fields such as optical, automobile, aerospace, bio-medical, and solar engineering (Angermann et al. 2008). And the precision and ultra-precision machining of hard and brittle materials depend on grinding technology of diamond grinding wheel (Aurich et al. 2009). Due to the characteristics and advantages of diamond grinding wheel, it becomes the perfect tool for choice of the hard and brittle materials.

9.2.1 Mechanical Mutual-Wear Truing

Due to the difficulty in truing of diamond wheel micro-tip, a mechanical truing was developed by the NC mutual-wear between grinding wheel and dresser (Xie et al. 2010). The GC dresser is driven by a linear interpolation motion along V-shaped line to true the diamond grinding wheel constantly, then gradually grinding the diamond wheel into a V-shaped tip (Xie et al. 2011).

In the dressing experiment, the #600 GC dresser was employed into the truing for #600 diamond grinding wheel. Figure 1 shows the NC mutual-wear truing of diamond wheel micro-tip. The rotary diamond wheel was driven along the crossed V-shaped tool paths to grind a GC dresser in NC grinding system, and then a wheel micro-tip profile was gradually produced with the depth of cut a through the NC mutual-wear between diamond wheel and dresser, whose wheel micro-tip angle α_i is equal to the angle of NC V-shaped tool paths.

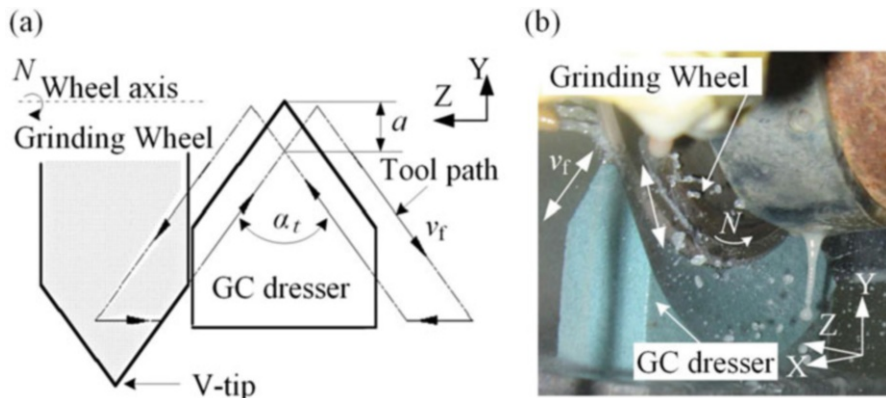


Fig. 1 Mechanical truing of diamond wheel micro-tip: (a) tool paths on YZ-section and (b) actual truing scene

Table 1 Mechanical truing conditions

NC grinder	Smrart B818
Diamond grinding wheel	SD600, Metal bonded, $N = 2000$ rpm
Tool paths	V-shaped linear interpolation movement
Dresser	#600 GC, Ceramic bond
Rough truing	$v_f = 500$ mm/min, $a = 10$ $\mu\text{m}/\Sigma$ $a = 100$ μm
Fine truing	$v_f = 500$ mm/min, $a = 5$ $\mu\text{m}/\Sigma$ $a = 50$ μm
Coolant	Water

The metal bond was chosen as the grinding wheel bond to ensure that the abrasive grains of diamond wheel micro-tip do not come off easily. The wheel micro-tip angle can be controlled by the angle of the V-shaped linear interpolation motion. The angle was set as 60° and the detailed dressing conditions are shown in Table 1.

Diamond wheel micro-tip shape was detected by grinding wheel in-process copying on the graphite board surface. The microscopic grain protrusion of grinding wheel micro-tip was observed by the scanning electron microscope (SEM).

Figure 2 shows the SD600 diamond grinding wheel micro-tip shape and microscopic grain protrusion after mechanical mutual-wear truing. Using NC mutual-wear truing, the diamond grinding wheel micro-tip was shaped and the micro-tip arc radius was 19.5 μm (see Fig. 2a). On the V-tip of the wheel, tiny diamond grains are sharpened and presented a V-shaped sharp corner along the cutting direction (see Fig. 2b). In addition, the rear of dressed diamond grains had no bond-tail, which was conducive to the hard and brittle material precision grinding. This is because there is an additional dressing force perpendicular to the cutting direction of the grinding wheel, which can grind off the bond-tail.

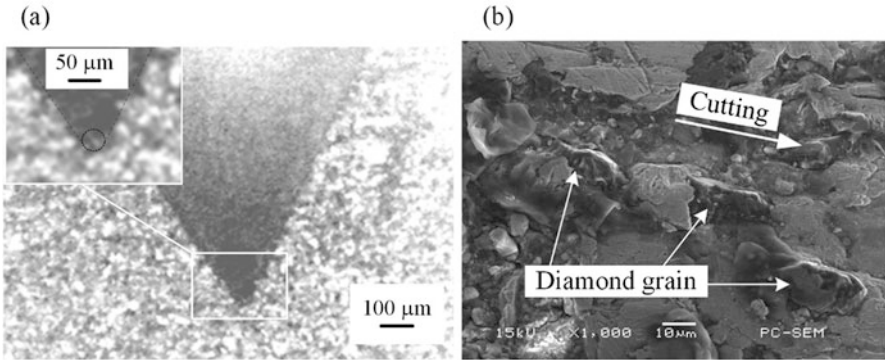


Fig. 2 The sharpened SD600 wheel after Medical Mutual-wear dressing: (a) wheel micro-tip shape and (b) microscopic grain protrusion

9.2.2 Electro-Contact Discharge (ECD) Truing

9.2.2.1 ECD Truing

Although an NC mechanical truing with coolant was successfully applied to metal-bonded #600 diamond wheel, its production efficiency was very low. To realize an eco-efficient truing of diamond wheel micro-tip for precision micro-grinding, a novel V-tip truing of metal bond diamond wheel is proposed using a hybrid of Dry ECD removal and mutual-wear between diamond wheel and electrode.

Figure 3 shows the ECD dressing principle of metal-bonded diamond wheel micro-tip. The ECD dressing was performed without any coolant. This is because the dry impulse discharge removal was less than the wet one, thus it may sharpen finer diamond grains from wheel working surface. The conductive chip is first gradually formed as soon as a diamond grain cuts electrode (see Fig. 3a). As the rolled-up chip approaches the metal bond to a certain extent, an impulse spark discharge occurs between the diamond wheel and the electrode (see Fig. 3b). After this impulse spark discharge, a discharge crater is formed on the metal bond surface of diamond wheel (see Fig. 3c). Gradually, the metal bond around grain is removed, and then the micron-scale diamond grain is protruded from wheel working surface.

Figure 4 shows ECD truing of diamond wheel micro-tip. Different from mechanical mutual-wear truing, the dresser was replaced by a conductive material, called electrode, and then continuous pulse voltages were applied to diamond wheel (positive pole) and electrode (negative pole). In this study, the wheel micro-tip angle α_t was designed as 60° ; thus the crossed angle of V-shaped tool paths was chosen as 60° in truing experiments. The detailed Dry ECD mutual-wear truing conditions are shown in Table 2.

Figure 5 shows the grain protrusion topography before and after ECD truing ($E = 7 \text{ V}$ and $f = 500 \text{ Hz}$). Before ECD truing, micro diamond grains were enmeshed with wheel metal bond, and their cutting edges were worn to be a near plate (see Fig. 5a). After truing, the diamond grains were well protruded from the metal bond surface, and their cutting edges were also sharpened (see Fig. 5b).

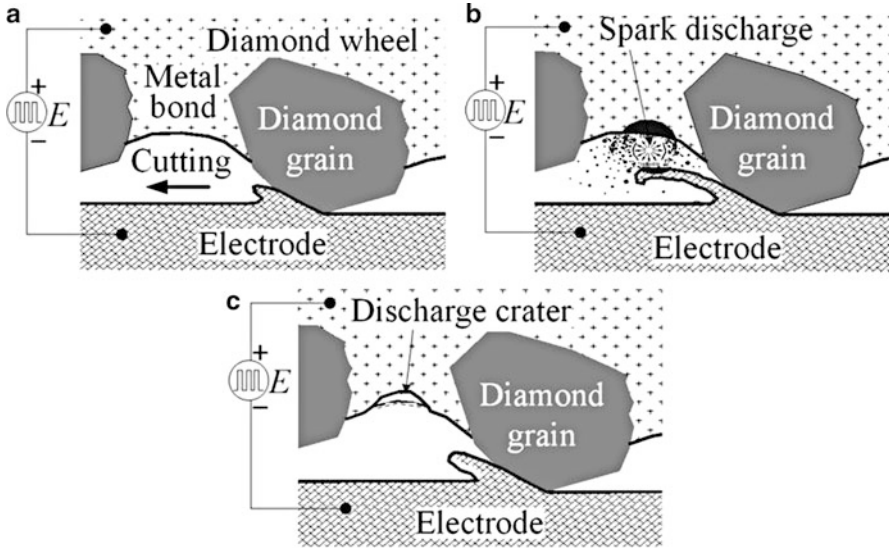


Fig. 3 ECD dressing principle: (a) electrode chip formation, (b) spark discharge occurrence, and (c) metal bond removal

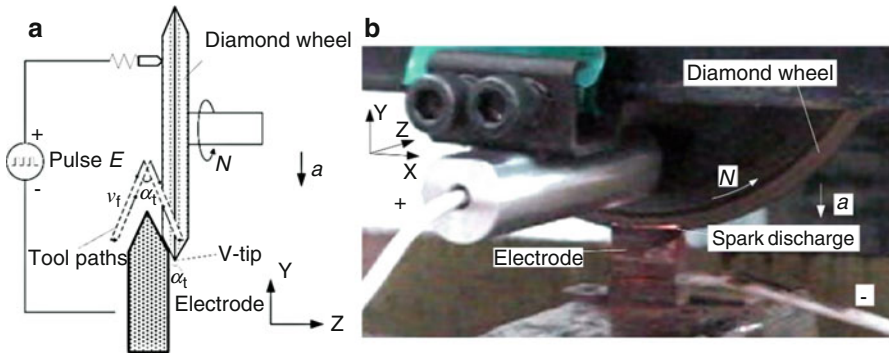


Fig. 4 ECD truing of diamond wheel micro-tip: (a) truing mode and (b) truing process

Table 2 Dry ECD mutual-wear truing conditions

NC grinder	Smrart B818
Diamond grinding wheel	SD600, Metal Bonded, $N = 3826$ rpm
NC tool paths	V-shaped linear interpolation movement
Electrode	Bronze and GC grains
Truing	$v_f = 200$ mm/min, $a = 3$ $\mu\text{m}/\Sigma$
Discharge variables	$a = 150$ μm
	Duty cycle = 50%
	$E = 1$ V, 3 V, 5 V, 7 V, 10 V
	$f = 100$ Hz, 500 Hz, 1000 Hz

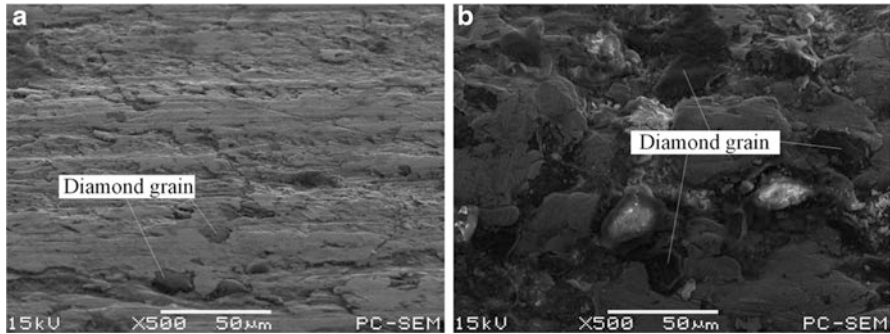


Fig. 5 Grain protrusion topography: (a) before ECD truing and (b) after ECD truing

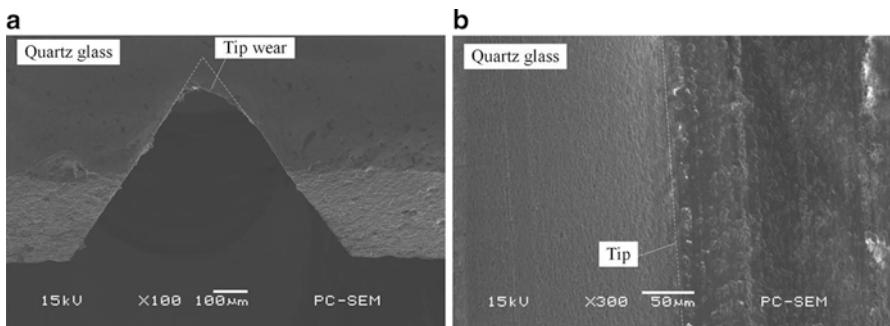


Fig. 6 SEM photos of microgrooved quartz glass: (a) microgroove profile and (b) microgroove tip surface

To observe grinding wheel micro-tip shape after ECD truing, an experiment of microgroove grinding on quartz glass substrate was conducted. Figure 6 shows SEM photos of ground microgroove of quartz glass substrate. It is shown that integrated microgroove was produced without any brittle crack edges after micro-grinding. However, micro shape deformation (see Fig. 6a) and surface damage (see Fig. 6b) happened on diamond wheel micro-tip. The reason is that when the microgroove depth was large, the diamond wheel micro-tip was easily worn.

9.2.2.2 Truing Setup

Figure 7 shows the mutual-wear truing setup in experiment. It can be used for both mechanical mutual-wear truing and Dry ECD mutual-wear truing. It was composed of NC system, grinder, diamond wheel, working table, straight polarity, and pulse power supply. The electrode was composed of a hybrid of bronze and #600 GC grains. The GC grains on electrode working surface may cut off arc discharge and prevent short circuit between diamond wheel and electrode during truing.

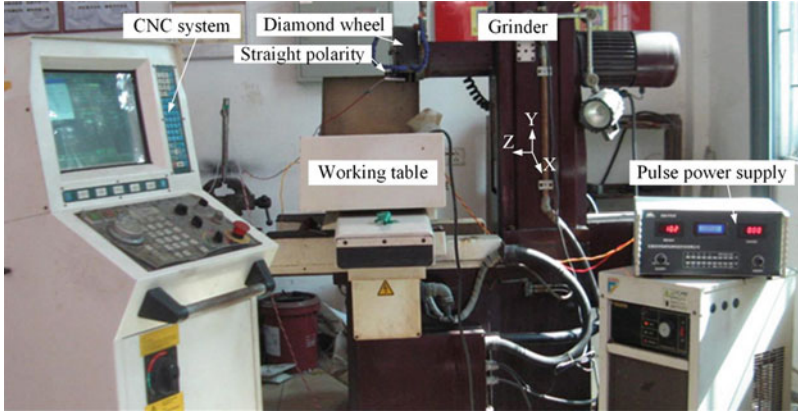


Fig. 7 Mutual-wear truing setup

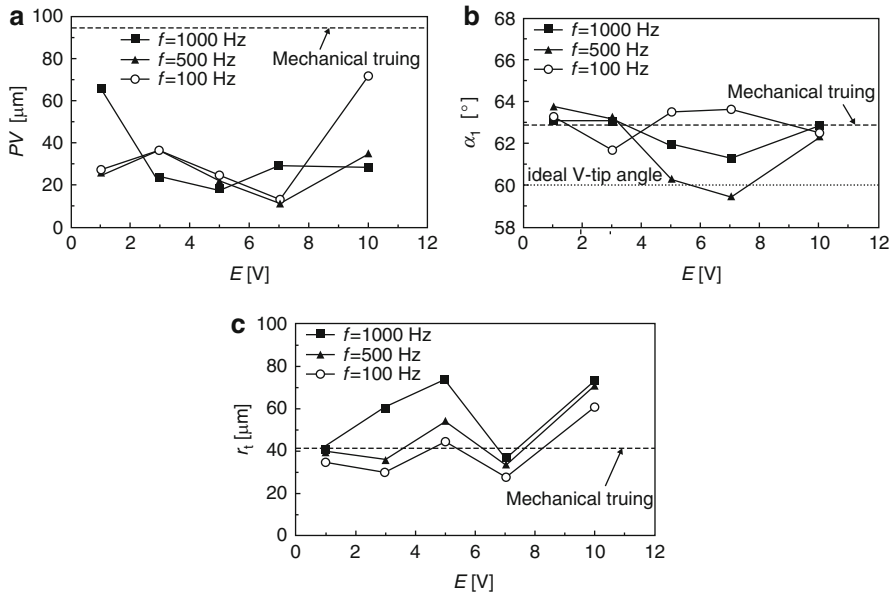


Fig. 8 Various parameters versus pulse voltage E and pulse frequency f : (a) wheel micro-tip form error PV and (b) wheel micro-tip angle α_t and (c) wheel micro-tip radius r_t

9.2.2.3 Comparison Between Two Truing Methods

By measuring the trued grinding wheel micro-tip profile, the truing effect of mechanical mutual-wear truing and dry ECD mutual-wear truing can be evaluated. Figure 8 shows various parameters versus pulse voltage E and pulse frequency f . The wheel micro-tip form error PV mainly ranged 10–40 μm , whereas it was 94 μm in the

case of mechanical truing. And the least wheel micro-tip form error PV may be achieved as the pulse voltage E ranged 5–7 V (see Fig. 8a). The trued wheel micro-tip angles may approach the ideal wheel micro-tip angle of 60° in the case of $E = 5\text{--}7$ V and $f = 500$ Hz, leading to the least wheel micro-tip angle (see Fig. 8b). The least wheel micro-tip radius of $26\ \mu\text{m}$ in the case of $E = 7$ V and $f = 100$ Hz was much less than the one of $42\ \mu\text{m}$ in the case of mechanical truing (see Fig. 8c).

Therefore, conclusion can be drawn that the ECD truing with suitable discharge variables may achieve less wheel micro-tip form error, less wheel micro-tip angle, and less wheel micro-tip radius than mechanical truing. The truing ratio and truing efficiency of ECD truing are much higher than mechanical truing. Besides, ECD truing needs no coolant. However, the truing equipment and operation of mechanical mutual-wear truing is much simpler and easier than ECD truing. What's more, the wheel micro-tip shape after ECD truing is not as good as mechanical mutual-wear truing.

9.2.3 Micro-Grinding Mechanism

Figure 9 shows the precision grinding machining principle of microgroove. In the precision grinding of microgroove, the flat diamond grinding wheel is trued into a V-shaped micro-tip. Then, the grinding wheel moves horizontally along the cutting direction, cutting the surface of workpiece with the depth of cut a . In the grinding, many diamond abrasive which distribute in the V-tip of diamond grinding wheel cut the workpiece in micro-nano scale constantly as tiny cutting edge, reaching the cutting condition of hard and brittle material in plastic domain.

Some researches show that the cutting depth in diamond micro-grinding of silicon wafer impacts on the conversion from brittle-mode removal to ductile-mode removal. As shown in Fig. 10, the micro diamond grains gradually cut in and cut

Fig. 9 Precision grinding principle of microgroove

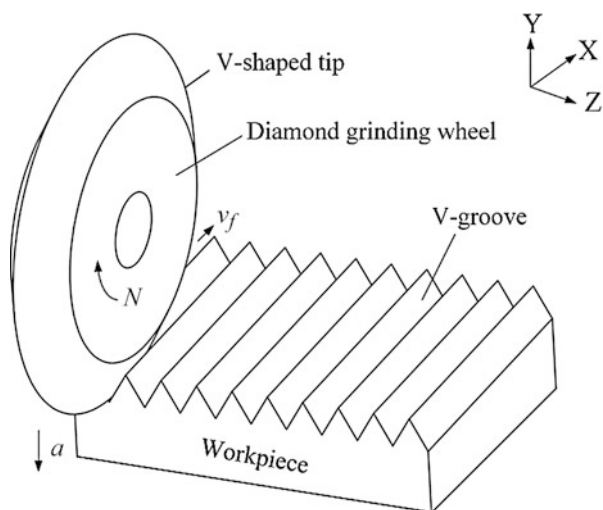
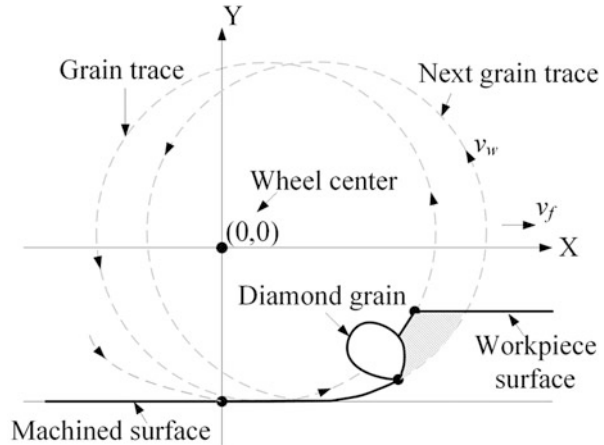


Fig. 10 Parameterization model of diamond micro-grinding



out the silicon surface with a given wheel speed v_w and feed speed v_f along the cycloid grain trace. If ductile-mode cutting is performed when the cutting depth is appropriate, the microgrooves are gradually produced by continuously replicating grain profiles on the silicon surface.

9.3 Micro-Grinding Optic Glass for Solar Electricity

It is known the fact that crystalline silicon (*c*-silicon) solar cells own poor absorption property (Bozzola et al. 2014). So other materials such as amorphous silicon (α -silicon) (Seungil et al. 2014) and organic materials (Li et al. 2012) whose absorption property is stronger are employed for thin film solar cells. However, they are not as competitive as crystalline silicon in terms of the conversion efficiency and, additionally, with limited photovoltaic performance like in ideal thermodynamic field, etc. (Shockley and Queisser 1961). Therefore, in order to improve the conversion efficiency while weaken no photovoltaic characteristics, new designs on optic glass for solar cells are proposed.

9.3.1 Precision Grinding of Microlens Array

In this study, two types of new designs are proposed as the surface of the glass substrate is plane and macro-freeform curved, while well-determined microlens array is fabricated on the surfaces. Here, micro-grinding is employed to reach the micron-scale forming accuracy.

9.3.1.1 Microlens Array on Plane Glass Substrate

The dimension of the glass substrate with plane surface is $50 \times 50 \times 3 \text{ mm}^3$ ($l \times w \times h$). As shown in Fig. 11, for the employability of micro-grinding, the

Fig. 11 Design of the microlens array

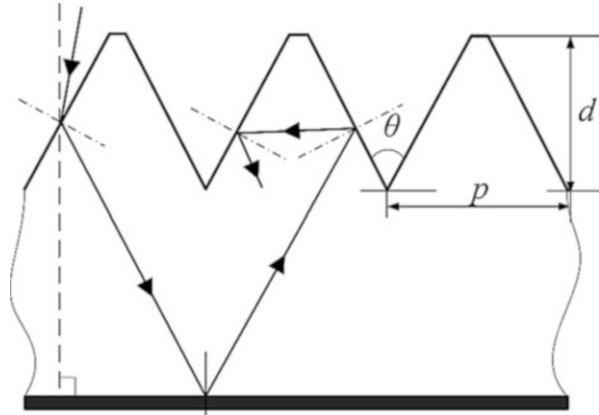


Table 3 Form-truing conditions of diamond wheel micro-tip

NC grinding machine	SMART B818
Diamond grinding wheel	SD 600, SD 3000, Resin bonded, $N = 2000$ rpm
Tool paths	Linear interpolation movement
Dresser	#600 GC, Ceramic bonded
Rough truing	$v_f = 500$ mm/min, $a = 10 \mu\text{m}/\Sigma$ $a = 100 \mu\text{m}$
Fine truing	$v_f = 100$ mm/min, $a = 5 \mu\text{m}/\Sigma$ $a = 50 \mu\text{m}$
Coolant	Water

microlens is designed as V-shaped whose base angle θ should locate between 52 and 115.2° and the aspect ratio (p/d) should be within 0.64 and 2.05 , according to calculation. In this study, 60° is chosen to be the base angle θ .

Before micro-grinding the microlens array, the diamond wheel was trued to be V-shaped. Mutual-wear happened and the grinding wheel was driven along the tool path that was similar to the theoretical contour of the V-shaped microlens with base angle θ of 60° . According to Sect. 9.1, no matter what the original shape of the grinding wheel is like, the working surface profile will finally be formed to V-shape with 60° base angle. The form-truing conditions are listed in Table 3.

The micro-grinding process of microlens array on the glass substrate is shown in Fig. 12. The well-trued grinding wheel was employed and the sharpened V-tip on the grinding wheel was taking effect to grind the microlens on the glass precisely with micron-scale single cutting depth. Along with a traverse grinding tool path, the microlens was gradually fabricated. The micro-grinding conditions are listed in Table 4.

With the purpose of reaching fine surface quality and high smoothness of the working surface of the workpiece, the spark-out grinding was performed to polish the surfaces after rough grinding and fine grinding (Fig. 13) shows the micrographics of microlens array before and after polishing.

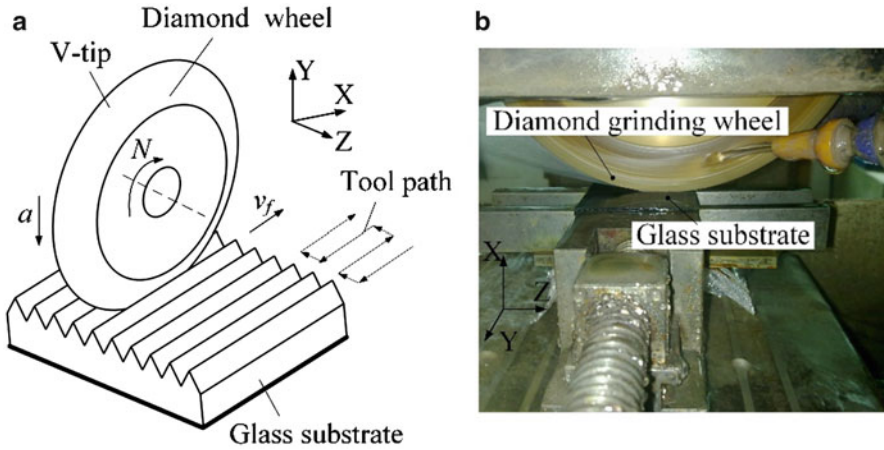


Fig. 12 Micro-grinding of microlens array on glass substrate: (a) machining scheme and (b) machining scene

Table 4 Micro-grinding conditions of microlens array fabrication

NC grinder	Smart B818
Diamond grinding wheel	SD 600, SD 3000, Resin bonded, $N = 2000$ rpm, $v_f = 2000$ mm/min
Tool paths	Level, reticulated cross
Rough grinding	SD 600 grinding wheel, $a = 2 \mu\text{m}/\Sigma$ $a = 450\text{--}750 \mu\text{m}$
Fine grinding	SD 3000 grinding wheel, $a = 1 \mu\text{m}/\Sigma a = 50 \mu\text{m}$
Coolant	Water

Surface profiler Talysurf CLI2000 was used to measure the surface profile. The surface roughness Ra of the microlens array without polishing was $1.84\text{--}2.27 \mu\text{m}$ while it was only $0.06\text{--}0.20 \mu\text{m}$ after the microlens array had been polished. And moreover, the surface quality of the microlens after polishing was noticeably smooth and integrated with mere edge-damage.

9.3.1.2 Microlens Array with Macro Curved Surface on Glass Substrate

The dimension of the glass substrate to fabricate microlens array with macro curved surface was $49.7 \times 49.7 \times 3.2 \text{ mm}^3$ ($l \times w \times h$). After a series of simulation to test several optic parameters, the depth of the microlens d was determined as $400 \mu\text{m}$, base angle of the microlens θ as 60° , and the macro curved surface was designed as an ellipsoidal surface as shown in Fig. 14.

As mentioned in Sect. 9.3.1.1, the diamond wheel's truing to be V-shaped by mutual-wear form-truing was conducted before micro-grinding the microlens array. Then, micro-grinding was performed, as shown in Fig. 15a, b and c. The grinding

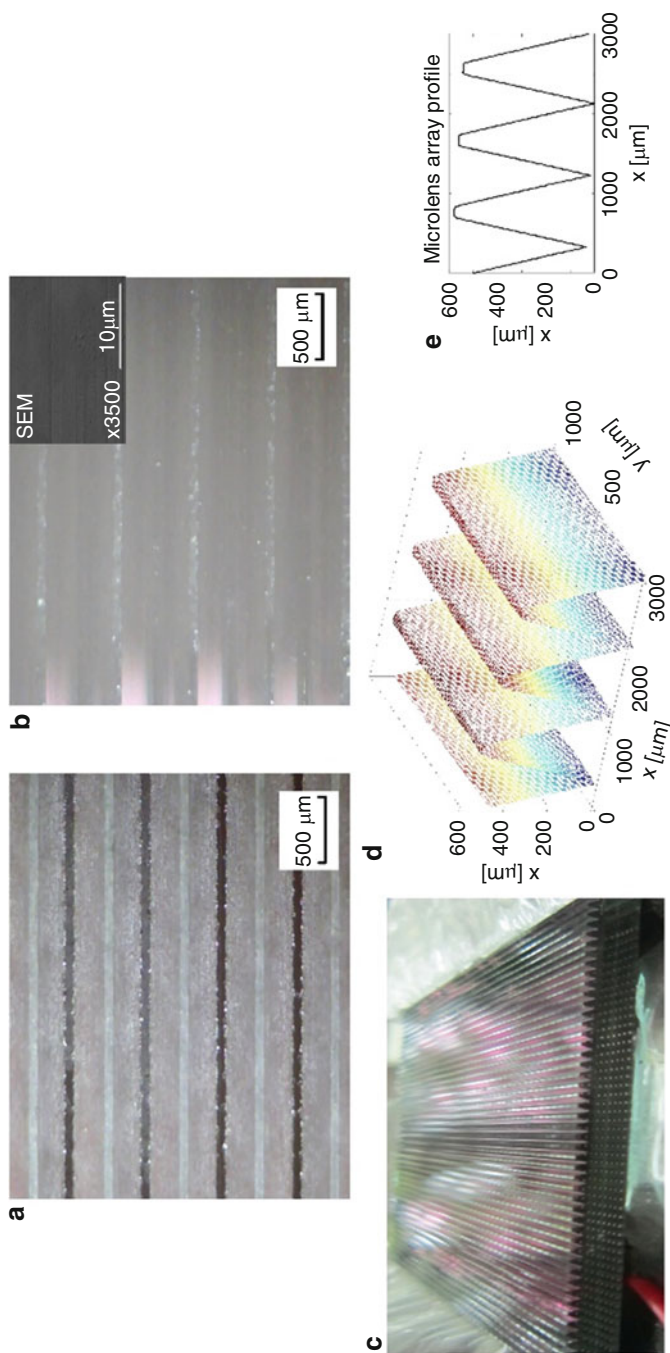


Fig. 13 Micrographics of microlens array (a) before and (b) after polishing, (c) photo and topographies of measured (d) 3D surface and (e) profile of polished microlens array

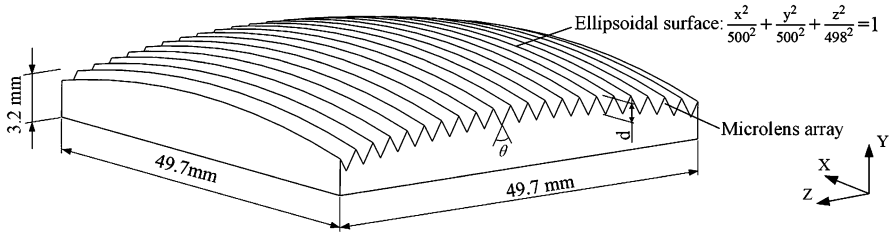


Fig. 14 Theoretical scheme of micro-prism with ellipsoidal surface

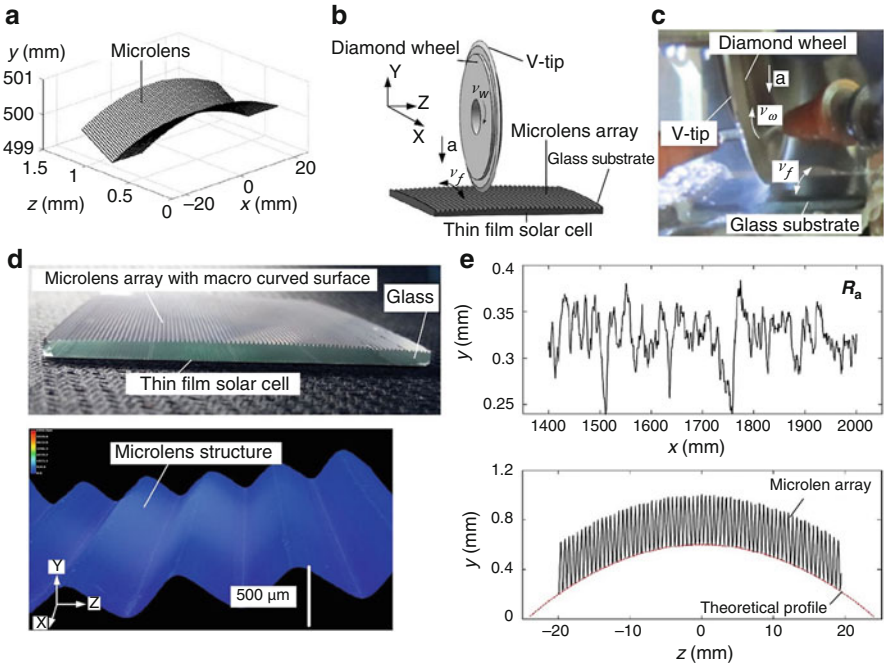


Fig. 15 Micro-grinding of microlens array with macro curved surface: (a) single microlens topography, (b) machining scheme, and (c) machining scene and machined microlens array; (d) photo and micro-topography of the surface profile and (e) profiles of surface roughness and microstructure

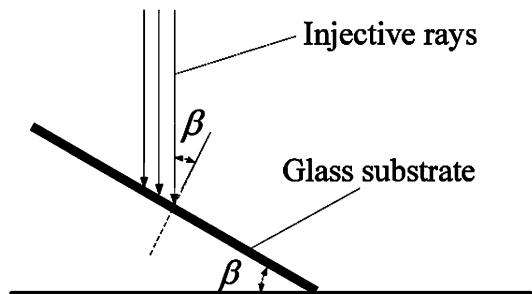
wheel ran along the curves on the theoretical ellipsoidal surface and, correspondingly, the V-tip of it formed the macro curved surface. The micro-grinding conditions are listed in Table 5.

The micro-topography in Fig. 15d and the profiles in Fig. 15e were measured by super depth microscope and surface profiler, respectively. It can be seen that the surface quality is fine and integrated. And the form error of the curve profile to the theoretical profile is 10.3 μm along the long edge of the glass substrate while that of

Table 5 Micro-grinding conditions of microlens array with macro curved surface fabrication

NC grinder	Smart B818
Diamond grinding wheel	SD 600, SD 3000, Resin bonded, $N = 2000$ rpm
Tool paths	Level, reticulated cross
Rough grinding	SD 600 grinding wheel, $v_f = 2000$ mm/min, $a = 10 \mu\text{m}/\Sigma a = 1180 \mu\text{m}$
Fine grinding	SD 3000 grinding wheel, $v_f = 400$ mm/min, $a = 5 \mu\text{m}/\Sigma a = 50 \mu\text{m}$
Coolant	Water

Fig. 16 The measurement of photovoltaic characteristic of solar cell: (a) measuring method and (b) measuring instrument



the microlens array depth to the theoretical depth of $400 \mu\text{m}$ is $5.1 \mu\text{m}$. In conclusion, NC micro-grinding is able to contribute to extremely fine and precise microlens array glass curved surface.

9.3.2 The Micro-Grinding Substrates for Electricity Generation

9.3.2.1 The Photovoltaic Characteristic of Glass Substrates for Solar Cell

In order to investigate the photovoltaic characteristic of glass substrates for solar cell, a solar simulator Sun 3000 was employed. The incident angle β was defined as the angle of injective rays and normal plane on glass substrate. It was used to evaluate the photovoltaic characteristic for scattered light (Fig. 16).

Figure 17 shows the experimental photovoltaic characteristic of microlens curved surface compared with the plane surface. In this experiment, the illumination $L_x = 500 \text{ W/m}^2$ was used to simulate the photovoltaic characteristic in dim condition and the illumination $L_x = 1000 \text{ W/m}^2$ was used to simulate the photovoltaic characteristic in bright condition. It is shown that the power conversion efficiency η of microlens curved surface decreased with increasing incident angle β (see Fig. 17a). Compared with the illumination $L_x = 500 \text{ W/m}^2$, the illumination $L_x = 1000 \text{ W/m}^2$ had a higher power conversion efficiency when the incident angle β was less than 60° and when β was larger than 60° , the opposite was true. In the condition of $L_x = 500 \text{ W/m}^2$, the microlens curved surface performed larger output power than plane surface and compared with $\beta = 10^\circ$; this difference is more pronounced at $\beta = 70^\circ$ (see Fig. 17b). In the condition of $\beta = 70^\circ$, the output power

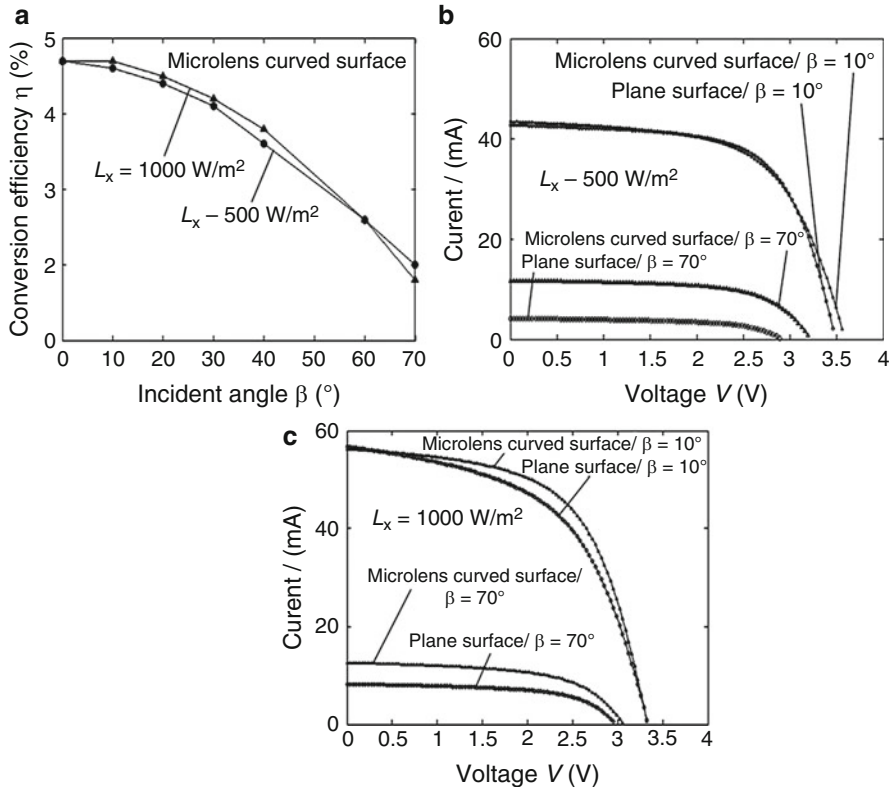


Fig. 17 The experimental photovoltaic characteristic of microlens curved surface: (a) power conversion efficiency η versus illumination intensity L_x , (b) I-V curves of $L_x = 500 \text{ W/m}^2$ and (c) I-V curves of $L_x = 1000 \text{ W/m}^2$

of $L_x = 1000 \text{ W/m}^2$ and $L_x = 500 \text{ W/m}^2$ were approximate for microlens curved surface while the $L_x = 1000 \text{ W/m}^2$ performed quite larger output power than the $L_x = 500 \text{ W/m}^2$ for plane surface (see Fig. 17b and c). It means that the microlens curved surface contributes to improving the photovoltaic characteristic for scattered light in dim condition.

9.3.2.2 The electricity Generation Ability of Glass Substrates for Solar Cell

Figure 18 shows the indoor electricity generation ability of the microlens structured solar cells. An incandescent lamp of 40 W was used as light source charging for the thin film solar cells and then the LED lamp was lighted (see Fig. 18a). It is shown that the microlens surface which had a brighter lamp generated open-circuit voltage V_{oc} of 0.4 V while the plane surface generated open-circuit voltage V_{oc} of 0.26 V (see

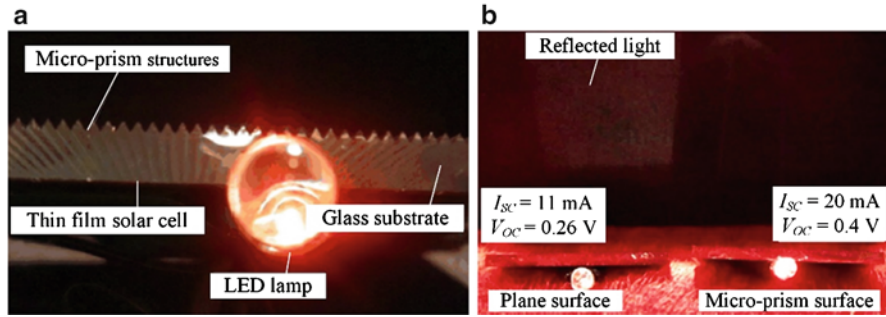


Fig. 18 Indoor electricity generation of thin film solar cell with microlens structures: (a) LED lamp in dim indoor and (b) the lighting comparison between microlens surface and plane surface

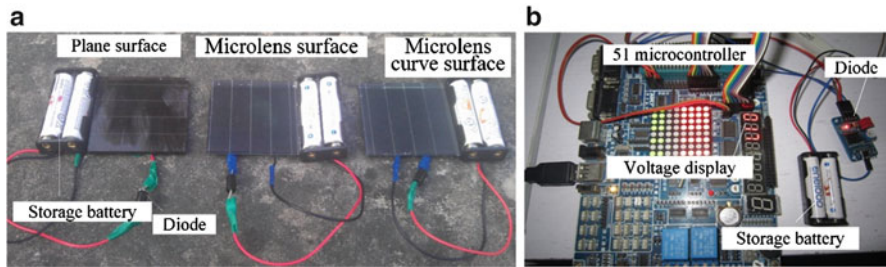


Fig. 19 The measurement setup of electricity generation ability: (a) outdoor charging process and (b) electric discharging process

Fig. 18b). As a result, the microlens structured solar cells has a better indoor electricity generation ability than the plane surface solar cells.

In order to evaluate the outdoor electricity generation ability of the microlens structured solar cells applied to a solar device, the No. 51 microcontrollers was used to control the test setups of electricity charge-discharge as shown in Fig. 19. In this experiment, the original TF solar cells were chosen as power source. They were divided into three groups. One group was fabricated with same dimensions of microlens surface, one group was fabricated with microlens curved surface, and the other group was prepared with plane surface. During this experiment, the all power sources were put outdoor for 7 h from 9:00 am to 4:00 pm to store electricity (see Fig. 19a). Then, the storage battery was discharged and the discharged time was used to evaluate the outdoor electricity generation ability (see Fig. 19b).

Figure 20 shows the outdoor electricity generation ability of the microlens structured solar cells. It is shown that the microlens curved surface had the longest discharge time T_d during sunny day and cloudy day. It increased the discharge time by 260% compared with the plane surface and 119% with the microlens surface during sunny day (see Fig. 20a). Moreover, the microlens curved surface increased

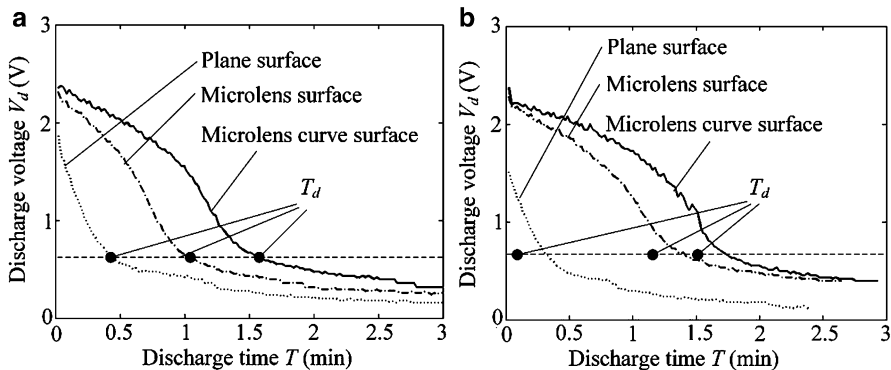


Fig. 20 Outdoor electricity generation of thin film solar cell with microlens structures: (a) discharge voltage V_d versus discharge time T in sunny day and (b) discharge voltage V_d versus discharge time T in cloudy day

the discharge time by 419% compared with the plane surface and 106% with the microlens surface (see Fig. 20b). The reason may be that the microlens curved surface can improve the photovoltaic characteristic for scattered light in weak-light condition.

What's more, a surprising finding is that the electricity generation produced by microlens curve surface in cloudy day was stronger than it in sunny day (see Fig. 20a and b). It is different from the result of plane surface. It may be explained by that the infrared light not only generated little photoelectric effect on the thin film solar cell, but also heated the the solar cell, which made effectiveness losing in sunny day. Moreover, the microlens curve surface had a broader perspective for light absorbing during cloudy day (Fig. 19b). As a result, the microlens curved surface has the ability to the weak-light electricity generation by absorbing ambient scattered light for thin film solar cell.

9.4 Micro-Grinding Silicon for Wetting

Nowadays, micro-structures on most of hard and brittle material surfaces such as silicon wafer can be fabricated by ultra-violet (UV) embossing (Escarré et al. 2011), laser machining (Romoli et al. 2011), chemical etching (Tieqiang et al. 2010), and single crystal diamond tool processing (Xie et al. 2009), but these technologies are of high energy consumption, low surface quality, or generate pollution emissions. Therefore, the diamond micro-grinding is employed to solve these problems and the critical value of brittle plastic transition can be easily controlled by cutting depth. In this study, gradient micro-V-microgrooved surfaces were precisely and smoothly fabricated using a new micro-grinding process. The objective is to investigate how these accurate micro-characterized variables systematically influence anisotropic wetting on such regular micro-V-microgrooved surfaces without surface chemical modification.

9.4.1 Micro Grinding of Gradient Array Micro-V-Microgrooved Silicon Surface

Figure 21 shows the fabrication scheme of microgroove array using a diamond wheel. In traditional plane grinding of inaccurate microgroove array (see Fig. 21a), many micro diamond grains are dispersed on parallel grinding wheel surface. Therefore, the rough and inaccurate microgroove array were produced by continuously replicating grain profiles on the silicon surface. So the microgroove angle is dominated by top grain angle (Xie et al. 2012). In micro-grinding of accurate microgroove array (see Fig. 21b), the micro-V-tip diamond grinding wheel was well-trued with V-shaped tip. This means the microgroove angles were identical on the silicon surface. The detailed grinding conditions are shown in Table 6.

In order to investigate how these accurate micro-characterized variables systematically influence the anisotropic wetting and droplet self-movement on such accurate microgroove array surfaces, the accurate microgroove array silicon surfaces were machined by using an NC mechanical micro-grinding process. Figure 22

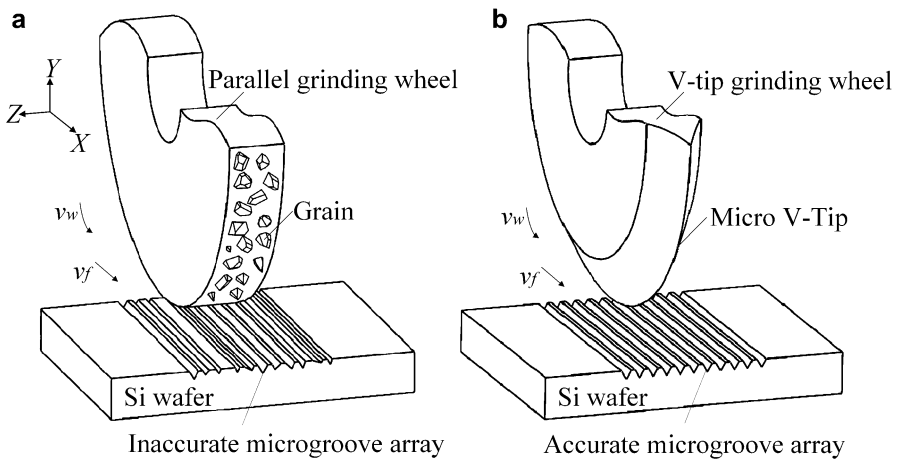
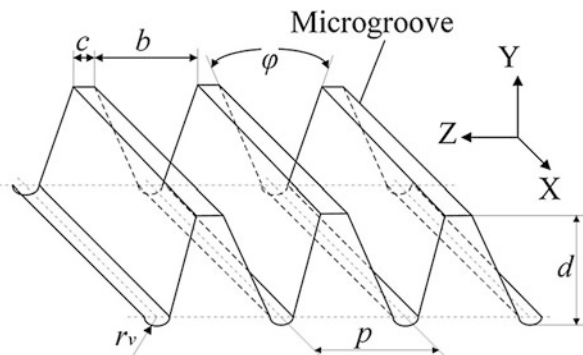


Fig. 21 The fabrication of microgroove array: (a) traditional plane grinding and (b) micro-grinding

Table 6 Gradient micro-grinding conditions

NC grinder	Smartr B818
Diamond grinding wheel	#3000, Resin-bonded, $N = 2000$ rpm, $v_f = 500$ mm/min
Tool paths	Level
Workpiece	Silicon{0 1 1}
Rough grinding	$a = 5 \mu\text{m}/\Sigma$ $a = 20\text{--}50 \mu\text{m}$
Fine grinding	$a = 1 \mu\text{m}/\Sigma$ $a = 10\text{--}20 \mu\text{m}$ spark grinding = 1
Coolant	Water

Fig. 22 The geometrical scheme of micro-characterized variables



shows the geometrical scheme of the microgroove array. The microgroove array is characterized with the depth d , top width c , pitch p , V-tip radius r_v of microgroove, and microgroove V-angle ϕ , respectively.

9.4.2 The Wetting of Accurate Microgroove Array

Figure 23 shows the topographies of the microgroove silicon surfaces along with scanning electron microscope (SEM) photos and their wetting characteristics. A white light interferometer (WLI: BMT SMS Expert 3D) was employed for the measurement of the microstructured 3D surfaces. An ACM 600 confocal microscopy was used here with its objective lens of 50 times lateral magnification, the vertical resolution of 30 nm, and the lateral resolution of 3 μm . The wetting characteristics were evaluated by the contact angles. They were measured by an optical contact-angle measuring device (Dataphysics OCA40 Micro, Filderstadt, Germany) using the sessile drop method. The distilled water droplets of 2 μl were placed on the samples with a micro-syringe. The determination error of the contact angle is estimated to be $\pm 0.1^\circ$. The measurements were conducted at a constant temperature of 26 $^\circ\text{C}$ and a relative humidity of 68%.

As shown in Fig. 23a and b, the rough and inaccurate microgroove array were produced by the micro cutting edges of diamond grains of #60 and #3000 diamond grinding wheels, respectively. As for the fabrication of accurate microgroove surfaces, the well-trued #3000 V-tip diamond wheel with V-tip angle designed as 60° was employed in precision micro-grinding. It is shown that the microgroove array were identical and accurate on the surfaces different microgroove pitches p (see Fig. 23c and d).

As Fig. 23a and b shows, the droplet shape on the inaccurate microgroove surfaces were near circle. The droplet may invade into the irregular structures, and be trapped by the structure edges, thus leading to confined spreading the silicon surface towards to water-repellent character. As for the accurate microgroove

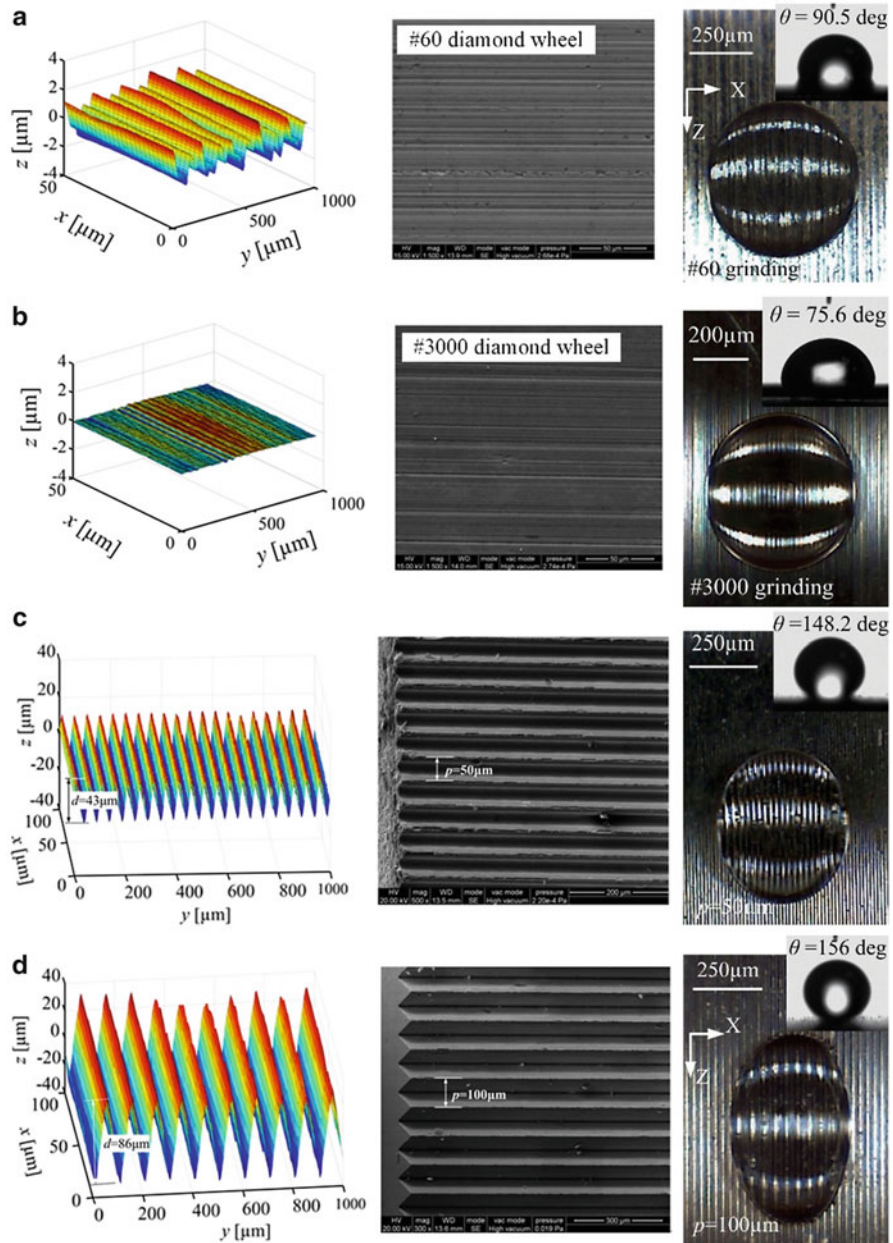


Fig. 23 The topographies of the micro-V-microgrooved silicon surfaces along with SEM photos and their wetting characteristics: (a) the inaccurate microgroove array ground by #60 and (b) #3000 diamond grinding wheel and the accurate microgroove array ground by trued #3000 diamond wheel with (c) $p = 50\mu\text{m}$ and (d) $p = 100\mu\text{m}$

surfaces shown in Fig. 23c and d, the droplet was formed from a near circle to an ellipse by changing microgroove pitch p . This particular drop shape leads to strongly differences of contact angles measured from difference directions. Here, the measuring direction of contact angles was perpendicular to microgroove longitudinal fins. It can also be seen that the contact angles increased with increasing of surface roughness. Besides, compared with the wetting behavior on accurate microgroove surfaces, the inaccurate microgroove surface did not appear such anisotropic property even though the microgrooves existed.

9.5 Micro-Grinding Quartz Glass for Microfluidic Chip

Quartz glass is a kind of high-purity noncrystalline silicon dioxide, and it is an excellent material for making microfluidic chip to improve the performance of microfluidic flowing because of the small expansion coefficient, preeminent thermal conductivity, chemical stability. However, quartz glass is also a kind of typical hard and brittle material, so the machining properties are very poor. It is very easy to appear some defects such as crack and damage at nanoscale during machining.

The etching process can be used to machine the micro V-shaped microchannel of quartz glass (Yuan et al. 2004), but it is difficult to control the shape precision, and the processing efficiency is also poor. The soft lithography was also applied to the forming of microchannel (Arscott 2014), but it leads to pollution. Hot embossing and injection molding of microchannel were rapid (Li et al. 2008; Yin et al. 2013), but they are poor compatibility in the glass material. Although the micromilling was used for ultra-rapid prototyping of plastic microfluidic devices, it is difficult to machine brittle glass like quartz glass (Chen et al. 2014). Micro grinding can be used to machine micro V-shaped slot lens structure (Xie et al. 2013), but the shape precision has not been studied in detail. Until now, it has not been reported how to grind quartz glass for microfluidic chip and how the micro-/nanoscale topographies of quartz glass chip microchannel actually influence the microfluidic flowing.

Based on the self-developed micro-tip dressing technology of super hard diamond wheels, a V-shaped microchannel precision grinding technology has been developed independently for quartz glass microfluidic chip.

9.5.1 Micro-Grinding of Microchannel on Microfluidic Chip

According to the truing method introduced in Sect. 9.1, the resin-bonded diamond grinding wheel with micro-tip were well trued. Then, they were employed into the micro grinding of the microchannel on microfluidic chip surface.

Figure 24 shows the micro-grinding of V-shaped microchannel on quartz glass. The rotating diamond wheel with micro-tip is used to fabricate the V-shaped microchannel. Driven by the rotational speed of grinding wheel N , the micro-

Fig. 24 Grinding of micro V-shaped microchannel on quartz glass. **(a)** The model of grinding V-shaped microchannel and **(b)** the actual machining scene

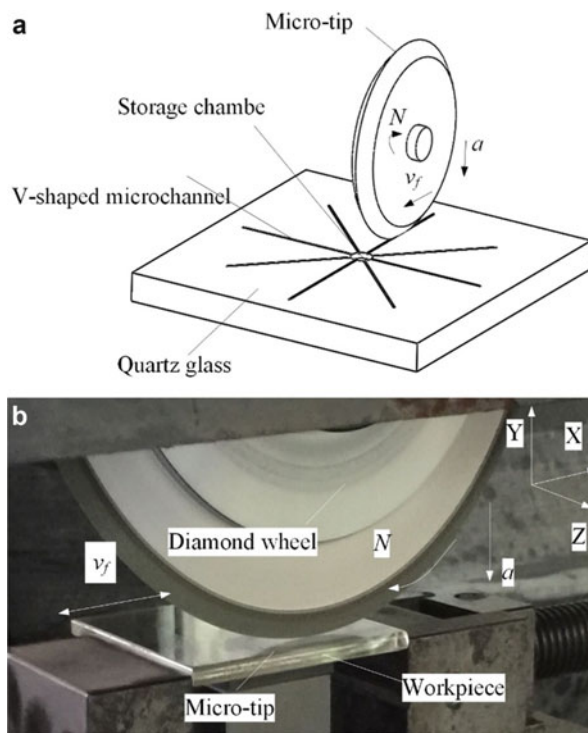


Table 7 Grinding conditions of micro V-shaped microchannel on quartz glass

	$N/(r \cdot \text{min}^{-1})$	$a/\mu\text{m}$	$v_f/(\text{mm} \cdot \text{min}^{-1})$	n_s	Coolant
Rough machining	1990	5	500	0	Water
Fine machining	1990	1	200	3	

diamond cutting edge on the micro-tip could remove the hard and brittle materials in smooth way. And according to the reciprocating motion of the grinding wheel and the longitudinal feeding on the micrometer scale, the high-precision micro-tip profile of grinding wheel is gradually replicated onto the quartz glass (see Fig. 24a). In order to improve machining accuracy, the cutting depth should be controlled within a small range, about 5 μm for rough machining and about 1 μm for fine machining. Hence, the angle of the grinding wheel micro-tip is in accordance with the angle of the micro V-shaped microchannel. Figure 24b shows the actual machining scene. The detailed grinding conditions are shown in Table 7.

Figure 25a shows the topography of quartz glass microfluidic chip with V-shaped microchannels. The microfluidic device is composed of storage chamber, V-shaped microchannel and microreactor chamber. The V-shaped microchannel is parameterized by the angle α , the depth d and the gradient η and the surface roughness R_a . This quartz glass microfluidic chip could be machined by the technology of micro V-shaped

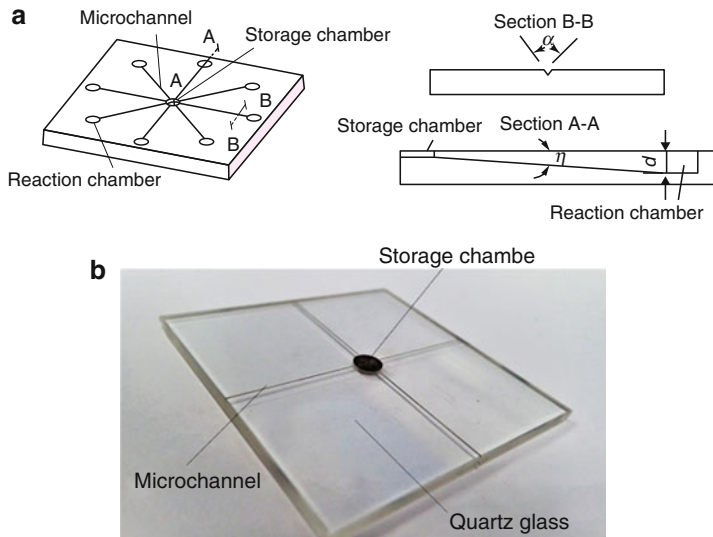


Fig. 25 The topographical scheme of microchannel on microfluidic chip. (a) The model of quartz glass microfluidic chip and (b) the machined microfluidic chip scene

microchannel precision grinding described above. In addition, in order to machine the microchannel with gradient η , the gradient of wheel path was also designed to be same as the gradient η of microchannel, so the cutting depth of grinding wheel would increase gradually with the wheel moving. Figure 25b shows the machined quartz glass microfluidic chip. Moreover, the microchambers and storage chamber were processed by the laser.

9.5.2 The Form Accuracy of Ground Microchannel

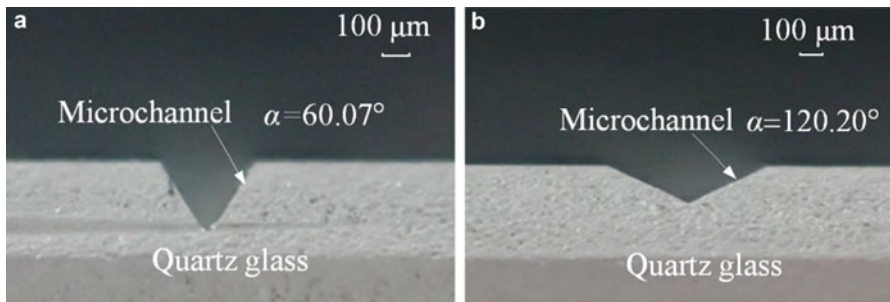
In the grinding and microfluid flowing experiments, the surface topography parameters of microchannel are shown in Table 8. Quartz glass and polymer, were chosen for comparison.

Figure 26 shows the profiles of micro-ground V-shaped microchannel. It is shown that there was no burrs on microchannel edges. The measured microchannel angles were 60.4° , 60.07° , and 59.8° for the designed $\alpha = 60^\circ$ and 119.0° , 120.2° , and 119.7° for the designed $\alpha = 120^\circ$. The machined microchannel angle error reached ± 0.4 and ± 1.0 . The micro-tip radius r was $10.7 \mu\text{m}$ for $\alpha = 60^\circ$ and $29.3 \mu\text{m}$ for $\alpha = 120^\circ$, respectively. This means that the micro-grinding can obtain the accurate and smooth microchannel with integrate edges and sharp tip.

Figure 27 shows the rough profile of microchannel surface of quartz glass. The two microchannels were ground by the SD600 wheel with $24 \mu\text{m}$ in diamond abrasive size and SD3000 wheel with $5 \mu\text{m}$ in diamond abrasive size respectively. It is shown

Table 8 The micro-nano surface topography parameters of microchannel and chip materials

Microchannel no.	Chip material	$\eta(^{\circ})$	$\alpha(^{\circ})$	Diamond wheel	$d(\mu\text{m})$
1	Quartz glass	0	60	SD600	300
2	Quartz glass	0	120	SD600	225
3	Polymer (PMMA)	0	60	SD600	300
4	Polymer (PMMA)	0.33	60	SD600	300
5	Polymer (PMMA)	0.43	60	SD600	300
6	Quartz glass	0	60	SD3000	300

**Fig. 26** The profiles of micro-ground microchannel angle α . (a) $\alpha = 60^{\circ}$ and (b) $\alpha = 120^{\circ}$

that the surface roughness reached 83.5 and 42.8 nm, respectively. Hence, smaller the diamond abrasive size, smoother the microchannel surface is. This also means that the abrasive size may be used to control the surface roughness of microchannel.

Figure 28 shows the photos of nanometer-scale surface cracks around microchannel tip of quartz glass. This is because that quartz glass has high hardness and poor fracture toughness, which make it hard and brittle, and the plastic region accuracy machining is difficult to be reached. So, the mechanical force of diamond wheel micro-tip produced the cracks on brittle workpiece. However, these cracks have an effect on the microfluidic flowing, and it is significant to be studied.

9.5.3 The Flowing Speed on Microfluidic Chip

In microfluidic devices, the microchannel size is less than 1 mm for microfluidic flowing. Figure 29 shows the photos of microfluidic flowing in the microchannel on quartz glass microfluidic chip. It is shown that a concave was formed in the front of flowing microfluid.

Figure 30 shows the photographs of microfluidic flowing speed v_m versus flowing length l for nanometer. The microfluid extended into the crack tips rapidly and the speed is faster than that inside microchannel, then the v_m was fluctuating along with flowing length l . The experiment proves that the nanometer-scale crack induction

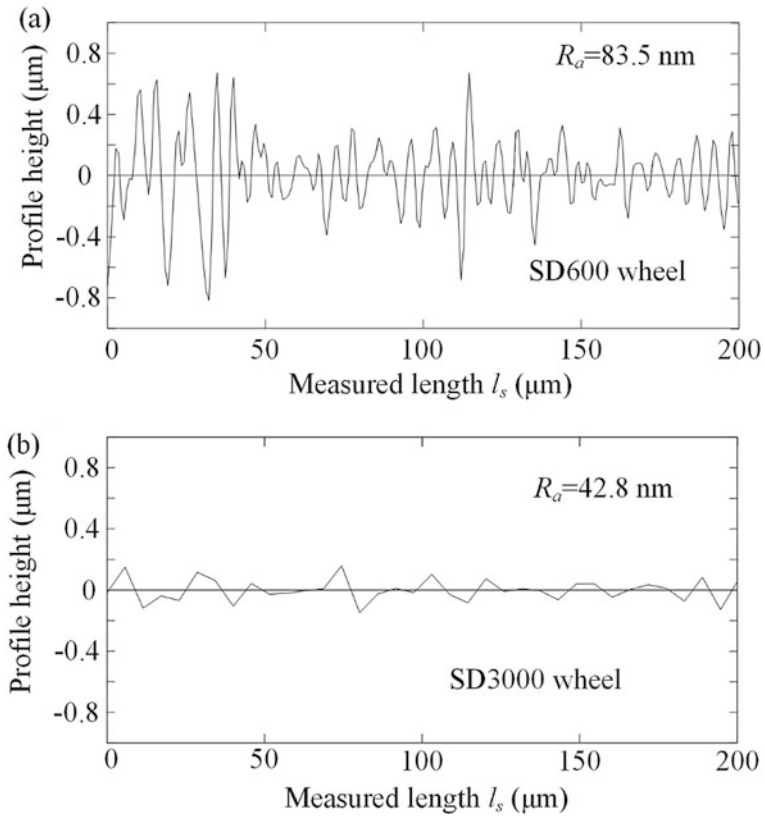


Fig. 27 The rough profile of quartz glass microchannel surface ground by different diamond wheels. (a) SD600 and (b) SD3000

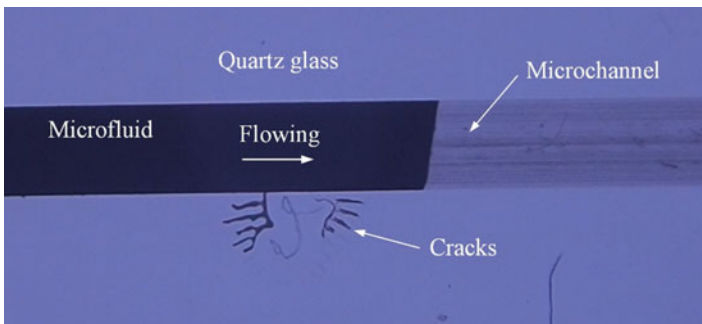


Fig. 28 The photos of microgrinding nanometer cracks

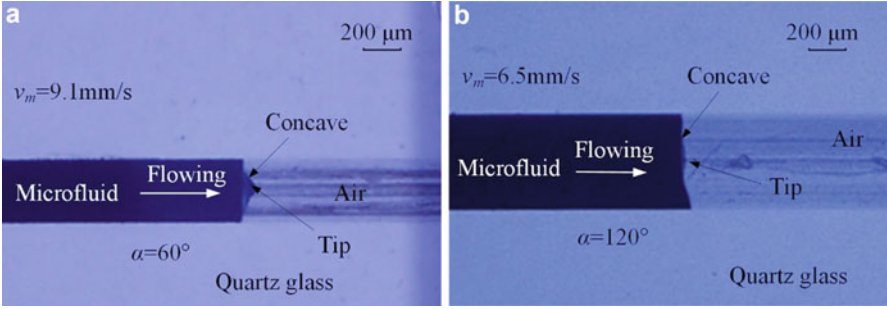
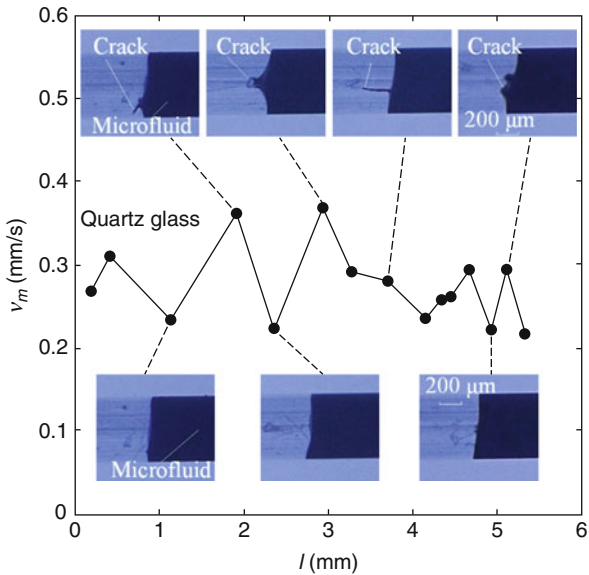


Fig. 29 The photos of microfluid flowing on quartz glass chip. (a) $\alpha = 60^\circ$ and (b) $\alpha = 120^\circ$

Fig. 30 Flowing speed v_m versus nanometer surface cracks along with flowing length l



improves the self-flowing speed by 27% compared with the smooth microchannel which means the nanometer-scale surface cracks could greatly induced the microfluidic flowing.

Figure 31 shows flowing speed v_m versus microchannel angle α , surface roughness R_a and microchannel gradient η along flowing length l . It is seen that the flowing speed v_m decreased with increasing the flowing length l by and large then trended to a stable value when the flowing length l was larger than 20 mm. And it also shows that the self-flowing speed may be increased by 20% when the microchannel tip angle is decreased to 60 from 120°, so small microchannel angle may speed the microfluidic flowing (see Fig. 31a), the smooth microchannel surface can improve

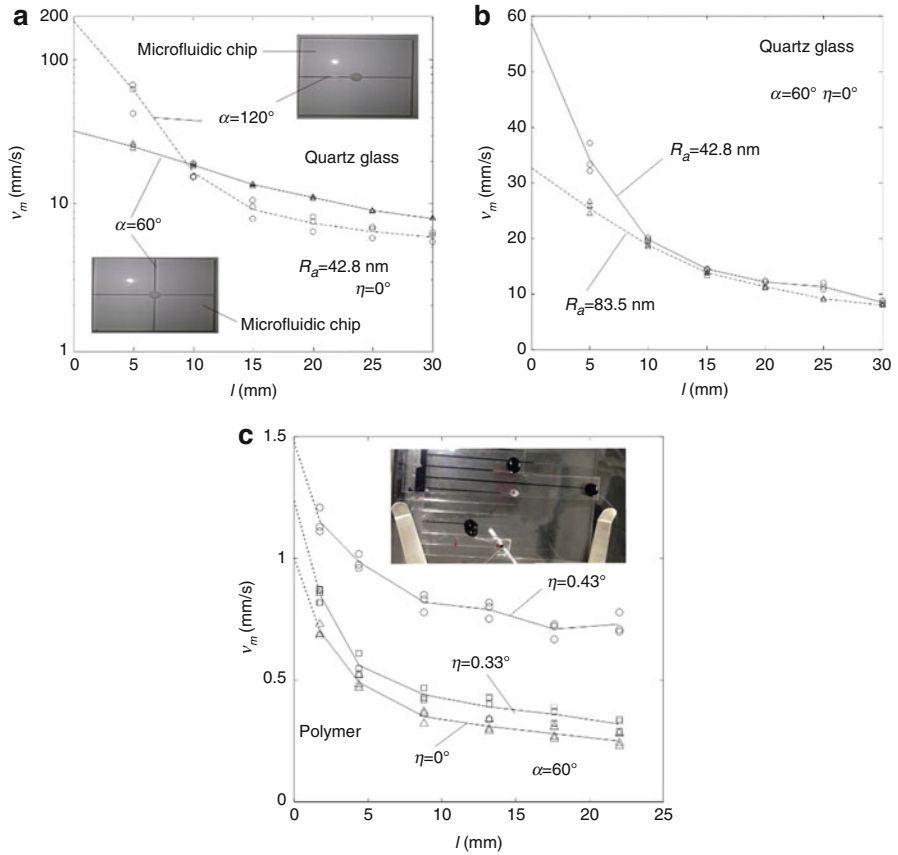


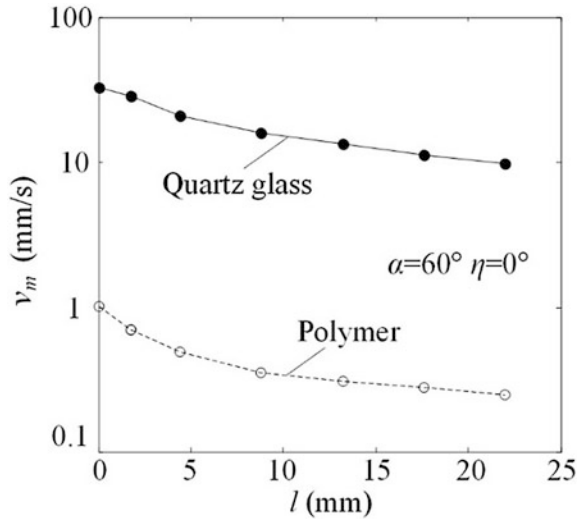
Fig. 31 Flowing speed v_m versus the characteristic parameters of microchannel: **(a)** Flowing speed versus microchannel angel α , **(b)** flowing speed versus surface roughness R_a , **(c)** flowing speed versus microchannel gradient η

the microfluidic flowing substantially compared with the rough microchannel surface (see Fig. 31b), and the flowing speed v_m increased with increasing the microchannel gradient η , so the microchannel gradient greatly contributes to the self-flowing (see Fig. 31c).

Figure 32 shows the flowing speed v_m versus chip materials along flowing length l . It is shown that the quartz glass as chip material may increase the flowing speed by about 40 times compared with the polymer, because the nanometer-scale crack induced the microfluidic flowing for quartz glass. This also means that quartz glass is a preminent material to make microfluidic chip.

In summary, quartz glass is a preminent material for microfluidic chip because it could improve the microfluid self-flowing speed. Besides, micro grinding with micro-tip wheel can be used for precision machining of microfluid chip on quartz glass.

Fig. 32 Flowing speed v_m versus chip materials along flowing length l



9.6 Summary

By using a diamond wheel micro-tip, the micro-grinding is able to fabricate the microgroove array on difficult-to-cut silicon and glass. The mechanical truing and the ECD truing may assure the profile accuracy and dressing of diamond wheel micro-tip. The on-machine dressing and ductile-mode grinding dominates the accuracy and smoothness microstructured array. In future, the on-line dressing of super-fine diamond wheel micro-tip will be developed to achieve smoother microstructured surface.

ECD truing can improve the truing efficiency by about 59 times against mechanical truing. The micro-grinding along with dressed #1500 diamond wheel micro-tip may fabricate the accurate and smooth microgrooves. The micro-ground form error, surface roughness, and micro-tip radius may reach 0.7–6%, 40–60 nm and 4–8 μm , respectively. In future, the micro-tip radius will reach 2 μm and less.

The microgroove lens can produce new micro-optics for absorbing scattered light and significantly enhance the electricity generation especially under weak-light. When the microlens array were ground on curved optical glass, it may increase the electricity generation by 260–419% against traditional plane surface and by 119–106% against general microlens array, respectively. In future, new functions will be developed.

Through micro-grinding, the accurate microgroove array on silicon may enhance the contact angle by 106% against the irregular microgrooved surface. It is able to convert the hydrophilicity from the super hydrophobicity without any chemical modification.

In micro-grinding of accurate microchannels on microfluidic chip of quartz glass, large microchannel gradient, small microchannel angle, and small surface roughness may increase the microfluidic flowing speed. Moreover, the glass microchannel with nano-scale cracks may improve the flowing speed by about 40 times against the polymer one without any cracks. In future, the nano-scale crack channels will be accurate.

References

- Angermann H, Rappich J, Korte L et al (2008) Wet-chemical passivation of atomically flat and structured silicon substrates for solar cell application. *Appl Surf Sci* 254(12):3615–3625
- Arscott S (2014) SU-8 as a material for lab-on-a-chip-based mass spectrometry. *Lab Chip* 14(19):3668–3689
- Aurich JC, Engmann J, Schueler GM et al (2009) Micro grinding tool for manufacture of complex structures in brittle materials. *CIRP Ann Manuf Technol* 58(1):311–314
- Bozzola A, Kowalczewski P, Andreani LC (2014) Towards high efficiency thin-film crystalline silicon solar cells: the roles of light trapping and non-radiative recombinations. *J Appl Phys* 115(9):094501
- Chaudhury MK, Whitesides GM (1992) How to make water run uphill. *Science* 256(5063):1539
- Chen PC, Pan CW, Lee WC, Li KM (2014) An experimental study of micromilling parameters to manufacture microchannels on a PMMA substrate. *J Adv Manuf Technol* 71:1623–1630
- Clinard FW Jr (1979) Ceramics for application in fusion systems. *J Nucl Mater* 85–86:393–404
- Dhupal D, Doloi B, Bhattacharyya B (2008) Pulsed Nd: YAG laser turning of micro-groove on aluminum oxide ceramic (AlO). *Int J Mach Tool Manu* 48(2):236–248
- Escarré J, Söderström K, Battaglia C, Haug FJ, Ballif C (2011) High fidelity transfer of nanometric random textures by UV embossing for thin film solar cells applications. *Sol Energy Mater Sol Cells* 95(3):881–886
- Filiz S, Conley CM, Wasserman MB, Ozdoganlar OB (2007) An experimental investigation of micro-machinability of copper 101 using tungsten carbide micro-endmills. *Int J Mach Tool Manu* 47(7):1088–1100
- Hsieh CC, Yao SC (2006) Evaporative heat transfer characteristics of a water spray on micro-structured silicon surfaces. *Int J Heat Mass Transf* 49(5):962–974
- Li JM, Liu C, Qiao HC, Zhu LY, Chen G, Dai XD (2008) Hot embossing/bonding of a poly (ethylene terephthalate) (PET) microfluidic chip. *J Micromech Microeng* 18(1):015008
- Li J, Liu JC, Gao CJ (2012) Improved efficiency of organic solar cells with modified hole-extraction layers. *J Polym Sci Polym Phys* 50(2):125–128
- Namba Y, Abe M, Kobayashi A (1993) Ultraprecision grinding of optical glasses to produce super-smooth surfaces. *CIRP Ann Manuf Technol* 42(1):417–420
- Neuhaus S, Spencer ND, Padeste C (2012) Anisotropic wetting of microstructured surfaces as a function of surface chemistry. *ACS Appl Mater Interfaces* 4(1):123
- Romoli L, Tantussi G, Dini G (2011) Experimental approach to the laser machining of PMMA substrates for the fabrication of microfluidic devices. *Opt Lasers Eng* 49(3):419–427
- Seungil P, Hyung YJ, Myeong JK, Jong HP, Keunjoo K (2014) Enhanced quantum efficiency of amorphous silicon thin film solar cells with the inclusion of a rear-reflector thin film. *Appl Phys Lett* 104:73–902
- Shockley W, Queisser HJ (1961) Detailed balance limit of efficiency of p-n junction solar cells. *J Appl Phys* 32(3):510
- Tieqiang W, Xiao L, Junhu Z et al (2010) Elliptical silicon arrays with anisotropic optical and wetting properties. *Langmuir ACS J Surf Colloid* 26(16):13715–13721
- Xie J, Wei F, Tamaki J (2009) Laser measurement and evaluation for brittle/ductile cutting of micro/nano scale V-shaped groove. *Opt Precis Eng* 17(11):2771–2778

- Xie J, Tan YW, Zheng JH, Jiang JH, Huang SL (2010) CNC mutual-wear micro truing technique of diamond wheel V-tip. *Diamond Abras Eng* 30(5):1–5
- Xie J, Zhuo YW, Tan TW (2011) Experimental study on fabrication and evaluation of micro pyramid-structured silicon surface using a V-tip of diamond grinding wheel. *Precis Eng* 35(1):173–182
- Xie J, Xie HF, Liu XR, Tan TW (2012) Dry micro-grooving on Si wafer using a coarse diamond grinding. *Int J Mach Tool Manu* 61:1–8
- Xie J, Li P, Wu KK et al (2013) Micro and precision grinding technique and functional behavior development of microstructured surfaces. *J Mech Eng* 49(23):182–190
- Yin XH, Cheng GM, Yang C (2013) Microinjection molding of microsystem components: new aspects in improving performance. *J Micromech Microeng* 23(9):093001
- Yuan J, Luo FG, Cao MC (2004) I/O fiber bundle arrays access device and its application in optical connection network. *Opt Commun Technol* 10:53–55. (in Chinese)



Anthony T. Beaucamp

Contents

10.1	Introduction	334
10.1.1	Principle of MFJP Process	334
10.1.2	Some Applications of MFJP	335
10.2	MFJP Process Parameters	338
10.2.1	Nozzle Outlet	339
10.2.2	Fluid Pressurization	340
10.2.3	Abrasive Particles	341
10.3	MFJP Process Mechanism	343
10.3.1	Development of Jet Plume and Impingement of Workpiece	343
10.3.2	Entrainment of Abrasive Particles by Carrier Fluid	345
10.3.3	Material Removal by Abrasive Impacts	348
10.3.4	Surface Integrity of Hard and Brittle Materials	353
10.4	Deterministic Finishing by MFJP	355
10.4.1	Influence Function	355
10.4.2	Forward Problem	356
10.4.3	Inverse Problem	356
10.5	MFJP Process Enhancements	359
10.5.1	Submerged MFJP	359
10.5.2	Air-Assisted MFJP	360
10.5.3	Ultrasonic Cavitation-Assisted MFJP	361
10.5.4	Non-Newtonian Fluid-Assisted MFJP	362
10.5.5	Magnetorheological Fluid-Assisted MFJP	362
10.5.6	Nozzle Array MFJP	363
10.5.7	Rotary Multi-MFJP	367
10.6	Summary and Outlook	367
	References	368

A. T. Beaucamp (✉)

Department of Micro-Engineering, Kyoto University, Kyoto, Japan

e-mail: beaucamp@me.kyoto-u.ac.jp

Abstract

Micro fluid jet polishing (MFJP) is a super-fine machining process in which a slurry of loose abrasives and carrier fluid is pressurized and pushed out through a nozzle orifice, generating a fluid beam of small diameter. Impingement of the beam onto a workpiece surface results in a submillimeter footprint of time-dependent material removal. The relatively benign processing pressure and abrasive grain size in MFJP, as compared to micro waterjet machining, assure a low material removal rate that promotes smoothing of the workpiece surface. In this chapter, the basic principles and applications of the MFJP process are first reviewed. Characterization of the process parameters, their typical value ranges, and best practice in implementing the MFJP process are discussed, together with an in-depth analysis of the process mechanism including jet plume formation, abrasive particles entrainment, material removal by particle impacts, and surface integrity considerations when using MFJP on hard and brittle materials. The basic principles of deterministic finishing by MFJP are discussed next, whereby a workpiece shape accuracy may be improved through iterative measurement and processing, with an introduction to the associated numerical methodology being provided. Finally, a number of enhancements to the MFJP process are considered, including submerged, air-assisted, ultrasonic cavitation-assisted, non-Newtonian, and magnetorheological fluid-assisted MFJP, as well as multi-jet designs of the nozzle cavity. Useful indicators are provided, as to the advantages and shortcomings of such enhancements.

Keywords

Finishing · Polishing · Fluid jet

10.1 Introduction

10.1.1 Principle of MFJP Process

Micro fluid jet polishing (MFJP) is used to refer to a class of material processing technologies in which loose abrasives (such as diamond or alumina) and a carrier fluid (typically water) are premixed into a slurry that is pressurized and pumped into a nozzle cavity which it then escapes through a small cylindrical outlet (Fähnle et al. 1998), as shown in Fig. 1a. The resulting fluid jet beam impinges the workpiece surface either perpendicularly or at a deflection angle, allowing individual abrasive particles entrained within the carrier fluid to impact the workpiece material, as shown in Fig. 1b. The full or even partial release of the abrasives kinetic energy results in removal of material from the workpiece surface without the need for a pad or cloth, as is typical in conventional polishing.

Some advantages of the MFJP process include the possibility of generating sub-millimeter diameter footprints of ductile mode material removal, as well as the ability to maneuver the thin beam of slurry around difficult areas such as bore holes, steeply concave surfaces, deeply recessed areas, and workpiece corners. Tool wear issues are

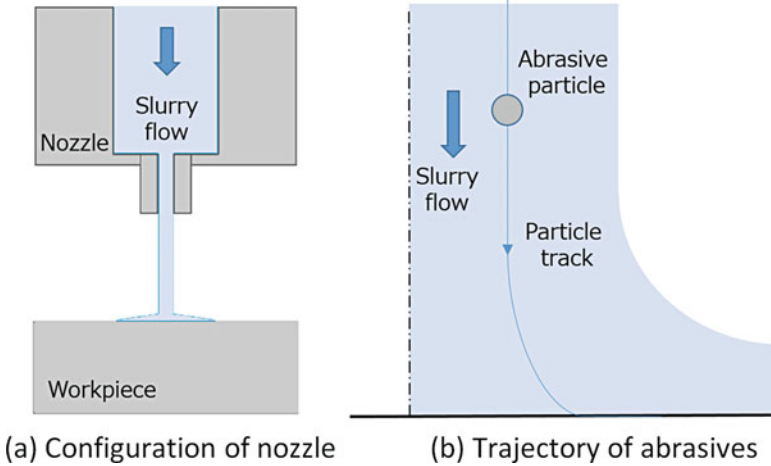


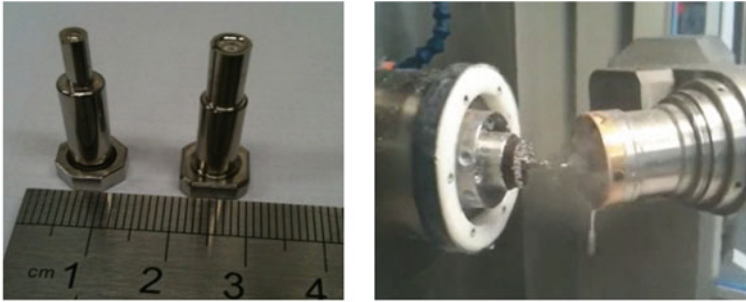
Fig. 1 Principle of micro fluid jet polishing (MFJP)

usually limited to the slow and progressive breakdown of abrasive particles, which can be predictively controlled by using abrasives of adequate hardness as compared to the workpiece material. Furthermore, the excellent stability of material removal rate achievable under well-controlled conditions (see Sect. 10.2) allows for usage of MFJP as a deterministic finishing process. Corrective polishing of optical surfaces to a geometrical shape accuracy less than 100 nm peak-to-valley (P-V) is routinely attainable, through variable feed scanning of the workpiece with the slurry beam.

10.1.2 Some Applications of MFJP

10.1.2.1 Polishing of Micro-Lens Molds

Fabrication of optical quality micro-lens molds and mold arrays is a key technological enabler for a number of industrial sectors, such as consumer cameras and smartphones, endoscopes, and fiber-optic end connectors to communication terminals. Single-lens optical designs usually rely on the use of aspheric surfaces, for correction of spherical aberrations. Such aspheric shapes may be generated by diamond turning or micro-grinding of materials such as electroless nickel or nickel alloys (for replication by plastic injection) and tungsten carbide or silicon carbide (for replication by glass injection). Post-polishing of the pre-machined surfaces is required in order to meet the stringent surface roughness (less than 2 nm Ra) and form accuracy (less than 60 nm P-V) requirements of visible light optical systems. As well as the small overall size of the optical aperture (usually less than 1–2 mm), the asphericity of the optical surface implies variations of the surface curvature that translates into surface features with a lateral resolution of few hundred microns, which are very challenging to polish with conventional compliant polishing tools.



a) Pair of aspheric micro-molds (b) Polishing of micro-mold on MFJP machine

Fig. 2 Polishing by MFJP of nickel-plated micro-molds, for replication of smartphone camera lenses

The ability to adapt the beam size to aspheric feature resolution thus makes MFJP a well-suited process for final finishing of micro-lens molds and mold arrays (Fig. 2).

10.1.2.2 Polishing of Micro-Channels

By operating MFJP with a small nozzle outlet of few hundred microns in diameter, polishing of microgrooves and channels is technologically possible. In the polishing of such features, it was observed that sidewalls of the grooves promote development of a stagnation effect area, which leads to higher velocity fluid flow that is aligned with the direction of the microstructures (Matsumura et al. 2011). Figure 3 shows an example of microgrooves, 100 μm wide and few microns deep, used for channeling of human cells on glass chips. The channels were pre-machined by micro-milling and finished by MFJP. Effective removal of milling marks and subsurface crack damage can be clearly observed, with final surface finish of 25 nm Ra.

10.1.2.3 Smoothing of Micro-Cusps

The periodic structures generated by fine pre-machining processes such as diamond turning and micro-grinding are of particular interest. The fine cusping left over from these processes is typically a few microns wide and only a few nanometers deep. Nevertheless, it can cause very noticeable degradation of the optical performance due to light diffraction and scattering; this phenomenon usually appears in the form of rainbow patterns when observing the surface at a glancing angle of incidence. Removal of such micro-cusps with compliant polishing tools can be exceedingly time-consuming, as these tools have a tendency to follow the patterns rather than cut through them. By comparison, the MFJP process has a remarkable propensity for smoothing fine regular structures on such pre-machined surfaces. Figure 4 shows a typical example of diamond turning marks on an electroless nickel plated surface, which were completely eradicated after the removal of a few hundred nanometers of material by MFJP (Beaucamp and Namba 2013).

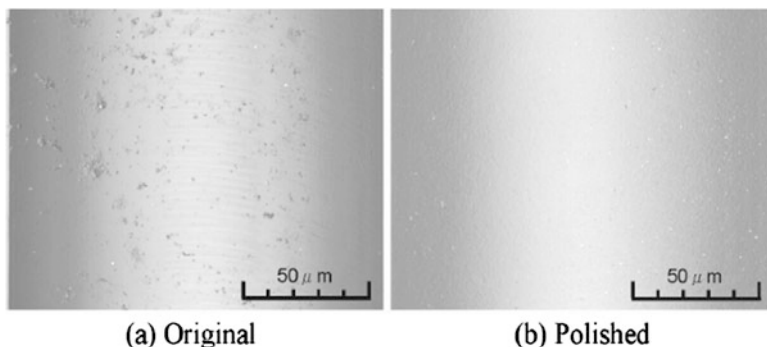


Fig. 3 Polishing of micro-milled channels by MFJP. (Matsumura et al. 2011)

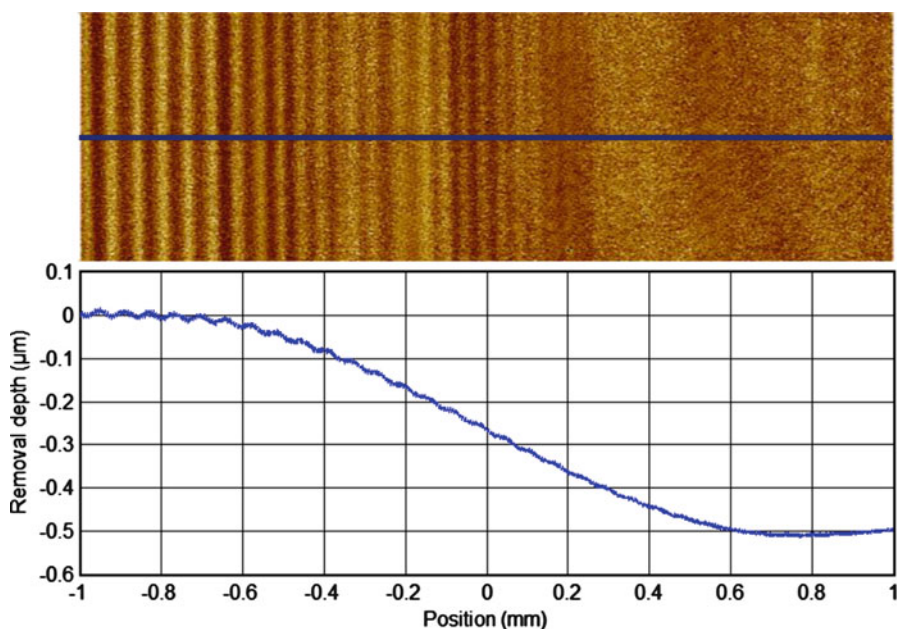
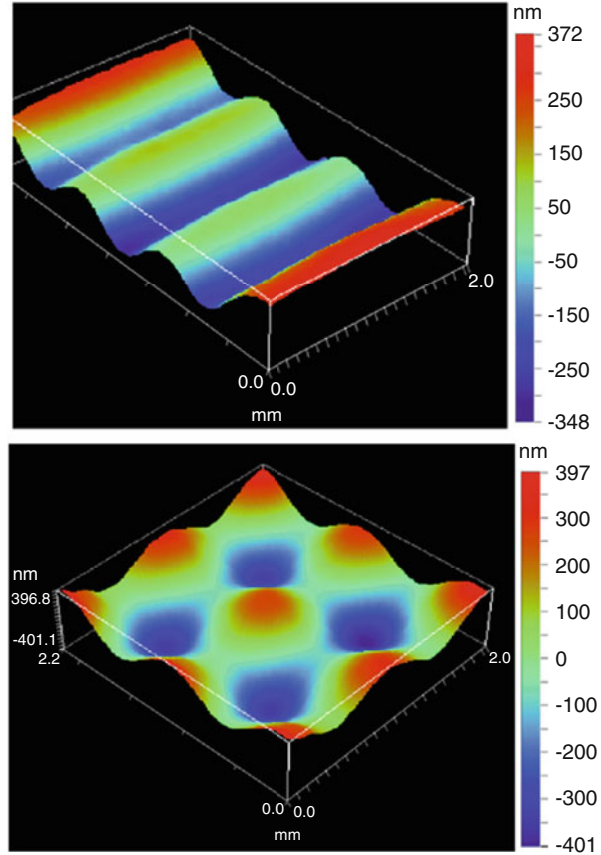


Fig. 4 Removal of diamond turning marks on electroless nickel plating by MFJP. (Beaucamp and Namba 2013)

10.1.2.4 Generation of Functional Surfaces

When operating under well-controlled conditions (see Sect. 10.2), evolution of the material removal rate in the MFJP process can become stable and predictable. It may then be employed to generate functional surfaces with regular patterns and structures that find application in microelectromechanical systems (MEMS), micro-fluidics, and controlled lubrication of surfaces. Based on scanning of the workpiece surface with a stable footprint, moderation of the beam displacement feed results in localized

Fig. 5 Generation of functional patterns on BK7 glass by MFJP. (Cao et al. 2016)



variations of the material removal depth and appearance of peaks and valleys. Using numerical methods such as point spread functions (see Sect. 10.4), functional patterns with a lateral resolution half that of the footprint can be polished onto the surface. This deterministic polishing method may be used either on glass plates for direct application or to process molding inserts made from nickel alloy or steel, from which plastic or glass plates can be replicated. Depth resolution of few nanometers, and accuracy of few dozen nanometers, can be technologically realized. Figure 5 shows some examples of functional patterns generated by MFJP on BK7 glass plates (Cao et al. 2016).

10.2 MFJP Process Parameters

The principal process parameters in MFJP are listed in Table 1, together with their typical value ranges. There are three main categories: (1) nozzle parameters, (2) fluid parameters, and (3) abrasive parameters. While there exists similarities with

Table 1 Typical process parameters in MFJP

Parameter type	Typical values
Nozzle parameters	
Nozzle outlet diameter	0.1–1.0 mm
Nozzle standoff distance	1.0–20 mm
Nozzle attack angle	90°
Fluid parameters	
Carrier fluid	Water
Fluid pressure	0.2–2.0 MPa
Abrasive parameters	
Abrasive type	Al ₂ O ₃ , CeO ₂ , SiC, diamond
Abrasive grain size	0.1–10 μm
Abrasive concentration	10–40 g/L

micro waterjet machining, such as the configuration of the nozzle and pressurization of the carrier fluid, processing conditions in MFJP are much more benign in order to ensure ductile cutting of the workpiece surface rather than brittle removal of material.

10.2.1 Nozzle Outlet

The nozzle outlet diameter typically ranges between 0.1 and 1.0 mm, with material removal rate increasing as a function of the squared value of this diameter (all other parameters being equal). When using smaller diameter outlets below 0.5 mm, the installation of an inline filter between the pump and nozzle cavity is recommended in order to avoid potential obstruction of the outlet. While conventionally drilled tapered stainless steel nozzles may be employed, the best practice is to use laser-drilled sapphire or diamond inserts, as these are machined with a higher degree of precision that results in noticeably narrower and more rotationally symmetric removal footprints, as shown in Fig. 6.

A further advantage in using laser-drilled inserts is the superlative sharpness of the bore edges, which promotes a strongly negative pressure gradient as the carrier fluid flows around the inner edge of the outlet. For inlet pressure more than around 0.4 MPa, fluid depressurization at this edge results in cavitation that leads to the development of a vena contracta region on the outlet wall close to this inner edge, as shown in Fig. 7. As fluid flows around the vena contracta, it temporarily detaches from the outlet wall. Under increased inlet pressure more than around 0.6 MPa, detachment of the carrier fluid reaches across the entire length of the nozzle outlet wall, thanks to a continuous layer of vaporized fluid. This condition, known as a hydraulic flip, brings two key advantages to the MFJP process: (1) narrowing of the fluid jet beam that offers enhanced processing resolution and (2) greatly enhanced longevity of the insert as abrasive particles seldom come into contact with the nozzle outlet wall.



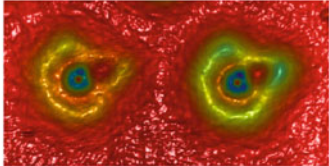
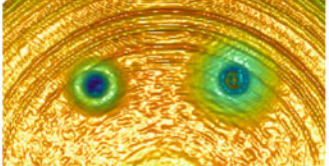
Nozzle Type	Tapered stainless-steel	Sapphire inserts
Illustration		
Experimental footprints		

Fig. 6 Experimental comparison of MFJP footprints generated with tapered stainless steel versus sapphire insert nozzle types

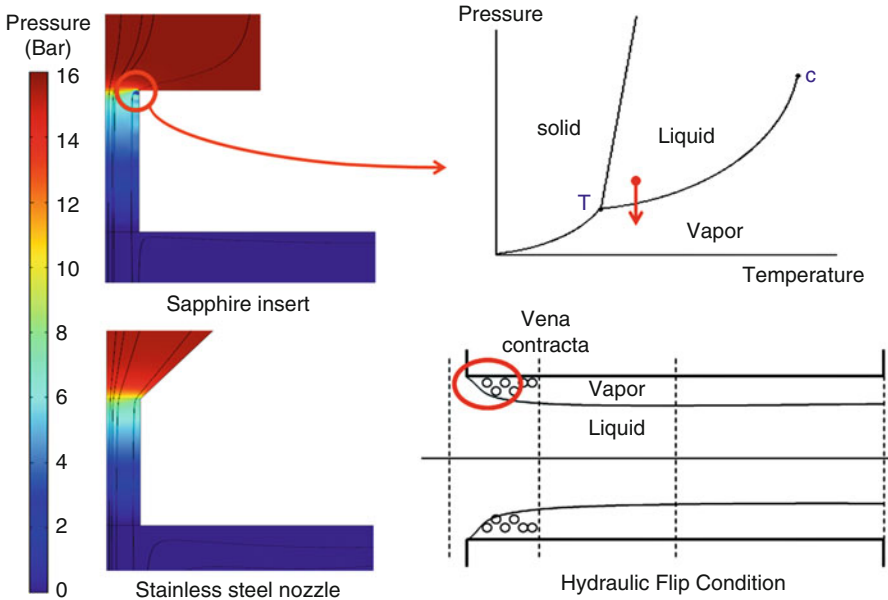
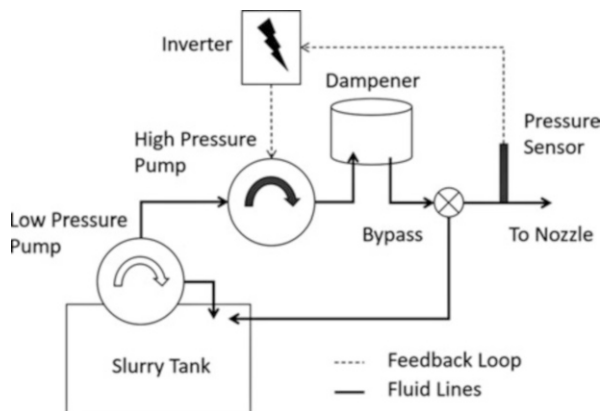


Fig. 7 Simulation of pressure field difference between sapphire and tapered stainless steel nozzle outlet and the resulting development of hydraulic flip condition in the case of sapphire inserts

10.2.2 Fluid Pressurization

Pressurization of the MFJP slurry at the nozzle inlet between 0.2 and 2.0 MPa is the typically recommended range, as it allows lower impact energy of the abrasive particles when compared to micro waterjet machining, ensuring that brittle damage

Fig. 8 Typical implementation of feedback-enabled fluid pressurization system in MFJP. (Beaucamp et al. 2012)



does not occur on the workpiece surface. Special care and attention should be paid when designing the fluid pressurization system, as oscillations of nozzle inlet pressure inevitably translates into oscillations of the material removal rate at the workpiece surface. Figure 8 shows a typical setup designed to reduce such nozzle inlet pressure oscillations (Beaucamp et al. 2012): in order to maximize efficiency of the pressurization system, a low-pressure pump acts as a fluid mixer (to keep abrasive particles in suspension) and feed-in to a high-pressure pump. The high-pressure pump may be of the plunger, diaphragm, or Archimedean screw type, with the latter usually preferred as it operates with lesser oscillations of the fluid pressure.

The pressurized fluid then flows through a dampener in order to reduce residual oscillations, after which it enters a variable bypass that allows a fraction of the fluid through to the nozzle inlet, while the rest flows back to the slurry tank. The bypass is useful for steering operation of the system toward high revolution of the pump, as high-frequency pressure oscillations are more effectively absorbed by the dampener. A pressure sensor is located between the bypass and nozzle inlet and connects to a control system that monitors fluid pressure and corrects residual fluctuations by feeding back to the inverter powering the high-pressure pump, as well as regulating the opening level of the bypass. The usefulness of this kind of advanced system, capable of pressure monitoring and feedback loop, has been demonstrated in the case of optical glass polishing (Beaucamp et al. 2012), with reduction in surface waviness from 16 nm down to 1.5 nm rms when the feedback loop is enabled.

10.2.3 Abrasive Particles

Typical abrasive particle size ranges between 0.1 and 10.0 μm . The selection of abrasive particle type depends mostly on the workpiece material, with typical recommendations as follows: Al_2O_3 for metals such as nickel and steel, CeO_2 for optical glass, and SiC or diamond for harder materials such as ceramics and superalloys. The influence of abrasive size and nozzle inlet pressure on the material removal rate and surface roughness has been well documented in the literature, such as in the case of

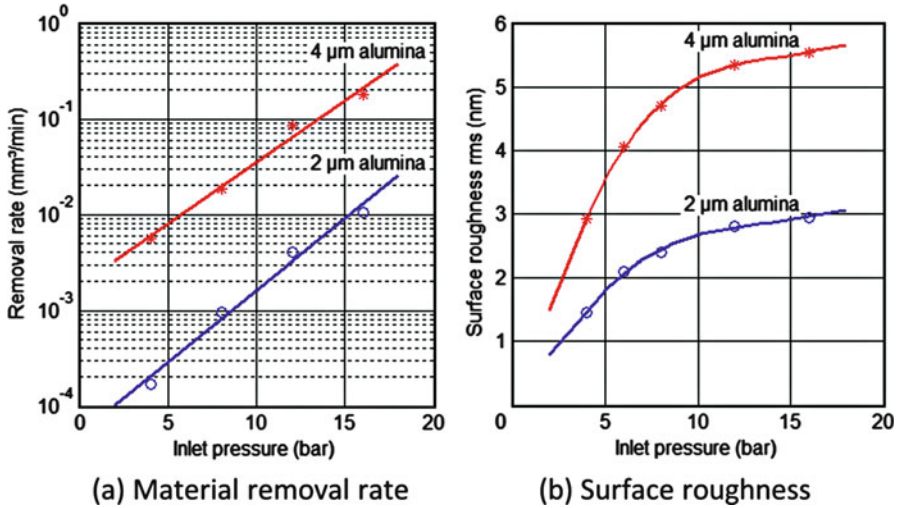


Fig. 9 Influence of abrasive size and inlet pressure on removal rate and surface roughness in MFJP. (Beaucamp and Namba 2013)

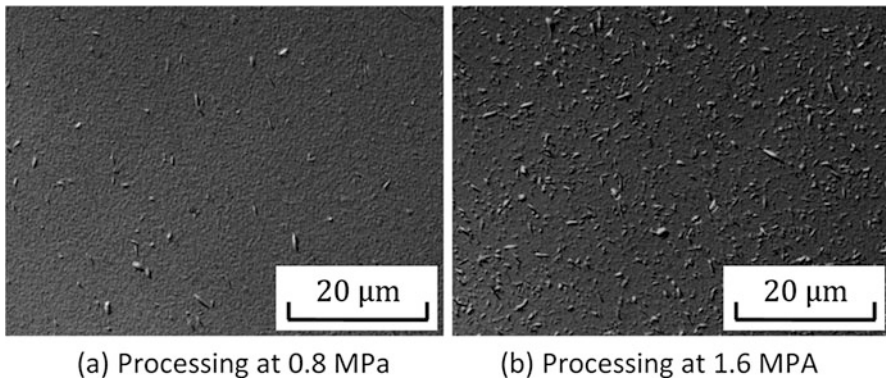


Fig. 10 Contamination of tungsten carbide surfaces by embedded 2 μm alumina abrasive particles after processing by MFJP. (Beaucamp et al. 2014)

optical glass (Booij 2003) and electroless nickel (Beaucamp and Namba 2013). As shown in Fig. 9, the material removal rate typically increases exponentially as a function of both inlet pressure and abrasive particle size, while surface roughness follows a more linear relationship of these parameters. These trends make MFJP an attractive process when used in multiple stages, with a first stage of larger abrasives used for bulk material removal without excessive degradation of surface roughness and a second stage of smaller abrasives used for final finishing of the surface.

Contamination of the workpiece surface by embedded abrasive particles may occur when processing by MFJP soft materials such as electroless nickel plating or nickel alloys. Fig. 10 shows an example, in which tungsten carbide surfaces were

contaminated by embedded alumina particles (Beaucamp et al. 2014). Whenever such embedding occurs, it can be very difficult to remove the abrasive particles from the surface (even with the use of ultrasonic vibration-assisted cleaning equipment). Contamination of the surface typically increases as a function of the MFJP inlet pressure, and as the inverse function of the abrasive particle size. Thus, in cases where contamination of the surface is observed, loading the carrier fluid with a slightly larger abrasive grit size while reducing the operating pressure of the system is recommended. This remedial action will usually maintain both the removal rate and surface roughness level, while drastically reducing surface contamination by the abrasives.

10.3 MFJP Process Mechanism

The process mechanism in MFJP can be broken down into four separate basic components: (1) development of the jet plume at the nozzle outlet and subsequent impingement of the workpiece surface, (2) entrainment of abrasive particles by the carrier fluid, (3) removal of workpiece material by abrasive particles grazing the surface, and (4) impact of the process on surface integrity when processing hard and brittle materials. Each of these components is separately detailed in the following sections.

10.3.1 Development of Jet Plume and Impingement of Workpiece

Considering that the carrier fluid is nearly incompressible at the typical operating pressure and temperature of the MFJP process, the average velocity of the jet plume at the nozzle outlet can be estimated from Bernoulli's equation:

$$P = \frac{1}{2} \rho v^2 \quad (1)$$

where P [Pa] is the inlet pressure, ρ [$\text{kg}\cdot\text{m}^{-3}$] is the carrier fluid density, and v [$\text{m}\cdot\text{s}^{-1}$] the fluid velocity at the nozzle outlet. For the typical operating pressure conditions of 0.2–2.0 MPa, nozzle outlet velocities thus range between 20 and 60 $\text{m}\cdot\text{s}^{-1}$.

More detailed modelling of the jet plume formation requires application of the Navier-Stokes equations to a two-phase flow computational fluid dynamics problem. In their incompressible form, the Navier-Stokes equations are reduced to the expression:

$$\rho \left(\frac{\partial v}{\partial t} + v \cdot \nabla v \right) = -\nabla P + \mu \nabla^2 v + F \quad (2)$$

where μ [Pa.s] is the fluid viscosity and F [N] represents external forces acting on the fluid. The left side of the equation generally represents the fluid inertia and the right

side the divergence of stress and other forces. The viscosity of a slurry mixture can be calculated from the volume fraction of solid particles in the carrier fluid using the Thomas equation, which arises from a combination of Brownian motion theory and experimental observations at high particle concentrations:

$$\mu_r = 1 + 2.5\phi + 10.05\phi^2 + Ae^{B\phi} \quad (3)$$

where μ_r is the relative viscosity of the slurry to that of water, ϕ the volume fraction of solid particles, and $A = 0.00273$, $B = 16.6$ (empirically derived constants).

When dealing with the two-phase propagation of slurry through surrounding air, a phase function ϕ is used to describe the interface between air and carrier fluid, with fluid density and viscosity being assigned for air or slurry on either side of this interface. From an initial state ϕ_0 , in which the carrier fluid fills the inside of the nozzle cavity and air occupies the outside, the interface is convected by the fluid velocity field. This evolution is described by the Cahn-Hilliard equation:

$$\frac{\partial\phi}{\partial t} + (\mathbf{v} \cdot \nabla)\phi = \nabla \cdot \gamma \nabla G \quad (4)$$

where γ [$\text{m}^3 \cdot \text{s} \cdot \text{kg}^{-1}$] is a mobility parameter controlling the relaxation time (used to prevent oscillations of the interface and improve numerical stability) and G [Pa] is the chemical potential of the system. The left side of the equation convects the air/slurry interface, while the right side seeks to minimize the total free energy of the system. While a system of two immiscible fluids has a free energy comprised of mixing, bulk distortion, and anchoring, in MFJP the problem may be simplified by retaining only the mixing energy, in which case the potential G is derived from the Ginzburg-Landau equation:

$$G = \lambda \left(-\nabla^2\phi + \frac{\phi(\phi^2 - 1)}{\varepsilon^2} \right) \quad (5)$$

where ε [m] is an arbitrary capillary width (thickness of the air/carrier fluid interface region) and λ [N] represents the mixing energy density. These two parameters are closely linked to the surface tension coefficient σ [N/m] through the expression:

$$\sigma = \frac{2\sqrt{2}}{3} \frac{\lambda}{\varepsilon} \quad (6)$$

Turbulence of the fluid flow through the outlet and near the workpiece surface requires adequate treatment by introducing turbulence model equations into the simulation. Table 2 shows a comparison of three of the most common turbulent flow models: k- ε , k- ω , and SST. The SST model is well suited to jet plume formation and impingement problems, as it combines robustness of the k- ω model in the near-wall regions (including the severe pressure gradient at the inner edge of the outlet) and numerical stability of the k- ε model in the free shear flow regions of the jet

Table 2 Comparison of three turbulent flow models

Model	$k-\varepsilon$	$k-\omega$	SST
Concept	2 transport equations: Turbulent kinetic energy k Turbulent dissipation ε	2 transport equations: Turbulent kinetic energy k Turbulent frequency ω	Combination of: $k-\omega$ in near-wall regions $k-\varepsilon$ in free stream regions
Pros/cons	+ Numerically robust – Valid only if fully turbulent – Poor results against severe pressure gradients	+ Superior treatment of near-wall regions + Suitable against severe pressure gradients – Flow separation can occur excessively in free streams	+ Well suited for laminar to turbulent flow transitions – Less suitable for free shear flow regions

plume. A complete formulation of the SST model is readily available in the literature (Menter 1994).

Figure 11 shows a typical time series simulation of jet plume development and surface impingement, based on the numerical method described above (Beaucamp et al. 2012). After initial formation of a wide front by the fluid, which pushes out the surrounding air, the fluid stream rapidly stabilizes into a near laminar flow condition out of the nozzle. As the MFJP beam impinges the workpiece surface, a high-pressure region is established at the center of the jet impact zone, with fluid thereupon flowing around this stagnation point.

Additionally, edge effects may require special consideration in the case of optical surface polishing. For this type of application, geometrical distortions of the surface such as edge roll and shaving is considered as one of the more critical technical issues, which can dominate the performance of an optical system. When running 3D computational fluid dynamics simulations, it was found that fluid velocity in the edge region can increase by a factor of 2 relative to the inner region, as shown in Fig. 12a and b (Guo et al. 2006).

Such distortion of the fluid velocity field influences material removal at the ragged edge of the workpiece (width of approximately 0.2 mm): the usually circular influence region widens along the edge and features excessive removal of material compared with the inner region, as shown in Fig. 12c. The accuracy of deterministic finishing algorithms is improved when taking this effect into account (see Sect. 10.4).

10.3.2 Entrainment of Abrasive Particles by Carrier Fluid

The motion of individual abrasive particles within the carrier fluid can be derived from the application of Newton's second law of motion to the slurry mix, whereby:

$$m_p \frac{\partial^2 \mathbf{p}}{\partial t^2} = \mathbf{F} \quad (7)$$

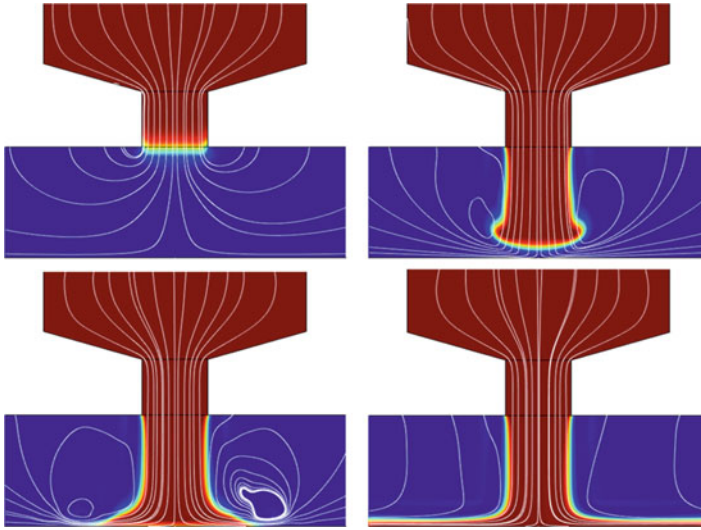


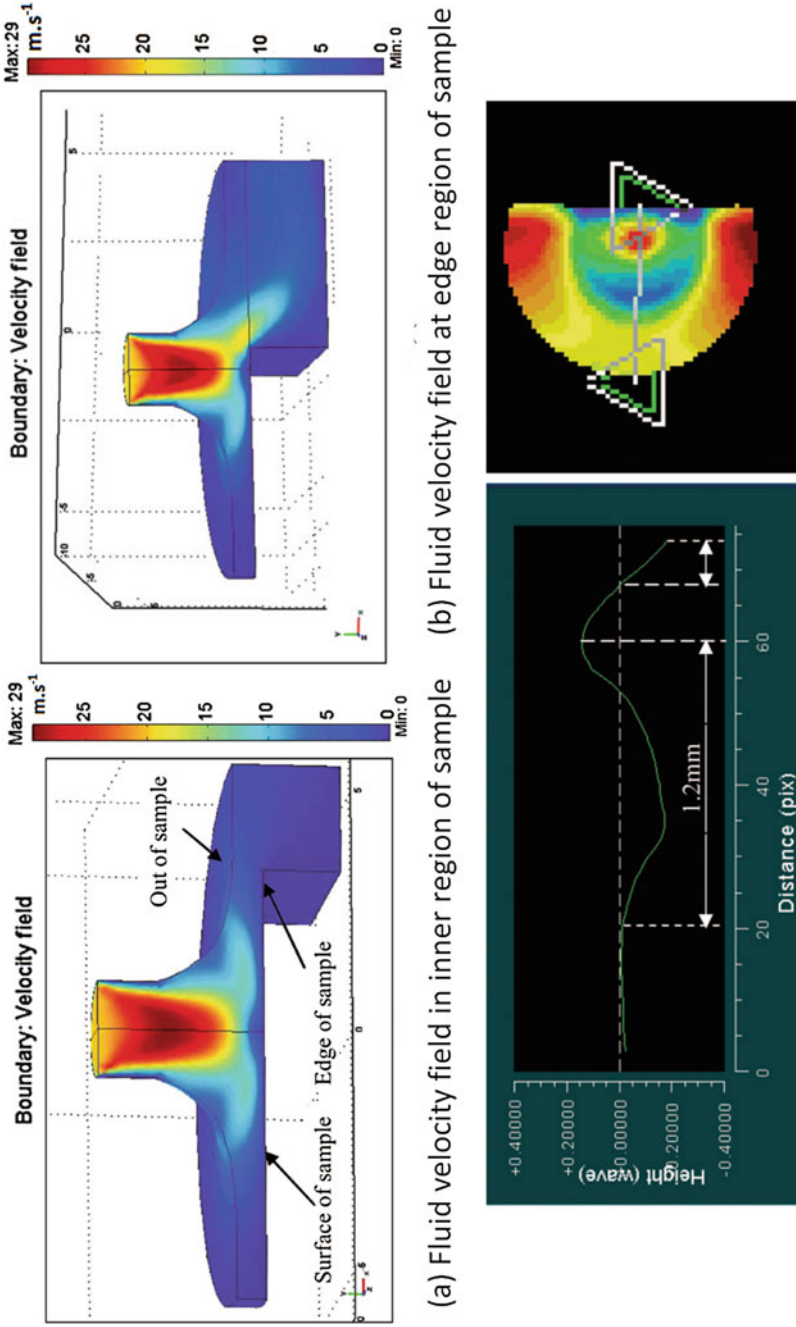
Fig. 11 Development of MFJP jet plume and impingement of workpiece surface. (Beaucamp et al. 2012)

where $p(t)$ is the trajectory of a single abrasive particle, m_p [kg] the abrasive particle mass, and F the sum of forces acting on the particle. External forces acting on a particle within a carrier fluid comprise gravitation, buoyancy, as well as collisions with other particles. In the case of MFJP, it is assumed that all these factors are small in comparison with the drag force issuing from the relative motions of the particle and high-velocity carrier fluid. This drag force can be estimated using Rayleigh's equation:

$$F = \rho C_D v^2 \frac{A}{2} \quad (8)$$

where C_D is the drag force coefficient (relating to the shape of the particle) and A [mm²] is the projected area of the particle relative to the fluid flow direction. Typically, abrasives follow the jet plume streamlines out of the nozzle and only start diverging in the region close to the workpiece surface, due to their downward momentum. Figure 13 shows an example of simulated abrasive particle tracks near the center of the jet impingement zone (Beaucamp et al. 2012). The color map denotes the velocity field of the carrier fluid, while individual particle trajectories are shown as black curves and can be seen to deviate from the carrier fluid velocity field in the vicinity of the stagnation region at the center of the impact zone. From these simulations, the spatial distribution of the abrasive particles' first impact point $\sigma_A(r)$ [mm⁻².s⁻¹] and their impact velocity vector $\vec{v}(r)$ can be estimated.

Figure 14 shows examples of simulations for the spatial distribution of abrasive particles' first impact on the workpiece surface and the impact velocity. The spatial distribution $\sigma_A(r)$ is a Gaussian-shaped curve, with a small depression at the center



(a) Fluid velocity field in inner region of sample (b) Fluid velocity field at edge region of sample

(c) Material removal profile at ragged edge of sample

Fig. 12 Characteristics of jet plume velocity field and material removal profile, between the inner and edge regions of a planar surface. (Guo et al. 2006)

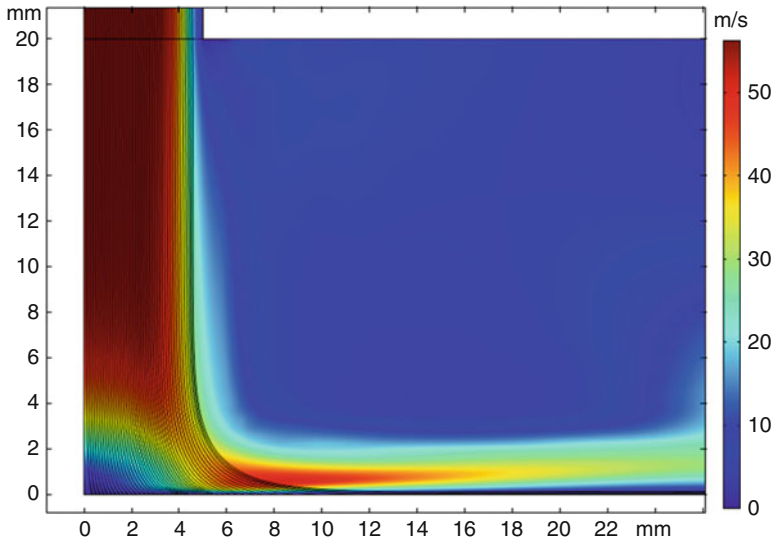


Fig. 13 Tracks of abrasive particle trajectories through the MFJP carrier fluid stream. (Beaucamp et al. 2012)

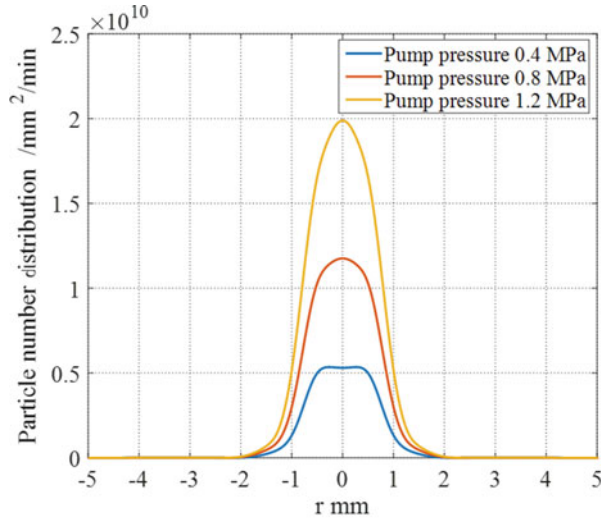
that corresponds to the increased fluid drag in the stagnation region of the impinging jet. At lower pump pressures such as 0.4 MPa, only a small number of abrasive particles actually reach the surface. The total number of particles reaching the surface increases approximately as a square law of the pump pressure for the typical operating range of the MFJP process. A similar law holds true when the abrasive grit diameter is increased. The impact velocity distribution $|\vec{v}|$ is an inverted W-shaped curve, with almost zero velocity at the center of the stagnation area and peak velocity at a radial distance of around 2 times the nozzle outlet half-diameter.

Experimental observation of abrasive particle tracks through the impact zone of the MFJP beam is possible through the use of particle image velocimetry (PIV). Abrasive particles can be coated with a fluorescent dye, which is activated by laser illumination of the fluid flow area captured by a high-speed camera. Figure 15 shows an example of CeO_2 particles coated with such fluorescent dye, and Fig. 16 shows a snapshot of the particles moving through an illuminated area close to the workpiece surface (Wäger et al. 2005). Experimental data for the particle trajectories has been found to agree reasonably well with predictions from computational fluid dynamics models.

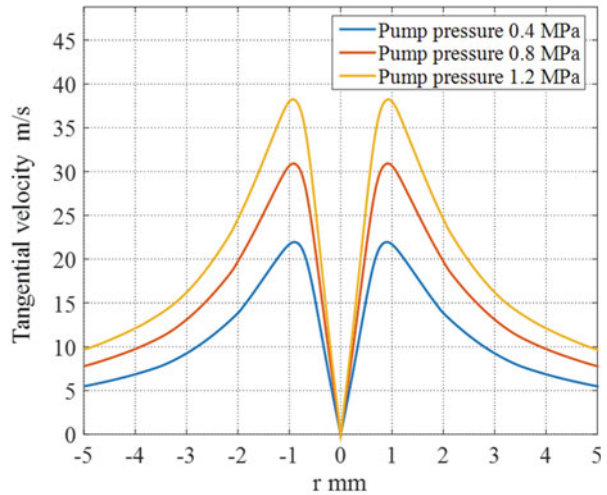
10.3.3 Material Removal by Abrasive Impacts

Modelling of material removal in abrasive waterjet cutting usually takes into account particle rotation due to the violent mixing of fluid and abrasives in the nozzle cavity, with particle rotation direction influencing the formation of chips on the workpiece surface. However, since the carrier fluid and abrasive particles in MFJP are premixed

Fig. 14 Simulations of MFJP abrasive particle impacts on the workpiece surface, as a function of pump pressure (Katsuura 2018)



(a) Spatial distribution of abrasive particles



(b) Impact velocity of abrasive particles

inside a slurry tank, the influence of particle rotation energy can be considered to be negligible when abrasives impact the surface. The impact velocity of abrasive particles on the workpiece surface can thus be decomposed into a normal component v_y [$\text{m}\cdot\text{s}^{-1}$] and tangential component v_x [$\text{m}\cdot\text{s}^{-1}$], as shown in Fig. 17a (Cao and Cheung 2014). As the abrasive particles impact the surface with an approach angle α , their normal component of velocity v_y is responsible for penetration of the workpiece material, which leads to deformation wear. The horizontal component of velocity v_x is responsible for cutting action of the particles. In the cutting process, two scenarios

Fig. 15 Cerium oxide particles coated with fluorescent die. (Wäger et al. 2005)

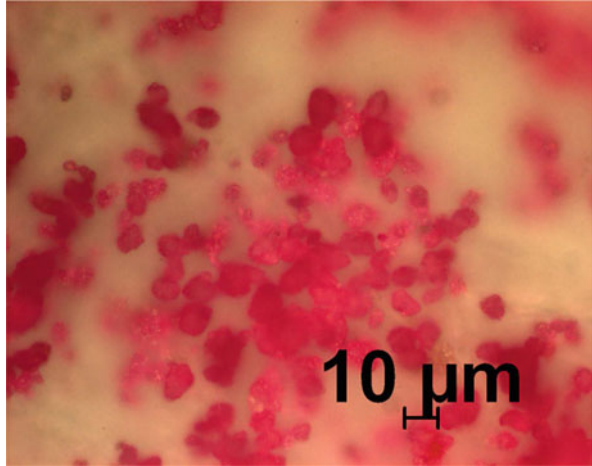
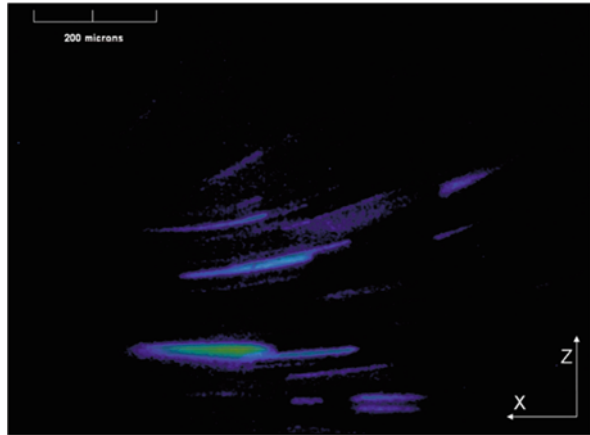


Fig. 16 Snapshot of abrasive particles motion close to the workpiece surface. (Wäger et al. 2005)



are possible: cutting type I in which the particle loses all its kinetic energy during the collision and cutting type II in which the particle loses only a fraction of its kinetic energy and bounces off the surface.

Assuming an abrasive hardness greater than that of the workpiece material, in which case deformation of the impacting particles may be neglected, the abrasives are modelled as cones of semi-angle θ hitting the surface with their cone axis perpendicular to the surface. As the cone indents the surface with an increasing depth d [mm], its cross-sectional area of indentation A_n [mm²] can be expressed as:

$$A_n = \pi d^2 \tan^2 \theta \quad (9)$$

The normal component of the equation of motion for abrasive particles, as they progressively indent the workpiece material, can then be written as:

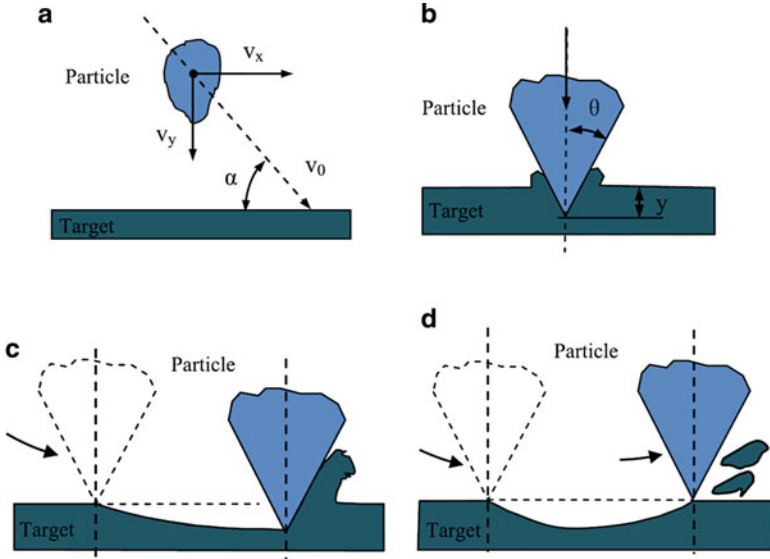


Fig. 17 Erosion behavior of abrasive particles in MFJP: (a) impact, (b) deformation wear, (c) material cutting type I, (d) material cutting type II. (Cao and Cheung 2014)

$$m_p \frac{\partial v_n}{\partial t} = P_n A_n \quad (10)$$

where P_n [Pa] is the normal component of plastic flow pressure acting over the area A_n , v_n [$\text{mm}\cdot\text{s}^{-1}$] is the normal velocity of the particle at a time t [s], and m_p [kg] is the mass of the abrasive particle. This equation can be solved under the initial condition $v_n(0) = v_y$ when the particle first contacts the surface, and $v_n(T) = 0$ when the particle fully indents the surface with a depth d_i , leading to an expression for the volume of indentation V_i [mm^3] when reaching the maximum indentation d_i [mm]:

$$V_i = \int_0^{d_i} A_n \partial y = \frac{m_p v_y^2}{2P_n} \quad (11)$$

The material displaced by indentation is associated with several phenomena: elastic deformation, plastic deformation, or wear removal as debris. However, owing to the low kinetic energy of abrasive particles in MFJP, the direct removal of material due to indentation-induced wear is usually negligible (except for brittle mode processing cases, see Sect. 10.3.4). This is confirmed by the noticeable absence of material removal at the center of the stagnation area, where particle trajectories are mostly normal to the surface.

Therefore, the main material removal mechanism in MFJP is ductile cutting of the surface under the lateral motion of the penetrating abrasives. Owing to springback of the material from the elastic component of deformation, the volume of ductile material removal by the indenting abrasives can be expressed as a fraction of the

integral along the cutting length L [mm] of the cross-sectional area of the engagement by abrasive particles A_t [mm²] (Huang et al. 2008), in the plane perpendicular to the direction of cutting:

$$V \propto \int_0^L A_t \partial x \quad (12)$$

The tangential component of force F_t experienced by the abrasive particle is proportional to the tangential component of the workpiece material plastic flow pressure P_t [Pa], applied against the cross-sectional area A_t , leading to the expression:

$$F_t \propto P_t A_t^b \quad (13)$$

where b ($0.5 \leq b \leq 1$) is a material-dependent exponent of the cross-sectional area. The energy equation of the particle can then be solved for the initial condition $v_t(0) = v_x$ and $v_t(T) = v_{\text{out}}$ reflecting the probability that a particle may escape the cutting zone with some residual tangential velocity v_{out} (cutting type II):

$$\int_0^L F_t \partial x \propto \frac{1}{2} m_p (v_x^2 - v_{\text{out}}^2) \quad (14)$$

By combining Eqs. 12–14, and substituting cV_x ($c \leq 1$) in place of V_{out} (c is the fraction of initial particle velocity on impact), the expression of the volume V [mm³] of material removed by a single particle can be simplified to a function of its normal and tangential impact velocities as follows:

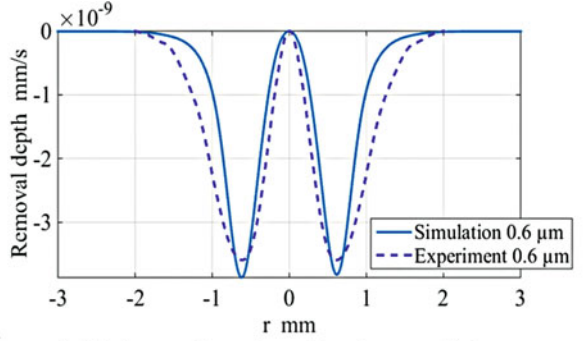
$$V(v_x, v_y) = k \left(\frac{1}{2} m_p v_x^2 \right) \left(\frac{1}{2} m_p v_y^2 \right)^{\frac{2(1-b)}{3}} \quad (15)$$

where k is a coefficient that depends on the workpiece material (compounding contributions from the plastic flow pressure and material springback) and which requires experimental calibration. The overall material removal rate E [mm³.s⁻¹] can finally be estimated by taking into account the rate of particles $\sigma_A(r)$ [mm⁻².s⁻¹] impacting a specific area of the workpiece surface, as follows:

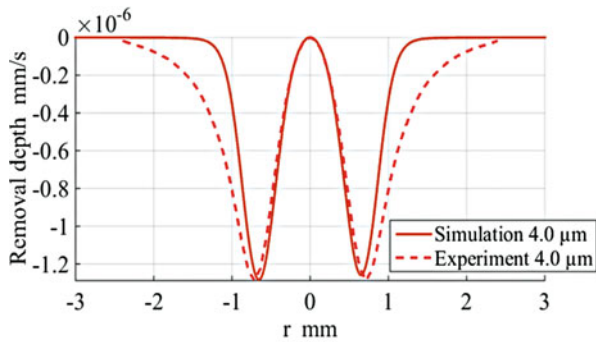
$$E(r) = \sigma_a(r) V(v_x(r), v_y(r)) \quad (16)$$

Some comparisons of removal depth distribution computed by simulations and measured in experiments are shown in Fig. 18. In the case of small abrasive particles with a diameter below 1 μm , the single particle impact model generally provides accurate estimates. However, as the particle size further increases, the removal footprint measured in experiments widens noticeably, due to further removal of material caused by secondary impacts of the abrasive particles. The influence of secondary impacts can be reflected by further tracing the particle trajectories to characterize the secondary impact distribution $\sigma'_A(r)$ and velocities

Fig. 18 Comparison of material removal footprints predicted by single particle impact model and measured experimentally. (Katsuura 2018)



(a) 0.6 μm diameter abrasive particles



(b) 4.0 μm diameter abrasive particles

$v'_x(r)$, $v'_y(r)$. The predictions from secondary impact models agree more closely with measured data in the case of abrasive particles with diameter above 1 μm (Katsuura 2018).

10.3.4 Surface Integrity of Hard and Brittle Materials

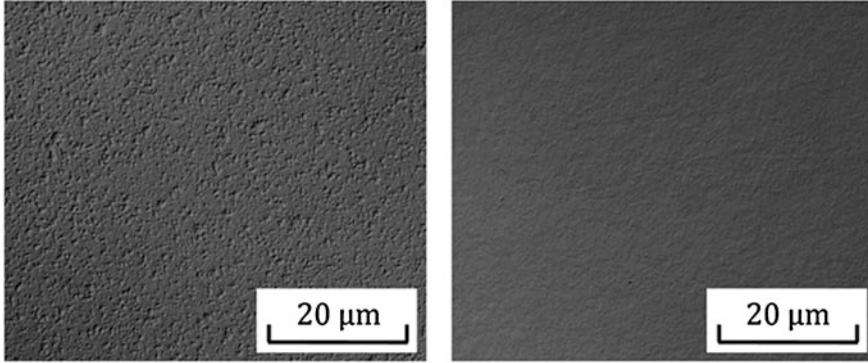
When processing hard and brittle materials, the potential occurrence of deformation wear on the workpiece by particle impacts should be given special attention. According to Bifano et al. (1991), there exists a critical indentation depth d_c of the abrasive particles, above which brittle fracture of the workpiece surface is expected to occur during machining. d_c [mm] can be expressed as a function of measurable material properties as follows:

$$d_c = 0.15 \left(\frac{E}{H} \right) \left(\frac{K_c}{H} \right)^2 \tag{17}$$

where E is the elastic modulus of the material, H the Vickers hardness, and K_c the fracture toughness. The validity of the coefficient 0.15 was verified for several

Table 3 Material properties of binderless carbide materials used in optical mold fabrication

Material properties	Silicon carbide	Tungsten carbide
Elastic modulus (E)	410 [GPa]	715 [GPa]
Fracture toughness (K_c)	4.6 [MPa.m ^{1/2}]	4.8 [MPa.m ^{1/2}]
Vickers hardness (H)	2800 [kg.Mm ⁻²]	2350 [kg.Mm ⁻²]
Critical depth of indentation (d_c)	59 [nm]	190 [nm]

(a) Brittle mode processing ($d_i > d_c$) (b) Ductile mode processing ($d_i < d_c$)**Fig. 19** Surface integrity of binderless tungsten carbide processed by MFJP. (Beaucamp et al. 2014)

ceramic materials including fused silica, Zerodur, and silicon carbide. It corresponds to an arbitrary 10% fracturing of the cut walls. Table 3 shows a summary of these material properties for silicon carbide and tungsten carbide, together with the resulting value for critical depth of indentation.

Given that the equivalent indentation depth d_i in MFJP can be expressed as function of process and material parameters, it is possible to use the critical indentation depth model to predict the approximate appearance of brittle damage on the workpiece surface, through the relationship $d_i > d_c$. By integration of Eq. 11, an expression of d_i is obtained as follows:

$$d_i = \left(\frac{3m_p v_y^2}{2\pi P_n \tan^2 \theta} \right)^{\frac{1}{3}} \quad (18)$$

Figure 19 shows a typical example of brittle material (binderless tungsten carbide) machined by MFJP, with the equivalent indentation depth d_i above (a) and below (b) the critical indentation depth d_c of the processed material. The impact on surface integrity is very clearly observable, with extensive pitting of the brittle mode machined surface versus smoothness of the ductile mode machined surface.

10.4 Deterministic Finishing by MFJP

An exploitable characteristic of MFJP is the time-dependent nature of material removal during processing. As such, the removal depth per unit of area is a factor of the equivalent time spent by the MFJP beam at a given location on the workpiece. This property can be harnessed to perform deterministic finishing of surfaces, in which the shape accuracy of a workpiece is improved through iterative processing by MFJP. This processing strategy is based on convolution of influence function (material removal footprint) data with tool path information to predict the outcome of a polishing run. The basic principles of deterministic finishing by MFJP are presented in the following sections.

10.4.1 Influence Function

While basic process simulations provide useful indicators of the extent and rate of material removal in MFJP, deterministic finishing usually requires very precise measurements of experimental influence functions. These are generated by impinging a static location on a sacrificial workpiece for a specific amount of dwell time. Figure 20 shows an example of such influence function spots generated on a piece of electroless nickel with a slurry of aluminum oxide at a concentration of 20 g.L^{-1} , pressurized at 0.8, 1.2, and 1.6 MPa (from left to right). The 10-s dwell time resulted in a maximum depth of 10 nm at 0.8 Mpa, and 40 nm at 1.6 MPa, as well as a slight variation in the extent of the footprint due to the varying degree of secondary impacting by the abrasive particles (see Sect. 10.3.3).

A continuous model of the footprint shape, as function of the various process parameters such as the nozzle standoff distance and inlet pressure, can be assembled using a mathematical object called multivariate spline. The concept consists of associating an N-dimensional process parameter space (denoted as u, v, \dots) with a Cartesian representation space (denoted as x, y, z) of the influence function. Based on a set of measured data (fixed points in the process parameter space, associated with 3D measurements of the influence function), a multivariate spline of the influence function (IF) can be constructed by the tensor product method resulting in the form:

$$IF(p_u, p_v) = \sum_{u=1}^U \sum_{v=1}^V B_{u,k}(p_u) B_{v,l}(p_v) A_{u,v} \quad (19)$$

where $B_{u,k}$ and $B_{v,l}$ are univariate B-splines of order k and l , respectively, and $A_{u,v}$ are coupling coefficients. This definition can be extended to any number of dimensions in the process parameter space, and the output provides a continuous morphing of the influence function shape between the experimentally collected data points.

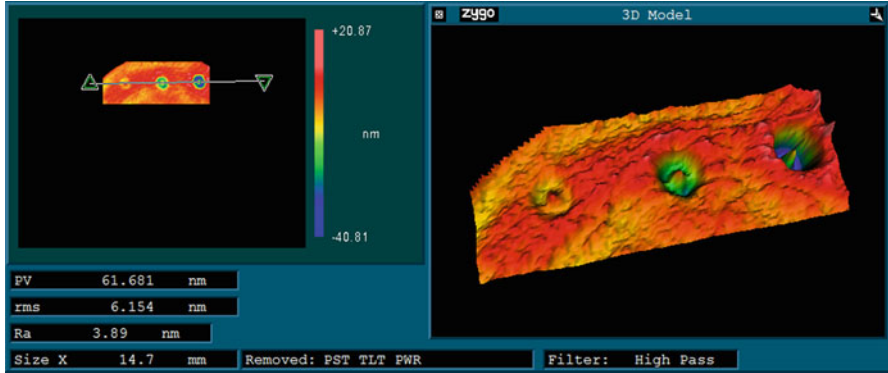


Fig. 20 Influence function spots generated on electroless nickel by 0.8, 1.2, and 1.6 MPa MFJP

10.4.2 Forward Problem

Processing a workpiece by deterministic MFJP usually involves rastering or spiraling the surface, with a track spacing that is a fraction of the influence function spot extent. Typical track spacing of between 5% and 10% of the spot extent is used to attenuate the appearance of cusping across the workpiece surface.

For numerical convenience, the continuous tool path may be discretized into a series of points $\{i \mid 0 \leq i \leq n\}$ as illustrated in Fig. 21. The MFJP beam dwells at each point for an equivalent time that is relative to the distance between points in the series and inverse to the feed of displacement of the beam across the surface. Inlet pressure and nozzle standoff distance may vary along this tool path, such that the process parameters may be expressed as function of i : $p_u(i), p_v(i), \dots$

The compound removal of material CR by the tool path (usually referred to as the forward problem) can be expressed as a discrete sum of the influence function's multivariate spline and dwell time map DT :

$$CR(p_u, p_v) = \sum_{i=0}^n DT(i) IF(p_u(i), p_v(i)) \tag{20}$$

While CR accounts for the material removal profile across the entire workpiece surface, individual points of the tool path vector only affect a localized area of the entire surface matrix.

10.4.3 Inverse Problem

The main attraction of deterministic finishing by MFJP lies in the ability to iteratively improve form accuracy, through repeated measurement and processing of a

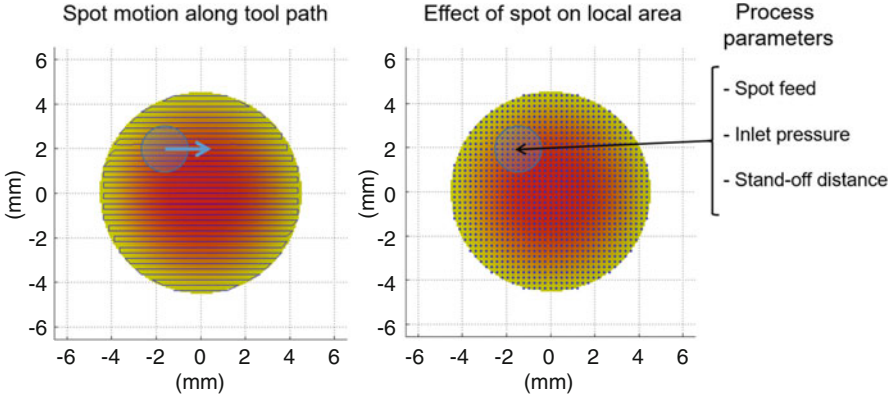


Fig. 21 Discretization of continuous tool path into dwell points visited by the MFJP influence function

workpiece. The objective function in this type of processing consists of minimizing the deviation between a target removal profile TR and the predicted compound removal profile CR :

$$f(p_u, p_v) = \sqrt{TR - CR(p_u, p_v)} \quad (21)$$

The scale of this numerical problem is vast: the process parameters p_u, p_v, \dots may vary across the entire series of tool path points, which makes this a numerical optimization problem with n^p input variables. In order to reduce the complexity of this problem, a typical approach consists of selecting initially constant values of the process parameters and treating the influence function as a point spread function (Fang et al. 2006). This permits initial assessment of the problem by deconvolution over the time domain, whereby:

$$DT * IF = CR \quad (22)$$

Limitations of the deconvolution method include the requirement for a non-varying influence function and the tool path covering a rectilinear grid. Thus, this method is used to compute an approximate solution, which can then be used as seed to a more advanced numerical optimization algorithm (such as evolutionary or Newtonian search).

An example of deterministic finishing by the inverse problem-solving method is shown in Fig. 22: an electroless nickel-plated aspheric molding die was generated by diamond turning to a form accuracy of 387 nm P–V. Through iterative measuring with a Fizeau interferometer and processing by deterministic MFJP, the form accuracy was improved down to 47 nm P–V. It is noteworthy that the process loop was realized on a standard polishing CNC machine, only capable of positioning with micron level accuracy.

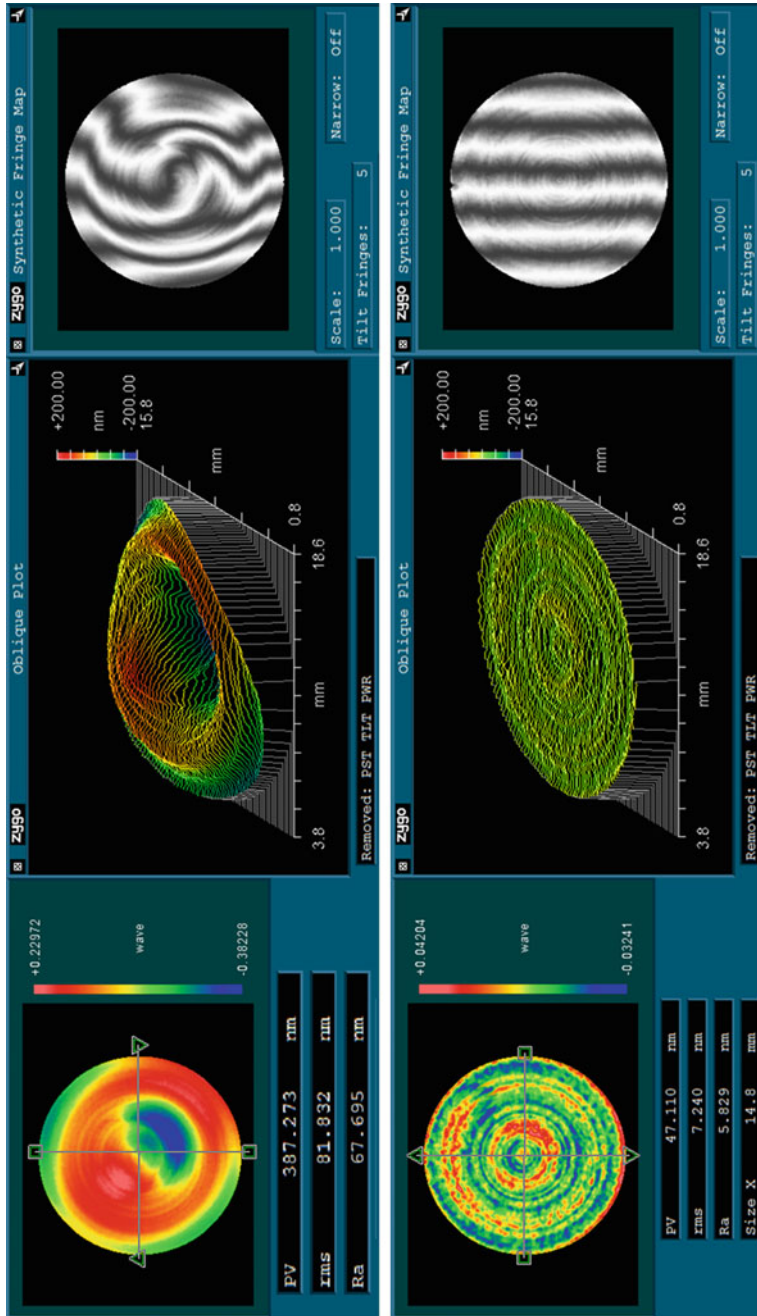


Fig. 22 Deterministic finishing of electroless nickel-plated aspheric molding die by MFJP

10.5 MFJP Process Enhancements

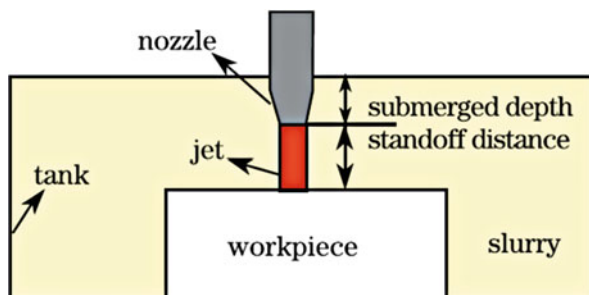
As discussed in Sect. 10.2.3, there exists in MFJP a strong correlation between abrasive size and inlet pressure on the one hand and removal rate on the other (Fig. 9). But increasing these factors in order to enhance material removal rate also leads to an increase in the normal component of velocity and potential degradation of the surface integrity (see Sect. 10.3.4). Thus, the MFJP process is usually constrained to lower material removal rates, and its scope for application was initially limited to finishing of near-perfect shape optical surfaces. However, a number of process enhancements have been proposed in order to increase the material removal rate, ranging from the injection of air bubbles to using arrays of nozzles. A number of these enhancements are discussed in this section.

10.5.1 Submerged MFJP

Submerged MFJP is a process variant in which the workpiece is plunged within a tank of circulating slurry, and the nozzle outlet is kept below the waterline of the tank, as shown in Fig. 23. Experimental data shows that material removal footprints generated in this operation method have a Gaussian-like appearance, instead of the W-shape common in standard MFJP. According to computational fluid simulations, the outflow of slurry from the nozzle outlet has to overcome greater resistance from surrounding slurry, than is the case in standard MFJP in which air is displaced. Accordingly, the tangential speed of the fluid along the workpiece surface is reduced, and abrasive particles rapidly lose their kinetic energy, the further away they travel from the center of the impingement region.

Material removal rate in submerged MFJP is somewhat lower than the standard process, with removal rate quickly tapering off as the standoff distance increases to more than 10 mm away from the workpiece surface. However, there are distinct advantages in submerged MFJP such as the Gaussian shape of influence functions, which performs better than a W-shape when using the process for deterministic finishing, and surface roughness that is around 50% lower than the standard process (all other parameters being equal). This improvement in surface roughness is understood to arise from the reduced likelihood of air bubbles becoming trapped

Fig. 23 Principle of submerged MFJP, in which the nozzle outlet is plunged within a tank of enveloping slurry (Shi et al. 2011)



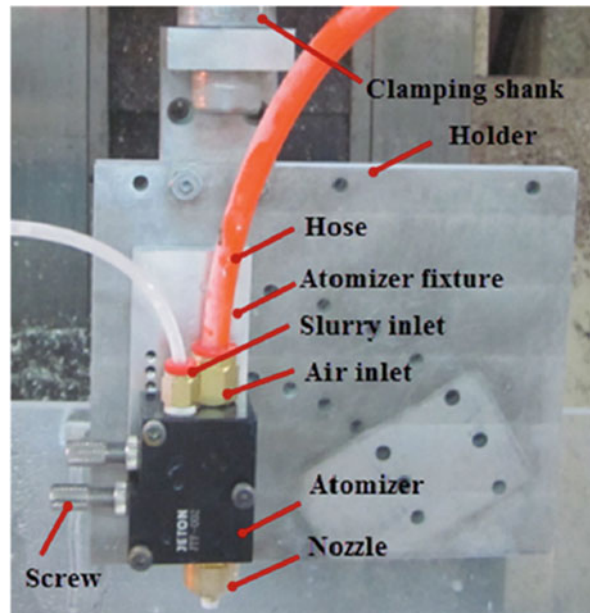
within the jet plume as it travels through surrounding slurry, as such air bubble can energize the impact of individual abrasives and detrimentally affect the surface.

10.5.2 Air-Assisted MFJP

One of the more intensely investigated line of research for the enhancement of material removal rate in MFJP has been the injection of air bubbles into the fluid jet stream, in order to energize the motion of abrasive particles within the carrier fluid. This effect can be achieved either by inclusion of a pulsating mixing valve that admits pressurized air up-front of the nozzle cavity (Messelink et al. 2005), or through the implementation of a special nozzle inside which slurry is drawn into an air stream by Venturi effect (Loc et al. 2013), an example of the latter being shown in Fig. 24.

In the case of both setups, material removal rate was found to greatly increase when compared to standard FJP (more than 1000%). However, the barely controllable mixing of slurry and air also has some side effects, such as a significant breakup of the jet plume at the nozzle outlet and rapid wear of the nozzle outlet walls. The resulting loss of process stability leads to large fluctuations of the removal rate and severe degradation of the surface roughness (more than 10,000%). For these reasons, air-assisted MFJP may qualify as a micro-blasting rather than micro-polishing process.

Fig. 24 Experimental setup of Venturi effect based air-driven MFJP system (Loc et al. 2013)



10.5.3 Ultrasonic Cavitation-Assisted MFJP

Ultrasonic cavitation-assisted MFJP is an enhancement in which microbubbles are generated directly within the nozzle, with the help of an acoustic transducer located at the back of the cavity. The main advantage of this method lies in the fact that both the size and number of microbubbles are controllable through the output frequency f [Hz] and power P [W] of the ultrasonic transducer. Figure 25 shows a typical implementation in which an acoustic lens is attached to the transducer (Beaucamp et al. 2017), such that pressure waves may be focused directly upstream of the nozzle outlet. Typical focal length value of the acoustic lens is 50 mm, with the nozzle cavity assuming a cone shape that matches the transducer diameter and focal length.

Typical operating frequency of the ultrasonic transducer is in the range 26–130 kHz and the output power in the range 50–400 W. The high intensity of the focused beam maximizes generation of cavitation bubbles, while proximity of the generation region to the nozzle outlet ensures delivery of microbubbles to the workpiece surface in the shortest time possible. The lifetime of microbubbles is measured in cycles of the acoustic waves, with a value of around 200 cycles typically observed in basic experiments. Table 4 shows the expected lifespan of cavitation microbubbles, as a function of the ultrasonic generation frequency. Accordingly, microbubbles should pass through the nozzle outlet and reach the workpiece within a few milliseconds. Integration of path time through the fluid stream computed numerically dictates that nozzle standoff distance should be no more than a few centimeters. This constraint can thus restrict applicability of ultrasonic cavitation-assisted systems in cases where recessed areas of a workpiece are more than a few centimeters deep.

Material removal rate increase of up to 380% compared to standard MFJP has been observed, when processing metals and glass by ultrasonic cavitation-assisted MFJP. Figure 26a shows that removal rate increases almost linearly as a function of ultrasonic output (ultrasonic frequency has a weaker impact on removal rate

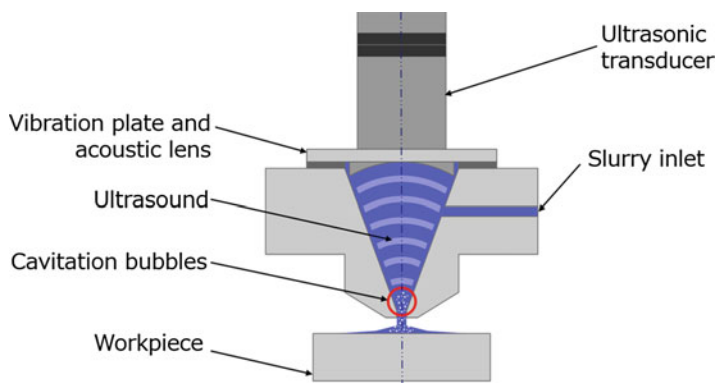


Fig. 25 Principle of ultrasonic cavitation-assisted MFJP (Beaucamp et al. 2017)

Table 4 Lifespan of microbubbles generated by ultrasonic cavitation (based on 200 cycles)

Transducer Frequency	26 kHz	78 kHz	130 kHz
Microbubble lifespan	7.2 ms	2.4 ms	1.4 ms

variation, the power output being equal). Crucially, surface roughness can be maintained or even slightly improved as shown in Fig. 26b. Thus, while the overall material removal rate boost of ultrasonic cavitation-assisted MFJP is lower than that of air-assisted systems, the maintaining of surface roughness is a considerable advantage.

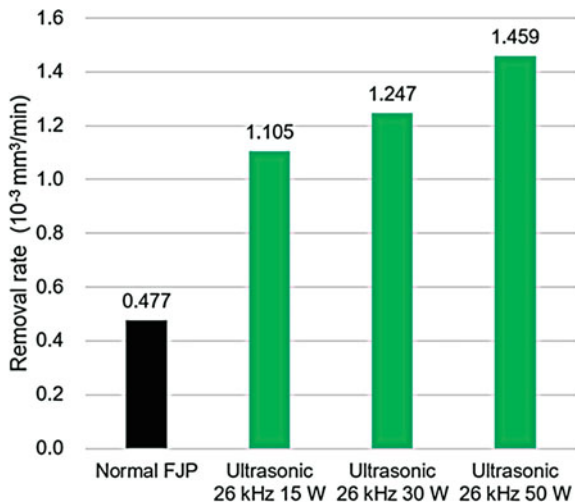
10.5.4 Non-Newtonian Fluid-Assisted MFJP

Fluids containing a dilute solution of long-chain polymers, such as polyacrylamide (PAM) and polyethylene oxide (PEO), are often described as non-Newtonian. Their viscosity and resistance to external deformation (elasticity) are dependent on the shear-rate and shear-rate history of the fluid, with the fluid viscosity typically increasing as the shear-rate increases. When using a non-Newtonian carrier fluid for MFJP processing, the shear-thickening effect is most noticeable in the near-wall region of the impinging jet, where a stagnation layer appears whenever an abrasive particle attempts to punch through the fluid and reach the workpiece surface, as shown in Fig. 27 (Kowsari et al. 2014). The extra drag experienced by the abrasive particles softens their impact on the surface, causing a noticeable reduction of the overall material removal rate. However, the possibility of increasing the elasticity of non-Newtonian fluids independently from their viscosity brings useful benefits, such as decreased jet plume instability (breakup) and improved focusing of the beam. In experimental tests, the width of channels machined with non-Newtonian fluids could be reduced by about 20% as compared to water-based MFJP (all other parameters being equal).

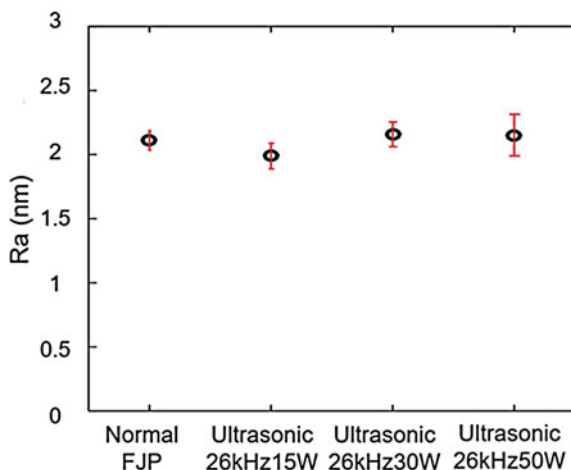
10.5.5 Magnetorheological Fluid-Assisted MFJP

Magnetorheological (MR) fluids are a type of carrier fluid that can greatly increase its apparent viscosity when subjected to an external magnetic field. MR fluids are typically loaded with micrometer-scale ferromagnetic particles, which under the influence of a magnetic field align themselves into lines of magnetic flux. In MR fluid-assisted MFJP, the jet plume is stabilized and stiffened by an axial magnetic field generated with the help of an electromagnet. This method has been shown to prevent breakup of the jet plume as the dense MR fluid exits the nozzle outlet (Tricard et al. 2006), as shown in Fig. 28. The stabilization persists for up to several meters, allowing for precise targeting of remote and difficult-to-access workpiece areas. Some advantages of this method include higher removal rate due to the increased apparent viscosity while maintaining nanometer-scale surface roughness, although the handling

Fig. 26 Comparison between standard and ultrasonic cavitation-assisted MFJP processing of BK7 optical glass (Beaucamp et al. 2017)
(a) Material removal rate
(b) Surface roughness



(a) Material removal rate



(b) Surface roughness

and recycling of MR fluid require highly specialized equipment and knowledge, which makes the implementation of a MR fluid-assisted MFJP setup somewhat challenging.

10.5.6 Nozzle Array MFJP

Precision artifacts made of repeating elements, such as the micro-lens arrays used in fiber-optic end connectors to telecommunications terminals (as well as replication molds for such artifacts), are well suited for parallelized processing by arrays of

Fig. 27 Extra drag experienced by abrasive particles near the workpiece surface, due to normal stress induced stagnation (Kowsari et al. 2014)

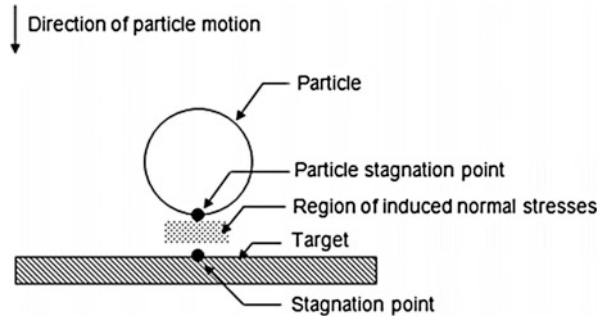
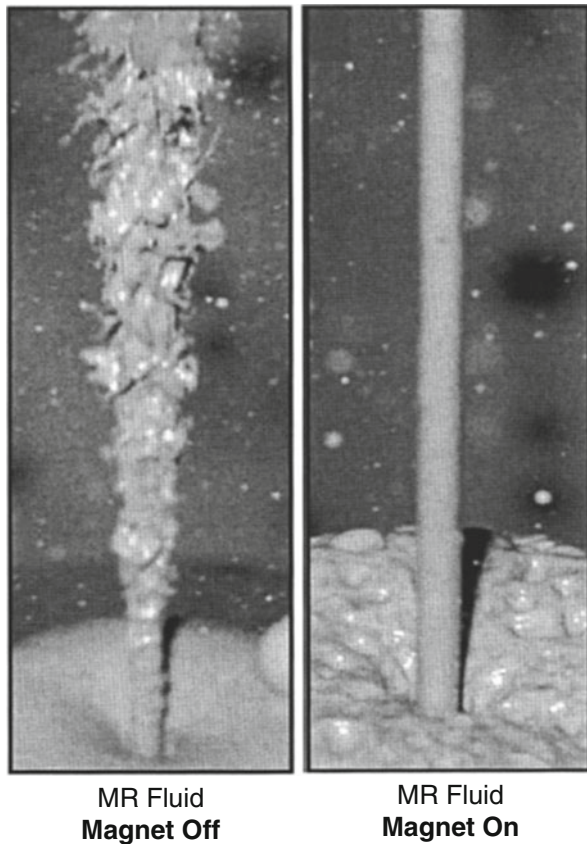


Fig. 28 Influence of magnetic field on the shape of a magnetorheological fluid jet beam (Tricard et al. 2006)



MFJP nozzles. As shown in Fig. 29, the array of nozzles may either match exactly the grid of micro-lenses or span a subset of the entire distribution (Wang et al. 2017). While basic implementations of the process may amount to the straightforward drilling of nozzle outlets into a base plate made of stainless steel, performance of nozzle array systems in terms of removal rate uniformity usually compares unfavorably against

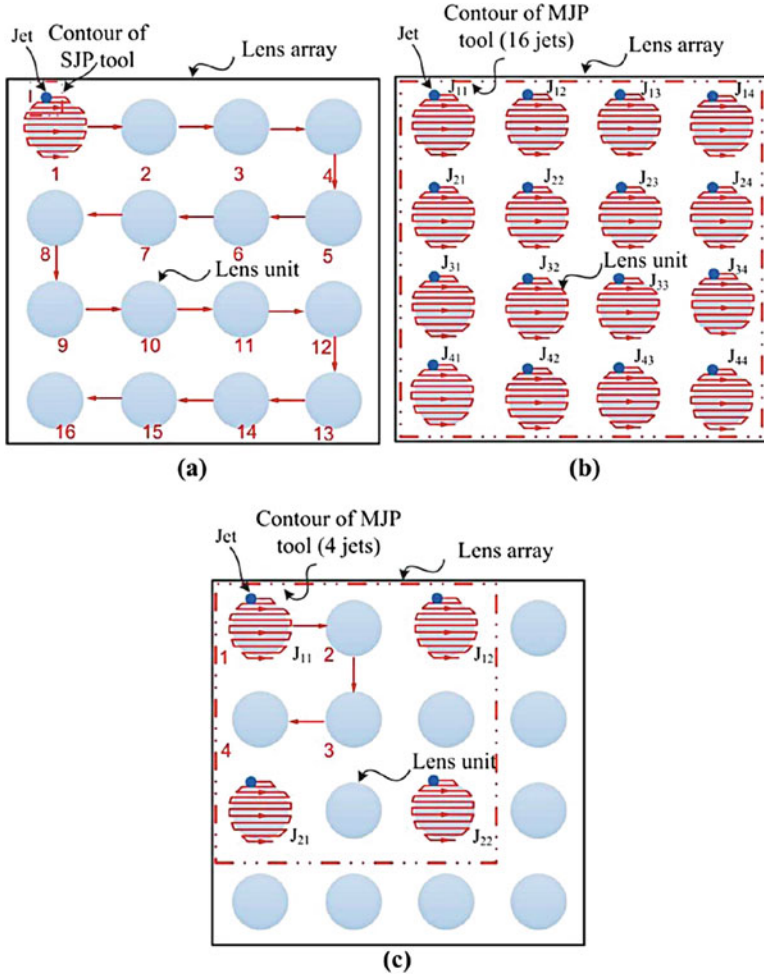


Fig. 29 Principle of lens array polishing with (a) single MFJP nozzle, (b) 4×4 array of nozzles, and (c) 2×2 array of nozzles (Wang et al. 2017)

single nozzle MFJP. The lower precision of conventionally drilled metal nozzles is one factor, which can be remediated by laser drilling of a large sapphire insert.

A less tractable factor is interference between impinging MFJP beams, as shown in Fig. 30. As the carrier fluid attempts to move across the workpiece surface and away from the impingement zone, interference in the fluid flow causes large variations in the maximum depth of material removal of beams issuing from the center and edge of the nozzle array, as well as the appearance of material removal interference patterns in between individual influence function spots. Reduction of these interference issues requires a minimum spacing between beams of several

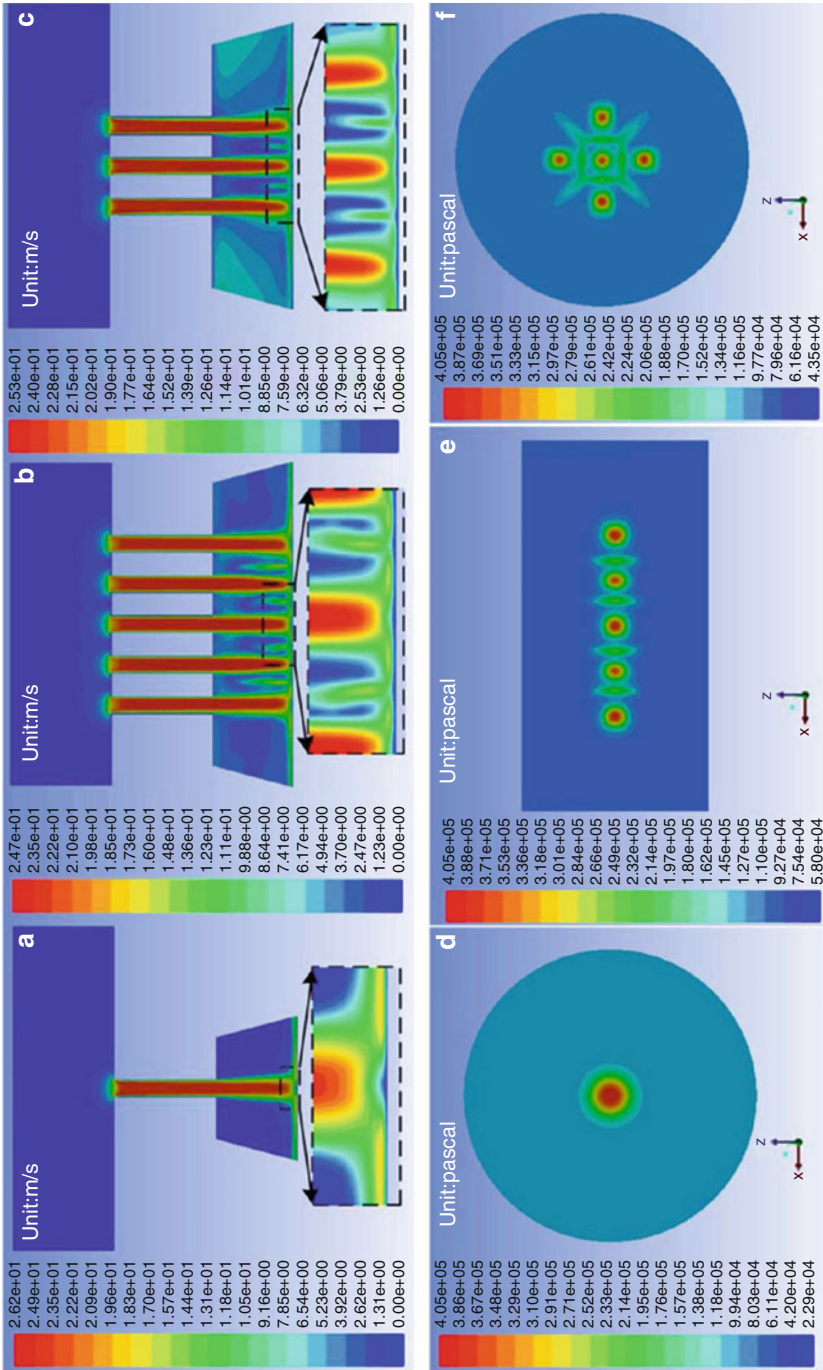
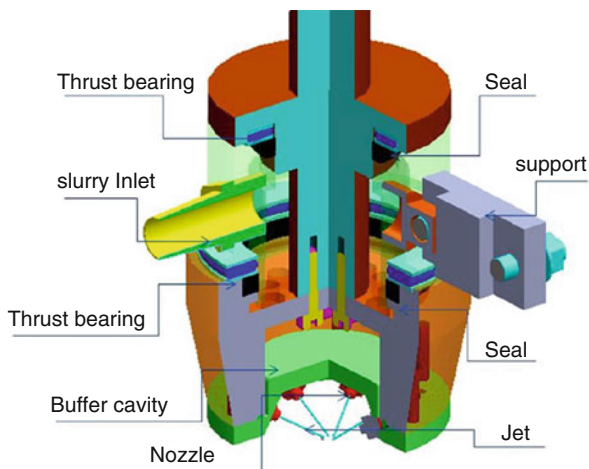


Fig. 30 Computational fluid simulation demonstrating MFJP beam interference in linear and radial arrangements of nozzle outlets (Wang et al. 2017)

Fig. 31 Design principle of rotary multi-jet polishing head (Shiou and Asmare 2015)



times the beam width, which makes the subset processing strategy shown in Fig. 29c the most practical.

10.5.7 Rotary Multi-MFJP

Combining several MFJP beams into a single influence function spot, from radially distributed inclined attack directions around a single impact zone, is another method that has been explored in order to enhance the material removal rate of the process. Figure 31 shows the design of a rotary multi-nozzle MFJP head, which offers the added benefit of suppressing directionality of the combined influence function spot (Shiou and Asmare 2015). The head consists of a shank coupled to a rotating shaft, supported by thrust bearings at the top and bottom of a static compartment. The pressurized slurry enters the top part of the cavity and flows out through a number of nozzle outlets attached to a plate at the bottom of the rotating shaft. Experimental data has found some unique advantages to this method, such as decreased surface roughness as the inlet pressure is increased between 0.4 and 0.8 MPa (a reverse trend to that observed in single jet MFJP). A dependency between surface roughness and angular rotation rate of the shaft was also observed, with an optimum speed of 20 rpm reported in the case of six nozzle outlets.

10.6 Summary and Outlook

In this chapter, micro fluid jet polishing (MFJP) was introduced as a flexible process for super-fine finishing of small and complex workpiece geometries. The principal advantages of MFJP include lack of tool wear, ease of access to deeply recessed areas, wide range of beam diameter from 0.1 to 1.0 mm, and the ability to reach

nanometer-level surface finish on various materials. Comprehensive modelling of the process has been published in the literature, covering all aspects from development of the jet plume to entrainment and impacting of the surface by abrasive particles. By application of these mathematical models, material removal rate in MFJP is eminently predictable and controllable, allowing for ultra-precise applications such as deterministic finishing and functional surface generation with nanometer-scale height resolution.

Some drawbacks have been highlighted, such as the potential occurrence of surface contamination by abrasives, which can be mitigated by increasing the particle size and decreasing the operating pressure, as well as the generally low material removal rate of the standard MFJP process. However, a number of enhancements can boost the material removal rate, such as air-assisted, ultrasonic cavitation-assisted, and multiple beam MFJP, while other enhancements such as submerged polishing and non-Newtonian carrier fluids can improve the achievable surface roughness.

Present limitations of MFJP include the minimum beam diameter achievable of 0.1 mm, due to the difficulty of drilling narrow holes in sapphire. It is however expected that advances in laser drilling and electro-discharge machining will allow for smaller nozzle diameter in the near future and permit smaller lateral feature size in functional surface generation. Another area for future improvement is expected in the use of finer nanoscale abrasives, in conjunction with the enhanced air-driven and ultrasonic systems. It is conceivable that surface machining on par with ultra-fine processes such as ion beam figuring may be possible with nanoparticle-loaded slurries.

References

- Beaucamp A, Namba Y (2013) Super-smooth finishing of diamond turned hard X-ray molding dies by combined fluid jet and bonnet polishing. *CIRP Ann Manuf Technol* 62(1):315–318
- Beaucamp A, Namba Y, Freeman R (2012) Dynamic multiphase modeling and optimization of fluid jet polishing process. *CIRP Ann Manuf Technol* 61(1):315–318
- Beaucamp A, Namba Y, Messelink W, Walker D, Charlton P, Freeman R (2014) Surface integrity of fluid jet polished tungsten carbide. *Procedia CIRP* 13:377–381
- Beaucamp A, Katsuura T, Kawara Z (2017) A novel ultrasonic cavitation assisted fluid jet polishing system. *CIRP Ann Manuf Technol* 66(1):301–304
- Bifano T, Dow T, Scattergood R (1991) Ductile-regime grinding: a new technology for machining brittle materials. *Trans ASME* 113:184–189
- Booij S (2003) Fluid jet polishing: possibilities and limitations of new fabrication technique. PhD thesis, Technische Universiteit Delft
- Cao Z, Cheung B (2014) Theoretical modelling and analysis of the material removal characteristics in fluid jet polishing. *Int J Mech Sci* 89:158–166
- Cao Z, Cheung C, Ren M (2016) Modelling and characterization of surface generation in fluid jet polishing. *Precis Eng* 43:406–417
- Fähnle O, van Brug H, Frankena H (1998) Fluid jet polishing of optical surfaces. *Appl Opt* 37:6771–6773
- Fang H, Guo P, Yu J (2006) Dwell function algorithm in fluid jet polishing. *Appl Opt* 45(18):4291–4296

- Guo P, Fang H, Yu J (2006) Edge effect in fluid jet polishing. *Appl Opt* 45(26):6729–6735
- Huang C, Chiovelli S, Minev P, Luo J, Nandakumar K (2008) A comprehensive phenomenological model for erosion of materials in jet flow. *Powder Technol* 187(3):273–279
- Katsuura T (2018) Characterization of process and mechanism in ultrasonic cavitation assisted fluid jet polishing. Master dissertation, Kyoto University
- Kowsari K, James D, Papini M, Spelt J (2014) The effects of dilute polymer solution elasticity and viscosity on abrasive slurry jet micro-machining of glass. *Wear* 309(1):112–119
- Loc P, Shiou F, Yu Z, Hsu H (2013) Investigation of optimal air-driving fluid jet polishing parameters for the surface finish of N-BK7 optical glass. *J Manuf Sci Eng* 135(1):011015
- Matsumura T, Muramatsu T, Fueki S (2011) Abrasive water jet machining of glass with stagnation effect. *CIRP Ann Manuf Technol* 60(1):355–358
- Menter Z (1994) Two-equation Eddy-viscosity turbulence models for engineering applications. *Am Inst Aeronaut Astronaut J* 32(8):1598–1605
- Messelink W, Waeger R, Wons T, Meeder M, Heiniger K, Faehnle O (2005) Prepolishing and finishing of optical surfaces using fluid jet polishing. *Proceeding of Optical manufacturing and testing VI*, San Diego, Vol 5869. International Society for Optics and Photonics, p 586908
- Shi C, Yuan J, Wu F, Wan Y (2011) Ultra-precision figuring using submerged jet polishing. *Chin Opt Lett* 9(9):092201
- Shiou F, Asmare A (2015) Parameters optimization on surface roughness improvement of Zerodur optical glass using an innovative rotary abrasive fluid multi-jet polishing process. *Precis Eng* 42:93–100
- Tricard M, Kordonski W, Shorey A, Evans C (2006) Magnetorheological jet finishing of conformal, freeform and steep concave optics. *CIRP Ann Manuf Technol* 55(1):309–312
- Wäger R, Messelink W, Looser H, Fähnle O, Heiniger K (2005) Particle tracking in a fluid jet polishing slurry flow. In: *SPIE Conference Optifab*, Rochester
- Wang C, Cheung C, Ho L, Liu M, Lee W (2017) A novel multi-jet polishing process and tool for high-efficiency polishing. *Int J Mach Tools Manuf* 115:60–73



Bonnet Polishing of Microstructured Surface

11

Lingbao Kong, Zhongchen Cao, and Laiting Ho

Contents

11.1	Introduction	372
11.2	Material Removal Characteristics in Bonnet Polishing	374
11.2.1	Experimental Design	375
11.2.2	Results and Discussion	375
11.3	Modeling and Theoretical Investigation of Material Removal	378
11.4	Generation of Microstructures by Bonnet Polishing	382
11.4.1	Polishing Mechanism by Multi-axis Ultra-precision Polishing	382
11.4.2	Surface Generation Mechanisms	382
11.5	Microstructured Surface Generation by Bonnet Polishing with Different Precess	392
11.5.1	Microstructured Surface Generation by Single Precess Polishing	395
11.5.2	Microstructured Surface Generation by Swing Precess Bonnet Polishing	399
11.6	Experimental Studies for Bonnet Polishing of Microstructured Surface	402
11.6.1	Group A: Effect of Parameters on the Generation of Structured Surfaces	402
11.6.2	5.2 Group B: Results of Experimental and Theoretical Investigation of Pattern Tests	407
11.7	Summary	416
	References	417

L. Kong (✉)

Shanghai Engineering Research Center of Ultra-Precision Optical Manufacturing, Fudan University, Shanghai, China

e-mail: LKong@fudan.edu.cn

Z. Cao

Key Laboratory of Advanced Ceramics and Machining Technology, Ministry of Education, Tianjin University, Tianjin, China

e-mail: Charles.cao@connect.polyu.edu.hk

L. Ho

Partner State Key Laboratory of Ultra-Precision Machining Technology, The Hong Kong Polytechnic University, Hung Hom, Hong Kong

e-mail: lai.ting.ho@polyu.edu.hk

© Springer Nature Singapore Pte Ltd. 2018

J. Yan (ed.), *Micro and Nano Fabrication Technology*, Micro/Nano Technologies,

https://doi.org/10.1007/978-981-13-0098-1_11

371

Abstract

Microstructured surfaces have been adopted in various and wide applications. Different types of microstructures made of ductile materials can be generated by cutting process, for example, turning and milling with specified diamond cutters. However, these processes generally are not capable to handle with hard and brittle materials which are called difficult-to-machine materials. Computer-controlled ultra-precision polishing with bonnet provides an enabling solution to generate microstructures due to its feasible influence function. With proper machining parameters, specified shape of the tool influence function is hence obtained, and then with aid of tool path planning, microstructured surface topography is generated, especially for those difficult-to-machine materials. In this chapter, research work for generating microstructured surface by computer-controlled ultra-precision bonnet polishing is presented. The material removal characteristics and tool influence function of bonnet polishing are explained, and a multi-scale material removal model and a surface generation model were developed. Surface generation of microstructures by single precess polishing and swing precess polishing is explained in details. A series of simulation and real polishing experimental studies are undertaken based on a seven-axis ultra-precision freeform polishing machine. The generated microstructured surfaces with various patterns have been analyzed. The research results have demonstrated that the proposed bonnet polishing provides an enabling and effective approach for generating microstructured surfaces.

Keywords

Ultra-precision machining · Computer controlled polishing · Bonnet polishing · Microstructured surface · Influence function · Precess polishing · Difficult-to-machine material · Multi-scale material removal · Surface generation · Modelling · Simulation

11.1 Introduction

Microstructured surfaces are usually possessing specially designed functional textures used in the development of high-precision applications such as optical (Beaucamp and Namba 2013), biomedical (Charlton and Blunt 2008), and automotive components (Cheung et al. 2010). Different scales of structures are found in various applications, for example, structured surfaces with a width of 2.0 mm and depth of 0.2 mm were intentionally machined (Zhou et al. 2006); 500- μm shark skin-like structures reduce wall shear stress (Bechert et al. 2000); pore surface can enhance the load capacity and stiffness of the fluid film between the seal-mating rings (Wakuda et al. 2003). Currently, three-dimensional (3D) structured surfaces are manufactured by different methods such as electroforming and laser machining, micro-milling or micro-grinding processes, etc. (Johansen et al. 2000; Chen et al. 2016; Shen et al. 2014; Schaller et al. 1999; Egashira et al. 2014). However, it is hard to control the form error and surface texture at different areas of such complex 3D structured surfaces by using these methods.

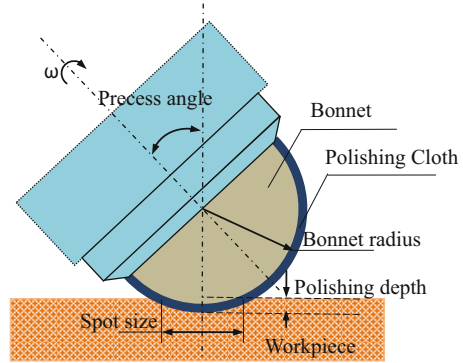
There are various types of computer-controlled polishing (CCP) used for the fabrication of precision components, such as CCP with small and large rotating tools (Beckstette et al. 1989), water jet polishing (Fähnle et al. 1998; Zhu et al. 2009), reactive or nonreactive ion beam polishing (Johnson and Ingersoll 1983; Sudarshan 1995; Zhao et al. 1990; Carter et al. 1993), etc. During the past few decades, much research has been performed on the modeling and simulation of surface generation in CCP processing (Schinhaerl et al. 2008a, b; Xi and Zhou 2005), as well as the modeling of polishing mechanics (Gee 1996). However, most of the previous research has been focused on the reduction of surface roughness and figuring of aspheric and freeform surfaces. At present, multi-axis computer-controlled ultra-precision polishing (CCUP) can be used for machining freeform surfaces with high form accuracy and good surface roughness. This is particularly true for machining difficult-to-machine and ferrous materials which are not amenable by using other ultra-precision machining technologies such as single-point diamond turning and ultra-precision raster milling.

So far, much research work has been undertaken on the study of surface generation in computer-controlled ultra-precision polishing and polishing mechanics (Cheung et al. 2011; Cao et al. 2016; Evans et al. 2003; Zeng and Blunt 2014). Currently, CCUP is found to be used to reduce surface roughness and figuring of aspheric and freeform surfaces (Namba et al. 2008; Shiou and Ciou 2008; Kumar et al. 2015). However, the use of CCUP for the generation of complex 3D structured surfaces for functional applications has received relatively little attention. Stout and Blunt (2001) stated that there is great demand in structured engineered parts. In order to reduce the manufacturing cost and find out more potential structures, it is necessary to explore more manufacturing processes to generate different 3D structured surfaces. There is a need for the development of a new and controllable polishing process to generate complex 3D structured surfaces to meet the demand for functional applications.

As a typical process of computer-controlled polishing, bonnet polishing is a computer-controlled sub-aperture polishing process that actively controls the position and orientation of the bonnet which is the spinning, inflated, and membrane tool as it sweeps through the polished surfaces (Walker et al. 2002a, b), as shown in Fig. 1. The polishing bonnet is covered with the polishing pad, and the slurry is dragged by the porous polishing pad into the interface between the pad and workpiece. Bonnet polishing was originally invented at London's Optical Sciences Laboratory and was then further developed by Zeeko Ltd. It has been exploited for commercial production of the IRP robotic polishing system (Walker et al. 2001). Bonnet polishing is particularly suitable for machining difficult-to-machine materials which are not amenable to using other ultra-precision machining technologies such as diamond cutting process. Polishing of such materials with sub-micrometer form accuracy and surface finish in the nanometric range is complex and multi-scale in nature. Bonnet polishing also has the advantage of high polishing efficiency, mathematically tractable influence function, and flexibly controllable spot size with variable tool hardness (Bingham et al. 2000).

In this chapter, research work for generating microstructured surface by computer-controlled ultra-precision bonnet polishing is based on single precess polishing

Fig. 1 Schematic illustration of bonnet polishing



and swing precess polishing. The material removal characteristics and tool influence function of bonnet polishing will be first explained, and multi-scale material removal model and a surface generation model were developed. Then surface generation of microstructures by single precess polishing and swing precess polishing is explained in details. A series of experimental studies are followed to demonstrate the microstructures generation by bonnet polishing, and the results are discussed, in order to better understanding the bonnet polishing process. A brief summary is provided at the end of the chapter. The proposed methods can be potentially used for fabricating microstructured surfaces with high surface finish, especially for difficult-to-machine and ferrous materials.

11.2 Material Removal Characteristics in Bonnet Polishing

In bonnet polishing, the material removal characteristics represent the distribution of the material removal rate across the size of the polishing tool. The material removal characteristics are referred to be the tool influence function (TIF), and they are assessed in terms of width, maximum depth, and volumetric material removal rate (Schinhaerl et al. 2007). Bonnet polishing involves forcing a spinning, inflated bonnet, covered with the polishing pad, against the polished surfaces flooded with a liquid slurry of abrasive particles. The slurry is dragged by the porous polishing pad into the interface between the pad and workpiece. The material removal in bonnet polishing is accomplished by the interactions between the polishing pad, workpiece, and abrasive particles. The mechanism of material removal is a complex process, which is affected by various parameters such as tool radius, precess angle, polishing depth, head speed, tool pressure, polishing time, polishing cloth, slurry concentration, particle size and material properties of particle and workpiece, etc. To better understand the pad-abrasive-workpiece contact mechanics and polishing mechanisms in bonnet polishing, a series of experimental and theoretical studies are undertaken to investigate the material removal characteristics in bonnet polishing first in this section, and this also helps to explain some common experience.

11.2.1 Experimental Design

An experiment is designed and aims to investigate the interactions among the polishing pad, workpiece, and abrasive particles. Three samples (A1, A2, A3) made of nickel copper (NiCu) were prepared by the Moore Nanotech 350FG using single-point diamond tooling and then polished on a Zeeko IRP 200 ultra-precision freeform polishing machine. Sample A1 was polished without water and abrasive particles, sample A2 was polished using pure water without abrasive particles, and sample A3 was polished using a slurry comprising 2.066 vol.% of Al_2O_3 abrasives with an average size of $3.22\ \mu\text{m}$. All these samples were polished under the identical polishing parameters as shown in Table 1, and they are measured by a Zygo Nexview 3D optical surface profiler and HITACHI TM3000 tabletop scanning electron microscope. With the consideration of the importance of dwell time map for the surface generation by bonnet polishing, the effect of polishing time on surface generation for various materials was studied in the other experiment. Three samples made of different materials of steel, optical glass (BK7), and NiCu were polished using a slurry comprising 2.066 vol.% of Al_2O_3 abrasives with an average size of $13.12\ \mu\text{m}$. All experiments were conducted on the Zeeko IRP 200 ultra-precision freeform polishing machine using the different polishing time of 60, 120, and 180 s, and the other parameters can be seen in Table 1.

11.2.2 Results and Discussion

11.2.2.1 Pad-Abrasive-Workpiece Interactions

Table 2 shows the experimental results for studying interactions between the pad, workpiece, and particles and indicates that sample A3 has the highest material removal rate, while the amount of material removal of sample A2 is smaller than that of sample A3, and sample A1 has the lowest material removal. It is also found that the polishing pad not only contributes to the material removal but also generates microscale scratches on the polished surface as shown in the scanning electronic microscopy (SEM) photographs in Table 2. The outcomes of these experiments can be summarized as follows:

- (i) The interaction between the pad and the polished surface decreases the material removal rate for the dry bonnet polishing process.
- (ii) The functions of the abrasive slurry in bonnet polishing including transport of abrasive to a loose abrasive process, flushing or the transport of the debris away from the abrasive process, culling in the contact area, mechanical lubrication of the abrasive contacts, etc.
- (iii) The material removal in bonnet polishing is shared by the polishing pad and the abrasives trapped in the pad-workpiece interface, and the amount of material removal by the polishing pad is much smaller than that by the abrasive particles.
- (iv) The material removal associated with plastic deformation of the polishing pad could produce the scratches and hence damage the surfaces being polished.

Table 1 Polishing parameters used in the experimental studies

Polishing pad	LP-66 (cerium oxide D'27)
Process angle	15°
Tool size	20 mm radius bonnet
Tool pressure	1.2 bar
Polishing depth	0.2 mm
Head speed	1200 rpm
Polishing time	60 s

Table 2 Experimental results for studying interactions (pad, workpiece, and particles)

Sample No.	Zygo photographs	SEM photographs (Center area)
A1 (No water and no abrasive particles)	<p>Maximum Depth: 4.490 μm</p>	<p>2.86 μm, 3.27 μm, 1.36 μm, 3.82 μm</p>
A2 (with water but no abrasive particles)	<p>Maximum Depth: 7.306 μm</p>	<p>1.91 μm, 1.77 μm</p>
A3 (with water and abrasive particles)	<p>Maximum Depth: 25.567 μm</p>	<p>136 nm, 272 nm, 409 nm, 409 nm</p>

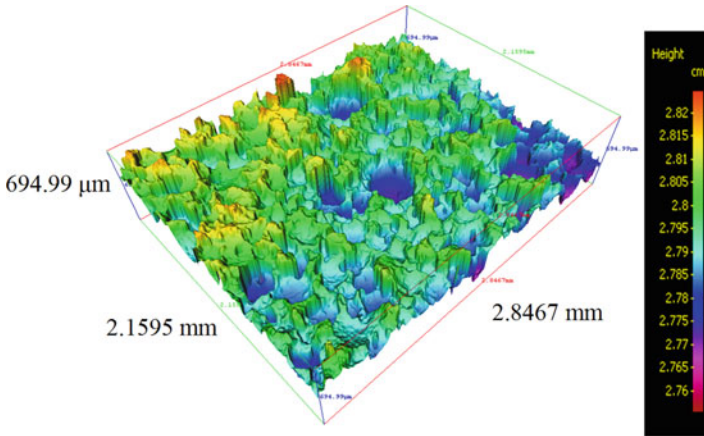


Fig. 2 The three-dimensional surface topography of the polishing pad

Figure 2 shows the surface topography of polishing pad measured by Alicona IFM G4 optical 3D measurement device. The geometry and the mechanical properties of the tallest asperities of the pad surface may play a dominant role in pad scratching. To obtain mirror surface finish without pad scratches, abrasive wear occurred in bonnet polishing should be dominated by plastic removal mode of abrasive particles, while the material removal caused by the polishing pad should be mitigated through flattening the asperities (Saka et al. 2010; Hutchings 1993; Kim et al. 2013), controlling the polishing depth and adopting appropriately the polishing pad owned low pad hardness.

11.2.2.2 Effect of Polishing Time

Since the surface generation by bonnet polishing is dominated by the influence function of the polishing tool instead of the geometry of the cutting tool itself, the surface generation mechanism of bonnet polishing is quite different from that of other ultra-precision machining processes such as single-point diamond turning and raster milling (Cheung et al. 2011). The tool influence function (TIF) affected by various factors is commonly regarded as a tool that is used in calibration, prediction, or form correction in the polishing process. With the data of the tool influence function, the polishing tool can be commanded where it should stay longer or shorter for removing more or less materials from the surface, respectively. In the second experiment, Fig. 3 shows that the removal volume increases linearly with increasing polishing time for all cases, and this infers that the material removal rate is constant when using only polishing time as a variable parameter while keeping other parameters constant. This infers that bonnet polishing is a relative and cumulative polishing process for various materials and the surface generation of bonnet polishing is a linearly cumulative effect of dwell time together with the constant material removal rate for identical polishing condition.

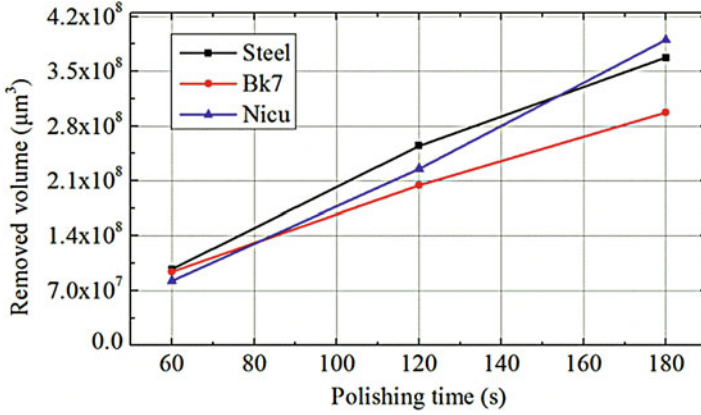


Fig. 3 The effect of polishing time on the surface generation

11.3 Modeling and Theoretical Investigation of Material Removal

It is well known that the surface generation of the polishing process can be regarded as the convolution of the influence function and the dwell time map along the pre-specific tool path. Hence the determination of the material removal characteristics and an optimized tool path generator is of paramount importance for modeling and simulation of the surface generation in bonnet polishing. A multi-scale material removal model is developed by the study of the contact mechanics, kinematics theory, and abrasive wear mechanism. Then the polishing tool path is planned based on the desired surface integrity of the optical surface to be generated using the predicted data of the material removal characteristics. Finally, the surface generation is simulated based on the developed multi-scale material removal model and polishing tool path planning.

Based on the experimental results of previous section, the material removal caused by the polishing pad is much less than that caused by the abrasive particles. Hence, it is assumed that material removal occurs primarily as a result of abrasive wear of the surface by the abrasive particles in the slurry. From the view of the mechanical behavior, the basic model of the material removal characteristics of bonnet polishing process can be described by Eq. 1 as shown in Fig. 4.

$$MRR(x, y, t) = N(k_{ac}, V_c, t, R_p, R_a, \sigma_z) \cdot E(\eta, P(x, y, R_b, d, \omega, Y, \nu, \varphi, \eta_1, \eta_2), V(x, y, S, \varphi, R_b, d), H_w, \beta) \tag{1}$$

where $MRR(x, y, t)$ is material removal at position (x, y) during the polishing time t ; the term $N(k_{ac}, V_c, t, R_p, R_a, \sigma_z)$ is the spatial distribution of active abrasive particles participated in the material removal which represents the effect of the

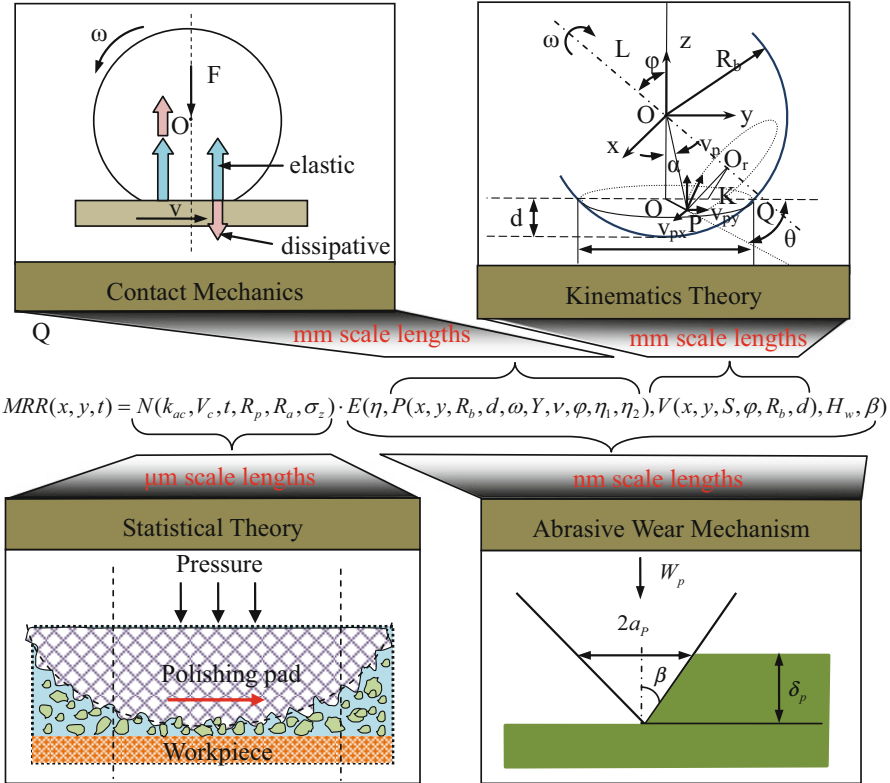


Fig. 4 Schematic illustration of the multi-scale mechanisms affecting the material removal characteristics in bonnet polishing

volume fraction V_c , the polishing time t , the radius of the abrasive particle R_p , the pad asperity radius R_a , the standard deviation of asperity heights σ_z , and the coefficient related to the particle size distribution and the hydrodynamics condition k_{ac} ; and the term $E(\eta, P(x, y, R_b, d, \omega, Y, \nu, \varphi, \eta_1, \eta_2), V(x, y, S, \varphi, R_b, d), H_w, \beta)$ is the volume removed by a single particle that describes the effect of the pressure distribution $P(x, y, R_b, d, \omega, Y, \nu, \varphi, \eta_1, \eta_2)$, the velocity distribution $V(x, y, S, \varphi, R_b, d)$, the hardness of polished workpiece H_w , the semi-angle of a cone particle β , and a volume fraction of a wear groove removed as a wear debris η .

The slurry particles involved in material removal are those that are embed in the surface of the compliant polishing pad, and they are dragged across the polished surface by the relative velocity between two surfaces, and the active number of these particles is generally related to the distribution of particle size, the hydrodynamics condition between the polishing pad and the workpiece, as well as the surface topography of the polishing pad and the target surface. To simplify the theoretical modeling, the pad-particle-workpiece contact is assumed to be solid-solid contact

neglecting the effect of the fluid flow, and the particle size is assumed to be constant which is the same as the average size of the particle distribution.

In the present study, statistical theories were used to model the surface topography of polishing pad assessed by the pad asperity radius R_a and the standard deviation of asperity heights σ_z (Kim et al. 2014; Greenwood and Williamson 1966). For relatively soft pad and low abrasive concentration, the active number of abrasive particles tends to be proportional to the real contact area and the slurry concentration (Fu et al. 2001; Luo and Dornfeld 2001, 2003). As a result, the active number of abrasive particles can be expressed by Eq. 2 as follows:

$$N(k_{ac}, V_c, t, R_p, R_a, \sigma_z) = K_{ac} \frac{V_c t}{R_p^2} \left(\frac{R_a}{\sigma_z} \right)^{1/2} \quad (2)$$

The effective contact area between the polishing pad and the entrained particle is approximately equal to πR_p^2 (Luo and Dornfeld 2001), and hence the force applied on an abrasive, W_p , can be expressed by Eq. 3:

$$W_p = \pi R_p^2 P(x, y, R_b, d, \omega, Y, \nu, \varphi, \eta_1, \eta_2) \quad (3)$$

In the bonnet polishing process, since the abrasive particles are sufficiently small and numerous in the contact region, the load carried by each tends to be below the critical value needed to cause cracking. Below this critical value, a hard abrasive particle would cause plastic deformation only, and the wear is undertaken by plastic processes without brittle fracture. Abrasive particles may roll and/or slide over the surface which involve in three distinct modes of plastic deformation including cutting, plowing, and wedge formation (Challen and Oxley 1979; Hutchings 1992). The transition from one mode to another and the relative efficiency of each mode may depend on the attack angle of particle, the normal load, the hardness of the material, and the state of lubrication (Hokkirigawa and Kato 1988). In the polishing process, lubrication of the slurry can lead to more particle cutting and reduce the couple necessary for particle rotation by lowering the friction between the particles and the surface (Bingley and Schnee 2005). In this study, an abrasive particle, assumed to be a cone of semi-angle β , is dragged across the surface in plastic contact which flows under an indentation pressure H_w . Since the depth of indentation, δ_p , is much smaller than the radius of the abrasive, the volume of wear debris produced by the cone particle per unit time can be expressed by Eq. 4 as follows:

$$\begin{aligned} E(\eta, P(x, y, R_b, d, \omega, Y, \nu, \varphi, \eta_1, \eta_2), V(x, y, S, \varphi, R_b, d), H_w, \beta) &= \eta \delta_p^2 \tan \beta V(x, y, S, \varphi, R_b, d) \\ &= \frac{2\eta W_p V(x, y, S, \varphi, R_b, d)}{\pi H_w \tan \beta} = \frac{2\eta R_p^2 P(x, y, R_b, d, \omega, Y, \nu, \varphi, \eta_1, \eta_2) V(x, y, S, \varphi, R_b, d)}{H_w \tan \beta} \end{aligned} \quad (4)$$

According to the kinematics theory, the relative velocity between the polishing pad and the target surface in the polishing area can be expressed as

$$V(x, y, S, \varphi, R_b, d) = \frac{\pi S}{30} \sqrt{(y \cot \varphi - (R_b - d))^2 (\sin \varphi)^2 + x^2 (\cos \varphi)^2} \quad (5)$$

where $x^2 + y^2 \leq (R_b)^2 - (R_b - d)^2$, S is angular velocity in rpm, φ is the inclination angle, d is the polishing depth in mm, and R_b is the radius of the bonnet in mm.

The pressure distribution between the polishing pad and the target surface is very complex and still not well understood as resulting from multiple influence factors including the elastic response of the polishing pad, the hydrodynamic forces due to fluid flow at the interface and the viscoelastic relaxation of the polishing bonnet, etc. In this study, the viscoelastic properties of the polyurethane pad is considered, and the polishing bonnet in contact with the flat workpiece surface was assumed to be a viscous sphere on a hard plane regardless of the contribution of slurry hydrodynamic pressure, pad asperities, contact-surface instability, and pad-abrasive-workpiece contact. According to Brilliantov and Poschel (1998), the total stress $P(x, y, R_b, d, x, y, R_b, d, \omega, Y, \nu, \varphi, \eta_1, \eta_2)$ is a sum of the elastic part of the stress tensor σ_{zz}^{el} and the dissipative part of the stress tensor σ_{zz}^{dis} . σ_{zz}^{el} is the known solution for the Hertz contact problem (Landau and Lifshitz 1959) as expressed by Eq. 6 as follows:

$$\sigma_{zz}^{el} = E_1 \frac{\partial u_z}{\partial z} + \left(E_2 - \frac{E_1}{3} \right) \left(\frac{\partial u_x}{\partial x} + \frac{\partial u_y}{\partial y} + \frac{\partial u_z}{\partial z} \right) = p_0 \left(1 - \frac{x^2}{a^2} - \frac{y^2}{a^2} \right)^{1/2} \quad (6)$$

where u_x , u_y , and u_z denote the x-, y-, and z-direction displacement field of the classic Hertz contact problem; $E_1 = Y/(1 + \nu)$ and $E_2 = Y/3(1 - 2\nu)$ denote the elastic material constants with Y and ν being the Young modulus and the Poisson ratio of the polishing pad, respectively; $a = \sqrt{dR_b}$ denotes the radius of contact area; and $p_0 = 3F_N/(2\pi a^2)$ denotes the maximum contact pressure; F_N is the total elastic force, acting by the surface (in normal direction) on the polishing pad as expressed in Eq. 7:

$$F_N = \frac{2}{3} \frac{Y}{(1 - \nu^2)} R_b^{1/2} d^{3/2} \quad (7)$$

According to the kinematics theory and contact mechanics (Brilliantov and Poschel 1998; Zheng et al. 2011; Johnson 1987), σ_{zz}^{dis} can be expressed as

$$\begin{aligned} \sigma_{zz}^{dis} &= \eta_1 \frac{\partial u_z}{\partial z} + \left(\eta_2 - \frac{\eta_1}{3} \right) \left(\frac{\partial u_x}{\partial x} + \frac{\partial u_y}{\partial y} + \frac{\partial u_z}{\partial z} \right) \\ &= \frac{(1 - 2\nu)(1 + \nu)}{Y} \cdot \frac{\omega \cos \varphi (2\eta_2 + \eta_1/3) p_0 x (R_b - d)}{a^2} \\ &\cdot \left(1 - \frac{x^2}{a^2} - \frac{y^2}{a^2} \right)^{-1/2} + \frac{(1 - \nu)^2}{Y} \cdot \frac{\omega \cos \varphi (2\eta_2 + \eta_1/3) \pi p_0 x}{2a} \end{aligned} \quad (8)$$

where \dot{u}_x , \dot{u}_y , and \dot{u}_z denote the time derivative of the displacement field in x-, y-, and z-direction, respectively; η_1 and η_2 are the coefficients of viscosity, related to shear and bulk deformation, respectively; ω is the angular velocity; and φ is the inclined angle.

As a result, the pressure distribution at the polishing contact area can be expressed by

$$\begin{aligned}
 P(x, y, R_b, d, \omega, Y, \nu, \varphi, \eta_1, \eta_2) &= \sigma_{zz}^{el} + \sigma_{zz}^{dis} \\
 &= p_0 \left(1 - \frac{x^2}{a^2} - \frac{y^2}{a^2} \right)^{1/2} + \frac{(1-2\nu)(1+\nu)}{Y} \cdot \frac{\omega \cos \varphi (2\eta_2 + \eta_1/3) p_0 x (R_b - d)}{a^2} \\
 &\quad \left(1 - \frac{x^2}{a^2} - \frac{y^2}{a^2} \right)^{-1/2} + \frac{(1-\nu)^2}{Y} \cdot \frac{\omega \cos \varphi (2\eta_2 + \eta_1/3) \pi p_0 x}{2a}
 \end{aligned} \quad (9)$$

11.4 Generation of Microstructures by Bonnet Polishing

11.4.1 Polishing Mechanism by Multi-axis Ultra-precision Polishing

As shown in Fig. 5, CCUP is implemented by using a seven-axis freeform polishing machine, Zeeko IRP200 from ZeekoTM Ltd. of the UK, in which four axes control the workpiece motion and the other three axes control the polishing head. There are mainly two types of polishing methods, one is mechanical polishing, and the other is fluid jet polishing. The bonnet polishing is the mechanical polishing (see Fig. 6), which makes use of a plastic bonnet covered with a polishing cloth for performing the polishing process.

11.4.2 Surface Generation Mechanisms

The CCUP is a complex process and is quite different from other ultra-precision machining processes such as single-point diamond turning and raster milling; the surface generation by CCUP is dominated by the polishing tool influence function (TIF) instead of the pure geometry of cutting tool. The influence function is affected by a number of factors such as workpiece material, polishing cloth, machining parameters, geometry of workpiece, polishing strategies, and especially the slurry. This provides an important means to generate structured surfaces. One of the key issues about CCUP is the investigation of TIF.

Any workpiece surfaces may be approximated locally by a convex, concave, or flat geometry. The influence function models are different for these three shapes, since the contact conditions between the workpiece and the polishing tool (e.g., bonnet) are different leading to varying deformations of the bonnet. As a result, the pressure distribution in the contact region and the magnitude of relative velocity between polishing tool and workpiece are different and hence the material removal rate (MRR). Moreover, the material removal characteristics of the polishing tool, the slurry, and the polishing cloth also play an important role in surface generation and have a significant impact on TIF. When establishing an integrated model to simulate and predict the surface generation in ultra-precision polishing process, all these factors need to be taken into account.

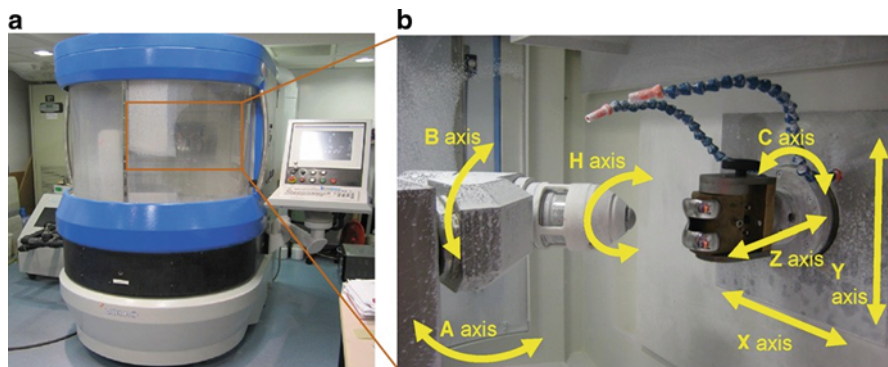


Fig. 5 Ultra-precision freeform polishing machine (Zeeko IRP200 from the UK): (a) polishing machine; (b) seven-axis motion of the machine

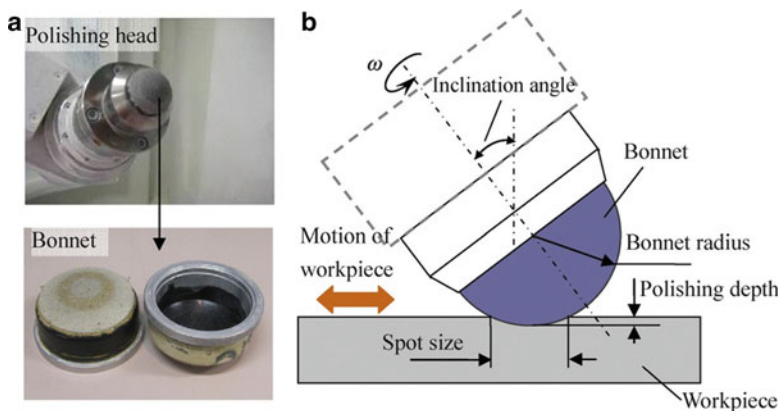


Fig. 6 Cutting mechanics for CCUP based on mechanical polishing: (a) polishing tools; (b) polishing geometry

11.4.2.1 Theoretical Modeling of Influence Function for Bonnet on a Fat Surface

One of the most important issues in the simulation of surface generation in CCUP is the determination of TIF, which indicates the tool material removal characteristics. The theoretical base of the surface topography simulation model is focused on the modeling of the TIF. Based on Preston’s Law (Preston 1927), the TIF is proportional to the polishing tool pressure on the surface of the workpiece and the relative velocity between the tool and the workpiece. Some previous research work (Walker et al. 2000, 2002, 2003) shows that the distribution of pressure of the tool appears to be in the shape of a Gaussian function. In the surface topography simulation model, a modified Gaussian function (MGF) is employed to construct the TIF in CCUP.

As shown in Fig. 7a, a Gaussian function is expressed as

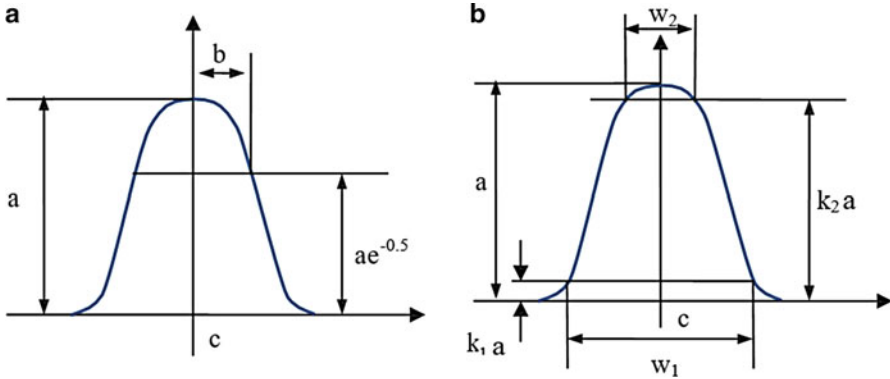


Fig. 7 Graphical illustrations for parameters in modified Gaussian function (MGF)

$$f(x) = a \exp\left(-\frac{1}{2} \left|\frac{x-c}{b}\right|^2\right) \tag{10}$$

Based on Eq. 10, the modified Gaussian function is expressed

$$f(x) = a \exp\left(-\frac{1}{2} \left|\frac{x-c}{b}\right|^2\right) \tag{11}$$

where a is the height of the curve’s peak and b controls the width of the curve, and this can be derived as the half width at the point with the curve height of a $a \exp(-0.5)$. The parameter λ can be derived as

$$\lambda = \frac{\ln(\ln(k_1)/\ln(k_2))}{\ln(w_1/w_2)} \tag{12}$$

where k_1 is a positive value near 0, w_1 is the width of the curve at the height of $k_1 a$, k_2 is a positive value near 1, and w_2 is the width of the curve at the height of $k_2 a$.

Fig. 8 shows the graphical illustration of polishing mechanism by a bonnet on a flat surface. d is the polishing depth in mm, R is the radius of the bonnet, ϕ is the diameter of spot size, and φ is the inclination angle. In Fig. 8b, O_b is the center of the bonnet, O_p is the center of the polishing area, P is a polishing point within the polishing area, L is the axis of rotation of the bonnet, Q is the intersection of line L with the polished surface area, O_r is the swing center of point P , r_p is the swing radius, $PK \perp O_p Q$, $PN \parallel O_b O_p$ and N is in the spherical surface with radius R and center O_b . Angular velocity expressed in vector form is (norm{direction}).

$$\omega = 2\pi S\{0, -\sin(\varphi), \cos(\varphi)\} \tag{13}$$

where S is the angular velocity.

The point $P(x_p, y_p, z_p)$ is a point in the contact area and is determined by angle α and θ , as shown in Fig. 8b. The vector of $\vec{O_b P}$ is represented as

Therefore,

$$r_P = \sqrt{|O_r K|^2 + |PK|^2} = \sqrt{((D \tan(\varphi) - y_p) \cos(\varphi))^2 + x_p^2} \quad (16)$$

$$|\mathbf{v}_r| = r_P |\boldsymbol{\omega}| = \frac{\pi}{30} S \sqrt{(D \tan(\varphi) - y_p)^2 + x_p^2} \quad (17)$$

The direction of the velocity \mathbf{v}_r at point P can be obtained by using vector operation (cross product):

$$\mathbf{v}_r = \boldsymbol{\omega} \times \overrightarrow{O_b P} = |\mathbf{v}_r| \{v_{rx}, v_{ry}, v_{rz}\} \quad (18)$$

The feed speed can be expressed as

$$\mathbf{v}_f = |\mathbf{v}_f| \{v_{fx}, v_{fy}, v_{fz}\} \quad (19)$$

For polishing a flat surface, the relative velocity at the point $P(x_p, y_p, z_p)$ is

$$v_p = \sqrt{(|\mathbf{v}_r|v_{rx} + |\mathbf{v}_f|v_{fx})^2 + (|\mathbf{v}_r|v_{ry} + |\mathbf{v}_f|v_{fy})^2} \quad (20)$$

The distribution of the pressure of the bonnet on the workpiece is taken as a Gaussian curve shape, which is expressed as a modified Gaussian function (MGF)

$$P(r) = a \exp\left(-\frac{1}{2} \left|\frac{r-c}{b}\right|^\lambda\right) \quad (21)$$

where $r = |PO_b| = D \tan(\alpha)$, $c = 0$; P_m is the maximum pressure at the center of the imprint. Therefore,

$$P(\alpha) = P_m \exp\left(-\frac{1}{2} \left(\frac{D \tan(\alpha)}{b}\right)^\lambda\right) \quad (22)$$

The parameter b controls the width of the curve, and λ determines the shape of the curve. The two parameters are determined by air pressure, polishing cloth material, etc.

According to Preston's Law, the integrated material removal rate (IMRR) is

$$M_p = k \cdot P_p \cdot V_p \cdot t_d \quad (23)$$

where M_p is the material removal at point P , k is Preston coefficient, P_p is polishing pressure, V_p is the magnitude of relative velocity at point P , and t_d is dwell time. As a result, MRR at point $P(\alpha, \theta)$ is

$$M_p(\alpha, \theta) = k \cdot P_m \cdot \exp\left(-\frac{1}{2} \left(\frac{D \tan(\alpha)}{b}\right)^\lambda\right) \cdot \left((|\mathbf{v}_r|v_{rx} + |\mathbf{v}_f|v_{fx})^2 + (|\mathbf{v}_r|v_{ry} + |\mathbf{v}_f|v_{fy})^2\right)^{1/2} \cdot t_d \quad (24)$$

The above equation is the polishing tool material removal characteristics, or influence function. A series of preliminary simulation and experimental studies based on the above theoretical model have been undertaken to generate various structured surfaces, which will be presented in the coming section.

11.4.2.2 Simulation Experiments for Generating Different Surface Patterns

Table 3 tabulates the design of the simulation experiments. Three groups of experiments are conducted under different spacing distance, different polishing depth, and different variable process angles, respectively. Figures 9, 10, and 11 show the different surface patterns generated by the designed three groups of the experiments. It is interesting to note that different structured surfaces can be generated by bonnet polishing with changing the polishing parameters and strategies, which provides some new approaches and solutions for producing structured surfaces, especially for the hard machining materials.

11.4.2.3 Real Polishing Experiments for Generating Different Surface Patterns

A series of practical polishing experiments have also been conducted in the present study to further validate the proposed model. The polishing machine used in the experiments is a seven-axis freeform polishing machine IRP200 manufactured by Zeeko Ltd., UK. Table 4 shows the polishing parameters, workpiece materials, slurries, and polishing tools employed in the polishing experiments.

To determine the tool influence function (TIF) in the polishing process, the test of TIF was firstly undertaken under the same polishing conditions but with a longer dwell time for the convenience of the data measurement. In the present study, the dwelling time for TIF test is 300 s. The polished surface for TIF test was measured by Talysurf PGI 1240 (Taylor-Hobson Ltd., UK), and the measured area data are shown in Fig. 12a. The measured data are processed in two steps. Firstly, the measured TIF data ($X = Y = 0$) are centered by x - y shift, and the data center is determined by an inscribed circle inside the rectangular formatted data (X - Y plane). Secondly, the data outside the inscribed circle (X - Y plane) are trimmed. Hence, the data is fitted to find the coefficients in the proposed model. Figure 12b shows the processed data which indicate TIF in the contact area of the polishing bonnet on the workpiece surface. As shown in Fig. 11, it is found that the TIF is asymmetric and

Table 3 Design of simulation experiments

No.	Parameters	Values	Notes
1	Spacing (mm)	spx 3 1.5 2 1.5 3 3.5	d = 0.3 mm; $\varphi = 15^\circ$
		spy 1.5 3 2 1.5 3 3.5	
2	Polishing depth (mm)	d 0.1 0.2 0.4 0.8 1 2	spx = spy = 3 mm; $\varphi = 15^\circ$
3	Inclination angle ($^\circ$)	φ 15 5 4 2 1 0.5	spx = spy = 3 mm; d = 0.3 mm

S = 1200 rpm; R = 20 mm; Pm = 1 Pa; Vf = 50 mm/min; K = $1e-8$

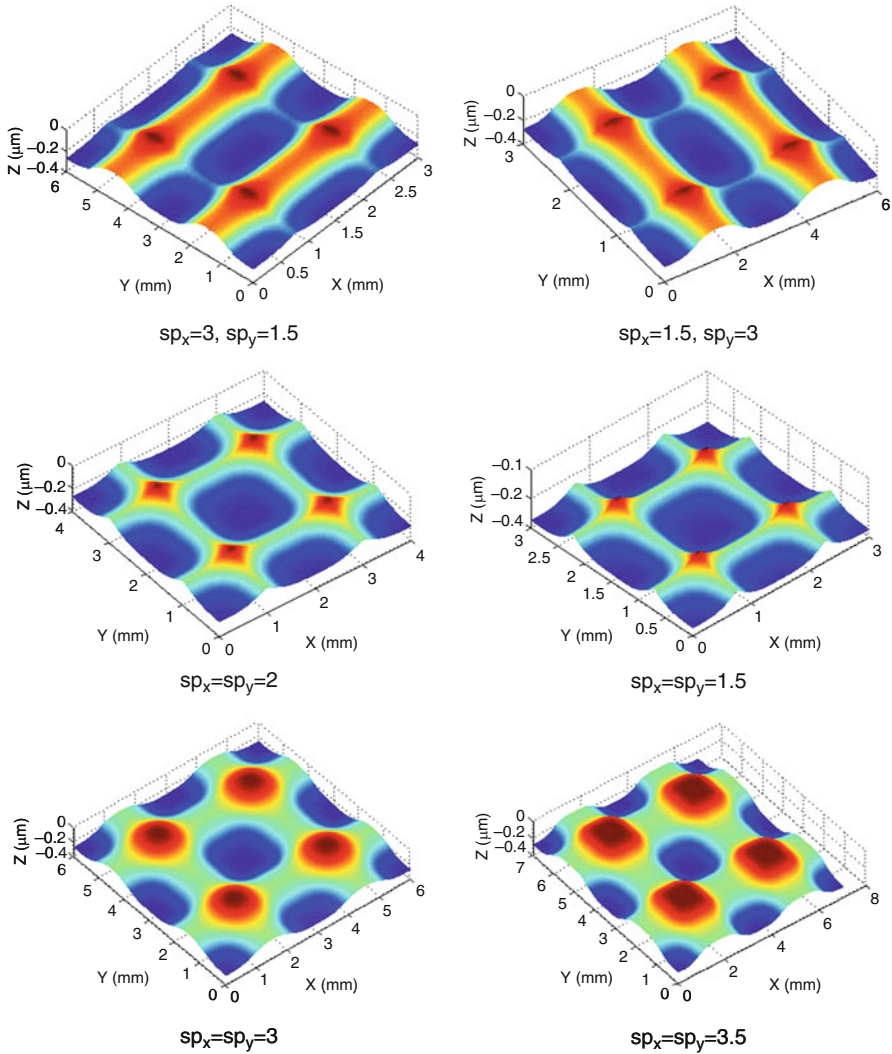


Fig. 9 Structured surface generation by different spacing in mm (horizontal spacing, sp_x ; vertical spacing, sp_y)

the reason for the asymmetry is due to the inclination angle of the bonnet on workpiece surface which causes the asymmetric relative velocity between the polishing tool and the workpiece surface, and hence the MRR is asymmetrical as referred to Eqs. 23 and 24. To find the coefficients in Eq. 24, nonlinear regression method is used based on the measured data for TIF test. The coefficients were found to be $k = 3.566 \times 10^{-8}$ (Preston coefficient), $b = 0.7446$, and $c = 3.0432$.

Figure 13 shows the mathematical extrapolation of tool influence function obtained in the polishing process. Figure 13a depicts the 3D topography, while

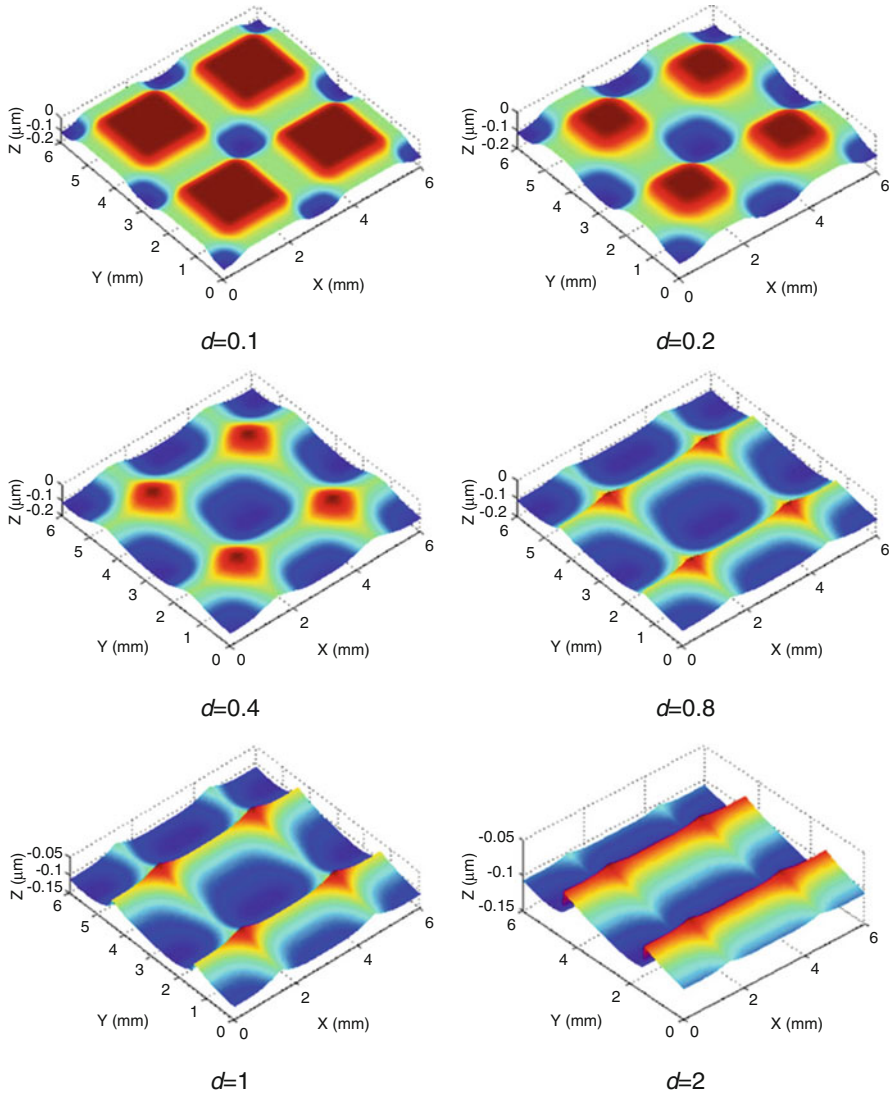


Fig. 10 Structured surface generation by different polishing depths in mm

Fig. 13b and c is the TIF profiles in XZ and YZ planes, respectively. It is interesting to note that the two profiles in XZ and YZ planes are different in shape. This makes the polishing process more flexible to generate different surface structures.

The polishing experiments are designed by using different polishing strategies with different spacing distances as show in Table 5. The topography of the polished workpiece surface was measured by a white-light interferometer Wyko NT 8000 from Veeco Instruments Inc., USA.

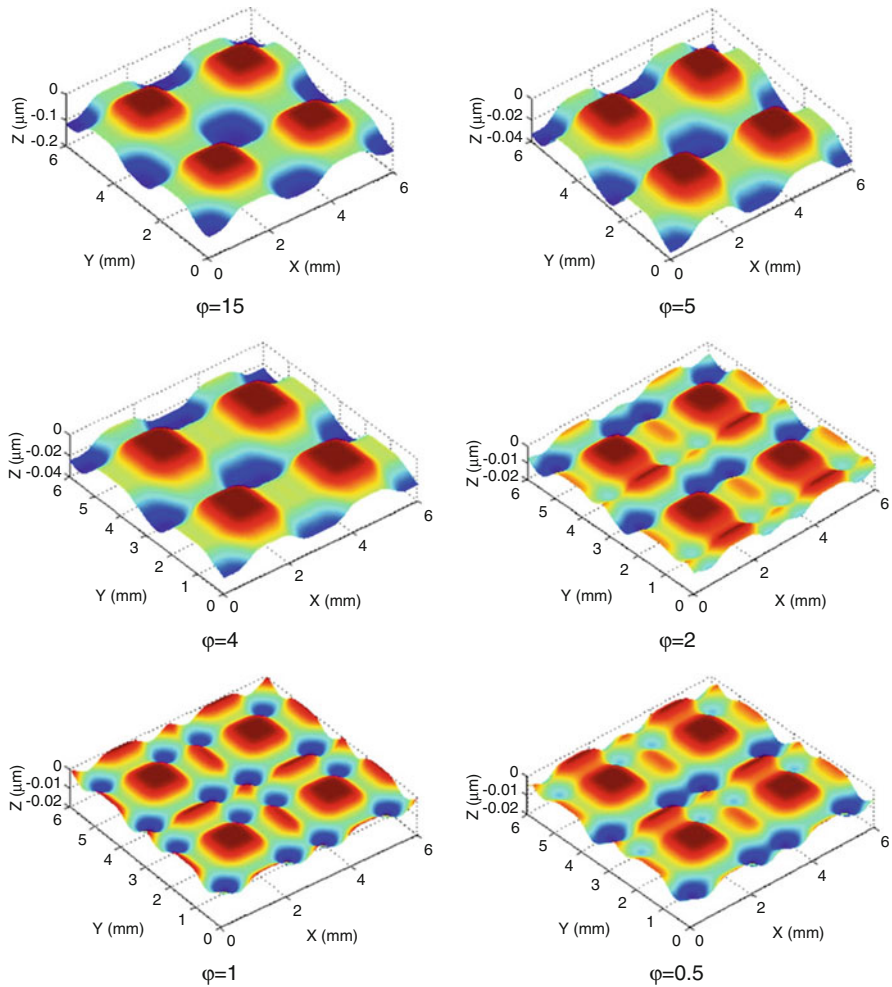


Fig. 11 Structured surface generation by different inclination angle in degrees

Table 4 Polishing parameters used in the experimental studies

Polishing mode	Raster
Inclination angle (deg)	15
Angular velocity (rpm)	1200
Polishing depth (mm)	0.3
Tool pressure (bar)	1
Surface feed (mm/min)	50
Tool size	20 mm radius bonnet
Polishing cloth	Cerium oxide D'16
Workpiece material	NiCu alloy

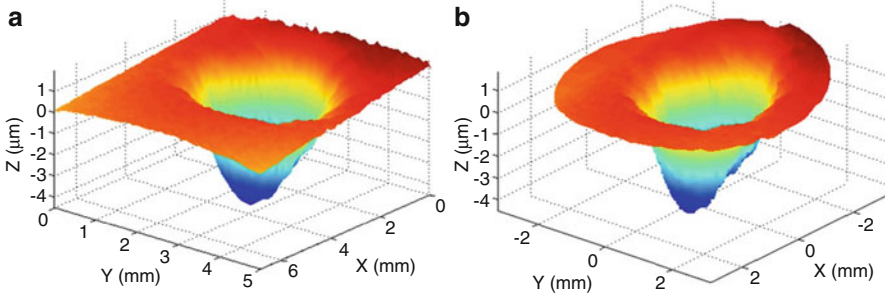


Fig. 12 (a) Measured TIF test data and (b) data after processing

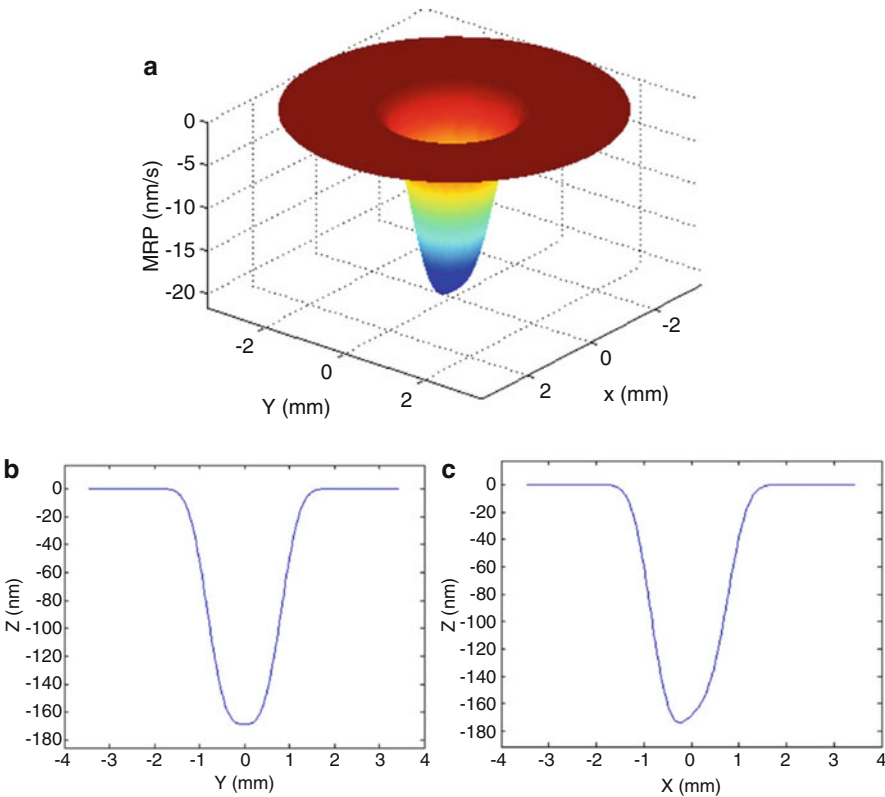


Fig. 13 Mathematical extrapolation of tool influence function (TIF) in the polishing process: (a) 3D topography; (b) in XZ plane; (c) in YZ plane

Table 6 illustrates the comparisons between the measured and the simulated results of the workpiece surface polished under various conditions, i.e., conditions A1–A5. It is interesting to note that the patterns of the predicted structured surfaces exhibit a good agreement with the measured structured surfaces. This

Table 5 Group A: experimental design for the raster polishing tests

Condition No.	1st step polishing	Spacing (mm)	2nd step polishing	Spacing (mm)
A1	H	3	V	3
A2	H	3	V	1
A3	V	1	H	3
A4	H	1	V	3
A5	V	3	H	1

H horizontal polishing, *V* vertical polishing

further validates the proposed model. This not only provides an important means for generating different surface structures or patterns by ultra-precision polishing approach but also makes the polishing process more controllable and predictable.

For further verification, some surface parameters (root-mean-squared value, Sq; peak-to-valley value, St) are determined for the measured surface data and the predicted ones. Figure 14 shows a graphic illustration of the comparison of the predicted and measured results. As shown in Fig. 14, the parametric values are of the same order of magnitude. It is also interesting to note that the predicted values of Sq are all larger than the measured values (except data no. A5), while the predicted values of St are all smaller than the measured ones. This can be explained as follows. The model proposed in the present study only considers the geometry of the TIF. In other words, the surface generation is predicted based on the shape of TIF.

However, the polishing process also involves other factors such as interference between two concessive polishing contacts, the influence of polishing fluid, and interaction between the workpiece material and abrasive particles in the polishing fluid. As a result, the predicted St is less, and the predicted Sq is larger than the measured values, since in the real polishing process, there are additional factors which remove high points on the surface. Moreover, there is a good agreement of the trend between the measured and predicted results. There exist some deviations between the measured and predicted results which are due to the fact that ultra-precision polishing is a complex machining process. The surface generation is affected by a lot of materials and process factors. Some other factors would need to be considered such as the effect of slurry, machine characteristics, dynamic factors, etc.

11.5 Microstructured Surface Generation by Bonnet Polishing with Different Precess

In bonnet polishing, there are different precess polishing, including single precess, continuous precess, and swing precess, as shown in Fig. 15. Figure 15a is the “single precess,” and Fig. 15b is “continuous precess” polishing regime (Beaucamp and Namba 2013), in which the precess angle is constant. Figure 15c and d shows the

Table 6 Comparison between the measured and simulated results for the structured surface generation

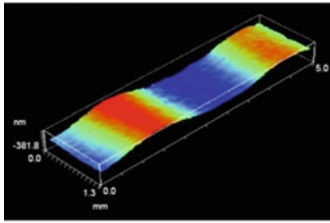
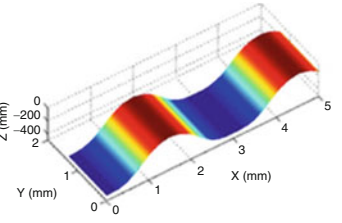
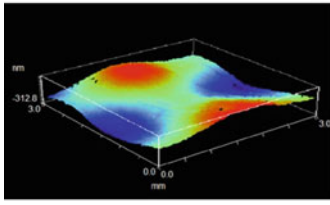
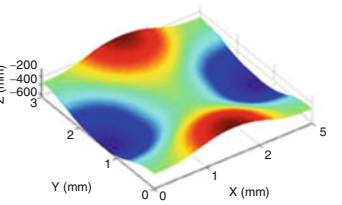
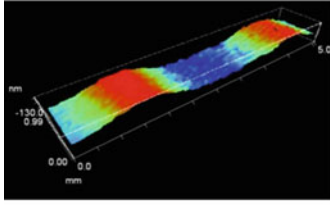
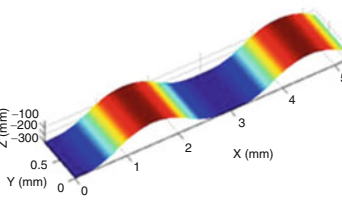
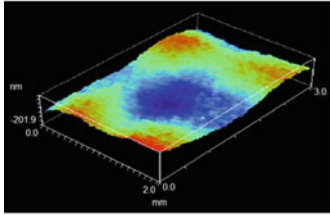
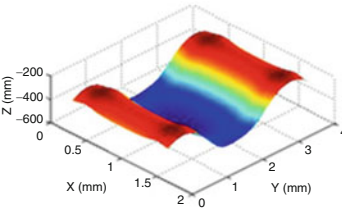
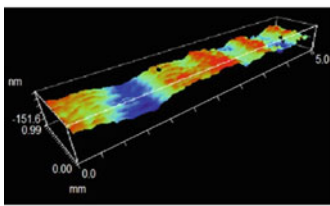
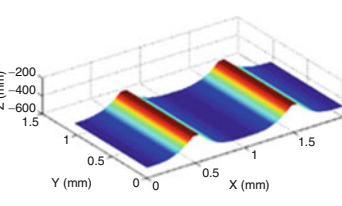
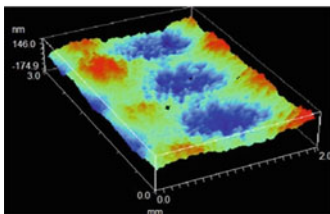
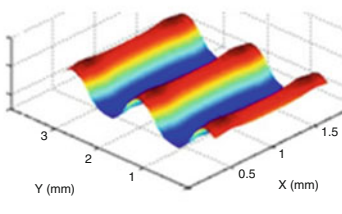
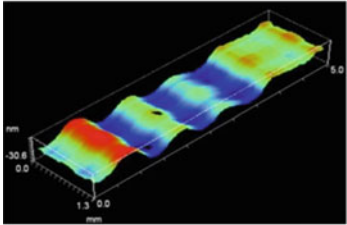
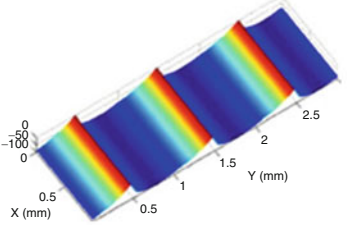
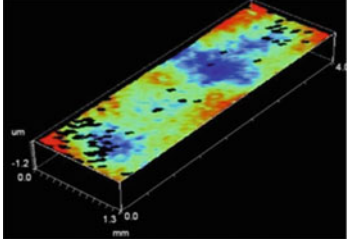
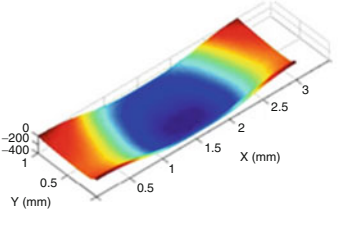
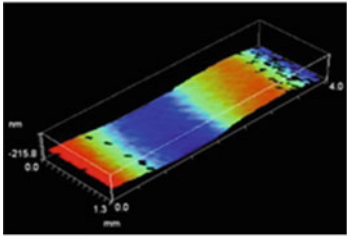
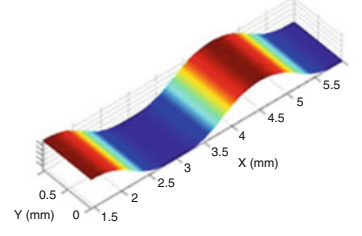
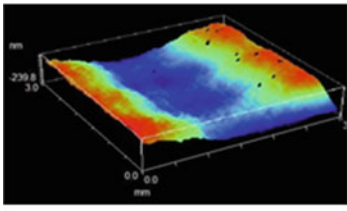
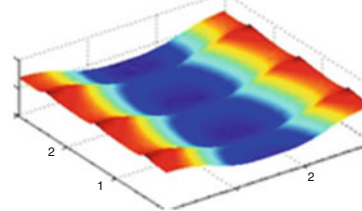
No.	Measured results	Simulation results*
A1		
		
A2		
		
A3		
		

Table 6 (continued)

No.	Measured results	Simulation results*
A4		
		
		
		

*Simulated time: 1.2 s.

two types of swing process bonnet polishing processes which include climb and vertical swing process bonnet polishing processes. In the vertical swing process bonnet polishing process, the swing plane of polishing spindle is perpendicular to the feed direction of the polishing tool, while the swing plane of polishing spindle consists of the normal direction of the target surface and the feed direction of the polishing tool in climb swing process bonnet polishing. The generation of complex 3D structured surfaces is affected by many factors which include point spacing, track

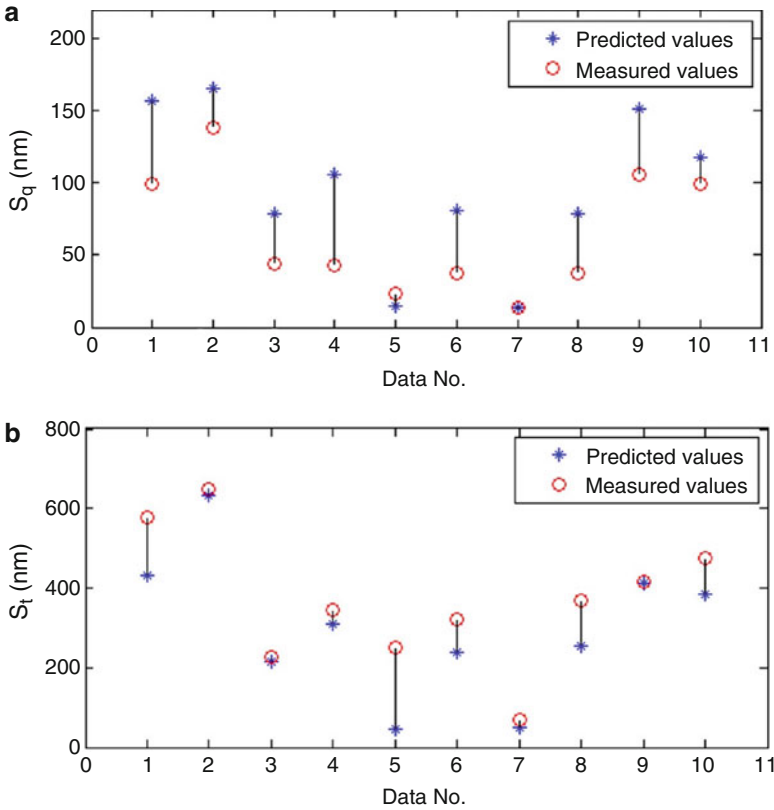


Fig. 14 A comparison between the measured and predicted results for the surface parameters: (a) root-mean-squared value (S_q) comparisons; (b) peak-to-valley value (S_t) comparisons

spacing, swing speed, swing angle, head speed, tool pressure, tool radius, feed rate, polishing depth, polishing cloth, polishing strategies, polishing slurry, etc.

11.5.1 Microstructured Surface Generation by Single Precess Polishing

In practice, polishing is a multistep process conducted by repeatedly running particular designed polishing cycles until the expected surface finish and form error are obtained. Within each cycle, the polishing tool sweeps through the polished surface under adopted polishing tool path and desired dwell time map. Hence, an important part of the surface generation model is dwell time and tool path planning (Tam et al. 1999) as considering time efficiency and surface quality improvement. Based on the discussion in previous sections, bonnet polishing appears to be a relative and cumulative polishing process for various materials, and the surface

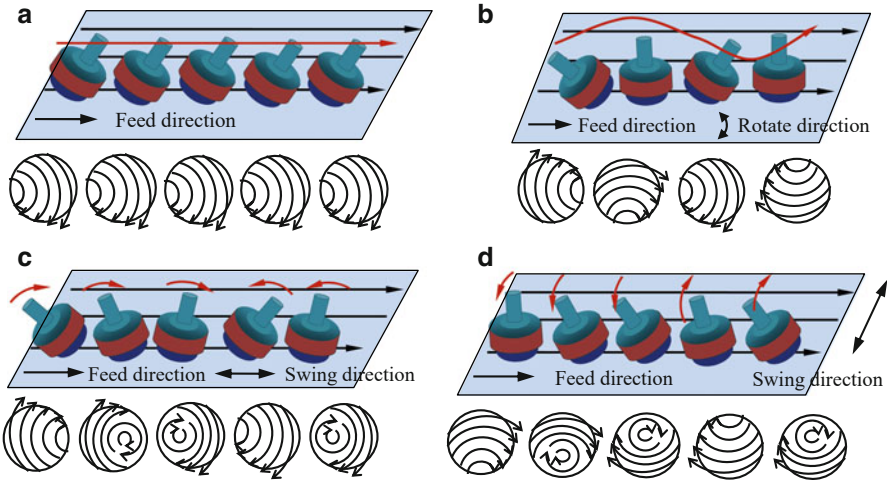


Fig. 15 (a) Single process, (b) continuous process, (c) climb swing process, and (d) vertical swing process bonnet polishing across the raster tool path

generation, ΔZ_i , of bonnet polishing can be assumed to be a linearly cumulative effect of dwell time, T_0 , together with the material removal rate, MRR_{ij} , under the same polishing condition as follows:

$$\Delta Z_i = \sum_{j=1}^N MRR_{ij} \cdot T_0, \quad (i = 1, 2, 3 \dots M) \quad (25)$$

where M is the sample point number, N is the trajectory point number along the polishing path, and MRR_{ij} is the material removal of j th sample point when the i th trajectory point along the polishing path is polished by the bonnet. The value of MRR_{ij} depends on the material removal rate and the contract area of the bonnet. It will be non-zero if the j th sample point locates within the contract area of the i th trajectory point and will be zero if the sample point locates outside the contract area.

In the present study, raster polishing was used to understand the surface generation mechanisms by single process bonnet polishing and verify the effectiveness of the surface generation model. The polishing conditions in all the paths are assumed to be constant, and hence the tool influence function is stable and constant, and the polishing paths are also assumed to be evenly spaced straight lines on a flat surface as can be seen in Fig. 16. When the predicted influence function follows straight path lines with a constant surface feed rate, the removal profile is constant along each and all the path lines. Hence, the material removal distribution is constant along the path line direction and waves in the orthogonal direction arising from the overlapping of the removal profiles affiliated with adjacent polishing path lines for the raster polishing. In this case, the surface generation may be simplified to be a 2D problem which can be solved numerically for given polishing path spacing and path number.

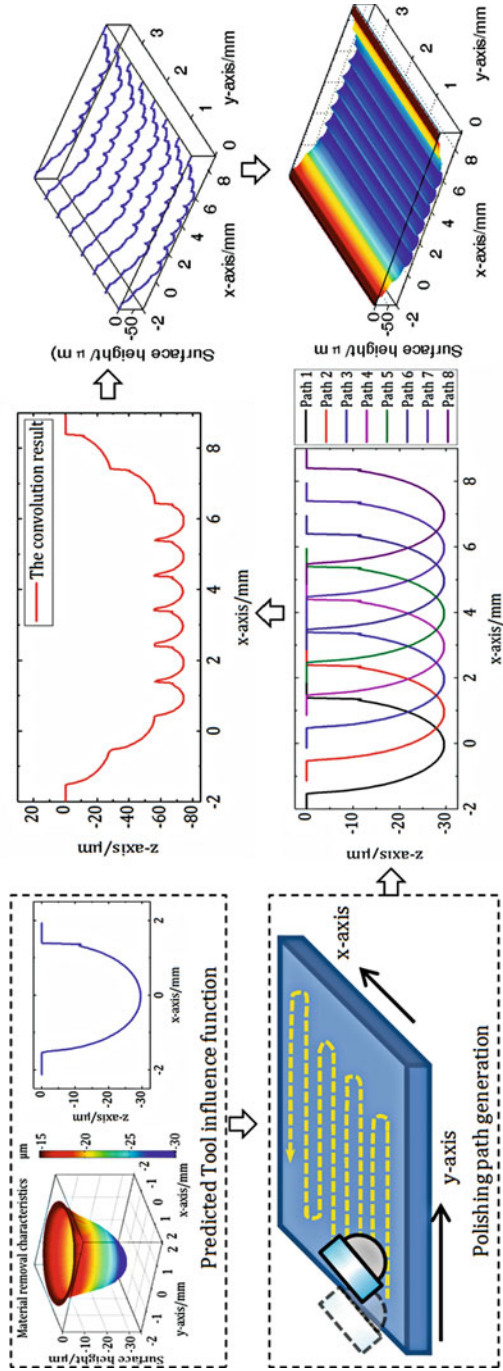


Fig. 16 A schematic diagram of the surface generation model by single process bonnet polishing in the raster polishing

The polishing path spacing represents the translation distance of removal profile along the orthogonal direction, and the feed rate determines the dwell time of each polished spot and hence the surface height of removal profile along the path line direction.

Experimental studies for single precess bonnet polishing by aster polishing were carried out. The polishing strategies used for generating the designed surface pattern are shown in Table 7, while the surface generation model has been purposely built and programmed by using MATLAB software package. Figure 17 shows a comparison between the measured and simulated results in the pattern test. It is found that the simulated surface pattern by the surface generation model agree well with that for the experimental results. The peak-to-valley (PV) value and the root-mean-squared (RMS) value are determined for the measured surface data and the predicted ones. The PV value of the predicted data is $0.803\ \mu\text{m}$, and the RMS value is $229\ \text{nm}$, while the PV value and RMS value of the measured surface data are $0.876\ \mu\text{m}$ and $110\ \text{nm}$, respectively. It is interesting to note that the parametric values are of the same order of magnitude. This further help to explain and predict the relative and cumulative polishing process and the linearly cumulative effect of dwell time together with the constant material removal rate under the identical polishing condition in surface generation of bonnet polishing.

To further verify the effectiveness of the surface generation model, a least-square-based surface matching method is used to evaluate the deviation of the measured

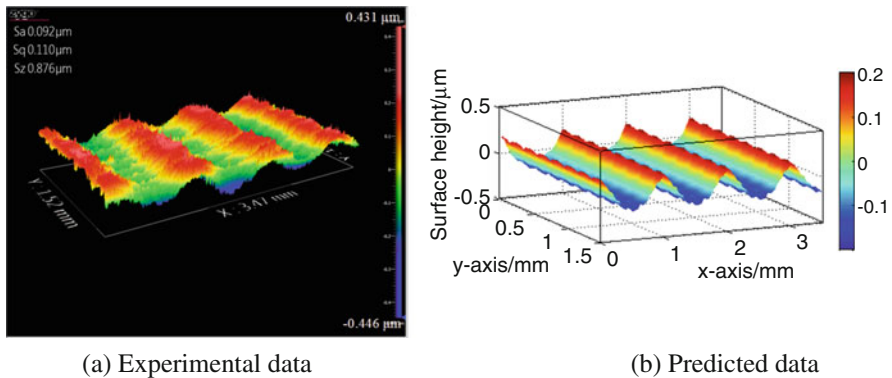


Fig. 17 Comparison between the measured and simulated results of the pattern test

Table 7 Parameters for generating surface pattern

Workpiece Material	Steel (S136)	Polishing mode	Raster
Surface feed	20 mm/min	Polishing cloth	LP-66
Polishing spacing	1 mm	Head speed	1200 rpm
Polishing depth	0.2 mm	Precess angle	15°
Tool pressure	1.2 bar	Slurry concentration	1:12
Tool radius	20 mm	Particle property	$3.22\ \mu\text{m}$ (Al_2O_3)

surface from the corresponding simulated surface (Ren et al. 2012). Due to the misalignment between the coordinate frames of the coordinate frames of the measured surface and the simulated surface, the surface matching is required to search for an optimal Euclidean motion for the measured surface so that it is well aligned with the simulated surface as close as possible. After that, the deviation of the simulated surface and the measured surface is considered to be the prediction error of the proposed model as shown in Fig. 18. It is turned out that the peak-to-valley (PV) value of the prediction error is $0.4231\ \mu\text{m}$ and the root-mean-squared (RMS) value is $64.8\ \text{nm}$. The result reveals that the surface generation model can be successfully used for predicting and better explaining the surface generation in bonnet polishing. This further validates the technical feasibility and effectiveness of the surface generation model in bonnet polishing.

11.5.2 Microstructured Surface Generation by Swing Precess Bonnet Polishing

11.5.2.1 Principle of Swing Precess Bonnet Polishing

It is well known that surface generation by bonnet polishing is dominated by the influence function of the polishing tool instead of the pure geometry of the cutting tool that is quite different from other ultra-precision machining processes such as single-point diamond turning and ultra-precision raster milling. Taking the advantages of high polishing efficiency and flexibly controlled influence function in the bonnet polishing process, the swing precess bonnet polishing (SPBP) method for generating microstructured surfaces is realized by the relative and cumulative process of varied tool influence function through the combination of specific polishing tool orientation and tool path. As shown in Fig. 19, the SPBP method is a sub-aperture finishing process in which the polishing spindle is swung around the normal direction of the target surface within the scope of swing angle while moving around the center of the bonnet.

11.5.2.2 Tool Path Generator for Swing Precess Bonnet Polishing

To realize swing precess bonnet polishing, a tool path generator (TPG) has been purposely built which is used for generating the CNC files for polishing as shown in Fig. 20. The TPG is composed of three modules which are input module, processing

Fig. 18 Evaluated prediction error of the testing pattern for bonnet polish

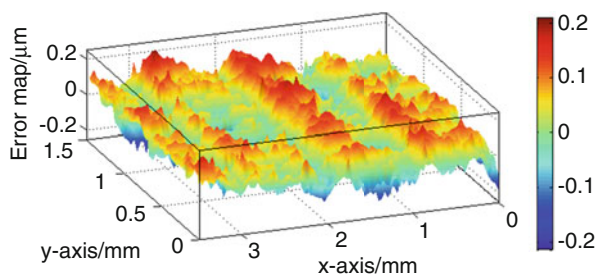


Fig. 19 Schematic diagram of swing process bonnet polishing

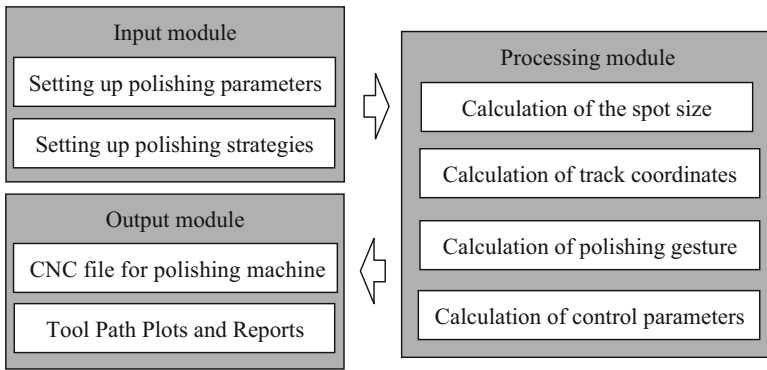
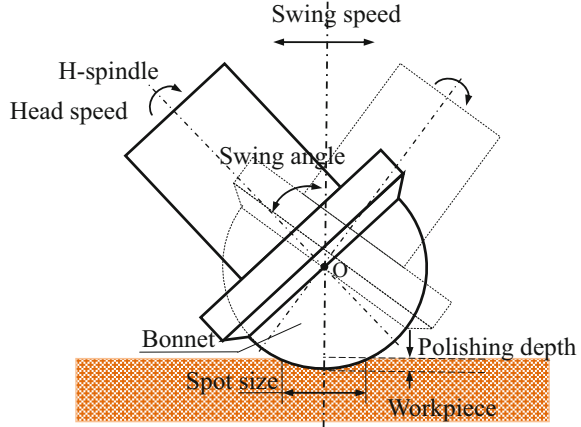


Fig. 20 Schematic diagram of tool path generator for SPBP

module, and output module. The input module is used to acquire the polishing parameters (e.g., head speed, spacing, tool pressure, bonnet radius, feed rate, etc.) and the polishing strategies (e.g., spacing and swing speed). Hence, the processing module determines the spot size, track coordinates, polishing gesture, and control parameters. The necessary CNC file of the SPBP tool path is generated by the output module. In this study, the TPG has been developed by the MATLAB programming software package. Hence, SPBP can be undertaken by a seven-axis polishing machine through two kinds of motions which include feed motion (X-, Y-, Z-, C-axis) and swing motion (A-, B-, H-axis), respectively.

11.5.2.3 A Multi-scale Material Removal Model for SPBP

Since the produced 3D structured surfaces are effected by various polishing parameters, the prediction model needs to be developed for effective selection of the polishing conditions and better understanding of the SPBP process. The surface generation of the polishing process can be regarded as the convolution of the

influence function and the dwell time map along the pre-specific tool path (Tam and Cheng 2010). To simulate the generation of 3D structured surfaces by SPBP, a multi-scale material removal model has been developed based on the prior work (Cao and Cheung 2016). The model is used for predicting the tool influence function in SPBP based on the study of contact mechanics, kinematics theory, and abrasive wear mechanism. The material removal of the SPBP can be expressed by

$$MRR(x, y, t) = \frac{2\eta K_{ac} V_c t V_r(x, y) P(x, y)}{H_w \tan \alpha} \left(\frac{R_a}{\sigma_z} \right)^{\frac{1}{2}} \quad (26)$$

where η is the volume fraction of a wear groove removed as wear debris, K_{ac} is the coefficient related to the particle size distribution and the hydrodynamics condition, V_c is the volume fraction of the polishing slurry, t is the polishing time, H_w is the hardness of polished workpiece, α is the semi-angle of the cone particle, R_a is the radius of the pad asperities, σ_z is the standard deviation of asperity heights, $V_r(x, y)$ is the relative velocity distribution between the polishing pad and the target surface in the polishing area, and $P(x, y)$ is the pressure distribution at the polishing contact area.

$$V(x, y, S, \varphi, R_b, d) = \frac{\pi S}{30} \sqrt{(y \cot \varphi - (R_b - d))^2 (\sin \varphi)^2 + x^2 (\cos \varphi)^2} \quad (27)$$

where $x^2 + y^2 \leq (R_b)^2 - (R_b - d)^2$, S is angular velocity in rpm, φ is the swing angle, d is the polishing depth in mm, and R_b is the radius of the bonnet in mm.

$$P(x, y, R_b, d, \omega, Y, \nu, \varphi, \eta_1, \eta_2) = p_0 \left(1 - \frac{x^2}{a^2} - \frac{y^2}{a^2} \right)^{1/2} + \frac{(1 - 2\nu)(1 + \nu)}{Y} \cdot \frac{\omega \cos \varphi (2\eta_2 + \eta_1/3) p_0 x (R_b - d)}{a^2} \cdot \left(1 - \frac{x^2}{a^2} - \frac{y^2}{a^2} \right)^{-1/2} + \frac{(1 - \nu)^2}{Y} \cdot \frac{\omega \cos \varphi (2\eta_2 + \eta_1/3) \pi p_0 x}{2a} \quad (28)$$

where $a = \sqrt{dR_b}$ denotes the radius of contact area and Y and ν are the Young modulus and the Poisson ratio, respectively, while η_1 and η_2 are the coefficients of viscosity related to shear and bulk deformation, respectively. ω is the angular velocity, and $p_0 = 3F_N/(2\pi a^2)$ denotes the maximum contact pressure, and F_N is the total elastic force, acting on the surface (in normal direction) α on the polishing pad:

$$F_N = \frac{2}{3} \frac{Y}{(1 - \nu^2)} R_b^{1/2} d^{3/2} \quad (29)$$

11.5.2.4 Surface Generation Model of Swing Precess Bonnet Polishing

A surface generation model has been developed for swing precess bonnet polishing based on the surface generation mechanism of the relative and cumulative removal process in the polishing process, together with the predicted tool influence function

by the multi-scale material removal model as described in previous section. As shown in Fig. 21, the track coordinates of the polishing bonnet, along with the polishing path, are determined in terms of polishing parameters and strategies. The tool influence function of every polishing point is then computed by the multi-scale material removal model with respect to the corresponding polishing gesture and track coordinates. Hence, the surface generation by SPBP is simulated by the aggregation of the amount of material removal of the superposed tool influence function at every sampling point, together with a Gaussian Process model (Williams and Rasmussen 2006).

11.6 Experimental Studies for Bonnet Polishing of Microstructured Surface

To realize the technological merits as well as the performance of the multi-scale material removal model and the surface generation model in this chapter, a series of experiments were conducted on a Zeeko IRP 200 ultra-precision freeform polishing machine, as shown in Fig. 22a. Cylindrical nickel copper samples with a diameter of 25.4 mm were machined by single-point diamond turning to ensure their consistent initial surface finish. The parameters used in single-point diamond turning include spindle speed, 1500 rpm; feed rate, 8 mm per min; depth of cut, 4 μm ; and tool radius, 2.47315 mm. The surface roughness and 3D surface topography of the samples were measured by a Zygo Nexview 3D optical surface profiler. As shown in Fig. 22b, the arithmetic roughness, R_a , of the samples before polishing is found to be 103 nm.

Two groups of experiments are designed, said Group A and Group B. In Group A of experiments, line tests of swing precess bonnet polishing were conducted with different polishing parameters in order to study the effect of polishing parameters on the generation of structured surfaces. Experiments conducted in Part B are pattern tests which aim to verify the feasibility of the proposed swing precess bonnet polishing method under various polishing conditions and evaluate the performance of the multi-scale material removal model and surface generation model for the swing precess bonnet polishing.

11.6.1 Group A: Effect of Parameters on the Generation of Structured Surfaces

11.6.1.1 Experimental Setup

This group of experiments aims to investigate how single process parameter affects the generation of 3D structured surface with swing precess bonnet polishing. The polishing parameters are selected based on the work range of typical parameters in bonnet polishing system (Zeng and Blunt 2014). Green silicon carbide (GC) grit #4000 and LP-26 polishing cloth were used. The tool radius, the tool pressure, and the spindle speed are 20 mm, 1.2 bar, and 1500 rpm, respectively. Other polishing settings are shown in Table 8. As shown in Fig. 23, the 3D structured surfaces

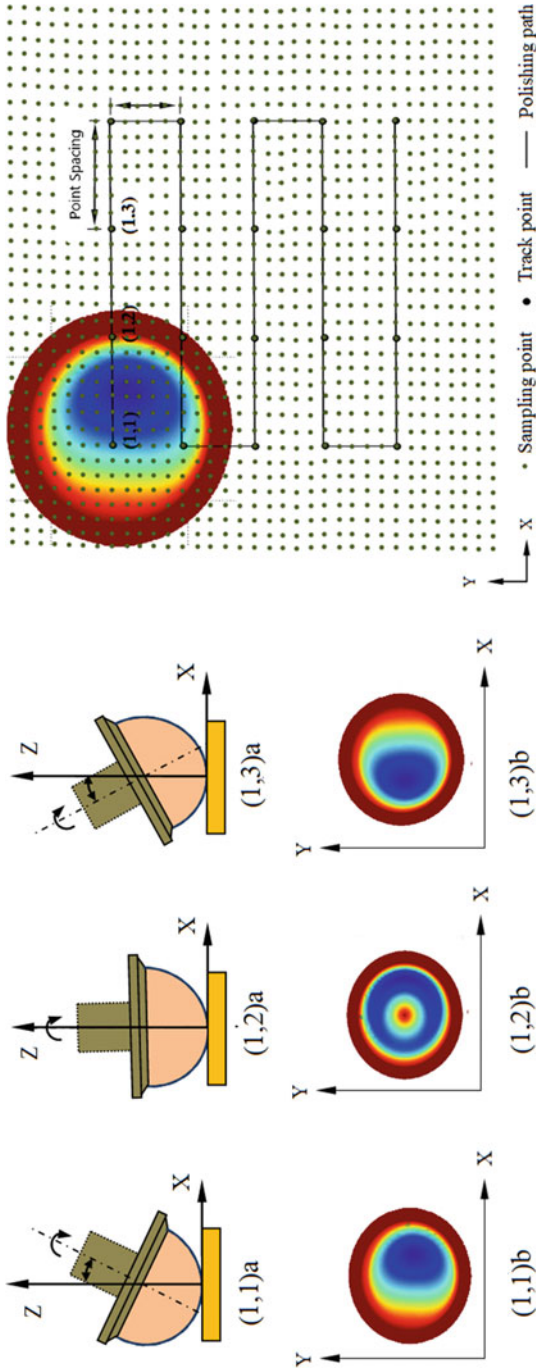


Fig. 21 Schematic diagram of the surface generation mechanisms of swing process bonnet polishing across the raster tool path

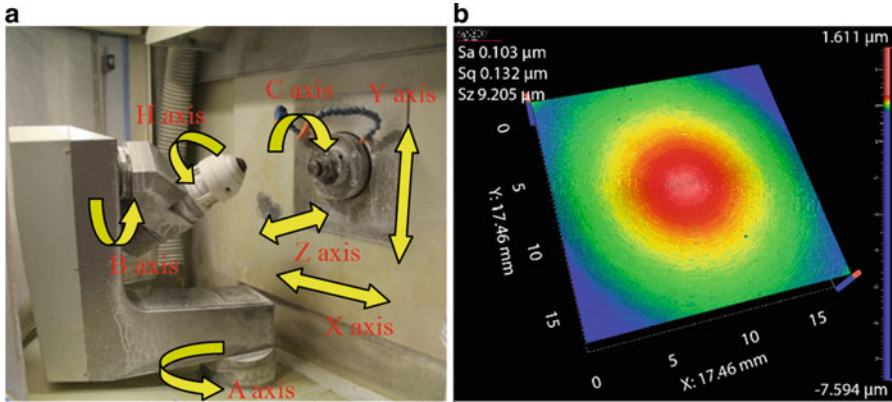


Fig. 22 (a) Zeeko IRP200 Ultra-precision freeform polishing machine and (b) measured surface topography of the samples before polishing

Table 8 Polishing parameters used in line tests of swing precess bonnet polishing

Sample No.	Parameters					
	Precess angle (°)	Tool offset (mm)	Feed rate (mm/min)	Spacing (mm)	Swing speed (°/min)	Swing direction
1	5	0.28	50	0.4	250	Climb
2	10					
3	15					
4	10	0.14	25	0.6	200	
5		0.42				
6		0.28	75	0.8	300	
7						
8						
9		50	0.4	250	Vertical	
10						
11						
12						

generated on the polished area were characterized by the peak-to-valley (PV) height, the width, and the length of a rectangle that can cover a cycle of the structure.

11.6.1.2 Results and Discussion

Figures 24, 25, 26, 27, 28, and 29 show the results of the characterization of the 3D structures generated by only a single one-way tool path. It is interesting to note that the shape of each cycle of the structures is varied under different polishing conditions. It is believed that this may affect the pattern of the 3D structures formed on a

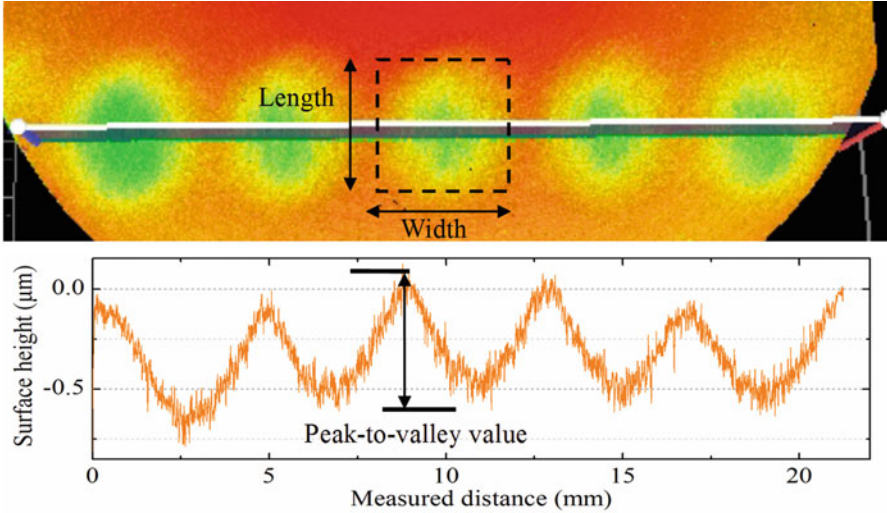


Fig. 23 Characterization of the surface feature parameters of the generated 3D structured structures

surface. Moreover, precess angles and feed rate significantly affect the density of the 3D structures, as shown in Figs. 24 and 25. The smaller the precess angle and the slower the feed rate, the higher the density of the 3D structures. Figure 26 shows that the density of the 3D structures increases with the increasing swing speed. This can be explained by

$$N = \frac{L\omega_s}{4F_r A} \quad (30)$$

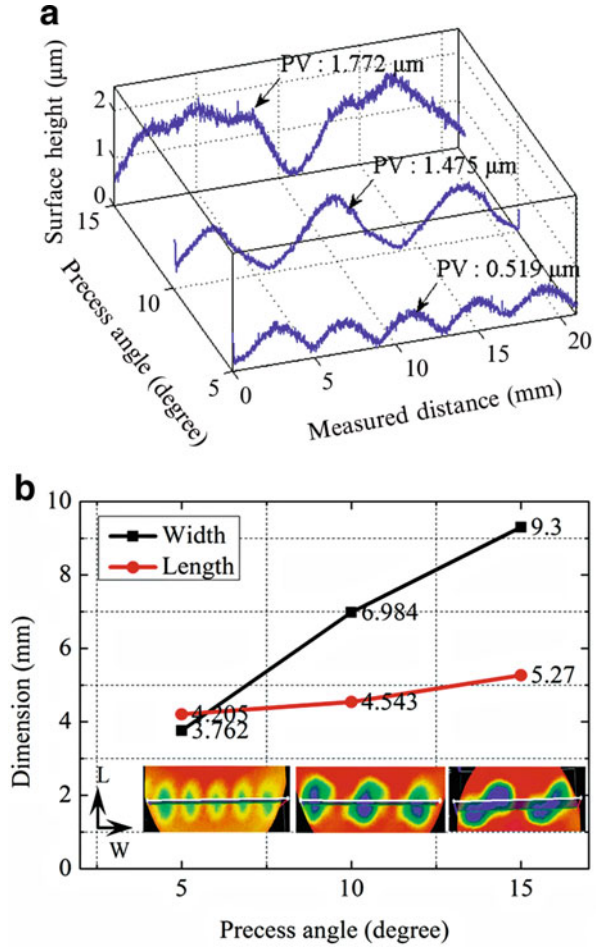
where N is the number of swing cycle, L is the length of the polishing area in mm, ω_s is the swing speed in degree per min, F_r is the feed rate in mm/min, and A is the precess angle in degree. The smaller the precess angle and the higher the swing speed mean the smaller the swing cycle, while the slower the feed rate means the longer polishing time. Hence, both of them cause the higher density of the structures.

Figures 24a and 25a show that the PV values increase as the precess angle and feed rate are increased. This can be explained by

$$T_c = \frac{4A}{\omega_s} \quad (31)$$

where T_c is time of each swing cycle. A larger precess angle means longer time of each swing cycle and hence causes a larger PV value. The smaller the feed rate means the higher the density of the structures, and this may cause the smaller PV values. Figure 24b shows that the width and the length of the 3D structures increase with increasing precess angle. Figure 25b shows that the width of the 3D structures

Fig. 24 Effect of precess angle on the surface generation in line test: (a) 2D cross-sectional profile with PV values and (b) width and length of the 3D structures



increases with increasing feed rate, while the length of the 3D structures shows no obvious variation trend. Precess angle 15°, feed rate 75 mm per min, and swing speed 200° per minute give similar 3D structures, which have a larger width-to-length ratio.

Figures 27, 28, and 29 show that the tool offset, point spacing, and swing direction have no significant influence on the density of the 3D structures. Figure 27a shows that the PV values of tool offset of 0.14 mm is obviously smaller than that of 0.28 and 0.42 mm, while Fig. 27b shows that the width and the length of the 3D structures increase with increasing the tool offset. This can be explained by a larger tool offset presenting a larger contact area and higher contact pressure and hence a higher material removal rate. Tool offsets of 0.28 and 0.42 mm give similar PV values, and this infers that there may exist a critical tool offset which if exceeded would lead to the breaking of the increment of PV values with the increasing tool offset.

Fig. 25 Effects of feed rate on the surface generation in line test: (a) 2D cross-sectional profile with PV values and (b) width and length of the 3D structures

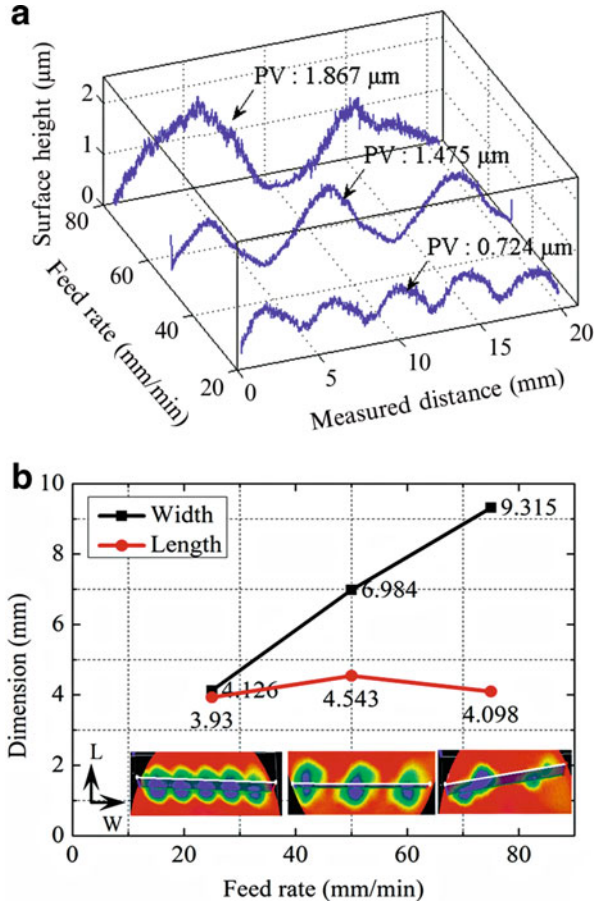


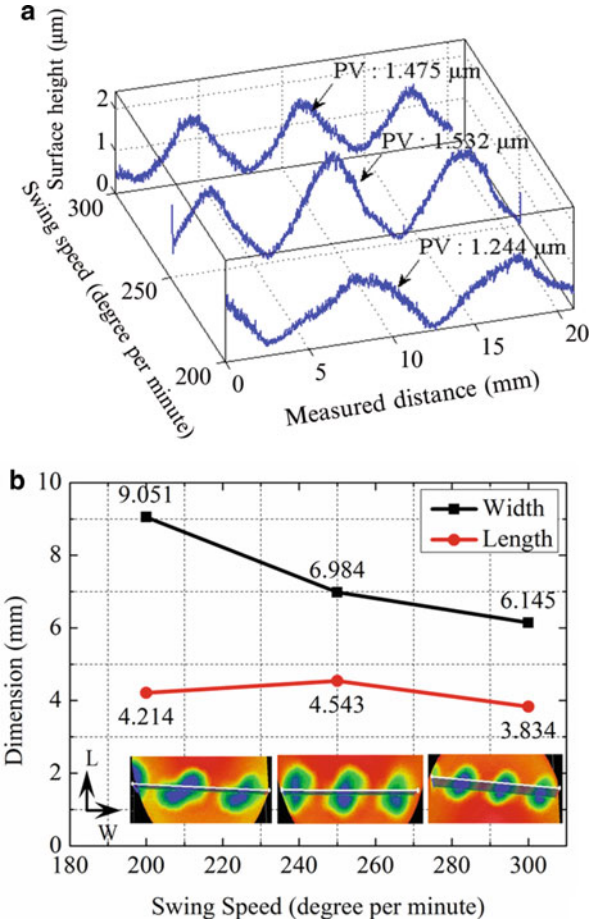
Figure 28 shows that the effect of point spacing on the peak-to-valley (PV) height, the width, and the length of the 3D structures is negligible. Figure 29 shows that the swing directions mainly affects the shape of the 3D structure but shows no significant influence on the PV values. Although experimental study was conducted on studying effect of the single process parameter on the generation of 3D structured surfaces, the significance of process parameters and the interactions among them should be further investigated in the further study.

11.6.2 5.2 Group B: Results of Experimental and Theoretical Investigation of Pattern Tests

11.6.2.1 Experimental Setup

In Group B, four sets of parameters were selected to generate 3D structured surfaces, as shown in Table 9. The tool pressure and the spindle speed were set at 1.2 bar and

Fig. 26 Effects of swing speed on the surface generation in line test: (a) 2D cross-sectional profile with PV values and (b) width and length of the 3D structures

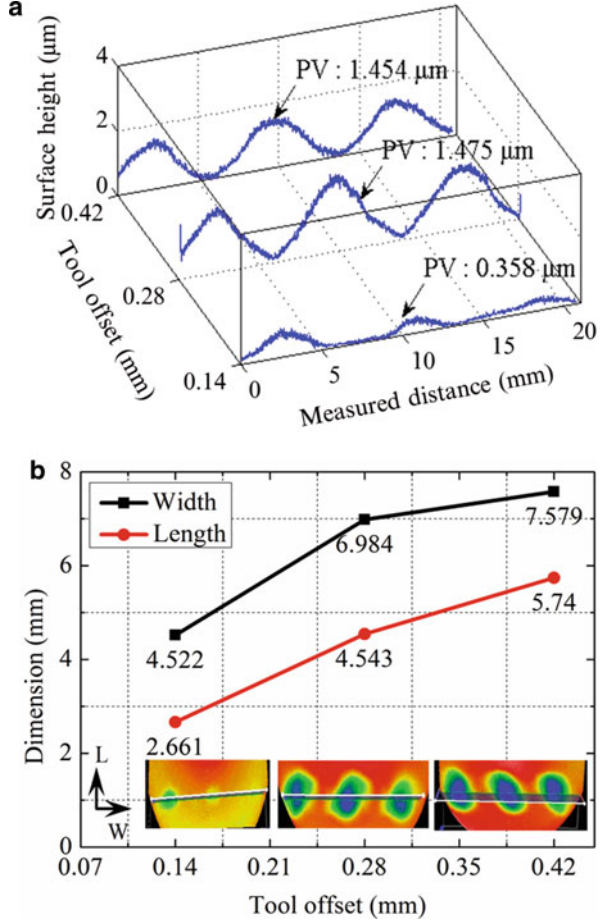


1500 rpm, respectively. Twelve samples were polished with three samples for each set.

11.6.2.2 The Repeatability Under Various Polishing Conditions

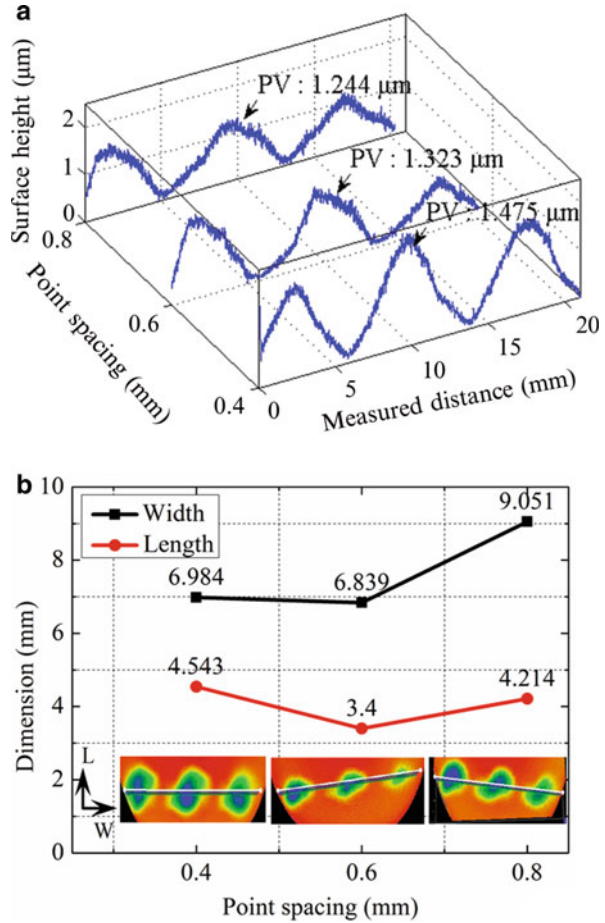
Table 10 shows the results of pattern tests measured by a Zygo Nexview 3D optical surface profiler, and Table 11 shows the photos of the patterns generated by swing precess bonnet polishing. It is interesting to note that complex 3D structured patterns are formed on the surfaces. The results show that different kinds of the complex 3D structured surfaces can be generated by using different polishing parameters. It is also found that the 3D topographies of the 3D structured patterns generated on the surfaces have a good consistency in surface shape when using the same polishing parameters. Since there are some noise points for the original measured data without filtering, especially for the case of set 3(b), the direct comparison of measured data for each set is not acceptable.

Fig. 27 Effect of tool offset on the surface generation in line test: (a) 2D cross-sectional profile with PV values and (b) width and length of the 3D structures



To further evaluate the feasibility and stability of the proposed SPBP method, the deviation of measured results with same polishing conditions was evaluated by the repeatability test. For every set of experiment, three measurement data were obtained, named set a, set b, and set c. The measurement data set a were used as the reference data. Then measurement data set b and measurement data set c were compared to the reference data. The error maps were then obtained, and the root-mean-square (RMS) value of the error maps were calculated and shown in Table 12. As shown in Table 13, the result shows that the RMS values of the error maps vary from 0.2 to 0.5 μm which demonstrate that the repeatability of the experiment is reasonable. This implies that swing precess bonnet polishing can be used for generating different kinds of 3D structured patterns in deterministic and stable way, especially for difficult-to-machine and ferrous materials. However, the deformation of polishing bonnet and the abrasion wear of the polishing cloth could affect the stability of the produced pattern, and hence both of them should be critically

Fig. 28 Effects of point spacing on the surface generation in line test: (a) 2D cross-sectional profile with PV values and (b) width and length of the 3D structures



controlled. The polishing conditions should also be further optimized for obtaining the structured patterns with high surface finish.

11.6.2.3 Experimental Verification of Surface Generation Model for SPBP

To evaluate the performance of the multi-scale material removal model and surface generation model for SPBP, the simulation experiments were conducted using the same polishing parameters with practical polishing experiments as shown in Table 9. Figure 30 shows the simulated 3D structured surface generated by the theoretical model. It is interesting to note that the surface topography of the simulated results shows a reasonably good agreement with that of the experimental data. This means that the theoretical model can be successfully used for the selection of polishing parameters for designed structured pattern and better understanding of the SPBP process.

Fig. 29 Effects of swing direction on the surface generation in line test: (a) 2D cross-sectional profile with PV values and (b) width and length of the 3D structures

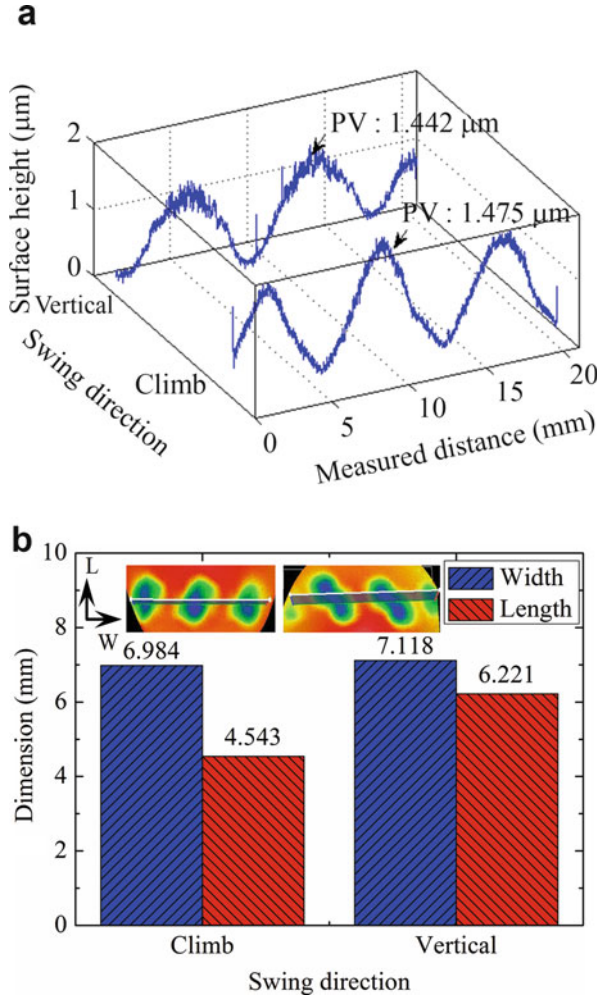


Table 9 Polishing parameters used in pattern tests of swing process bonnet polishing

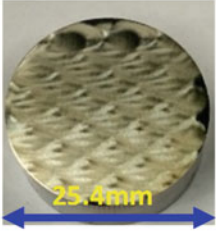
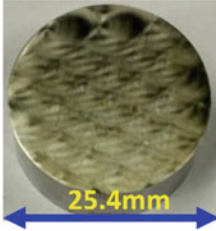
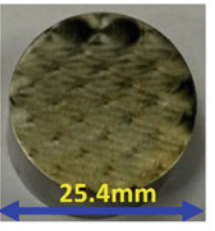
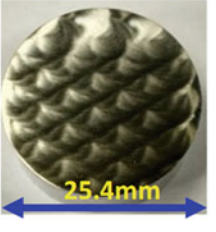
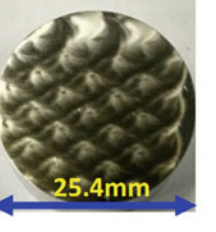
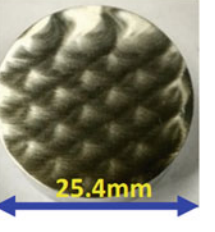
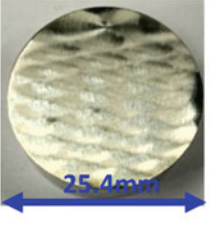
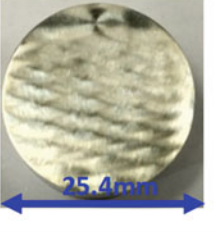
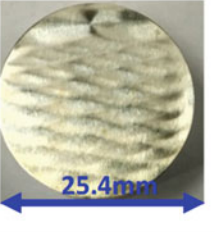
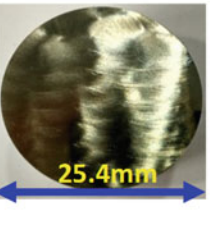
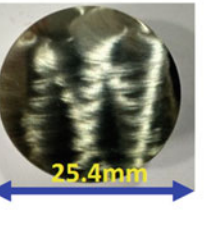
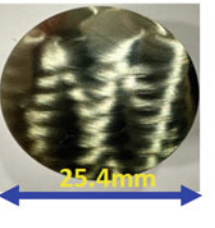
Parameter set no.	Parameters					
	Precess angle (°)	Tool offset (mm)	Feed rate (mm/min)	Spacing (mm)	Swing speed	Swing direction
1	10	0.28	50	0.4	300	Climb
2						Vertical
3	15			0.6	250	Climb
4						Vertical

Table 10 Measured topography of structured pattern generated by swing precess bonnet polishing

Set no.	3D surface topography measured by a Zygo Nexview 3D Optical Surface Profiler		
	a	b	c
1			
3			

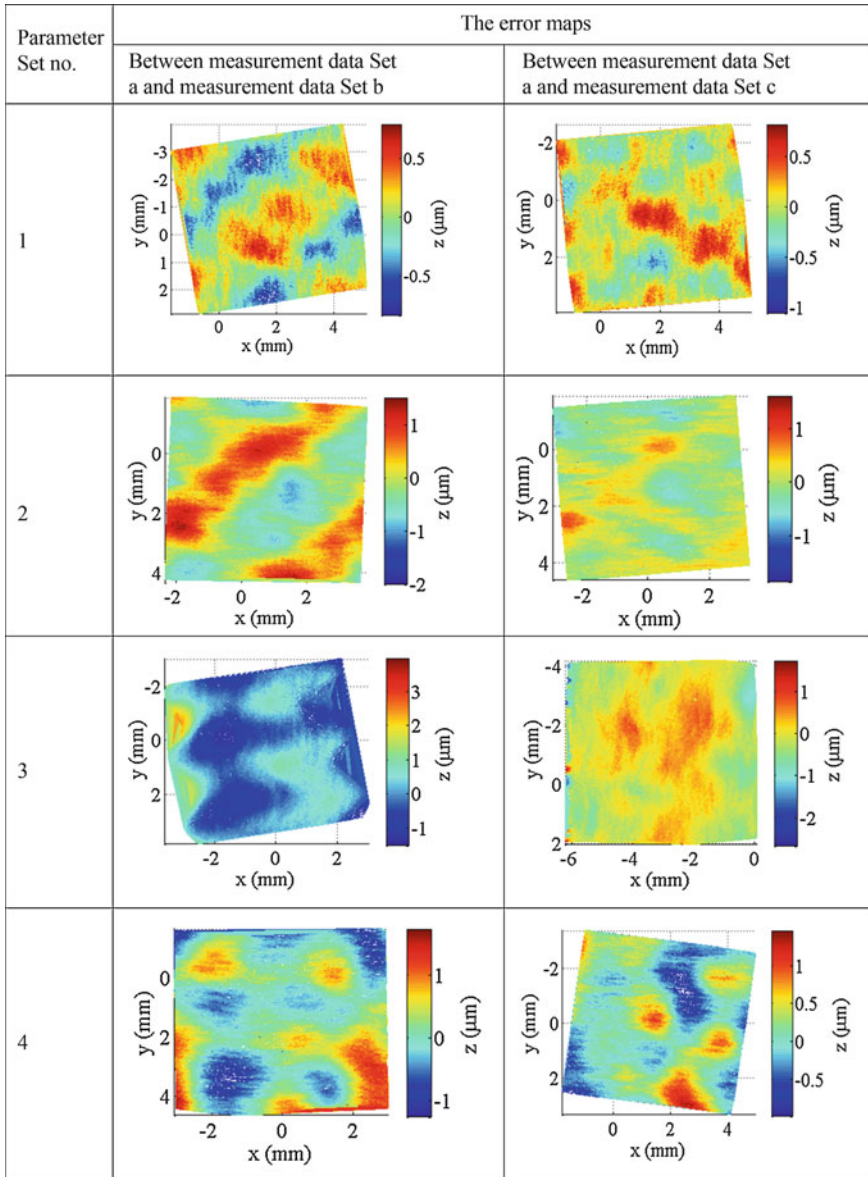
To compare the simulation results and measured results quantitatively, the measured results have to be registered to the simulated results by a freeform surface characterization method which has been purposely built based on an iterative closest point (ICP) method (Besl and Mckay 1992). To improve the accuracy and robustness of the registration process, the simulated surface was first filtered with a Gaussian zero-order regression filter (Brinkmann et al. 2001). Hence, the measured surface was registered to the filtered simulated surface with the ICP method, and the transformation matrix was obtained. Based on the calculated transformation matrix, the error map showing the deviation of the simulation results and the measured

Table 11 Photos of structured pattern generated by swing precess bonnet polishing

Set no.	Photos of samples		
	a	b	c
1			
2			
3			
4			

results was determined by registering the measured results with the original simulated results. Figure 31 shows the surface matching and error evaluation process for case parameter set 4. As shown in Fig. 31a and b, the simulated topography and measured topography of the complex 3D structured surface generated by SPBP are found to agree well. To further verify the performance of the models quantitatively,

Table 12 The error maps of experimental results for pattern tests



the deviation of the measured surface from the corresponding simulated surface was determined by the freeform surface characterization method. Figure 31c shows the results after registration of the measured surface and the simulated surface, while Fig. 31d shows the deviation between the simulated and measured results.

Table 13 The root-mean-squared (RMS) value of the error maps of experimental results for pattern tests

Parameter set no.	The root-mean-squared value of the error maps (μm)	
	Between measurement data set a and measurement data set b	Between measurement data set a and measurement data set c
1	0.2556	0.2221
2	0.5020	0.2528
3	0.5530	0.3330
4	0.4791	0.3710

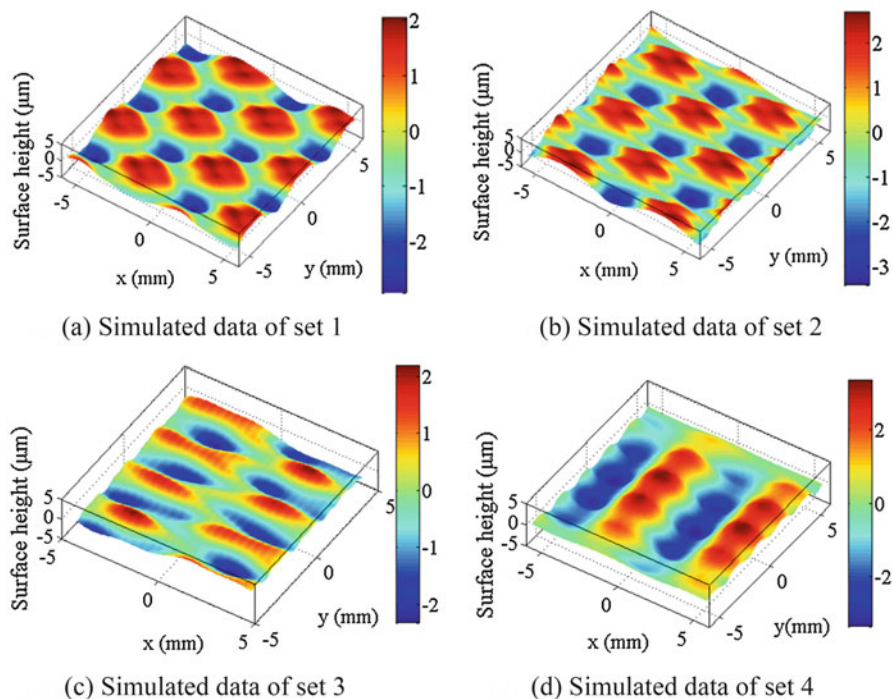


Fig. 30 Simulated topography of structured pattern by the developed theoretical model

Table 14 shows the comparison results between the simulated and measured results of swing precess bonnet polishing. The simulated results were found to agree reasonably well with the experimental results with the root-mean-squared (RMS) value of the prediction error from 0.1 to 0.5 μm . Since the surface generation of SPBP is the relative and cumulative process of varied tool influence function, the prediction error of surface generation model is the accumulation of the error of material removal model under different polishing gestures. The comparison results show that the theoretical model can be successfully used for the prediction and better understanding of the SPBP process.

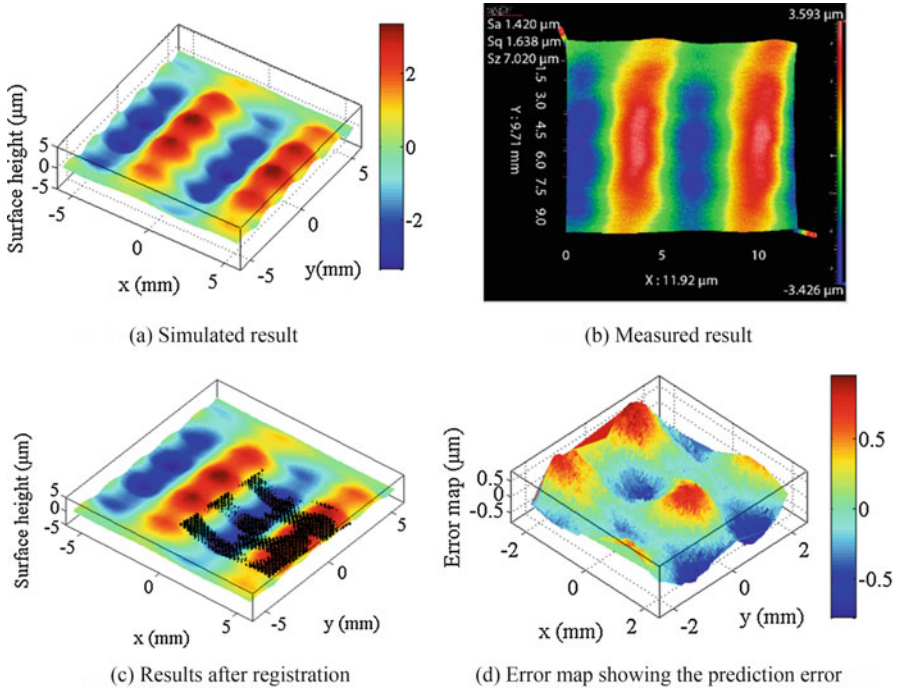


Fig. 31 The surface matching and error evaluation process for case set 4

Table 14 The root-mean-squared (RMS) value of the error maps between the simulated and experimental results

Parameter set no.	The root-mean-squared value of the error maps (μm)		
	Measured data set a – simulated data	Measured data set b – simulated data	Measurement data set c – simulated data
1	0.476	0.3665	0.4922
2	0.4402	0.3103	0.3723
3	0.134	0.1708	0.1576
4	0.2723	0.2143	0.2211

11.7 Summary

Microstructured surfaces are surfaces possessing specially designed functional textures which are widely used in the development of a wide range of products such as structured surfaces for improving adhesion property of the mold and die and fluid films sealing. However, they are difficult to be fabricated to high precision and high accuracy by traditional machining technology. As one of the computer-controlled ultra-precision polishings (CCUP), bonnet polishing is an enabling machining

technology which is capable of fabricating ultra-precision freeform surfaces made of difficult-to-machine materials with sub-micrometer form accuracy and surface roughness in the nanometer range. It addresses the limitations of materials that can be machined by single-point diamond turning or ultra-precision raster milling processes. However, most of the previous research work has focused on the control of surface finish and the control of form errors of the surfaces. Research on the generation of microstructured surface by bonnet polishing has received relatively little attention.

In this chapter, a theoretical and experimental investigation of microstructured surface generation by using bonnet polishing was presented. The surface generation by bonnet polishing has been studied which include the theoretical and experimental analysis of material removal rate (MRR) or tool influence function (TIF) which significantly affects the surface generation in bonnet polishing. A surface topography simulation model has been built, and hence a model-based simulation system has been established for the modeling and simulation of microstructured surface generation by using bonnet polishing. A series of simulation and practical polishing experiments have been undertaken to verify the surface topography simulation model and to evaluate the performance of the model-based simulation system. The experimental results provide an important means to demonstrate the capability of the model-based simulation system in the prediction of surface generation in terms of the form error and various patterns of the 3D microstructures generated by using bonnet polishing.

References

- Beaucamp A, Namba Y S-s (2013) finishing of diamond turned hard X-ray molding dies by combined fluid jet and bonnet polishing. *CIRP Ann Manuf Technol* 62:315–318
- Bechert DW, Bruse M, Hage W, Meyer R (2000) Fluid mechanics of biological surfaces and their technological application. *Naturwissenschaften* 87:157–171
- Beckstette K, Kuechel M, Heynacher E (1989) Large mirror figuring and testing. *Astrophys Space Sci* 160(October (1–2)):207–214
- Besl PJ, McKay ND (1992) A method for registration of 3-D shapes. *IEEE Trans Pattern Anal Mach Intell* 14:239–256
- Bingham RG, Walker DD, Kim DH, Brooks D, Freeman R, Riley DA (2000) Novel automated process for aspheric surfaces. *Curr Dev Lens Des Opt Sys Eng* 4093:445–450
- Bingley MS, Schnee S (2005) A study of the mechanisms of abrasive wear for ductile metals under wet and dry three-body conditions. *Wear* 258:50–61
- Brilliantov NV, Poschel T (1998) Rolling friction of a viscous sphere on a hard plane. *Europhys Lett* 42:511–516
- Brinkmann S, Bodschinna H, Lemke HW (2001) Accessing roughness in three-dimensions using Gaussian regression filtering. *Int J Mach Tool Manu* 41:2153–2161
- Cao ZC, Cheung CF (2016) Multi-scale modeling and simulation of material removal characteristics in computer-controlled bonnet polishing. *Int J Mech Sci* 106:147–156
- Cao ZC, Cheung CF, Ren MJ (2016) Modelling characterization of surface generation in Fluid Jet Polishing. *Precis Eng* 43:406–417
- Carter G, Nobes MJ, Katardjiev IV (1993) The theory of ion beam polishing and machining. *Vacuum* 44(3/4):303–309

- Challen JM, Oxley PLB (1979) An explanation of the different regimes of friction and wear using asperity deformation models. *Wear* 53:229–243
- Charlton P, Blunt L (2008) Surface and form metrology of polished “freeform” biological surfaces. *Wear* 264:394–399
- Chen PY, Jywe WY, Wang MS, Wu CH (2016) Application of blue laser direct-writing equipment for manufacturing of periodic and aperiodic nanostructure patterns. *Precis Eng* 46:263–269
- Cheung CF, Ho LT, Charlton P, Kong LB, To S, Lee WB (2010) Analysis of surface generation in the ultraprecision polishing of freeform surfaces. *Proc Inst Mech Eng B J Eng Manuf* 224:59–73
- Cheung CF, Kong LB, Ho LT, To S (2011) Modelling and simulation of structure surface generation using computer controlled ultra-precision polishing. *Precis Eng* 35:574–590
- Egashira K, Kumagai R, Okina R, Yamaguchi K, Ota M (2014) Drilling of microholes down to 10 μm in diameter using ultrasonic grinding. *Precis Eng* 38:605–610
- Evans CJ, Paul E, Dornfeld D, Lucca DA, Byrne G, Tricard M et al (2003) Material removal mechanisms in lapping and polishing. *Cirp Ann Manuf Technol* 52:611–633
- Fähnle OW, van Brug H, Frankena HJ (1998) Fluid jet polishing of optical surfaces. *Appl Opt* 37(28):6771–6773
- Fu GH, Chandra A, Guha S, Subhash G (2001) A plasticity-based model of material removal in chemical-mechanical polishing (CMP). *IEEE Trans Semicond Manuf* 14:406–417
- Gee AE (1996) Modelling the mechanics of free particulate abrasive polishing from the viewpoint of single-point processes. *SPIE* 2775:611–618
- Greenwood J, Williamson J (1966) Contact of nominally flat surfaces. *Proc R Soc Lond A Math Phys Sci* 295:300–319
- Hokkirigawa K, Kato K (1988) An experimental and theoretical investigation of ploughing, cutting and wedge formation during abrasive wear. *Tribol Int* 21:51–57
- Hutchings IM (1992) *Tribology: friction and wear of engineering materials*. Arnold, London
- Hutchings IM (1993) Mechanisms of wear in powder technology – a review. *Powder Technol* 76:3–13
- Johansen LS, Ginnerup M, Ravnkilde JT, Tang PT, Lochel B (2000) Electroforming of 3D microstructures on highly structured surfaces. *Sensors Actuators A Phys* 83:156–160
- Johnson KL (1987) *Contact mechanics*. Cambridge University Press, Cambridge
- Johnson LF, Ingersoll KA (1983) Ion polishing with the aid of a planarizing film. *Appl Opt* 22(8):1165–1167
- Kim S, Saka N, Chun JH, Shin SH (2013) Modeling and mitigation of pad scratching in chemical–mechanical polishing. *CIRP Ann Manuf Technol* 62:307–310
- Kim S, Saka N, Chun J-H (2014) The effect of pad-asperity curvature on material removal rate in chemical-mechanical polishing. *Procedia CIRP* 14:42–47
- Kumar S, Jain VK, Sidpara A (2015) Nanofinishing of freeform surfaces (knee joint implant) by rotational-magnetorheological abrasive flow finishing (R-MRAFF) process. *Precis Eng* 42:165–178
- Landau LD, Lifshitz EM (1959) *Theory of elasticity*. Pergamon Press, London
- Luo JF, Dornfeld DA (2001) Material removal mechanism in chemical mechanical polishing: theory and modeling. *IEEE Trans Semicond Manuf* 14:112–133
- Luo JF, Dornfeld DA (2003) Effects of abrasive size distribution in chemical mechanical planarization: modeling and verification. *IEEE Trans Semicond Manuf* 16:469–476
- Namba Y, Shimomura T, Fushiki A, Beaucamp A, Inasaki I, Kunieda H et al (2008) Ultra-precision polishing of electroless nickel molding dies for shorter wavelength applications. *Cirp Ann Manuf Technol* 57:337–340
- Preston FW (1927) The theory and design of plate glass polishing machines. *J Soc Glas Technol* 11:214–256
- Ren MJ, Cheung CF, Kong LB (2012) A task specific uncertainty analysis method for least-squares-based form characterization of ultra-precision freeform surfaces. *Meas Sci Technol* 23:054005

- Saka N, Eusner T, Chun JH (2010) Scratching by pad asperities in chemical–mechanical polishing. *CIRP Ann Manuf Technol* 59:329–332
- Schaller T, Bohn L, Mayer J, Schubert K (1999) Microstructure grooves with a width of less than 50 μm cut with ground hard metal micro end mills. *Precis Eng* 23:229–235
- Schinhaerl M, Rascher R, Stamp R, Smith G, Smith L, Pitschke E, Sperber P (2007) Filter algorithm for influence functions in the computer controlled polishing of high-quality optical lenses. *Int J Mach Tool Manu* 47:107–111
- Schinhaerl M, Smith G, Stamp R, Rascher R, Smith L, Pitschke E et al (2008a) Mathematical modelling of influence functions in computer-controlled polishing: part I. *Appl Math Model* 32(12):2888–2906
- Schinhaerl M, Smith G, Stamp R, Rascher R, Smith L, Pitschke E et al (2008b) Mathematical modelling of influence functions in computer-controlled polishing: part II. *Appl Math Model* 32(12):2907–2924
- Shen JC, Jywe WY, Wu CH (2014) Control of an equipment for fabricating periodic nanostructure. *Precis Eng* 38:391–397
- Shiou FJ, Ciou HS (2008) Ultra-precision surface finish of the hardened stainless mold steel using vibration-assisted ball polishing process. *Int J Mach Tool Manu* 48:721–732
- Stout KJ, Blunt L (2001) A contribution to the debate on surface classifications – random, systematic, unstructured, structured and engineered. *Int J Mach Tool Manu* 41:2039–2044
- Sudarshan TS (1995) Polishing of diamond films – a review. In: Jeandin TS, Sudarshan M (eds) *Surface modification technologies VIII*. The Institute of Materials, London
- Tam HY, Cheng HB (2010) An investigation of the effects of the tool path on the removal of material in polishing. *J Mater Process Technol* 210:807–818
- Tam HY, Lui OCH, Mok ACK (1999) Robotic polishing of free-form surfaces using scanning paths. *J Mater Process Technol* 95:191–200
- Wakuda M, Yamauchi Y, Kanzaki S, Yasuda Y (2003) Effect of surface texturing on friction reduction between ceramic and steel materials under lubricated sliding contact. *Wear* 254: 356–363
- Walker DD, Brooks D, Freedman R, King A, McCavana G, Morton R, Riley D, Simms J (2000) First aspheric form and texture results from a production machine embodying the precessions process. In: *Optical manufacturing and testing IV*, Proceedings of SPIE, vol 4451, pp 267–76
- Walker DD, Brooks D, Freeman R, King A, McCavana G, Morton R, Riley D, Simms J (2001) The first aspheric form and texture results from a production machine embodying the precession process. In: *Optical manufacturing and testing*, vol 4451, pp 267–276
- Walker DD, Beaucamp ATH, Brooks D, Freeman R, King A, McCavana G, Morten R, Riley D, Simms J (2002a) Novel CNC polishing process for control of form and texture on aspheric surfaces. *Curr Dev Lens Des Opt Eng III* 4767:99–105
- Walker DD, Freeman R, McCavana G, Morton R, Riley D, Simms J, Brooks D, Kim ED, King A (2002b) The Zeeko/UCL process for polishing large lenses and prisms. *Large Lens Prism* 4411:106–111
- Walker DD, Beaucamp AT, Bingham RG, Brooks D, Freeman R, Kim SW, King AM, McCavana G, Morton R, Riley D, Simms J (2002c) Precessions process for efficient production of aspheric optics for large telescopes and their instrumentation. In: Atad-Ettinger E, D’Oro S (eds) *Specialized optical developments in astronomy*, Proceedings of SPIE, vol 4842, pp 73–84
- Walker DD, Brooks D, King A, Freeman R, Morton R, McCavana G, Kim S-W (2003) The ‘Precessions’ tooling for polishing and figuring flat, spherical and aspheric surfaces. *Opt Express* 11(8):958–964
- Williams CK, Rasmussen CE (2006) *Gaussian processes for machine learning*, vol 2. MIT Press, Cambridge, MA, p 4
- Xi F, Zhou D (2005) Modelling surface roughness in the stone polishing process. *Int J Mach Tool Manu* 45:365–372

- Zeng SY, Blunt L (2014) Experimental investigation and analytical modelling of the effects of process parameters on material removal rate for bonnet polishing of cobalt chrome alloy. *Precis Eng* 38:348–355
- Zhao T, Grogan DF, Bovard BG, Macleod HA 1990 Diamond film polishing with argon and oxygen ion beams. In: *Diamond optics III*, SPIE proceedings, vol 1325, pp 142–51
- Zheng QJ, Zhu HP, Yu AB (2011) Finite element analysis of the rolling friction of a viscous particle on a rigid plane. *Powder Technol* 207:401–406
- Zhou H, Shan HY, Tong X, Zhang ZH, Ren LQ (2006) The adhesion of bionic non-smooth characteristics on sample surfaces against parts. *Mater Sci Eng A* 417:190–196
- Zhu HT, Huang CZ, Wang J, Li QL, Che CL (2009) Experimental study on abrasive waterjet polishing for hard–brittle materials. *Int J Mach Tools Manuf* 49(78):569



Soft-Brittle Semiconductors Polishing with Environment-Friendly Slurries

12

Zhenyu Zhang, Bo Wang, and Dongming Guo

Contents

12.1	Introduction	422
12.2	Traditional Machining Challenges for Soft-Brittle Semiconductors	423
12.3	Soft-Brittle Semiconductors Polishing with Environment-Friendly Slurries	426
12.3.1	Cadmium Zinc Telluride Semiconductors	426
12.3.2	Mercury Cadmium Telluride Semiconductors	432
12.4	Summary and Future Directions	441
	References	442

Abstract

A novel approach of chemical mechanical polishing (CMP) is developed for cadmium zinc telluride (CdZnTe or CZT) wafers. The approach uses environment-friendly slurry that consists of mainly silica, hydrogen peroxide, and citric acid. This is different from the previously reported slurries that are usually composed of strong acid, alkali, and bromine methanol and are detrimental to the environment and operators. Surface roughness 0.5 and 4.7 nm are achieved for R_a and peak-to-valley (PV) values, respectively, in a measurement area of $70 \times 50 \mu\text{m}^2$, using the developed novel approach.

A novel approach of CMP is developed for mercury cadmium telluride (HgCdTe or MCT) semiconductors. Firstly, fixed-abrasive lapping is used to machine the MCT wafers, and the lapping solution is deionized water. Secondly, the MCT wafers are polished using the developed CMP slurry. The CMP slurry consists of mainly SiO_2 nanospheres, H_2O_2 , and malic and citric acids, which are different from previous CMP slurries, in which corrosive and toxic chemical

Z. Zhang (✉) · B. Wang · D. Guo

Key Laboratory for Precision and Non-Traditional Machining Technology of Ministry of Education, Dalian University of Technology, Dalian, China

e-mail: zzy@dlut.edu.cn

© Springer Nature Singapore Pte Ltd. 2018

J. Yan (ed.), *Micro and Nano Fabrication Technology*, Micro/Nano Technologies,

https://doi.org/10.1007/978-981-13-0098-1_12

421

reagents are usually employed. Finally, the polished MCT wafers are cleaned and dried by deionized water and compressed air, respectively. The novel approach of CMP is environment-friendly. Surface roughness R_a and peak-to-valley (PV) values of 0.45 and 4.74 nm are achieved, respectively, on MCT wafers after CMP. The first and second passivation processes are observed in electrochemical measurements on MCT wafers. Fundamental polishing mechanisms are also investigated in terms of X-ray photoelectron spectroscopy (XPS) and electrochemical measurements.

Keywords

Chemical mechanical polishing · Environment-friendly slurry · Soft-brittle crystals · Alloy · CdZnTe

12.1 Introduction

Ultrasmooth and ultralow damage surface is usually used in semiconductor, micro-electronic, and optoelectronic industries. Chemical mechanical polishing (CMP) has a unique combination of chemical and mechanical effects, resulting in material removal at atomic level and obtaining ultrasmooth and ultralow surfaces (Lin et al. 2018; Wang et al. 2017). CMP usually employs slurry consisting of abrasives, oxidant, complexing agent, etc. Slurry oxidizes the surface of workpiece, forming an oxidized layer. Complexing agent is applied to combine the ions generated in chemical reactions, producing an adsorption layer. Layers induced by chemical reactions in CMP are normally soft, and they are removed by silica abrasive, as illustrated in Fig. 1. During CMP, a wafer workpiece is rotated around its axis while

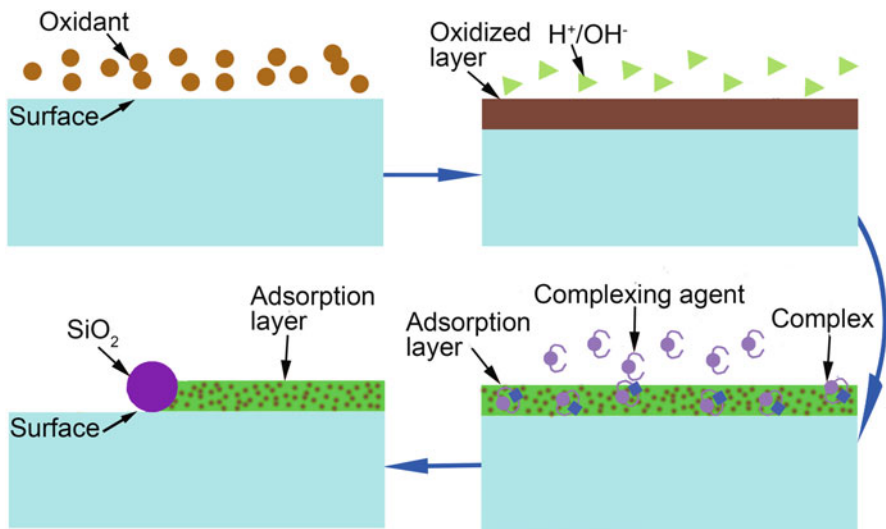


Fig. 1 Schematic diagrams of reaction between slurry and workpiece in CMP process

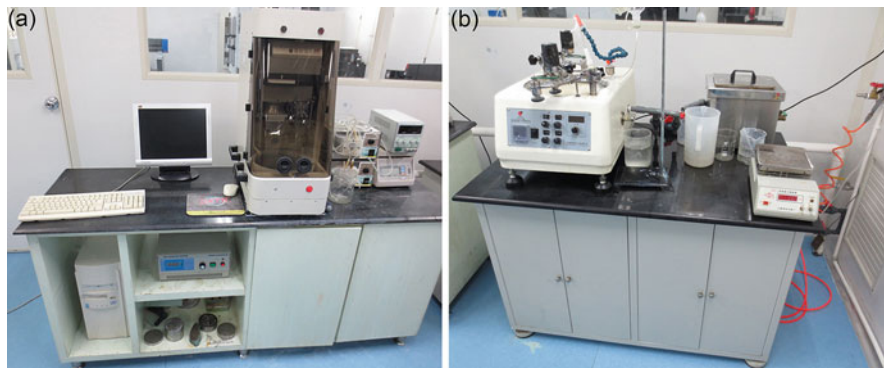


Fig. 2 CMP polishers (a) with and (b) without force sensors

it is pressed facedown by a carrier against a rotating polishing pad. CMP is performed by a polisher, as pictured in Fig. 2. CMP slurry plays an important role to obtain ultrasmooth and ultralow surfaces.

Cadmium zinc telluride (CdZnTe or CZT) is a representative for the third-generation soft-brittle semiconductors in room temperature radiation detection, as well as a substrate for epitaxial growth of lattice-matched mercury cadmium telluride (HgCdTe or MCT) films used for infrared detectors (Cohen et al. 2010; Yang et al. 2011; Ruzin et al. 2012). Furthermore, CZT is widely used in medical imaging, homeland security, and spaceborne X-ray and gamma-ray astronomy (Cohen et al. 2010; Androulakis et al. 2011; Zhang et al. 2015b). This is attributed to its high gamma-ray absorption coefficient and high electrical resistivity, derived from the high atomic number and wide bandgap, respectively (Cohen et al. 2010).

Mercury cadmium telluride ($\text{Hg}_{1-x}\text{Cd}_x\text{Te}$ or MCT) has become the most versatile semiconductor for infrared (IR) detectors, in terms of their tunable band gaps over the entire IR range (Lei et al. 2015; Rogalski 2005; Zha et al. 2008; Venkatasamy et al. 2007; Zhang et al. 2013a). At present, MCT is the most widely used variable gap semiconductor for IR photodetectors (Rogalski 2005). In addition, MCT is nearly ideal for IR detector system, remaining the leading semiconductor in IR detectors.

12.2 Traditional Machining Challenges for Soft-Brittle Semiconductors

CZT has soft and brittle nature (Zhang et al. 2012b), which is different from the first- and second-generation semiconductors with hard and brittle characteristics, such as silicon (Si) (Zhang et al. 2011) and gallium arsenide (GaAs), respectively, making it a hard-to-machine material. For instance, the hardness and fracture toughness of CZT are 1.21 GPa (Zhang et al. 2008) and $0.158 \text{ MPa} \cdot \text{m}^{0.5}$, respectively (Zhang et al. 2013b), which are one twelfth (14.5 GPa) (Zhang et al. 2015a) and one sixth ($0.9\text{--}1.1 \text{ MPa} \cdot \text{m}^{0.5}$) (Qiao and Chen 2008) those of an Si crystal, correspondingly

(Chandra et al. 2014). This results in the corrosive rivers, abrasive embedding, scratch, and pit induced by traditional machining on CZT semiconductors, as illustrated in Fig. 3.

Surface roughness has a significant effect on the electrical property and performance of CZT detectors, and therefore atomically smooth and defect-free surfaces are necessary to the high-performance CZT-based detectors (Tari et al. 2014; Hossain et al. 2014). Thus, the surface roughness root-mean-square (rms) < 1 nm is required for a high-performance CZT detector (Hossain et al. 2014; Pelenc et al. 2014). For this reason, surface processing techniques for CZT wafers have attracted attentions and are investigated intensively (Hossain et al. 2014; Pelenc et al. 2014; Zazvorka et al. 2014; Duff et al. 2008; Teague et al. 2011; Aqariden et al. 2012; Zheng et al. 2011; Ivanits'ka et al. 2011). Currently, lapping, mechanical polishing, chemical mechanical polishing (CMP), and chemical etching are usually employed to machine a CZT wafer. Firstly, free abrasives of alumina are widely used to lap and polish the surfaces of CZT wafers with different grain sizes in a sequence (Zazvorka et al. 2014; Duff et al. 2008). Nitric acid (HNO_3) and bromine methanol (BM) are normally used in CMP (Hossain et al. 2014; Lucile et al. 2011) and chemical etching (Zazvorka et al. 2014; Duff et al. 2008), respectively, to machine CZT wafers.

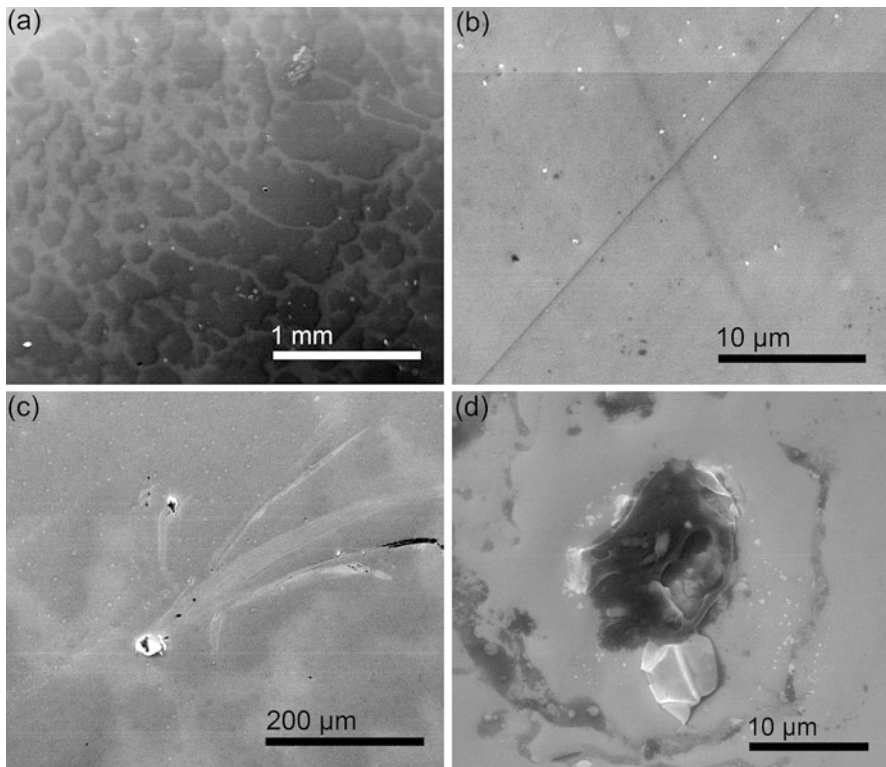


Fig. 3 (a) Corrosive rivers, (b) abrasive embedding, (c) scratch, and (d) pit induced by traditional machining on CZT semiconductors

Nonetheless, free abrasives of alumina are easy to embed in a CZT surface during lapping and polishing (Teague et al. 2011). After embedding, the abrasives are difficult to remove in the successive processes. This results in the high surface roughness and low surface quality. Moreover, HNO_3 is highly corrosive, and BM is toxic to the environment and operators. Hereby, it is necessary to develop a novel environment-friendly approach of CMP for CZT wafers to overcome the disadvantages of the conventional approaches.

Surface roughness is generally related to the measured area, i.e., smaller area leads to lower surface roughness. For example, surface roughness arithmetic average R_a and PV values of 0.32 and 3.29 nm are reported, respectively, using atomic force microscopy (AFM) with a scanning area of $0.5 \times 0.5 \mu\text{m}^2$ on a CZT surface (Hossain et al. 2014). With an increase in the scanning area to $5 \times 5 \mu\text{m}^2$, R_a and PV values increase to 0.94 and 20.2 nm, correspondingly (Hossain et al. 2014). These CZT wafers are polished by HNO_3 and BM (Hossain et al. 2014). Surface roughness rms of 0.74 nm is obtained on a CZT surface using AFM with a scanning area of $1 \times 1 \mu\text{m}^2$ after CMP and chemical etching (Pelenc et al. 2014). The rms value increases to 1.181 nm in a scanned surface of $20 \times 20 \mu\text{m}^2$ which is mechanically polished by free abrasives of alumina, followed by chemical polishing of bromine, ethylene glycol, and sodium hydroxide (NaOH) (Aqariden et al. 2012). Bromine and ethylene glycol are toxic, and NaOH is much corrosive. Surface roughness R_a reaches to 1.8 nm measured by AFM with a scanning area of $2 \times 2 \mu\text{m}^2$, which is produced after mechanical polishing by free abrasives of alumina and diamond, followed by chemical etching of BM (Zheng et al. 2011). For decreased toxicity, iodine is dissolved in methanol replacing bromine in chemical etching of CZT wafers after mechanical polishing by diamond pastes, and R_a and PV values are 1.563 and 15.85 nm (Ivanits'ka et al. 2011), respectively, with a measurement area of $180 \times 130 \mu\text{m}^2$. However, both iodine and methanol are toxic, despite less toxicity of iodine than that of bromine. Surface roughness rms and PV values are 2.063 and 27.834 nm, respectively, on the CZT surfaces after mechanical polishing by alumina abrasives (Zazvorka et al. 2014). Surface roughness increases to 3.855 and 95.762 nm, correspondingly after chemical etching using BM. As a result, BM deteriorates the surface roughness, rather than improving it. Undoubtedly, CMP and chemical etching play an important role to decreasing the surface roughness of the CZT wafers. It is a challenge to develop a novel environment-friendly approach to achieve the surface roughness <1 nm with a measurement area of $50 \times 50 \mu\text{m}^2$.

Hg-Te bonds in MCT are extremely weak, resulting in its soft and brittle nature (Rogalski 2005; Zhang et al. 2013a, b). This makes MCT become a difficult-to-machine material. For instance, the hardness of MCT varies from 0.5 to 0.66 GPa (Martyniuk et al. 2005; Zhang et al. 2012a), which is approximately one twentieth that of silicon (Si) (12–14 GPa). The fracture toughness of MCT is $0.158 \text{ MPa} \cdot \text{m}^{0.5}$, which is about one sixth that of Si ($0.9\text{--}1.1 \text{ MPa} \cdot \text{m}^{1/2}$) (Zhang et al. 2013b; Martyniuk et al. 2005). Surface roughness plays an important role to the IR performance of MCT detectors, and therefore the surface roughness of MCT wafers demands less than 1 nm, despite of their soft and brittle nature. This is a stringent requirement for MCT wafers, prior to becoming a high-performance IR detector. The

conventional machining consists of successive processes for MCT wafers (Garg et al. 2007; Singh et al. 2006, 2008; Sang et al. 2000). An MCT wafer is usually lapped using free abrasives with sizes at several microns (Garg et al. 2007) and then chemically polished by abrasives with sizes at submicron, finally followed by chemical etching using bromine methanol solution (Singh et al. 2006, 2008; Sang et al. 2000). These processes have kept basically constant since 2000 year. Nonetheless, bromine and methanol are toxic to both the operators and environment. Scratches are obvious even after the final mechanical polishing by abrasives with size of 50 nm (Singh et al. 2006). Furthermore, chemical etching using bromine methanol renders the richness of tellurium element on the MCT surfaces (Singh et al. 2006, 2008). Surface roughness root-mean-square (rms) of 1 nm is reported after chemical etching by bromine methanol (Singh et al. 2006). However, the rms is measured by atomic force microscopy (AFM) with a scanning area of $1 \times 1 \mu\text{m}^2$. With increasing a measurement area, surface roughness rms increases usually to several nanometers. Few machining process is reported on MCT wafers, as well as related surface science, except for their conventional machining processes. Hence, it is surprising that a novel approach of CMP and its surface science remain virgin ground for MCT wafers, which dominate the performance of IR detectors in a large body of work. No need to reticence, it is a challenge to develop a novel approach of CMP using environment-friendly slurry for MCT semiconductors.

12.3 Soft-Brittle Semiconductors Polishing with Environment-Friendly Slurries

12.3.1 Cadmium Zinc Telluride Semiconductors

The as-received $\text{Cd}_{0.96}\text{Zn}_{0.04}\text{Te}$ (111) wafers were 10 mm in length, 10 mm in width, and 1.5 mm in thickness, which were grown by the modified Bridgman method (Cohen et al. 2010). A precision polisher (YJ-Y380 of Shenyang Yanjia Co., Ltd. China) was employed to lap and polish the CZT wafers. SiC waterproof papers were put on a stainless steel plate as lapping pads. Four CZT wafers were fixed using a 502 glue on an aluminum plate of 150 mm in diameter uniformly along its periphery. CZT wafers were lapped using SiC papers with mesh sizes in a sequence of 2500, 5000, and 8000, and lapping time was set at 3, 2, and 2 min, respectively. During lapping, the pressure of the lapping plate was 20 kPa, and rotation speeds of both the CZT wafers and SiC papers were 65 rpm. After lapping, the CZT wafers were cleaned using deionized wafer and dried by compressed air for further characterization by an optical microscope (Olympus).

After the optical characterization, the SiC papers were replaced by floss polishing pads on the stainless steel plate. The morphology and size of SiO_2 spheres were measured by transmission electron microscopy (TEM, Tecnai spirit, FEI, Netherlands). The SiO_2 spheres were used to produce silica slurry with a pH value ranging from 7 to 7.5 and a weight percentage of 60%. The oxidant was H_2O_2 solution that had a volume percentage of 40%. A volume ratio of 7:4 between the silica slurry and

H_2O_2 solution was used to prepare the CMP slurry for the CZT wafers. Citric acid was used as a pH adjustor. The pH value of the CMP slurry varied from 4 to 4.5, which was decreased by the citric acid. During CMP, the rotation speeds of both the CZT wafers and floss polishing pads were 65 rpm. The polishing pressure and time were 30 kPa and 25 min, respectively. After CMP, the CZT wafers were cleaned and dried using deionized water and then compressed air.

Except the optical characterization, surface roughness and morphology of the CZT wafers were also measured by a precision noncontact surface profilometer (NewView 5022, Zygo, USA). X-ray photoelectron spectroscopy (XPS) was obtained by a VG ESCALAB MKII spectrometer with a magnesium $\text{K}\alpha$ excitation source. Electrochemical measurement was performed on an advanced electrochemical system (PARSTAT 2273, Princeton Applied Research, Ametek, Inc.). The referenced and auxiliary electrodes were saturated calomel electrode (SCE) of potassium chloride (KCl) and platinum (Pt) with purity of 99.99%, respectively. In electrochemical measurement, the pH values of H_2O_2 , citric acid, and mixed slurry consisting of H_2O_2 , SO_2 , and citric acid were 2.89, 4.45, and 7.61, respectively.

Figure 4a shows the rough surface of the as-received CZT wafer after multi-wire sawing. Figure 4b shows an optical image of lapped surface on a CZT wafer. There were neither embedded grains nor cracks, except for micro-scratches. Figure 4c

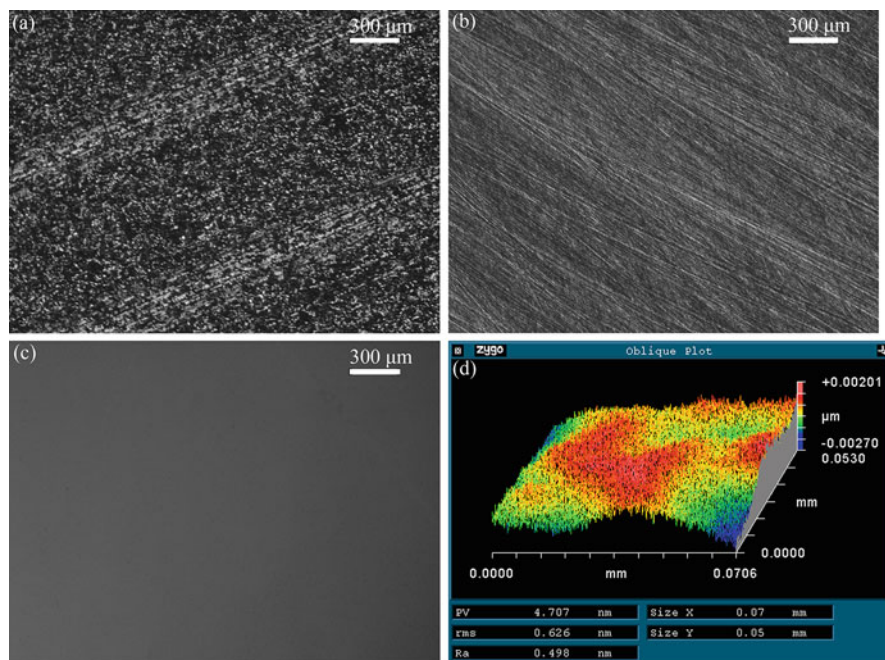


Fig. 4 Optical images of (a) as-received, (b) lapped using SiC waterproof papers with mesh size of #2500, (c) polished by the developed approach of CMP CZT wafers, and (d) surface roughness and morphology measured by a surface profilometer (NewView 5022) after CMP

shows the polished surface after CMP using the proposed approach. The polished surface looked like a mirror and was perfectly smooth, free of scratches and cracks. The surface roughness R_a , rms, and PV values were 0.498, 0.626, and 4.707 nm, respectively, with a measurement area of $70.6 \times 53 \mu\text{m}^2$. Therefore, the object of surface roughness rms < 1 nm is achieved using a novel approach with a measurement area of $50 \times 50 \mu\text{m}^2$.

Figure 5 shows the XPS spectra of tellurium (Te) element on different CZT surfaces. All the three surfaces exhibit the $\text{Te}^0 3d_{5/2}$, $\text{Te}^{4+} 3d_{5/2}$, $\text{Te}^0 3d_{3/2}$, and $\text{Te}^{4+} 3d_{3/2}$ peaks on the as-received CZT wafers, citric acid, and mixed slurry consisting of H_2O_2 , SiO_2 , and citric acid, as shown in Fig. 5a, c, and d, respectively, except for $\text{Te}^{4+} 3d_{5/2}$, $\text{Te}^{4+} 3d_{3/2}$, and extremely weak $\text{Te}^0 3d_{5/2}$ peaks on the CZT surface induced by H_2O_2 , as seen in Fig. 5b (Cheng et al. 2007; Li and Jie 2006).

Figure 6 shows XPS spectra of the cadmium (Cd) element on various CZT wafers. The XPS spectra of the as-received CZT surface reveal $\text{Cd}^0 3d_{5/2}$ and $\text{Cd}^0 3d_{3/2}$ peaks, as illustrated in Fig. 6a, which are different from the $\text{Cd}^{2+} 3d_{5/2}$ and $\text{Cd}^{2+} 3d_{3/2}$ peaks generated by H_2O_2 , citric acid, and mixed slurry of H_2O_2 , SiO_2 , and citric acid, as observed in Fig. 6b, c, and d, correspondingly (Aqariden et al. 2012; Okwechime et al. 2014).

Figure 7 shows the electrochemical curves of H_2O_2 , SiO_2 , citric acid, and mixed slurry made of H_2O_2 , SiO_2 , and citric acid as a function of potential versus SCE. The corrosion potential is also referred to open-circuit voltage (OCV). The corrosion

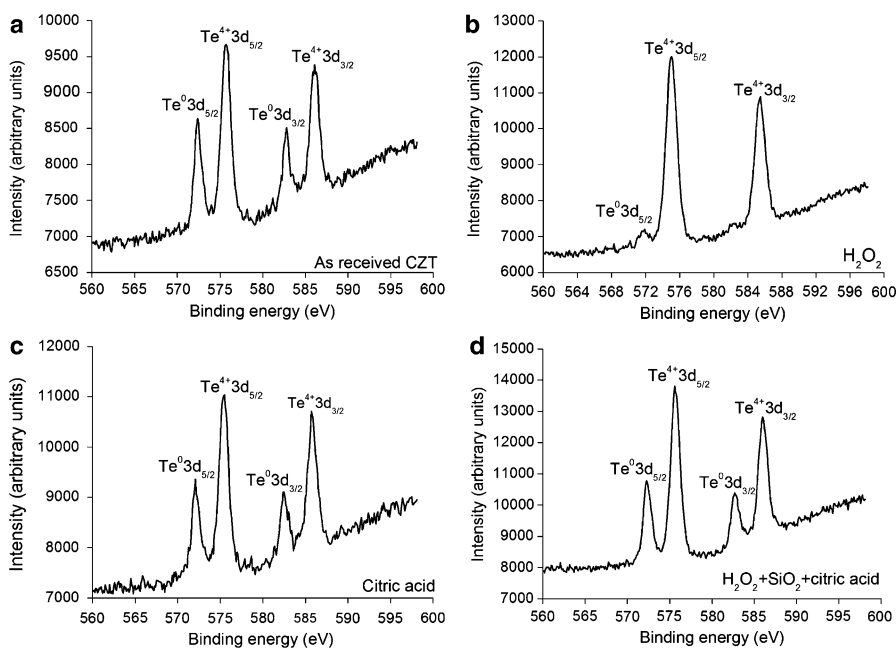


Fig. 5 XPS spectra of Te element on CZT surfaces of (a) as-received, (b) H_2O_2 , (c) citric acid, and (d) mixed slurry consisting of H_2O_2 , SiO_2 , and citric acid

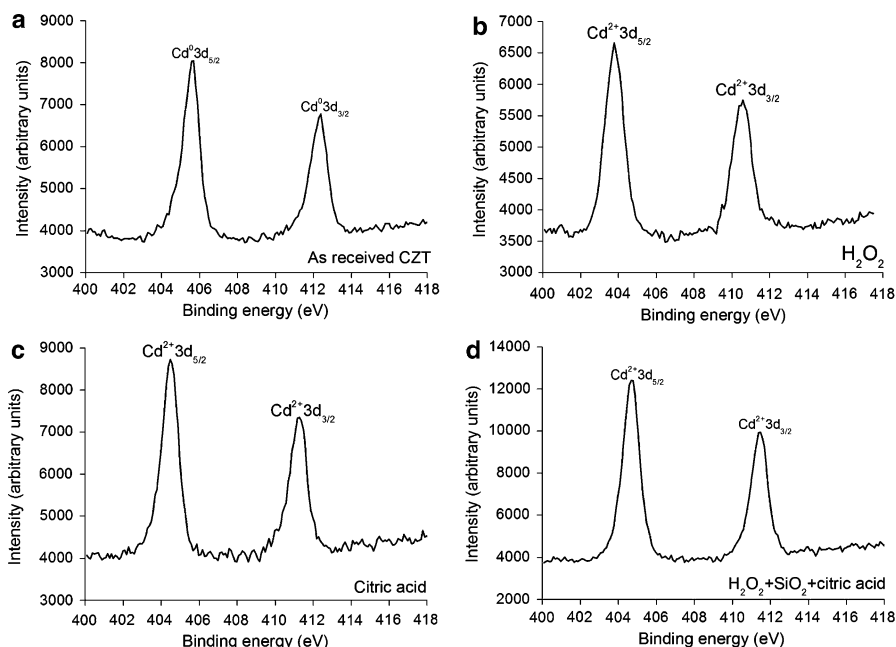
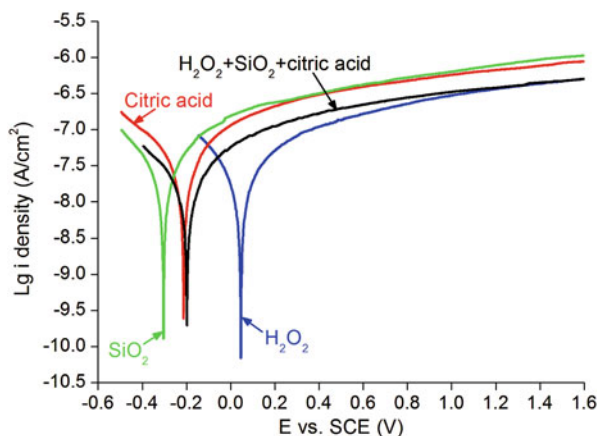


Fig. 6 XPS spectra of Cd element on CZT surfaces of (a) as-received, (b) H_2O_2 , (c) citric acid, and (d) mixed slurry including H_2O_2 , SiO_2 , and citric acid.

Fig. 7 Electrochemical curves of H_2O_2 , SiO_2 , citric acid, and mixed slurry made of H_2O_2 , SiO_2 , and citric acid as a function of potential versus SCE



potentials of SiO_2 , citric acid, mixed slurry, and H_2O_2 are -0.31 , -0.21 , -0.2 , and $+0.05$ V, respectively, and their passivation current densities are $10^{-6.5}$, $10^{-6.53}$, $10^{-6.77}$, and $10^{-6.96}$ A cm^{-2} , correspondingly, at the potential versus SCE of $+0.4$ V. At potential versus SCE of $+1.2$ V, the passivation current densities are $10^{-6.45}$, $10^{-6.43}$, $10^{-6.17}$, and $10^{-6.11}$ A cm^{-2} , for H_2O_2 , mixed slurry, citric acid, and SiO_2 , respectively (Feng and Gu 2013; Chaure et al. 2008).

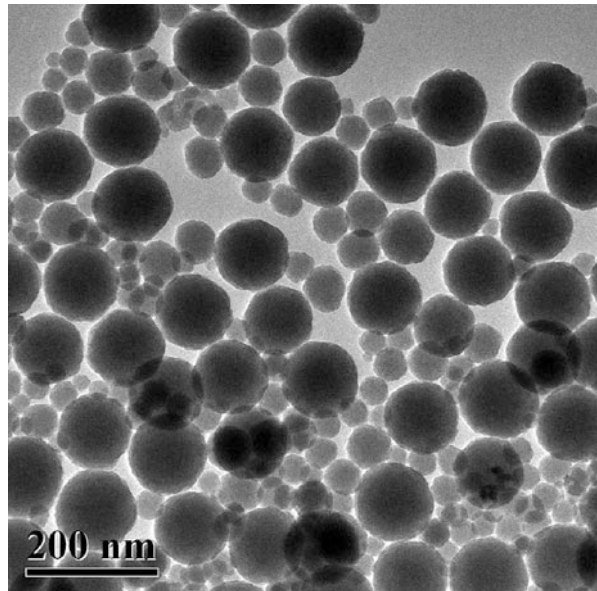
Fixed abrasives of SiC grains are used during lapping processes, which are effective in eliminating the embedding of free abrasives, as shown in Fig. 3b. The fixed-abrasive lapping is different from the previous findings, in which free abrasives are usually employed. Ultrafine SiC grains, such as mesh sizes of 2500, 5000, and 8000, are efficient in decreasing surface roughness, saving time and cost of CMP.

In the CMP slurry, H_2O_2 slowly decomposes into water and oxygen gas in air,



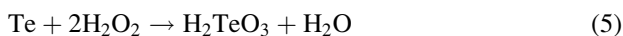
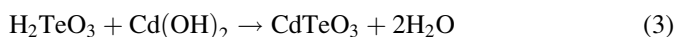
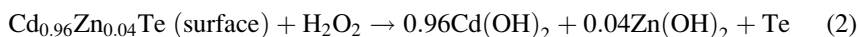
H_2O_2 solution is used as a medical disinfectant. In this work, H_2O_2 solution is diluted by silica slurry and citric acid solution, and it is environment-friendly. Even the mixed slurry composed of H_2O_2 , SiO_2 , and citric acid flushes hands, and the hands will turn into light yellow. After water flushing, the light yellow color fades. Silica slurry contains SiO_2 and deionized water. SiO_2 distributes widely in nature and occupies a weight percentage of 12% in the earth crust, such as stones mainly consisting of SiO_2 and calcium carbonate (CaCO_3). The size of SiO_2 spheres played a significant effect on the material removal rate (Zhang et al. 2010), and therefore the diameters of SiO_2 spheres varied from 25 to 118 nm, as shown in Fig. 8. Generally speaking, the distribution of particle size is important to controlling surface roughness, i.e., either a high material removal rate with large particles or low surface roughness with relatively small particles. An appropriate distribution of particle size could obtain a balance between the material removal rate and surface roughness, resulting in a relatively high material removal rate and low surface roughness. Thus, the distribution of particle size in this study expects to produce coherent effect for the material removal rate and surface roughness and achieve ultralow surface roughness

Fig. 8 TEM image of silica spheres with diameters ranging from 25 to 118 nm



at a relatively high material removal rate. Citric acid is a drink and is popular in the food industry. During the final step of cleaning the CZT wafers, deionized water and compressed air are used to displacing the previously toxic etchants and cleaning agents, such as BM^{20} , bromine-based etchants (Hossain et al. 2014), methanol (Aqariden et al. 2012), and ethanol (Lucile et al. 2011). Both deionized water and compressed air are natural. Thus, the novel CMP approach for CZT wafers are environment-friendly and can be applied to lapping, CMP, and cleaning processes.

Fundamental polishing mechanisms are investigated using XPS and electrochemical measurements. In Fig. 7, the passivation current density of the H_2O_2 solution is the lowest among the four solutions, implying that the most compact passivation films can be formed on the CZT wafers. Citric acid is a pH adjustor in the CMP slurry, and its passivation effect is similar to that of the silica slurry. This is attributed to the similar curves of passivation current density between the citric acid and the silica slurry. In the mixed slurry, the corrosion potential decreases from +0.05 of H_2O_2 solution to -0.2 V, diluting by SiO_2 slurry and citric acid. This leads to decreasing of the pH value of the H_2O_2 solution from 2.89 to 7.61 of the mixed slurry, whereas the passivation current density of the mixed slurry is the same as that of the H_2O_2 solution after potential versus SCE at +1.2 V. Consequently, H_2O_2 solution dominates the passivation current density, playing a key role in dissolving the CZT wafers and forming an ultrasurface with the lowest surface roughness. Thereby, the chemical reaction equations of the H_2O_2 solution are proposed with CZT wafers (Dean 1999; Wang et al. 2005; Chen 1994):

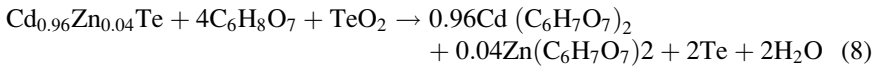


In Figs. 5a and 6a, $\text{Cd}^{0}3\text{d}$, $\text{Te}^{0}3\text{d}$, and $\text{Te}^{4+}3\text{d}$ are present. $\text{Cd}^{0}3\text{d}$ and $\text{Te}^{0}3\text{d}$ are derived from $\text{Cd}_{0.96}\text{Zn}_{0.04}\text{Te}$ surface. $\text{Te}^{4+}3\text{d}$ valence state comes from the following chemical reaction:



This is because of the as-received CZT wafers that are exposed in air after multi-wire sawing from an ingot of CZT. Te usually enriches on the surfaces of the CZT wafers, and therefore Eq. 7 prevails. Accordingly, Cd is at the state of $\text{Cd}^{0}3\text{d}$. With Eqs. 2, 3, 4, 5, and 6, the final reaction products are CdTeO_3 , ZnTeO_3 , and TeO_2 under the function of the H_2O_2 solution. This is verified by the $\text{Te}^{4+}3\text{d}$ valence state in Fig. 5b. As $\text{Cd}(\text{OH})_2$ and $\text{Zn}(\text{OH})_2$ are dissolved in H_2O_2 and mixed slurry with ion state, Eqs. 3 and 4 have priority than Eq. 5 for an elementary substance. In the

high concentration of the H_2O_2 solution, Eq. 5 reacts effectively, leading to an extremely small amount of Te left, as illustrated in Fig. 5b. However, in the mixed slurry, the H_2O_2 solution is greatly diluted to a pH value of 7.61; Eq. 5 reacts ineffectively, resulting in a large amount of Te appeared, as drawn in Fig. 5d. With the effect of H_2O_2 , $\text{Cd}(\text{OH})_2$ and CdTeO_3 are produced, which are presented in Eqs. 2 and 3, respectively. This is confirmed by Fig. 6b and d in the H_2O_2 and mixed slurry, correspondingly. Citric acid ionizes hydrogen (H) ions. The following equation happens:



With Eq. 8, $\text{Cd}^{2+}3\text{d}$ is found in Fig. 5c. Citric acid is a pH adjustor; passivation effect is similar to that of the silica slurry, as shown in Fig. 7. As a result, the dissolving effect of the citric acid for the CZT wafers is comparatively weak, resulting in both $\text{Te}^{4+}3\text{d}$ and $\text{Te}^{0}3\text{d}$ in Fig. 4c. On the other hand, CZT crystals are easy to slip under stress even induced by high-speed grinding, rather than forming amorphous phase, in terms of their low stacking fault energy ($9.7 \pm 1.7 \text{ mJ m}^{-2}$) (Zhang et al. 2012b, 2013b). In consequence, the polished surfaces of CZT wafers are usually crystalline (Zhang et al. 2016b).

12.3.2 Mercury Cadmium Telluride Semiconductors

As-received $\text{Hg}_{0.22}\text{Cd}_{0.78}\text{Te}$ (111) wafers were grown using modified Bridgman method and used as specimens (Zhang et al. 2012a). The wafers were 10 mm in diameter and 0.8 mm in thickness. Both approaches were employed to machine the MCT wafers: one is the conventional polishing, and another is the novel approach of CMP. In conventional polishing, free abrasives of alumina were used with size of 1 μm , and the polishing pad was the nubuck leather. Three MCT wafers were distributed on the periphery of a circular plate of aluminum alloy in diameter of 150 mm. During conventional polishing, both the rotation rates of polishing pads and MCT wafers were 40 rpm. The pressure and polishing time on the MCT wafers were 15 kPa and 10 min, respectively.

Fixed-abrasive waterproof papers of alumina were employed to lap the MCT wafers. The lapping slurry was deionized water. The waterproof papers were glued on a stainless steel plate and used as the lapping pads. The MCT wafers were lapped by abrasive papers with sizes in a sequence of 5, 2, and 1 μm . The lapping slurry was deionized water. The lapping pressure and time were 15 kPa and 10 s. The rotation rates of both MCT wafers and lapping pads were 40 rpm. After lapping, the MCT wafers were flushed and dried by deionized water and compressed air, respectively. The lapping pads were replaced by polishing pads of nubuck leather. Hydrogen peroxide (H_2O_2) was used as the oxidant with volume percentage of 30%. The pH adjustor was citric and malic acids. SiO_2 slurry had a weight percentage of 50%. The polishing slurry of CMP mainly consisted of H_2O_2 , SiO_2 , and citric and malic acids.

The pressure and time of CMP were 22 kPa and 20 min, respectively. During the CMP, the rotation rates of both MCT wafers and polishing pads were 60 rpm. The optimal volume ratio of SiO_2 and H_2O_2 to malic and citric acids was 10:4:5. The optimal pH value of the CMP slurry varied from 4 to 5 adjusted by malic and citric acids. After CMP, the MCT wafers were cleaned and dried using deionized water and compressed air, respectively.

Surface morphology was characterized using an optical microscope (Olympus MX40, Japan). Surface roughness was measured by a precision noncontact surface profilometer (Zygo, NewView 5022, USA). SiO_2 nanospheres were characterized using a TEM (Tecnai spirit, FEI, Netherlands). Electrochemical measurements were conducted by an advanced electrochemical system (PARSTAT 2273, Princeton Applied Research, Ametek, Inc.). The pH values were 2.95, 4.56, 8.43, and 7.54 in electrochemical measurements for H_2O_2 , malic and citric acids, SiO_2 , and mixed slurry consisting of H_2O_2 , SiO_2 , and malic and citric acids, respectively. SCE of KCl and platinum with purity of 99.99% were used for referenced and auxiliary electrodes, respectively. XPS spectra were measured using a VG ESCALAB MKII spectrometer with a magnesium $\text{K}\alpha$ excitation source.

Figure 9 shows the optical images on an MCT wafer after free abrasive polishing. Scratches and embedded abrasives are observed on the MCT wafer. Embedded abrasives of alumina are full of on the polished surface, even after flushing of deionized water and dried by compressed air.

Figure 10 shows the optical images of surface morphologies after fixed-abrasive lapping by alumina with a size of 5 μm and CMP using slurry consisting of SiO_2 and H_2O_2 with a volume ratio of 5:1. There are no embedded abrasives and cracks on the lapped surface of MCT wafers, except for uniform and subtle scratches, as shown in Fig. 10a and b. The polished surface has shallow scratches, as observed in Fig. 10c and d, even after CMP using slurry consisting of SiO_2 and H_2O_2 with a volume ratio of 5:1. This is attributed to the absence of malic and citric acids and deviation of H_2O_2 from the optimal volume ratio of SiO_2 to H_2O_2 for 5:2.

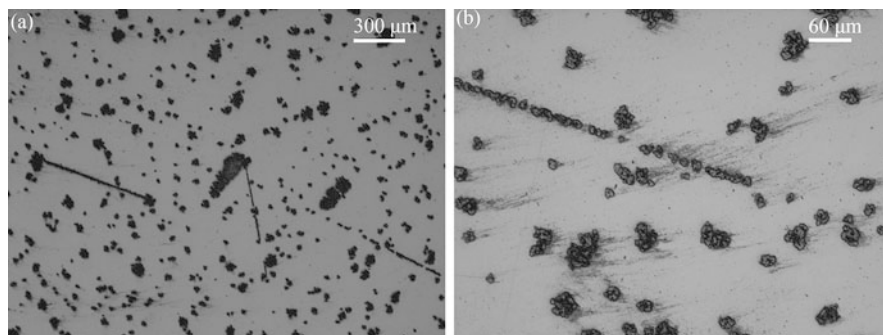


Fig. 9 Optical images on an MCT wafer after free abrasive polishing

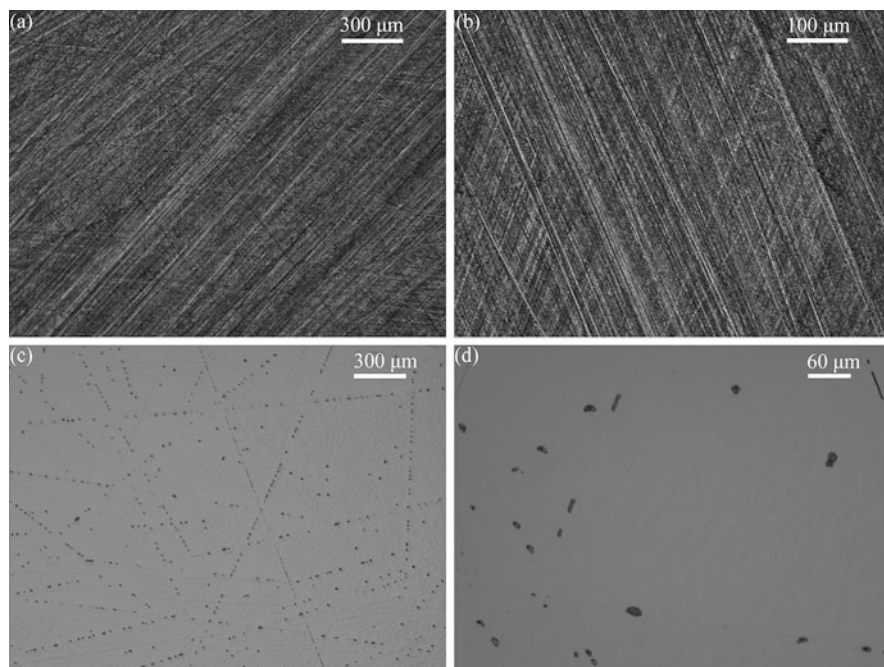


Fig. 10 Optical images of surface morphologies after fixed-abrasive lapping (a), (b) by alumina with a size of 5 μm and CMP (c), (d) using slurry consisting of SiO_2 and H_2O_2 with a volume ratio of 5:1

Figure 11 shows the TEM image of SiO_2 nanospheres in SiO_2 slurry after evaporation of solution. SiO_2 nanospheres have diameters varying from 20 to 120 nm and mainly distribute at four diameters of 20, 40, 60, and 120 nm.

Figure 12 shows the optical image and surface roughness on MCT wafers after CMP using environment-friendly CMP slurry with optimal volume ratio. The polished surface looks like a mirror, neither scratches, embedded abrasives, nor cracks on the MCT wafers, as illustrated in Fig. 12a. Surface roughness arithmetic average R_a , rms, and peak-to-valley (PV) values are 0.447, 0.553, and 4.736 nm, respectively, with a measurement area of $50 \times 70 \mu\text{m}^2$ on an MCT wafer after CMP using environment-friendly CMP slurry, as seen in Fig. 12b. The ultralow surface roughness verifies the validity of developed novel approach of CMP, using environment-friendly CMP slurry for such a large measurement area.

Figure 13 reveals the XPS spectra of Te elemental valence states on as-received, and H_2O_2 , malic and citric acids, and mixed slurry polished MCT wafers. Both $\text{Te}^{0}3\text{d}$ and $\text{Te}^{4+}3\text{d}$ peaks are present on an as-received MCT wafer, whereas only $\text{Te}^{0}3\text{d}$ peaks are observed on an MCT wafer after CMP using mixed slurry consisting of H_2O_2 , SiO_2 , and malic and citric acids (Singh et al. 2008; Cheng et al. 2007; Li and Jie 2006). $\text{Te}^{4+}3\text{d}$ peaks are very weak on MCT wafers after polishing, respectively, by H_2O_2 and malic and citric acids. Moreover, the

Fig. 11 TEM image of SiO₂ nanospheres in SiO₂ slurry after evaporation of solution

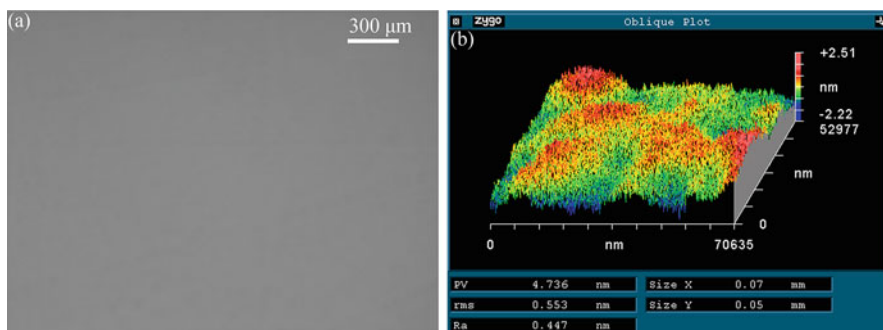
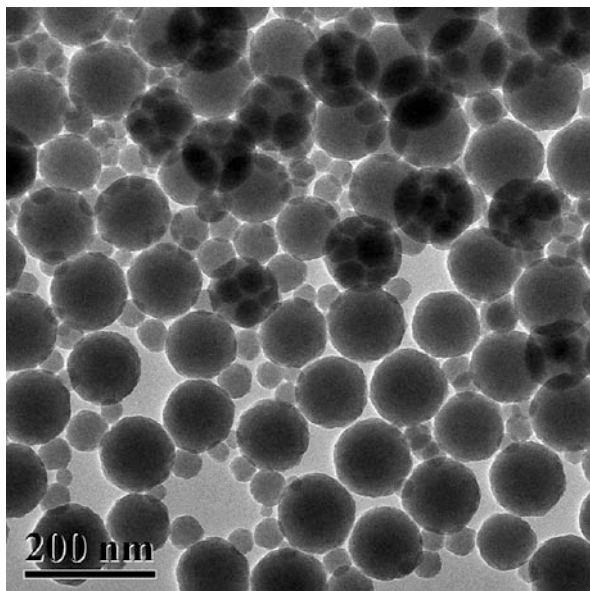


Fig. 12 Optical image (a) and surface roughness (b) on MCT wafers after CMP using environment-friendly CMP slurry with optimal volume ratio

Te⁴⁺3d peaks on an MCT wafer polished by malic and citric acids are weaker than those by H₂O₂.

Figure 14 illustrates the XPS spectra of Cd elemental valence states on as-received, and H₂O₂, malic and citric acids, and mixed slurry polished MCT wafers. Cd⁰3d peaks appear on all the polished MCT wafers, except the Cd²⁺3d peaks on the as-received MCT wafers (Aqariden et al. 2012; Okwechime et al. 2014).

Figure 15 shows the XPS spectra of Hg elemental valence states on as-received, and H₂O₂, malic and citric acids, and mixed slurry polished MCT wafers. Hg²⁺4f peaks are present on all the MCT wafers (Ramiro et al. 2001; Yang et al. 2015; Li et al. 1999).

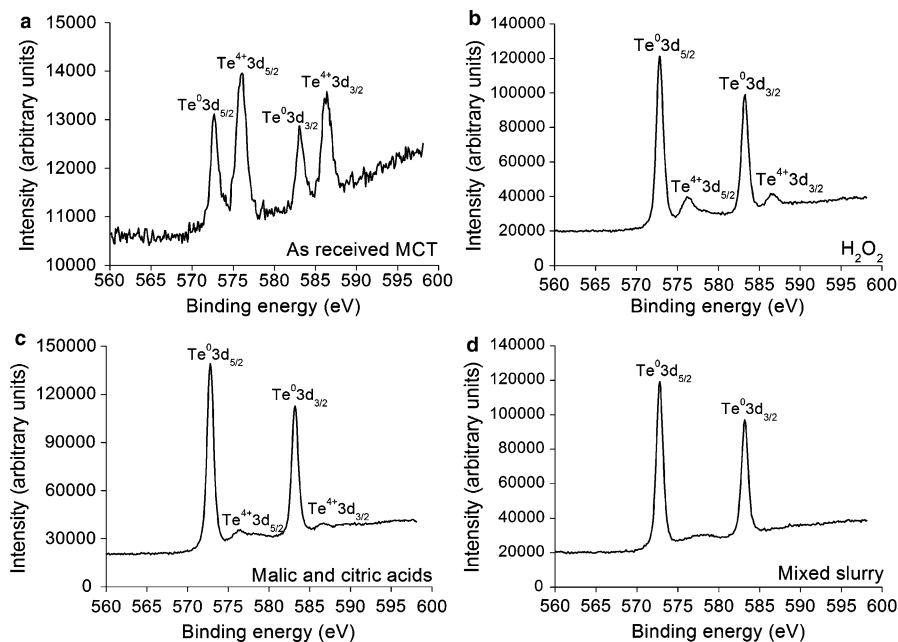


Fig. 13 XPS spectra of Te elemental valence states on (a) as-received, and (b) H_2O_2 , (c) malic and citric acids, and (d) mixed slurry polished MCT wafers

Figure 16 displays the electrochemical curves of current density as a function of potential versus SCE on MCT wafers polished by different slurry. Two passivated films are formed in each electrochemical curve. The corrosion potential of SiO_2 is 0.06 V. The first passivated film of SiO_2 is generated at 0.15 V and stable at current density of $10^{-5.8} \text{ A cm}^{-2}$ until 0.36 V. The second passivated film of SiO_2 is produced at 0.68 V and stable at current density of $10^{-4.8} \text{ A cm}^{-2}$ till 0.88 V. The corrosion potential of malic and citric acids shifts positively to 0.12 V. The first passivated film in malic and citric acids is formed at 0.16 V, and its current density is lower than that of SiO_2 with increasing potential versus SCE from 0.18 to 0.4 V. The second passivated film is produced at 1.0 V, corresponding to the current density of $10^{-2.6} \text{ A cm}^{-2}$, basically stable and slightly lower with the increasing potential versus SCE. This is two orders of magnitude higher than $10^{-4.8} \text{ A cm}^{-2}$ of SiO_2 . The corrosion potential of H_2O_2 is the highest at 0.36 V. However, there is no obvious transformation zone between the first and second passivated films of H_2O_2 . The current density of H_2O_2 is $10^{-3.7}$ at 1.0 V, which is in the middle between those of SiO_2 and malic and citric acids. The corrosion potential of mixed slurry is 0.18 V, consisting of H_2O_2 , SiO_2 , and malic and citric acids, which is higher than those of SiO_2 and malic and citric acids slurry. The current density of the first passivated film in mixed slurry is lower than that in SiO_2 , whereas the second passivated film of the former is approximately the same current density that of the latter. The malic and citric acids and mixed slurry have the lowest current density in the first and second passivated films among four solutions,

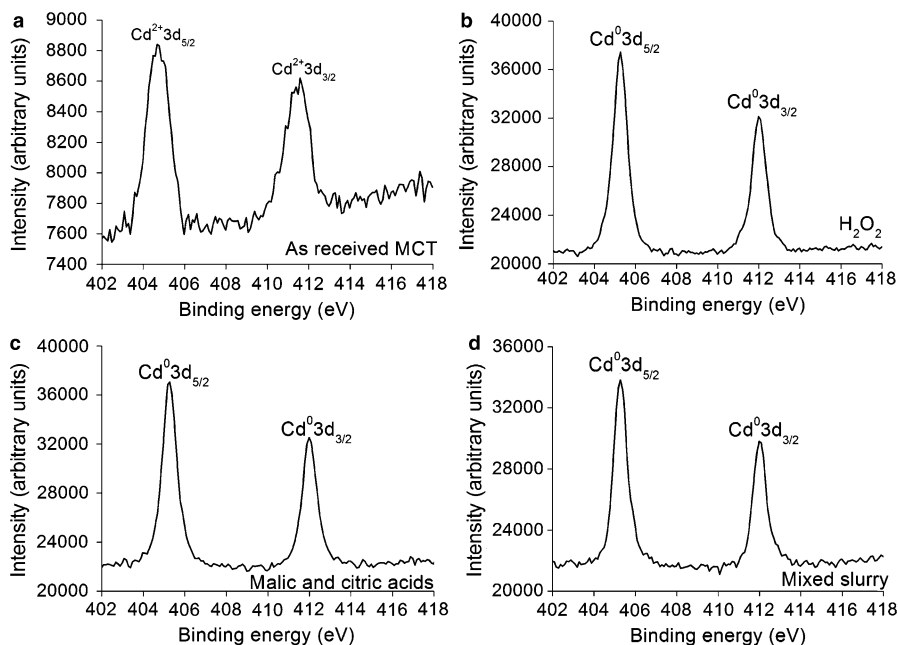


Fig. 14 XPS spectra of Cd elemental valence states on (a) as-received, and (b) H_2O_2 , (c) malic and citric acids, and (d) mixed slurry polished MCT wafers

respectively, meaning the malic and citric acids and mixed slurry dominate the first and second passivation process, correspondingly.

As MCT has soft and brittle nature, free abrasives of alumina are easy to embedding on the MCT wafers, as shown in Fig. 3. After embedding, it is difficult to remove the abrasives in the successive processes, resulting in the deteriorating of surface roughness. This is employed in the conventional machining processes for MCT semiconductors.

To avoid the embedding of free abrasives, fixed-abrasive lapping is used to machine the MCT wafers. Neither embedded abrasives nor cracks are found on the MCT wafers, except for uniform and subtle scratches, as observed in Fig. 10a and b. The hardness of MCT is only 0.5 GPa (Martyniuk et al. 2005; Zhang et al. 2012a), which is much softer than 17 GPa of alumina (Ahmad et al. 2015). Thus, ultrafine abrasives of alumina are used during lapping, obtaining lower surface roughness and saving time and cost for following CMP process. If the volume concentration of H_2O_2 is not appropriate, subtle scratches are left after CMP. Hereby, H_2O_2 plays an important role in removing the scratches, as illustrated in Fig. 10c and d.

The diameters of SiO_2 nanospheres distribute mainly at 20, 40, 60, and 120 nm, as observed in Fig. 11, leading to synergistically removing the passivated films formed in CMP. At an optimal volume concentration of ingredients, surface roughness R_a , rms, and PV values of 0.45, 0.55, and 4.74 nm are achieved, respectively, with a measurement area of $70 \times 50 \mu\text{m}^2$, as shown in Fig. 12b. Thereby, the

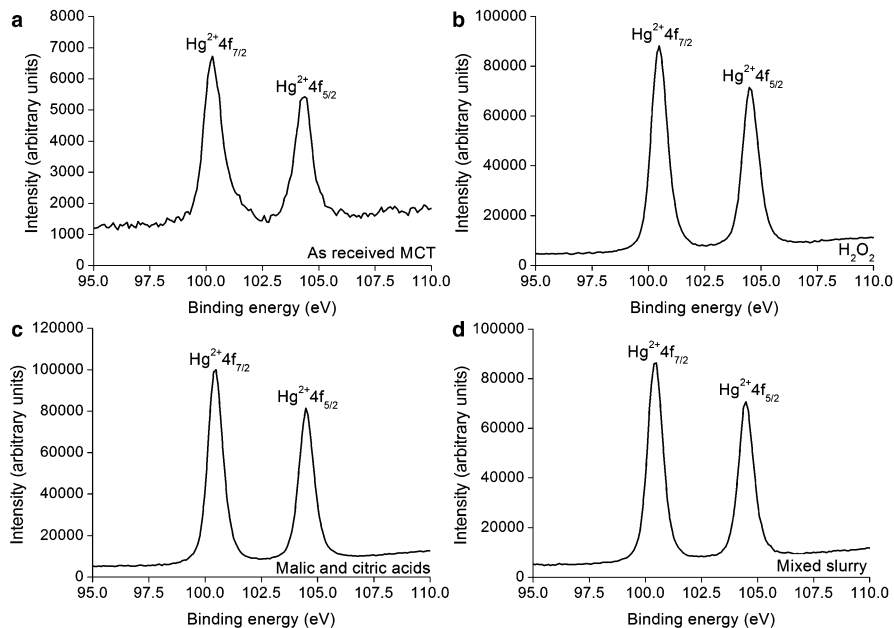
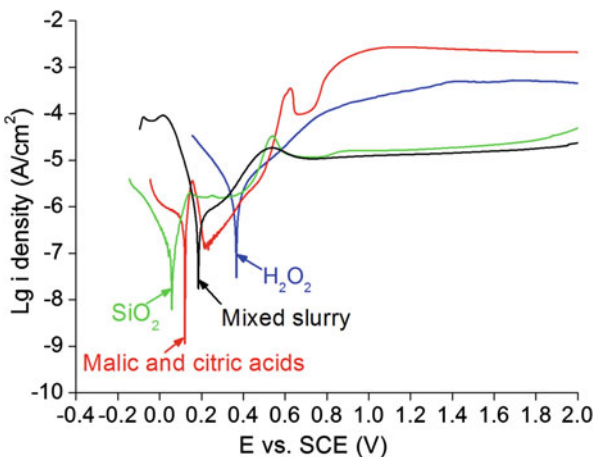


Fig. 15 XPS spectra of Hg elemental valence states on (a) as-received, and (b) H_2O_2 , (c) malic and citric acids, and (d) mixed slurry polished MCT wafers

Fig. 16 Electrochemical curves of current density as a function of potential versus SCE on MCT wafers polished by different slurries

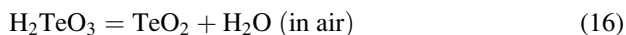
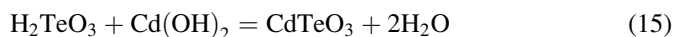
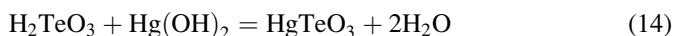
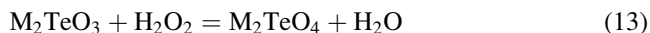
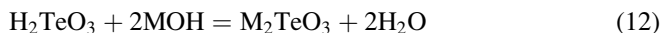
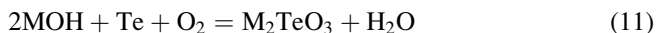
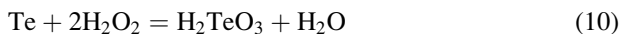
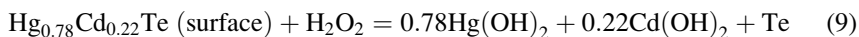


developed novel approach of CMP is extremely effective, to achieving mirror-like surface for MCT semiconductors with ultralow surface roughness.

The developed novel CMP slurry mainly consists of SiO_2 , H_2O_2 , and malic and citric acids. SiO_2 is commonly found in nature as quartz, and it is the major constituent of sand. Accordingly, SiO_2 is environment-friendly. H_2O_2 solution is

diluted by water and has a volume percentage of 30%. H_2O_2 solution decomposes into oxygen gas and water in air slowly, and it is environment-friendly. In the developed CMP slurry, H_2O_2 solution is further diluted by SiO_2 slurry and malic and citric acids. A finger dips in the mixed slurry containing H_2O_2 solution, and it turns light yellow. After flushing by tap water, the light yellow fades and the finger recovers the pristine color. Malic and citric acids are drinks and popular in food industry. Consequently, malic and citric acids are environment-friendly. Accordingly, the developed CMP slurry is environment-friendly. Fixed-abrasive lapping uses the waterproof alumina papers as lapping pads, and the lapping solution is deionized water. After the CMP, deionized water and compressed air are used to clean and dry the MCT wafers, respectively. During CMP, neither strong corrosive acids and alkali nor toxic chemical reagents are used, and the novel approach of CMP is environment-friendly.

Combining Figs. 10c and 16, H_2O_2 and SiO_2 dominate the forming of second passivated film, and the most scratches are removed, leaving subtle scratches on polished MCT wafers. SiO_2 slurry is composed of nanospheres, as shown in Fig. 11. To disperse the nanospheres, OH^- is added into the SiO_2 solution, resulting in the alkaline characteristic of SiO_2 solution with pH value of 8.43. Wherefore, following equations are proposed (Wang et al. 2005; Dean 1999):



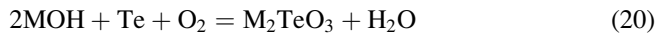
In Eqs. 11, 12, and 13, the M represents metal ions in SiO_2 slurry. Because H_2O_2 dissolves MCT well, most scratches are removed after CMP with low volume concentration of H_2O_2 , as observed in Fig. 10c.

MCT contains the Hg element, and it is easy to oxidize.

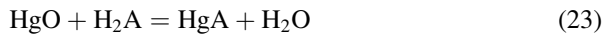
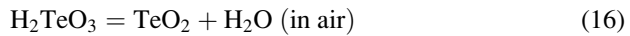
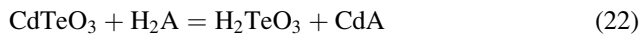
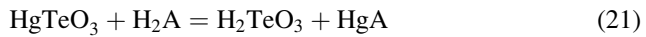


If MCT wafers are exposed in air for a bit long time, HgTeO_3 and CdTeO_3 are present (Singh et al. 2008). For a short time in air, the reaction of Eq. 17 prevails, and

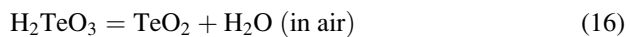
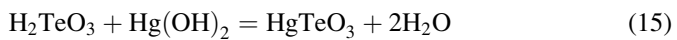
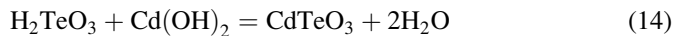
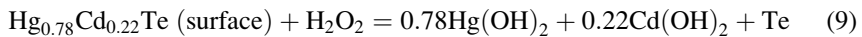
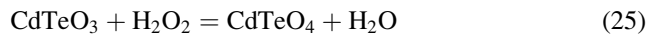
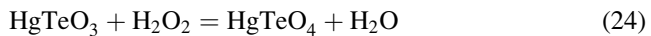
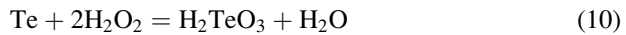
therefore Hg^{2+} 4f are found prior to and after CMP on MCT wafers. Equation 19 needs a bit more time to complete, and only Cd^{0} 3d appears after removing the oxidized film of CdTeO_3 on MCT wafers using H_2O_2 , malic and citric acids, and mixed slurry, respectively, as shown in Fig. 14. In MCT, the elemental concentration of Hg is more than Cd, and Eq. 18 dominates the oxidizing process. Consequently, HgTeO_3 are prominent in the oxidized film. During the first passivation process, malic and citric acids have the lowest current density, as shown in Fig. 16, indicating the less HgTeO_3 left induced by malic and citric acids than by H_2O_2 solution. This results in the weaker Te^{4+} 3d peaks of malic and citric acids than those of H_2O_2 solution, as illustrated in Fig. 13b and c. The mixed slurry has comprehensive advantages integrating the first and second passivation processes, compared to those in single H_2O_2 solution and malic and citric acids. Thus, the HgTeO_3 are dissolved completely in the mixed slurry; Te^0 3d are present after CMP, as revealed by Fig. 13d. During the first passivation process, the following equations are presented. For SiO_2 solution includes OH^- ions (Wang et al. 2005; Dean 1999):



For malic and citric acids contain H^+ ions,



In Eqs. 21, 22, and 23, A denotes an acid in malic and citric acids. For H_2O_2 solution,



During the first passivation process in SiO_2 slurry, only Eq. 20 takes place, resulting in its stable passivated current density, as shown in Fig. 16. For malic

and citric acids, Eqs. 21, 22, 23, and 24 happen simultaneously; the passivated current density varies sharply. For H_2O_2 solution, Eqs. 9, 10, 14, 15, and 16 occur in both the first and second passivation processes, and therefore there is no obvious transformation zone between the first and second passivated films, as indicated in Fig. 16. The pH value of the environment-friendly CMP slurry varies from 4 to 5, which is adjusted by malic and citric acids, due to the dominating effect of malic and citric acids in the first passivation process. This is to achieve a good passivated effect using the environment-friendly CMP slurry, in terms of the extremely weak passivation effect of malic and citric acids in the second passivation process, as illustrated in Fig. 16 (Zhang et al. 2016a).

12.4 Summary and Future Directions

In summary, fixed abrasives of SiC are used in lapping CZT wafers to eliminate effectively the embedded free abrasives to save time and cost for subsequent CMP processes. A novel CMP approach is proposed in which the newly developed slurries consist of mainly H_2O_2 , SiO_2 , and citric acid. The novel approach is environment-friendly. H_2O_2 solution dominates the passivation process, which is confirmed by electrochemical measurement. With the best passivation effect of H_2O_2 solution among four solutions, relatively strong $\text{Te}^{4+}3d$ peaks and an extremely small $\text{Te}^{0}3d_{5/2}$ peak are found.

A novel approach of CMP is proposed for MCT semiconductors. The whole machining process consists of lapping, CMP, and cleaning, which are environment-friendly. This is different from conventional machining processes, in which free abrasive lapping and polishing are usually used, followed by chemical etching using bromine methanol. Bromine methanol is toxic to both the environment and operators, which is necessary to be replaced by environment-friendly slurry. In electrochemical measurements, the first and second passivation processes are confirmed. The first passivation process is related to the dissolution of oxidized films formed on the MCT wafers. The second passivation process is to dissolve the MCT wafers. During the first process, malic and citric acids play a leading role, and the mixed slurry dominates the second process. The fundamental mechanisms of passivation processes are investigated using XPS and electrochemical measurements. Chemical reaction equations are proposed to elucidate the nature of developed novel approach of CMP for MCT semiconductors.

CMP is the most expensive and complicated process for soft-brittle semiconductors, due to the operation, transportation, storage, and posttreatment. Environment-friendly slurries are the tendency of development for soft-brittle semiconductors, as well as for the CMP industry. The developed environment-friendly slurries are used for soft-brittle semiconductors. They will be enlarged for the applications in CMP of nickel and titanium alloys (Zhang et al. 2018), and other metals.

References

- Ahmad I, Islam M, Abdo HS, Subhani T, Khalil KA, Almajid AA, Yazdani B, Zhu YQ (2015) Toughening mechanisms and mechanical properties of graphene nanosheet-reinforced alumina. *Mater Des* 88:1234–1243. <https://doi.org/10.1016/j.matdes.2015.09.125>
- Androulakis J, Peter SC, Li H, Malliakas CD, Peters JA, Liu ZF, Wessels BW, Song JH, Jin H, Freeman AJ, Kanatzidis MG (2011) Dimensional reduction: a design tool for new radiation detection materials. *Adv Mater* 23:4163–4167. <https://doi.org/10.1002/adma.201102450>
- Aqariden F, Tari S, Nissanka K, Li J, Kioussis N, Pimpinella RE, Dobrowolska M (2012) Influence of surface polishing on the structural and electronic properties of CdZnTe surfaces. *J Electron Mater* 41:2893–2898. <https://doi.org/10.1007/s11664-012-2126-2>
- Chandra A, Anderson G, Melkote S, Gao W, Haitjema H, Wegener K (2014) Role of surfaces and interfaces in solar cell manufacturing. *CIRP Ann Manuf Technol* 63:797–819. <https://doi.org/10.1016/j.cirp.2014.05.008>
- Chaure NB, Chaure S, Pandey RK (2008) Cd_{1-x}Zn_xTe thin films formed by non-aqueous electrochemical route. *Electrochim Acta* 54:296–304. <https://doi.org/10.1016/j.electacta.2008.07.081>
- Chen SC (1994) Important inorganic chemical reactions, 3rd edn. Shanghai Press of Science and Technology, Shanghai, p 947
- Cheng X, Zhu SF, Zhao BJ, He ZY, Gao DY, Fang J (2007) Effect of surface preparation on the properties of Au/p-Cd_{1-x}Zn_xTe. *Appl Surf Sci* 253:8404–8407. <https://doi.org/10.1016/j.apsusc.2007.04.008>
- Cohen TG, Sinkevich O, Levinshtein M, Ruzin A, Goldfarb I (2010) Atomic structure and electrical properties of In(Te) nanocontacts on CdZnTe(110) by scanning probe microscopy. *Adv Funct Mater* 20:215–223. <https://doi.org/10.1002/adfm.200900812>
- Dean JA (1999) Lange's handbook of chemistry, 15th edn. McGraw-Hill Company, New York, pp 8124–8139
- Duff MC, Hunter DB, Burger A, Groza M, Buliga V, Black DR (2008) Effect of surface preparation technique on the radiation detector performance of CdZnTe. *Appl Surf Sci* 254:2889–2892. <https://doi.org/10.1016/j.apsusc.2007.10.064>
- Feng YY, Gu M (2013) The electrochemical behavior of tellurium on GCE in sol and solutions. *Electrochim Acta* 90:416–420. <https://doi.org/10.1016/j.electacta.2012.12.067>
- Garg A, Kapoor A, Tripathi KN, Bansal SK (2007) Laser induced damage studies in mercury cadmium telluride. *Opt Laser Technol* 39:1319–1327. <https://doi.org/10.1016/j.optlastec.2006.12.002>
- Hossain A, Bolotnikov AE, Camarda GS, Cui Y, Jones D, Hall J, Kim KH, Mwathi J, Tong X, Yang G, James RB (2014) Novel approach to surface processing for improving the efficiency of CdZnTe detectors. *J Electron Mater* 43:2771–2777. <https://doi.org/10.1007/s11664-013-2698-5>
- Ivanits'ka VG, Moravec P, Franc J, Tomashik VM, Tomashik ZF, Masek K, Chukhnenko PS, Hoschl P, Ulrych J (2011) Chemical polishing of CdTe and CdZnTe in iodine-methanol etching solutions. *J Electron Mater* 40:1802–1808. <https://doi.org/10.1007/s11664-011-1649-2>
- Lei W, Antoszewski J, Faraone L (2015) Progress, challenges, and opportunities for HgCdTe infrared materials and detectors. *Appl Phys Rev* 2:041303. <https://doi.org/10.1063/1.4936577>
- Li Q, Jie WQ (2006) Surface passivation and electrical properties of p-CdZnTe crystal. *Semicond Sci Technol* 21:72–75. <https://doi.org/10.1088/0268-1242/21/1/013>
- Li YD, Ding Y, Liao HW, Qian YT (1999) Room-temperature conversion route to nanocrystalline mercury chalcogenides HgE (E = S, Se, Te). *J Phys Chem Solids* 60:965–968. [https://doi.org/10.1016/S0022-3697\(98\)00349-7](https://doi.org/10.1016/S0022-3697(98)00349-7)
- Lin ZC, Wang RY, Ma SH (2018) Theoretical model and experimental analysis of chemical mechanical polishing with the effect of slurry for abrasive removal depth and surface morphology of silicon wafer. *Tribol Int* 117:119–130. <https://doi.org/10.1016/j.triboint.2017.08.021>
- Martyniuk M, Sewell RH, Musca CA, Dell JM, Faraone L (2005) Nanoindentation of HgCdTe prepared by molecular beam epitaxy. *Appl Phys Lett* 87:251905. <https://doi.org/10.1063/1.2143411>

- Okwechime IO, Egarievwe SU, Hossain A, Hales ZM, Egarievwe AA, James RB (2014) Chemical treatment of CdZnTe radiation detectors using hydrogen bromide and ammonium-based solutions. *Proc SPIE Int Soc Opt Eng* 9213:92130Y. <https://doi.org/10.1117/12.2063067>
- Pelenc D, Merlin J, Etcheberry A, Ballet P, Baudry X, Brellier D, Destefanis V, Ferron A, Fougères P, Giotta D, Grangier C, Mollard L, Perez A, Rochette F, Rubaldo L, Vaux C, Vigneron J, Zanatta JP (2014) Development of a method for chemical-mechanical preparation of the surface of CdZnTe substrates for HgCdTe-based infrared focal-plane arrays. *J Electron Mater* 43:3004–3011. <https://doi.org/10.1007/s11664-014-3175-5>
- Qiao Y, Chen J (2008) Resistance of through-thickness grain boundaries to cleavage cracking in silicon thin films. *Scr Mater* 59:251–254. <https://doi.org/10.1016/j.scriptamat.2008.03.022>
- Ramiro J, Galan L, Camarero EG, Montero I, Laaziz Y (2001) X-ray photoelectron spectroscopy of electrodeposited cadmium mercury telluride thin films and their native surface oxides. *J Mater Res* 16:1942–1952. <https://doi.org/10.1557/JMR.2001.0266>
- Rogalski A (2005) HgCdTe infrared detector material: history, status and outlook. *Rep Prog Phys* 68:2267–2336. <https://doi.org/10.1088/0034-4885/68/10/R01>
- Ruzin A, Sinkevich O, Cohen TG, Goldfarb I (2012) Anomalous behavior of epitaxial indium nanocontacts on cadmium-zinc-telluride. *Appl Phys Lett* 101:132108. <https://doi.org/10.1063/1.4754706>
- Sang WB, Ju JH, Shi WM, Qian YB, Wang LJ, Xia YB, Wu WH, Fang JX, Li YJ, Zhao J, Gong HM (2000) Comparison of physical passivation of $Hg_{1-x}Cd_xTe$. *J Cryst Growth* 214:265–268. [https://doi.org/10.1016/S0022-0248\(00\)00085-3](https://doi.org/10.1016/S0022-0248(00)00085-3)
- Singh RR, Kaushik D, Gupta D, Sharma RK, Pandey RK (2006) Investigation of passivation processes for HgCdTe/CdS structure for infrared application. *Thin Solid Films* 510:235–240. <https://doi.org/10.1016/j.tsf.2005.12.201>
- Singh RR, Kaushik D, Sharma M, Gupta DK, Pandey RK (2008) Studies on surface processing and passivation of p- $Hg_{1-x}Cd_xTe$. *Semicond Sci Technol* 23:015016. <https://doi.org/10.1088/0268-1242/23/1/015016>
- Tari S, Aqariden F, Chang Y, Ciani A, Grein C, Li J, Kioussis N (2014) Structural and electronic properties of gold contacts on CdZnTe with different surface finishes for radiation detector applications. *J Electron Mater* 43:2978–2983. <https://doi.org/10.1007/s11664-014-3167-5>
- Teague LC, Duff MC, Cadieux JR, Soundararajan R, Shick CR, Lynn KG (2011) Characterization of etch pit formation via the Everson-etching method on CdZnTe crystal surfaces from the bulk to the nanoscale. *Nucl Instrum Methods Phys Res Sect A* 652:178–182. <https://doi.org/10.1016/j.nima.2010.09.061>
- Venkatasamy V, Jayaraju N, Cox SM, Thambidurai C, Stickney JL (2007) Studies of $Hg_{1-x}Cd_xTe$ formation by electrochemical atomic layer deposition and investigations into bandgap engineering. *J Electrochem Soc* 154:H720–H725. <https://doi.org/10.1149/1.2745677>
- Wang XQ, Jie WQ, Li Q, Gu Z (2005) Surface passivation of CdZnTe wafers. *Mater Sci Semicond Process* 8:615–621. <https://doi.org/10.1016/j.mssp.2005.11.001>
- Wang L, Zhou P, Yan Y, Zhang B, Kang RK, Guo DM (2017) Chemical-mechanical wear of monocrystalline silicon by a single pad asperity. *Int J Mach Tools Manuf* 120:61–71. <https://doi.org/10.1016/j.ijmactools.2017.05.001>
- Yang G, Bolotnikov AE, Cui Y, Camarda GS, Hossain A, Kim KH, Gul R, James RB (2011) Low-temperature spatially resolved micro-photoluminescence mapping in CdZnTe single crystals. *Appl Phys Lett* 98:261901. <https://doi.org/10.1063/1.3603930>
- Yang J, Hu YP, Tan JW, Jia L, Zhua YH, Yu JS (2015) Ultra-bright near-infrared-emitting HgS/ZnS core/shell nanocrystals for in vitro and in vivo imaging. *J Mater Chem B* 3:6928–6938. <https://doi.org/10.1039/c5tb01034a>
- Zazvorka J, Franc J, Moravec P, Jesenska E, Sedivy L, Ulrych J, Masek K (2014) Contactless resistivity and photoconductivity correlation to surface preparation of CdZnTe. *Appl Surf Sci* 315:144–148. <https://doi.org/10.1016/j.apsusc.2014.07.104>
- Zha FX, Zhou SM, Ma HL, Yin F, Zhang B, Li TX, Shao J, Shen XC (2008) Laser drilling induced electrical type inversion in vacancy-doped p-type HgCdTe. *Appl Phys Lett* 93:151113. <https://doi.org/10.1063/1.3001930>

- Zhang ZY, Gao H, Jie WQ, Guo DM, Kang RK, Li Y (2008) Chemical mechanical polishing and nanomechanics of semiconductor CdZnTe single crystals. *Semicond Sci Technol* 23:105023. <https://doi.org/10.1088/0268-1242/23/10/105023>
- Zhang ZF, Liu WL, Song ZT (2010) Particle size and surfactant effects on chemical mechanical polishing of glass using silica-based slurry. *Appl Opt* 49:5480–5485. <https://doi.org/10.1364/AO.49.005480>
- Zhang ZY, Huo FW, Wu YQ, Huang H (2011) Grinding of silicon wafers using an ultrafine diamond wheel of a hybrid bond material. *Int J Mach Tools Manuf* 51:18–24. <https://doi.org/10.1016/j.ijmachtools.2010.10.006>
- Zhang ZY, Song YX, Huo FW, Guo DM (2012a) Nanoscale material removal mechanism of soft-brittle HgCdTe single crystals under nanogrinding by ultrafine diamond grits. *Tribol Lett* 46:95–100. <https://doi.org/10.1007/s11249-012-9924-9>
- Zhang ZY, Xu CG, Zhang XZ, Guo DM (2012b) Mechanical characteristics of nanocrystalline layers containing nanotwins induced by nanogrinding of soft-brittle CdZnTe single crystals. *Scr Mater* 67:392–395. <https://doi.org/10.1016/j.scriptamat.2012.05.033>
- Zhang ZY, Li FY, Ma GJ, Kang RK, Guo XG (2013a) Ultrahigh hardness and improved ductility for nanotwinned mercury cadmium telluride. *Scr Mater* 69:231–234. <https://doi.org/10.1016/j.scriptamat.2013.04.007>
- Zhang ZY, Zhang XZ, Xu CG, Guo DM (2013b) Characterization of nanoscale chips and a novel model for face nanogrinding on soft-brittle HgCdTe films. *Tribol Lett* 49:203–215. <https://doi.org/10.1007/s11249-012-0058-x>
- Zhang ZY, Wang B, Kang RK, Zhang B, Guo DM (2015a) Changes in surface layer of silicon wafers from diamond scratching. *CIRP Ann Manuf Technol* 64:349–352. <https://doi.org/10.1016/j.cirp.2015.04.005>
- Zhang ZY, Yang S, Guo DM, Yuan BY, Guo XG, Zhang B, Huo YX (2015b) Deformation twinning evolution from a single crystal in a face-centered-cubic ternary alloy. *Sci Rep* 5:11290. <https://doi.org/10.1038/srep11290>
- Zhang ZY, Wang B, Zhou P, Guo DM, Kang RK, Zhang B (2016a) A novel approach of chemical mechanical polishing using environment-friendly slurry for mercury cadmium telluride semiconductors. *Sci Rep* 6:22466. <https://doi.org/10.1038/srep22466>
- Zhang ZY, Wang B, Zhou P, Kang RK, Zhang B, Guo DM (2016b) A novel approach of chemical mechanical polishing for cadmium zinc telluride wafers. *Sci Rep* 6:26891. <https://doi.org/10.1038/srep26891>
- Zhang ZY, Shi ZF, Du YF, Yu ZJ, Guo LC, Guo DM (2018) A novel approach of chemical mechanical polishing for a titanium alloy using an environment-friendly slurry. *Appl Surf Sci* 427:409–415. <https://doi.org/10.1016/j.apsusc.2017.08.064>
- Zheng Q, Dierre F, Crocco J, Carcelen V, Bensalah H, Plaza JL, Dieguez E (2011) Influence of surface preparation on CdZnTe nuclear radiation detectors. *Appl Surf Sci* 257:8742–8746. <https://doi.org/10.1016/j.apsusc.2011.05.098>



Three-Dimensional Fabrication of Micro-/Nanostructure Using Scanning Probe Lithography

13

Yanquan Geng and Yongda Yan

Contents

13.1	Introduction	446
13.2	Principle of AFM Tip-Based Mechanical Nanomachining	447
13.3	Fabrication of 3D Nanostructure by Material Removal	449
13.3.1	Selection of Feed Direction	449
13.3.2	Fabrication 3D Nanostructure by Controlling the Applied Normal Load	452
13.3.3	Fabrication 3D Nanostructure by Controlling the Feed Value	457
13.4	Fabrication of 3D Nanostructure by Stick-Slip Process	461
13.5	Fabrication of 3D Nanostructure by Combining the Material Accumulation and the Machined Nanogroove	470
13.6	Summary and Outlook	472
	References	475

Abstract

As one of the tip-based nanofabrication approaches, the atomic force microscope (AFM) tip-based nanomechanical machining method has been successfully utilized to fabricate three-dimensional (3D) nanostructure. First, the principle of AFM tip-based mechanical nanomachining is introduced, which includes contact and tapping modes. Second, fabrication of 3D nanostructure by material removal is presented. This part contains force- and feed-control approaches. Third, ripple-type nanostructure machined with stick-slip process is described. This method is usually implemented on the polymer materials. Finally, a novel machining method combining the material pileup and the machined groove to form a 3D nanostructure is presented. It is expected that this chapter will serve to aid in the advance of the fabrication of 3D nanostructure and expand its applications in various fields.

Y. Geng · Y. Yan (✉)
Center for Precision Engineering, Harbin Institute of Technology,
Harbin, Heilongjiang, China
e-mail: yanyongda@hit.edu.cn

Keywords

Atomic force microscopy · Nanomechanical machining · 3D nanostructure

13.1 Introduction

With the rapid development of the nanotechnology, more and more nanostructures have been used in various fields, such as nanofluidic (Peng and Li 2016; Duan et al. 2016), nanosensor (Kim et al. 2009; Barton et al. 2010), and nanooptics (Kumar et al. 2012; Dregely et al. 2013). However, how to fabricate the nanostructure with desired dimensions is still a hot and difficult problem. There are a number of methods to produce three-dimensional (3D) nanostructure, including nanoimprint lithography (Liang and Chou 2008), focused ion-beam nanolithography (FIB) (Menard and Ramsey 2011), and electrochemical machining (Zhan et al. 2016). However, due to the properties of complexity, low throughput, and/or cost of implementation, these approaches are restricted for more extensive applications.

The atomic force microscopy (AFM) tip-based nanofabrication method has been proved as a powerful and feasible approach to create nanostructure with high quality, due to the advantages of nanoscale machining accuracy, wide range of applicable materials, atmospheric environment requirement, and low cost (Yan et al. 2015). The AFM tip-based nanofabrication method includes dip-pen nanolithography (Richard et al. 1999), thermochemical nanolithography (Pires et al. 2010), local anode oxidation (Dagata 1995), and nanomechanical machining methods (Yan et al. 2015). The nanomechanical machining method is the easiest and most flexible approach among the various AFM tip-based nanofabrication techniques. Some scholars have utilized this nanomechanical machining method to fabrication nanogroove (Geng et al. 2014), 2D (Brousseau et al. 2013), and 3D (Yan et al. 2010) nanostructures on different materials, such as metal (Geng et al. 2013a), polymer (Geng et al. 2016a), and semiconductor (Lin and Hsu 2012). The fabrication of 3D nanostructure is the most complicated and difficult. Mao et al. found that the material cannot be removed effectively to form the material pileup when using the silicon AFM tip to conduct nanoscratching (Mao et al. 2009). Thus, the authors utilized the material pileup to form 3D nanostructure by controlling the scratching trajectory. Based on this method, a steric Taiwan map has been fabricated (Mao et al. 2009). However, the machining accuracy and repeatability of this method is needed to be improved. Yan et al. used gray-scale map to fabricate human face on the aluminum alloy surface (Yan et al. 2010). They employed a 3D high-precision stage to take the place of the original stage of the AFM. During the machining process, the AFM tip remained stationary, and the motion of the sample is controlled by the 3D high precision using the gray-scale map. The relative displacement between the sample and the AFM tip can result in the change of the deflection of the tip cantilever, which can thus cause the variation of the applied normal load by the AFM tip on the sample surface to achieve the fabrication of 3D nanostructure. However, in this proposed method, the relationship

between the machining parameters and the machined depth was not given. Thus, the dimensions of the machined 3D nanostructure are unpredictable.

In this chapter, we review several approaches to fabricate 3D nanostructure with desired dimensions by using the AFM tip-based nanomechanical machining technique. These methods will advance the application of the AFM tip-based nanomechanical machining technique in various fields.

13.2 Principle of AFM Tip-Based Mechanical Nanomachining

Since the AFM was invented in 1986 by Binnig et al. (1986), it has been considered as a profiler with nano-precision. The interaction force between the tip and the sample surface is usually set as several hundred nano-newtons to guarantee no damage occurring when measuring the target surface. However, when this force increases to several micro-newtons, the plastic deformation of the sample surface may be occurring during the scanning process, especially for the soft materials. Some scholars utilized this principle to conduct nanomachining on the surface with good quality, due to the motion limitation of the AFM PZT in z direction. The mechanical machining mode of the AFM tip-based nanofabrication technique mainly includes contact and tapping modes, which corresponds to the typical scanning modes of the AFM. For the contact mode, the interaction force between the tip and the sample is controlled by the deflection of the cantilever of the AFM tip. This applied normal load can be kept constant by adjusting the deflection of the tip cantilever. The deflection of the cantilever is controlled by the motion of the AFM PZT in z direction through an optical lever system. Thus, to achieve 3D nanostructure, one method can be changing the applied normal load according to the corresponding machined depth by controlling the vertical motion of the AFM PZT in z direction. The applied normal load can be calculated by:

$$F_N = K_N \cdot s \cdot V_{\text{setpoint}} \quad (1)$$

where K_N is the normal spring constant of the tip cantilever, s is the sensitivity of the position sensitive detector (PSD), and V_{setpoint} is represented the vertical voltage value preset by the user. The product of s and V_{setpoint} is the deflection of the tip cantilever in the vertical direction. Thus, the applied normal load can be controlled by the preset value of V_{setpoint} directly.

For the tapping mode, the interaction force is not only related to the properties of the tip and sample including tip radius, spring constant of the tip cantilever, and the mechanical properties of the sample material, but also concerned with the preset machining parameters, such as the driven amplitude, the driving frequency, and the tip-sample distance (Chen et al. 1994; Salapaka et al. 2000; Tamayo and Garcia 1996). The tapping mode of the AFM tip is always assumed as a damping oscillator system. This system is driven by a sinusoidal force, and the substrate is deformable, which can be expressed by (Liu et al. 2012):

$$m \frac{d^2 z}{dt^2} = -K_N z - \frac{m\omega_0}{Q} \frac{dz}{dt} + F_0 \sin(\omega t) + F(z_c, z) \quad (2)$$

where m is the effective mass of this oscillator system, which can be obtained by K_N/ω_0^2 . ω_0 is the angular resonance frequency, and Q is the quality factor of the tip cantilever. The driven force can be expressed as $F_0 \sin(\omega t)$. F_0 can be calculated as $K_N \times A_m$; A_m is the driven amplitude. $F(z_c, z)$ represents the interaction force between the tip and the sample at one position deviated from the center of the vibration in the vertical direction, z , and z_c is the tip-sample separation without the oscillation of the cantilever. In terms of the vertical position z , $F(z_c, z)$ can be divided into two scenarios: when the distance between the tip and the sample is larger than a certain value a_0 , the van der Waals model should be employed to obtain $F(z_c, z)$; while, when the tip-sample distance is smaller than this value a_0 , the Hertz contact model should be used to calculate $F(z_c, z)$. Thus, $F(z_c, z)$ can be expressed as (Liu et al. 2012):

$$F(z_c, z) = \begin{cases} -\frac{AR}{6(z_c + z)^2} & z_c + z > a_0 \\ -\frac{AR}{6a_0^2} + \frac{4E^* \sqrt{R}}{3} (a_0 - z - z_c)^{3/2} & z_c + z \leq a_0 \end{cases} \quad (3)$$

where A is the Hamaker constant. R and E^* are the radius of the tip and the effective Young's modulus of the sample, which can be calculated as:

$$\frac{1}{E^*} = \frac{(1 - \nu^2)}{E} + \frac{(1 - \nu_1^2)}{E_1} \quad (4)$$

where E and ν are the Young's modulus and the Poisson's coefficient of the sample, respectively, and E_1 and ν_1 are the Young's modulus and the Poisson's coefficient of the tip material, respectively.

During the machining process of one structure, the tip and sample are usually prearranged. Thus, the interaction force is always controlled by the machining parameters when implementing nanoscratching using tapping mode, which cannot be obtained directly. Comparison of the contact and tapping modes, it can be observed the interaction force can be controlled more easily by the contact mode, as shown in Eq. 1. For this reason, the contact mode is usually selected to conduct nanofabrication of the 3D nanostructures (Yan et al. 2010). However, due to the intermittent interaction between the tip and the sample, scratching with tapping mode is proved as an efficient approach for reduction of tip wear (He et al. 2018). Therefore, some scholars utilized the tapping mode to carry out a long-term scratching process with a silicon AFM tip (He et al. 2018; Heyde et al. 2001).

The AFM tip-based nanomechanical machining method has been used to fabricate nanostructure on various materials, such as semiconductor, metal, and polymer (Yan et al. 2015). For the semiconductor and metal material, a relatively large normal load is needed to create structures. The tip wear cannot be neglected, especially for

the semiconductor materials due to owning a relatively large hardness. Thus, the diamond- or diamond-like-coated AFM tip is always chosen to reduce the tip wear, while the typical silicon tip is usually selected to scratch on the polymer material. The possible reason can be explained as follows. The polymer material is easy processing due to its small hardness, and the silicon tip is completely competent to carry out a long-term scratching process. Moreover, the radius of the silicon tip is relatively small, which can be used to fabricate nanostructures with more accurate dimensions, and the low price of the silicon tip is another advantage. Therefore, the selection of the tip used for machining is dependent on the sample material.

13.3 Fabrication of 3D Nanostructure by Material Removal

13.3.1 Selection of Feed Direction

In order to fabricate 3D nanostructure, a feed value with a direction perpendicular to the scratching direction is needed to expand the width (Geng et al. 2016b), rather than a single scratch for machining nanoline. Thus, in this case, the normal load is not the only factor for controlling the machined depth. The feed value also has a large influence on the dimensions of the structures. In the machining process of 3D nanostructure, the feed direction is a key factor due to the asymmetrical geometry of the AFM tip, which needs to be studied first. In terms of the tip-sample relative displacement and the geometry of the tip, three typical feed directions, named edge-forward, face-forward, and sideface-forward, are investigated, as shown in Fig. 1. For the edge-forward feed direction, the sample is controlled to move parallel and toward the tip cantilever after a single scratch to complete one feed operation, as shown in Fig. 1a. Oppositely, the sample moves parallel but away from the tip cantilever in the face-forward feed direction, as shown in Fig. 1b. While, for the sideface-forward, the sample is controlled to move perpendicular to the tip cantilever, as shown in Fig. 1c. Due to the feeds are usually selected as very small values, such as tens to hundreds of nanometers, only the corresponding edge or the face of the tip takes part in the scratching process. Taking a diamond tip as an example, the OA edge of the tip, shown in Fig. 1d, participates in the scratching process with the edge-forward feed direction. In the face-forward feed direction, both the edge OB and OC may take part in the scratching process. Thus, we consider plane BOC playing the main role for the material removal. For the sideface-forward feed direction, only the edge OB or OC participates in the scratching process.

In our pervious study (Geng et al. 2016b), scratching tests were carried out on the 2A12 aluminum alloy surface with a diamond AFM tip to study the influence of the feed directions on the machined outcomes. The surface of the sample was per machined by the single-point diamond turning, and the surface roughness can reach 5 nm approximately. Figures 2 and 3 show the SEM and AFM images of the nanochannels machined with the three typical feed directions. The conventional zigzag trajectory was selected. The feed and normal load were set as 120 nm and 67 μN , respectively. The SEM images were taken just after the machining process,

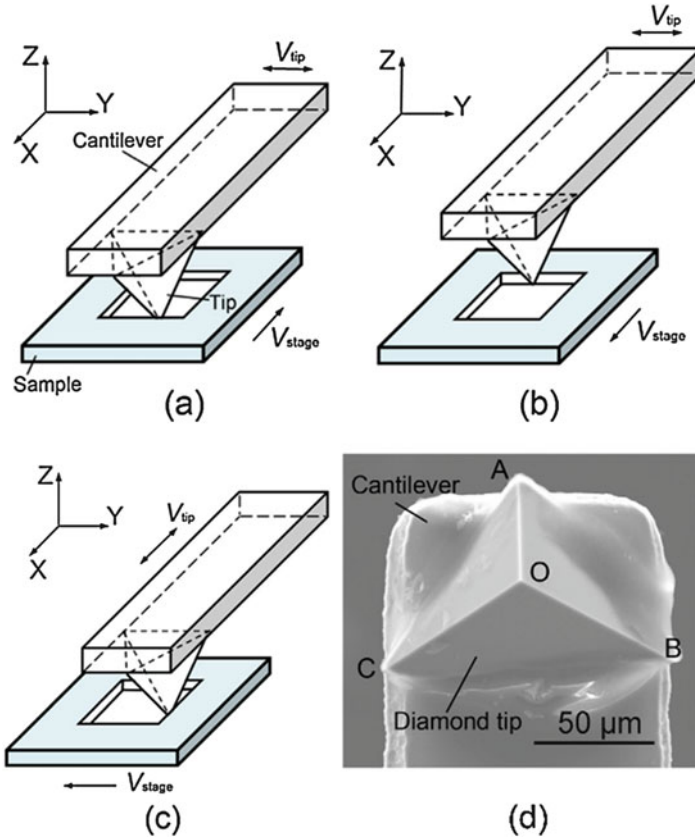


Fig. 1 Three typical feed directions and the SEM image of the diamond tip: (a) edge-forward, (b) face-forward, (c) sideface-forward, and (d) SEM image of the tip (Reproduced with permission from Geng et al. 2016b)

and the AFM images were obtained after washing the sample in alcohol solution for about 10 min to remove the chips generated in the machining process. As shown in Fig. 2a and d, continuous chips are formed when scratching with edge-forward feed direction. It can be observed from the magnified image of the chips in Fig. 2d that one side of the chip has a sawtooth shape. This has been explained that both cutting and plowing machining states occur to generate this sawtooth shape (Geng et al. 2016b). However, the formation of the continuous chips indicates that cutting state plays the main role in the machining process. Moreover, it can be found from Fig. 3a that no chip was adhered on the sides of the nanochannel. This means the chips can be washed away easily before scanning by the AFM, which is attributed to the sawtooth shape on one side of the chips. The sawtooth shape can result in the chips being broken easily. From the cross section of the nanochannel shown in Fig. 3a, a nanochannel with relative good quality was obtained when machining by the edge-

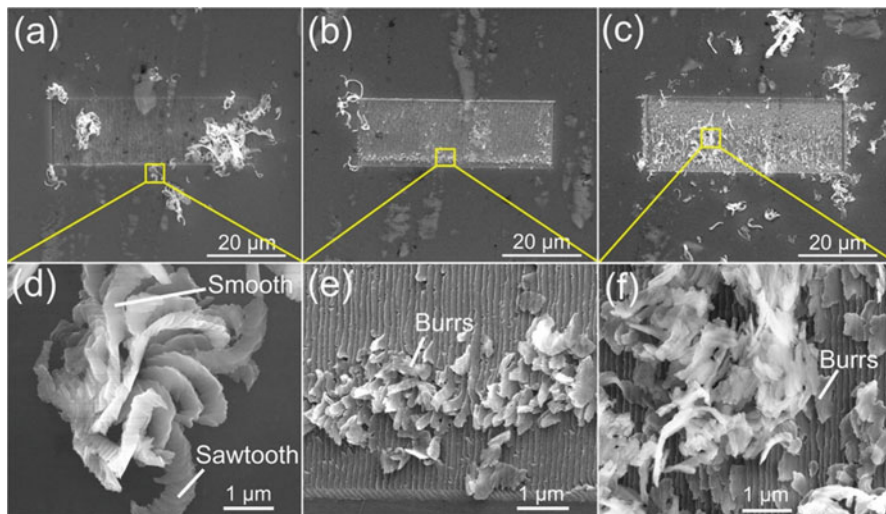


Fig. 2 SEM images of the nanochannels machined with three typical feed directions: (a) edge-forward, (b) face-forward, and (c) sideface-forward (Reproduced with permission from Geng et al. 2016b)

forward feed direction. The machined depth was measured as 208 nm approximately (Geng et al. 2016b). As shown in Fig. 2b and e, prominent burrs can be found in the processed area when implementing scratching process with the face-forward feed direction. From the AFM image shown in Fig. 3b, it can be seen that no obvious depth obtained after machining with the face-forward feed direction. This indicates that the materials cannot be removed effectively, and plowing machining state plays an important role in this case. The possible reason for this is the extremely small attack angle of the main cutting edge (Geng et al. 2016b). Thus, the face-forward feed direction is not suitable for the fabrication of 3D nanostructure. For the sideface-forward feed direction, both the chips and the burrs can be generated during the machining process, as shown in Fig. 2c and f. In this condition, the attack angles of the trace and retrace in the reciprocating motion are different, which are about 26.5° and 63.5° , respectively. For the attack angle of 26.5° , the plowing mechanism may occur, which leads to burr formation, while, in the opposite motion, the attack angle can reach 63.5° , which results in the generation of the chips. However, the clearance angle is estimated only 26.5° in this case. This relatively small clearance angle may not be enough to form the continuous chips. The coexisting of the chips and burrs is attributed to the variation of the attack angles in the reciprocating motion. In addition, it can be observed from Fig. 3c that there is a large variation of the machined depth along the width and length cross section, which is caused by the unitability of the machining process in the reciprocating motions. Thus, considering the consistency of the machined depth and the surface quality, the sideface-forward feed direction is also not suitable for the fabrication of the 3D nanostructure.

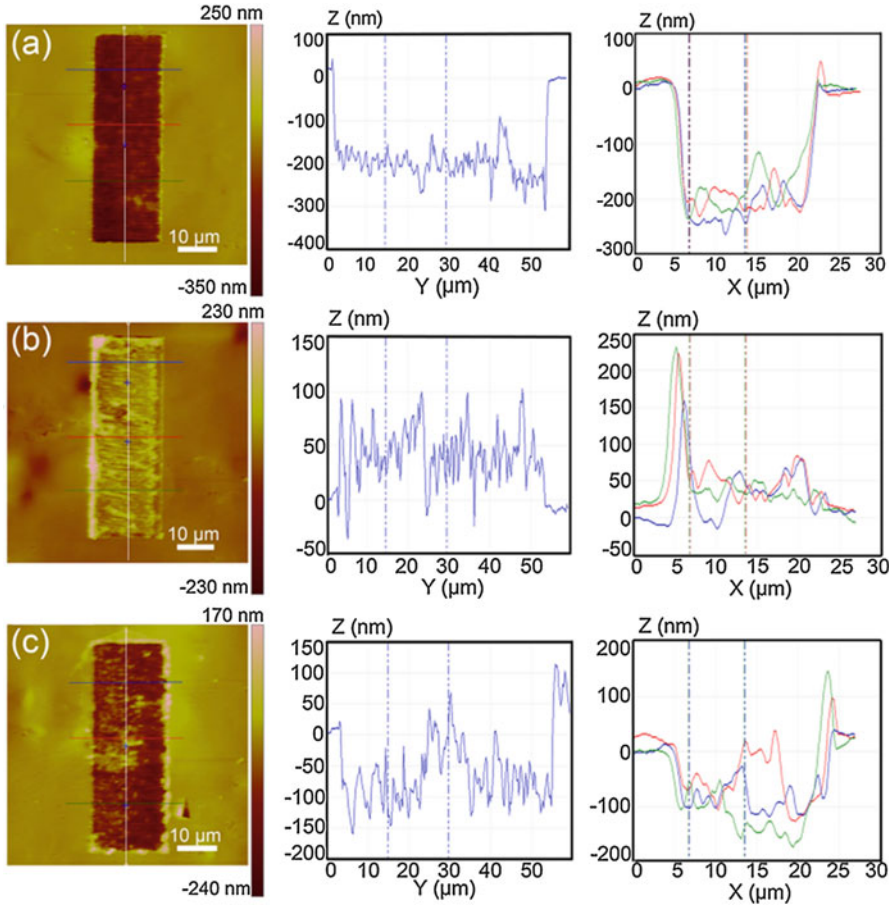


Fig. 3 AFM images and the corresponding cross sections of the nanochannels machined with three typical feed directions: (a) edge-forward, (b) face-forward, and (c) sideface-forward (Reproduced with permission from Geng et al. 2016b)

13.3.2 Fabrication 3D Nanostructure by Controlling the Applied Normal Load

As described in Sect. 3.1, the edge-forward feed direction is the best among the three typical feed directions. Thus, in the machining process of 3D nanostructure, edge-forward feed direction is selected. Moreover, as discussed in Sect. 3.1, the machined depth of the nanostructure is related to the applied normal load and the feed values, which is also studied in our previous study (Geng et al. 2013a). Thus, both the applied normal load and the feed values can be used to control the machined depth to achieve 3D nanostructures. Most scholars utilized the intuitive force-control approach to fabricate nanostructures with fluctuant machined depth, and the feed is kept as a constant value, as shown in Fig. 4a. In order to better understand the

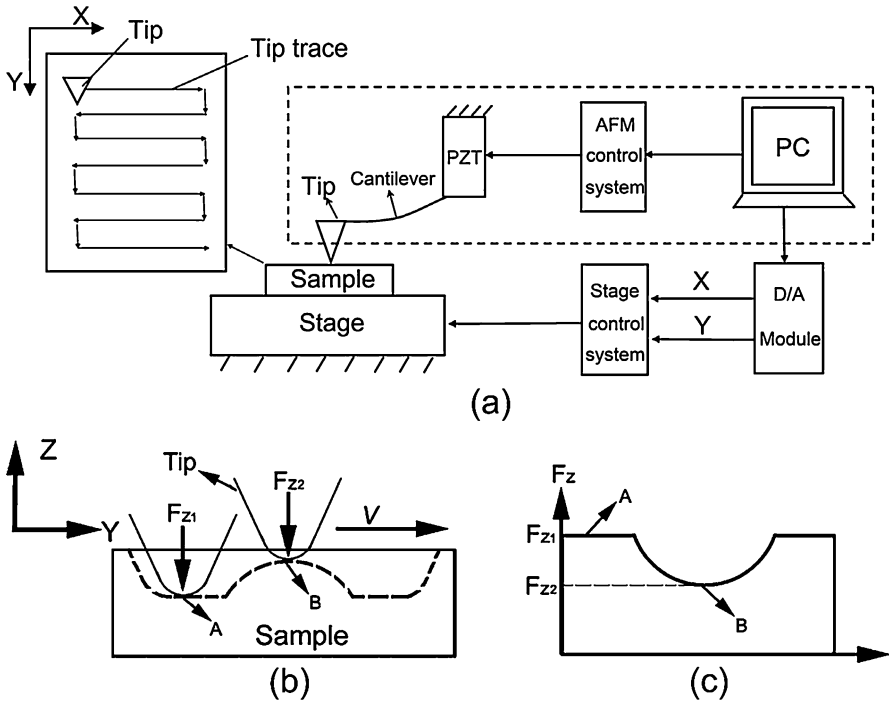


Fig. 4 (a) Schematic of the modified AFM tip-based nanomachining system. (b) The dotted line shows a 3D nanostructure required to be machined. (c) Corresponding force single in machining the 3D nanostructure shown in (b) (Reproduced with permission from Yan et al. (2010) and Geng et al. (2013b))

nanomachining process and guarantee the machining quality, a rectangular tip trajectory is usually selected. Unlike the traditional processing, the relationship between the applied normal load and the machined depth should be investigated first for the AFM tip-based nanomachining. It can easily be imagined that the machined depth increases with the normal load going up. Figure 4b shows the cross section of the desired nanostructure, and Fig. 4c illustrates the corresponding normal loads needed to be applied on the surface. It can be observed that the deeper point of the machined depth needs a relatively large normal load. Due to the large pileup formed in the machining process (Geng et al. 2016a), the polymer material is not suitable for this material removal approach to fabricate 3D nanostructure. Thus, the metal is usually selected as the sample material in this method. In the nanomachining process of the metal material, the plastic deformation is the dominant mechanism of energy dissipation (Bhushan 2002), and the influence of the elastic recovery can be neglected. For this reason, the nanomachining process can be treated as a hard particle sliding over a soft sample surface (Geng et al. 2013b). The applied normal load (F_N) can be calculated by the product of the yield pressure of the sample material (σ_p) and the horizontally projected area of the tip-sample interface (A_T), as

expressed in Eq. 5 (Bowden and Tabor 1950). σ_p is the property of the material, which can be obtained by the nanoindentation process. A_T has a relationship with the machined depth (h). Thus, the relationship between F_N and h can be derived by Eq. 5.

$$F_N = \sigma_p \cdot A_T \tag{5}$$

Figure 5a shows the 3D view of the nanomachining process. “1” and “2” denoted in this figure show the previous and latter tip paths, respectively. “3” marked with red line represents the interface between the tip and the sample material. Figure 5b shows the top view of the machining process. “1” and “2” indicated in this figure

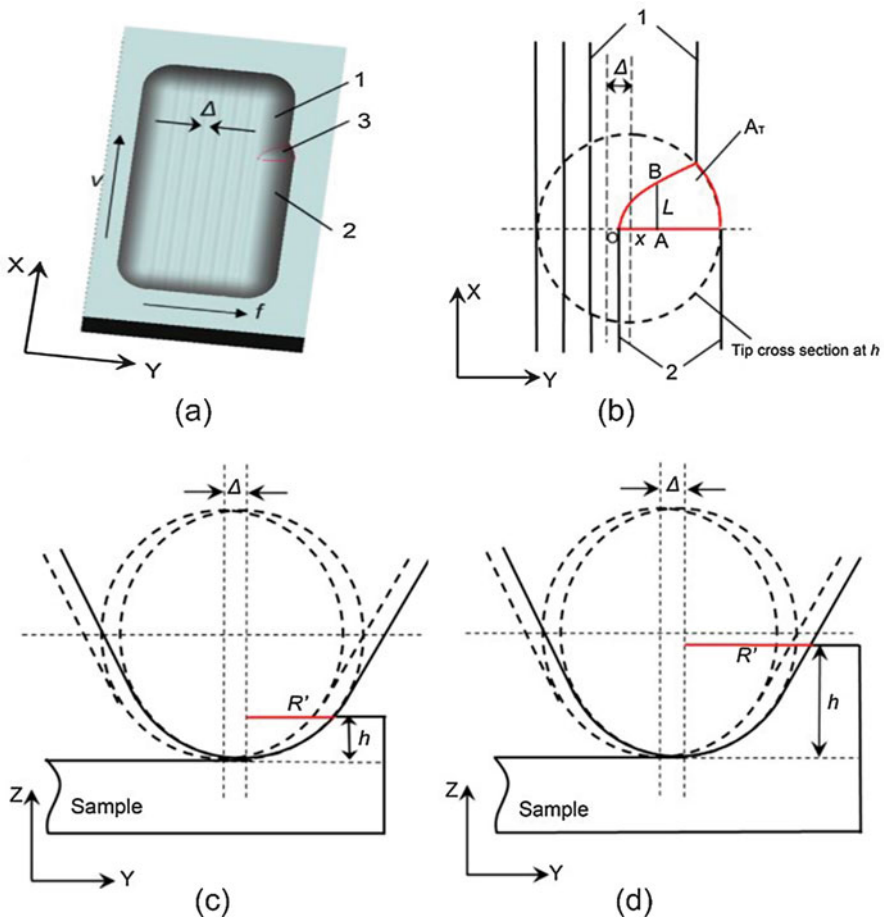


Fig. 5 (a) Schematic 3D view of nanomachining processing. (b) The top view of the machining process. Front views of the nanostructure fabrication process when $h < h_1$, (c) and when $h > h_1$, (d) (Reproduced with permission from Geng et al. 2013b)

show the edges of the previous and latter tip paths corresponding to the paths shown in Fig. 5a. The red line in Fig. 5b illustrates the horizontal projection of the interface between the tip and the sample (A_T). In order to study the machined depth, the relationship between A_T and h needed to be considered first. To simplify the calculation, the AFM tip is usually assumed as a cone with a spherical apex (Geng et al. 2013b). Thus, in term of the machined depth, the nanomachining process can be divided into two scenarios: h is larger than the critical depth (h_1) and h is smaller than h_1 . The critical depth is the vertical distance from the top of the tip to the connection ring of the cone and the spherical apex, which can be calculated by $R_0(1-\sin\alpha)$. R_0 is the radius of the spherical apex, and α is the tip semi-angle. As shown in Fig. 5b, A_T can be obtained by integrating L with respect to x and adding an arc area, which can be calculated by symbolic computation expressed as (Geng et al. 2013b):

$$A_T = \frac{1}{3}(2R' - \Delta) \cdot \sqrt{(2R' - \Delta) \cdot \Delta} + \frac{1}{2} \arccos \frac{R' - \Delta}{R'} \cdot R'^2 - \frac{1}{2}(R' - \Delta) \sqrt{R'^2 - (R' - \Delta)^2} \quad (6)$$

where Δ is the feed value and R' represents the radius of the cross section of the tip at the depth of h , as shown in Fig. 5c and d. In terms of h , R' can be obtained as follows (Geng et al. 2013b):

$$\begin{cases} R' = \sqrt{R_0^2 - (R_0 - h)^2} & h < h_1 \\ R' = (h - R_0(1 - \sin \alpha)) \cdot \tan \alpha + R_0 \cos \alpha & h > h_1 \end{cases} \quad (7)$$

Thus, if nanostructure with a depth is desired to be machined, an applied normal load can be determined from Eqs. 5, 6, and 7 when the feed value is fixed. However, we know that the feed value cannot be extremely small, which can result in the plowing machining state and the bottom of the structure with a relatively large roughness. This is because the edge of the tip is not extremely sharp, which is about 40 nm for the diamond tip (Geng et al. 2013b). Thus, a minimum value of the feed is usually selected as 30 nm. In addition, the feed can also not be chosen a large value. When the feed is larger than a certain value, the tip paths are independent of each other, and the nanochannel cannot be generated (Geng et al. 2013b). Considering the surface quality of machined structure, a maximum feed value is selected as 130 nm. Thus, a moderate feed value should be chosen to guarantee the surface quality of the machined nanostructure.

In our previous study (Geng et al. 2013b), we selected a moderate feed of 60 nm and a reasonable range of machined depth to fabricate sinusoidal nanostructure, as shown in Fig. 6a. Figure 6b shows the corresponding normal load calculated by Eqs. 5, 6, and 7. The scratching speed is set as 10 $\mu\text{m/s}$, and the width of the structure is 18 μm . Figure 6c shows the AFM image of the machined sinusoidal nanostructure, and Fig. 6d shows the corresponding cross section compared with the desired machined depths. It can be indicated that the machined depth is closed to the

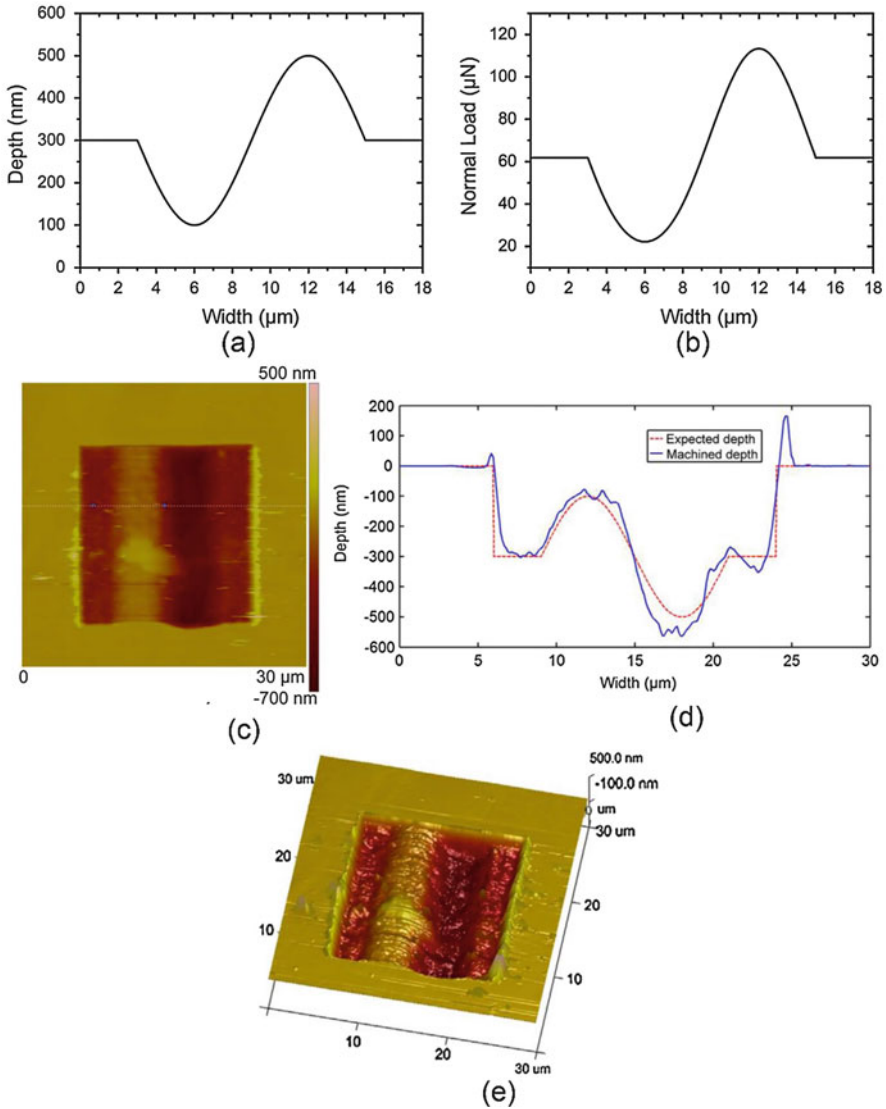


Fig. 6 (a) The expected depth of the nanostructure with sinusoidal waveform. (b) The corresponding normal load. (c) The AFM image of the fabricated nanostructure. (d) The corresponding cross-sectional AFM image comparing with the expected depth. (e) 3D AFM image of the machined nanostructure (Reproduced with permission from Geng et al. 2013b)

expected depth, and the sinusoidal nanostructure can be observed clearly from the 3D AFM image of the machined structure, as shown in Fig. 6e. Therefore, the AFM tip-based load-control nanomachining approach has been proven by this work, which can be used to fabricate 3D nanostructure with expected dimensions.

13.3.3 Fabrication 3D Nanostructure by Controlling the Feed Value

As mentioned in Sect. 3.1, the feed value is also a key factor for the machined depth. In the load-control nanomachining method, each point on the nanostructure requires a specific normal load and the accurate location, which may result in relatively time-consuming, while the feed-control approach only needs the feed values for each machined depth and the applied normal load is kept constant. This machining process can be changed into a design of the scratching trajectory. This means the stage can be separated from the AFM system and move to any other AFM system to conduct nanomachining of 3D nanostructure without programming to control the normal load. The AFM is like a tool rest to provide a constant normal force. This approach can be used as a 3D nanostructure machining module in some applications with the advantage of easy operation and high efficiency (Geng et al. 2016c, 2017a). However, the disadvantage of this method is the machined depth along the scratching path should be constant, which may confine the application of this feed-control method.

In this method, the feed is enabled variationally by controlling the scratching trajectory during machining, as shown in Fig. 7a. Figure 7b shows the cross section of the structure with the expected depth, and Fig. 7c illustrates the schematic of the corresponding feed values needed. In particular, the positions A and B shown in Fig. 7b represent the deepest and shallowest points of the structure, respectively. Δ_1 and Δ_2 denoted in Fig. 7c show the feed values required at points A and B, respectively. It can be observed clearly that the depth at point A is larger than that at point B, while Δ_1 is smaller than Δ_2 . In addition, the edge-forward is also selected as the feed direction to guarantee the machining quality, and the feed values in the range from 30 nm to 130 nm are chosen.

Comparing with the force-control machining method, this proposed approach should consider the change of the feed value and the depth between the two adjacent scratching paths (Geng et al. 2017a). Figure 8a and b shows the top view of the machining processes with the depth decreasing and increasing, respectively. Figure 8c and d shows the corresponding side view of the machining process. The red and green solid lines in Fig. 8a and b represent the edges of the previous and latter scratching paths, and the dotted cycles denote the horizontal cross section of the AFM tip at the sample surface. Moreover, the blue curved line is the horizontal projection of the interface between the tip and the sample. The red dotted line and green solid line in Fig. 8b represent the vertical cross section of the AFM tip for the previous and latter scratching paths, respectively.

1. As shown in Fig. 8a, when the depth is decreasing, that is, the feed is increasing, it can be observed easily that the radius of the red dotted cycle is larger than that of the green dotted cycle. Similar to the force-control method, the area OCD (S_{OCD}) can be obtained by integrating L with respect to x , as expressed by (Geng et al. 2017a):

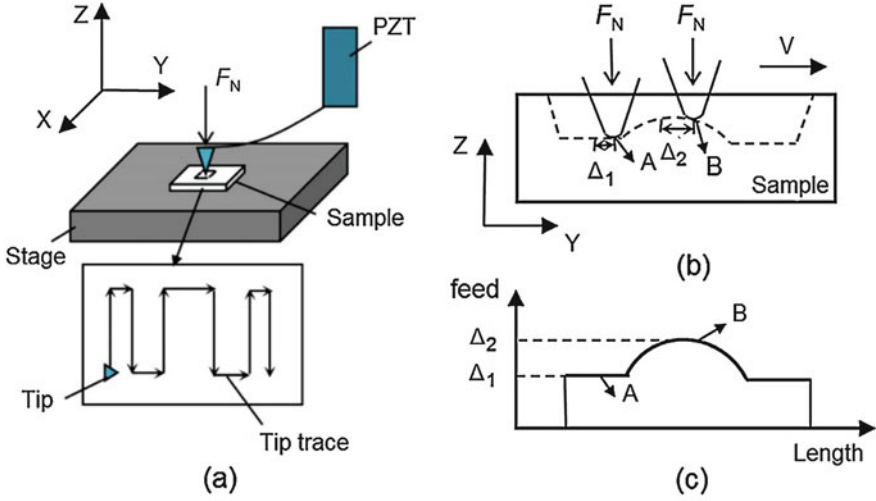


Fig. 7 (a) Schematic of AFM-based mechanical machining process using the feed-control approach. (b) The dotted line denotes a 3D nanostructure desired to be machined. (c) Feed control signal variation during the machining process of the 3D nanostructure shown in (b) (Reproduced with permission from Geng et al. 2017a)

$$\begin{aligned}
 S_{OCD} = & \int_0^L \sqrt{R_0^2 - (R_0^2 - h_c^2)} - \sqrt{R_0^2 - (R_0 - (h_r + \Delta h))^2} Ld \\
 & x - \int \frac{(R_0 \cos \alpha + (h_c + \Delta h - (R_0 - R_0 \sin \alpha)) \tan \alpha) - \sqrt{R_0^2 - (R_0 - (h_r + \Delta h))^2}}{\sqrt{R_0^2 - (R_0^2 - h_c^2)} - \sqrt{R_0^2 - (R_0 - (h_r + \Delta h))^2}} Ld \\
 & x \int \frac{R_1' - \sqrt{R_0^2 - (R_0 - (h_r + \Delta h))^2}}{(R_0 \cos \alpha + (h_c + \Delta h - (R_0 - R_0 \sin \alpha)) \tan \alpha) - \sqrt{R_0^2 - (R_0 - (h_r + \Delta h))^2}} Ldx
 \end{aligned} \tag{8}$$

where Δh is the difference between the two adjacent paths. h_r is the height of the intersection point between the previous and latter paths denoted by point “O” with respect to the deepest point of the current path, as shown in Fig. 8e, which can be calculated by (Geng et al. 2017a):

$$\sqrt{R_0^2 - (R_0 - h_r)^2} + \sqrt{R_0^2 - (R_0 - (h_r + \Delta h))^2} = \Delta \tag{9}$$

The area CDE (S_{CDE}) can be calculated by (Geng et al. 2017a):

$$S_{CDE} = \frac{1}{2} \arccos \left(\frac{R_1' - \Delta}{R_2'} \right) \cdot R_2'^2 - \frac{1}{2} (R_1' - \Delta) \sqrt{R_2'^2 - (R_1' - \Delta)^2} \tag{10}$$

where R_1' and R_2' are the radii of the horizontal cross section of the AFM tip at the sample surface for the previous and latter paths, which can be expressed by (Geng et al. 2017a):

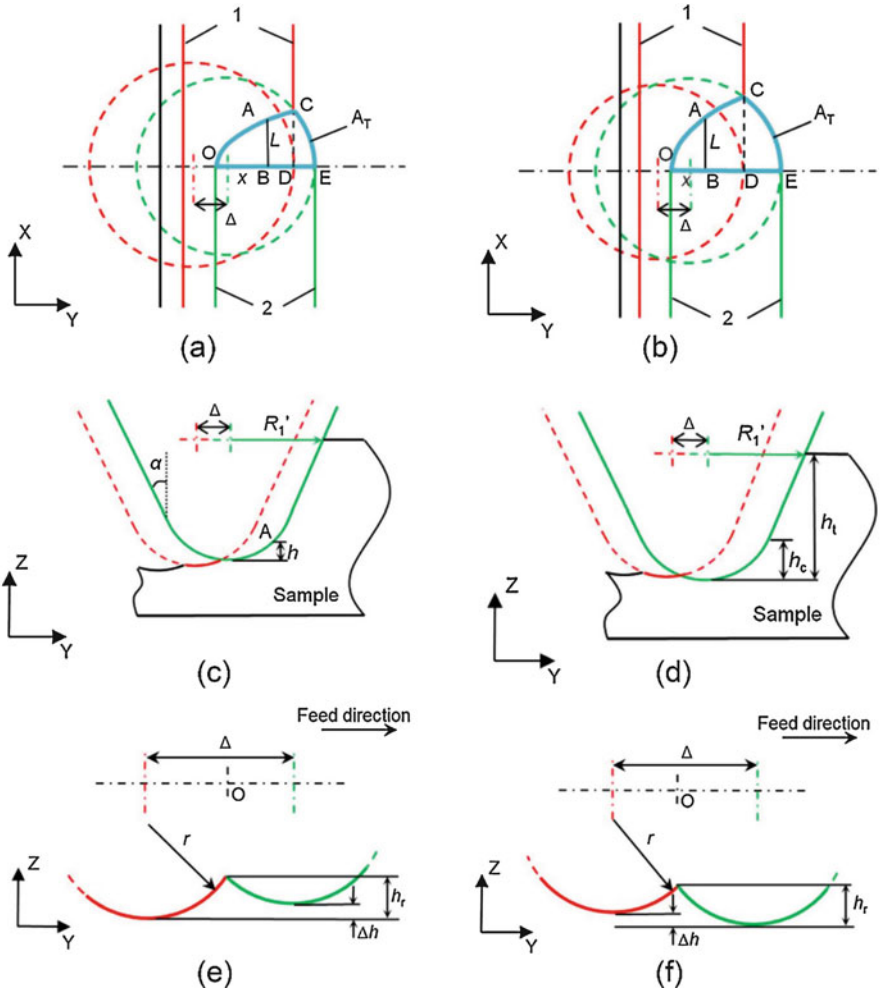


Fig. 8 Top views of the machining process when the feed is increasing (a) and when the feed is decreasing (b). Front views of the machining process when the feed is increasing (c) and when the feed is decreasing (d). Side views of the 3D-MNS fabrication process. Feed increasing (e) and feed decreasing (f) (Reproduced with permission from Geng et al. 2017a)

$$\begin{cases} R_1' = R_0 \cos \alpha + (h + \Delta h - (R_0 - R_0 \sin \alpha)) \tan \alpha \\ R_2' = R_0 \cos \alpha + (h - (R_0 - R_0 \sin \alpha)) \tan \alpha \end{cases} \quad (11)$$

Thus, A_T can be obtained by the sum of S_{OCD} and S_{CDE} .

2. When the depth is increasing and the feed values decreases, the radius of the green dotted cycle is larger than that of the red one, as shown in Fig. 8b. In this case, S_{OCD} can be obtained by (Geng et al. 2017a):

$$\begin{aligned}
 S_{\text{OCD}} = & \int_0^{\sqrt{R_0^2 - (R_0^2 - (h_c - \Delta h)^2)} - \sqrt{R_0^2 - (R_0 - (h_r - \Delta h))^2}} Ld \\
 & x - \int_{\sqrt{R_0^2 - (R_0^2 - (h_c - \Delta h)^2)} - \sqrt{R_0^2 - (R_0 - (h_r - \Delta h))^2}}^{(R_0 \cos \alpha + (h_c + \Delta h - (R_0 - R_0 \sin \alpha)) \tan \alpha) - \sqrt{R_0^2 - (R_0 - (h_r - \Delta h))^2}} Ld \quad (12) \\
 & x \int_{(R_0 \cos \alpha + (h_c - (R_0 - R_0 \sin \alpha)) \tan \alpha) - \sqrt{R_0^2 - (R_0 - (h_r - \Delta h))^2}}^{R_1' - \sqrt{R_0^2 - (R_0 - (h_r - \Delta h))^2}} Ldx
 \end{aligned}$$

The relationship between h_r and Δ is now changed to (Geng et al. 2017a):

$$\sqrt{R_0^2 - (R_0 - h_r)^2} + \sqrt{R_0^2 - (R_0 - (h_r - \Delta h))^2} = \Delta \quad (13)$$

The area CDE (S_{CDE}) can also be calculated by Eq. 10 given for the previous scenario. However, in this case, R_1' and R_2' should be changed to (Geng et al. 2017a):

$$\begin{cases} R_1' = R_0 \cos \alpha + (h - \Delta h - (R_0 - R_0 \sin \alpha)) \tan \alpha \\ R_2' = R_0 \cos \alpha + (h - (R_0 - R_0 \sin \alpha)) \tan \alpha \end{cases} \quad (14)$$

Thus, A_T can also be obtained by summing S_{OCD} and S_{CDE} .

In our previous study (Geng et al. 2017a), we found that the slope values of the nanostructures can only be selected in the range from -12° to $+12^\circ$ to guarantee a machining error within 10% when conducting machining process on the single-crystal copper surface with the (110) crystallographic plane. The sample surface was polished by the manufacturer, and the roughness (R_a) is less than 5 nm, which is measured by the tapping mode of the AFM system. The possible reasons for the selection range of the slope value have been given as follows. First, the adjacent scratching paths should not affect each other during the machining process to guarantee the machining quality. Thus, applying Eqs. 13 and 14, an inequation can be derived as follows (Geng et al. 2017a):

$$\frac{\Delta h}{\Delta} < \tan \left(\frac{\pi}{2} - \alpha \right) \quad (14)$$

The ratio of Δh and Δ is defined as the slope of the nanostructure. The AFM tip used in our previous study (Geng et al. 2017a) is 60° based on the SEM image. Thus, it can be found from Eq. 14 that the slope of the expected nanostructure should be less than 30° . In addition, the relationship between the feed value and the machined depth is usually obtained by the machining experiments of the cavities with planar floor surfaces, for the cavities with planar floor surfaces are machined with the constant-feed method and the point “O” shown in Fig. 8a and b should be in the middle of the green and red dotted cycles. However, it can be observed for Eq. 9 that the point “O” is closed to the center of the green dotted cycle for the latter path in the case of the machined depth decreasing, as shown in Fig. 8c, while the point “O” is closed to the center of the red dotted cycle for the previous path in the case of the machined depth increasing, as shown in Fig. 8f. Thus, the length of the integral for

A_T (OE shown in Fig. 8a and b is smaller in the case of depth decreasing and larger in the condition of depth increasing, compared with the situation of machining the planar floor surface. Moreover, it can be found from Fig. 8a and b that L is smaller in the case of the depth decreasing and larger in the condition of depth increasing compared with the situation of machining the planar floor surface. Thus, from Eqs. 8, 10, and 12, it can be indicated that the sum of S_{OCD} and S_{CDE} , that is, A_T , is smaller in the case of depth decreasing and larger in the condition of depth increasing. With the same normal load, if A_T is smaller, the AFM tip should be penetrated deeper in the case of the depth decreasing. This can result in the slope of the structure smaller than the setting value. While, if A_T becomes larger, the depth penetrated by the AFM tip should be shallower in the condition of the depth increasing. This can also cause the reduce of the slope of the structure. Therefore, by utilizing the relationship between the feed values and depth obtained by machining the cavities with planar floor surfaces to fabricate 3D nanostructure, the obtained slope of the structure should be less than that of the expected value. Moreover, the larger slope is chosen, the difference between the achieved and desired values is larger. Thus, to guarantee the machining error less than 10%, the slope in the range from -12° to $+12^\circ$ can be selected.

Based on the above discussion, typical sinusoidal waveform nanostructures were fabricated to demonstrate the feasibility of the feed-control nanomachining approach in our previous study (Geng et al. 2017a). The period of the desired sinusoidal waveform nanostructures (T) should satisfy the inequation as described below:

$$T \geq \frac{2\pi a_s}{\tan(\theta_c)} \quad (14)$$

where a_s represents the amplitude of the structure, and θ_c is the critical value of the slope, which should be 12° . If the amplitude is selected as 80 nm, the period (T) should be larger than or equal to 2.4 μm . When the amplitude is chosen as 125 nm, the minimum value of the period can be calculated as 3.74 μm . Thus, we chose two group machining parameters to conduct the machining processes of the typical sinusoidal waveform nanostructures. The first one is machining with the normal load of 102.4 μN , the amplitude of 80 nm, the base depth of 240 nm, and the period of 2.4 μm . The second one is fabricating with the normal load of 145.1 μN , the amplitude of 125 nm, the base depth of 275 nm, and the period of 4 μm . The 2D and 3D AFM images of the two sinusoidal waveform nanostructures are shown in Fig. 9a and b, respectively. From the cross sections of the machined nanostructure, it can be indicated that the results are consistent with the desired values. This can prove the feasibility of the feed-control approach to fabricate 3D nanostructure with expected dimensions.

13.4 Fabrication of 3D Nanostructure by Stick-Slip Process

Comparing with the metal material, the polymer can hardly be removed by the AFM tip with the formation of the chips. This is because the polymer material is usually accumulated on the sides of the groove to generate material pileups during the

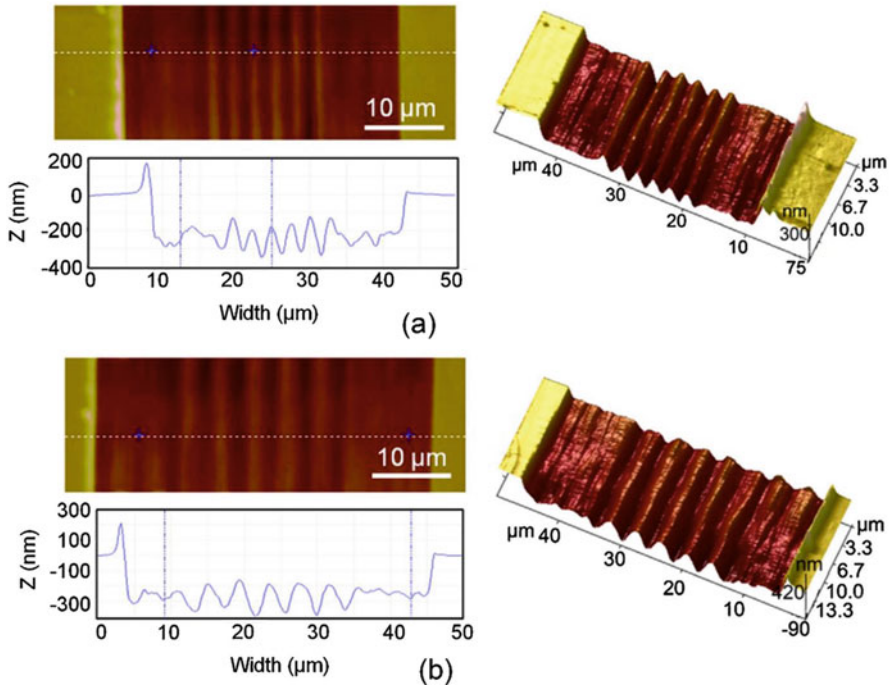


Fig. 9 AFM images of the machined nanochannels with desired sinusoidal waveforms nanostructures: (a) the period of 2.4 μm and (b) the period of 4 μm (Reproduced with permission from Geng et al. 2017a)

scratching process. Nano-periodic pattern was first found during investigating nano-tribological behavior of the polymer material with the AFM tip (Aoike et al. 2001). This ripple-type nanostructure is perpendicular to the scratching direction. However, the ripple-type nanostructure was always formed by more than 10 times of reciprocal scanning on the sample surface with an extremely small normal load (several nano-newton) (Aoike et al. 2001), which is not suitable to be considered as a novel nanofabrication method due to the time-consuming of the process and uncertainty of the dimensions of the obtained structures. Thus, fabrication the ripple-type nanostructure with only one scratching process is needed. Moreover, the investigation of the approach to control the period and amplitude of the ripple-type nanostructure is also required. D'Acunto et al. (2007) proved that the ripple-type nanostructure can be formed with only one scanning process on PCL and PET polymer film surfaces by using a relatively small normal load (several nano-newton). However, the amplitude is very small and uncontrollable. Thus, in our previous study (Sun et al. 2012), we considered enlarging the applied normal load (tens of micro-newton) to increase the amplitude of the ripple-type structure and controlling the period and amplitude for one-scan machining process. The formation mechanisms for the ripple-type nanostructure are usually explained as Schallamach waves,

stick-slip process, fracture mechanisms, and erosion-diffusion process (Aoike et al. 2001; Yang et al. 2013; Dinelli et al. 2005; Surtchev et al. 2005; Elkaakour et al. 1994), which are different from the material removal mechanism in the machining process of metal material. Thus, the influence of the scratching parameters on the machining results is also different. Similarly, the scratching trajectory and feed direction are also needed to be studied first.

Figure 10 shows the three typical machining trajectories in the scratching process on the polymer surface, which are zigzag, rectangular, and line-scratch types. For the zigzag tip trace, the AFM tip is controlled by the AFM scanner along the X and Y directions to achieve the tip trace, as shown in Fig. 10a and b, which is the same with the scanning process of the AFM system. The rectangular trajectory is obtained by the relative motion between the tip and the sample along the X and Y directions, as shown in Fig. 10c and d. The position of the AFM tip is kept constant in the horizontal plane, and the sample is driven by the high precision. The vertical position of the AFM tip can be adjusted by the AFM scanner in Z direction to keep the normal load constant during the machining process. As shown in Fig. 10e and f, the movement of the sample is also controlled by the high-precision stage, and the position of the AFM tip is also kept constant in the horizontal plane. However, after the tip accomplishing one scratch, the sample is controlled to conduct the vertical downward motion by the high-precision stage. This can cause the tip separating with the sample surface due to the limitation of the AFM scanner in Z direction. This operation is similar as the tip lifting up, which is denoted by BB' shown in Fig. 10f. Then, the sample is controlled to return the initial point of the scratch, denoted by B'A' in Fig. 10f. After the sample reaching point A', it moves upward to contact with the AFM tip again. This step is similar with the approaching process. A feed is then conducted toward the positive direction of X axis to accomplish one scratching cycle. In our pervious study (Yan et al. 2012), experimental tests were carried out to compare these three scratching trajectories.

Figure 11 shows the AFM images of the ripple-type nanostructures machined with the zigzag and rectangular trajectories, respectively. The machining ranges are $10\ \mu\text{m} \times 10\ \mu\text{m}$ and $8\ \mu\text{m} \times 8\ \mu\text{m}$, respectively. The feed is set as 10 nm, and the normal load is selected as $5.2\ \mu\text{N}$. The feed direction is chosen as the edge-forward. The dislocation phenomenon of the cross sections of the AFM image at three different points can be observed easily from Fig. 11b, which is machined with the zigzag trajectory, while the cross sections of the AFM image are consistent with each other when machining with the rectangular trajectory, as shown in Fig. 11d. The possible reason can be given as follows. For the zigzag trajectory, the feed in one scratching cycle is not kept constant, which is smallest at the beginning and largest at the end of the scratching cycle. Moreover, due to the reciprocating motion of the AFM tip, the beginning and the end points are alternant for the adjacent scratching cycles. Here, we utilize the stick-slip and crack formation processes to explain the machining results (Elkaakour et al. 1994). When scratching on the surface of the polymer material, a material pileup can be generated, and a lateral force can thus be applied on the tip apex. This lateral force (F_l) can be expressed by Eq. 15, which is resulted from the elastic energy stored in the substrate (Elkaakour et al. 1994).

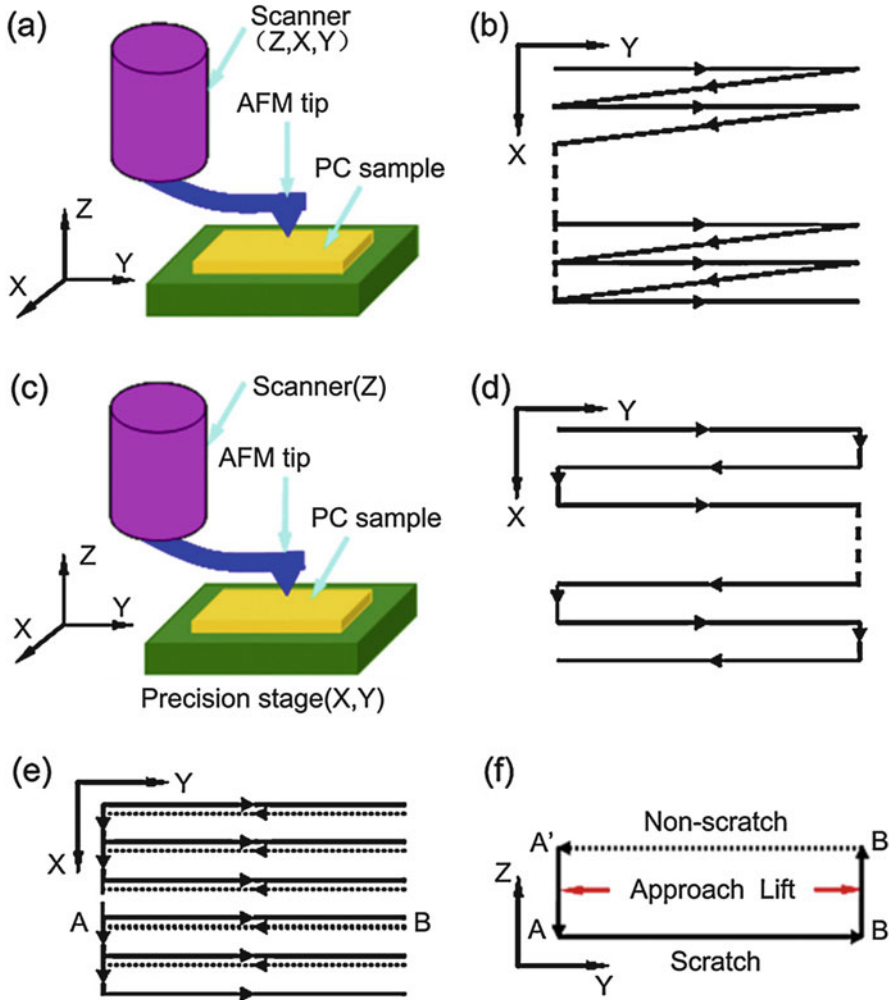


Fig. 10 Schematic illustration of the machining systems and the corresponding tip traces. (a) The AFM system, (b) the zigzag trajectory, (c) the modified AFM system, (d) the rectangular trace, (e) the line-scratch trace of the modified AFM system, and (f) the tip’s motion in each line of (e) (Reproduced with permission from Yan et al. 2012)

$$F_t = \frac{Eah \tau}{2} \frac{1}{L} \tag{15}$$

where E , a , and h are Young’s modulus of the substrate, the radius of the tip-sample contact area, and the machined depth, respectively. L and τ represent the length of the internal defect and strain yielded, respectively (Elkaakour et al. 1994). When this lateral force (F_t) reaches a critical value (F_{tc}), the AFM tip can slide over the material pileup instead of pushing the polymer material to form a groove (Elkaakour et al.

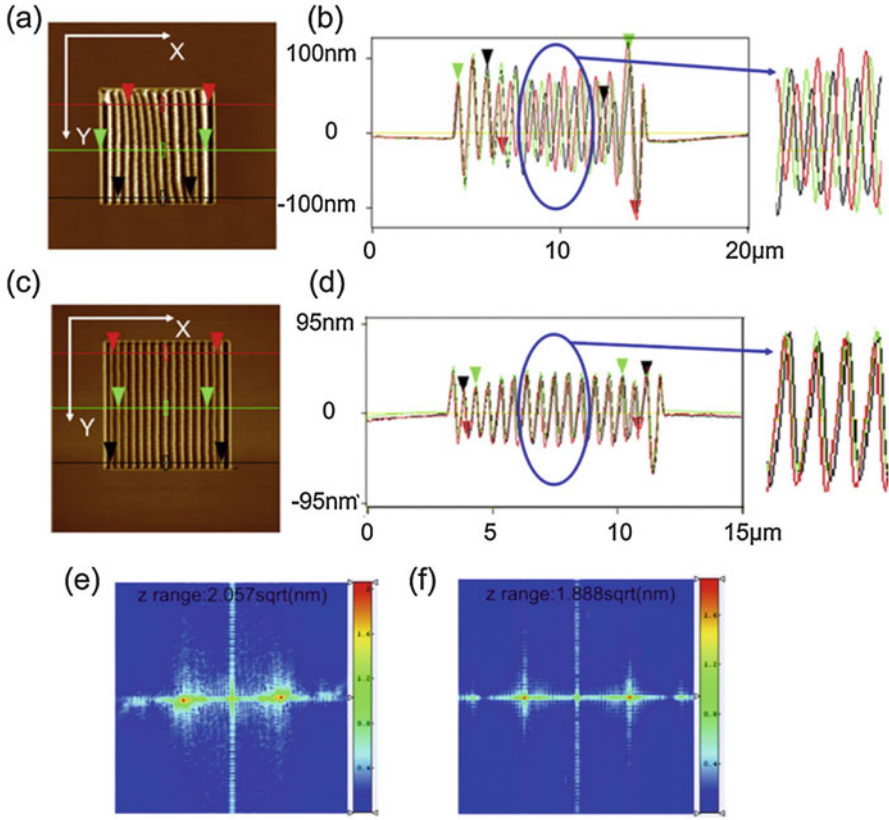


Fig. 11 The morphologies and the corresponding FFT of the sample surface for once scratching with the AFM system and the modified AFM system, respectively (Reproduced with permission from Yan et al. 2012)

1994). This critical force value (F_{tc}) is related to the friction coefficient, applied normal load, radius of the AFM tip, and surface energy term (Elkaakour et al. 1994). If the feed is changing all the time during the machining process, that is, the radius of the tip-sample contact area and machined depth changing, the lateral force (F_t) is thus changed. The scratching length to form one peak of the ripple structure is also changing in one cycle, which may cause the dislocation of the cross sections. This may also result in the inconsistent amplitude of the ripple structure, as shown in Fig. 11b. For the rectangular trajectory, the feed value is kept constant in one scratching cycle. The lateral force (F_t) applied on the apex of the tip is changeless during the machining process. Thus, the period and amplitude of the ripple nanostructure is stable. It can be indicated that the rectangular trajectory is more suitable than the zigzag trace considering the machining quality of the ripple-type nanostructure. The AFM image was also analyzed in our previous study using the means of the fast Fourier transform (FFT) function, as shown in Fig. 11e and f (Yan et al. 2012). It

can be observed that the structure machined with the rectangular trajectory shows a better periodical property than that machined with the zigzag trajectory, which agrees well with the above discussion.

To study the difference between the rectangular and the line-scratch trajectories, a small feed of 10 nm is selected. When scratching with the rectangular trace, the machining range is chosen as $8\ \mu\text{m} \times 8\ \mu\text{m}$, and the normal load is set as $2.5\ \mu\text{N}$. For the line-scratch trajectory, the machining range is select as $10\ \mu\text{m} \times 10\ \mu\text{m}$, and the normal load is chosen as $2\ \mu\text{N}$. Figure 12a and b shows the AFM images of the structures machined with the rectangular and the line-scratch trajectories, respectively. It can be observed that only one groove and ridge, rather than ripple-type

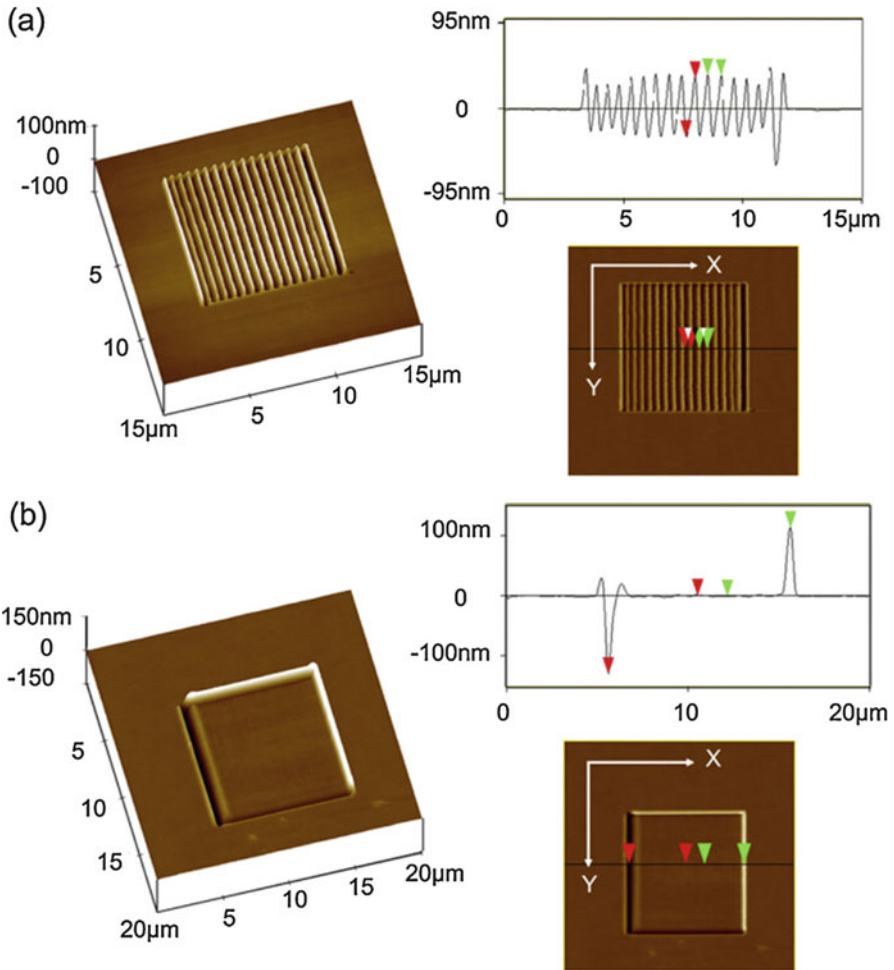


Fig. 12 The morphologies of the scratched sample surface with the feed of 10 nm: (a) rectangular trajectory and (b) line-scratch trajectory (Reproduced with permission from Yan et al. 2012)

nanostructure, can be formed when machining with the line-scratch trajectory. The reason for this phenomenon is attributed to the different scratching paths for the rectangular and the line-scratch trajectories. As shown in Fig. 12b, the left side of the cross section of the AFM image is the beginning point of the scratching process. A groove with a relatively large depth can be found at the beginning point in this case. Figure 13a–d shows the schematic of the front view of the scratching process with the line-scratch trajectory (Yan et al. 2017). As shown in Fig. 13a, the AFM tip penetrates into the sample surface with a preset normal load. After the tip scratching with a small length, one side of the tip is separated from the sample. Thus, the tip is pressed into the sample deeper to balance the normal load, and the height of the material pileup becomes larger due to the increase of the machined depth, as shown in Fig. 12b. With the increase of the material accumulation on the front of the main cutting surface of the AFM tip, the tip should move upward to keep the efficient contact area between the tip and the sample constant, as shown in Fig. 12c. The lateral force (F_t) applied on the tip apex generated by the material pileup is not large enough to reach the critical force value (F_{tc}). Thus, the tip cannot slide over the material pileup. Instead, the material pileup is pushed to the end point by the AFM tip, as shown in Fig. 12d, which is formed the ridge structure at the right side of the structure observed in the cross section of the AFM image. For the rectangular trajectory, the AFM tip is carried out a reciprocating motion. Some material can be pushed to the beginning side of the structure. Thus, the height of the material accumulated at the beginning side of the structure is relatively larger than that machining with the line-scratch trajectory. Figure 13e and f shows the schematic of the front view of the scratching process with the rectangular trajectory (Yan et al. 2017). Due to the large material pileup at the beginning point, the depth penetrated by the AFM tip is smaller, as shown in Fig. 13e. As a result, the height of the material accumulated on the front of the main cutting surface of the AFM tip should be also

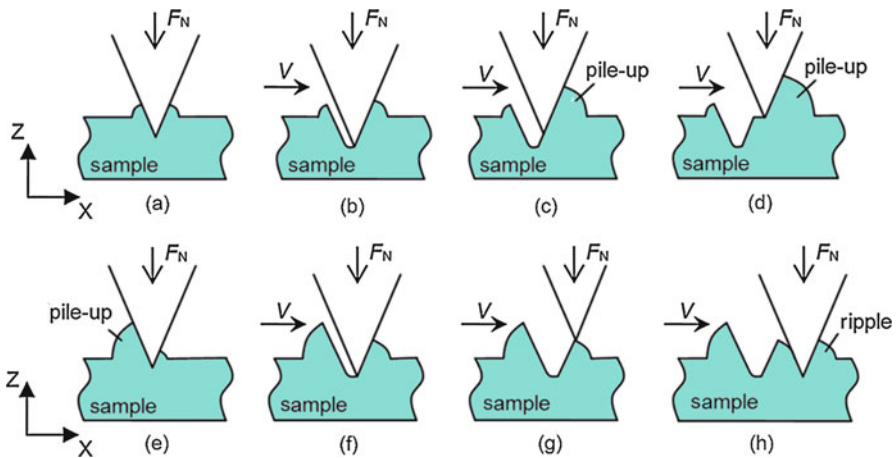


Fig. 13 Formation process of the ripple-type nanostructure: (a–d) scratching with the line-scratch trajectory and (e–h) scratching with rectangular trajectory

smaller, as shown in Fig. 13f. Both the substrate material and the pileup take part in contacting with the AFM tip. In this case, the lateral force (F_T) may be large enough to reach the critical force value (F_{Tc}) to slide over the pileup, as shown in Fig. 13g. The AFM tip then presses into the sample surface again to form another hump, as shown in Fig. 13h. Therefore, it can be indicated that the scratching trajectory has a large influence on the formation of the ripple-type nanostructure, and the rectangular trajectory is the most suitable for the machining of ripple-type nanostructure.

We also investigated the influence of the feed direction on the formation of the ripple-type nanostructure (Yan et al. 2014). The edge-forward, an included angle of 45° and 90° with the edge-forward feed directions were selected, which are named as 0° , 45° , and 90° , respectively. The zigzag trajectory was chosen, the machining area was set as $15 \mu\text{m} \times 15 \mu\text{m}$, and the scratching velocity was $30 \mu\text{m/s}$. Figure 14a shows the machining parameters selected for the scratching tests. Figure 14b–d shows the relationship between the period of the ripple-type nanostructure, applied normal load, and feed value. It can be observed that the feed direction has a large influence on the formation of the ripple-type nanostructure. This reason can be explained as follows. Different cutting angles for various feed directions affect the contact area between the tip and the sample material. In addition, the deformation of the tip cantilever is also changed with different scratching directions, which affects

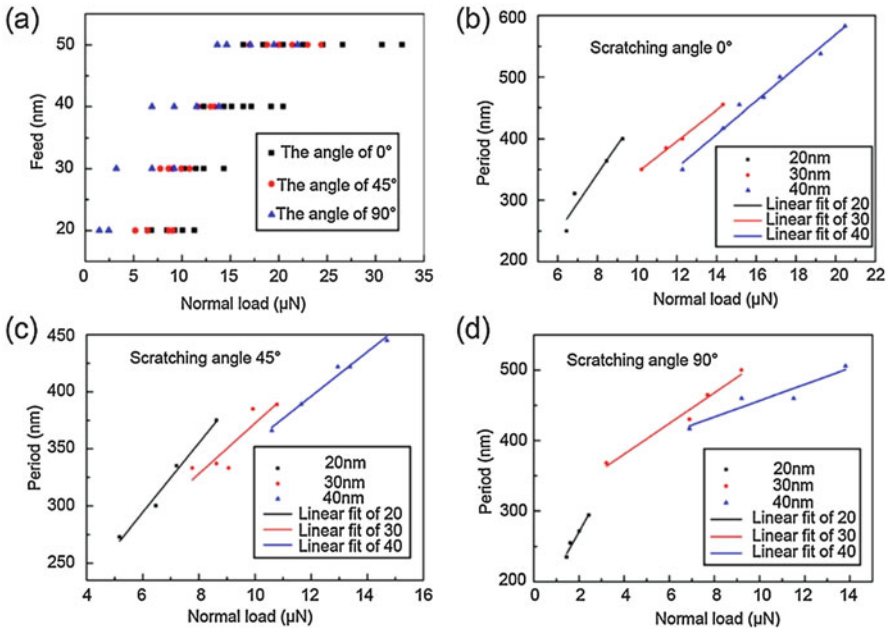


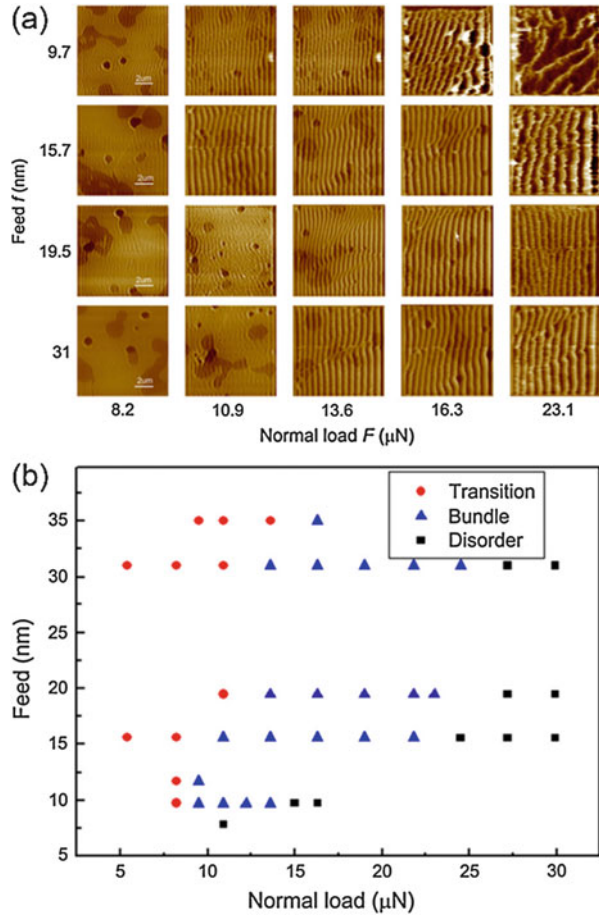
Fig. 14 The relationship between the feed, normal load, and ripple formation. Effects of feed and normal load on (a) ripple formation and (b–d) the period of ripples for different scratching angles (Reproduced with permission from Yan et al. 2014)

the actual normal load applied on the sample surface (Yan et al. 2014). The tip-sample contact area and the actual normal load can affect the lateral force (F_t) applied on the tip apex and the critical force value (F_{tc}), which can thus result in the changing of the period and amplitude of the machined ripple-type nanostructure. Based on the results shown in Fig. 14, it can be indicated that the period scope for the ripple-type nanostructure follows the order $0^\circ > 90^\circ > 45^\circ$ for the three feed directions.

In order to fabricate ripple-type nanostructure with controllable period and amplitude, the influence of the machining parameters, including the applied normal load and the feed value, on the results should also be studied. In our previous (Sun et al. 2012), five normal loads of 10.9 μN , 13.6 μN , 16.3 μN , and 23.1 μN were selected, and four feed values of 9.7 nm, 15.7 nm, 19.5 nm, and 31 nm were chosen to conduct scratching tests on PC sample surface. The rectangular trajectory and edge-forward feed direction were employed. Figure 15 shows the AFM images of the obtained nanostructures and the feasibility analysis of the selected machining parameters, respectively. It can be observed from Fig. 15a that the ripple nanostructure cannot be formed when scratching with small normal loads and relatively large feed values, such as the normal loads of 8.2 μN and 10.9 μN , and the feed values of 19.5 nm and 31 nm. As mentioned above, the normal force and the feed value can affect the lateral force applied on the tip apex (F_t) and the critical force value (F_{tc}). If the F_t cannot reach the critical force value F_{tc} , the ripple-type nanostructure cannot be formed. When scratching with a small normal load and large feed value, the machined depth is relatively small, which will cause a relatively small lateral force (F_t). Thus, in these cases, the lateral force may be not larger enough for the AFM tip sliding over the pileup to form the ripple-type structure. It can also be found from Fig. 15a that the deformation of the ripple-type nanostructure occurs when scratching with a relatively large normal load, such as 16.3 μN and 23.1 μN . In particular, the nanostructure becomes disordered with a small feed value, such as 9.7 nm. This phenomenon can be explained as follows. When the normal load is relatively large and the feed is relatively small, the latter scratching path can affect the pervious scratching path a lot, which results in the formation of the disorder nanostructure, rather than the ripple-type nanostructure. In order to obtain the influence of the normal and feed value more clearly, the feasibility analysis was conducted (Sun et al. 2012). The result of the feasibility analysis is shown in Fig. 15b. We defined the “Transition” state as the indistinct structure, such as the morphology obtained with the normal load of 8.2 μN and the feed of 9.7 nm. The “Bundle” state means the formation of the regular ripple-type nanostructure. The “Disorder” state indicates the generation of the disordered nanostructure. From Fig. 15b, the range of the normal load and the feed value for generation ripple-type nanostructure can be obtained, which can give an instruction on the machining parameters selection for the fabrication of the ripple-type nanostructure with good quality (Sun et al. 2012).

Figure 16a shows the relationship between the feed value, the period, and the amplitude of the ripple-type nanostructure. It can be observed that both the period and the amplitude are increasing slightly with the feed going up when scratching

Fig. 15 (a) AFM image of the machined nanostructure with different normal loads and feeds. (b) Effects of the feed and the normal load on formation states of ripple structures (Reproduced with permission from Sun et al. 2012)

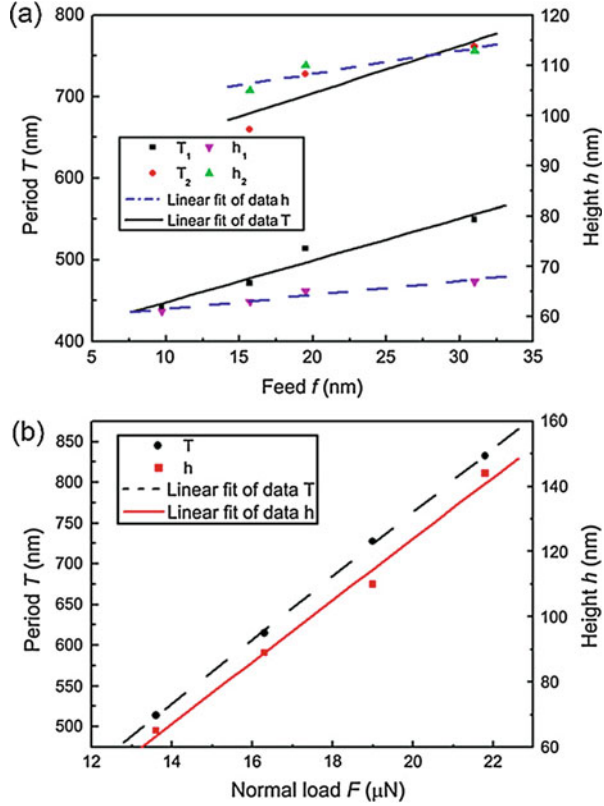


with the normal load of 13.6 μN and 19.0 μN . Figure 16b shows the relationship between the normal load, the period, and the amplitude of the ripple-type nanostructure. It can be found that both the period and the amplitude increase dramatically with the normal load going up when scratching with the feed of 19.5 nm. Therefore, we can conclude that the normal load has a greater influence on the machining outcomes than the feed value.

13.5 Fabrication of 3D Nanostructure by Combining the Material Accumulation and the Machined Nanogroove

Recently, an easy and novel approach to fabrication 3D nanostructure was proposed in our pervious study (He et al. 2018). As shown in Fig. 17a, we knew that a large pileup can be formed when scratching on the polymer material with an AFM tip. The proposed method is just considered simply combining the material pileup and the

Fig. 16 (a) Relationships between the period, the height amplitude, and the feed value. (b) Relationships between the period, the amplitude, and the normal load (Reproduced with permission from Sun et al. 2012)



machined groove to form a 3D nanostructure by controlling the separation distance between parallel adjacent scratching paths. Comparing these methods mentioned above, this approach shows the properties of high efficiency, easy operation, and high feasibility for various applications. Considering the sample material, the tapping mode and silicon AFM tip are employed. Due to the geometrical asymmetry of the silicon tip, the scratching direction has a large influence on the profile of the machined groove, as shown in Fig. 17b. The sample material is a poly(methyl methacrylate) (PMMA) thin film. Figure 18a shows the AFM image of the typical groove machined with sideface-forward scratching direction (denoted 90° in Fig. 17a), in which the scratching direction is perpendicular to the tip cantilever. Figure 18b presents the AFM image of the typical groove machined with edge-forward scratching direction (denoted 0° in Fig. 17a), in which the scratching direction is parallel to the tip cantilever. It can be observed that the material is only accumulated on one side of the groove when scratching with sideface-forward scratching direction, while, for the edge-forward scratching direction, the material pileup can be found on both sides of the groove. The period is defined as the total width of the groove and pileup, as shown in Fig. 18. The height and the depth can be measured by the cross section of the AFM image.

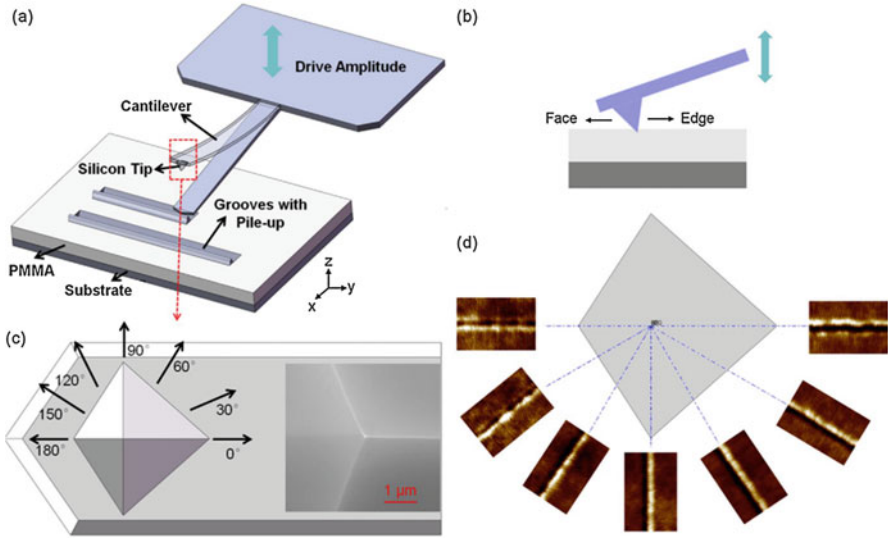


Fig. 17 (a) Schematic of grooves with pileup fabrication on a PMMA thin film using tapping mode. (b) Edge- and face-forward writing directions. (c) Geometry of a silicon tip. (d) AFM images of grooves obtained from different scanning directions (Reproduced with permission from He et al. 2018)

We selected sideface-forward scratching direction to conduct the machining process of the 3D nanostructure because the pileup only exists on one side of the groove and the other side can be connected with the material pileup of adjacent groove. The separation distance between parallel adjacent scratching paths can be chosen as the corresponding period of the groove. Figure 19 shows the machined 3D nanostructure with the wavelength of 30 nm and 40 nm. It can be found that the machining quality of the structure is good. The wavelength of the machined structure is determined by the period of the groove, and the amplitude is controlled by the machined depth of the groove. From Fig. 19, it can be indicated that this proposed method is feasible to fabricate 3D nanostructure.

13.6 Summary and Outlook

The AFM tip-based nanomechanical machining method shows advantages of nano-scale machining accuracy, wide range of applicable materials, atmospheric environment requirement, and low cost. In this chapter, we introduce several approaches based on this technique to fabricate 3D nanostructure with desired dimensions.

1. The force-control method is the most intuitive way to fabricate nanostructures with fluctuant machined depth. The feed value is kept constant during the whole scratching process. The relationship between the machined depth, applied normal,

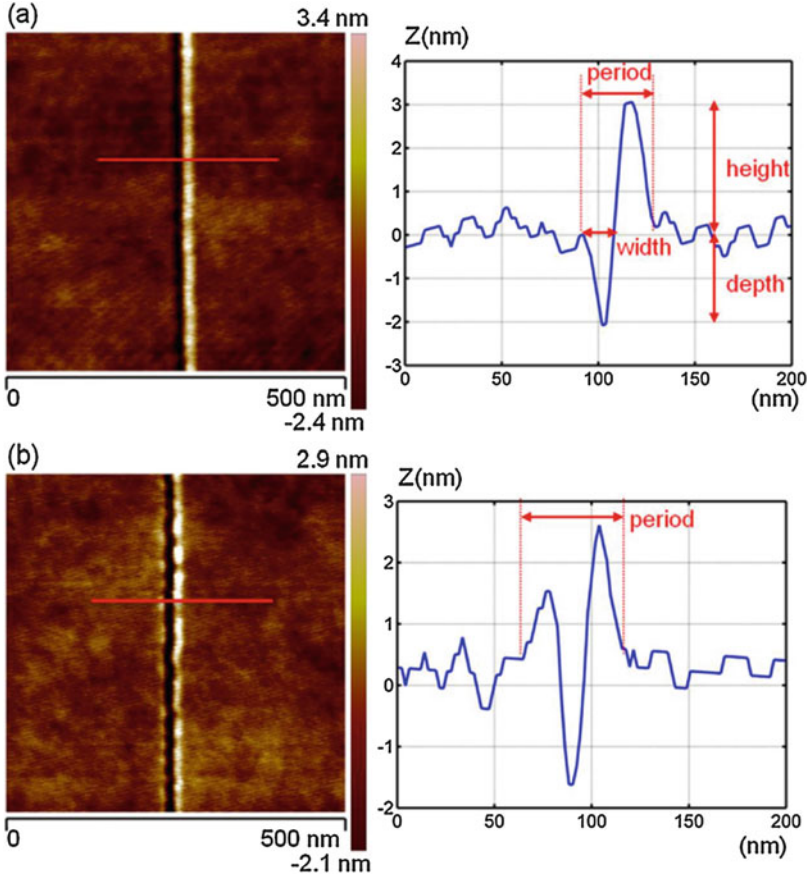


Fig. 18 AFM images and cross sections of grooves fabricated with (a) pileup accumulated at 90° along one side and (b) pileup accumulated at 0° along both sides (Reproduced with permission from He et al. 2018)

and feed value can be obtained by calculation of the tip-sample contact area. However, in the load-control method, each point on the nanostructure requires a specific normal load and the accurate location. This may result in relatively time-consuming.

2. For the feed-control approach, only the feed values for each machined depth is needed. The applied normal load is kept constant. This machining process can be changed into a design of the scratching trajectory, which can improve the machining efficiency.
3. 3D ripple-type nanostructure can be fabricated on the surface of the polymer material by the stick-slip process. This ripple-type nanostructure is perpendicular to the scratching direction. The applied normal load, tip-sample contact area, geometrical shape of the tip, and deformation of the tip cantilever have a large

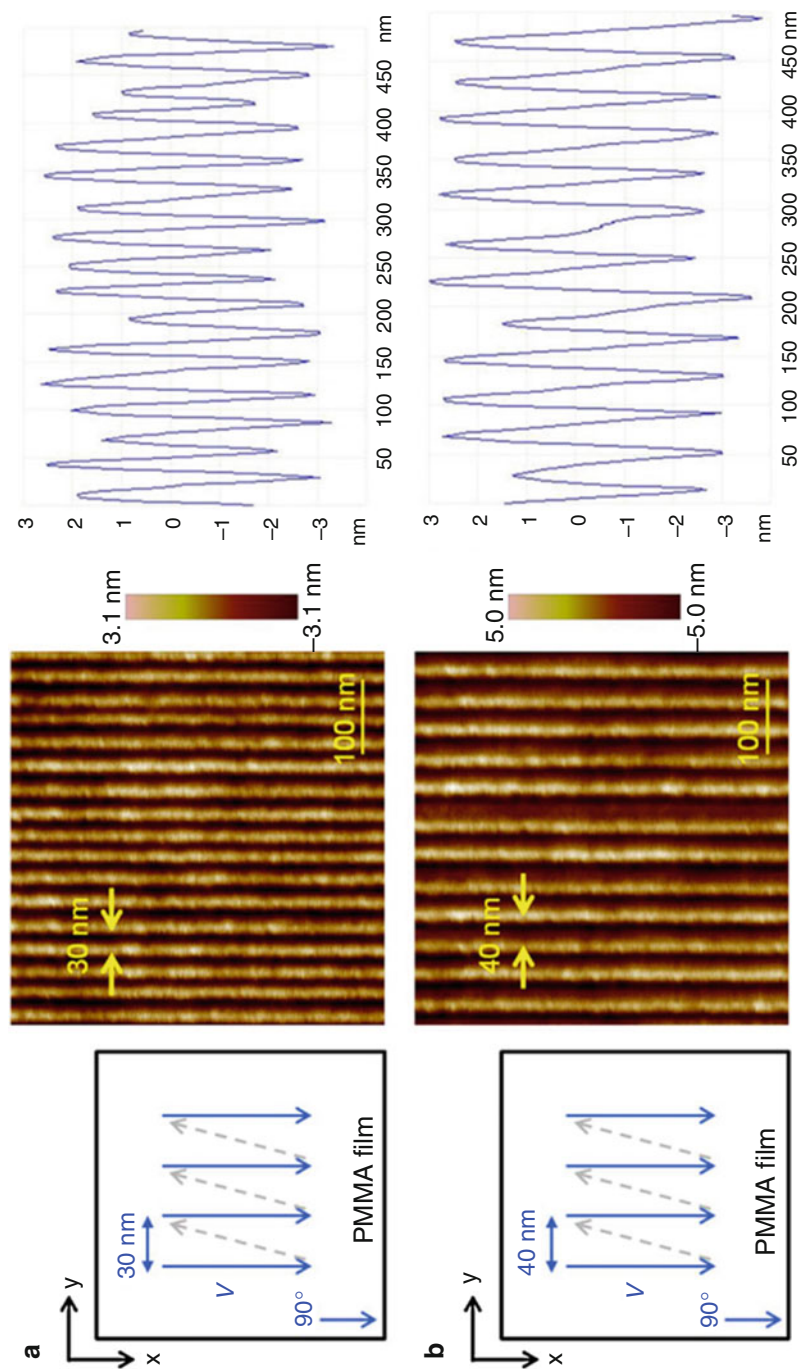


Fig. 19 Schematic of tip traces and AFM images of arrays of grooves obtained in the direction of 90° for a feed of (a) 30 nm and (b) 40 nm (Reproduced with permission from He et al. 2018)

influence on the formation of the ripple nanostructure. The relationship between the period and amplitude of the ripple nanostructure and the machining parameters can be obtained by the experimental tests.

4. The last method described in this chapter is just considered simply combining the material pileup and the machined groove to form a 3D nanostructure. The waveform of the structure is controlled by the separation distance between parallel adjacent scratching paths. Comparing these methods mentioned above, this approach shows the properties of high efficiency, easy operation, and high feasibility for various applications.

Although the AFM tip-based nanomechanical machining technique has already been used for the fabrication of 3D nanostructure, it is still in its infancy for the applications in many fields. Thus, much research in this area is needed to be considered.

1. *Fabrication 3D nanostructure on curved surface* To date, nanogroove and nanopit structures have been fabricated on the micro-ball, which has the potential to prepare the inertial confinement fusion (ICF) target with the expected dimension defects (Geng et al. 2017b). However, more complex nanostructures, such as 3D nanostructures, are required to simulate the arbitrary defects to advance the ICF field. Thus, in the future, 3D nanostructure on the curved surface can be machined by combination of the methods described in this chapter and the new device proposed in (Geng et al. 2017b).
2. *Promotion of the application* Using this technique, complex 3D nanostructure with expected dominations has already been fabricated successfully. However, no research related to the application of the 3D nanostructure machined by this technique has been reported yet. Thus, in the future, more attention should be given to the combination of this technique with other micro-/nanofabrication methods, such as wet etching, lift-off process, and optical lithography, to gain more interesting results, which can advance the application of this technique.
3. *Combination of multiple recourse effects* The mechanical effect combining the chemical and thermal energy or other recourses may lead to reducing the tip wear and improving the processing efficiency. This can contribute to create novel nanofabrication approaches.

References

- Aoike T, Uehara H, Yamanobe T et al (2001) Comparison of macro- and nanotribological behavior with surface plastic deformation of polystyrene. *Langmuir* 17(7):2153–2159
- Barton RA, Ilic B, Verbridge SS et al (2010) Fabrication of a nanomechanical mass sensor containing a nanofluidic channel. *Nano Lett* 10:2058–2063
- Bhushan B (2002) Introduction to tribology. Wiley, New York
- Binnig G, Quate CF, Gerber C (1986) Atomic force microscope. *Phys Rev Lett* 56(9):930–933
- Bowden FP, Tabor D (1950) The friction and lubrication of solids. Oxford University Press, Oxford

- Brousseau EB, Arnal B, Thiery S, et al (2013) Towards CNC automation in AFM probe-based nano machining. In: International conference on micromanufacture, Victoria, p 95
- Chen J, Workman RK, Sarid D et al (1994) Numerical simulations of a scanning force microscope with a large-amplitude vibrating cantilever. *Nanotechnology* 5(4):199–204
- D'Acunto M, Napolitano S, Pingue P et al (2007) Fast formation of ripples induced by AFM: a new method for patterning polymers on nanoscale. *Mater Lett* 61:3305–3309
- Dagata JA (1995) Device fabrication by scanned probe oxidation. *Science* 270(5242):1625–1626
- Dinelli F, Leggett GJ, Shipway PH (2005) Nanowear of polystyrene surfaces: molecular entanglement and bundle formation. *Nanotechnology* 16(6):675–682
- Dregely D, Neubrech F, Duan H et al (2013) Vibrational near-field mapping of planar and buried three-dimensional plasmonic nanostructures. *Nat Commun* 4:2237
- Duan C, Alibakhshi MA, Kim DK et al (2016) Label-free electrical detection of enzymatic reactions in nanochannels. *ACS Nano* 10:7476–7484
- Elkaakour Z, Aime JP, Bouhacina T et al (1994) Bundle formation of polymers with an atomic-force microscope in contact mode—a friction versus peeling process. *Phys Rev Lett* 73(24):3231
- Geng Y, Yan Y, Zhao X et al (2013a) Fabrication of millimeter scale nanochannels using the AFM tip-based nanomachining method. *Appl Surf Sci* 266:386–394
- Geng YQ, Yan YD, Xing YM et al (2013b) Modelling and experimental study of machined depth in AFM-based milling of nanochannels. *Int J Mach Tools Manuf* 73:87–96
- Geng Y, Yan Y, Yu Y et al (2014) Depth prediction model of nanogrooves fabricated by AFM-based multi-pass scratching method. *Appl Surf Sci* 313:615–623
- Geng Y, Yan Y, Hu Z et al (2016a) Investigation of the nanoscale elastic recovery of a polymer using an atomic force microscopy-based method. *Meas Sci Technol* 27:015001
- Geng Y, Yan Y, Brousseau E et al (2016b) Processing outcomes of the AFM probe-based machining approach with different feed directions. *Precis Eng* 46:288–300
- Geng Y, Yan Y, Brousseau E et al (2016c) Machining complex three-dimensional nanostructures with an atomic force microscope through the frequency control of the tip reciprocating motions. *J Manuf Sci Eng* 138:124501
- Geng Y, Yan Y, Brousseau E et al (2017a) AFM tip-based mechanical nanomachining of 3D micro and nano-structures via the control of the scratching trajectory. *J Mater Process Technol* 248:236–248
- Geng Y, Wang Y, Yan Y et al (2017b) A novel AFM-based 5-axis nanoscale machine tool for fabrication of nanostructures on a micro ball. *Rev Sci Instrum* 88(11):115109
- He Y, Yan Y, Geng Y et al (2018) Fabrication of periodic nanostructures using dynamic plowing lithography with the tip of an atomic force microscope. *Appl Surf Sci* 427:1076–1083
- Heyde M, Rademann K, Cappella B et al (2001) Dynamic plowing nanolithography on polymethylmethacrylate using an atomic force microscope. *Rev Sci Instrum* 72:136–141
- Kim SJ, Li LD, Han J (2009) Amplified electro kinetic response by concentration polarization near nanofluidic channel. *Langmuir* 25(13):7759–7765
- Kumar K, Duan H, Hegde RS et al (2012) Printing colors at the optical diffraction limit. *Nat Nanotechnol* 7(9):557–561
- Liang X, Chou SY (2008) Nanogap detector inside nanofluidic channel for fast real-time label-free DNA analysis. *Nano Lett* 8(5):1472–1476
- Lin ZC, Hsu YC (2012) A calculating method for the fewest cutting passes on sapphire substrate at a certain depth using specific down force energy with an AFM probe. *J Mater Process Technol* 212:2321–2331
- Liu W, Yan Y, Hu Z et al (2012) Study on the nano machining process with a vibrating AFM tip on the polymer surface. *Appl Surf Sci* 258:2620–2626
- Mao Y, Kuo K, Tseng C et al (2009) Research on three dimensional machining effects using atomic force microscope. *Rev Sci Instrum* 80:0651056
- Menard LD, Ramsey JM (2011) Fabrication of sub-5 nm nanochannels in insulating substrates using focused ion beam milling. *Nano Lett* 11(2):512–517

- Peng R, Li D (2016) Fabrication of polydimethylsiloxane (PDMS) nanofluidic chips with controllable channel size and spacing. *Lab Chip* 16:3767–3776
- Pires D, Hedrick JL, Silva AD et al (2010) Nanoscale three-dimensional patterning of molecular resists by scanning probes. *Science* 328:732–735
- Richard DP, Jin Z, Feng X et al (1999) ‘Dip-pen’ nanolithography. *Science* 283(5402):661–663
- Salapaka MV, Chen DJ, Cleveland JP (2000) Linearity of amplitude and phase in tapping-mode atomic force microscopy. *Phys Rev B* 61(2):1106–1115
- Sun Y, Yan Y, Hu Z et al (2012) 3D polymer nanostructures fabrication by AFM tip-based single scanning with a harder cantilever. *Tribol Int* 47:44–49
- Surtchev M, de Souza NR, Jerome B (2005) The initial stages of the wearing process of thin polystyrene films studied by atomic force microscopy. *Nanotechnology* 16(8):1213–1220
- Tamayo J, Garcia R (1996) Deformation: contact time, and phase contrast in tapping mode scanning force microscopy. *Langmuir* 12(18):4430–4435
- Yan Y, Hu Z, Zhao X et al (2010) Top-down nanomechanical machining of three-dimensional nanostructures by atomic force microscopy. *Small* 6(6):724–728
- Yan Y, Sun Y, Yang Y et al (2012) Effects of the AFM tip trace on nanobundles formation on the polymer surface. *Appl Surf Sci* 258:9656–9663
- Yan Y, Sun Y, Li J et al (2014) Controlled nanodot fabrication by rippling polycarbonate surface using an AFM diamond tip. *Nanoscale Res Lett* 9:372
- Yan Y, Geng Y, Hu Z (2015) Recent advances in AFM tip-based nanomechanical machining. *Int J Mach Tools Manuf* 99:1–18
- Yan Y, Cui X, Geng Y et al (2017) Effect of scratching trajectory and feeding direction on formation of ripple structure on polycarbonate sheet using AFM tip-based nanomachining process. *Micro Nano Lett* 12(12):1011–1015
- Yang S, Yan Y, Liang Y et al (2013) Effect of the molecular weight on deformation states of the polystyrene film by AFM single scanning. *Scanning* 35(5):308–315
- Zhan DP, Han LH, Zhang J et al (2016) Confined chemical etching for electrochemical machining with nanoscale accuracy. *Acc Chem Res* 49(11):2596–2604

Part III

High-Energy Beam Machining Technology



Mitsuhiro Terakawa

Contents

14.1	Introduction	482
14.2	Ultrafast Laser Ablation: Material Removal	483
14.2.1	Fundamentals of Ultrafast Laser Ablation	483
14.2.2	Laser Processing of Transparent Materials	486
14.2.3	Precise Processing beyond the Diffraction Limit	488
14.3	Laser Additive Manufacturing	492
14.3.1	Two-Photon Polymerization	492
14.3.2	Two-Photon Reduction of Metal Ions	492
14.3.3	Simultaneous Induction of Photopolymerization and Photoreduction	495
14.4	Conclusions and Perspectives	496
	References	497

Abstract

A laser enables the confinement of optical energy to a limited small space, resulting in a highly controllable processing zone with high fabrication preciseness. Laser direct writing (LDW) is a fabrication method for structures in a laser-irradiated space or a scanned space and includes subtractive, additive, or modification processing. Laser ablation is a typical subtractive process method where material removal occurs at the laser-irradiated area, while laser sintering, photopolymerization, and photoreduction are widely known as additive methods. The femtosecond laser is a powerful tool for highly precise processing of various kinds of materials and realizes exclusive processing technologies. An understanding of the fundamentals is essential to maximize the outcome of femtosecond

M. Terakawa (✉)

Department of Electronics and Electrical Engineering, Keio University, Yokohama, Japan
e-mail: terakawa@elec.keio.ac.jp

LDW. In this chapter, femtosecond LDW is described for both subtractive and additive material processing, starting with the fundamentals to understand the processing characteristics. Advantages and capabilities of femtosecond LDW are described with reference to recent studies.

Keywords

Laser Processing · Femtosecond Laser · Additive Laser Manufacturing · Photopolymerization · Photoreduction

14.1 Introduction

The term “laser direct writing” (LDW) indicates a method to fabricate a structure in a laser-irradiated or laser-scanned space, just like writing with a pen. LDW enables fabrication of arbitrarily designed structures without using pre-patterned templates such as photomasks. In the case of writing with a pen, the adhesion of ink particles is the basic mechanism, which is an additive approach. The definition of LDW includes subtractive (negative mass change), additive (positive mass change), and modification (no mass change) methods. The typical process of the subtractive method is laser ablation, where material removal occurs at the laser-irradiated area, while laser sintering, photopolymerization, and photoreduction are widely known as additive methods. Waveguide fabrication by changing the refractive index in a glass by femtosecond laser irradiation can be categorized as a modification method.

Lasers enable the confinement of energy in a limited small space, resulting in a highly controllable processing zone with high preciseness of fabrication. Computer-aided laser scanning realizes high-speed manufacturing of arbitrary shapes. Lasers that generate laser pulses longer than several nanoseconds can also be applied to many cases of LDW; however, a femtosecond laser is a powerful tool for the high-precision processing of various kinds of materials because of its exclusive features. Although the development of ultrashort-pulsed lasers traces back to the technology of mode-locking in the 1960s, the femtosecond laser that was capable of material processing was commercially supplied in 1991. Since then, various sophisticated ultrashort-pulsed lasers have been available commercially. Such lasers have been used in many industrial applications including the microfabrication of semiconductor devices, displays, and medical stents.

Despite the fact that ultrashort-pulsed lasers are being used in industries, the fundamentals of ultrafast laser processing are still attracting the interest of scientists and researchers because of its physics and unique phenomena. Compared to nanosecond lasers, femtosecond laser processing enables nonthermal processing with an extremely small heat-affected zone (HAZ) and exclusive processing technology for various materials including the internal processing of transparent materials by non-linear optical interaction. An understanding of fundamentals is essential to maximize the ability of femtosecond laser processing and to create a new fabrication technology.

In this chapter, femtosecond LDW is described for both subtractive and additive material processing, starting with the fundamentals to understand the processing

characteristics. Advantages and capabilities of femtosecond LDW are shown in reference to recent studies.

14.2 Ultrafast Laser Ablation: Material Removal

Laser ablation is the process of removing material mostly from the surface of a solid by laser irradiation, i.e., it is a subtractive process. Laser energy should be transferred to a material via optical absorption; therefore, the outcome of the laser ablation largely depends on the laser wavelength and absorption property of a material at that wavelength. Energy transfer to a material is large when the absorption coefficient is large, but a femtosecond laser enables the processing of transparent materials which show little linear optical absorption, allowing it to process metals, dielectrics, semiconductors, polymers, and even biological materials. In this section, the fundamentals of femtosecond laser ablation are described to understand the processing properties and to provide a basic understanding for maximizing the capability of femtosecond laser ablation. Femtosecond laser processing of transparent materials is also explained, followed by challenges to overcome the limit of fabrication preciseness.

14.2.1 Fundamentals of Ultrafast Laser Ablation

To better understand the properties of femtosecond laser processing, two major points of view are necessary: ultrashort interaction time and high intense optical field. Since the duration of a femtosecond laser pulse is several tens to hundreds of femtoseconds, the duration is much shorter than the electron-to-lattice energy relaxation time of a few picoseconds. The ultrafast phenomena and the mechanisms of femtosecond laser ablation have been discussed substantially and have been described in many review papers (Sundaram and Mazur 2002; Eaton et al. 2012; Krüger and Kautek 2004; Gattass and Mazur 2008). When a laser pulse is irradiated, electrons in a material absorb laser pulse energy and collide with other electrons in the femtosecond timescale (carrier-carrier scattering) until an equilibrium is reached. At this point, the electrons and lattice are in a non-equilibrium state. Part of the energy absorbed by the electrons is then transferred to the lattice (electron-lattice scattering), resulting in an increase in lattice temperature. The oscillation of the lattice propagates as phonons. These phenomena occur within a few picoseconds. In the case of laser processing using lasers which have pulse durations longer than nanoseconds, the laser pulse duration is long enough to be a heating source because the electrons and the lattice reach an equilibrium state within a laser pulse. Material removal occurs by thermal ablation via the liquid phase in subtractive laser processing using nanosecond lasers. In the case of femtosecond laser ablation, the laser pulse, i.e., energy input, completes before electron-lattice scattering and before thermally exciting ions. Therefore, a two-temperature model was used to analyze the femtosecond laser phenomena to simulate electron and lattice temperatures

individually (Kaganov et al. 1957; Anisimov et al. 1974). A phase transition occurs because of the rapid increase of electron temperature in the case of metals, while Coulomb explosion is associated with the case of dielectrics. Momma et al. showed smaller HAZ on metal by using a femtosecond laser by comparing results with different pulse durations ranging from 200 fs to 5 ns (Momma et al. 1996; Chichkov et al. 1996). A femtosecond laser pulse allows the direct excitation of electrons to an ionization state by generating enough seed electrons in tens of femtoseconds. Femtosecond laser ablation is called “nonthermal ablation” because the increase in lattice temperature, which results in a mediating liquid phase, is not required in its mechanism.

In practical processing, a small degree of heat effect occurs in femtosecond laser ablation. The excess energy at material removal is transferred from the electron system to the lattice system and appears as heat increase. The heat effect increases when the repetition rate of femtosecond laser pulses is high because successive pulses reach the material before the completion of heat relaxation after the previous pulse, resulting in an accumulation of heat. Eaton et al. investigated the cumulative heating in borosilicate glass by using a near-infrared femtosecond laser by changing the repetition rate from 100 kHz to 1 MHz (Eaton et al. 2005). As a result, cumulative heating was evident at repetition rates higher than 200 kHz (Fig. 1). They also reported material dependence of cumulative heating by showing negligible cumulative heating on fused silica in the range of their experimental conditions.

Since the energy of a femtosecond laser pulse is confined to an ultrashort timescale, a high intense optical field reaching above 10^{12} W/cm² of peak intensity is easily obtained even though the total energy of the pulse is moderate, thereby allowing exclusive processing methods. In general, optical energy sufficient for a discrete energy level is required for the absorption of a laser pulse by an electron system. The high density of photons in a femtosecond laser pulse allows for the

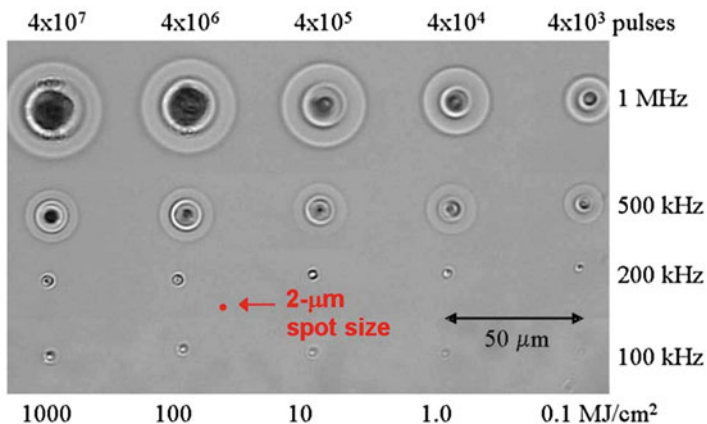


Fig. 1 Optical microscope images showing HAZ created in AF45 borosilicate glass with femtosecond laser. Total pulse (top) and fluence accumulation (bottom) are shown for each column, and laser repetition rate is indicated for each row. Laser direction is normal to page (Eaton et al. 2005)

overlapping of multiphotons which contribute to the excitation from one energy state to a higher state if the sum of the multiphoton energies is equal to or higher than the energy difference between the states (Fig. 2). This is possible because a photon is a boson. In the case of an intense femtosecond laser pulse, phenomena in addition to multiphoton ionization should be considered. For example, the intense electric field of a laser pulse affects the Coulomb potential; consequently, the ionization process in transparent materials depends on the laser intensity. The Keldysh parameter has been proposed to classify these phenomena (Keldysh 1965).

$$\gamma = \frac{E_g}{2U_p}$$

Here, E_g and U_p are the bandgap energy of a material and the ponderomotive energy, respectively. Multiphoton ionization, tunnel ionization, and barrier-suppression ionization occur depending on the incident laser intensity. Such phenomena induced by a femtosecond laser pulse provide precise processing even for transparent materials which have little linear optical absorption. Du et al. studied the ablation threshold of fused silica with a laser pulse ranging from 150 fs to 7 ns (Du et al. 1994). They observed an aberration from the $\tau^{1/2}$ law (thermal diffusion process) with laser pulses shorter than 10 ps. Stuart et al. combined Keldysh's multiphoton absorption theory with avalanche ionization after excitation and contributed a model for the laser ablation of transparent materials (Stuart et al. 1996). Laser ablation of transparent materials is described in detail in the next subsection.

The femtosecond laser is also a powerful tool for the laser ablation of metals. The energy of a laser pulse is absorbed to free electrons that exist in metals by classical absorption. Evaporation occurs before melting at femtosecond laser ablation, resulting in a small HAZ. The ablation threshold depends on the material and can

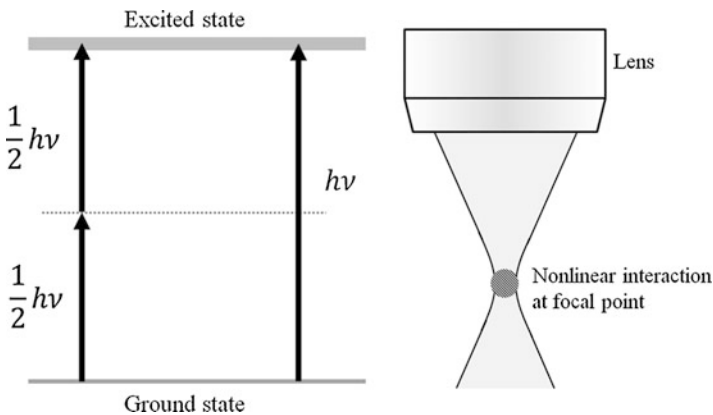


Fig. 2 Schematic diagram of two-photon absorption. Nonlinear interaction occurs at focal point of laser pulse where the photon density is high

be explained by the electron-to-lattice relaxation time. For metals with long relaxation times, such as Au, the energy absorbed at the surface diffuses into the material by energy transfer of ballistic electrons, followed by a decrease in the energy density at the surface. For metals with a short relaxation time, such as Ni, the energy transfer by ballistic electrons at long distances does not occur because of the rapid cooling of the thermal electron, which shows little decrease in surface energy density. Therefore, Au has a higher laser ablation threshold compared to that of Ni (Wellershoff et al. 1999).

14.2.2 Laser Processing of Transparent Materials

Transparent materials including various polymers have less linear optical absorption at visible to near-infrared wavelengths. UV lasers have been used for its surface processing; however, femtosecond lasers having high peak intensity provide precise processing by using visible to near-infrared wavelengths.

Various studies have been reported on the femtosecond laser ablation of polymers after the study on polymethyl methacrylate reported by Srinivasan et al. in 1987 (Srinivasan et al. 1987). Lively discussion on the mechanism of laser ablation of polymers still continues at present. Models based on photothermal, photochemical, and photophysical points of view have been proposed (Bityurin et al. 2003). Even for polymers, the mechanism can be systematically discussed as processes of energy absorption, electron transition, and relaxation. Among transparent materials, polymers have localized electrons in molecules; therefore, differences between energy levels are small because of low individual kinetic energies. Electrons in a polymer occupy hybrid orbits, and thus many narrow levels exist in the energy levels of electrons. The mechanism of laser ablation is highly related to the output of femtosecond laser processing of polymers. For example, laser wavelengths affect the biodegradability of poly(lactic-co-glycolic acid) (PLGA), a typical biodegradable polymer, following femtosecond laser irradiation (Shibata et al. 2016). The degradation rate of the 400-nm-laser-irradiated PLGA film was much greater than that of the 800-nm-laser-irradiated PLGA film (Fig. 3). The acceleration of the biodegradation could be attributed to the decrease in molecular weight induced by the efficient chemical bond dissociation.

Femtosecond laser ablation is very useful for polymer materials that have a low melting temperature because of the low heat effect. Aguilar reported that a small amount of melting was observed with the femtosecond laser ablation of polycaprolactone (PCL) and polyglycolic acid compared to that of a nanosecond laser (Aguilar et al. 2005). The fabrication of coronary stents using femtosecond lasers has shown a significantly smaller HAZ compared with that of a CO₂ laser (Tönshoff et al. 2000). A grating structure was fabricated with a femto second laser on the surface of poly-L-lactic acid (PLLA)-PCL copolymer for cell adhesion and alignment by Yeong et al. (2010).

By focusing a femtosecond laser pulse inside a transparent material, nonlinear optical interaction is induced at the spot of high photon density. If the laser intensity is lower than the threshold for generating macroscopic cracks, a material can be

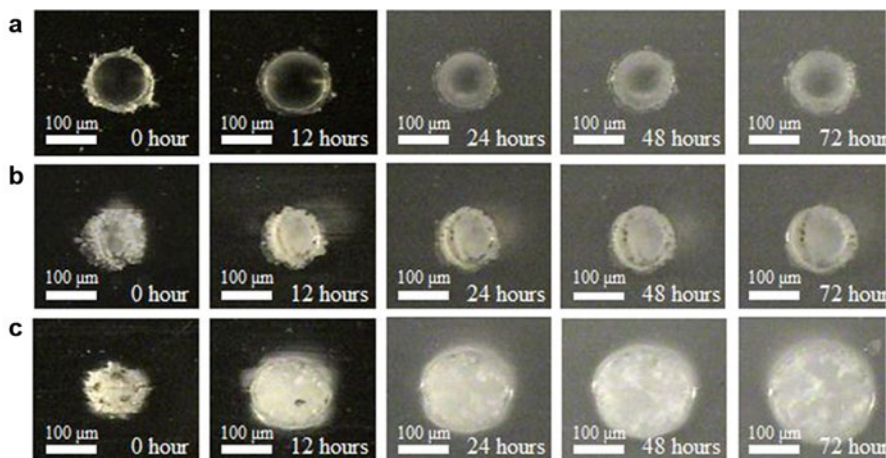


Fig. 3 Craters formed on PLGA films. The time shown in each figure indicate the time of the samples immersed in PBS at 37 °C. Scale bars represent 100 μm. (a) The crater formed by mechanically milling. (b) The laser ablation crater under the condition of 800 nm. (c) The laser ablation crater under the condition of 400 nm (Shibata et al. 2016)

modified without changing its geometrical shape. The phenomena can be used to change the refractive index of a material. Previously, excimer lasers were used to change the refractive index of glass materials containing UV-sensitive compounds such as GeO₂ in the fabrication of optical waveguides. The femtosecond laser-based method that enables modification inside a transparent material attracted great interest for the fabrication of three-dimensional (3D) optical devices.

When it comes to higher photon density, subtractive processing inside a material is realized, i.e., creating a space or void inside a material (Fig. 4; Terakawa et al. 2010). Femtosecond laser provides an exclusive method to process at the focus point of a laser pulse while preserving the material surface and the optical path. Nonlinear interaction at the focus point creates a localized interaction in a limited space. Focused femtosecond laser pulses induce multiphoton ionization on a focal spot inside transparent materials, followed by a rapid increase in the density of free electrons through avalanche ionization. The defect formation and the compaction in an interacting zone produce changes in material density. By focusing a relatively high-energy laser pulse, a micro-explosion can be induced by the focused laser pulse to fabricate voids inside a transparent material (Gattass and Mazur 2008; Glezer and Mazur 1997; Watanabe et al. 2000). The size of the fabricated void is smaller than the focal spot size because the multiphoton absorption mainly takes place in the center of the focused area. The fabricated void consists of a gas phase because of a reduction of the host material (Tönshoff et al. 2000). This process has been applied to the fabrication of 3D void structures for applications including microfluidics (Fig. 5; Wu et al. 2014; Zhang et al. 2017). Femtosecond laser processing inside a material has also been applied to soft materials including biological tissues and cells, in which water makes up a large proportion of the material (Vogel et al. 2005).

Fig. 4 Periodically arrayed voids fabricated inside a fused silica by using 800-nm femtosecond laser. The void was fabricated with ten successive laser pulses irradiation (Terakawa et al. 2010)

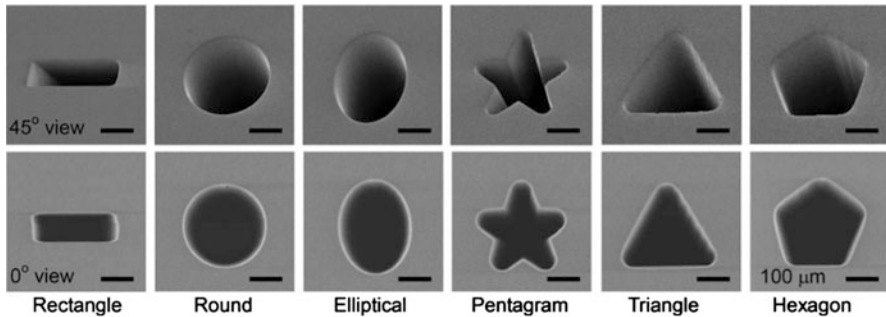
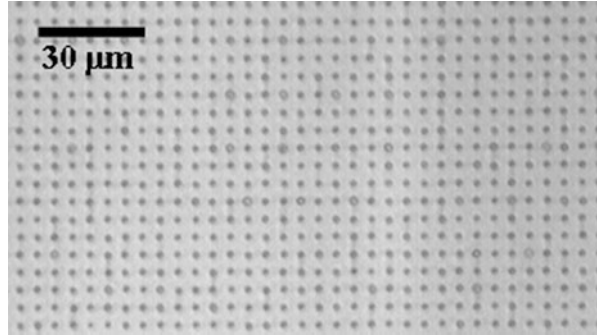


Fig. 5 Forty-five-degree tilted and top-view SEM images of cross sections of 3D microchannels (Wu et al. 2014)

Unlike the case of using nanosecond lasers which generate shock waves by rapidly heating a liquid, femtosecond lasers enable processing at a submicron scale with HAZ small enough to perform eye surgery that preserves an eye's surface and surgery of organelles inside a single cell (Salomao and Wilson 2010).

14.2.3 Precise Processing beyond the Diffraction Limit

The theoretical resolution of the minimum size of the focal spot of light is governed by the Abbe criterion in far-field optics. The processing area/volume is comparable to the interaction area/volume in laser processing by linear interaction; therefore, the minimum size that can be obtained with laser processing is regarded to be larger than several hundred nanometers, which is comparable to or larger than that of the laser wavelength. The conventional way to improve processing preciseness is the utilization of shorter laser wavelengths, and shorter optical sources were developed, e.g., development of lithography technology for semiconductors. Femtosecond laser processing overcomes the limitation of preciseness and has been experimentally demonstrated by several methods. One of the widely known methods for overcoming the diffraction limit in femtosecond LDW is based on the thresholds of nonlinear

interaction. Considering the Gaussian distribution of a laser beam intensity, multiphoton absorption and other nonlinear phenomena occur only in the central area of the beam distribution higher than the threshold (Fig. 6). By precisely controlling the laser intensity, the nonlinear interaction area can be controlled beyond the diffraction limit, resulting in an improvement of fabrication resolution. Liao et al. successfully formed a 50-nm-wide channel on silicate glass by combining the technique with the concept of a single cycle of the modulated energy distribution (Liao et al. 2013). Liu et al. demonstrated the formation of nanogrooves by femtosecond LDW (Fig. 7; Liu et al. 2014). Not only the nonlinear interaction but also the extremely limited HAZ contributed to achieve highly precise processing.

Another approach to overcome the diffraction limit is the utilization of near-field light (Terakawa et al. 2012). Laser irradiation to a nanoscale structure induces enhanced near-field light around a structure. The enhanced light is not limited by the diffraction limit of geometric optics and can be localized in the nanoscale. For example, laser irradiation to metal or dielectric spheres induces a localized enhanced optical field around the spheres. The generated light decays proportionally to r^{-3} , but the intensity of the localized light is much higher than that of the incident laser intensity. The near-field scattering is explained by the Mie scattering theory in the case of dielectric spheres, where the scattering cross section can be derived from the size of a sphere and by the permittivity. The scattering field depends on the polarization mode in a sphere; a strong enhancement is obtained when the mode is in resonance. In the case of metal spheres, collective oscillation of electrons governed by the plasmon polariton is induced at the surface of the spheres, and then an

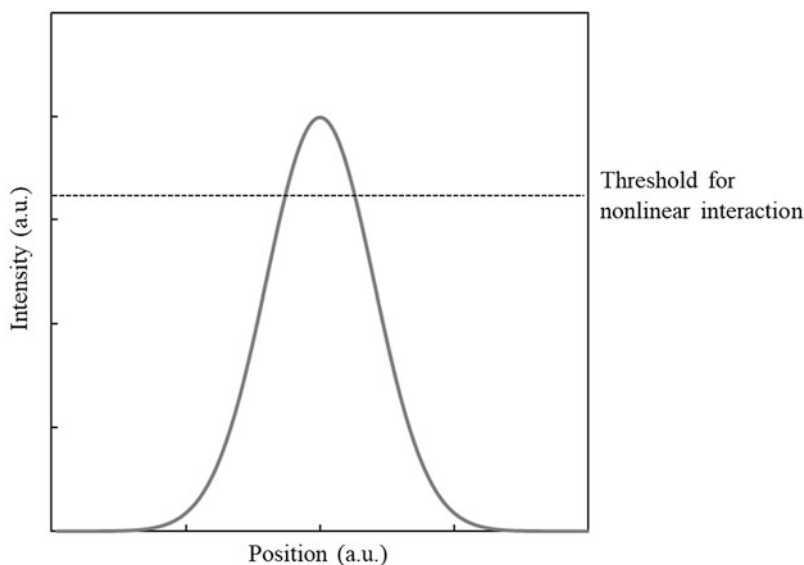


Fig. 6 Gaussian distribution, multiphoton absorption, and other nonlinear phenomena occur only in the central area of the beam distribution higher than the threshold

electromagnetic field is generated around the sphere. In addition, the electromagnetic field is largely affected by the electromagnetic coupling between the metal sphere and the substrate (work). By using an enhanced and localized optical near-field, precise laser processing in the nanoscale can be achieved (Terakawa and Nedyalkov 2016). An enhanced and localized optical near-field can be generated with a nano-second laser; however, a femtosecond laser provides precise processing with a small HAZ for many materials including wide-bandgap materials. Figure 8 shows

Fig. 7 SEM image of nanogrooves fabricated by femtosecond laser irradiation (Liu et al. 2014)

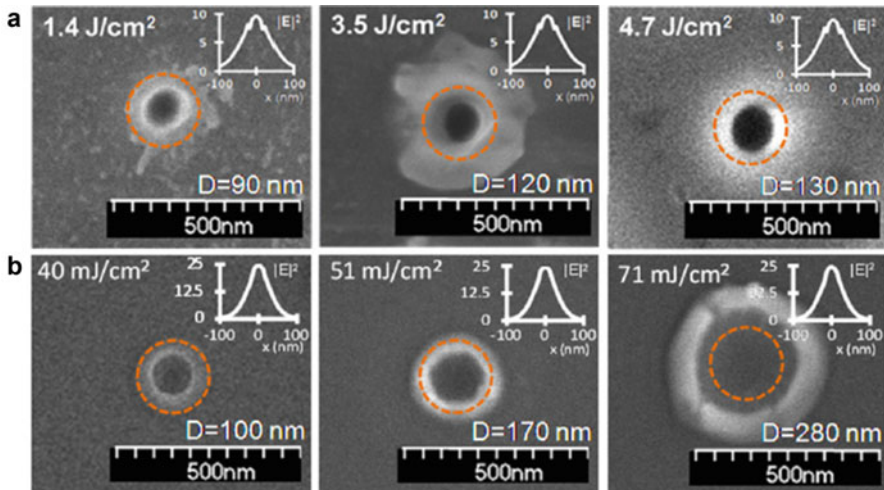
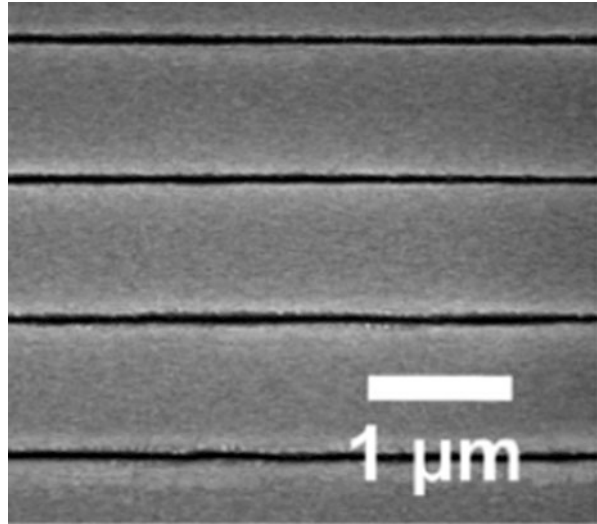


Fig. 8 SEM images of fabricated nanoholes using a 200-nm amorphous TiO_2 particle on (a) SiO_2 and (b) Si substrate surfaces with different laser fluencies. The dashed line shows delineation of the applied particle. (Reproduced with permission from Tanaka et al. 2010)

nanoholes fabricated by the femtosecond laser irradiation of a 200-nm diameter TiO_2 sphere (Tanaka et al. 2010). The wavelength was 400 nm, which is much longer than the 100-nm diameter of the nanohole.

The metallic tips of a scanning tunneling microscope, an atomic force microscope, or the aperture tip of a near-field scanning optical microscope can also write a 2D structure with an optical near-field. The aperture tip used for a near-field scanning optical microscope, whose diameter is in the range of nanometers, was investigated for nanoablation (Chong et al. 2010). In this method, the laser beam was guided through the optical fiber and irradiated a substrate surface as an evanescent wave around the aperture. Ablation characteristics are strongly dependent on the distance between the tip and the sample surface in these methods. An increase in the distance between the tip and sample surface incapacitates nanoablation.

Microspheres, instead of nano-sized sharp tips, can also be used for LDW. The Arnold group demonstrated the optical trapping of a microsphere with a Bessel beam. Although they used a nanosecond laser, they demonstrated the writing of an arbitrary pattern of a 100-nm-wide trench. The near-field direct writing of the subwavelength nanopatterning was performed by scanning laser beam by trapping the microsphere (Fig. 9; McLeod and Arnold 2008). It is notable that, by using a Bessel beam, trapped microspheres show self-positioning in the propagation direction for surface roughness.

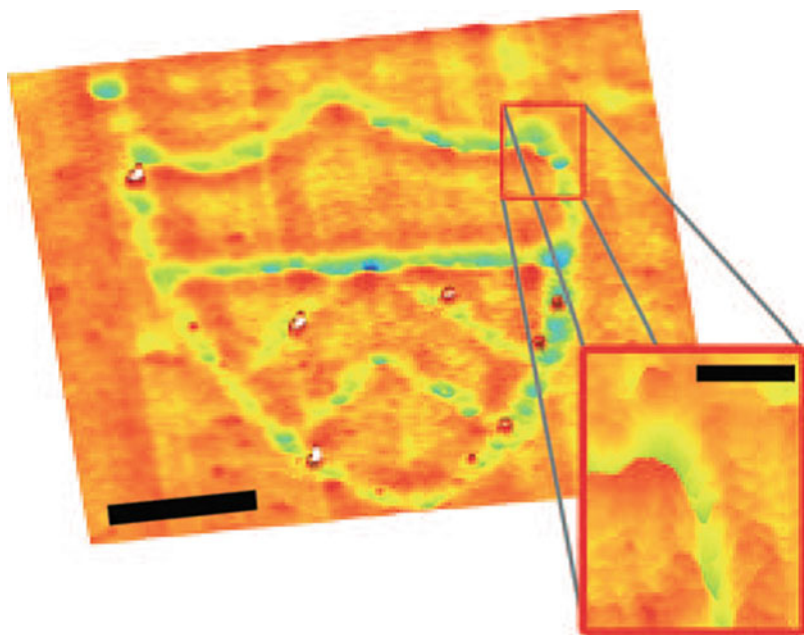


Fig. 9 Princeton University logo nanopatterned on polyimide film using optically trapped sphere. Main scale bar, 2 μm ; inset scale bar, 1 μm . (Reproduced with permission from McLeod and Arnold 2008)

14.3 Laser Additive Manufacturing

LDW in additive processing forms a structure whereby the mass change in the laser-irradiated area or volume after the laser irradiation is positive. Additive LDW methods can be categorized as laser sintering, photopolymerization, and photoreduction. Laser sintering is a method to sinter powdered material and is widely known as a method of 3D printing. Since the role of laser irradiation in laser sintering is a heating source for melting and welding powdered material, a femtosecond laser is less commonly used, but laser sintering by highly controlled cumulative heating was recently reported by using a high-repetition-rate femtosecond laser (Kaden et al. 2017). The advantage of nonlinear interaction with localized laser intensity is obviously shown in a structure formed by photopolymerization and photoreduction, which allows the fabrication of an arbitrary 3D structure with high preciseness. In this section, the LDW of a polymer structure by polymerization via multiphoton excitation is described, followed by the photoreduction of metal ions for fabricating metal structures. In addition, emerging developments in simultaneous induction of photopolymerization and photoreduction for fabricating composite structures are introduced in reference to research performed after 2010.

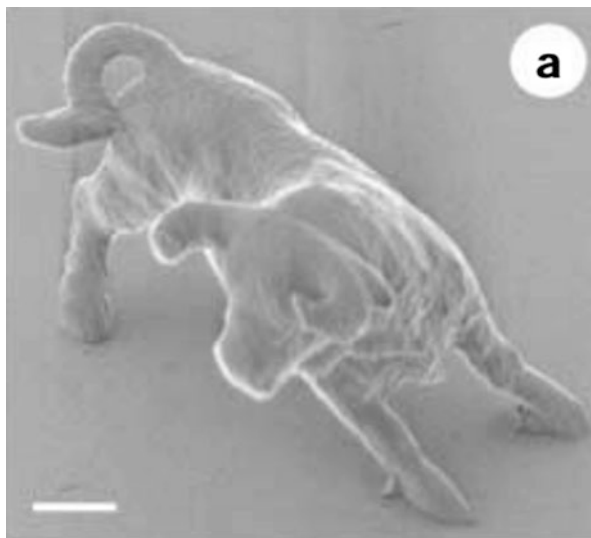
14.3.1 Two-Photon Polymerization

A pioneering study on the fabrication of 3D polymer structures by two-photon or multiphoton polymerization was reported 20 years ago (Maruo et al. 1997). Since then, the method has developed substantially with a number of significant publications. Details can be found in a book (Baldacchini 2016) and review paper (Malinauskas et al. 2016) published in 2016. In principle, a 3D polymer structure is formed via multiphoton absorption by the irradiation of focused ultrashort laser pulses to photo-curable polymers. Similar to nonlinear laser ablation beyond the diffraction limit, the volume for polymerization can be smaller than the diffraction limit by controlling the laser intensity distribution in relation to the threshold of multiphoton absorption. One of the most widely known structures fabricated by this method is the micro-bull structure reported by the Kawata group (Fig. 10; Kawata et al. 2001). Three-dimensional structures were fabricated with high preciseness by scanning focused femtosecond laser pulses. The fabrication system based on multiphoton polymerization has been used for many purposes and applications and is available commercially. Since the threshold of multiphoton polymerization is relatively low, amplifier system for a femtosecond laser is not necessary, while an amplifier system is required in many cases for subtractive processing. This can decrease the total cost of a system for multiphoton polymerization.

14.3.2 Two-Photon Reduction of Metal Ions

Formation of metal by reduction of metal ions is widely known as the silver mirror reaction. Most metal ions show high absorbance at UV wavelengths and can be

Fig. 10 Bull sculpture produced by two-photon polymerization. Scale bars, 2 μm . (Reproduced with permission from Kawata et al. 2001)



reduced by using a UV lamp. Femtosecond lasers enable the localized interaction at the focal point by multiphoton absorption, resulting in the formation of metals by the reduction of metal ions. In 2005, Baldacchini et al. fabricated a silver-wire structure by irradiating 780-nm focused femtosecond laser pulses to a mixed liquid of silver nitrate and polyvinylpyrrolidone on glass (Baldacchini et al. 2005). The unsolidified portion of the mixture was removed after the fabrication. Maruo et al. fabricated a 200-nm-thick silver nanowire in 2008 using a 752-nm femtosecond laser (Maruo and Saeki 2008). They also reported the electrical conductivity of the structure. One of the advantages of multiphoton photoreduction is the ability to fabricate 3D structures with a scanning laser beam. Tanaka et al. fabricated a self-standing structure on a glass substrate using this method (Tanaka et al. 2006). It should be noted that a supporting medium that preserves the shape of the fabricating structure during laser scanning can also be used. Qiu et al. demonstrated the two-photon reduction of Sm^{3+} and Sm^{2+} inside a sodium aluminoborate glass in 1999 (Qiu et al. 1999). Wu et al. fabricated a silver ring structure with silver-doped sol-gel materials (Wu et al. 2000). Multiphoton reduction can be categorized as additive processing if the fabrication is conducted in a liquid or if the metal-ion-containing material is removed after the fabrication. However, the method can also be described as modification processing if the supporting medium is preserved after the fabrication.

In mid- to late 2010, research on the fabrication of metal structures on or in soft materials such as polymers were reported by different groups. He et al. fabricated a 2D silver nanowire structure on a polyethylene terephthalate sheet and demonstrated its electrical conductivity after bending (He et al. 2017). In addition to a femtosecond laser beam for two-photon reduction, they employed a CW laser for optical trapping to fabricate highly dense wires. A pioneering study on photoreduction in gelatin was reported in 2015 by Kang et al. using a 795-nm femtosecond laser (Kang et al. 2015). The fabrication of silver-line structures in synthetic polymer-based hydrogel was demonstrated in 2016 (Fig. 11; Terakawa et al. 2016). The shrinking and swelling of

a fabricated silver structure dependent on the water content of the hydrogel was demonstrated (Fig. 12); it is probable that the structure was composed of nanoparticle aggregates. A 522-nm wavelength femtosecond laser beam improved the efficiency and quality of fabrication of a precise silver-wire grating pattern (Machida et al. 2018). The silver grating fabricated inside the hydrogel produced an optical diffraction pattern to a CW laser beam with equally spaced diffraction spots, which validates the periodicity of the silver grating with a uniform silver-line width (Fig. 13).

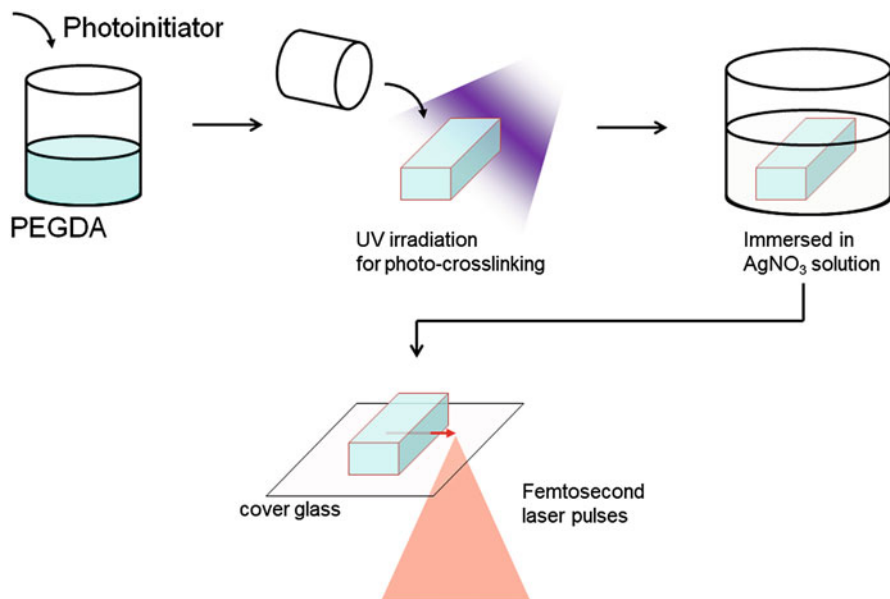


Fig. 11 Schematic illustration of the experimental procedure for fabrication of silver structures inside a hydrogel by using femtosecond laser

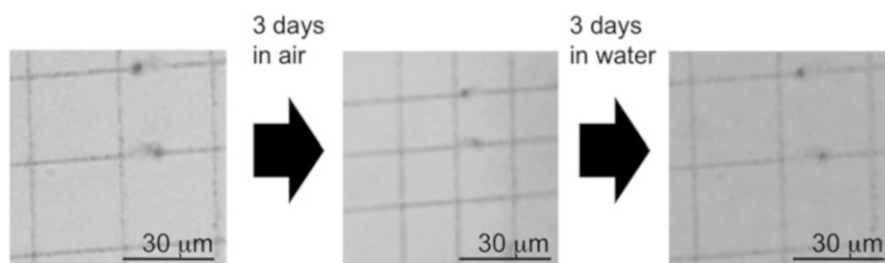


Fig. 12 Optical microscopy images of silver microstructure fabricated in a hydrogel by using 800-nm femtosecond laser pulses. Hydrogel was immersed in water for 1 day after fabrication, was kept in air for 3 days at room temperature, and was soaked again in water and maintained there for 3 days (Terakawa et al. 2016)

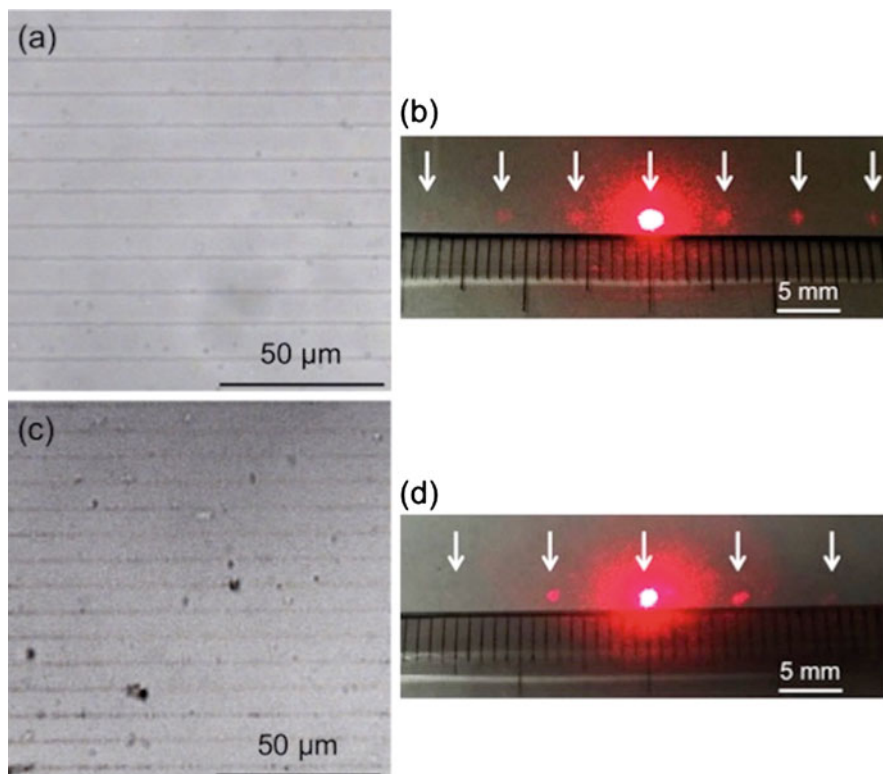


Fig. 13 Bright-field microscope images of silver gratings fabricated by multiphoton photoreduction inside hydrogel and corresponding optical diffraction patterns obtained before and after shrinking of the hydrogel. (a) Bright-field microscope image of silver grating fabricated inside hydrogel before shrinking, (b) optical diffraction pattern obtained with silver grating shown in (a) (distance between diffraction spots was approximately 6.2 mm), (c) bright-field microscope image of silver grating after shrinking of hydrogel, and (d) optical diffraction pattern obtained with silver grating shown in (c) (distance between the diffraction spots was approximately 7.5 mm). White arrows in (b) and (d) indicate diffraction spots (Machida et al. 2018)

14.3.3 Simultaneous Induction of Photopolymerization and Photoreduction

Photopolymerization and photoreduction can be induced by using a femtosecond laser oscillator without an amplifier system. The thresholds of the two reactions are not so different. When both polymerization and reduction were induced simultaneously by laser scanning, a one-step fabrication of a composite structure was produced by LDW (Shukla et al. 2011; Blasco et al. 2016; Sun et al. 2015; Nakamura et al. 2016; Liu et al. 2016). Shukla et al. performed LDW on a conductive SU8/Au composite using an 800-nm femtosecond laser in 2011 (Shukla et al. 2011). In 2016, Blasco et al. fabricated perpendicular connections with microarches made with water-soluble polymers and HAuCl_4 as a gold precursor by simultaneous reactions (Blasco et al. 2016).

A silk/metal composite microstructure was also fabricated (Sun et al. 2015). A silver/poly(dimethylsiloxane) (PDMS) composite microline structure was fabricated by simultaneous induction of photoreduction and photopolymerization by using a femtosecond laser (Fig. 14; Nakajima et al. 2017). The fabricated line structures exhibit electrical conductivity, and the resistances of the structures increase when they are subjected to mechanical force owing to the flexibility of the structure (Fig. 15).

14.4 Conclusions and Perspectives

Laser direct writing by using femtosecond laser was described in this chapter from its fundamentals to practical advantages. Femtosecond LDW can be applied to both subtractive and additive processes, where processing preciseness and characteristics correlate highly with the fundamentals. Therefore, not only trial and error but also understanding the fundamentals is essential for optimizing the output of the process. Although the throughput of laser processing was not described in this chapter, high-speed laser scanning using fast spinning mirrors and multi-spot processing has been implemented to establish LDW technology. Various 3D structures and applications have been previously created by LDW (Malinauskas et al. 2016; Sugioka 2017; Selimis et al. 2015).

Since LDW is a simple process that involves only scanning focused laser pulses, LDW is highly applicable to a production line for customization controlled by computer-aided systems. Laser-based fabrication technology is compatible to the smart manufacturing system in Internet of Things (IoT) and thus plays a considerable role in the transition from mass production to mass customization. For example, the shape and size of a device should be customized to that of each patient in medical applications. The versatility of laser processing for various materials has great potential for the future production technologies for novel devices.

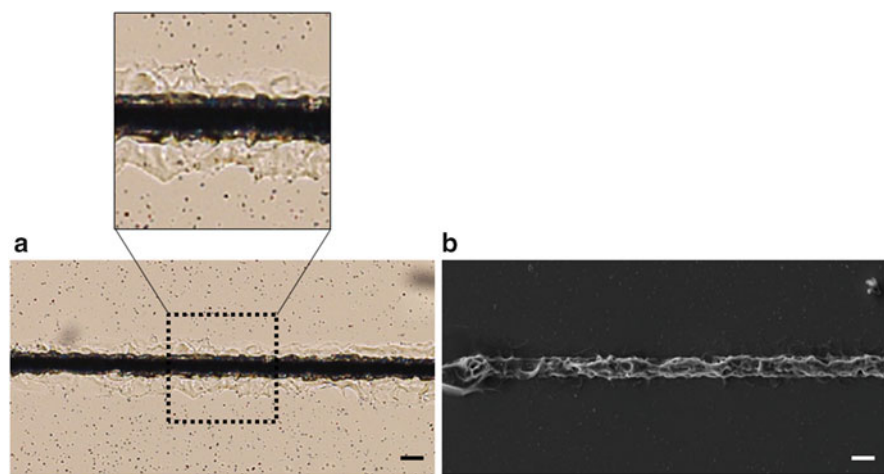


Fig. 14 Optical microscopy image (a) and SEM image (b) of the silver/PDMS composite structure fabricated by femtosecond laser. Scale bars indicate 25 μm (Nakajima et al. 2017)

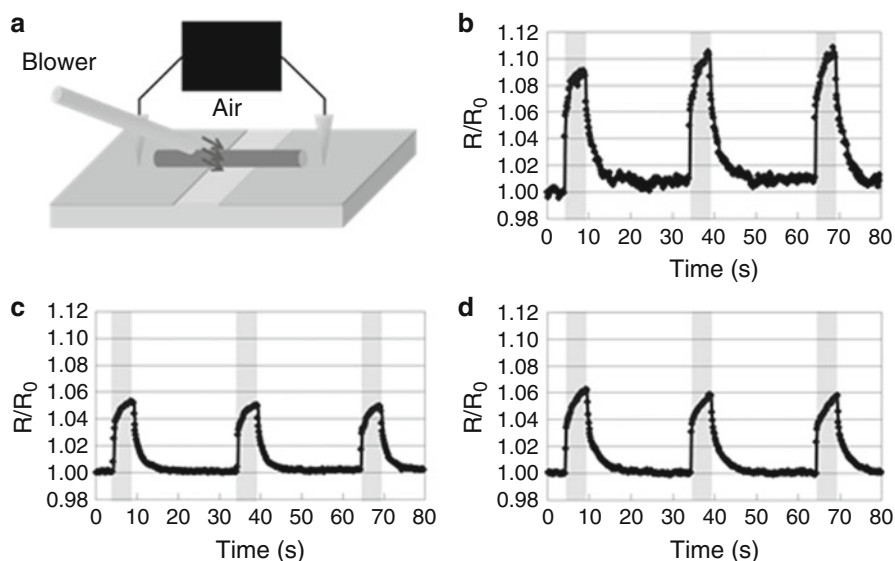


Fig. 15 (a) Experimental configuration for pressure sensing by using the structures fabricated by femtosecond laser. (b–d) Temporal resistance profiles of the silver/PDMS composite line structures during air-blowing. Different numbers of laser scans were used: (a) 4, (b) 10, and (c) 20 scans (Nakajima et al. 2017)

References

- Aguilar CA, Lu Y, Mao S, Chen S (2005) *Biomaterials* 26:7642
- Anisimov SI, Kapeliovich BL, Perelman TL (1974) *JETP* 39:375
- Baldacchini T (ed) (2016) *Three-dimensional microfabrication using two-photon polymerization*. Elsevier, Oxford
- Baldacchini T, Pons A-C, Pons J, LaFratta CN, Fourkas JT, Sun Y, Naughton MJ (2005) *Opt Express* 13:1275
- Biturkin N, Luk'yanchuk BS, Hong MH, Chong TC (2003) *Chem Rev* 103:519
- Blasco E, Müller J, Müller P, Trouillet V, Schön M, Scherer T, Barner-Kowollik C, Wegener M (2016) *Adv Mater* 28:3592
- Chichkov BN, Momma C, Nolte S, von Alvensleben F, Tünnermann A (1996) *Appl Phys A Mater Sci Process* 63:109
- Chong TC, Hong MH, Shi LP (2010) *Laser Photon Rev* 4:123
- Du D, Liu X, Korn G, Squier J, Mourou G (1994) *Appl Phys Lett* 64:3071
- Eaton SM, Zhang H, Herman PR, Yoshino F, Shah L, Bovatsek J, Arai AY (2005) *Opt Express* 13:4708
- Eaton SM, Cerullo G, Osellame R (2012) *Top Appl Phys* 123:3
- Gattass RR, Mazur E (2008) *Nat Photon* 2:219
- Glezer EN, Mazur E (1997) *Appl Phys Lett* 71:882
- He G-C, Zheng M-L, Dong X-Z, Jin F, Liu J, Duan X-M, Zhao Z-S (2017) *Sci Rep* 7:41757
- Kaden L, Matthäus G, Ullsperger T, Engelhardt H, Rettenmayr M, Tünnermann A, Nolte S (2017) *Appl Phys A Mater Sci Process* 123:595
- Kaganov MI, Lifshitz IM, Tanatarov LV (1957) *JETP* 4:173

- Kang S, Vora K, Mazur E (2015) *Nanotechnology* 26:121001
- Kawata S, Sun H-B, Tanaka T, Takada K (2001) *Nature* 412:697
- Keldysh LV (1965) *JETP* 20:1307
- Krüger J, Kautek W (2004) *Adv Polym Sci* 168:247
- Liao Y, Cheng Y, Liu C, Song J, He F, Shen Y, Chen D, Xu Z, Fan Z, Wei X, Sugioka K, Midorikawa K (2013) *Lab Chip* 13:1626
- Liu J, Jia T, Zhou K, Feng D, Zhang S, Zhang H, Jia X, Sun Z, Qiu J (2014) *Opt Express* 22:32361
- Liu Y, Hu Q, Zhang F, Tuck C, Irvine D, Hague R, He Y, Simonelli M, Rance G, Smith E, Wildman R (2016) *Polymers* 8:325
- Machida M, Nakajima Y, Torres-Mapa ML, Heinemann D, Heisterkamp A, Terakawa M (2018) *Sci Rep* 8:187
- Malinauskas M, Žukauskas A, Hasegawa S, Hayasaki Y, Mizeikis V, Buividas R, Juodkazis S (2016) *Light Sci Appl* 5:e16133
- Maruo S, Saeki T (2008) *Opt Express* 16:1174
- Maruo S, Nakamura O, Kawata S (1997) *Opt Lett* 22:132
- McLeod E, Arnold CB (2008) *Nat Nanotechnol* 3:413
- Momma C, Chichkov BN, Nolte S, von Alvensleben F (1996) *Opt Commun* 129:134
- Nakajima Y, Obata K, Machida M, Hornholz A, Koch J, Suttmann O, Terakawa M (2017) *Opt Mater Express* 7:4203
- Nakamura R, Kinashi K, Sakai W, Tsutsumi N (2016) *Phys Chem Chem Phys* 18:17024
- Qiu J, Miura K, Suzuki T, Mitsuyu T, Hirao K (1999) *Appl Phys Lett* 74:10
- Salomao MQ, Wilson SE (2010) *J Cataract Refract Surg* 36:1024
- Selimis A, Mironov V, Farsari M (2015) *Microelectron Eng* 132:83
- Shibata A, Yada S, Terakawa M (2016) *Sci Rep* 6:27884
- Shukla S, Vidal X, Furlani EP, Swihart MT, Kim KT, Yoon YK, Urbas A, Prasad PN (2011) *ACS Nano* 5:1947
- Srinivasan R, Sutcliffe E, Braren B (1987) *Appl Phys Lett* 51:1285
- Stuart BC, Feit MD, Herman S, Rubenchik AM, Shore BW, Perry MD (1996) *J Opt Soc Am B* 13:459
- Sugioka K (2017) *Nanophotonics* 6:393
- Sun Y, Li Q, Sun S, Huang J, Zheng B, Chen Q, Shao Z, Sun H (2015) *Nat Commun* 6:8612
- Sundaram SK, Mazur E (2002) *Nat Mater* 1:217
- Tanaka T, Ishikawa A, Kawata S (2006) *Appl Phys Lett* 88:081107
- Tanaka Y, Obara G, Zenidaka A, Terakawa M, Obara M (2010) *Appl Phys Lett* 96:261103
- Terakawa M, Nedyalkov NN (2016) *Adv Opt Technol* 5:17
- Terakawa M, Toratani E, Shirakawa T, Obara M (2010) *Appl Phys A Mater Sci Process* 100:1041
- Terakawa M, Takeda S, Tanaka Y, Obara G, Miyanishi T, Sakai T, Sumiyoshi T, Sekita H, Hasegawa M, Viktorovitch P, Obara M (2012) *Prog Quantum Electron* 36:194
- Terakawa M, T-Mapa ML, Takami A, Heinemann D, Nedyalkov NN, Nakajima Y, Hörtdt A, Ripken T, Heisterkamp A (2016) *Opt Lett* 41:1392
- Tönshoff HK, Ostendorf A, Nolte S, Korte F, Bauer T (2000) *Proc SPIE* 4088:136
- Vogel A, Noack J, Hüttman G, Paltauf G (2005) *Appl Phys B Lasers Opt* 81:1015
- Watanabe W, Toma T, Yamada K, Nishii J, Hayashi K, Itoh K (2000) *Opt Lett* 26:1669
- Wellershoff SS, Hohlfeld J, Gudde J, Matthias E (1999) *Appl Phys A Mater Sci Process* 69:S99
- Wu P-W, Cheng W, Martini IB, Dunn B, Schwartz BJ, Yablonovitch E (2000) *Adv Mater* 12:1438
- Wu D, Wu S, Xu J, Niu L, Midorikawa K, Sugioka K (2014) *Laser Photonics Rev* 8:458
- Yeong WY, Yu H, Lim KP, Ng KLG, Boey YCF, Subbu VS, Tan LP (2010) *Tissue Eng Part C Methods* 16:1011
- Zhang P, Chen L, Wang F, Tu P (2017) *Microw Opt Technol Lett* 59:1993



Hu Huang and Jiwang Yan

Contents

15.1	Introduction	500
15.2	Potential Methods for Patterning Metallic Glass	501
15.2.1	Mechanical Machining	501
15.2.2	Thermoplastic Shaping	501
15.2.3	Chemical Etching	502
15.2.4	Laser Irradiation	503
15.3	Laser Patterning of Crystalline Materials	503
15.4	Nanosecond Laser Patterning of Metallic Glass	505
15.4.1	Single Laser Pulse Irradiation	505
15.4.2	Line Laser Irradiation	509
15.5	Application in Enhancing Surface Hydrophobicity	522
15.6	Summary and Outlook	524
	References	524

Abstract

Metallic glass (MG) with a long-range topological disorder structure exhibits some unique mechanical, physical, and chemical properties compared to its crystalline counterpart, such as high hardness and strength, large elastic limit as well as superior resistance to wear and corrosion. These features make MGs to be regarded as very promising materials. Recent studies indicate that patterned MG

H. Huang (✉)

School of Mechanical Science and Engineering, Jilin University, Changchun, Jilin, China

Department of Mechanical Engineering, Faculty of Science and Technology, Keio University, Yokohama, Japan

e-mail: huanghu@jlu.edu.cn

J. Yan

Department of Mechanical Engineering, Keio University, Yokohama, Japan

e-mail: yan@mech.keio.ac.jp

surface with micro-/nanostructures on it can hugely enhance its biological activity and compatibility, catalytic activity, and hydrophobicity, extending the application of MGs in biomedicine, waterproof material, industrial catalysis, sewage treatment, etc. This chapter summarizes the potential methods for patterning MGs firstly, mainly including mechanical machining, thermoplastic shaping, chemical etching, and laser irradiation. Then, the emphasis is on nanosecond pulsed laser patterning of MGs, and its recent achievement and development will be addressed. The surface structures patterned by single nanosecond pulsed laser irradiation as well as line laser irradiation under various experimental parameters and environmental atmospheres will be introduced, and their formation mechanisms will be discussed. Accordingly, a new surface patterning method of MGs, i. e., nanosecond pulsed laser irradiation inducing selective thermoplastic extrusion in nitrogen gas, will be provided. Furthermore, the effect of patterned microstructures on the surface hydrophobicity will be briefly discussed.

Keywords

Metallic glass · Surface patterning · Nanosecond laser irradiation · Hierarchical micro-/nanosstructure · Application

15.1 Introduction

Metallic glass (MG) with a long-range topological disorder structure exhibits some unique mechanical, physical, and chemical properties compared to its crystalline counterpart, such as high hardness and strength, large elastic limit, as well as superior resistance to wear and corrosion (Byrne and Eldrup 2008; Plummer and Johnson 2015; Trexler and Thadhani 2010; Wang 2012). These features make MGs to be regarded as very promising structural, engineering, and sports materials (Inoue and Takeuchi 2010; Khun et al. 2016). For example, they are attractive materials for high-end products and high value-added metal components such as electronic frames, sport products, precision surgical instruments, and micro-electromechanical devices (Marti 2007; Plummer and Johnson 2015; Schroers 2013; Telford 2004).

For applications of MGs in the aforementioned fields, the smooth and featureless surface is commonly used. Being different from those applications, recent studies (Chen et al. 2011; Chen et al. 2013; Ketov et al. 2015; Zhao et al. 2009) indicate that compared to smooth surface, patterned MG surface with micro-/nanostructures on it shows some specific features in the aspect of biological activity and compatibility, catalytic activity, and hydrophobicity because of its high effective surface area, and these features enhance the application prospect of MGs in biomedicine, waterproof material, industrial catalysis, sewage treatment, etc. For example, gold-based MG with a heterogeneously granular structure (Chen et al. 2011) exhibits a high catalytic activity in the oxidation of organosilane compounds with water. Zr-Pd MG thin films with a similar nanometer-scale surface structure (Ketov et al. 2015) show good biocompatibility for potential applications in biochemistry and

implant engineering. Pd-based MG surface with hierarchical micro-/nanostructures shows superhydrophobicity, while the corresponding smooth surface shows intrinsic hydrophilicity (Ma et al. 2014).

To enhance their application in these fields, surface patterning of MGs is of great importance (Chen et al. 2011; Ketov et al. 2015; Zhao et al. 2014). However, those unique mechanical, physical, and chemical properties mentioned above, on the other hand, bring difficulties for patterning of MGs, and efficient and controllable fabrication of large-area micro-/nanostructures on MG surface is urgently required.

15.2 Potential Methods for Patterning Metallic Glass

There are four potential methods to pattern MG surface, including mechanical machining, thermoplastic shaping, chemical etching, and laser irradiation. In this section, the characteristics of each method will be briefly introduced.

15.2.1 Mechanical Machining

Although mechanical machining, typically diamond cutting (Brinksmeier et al. 2010; Guo et al. 2014a; Xu et al. 2014), has been widely used to fabricate micro-/nanostructures on the surface of soft metals because of its flexibility, such as copper by tuning tool paths (Zhu et al. 2015), it may be not suitable for MGs. The high hardness of MGs (usually six to eight times of copper) accelerates the tool wear which further affects the uniformity and accuracy of the cutting surface (Bakkal et al. 2004a; Fujita et al. 2005). For some hard-brittle MGs, mechanical machining becomes more difficult. For example, most of Fe-based MGs show high hardness (~12 GPa) but very low fracture toughness (~10 MPa m^{1/2}) (Lewandowski et al. 2005), although some Fe-based MGs with enhanced ductility have been reported recently (Guo et al. 2014b). Furthermore, very low thermal conductivity of MGs results in a high local temperature in the cutting region especially during high-speed cutting. Thus, oxidation and crystallization of MGs may occur (Bakkal et al. 2004b) which probably affect their amorphous performances (Gilbert et al. 1997; Nagendra et al. 2000). In addition, high local temperature will also increase the adhesion between the chip and tool, leading to the formation of built-up edge on the rake face and thus affect the subsequent cutting process (Bakkal et al. 2004a; Huang et al. 2012). Hence, fabrication of micro-/nanostructured surfaces on MGs by mechanical machining is still challenging.

15.2.2 Thermoplastic Shaping

Taking the feature of viscous state in the supercooled temperature region (between the glass transition and crystallization temperature), thermoplastic shaping is reported to form micro-/nanostructured surfaces on MGs (He et al. 2016a; Hu et al. 2015;

Kumar et al. 2009). For example, by thermoplastic shaping, Xia et al. (2012) use a silicon mold to pattern honeycomb microstructures on Pd-based MG surface, achieving superhydrophobicity. Using the similar method, Ma et al. (2014) pattern hierarchical micro-/nanostructures on Pd-based MG surface, and the surface characteristic is changed from hydrophilicity (smooth surface) to superhydrophobicity (patterned surface).

Although thermoplastic shaping provides a unique way to pattern the MG surface, some shortcomings exist which hinder its wide application. Firstly, the patterned structures completely rely on the structures preformed on the mold surface, and thus the fabrication flexibility is relatively low. Secondly, the materials used for mold, such as silicon and Al_2O_3 , are commonly hard-brittle materials, and fabrication of this kind of mold usually requires expensive or complex processing technologies such as femtosecond laser, photolithography, ion etching, etc. (Kumar et al. 2009; Ma et al. 2014; Xia et al. 2012). Thus, the fabrication cost is high, and, additionally, it is very hard to fabricate the mold with large-area complex micro-/nanostructures. Thirdly, the mold is easy to fracture under circularly thermal and mechanical stress during thermoplastic shaping, which greatly decreases the mold lifetime (Plummer and Johnson 2015). Fourthly, because of the capillary effect as well as other reasons, MG materials are very hard to completely fill the micro-/nanostructured mold (Kumar et al. 2009; Liu and Schroers 2015; Sarac et al. 2017). Fifthly, demolding process that separates the sample with the mold is quite difficult, and in this process, both mold and sample surfaces are easily damaged. Currently, after thermoplastic shaping, the mold is directly etched by acid or alkali (Hasan and Kumar 2016; Kumar et al. 2009; Liu and Schroers 2015; Xia et al. 2012), and one mold is commonly used only one time, which further increases the cost and pollutes the environment. Sixthly, crystallization may occur during the thermoplastic shaping because it is very hard to control a uniform forming temperature (Kaltenboeck et al. 2014; Plummer and Johnson 2015), especially for MGs with a narrow supercooled temperature region. Thus, thermoplastic shaping may be suitable for some specific applications using smooth surface, but for patterning micro-/nanostructures on MG surface, many problems as mentioned above should be carefully considered.

15.2.3 Chemical Etching

Chemical etching is another method to pattern MGs. The MGs consisting of active elements can react with some specific chemical reagent, by which the MG surface is selectively etched and thus patterned. Zhao et al. (2009) use double-distilled water to etch CaLi-based MG, forming micro-/nanoscale hierarchical surface structures. The etched surface is further chemically modified with fluoroalkylsilane coating. By this combined chemical method, the surface of CaLi-based MG is tuned from hydrophilicity to both superhydrophobicity and superoleophobicity. This method can be combined with thermoplastic shaping to

generate micro-/nanohierarchical surface structures, which can further improve the surface hydrophobicity (Li et al. 2013).

Compared to mechanical machining and thermoplastic shaping, chemical etching process is relatively simple. However, this method is only available for some specific MGs that consist of active elements, and the etched structures, on the other hand, are hard to control. Furthermore, for applications in various MGs, the chemical reagent should be specific which is difficult to select. Additionally, because of using chemical reagent, this method is not environmentally friendly.

15.2.4 Laser Irradiation

When a high-power laser pulse interacts with material surface, the irradiated region may experience melting, vaporization, and boiling, accompanying with material ejection because of recoil pressure. Thus, dimple-like microstructures, linear micro-grooves, and crossed grooves could be patterned on materials surface via laser irradiation.

For applications of laser irradiation in MGs, some micro-/nanostructures are recently reported in the irradiated region when exploring nanosecond pulsed laser-MG interaction under both single laser pulse and line laser irradiation (Huang et al. 2016a; Huang and Yan 2017; Jiang et al. 2015; Liu et al. 2011; Williams and Brousseau 2016), which may open up new ways to pattern MG surface. Compared to the patterning methods mentioned above, laser irradiation method is applicable for almost all kinds of MGs because of their high absorption of laser energy, and the process is highly efficient and environmentally friendly. Thus, laser irradiation is a promising method to pattern large-area micro-/nanostructures on MG surface. As MGs are sensitive to temperature and oxygen, laser irradiation conditions should be carefully considered to avoid crystallization and oxidation.

15.3 Laser Patterning of Crystalline Materials

Laser irradiation with various pulse widths, typically femtosecond, picosecond, and nanosecond, has been widely adopted to fabricate micro-/nanostructures on crystalline material surfaces that possess unique optical, photoelectric, catalytic, mechanical, and wetting properties (Jagdheesh 2014; Martinez-Calderon et al. 2016; Ta et al. 2015; Vorobyev and Guo 2015; Yang et al. 2014). For example, hierarchical micro-/nanostructures as shown in Fig. 1a–c are created on metal surface by femtosecond pulsed laser irradiation (Vorobyev and Guo 2015), resulting in combined effects of dramatically enhanced broadband absorption, super-hydrophobicity, and self-cleaning. Using picosecond pulsed laser irradiation, micro-pillars are patterned on alumina (Al_2O_3) surface as shown in Fig. 1d–f (Jagdheesh 2014), which hugely enhance the surface hydrophobicity. Via nanosecond pulsed laser ablation, micro-/nanostructures as shown in Fig. 1g–i are patterned on silicon surface (Yang et al. 2014), resulting in decreased reflectivity, which has potential

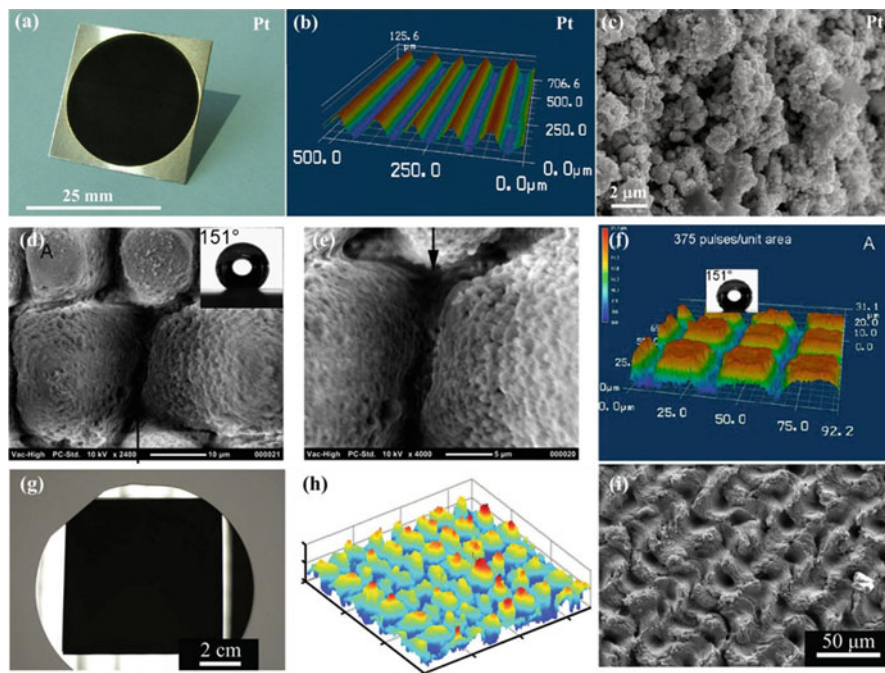


Fig. 1 Examples showing laser patterning of crystalline materials: (a–c) platinum patterned by femtosecond pulsed laser irradiation; (d–f) alumina (Al_2O_3) patterned by picosecond pulsed laser irradiation; (g–i) silicon patterned by nanosecond pulsed laser irradiation (Reproduced from Vorobyev and Guo 2015; Jagdheesh 2014; Yang et al. 2014)

applications in solar cells. Although femtosecond and picosecond pulsed laser irradiation is much easier to generate micro-/nanostructures on the surface compared to nanosecond pulsed laser irradiation, the corresponding laser systems are quite expensive compared to the nanosecond pulsed laser system, which greatly hinders their practical applications especially in industry. From this point, exploring new surface patterning methods or mechanisms by means of nanosecond pulsed laser is significant and meaningful.

On the other hand, although laser irradiation has been widely used for surface patterning of crystalline materials and a lot of literatures have been published, it is relatively new for applications in patterning of MGs. According to the basic process of laser irradiation of materials, laser patterning of MGs is feasible. However, being different from crystalline materials, MGs are a relatively novel class of non-crystalline materials which are formed by fast cooling of high viscous melts. Thus, their formation is very sensitive to the temperature as well as heating/cooling rate. As laser irradiation especially using nanosecond pulsed laser is a thermal process, crystallization may occur during the patterning process. Furthermore, the viscosity of MGs hugely depends on the temperature, and thus some unique microstructures may be formed due to the temperature gradient during pulsed laser irradiation

resulting in various flow abilities of MG materials. Accordingly, laser patterning of MGs requires further exploration.

In this chapter, recent achievement and development in surface patterning of MGs by means of nanosecond pulsed laser will be introduced and discussed. Corresponding to different experimental conditions such as single laser pulse, line laser irradiation, various laser power intensities, laser scanning speeds, overlaps, environmental atmospheres, etc., the surface microstructures as well as their formation mechanisms will be comparatively analyzed. Accordingly, a new surface patterning method of MGs, i.e., nanosecond pulsed laser irradiation inducing selective thermoplastic extrusion in nitrogen gas, will be provided. Furthermore, the effect of patterned microstructures on the surface hydrophobicity will be briefly discussed.

15.4 Nanosecond Laser Patterning of Metallic Glass

15.4.1 Single Laser Pulse Irradiation

Single laser pulse irradiation is a useful method to investigate the mechanism for laser-material interaction. By this method, Liu et al. (Jiang et al. 2015; Liu et al. 2011, 2012) study the response of $Zr_{41.2}Ti_{13.8}Cu_{10}Ni_{12.5}Be_{22.5}$ (commonly named Vit 1) MG to the nanosecond pulsed laser, and some unique surface micro-/nano-structures are observed in the irradiated region, and their formation mechanisms are discussed correspondingly.

15.4.1.1 Formation of Ripple

Figure 2 shows the irradiated morphology of Vit 1 MG after single laser pulse irradiation by using a Q-switched Nd:YAG solid-state laser (wavelength of 532 nm, pulse width of 10 ns, laser power intensity of $\sim 2.5 \times 10^{13}$ W/m²). As shown in Fig. 2a, at the center of the irradiated region, a concentrated ablated region exists which can be clearly seen from the high magnification view in Fig. 2b. The formation of ablated region implies that ablation-induced plasma plume would occur because of the pulse energy higher over the ablation threshold of Vit 1. Outside the ablated region as shown in Fig. 2c as well as its enlarged view in Fig. 2d, the material might undergo melting in the region from the outer boundary of the ablated region to the edge of the irradiated region. Furthermore, some concentric ripples at a microscale are formed prior to the material resolidification, which can be further clearly observed in the enlarged view as shown in Fig. 2e (enlarged view of area D) and Fig. 2f (enlarged view of area E). From Fig. 2d and e, the ripple spacing is approximately evaluated to be about 5 μ m. At the edge of the irradiated region as shown in Fig. 2f, the ripple spacing decreases because of the solid boundary effect, but it is still much larger than the laser wavelength of 532 nm, which indicates that the formation of ripples does not result from the light interference effect and other reasons should exist. Being similar to an unstable interface between the wind and the water when the wind skitters along the water surface, the hydrodynamic mechanism

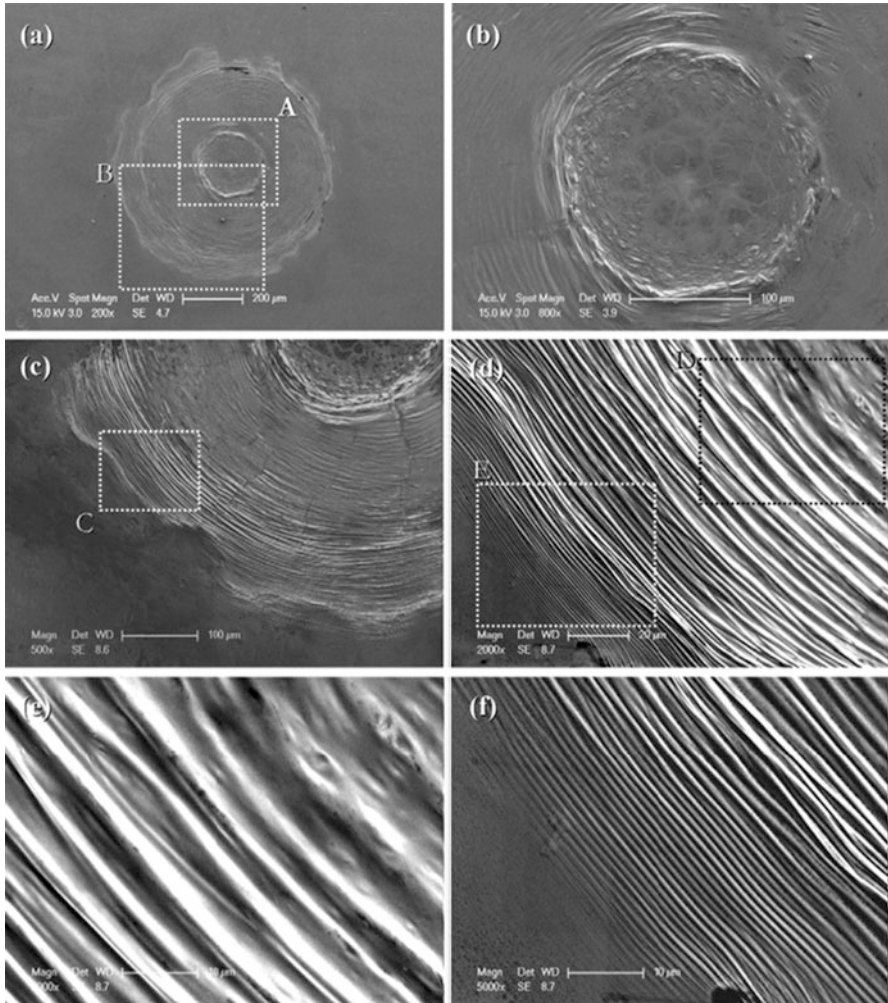


Fig. 2 The irradiated morphologies of $Zr_{41.2}Ti_{13.8}Cu_{10}Ni_{12.5}Be_{22.5}$ (Vit 1) MG after single laser pulse irradiation by using a Q-switched Nd:YAG nanosecond pulsed laser (wavelength, 532 nm; pulse width, 10 ns; laser power intensity, $\sim 2.5 \times 10^{13}$ W/m²) (Reproduced from Liu et al. 2011)

is adopted to explain the formation of ripple-type surface where the molten Vit 1 at the irradiated region works as “water” and expansion of the high-pressure plasma plume generates the “wind.” Accordingly, two fluid layers, the laser-induced plasma plume and the molten Vit 1 pool, with different density and horizontal velocity exist, which is similar to the configuration of Kelvin-Helmholtz (K-H) instability. By theoretical analysis and calculation, the predicted ripple spacing by K-H instability mechanism agrees well with the actually measured spacing. Thus, the surface

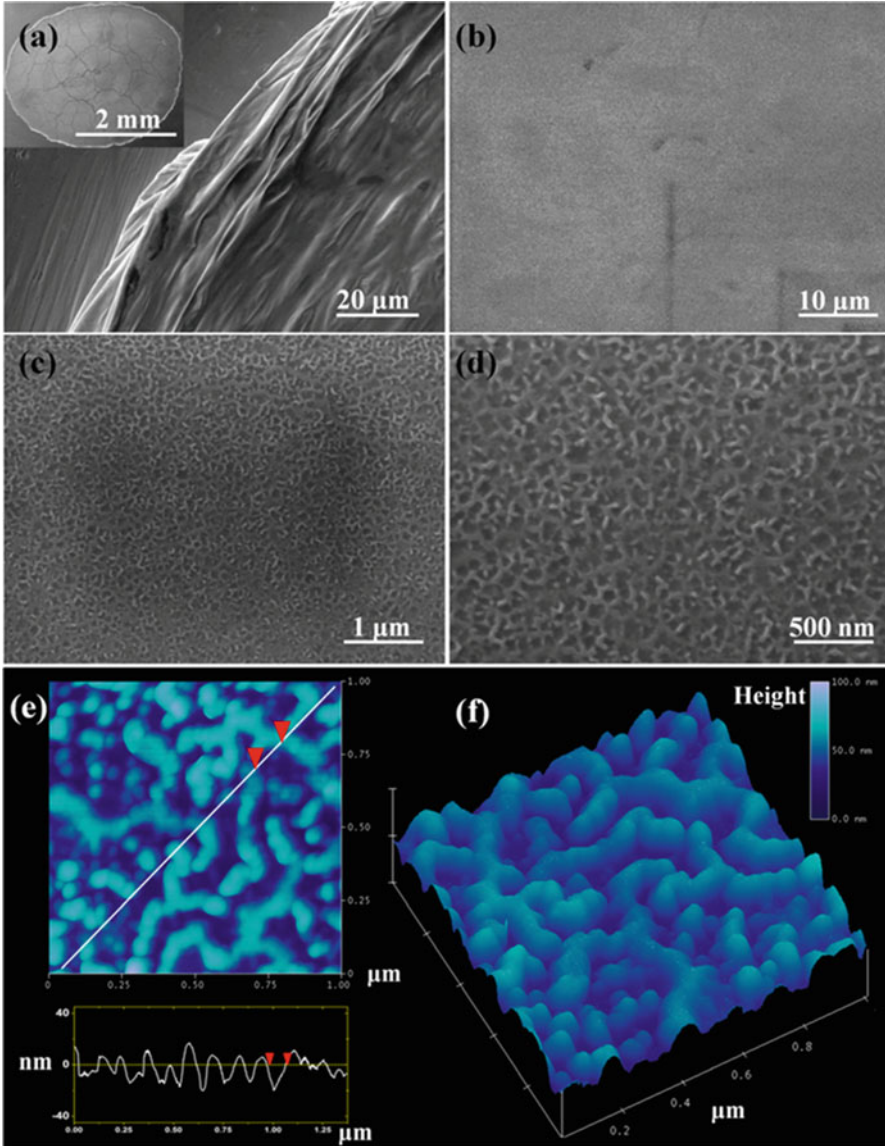


Fig. 3 The irradiated morphologies of Vit 1 MG after single laser pulse irradiation by using a Q-switched Nd:YAG nanosecond pulsed laser (wavelength, 1064 nm; pulse width, 10 ns; laser power intensity, $\sim 1.1 \times 10^{13}$ W/m²) (Reproduced from Jiang et al. 2015)

rippling phenomenon can be ascribed to the K-H instability at the interface between the molten layer and the expanding plasma plume. Furthermore, the ripple spacing is affected by the density, transverse velocity of the plasma plume, and the surface tension of the molten layer.

15.4.1.2 Formation of Porous Nanostructure

During the investigation of superheating and explosive boiling of MG induced by a high-power nanosecond laser pulse, a unique porous structure is further reported when observing the laser irradiated region by a high-resolution scanning electron microscope (HRSEM) and atomic force microscope (AFM) (Jiang et al. 2015). In this study, single laser pulse irradiation is performed by using a Q-switched Nd:YAG nanosecond pulsed laser with a wavelength of 1064 nm, pulse width of 10 ns, and laser power intensity of $\sim 1.1 \times 10^{13}$ W/m², and the irradiated morphology of Vit 1 MG is presented in Fig. 3. Besides the ripples observed at the edge of the irradiated region as shown in Fig. 3a which are similar to those as shown in Fig. 2, a porous structure consisting of 100 nm scale voids appears at the entire irradiated region, and the distribution of these voids is quite homogeneous as shown in Fig. 3b–d. The AFM morphologies in Fig. 3e and f confirm that the porous nanostructure exhibits a striated pattern and the striae spacing is about 120 nm being the same scale as the characteristic size of voids. The formation of the porous nanostructure is theoretically ascribed to a liquid-gas spinodal phenomenon. A spatial separation would occur via a spinodal process between the vaporized gas and the residual liquid. The ejection of the vapor bubbles generates the homogenous nanovoids, and resolidification of the residual liquid forms the walls of these nanovoids.

15.4.1.3 Formation of Saffman-Taylor Fingering

The surface micro-/nanostructures shown in Figs. 2 and 3 are induced by single nanosecond pulsed laser irradiation in air. During the investigation of laser-Vit 1 MG interaction in a liquid-confined environment, an interesting irradiated surface morphology is observed as shown in Fig. 4. The single laser pulse irradiation is performed by using a Q-switched Nd:YAG nanosecond pulsed laser with a wavelength of 532 nm, pulse width of 10 ns, and laser power intensity of $\sim 2.38 \times 10^{14}$ W/m².

As shown in Fig. 4a, the irradiated region mainly consists of two areas, a relatively smooth central area “I” and a rough outer area “II” with the starfish-shaped boundary. In Fig. 4b–d, near the edge of the irradiated region, many ripples appear, and cell-like vein patterns are formed in the rough area “II” which are very similar to the surface pattern of fractured Vit 1 MG under uniaxial compression. Along with the appearance of cell-like patterns, many melted droplets and pores exist as shown in Fig. 4d, suggesting that strong thermo-mechanical process, for example, material ejection, should have occurred in this area. Fig. 4e and f gives a close-up view of area “E” in Fig. 4a, showing details of the “arms of the starfish” where interesting fingering phenomenon is observed. The surface morphology shown in Fig. 4 could be explained by the phase explosion mechanism. As high-power pulse laser acts on the Vit 1 surface, phase explosion occurs, resulting in ejection of material in the form of a plume which further acts on the molten Vit 1 layer because of the confinement of water. The interaction between the plume and the molten Vit 1 layers leads to the hydrodynamic instability phenomenon, and thus Saffman-Taylor fingering is formed as shown in Fig. 4e and f.

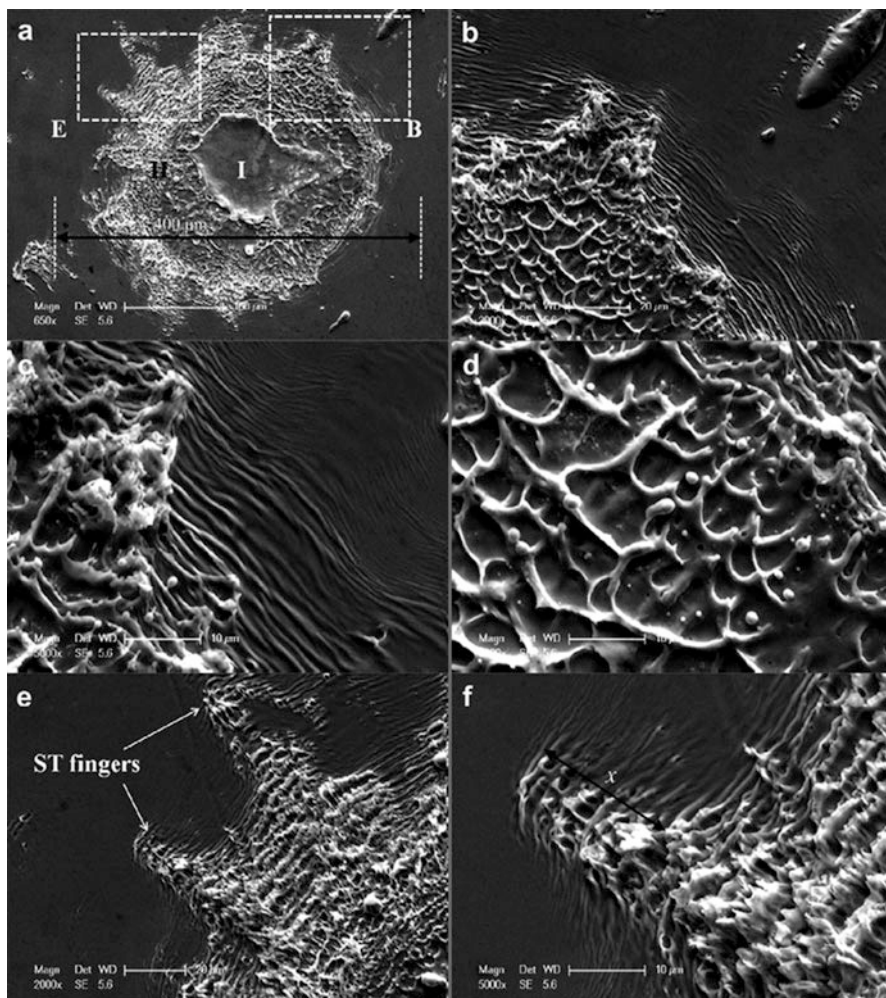


Fig. 4 The irradiated morphologies of Vit 1 MG after single laser pulse irradiation in a water environment by using a Q-switched Nd:YAG nanosecond pulsed laser (wavelength, 532 nm; pulse width, 10 ns; laser power intensity, $\sim 2.38 \times 10^{14}$ W/m²) (Reproduced from Liu et al. 2012)

15.4.2 Line Laser Irradiation

In Sect. 4.1, surface ripple, porous nanostructure, cell-like vein pattern, and Saffman-Taylor fingering are generated by using single nanosecond laser pulse irradiation. Analyzing the formation mechanisms of these micro-/nanostructures enhances the understanding of the complex nanosecond pulsed laser-MG interaction. However, from the point of view of practical application, patterning of large-area micro-/nanostructures on MG surface is necessary which requires large-area irradiation, pulse by pulse and line by line. In this aspect, Huang et al. (2016a, b; Huang and

Yan 2017) carry out some studies by line nanosecond pulsed laser irradiation. As MG is sensitive to oxygen, various environmental atmospheres, vacuum, argon, and nitrogen shield gases are used, resulting in some unique surface micro-/nanostructures. Accordingly, a new laser patterning method of MGs is proposed.

15.4.2.1 Line Laser Irradiation in Vacuum

By single laser pulse irradiation, a micro-crater with some specific micro-/nanostructures on it as discussed in Sect. 4.1 can be formed. Accordingly, a simple idea to generate micro-/nanostructure patterns on MG surface by line laser irradiation is as follows. If line irradiation is implemented along two directions with an overlap between two craters, a layer of laser pulse tracks can be patterned on MGs. Furthermore, when the laser intensity is sufficiently high, the irradiated materials may experience phase changes, vaporization, boiling, and even explosive boiling, accompanying with the ejection of a high-temperature matter because of the recoil pressure (Bulgakova and Bulgakov 2001; Jiang et al. 2015; Miotello and Kelly 1995; Williams and Brousseau 2016; Yoo et al. 2000). By redeposition of the vapor particles in the adjacent irradiated region, a layer of MG thin film is expected to be formed over the first layer of laser pulse tracks. Thus, hierarchical micro-/nanostructures could be patterned on the MG surface.

According to this idea, line laser irradiation of Vit 1 MG is attempted in vacuum by using a Nd:YAG nanosecond pulsed laser with a wavelength of 532 nm, pulse width of 15.4 ns, pulse frequency of 1 kHz, and laser beam diameter of $\sim 85 \mu\text{m}$. The pulse overlap rate r between two adjacent scanning lines is 53%. Various peak laser power intensities and scanning speeds are selected. The typical experimental results are shown as follows.

Figure 5 presents representative optical morphologies of the laser irradiated region under a peak laser power intensity of $3.6 \times 10^{12} \text{W/m}^2$ and scanning speed of 10 mm/s. In Fig. 5a, a rectangle irradiated region is formed on the MG surface where many remarkable laser pulse tracks are observed in its local enlarged view in Fig. 5b. The 3D morphology as well as the cross-sectional profiles in Fig. 5c–e confirms that a layer of laser pulse tracks in micron scale has been successfully formed in the irradiated region, leading to the effective surface area of irradiated region being 1.57 times of the corresponding flat surface area. Furthermore, by changing the laser scanning speed, power, and overlap rate, the microstructure and height shown in Fig. 5 can be tuned easily, resulting in various effective surface areas.

Figure 6 presents the SEM morphologies of line laser pulse irradiated region with various magnifications corresponding to the optical morphologies in Fig. 5, showing more detailed microstructures. Apart from the individual laser pulse tracks which have been observed in Fig. 5, a cotton-like film with nanometer-scale microstructure is uniformly distributed on the top surface of each pulse track in region 1. Similarly, this cotton-like film is also formed in region 2 although no direct laser irradiation is performed in this region. Accordingly, hierarchical micro-/nanostructures, micron-scale laser pulse tracks covered by a cotton-like film with nanometer-scale microstructure, are confirmed that have formed in the laser irradiated region.

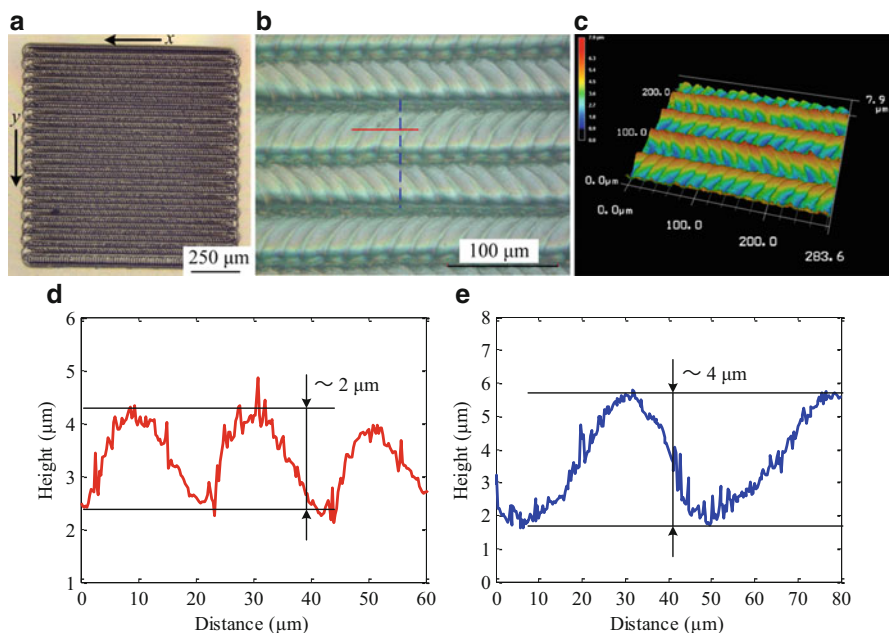


Fig. 5 Optical morphologies and profiles of Vit 1 MG after line laser pulse irradiation by using a Nd:YAG nanosecond pulsed laser with a wavelength of 532 nm, pulse width of 15.4 ns, pulse frequency of 1 kHz, peak laser power intensity of $3.6 \times 10^{12} \text{ W/m}^2$, and scanning speed of 10 mm/s. The pulse overlap rate between two adjacent scanning lines is 53% (Reproduced from Huang et al. 2016a)

To further confirm that hierarchical micro-/nanostructures can be formed under various laser irradiation parameters, Fig. 7 presents representative SEM morphologies under a higher peak laser power intensity of $5.8 \times 10^{12} \text{ W/m}^2$ (Fig. 7a–c) and a lower scanning speed of 1 mm/s (Fig. 7d–f). Other parameters for Fig. 7 are the same to those for Figs. 5 and 6. It is noted that hierarchical micro-/nanostructures are also generated for these two parameters. In Fig. 7a–c, laser pulse tracks with more remarkable wrinkle appear compared to those in Fig. 6b. With the increase of the laser power intensity, more materials are heated during a single pulse, and the recoil pressure should also be enhanced. Thus, more materials are pushed to flow outside the crater, leading to more remarkable wrinkle. In Fig. 7d, laser pulse tracks become nonuniform. In this case, although the laser power intensity for a single pulse is the same to that in Fig. 6, more laser pulses are applied for the same irradiated region because of the low laser scanning speed, resulting in an increased overlapped region along a scanning line. Therefore, more heat is accumulated in a single pulse region, leading to the irregular laser pulse tracks in Fig. 7d. Furthermore, instead of the cotton-like nanostructure in Fig. 6d and f, particle-like nanostructures as shown in Fig. 7c and f are formed on the surface of laser pulse tracks, demonstrating that more materials are ejected in these two cases because of the increased laser power and

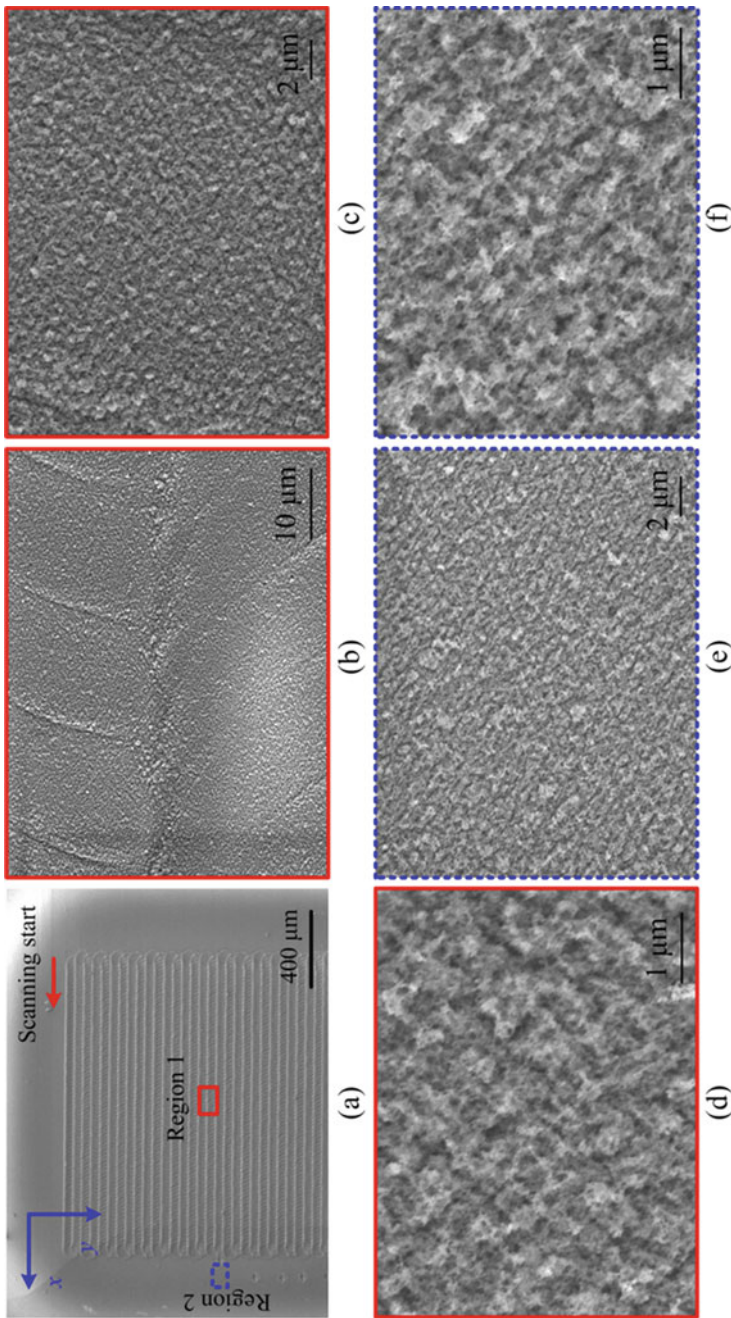


Fig. 6 SEM morphologies of the line laser irradiated surface at different regions and magnifications (Reproduced from Huang et al. 2016a)

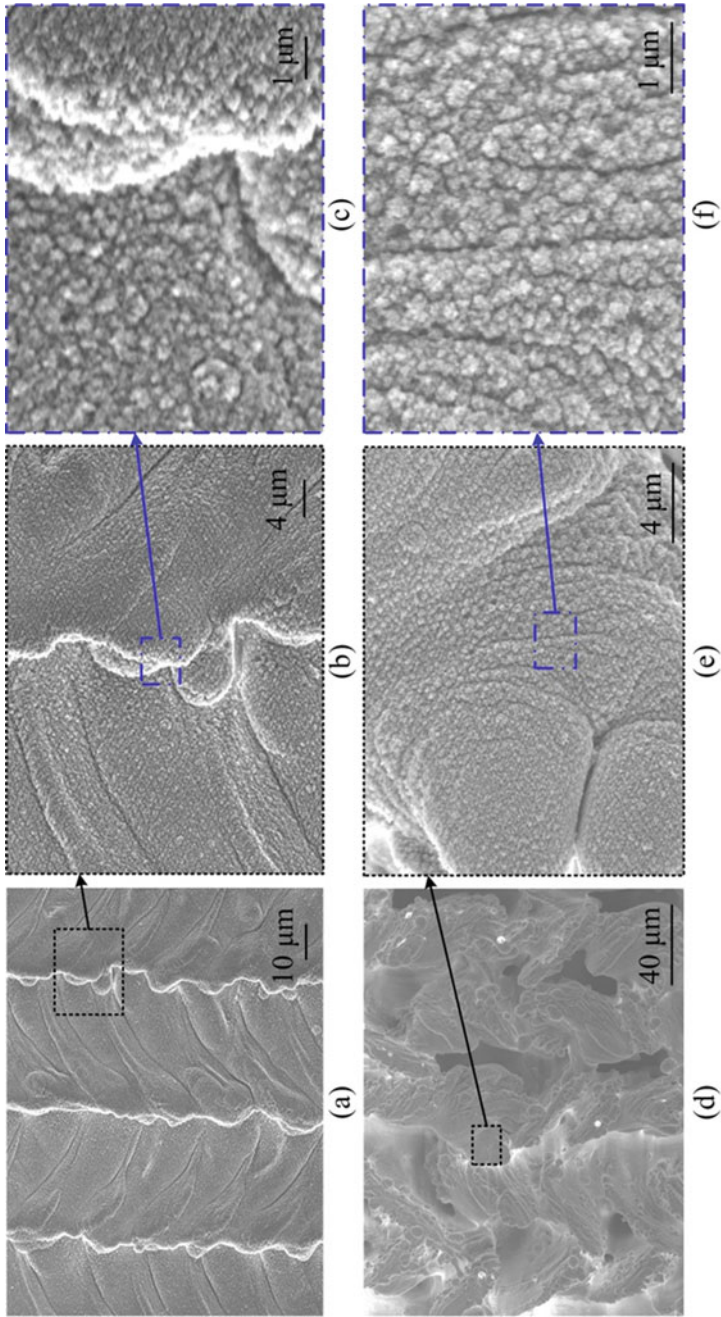


Fig. 7 SEM morphologies under a higher peak laser power intensity of $5.8 \times 10^{12} \text{ W/m}^2$ (a–c) and a lower scanning speed of 1 mm/s (d–f). Other parameters for the figure are the same for Figs. 5 and 6 (Reproduced from Huang et al. 2016a)

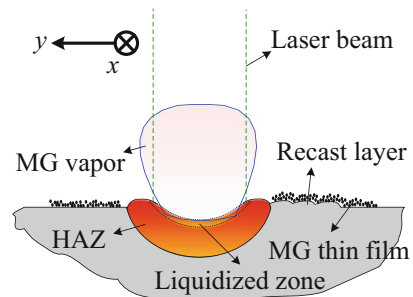
decreased scanning speed. The change in hierarchical micro-/nanostructures also leads to various effective surface areas. Corresponding to the morphologies in Fig. 7a and d, the effective surface areas measured by the 3D laser scanning microscope are 5.1 and 24.3 times of the flat surface area.

As MG is very sensitive to heat which could be easily accumulated during line nanosecond pulsed laser irradiation, the irradiated region is characterized by X-ray diffractometer (XRD), and the element mapping is performed by an energy dispersive X-ray spectroscopy (EDX). The XRD patterns and EDX element mappings show that the irradiated region with hierarchical micro-/nanostructures retains the amorphous characteristic and its elements are distributed uniformly, indicating that line laser irradiation under current experimental conditions does not result in phase separation or element enrichment.

By theoretical calculation and analysis of the surface temperature and vapor pressure, it is derived that only normal vaporization occurs corresponding to the experimental conditions in Fig. 6 rather than explosive boiling. Accordingly, the possible formation mechanism of the hierarchical micro-/nanostructures is illustrated in Fig. 8.

Laser energy is absorbed by the MG, causing very fast temperature raise of the irradiated region. For line irradiation, residual heat in previous irradiation also contributes to the fast temperature raise of subsequent irradiation especially for a low scanning speed. In the center region, some materials are liquidized. Compared to femtosecond pulsed laser, nanosecond pulsed laser has a relatively long duration, and thus a large heat affected zone (HAZ) is formed underneath the liquidized materials as well as on the top surface. Materials in the liquidized zone and HAZ have enhanced flow. With the role of the recoil pressure generated by vaporization, some liquidized materials and some materials in HAZ are pushed toward the edge of the crater, forming the laser pulse tracks. On the other hand, some materials in the center region are vaporized as very fine vapor particles. As time goes on, the vaporized materials are cooled and then deposited and resolidified on the surface of the adjacent irradiated regions as well as unirradiated regions. With accumulation of the deposited materials particle by particle and layer by layer, a MG thin film with nanostructures as shown in Figs. 6d, f and 7c, f is formed on the top surface of the irradiated region as well as the surrounded HAZ. The MG thin film with

Fig. 8 Diagram of the possible formation mechanism of the hierarchical micro-/nanostructures (Reproduced from Huang et al. 2016a)



nanostructures formed in the HAZ provides a believable evidence for aforementioned formation mechanism.

According to the experimental results and mechanism analysis mentioned above, line nanosecond pulsed laser irradiation in vacuum is a method to pattern large-area hierarchical micro-/nanostructures on MG surface, i.e., a layer of micron-scale laser pulse tracks covered by a cotton-like MG thin film with nanometer-scale microstructure.

15.4.2.2 Line Laser Irradiation in Various Shield Gases

For laser processing of MGs, shield gases such as argon and nitrogen (Pauly et al. 2013), are commonly used to avoid oxidation and crystallization. Although shield gases do not react with MGs at ambient temperature and pressure, chemical reactions might be activated when MGs are in complex states such as molten, vaporized, and boiled states during nanosecond pulsed laser irradiation because of their naturally metastable states (Jiang et al. 2015). As shown in Fig. 9, a recently comparative

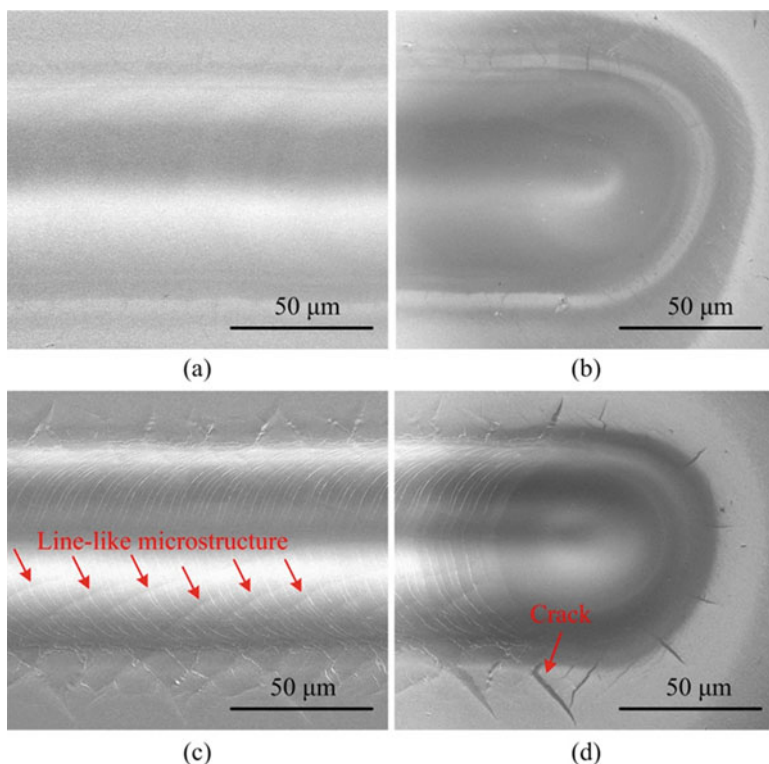


Fig. 9 SEM morphologies of single line laser irradiated regions under the same experimental conditions except for the difference in shield gas: (a) and (b) argon gas; (c) and (d) nitrogen gas (Reproduced from Huang et al. 2016b)

experiments show that compared to argon gas, nitrogen gas remarkably promotes the formation of cracks during nanosecond pulsed laser irradiation of Vit 1 MG.

The difference in crack is further highlighted in their corresponding optical morphologies as shown in Fig. 10. Taking a high contrast of the optical microscope, cracks are visually enhanced compared to those in Fig. 9. In Fig. 10a and b, small cracks are also observed around the irradiated regions generated in argon gas. Similar to those in Fig. 9c, remarkable cross cracks are clearly observed in Fig. 10c and d. According to the morphology in Fig. 10d, the line-like microstructure in Fig. 9c is confirmed to be cracks. By varying the laser power and scanning speed, it is further confirmed that with increase of the peak laser power intensity or decrease of the laser scanning speed, crack formation during line laser irradiation in nitrogen gas is enhanced. By XRD and Raman spectrum analysis, it is derived that the promoted crack formation in nitrogen gas results from the formation of ZrN, which enhances the thermal mismatch between the molten layer and substrate, resulting in high thermal stress at their interface during resolidification because of thermal contraction and solidification shrinkage.

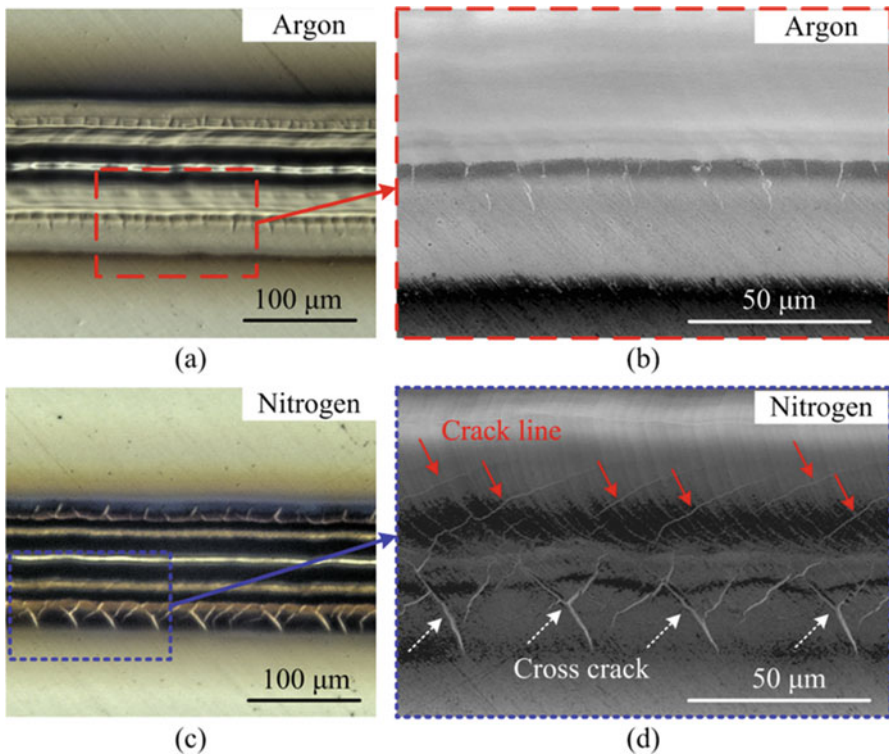


Fig. 10 Optical morphologies of single line laser irradiated regions, corresponding to the SEM morphologies in Figs. 9a and 8c (Reproduced from Huang et al. 2016b)

15.4.2.3 Patterning Metallic Glass in Nitrogen Gas

Crack is commonly regarded as a kind of defect that affects the performances and service life of a product. However, some studies indicate that crack shows some unique physical and electrical response to a laser beam compared to the surrounding surface region, i.e., enhanced laser absorption and higher localized thermal resistivity (Bloembergen 1973; Feit and Rubenchik 2003; Li et al. 2011; Myrach et al. 2016; Schlichting et al. 2012). Because of these characteristics, laser irradiation in combination with infrared thermography has been used to detect cracks (Li et al. 2011; Myrach et al. 2016; Schlichting et al. 2012). For Vit 1 MG as mentioned above, cracks can be effectively generated by nanosecond pulsed laser irradiation in nitrogen gas (Huang et al. 2016b). If the laser irradiation condition is suitably controlled to make the temperature of MG material around cracks over the glass transition point while the temperature of the surrounding surface region below the glass transition point, the MG material around the cracks might undergo local thermal expansion and deformation because of their superplastic flow characteristics (Kumar et al. 2009; Li et al. 2016; Schroers 2010). This effect might be able to generate unique micro-/nanostructures on the MG surface.

Based on this idea, multiline laser irradiation of Vit 1 is attempted in nitrogen gas by using a Nd:YAG nanosecond pulsed laser with a wavelength of 532 nm, pulse width of 15.4 ns, pulse frequency of 1 kHz, and laser beam diameter of $\sim 85 \mu\text{m}$. Hierarchical surface structures as shown in Fig. 11 are successfully patterned on the Vit 1 MG surface. In Fig. 11a, microgroove and pileup are formed in the irradiated region because of the accumulation effect of multi-pulse laser irradiation along a scanning line, which is similar to the laser pulse tracks shown in Fig. 5. Line cracks being the same to those shown in Figs. 9 and 10 are distributed on the irradiated surface. Interestingly, periodically cross-shaped microstructures are observed between two laser scanning lines, and their formation positions are much closer to the side of microgroove that is near the next scanning line. In Fig. 11b and c, some MG materials are protruded on the microgroove surface at the positions of line cracks and laser pulse tracks, demonstrating that the formation of cross-shaped

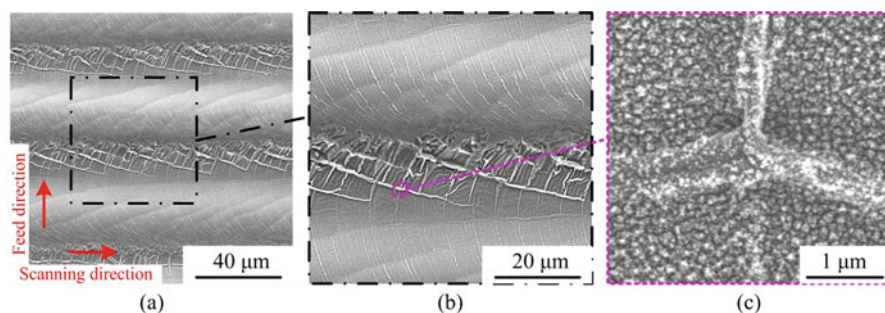


Fig. 11 SEM morphologies of the irradiated Vit 1 MG surface in nitrogen gas under a peak laser power intensity of $1.3 \times 10^{12} \text{ W/m}^2$, a scanning speed of 1 mm/s, and a pulse overlap rate r of 47% (Reproduced from Huang and Yan 2017)

protrusions is related to both the line cracks and laser pulse tracks. Furthermore, in Fig. 11c, cross-shaped protrusions as well as surrounding surface are covered by nanoparticles, which are generated by redeposition of the vaporized materials (Huang et al. 2016a). Accordingly, three kinds of surface structures, namely, microgrooves, cross-shaped protrusions, and nanoparticles, have been formed on Zr-based MG surface by nanosecond pulse laser irradiation in nitrogen gas.

Furthermore, experimental results show that the patterned surface structures are affected by the scanning speed, laser power intensity, and pulse overlap rate. When the scanning speed increases to 5 and 10 mm/s, the laser pulse tracks become much clearer with increased width, but the cross-shaped protrusions are not observed. This is due to the decreased overlap width along a scanning line as well as decreased heat accumulation for the increased scanning speeds, which reduces the formation of ZrN, agreeing well with the XRD results that increased scanning speeds suppress the ZrN peaks (Huang et al. 2016b). Thus, the formation of radial cracks and line cracks is suppressed. As the formation of cross-shaped protrusions is related to the line cracks, hence, cross-shaped protrusions are also suppressed for increased laser scanning speeds.

When increasing the peak laser power intensity, although the irradiated surfaces become irregular and it is difficult to distinguish the microgrooves and laser pulse tracks, cross-shaped protrusions with increased width can be formed on the wrinkled surfaces. Furthermore, by varying the pulse overlap rate, the irradiated surface shows various morphologies as presented in Fig. 12. In Fig. 12a–c, with a large pulse overlap rate r of 82%, the whole irradiated surface is almost covered by the cross-shaped protrusions, which are separated by a narrow laser interactive region. Furthermore, the cross-shaped protrusions as well as surrounding surfaces are covered by nanoparticles, similarly to that shown in Fig. 11c. With decrease in the pulse overlap rate r from 82% to 29%, the position of cross-shaped protrusions moves from the side of microgrooves being close to preceding scanning lines to another side being close to the next scanning lines. Results in Fig. 12 indicate that by controlling the pulse overlap rate r , the cross-shaped protrusions can be tuned to form at various positions of a single scanning line. Furthermore, by comparing the SEM morphologies in Fig. 12a and d–f which are obtained at the same magnification, it is noted that with decrease in r , the size of the cross-shaped protrusions also decreases. This could be ascribed to the following three reasons. Firstly, less ZrN is generated with decrease in r as confirmed by XRD, possibly resulting in small line cracks. Secondly, fewer MG materials are vaporized and re-deposited because of the less irradiation time and heat accumulation with decrease in r . Thirdly, with a decreased r , for example, $r = 29\%$, redeposition of vaporized fine particles may occur only in the very adjacent laser scanning line, while it may occur in the subsequent several laser scanning lines for a large r , for example, $r = 82\%$.

The analysis of SEM morphologies suggests that the formation of cross-shaped protrusions is originated from both the line cracks and laser pulse tracks. Further AFM morphologies as shown in Fig. 13 indicate that compared to the slightly concave line cracks as well as very small and narrow laser pulse tracks, the cross-shaped protrusions are convex with a height of hundreds of nanometers, suggesting

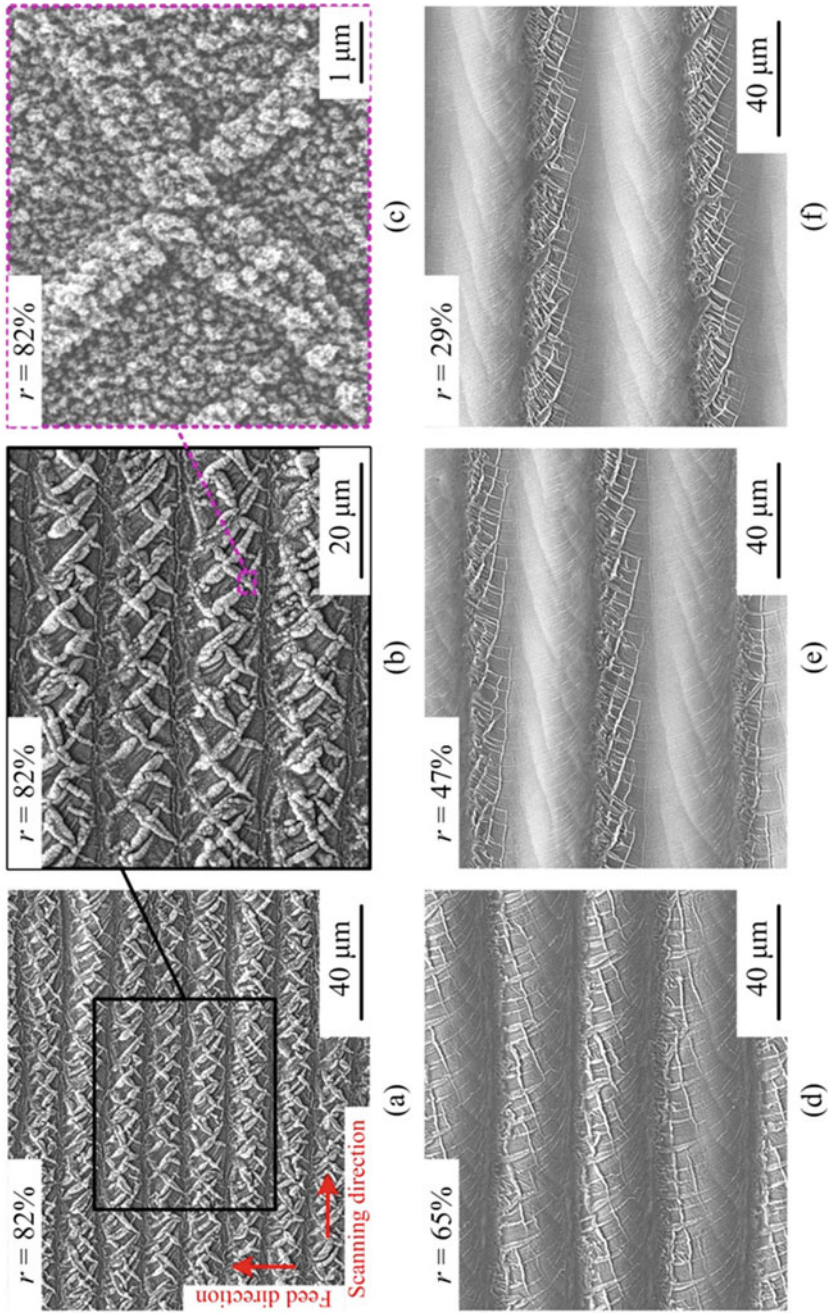


Fig. 12 SEM morphologies of the irradiated MG surfaces under various pulse overlap rates: (a–c) $r = 82\%$, (d) $r = 65\%$, (e) $r = 47\%$, and (f) $r = 29\%$. Other experimental conditions are the same to those in Fig. 11 (Reproduced from Huang and Yan 2017)

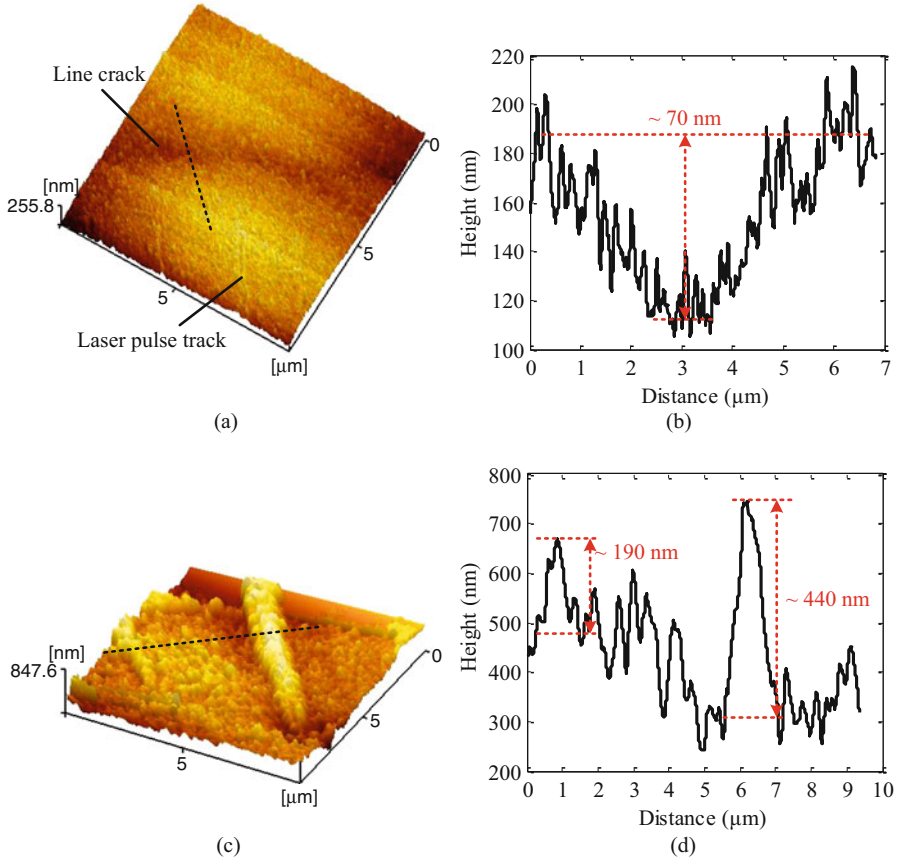


Fig. 13 AFM morphologies and profiles around a line crack (a and b) and a cross-shaped protrusion (c and d) (Reproduced from Huang and Yan 2017)

that MG materials are selectively extruded from both the line cracks and laser pulse tracks during the subsequent laser scanning lines. This scenario is reasonable in consideration of enhanced laser energy absorption (Bloembergen 1973; Feit and Rubenchik 2003; Myrach et al. 2016) and higher localized thermal resistivity (Li et al. 2011; Myrach et al. 2016; Schlichting et al. 2012) at positions of the line cracks and laser pulse tracks, compared to surrounding irradiated surfaces.

Accordingly, taking line cracks, for example, Fig. 14 illustrates the possible formation mechanism of cross-shaped protrusions. In Fig. 14a, microgrooves and pileups with line cracks on their surface as shown in Fig. 11a are generated on the MG surface along a laser scanning line after nanosecond pulsed laser irradiation in nitrogen gas using a Gauss beam with a peak laser power intensity I_0 and a laser beam radius R defined by I_0/e^2 . Over the beam radius R , MG surface may be only heated as HAZ because of relatively low laser power intensity. After one line scanning, laser beam is shifted with a given pulse overlap rate r , for example,

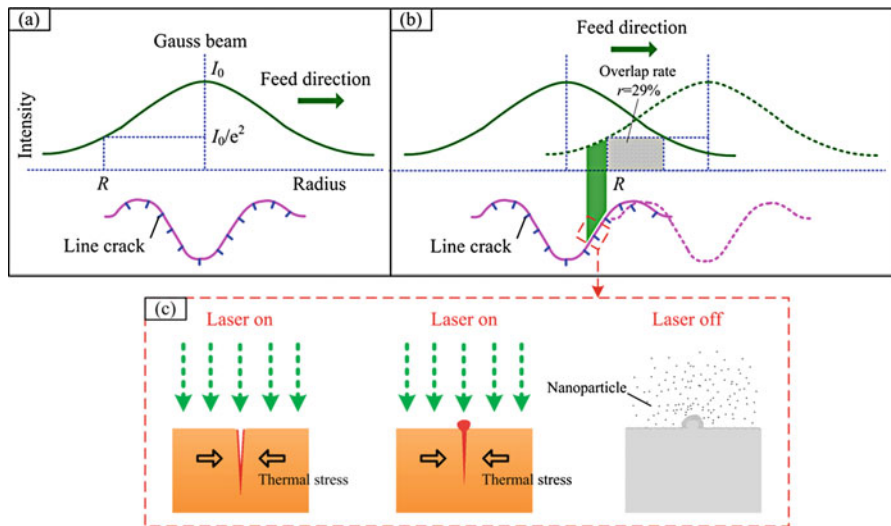


Fig. 14 Schematic diagrams illustrating the formation mechanism of cross-shaped protrusions. (a) Formation of line cracks after single line scanning, (b) interaction of two scanning line with a pulse overlap rate r of 29%, and (c) local enlarged view in (b) showing the laser-MG interaction around a line crack during laser on and off (Reproduced from Huang and Yan 2017)

$r = 29\%$ shown in Fig. 14b, and then continued scanning along a line. As shown in Fig. 14b, some line cracks formed by the preceding laser scanning line are still in the irradiation range of Gauss laser beam. In consideration of their enhanced laser energy absorption and high localized thermal resistivity, the line cracks being very close to the overlap region as shown in Fig. 14b could be affected by the laser beam over the beam radius R . Fig. 14c presents the local enlarged view of Fig. 14b, illustrating the possible laser-MG interaction around a line crack being close to the overlap region during laser on and off. When laser is on, the line crack as well as surrounding surface is heated, and meanwhile, thermal expansion-induced thermal stress is generated inside the heated region. Because of high laser energy absorption and localized thermal resistivity, the local temperature at a crack increases fast, and it could be over the glass transition point. Because of low laser power intensity over the beam radius R , the surrounding surface is only heated, and the temperature is still below the glass transition point. It is well known that MGs over the glass transition temperature have superplasticity, which is the foundation for widely used thermo-plastic forming of MGs (Hasan et al. 2015; Hu et al. 2015; Kumar et al. 2009; Li et al. 2016; Plummer and Johnson 2015; Sarac et al. 2012; Schroers 2010; Xia et al. 2012). Thus, with the role of thermal stress, some MG materials are selectively extruded from the line cracks as shown in Fig. 14c. Additionally, the recoil pressure generated by material vaporization in adjacent laser scanning lines results in the overall deformation of MG materials in the overlap region toward the direction of preceding scanning lines, and this may also contribute to the extrusion of MG materials from the line cracks. Similar processes could also occur at the position

of laser pulse tracks. The extruded MG materials from the line cracks and laser pulse tracks interlace with each other, forming the embryo of the cross-shaped protrusions. During laser off, vaporized fine particles are readily redeposited on the surface of cross-shaped protrusions because of their increased surface area, and, thus, the cross-shaped protrusions further grow up with nanoparticles covered. By tuning the pulse overlap rate r , MG materials can be controlled to be extruded from the line cracks and laser pulse tracks at various positions of a single scanning line, and thus the cross-shaped protrusions are generated at various positions as shown in the comparative results in Fig. 12.

According to the experimental results and mechanism analysis mentioned above, line nanosecond pulsed laser irradiation in nitrogen gas provides an effective method to pattern large-area hierarchical micro-/nanostructures on MG surface, and the corresponding surface structures are easily tuned by varying the experimental parameters, typically as peak laser power intensity and pulse overlap rate. Compared to the surface structure formed by line nanosecond pulse laser irradiation in vacuum, the structure patterned by line laser irradiation in nitrogen is more complex and three-dimensional, which may have special performances and applications. Furthermore, the formation of ZrN in the MG matrix as a MG composite could change its surface mechanical properties, which requires further investigation.

15.5 Application in Enhancing Surface Hydrophobicity

It is commonly reported that the structured surface can effectively enhance its hydrophobicity (Li et al. 2013; Ma et al. 2014; Xia et al. 2012), and this effect is also confirmed for nanosecond laser patterned MG surface. For example, Fig. 15a–c shows the comparative results of water contact angle between the as-cast and laser patterned MG surfaces with the morphologies shown in Fig. 12a and e. The featureless smooth surface of the as-cast MG after grinding and polishing only induces a contact angle of 96° in Fig. 15a. With the hierarchical surface structures as shown in Fig. 15a formed by line laser irradiation in nitrogen gas with a pulse overlap rate r of 82%, the contact angle remarkably increases to 140° in Fig. 15b. Furthermore, with a decreased r of 47%, the contact angle also remarkably increases to be 144° . As shown in Fig. 12a and e, the surface morphologies for $r = 82\%$ and 47% are hugely different. For the case of $r = 47\%$, deeper and wider microgrooves with fewer cross-shaped protrusions are generated because of large distance between two adjacent scanning lines, while for $r = 82\%$, the microgrooves are shallow and narrow because of the small distance between two adjacent scanning lines. This difference in surface structure may suggest different mechanisms resulting in increase in contact angle under various pulse overlap rates r . It is well known that a composite of solid-liquid-air interface will be formed when the water droplet contacts with a heterogeneous surface (He et al. 2016b; Li et al. 2013). According to the modified Cassie-Baxter model (Cassie and Baxter 1944), the contact angle θ_{CB} on a structured surface and the contact angle θ_C on a smooth surface with identical chemical composition satisfy the following equation:

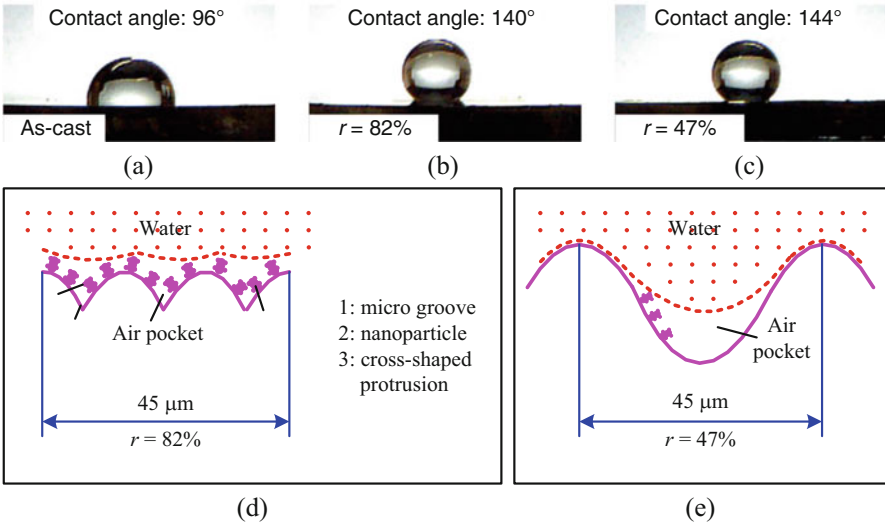


Fig. 15 Contact angle of as-cast (a) and laser patterned MG surface with $r = 82\%$ (b) and 47% (c). (d) and (e) Local contact statuses between the water droplet and the laser patterned surfaces corresponding to $r = 82\%$ and 47% , respectively (Reproduced from Huang and Yan 2017)

$$\cos \theta_{CB} = f_{s-l}(\cos \theta_C + 1) - 1 \quad (1)$$

where f_{s-l} is the area fraction of the solid-liquid interface and θ_C here is 96° according to Fig. 15a. As the contact angle for $r = 82\%$ and 47% is almost the same, it means that almost the same area fraction of the solid-liquid interface, i.e., almost the same area fraction of the air-liquid interface, is generated under these two cases although their surface structures are hugely different. According to the residual morphologies in Fig. 12a and e, Fig. 15d and e illustrates the possible local contact statuses between the water droplet and the structured surfaces corresponding to $r = 82\%$ and 47% , respectively. For $r = 47\%$, the microgrooves on the irradiated surface are relatively deep and wide, and the surface of microgrooves is relatively smooth with fewer cross-shaped protrusions. Thus, a large amount of air could be trapped in the microgrooves as shown in Fig. 15e, resulting in large area fraction of the air-liquid interface. In this case, microgrooves may play a dominant role in increasing the contact angle. For $r = 82\%$, a large amount of air could be trapped in hierarchical surface structures forming the air-liquid interface as shown in Fig. 15d, especially the uniformly distributed cross-shaped protrusions covered by nanoparticles because of their large effective surface area (Li et al. 2013). Furthermore, corresponding to the same length of $45 \mu\text{m}$, the amount of the repeated surface structures for $r = 82\%$ is three times of that for $r = 47\%$. Thus, although the microgrooves are relatively shallow and narrow, a large area fraction of the air-liquid interface could also be generated, increasing the contact angle. Although the dominant reason leading to the increase in contact angle for various pulse overlap

rates r may be different, the comparative results in Fig. 15 indicate that the patterned MG surface by nanosecond pulsed laser irradiation in nitrogen gas can efficiently increase the water contact angle, i.e., the hydrophobicity, which will enrich the functional applications of MG as structural and engineering materials. Furthermore, by optimizing the laser irradiation parameters that induce suitable surface structures, it is believed that the surface hydrophobicity could be further improved.

15.6 Summary and Outlook

Although nanosecond pulsed laser irradiation has been widely used for patterning of various materials, it is relatively new for application in patterning of MGs with both glassy-state structure and metallic-bonding character. However, some research progress has been achieved in recent years. By single laser pulse irradiation, some unique surface structures such as ripple, porous nanostructure, and Saffman-Taylor fingering can be formed on Vit 1 MG surface. When line laser irradiation is performed, large-area hierarchical micro-/nanostructures can be patterned, but the detailed structures strongly depend on the laser irradiation parameters as well as environmental atmosphere. Anyhow, it is suggested that nanosecond pulsed laser irradiation is a usable method to pattern MG surface. Furthermore, the patterned surface structures hugely increase the effective surface area as well as surface hydrophobicity, which will enhance the application of MGs as functional materials. As discussed in this chapter, the current research on laser patterning of MGs mainly focuses on the fundamental aspect, i.e., the formation mechanisms of various micro-/nanostructures induced by laser irradiation. In the future, more practical applications of laser patterned MGs in biomedicine, waterproof material, industrial catalysis, and sewage treatment should be further explored.

Acknowledgments This work was supported by the National Natural Science Foundation of China (Grant No. 51705197), Grant-in-Aid for JSPS Fellows (Grant No. 26-04048), and Young Talent Lift Project of China Association for Science and Technology (CAST) and Chinese Mechanical Engineering Society (CMES).

References

- Bakkal M, Shih AJ, Scattergood RO (2004a) Chip formation, cutting forces, and tool wear in turning of Zr-based bulk metallic glass. *Int J Mach Tools Manuf* 44:915–925
- Bakkal M, Liu CT, Watkins TR et al (2004b) Oxidation and crystallization of Zr-based bulk metallic glass due to machining. *Intermetallics* 12:195–204
- Bloembergen N (1973) Role of cracks, pores, and absorbing inclusions on laser-induced damage threshold at surfaces of transparent dielectrics. *Appl Opt* 12:661–664
- Brinksmeier E, Riemer O, Glabe R et al (2010) Submicron functional surfaces generated by diamond machining. *CIRP Ann Manuf Technol* 59:535–538
- Bulgakova NM, Bulgakov AV (2001) Pulsed laser ablation of solids: transition from normal vaporization to phase explosion. *Appl Phys A Mater Sci Process* 73:199–208

- Byrne CJ, Eldrup M (2008) Materials science – bulk metallic glasses. *Science* 321:502–503
- Cassie ABD, Baxter S (1944) Wettability of porous surfaces. *Trans Faraday Soc* 40:546–551
- Chen N, Frank R, Asao N et al (2011) Formation and properties of Au-based nanograin metallic glasses. *Acta Mater* 59:6433–6440
- Chen N, Shi XT, Witte R et al (2013) A novel Ti-based nanoglass composite with submicron-nanometer-sized hierarchical structures to modulate osteoblast behaviors. *J Mater Chem B* 1:2568–2574
- Feit MD, Rubenchik AM (2003) Influence of subsurface cracks on laser induced surface damage. In: SPIE boulder damage symposium XXXV annual symposium on optical materials for high power lasers, Boulder, Colorado, 22–24 Sept 2003
- Fujita K, Morishita Y, Nishiyama N et al (2005) Cutting characteristics of bulk metallic glass. *Mater Trans* 46:2856–2863
- Gilbert CJ, Ritchie RO, Johnson WL (1997) Fracture toughness and fatigue-crack propagation in a Zr-Ti-Ni-Cu-Be bulk metallic glass. *Appl Phys Lett* 71:476–478
- Guo P, Lu Y, Ehmann KF et al (2014a) Generation of hierarchical micro-structures for anisotropic wetting by elliptical vibration cutting. *CIRP Ann Manuf Technol* 63:553–556
- Guo SF, Qiu JL, Yu P et al (2014b) Fe-based bulk metallic glasses: Brittle or ductile? *Appl Phys Lett* 105:161901
- Hasan M, Kumar G (2016) High strain rate thermoplastic demolding of metallic glasses. *Scr Mater* 123:140–143
- Hasan M, Schroers J, Kumar G (2015) Functionalization of metallic glasses through hierarchical patterning. *Nano Lett* 15:963–968
- He P, Li LK, Wang F et al (2016a) Bulk metallic glass mold for high volume fabrication of micro optics. *Microsyst Technol* 22:617–623
- He YX, Peng Y, Li Z et al (2016b) Bio-inspired multifunctional metallic glass. *Sci China Chem* 59:271–276
- Hu Z, Gorumlu S, Aksak B et al (2015) Patterning of metallic glasses using polymer templates. *Scr Mater* 108:15–18
- Huang H, Yan JW (2017) Surface patterning of Zr-based metallic glass by laser irradiation induced selective thermoplastic extrusion in nitrogen gas. *J Micromech Microeng* 27:075007
- Huang H, Zhao HW, Shi CL et al (2012) Effect of residual chips on the material removal process of the bulk metallic glass studied by in situ scratch testing inside the scanning electron microscope. *AIP Adv* 2:042193
- Huang H, Jun N, Jiang MQ et al (2016a) Nanosecond pulsed laser irradiation induced hierarchical micro/nanostructures on Zr-based metallic glass substrate. *Mater Des* 109:153–161
- Huang H, Noguchi J, Yan JW (2016b) Shield gas induced cracks during nanosecond-pulsed laser irradiation of Zr-based metallic glass. *Appl Phys A Mater Sci Process* 122:881
- Inoue A, Takeuchi A (2010) Recent development and applications of bulk glassy alloys. *Int J Appl Glas Sci* 1:273–295
- Jagdheesh R (2014) Fabrication of a superhydrophobic Al_2O_3 surface using picosecond laser pulses. *Langmuir* 30:12067–12073
- Jiang MQ, Wei YP, Wilde G et al (2015) Explosive boiling of a metallic glass superheated by nanosecond pulse laser ablation. *Appl Phys Lett* 106:021904
- Kaltenboeck G, Harris T, Sun K et al (2014) Accessing thermoplastic processing windows in metallic glasses using rapid capacitive discharge. *Sci Rep* 4:6441
- Ketov SV, Shi XT, Xie GQ et al (2015) Nanostructured Zr-Pd metallic glass thin film for biochemical applications. *Sci Rep* 5:7799
- Khun NW, Yu H, Chong ZZ et al (2016) Mechanical and tribological properties of Zr-based bulk metallic glass for sports applications. *Mater Des* 92:667–673
- Kumar G, Tang HX, Schroers J (2009) Nanomoulding with amorphous metals. *Nature* 457:868–872
- Lewandowski JJ, Wang WH, Greer AL (2005) Intrinsic plasticity or brittleness of metallic glasses. *Philos Mag Lett* 85:77–87

- Li T, Almond DP, Rees DAS (2011) Crack imaging by scanning pulsed laser spot thermography. *NDT&E Int* 44:216–225
- Li N, Xia T, Heng LP et al (2013) Superhydrophobic Zr-based metallic glass surface with high adhesive force. *Appl Phys Lett* 102:251603
- Li N, Chen W, Liu L (2016) Thermoplastic micro-forming of bulk metallic glasses: a review. *JOM J Miner Met Mater Soc* 68:1246–1261
- Liu Z, Schroers J (2015) General nanomoulding with bulk metallic glasses. *Nanotechnology* 26:145301
- Liu Y, Jiang MQ, Yang GW et al (2011) Surface rippling on bulk metallic glass under nanosecond pulse laser ablation. *Appl Phys Lett* 99:191902
- Liu Y, Jiang MQ, Yang GW et al (2012) Saffman-Taylor fingering in nanosecond pulse laser ablating bulk metallic glass in water. *Intermetallics* 31:325–329
- Ma J, Zhang XY, Wang DP et al (2014) Superhydrophobic metallic glass surface with superior mechanical stability and corrosion resistance. *Appl Phys Lett* 104:173701
- Marti K (2007) Sampling the sun. *Science* 318:401–402
- Martinez-Calderon M, Manso-Silvan M, Rodriguez A et al (2016) Surface micro- and nano-texturing of stainless steel by femtosecond laser for the control of cell migration. *Sci Rep* 6:36296
- Miotello A, Kelly R (1995) Critical-assessment of thermal models for laser sputtering at high fluences. *Appl Phys Lett* 67:3535–3537
- Myrach P, Polomski B, Le Claire E et al (2016) Thermographic crack detection in hot steel surfaces. In: 19th world conference on non-destructive testing, Munich, Germany, 13–17 June 2016
- Nagendra N, Ramamurty U, Goh TT et al (2000) Effect of crystallinity on the impact toughness of a La-based bulk metallic glass. *Acta Mater* 48:2603–2615
- Pauly S, Lober L, Petters R et al (2013) Processing metallic glasses by selective laser melting. *Mater Today* 16:37–41
- Plummer J, Johnson WL (2015) Is metallic glass poised to come of age? *Nat Mater* 14:553–555
- Sarac B, Ketkaew J, Popnoe DO et al (2012) Honeycomb structures of bulk metallic glasses. *Adv Funct Mater* 22:3161–3169
- Sarac B, Bera S, Balakin S et al (2017) Hierarchical surface patterning of Ni- and Be-free Ti- and Zr-based bulk metallic glasses by thermoplastic net-shaping. *Mater Sci Eng C Mater Biol Appl* 73:398–405
- Schlichting J, Ziegler M, Maierhofer C et al (2012) Flying laser spot thermography for the fast detection of surface breaking cracks. In: 18th world conference on nondestructive testing, Durban, South Africa, 16–20 Apr 2012
- Schroers J (2010) Processing of bulk metallic glass. *Adv Mater* 22:1566–1597
- Schroers J (2013) Bulk metallic glasses. *Phys Today* 66:32–37
- Ta DV, Dunn A, Wasley TJ et al (2015) Nanosecond laser textured superhydrophobic metallic surfaces and their chemical sensing applications. *Appl Surf Sci* 357:248–254
- Telford M (2004) The case for bulk metallic glass. *Mater Today* 7:36–43
- Trexler MM, Thadhani NN (2010) Mechanical properties of bulk metallic glasses. *Prog Mater Sci* 55:759–839
- Vorobyev AY, Guo CL (2015) Multifunctional surfaces produced by femtosecond laser pulses. *J Appl Phys* 117:033103
- Wang WH (2012) The elastic properties, elastic models and elastic perspectives of metallic glasses. *Prog Mater Sci* 57:487–656
- Williams E, Brousseau EB (2016) Nanosecond laser processing of Zr₄₁.2Ti₁₃.8Cu₁₂.5Ni₁₀Be_{22.5} with single pulses. *J Mater Process Technol* 232:34–42
- Xia T, Li N, Wu Y et al (2012) Patterned superhydrophobic surface based on Pd-based metallic glass. *Appl Phys Lett* 101:081601
- Xu SL, Shimada K, Mizutani M et al (2014) Fabrication of hybrid micro/nano-textured surfaces using rotary ultrasonic machining with one-point diamond tool. *Int J Mach Tools Manuf* 86:12–17

- Yang J, Luo FF, Kao TS et al (2014) Design and fabrication of broadband ultralow reflectivity black Si surfaces by laser micro/nanoprocessing. *Light Sci Appl* 3:e185
- Yoo JH, Jeong SH, Mao XL et al (2000) Evidence for phase-explosion and generation of large particles during high power nanosecond laser ablation of silicon. *Appl Phys Lett* 76:783–785
- Zhao K, Liu KS, Li JF et al (2009) Superamphiphobic CaLi-based bulk metallic glasses. *Scr Mater* 60:225–227
- Zhao M, Abe K, Yamaura S et al (2014) Fabrication of Pd-Ni-P metallic glass nanoparticles and their application as highly durable catalysts in methanol electro-oxidation. *Chem Mater* 26:1056–1061
- Zhu ZW, To S, Zhang SJ (2015) Theoretical and experimental investigation on the novel end-fly-cutting-servo diamond machining of hierarchical micro-nanostructures. *Int J Mach Tools Manuf* 94:15–25



Noritaka Kawasegi

Contents

16.1	Introduction	530
16.2	Interaction of Ion with Solid and Damage Creation	531
16.3	Structure Fabrication by Sputtering	534
16.3.1	Dependence of Machining Characteristics on Irradiation Parameters	534
16.3.2	Application of Sputtering	537
16.4	Structure Fabrication by a Combination with Etching	541
16.4.1	Structure Fabrication Using the Etch Stop Effect	541
16.4.2	Structure Fabrication Using the Etching Enhancement Effect	544
16.5	Summary and Outlook	549
	References	551

Abstract

Ion beam machining is a powerful tool for the micro- and nanoscale fabrication of various materials utilizing the phenomenon of the interaction of the irradiated ions with a target material. The interaction causes a sputtering phenomenon, which can be utilized for micro- and nanomachining. The interaction simultaneously causes damage to the machined area, which degrades the characteristics of the machined material. However, the damaged layer can be used to fabricate structure by combining it with an etching method. In this chapter, the characteristics and application of ion beam machining, especially for silicon and diamond, are described. The basis of the interaction and damage creation is described. Then, two types of ion beam machining method (direct sputtering and a combination

N. Kawasegi (✉)

Toyama Industrial Technology Center, Takaoka-shi/Toyama, Japan

e-mail: kawasegi@itc.pref.toyama.jp

method of ion beam irradiation and etching) are described in detail. For ion beam sputtering, the effect of irradiation parameters on the sputtering characteristics, and the application of this method, is introduced. For the combination method of ion beam irradiation and etching, the characteristics and application to unique structure fabrication are described.

Keywords

Ion beam · Focused ion beam · Sputtering · Silicon · Diamond · Etching · Microfabrication · Dose · Ion energy

16.1 Introduction

Micro- and nanofabrication technology is an important field of research, and numerous attempts have been made to improve this technology in recent years. This technology is required in various industrial fields such as electronic, photonic, and biomedical engineering to miniaturize machine components. Through miniaturization, the integration and parallelization of components in a machine device are possible, leading to reductions in dead space and fabrication cost. A high-performance device can be fabricated using the changes in physicochemical behavior owing to scaling effects; the resonance frequency, thermal response, and chemical reaction increase with miniaturization. These characteristics are particularly effective in devices such as sensors and reactors. Devices that maximize these effects include microelectromechanical systems and nanoelectromechanical systems, which consist of micro-/nanometer-scale mechanical components.

The fabrication methods for these components are based on photolithography (Elwenspoek and Jansen 1998), which is a fabrication method used for semiconductor devices. This technology was developed based on Moore's law and can fabricate sub-100-nm patterns. This method consists of exposure through a mask, development, and wet or dry etching and is effective for the high-volume production of devices. However, the machined material is limited to silicon, gallium arsenide, and other semiconductor materials, and this method is adversely inefficient in special structure fabrications with low-volume production. In addition, this method is based on a two-dimensional process, and the shapes of the fabricated structures are limited to two-and-a-half-dimensional shapes, i.e., structures of arbitrary but uniform height. Therefore, the fabrication technique for complex structures, i.e., three-dimensional structures, in various materials is required for various industrial applications. Several successful fabrication attempts have been made by other methods. In particular, ion beam machining is an effective tool for micromachining and fabricating microstructures.

In this chapter, the characteristics and applications of ion beam machining are described. The basic characteristics and typical machining methods such as sputtering and a combination with etching methods are described, especially for silicon and diamond that have superior characteristics and have been widely researched.

16.2 Interaction of Ion with Solid and Damage Creation

Ion beam machining is achieved by irradiating accelerated ions to a solid surface and utilizing the effects of interactions between the irradiated ions and the target atoms. This phenomenon can be used for the micro- and nanofabrication of various materials. Herein, the interaction and damage creation are described.

Ion beam machining applies positive ions with several tens to several mega-electron volts of kinetic energy and irradiates them to solid materials. The irradiated ions intrude into the target materials, causing elastic and/or inelastic collisions with the target atoms, and then remain in the target material or are backscattered from the material. If a target atom receives energy over the displacement energy (e.g., 15–20 eV for silicon (Miller et al. 1994)) from an irradiated ion, the atom is knocked out of the original lattice site. Then, the atom causes continuous collisions with other target atoms, resulting in a massive magnitude of collision. This continues until the energy of the atom is less than the displacement energy. This phenomenon is called cascade collision. In addition, if target atoms near the surface have binding energy over the surface, they are removed from the surface. This phenomenon is called sputtering. The sputtering can be used for micromachining and the formation of thin film by depositing the sputtered atoms on other materials. By applying the remaining ions in the target atom, ion irradiation can be used for doping.

Because ion irradiation machining is achieved by utilizing these phenomena, it affects the crystal structure in the machined area, resulting in the creation of defects and phase transitions. Figure 1 shows cross-sectional transmission electron microscope (TEM) images and nanoelectron diffraction (nano-ED) patterns of 30-keV Ga-ion-irradiated silicon at different doses (Kawasegi et al. 2006a). Damaged layers are formed in ion-irradiated areas. Under a low-dose condition, a damaged area, which has the same pitch as the irradiation pitch (250 nm), is formed on the silicon substrate, as indicated by the nano-ED image in Fig. 1c, which shows a diffuse ring pattern. This indicates that an amorphous phase is formed in the irradiated area, and the layer expands to a depth of approximately 70 nm, as can be observed in Fig. 1a. On the other hand, a thicker and wider amorphous phase is formed under a high-dose condition than under a low-dose condition, and the layer is formed from the surface, as shown in Fig. 1b.

The distribution of the ions and the defects in the target material can be obtained by a simulation. Figure 2 shows ions and damage distribution in silicon irradiated by a 30-keV Ga ion, calculated by the Stopping and Range of Ions in Matter (SRIM) Monte Carlo simulation (Ziegler et al. 1985). The peak value of the ions and the defect distribution are observed at the interior of the silicon substrate at a depth of 19 nm. In addition, the distribution of Ga ions exists deeper than that of the irradiation-induced defect. The irradiated ions do not have enough energy to form massive cascades near the end of the ion tracks. Therefore, the distribution of defects is shallower than that of irradiated ions. The phase transition of the target material is related to the defect creation as described below. Therefore, the depth distribution of the defect is similar to that of the TEM observation in Fig. 1.

The mechanism of defect creation has been extensively investigated for silicon by experimental methods such as a transmission electron microscope (TEM) and X-ray

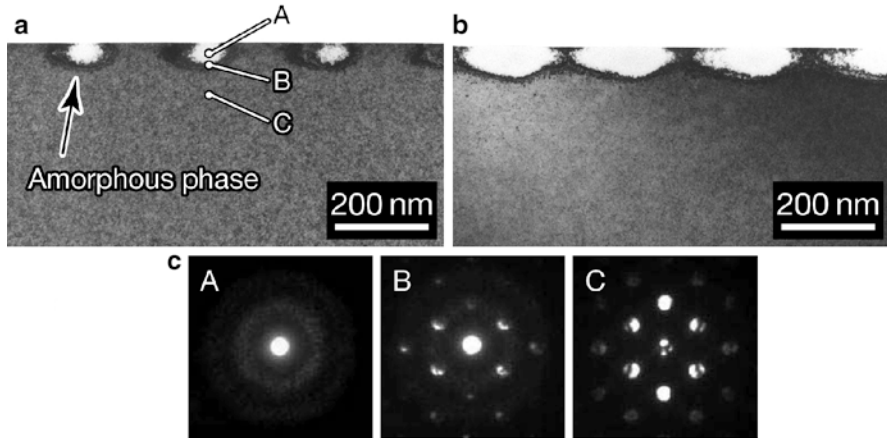
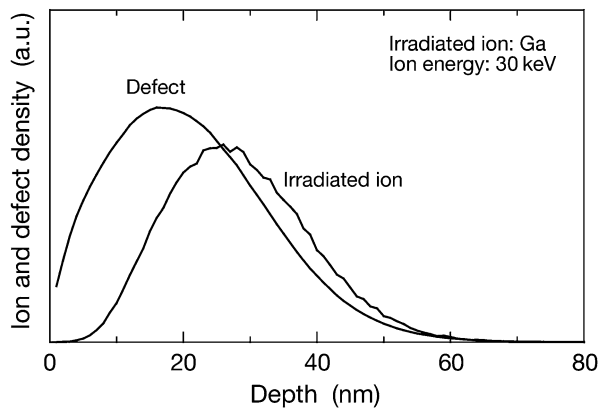


Fig. 1 Bright-field cross-sectional TEM image of 30-keV Ga-irradiated silicon at (a) lower dose and (b) higher dose. (c) Electron diffraction pattern of irradiated area denoted by A, B, and C in (a) (Reprinted from Kawasegi et al. 2006a. Copyright 2006, The Japan Society of Mechanical Engineers)

Fig. 2 Ion and defect distribution for silicon substrate after irradiation with 30-keV Ga ions, calculated by SRIM Monte Carlo simulation



diffraction and by simulation methods such as molecular dynamics (MD) and Monte Carlo simulations. The interaction causes thermal spikes to the material in addition to a cascade. This leads to the melting of the material, resulting in the formation of amorphous pockets (Diaz de la Rubia and Gilmer 1995; Caturla et al. 1996). The solidification rate is between 10^{14} and 10^{15} K/s, which is significantly higher than the critical rate for the amorphization (Brown et al. 1994). A part of the defect created by ion irradiation simultaneously disappears by the annealing, owing to heat induced by ion irradiation. This results in the recrystallization and inhibition of the amorphization. The morphologies of the crystal structure and defect are determined by these complex phenomena of amorphization and recrystallization.

A point defect created by ion irradiation is accumulated by the continuous irradiation, resulting in the formation of vacancies and interstitial clusters

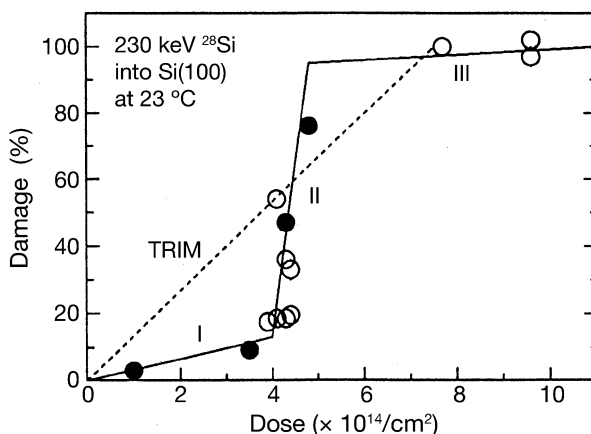
(Battaglia et al. 1990; Knights et al. 1999). These cluster defects act as the core of the amorphization and cause larger magnitudes of amorphization (Holland et al. 1989; Motooka et al. 1997). Therefore, the magnitude of the amorphization relates to that of the defect, and the amorphization is initially caused at the point of the maximum defect density (Motooka and Holland 1991).

The morphology of the amorphization depends on the ion irradiation conditions, similar to the defect density. Figure 3 shows the effect of the ion dose on the change in the defect density of silicon (Bai and Nicolet 1991). The creation process of the defect shows distinguishing trend which is different from that of the simulation. The defect density and the rate of increase in defects are marginal at low-dose conditions (Region I). Next, the defect rapidly increases when the dose reaches a critical dose value (Region II). Then, it saturates after a large dose of irradiation (Region III). Region I is associated with simple defects in crystalline silicon. Region II shows the formation of an amorphous phase and a mixture of crystalline and amorphous silicon structures. Region III shows the formation of an amorphous silicon structure, and further irradiation causes only the expansion of the amorphous region (Wang et al. 1985). The drastic change in density from Region I to Region II is caused by the nucleation of amorphous silicon when the defect density exceeds the critical dose value. The presence of the amorphous phase accelerates further amorphization, and a rapid increase is observed (Holland et al. 1989).

The trend of the defect creation is different from that for the species of ions (Baranova et al. 1973). A similar trend with that in Fig. 3 is observed for light ions such as Sb^{11} and C^{12} . In contrast with these ion irradiations, the boundaries of Regions I and II disappear during heavy-ion irradiation such as Sb^{121} and Ar^{40} , and the defect density increases from the low-dose condition. The heavy-ion irradiation directly creates an amorphous region from the ion impact, whereas the light ions can create isolated point defects and/or defect clusters (Howe and Rainville 1981; Narayan et al. 1985). Therefore, a continuous increase is observed from the low-dose condition during heavy-ion irradiation.

The ion energy affects the project rage of defects rather than the defect density and does not affect the threshold dose value for amorphization (Dennis and Hale 1976).

Fig. 3 Defect density dependence on dose at various species of ion irradiation (Reprinted from Bai and Nicolet. 1991. Copyright 1991, AIP Publishing LLC)



Therefore, an increase in the ion energy causes the depth range of the amorphous phase formed in the target material.

For diamond material, defect creation and phase transition occur similar to those for silicon, and the amorphization of diamond has been widely investigated. McKenzie et al. investigated the threshold dose for amorphization using TEM observations using 30-keV Ga-ion irradiation (McKenzie et al. 2011b). At a low dose of less than 3×10^{13} ions/cm², the diamond maintains its crystal structure. Significant defects are created at 1×10^{14} ions/cm². The threshold dose for amorphization is 2×10^{14} ions/cm², and a complete amorphous phase is formed in the irradiated area. Rubanov compared a cross-sectional TEM image of diamond irradiated by a 30-keV Ga ion with the defect density calculated by an SRIM Monte Carlo simulation (Rubanov and Suvorova 2011). The morphology of the amorphous phase is different from that of the dose. The amorphous phase is formed in the interior of the diamond, and a thin cap crystalline diamond is formed above the amorphous phase at a low dose because the amorphous layer is initially formed in the interior of the diamond, where most of the irradiated ions have ceased and have low energies. They determined that the threshold defect density for amorphization is $5.2 \pm 0.4 \times 10^{22}$ vacancies/cm³. The threshold defect density for amorphization was investigated also by various methods (Uzan-Saguy et al. 1995; Hickey et al. 2009).

Ion beam machining, especially for sputtering, is caused by the interaction of irradiated ions with the target material. Therefore, this method involves defect and phase transitions. The defect and phase transitions typically degrade the performance of the fabricated structure because the property is different from the original target material. However, this phenomenon can be utilized for structural fabrication. These techniques are described in the following sections.

16.3 Structure Fabrication by Sputtering

16.3.1 Dependence of Machining Characteristics on Irradiation Parameters

Sputtering is caused by the interaction of irradiated ions with a target material, and the phenomenon knocked the target atoms from the surface. By using this phenomenon, atomic-scale machining is possible. The sputtering method is widely used for preparation of TEM samples, which requires a thin sample of several hundreds of nanometers in thickness by a focused ion beam (FIB). FIB is particularly suitable for micro- or nanometer-scale machining owing to its high-resolution controllability. FIB can irradiate ion beams focused over a range from a few nanometers to a few micrometers and accelerate an ion energy of several tens of kilo electron volts.

The machining characteristics of the ion beam change by the ion irradiation parameters including dose, ion energy, incident angle, and species of ion. Figure 4 shows the change in depth of a single-crystal diamond surface irradiated by 40-keV Ga ions, plotted as a function of ion dose (Kawasegi et al. 2017b). Distinguishing phenomena are observed at low doses, and the irradiated area protrudes by 1–5 nm, as

Fig. 4 Changes in depth of FIB-irradiated area, plotted as a function of dose. Diamond surface is irradiated with Ga ions of energy 40 keV at various doses (Reprinted from Kawasegi et al. 2017b. Copyright 2017, Elsevier)

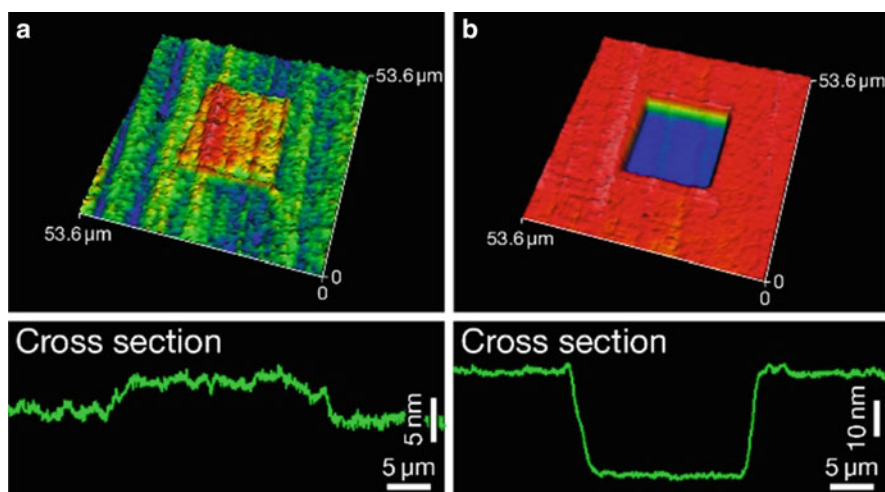
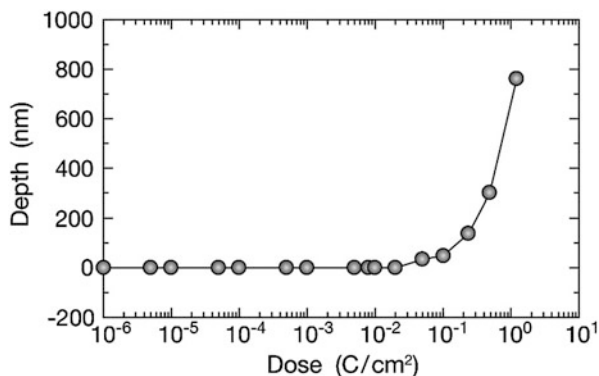
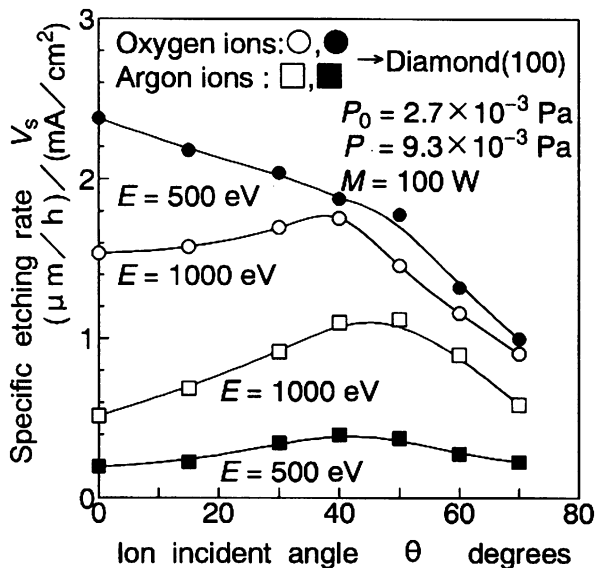


Fig. 5 Surface topography of diamond surface irradiated by Ga ions of energy 40 keV at dose of (a) 10 mC/cm² and (b) 100 mC/cm², measured using a coherence scanning interferometer (Reprinted from Kawasegi et al. 2017. Copyright 2017b, Elsevier)

shown in Fig. 5a. This phenomenon is called the swelling effect (Prins et al. 1986) and results from volume expansion caused by the formation of non-diamond phases induced by the FIB irradiation. Over a dose of 10 mC/cm², the irradiated area is sputtered, and a concave structure is fabricated, as shown in Fig. 5b. Therefore, the threshold dose value for diamond is about 10 mC/cm² in this condition.

The incident angle (the angle against the normal direction of the surface) is an important factor in determining the sputtering rate. In addition, by using a specific species of ion, a chemical reaction is obtained in addition to the physical sputtering, and highly efficient machining is possible. Figure 6 shows the specific etching rate of the diamond irradiated by ion beams at various incident angles (Kiyohara and Miyamoto 1996). To verify the effect of the chemical reaction, reactive ion O and nonreactive ion Ar are irradiated. For Ar-ion irradiation, the etching rate increases with the incident angle

Fig. 6 Dependence of specific etching rate of diamond on ion incident angle and species of ions (Reprinted from Kiyohara and Miyamoto 1996. Copyright 1996, The Japan Society for Precision Engineering)



because the energy of the ion is easy to transfer to the target atoms at the surface. However, it decreases at an incident angle over 50° owing to the backscattering of the ions at the surface. A similar trend is observed for 30-keV Ga-ion irradiation to silicon though the peak angle is different and obtained at 80° (Vasile et al. 1999). For the O-ion irradiation, the trend in the etching rate is different from that of the Ar-ion irradiation. The etching rate is significantly higher than that of Ar-ion irradiation, especially at low incident angles, because O ions induce a chemical reaction with the diamond, i.e., the reaction of C and O atoms to CO and CO₂. For an ion energy of 500 eV, the chemical reaction dominates the etching, and the maximum etching rate is observed at 0° . However, the rate of physical sputtering increased with the ion energy, and a trend similar to that of Ar irradiation is obtained at 1000 eV. Therefore, high-efficiency ion beam machining is possible by applying chemical reactions to the physical sputtering.

For the machining of silicon, a widely used similar technique is reactive ion etching (RIE) (Kovacs et al. 1998). In this method, reactive ions such as SF₆ are used and irradiated to the silicon surface. The ions react to the silicon surface and convert to SiF₄. By combining this chemical reaction with physical sputtering, highly efficient patterning is possible. This method is used to fabricate high-aspect-ratio structures in the photolithographic process with the Bosch process, which protects the side wall of the structure to prevent side etching.

For nano- to micrometer-scale structure fabrication, FIB is a powerful tool because structures can be fabricated by scanning a beam with a minimum diameter of several tens of nanometers to arbitrary positions. To scan an area, the surface is digitally scanned, and the irradiated area consists of a series of irradiation points. Since the machining characteristics are affected by the irradiation parameters, scanning parameters such as the dwell time (irradiation time per single irradiation point) and number of scans also affect the shape of the fabricated structure. Figure 7 shows SEM images of a diamond surface area

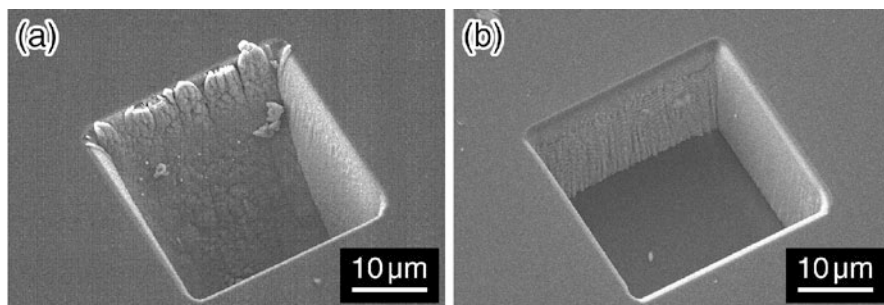


Fig. 7 SEM image of 40-keV Ga ion-irradiated area at dose of 30 C/cm^2 with (a) long and (b) short dwell-time conditions

($30 \times 30 \mu\text{m}^2$ area) irradiated by 40-keV Ga ions at a dose of 30 C/cm^2 . Although the diamond is irradiated at the same dose, the dwell time and number of machinings are different; i.e., the surface in Fig. 7a is irradiated at a long dwell time with a low number of scanning times, and the surface in Fig. 7b is irradiated at a short dwell time with a high number of scanning times. As can be seen, the shape of the machined area is different. The former has a deeper sloped surface. However, the latter has a flat surface.

The reason for the difference in shape of the irradiated area can be described as follows (Yamaguchi et al. 1984). For a long dwell time, a locally deep and sloped dotted surface is formed at the irradiated point. The formation of the sloped dotted surface causes an increased sputtering rate at the next scanning point owing to the high incident angle against the sloped surface. This results in the formation of a deeper machined area. However, the sputtered ions redeposit to the machined area, and the previously machined area is buried. Therefore, a deep but sloped surface is formed. For the short-dwell-time irradiation with a high number of scans, the slope angle is small at a single irradiation point, and the sputtering rate is smaller compared with that of the long-dwell-time irradiation. The entire area is uniformly machined and somewhat shallow, but a uniform surface is formed. These results indicate that scanning parameters must also be optimized to fabricate precise structures in FIB.

16.3.2 Application of Sputtering

By using these characteristics, the ion beam sputtering technique is applied in various fields. Miyamoto et al. applied this technique to repolish a diamond indenter for a Vickers hardness tester (Miyamoto 1987). The diamond indenter is used to measure the hardness by indenting it to a material and therefore becomes worn after repetitive usage. To repolish the indenter, a broad Ar-ion beam is irradiated from the upside utilizing the differences between the characteristics caused by the irradiation parameters. The incident angle at the apex is 0° , and the sputtering rate is slow. However, that at the inclined side wall is high because of the high incident angle. Therefore, the apex becomes sharper with the ion irradiation, and a sharp apex of the indenter can be

formed. For microfabrication using broad ion beam, an etching mask is necessary to fabricate arbitrarily shaped structures. Taniguchi et al. applied spin-on-glass (SOG) mask patterned by electron beam lithography (Taniguchi et al. 2006a). The maximum selectivity of diamond and SOG is investigated, and diamond field electron emitter arrays, with 30 nm of curvature radius, 2.58 μm of base radius, and 5.86 μm of height, are fabricated by the oxygen reactive ion beam etching, as shown in Fig. 8. This result indicates that ion beam machining is effective for fabrication of diamond structures.

For nano- to micrometer-scale fabrication, FIB is a powerful tool with a fine-diameter scanning beam. To fabricate arbitrarily shaped structures, precise control of the position and irradiation parameters is necessary because the shape of the fabricated structure cannot be geometrically determined as in mechanical cutting. Vasile et al. developed an ion milling program and fabricated three-dimensional structures, as shown in Fig. 9 (Vasile et al. 1997). They mainly controlled the dwell time and pixel address to fabricate arbitrary shapes of structures, and a three-dimensional shape similar to that expected

Fig. 8 SEM image of fabricated diamond field electron emitter arrays (Reprinted from Taniguchi et al. 2006a. Copyright 2006, Elsevier)

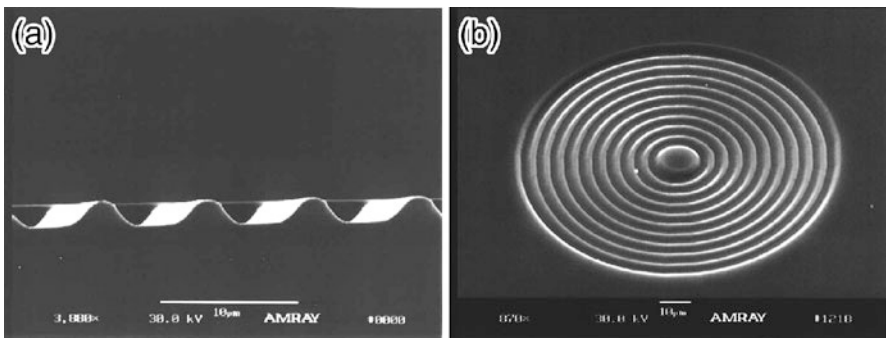
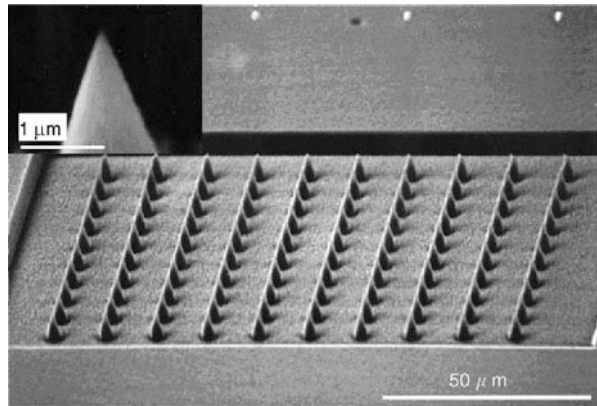


Fig. 9 SEM images of structures fabricated by applying ion milling program. (a) Edge view of sinusoidal pattern ion milled in Si (100) on 60 μm \times 30 μm pixel pattern. (b) Rotationally symmetric sine pattern ion milled in Si (100) on annulus pattern (Reprinted from Vasile et al. 1997. Copyright 1997, AIP Publishing LLC)

could be fabricated. It is mentioned that the sputter yield at a high incident angle, pixel size, and beam diameter are also important in controlling the shape of the structures.

Compared with silicon, the fabrication of a diamond structure is limited by conventional methods because of diamond's superior characteristics. Therefore, FIB is a more efficient method for microfabrication. Benjamin fabricated a triangle-faced single-crystal diamond cantilever applicable to chemical and biological sensors (Benjamin et al. 2010). The cantilever shape was cut by irradiating a Ga-ion beam at an angle to the surface, and various shapes of three-dimensional cantilevers were fabricated even for diamond, as shown in Fig. 10. FIB milling causes damage such as non-diamond phases and Ga implantation, which are removed by heat treatment. Diamond structures have excellent properties such as high hardness, low friction, and low chemical reaction. Therefore, such three-dimensional structures are suitable for microelectromechanical system (MEMS) applications.

For mechanical applications such as mold and cutting tools, superior hardness and wear resistance are required for the mold material. In general, silicon and nickel phosphorus, fabricated by photolithography and mechanical cutting methods, are used for molds. By using diamond as a mold material, superior wear resistance is achieved. Although the diamond is used as a tool material in precision cutting, the shape of the cutting edge is limited because the shape is formed by mechanical polishing. Arbitrary

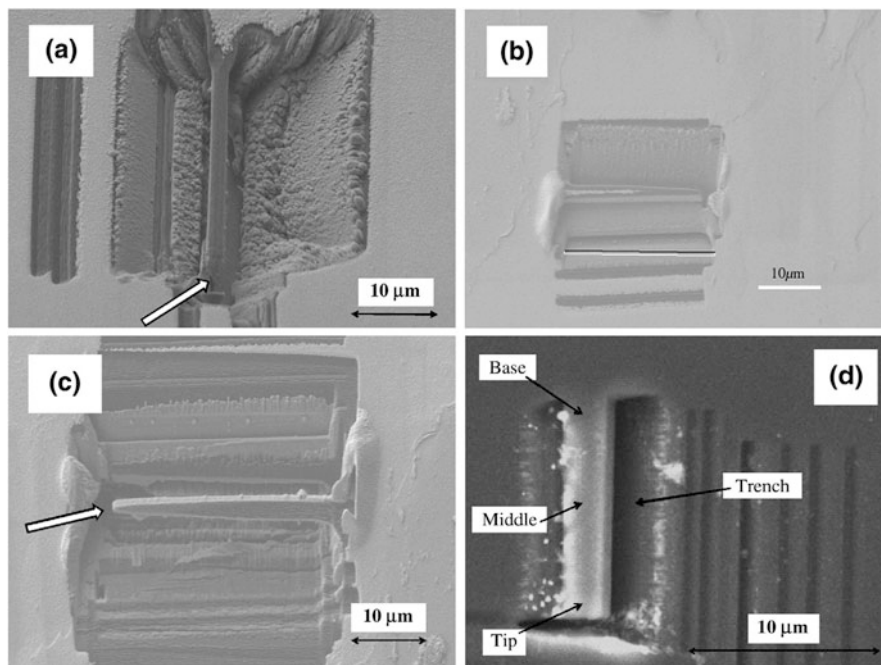


Fig. 10 Various shaped cantilevers fabricated by FIB milling (Reprinted from Benjamin et al. 2010. Copyright 2010, Elsevier)

complex and minute shapes of a diamond cutting edge enable us to form various microshapes by mechanical cutting.

McKenzie et al. fabricated specially shaped diamond nanoindenter tips by means of FIB-induced resistless hard mask formation, followed by O- and Ar-ion beam irradiation (McKenzie et al. 2011a). FIB with a Ga-ion beam was used to form patterns consisting of an amorphous carbon layer that was Ga-rich. This area acted as a mask against both reactive O and nonreactive Ar-ion beam machining, and a convex diamond pattern could be fabricated, as shown in Fig. 11. Imprinting of gold and silicon with features less than 100 nm was successfully performed, indicating that ion beam milling is effective for fabricating micropatterns on such microindenters made of diamond material. Takano et al. fabricated microtools used for microcutting with an atomic force microscope (AFM) (Takano et al. 2014).

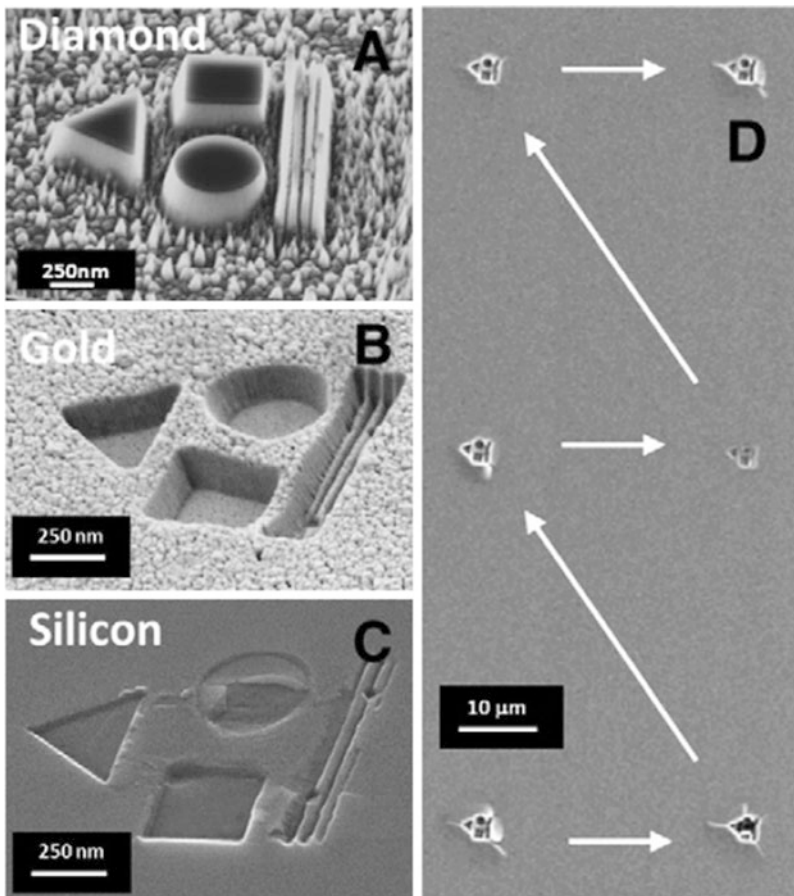


Fig. 11 (a) Diamond nanoimprint die fabricated by Ga implant mask. (b) Gold and (c) silicon patterns fabricated by imprinting diamond die. (d) Array of six consecutive imprints into silicon at imprint stress of 14.6 GPa (Reprinted from McKenzie et al. 2011a. Copyright 2011, Elsevier)

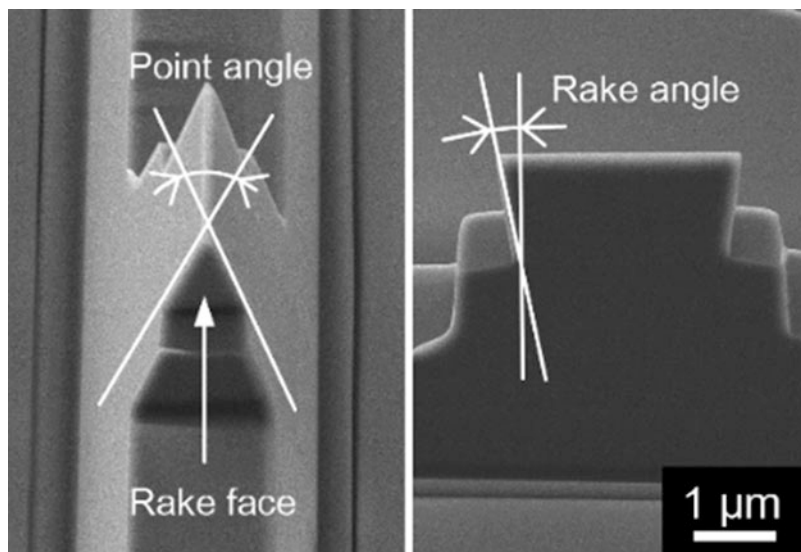


Fig. 12 Diamond cutting edge fabricated by FIB milling. Diamond tip of cantilever is fabricated by silicon mold fabrication and CVD diamond deposition and then milled by FIB (Reprinted from Takano et al. 2014. Copyright 2014, The Japan Society for Abrasive Technology)

Superior wear resistance and transcribility is required for cutting tools. A pyramidal diamond tip, fabricated by silicon mold fabrication and the chemical vacuum deposition (CVD) diamond deposition method (Kawasegi et al. 2006c), was machined by FIB. An arbitrary shape of the cutting edge was fabricated, as shown in Fig. 12. A machining experiment using AFM indicated that sharp grooves can be fabricated by the fabricated tools, and the machining characteristics change by the tool shape. Therefore, FIB milling is effective for fabricating minute tool shapes that cannot be fabricated by a conventional mechanical polishing method.

16.4 Structure Fabrication by a Combination with Etching

16.4.1 Structure Fabrication Using the Etch Stop Effect

In this section, a microfabrication method using a combination of ion beam irradiation and etching is described. The ion beam irradiation induces a damaged layer in the target material, which typically degrades the performance of the fabricated structure. However, this damaged area acts as a mask or is selectively removed by various methods. This phenomenon can be used to fabricate various unique structures.

The combination method of ion irradiation and etching is mainly applied to single-crystal silicon devices. A silicon surface irradiated with ion beams resists some etchants such as potassium hydroxide (KOH) (Berry and Caviglia 1983; Schmidt et al. 1997), tetramethylammonium hydroxide (TMAH) (Masahara et al. 2003), sodium

hydroxide (NaOH) (Edenfeld et al. 1994), and hydrazine (Koh et al. 2000, 2001). Thus, protruding structures can be fabricated on the irradiated area. This phenomenon is not dependent on the species of irradiated ions and has been reported after irradiating Ga (Berry and Caviglia 1983; Steckl et al. 1992), Si (Steckl et al. 1992; Fuhrmann et al. 1999), Au (Steckl et al. 1992), BF_2 (Koh et al. 2000), Ni (Ferrer et al. 2004), and P (Masahara et al. 2003) ions.

The “etch stop” effect of the ion-irradiated area is caused by the formation of an amorphous phase owing to ion irradiation. Fuhrmann et al. investigated the effect of irradiation-induced doping, amorphization, defects, and surface oxidation on the etch stop at different temperatures using H-passivated silicon (Fuhrmann et al. 1999). They concluded that several complex effects, including oxidation and amorphization, led to a decrease in the etch rate of the irradiated area against KOH. The etch stop of silicon is caused by the irradiation of different species of ions, even for silicon, which is the same species atom as the target atom. The maximum etch resistance against KOH is observed in the interior of the silicon rather than on the surface (Kawasegi et al. 2004). The rate of the etch stop could be controlled by the ion irradiation conditions, which do not cause drastic changes in the thickness and/or density of the formed oxide. Therefore, the etch stop in silicon is mainly caused by the amorphization of the silicon, although it is partly owing to oxidation.

The etch stop effect is effective for fabricating structures on large area because the ion irradiation time is significantly shorter than that required for the sputtering process. A wet chemical etching process can be used to remove a large amount of material in a short time. Therefore, highly efficient and unique structure fabrication is possible with this method. Several attempts have been made to fabricate various structures, including grating and dot patterns. These experiments used 10–60-keV ion beams and irradiated the ions with a dose ranging from 10^{13} to 10^{16} ions/cm². This method can also be used to fabricate a structure that cannot be achieved by conventional lithographic techniques and direct sputtering method. Berry and Caviglia fabricated grating pattern structures on a silicon surface with a minimum line width of 140 nm using an ion beam with a spot size ranging from 50 to 70 nm, followed by etching in KOH, as shown in Fig. 13 (Berry and Caviglia 1983). They demonstrated that this method could be used to fabricate submicron-size structures efficiently because a photomask is not necessary and the patterning speed is fast. Since ion irradiation can fabricate a thin etching mask that has a high etch resistance, the mask region can be used as part of the structure. The silicon substrate on the nonirradiated surface and under the irradiated areas is anisotropically etched to create an undercut. Consequently, thin freestanding ion-doped structures are formed on the silicon structures. The minimum line width can be controlled by the ion dose and the etch time. Several attempts have been made to fabricate freestanding silicon structures using a sufficient dose of ion irradiation followed by wet etching (Schmidt et al. 1997; Steckl et al. 1992; Sievilä et al. 2010).

Several researchers attempted to apply these methods to various device constructions. Koh et al. (2000) and Ferrer et al. (2004) fabricated convex silicon nanopyramid array patterns by Si, P, BF_2 , and N ion irradiation and N_2H_4 etching, as shown in Fig. 14. A simple process can be used to fabricate a convex nanopyramid array with a

Fig. 13 SEM image of freestanding gallium-doped silicon lines of 140 nm of width and 20 nm of thickness formed by ion implantation, which causes etch to undercut the implant region (Reprinted from Berry and Caviglia 1983. Copyright 1983, AIP Publishing LLC)

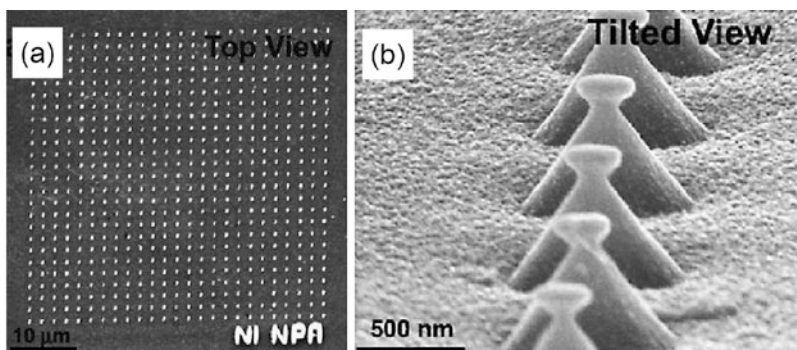
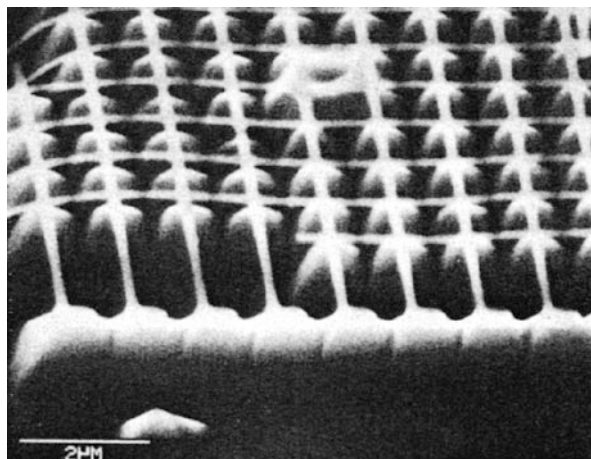


Fig. 14 SEM image of convex nanopillar array fabricated using 30-keV Ni ion irradiation at dose of 5×10^{15} ions/cm² with 2- μ m pitch: (a) top view and (b) tilted view (Reprinted from Ferrer et al. 2004. Copyright 2004, Elsevier)

2- μ m pitch. Ion beam irradiation can also be used to control the properties of the material based on ion implantation. The electrical properties of the apex of the pyramid can be controlled by dopant ion irradiation. This structure can be used for high-density field emitter arrays and biomolecule detection, such as for a deoxyribonucleic acid (DNA) tip. Masahara et al. fabricated ultrathin silicon walls by ion irradiation and TMAH etching (Masahara et al. 2003). A thin wall, 100 nm high and 16 nm wide, is fabricated without the damage caused in the RIE process. Such a wall can be used as a double-gate metal-oxide-semiconductor field-effect transistor.

The height of these structures is uniform because the ion irradiation-induced etching masks have sufficient etch resistance, similar to conventional photolithographic techniques. The etch resistance of the irradiated area is caused by the formation of the damaged layer. By controlling the thickness and/or etch resistance of the damaged layer, the height can be controlled.

Figure 15a shows the dependence the height of the structure on the ion dose after etching in KOH for 5 min (Kawasegi et al. 2004). The etch rate of the irradiated area decreased with an increase in the ion dose up to $10.0 \mu\text{C}/\text{cm}^2$ so that higher structures are fabricated at higher dose conditions. For a dose of $10.0 \mu\text{C}/\text{cm}^2$, the etch rate and height are nearly constant at approximately 24 nm/min and 85 nm, respectively. For doses less than $10.0 \mu\text{C}/\text{cm}^2$, an amorphous phase induced by the ion irradiation is etched. The etch resistance varied according to the ion doses, and consequently, structures of various heights can be fabricated due to the time lag of the dissolution in KOH. A thick and highly dense amorphous phase formed on the irradiated area for higher ion doses of irradiation, resulting in a high etch resistance against KOH. The height of the resulting structure is approximately 35 nm less than that of the non-etched area because the FIB-induced amorphous phase is formed in the interior of the silicon. Therefore, the maximum etch resistance occurred in the interior of the silicon, and the resulting height is somewhat less than that of the non-etched area. Figure 15b shows an AFM topography image of the dome-shaped structures fabricated by changing dose (Kawasegi et al. 2004). By using characteristics of height dependence on the dose in Fig. 15a, smooth and sloped three-dimensional structure can be fabricated by continuously changing the ion dose.

16.4.2 Structure Fabrication Using the Etching Enhancement Effect

A silicon surface irradiated by an ion beam is selectively etched in hydrofluoric acid (HF) (Gianola 1957; Gibbons et al. 1969) and phosphoric acid (H_2PO_4) (Komuro et al. 1983), and concave structures are fabricated on the irradiated area. This phenomenon is in contrast with that of alkaline etching. This phenomenon also does not depend on the species of the irradiated ions but is caused by the dissolution of the damaged region induced by the ion irradiation. This phenomenon is also used to measure the morphology of the damaged region (Baba et al. 1997) as well as creating structures. Gibbons et al. investigated the effect of the ion energy on the depth of a structure using 25- to 75-keV Ne- and Ar-ion beams (Gibbons et al. 1969). The depth of the structures increased with the ion energy, eventually creating 30–300-nm-deep structures. They indicated that the depth could be estimated using the theory of Lindhard et al. (1963). This result is useful in designing the shape of the structure.

These ion irradiation-induced phenomena can be caused on various sample surfaces other than silicon. This is effective for industrial applications because fabrication techniques based on semiconductor devices are limited to silicon and a few other materials. Zr-based metallic glass, a newly developed amorphous alloy (Inoue 2000) irradiated with Ga ions, is rapidly etched in a HNO_3 -based solution owing to the decrease in the etch resistance of the native oxide (Kawasegi et al. 2006b). This technique can create structures with a depth of several tens to hundreds of nanometers. This is suitable for structuring metallic glass since no other effective method exists for fabricating these submicron-scale structures. MeV ion irradiation induces significantly deeper damaged regions with a depth of several micrometers and can induce a latent track damage region in amorphous SiO_2 and TiO_2 substrates,

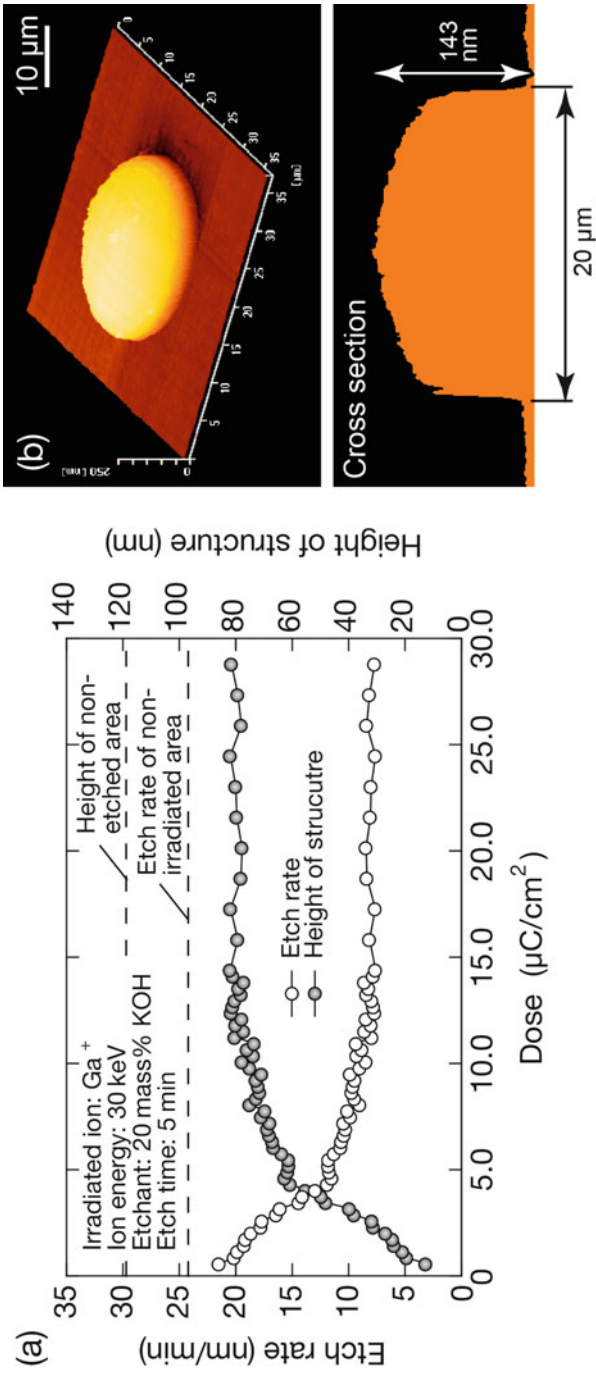


Fig. 15 (a) Change in height of structure for various ion doses. Silicon surface is irradiated by Ga ions and then etched in KOH for 5 min. (b) AFM topography image of dome structure fabricated by changing ion dose (Reprinted from Kawasegi et al. 2004. Copyright 2004, The Japan Society of Mechanical Engineers)

which subsequently can induce etching enhancements in HF (Awazu et al. 2000; Nomura et al. 2003). This is effective for fabricating high-aspect ratio structures for optics and photonic devices. Ion beam irradiation can be used instead of electron beam irradiation as a resist exposure owing to its high sensitivity and low amount of scattering. Ion beam irradiation is also used to expose a spin-on-glass (SOG) and poly-methyl methacrylate (PMMA) resist to create a template for nanoimprint lithography and can fabricate a replicated pattern with a 59.8-nm gap (Taniguchi et al. 2006b). A more rapid exposure is achieved by using a highly charged ion beam, which enhances the etch rate of PMMA (Momota et al. 2006). This highlights the distinctive phenomena of ion beam lithography for effective structure fabrication.

Since the morphology of the amorphous phase depends on the irradiation parameters, the shape of the fabricated structure changes with that of the amorphous phase. Fig 16a and b show AFM topography images of the silicon surface irradiated with 30-keV Ga ions at doses in a range of 0.2–27.1 $\mu\text{C}/\text{cm}^2$, before and after etching in hydrofluoric acid (HF) for 20 min, respectively (Kawasegi et al. 2006a). The irradiated area protruded to a height of 1–2 nm after irradiation owing to the swelling effect. The irradiated areas are selectively etched in HF, whereas the nonirradiated areas are scarcely etched. Therefore, concave structures with various depths are fabricated on the irradiated area over a dose of 20.4 $\mu\text{C}/\text{cm}^2$. For the low dose, the surface crystalline layer has an etch resistance against HF even at the irradiated area, due to the surface crystalline layer. The irradiated areas are etched, and a deeper structure is fabricated with increasing doses because of the longitudinal expansion of the amorphous phase. Hence, the depth of the structure can be controlled by the ion dose. By using this phenomenon, multiple-depth patterning is possible, as shown in Fig. 16c. A Fresnel lens pattern structure with a smooth curved surface can be fabricated by gradually changing the ion dose, indicating that this method is effective for fabricating multiple-depth structures on a silicon surface. Deeper structures can also be fabricated by applying high-energy ion irradiation (Kawasegi et al. 2007).

For diamond materials, non-diamond phases are formed via irradiation with high-energy ions, and this area can be selectively etched using a number of methods including heating in an oxygen atmosphere (Parikh et al. 1992; Kawasegi et al. 2014), wet chemical etching (Prins 1989; Olivero et al. 2006), electrochemical etching (Marchywka et al. 1993; Posthill et al. 1996), and deep ultraviolet laser irradiation (Kawasegi et al. 2017a). This method is applied to separate diamond plates from a bulk diamond by using MeV ion irradiation followed by etching. The high-energy ion irradiation can form a damaged layer only in a particular depth range. Therefore, a thin plate can be separated by etching the damaged layer. Parikh et al. applied this technique to fabricate a diamond plate by 4-MeV C-ion implantation or 5-MeV O-ion implantation in natural diamond (Parikh et al. 1992). In this method, the etching characteristics are different owing to the species of irradiated ions. For the C-ion implantation, the buried damaged layer is graphitized by annealing in a vacuum and is then etched in either chromic acid solution or by heating in oxygen. For the O-ion implantation, the methods of vacuum annealing and/or annealing in O_2 are applied. In this case, the implanted O is supplied internally to the graphic layer and is converted to carbon oxide, and diamond sheets

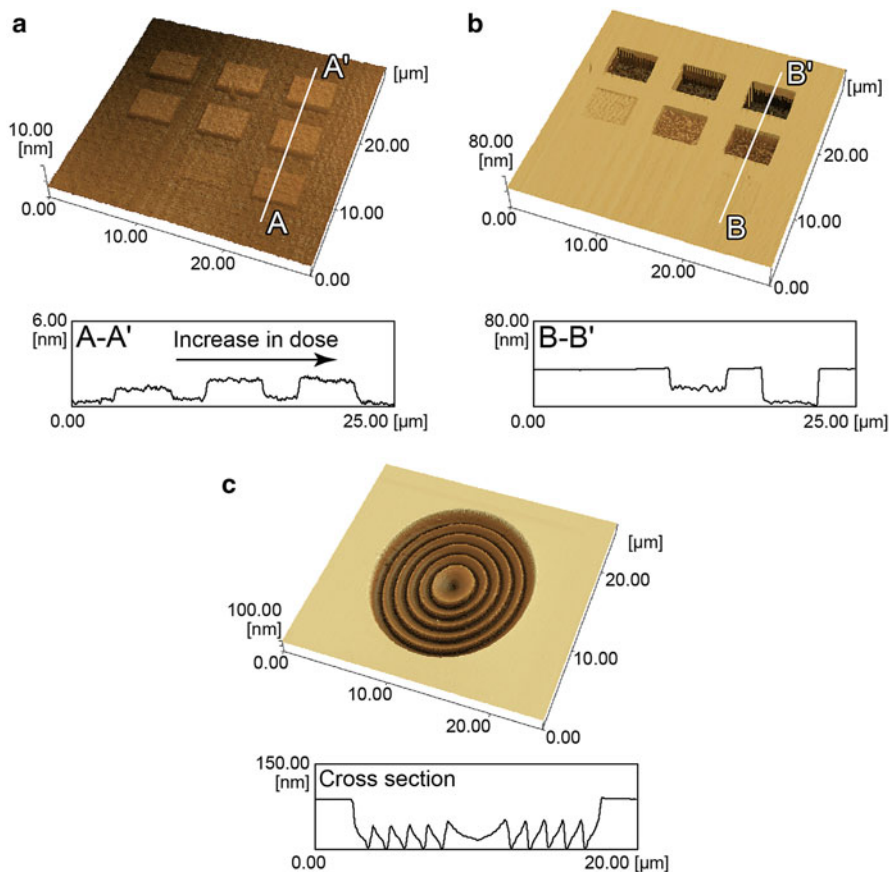


Fig. 16 AFM topography image of 30-keV Ga ion-irradiated silicon surface at doses of 0.2 to 27.1 $\mu\text{C}/\text{cm}^2$ (a) before and (b) after etching in HF for 20 min. (c) AFM topography image of Fresnel lens pattern structure fabricated using FIB irradiation with various ion doses followed by wet chemical etching in HF for 20 min (Reprinted from Kawasegi et al. 2006a. Copyright 2006, The Japan Society of Mechanical Engineers)

up to 4×4 mm in size are separated from a bulk diamond. This technique can also be applied to the separation of a CVD diamond plate, indicating that this technique is effective for this purpose (Mokuno et al. 2008).

The morphology of the damaged layer is controlled by the ion irradiation conditions similar to those of the silicon in Fig. 16. By using different species of ion irradiation facilities, unique structures can be fabricated. Olivero et al. fabricated a freestanding single-crystal diamond microstructure and an optical waveguide structure by using a combination of MeV ions and FIB irradiation (Olivero et al. 2006). A buried, highly damaged layer was created by MeV He ion irradiation at a dose of 1.5×10^{17} ions/cm². By using a MeV ion beam, the damaged layer was created at a depth of ~ 3.5 μm below the surface. Following the irradiation, the irradiated surface was patterned by FIB with

a 30-keV Ga-ion beam, and micrometer-width linear trenches deep enough to expose the buried layer were milled. Then, it was annealed at 500 °C to convert the damaged layer to tetrahedral amorphous carbon. The exposed damaged layer was etched in boiling acid ($\text{H}_2\text{SO}_4/\text{HClO}_4/\text{HNO}_3$), and then the freestanding structure could be fabricated, as shown in Fig. 17. Therefore, this technique is effective for such unique structure fabrications. Fairchild et al. fabricated single-crystal diamond membrane structures using a similar technique, such as a microring of 3 μm in diameter with a cross section of 280 nm \times 330 nm and a micro-/nanometer-scale cantilever (Fairchild et al. 2008). The shapes of these structures cannot be fabricated by a direct machining method. In addition, the crystal structure is nearly diamond because the damaged layer is removed, and therefore structures fabricated by this method have advantages in terms of their mechanical properties.

For FIB irradiation, the depth of the fabricated structures is controlled by ion irradiation conditions such as the dose and ion energy, although the depth is limited owing to the low ion energy. Multiple-depth patterns were fabricated on a diamond

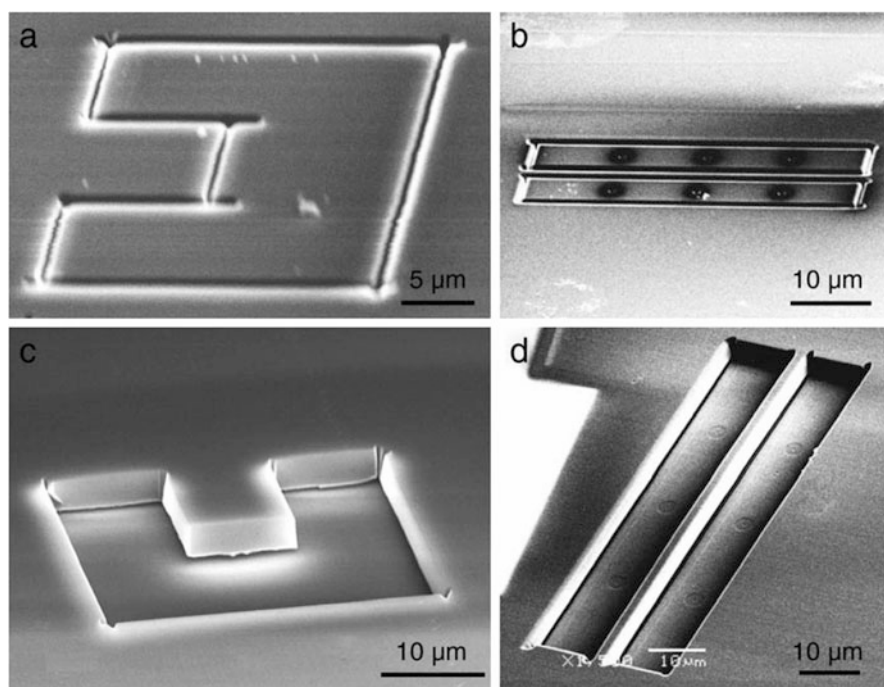


Fig. 17 SEM images of microstructures machined in single-crystal diamond. (a) and (b) show the FIB-patterned regions for the fabrication of a cantilever and waveguide structure, respectively. The diamond surface was irradiated by 2-MeV He ions, and then linear trenches were milled by FIB to expose the buried sacrificial layer to the surface in the desired shapes. (c) and (d) show the three-dimensional structures, respectively, in the same samples after the completion of the lift-off step. Reprinted from (Olivero et al. 2006) Copyright 2006, Elsevier

surface by the creation of an FIB-induced damaged layer and heating in air (Kawasegi et al. 2016), similar to that of silicon in Fig. 16. This technique is effective especially for tribological applications because the texturing on a solid surface is effective in improving the frictional characteristics of the surface, and the texture shape is important in this application (Blatter et al. 1998; Kawasegi et al. 2009).

As for the sputtering method, the damaged layer is formed on the machined surface and induces the degradation of the superior characteristics of the diamond. Therefore, the method of ion irradiation and etching is also effective for the removal of the damaged layer in addition to the structural fabrication. The damaged layer and implanted Ga ions degrade the characteristics of the photonic diamond structure fabricated by FIB. Bayn et al. added exposure to hydrogen plasma, followed by chemical etching in boiling acid (Bayn et al. 2011). The surface was characterized by time-of-flight secondary ion mass spectrometry (TOF-SIMS) and photoluminescence (PL), and the results indicated that the Ga-rich layer was removed, resulting in the improvement of the photonic properties. The photonic properties, irradiated by the oxygen FIB-milled surface, were also improved by H₂O-mediated electron beam-induced etching (Martin et al. 2015).

The single-crystal diamond is also used in cutting tools for ultraprecision mechanical machining because of its superior wear resistance, high transcribability, sharp cutting edge, low affinity, and other desirable properties. FIB is an effective means of fabricating micro- to nanometer-scale tool shapes. However, FIB-induced damage causes degradation of the machining characteristics, including a large tool wear, a large amount of adhesion, and a poorly machined surface. Kawasegi et al. applied this technique to remove the FIB-induced damaged layer on a diamond tool surface by heating in air (Kawasegi et al. 2014). The result indicated that the tool wear, adhesion, and machined surface were improved, and similar machining characteristics with a non-FIB-irradiated tool were obtained. In addition, an FIB irradiation and heat treatment technique was applied to texture fabrication on a diamond tool surface, and a texture that was 42 nm deep and 1.8 μm wide was fabricated, as shown in Figs. 18a and 17b (Kawasegi et al. 2017a). The tool texturing improved the friction and resultant cutting force while machining an aluminum alloy and NiP, as shown in Fig. 18c. This indicates that the texturing on a diamond tool surface is effective in improving the machining characteristics of the tool.

16.5 Summary and Outlook

In this chapter, the characteristics and applications of ion beam machining are described. Ion beam irradiation induces interaction of the irradiated ions with the target material, and this phenomenon can be applied to micro- to nanometer-scale machining. The sputtering method, especially when using FIB, is effective for fabricating three-dimensional structures. This method has advantages over the photolithographic technique in low-volume production because the machined material of the photolithographic technique is limited mainly to semiconductor material and the structure shape is also limited. In the solo direct sputtering method, a damaged layer,

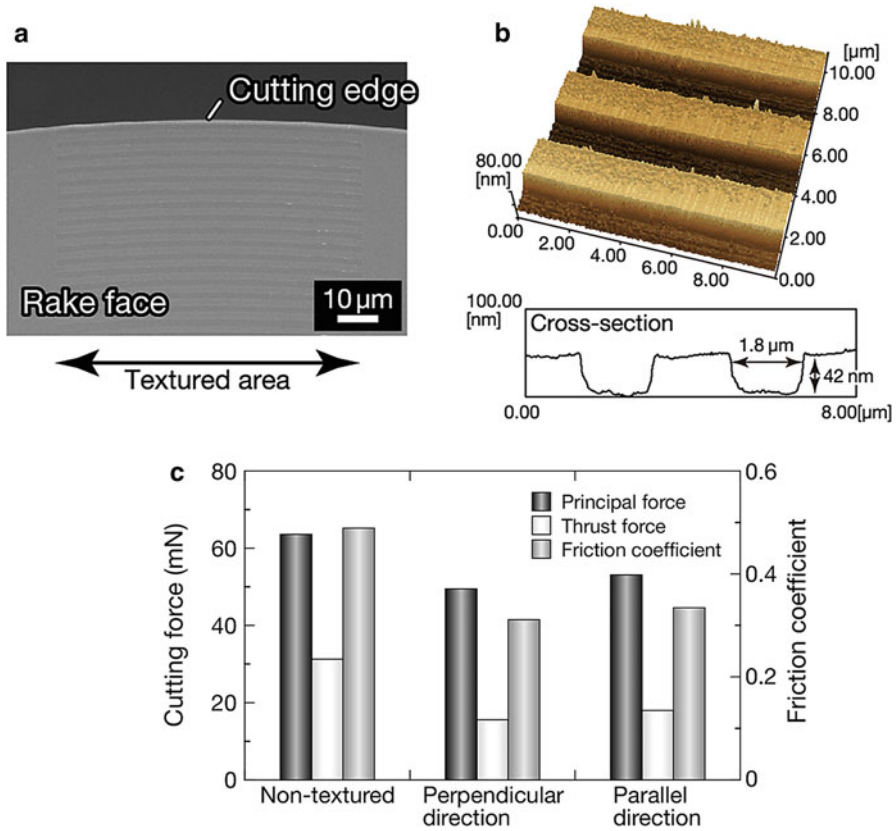


Fig. 18 Textured diamond cutting tool fabricated by FIB irradiation and subsequent heat treatment: (a) SEM image of rake face of textured diamond cutting tool surface, (b) enlarged image of texture measured by AFM, and (c) comparison of cutting forces while machining aluminum alloy with nontextured tool and tools textured in perpendicular and parallel to the chip flow direction (Reprinted from Kawasegi et al. 2017a. Copyright 2017, Elsevier)

which degrades the characteristics of the material, is formed on the surface. If the damaged layer adversely affects the performance of the fabricated device, the etching method is effective to remove this layer. The combined method of ion beam irradiation and etching can fabricate unique structures such as freestanding structures and three-dimensional structures. In addition, the damaged layer, which degrades the original material performance, can be removed in this method. A great advantage of ion beam machining is that it is applicable to diamonds that have superior mechanical, electrical, and chemical properties. This method is critically useful in the micro- to nanoscale machining of diamonds. Therefore, ion beam machining is expected to become an essential tool for emerging nanotechnology and nanoscience applications related to electronic, photonic, biomedical, and nanosystem engineering.

References

- Awazu K, Ishii S, Shima K, Roorda S, Brebner JL (2000) Structure of latent tracks created by swift heavy-ion bombardment of amorphous SiO₂. *Phys Rev B* 62:3689–3698
- Baba A, Bai D, Sadoh T, Kenjo A, Nakashima H, Mori H, Tsurushima T (1997) Behavior of radiation-induced defects and amorphization in silicon crystal. *Nucl Instrum Methods Phys Res Sect B* 121:299–301
- Bai G, Nicolet MA (1991) Defects production and annealing in self-implanted Si. *J Appl Phys* 70:649–655
- Baranova EC, Gusev VM, Martynenko YV, Starinin CV, Haibullin IB (1973) On silicon amorphization during different mass ion implantation. *Radiat Eff* 18:21–26
- Battaglia A, Priolo F, Rimini E (1990) Ion-induced annealing and amorphization of isolated damage clusters in Si. *Appl Phys Lett* 56:2622–2624
- Bayn I, Bolker A, Cytermann C, Meyler B, Richter V, Salzman J, Kalish R (2011) Diamond processing by focused ion beam – surface damage and recovery. *Appl Phys Lett* 99:183109
- Benjamin Z, KupferRezal KA, Aiman Z, Richard BJ (2010) Fabrication and characterisation of triangle-faced single crystal diamond micro-cantilevers. *Diam Relat Mater* 19:742–747
- Berry IL, Caviglia AL (1983) High resolution patterning of silicon by selective gallium doping. *J Vac Sci Technol B* 1:1059–1061
- Blatter A, Maillat M, Pimenov SM, Shafeev GA, Simakin AV (1998) Lubricated friction of laser micro-patterned sapphire flats. *Tribol Lett* 4:237–241
- Brown RA, Maroudas D, Sinno T (1994) Modelling point defect dynamics in the crystal growth of silicon. *J Cryst Growth* 137:12–25
- Caturla MJ, Diaz de La Rubia T, Marques LA, Gilmer GH (1996) Ion-beam processing of silicon at keV energies: a molecular-dynamics study. *Phys Rev B* 54:16683–16695
- Dennis JR, Hale EB (1976) Energy dependence of amorphizing implant dose in silicon. *Appl Phys Lett* 29:523–524
- Diaz de la Rubia T, Gilmer GH (1995) Structural transformations and defect production in ion implanted silicon: a molecular dynamics simulation study. *Phys Rev Lett* 74:2507–2510
- Edenfeld KM, Jarausch KF, Stark TJ, Griffis DP, Russell PE (1994) Force probe characterization using silicon three-dimensional structures formed by focused ion beam lithography. *J Vac Sci Technol B* 12:3571–3575
- Elwenspoek M, Jansen HV (1998) *Silicon micromachining*. Cambridge University Press, Cambridge
- Fairchild BA, Olivero P, Rubanov S, Greentree AD, Waldermann F, Taylor RA, Walmsley I, Smith JM, Huntington S, Gibson BC, Jamieson DN, Praver S (2008) Fabrication of ultrathin single-crystal diamond membranes. *Adv Mater* 20:4793–4798
- Ferrer D, Shinada T, Tanii T, Kurosawa J, Zhong G, Kubo Y, Okamoto S, Kawarada H, Ohdomari I (2004) Selective growth of carbon nanostructures on nickel implanted nanopyramid array. *Appl Surf Sci* 234:72–77
- Fuhrmann H, Döbeli M, Mühle R (1999) Focused ion-beam structuring of Si and Si/CoSi₂ heterostructures using adsorbed hydrogen as a resist. *J Vac Sci Technol B* 17:945–948
- Gianola UF (1957) Damage to silicon produced by bombardment with helium ions. *J Appl Phys* 28:868–873
- Gibbons JF, Hechtl EO, Tsurushima T (1969) Ion-bombardment-enhanced etching of silicon. *Appl Phys Lett* 15:117–118
- Hickey DP, Jones KS, Elliman RG (2009) Amorphization and graphitization of single-crystal diamond – a transmission electron microscopy study. *Diam Relat Mater* 18:1353–1359
- Holland OW, Pennycook SJ, Albert GL (1989) New model for damage accumulation in Si during self-ion irradiation. *Appl Phys Lett* 55:2503–2505
- Howe LM, Rainville MH (1981) Features of collision cascades in silicon as determined by transmission electron microscopy. *Nucl Instrum Methods* 182/183:143–151

- Inoue A (2000) Stabilization of metallic supercooled liquid and bulk amorphous alloys. *Acta Mater* 48:279–306
- Kawasegi N, Shibata K, Morita N, Yamada S, Takano N, Oyama T, Ashida K, Taniguchi J, Miyamoto I (2004) 3D micro-fabrication using combination technique of nano-scale processing and chemical etching: 2nd report, possibility of 3D micro-fabrication using focused ion beam process. *Trans Jpn Soc Mech Eng Ser C* 70:2541–2547. (in Japanese)
- Kawasegi N, Morita N, Yamada S, Takano N, Oyama T, Ashida K, Taniguchi J, Miyamoto I (2006a) Three-dimensional nanofabrication utilizing selective etching of silicon induced by focused ion beam irradiation. *JSME Int J Ser C* 49:583–589
- Kawasegi N, Morita N, Yamada S, Takano N, Oyama T, Ashida K, Taniguchi J, Miyamoto I, Momota S, Ofune H (2006b) Rapid nanopatterning of a Zr-based metallic glass surface utilizing focused ion beam induced selective etching. *Appl Phys Lett* 89:143115
- Kawasegi N, Takano N, Oka D, Morita N, Yamada S, Kanda K, Takano S, Obata T, Ashida K (2006c) Nanomachining of silicon surface using atomic force microscope with diamond tip. *ASME J Manuf Sci Eng* 128:723–729
- Kawasegi N, Morita N, Yamada S, Takano N, Oyama T, Momota S, Taniguchi J, Miyamoto I (2007) Depth control of a silicon structure fabricated by 100q keV Ar ion beam lithography. *Appl Surf Sci* 253:3284–3291
- Kawasegi N, Sugimori H, Morimoto H, Morita N, Hori I (2009) Development of cutting tools with microscale and nanoscale textures to improve frictional behavior. *Precis Eng* 33:248–254
- Kawasegi N, Ozaki K, Morita N, Nishimura K, Sasaoka H (2014) Single-crystal diamond tools formed using a focused ion beam: tool life enhancement via heat treatment. *Diam Relat Mater* 49:14–18
- Kawasegi N, Kuroda S, Morita N, Nishimura K, Yamaguchi M, Takano N (2016) Removal and characterization of focused-ion-beam-induced damaged layer on single crystal diamond surface and application to multiple depth patterning. *Diam Relat Mater* 70:159–166
- Kawasegi N, Ozaki K, Morita N, Nishimura K, Yamaguchi M (2017a) Development and machining performance of a textured diamond cutting tool fabricated with a focused ion beam and heat treatment. *Precis Eng* 49:311–320
- Kawasegi N, Yamaguchi M, Kozu T, Morita N, Nishimura K (2017b) Sub-micrometer scale patterning on single-crystal diamond surface using focused ion beam and deep ultraviolet laser irradiations. *Precis Eng* 50:337–343
- Kiyohara S, Miyamoto I (1996) Oxygen ion beam etching of single crystal diamond chips using an ECR-type ion source. *J Jpn Soc Prec Eng* 62:1459–1463. (in Japanese)
- Knights AP, Malik F, Coleman PG (1999) The equivalence of vacancy-type damage in ion-implanted Si seen by positron annihilation spectroscopy. *Appl Phys Lett* 75:466–468
- Koh M, Sawara S, Goto T, Ando Y, Shinada T, Ohdomari I (2000) New process for si nanopyramid array (NPA) fabrication by ion-beam irradiation and wet etching. *Jpn J Appl Phys* 39: 2186–2188
- Koh M, Goto T, Sugita A, Tanii T, Iida T, Shinada T, Matsukawa T, Ohdomari I (2001) Novel process for high-density buried nanopyramid array fabrication by means of dopant ion implantation and wet etching. *Jpn J Appl Phys* 40:2837–2839
- Komuro M, Hiroshima H, Tanoue H, Kanayama T (1983) Maskless etching of a nanometer structure by focused ion beams. *J Vac Sci Technol B* 1:985–989
- Kovacs GTA, Maluf NI, Petersen KE (1998) Bulk micromachining of silicon. *Proc IEEE* 86:1536–1551
- Lindhard J, Scharff M, Schiott HE (1963) Range concepts and heavy ion ranges. *Mat Fys Medd Dan Vid Selsk* 33:1–42
- Marchywka M, Pehrsson PE, Binari SC, Moses D (1993) Electrochemical patterning of amorphous carbon on diamond. *J Electrochem Soc* 140:L19–L22
- Martin AA, Randolph S, Botman A, Toth M, Aharonovich I (2015) Maskless milling of diamond by a focused oxygen ion beam. *Sci Report* 5:8958

- Masahara M, Matsukawa T, Ishii K, Liu Y, Nagao M, Tanoue H, Tanii T, Ohdomari I, Kanemaru S, Suzuki E (2003) Fabrication of ultrathin Si channel wall for vertical double-gate metal-oxide-semiconductor field-effect transistor (DG MOSFET) by using ion-bombardment-retarded etching (IBRE). *Jpn J Appl Phys* 42:1916–1918
- McKenzie W, Pethica J, Cross G (2011a) A direct-write, resistless hard mask for rapid nanoscale patterning of diamond. *Diam Relat Mater* 20:707–710
- McKenzie WR, Quadir MZ, Gass MH, Munroe PR (2011b) Focused ion beam implantation of diamond. *Diam Relat Mater* 20:1125–1128
- Miller LA, Brice DK, Prinja AK, Picraux ST (1994) Molecular dynamics simulations of bulk displacement threshold energies in Si. *Radiat Eff Defects Solids* 129:127–131
- Miyamoto I (1987) Ultra fine finishing of diamond tools by ion beams. *Precis Eng* 9:71–78
- Mokuno Y, Chayahara A, Yamada H (2008) Synthesis of large single crystal diamond plates by high rate homoepitaxial growth using microwave plasma CVD and lift-off process. *Diam Relat Mater* 17:415–418
- Momota S, Nojiri Y, Hamagawa Y, Hamaguchi K, Taniguchi J, Ohno H (2006) Application of highly charged Ar ion beams to ion beam lithography. *Nucl Instrum Methods B* 242:247–249
- Motooka T, Holland OW (1991) Amorphization processes in self-ion-implanted Si: dose dependence. *Appl Phys Lett* 58:2360–2362
- Motooka T, Harada S, Ishimaru M (1997) Homogeneous Amorphization in high-energy ion implanted Si. *Phys Rev Lett* 78:2980–2982
- Narayan J, Oen OS, Fathy D, Holland OW (1985) Atomic structure of collision cascades in ion-implanted silicon and channeling effects. *Mater Lett* 3:67–72
- Nomura K, Nakanishi T, Nagasawa Y, Ohki Y, Awazu K, Fujimaki M, Kobayashi N, Ishii S, Shima K (2003) Structural change induced in TiO_2 by swift heavy ions and its application to three-dimensional lithography. *Phys Rev B* 68:064106
- Olivero P, Rubanov S, Reichart P, Gibson BC, Huntington ST, Rabeau JR, Andrew DG, Salzman J, Moore D, Jamieson DN, Praver S (2006) Characterization of three-dimensional microstructures in single-crystal diamond. *Diam Relat Mater* 16:1614–1621
- Parikh NR, Hunn JD, McGucken E, Swanson ML, White CW, Rudder RA, Malta DP, Posthill JB, Markunas R (1992) Single-crystal diamond plate liftoff achieved by ion implantation and subsequent annealing. *Appl Phys Lett* 61:3124–3126
- Posthill JB, Malta DP, Humphreys TP, Hudson GC, Thomas RE, Rudder RA, Markunas RJ (1996) Method of fabricating a free-standing diamond single crystal using growth from the vapor phase. *J Appl Phys* 79:2722–2727
- Prins JF (1989) Preparation of ohmic contacts to semiconducting diamond. *J Phys D Appl Phys* 22:1562–1564
- Prins JF, Derry TE, Sellschop JPF (1986) Volume expansion of diamond during ion implantation. *Phys Rev B* 34:8870–8874
- Rubanov S, Suvorova A (2011) Ion implantation in diamond using 30 keV Ga^+ focused ion beam. *Diam Relat Mater* 20:1160–1164
- Schmidt B, Bischoff L, Teichert J (1997) Writing FIB implantation and subsequent anisotropic wet chemical etching for fabrication of 3D structures in silicon. *Sensors Actuators A* 61:369–373
- Sievilä P, Chekurov N, Tittonen I (2010) The fabrication of silicon nanostructures by focused-ion-beam implantation and TMAH wet etching. *Nanotechnology* 21:145301
- Steckl AJ, Mogul HC, Mogren S (1992) Localized fabrication of Si nanostructures by focused ion beam implantation. *Appl Phys Lett* 60:1833–1835
- Takano N, Sonobe S, Yamada S, Morita N (2014) Study on micromachining using diamond array tool (4th report: high efficiency micromachining using AFM cantilever). *J Jpn Soc Abras Technol* 58:446–450. (in Japanese)
- Taniguchi J, Koga K, Kogo Y, Miyamoto I (2006a) Rapid and three-dimensional nanoimprint template fabrication technology using focused ion beam lithography. *Microelectron Eng* 83:940–943

- Taniguchi J, Ohno K, Kawabata Y, Miyamoto I (2006b) Ion-beam processing of single crystal diamond using SOG mask. *Vacuum* 80:793–797
- Uzan-Saguy C, Cytermann C, Brener R, Richter V, Shaanan M, Kalish R (1995) Damage threshold for ion-beam induced graphitization of diamond. *Appl Phys Lett* 67:1194–1196
- Vasile MJ, Niu Z, Nassar R, Zhang W, Liu S (1997) Focused ion beam milling: depth control for three-dimensional microfabrication. *J Vac Sci Technol B* 15:2350–2354
- Vasile MJ, Xie J, Nassar R (1999) Depth control of focused ion-beam milling from a numerical model of the sputter process. *J Vac Sci Technol B* 17:3085–3090
- Wang KW, Spitzer WG, Hubber GK, Sadana DK (1985) Ion implantation of Si by ^{12}C , ^{29}Si , and ^{120}Sn : amorphization and annealing effects. *J Appl Phys* 58:4553–4564
- Yamaguchi H, Shimase A, Haraichi S, Miyauchi T (1984) Characteristics of silicon removal by fine focused gallium ion beam. *J Vac Sci Technol B* 3:71–74
- Ziegler JF, Biersack J, Littmark U (1985) *The stopping and range of ions in matters*. Pergamon Press, New York



Jun Taniguchi

Contents

17.1	Introduction	556
17.2	The Principles of Electron-Beam Lithography	556
17.2.1	Basic Principles of Electron Beams and Electron-Beam Lithography Systems	556
17.2.2	Improvement of the Throughput of EBL	558
17.2.3	Principle of Electron-Beam Lithography	559
17.3	Applications of Electron-Beam Lithography	560
17.4	Three-Dimensional Patterning by Electron-Beam Lithography	562
17.5	Example of an EBL Process for a Flat Substrate	566
17.5.1	EB Resist Details	566
17.5.2	An Example of an EBL Process	566
17.5.3	Three-Dimensional Variable Acceleration Voltage EBL	569
17.6	Electron-Beam Lithography for Roll-Shaped Surfaces	571
17.7	Summary and Outlook	574
	References	574

Abstract

Electron-beam (EB) machining is a powerful method for micro- and nano-fabrication because the beam can be focused to a diameter of the order of a few nanometers. This property permits the fabrication of nanoscale patterns by using an EB-sensitive polymer (resist) in a process called EB lithography (EBL). EBL is an advanced technique that can be used to produce three-dimensional structures by changing the EB dose or varying the EB acceleration voltage. In addition, EBL can be used to fabricate fine patterns on three-dimensional curved surfaces such

J. Taniguchi (✉)

Faculty of Industrial Science and Technology, Department of Applied Electronics, Tokyo University of Science, Tokyo, Japan
e-mail: junt@te.noda.tus.ac.jp

as roll-shape molds or lenses. To understand EBL, it is necessary to understand EB machines, EB resists, the principles of EBL, and the EBL process. This chapter explains these basic topics and describes advanced three-dimensional shape fabrication and EBL for three-dimensional surface fabrication.

Keywords

Electron beam (EB) · Resist · Three-dimensional patterning · Mold · Nanoimprint

17.1 Introduction

Electron beams (EBs) are widely used in analysis and in fabrication. In analysis, EBs are used to obtain atomic-scale images through transmission electron microscopy or to examine the morphologies of surfaces by means of scanning electron microscopy (SEM). EBs can also be used to investigate crystal orientation through low-energy electron diffraction or by reflective high-energy electron diffraction.

In fabrication, EBs can be used for welding, drilling holes, curing, or lithography. EB welding and hole drilling utilize the heat resulting from EB irradiation and operate on a submillimeter scale. EB curing can be used to harden resins to produce micrometer-scale patterns, whereas EB lithography (EBL) can be used to fabricate nanoscale patterns, because an EB can be focused so that its diameter is of the order of less than a few nanometers. Section 2 provides a description of the use of EBL techniques in micro- and nanoscale machining.

17.2 The Principles of Electron-Beam Lithography

Before providing an explanation of EBL, this section describes the basic principles of EBs and EB equipment. Finally, processes for improving the throughput of EBL are described and compared.

17.2.1 Basic Principles of Electron Beams and Electron-Beam Lithography Systems

EBs are generated by thermionic emission or field emission in a vacuum environment. A tungsten hairpin-type cathode is usually used as the source of thermionic emissions, and the resulting electrons are accelerated toward a nearby anode. Similarly, a needle-shape tungsten electrode is used in field emission devices, and the generated electrons are accelerating by an anode. The emitted EB is focused to a diameter of a few nanometers by means of electrostatic or electromagnetic lenses. In the case of patterning, a deflection electrode causes the EB to scan a required pattern, which can be designed by using a computer-aided design (CAD) system. A schematic representation of an EBL system is shown in Fig. 1.

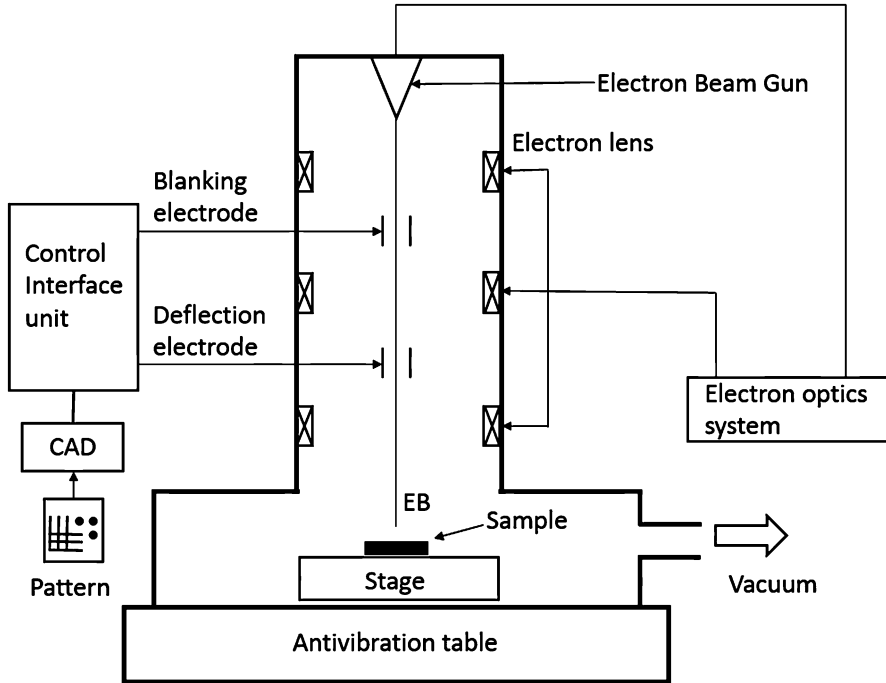


Fig. 1 Schematic representation of an EBL system

An EB is generated and accelerated by an EB gun system and subsequently irradiates a sample that is placed on a sample stage. The sample usually consists of an EB resist on a suitable substrate. In the finest case, electron lenses focus onto a segment of the sample measuring a few nanometers, and the focused EB is called a “point beam.” In reality, the diameter of the EB depends on the EB current, but here we will discuss the ideal case only.

The EB gun and lenses are controlled by an electron optics system. The EB passes through an area that is evacuated by a vacuum pump system, typically to a pressure of less than 10^{-6} Pa at the EB gun and less than 10^{-4} Pa near the sample stage. The sample stage is mounted on an antivibration table to avoid transmission of vibrations from the surroundings. To obtain a fine pattern on a sample, the desired pattern is initially designed by using a CAD system. In a simple system, a bitmap pattern file from a PC can be used for EBL. The pattern data are transferred to a control interface unit that controls an EB blanking electrode and an EB deflection electrode. The blanking electrode can switch the EB into an on state or an off state, whereas the deflection electrode is responsible for scanning the EB. These electrodes are then able to generate a pattern in a layer of resist material present on the surface of the substrate. If a black area in the designed pattern is required, the blanking electrode switches the beam on while it scans that area, whereas the blanking electrode similarly switches the beam off to produce a white area. The deflection electrode

scans each black area in a series of continuous lines, without switching the EB off. The size of the resulting pattern on the EB resist is determined by the magnification of the EB scanning area. In the case of a point beam, EB exposure times are very long, because the diameter of the EB spot is of the order of a few nanometers, whereas the patterned area typically measures 10×10 mm, which is a comparatively a very large area for such a small spot size. To reduce exposure times, shaped EB is used. This technique is described in Sect. 2.2.

17.2.2 Improvement of the Throughput of EBL

The shapes of EBs can be classified into three groups, as shown in Fig. 2.

The point beam is a focused EB that can delineate a fine pattern on an EB resist but requires lengthy exposure because the exposed area is very small, usually of the order of nanometers. To ameliorate this problem, beams with a larger area, such as stencil beams (Fig. 2b) or variable-shaped beams (Fig. 2c), are used. In the former, the target area is irradiated by a large-diameter EB through a stencil mask that contains holes or perforated patterns through which the resist is partially exposed to the EB, permitting a much larger area to be processed within a given time, thereby improving the overall throughput of the system. However, the stencil mask is generally located about $50 \mu\text{m}$ above the substrate, and the resulting gap causes blurring of the EB. Consequently, this type of EB lithography has a resolution limit of about 50 nm .

With variable-shaped beams, as shown in Fig. 2c, the arrangement is similar to that for a stencil-type beam, but the lens system is located below the stencil mask. When the EB has passed through the apertures in the stencil mask, its diameter is reduced by the lens system to permit the production of a finer pattern in the target area. This system provides both high resolution and high throughput but is very expensive and, consequently, is generally only used to produce photomasks for the manufacture of large-scale integrated circuit. Consequently, the equipment is usually referred to as a “mask writer.” Because of the expense of the equipment, photomasks are costly to produce.

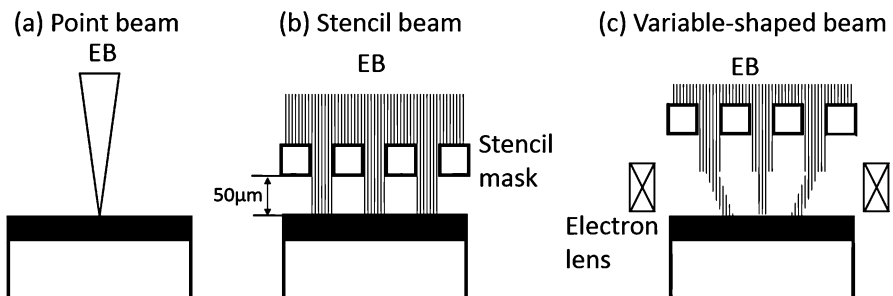


Fig. 2 Classification of EBs by shape: (a) point beam, (b) stencil beam, (c) variable-shaped beam

Shapes are produced in variable-beam EB equipment as follows. If, for example, a rectangular pattern is required, the EB passes through a rectangular-shaped aperture in the stencil mask. The diameter of the EB that passes through the rectangular shape is then reduced by an electron lens, to irradiate a smaller rectangular shape on the EB resist. In the research phases of manufacture, where the areas subjected to EBL are small, point beams and stencil beams are generally used. The principles of EBL are explained in Sect. 2.3 below.

17.2.3 Principle of Electron-Beam Lithography

In EBL, fine patterns are produced in a resist material that can subsequently be subjected to dry etching or lift-off processes. In this section, typical fine patterning processes are explained, an example of which is shown in Fig. 3. Various substrates can be used, for example, silicon wafers, quartz substrates, composite semiconductors (GaN, GaAs), or mask blanks. Mask blanks, which are subsequently used to produce photomasks, consist of a layer of chromium deposited on a quartz substrate. In the example shown in Fig. 3, a thermally oxidized silicon wafer is used as the substrate.

First, an EB resist is coated onto the silicon substrate (Fig. 3(1)), usually by spin coating. The EB resist is a material whose solubility is altered by exposure to an EB. The EB resist coating is then irradiated with an EB through a patterned mask (Fig. 3 (2)). The exposed areas are developed by immersion in a liquid developer and can either be removed by the developer, leaving unexposed areas (positive-type resist). Or the unexposed areas are removed, leaving the exposed areas (negative-type resist). The resulting patterned resists can be subjected to various semiconductor

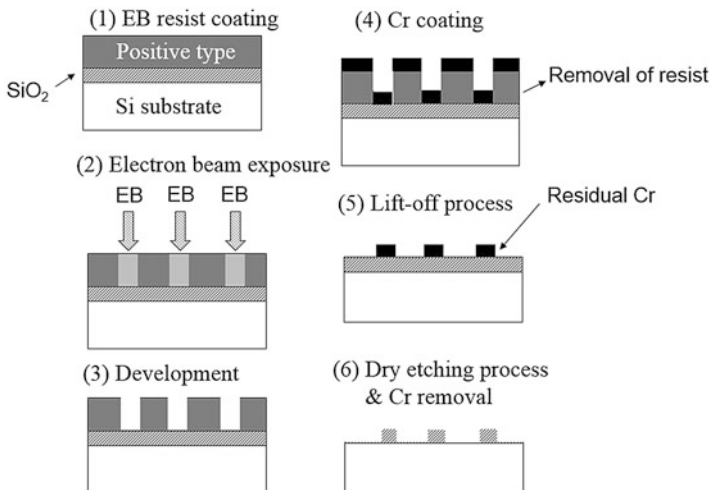


Fig. 3 The electron-beam lithography process and subsequent production of a nanoscale pattern

manufacturing processes, such as dry etching, ion implantation, or metal wiring. In the process illustrated in Fig. 3, these processes are applied to produce a raised pattern on which, after development (Fig. 3(3)), chromium is deposited by vacuum evaporation (Fig. 3(4)). In this case, the thickness of the Cr layer is less than that of the remaining resist. After coating with the Cr layer, the resist is dissolved by immersion in a solvent. For example, poly(methyl methacrylate) EB resist can be dissolved in acetone. In removing the resist layer, it is essential that the Cr coating does not cover the side walls of resist layer; this is why the Cr layer must be thinner than the height of the residual resist. After removal of the resist layer, the Cr patterns remain on the substrate. This process is referred to as a “lift-off” process. The resist is lifted off along with its Cr coating, and the excess Cr is washed away. As a result, Cr patterns on the substrate are obtained in the regions where no resist remained after the EB irradiation and development processes (Fig. 3(5)). The resulting Cr mask is used in a dry etching process in which the silicon or silicon dioxide substrate is removed in uncovered areas exposed to a plasma generated from an active gas, such as CF_4 , SF_6 , or CHF_3 , at a low pressure, whereas the substrate in regions protected by a Cr coating is relatively unaffected. In Fig. 3(6), the silicon dioxide layer is etched by dry etching with CHF_3 through a Cr mask, and after the etching process, the Cr is dissolved by immersion in an appropriate solvent. In this process, the EB resist is removed, so this layer is referred to as a “sacrificial layer.” Although the sacrificial layer is not present in the final lithograph, it is responsible for generating nanoscale patterns, and it determines their resolution.

A chemically amplified resist (CAR) can be used to reduce exposure times in EB lithography. The CAR contains an acid generator that promotes a chemical reaction in the EB-exposed area of the resist, as follows. The EB-exposed resist is subjected to heating, in a process referred to as a “postexposure bake.” During this process, an acid generator produces an acid in EB-exposed areas, which enhances the resist reactions in these regions. Development is then carried out. In this case, exposure to fewer electrons is needed in the EBL process, because the acid assists the chemical reaction of the resist, thereby reducing the overall time required for the process.

EB resists are mainly categorized as organic or inorganic. Organic EB resists are used for most process, whereas inorganic resists, which have a high resolution or high hardness, are used in producing molds for nanoimprint lithography. EB resists have recently become available for various purposes, so some applications of EB lithograph and EB resists are explained in Sect. 3.

17.3 Applications of Electron-Beam Lithography

EBL is useful for generating patterns on a scale of less than 300 nm; for larger scales of around 500 nm, for example, in the production of V-shape trenches or diffracting gratings, other technologies, such as photolithography, laser direct lithography, or fine precision cutting, are available. Therefore, the achievement of a resolution of less than 300 nm was the first target of EBL. Super-resolution laser lithography or two-photon absorption three-dimensional (3D) curing processes have a resolution of

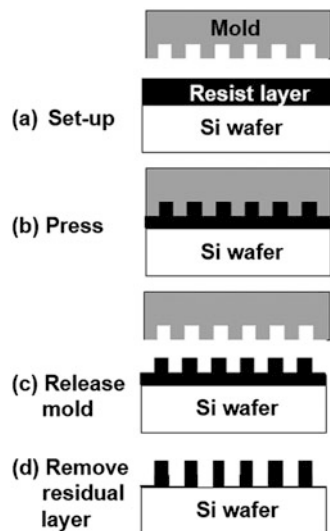
80 nm so that EBL is the only possible technique for achieving resolutions of below 80 nm. Semiconductor mass production technology can make less than 20 nm resolution pattern; however, this technology requires expensive photolithography tools such as steppers and scanners. Thus, in this case, semiconductor mass production technology is eliminated for comparison.

The finer delineation available in EBL requires prolonged exposures; however, a technique known as nanoimprint lithography (NIL) can compensate for the consequent time loss. The term “nanoimprint” first appeared as “nanoimprint lithography,” used by Professor S. Y. Chou in 1995 (Chou et al. 1995). “Imprint” in this context means to press and produce engraved marks, and so it has a similar meaning to pressing, embossing, or printing. The NIL process is illustrated in Fig. 4.

First, a nanoscale-patterned mold and a silicon wafer with a resist layer are prepared (Fig. 4a). One of two types of resist layer is generally used: a thermoplastic polymer or a photocurable polymer. Thermoplastic polymers are solid at room temperature but begin to flow (melt) on heating. Thus, the shape of a thermoplastic polymer can be deformed by heating and pressing with a mold. Photocurable polymers are liquid at room temperature and are therefore easily deformed by pressing with a mold; however, they solidify on exposure to UV radiation, typically from a mercury lamp (wavelength: 365 nm). Silicon wafers do not transmit UV radiation, so the mold must be transparent in the UV region, and is therefore usually made from quartz or sapphire, which both transmit UV radiation.

After the pattern for transfer has been produced, the mold is pressed onto a resist layer on a silicon wafer (Fig. 4b). The resist layer is then solidified and the mold is released from it (Fig. 4c). At this stage, convex parts of the mold generate corresponding concave parts in the resist layer, but they do not make contact with the silicon wafer. As a result, a residual layer of the resist normally remains on the

Fig. 4 Nanoimprint lithography process



silicon wafer. This residual layer is unnecessary and is removed by oxygen plasma ashing or a similar method (Fig. 4d).

The advantages of NIL are as follows. First, it is a simple process, and therefore cost-effective. Once a nanoscale mold has been prepared, numerous patterns with a nanoscale resolution can be produced at low cost. Furthermore, the NIL process is capable of producing features with a sub-10-nm resolution (Chou et al. 1997).

NIL can also be applied in other fields, such as 3D pattern transfer. When NIL is used in the manufacture of semiconductors, the residual layer must be removed, but in other fields, it is not necessary to remove it. When the residual layer is removed, a mask pattern for silicon is obtained, but this is a two-dimensional pattern; that is, the silicon surface is partially coated with a resist mask. On the other hand, if a mold pattern with a three-dimensional (3D) pattern is used, the nanoimprint process creates a 3D replica. This kind of 3D fabrication is difficult to achieve by photolithography. Furthermore, 3D replica patterns are widely used as optical elements, for example, moth-eye antireflective structures, diffraction gratings, Fresnel lenses, polarizers, subwavelength plates, or wire-grid polarizers; they are also used in surface-modified structures, such as cell culture plates, hydrophobic surfaces (lotus-effect surfaces), or adhesive surfaces, such as biomimetic gecko finger structures. Consequently, NIL is widely used in 3D nanofabrication, and processes for fabricating the 3D molds are important. EBL can be used to generate 3D patterns, so 3D patterning by EBL is explained in Sect. 4

17.4 Three-Dimensional Patterning by Electron-Beam Lithography

A method for fabricating a 3D pattern on an EB resist is shown in Fig. 5. Both positive-type and negative-type resists can be treated by the same procedure. First, the EB resist is coated onto a substrate. After a prebake to evaporate excess solvent, the EB resist is exposed to a variable dose of EB [EB dose = (EB current \times EB exposure time)/area]. In this case, the EB current is kept constant, and the exposure time is altered to change the EB dose. Because the number of electrons per unit area is proportional to the EB dose, the degree of change induced in the resist is dependent on the EB dose. As the EB dose is changed in various areas, a gradation in the number of electrons impinging those areas is produced (Fig. 5, upper). After development, a large EB dose produces a deep groove, and a small EB dose produces a shallow groove in a positive-type resist, whereas a large EB dose produces a high wall, and a small EB dose produces a low wall in a negative-type resist. Consequently, 3D resist patterning is possible by EBL.

However, the method of varying the EB dose has disadvantages. In the case of a positive-type EB resist, a large EB dose creates a deep groove pattern but simultaneously increases the width of the pattern (Fig. 6, left), making fine patterning difficult.

To avoid this increase in the pattern width, a technique known as variable acceleration voltage EBL has been developed (Fig. 6, right) (Ishii and Taniguchi

Fig. 5 Method for the fabrication of 3D patterns in EB resists

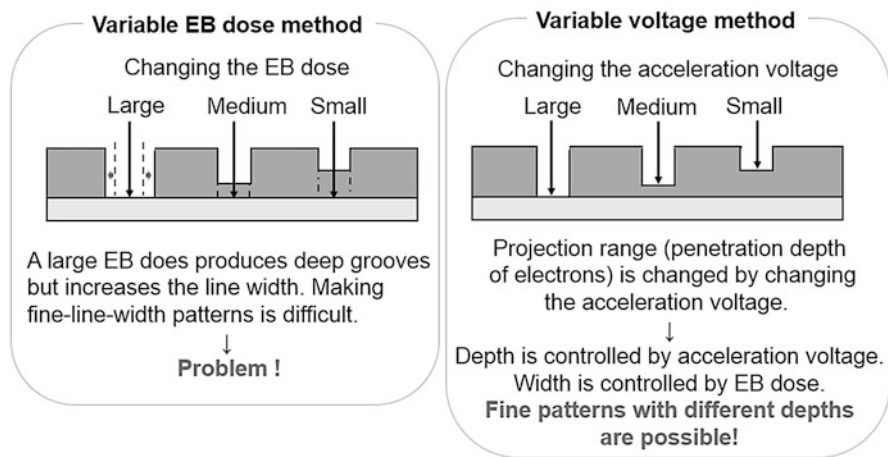
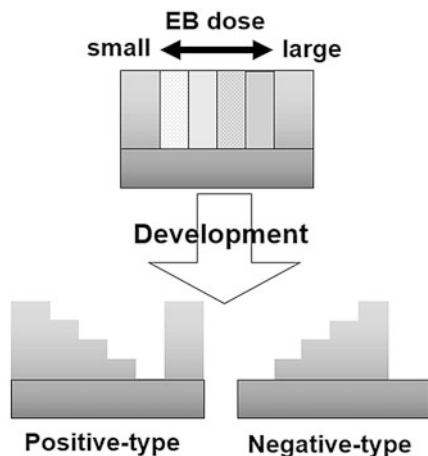


Fig. 6 Variable acceleration voltage method for 3D patterning

2007). The acceleration voltage determines the projection range (the penetration depth) of the beam in the EB resist. Changing the acceleration voltage therefore permits control of the groove depth in a positive-type resist. A higher acceleration voltage produces a deeper groove, whereas a lower acceleration voltage produces a shallower groove. In this method, groove depths are controlled by changing the acceleration voltage, and pattern widths are controlled by changing the EB dose. By using this method, a depth control of 5 nm is possible, and, simultaneously, 100 nm line patterns can be delineated. The experimental details are discussed in Sect. 5.

Another method for producing 3D patterns involves repeated EBL and dry etching processes. This method can be used to produce binary optics elements and is illustrated in Fig. 7.

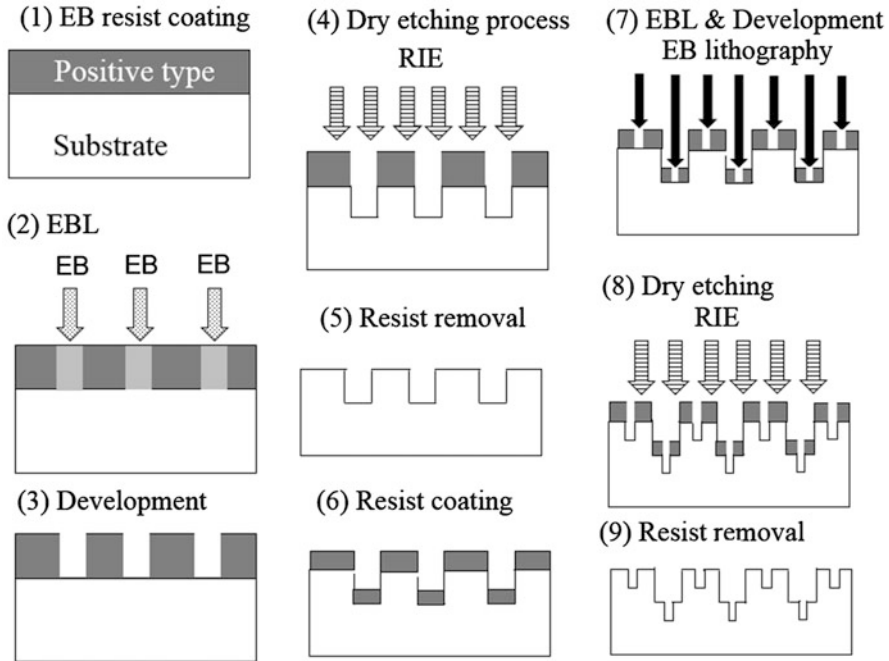


Fig. 7 Repeated EBL and dry etching process for making binary optics element

First, the substrate is coated with an EB resist (Fig. 7(1)). In this case a positive-type EB resist is used. EBL is then performed (Fig. 7(2)) and the pattern is developed (Fig. 7(3)). After development, dry etching is carried out by using the developed EB resist as a mask (Fig. 7(4)). Dry etching with reactive ions in a plasma removes the resist from the substrate (Fig. 7(5)). The resulting substrate has a two-level surface, which is then coated with a fresh layer of EB resist (Fig. 7(6)) so that the tops and the bottoms of the groove surfaces are covered with the resist. A second cycle of EBL is performed (Fig. 7(7)), and the surfaces at both the tops and bottoms of grooves are exposed to the EB. After development, masks for RIE are formed on both the top and bottom surfaces of the grooves. The resulting developed EB resist masks are again subjected to dry etching (Fig. 7(8)) to remove the resist, leaving a four-level surface (Fig. 7(9)).

A single cycle of EBL and dry etching generates a two-level surface. Two cycles of EBL and dry etching create a four-level surface. Therefore, n repetitions of the process produce a surface with 2^n levels. However, the resulting pattern has a jagged surface so that the production of curved structures, such as lenses or mirrors, requires a large number of cycles. Usually, three or more cycles are used, producing eight or more levels. This process is capable of fabricating fine and precise 3D pattern, but there are some problems. One is that the process is complicated, so alignment errors tend to occur; another is that a long total EBL time is required.

Technologies for producing 3D shapes and their features are summarized in Table 1.

Mechanical cutting is now greatly advanced, and a high-precision cutting machine can cut groove patterns a few hundred nanometers in depth, depending on the shape of the cutting tool and accuracy of the machine; this technique has the merit of providing a very rapid rate of removal. Deposition processes such as the focused ion beam–chemical vapor deposition (FIB-CVD) process can fabricate patterns with a resolution of less than 100 nm in width and depth, but this process is very slow because the 3D shape is created by FIB irradiation, and the area of FIB spot is only about 10 nm in diameter (Matsui et al. 2000). In addition, the CVD process requires a dwell time so that FIB irradiation times tend to be long. A similar problem is encountered in spot EBL. Semiconductor fabrication processes tend to involve a photolithography-based technique or EBL. Photolithography-based techniques include gray-scale lithography or repeat of photolithography and dry etching processes. Photolithography is a similar process to EBL. A photomask is used to produce a light-exposed area and an unexposed area. In this case, the semiconductor lithography tool, such as contact aligner, stepper or scanner, and resolution of photomask, determines the resolution of the photoresist. Steppers, scanners, and photomasks are very expensive, and therefore their use is generally limited to semiconductors for mass production. Gray-scale lithography uses a photomask that has gradual changes in transparency. It is a very fast process, but its resolution

Table 1 Fabrication processes for 3D shapes and their features

Category	3D process	Line width	Depth control	Process time
Mechanical cutting	High-precision cutting machine	Depends on cutting toll (250 nm)	Machine dependent	Fast
Deposition technique	FIB-CVD ^a	80 nm	100 nm	Very slow
Semiconductor processes (photolithography or EBL)	Gray-scale photolithography	Mask dependent (submicron)	Mask dependent (submicron)	Very fast
	Photolithography + dry etching	Photomask dependent (submicron)	Dry etching process dependent (nanoscale)	Slow
	EBL + dry etching	EBL dependent (<100 nm)	Dry etching process dependent (nanoscale)	Ultraslow
	Variable dose EB	500 nm	50 nm	Very slow
	Variable acceleration voltage EB	40 nm	5 nm	Very slow

^aFocused ion beam–chemical vapor deposition

depends on the gray-scale photomask, which can be difficult to fabricate and has a resolution of a submicrometer order. On the other hand, a repeated photolithography–dry etching process, which is similar the repeated EBL–dry etching, can improve depth resolution; however, the process is slow because of the repetition of photolithography and dry etching. Repeated EBL–dry etching has a high resolution in terms of both the width and the depth of lines, but the process times are also extremely lengthy. The variable-dose EB method can produce 3D shapes of a submicron order, but the process is very slow. Variable acceleration voltage EB permits the fabrication of 3D shapes of less than 100 nm in size, but the process is also very slow. In summary, EBL has the merit of a high resolution in both width and depth of lines, but because the EB exposure time is very long, EBL is generally used to fabricate high-resolution and high value-added items.

In this section, basic and advanced EBL processes have been explained, and the classification of 3D fabrication processes has been discussed. In Sect. 5 an example of an EBL process is explored.

17.5 Example of an EBL Process for a Flat Substrate

17.5.1 EB Resist Details

The properties of some commercially available EB resists are listed in Table 2, including the manufacturer, type, thickness, resolution, sensitivity, and developer. Resist thickness is controlled by the speed of rotation of the spin coater, and some typical conditions are shown in Table 2. The sensitivity is the EB dose required to ensure that material is removed from an exposed area. Both the resolution and the sensitivity depend on the EB acceleration voltage, so typical acceleration voltages are listed. A high acceleration voltage can focus the EB to a smaller diameter, so 50 kV EB machines are generally used. CARs or chemically semi-amplified resists (CSARs) have a high sensitivity, reducing exposure times and permitting a high throughput. However, after development, CAR-type resists have a greater line width (low resolution) and high line edge roughness. It is therefore important to achieve a balance between resolution and sensitivity (throughput) when choosing an EB resist. CAR resists need a postexposure bake. For example, FEP-171 has to be heated at 110 °C for 90 s. In the case of negative-type EB resists, high resolutions are difficult to obtain. However, in 2001 hydrogen silsesquioxanes were shown to act as high-resolution negative-type EB resists (Namatsu et al. 1998), and these are now widely used. Tetramethylammonium hydroxide (TMAH) is an alkaline developer, and this developer is widely used for development of semiconductor photoresist.

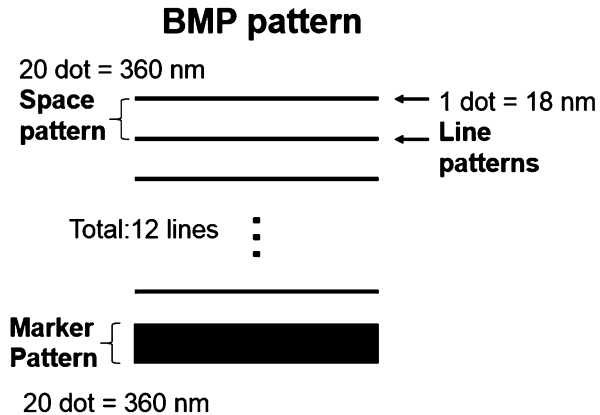
17.5.2 An Example of an EBL Process

Here, an example of an EBL process is described. Figure 8 shows the design of a pattern for EB writing. In this case, a scanning electron microscope with a pattern

Table 2 Commercially available EB resists

Resist	Maker	Posi/ Nega	CAR/non- CAR	Thickness	Resolution	Sensitivity [$\mu\text{C}/\text{cm}^2$]	Developer	Reference
CSAR62 (AR-P6200-09)	Allresist GmbH	Positive	CSAR	200 nm	10 nm	55(30 kV)	AR 600-	ALLRESIST (2017)
				(4000 rpm)	(30 kV)		546	
PMMA950k	EM Resist	Positive	Non-CAR	1000 nm	10–20 nm	200–500	MIBK:	EM Resist, PMMA (2015a)
				(4000 rpm)			IPA	
SML100	EM Resist	Positive	Non-CAR	100 nm	< 10 nm	378(50 kV)	MIBK:	EM Resist, SML (2015b)
				(5000 rpm)			IPA	
ZEP520A	Zeon	Positive	Non-CAR	500 nm	10–20 nm	20–25	1: 3	Gangnaik et al. (2014)
				(2000 rpm)			ZED-N50	
FEP-171	Fujifilm	Positive	CAR	2500 nm	Sub-	15 (50 kV)	TMAH	Paulsson et al. (2005)
				(2000 rpm)	100 nm		2.38%	
SAL 601	Shipley	Negative	CAR	200 nm	< 50 nm	30–40	MF319	Claßen et al. (1994)
				(4000 rpm)	(100 kV)			
HSQ	Dow corning	Negative	Non-CAR	10–20 nm	< 10 nm	110(70 kV)	TMAH	Grigorescu et al. (2007)
				(3000 rpm)	(100 kV)		2.38%	
				※HSQ: MIBL				
				1: 7				

Fig. 8 Pattern design for EB writing



generator is used as the EBL machine. This pattern generator can read the EB writing pattern from a bitmap file and use it to direct the EB. The black area of the bitmap pattern corresponds to beam on, whereas the white area is beam off. The size of 1 pixel on the bitmap pattern is determined by the magnification of the scanning electron microscope and the number of divisions in the scan area. In the case of Fig. 8, the scan length is 180 μm , and the number of divisions is 10,000, so 1 pixel has a diameter of 18 nm. Each line connects a series of single pixels (dots), so its designed width is 18 nm. Similarly, the space distance is 360 nm, and the line width of the marker pattern is 360 nm. The marker pattern is useful for detecting the EBL area.

Next, the process for fabricating fine patterns by EBL is explained. First, a positive-type EB resist (ZEP520A) is coated on a 10-mm-square section of a silicon substrate by using a spin coater (Fig. 9(1)) at a rotation speed of 10,000 rpm for 20 s to give a resist layer with a thickness of 300 nm.

A prebake is then carried out at 80 $^{\circ}\text{C}$ for 5 min on a hot plate (Fig. 9(2)) and at 180 $^{\circ}\text{C}$ for 20 min in an oven (Fig. 9(3)). The prepared EB resist is subjected to EBL (Fig. 9(4)) at an acceleration voltage of 10 kV and an EB current of 10 pA by using the bitmap pattern shown in Fig. 8. A relatively low acceleration voltage is used so that the diameter of the EB is about 10 nm. After EBL, development is carried out (Fig. 9(5)), and the developed patterns are examined by SEM (Fig. 9(6)).

The results of the observation are shown in Fig. 10. Twelve fine lines are delineated. Because the EB resist was a positive type, groove patterns are observed. The enlarged view (bottom right) shows a 60-nm-wide line. The design width was 18 nm, but the width of the resulting pattern was 60 nm. This is because the EB diameter was 10 nm and the thickness of the resist was 300 nm. The resolution depends on the beam diameter and the resist thickness. In this case, the EB diameter was relatively large (10 nm), and the resist layer was relatively thick (300 nm). In the case of a thick resist, a large EB dose is required to remove the resist, which means the Si substrate is exposed at the bottom of the grooves so that the width of the developed line tends to increase.

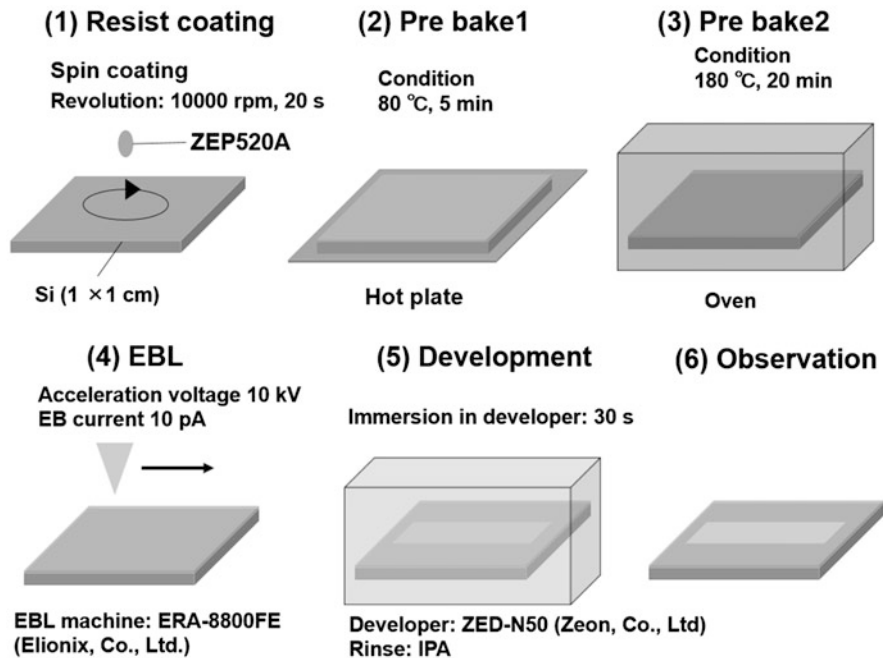
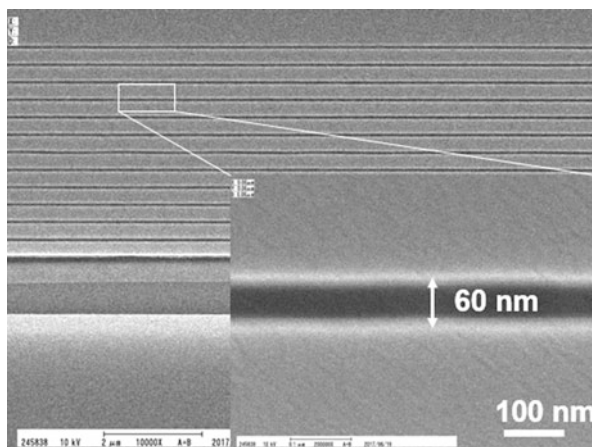


Fig. 9 Fabrication process of a fine pattern by using EBL

Fig. 10 Observed fine patterns



17.5.3 Three-Dimensional Variable Acceleration Voltage EBL

Next, the fabrication of three-dimensional patterns by variable acceleration voltage EBL is considered. In this case, a siloxane is used as the EB resist. This is an inorganic glass-like material, and consequently has high mechanical toughness, making it suitable for use in NIL molds. Once a siloxane resist has been developed,

the 3D pattern fabricated in the EB resist can be used directly as an NIL mold. Figure 11 shows cross-sectional views of a developed EB resist surface. The EB acceleration voltages were changed to 1, 2, 3, 4, and 5 kV, and the EB doses were set to $300 \mu\text{C}/\text{cm}^2$ for 1–4 kV and to $400 \mu\text{C}/\text{cm}^2$ for 5 kV. The developer was a buffered solution containing hydrofluoric acid, which permits siloxanes to be used as positive-type EB resists. The SEM micrograph clearly shows changes in depth, while the linewidths are less than 100 nm. In the case of the variable EB dose method, the linewidth increased with increasing EB dose. Therefore, the developed depth can be controlled by the variable acceleration voltage method, whereas the linewidth can be controlled by changing the EB dose.

Next, ultraviolet (UV) NIL is carried out by using the developed EB resist surface and a UV-curable acrylate resin at a pressure of 1.5 MPa for 60 s. The resulting UV-NIL pattern is shown in Fig. 12. The SEM micrograph shows that patterns with a linewidth of 100 nm line were transferred. In addition, the transferred height varied with the acceleration voltage. Therefore, EBL can be used to fabricate 3D molds, and the resulting patterns can be rapidly replicated by means of NIL.

Up to now, EBL for flat surfaces has been discussed exclusively. EBL for curved surfaces is challenging but is expected to have high value-added applications. For example, EBL for lens surfaces can be used to produce moth-eye structures capable of suppressing light reflection. Furthermore, tiny globes have been fabricated by EBL on polystyrene spheres. In this case, the spheres were coated with EB resist by dipping them in the liquid resist. After prebaking the resist, EBL was carried out over the entire surface of the sphere. Another powerful application of EBL is in the manufacture of roll molds for use in roll-to-roll (RTR) NIL techniques with fine patterns. Section 6 describes the use of EBL in the manufacture of roll molds.

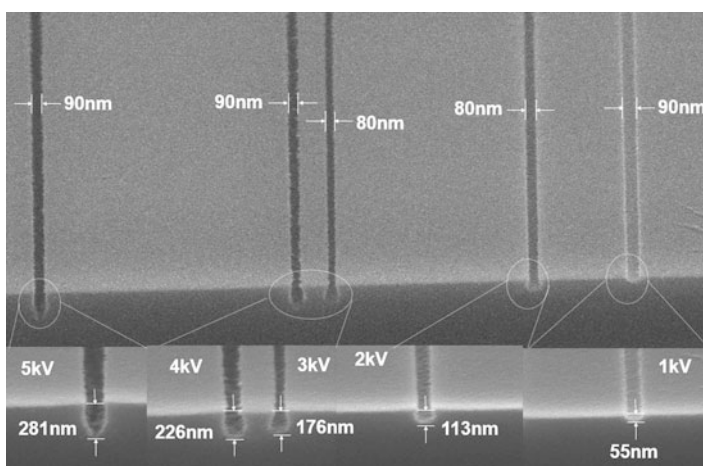


Fig. 11 Cross-sectional view of the developed EB resist surface

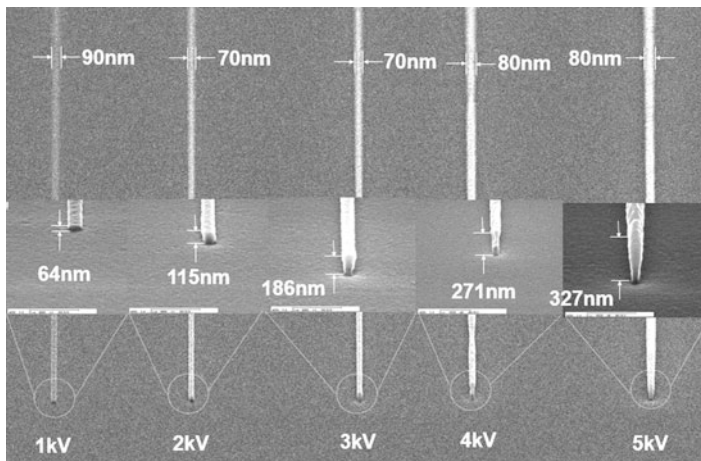


Fig. 12 Cross-sectional view of UV-NIL patterns

17.6 Electron-Beam Lithography for Roll-Shaped Surfaces

Roll-to-roll UV-NIL (RTR-UVNIL), which uses a roll mold, has great potential to improve manufacturing throughput because it is capable of transferring a nano-pattern continuously at a very high speed (e.g., 18 m/min) (Taniguchi et al. 2012). In addition, the force required to release the substrate from the mold in RTR-UVNIL is smaller than that in planar NIL, because the roll mold only makes a linear contact with the substrate (Moro et al. 2014). Large-scale planar NIL processes require high pressures with heavy machinery; consequently, it is more effective to transfer patterns onto a large area by RTR-UVNIL. However, there are difficulties in fabricating roll molds. A roll mold for RTR-UVNIL is typically prepared by attaching several individual planar replica molds onto a roll substrate. The resulting roll mold contains seams, which produce a decrease in product yield. A seamless roll mold can be obtained by mechanical cutting or laser cutting, although it is difficult to achieve sub-100 nm resolutions in this case. Self-organized structures, such as those produced by aluminum anodic oxidation, have no seams, and the pattern sizes fabricated by these techniques are very fine. However, it is difficult to produce pattern shapes to a required design by this method. Therefore, there is a need for a fabrication method that can produce seamless roll molds of sub-100 nm resolution with intricate designs.

Figure 13 shows the process of EB direct writing with a rotating roll mold (Taniguchi and Aratani 2009). In this case a cylindrical aluminum substrate of diameter 27.9 mm was used. ZEP520A (Zeon Corp., Tokyo) was used as an EB resist and was developed by using the appropriate chemical (ZED-N-50). First, ZEP520A was diluted to 50% with ZEP-A to reduce its viscosity. Then, the roll substrate was inserted into the diluted ZEP520A resist at a speed of 3 mm/s, kept in

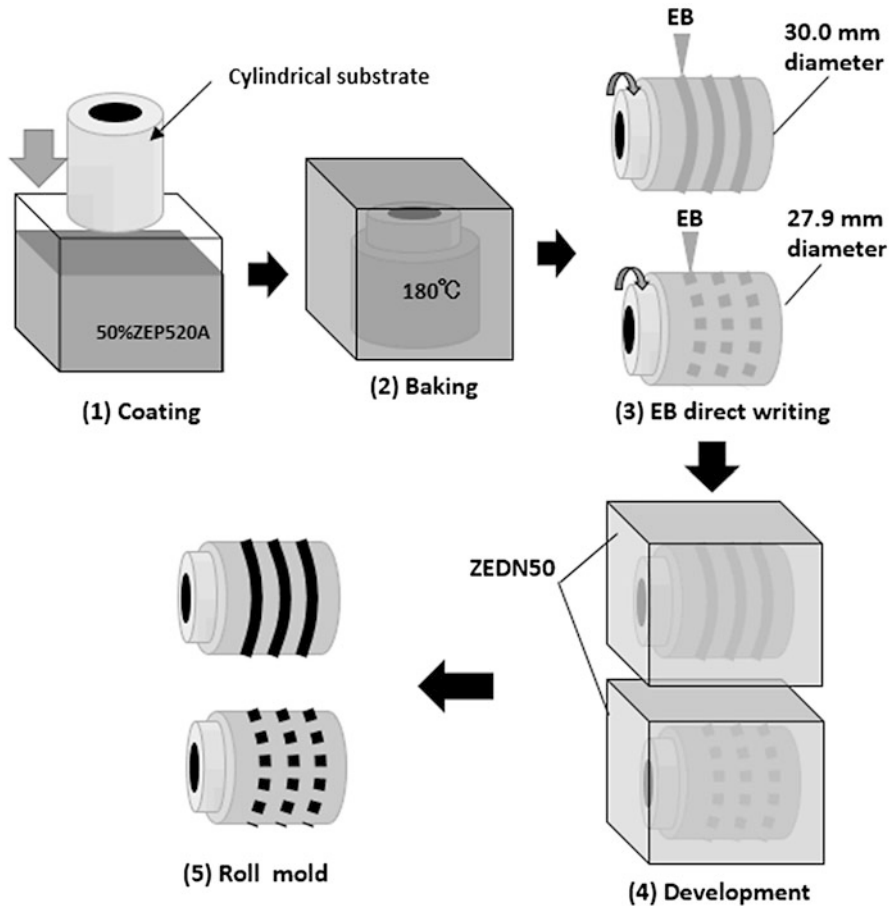


Fig. 13 Fabrication process for a roll mold

the solution for 5 s and then pulled out at a speed of 0.2 mm/s (Fig. 13(1)). The sample was then baked in air at 180 °C for 20 min (Fig. 13(2)). The thickness of resulting EB resist coating was 100 nm. The resist-coated substrate was then mounted in a scanning electron microscope customized to permit direct EB writing (Fig. 13(3)) by replacing the sample stage with a jig for roll mold EBL. This consists of an in-house-manufactured system comprising a rotating shaft and a vacuum seal containing a magnetic fluid. Rotation generated in the ambient atmosphere is passed to the vacuum EB-exposed area through the magnetic fluid seal. This EB writing system can switch the beam on or off (chopping) by means of a blanking signal generated by a personal computer while the roll mold is rotated, resulting in the fabrication of a pattern of dots.

The size of each dot is controlled by changing the number of chopping signals input over one rotation of the roll. In a typical study, the number of chopping signals

was varied from 520,000 to 2,080,000 per rotation. (Here, the minimum size of a dot was $27.9 \text{ mm} \times \pi/2,080,000 = 42.1 \text{ nm}$.) The frequency of the EB blanking signal and the speed of rotation were adjusted to obtain the same EB dose with different numbers of signals. After EB writing, the roll substrate was developed in ZED-N-50 and rinsed in propan-2-ol (IPA) (Fig. 13(4)). Because ZEP520A is a positive-type EB resist, the EB-exposed area was removed by development.

By using a similar approach, a line-and-space pattern was also generated. In this case, the EB dose was controlled by changing the rotation speed while the EB remained on. The required EB dose can be calculated by using the following expression:

$$\text{EB dose} = (\text{EB current} \times \text{unit drawing time}) / (\text{beam diameter} \times \text{unit drawing length}). \quad (1)$$

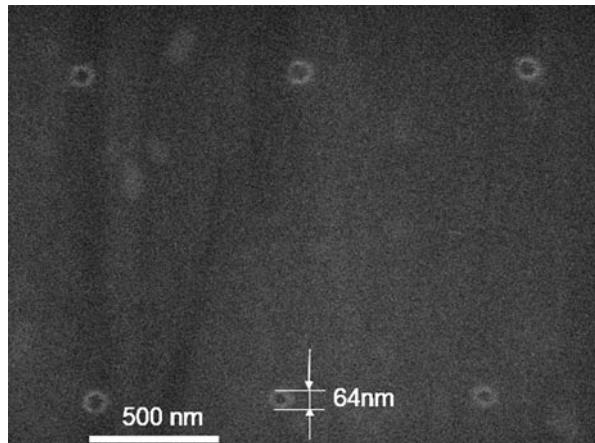
The EB parameters were as follows: acceleration voltage, 30 kV; EB dose, $1371 \mu\text{C}/\text{cm}^2$ per dot design of 42.1 nm; and EB current, 20 pA. The beam diameter was approximately 10 nm, and the vacuum pressure during EB writing was less than 5.0×10^{-4} Pa. Figure 14 shows an SEM micrograph of the resulting fine dot pattern. The finest diameter was 64 nm. However, this dot pattern did not appear across the entire circumference of the roll substrate because an eccentricity in the rotation of the rotating stage or of the roll caused the EB to defocus. Therefore, an additional autofocus system is required if finer patterns are to be fabricated on a roll mold.

Next, the finest line-and-space pattern was delineated by using a 30 kV EB. In this case, a cylindrical aluminum substrate of diameter 30 mm was used under the following conditions: acceleration voltage, 30 kV; EB current, 10 pA; dose, $120 \mu\text{C}/\text{cm}^2$; and rotation speed, 1.2 rpm.

Figure 15 shows the resulting finest line-and-space pattern at 90° intervals.

The figure shows that 60 nm line-and-space patterns were successfully fabricated across the entire circumference of the roll mold, demonstrating that such pattern can

Fig. 14 SEM image of finest dot pattern at 30 kV



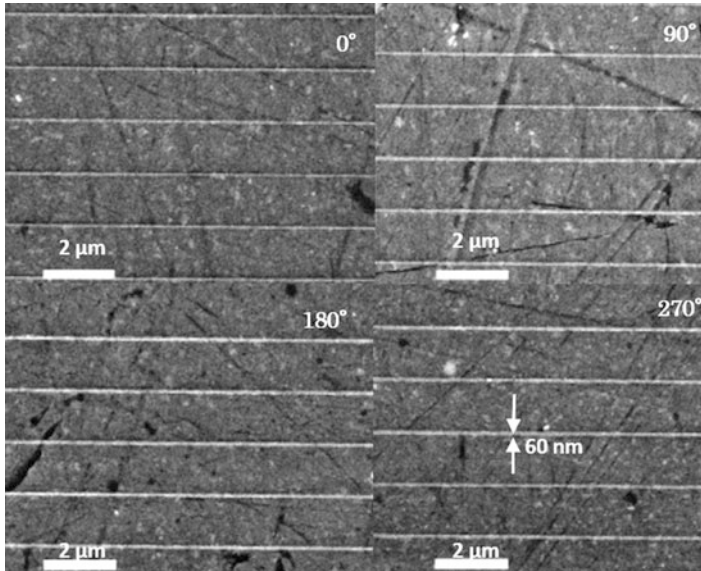


Fig. 15 SEM image of line-and-space patterns at 90° intervals

be fabricated on a roll substrate by using a single point EB. This type of line-and-space pattern can be used to fabricate diffraction gratings or bases of wire grid polarizers, usually by means of RTR-NIL technology.

17.7 Summary and Outlook

EB machining is widely used in industry and in laboratory-level studies. In the field of nanofabrication, EB lithography is a powerful tool for writing EB resists. The EB resist is a sacrificial layer that has various applications. Recently advances in EBL permit the manufacture of 3D resist patterns or patterns on curved surfaces that can be used as NIL molds. Once such a mold is fabricated, transfer is very rapid, making EBL a key technology for nanopatterning in mass production. Although this chapter concentrates on point-beam technologies, novel alternative technologies are required to improve throughput. One such novel technology, involving writing with a system of multiple EBs system, is being studied, and, although this technology can improve throughput, the problem of achieving an adequate resolution remains.

References

ALLRESIST (2017) allresist_produkinfos_ar-p6200. http://www.allresist.com/wp-content/uploads/sites/2/2016/12/allresist_produkinfos_ar-p6200_englisch.pdf. Accessed 15 Feb 2018

- Andok R, Bencurova A, Vutova K et al (2016) Study of the new CSAR62 positive tone electron-beam resist at 40 keV electron energy. *J Phys Conf Ser IOP Pub* 700:012030. <https://doi.org/10.1088/1742-6596/700/1/012030>
- Chou SY, Krauss PR, Renstrom PJ (1995) Imprint of sub-25 nm vias and trenches in polymers. *Appl Phys Lett* 67:3114–3116. <https://doi.org/10.1063/1.114851>
- Chou SY, Krauss PR, Zhang W et al (1997) Sub-10 nm imprint lithography and applications. *J Vac Sci Technol B* 15:2897–2904. <https://doi.org/10.1116/1.589752>
- Cläßen A, Kuhn S, Straka J et al (1994) High voltage electron beam lithography of the resolution limits of SAL 601 negative resist. *Microelectron Eng* 17:21–24. [https://doi.org/10.1016/0167-9317\(92\)90007-E](https://doi.org/10.1016/0167-9317(92)90007-E)
- EM Resist (2015a) PMMA resist product information. <http://www.emresist.com/downloads/PMMA%20Resist-Product%20Info.pdf>. Accessed 15 Feb 2018
- EM Resist (2015b) SML resist product information. <http://www.emresist.com/downloads/SML%20Resist%20Product%20Information.pdf>. Accessed 15 Feb 2018
- Gangnaik A, Georgiev YM, McCarthy B et al (2014) Characterisation of a novel electron beam lithography resist, SML and its comparison to PMMA and ZEP resists. *Microelectron Eng* 123:126–130. <https://doi.org/10.1016/j.mee.2014.06.013>
- Grigorescu AE, Van der Krogt MC, Hagen CW et al (2007) 10 nm lines and spaces written in HSQ, using electron beam lithography. *Microelectron Eng* 84:822–824. <https://doi.org/10.1016/j.mee.2007.01.022>
- Ishii Y, Taniguchi J (2007) Fabrication of three-dimensional nanoimprint mold using inorganic resist in low accelerating voltage electron beam lithography. *Microelectron Eng* 84:912–915. <https://doi.org/10.1016/j.mee.2007.01.133>
- Lopez GG (2016) ZEP520A spin curves and dilution characterization. https://repository.upenn.edu/cgi/viewcontent.cgi?article=1032&context=scn_protocols. Accessed 15 Feb 2018
- Matsui S, Kaito T, Fujita J et al (2000) Three-dimensional nanostructure fabrication by focused-ion-beam chemical vapor deposition. *J Vac Sci Technol B* 18:3181–3184. <https://doi.org/10.1116/1.1319689>
- Moro M, Taniguchi J, Hiwasa S (2014) Fabrication of antireflection structure film by roll-to-roll ultraviolet nanoimprint lithography. *J Vac Sci Technol B* 32:06FG09-1–06FG09-9. <https://doi.org/10.1116/1.4901877>
- Namatsu H, Takahashi Y, Yamazaki K et al (1998) Three-dimensional siloxane resist for the formation of nanopatterns with minimum linewidth fluctuations. *J Vac Sci Technol B* 16:69–76. <https://doi.org/10.1116/1.589837>
- Paulsson A, Xing K, Fosshaug H et al (2005) Managing effects in CD control from PED and PEB in advanced DUV photomask manufacturing using FEP-171 resist. *Adv Resist Technol Process XXII* 5753:1119–1129. <https://doi.org/10.1117/12.599938>
- Taniguchi J, Aratani M (2009) Fabrication of a seamless roll mold by direct writing with an electron beam on a rotating cylindrical substrate. *J Vac Sci Technol B* 27:2841–2845. <https://doi.org/10.1116/1.3237141>
- Taniguchi J, Yoshikawa H, Tazaki G et al (2012) High-density pattern transfer via roll-to-roll ultraviolet nanoimprint lithography using replica mold. *J Vac Sci Technol B* 30:06FB07-1-06FB07-5. <https://doi.org/10.1116/1.4758922>
- Zeon (2003) ZEP520A datasheet. <http://www.nanophys.kth.se/nanophys/facilities/nfl/resists/zep520a-7-2.pdf>. Accessed 15 Feb 2018



Microfabrication by Laser Lithography Combined with Ion Etching

18

Zhiyu Zhang, Ruoqiu Wang, and Donglin Xue

Contents

18.1	Introduction	578
18.1.1	Application of Microstructures	578
18.1.2	Fabrication of Microstructures	579
18.2	Photolithography	580
18.2.1	Mask Lithography	580
18.2.2	Maskless Lithography	581
18.3	Gaussian Ion Etching	584
18.3.1	Basic Concept of Gaussian Ion Etching	584
18.3.2	Dwell-Time Algorithm	586
18.3.3	Etching Uniformity and Etching Accuracy	588
18.4	Applications	589
18.4.1	CGH for Wave-Front Compensation	590
18.4.2	Fabrication of Four-Level Fresnel Zone Lens	592
18.4.3	Replication of the FZL to Polyimide Membrane	598
18.5	Summary and Outlook	601
	References	602

Abstract

Microstructures can enhance the functionality of surfaces in many ways. For the field of optics, the diffraction of light becomes dominant when the size of microstructures is in the order of the applied wavelength. Such diffraction microstructures are being used in many optical applications such as optical imaging, beam splitting, and light concentration. Recently, there are increasing demands for large-aperture diffraction optical elements. Due to strict requirements on both dimensional accuracy and surface roughness, fabrication of such diffraction

Z. Zhang (✉) · R. Wang · D. Xue
Changchun Institute of Optics, Fine Mechanics and Physics, Chinese Academy of Sciences,
Changchun, Jilin, China
e-mail: zhangzhiyu@ciomp.ac.cn

elements has many unique challenges. In responding to these needs, a high-efficiency hybrid technology including laser-scanning lithography combined with argon ion etching was developed. Moreover, the replication process of microstructures from glass substrate to ultrathin polymer membrane was also developed to lower the manufacturing cost for meeting the needs of mass production. The developed technologies could be utilized to fabricate large-aperture diffractive optical elements in a variety of future applications.

Keywords

Laser lithography · Ion etching · Diffractive optical elements · Fresnel zone lens · Micro and nano Fabrication

18.1 Introduction

18.1.1 Application of Microstructures

In recent years, microstructured surface is finding an increasing number of diverse applications such as microfluidics, bionics, and optics (Meier 2015; Chavoshi and Luo 2015; Chang et al. 2016). For example, in the microchannels of a typical microfluidic chip, a variety of microstructured components such as micropumps, microvalves, micromixers, and microactuators have been designed to successfully achieve the functions such as flow driving, flow mixing, cell collection, and cell sorting. Microstructured surfaces can also enhance the functionality of surfaces in many ways such as self-cleaning, hydrophobicity, and hydrophilicity. Interestingly, numerous natural surfaces contain microstructures that enable the ability to repel water in a certain direction. Recently, a unique multiscale structure involving duck-billed microcavities with arch-shaped open sharp edges and gradient wedge corners was discovered on the peristome surface of *Nepenthes alata* (Chen et al. 2016, 2017). This unique microstructure has gradually attracted worldwide attention owing to its 2D unidirectional liquid spreading on the surface with fast speed and long-distance properties, which has potential applications in various fields, such as fog harvesting, filtration, and microfluidic devices.

For the field of optical engineering, microstructures are even more important, since diffraction phenomenon becomes dominant when the typical feature size of microstructures is in the order of the applied wavelength or below. Such microstructured optical elements could be used in many optical applications. For instance, a diffraction grating is a typical optical component with a periodic microstructure, which splits and diffracts light into several beams traveling in different directions. The directions of these beams depend on the spacing of the grating and the wavelength of light. For another instance, a Fresnel zone lens (FZL) can be considered as a circular grating with variable periodicity. Unlike lenses or curved mirrors, the FZL is used to focus light by diffraction other than refraction or reflection (Cao and Jahns 2004). The FZL also features line widths that gradually decrease from center zones to outer zones, with the outermost zone possessing the narrowest line width. The FZL is frequently used in a variety of optical systems, such as soft X-ray

microscopy (Chao et al. 2005), microwave antennas (Wiltse 2005), beam shaping (Streibl 1989), and even next-generation giant space telescopes (Atcheson et al. 2014).

As a summary, the general characteristics of the abovementioned microstructures are as follows: (1) transverse size in micrometer level, from several μm up to hundreds of μm ; (2) tight tolerances, typically better than $1\ \mu\text{m}$; (3) smooth surface finish, in general surface roughness (Ra) in nanometer order; and (4) a variety of substrate materials such as metal, glass, ceramics, polymer, etc.

18.1.2 Fabrication of Microstructures

Several technologies including diamond turning, ultrafast laser ablation, and laser lithography have been adopted to fabricate optical microstructures. Ultraprecision diamond turning has proven to be suitable and effective to achieve excellent precision in fabrication of high-performance optical microstructures (Yan et al. 2005, 2010, 2012). It enables the machining of grooves with a width ranging from few to several hundred micrometers and a depth ranging from a few hundred nanometers to several micrometers. For example, fabrication of large-area diffraction gratings has been achieved on a soft aluminum substrate with a diamond tool. The groove densities could be up to 10,000 lines/mm with the ultraprecision grating ruling machine. On the other hand, fabrication of the Fresnel zone lens (FZL) by diamond turning on ductile metals such as oxygen-free copper, electroless-plated nickel, and single-crystal germanium has also been extensively reported. The fabricated microstructures are mainly continuous in the feeding direction. Even more complicated microstructures could be realized by using fast tool servo or slow slide servo, which enables a dynamic tool adjustment. However, the low material removal efficiency for diamond turning of large-area microstructured surface becomes a problem.

Ultrafast laser ablation with instantaneous high-density energy has shown to be an efficient and environmentally friendly method for the fabrication of microstructures (Phillips et al. 2015; Okamuro et al. 2010). For example, femtosecond laser direct writing was used to fabricate microstructures such as micro-dimple arrays and gratings on a variety of substrates, e.g., optical glass, sapphire, polymer, and even organic resist layer. However, the irradiated surface always has unqualified roughness for direct use in optical application. In addition, laser ablation treatment always changes the crystal structure of material and induces thick amorphous layer, which will alter the physical/optical properties of the irradiated surface. These problems are harmful to the excellent performance, hindering the further promotion of this technique for applications in optical application.

Different from above, many researchers have demonstrated the effective fabrication of high-quality diffraction microstructures by virtue of photolithography (Taghizadeh et al. 1997; Guo et al. 2018). The state-of-the-art fabrication process of the diffraction microstructures contains two steps: the generation of diffraction microstructures on a photoresist via photolithography and its transfer to a substrate by wet or dry chemical etching. The former step controls the horizontal width of the diffraction microstructures, while the latter one determines its vertical depth. It is

proved that the generation of large-area diffraction microstructures on photoresist layer could be realized using a high-precision photolithography technique. However, owing to the lack of etching technology during microstructure transfer step, it is difficult to simultaneously achieve both an accurate etching depth and a high uniformity of etching on a large substrate.

The variations in etching depth significantly decrease the diffraction efficiency of the fabricated diffraction microstructures, while nonuniform etching would cause fluctuations of the diffraction efficiency across the entire substrate surface (Zhang et al. 2017). As an example, the diffraction efficiency of a four-level FZL would theoretically decrease from 81.16% to 78.15% if the etching depth exhibits a 10% deviation from the designed value during each overlay photolithography process (Xu et al. 1998).

Reactive-ion etching (RIE) is frequently reported as a typical technology used for dry etching of fused silica (Kowalik et al. 2002). The RIE process can provide high-quality quasi-isotropic etching, which makes it possible to vary the etching directionality between isotropic and anisotropic using fluorine-based gas (CHF_3 or CF_4) and O_2 gases at various flow rates. During etching, F radicals provide the chemical etching of SiO_2 by formation of volatile SiF_4 (Ying et al. 2009). Generally, the etching rate ratio of photoresist and the SiO_2 glass could be matched by adjusting their own gas flow rates of the mixed gas of CHF_3 and O_2 (Steingoetter et al. 2003).

The depth uniformity of etched surface is one of the most important evaluating indicators for a large substrate, which is usually determined by the related ion energy distribution. To our best knowledge, the depth uniformity achieved by a commercial RIE equipment for a diameter up to 200 mm typically does not decrease below 5%. According to the current manufacturing capacity, it is very difficult to fabricate a large-area electrode plate with acceptable energy distribution. To improve depth uniformity during large-area etching, a scanning linear ion source has been reported. However, the modified linear ion etching process still exhibited variable energy densities, causing the decrease in the etching uniformity (Nakano et al. 2012).

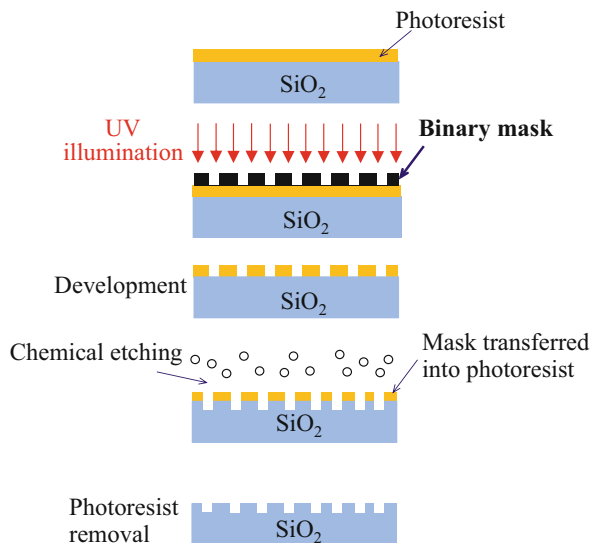
In this chapter, some new achievements in photolithography and ion etching were summarized. A strip-scanning laser system was used to rapidly expose the large-area diffraction microstructures on photoresist layer with high precision. An argon (Ar) ion beam characterized by a Gaussian energy distribution was developed for large-area physical etching. Both depth uniformity and depth accuracy were achieved simultaneously by optimizing the etching time at each etching coordinate. The uniqueness of our work lies in the combination of laser-scanning lithography and the Ar ion physical etching, which could be applied to the fabrication of large-aperture (up to 1500 mm) diffractive optics.

18.2 Photolithography

18.2.1 Mask Lithography

Traditionally, the fabrication process for producing diffractive optics in glass is mask photolithography followed by wet chemical etching, as shown in Fig. 1. In this process, the substrate (usually fused silica) is coated with a thin layer of

Fig. 1 Schematic of the conventional photolithographic process



light-sensitive photoresist. Then, a 1:1 replication process is applied to duplicate the patterns from a binary mask to the photoresist layer by proximity exposure. After development, the fused silica substrate with patterned photoresist layer was immersed into a buffered hydrofluoric acid solution (HF). Finally, the patterns on photoresist layer could be transferred to the unprotected fused silica substrate due to the chemical reaction between SiO_2 and HF. Moreover, multi-level structures could be realized by overlay photolithography using two or more masks.

Although all the conventional mask photolithography combined with wet chemical etching has demonstrated feasibility, it is not desirable to realize high accuracy and complex diffraction microstructures on fused silica substrate. The main drawbacks of mask photolithography are that it is not effective for non-planar surfaces due to the substrate curvature, and it induces the precision degradation during pattern replication. Moreover, it is very hard to obtain uniform depth for the subsequent wet chemical etching, mainly due to the characteristics of isotropic corrosion of wet etching, and also the significant undercutting induced bowl-like crater in the obtained microstructures as shown in Fig. 2.

18.2.2 Maskless Lithography

In this chapter, we modify the above process in a number of ways to eliminate a variety of fabrication errors. The process for fabrication of microstructures by maskless laser-scanning lithography is shown in Fig. 3, which consists of the following main steps: photoresist coating, laser exposure, development, ion etching, and photoresist stripping. In this process, the substrate is firstly coated with positive photoresist by spin coating to achieve a uniform thin layer, usually with a uniformity

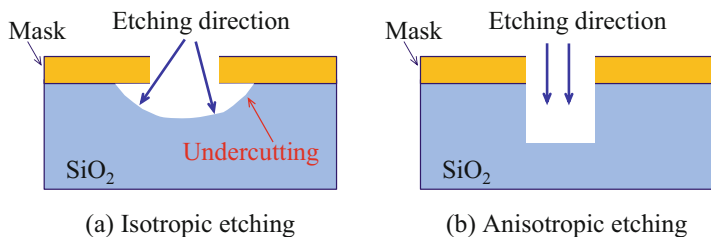
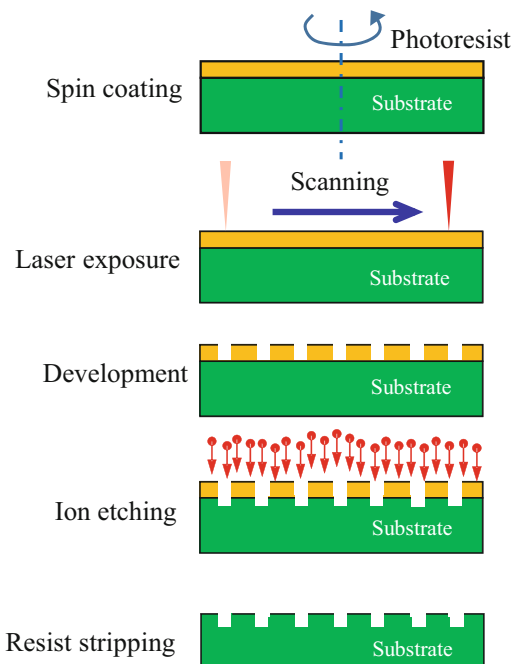


Fig. 2 Schematic of (a) undercutting in isotropic etching and (b) anisotropic etching

Fig. 3 Schematic of maskless lithography combined with ion etching



of within 5–10 nm. Then, the photoresist is exposed using a focused scanning laser beam that is moved by means of a motorized stage. The exposure to laser light causes a chemical change that allows the exposed portion to be rapidly dissolved by an alkaline solution called as developer. After development, the microstructures appear on the photoresist layer. Subsequently, the anisotropic ion etching is used to remove the uppermost layer of the substrate in the areas that are not protected by photoresist. After etching, the photoresist is no longer needed and removed from the substrate. Finally, the designed microstructures on substrate could be precisely achieved.

In the present work, a DWL4000 laser-scanning lithography system as shown in Fig. 4a (produced by Heidelberg Instruments, Germany) was used to generate

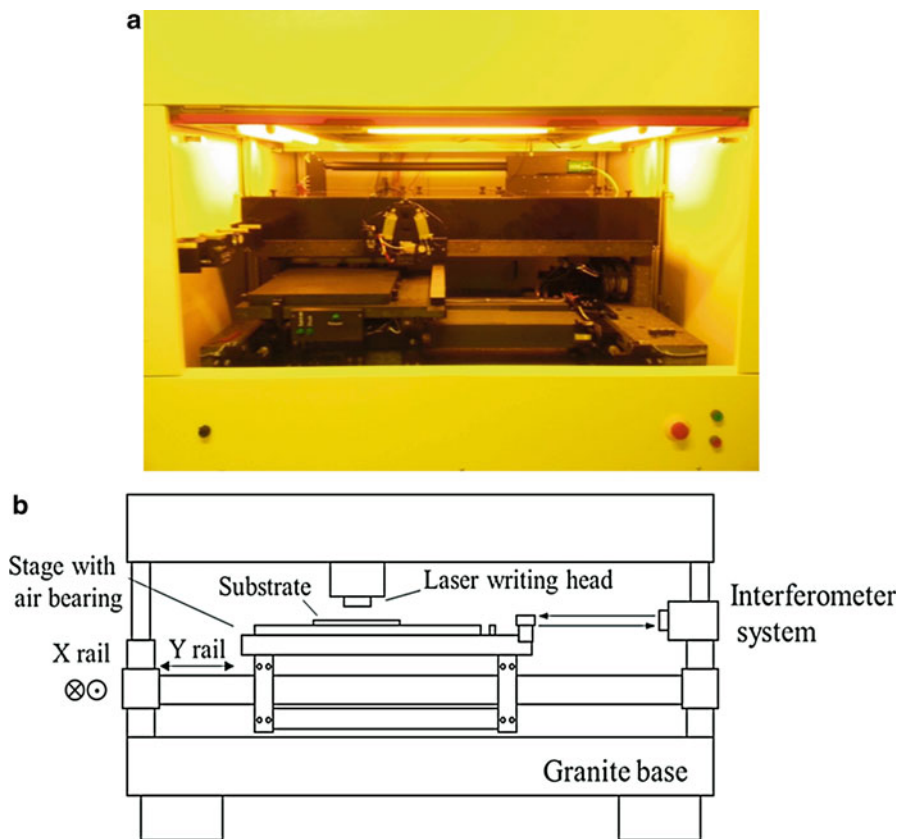


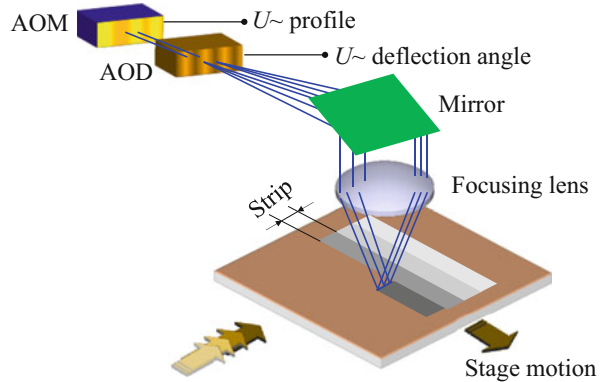
Fig. 4 (a) Photo and (b) schematic diagram of DWL4000 laser lithography system

the diffraction microstructures. The DWL4000 is a large-area, high-resolution laser writing system developed to expose the substrate coated with a photoresist coating layer. The lithography system can expose a maximum substrate of up to $400 \text{ mm} \times 400 \text{ mm}$ with positioning precision of 10 nm. Figure 4b shows a schematic illustration of the structure system of the DWL4000 laser lithography machine.

The optical system of DWL4000 uses a continuous-wave laser with 405 nm wavelength. This optical system has a high-NA objective lens module, which allows the minimum structure size to be smaller than 600 nm, and the size of Gaussian laser spot was $0.7 \mu\text{m}$ in full width.

Figure 5 shows the laser-scanning exposure method called strip scanning, which significantly enhances the exposure speed using an acousto-optic deflector (AOD) technology, thus generating a high-frequency laser scan with a resulting sweep rate of more than 55 kHz. The scanning angle is imaged into the back focal plane of the write lens resulting in a telecentric scanning arrangement, so that the laser beam is

Fig. 5 The strip scanning method using an acousto-optic deflector (AOD)



always perpendicular to the substrate. As a result, a highest writing speed of $1120 \text{ mm}^2/\text{min}$ could be accomplished. The design file which was acquired from the self-developed software was used to drive the DWL4000 system to fabricate the microstructures.

18.3 Gaussian Ion Etching

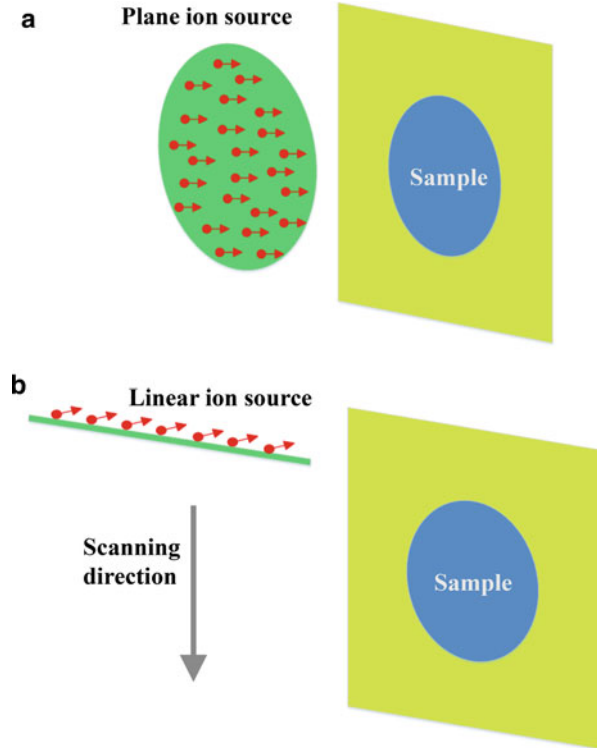
18.3.1 Basic Concept of Gaussian Ion Etching

Since the 1970s, ion beam technology has been successfully developed in the corrective polishing of reflecting mirrors. The inert gas ions (mostly Ar ions) with high energy and spatial distribution interact with the atoms on workpiece surface to realize the strictly controlled material removal, by which atomic-scale removal could be theoretically achieved (Allen and Romig 1990). The ion beam source is one of the main components in ion beam equipment which is controlled by its motion system to realize required dwell time distributions over the etching surface. In addition, it was called a point source ion beam due to its Gaussian-shape energy distribution.

In order to elucidate the working mechanism of the point source etching process, it can be compared with that of a plane etching technique. Figure 6a shows a typical plane source etching system, which is typically used in the RIE process. Because the utilized ion source is motionless during etching, its size determines the maximum substrate size, while the energy distribution of the plane ion source defines the etching precision of the treated samples. Therefore, the working area of a commercially available RIE system is typically not larger than 8 in. (around 200 mm) as it is difficult to fabricate a larger plane source with desired energy uniformity.

To precisely fabricate diffraction microstructures on a large-area substrate, a scanning etching method as shown in Fig. 6b that utilizes a linear ion source has been developed. One limitation of the linear ion source technique is that the aperture

Fig. 6 Schematics of the etching techniques using (a) a stationary plane source and (b) a scanning linear source



size of the etched substrate is restricted by the source length. Furthermore, the ion intensity of a large-sized linear source exhibits unavoidable fluctuations in different regions (Guo et al. 2018), which cause etching nonuniformity in the substrate surface. To achieve high-accuracy etching using the linear source method, the calibration of the resulting ion intensity distribution as well as the use of a complicated endpoint detection system is required (Zhang et al. 2009), which significantly reduces the etching efficiency.

In the present work, a novel etching technology using a scanning point ion source was developed to overcome the abovementioned limitations. As shown in Fig. 7a, the point ion source has a Gaussian-shape energy distribution. By scanning the point source along a raster path as shown in Fig. 7b, the size of the etched substrate is not limited by the size of the ion source. Thus large-area etching could be easily achieved. Most importantly, the etching time T_i at a specified etching point along the scanning path is one of the variables in the optimization algorithm and could be utilized for improving the etching uniformity.

In addition, because the point source ion beam technique was originally used for the corrective polishing of aspherical and freeform surfaces (Chkhalo et al. 2016), the etching of large-aperture diffraction microstructures via this method enables simultaneous etching and corrective polishing of the treated substrate.

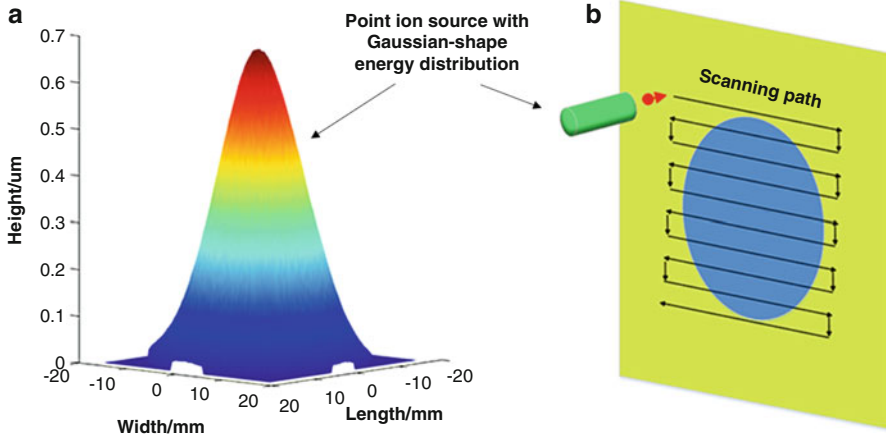


Fig. 7 Schematic of the etching procedure using a point source ion beam, which is scanned along the raster path

18.3.2 Dwell-Time Algorithm

Due to a stable etching rate which is better than traditional wet etching, ion beam etching plays an important role in optical fabrication. According to the sputtering theory, the peak value of the removal rate is proportional to the peak value of the scanning result by Faraday cup. The removal rate for the same material could be written as

$$R = J(x, y) * K \quad (1)$$

where R is the velocity of the material removal rate, K is a coefficient that depends on the material which is a constant for the same material, and J describes the energy distribution of the ion beam. The removal function of ion beam is in Gaussian shape, which could be expressed by the maximum rate and the full-wave half maximum.

As for the computer-controlled optical surfacing (CCOS) process, according to the Princeton hypothesis (Pereston 1927), the relationship between the material removal volume $d(x, y)$ and the polishing time t at the coordinate point (x, y) could be expressed by the linear equation

$$d(x, y) = r(x, y) * t \quad (2)$$

where $d(x, y)$ is the removal function during the polishing process. Because the value of the Gaussian removal function calculated at an arbitrary point also contributes to the material removal at the neighboring points, the entire substrate aperture can be uniformly polished by performing a reasonable scanning along a specified path. The utilized material removal model can be expressed via the following convolution equation:

$$D(x, y) = R(x, y) ** T(x, y) \quad (3)$$

where $D(x, y)$ is the distribution of the material removal function across the entire aperture, $R(x, y)$ is the actual removal function measured by a ZYGO interferometer, and the mathematical operator $**$ represents the convolution operation. When these two parameters are determined, the accurate characterization of material removal process depends on the optimization of $T(x, y)$, which corresponds to the distribution of the dwell time.

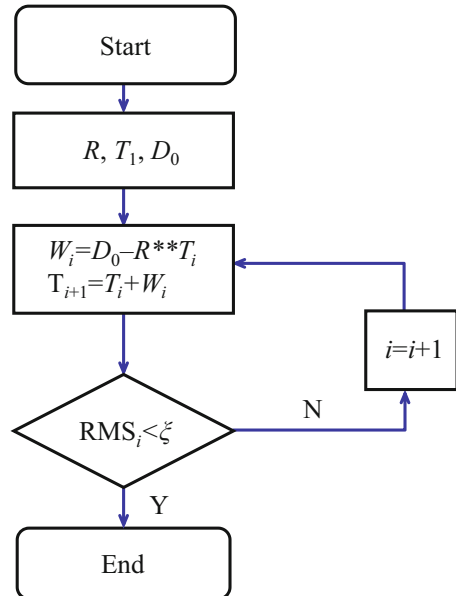
In this work, the abovementioned material removal model was used for characterizing the etching process of diffraction structures for the first time. During etching, the generation of etched microstructures is equivalent to the uniform removal of plane surfaces during the CCOS process. After the designed depth of the etched FZL is determined, the etching time at each point can be calculated using a dwell-time algorithm (Wang et al. 2014). In this algorithm, the etching depth error W_i and distribution of dwell time T_i during the optimization step i can be expressed as

$$W_i = D_0 - R ** T_i$$

$$T_{i+1} = T_i + W_i \quad (4)$$

where D_0 is the theoretical value of the material removal function. The iteration finishes when the root mean square (RMS) of the etching depth error becomes sufficiently small. In the present work, the acceptable value of RMS was defined as ξ (Fig. 8).

Fig. 8 Diagram of the optimization algorithm for the dwell time



18.3.3 Etching Uniformity and Etching Accuracy

As illustrated in Fig. 9, the point source with a Gaussian-shape energy distribution was installed on the utilized instrument (IBF1500, manufactured by Neue Technologien, Germany) for scanning etching of the area with dimensions of $1500\text{ mm} \times 1500\text{ mm}$. The movement of the point source ion beam was precisely controlled by a three-axis motor system. Etching performances for the point source ion system depend strongly on many processing parameters, such as gas pressure, flow rates, and RF power. During etching, the flow rate of the etching gas was set to 3 sccm, the RF power was set to 100 W, and the working distance was set to 40 mm. Under the above conditions, the corresponding etching rate was $0.1814\text{ mm}^3/\text{min}$.

To investigate the performances of the proposed etching method, eight groups of patterns with increasing depths ranging from 125 nm to 1000 nm were etched into fused silica. Moreover, the line widths of each group also varied from $2\text{ }\mu\text{m}$ to $100\text{ }\mu\text{m}$. The relationship between the etching uniformity and the increasing etching depths for different line widths is presented in Fig. 10, while the etching depths measured at different line widths are given in Fig. 11.

As shown in Fig. 10, when etching depth is lower than 800 nm, the nonuniformity of etching depth is smaller than 3 nm. When etching depth is higher than 800 nm, the nonuniformity gradually increases from 3 nm to 5 nm with the increasing etching depth. Therefore, the proposed etching method can significantly improve the etching uniformity, especially when the etching depth is lower than 800 nm.

Based on the above investigation, it can be concluded that not only excellent depth uniformity but also very accurate depths can be achieved using the Gaussian-shape Ar ion etching. Although there are many advantages of the developed etching method, there is also a need to pay special attention to the phenomenon of line with expansion. As shown in Fig. 11, the line width values increase along with the increasing etching depths. It is also seen that the expansion values have little relationship with different line widths. The obvious expansion of line width is probably caused by the poor etching resistance of the used photoresist (AZ4562).

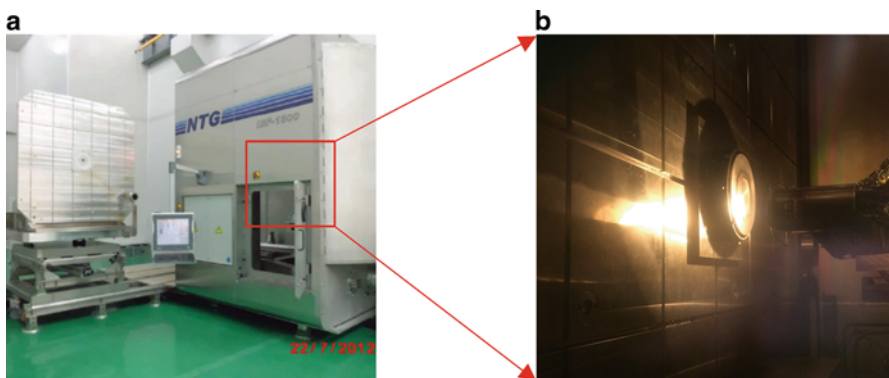


Fig. 9 (a) Ion etching machine, (b) during etching

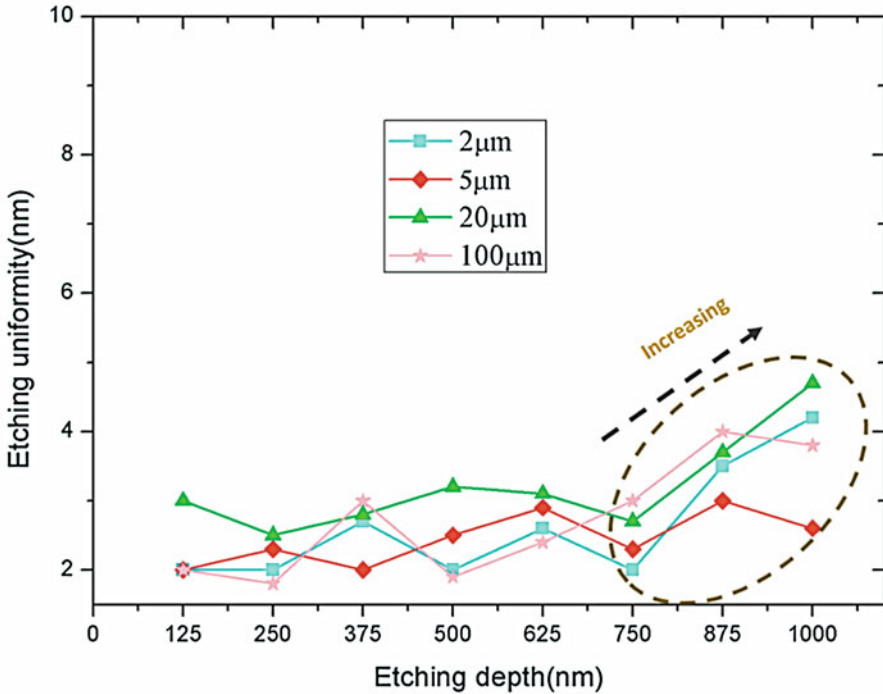


Fig. 10 Etching uniformity values observed for various line widths with different etching depths

There are two solutions for the suppression of line with expansion. One solution is to use hard photoresist (e.g., AZ6130) which has excellent corrosion resistance. The other one is to quantitatively compensate the line with expansion during exposure. The measured broadening rate for AZ4562 photoresist with a thickness of 1 μm is 0.24 $\mu\text{m}/100\text{ nm}$.

18.4 Applications

Due to the special dispersion characteristics, diffractive optical elements (DOEs) are used in numerous applications, ranging from spectroscopy to imagination, optical data storage, biomedical applications, and even laser material processing (cutting, welding, engraving). In the following section, the fabrication of two typical DOEs using the combination of laser-scanning lithography and Ar ion etching is introduced. The first one is the fabrication of computer-generated hologram (CGH) used as a wave-front compensator for the shape accuracy testing of aspherical surface. The other one is the fabrication of four-level Fresnel zone lens (FZL) on fused silica substrate for the establishment of next-generation diffraction imaging system. Moreover, the precise replication of the FZL from fused silica substrate to polyimide membrane is also demonstrated.

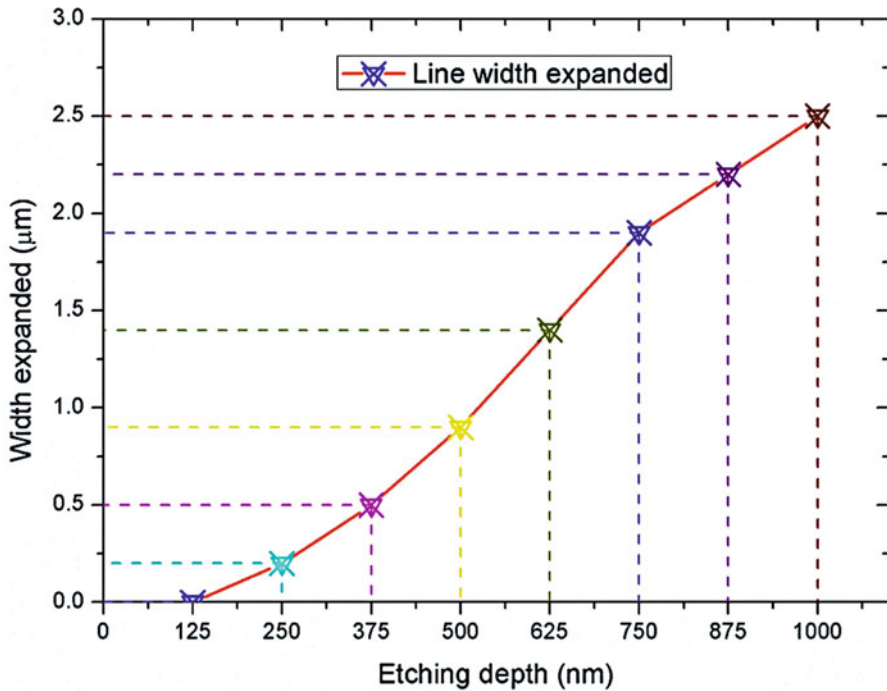


Fig. 11 Line width expansion with increasing etching depths

18.4.1 CGH for Wave-Front Compensation

18.4.1.1 Introduction of the CGH

Aspherical surfaces have been widely used in optical systems to provide improved imaging performances as well as reduced size and minimized weight. Shape accuracy of aspherical surface is one of the most important factors to affect the imaging performance. Shape error of aspherical surface could be measured by profilometer (mechanical or optical probe) or interferometers. The latter has become a standard testing method for optical surfaces. Interferometers use coherent light to measure spherical or flat surface to nanometer-order surface errors. However, interferometers cannot be used directly to measure aspherical surfaces. Interferometric null test using compensators is widely adopted in aspherical testing. Using compensated wave front, the aspheric surface and its compensator are tested just as testing a general sphere.

Computer-generated holograms (CGHs) are an effective way to compensate wave front in testing of aspheric surfaces (Zhou and Burge 2007). Figure 12 shows the schematic of testing an aspherical surface using CGH, which changes spherical wave front to aspherical. Then the light retroreflects from the test surface and goes back to the interferometer. The high-degree flexibility in generating complex wave fronts has made CGHs extremely useful while comparing with conventional null-lens compensators.

Figure 13 shows a typical CGH pattern, which looks like a wavy line fabricated onto a substrate. The dimensions of CGH pattern are designed by diffraction grating equation. In order to realize high-precision testing, the wave-front error of the CGH is required to be tiny enough to improve the degree of certainty in the test results. In addition to precision, it is necessary to have sufficient diffraction efficiency to broaden the range of use. In order to improve the diffraction efficiency, it is usually necessary to etch the CGH pattern on fused silica substrate to form a phase-type CGH.

18.4.1.2 Fabrication of the CGHs

In the present work, the CGH patterns are generated using laser-scanning lithographic techniques. After that, the CGH patterns were transferred into fused silica substrate using Ar ion etching. An amplitude-type and a phase-type CGH on the substrate with a diameter of 80 mm is shown in Fig. 14a, b, respectively. Figure 15a, b shows the micrographs of fabricated CGH pattern on the phase-type CGH. It can be seen that the profile of the groove was clearly fabricated. The minimum width of the groove is $1.8\ \mu\text{m}$ with a sidewall angle of about 70° . Results show that the duty ratio is near to 50% and the mean depth is 230 nm with a 2% depth uniformity. The diffraction efficiency is about 22.4%, measured at +1 diffraction order.

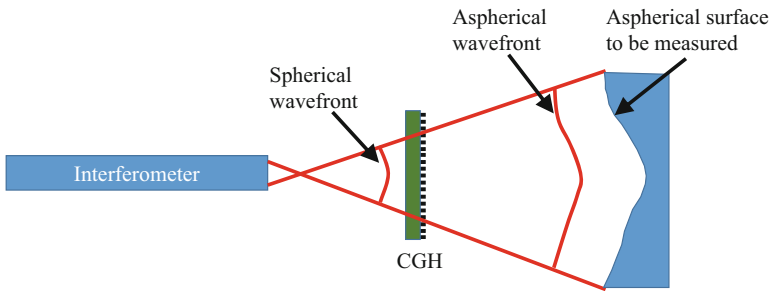


Fig. 12 Schematic for testing an aspheric surface using CGH

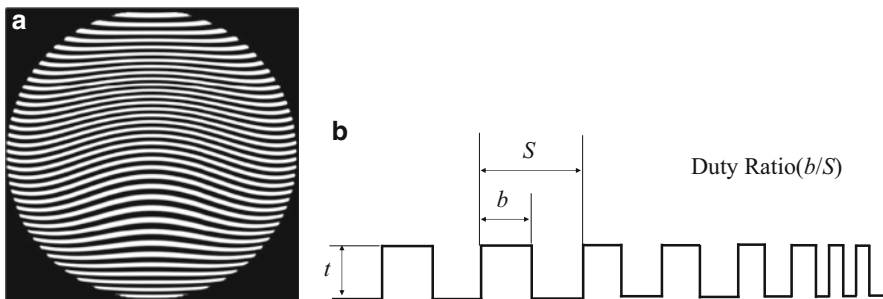


Fig. 13 A part of the designed pattern for a CGH: (a) up view, (b) side view

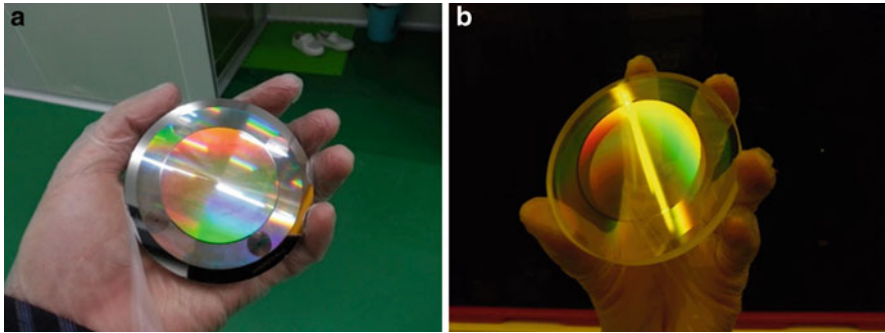


Fig. 14 Photos of (a) amplitude-type and (b) phase-type CGHs

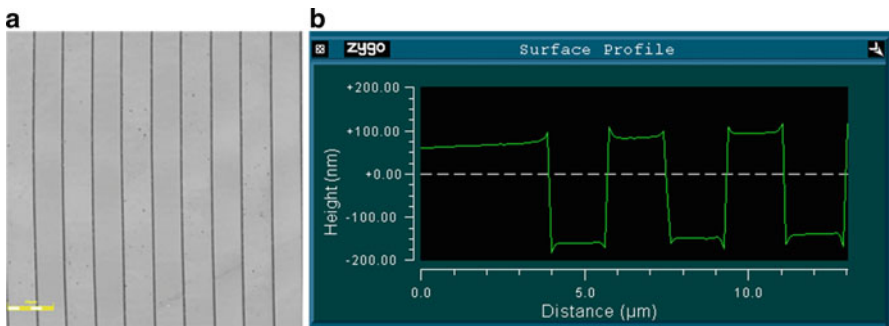


Fig. 15 Local topography of a phase-type CGH: (a) top view, (b) cross-section profile

In order to analyze the fabrication error of the CGH, a standard spherical surface having ultrahigh shape accuracy (negligible shape error) was tested using the fabricated CGH as shown in Fig. 16a. Results show that the measured shape error was 0.006λ RMS (approximate to 3.79 nm, $\lambda = 632.6$ nm) as shown in Fig. 16b, indicating that the fabrication error is tiny and the fabricated CGH could sufficiently meet the requirement of measurement. In fact, an aspherical surface was tested by using another CGH fabricated according to its aspherical parameters. Figure 17 shows a measurement result of the aspherical surface, having shape accuracy of 0.024λ RMS. It indicates that the fabricated CGH has been successfully applied in high-precision measurement of aspherical surfaces.

18.4.2 Fabrication of Four-Level Fresnel Zone Lens

18.4.2.1 Introduction of the Four-Level FZL

The FZL which is achieved by etching a set of concentric rings in an optical substrate could be used as a diffractive lens to focus light. Moreover, due to the

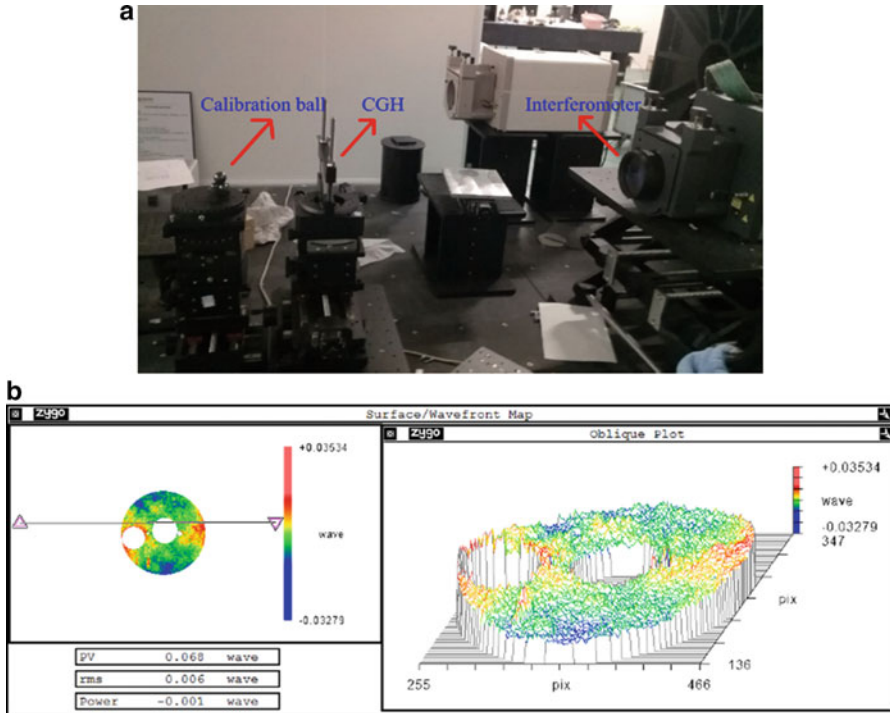


Fig. 16 (a) Setup for measurement of a standard spherical ball, (b) obtained result

advantages of lightweight, deployable, and relaxed tolerance, the extremely large FZLs fabricated on a thin polyimide membrane are expected to act as the primary lens to build the space-based telescopes (Barton et al. 2001; Wang et al. 2016).

Low diffraction efficiency is one of the most important drawbacks for FZLs in optical imaging application. It is known that the diffraction efficiency of FZLs could be improved by designing a multilevel surface to approximate a continuous phase distribution. In the present work, a four-level membrane FZL with a diameter of 320 mm was fabricated. Figure 18 shows the schematic of the central zone of the four-level FZL. Table 1 lists its parameters.

18.4.2.2 Fabrication of the Four-Level FZL

Figure 19 shows the fabrication process of the FZLs on fused silica substrate. The patterns of the first half period were directly exposed in photoresist using laser-scanning lithography as shown in Fig. 20a. After hardbake, the patterns on developed photoresist were etched into the fused silica substrate using the Ar ion etching as shown in Fig. 20b. Repeating the same process, the patterns of the second half period were etched into the fused silica substrate with double depth in

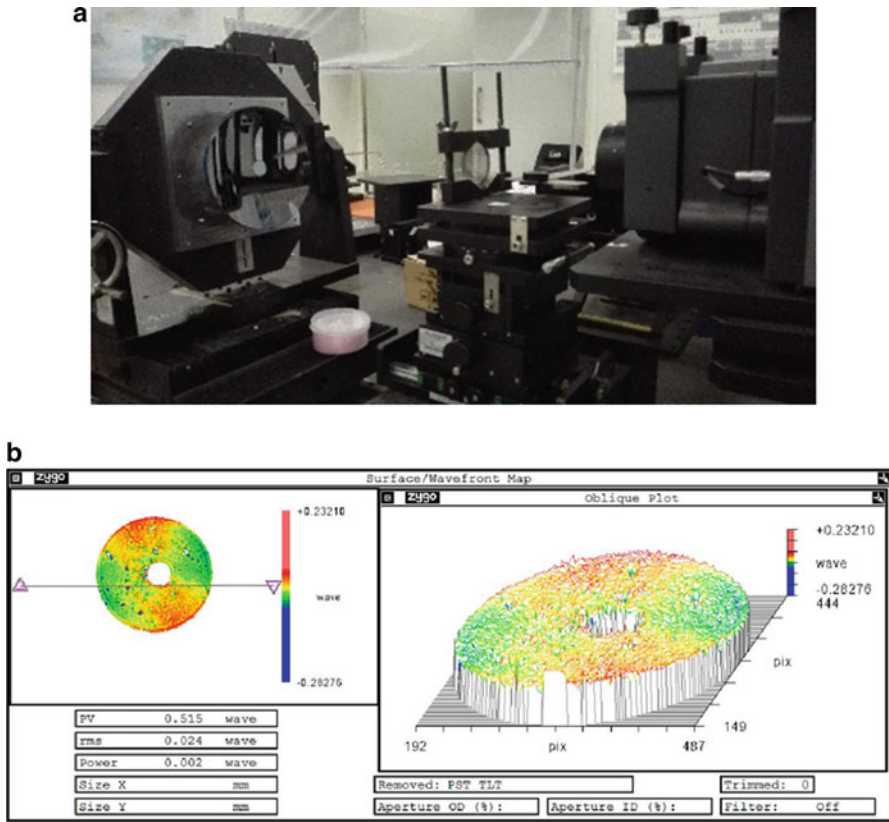


Fig. 17 (a) Setup for measurement of an aspherical surface, (b) obtained result

Fig. 18 Schematic of the central zone of the four-level FZL

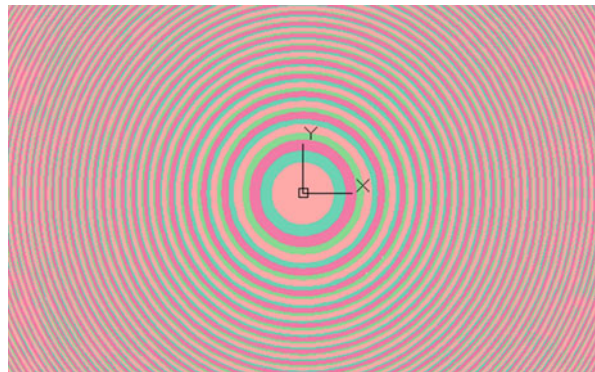
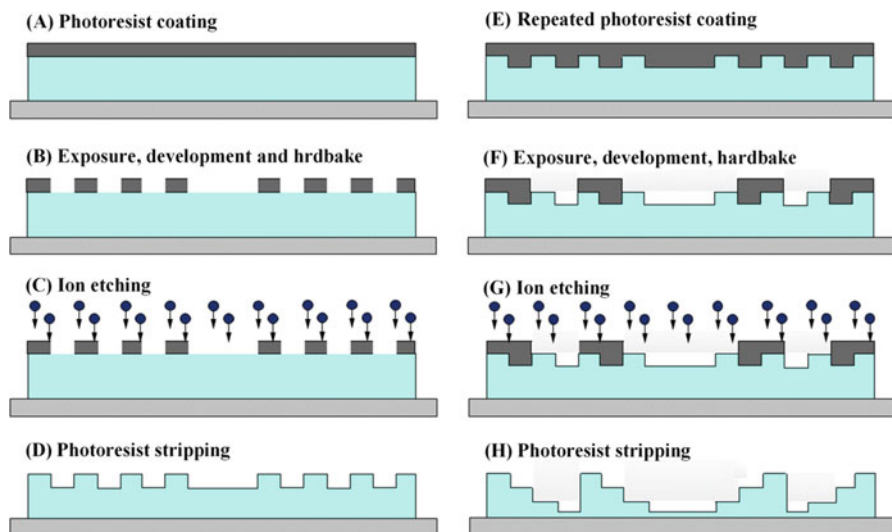
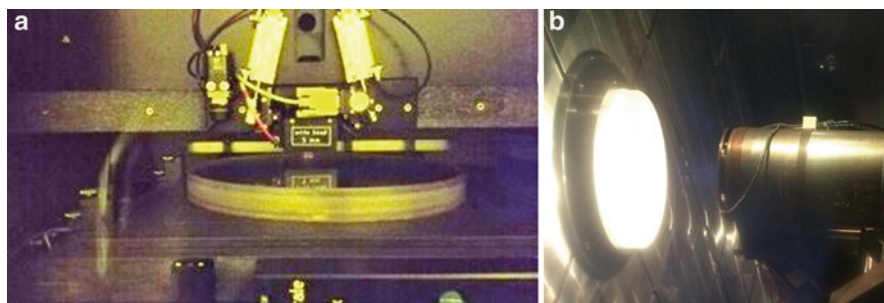


Table 1 Parameters of the four-level FZL

Items	Value
Main wavelength (nm)	632.8
Effective aperture (mm)	300
Focal length (m)	30
Band number	2372
Step number	4
Maximum line width (μm)	1276.15
Minimum ring width (μm)	31.75

**Fig. 19** Fabrication flow of a four-level FZL by overlay exposure**Fig. 20** Photos of the fused silica substrate: (a) during exposure, (b) during etching

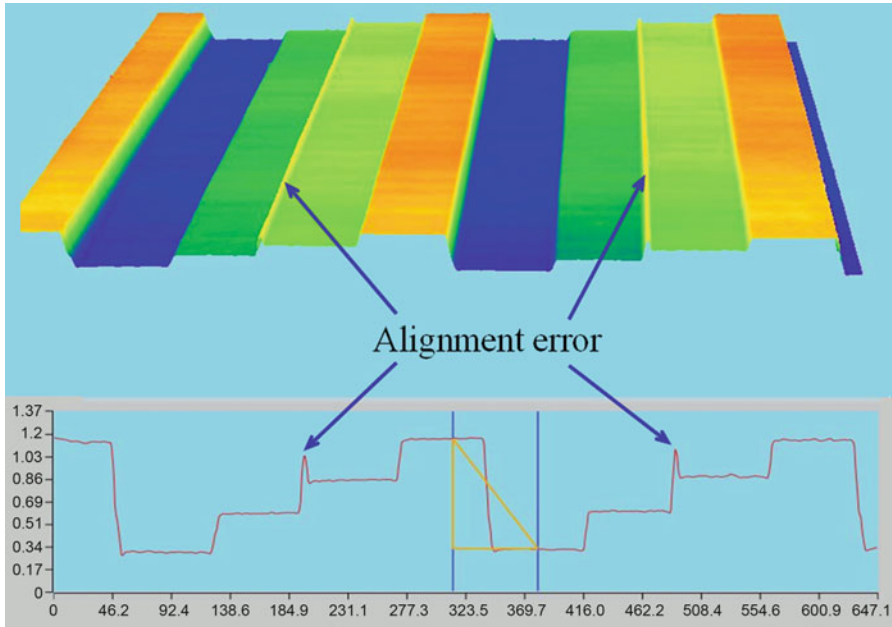


Fig. 21 The four-level microstructures on fused silica substrate. Top: 3D topography. Bottom: its cross-section profile

the first etching. Finally, the four-level FZL on fused silica substrate was achieved.

Subsequently, the fabricated four-level microstructures on fused silica substrate were measured using laser-scanning confocal microscope. Figure 21 shows a 3D topography (top) and its cross-section profile (bottom) at the outermost period of the Fresnel microstructures. The designed four-level microstructure could be obtained. However, a sharp spike could be seen on the connection portion between adjacent levels in each single period, which was induced by the alignment error of the positioning marks before the second exposure. Although these spikes could be dissolved using a buffered HF acid etchant (Britten et al. 2014), however, the misalignment of the two half-period patterns could not be removed, which decreases the diffraction efficiency of the Fresnel lens during optical imaging application.

In order to resolve this problem, a pattern of a vernier caliper as shown in Fig. 22 was exposed to the photoresist through twice exposure: the first exposure for the main ruler and the second exposure for auxiliary ruler. Therefore, the alignment error along both X and Y directions could be read out other than manually measured. Figure 23 shows the line position before and after the alignment compensation using the mechanism of vernier caliper. At last, the alignment error could be reduced below 200 nm.

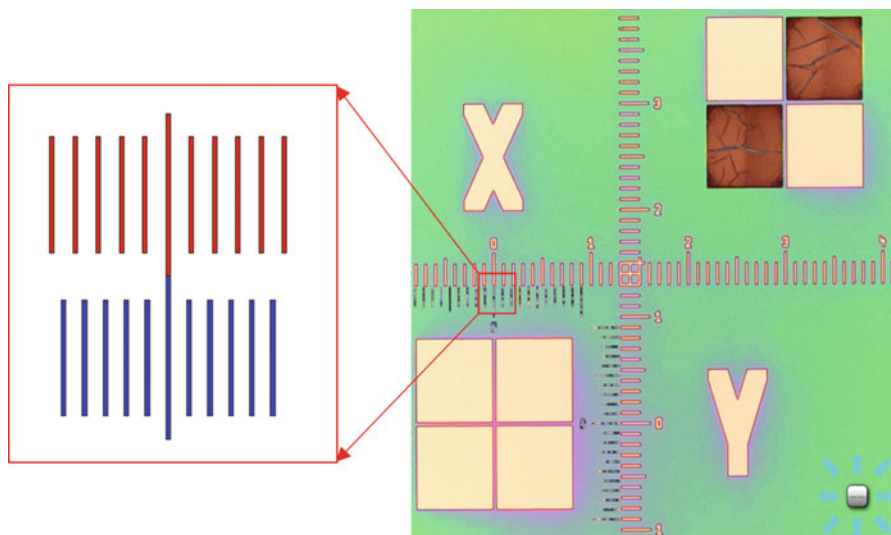


Fig. 22 Elimination of the alignment error by the mechanism of vernier caliper

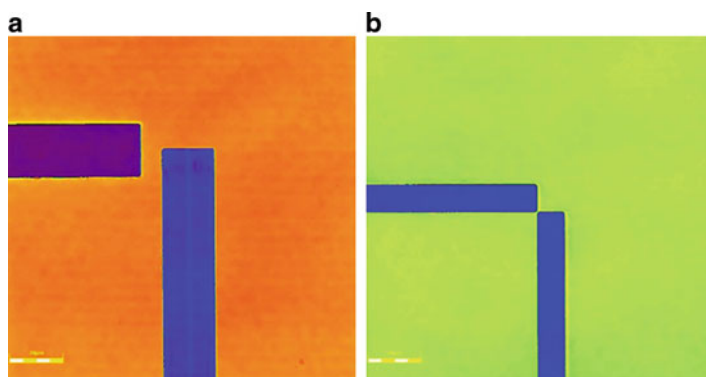


Fig. 23 Line positions before (a) and after (b) alignment compensation

Figure 24 shows a 3D topography (top) and its cross-section profile (bottom) at the outermost period of the Fresnel microstructures. It can be seen that the spikes were completely eliminated. The calculated diffraction efficiency was 66.4% by averaging all measured data. Moreover, the obtained results show that etching depth uniformity in full aperture could be reduced within 1%, which was sufficiently accurate to meet the use requirements of FZL.

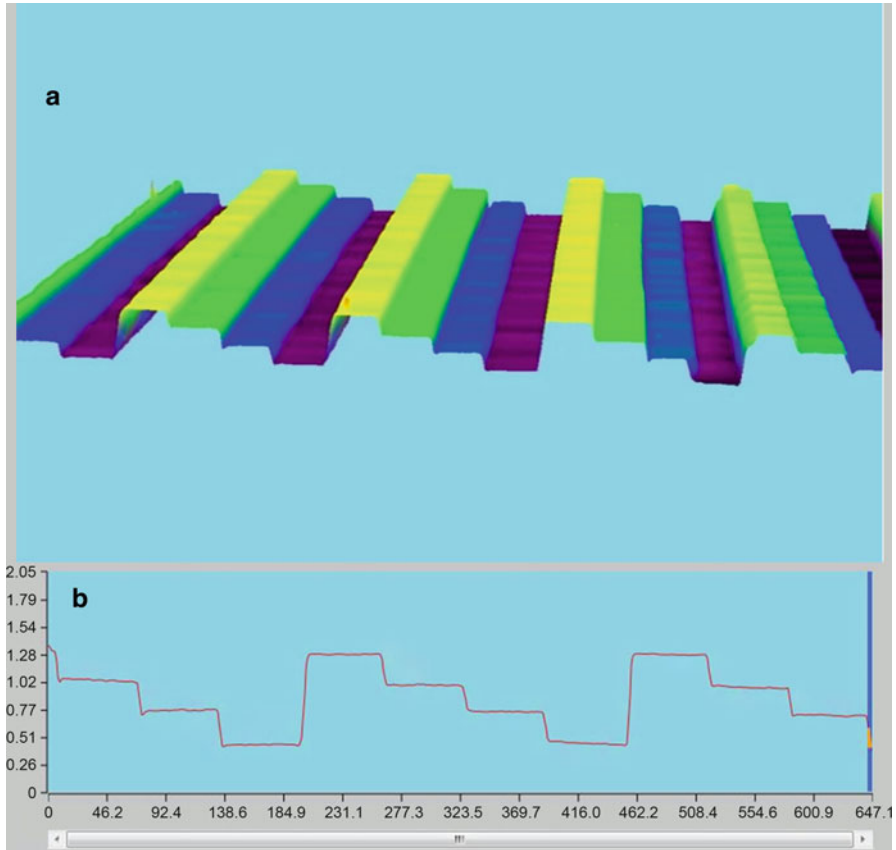


Fig. 24 Microstructures on fused silica substrate after alignment compensation: (a) 3D topography, (b) its cross-section profile

18.4.3 Replication of the FZL to Polyimide Membrane

18.4.3.1 Replication Procedures

Figure 25 shows the replication process of diffraction microstructures to polyimide membrane. At first, the liquid polyimide is cast onto the fused silica substrate with the fabricated four-level FZL described in the section above and then cured to membrane in place by spin coating. After spin coating, the membrane with the substrate is preheated on a hot plate. When the solvent in liquid polyimide is completely steamed out, the membrane with the substrate is transferred into vacuum oven and continuously heated up to the glass transition temperature of polyimide (350 °C) for 1 h to completely imidize the polyimide. When cooling to room temperature, the membrane is separated from the substrate and supported by a circular fixture.

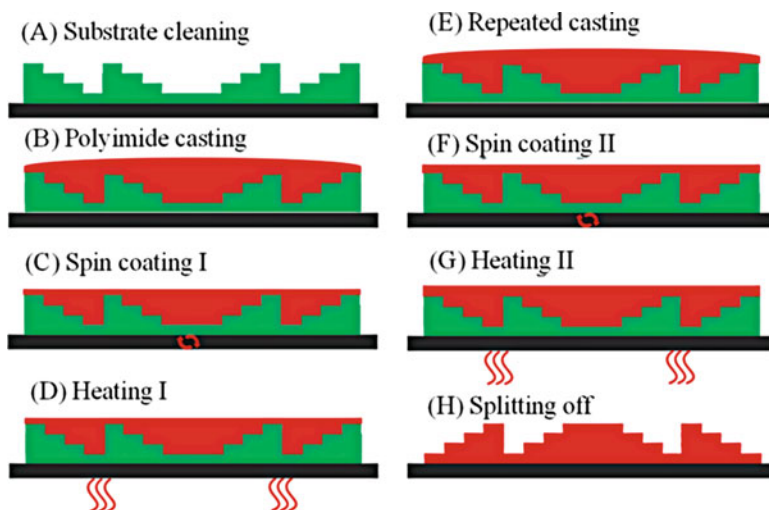


Fig. 25 Replication flow of a four-level FZL to polyimide membrane

Based on the abovementioned replication flow, the four-level FZL on polyimide membrane was achieved. A photograph of one such membrane is shown in Fig. 26. As a result, the Fresnel microstructures have been well transferred to the membrane with the evidence of sharp edges and steep sidewalls demonstrated in the following section.

18.4.3.2 Evaluation of the Replication Process

In order to investigate the replication performance, a pattern with various line widths from 1 to 100 μm was etched on fused silica plate and replicated into polyimide membrane, as is done in the above section. Figure 27 shows the photos and selected line width images of fused silica mold and replicated polyimide membrane. The line widths and step depths were measured and compared to the same positions on fused silica mold.

As shown in Fig. 28a, the black line represents the width transfer errors, while the red line represents the deviation with the designed values. It can be seen that the width transfer errors are less than 1%, indicating that the transfer process is effective to achieve high-precision replication of the FZL profiles. Figure 28b shows the measured depths for each step of the four-level structure (D1, D2, and D3). As a result, the depth transfer error is less than 6%, and the deviation to the designed step depth is approximately 10%. The transfer error is mainly due to the shrinkage of membrane when separated from substrate. In order to compensate shrinkage, the membrane should be appropriately extended and then fastened to the circular fixture.

At last, surface roughness of the fabricate microstructures was also measured. As shown in Fig. 29, the surface roughness of the polyimide membrane is about 1.5 nm Ra, basically consistent with that of the fused silica. However, some scratches could

Fig. 26 Replicated four-level FZL to polyimide membrane

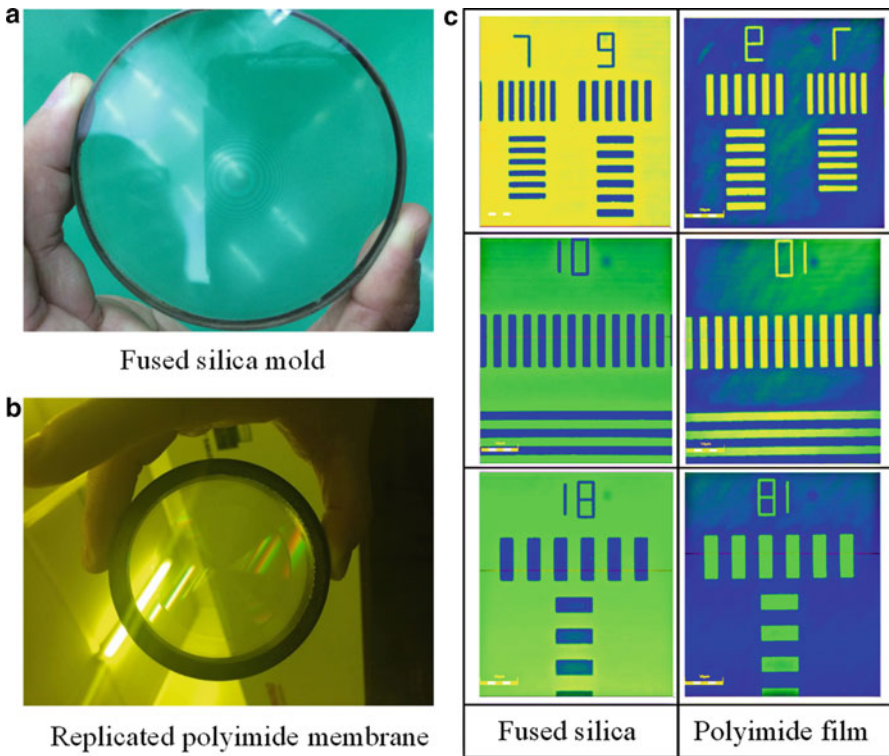
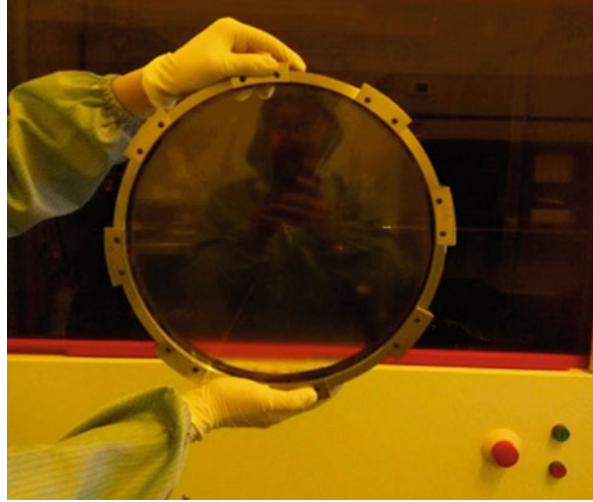
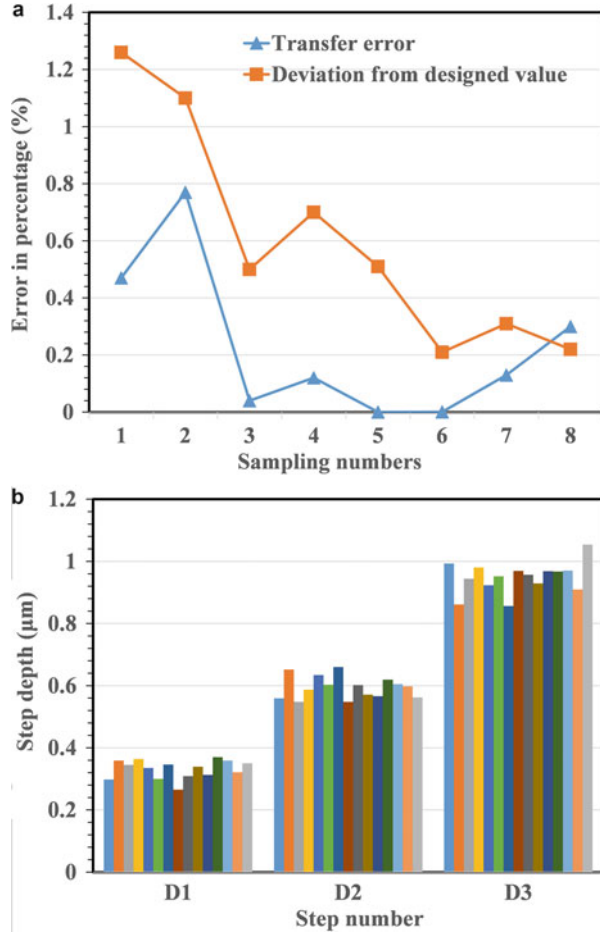


Fig. 27 Photos and images for the microstructure comparison between fused silica mold and replicated polyimide membrane

Fig. 28 (a) Line widths and (b) step depths on polyimide membrane surface



be found on the polyimide membrane, which were introduced during cleaning of the soft polyimide surface.

18.5 Summary and Outlook

In this chapter, the combined use of laser lithography and ion etching was summarized. The strip-scanning laser system was used to generate microstructures on photoresist layer with high precision. The Ar ion beam characterized by a point ion source with Gaussian energy distribution was applied to transfer the microstructures from the photoresist to the fused silica substrate. Moreover, the replication process of a four-level Fresnel zone lens from fused silica substrate to polyimide membrane was also developed as a route to mass replication of diffraction optics.

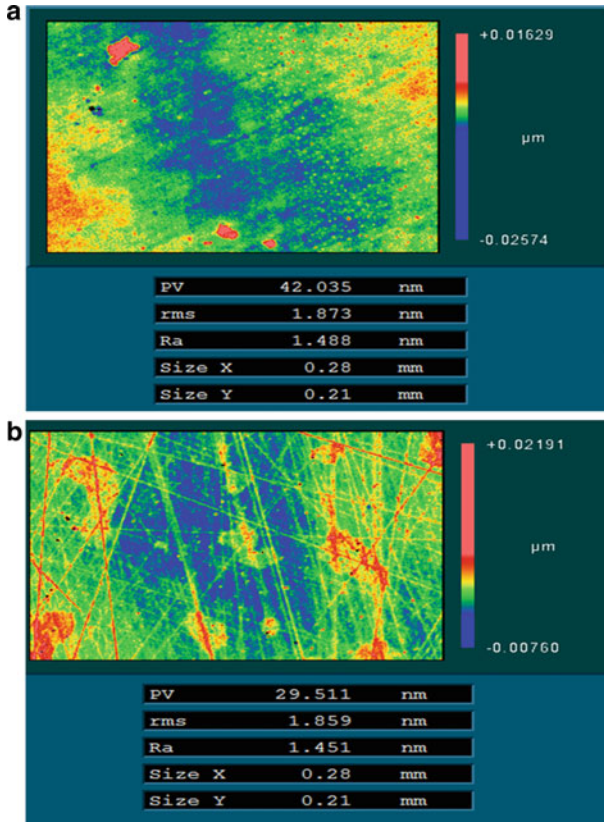


Fig. 29 Surface roughness: (a) fused silica, (b) polyimide membrane

This research work provides a cost-effective method for microfabrication of high-performance optical components, which has great potential for applications in visible and infrared optical applications such as cell phone camera, CMOS sensor, night-driving assistance, as well as next-generation space telescope. The achievements obtained in the work could also be used in the development of high-power laser, flat-panel display, solar photovoltaic system, and other high-value-added optical products.

References

- Allen LN, Romig HW (1990) Demonstration of an ion-figuring process. Proc SPIE 1333:164–170
- Atcheson P, Domber J, Whiteaker K, Britten JA, Dixit SN, Farmer B (2014) MOIRE-ground demonstration of a large aperture diffractive transmissive telescope. Proc SPIE 9143:9143W

- Barton I, Britten J, Dixit S, Summers L, Thomas I, Rushford M, Lu K, Hyde R, Perry M (2001) Fabrication of large-aperture lightweight diffractive lenses for use in space. *Appl Opt* 40(4): 447–451
- Britten JA, Dixit SN, Debruyckere M, Steadfast D, Hackett J, Farmer B, Poe G, Patrick B, Atcheson PD, Domber JL (2014) Large-aperture fast multilevel Fresnel zone lenses in glass and ultrathin polymer films for visible and near-infrared imaging applications. *Appl Opt* 53:2312–2316
- Cao Q, Jahns J (2004) Comprehensive focusing analysis of various Fresnel zone plates. *J Opt Soc Am A* 21:561–571
- Chang T, Chen Z, Lee Y, Li Y, Wang C (2016) Ultrafast laser ablation of soda-lime glass for fabricating microfluidic pillar array channels. *Microelectron Eng* 158(1):95–101
- Chao W, Harteneck BD, Liddle JA, Anderson EH, Attwood DT (2005) Soft X-ray microscopy at a spatial resolution better than 15 nm. *Nature* 435:1210
- Chavoshi SZ, Luo X (2015) Hybrid micro-machining processes: a review. *Precis Eng* 41:1–23
- Chen H, Zhang P, Zhang L, Liu H, Jiang Y, Zhang D, Han Z, Jiang L (2016) Continuous directional water transport on the peristome surface of *Nepenthes alata*. *Nature* 532:85–89
- Chen H, Zhang L, Zhang P, Zhang D, Han Z, Jiang L (2017) A novel bioinspired continuous unidirectional liquid spreading surface structure from the peristome surface of *Nepenthes alata*. *Small* 13:1601676
- Chkhalo NI, Churin SA, Mikhaylenko MS, Pestov AE, Polkovnikov VN, Salashchenko NN, Zorina MV (2016) Ion-beam polishing of fused silica substrates for imaging soft X-ray and extreme ultraviolet optics. *Appl Opt* 55:1249–1256
- Guo C, Zhang Z, Xue D, Li L, Wang R, Zhou X, Zhang F, Zhang X (2018) High-performance etching of multilevel phase-type Fresnel zone plates with large apertures. *Opt Commun* 407:227–233
- Kowalik A, Jaroszewicz Z, Gora K (2002) Diffractive optical elements obtained using electron-beam writer and reactive ion etching. *Proc SPIE* 4887:141–147
- Meier A (2015) Diamond turning of diffractive microstructures. *Precis Eng* 42:253–260
- Nakano S, Nakahara S, Singubara S (2012) Fabrication of the multi-level phase type hologram for display using the laser direct write lithography system. *Proc SPIE* 8281:828116
- Okamuro K, Hashida M, Miyasaka Y, Ikuta Y, Tokita S, Sakabe S (2010) Laser fluence dependence of periodic grating structures formed on metal surfaces under femtosecond laser pulse irradiation. *Phys Rev B* 82:1–5
- Pereston FW (1927) The theory and design of plate glass polishing machines. *J Soc Glass Technol* 11:214–256
- Phillips KC, Gandhi HH, Mazur E, Sundaram SK (2015) Ultrafast laser processing of materials: a review. *Adv Opt Photon* 7(4):684–704
- Steingöetter I, Grosse A, Fouckhardt H (2003) Very deep fused silica etching. *Proc SPIE* 4984:234–243
- Streibl N (1989) Beam shaping with optical array generators. *J Mod Opt* 36:1559–1573
- Taghizadeh MR, Blair P, Layet B, Barton IM, Waddie AJ, Ross N (1997) Design and fabrication of diffractive optical elements. *Microelectron Eng* 34:219–242
- Wang C, Yang W, Wang Z, Yang X, Hu C, Zhong B, Guo Y, Xu Q (2014) Dwell-time algorithm for polishing large optics. *Appl Opt* 53:4752–4760
- Wang R, Zhang Z, Guo C, Xue D, Zhang X (2016) Effects of fabrication errors on diffraction efficiency for a diffractive membrane. *Chin Opt Lett* 14(12):120501-1–120501-6
- Wiltse JC (2005) Zone plate designs for terahertz frequencies. *Proc SPIE* 5790:167–179
- Xu P, Li J, Bu G, Tang J, Guo L, Guo Y (1998) Fabrication error analysis of 4-step binary optic elements. *Chin J Lasers* 13:301–311
- Yan J, Maekawa K, Tamaki J, Kuriyagawa T (2005) Micro grooving on single-crystal germanium for infrared Fresnel lenses. *J Micromech Microeng* 15:1925–1931
- Yan J, Zhang Z, Kuriyagawa T (2010) Fabricating micro-structured surface by using single-crystalline diamond endmill. *Int J Adv Manuf Technol* 51:957–964

- Yan J, Watanabe K, Nakagawa Y (2012) Fabrication of thin-film Fresnel optics by combining diamond turning and MEMS techniques. *Proc CIRP* 4:146–150
- Ying X, Zhang X, Liu G, Liu Y, Xu D, Tian Y (2009) Methods for improving ion beam etching uniformity of large-sized DOEs. *Proc SPIE* 7282:728210
- Zhang X, Xiong Y, Liu Q, Tian Y (2009) Methods for increasing the etching uniformity of ion beam multiple mask. *Proc SPIE* 7282:728213
- Zhang Z, Guo C, Wang R, Hu H, Zhou X, Liu T, Xue D, Zhang X, Zhang F, Zhang X (2017) Hybrid-level Fresnel zone plate for diffraction efficiency enhancement. *Opt Express* 25(26):33676–33687
- Zhou P, Burge JH (2007) Optimal design of computer-generated holograms to minimize sensitivity to fabrication. *Opt Express* 15(23):15410–15417

Part IV

Molding/Forming/Self-Organization Technology



Paritat Muanchan and Hiroshi Ito

Contents

19.1	Introduction	608
19.2	Replication Technology	609
19.2.1	Background and History	609
19.2.2	Category of Replication Technology for Micro-/Nano Structures	611
19.2.3	Summary and Outlook	612
19.3	Micro-/Nano-injection Molding	612
19.3.1	Background and History	612
19.3.2	Thin-Wall Products	615
19.3.3	Tiny Products	617
19.3.4	Products with Micro-/Nanosurface Structures	619
19.3.5	Summary and Outlook	622
19.4	Micro-/Nano-imprinting	623
19.4.1	Background and History	623
19.4.2	Thermal and UV Micro-/Nano-imprinting	624
19.4.3	Rapid Fabrication Using Roll-to-Roll Micro-/Nano-imprinting	628
19.4.4	Summary and Outlook	631
19.5	Future Trends of Replication Technology	632
	References	633

Abstract

This chapter is intended to review the state of the art of surface replication technologies related to polymer processing for shaping micro-/nanostructures. The essence of this chapter is presentation of the capability of the high-precision polymer processing technology of micro-/nano-injection molding and micro-/nano-imprinting. Micro-/nano-injection molding is not merely a capability for

P. Muanchan · H. Ito (✉)

Department of Organic Materials Science, Yamagata University, Graduate School of Organic Materials Science, Yamagata, Japan

e-mail: hiroshi@yz.yamagata-u.ac.jp

© Springer Nature Singapore Pte Ltd. 2018

J. Yan (ed.), *Micro and Nano Fabrication Technology*, Micro/Nano Technologies,

https://doi.org/10.1007/978-981-13-0098-1_19

607

replication of micro-/nanostructures. This chapter explains that thin-wall products and tiny products can be produced effectively using micro-/nano-injection molding. A discussion of micro-/nano-imprinting emphasizes the progress of plate-to-plate and roll-to-roll methods for thermal and ultraviolet (UV) micro-/nano-imprinting. The explanations of those replication technologies in this chapter mainly address the following details: background and history, current situations and issues, progress in fundamental development, potential for development, and a forecast of future trends of research in this field.

Keywords

Replication technology · Micro-/nano-injection molding · Micro-/nano-imprinting

19.1 Introduction

From the advent of the Industrial Revolution in the eighteenth century through the mid-twentieth century, several manufacturing processes have been fully developed at a millimeter scale for polymer materials of various kinds (Taniguchi et al. 2013). Currently, operations have been scaled down to micro-/nanoscales. Particularly, surface structural development by replication technologies is progressing dramatically to miniaturization produce ultrafine structures. Especially in the last two decades, numerous studies have specifically examined research and development of microelectromechanical systems (MEMS). Intense research interest has prevailed in production technologies of micro-/nanostructures because of growing emphasis on MEMS (Ito et al. 2005). To augment the value-added by these products, the variety of applications along with structural development created by engineering design and polymer processing demand much attention. As one example, in the medical field, microneedle arrays have been produced to control drug delivery (Lutton et al. 2015), with nanopillar/nanofiber arrays that have bactericidal effects (Li 2016; Muanchan et al. 2017), etc. Several micro-/nanosurface structures with superhydrophobic properties have been commercialized at an industrial level. For optical devices, special attention has been devoted to development of antireflective nanosurface features designed using architectural engineering and inspired by nature (Chu et al. 2014).

Consistent with rapidly expanding research in this field, several replication technologies in polymer molding processes are being developed as industrial-scale manufacturing processes. Micro-/nano-injection molding is extremely useful at the industrial level because of its high productivity and high precision. However, in some cases, polymer solidification at mold wall surfaces and trapping of air inside the mold cavity are salient difficulties that arise when using this process. Furthermore, micro-/nano-injection molding has operational constraints for replication of thin-film products. To overcome these difficulties, a micro-/nano-imprint (plate-to-plate system) has been developed as high-precision technology for replicating micro-/nanostructures. Micro-/nano-imprint having high capability to produce the

ultrahigh aspect ratios (length/diameter) can be scaled down close to 25 nm diameter or less (Xia and Chou 2008). Although this technology is a high-precision method, the operational delay is an important impediment for industrial level and commercial development because of batch-type processing steps. Progress in micro-/nano-imprint is developed continuously from the point of view of the plate-to-plate system. Roll-to-roll micro-/nano-imprinting has been regarded as compensating for low-productivity issues in the plate-to-plate system by enabling continuous processing. The excellent large area of production with the rapid processing is preferred for industrial-scale production over micro-/nano-injection molding and micro-/nano-imprinting (plate-to-plate system). However, in terms of precision, roll-to-roll imprinting remains insufficient for replicating high-aspect-ratio features and complex structures because of the short contact time (imprint time) and low compression force (imprint pressure) for imprint mechanisms in this process. Moreover, reliability in the long-cycle imprint and optimization of imprint conditions such de-molding step must be improved.

All replication technologies described above have their particular benefits and shortcomings. Therefore, many reports have described specific examinations of progress in research development for improving the capability of replication performance. This chapter proposes a timeline of the development of those replication technologies. It is covered in the background and history, current status and critical issues, opportunities for development, and future trends of these replication technologies.

19.2 Replication Technology

19.2.1 Background and History

Throughout the long history of material development, various materials such as wood and stone have been used to produce appliances to fit the basic needs of daily life (Taniguchi et al. 2013). After passage through a long period of development, metal materials are widely used by our civilization, especially as frames of various constructions and artifacts. However, humans demand continuous development for their convenience. Currently, polymeric materials have become versatile materials with excellent characteristics that make them lighter, cheaper, and more flexible than earlier materials. Natural rubber was the first polymer material used by humans. Thereafter, natural cellulose progressed intensively in a short period. Synthetic resins also enable production. They have become an indispensable product supporting modern society. Replacement of the use of metal materials and ceramic materials by polymer materials is increasing intensely. Various applications are anticipated from polymer products such as housewares, electrical, automotive, and optical devices, especially for engineering plastics having properties approaching those of such materials.

Thermoplastics are polymer materials used almost exclusively because of their good processability for all dimension scales. They can be melted and hardened repeatedly without alteration of their molecular chains or chemical structures. Thermoplastics are classifiable in three categories: (1) amorphous polymers, with

arbitrary molecular structure; (2) crystalline or semicrystalline polymers, with molecules ordered in a crystalline manner; and (3) thermoplastic elastomers, which are rubbery, elastic polymers. In terms of thermosetting plastics and other thermal/UV-curable materials, these materials are formed with cross-linking points between their molecular chains when heat or UV radiation is applied. Such wide use of polymer materials is generally attributable to the replication techniques used for shaping the material surface structures according to their desired applications.

Research related to material development can improve material properties well. Materials require the development of a structure for advanced properties. Products with micro-/nanosurface structures of various shapes can offer specific properties that are useful for the sustainable development of future society. For this reason, replication technology is regarded as committing the key of success in the structural development of material surfaces. Various geometrical micro-/nanostructures on polymer surfaces are designed based on inspiration from nature and are designed using architectural engineering, thereby offering a broad range of novel functionalities and applications as presented below (Holzer et al. 2010):

- Control of hydrophilic or hydrophobic properties
- Ease of empty properties
- Moth eye antireflective effects
- Sensor/security features
- Control of tribological properties
- Optical waveguide structures
- Biological adhesives
- Surface patterns for guided self-assembly

For diverse applications, products with micro-/nanosurface structures have been produced. For example, many regenerative medical techniques have been proposed using tissue scaffolds with ultrafine structures. Microneedle arrays are used to control drug delivery and drug release. Hierarchical micro-/nano surface structures (hybrid structures) are producible to have both high water-repellent properties and self-cleaning properties (Chu et al. 2014, 2015). Optical sensors using surface plasmons have been produced, along with vertically aligned nanostructures with adhesive properties, bactericidal action, hydrophobic properties, and antireflective properties (Xie et al. 2017). Some micro-/nanostructures have antireflective functions (Kayano et al. 2011). In the electrical field, development of transistors, memory, and sensing devices using carbon-based materials and miniaturization in central processing units (CPUs) are progressing rapidly (Naeemi and Meindl 2009). Data storage devices with novel patterned media for high-density memory are being considered (Bandić et al. 2008). In the energy field, film surfaces with nanostructures are used for electrolyte membranes of fuel cells (Zhang et al. 2007, 2009). These micro-/nanofeatures also provide high performance with additional functionality. In actuality, demand for these products in the global market continues to increase rapidly. Consequently, several replication technologies are being pursued to develop capabilities for high precision and high productivity for shaping ultrafine structures.

19.2.2 Category of Replication Technology for Micro-/Nano Structures

Replication technologies by which micro-/nanostructures are produced by transferring the designed structures from a high-resolution mold to target surfaces have an important role in the manufacture of ultrafine structures. Various micro-/nanostructure fabrication methods have been reported. As one example, photolithography is used widely in the mass production of semiconductors and integrated circuits and nanofluidic applications because it can efficiently create ultrafine structures with a large area and low cost of manufacturing (Kim et al. 2015). Nevertheless, costs of facilities for this process are extremely high. Moreover, sacrificed materials must be removed to produce the final structure. Deep reactive ion etching (RIE) processing using inductively coupled plasma (ICP) can produce ultrafine structures with high aspect ratios (Li et al. 2016). The LIGA process (LIGA is a German acronym for lithography, electroplating, and polymer replication introduced in 1982) using X-rays or irradiating synchrotron radiation is well known as an outstanding method for producing ultrafine structures with high aspect ratios (Chang and Kim 2000). Other techniques such as electron beams (EBs) and focused ion beams (FIBs) are widely used to fabricate various ultrafine structures. Those techniques above present high capability with many merits for fabricating micro-/nanostructures, but they remain unsuitable for mass production because they typically require greater amounts of time than large-scale area processes (Jarupoonphol et al. 2002). Given such circumstances, polymer molding processes such as micro-/nano-injection molding and micro-/nano-imprint are regarded as effective technologies that are expected to be suitable methods for mass production because they lead to high precision, low production costs, high production rates, and simple processing steps.

Molding processes related to polymer processing technologies for development of various structures are well known as replication technologies to transfer the desired shape directly to polymer materials. Furthermore, molding processes are capable of achieving extremely high resolution (feature size below 100 nm) and for combining the high resolution of ultrafine structures with alignment and assembly features in large area production from the millimeter to centimeter regime. Basic polymer molding comprises three steps, as explained below (Taniguchi et al. 2013).

1. Fluidization

- Thermosetting/UV-curing resins are liquid, but thermoplastic resins are melted by heating processes.
- Material precursors must be fluidized to shape structures in the next step.

2. Replication

- Fluidized polymers are molded in the stamp or injected into the mold with the desired shape.
- Flowability of polymer materials at the micro-/nanoscale is driven by application of high pressure to materials to shape with the stamp/mold.
- Effects of the interfacial surface tension of materials become greater when the replication shape becomes smaller.

3. Heating (or UV exposure)/cooling and de-molding

- During the shaping mechanism, the thermosetting resin is heated, UV resin is cured with UV irradiation, and thermoplastic is cooled to form the molded shape.
- Stress occurs in the products in this mechanism. It usually occurs that the product shape changes and optical characteristics might be lost.

Some overlap will occur in three processing steps above for practical processing. For example, micro-/nano-injection molding during steps 2 and 3 progresses simultaneously inside a die; micro-/nano-imprinting occurs within one machine covering steps 1–3. An outline of the fundamental replication steps of micro-/nano-injection molding and micro-/nano-imprint (hot embossing) processes for thermoplastics is presented in Fig. 1 (upper). In micro-/nano-injection molding processing, the following occurs: (1) the molding tool is closed and heated above the glass transition temperature (T_g) or melting point temperature (T_m) of the polymer. (2) Polymer is injected and compressed to form the structures within the mold cavity. (3) The tool and polymer are cooled. Finally, the molded products are then de-molded. For micro-/nano-imprinting, the following occurs: (1) Polymer film is inserted into the imprint machine. (2) The imprint machine heats the polymer above its softening temperature, following by compression. (3) After the polymer is cooled, the product is de-molded. Capability of molding processes in the range of dimension scales of micro-/nanoscale ranges is implied as shown in Fig. 1 (lower).

19.2.3 Summary and Outlook

This section explained the importance of polymer materials. Features with specific functions of polymers can be improved not only in the field of material development at the molecular level. They can also be improved by structural development, especially in terms of surface improvement with the micro-/nanostructures. Several replication techniques have been introduced for replicating micro-/nanostructures. They can be evaluated in terms of their benefits of production costs, rapid production rates, simple processing, precision, and the lack of harsh chemicals used. All are major factors for the sustainable development of replication technology. For these reasons, molding processes including micro-/nano-injection molding and micro-/nano-imprint play an important role as a surface replication technology used for polymer materials.

19.3 Micro-/Nano-injection Molding

19.3.1 Background and History

In recent years, demand for micro-/nanoproducts has increased continuously to support miniaturization. The weight and size of these small components require high-precision fabrication technologies to shape the target structures. For use in

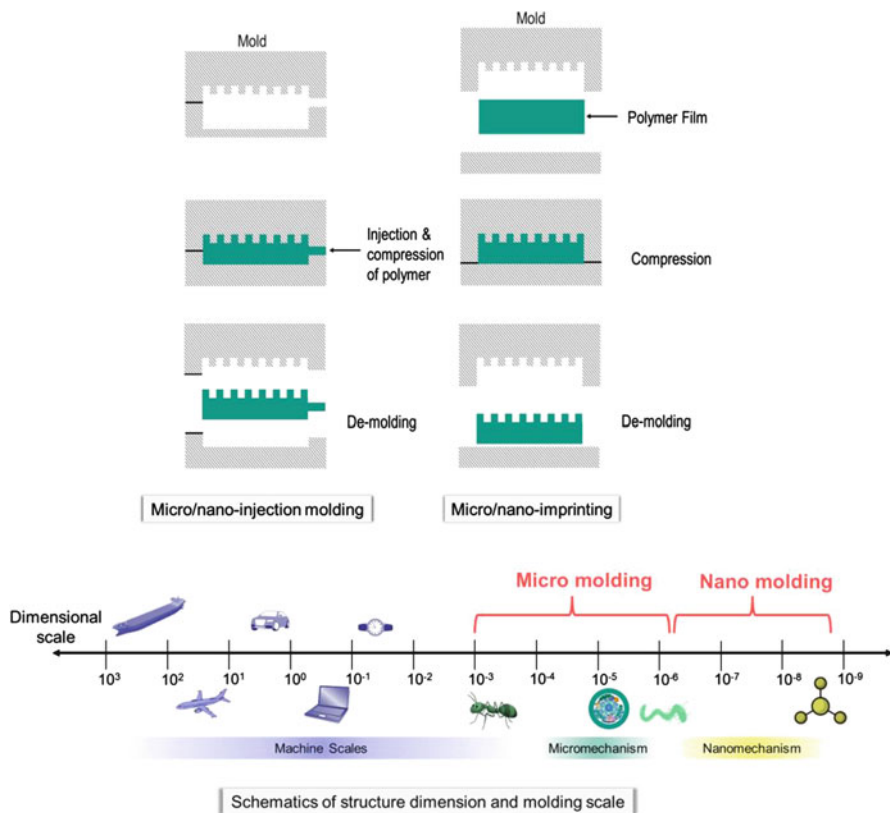


Fig. 1 Molding processes for replication technology

economically feasible processes, micro-/nano-injection molding is a key technology because it supports mass production capability, with consequent low production costs and stable mechanisms. Micro-/nano-injection molding process is a structure transfer technique from metallic molds to polymer materials that are capable of working to produce micro-/nanofeatures. Micro-/nano-injection molding was first developed from the 1980s from conventional injection molding. Nevertheless, it still has inadequate performance in many respects (Giboz et al. 2007). In the 1990s, an advanced micro-injection molding machine was developed to produce micro-molded products. With continuous development, micro-injection molding might eventually have high capability for making products with micro-/nanostructures as a micro-/nano-injection molding process. Currently, this process offers several benefits in terms of mass production with high precision in the field of replication technology. It is also being used commercially to produce devices of various types (Taniguchi et al. 2013). Additionally, it can serve as a production technique for small products with higher-order structures. An outline of the micro-/nano-injection molding machine is presented in Fig. 2.

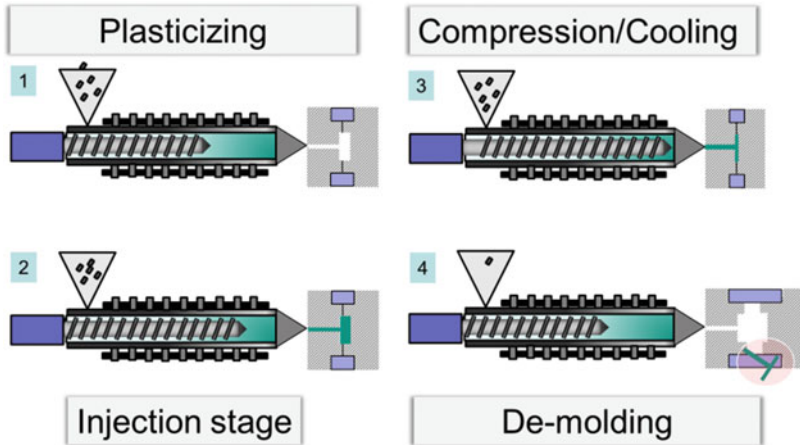


Fig. 2 Schematic of micro-/nano-injection molding machine

Micro-/nano-injection molding process consists of two main stages: injection and compression. In the injection stage, polymer granules are transferred from a hopper into a plasticizing unit to reach a molten or softened state. Subsequently, the molten polymer is injected into the mold cavity free from the clamping force. During compression, a mold with the injected polymer is compressed by clamping force, thereby reducing the cavity thickness to the final thickness of the part. During this stage, molten polymer is forced by the holding pressure for a specific time to compensate for material shrinkage. After a sufficient holding time, molten polymer is solidified by cooling processes. After the polymer is shaped completely with the mold, it is ejected from the mold. Then this cycle is repeated. Variables that affect product quality are classifiable into four categories: mold and component design, molding machine performance, material characteristics, and processing conditions. In addition, this method with high shearing can reduce the molecular orientation. It is noteworthy that the high shear rate occurring in the micro-/nano-injection molding process exhibits high shear-thinning rheology, which enhances the material filling ability within the mold cavity at the lowest practical injection pressure.

Products of micro-/nano-injection molding have been classified into three categories as the following (Ito et al. 2009):

1. Thin-wall products (micro-injection molding)
Molded products with microscale precision such as super-thin-wall molded products
2. Tiny products (micro-injection molding)
Molded products with less than 1 mg pellet weight
3. Products with micro-/nanosurface structures (micro-/nano-injection molding)
Molded products in the term of surface replication

This section next describes all three categories of products obtained using the micro-/nano-injection molding process.

19.3.2 Thin-Wall Products

Reduction of the dimension scale to a few hundred micrometers can be affected by many processing features in micro-injection molding. Those factors differ from conventional injection molding, in such cases of higher melt and mold temperature and higher injection pressure and speed. The shear-thinning effect can theoretically decrease the polymer viscosities, which allows higher flowing ability in micro-cavities. The rheological behavior of the flowing in microcavities can deviate or might differ from the description by conventional rheology laws. Therefore, fundamental study of structure development in micro-injection molding is necessary to clarify production of various thin-wall products. Furthermore, for both conventional injection molding and micro-injection molding, because molded products are affected by dimensional variation (shrinkage), it is important to minimize the discrepancy between mold design and final product dimensions, especially for applications that require high-precision products.

The first study of structure development in micro-injection molding process limits their scope for specific examination of the processability and surface structure observation for producing small components. However, it is noteworthy that the molding conditions have a marked effect on structure development and the final properties of molded products. Therefore, precise evaluation methods are indispensable for investigation of the relation between molding conditions and structures and physical properties of molded products. Herein, fundamental research related to structural development in micro-injection molding will be clarified by the case study presented below (Ito et al. 2005).

For this case study, we used selected model materials: isotactic polypropylene (PP) as the semicrystalline polymer and cyclo-olefin copolymer (COC) as the amorphous polymer. Figure 3 shows an outline of the molded product. Respective dimensions of the central region were 0.1, 0.3, 0.5, and 1.0 mm thickness with 40 mm length. Effects of the mold wall temperature and cavity thickness on the structures and various properties of molded products were assessed experimentally using some characterization methods.

Photograph results revealed that the flow length in the case of 0.3-mm-thick molded product was approximately 40 mm for all process conditions. However, 5 mm flow length was found for 0.1 mm thickness. The flow length decreased concomitantly with decreasing cavity thickness because the cooling rate for melted resin increases when the thickness decreases. At higher cooling rates, the viscosity of melted resin was increased immediately. The melted resin solidified rapidly. Increased molecular orientation with decreasing mold cavity thickness was obtained for both PP and COC. Lower birefringence value of the molded products at position C than those of positions A and B was observed. The increased birefringence with decreasing mold temperature resulted from the increase of

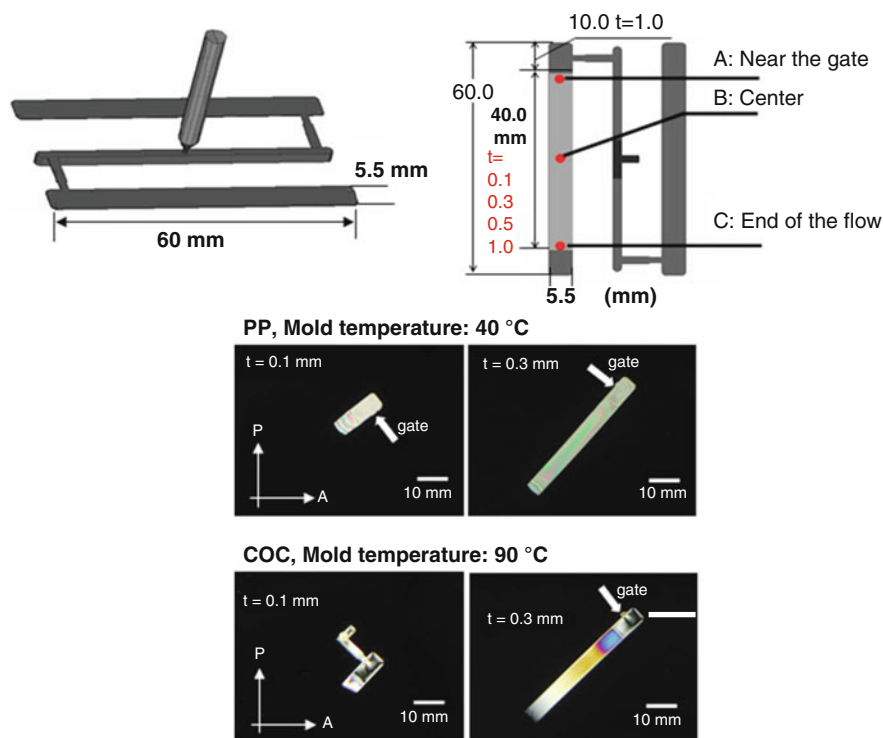


Fig. 3 Shape of PP- and COC-molded products

shear stress. Also, the optical anisotropy was increased. Wide-angle X-ray diffraction (WAXD) patterns of PP-molded products demonstrated that the molecular orientation in the machine direction (MD) is particularly high at position A (near the gate), implying that higher orientation-induced crystallization occurred because of the high shear flow in this region. The molecular orientation in the MD direction was decreased at position C (distant from the gate). Cross-sectional views of PP-molded products observed using polarizing microscopy show the skin–core structure. The skin region, including the shear layer, became thinner at position C. In addition, the tensile strength and elongation at the break of molded products were closely related to the molecular orientation. Results of tensile tests showed that elongation at the break of the moldings of 0.3 mm thickness was lower than those of 0.5 and 1.0 mm thickness. For 0.3 mm thickness, Young's modulus decreased. Elongation at the break increased in spite of high molecular orientation.

Many studies have been undertaken to advance fundamental research to produce plastic lenses, as in an earlier study of the thin-wall products. High-density polyethylene (HDPE) condenser lenses can be used in infrared radiation (IR) systems such as radiation thermometers and thermal imaging systems. Actually, HDPE lenses with the disk-shaped finished mirrorlike surface have been produced (Kaneda et al. 2016, 2017). Results of the obtained HDPE lenses showed IR transmittance higher than

65% with low visibility ray (VR) transmittance of less than 7%. These experiment results demonstrated the effects of important factors affecting IR and VR transmittance properties under process conditions of the micro-injection molding include surface roughness, thickness, crystallinity, internal structure, and molecular orientation (skin–core structure) of HDPE-molded products. The results suggest that IR transmittance becomes higher with a thin skin layer having small molecular orientation and low crystallinity. The VR transmittance becomes lower with lower molecular orientation in the shear–core layer.

19.3.3 Tiny Products

Tiny products from micro-injection molding are useful in diverse industries related to medical and pharmaceutical, electronics, telecommunication, automotive, aerospace, and petroleum technology fields. Tiny plastic products are increasingly demanded because of their economical and benefits attributable to various properties when compared with metal tiny products (from powder micro-injection molding). Typically, they have lighter weight, better processability, and remarkably higher mechanical properties, especially in terms of stiffness and flexural modulus. Table 1 presents a tiny product application.

Plastic microgears are preferred for tribological performance because of their high wear resistance with low friction. Therefore, several research groups have

Table 1 Application of tiny products

Applications	Tiny products	Materials
Micromechanical	Locking lever Latch (watch industry) Catch wheel (micro switch) Micro gear wheel Ex: Dented wheel, rotor with gear wheel, gear wheel, spur wheel, spiral gear, worm wheel	Polyoxymethylene (POM) Polyetheretherketone (PEEK) Polyamide (PA) Etc.
Medical	Microfilter Implantable chip Bearing shell/bearing cap Sensor housing implantable Impeller Vascular clamp Operating pin Gear plate Sleeve	Polylactic acid (PLA) Polycarbonate (PC) Polymethylmethacrilate (PMMA) Etc.
Optical and electronic	Microlens Microdisk Coax plug/switch MID (mobile phone) Micro connectors	PMMA PC Liquid crystal polymer (LCP) Polyethylene (PE) Etc.

sought to explore microgears with micro-injection molding process for both simulation and experimentation. Several plastics have been used to produce microgears (Otmani et al. 2016). Actually, because of its benefits of good processability, high thermal stability, high toughness, and high chemical resistance, PA is used widely to produce microgears. Some reports have described the use of carbon fiber reinforced nylon66 microgears in highly stressed tooth parts, whereas neat nylon66 is used in hub parts. Numerous reports have described experimental investigations of microgear production with determination of the optimum conditions for HDPE, PP, POM, and COC, particularly addressing microgear mechanical properties and geometry. Actually, PEEK is used for flexspline parts for a harmonic gear drive. Other tiny products in such cases of microdisks with weight of less than 1 mg can also be produced using micro-injection molding (Ito et al. 2006). In one study, POM, PP, and PC were used. Higher-order structures and physical properties of the microdisks were investigated (Fig. 4). For PC, birefringence in the flow direction (FD–FD') plane was low at the microdisk edge (at the flow end). It became higher between the gate and the edge. Birefringence showed the highest value at 0.1 mm thickness and obtained negative values at 0.3 and 0.5 mm thickness. At this end of the flow position, polymer flowed along the circumference of the microdisk shape. Higher molecular orientation was observed along this direction.

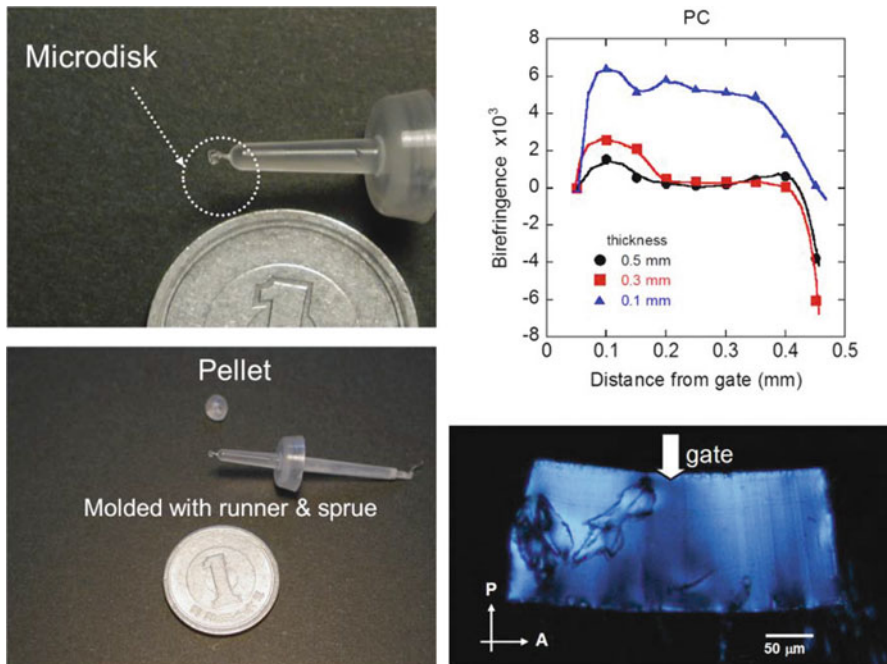


Fig. 4 Microdisk product with birefringence property

19.3.4 Products with Micro-/Nanosurface Structures

Replication products with quality improvement have been demanded for devices that require high precision and high performance. Especially, micro-/nano-level production control is extremely important for optical devices, information and communication devices, and medical applications. Replication methods using micro-/nano-injection molding can alleviate shortcomings of conventional injection molding. For example, conventional injection molding has caused uneven surface replication and structural distribution, which are daunting obstacles against the production of optical devices such as optical memory disks such as CDs and DVDs, pick-up lenses, and optical light guides.

The case study presented in this section clarifies the processability of micro-/nano-injection molding and the capability of the replication of micro-/nanostructures on the optical plastics. Optical polymers of four types were used for one study: COC, PP, PC, and PMMA (Ito et al. 2009). Micropatterns of microgrids and lines and spaces, and nanopatterns of line and spaces, were designed, respectively, for the mold (Fig. 5). Results show that the height replication ratio of micro-/nanopatterns increased concomitantly with increasing injection speed, injection temperature, mold temperature, and holding pressure. Higher optical anisotropy near the gate than at other positions was observed. For the micropatterns, results show that the convex part on the replicated surface exhibited lower molecular orientation in this feature. In the case of nanopatterns, negative birefringence in the flow direction was observed as higher than at the skin–shear region because the molecular orientation axis was oriented along the thickness direction during deformation in the de-molding step. Nanopatterns showed high thermal stability with annealing temperature 20 °C below T_g .

Rapid solidification in micro-/nano-injection molding is an important phenomenon hindering the replication of micro-/nanostructures. Even if the operability and processability can be enhanced by increasing the injection temperature, the cycle time lengthens. Programming a high injection speed also has a strong effect on the final products. Heat transfer development must be investigated for micro-/nano-injection molding. Replication of a PC surface using zirconia ceramic as the heat insulator mold has been reported (Kayano et al. 2011). Replicated micro-/nanostructures on a PC surface showed higher light transmission because of the better replication capability with less light reflection at the surface than with a conventional mold. Moreover, lower molecular orientation of the molded products from the insulation mold was obtained in comparison to those from a conventional mold. Surface replication by micro-/nano-injection molding of polystyrene (PS) was performed using 30-nm-diameter anodic aluminum oxide (AAO). Results showed that high replication capability of nanorod surface features with 30 nm diameter is obtainable. Results suggest that replication accuracy can be improved using a heat insulator and a higher flow grade of polymers (Ito et al. 2011).

Surface replication using micro-/nano-injection molding was applied to polymer composites as it was for powder injection molding of metals. This method enables near-net-shape fabrication of microstructures. Development of this method emphasizes reduction of posttreatment processes. For example, replication of PP/hexagonal

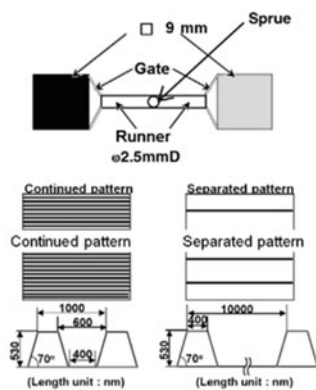
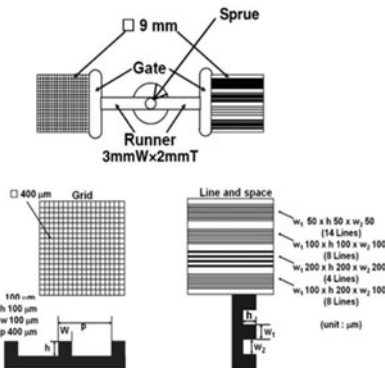
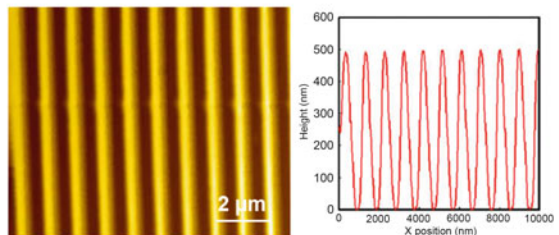
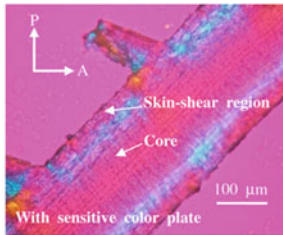
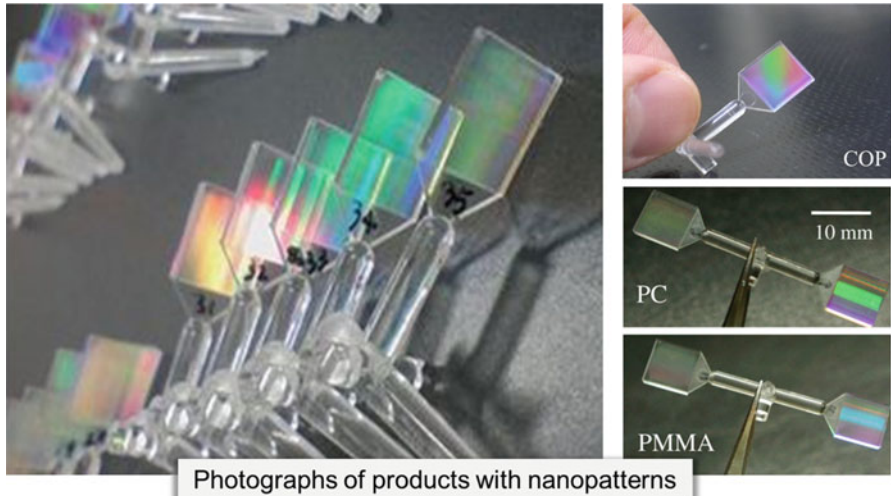


Fig. 5 Products with micro-/nanopatterns

boron nitride (h-BN) composites has been reported. The mold shape of lines and spaces in the dimension of the microfeature surface of 10–20 μm width \times 10–40 μm height was used in an experiment described in the literature (Ito et al. 2007). The replication ratio of the micropatterns and flow length of composite molded products was improved by compounding the h-BN filler. Thermal diffusivity increased concomitantly with increasing h-BN content. However, the thermal property was mainly dependent upon the h-BN filler orientation. The result suggests the importance of controlling the filler orientation to improve heat-release characteristics. In the area of medical application, microneedle arrays have been investigated extensively in recent decades with application for control of drug release and drug delivery. Generally, polymers show lower strength than silicon, metals, ceramics, and glass, but they present better toughness than either glass or ceramic. Furthermore, lower production cost is an impressive benefit of polymer materials. Therefore, polymer materials are promising for use as alternative materials for microneedle array production. Especially, biodegradable polymers are extremely interesting because of their outstanding biocompatibility, biodegradability, low cost, and low toxicity. Ito and co-workers (2010–2017) fabricated numerous microneedle array structures (50–100 μm feature size) on various polymer surfaces such as PP, PC, PMMA, PLLA, and PLA/hydroxyapatite (HA) composite. Maximum replication ratios reaching 100% can be obtained perfectly in this work. In addition, several plastic molding processes, not only micro-/nano-injection molding, which they have performed but also cover to micro-/nano-imprinting for both plate-to-plate and roll-to-roll systems for the replication of microneedle arrays. For hydrophobic surface application, micro-hierarchical structures can also be replicated using micro-/nano-injection processes (Chu et al. 2014). Figure 6 presents a scanning electron microscope (SEM) image showing PMMA with well-ordered arrays. The maximum value of water contact angle about 130° is obtainable. The water contact angles increased concomitantly with increasing height replication ratios of the hybrid structures.

In micro-/nano-injection molding process, both the injection step and cooling step of polymer materials progressed simultaneously because molten polymer is injected at high temperatures into a mold cavity at a low temperature. Therefore, surface layer solidification is expected to occur at the boundary area between mold wall surface and polymer (Fig. 7). Formation of a solidified surface layer influences the injection ability of molten polymer, the shape accuracy, and features of the molded product. Therefore, it is difficult to transcribe micro-/nanostructures perfectly at the mold surface. For thickness of the solidified surface layer that is sufficiently high against the gap of the mold cavity, a large pressure drop in the filling step occurs. For that reason, the molded products become imperfect (short shot). Moreover, polymer molecules at the boundary area and main current are stretched extremely in the flow direction, which influences the molecular orientation. Molecular orientation causes mechanical and optical anisotropy. It often disrupts reduction of the product quality of precision parts and optical devices. For this reason, controlling the solidified surface layer growth becomes extremely important to improve the molded product quality. The other fatal issue is the air trap within the mold cavity. Simulation data that agree with the experimentally obtained results demonstrate the possibility

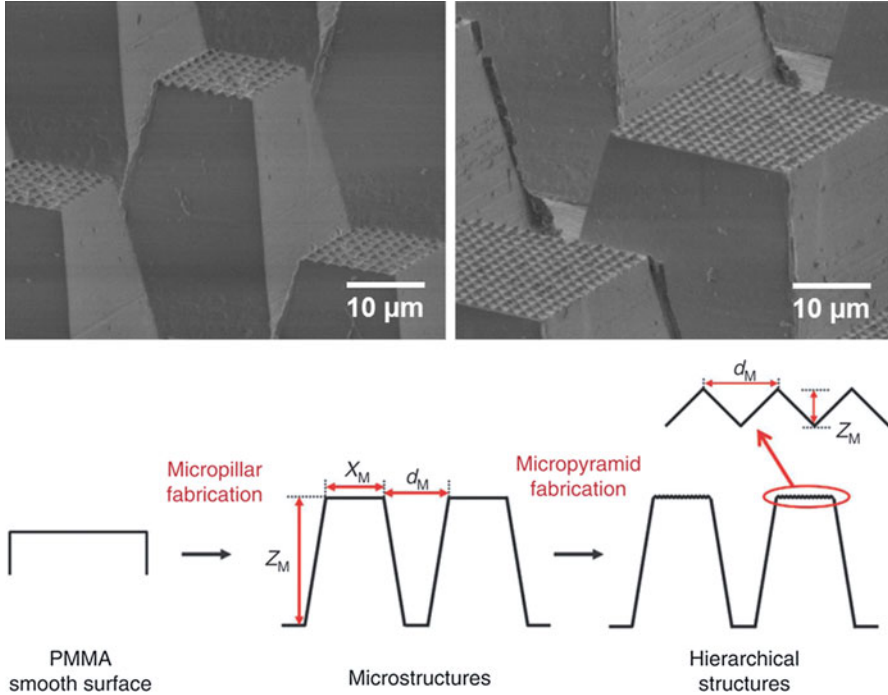


Fig. 6 Microhybrid structures of pyramid arrays

of air trap generation during the filling step in the micro-/nano-injection molding process (Fig. 7) (Tada et al. 2010). Results demonstrated that the air traps occurring during the filling step are strongly related to the replicated shape and replication rate. Overcoming this difficulty in the case of the solidification requires separate operational steps for transcriptions of the tiny shape step and the cooling step. In addition, high precision of the compression step with high capability of the vacuum system must be developed to resolve air trap difficulties. From these perspectives, thermal micro-/nano-imprint processes have been introduced.

19.3.5 Summary and Outlook

Surface replication technology using micro-/nano-injection molding can be used effectively to fabricate structures of various kinds in this scale range, as described in reports of earlier studies. This process is also widely recognized as a rapid production method with high precision. Nevertheless, this process retains important limitations to replication capability because of rapid solidification and air trapping inside the mold cavity. Rapid solidification occurs at the boundary area between the mold wall surface and polymer. These difficulties have caused the flowing ability of the melted polymer, by which incomplete filling of material within the mold occurs. For this reason, replacement of a conventional mold by a metal material or a heat-insulated mold

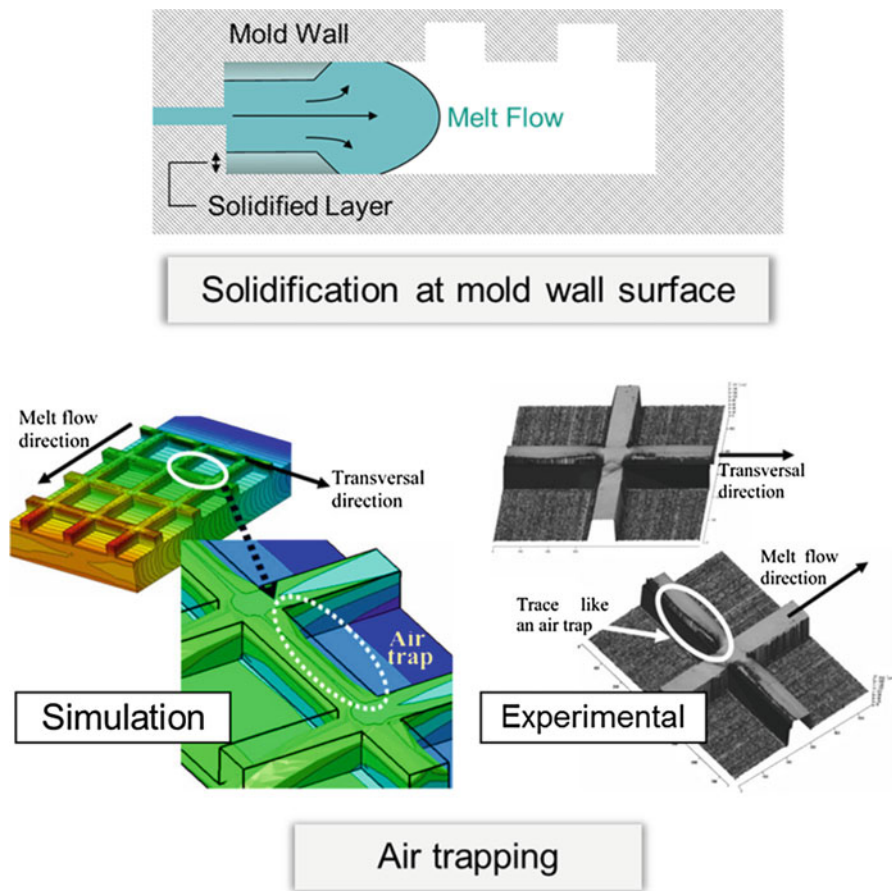


Fig. 7 Surface solidification at mold wall (upper) and air trap difficulties (lower) in micro-/nano-injection molding process

such as the ceramic material has attracted great interest. In addition, the de-molding step affects the molecular orientation of the mold products, which is important for the development of the high-precision devices such as optical devices and information and communication devices. In this field, avoiding uneven surface replication and control of the molecular orientation of the molded products are important.

19.4 Micro-/Nano-imprinting

19.4.1 Background and History

Micro-/nano-imprinting was first introduced in 1995 because it presented benefits in terms of simple, low-cost, and high-throughput processing (Taniguchi et al. 2013). In terms of the replication capability, micro-/nano-imprinting has been shown to

have more benefits than micro-/nano-injection molding for the following reasons: higher transcription of micro-/nanostructures, lower residual deformation, and lower residual molecular orientation. This process is effective for the production of micro-/nanostructures on a thin substrate such as a thin film, which cannot be produced easily using micro-/nano-injection molding process. Moreover, it can resolve difficulties of rapid solidification and air trapping in micro-/nano-injection molding as described above. Micro-/nano-imprinting can fabricate several 2D and 3D structures with feature sizes ranging from micrometer down to sub-10-nm scale. In actuality, they have already been fabricated. However, it is noteworthy that micro-/nanostructures must have a straight shape in accordance with the stroke direction of the stamp. Two main categories of micro-/nano-imprint processes exist based on the phase change system: thermal micro-/nano-imprinting (hot embossing) and UV micro-/nano-imprinting. The first introduction of thermal micro-/nano-imprint lithography was expected for replicating a softened thermoplastic resist. Later, with irradiation of UV light into the imprint machine, UV micro-/nano-imprinting was developed with suitability to UV-curable materials. Based on the production procedure and contact type between mold and polymer, thermal and UV micro-/nano-imprint processes are definable in categories of three types: plate-to-plate (batch process), roll-to-plate (semicontinuous process), and roll-to-roll (continuous process). Processes of these three types have been presented in terms of their benefits and shortcomings. This section introduces plate-to-plate and roll-to-roll processes for thermal and UV micro-/nano-imprinting.

19.4.2 Thermal and UV Micro-/Nano-imprinting

In a top-down approach, the surface pattern of a stamp is transferred to a polymer surface by mechanical compression for shaping structures. In terms of thermal micro-/nano-imprinting, a shaping pattern can be transferred by variation of polymer film thermomechanical properties by heating and cooling processes. A process diagram of thermal micro-/nano-imprinting is presented in Fig. 8.

During thermal micro-/nano-imprinting, the polymer substrate and stamp are heated higher than T_g of the polymer or a temperature required for shape transference. In this step, the polymer substrate must be softened or fluidized to fill into the mold cavities when driven by sufficient imprint pressure and time. This elevated temperature has caused material rheology including reduction of viscosity, elastic modulus, and yield strength. In thermal micro-/nano-imprinting, several imprint pressures are often applied. The stamp must have constant strength under compression, even at elevated temperatures. For this reason, silicon, silicon carbide, glassy carbon, tantalum, and electroplated nickel (often used in micro-/nano-injection molding) are often used as stamps for thermal micro-/nano-imprinting. After transcription or transference of the structures from the mother stamp to the polymer, the stamp is cooled to below T_g to promote the solidification of the polymer. Subsequently, it can be removed from the stamp (de-molding). In this case, the heating-cooling steps with a short cycle time become an important target for

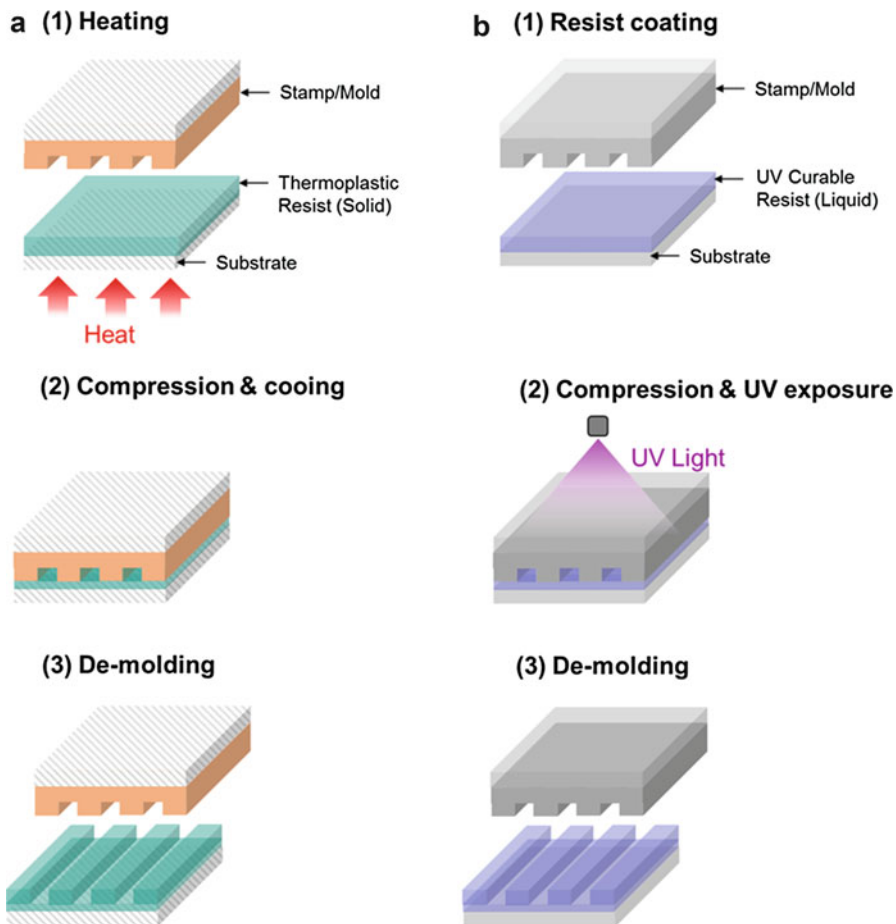


Fig. 8 Typical imprint steps for (a) thermal and (b) UV micro-/nano-imprinting

productivity improvement. However, under a cooling step, the patterned structures might be destroyed because of the shrinkage difference between the polymer, and the stamp is enlarged especially when the substrate is large. In addition, the de-molding step becomes difficult when applying the high imprint temperature and imprint pressure. Therefore, numerous studies have specifically investigated the development of de-molding steps, especially in the scope of the mold-releasing agents and the design of mold structures.

Nowadays, progress in thermal micro-/nano-imprinting has been growing rapidly. The Research Center for GREEN Materials and Advanced Processing (GMAP) presented their capability of replicating various structures with the variety of applications. For example, common polymers and biodegradable polymers such as PP, PC, and polyvinyl alcohol (PVA) were selected to produce microneedle arrays with

50–100 μm feature size. Results revealed that the high capability of thermal micro-/nano-imprinting with maximum replication ratios structures up to 95% is obtainable. In addition, PVA microneedle arrays coated with hyaluronic acid (HA) can be fabricated using this process (Fig. 9). Hydrophobic surfaces have been produced with various design structures using thermal micro-/nano-imprinting. For example, the hierarchical structure with micro-/nanostructures (hybrid structure) of PS having high water-repellent properties has been produced (Fig. 9) (Chu et al. 2015). In this fabrication technique, a concave microstructure was first produced by precision machine tooling followed by vertical patterning aligned nanostructures using thermal micro-/nano-imprinting with an AAO nanoporous template (25 nm pore diameter). Using AAO templates, they can also, respectively, produce PS and PP nanofiber arrays (50 nm diameter) with ultrahigh aspect ratios up to 1,000 and 2,600 (Muanchan et al. 2017). Vertically aligned nanostructures of polymer composite and polymer blend materials were also produced using AAO templates (100 nm diameter). Highly durable structures in the shape of micropyramid arrays

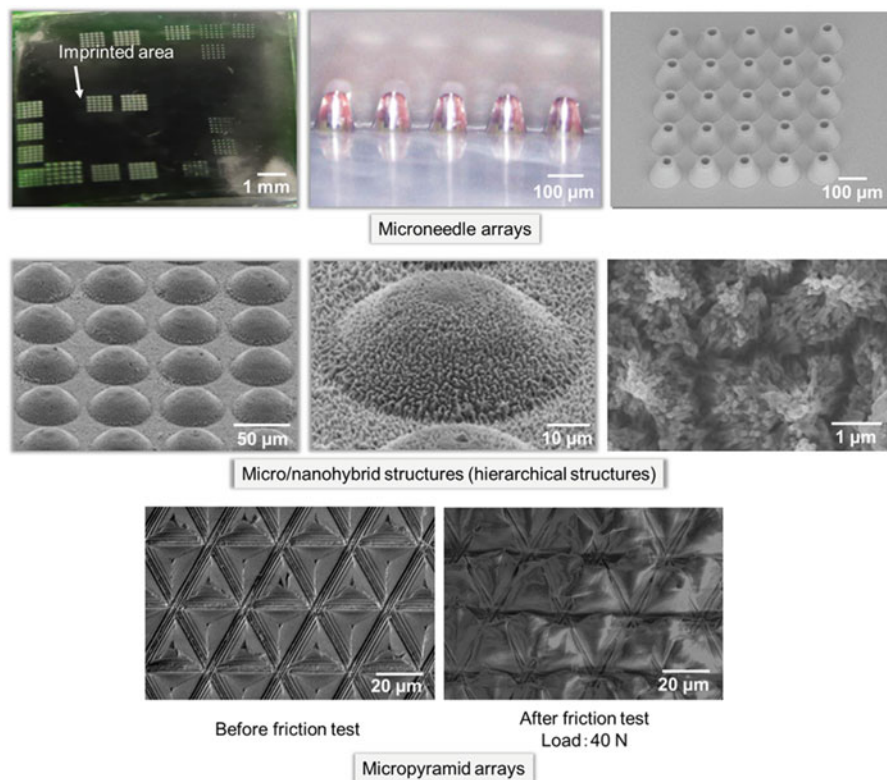


Fig. 9 Products with several micro-/nanostructures obtained using thermal micro-/nano-imprinting (plate-to-plate) (Source: Research Center for GREEN Materials and Advanced Processing (GMAP), Yamagata University)

are producible with the superhydrophobic property of low-density polyethylene (LDPE) (Fig. 9). It is particularly interesting that they can also replicate microstructures on natural rubber surfaces including micropyramid arrays and microlines and spaces (Fig. 9).

In the case of UV micro-/nano-imprinting, it can be operated by shaping a liquid of curable resin followed by UV curing for hardening. The outline of UV micro-/nano-imprint processes is presented schematically in Fig. 8. Two main processing steps are the imprint step (compression) and the UV-curing step. Hardening of the resist because of cross-linking under the UV-curing process is similar to the cooling step in thermal micro-/nano-imprinting. In the case of the stamp, it must be transparent to UV light: quartz or sapphire is often used. UV micro-/nano-imprinting has several benefits: it can operate at room temperature, which eliminates thermal expansion issues. The low viscosity of liquid photoresist (UV-curable material) allows imprinting conditions to be conducted at lower imprint pressures with shorter imprint times than thermal micro-/nano-imprinting. Therefore, UV micro-/nano-imprinting can eliminate the cycle time of heating–cooling steps that enhance the productivity, which is preferred for an industrial scale. Using a batch method, multiple layers such as segmental microchannels that can be applied for polymer optical waveguide materials can be fabricated using UV micro-/nano-imprinting (Fig. 10).

Comparison of typical processes used for thermal micro-/nano-imprinting and UV micro-/nano-imprinting are presented in Table 2 (Schift and Kristensen 2010).

Recently, thermal and UV micro-/nano-imprinting hybrid technology has been introduced by Obducat (Lund, Sweden). This machine can operate effectively at the simultaneous state for thermal and UV functions. During the imprint step, the applied

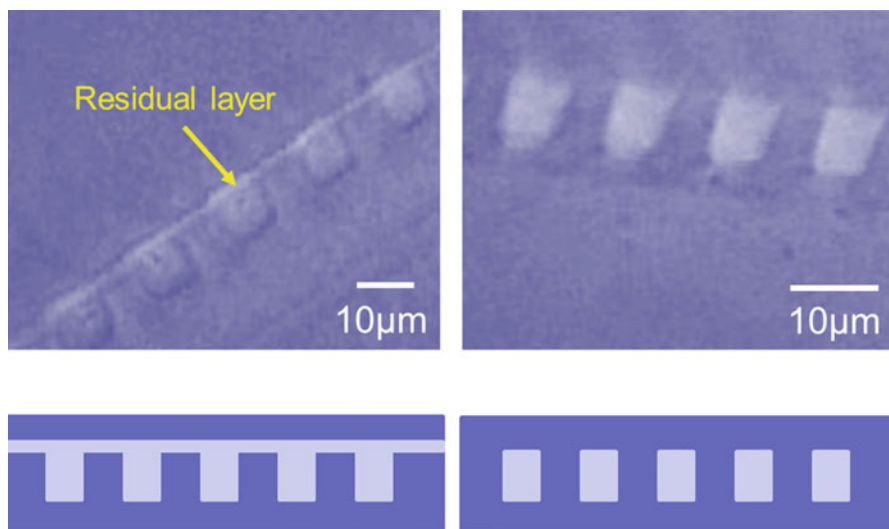


Fig. 10 Segmented microchannels obtained using UV micro-imprinting (Source: Research Center for GREEN Materials and Advanced Processing (GMAP), Yamagata University)

Table 2 Characteristics of thermal micro-/nano-imprinting (hot embossing) and UV micro-/nano-imprinting

Characteristics	Thermal micro-/nano-imprinting	UV micro-/nano-imprinting
Process and procedure	Melting on polymer film Compression of stamp Cooling step De-molding step	Pouring liquid resin Compression of stamp (low pressure) UV exposure step De-molding step
Resist material	Solid, thermoplastics	Liquid, UV-curable
Stamp material	Si, SiO ₂ , Ni	Glass, SiO ₂ Transparent
Imprint pressure (bar)	20–100	0–5
Imprint temperature (°C)	100–200	20–30 (ambient)
Imprint time (min)	A few s to a few min	Less than 1 min
De-molding temperature (°C)	20–80	20–30 (ambient)
Stamp contact	Facilitated by bending	Planarization layer

heat softens the polymer resist, forming a solid at temperatures lower than T_g , whereas the UV-curing process can solidify the resist by cross-linking. Ito and co-workers (GMAP) investigated hybrid imprinting for a curved surface, which is important for the development of smart contact lenses. They require circuit wiring on the lens itself.

19.4.3 Rapid Fabrication Using Roll-to-Roll Micro-/Nano-imprinting

Plate-to-plate and roll-to-plate imprinting present numerous benefits with high imprinting force and small machine size. With the high imprinting force and the higher capability of the de-molding step, plate-to-plate and roll-to-plate imprinting can produce higher-resolution imprinted structures than roll-to-roll method can, especially in terms of the high aspect ratios. However, roll-to-roll imprinting is particularly interesting: it can offer outstanding production rates with extremely high throughput that is suitable for manufacturing for all entire processes when compared to either plate-to-plate or roll-to-plate imprinting. These merits of roll-to-roll imprinting have led to the investigation of processes to improve the process capability for use in industrial applications (Taniguchi et al. 2013). For instance, the Technical Research Center of Finland has achieved imprint rates up to 20 m/min using wrapped nickel-electroplated foil on the imprint roller. Tokyo University of Science has proposed that roll-to-roll imprinting can operate with maximum imprinting speeds of 18 m/min using high-intensity UV-LED illumination. Yonsei University expanded the roll-to-roll imprinting capability for replicating rigid materials such as glass. Furthermore, the Research Center for GREEN Materials and Advanced Processing (GMAP) at Yamagata University has produced several micro-/nanoproducts with higher-order structures using roll-to-roll

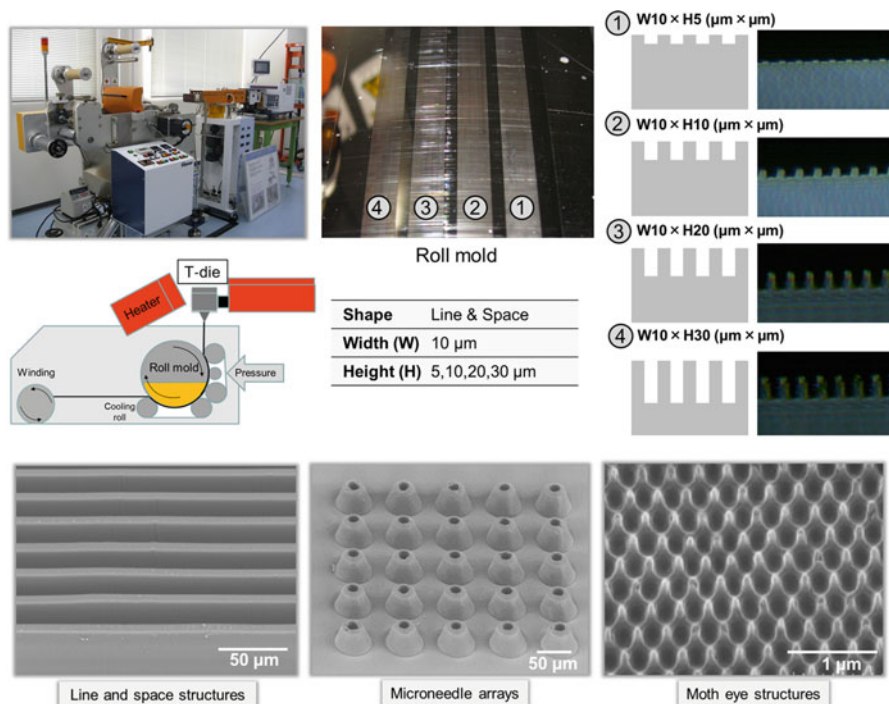


Fig. 11 Roll-to-roll thermal micro-/nano-imprinting system (Source: Research Center for GREEN Materials and Advanced Processing (GMAP), Yamagata University)

imprinting as shown in Figs. 11 and 12 (thermal and UV processes). For example, structural development of microstructures of lines and spaces can be clarified simply using the hybrid aspect ratios of the stamp (Egawa et al. 2014). In this experiment, the lines and spaces (10 μm width \times 30 μm height) are producible with the maximum replication ratio of 100% at the roll speed of 0.7 m/min. Microneedle arrays have also been produced with the maximum replication ratio about 95% at the roll speed of 0.5 m/min. In addition, nanostructures inspired by a moth eye (300 nm feature), which applies to anti-reflection products, can be produced at 0.5 m/min roll speed.

Although roll-to-roll imprinting has great value for production process at an industrial level, it still entails many difficulties that demand research and development, especially in the de-molding step. In the case of the roll-to-roll thermal micro-/nano-imprinting, incompletely imprinted structures are often obtained because of roll mold destruction. For example, incomplete microneedle structures of PP materials were found when the operational conditions were inappropriate. In the study described here, cross-linked liquid silicone rubber (LSR) was used selectively as the mold. The LSR mold destruction occurred when operating with an imprinting temperature at which storage modulus of PP is much higher than LSR during the de-molding and cooling steps, as shown in Fig. 13. This

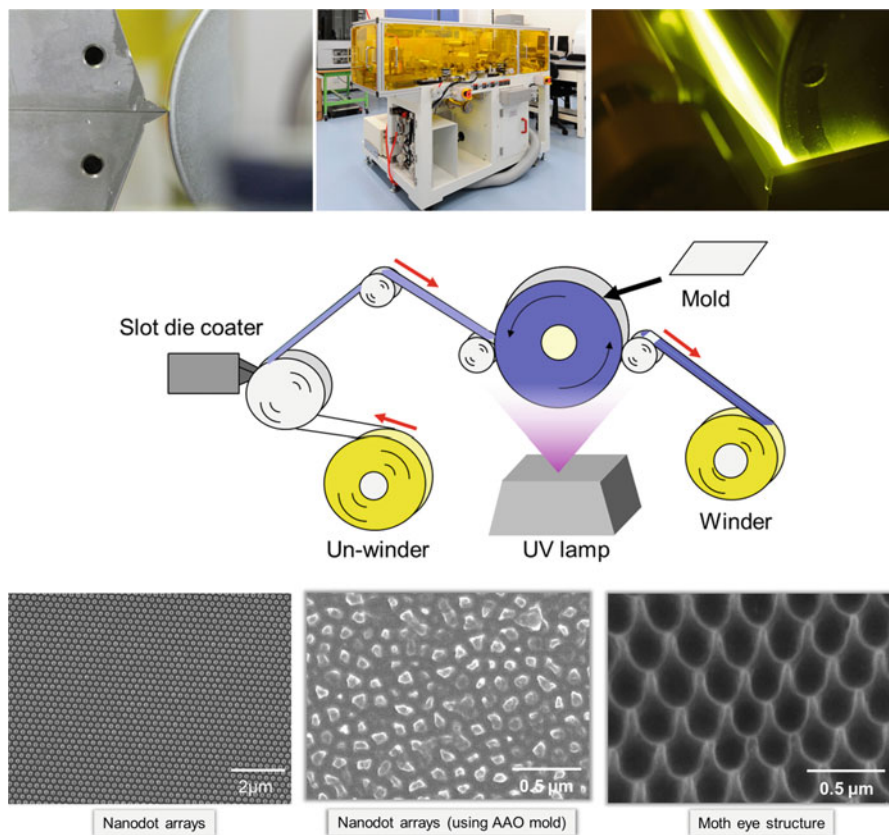


Fig. 12 Roll-to-roll UV micro-/nano-imprinting system (Source: Research Center for GREEN Materials and Advanced Processing (GMAP), Yamagata University)

difficulty can be resolved by increasing the imprinting temperature, which can maintain the condition which PP has a lower storage modulus than the LSR mold during molding step. In the case of roll-to-roll UV micro-/nano-imprinting, incomplete or destroyed imprinted structures might occur, especially when the cycle time of the imprint is increased. This difficulty results from contamination occurring on the mold surfaces with residual materials from the previous cycles (Fig. 14). Operational roll-to-roll UV micro-/nano-imprinting also requires feasible conditions for peeling-off or de-molding processes (Schift 2008). Earlier reports clarified that conversion of the UV resin is necessary during the de-molding step in terms of the UV intensity and imprinting speed (Taki et al. 2016) (Fig. 15). Another important issue in roll-to-roll imprinting is that the fabrication of roll molds is difficult and expensive. Widely used materials for producing conventional molds include polyurethane acrylate (PUA), polytetrafluoroethylene (PTFE), and ethylene tetrafluoroethylene (ETFE).

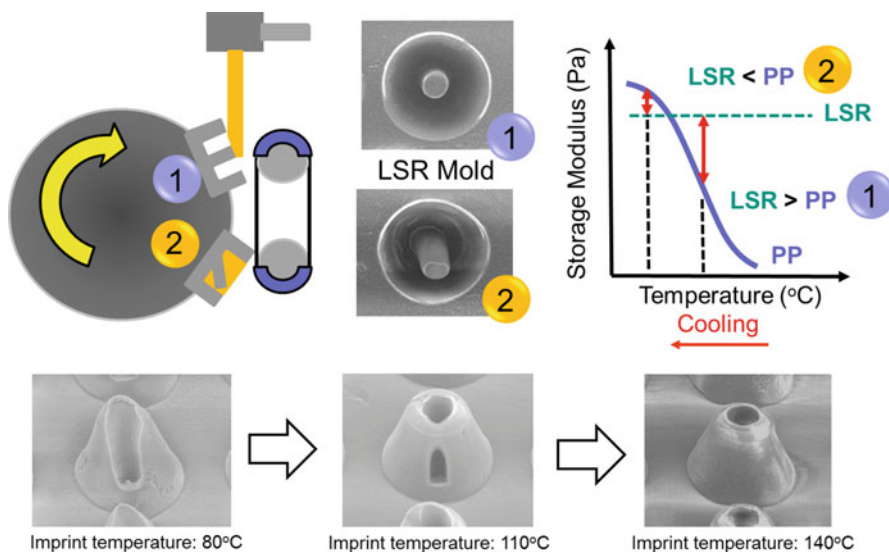


Fig. 13 Difficulties of roll-to-roll thermal micro-/nano-imprinting (Source: Research Center for GREEN Materials and Advanced Processing (GMAP), Yamagata University)

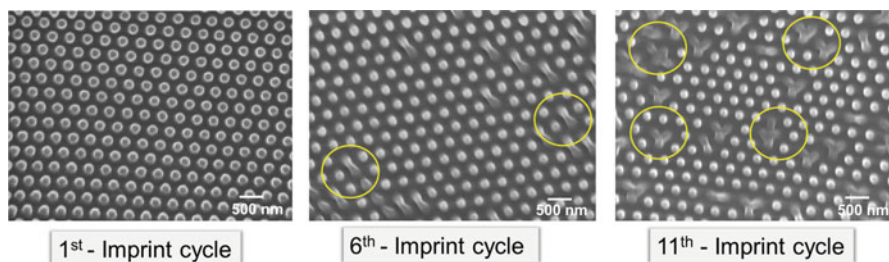


Fig. 14 Defect of process capability of roll-to-roll UV micro-/nano-imprinting (Source: Research Center for GREEN Materials and Advanced Processing (GMAP), Yamagata University)

19.4.4 Summary and Outlook

In terms of comparison of replication performance, micro-/nano-imprinting offers both benefits and shortcomings compared to micro-/nano-injection molding. Plate-to-plate imprinting is more capable in terms of precision, but it is not preferred for processes that require a high rate of production. Roll-to-roll imprinting can offer rapid production with a large imprint area but with the attendant difficulty in replicating the high aspect ratios and other complex structures. Recently, many research groups are striving to development roll-to-roll imprinting because of its applicability to rapid fabrication processes.

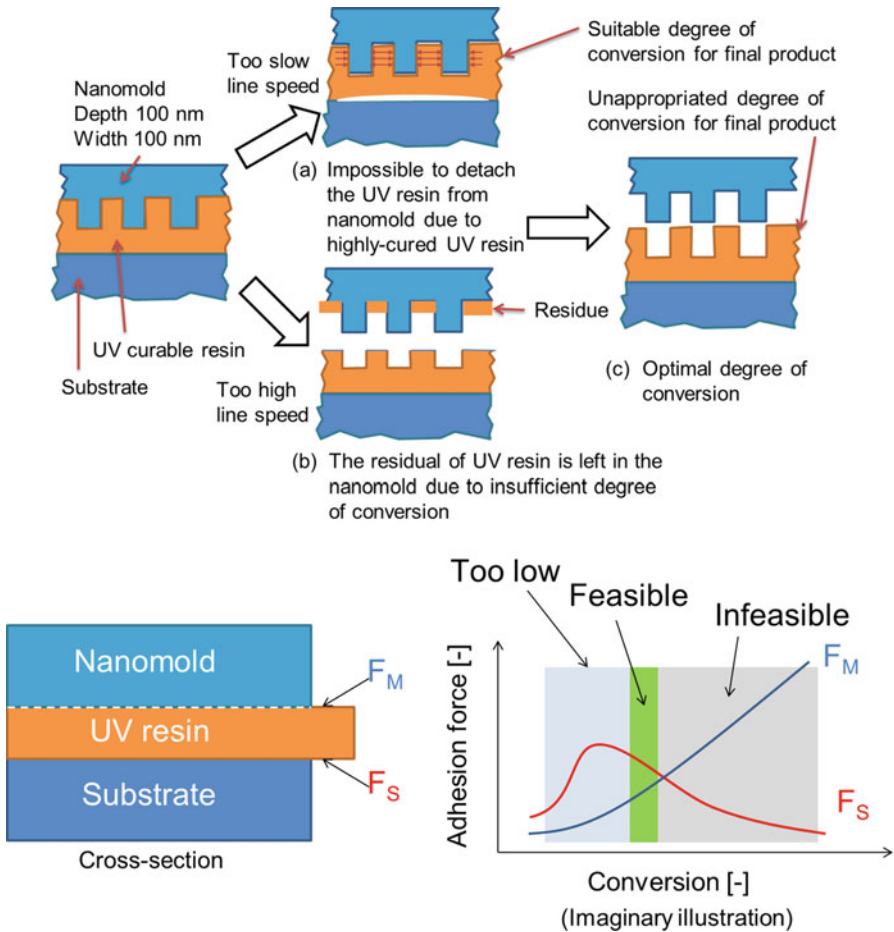


Fig. 15 Reduction of process capability of roll-to-roll UV micro-/nano-imprinting

19.5 Future Trends of Replication Technology

Products with micro-/nanostructures are attracting attention: various electronic devices, medical devices, optical devices, MEMS, and sensor devices. Many methods are transferable to mass production scales at the industrial level. For example, functional films having microsurface structures with ultra-water/oil repellency and high friction properties can be commercialized in the field of food packaging, coverings of electrical devices, and so on. In this field, improvement of mechanical robustness such as the durability of microstructures holds potential for the development for some cases of materials and structures. Some parts are indeed being transferred to the industrial level. In the medical field, micro-/nanofluidics in the microchannel of the microchips are under investigation for use in diagnostic

applications. Microneedle arrays incorporate various biodegradable polymers. Nanopillar arrays have been inspired by the characteristics of gecko feet, offering high friction property together with high water repellence is still attracting development for novel applications that include bactericides (these nanopillar arrays are inspired by cicada wings). In the case of optical devices, microlenses and the optical waveguides continue to attract attention for improvement of precision production capabilities. Resists are used for photolithography and in the field of electronics. Printed circuit boards are used for both of flat and curved substrate films. Furthermore, various novel applications have been created through inspiration from nature and architectural engineering design. To date, progress in replication technology by polymer molding processes has developed continuously in research areas such as suitable materials for molds and resins, machine design, characterization and evaluation technologies, molding technique, and de-molding techniques. For sustainable development, many research groups are specifically pursuing environmentally friendly products offering high moldability, simple processing, short-time, long life-cycle time, and continuous processing. In the field of micro-/nanotechnology, China has a strong position in the development of micro-/nanotechnology with many publications, patents, and reports. Future trends in replication technology in this area are expected to include exploration of novel materials that enable micro-/nanomolding processes (i.e., polymer composites, polymer blends, novel thermoplastic elastomers, rubbers), new die processing, new molding apparatus and processing technology, surface treatment technology, process monitoring and numerical analysis, precise evaluation technology for higher-order structures (especially in physical properties), and development of observation technology.

References

- Bandić ZZ, Litvinov D, Rooks M (2008) Nanostructured materials in information storage. *MRS Bull* 33:831–834
- Chang H, Kim Y (2000) UV–LIGA process for high aspect ratio structure using stress barrier and C-shaped etch hole. *Sens Actuators A* 84:342–350
- Chu D, Nemoto A, Ito H (2014) Hydrophobic property of hierarchical polymer surfaces fabricated by precision tooling machine. *J Polym Eng* 34:1–6
- Chu D, Nemoto A, Ito H (2015) Biomimetic superhydrophobic polymer surfaces by replication of hierarchical structures fabricated using precision tooling machine and anodized aluminum oxidation. *Microsyst Technol* 21:123–130
- Egawa T, Taki K, Ito H et al (2014) Surface replication and higher order structure of amorphous polymer film with nano surface structure fabricated by roll to roll imprinting process. Paper presented at international symposium on fiber science and technology, Tokyo, 29 Sept–1 Oct 2014
- Giboz J, Coppo T, Mélé P (2007) Microinjection molding of thermoplastic polymers: a review. *J Micromech Microeng* 17:R96–R109
- Holzer C, Gobrecht J, Solak H (2010) Replication of micro- and nanostructures on polymer surfaces. *Macromol Symp* 296:316–323
- Ito H, Yagisawa Y, Saito T et al (2005) Structural development in thin-wall injection molding process. *Theor Appl Mech Japan* 54:263–268
- Ito H, Kaxama K, Kikutani T (2006) Micro-scale disk in ultra miniature injection molding. *SPE ANTEC Tech Paper*, Charlotte, May 7–11 2006

- Ito H, Kazama K, Kikutani T (2007) Surface replication and structural development in micro-molding for micro/nanocomposites. Paper presented at the 2007 International manufacturing science and engineering conference (MSEC2007), Atlanta, 15–18 Oct 2007
- Ito H, Suzuki H, Kikutani T et al (2009) Polymer structure and properties in micro- and nano-molding process. *Curr Appl Phys* 9:19–24
- Ito H, Haryu A, Takahagi S et al (2011) Precision polymer nano-molding with anodic aluminum template. *SPE ANTEC Tech Paper*, Boston, 1–5 May 2011
- Jarupoonphol W, Ochiai C, Takai M et al (2002) Prototyping of field emitter array using focused ion and electron beams. *Jpn J Appl Phys* 41:4311–4313
- Kaneda R, Takahashi T, Ito H (2016) Optical properties of HDPE in injection molding and injection press molding for IR system lenses. *Int Polym Process* 31:385–392
- Kaneda R, Takahashi T, Ito H (2017) Optical properties of HDPE in injection molding and injection press molding for IR system lenses part II: mold temperature and surface roughness effects on injection molding. *Int Polym Process* 32:237–244
- Kayano Y, Zouta K, Ito H (2011) Replication properties and structure of PC in micromolding with heat insulator mold using zirconia ceramic. *Int Polym Process* 26:304–312
- Kim M, Ha D, Kim T (2015) Cracking-assisted photolithography for mixed-scale patterning and nanofluidic applications. *Nat Commun* 6:6247. (1–8)
- Li X (2016) Bactericidal mechanism of nanopatterned surfaces. *Phys Chem Chem Phys* 18:1311–1316
- Li Z, Chen Y, Zhu X et al (2016) Fabrication of single-crystal silicon nanotubes with sub-10nm walls using cryogenic inductively coupled plasma reactive ion etching. *Nanotechnology* 27:365302. (1–9)
- Lutton REM, Larrañeta E, Kearney M et al (2015) A novel scalable manufacturing process for the production of hydrogel-forming microneedle arrays. *Int J Pharm* 494:417–429
- Muanchan P, Kyotani T, Ito H et al (2017) One-dimensional polymer nanofiber arrays with high aspect ratio obtained by thermal nanoimprint method. *Polym Eng Sci* 57:214–223
- Naemi A, Meindl JD (2009) Carbon nanotube interconnects. *Annu Rev Mater Res* 39:255–275
- Otmani R, Kandoussi K, Kamal MR et al (2016) Morphology and flow effect of micro-injection-molded plastic microgears. *Polym Adv Technol* 28:511–515
- Schift H (2008) Nanoimprint lithography: an old story in modern times? A review. *J Vac Sci Technol B* 26:458–480
- Schift H, Kristensen A (2010) Nanoimprint lithography – patterning of resists using molding. In: Bhushan B (ed) *Springer handbook of nanotechnology*. Springer, Berlin/Heidelberg, pp 271–312
- Tada K, Fukuzawa D, Ito H et al (2010) Numerical simulation for flow behaviour on micro- and nanomoulding. *Plast Rubber Compos* 39:321–326
- Taki K, Kondo S, Ito H (2016) Effects of UV intensity, line-speed, and light distribution on conversion and surface elastic modulus of roll-to-roll UV-cured film. *J Photopolym Sci Technol* 29:835–840
- Taniguchi J, Ito H, Mizuno J, Saito T (eds) (2013) *Nanoimprint technology: nanotransfer for thermoplastic and Photocurable polymers*. Wiley, Chichester
- Xia Q, Chou SY (2008) Fabrication of sub-25 nm diameter pillar nanoimprint molds with smooth sidewalls using self-perfection by liquefaction and reactive ion etching. *Nanotechnology* 19:455301. (1–4)
- Xie H, Huang H, Peng Y (2017) Rapid fabrication of bio-inspired nanostructure with hydrophobicity and antireflectivity on polystyrene surface replicating from cicada wings. *Nanoscale* 9:11951–11958
- Zhang Y, Lu J, Shimano S et al (2007) Nanoimprint of proton exchange membrane for MEMS-based fuel cell application. Paper presented at 6th international IEEE conference on polymers and adhesives in microelectronics and photonics, Odaiba, 15–18 Jan 2007
- Zhang Y, Lu J, Wang Q et al (2009) Nanoimprint of polymer electrolyte membrane for micro direct methanol fuel cell application. *ECS Trans Micro Power Sources* 16:11–17



Precision Molding of Microstructures on Chalcogenide Glass for Infrared Optics

20

Tianfeng Zhou

Contents

20.1	Introduction	636
20.1.1	The Application of Chalcogenide Glass in Infrared Optics	636
20.1.2	Methods to Fabricate Microstructures on Chalcogenide Glass	638
20.1.3	Precision Molding Technique	639
20.2	Modeling and Simulation of Chalcogenide Glass Microstructure Molding	641
20.2.1	Modeling of Viscoelastic Constitutive of Chalcogenide Glass	642
20.2.2	Simulation of Microstructure Molding Process	643
20.3	Molding Process of Microstructures on ChG	647
20.3.1	Chalcogenide Glass Molding Machine	647
20.3.2	Chalcogenide Glass Molding Condition and Quality Control	648
20.4	Summary	658
	References	658

Abstract

Chalcogenide glass (ChG), as an alternative material in place of single-crystal germanium, is increasingly used in thermal imaging, night vision, and infrared guidance systems, etc., and microstructure array on the infrared component is widely used in micro-optical systems owing to their excellent formability through precision glass molding (PGM), which can achieve low cost and high efficiency compared with other microstructural manufacturing technologies. To describe the thermomechanical properties of ChG, the viscoelastic constitutive of ChG is modeled and used in finite element simulation to study the influence of process parameters on the forming stress. The processing parameters are studied

T. Zhou (✉)

Key Laboratory of Fundamental Science for Advanced Machining, Beijing Institute of Technology, Beijing, China

e-mail: zhoutf@bit.edu.cn

© Springer Nature Singapore Pte Ltd. 2018

J. Yan (ed.), *Micro and Nano Fabrication Technology*, Micro/Nano Technologies,

https://doi.org/10.1007/978-981-13-0098-1_20

635

to reduce the occurrence of microdimples and optimize the molding conditions. Finally, microstructure arrays are molded using spherical ChG preform and the optimal molding materials are identified.

Keywords

Chalcogenide glass · Microstructure array · Precision glass molding · Finite element simulation · Microdimples

20.1 Introduction

Infrared materials are gaining growing attention for their wide applications, such as thermal imaging and night vision (Tang et al. 2010; Bureau et al. 2004). In the past decades, single-crystal germanium has been used exclusively in infrared optical systems though it is rare and expensive (Zhang et al. 2003a). Chalcogenide glass (ChG), which is a kind of artificial material made of mainly chalcogens (S, Se, and Te) and some other elements, shows a wide transmission wave band from near to far infrared wavelength. In comparison, oxide glasses are limited to near and intermediate infrared wave band because of the strong infrared absorption of metal-oxygen bond vibrations. Compared with single-crystal germanium, ChG is much more economic and has more excellent properties of athermalization and achromatism (Yu 2007), and it is deemed as an alternative for single-crystal germanium in various infrared systems (Cha et al. 2010). Microstructure as well as microstructure array on the optical component is widely used in micro-optical systems due to its excellent optical properties and robust thermomechanical performance. The surface microstructures of the infrared optical elements can improve the infrared thermal imaging quality and eliminate the aberration, and the microstructure array is widely used to simplify and improve the optical system, achieving special requirements. ChG lenses, including spherical lens, aspherical lens, and free-form curved surface, are mainly fabricated by single-point diamond turning. Due to the limitations of the current processing technology and materials, the research of microstructures for infrared optical components is still in the initial stage.

ChG is not only an excellent infrared material but also has similar properties as optical glass, especially the high-temperature viscoelasticity and deformation characteristics. Therefore, precision glass molding (PGM) is able to form microstructures on ChG glass. It is of great significance to promote the development of processing microstructures on ChG infrared components through precision molding.

20.1.1 The Application of Chalcogenide Glass in Infrared Optics

Infrared transmittance of infrared glass is above 50%, and it can block visible light. According to the basic composition of infrared glass, it can be divided into oxide glass and ChG. Ordinary oxide glass cannot transmit the infrared radiation when the

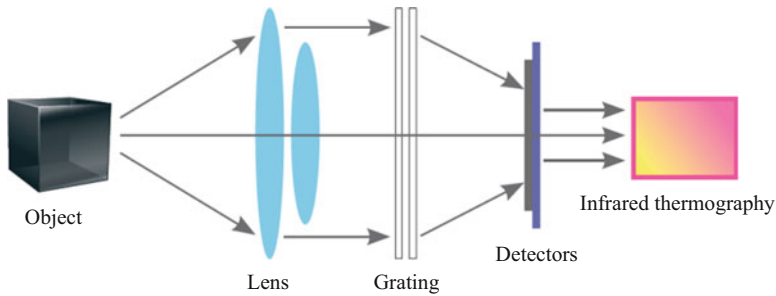


Fig. 1 Schematic diagram of an infrared thermal imaging system

wavelength is greater than $7 \mu\text{m}$, due to the strong infrared absorption of metal-oxygen bond vibrations. ChG extends the infrared transmission band from near to far infrared wavelength and has a preferable infrared transmittance. In addition, ChG has low-temperature coefficient and dispersion coefficient and unique photosensitive properties. ChG has been widely used in the infrared optical fiber sensors, infrared imaging lens, energy transmission, nonlinear optics, optical information processing, frequency multiplier, inorganic optical lithography, and other modern integrated optical systems and electronic device fields (Xue et al. 2003; Gai et al. 2010; Luo et al. 2010). ChG is considered to be the core material of the new generation of infrared optical systems.

20.1.1.1 Thermal Imaging System

Infrared thermal imaging technology is a sophisticated technology integrating optics, mechanics, electronics, and other advanced technologies (Eisenberg et al. 2000). Figure 1 shows the infrared thermal imaging system. The infrared detector and infrared lens are used to accept the infrared radiation energy distribution of measured target, which reflects in the photosensitive element of infrared detector to obtain infrared thermography. Generally speaking, the infrared thermal imaging system transforms the invisible infrared radiation of the object into the visible thermal image. The different colors of the thermal image represent the different temperatures corresponding with the heat distribution of the measured object.

Infrared detector is a very important component of infrared thermal imaging system. The detection capability of infrared detector can be improved by coupling ChG microlens array with infrared detector. Then, the incident beam of infrared radiation can be effectively converged on the photosensitive surface, which has a gathering energy effect and can improve the utilization rate of light energy. At the same time, ChG microlens array has the cold shield effect. The incident angle of infrared radiation is limited to ensure that each photosensitive element of the infrared detector has the same incident angle. In addition, each photosensitive element has the same background radiation that is greatly reduced, and the noise is dropped.

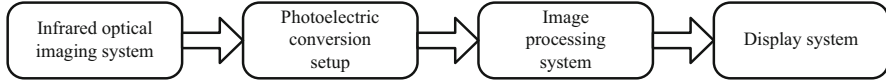


Fig. 2 Schematic diagram of a night vision system

20.1.1.2 Night Vision System

The infrared night vision apparatus consists of an infrared optical imaging system and a photoelectric conversion system. It can be divided into two types: active and passive. The former one uses infrared searchlight to irradiate the target and receives the reflected infrared radiation to form image. The latter one, which is also known as thermal imager, does not emit infrared radiation. This means that the thermal image is formed based on infrared radiation of the target itself (Lu et al. 2013).

As shown in Fig. 2, the general structure of the night vision system mainly includes four parts. The photoelectric conversion device converts the infrared radiation into the image visible to human eyes, and then the image is showed on the display screen after denoising, reshaping, and amplifying. Infrared lens is an important part of night vision system, which is responsible for transmitting infrared radiation of the target. At present, the material of infrared lens is generally germanium, silicon, and zinc selenide. These materials have a large temperature coefficient of refractive index. When the temperature changes, the behaviors of thermal difference and performance degradation will occur. The increase of system volume caused by temperature change needs to be compensated. The night vision system designed with ChG and diffractive optical elements can realize the temperature adaptation control system and make the system image well even in a large temperature range.

20.1.1.3 Infrared Window

With the establishment of aerospace integration, infrared guidance and other infrared optical system are becoming more and more important in the modern society. Infrared window is the key component to ensure these systems work properly. Large diameter, high infrared transmittance, high optical uniformity, and good thermal mechanical properties are the common requirements of infrared windows for the next generation of infrared systems (Xie et al. 2012).

The lack of infrared windows with large size and high performance has become an important factor restricting the development of the photoelectric system, as well as one of the factors to decide the price of some important system in many cases (Zhang et al. 2011). ChG material has obvious advantages in large-size preparation and the molding process, which costs lower than the machining process. Therefore, it is an important material for the new generation of infrared window.

20.1.2 Methods to Fabricate Microstructures on Chalcogenide Glass

In order to meet the application requirements of microstructures on infrared optical components, various microstructure fabrication techniques have been developed.

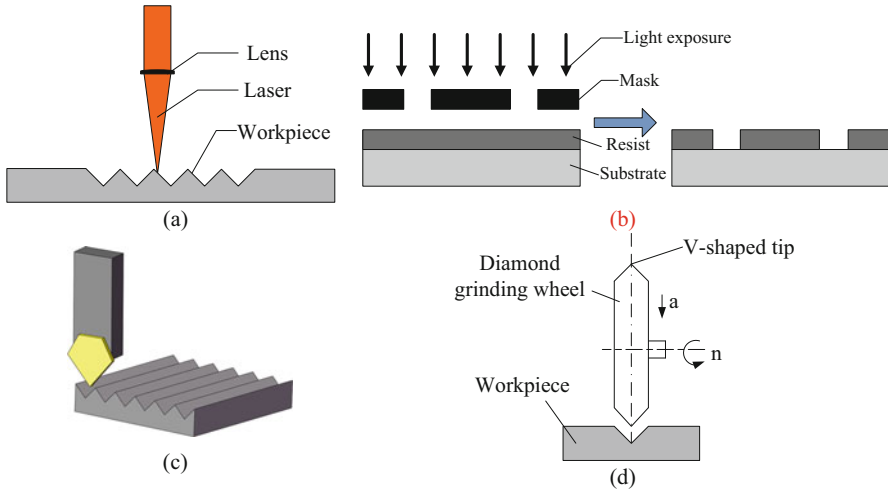


Fig. 3 Methods to fabricate microstructures on ChG: (a) laser processing, (b) photolithography, (c) single-point diamond turning, (d) CNC grinding and polishing

For example, based on energy-assisted machining, the focused ion beam machining and laser processing can fabricate surface microstructures directly in optical components. However, these two methods are complex in processing, high in cost, and poor in microstructure uniformity (Naessens et al. 2003; Hisakuni and Tanaka 1995; Chiu and Lee 2011). The surface microstructures on infrared glass can also be processed by photolithography, but the shape and size of the microstructures are limited (Manevich et al. 2008). Using traditional machining techniques such as single-point diamond turning or CNC grinding and polishing, complex surface microstructures can be fabricated. The surface microstructures have ultrahigh shape accuracy. However, these methods still have many problems such as high cost and poor efficiency. They are not able to meet the needs of the market (Davies et al. 2002). Precision molding can solve the problems of the above processing technology, and it is the most promising technology to form surface microstructures on ChG (Fig. 3).

20.1.3 Precision Molding Technique

Compared with single-crystal germanium, ChG is an amorphous material without fixed melting point. The viscosity of ChG gradually decreases during heating until it is suitable for the precision molding to process surface microstructures (Zhang et al. 2003b). The precision molding has high processing efficiency and can achieve mass production to reduce the processing cost with a good forming accuracy of surface microstructures. Therefore, it has a broad prospect for development and application.

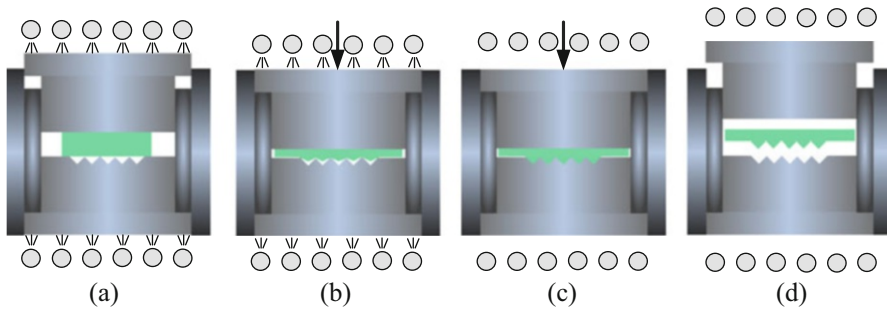


Fig. 4 Four stages of a precision molding cycle: (a) heating, (b) pressing, (c) annealing, and (d) cooling

20.1.3.1 Fundamental of Chalcogenide Glass Molding Process

In a precision molding cycle, the molds and ChG are heated simultaneously. The ChG is heated above softening point and fully softened. Then the upper mold is moved down to compress the ChG preform, and the stress is relaxed by holding the pressing load without further deformation for a short time. After that, the ChG is annealed at a slow cooling rate. Finally, the formed ChG is cooled to ambient temperature rapidly and released from the molds, and the surface microstructures of the molds are replicated to the ChG surface. Hence, ChG molding process can be divided into four stages, heating, pressing, annealing, and cooling, as shown in Fig. 4.

The surface microstructures with different shapes can be processed by changing the shape of the mold's surface microstructures. A set of molds can be used to form large quantities of ChG, so the precision molding has great advantages in the mass production of surface microstructures on ChG. The precision molding process is simple and the production efficiency can be greatly improved. It has been corroborated that the molding process would not deteriorate the infrared transmittance of ChG (Liu et al. 2012). Therefore, this technology has received extensive attention from various research institutions and enterprises in the world.

20.1.3.2 Chalcogenide Glass Materials for Microstructure Molding

ChG can be divided into sulfide glass, selenide glass, and telluride glass according to the elemental composition. The As-S and Ge-S glass are the earliest studies of sulfide glasses. As-S glass has the advantages of good infrared transmittance, high refractive index, low sound speed, and high quality factor. However, there are also some shortcomings such as high intrinsic loss, low mechanical strength, and poor chemical stability. In order to improve the comprehensive properties of As-S glass, the preparation and properties of Ge-As-S glass have been studied. The results show that the density, hardness, softening temperature, and chemical stability of glass increase and the expansion coefficient decrease with the content increase of element Ge. The transmittance region of Ge-As-S glass is $0.6 \mu\text{m} \sim 11 \mu\text{m}$ (Zhang et al. 2003a, b).

Selenide glass is easier than sulfide glass to prepare due to the higher rate of chemical reaction between Se and other elements, as well as the lower pressure when Se melts. The Ge-As-Se and Ge-Sb-Se glass in selenide glasses are most suitable for infrared optical system. Ge-As-Se glass is of intrinsic optical stability and has a wide glass forming range. The Ge-As-Se glass has a great transmittance of long wave infrared, the transmittance range of which is $0.8 \mu\text{m} \sim 15 \mu\text{m}$.

20.1.3.3 Mold Materials for Chalcogenide Glass Molding

The molds are the key items for forming high-precision optical components, the quality of which directly affects the quality of the final component. The differences of mold materials will lead to great differences in the internal stress distribution, the surface roughness, and the surface shape of the formed ChG. In order to obtain high-quality molded component, the selection of ChG mold material is of great importance. The molds are under the conditions of high temperature and high pressure during the forming process for a long time, so the material selection of the molds is mainly considered from the aspects of high-temperature stability, heat-shock resistance, stress release property, hardness and strength, mechanical performance, etc. In addition, in order to avoid deterioration of infrared optical properties, the mold material cannot react with oxygen or ChG. The thermal expansion coefficient of the mold material needs to be small to reduce the shape error of the formed glass, making the mold and glass easier to separate, avoiding the adhesion between the mold and the formed glass after annealing and cooling. The mold materials, including cemented carbide, cermet, and heat-resisting stainless steel with Ni-P plating, are available for molding.

20.1.3.4 Mold Coating

As a result of the adhesion between the mold and the formed glass, the shape error and surface roughness of the formed glass will increase, and the surface of the mold will be damaged leading to the decrease of the mold's service life. In order to ensure the forming quality and extend the life of the mold, it is an efficient way to have a release film on the mold surface. The film material is closely related to the mold material and can prevent chemical reactions between the mold and the glass. For example, the surface of cemented carbide substrate can be plated with precious metal alloy, titanium nitride coating, hard carbon, diamond-like carbon, and other carbon coating.

20.2 Modeling and Simulation of Chalcogenide Glass Microstructure Molding

ChG is a typical amorphous material, and its material properties are affected by temperature. When the temperature increases gradually, the ChG is gradually softened from hard brittle state to viscoelastic state. It is important to learn the thermal deformations during glass molding process by figuring out the material properties and processing properties of ChG under high temperatures.

20.2.1 Modeling of Viscoelastic Constitutive of Chalcogenide Glass

Viscoelasticity is a time-dependent response of a material to stress or strain. At a constant load, the ChG strain is made up of instantaneous strain (elastic effect) and a continual strain as a function of time (viscous effect). This time-dependent deformation under a constant load is termed creep. On the other hand, when a constant strain is applied, the stress relaxes with the increase of time, which is termed stress relaxation. Creep and stress relaxation are the two main characteristics of deformation behavior during molding process.

Viscoelastic constitutive models are necessary to analyze the time-dependent creep behavior and stress relaxation of ChG at high temperatures. The simple Maxwell model, the Kelvin model, the Burgers model, and the generalized Maxwell model are four typical constitutive models (Pipkin 1972), which allow the rate of the inelastic strain change to be a function of the total stress and previous strain. These models can be expressed by a series of springs and dashpots. The simple Maxwell model can fit stress relaxation but is not suitable for modeling creep. The Kelvin model is unable to describe the time-dependent change of stress during creep. The Burgers model can simulate creep perfectly. It can be used to simulate stress relaxation too, but it was found that a deviation always happens at the beginning of the stress relaxation (Zhou et al. 2009). Therefore, among the four kinds of models, the generalized Maxwell model might be the best one to describe creep and stress relaxation in the viscoelastic deformation of glass at high temperatures (Zhou et al. 2011). The generalized Maxwell model is based on a single Maxwell model, formed by a spring and multiple Maxwell models in parallel as shown in Fig. 5.

According to the Boltzmann superposition principle, the time-dependent response of the generalized Maxwell model can be described by Eq. 1:

$$\sigma(t) = \int_0^t G(t - \tau) \frac{d\varepsilon}{d\tau} d\tau \quad (1)$$

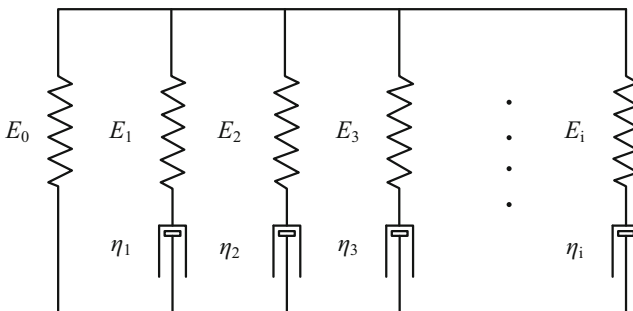


Fig. 5 The generalized Maxwell model

where the integral is evaluated for current time t based on past time τ . $G(t-\tau)$ is not a constant value, which can be described by the Prony series:

$$G(t) = G_0 \sum_{i=1}^n \omega_i e^{-\frac{t}{t_{ri}}} \quad (2)$$

where $G(t)$ is the relaxation modulus, G_0 is the elasticity modulus of the spring, ω_i is the weight coefficient of single Maxwell model, and t_{ri} is the relaxation time. The weight coefficients and the relaxation time can be described by the following two equations:

$$\sum_{i=1}^n \omega_i = 1 \quad (3)$$

$$t_{ri} = \frac{\eta_i}{G_i} = \frac{\eta_i}{G_0 \times \omega_i} \quad (4)$$

where η_i is the viscosity of each dashpot.

20.2.2 Simulation of Microstructure Molding Process

Finite element method (FEM) is a well-known and widely applied method, so its fundamentals need not be reviewed here. In order to give an example to demonstrate the simulation of microstructure molding, a commercial nonlinear FEM software ABAQUS/Explicit is used, and the ChG $\text{Ge}_{22}\text{Se}_{58}\text{As}_{20}$ is chosen to be preform material with its thermal and mechanical properties listed in Table 1. The program is capable of simulating large deformation of material flow under isothermal or non-isothermal conditions. It is able to analyze complex models such as mechanics and thermal field coupling problems. It can be used to visualize the glass molding process and monitor some difficult-to-measure variables including strain/stress distribution and internal temperature variation.

It will take a larger workload and need more computation time when three-dimensional model is used for the finite element simulation analysis, and the

Table 1 Thermo-mechanical properties of ChG $\text{Ge}_{22}\text{Se}_{58}\text{As}_{20}$

Property	Value
Density ρ (g/cm^3)	4.41
Young's modulus E (GPa)	18.2
Poisson's ratio ν	0.28
Transition temperature T_g ($^{\circ}\text{C}$)	282
Softening temperature T_s ($^{\circ}\text{C}$)	352
Thermal expansion coefficient ($10^{-6}/\text{K}$)	17

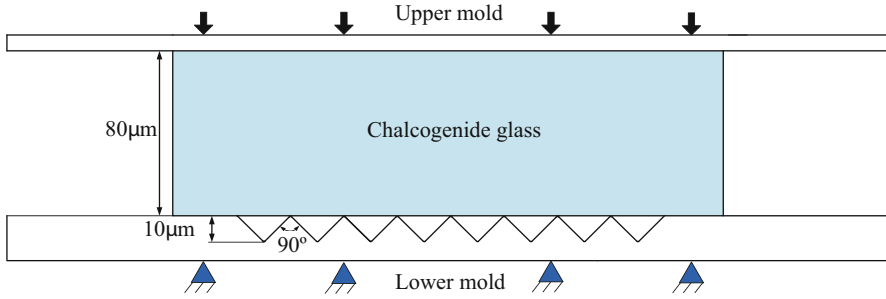


Fig. 6 The two-dimensional simulation model of microstructure molding

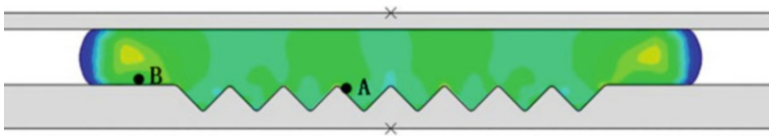


Fig. 7 Two representative special points of microstructure simulation

simulation process is prone to errors. It is much easier to simplify the microstructure molding into a two-dimensional simulation model as shown in Fig. 6.

The flat upper mold can be moved downward to press the softened ChG. The lower mold with microstructures is fixed. In order to avoid the stress convergence in the contact region and save remeshing time at the sharp corners during the molding simulation, the sharp corners of the microstructures are rounded with a small radius of $0.5\ \mu\text{m}$. As the ChG preform is pressed at a uniform temperature, as the same as the molds, the pressing stage can be treated as isothermal process without heat transfer.

In the molding process, the stress distribution of the ChG can reflect its forming feasibility. It can be shown where forming defects are easy to occur because of the stress concentration. The magnitude of the stress can be used to determine the magnitude of the residual stress, the annealing scheme, and the annealing time. Therefore, studying the stress distribution is helpful to plan the experiment scheme and get the optimized formed microstructure glass. Furthermore, molding temperature and other technological parameters seriously affect the forming stress distribution and magnitude of the ChG. Hence, it is essential to study the molding parameters' affection and optimize the technological parameters.

In order to study the effect of the technological parameters on the internal stress distribution of ChG, two representative special points are selected in the simulation model of the ChG, as shown in Fig. 7. The point A is in the contact area between the ChG and the top of the mold microstructure. The point B is in the contact area of the ChG and the mold surface without microstructure.

20.2.2.1 Effect of Molding Temperature on Forming Stress of Microstructure

It is crucial to choosing the appropriate molding temperature to guarantee the forming quality of the ChG microstructure. If the molding temperature is too low, the ChG cannot be fully softened, and it cannot fill the cavities of microstructure on the mold. Then a greater pressure is needed to achieve better filling effects, and the residual stress of ChG will increase, which leads to a greater shrinkage in the annealing stage. If the molding temperature is too high, it may cause the interface adhesion between the mold and the ChG (Monfared et al. 2017). In addition, high temperature leads the cooling temperature range to increase, and the ChG shrinks more serious during the cooling stage of molding process. All in all, excessive temperature results in difficulties in guaranteeing the shape and surface accuracy of the microstructure and even reduces the mold life. Previous research findings show that the ChG can better duplicate the surface morphology of the mold when the temperature is above the softening temperature (Monfared et al. 2017).

The effects of molding temperature are studied by FEM at 382 °C, 392 °C, 402 °C, and 412 °C, respectively. The pressing velocity is set to 0.001 mm/s, and the molding time is set to 20 s. The friction coefficient is specified to 0.1. Figure 8 shows the changes in the equivalent stresses of point A and point B at different temperatures from 382 °C to 412 °C. When the temperature of the ChG rises continuously, the internal stress of ChG decreases gradually. According to the simulation results, considering the longer service life of the mold and the shorter heating time, the molding temperature is chosen as 392 °C for the later demonstration.

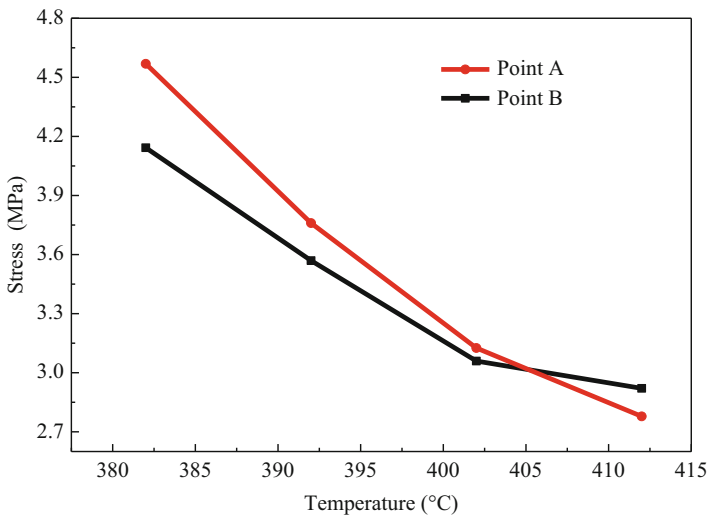


Fig. 8 Effect of molding temperature on internal stress of ChG

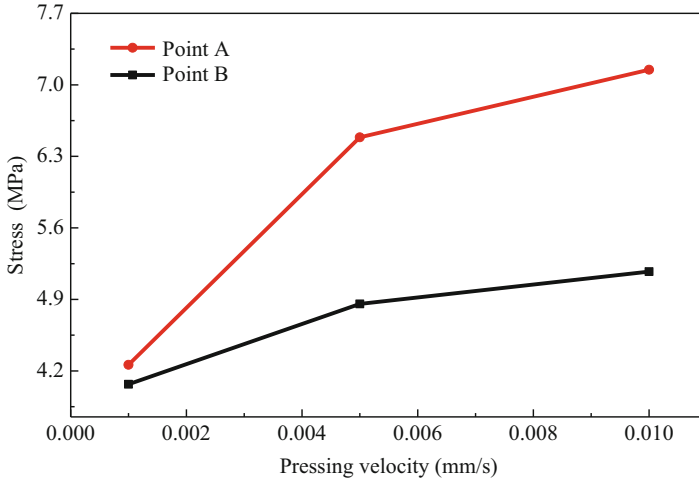


Fig. 9 Effect of pressing velocity on internal stress of ChG

20.2.2.2 Effect of Pressing Velocity on Forming Stress of Microstructure

In order to study the influence of the pressing velocity on the internal stress of ChG after precision molding, the pressing velocities are set to three levels, 0.001 mm/s, 0.005 mm/s, and 0.01 mm/s, respectively. Changing the length of the analysis step ensures that the displacement is 0.02 mm. The molding temperature is fixed at 392 °C and the coefficient of friction is set to 0.1. The simulation results of these three groups are shown in Fig. 9.

The stresses of point A and point B increase gradually with the increase of pressing velocity. The ChG preform is in a stable equilibrium state, and the internal molecular structure is relatively stable before the precision molding. After the pressure is applied, the ChG begins to flow passively and fill the cavities of the mold microstructures. The greater the pressing velocity is, the faster the strain rate of the ChG is. A shorter time is needed to fill the mold cavities, and the relaxation time is also shorter. The stress is released less, and the internal stress of ChG is greater. Therefore, under the premise of ensuring the production efficiency and filling quality, the lower pressing velocity is preferred. According to the simulation results, 0.001 mm/s is chosen as the pressing velocity in this later demonstration.

20.2.2.3 Effect of Friction Coefficient on Forming Stress of Microstructure

In the molding process, the friction force will significantly affect the forming stress of the microstructure and service performance of the molded components. According to the previous simulation results, the molding temperature is set as 392 °C, and the pressing velocity is set to 0.001 mm/s. The molding time is 20 s. In the simulation model, three groups of friction coefficient are set to 0.1, 0.3, and 0.5, respectively. The variation of the internal stresses of the ChG with the friction coefficient is shown in Fig. 10.

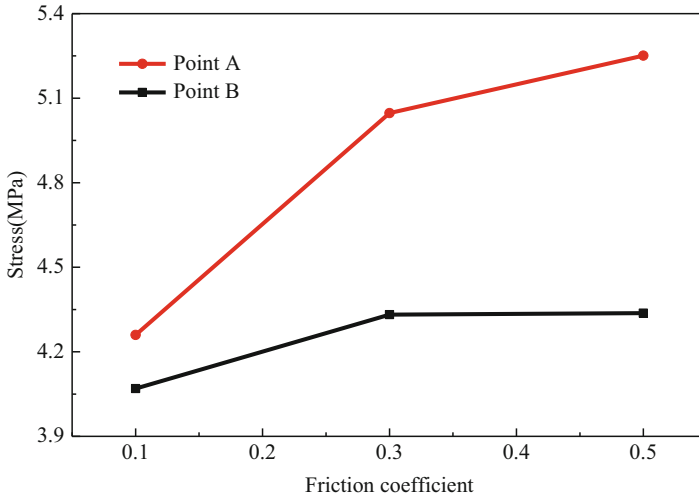


Fig. 10 Effect of friction coefficient on internal stress of ChG

The internal stresses of ChG rise with the increase of friction coefficient, which means the residual stress rises with the increase of the friction force. After the friction coefficient is increased to 0.3, the stress increasing rate decreases. When the friction coefficient is larger, the flow deformation of ChG on the mold surface is poorer, and the filling in the microstructure cavities is hindered. The above forming defects will all affect the optical performance of the molded infrared optical components. Therefore, the friction coefficient between the mold and the ChG should be reduced as much as possible to reduce the internal stress in the forming process of the ChG, which sets demands for ultraprecision molds.

20.3 Molding Process of Microstructures on ChG

The ChG technological parameters of the molding process can be optimized based on the above FEM simulation results. In order to introduce the molding process of microstructure on ChG, precision glass molding experiment is carried out with an ultraprecision glass molding machine. Then the forming quality of the microstructures is analyzed by comparing the microstructures on the ChG and the mold.

20.3.1 Chalcogenide Glass Molding Machine

The ChG molding machine used in this experiment consists of two parts, the main equipment and the peripheral devices. It mainly includes multistation molding machine, water cooler, air compressor, and nitrogen container. The multistation molding machine is the main equipment for precision molding experiment. It

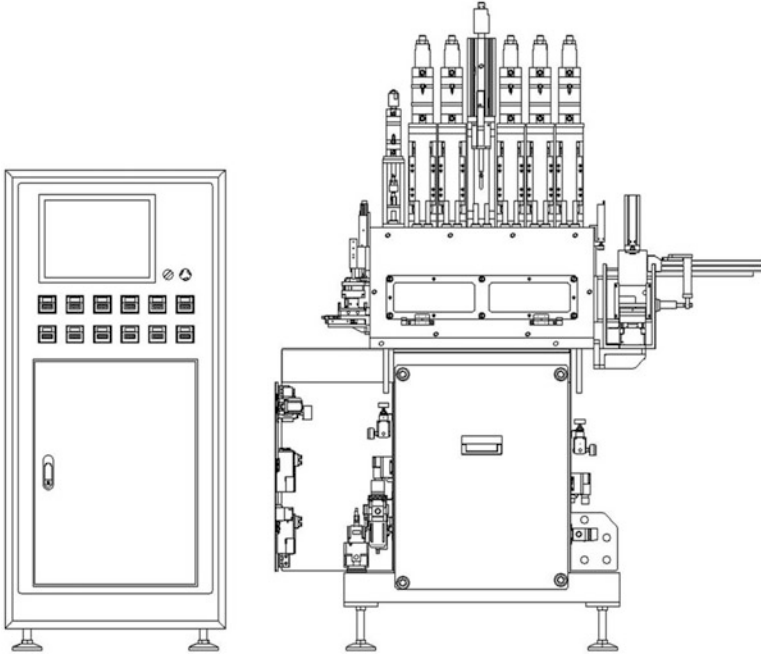


Fig. 11 The ChG multistation molding machine

contains seven station controllers, temperature and pressure control system, cooling system, and automatic conveying devices, as shown in Fig. 11. The peripheral devices include a water cooler, an air compressor, and a liquid nitrogen container.

Multistation molding machine consists of seven stations. From right to left, there are three preheating stations heating the ChG preform and the molds to the molding temperature. Then, a molding station presses the ChG to copy the surfaces of the mold to the surfaces of the ChG. Next, two annealing stations are used to anneal the ChG and eliminate the residual stress. Finally, a cooling station cools the formed glass rapidly to room temperature. The microstructures on ChG can be processed through the seven stations. The water cooler provides cooling water circulation for the cooling of the mold, the ChG, and the machine body. The air compressor provides compressed air to drive the up and down motion of cylinders in these seven stations and motion of automatic conveying devices in the molding process. The liquid nitrogen container continuously delivers nitrogen to avoid the ChG, the mold, and the interior of the machine body being oxidized by air.

20.3.2 Chalcogenide Glass Molding Condition and Quality Control

20.3.2.1 Chalcogenide Glass Molding Condition and Optimization

The ChG molding conditions can be partly confirmed by the FEM simulation results. Before the microstructure molding experiments, the cylindrical molding tests can be

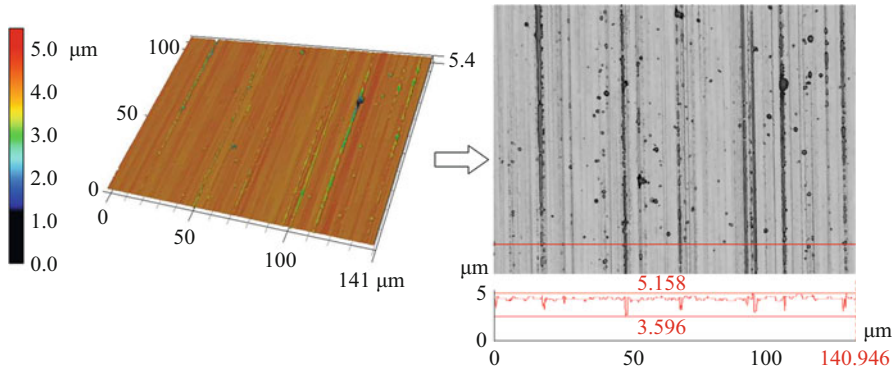


Fig. 12 The surface morphology and contour of a formed pillar at the molding temperature of 382 °C

conducted to explore the other microstructure molding conditions. The cylindrical molding experiments were conducted using molding temperatures at 382 °C and 392 °C under a pressing force of 1362 N. Many microdimples were observed on the ChG pillars, as shown in Fig. 12. The same observations were made using confocal laser scanning microscopy. The scratch-like surface defects were actually caused by coalesced dimples. The maximum peak-to-valley height difference was 1.562 μm, which is within the infrared transmission waveband of Ge₂₂Se₅₈As₂₀ and reduces the infrared transmittance. To guarantee infrared transmittance, microdimples must be suppressed.

To reduce the microdimples, gas generation should be reduced, and gas escape should be improved. For gas generation, the solubility of gas has been studied, and it can be expressed using A. Sieverts' square root law (Gupta 2006):

$$S = k\sqrt{P}e^{-\Delta H/(RT)} \quad (5)$$

where S is the dissolved concentration, k is a constant, P is the gas partial pressure, ΔH is the dissolution heat, R is the gas constant, and T is temperature. The movements of the molecules become more intense as the temperature increases, leading to more reactions, smaller gas solubility, and more gas generation. Pressure is another contributor that affects the gas solubility, in addition to the temperature. The gas density is greater with the increasing pressure, so the free molecular motion decreases, and the gas increasingly dissolves, as expressed by Eq. 5. According to Dalton's law of partial pressure, the total pressure is equal to the sum of the partial pressures of the mixed gas (Silberberg 2000). Meanwhile, based on Newton's third law (Kelley and Leventhal 2017), the total pressure increases with the increase in the pressing force. This law indicates that the gas solubility increases with the increase in the pressing force.

To quantify the effect of the temperature, the area ratios of the microdimples were evaluated. Avoiding the obvious molding defects, five measuring points are equidistantly chosen in the direction of diameter on the upper surface of a formed pillar,

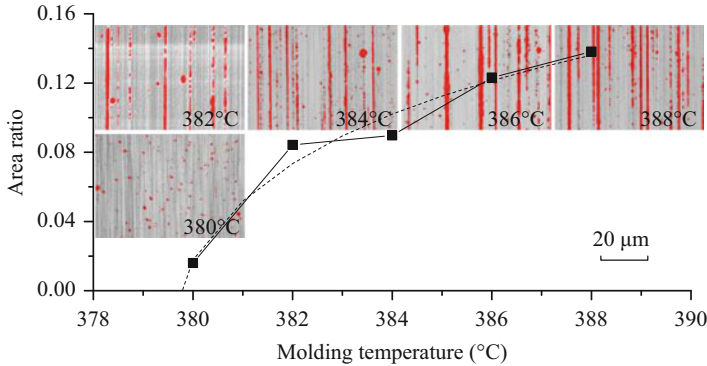


Fig. 13 Area ratios of the microdimples at different molding temperatures under a pressing force of 1362 N

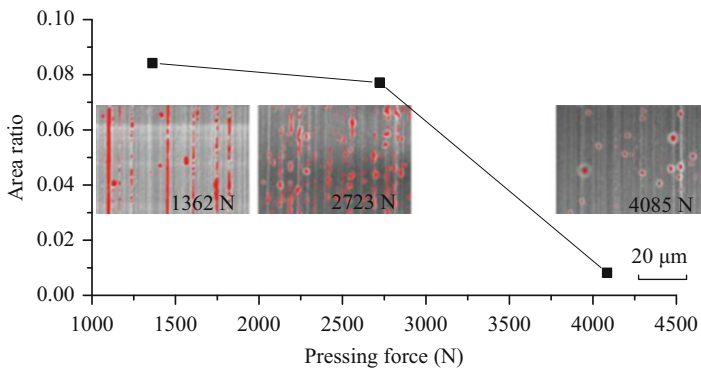


Fig. 14 Area ratios of the microdimples of formed pillars under different pressing forces at 382 °C

of which the third point is in the center, and the average area ratio values are obtained. In order to make the results more vivid, the central measurement point images are shown in data maps. The area ratio of the latter is also measured by this method. The area ratios of the microdimple areas increased almost logarithmically with the molding temperature, as shown in Fig. 13. By extrapolating the trend line in Fig. 13, we could estimate that the temperature for preventing microdimple was approximately 379.8 °C. However, this temperature is too low and could lead to surface scratching. In our experiment, surface scratches remained even after molding at 380 °C. Therefore, it was inferred that the optimum temperature would be between 380 °C and 382 °C. In the subsequent study, we fixed the molding temperature at 382 °C and focused on other parameters that could minimize the effects of gas release when gas release was inevitable.

Meanwhile, the area ratios of the microdimples with different pressing forces were also evaluated. As shown in Fig. 14, the area ratios of the microdimples

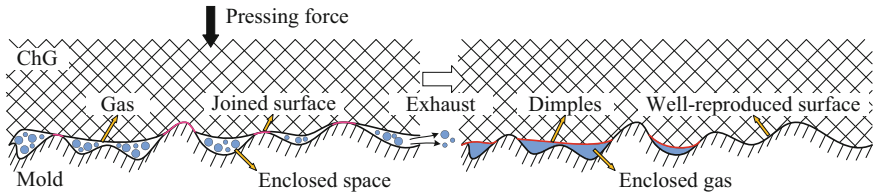


Fig. 15 Schematic diagram of the microdimple formation during glass molding process

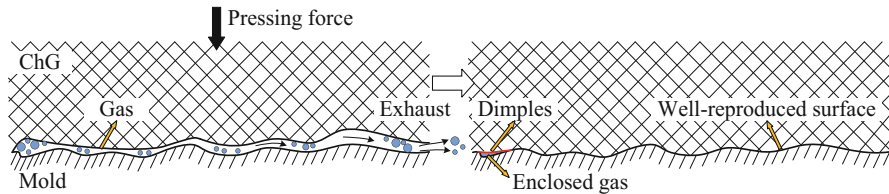


Fig. 16 Schematic diagram of the microdimple formation during glass molding process with a high-precision mold

decrease with the increase in the pressing force at a molding temperature of 382 °C. They decrease slowly from 1362 N to 2723 N and then decrease rapidly from 2723 N to 4085 N. Therefore, it can be assumed that if the contact pressure is larger than the saturated vapor pressure of the ChG, the gas will no longer be generated.

To decrease the occurrence of microdimples on the glass surface, the effect of the contact surface roughness was studied. Due to the surface microstructures of the mold and glass, the enclosed spaces resulted in a lower local pressure, as shown in Fig. 15. The pressure of the enclosed spaces was lower than the saturated vapor pressure of ChG, which intensified the evaporation of selenide gases and led to the morphology that exhibited incomplete reproduction and microdimples. However, the pressure of the joined surfaces was much higher than the saturated vapor pressure of ChG, and hence, these surfaces were reproduced in full. When the contact surfaces were smoother, the number of enclosed spaces was lower, and the gas generation decreased. In contrast, the enclosed spaces resulted in enclosed gas, which impeded gas escape. When the contact surfaces were smoother, the gas escaped more completely, as shown in Fig. 16, which also led to a better surface quality.

To verify the contact surface roughness effect, three groups of molds were prepared with surface roughness (R_a) values of 7 nm, 62 nm, and 835 nm, respectively. The surface roughness (R_a) of the glass preform was 10 nm. The glass molding experiments were carried out under the pressing force of 4085 N at the molding temperature of 382 °C. Figure 17 shows the area ratios of the microdimples under different mold surface roughness values. It can be concluded that smoother mold surfaces led to fewer microdimples, which verified the notion of the effect of the contact surface roughness, as shown in Figs. 15 and 16. When the mold surface

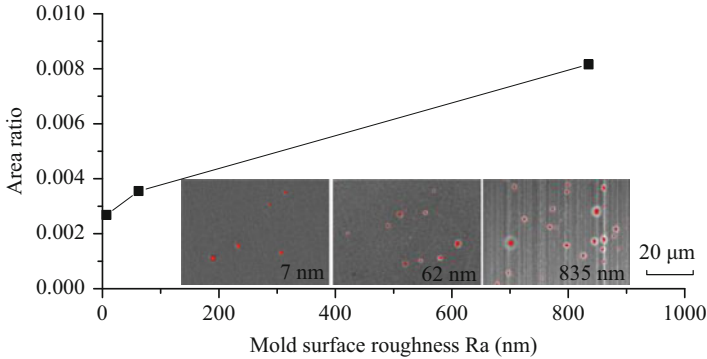
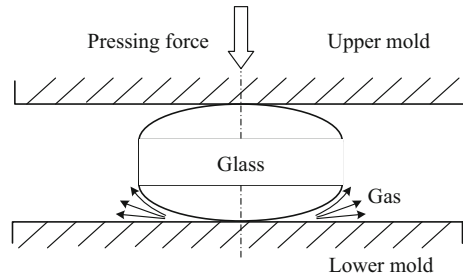


Fig. 17 Area ratios of the microdimples of the formed pillars with different mold surface roughness values under the pressure force of 4085 N at the molding temperature of 382 °C

Fig. 18 Gas escape mode during the spherical glass molding process



roughness (Ra) was 7 nm, the area ratio of the microdimples reached its minimum value. Moreover, 7 nm meets the precision requirement of infrared optical applications, so it was chosen for the next study.

When the glass surface is more curved with a smaller radius, the gas escape becomes easier as shown in Fig. 18, and the area of contact surface is smaller when the displacement is the same, which means the pressure is larger under the same force at the same displacement. Both of these two reasons can reduce microdimples as mentioned above. The effect of the surface curvature of the glass preforms was also studied. The mold surfaces were planar with a roughness (Ra) of 7 nm. The glass preforms had spherical surfaces with different curvature radii. It is impracticable to control a uniform pressure between contact surfaces. Therefore, in our experimental study of the effect of surface curvature, we can only guarantee external force to be the same. It can be seen from Fig. 19 that the area ratios of the microdimples of the formed pillars decreased or were even completely eliminated, with the decrease in the glass curvature radius. The surface roughness (Ra) of a formed pillar without microdimple can reach 20 nm.

Another experimental scheme to study the contact surface curvature effect included reducing the curvature radius of the mold surface, as shown in Fig. 20a. The glass surface was plain with a roughness (Ra) of 10 nm. The upper mold had a

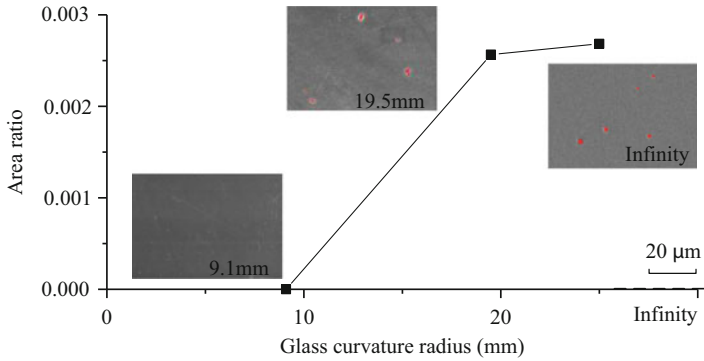


Fig. 19 Area ratios of the microdimples of the formed lenses with different glass surface curvature radii under 4085 N with a molding temperature of 382 °C

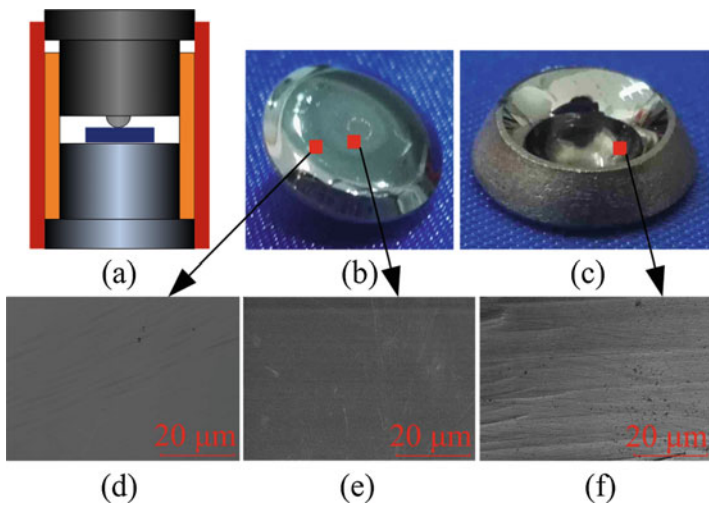
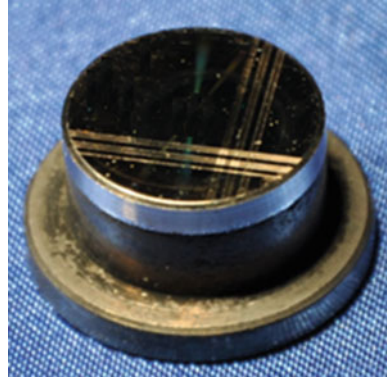


Fig. 20 Glass molding experiments with spherical molds: (a) experimental scheme, (b) the lower surface of a formed pillar, (c) the upper surface of a formed pillar, (d) the micromorphology of the convex surface, (e) the micromorphology of the flat surface, and (f) the micromorphology of the concave surface

spherical surface with a curvature radius of 2.5 mm. After the experiment, the formed pillar had a convex surface, a flat surface, and a concave surface as shown in Fig. 20d, e, f respectively. Moreover, microdimples were not present on these surfaces, which means that the microdimples could be eliminated by reducing the curvature radius of the mold. It was also concluded that the gas generation and escape could be improved by enlarging the curvature difference between the glass surface and the mold surface, either by reducing the curvature radius of the glass or the molds.

Fig. 21 The lower mold with microgrooves on its surface



20.3.2.2 Microstructure Shape and Morphology Control

The microstructure molding experiment is conducted by using spherical preform glass, and the microstructures include microgrooves and microlens arrays. The lower mold with some microgrooves on its surface based on above research is shown in Fig. 21.

According to the optimum technological parameters, the molding temperature is set to 382 °C, and molding time is set to 20 s. Microscopic observations of the ChG surface and the mold surface are performed using a confocal laser scanning microscope, and the microscopic observations of the microstructures are shown in Fig. 22. It can be found that there is no interfacial adhesion occurring in the edges of ChG, and the forming quality of microgrooves is excellent.

The contour curves of the microgrooves of the ChG surface and mold surface are extracted to analyze the forming quality of the microgrooves, as shown in Fig. 23. The filling rate is 97.43%, and the filling error is 2.57%. It can be seen from the contour curve that the top of the microgroove is sharp, although the forming quality of bottom is a little worse. Therefore, the molding process can better ensure the replication accuracy of the microgroove.

In the microlens arrays mold preparation, the upper and lower molds are generated on the Ni-P plating layer by diamond cutting, using a round diamond tool. Then, microlens arrays are generated by feeding the diamond tool with three-axle linkage and using a high-speed diamond-ball nose-end milling tool with an included fillet radius of 500 μm and shank diameter of 6 mm. Figure 24a is the microscopic image of microlens arrays on the Ni-P mold. The diameter of the microlens is 80 μm, and the height of the microlens is 1 μm. The microlens array was fabricated by the precision glass molding. Figure 24b is the microscopic image of microlens arrays on the chalcogenide glass.

Figure 25 shows the microlens arrays profile of mold and chalcogenide glass. The average error of the height is 0.034 μm. We can see that the forming quality is high and it is suitable for the fabrication of microstructure infrared optical components.

20.3.2.3 Molding Defect and Minimization

Although the ChG microstructure molding has high replication accuracy, there are still some defects. Most ChGs have a greater saturated vapor pressure, which enables

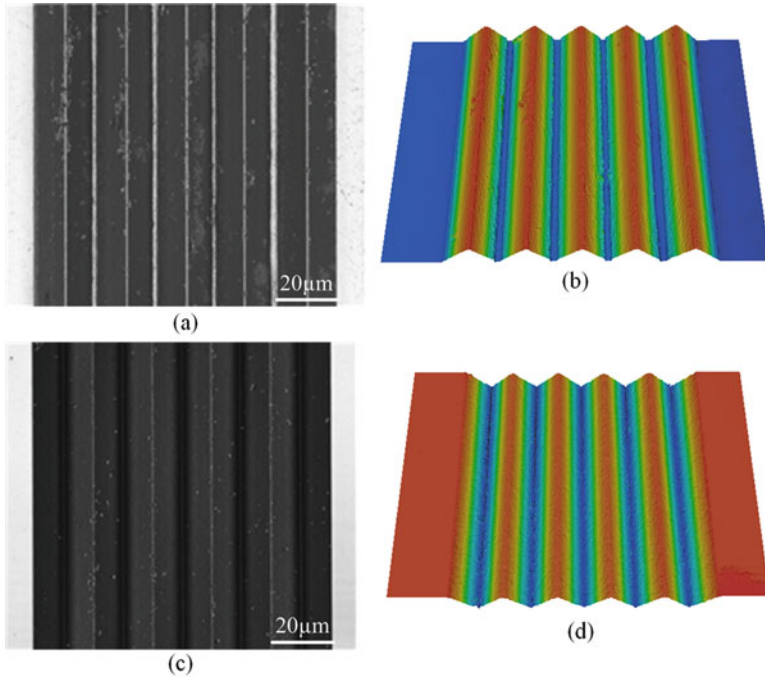
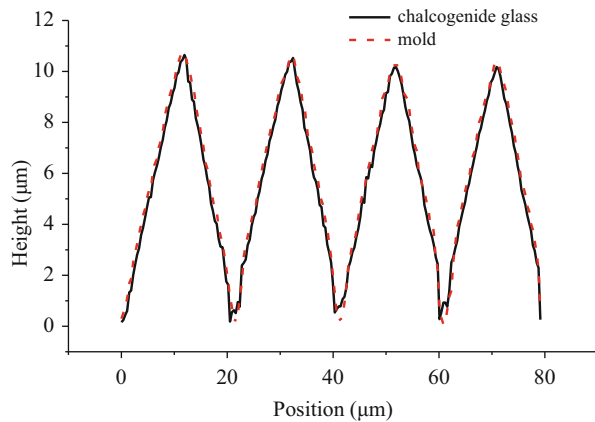


Fig. 22 Micrograph of microgrooves: (a) microgrooves of ChG, (b) 3D morphology of ChG microgrooves, (c) microgrooves of mold, (d) 3D morphology of mold microgrooves

Fig. 23 Microgroove profile of mold and ChG after experiment



the release of trace gases during the molding process. When these gases cannot escape, the lens shape and surface quality (Hilton 2010) are severely impaired. Also, interface adhesion exists in the molding process which reduces the forming quality of the optical components. It deteriorates the surface quality of the mold and has an important influence on the forming process (Saiz et al. 2008; Rieser et al. 2008).

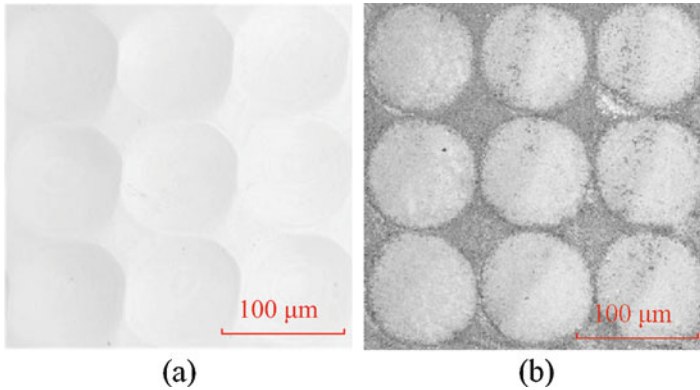
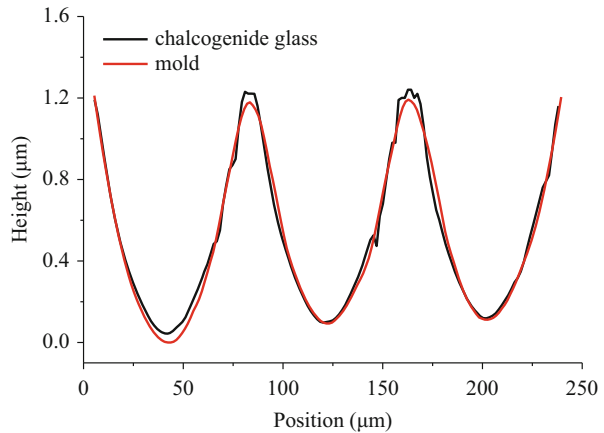


Fig. 24 Ni-P plating mold with microlens arrays: (a) microscopic image of microlens arrays on the mold and (b) microscopic image of microlens arrays on the chalcogenide glass

Fig. 25 Microlens arrays profiles of mold and molded chalcogenide glass

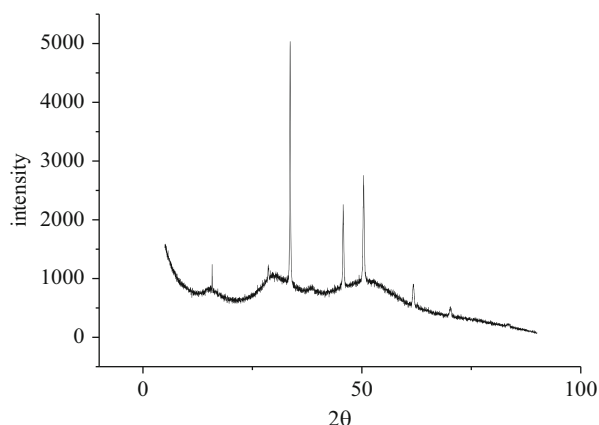


Atomic diffusion will come up between the surfaces of the ChG and the mold in the molding process. The motion of atoms is violent, and the diffusion phenomenon is serious at high temperature (Wang et al. 2014), which will lead to the change of optical property of ChG and thermomechanical property of mold material. Then the interface adhesion will be more serious (Suryanarayana and Bulk 2013). The diffusion degree of atoms is related to the material properties of the contact surface. Therefore, it is necessary to study the influence of the mold materials on interface adhesion. Three kinds of mold materials which are widely used in molding process are selected. They are cemented carbide, Ni-P coating mold, and heat-resisting stainless steel.

Experiments are carried out using these three kinds of mold materials. The surfaces of the ChG and the mold are analyzed by scanning electron microscope (SEM) and energy spectrum analysis (EDS). The atomic diffusion is studied by comparing the atomic composition of ChG preform with the mold.

Table 2 Atomic percentage of ChG formed by using different mold materials

Chemical element		Mg	Fe	Ge	As	Se	Ni
ChG preform		6.94		22.73	16.89	53.44	
Formed ChG	Cemented carbide	4.45		21.19	19.49	54.87	
	Heat-resistant stainless steel	8.21	4.24	21.81	13.91	47.23	4.6
	Ni-P coating mold	1.45		11.96	11.91	32.31	42.36

Fig. 26 The diffraction pattern of ChG formed by using Ni-P coating mold

The atomic percentage of formed ChG is shown in Table 2. It can be seen that there is no atomic percentage change in ChG after forming by using cemented carbide mold which is of the stable chemical property and high chemical bond dissociation energy (Cottrell 1958). So there is no atoms diffusion between the ChG and the mold even at high temperature.

The surface of ChG formed by using heat-resisting stainless steel mold contains small amounts of nickel Ni and iron Fe. It can be seen that some atoms of the heat-resistant stainless steel mold diffuse to the ChG surface, and the interface adhesion between the mold and the ChG is slight. The interface adhesion between ChG and the mold is most serious when using Ni-P coating mold. X-ray diffraction (XRD) is used to analyze the composition of ChG formed by using Ni-P coating mold. The diffraction pattern is shown in Fig. 26.

There are obvious diffraction peaks in the diffraction pattern. Compared with the standard diffraction pattern, the diffraction peak can be determined as crystal $\text{As}_{10}\text{Ni}_{8.8}\text{Pd}_{1.2}$. Hence in the molding process, the ChG react with Ni-P coating mold. Therefore, the adhesion of the ChG is more serious when the Ni-P coating mold is used. Cemented carbide mold can avoid the phenomenon of interfacial adhesion and is the suitable mold material for ChG forming process through comparative analysis.

20.4 Summary

The precision molding of microstructures on ChG can fabricate the microstructure infrared optical elements with excellent surface morphology. Compared with other microstructural manufacturing technologies, the molding process can achieve low cost and high efficiency machining of microstructures. The following conclusions are obtained:

1. The application of ChG in infrared optics and the advantages of ChG materials are introduced. The precision molding technology is compared with other microstructure processing methods, and the advantages and practical value of it are expounded.
2. The viscoelastic constitutive of ChG is modeled. A two-dimensional simulation model of ChG microstructure is established, and the influence of process parameters on the forming stress of ChG microstructures is studied.
3. To reduce the occurrence of microdimples, the processing parameters, including the temperature, pressure, surface roughness, and curvature difference, are studied to decrease the gas generation and increase the gas escape. Based on the optimization of ChG molding conditions, microstructure arrays are fabricated by molding process using spherical ChG preform. The optimal molding materials are identified.

However, the elements of sulfur (S), selenium (Se), and tellurium (Te) in ChG are easily influenced by environment. Meanwhile, the ChG has high refractive index and large reflection loss. In order to improve the infrared optical performance of the ChG, antireflective film technology needs to be further explored which will effectively reduce the infrared reflection loss of ChG and improve the infrared optical transmittance. Hence, we should apply an antireflective coating on the ChG microstructures after molding, and the maximum utility of ChG microstructures in the infrared optical systems can be achieved.

References

- Bureau B, Zhang X, Smektala F et al (2004) Recent advances in chalcogenide glasses. *J Non Cryst Solids* 345-346(20):276–283
- Cha D, Kim H, Park H et al (2010) Effect of temperature on the molding of chalcogenide glass lenses for infrared imaging applications. *Appl Optics* 49:1607–1613
- Chiu C, Lee Y (2011) Fabricating of aspheric micro-lens array by excimer laser micromachining. *Opt Lasers Eng* 49(9–10):1232–1237
- Cottrell T (1958) *The strengths of chemical bonds*. Butterworths Scientific Publications, London
- Davies M, Evans C, Bergner B (2002) Application of precision diamond machining to the manufacture of microphotronics components. *Proc SPIE Int Soc Opt Eng* 5183(2):94–108
- Eisenberg N, Klebanov M, Lyubin V et al (2000) Infrared microlens arrays based on chalcogenide photoresist, fabricated by thermal reflow process. *J Optoelectron Adv Mater* 2(2):147–152
- Gai X, Han T, Prasad A et al (2010) Progress in optical waveguides fabricated from chalcogenide glasses. *Opt Express* 18(25):26635–26646
- Gupta C (2006) *Chemical metallurgy: principles and practice*. Wiley, Hoboken

- Hilton A (2010) Chalcogenide glasses for infrared optics. McGraw-Hill Companies, Inc, New York
- Hisakuni H, Tanaka K (1995) Optical fabrication of microlenses in chalcogenide glasses. *Opt Lett* 20(9):958
- Kelley J, Leventhal J (2017) Newtonian physics problems in classical and quantum mechanics. Springer International Publishing, Berlin
- Liu W, Shen P, Jin N (2012) Viscoelastic properties of chalcogenide glasses and the simulation of their molding processes. *Infrared Laser Eng* 19(3):422–425
- Lu Y, Song B, Xu T et al (2013) Design of refractive-diffractive night vision system based on chalcogenide glass. *Laser Optoelectron Progress* 50(12):168–174
- Luo S, Huang F, Zhan D, et al (2010) Development of chalcogenide glasses for infrared thermal imaging system. *Laser & Infrared* 40(1):9–13
- Manevich M, Klebanov M, Lyubin V et al (2008) Gap micro-lithography for chalcogenide micro-lens array fabrication. *Chalcogenide Lett* 5(4):61–64
- Monfared A, Liu W, Zhang L (2017) On the adhesion between metallic glass and dies during thermoplastic forming. *J Alloys Compd.* <https://doi.org/10.1016/j.jallcom.2017.04.005>
- Naessens K, Ottevaere H, Daele P et al (2003) Flexible fabrication of microlenses in polymer layers with excimer laser ablation. *Appl Surf Sci* 208(1):159–164
- Pipkin A (1972) Lectures on viscoelasticity theory. Springer, Berlin
- Rieser D, Spieß G, Manns P (2008) Investigations on glass-to-mold sticking in the hot forming process. *J Non Cryst Solids* 354(12–13):1393–1397
- Saiz E, Cannon R, Tomsia A (2008) High-temperature wetting and the work of adhesion in metal/oxide systems. *Annu Rev Mat Res* 38(38):197–226
- Silberberg M (2000) Chemistry: the molecular nature of matter and change. McGraw-Hill Companies, Inc, New York
- Suryanarayana C, Bulk IA (2013) metallic glasses. *Phys Today* 66(2):32–37
- Tang B, Yang Y, Fan Y et al (2010) Barium gallogermanate glass ceramics for infrared applications. *J Mater Sci Technol* 26(6):558–563
- Wang J, Fan J, Zhang Y et al (2014) Diffusion bonding of a Zr-based metallic glass in its supercooled liquid region. *Intermetallics* 46(1):236–242
- Xie Q, Yi L, Pan S (2012) The development and application of the materials for infrared windows and domes. *Infrared Technol* 10:559–567
- Xue J, Man X, Gong Y et al (2003) Preparation, characteristic and application of chalcogenide glasses. *Optoelectronic Technology & Information* 16(4):28–31
- Yu H (2007) Infrared optical materials. National Defense Industry Press, Beijing. (in Chinese)
- Zhang X, Ma H, Lucas J (2003a) Applications of chalcogenide glass bulks and fibres. *J Optoelectron Adv Mater* 5(5):1327–1333
- Zhang X, Guimond Y, Bellec Y (2003b) Production of complex chalcogenide glass optics by molding for thermal imaging. *J Non Cryst Solids* 327(4):519–523
- Zhang L, Chen L, Fan Y et al (2011) Development of mid-infrared transmitting glasses window and applications. *Acta Opt Sin* 31(9):0900134
- Zhou T, Yan J, Masuda J et al (2009) Investigation on the viscoelasticity of optical glass in ultraprecision lens molding process. *J Mater Process Technol* 209(9):4484–4489
- Zhou T, Yan J, Masuda J et al (2011) Investigation on shape transferability in ultraprecision glass molding press for microgrooves. *Precis Eng* 35(2):214–220



Press Molding of Hybrid Fresnel Lenses for Infrared Applications

21

Ahmad Rosli Abdul Manaf and Jiwang Yan

Contents

21.1	Introduction	662
21.2	IR Lens Materials and Structures	663
21.2.1	IR Lens Materials	663
21.2.2	Hybrid Optical Lens	664
21.2.3	Si-HDPE Hybrid Lens	666
21.3	Hybrid Fresnel Lens Design	668
21.4	Mold Fabrication	673
21.5	Press Molding for Hybrid Lenses	674
21.6	Fresnel Lens Form Accuracy	678
21.7	Lens Performance Evaluation	682
21.7.1	Modulation Transfer Function	682
21.7.2	Night Mode Imaging	684
21.7.3	Thermography Imaging	687
21.8	Summary and Outlook	688
	References	688

Abstract

Infrared (IR) imaging systems are extensively used in various kinds of applications such as search and rescue, security surveillance, car driving assistance, and also engineering thermography. The demand for new technology and new material for fabricating IR lenses is rapidly rising. In this chapter, a press molding method of silicon-high density polyethylene (Si-HDPE) hybrid Fresnel lenses for IR application will be introduced. A novel double lens system, which comprises a spherical and an aspherical planoconvex-shaped Fresnel lens, was adopted to the

A. R. Abdul Manaf (✉)

Faculty of Manufacturing Engineering, Universiti Malaysia Pahang, Pekan, Pahang, Malaysia

e-mail: arosli@ump.edu.my

J. Yan

Department of Mechanical Engineering, Keio University, Yokohama, Japan

© Springer Nature Singapore Pte Ltd. 2018

J. Yan (ed.), *Micro and Nano Fabrication Technology*, Micro/Nano Technologies,

https://doi.org/10.1007/978-981-13-0098-1_21

661

lens design. The press molding parameters that influence the lens form accuracy are investigated. The lens design, lens performance, and the lens application during the night vision imaging will also be given. To demonstrate the application of the hybrid lens in IR field, an imaging trial was performed by using a home-built optical system. To verify the optical capabilities of the lenses, the images were captured with the fabricated lenses and compared with the simulated results. The required imaging quality was realized for both night vision and thermography applications.

Keywords

Hybrid optics · Infrared lens · Press molding · Fresnel · Night imaging

21.1 Introduction

The demand for IR imaging systems is rapidly rising, particularly in the applications of rescue, night surveillance, night driving assistance, as well as thermography, among others. The current trends of IR optical development are toward the miniaturization of the IR imaging system's size, which would, in turn, reduce the production cost of such systems. This has led the research community at large to investigate alternative IR substrate, mainly for the fabrication of the IR lenses through cost-effective methods while maintaining the integrity of the IR transmittance.

More often than not, germanium (Ge) has been considered as a popular choice for IR substrate and is widely used as IR lenses due to its excellent transmittance properties, especially in the mid-to-far IR region. Conversely, silicon (Si) has been identified as a suitable alternative to the bulky, heavy, and expensive Ge. Nonetheless, it is worth noting that both materials have its drawbacks. Besides the lower cost and lighter weight of Si, it possesses higher IR absorbance as compared to Ge. The machining of both materials into a thin Fresnel shape is seen as a solution to improve the IR transmittance of Si, as well as to reduce the weight of the Ge lens. In the Fresnel lens design, the concave or convex lens curvature is collapsed into a series of concentric narrow rings, while the optical characteristics of a normal planoconcave or planoconvex lens are retained. However, ultraprecision machining is required to realize the ductile cutting mode for both Ge and Si substrate. Extremely sharpened diamond tools are also necessary for the cutting process due to the hard and brittle characteristics of the substrates. This machining requirement has also led to the increase in production cost due to the higher tool wear rate, especially in machining Si, which in turn diminishes the dimensional accuracy of the machining process.

In recent years, the employment of the glass molding press (GMP) in forming glass lens for visible optical systems has received due attention. During the GMP process, the glass is heated above the glass transition temperature and pressed to form the lens structures. However, due to temperature limitations, this method is not suitable to be used to form a Ge and Si lens which requires high temperature.

Recently, the use of polymers for IR applications such as high-density polyethylene (HDPE) has been reported. HDPE is easy to be shaped by using thermal

manufacturing processes into complicated shapes, such as microgrooves and dimples. Although it offers a cheaper solution in comparison to Ge and Si, these types of polymers suffer from high IR absorbance. The lenses made by using HDPE needs to be formed in a minimal thickness to improve the IR transmittance. However, a thin HDPE lens is not suitable due to the low stiffness of the polymer that tends to deflect. A Si-HDPE hybrid substrate is proposed by the present authors for producing IR Fresnel lens. It combines the advantages of both materials, i.e., the high stiffness, high thermal stability and high IR transmittance of Si, and high formability of HDPE. In a previous study, an ultrathin Si-HDPE hybrid substrate for IR microlens arrays was press molded by attaching an extremely thin (~80 micron-thick) HDPE film onto a thin and flat Si wafer without adhesives through press molding (Abdul Manaf and Yan 2016).

The design and press molding of Fresnel structures onto an extremely thin polymer layer of a Si-HDPE hybrid substrate will be discussed in this chapter. Press molding is selected due to its effectiveness in forming microstructures and high aspect ratio optical components of glass and polymers, compared to the time-consuming diamond turning process. The press molding conditions are precisely controlled for obtaining the form accuracy and image quality of the pressed lenses.

This chapter discusses the design and fabrication of an ultrathin Si-HDPE hybrid Fresnel lens for night vision imaging systems. A novel double lens system by combining a spherical and an aspherical planoconvex-shaped Fresnel lens were implemented as the use of single Fresnel lens in imaging is not suitable as it suffers chromatic aberration. The press molding parameters control and its influence on Fresnel form accuracy were investigated. In addition, the optical performance of the fabricated lens systems was demonstrated by using a home-built optical system. As a form of validation toward the lens optical function, the performance of fabricated lenses was also compared with the simulated results. Finally, a combination of Si-HDPE hybrid Fresnel lens with Ge lens was attempted to investigate the improvement of the image quality, and it was demonstrated that a better imaging quality was realized.

21.2 IR Lens Materials and Structures

21.2.1 IR Lens Materials

IR lens material selection is very important to ensure that the IR radiation can be transmitted and captured by the IR imaging camera. Hitherto, several IR lens materials with different characteristics have been widely used. The most popular material is Ge, in which it possesses excellent transmittance rate in the mid-to-far IR region. However, it is bulky, heavy, and expensive (Kulakova et al. 2010). Machining Ge into a thin Fresnel shape enables the reduction of the lens weight (Grulois et al. 2015). Since Ge substrate is a difficult to machine material due to its brittle characteristic, an extremely sharp diamond point tool is required to enable the ductile mode cutting condition.

Another solution is Si which is relatively lower in cost as compared to Ge. Moreover, Si is lighter in weight compared to Ge; however, the IR absorbance is higher. To reduce the IR absorbance, the thickness needs to be maintained as thin as possible. The Fresnel lens structure can be applied to the Si to improve its IR transmittance as the thickness is reduced (Grulois et al. 2014). As for the Fresnel lens design, the concave or convex lens was broke down into a series of flat diffractive surfaces. Meanwhile, the optical characteristics of both lenses are still maintained. However, similar to Ge, Si is also a difficult machining material. Hence, the cutting tool will wear out quickly during machining, and in turn, leading to high machining cost (Yan et al. 2001, 2005; Yan et al. 2003).

Chalcogenide glass is another alternative material for the IR lenses owing to its desirable IR characteristics. It possesses an excellent transmittance in 8–12 μm IR region (Yang et al. 2016). The lenses made of the material can be fabricated by using glass molding press machine. However, extra precaution needs to be considered and the environment is required to be controlled as the material is toxic due to the chemical contents (Namnabat et al. 2014). Moreover, the material is also subjected to the index changes during fabrication, in which it will affect the lens performance (Deegan et al. 2015).

In recent years, a polymer has been reported to be used as IR lens material which offers a cheaper option. HDPE polymer has received due attention by researchers primarily due to its good IR transmittance (Claytor and Claytor 2003). It is also worth to note that the material could be easily shaped into complicated shapes, such as microgrooves and dimples, via thermal forming method. Conversely, HDPE suffers from high IR absorbance as compared to Ge and Si, respectively. In order to mitigate the aforementioned limitation, the thickness needs to be very small to achieve an acceptable level of IR transmittance. Nonetheless, due to its flexible characteristics, it tends to deflect, and it is hard to retain its lens shape when extra-thin HDPE lens is formed.

21.2.2 Hybrid Optical Lens

A combination of different optical materials to improve the optical properties of the camera systems, as well as to lower down the fabrication cost, has been proposed by many researchers in the past. Ultraviolet (UV) curable resin was the earliest method used to fabricate a glass-polymer hybrid lens whereby resin is applied to the substrate, and subsequently, cured by UV light (Zwiers and Dortant 1985; Goss 2002; Huang et al. 2013a, b). Before the UV curing (hardening) process begins, a UV resin is placed within the lens mold. After that, the glass lens is placed on top of the UV resin, while the resin is cured with the aid of UV light. The process of UV curing resin is illustrated in Fig. 1. This method provides a strong adhesion between the two materials.

Another method used to fabricate a glass-polymer hybrid lens is injection molding. This method has a special design of the injection mold that controls the lens's characteristics. To use this method, the glass is first inserted into the mold, then the

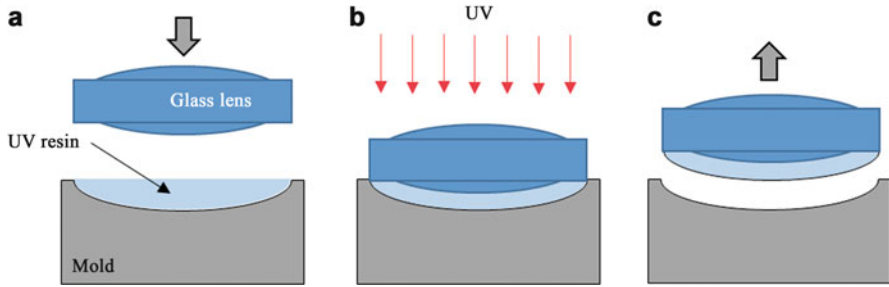
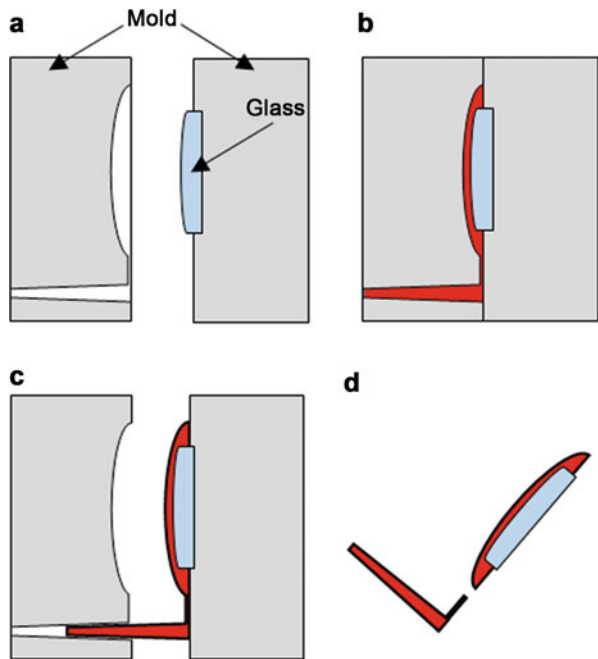


Fig. 1 Hybrid glass-polymer UV curing process: (a) placement of UV resin and glass lens, (b) UV curing process, and (c) demolding

Fig. 2 Fabrication of glass-polymer hybrid lens by using injection molding: (a) a glass lens is inserted into the mold, (b) the mold is closed and polymer injected into the mold, (c) the mold is opened, and (d) the glass-polymer hybrid lens is completed



molten polymer is injected to cover one side of the glass (Li and Yi 2013), as shown in Fig. 2. The resulting lens assembly is held by the flange of the polymer lens. Most importantly, this process allows the production of the lens in a large quantity at a cheaper cost with lower cycle time. A similar process is used to fabricate silicone-glass hybrid lenses for photovoltaic application (Askins et al. 2011).

Figure 3 exhibits the compression molding process, which is another method used to fabricate glass-polymer hybrid lens. Through this method, a glass lens is molded and used as the lower cavity. Then, the polymer is inserted on top of the glass to be heated and pressed. The polymer is adhered to the glass by the heating and cooling of the polymer during compression. The adhesion can be improved by applying hot

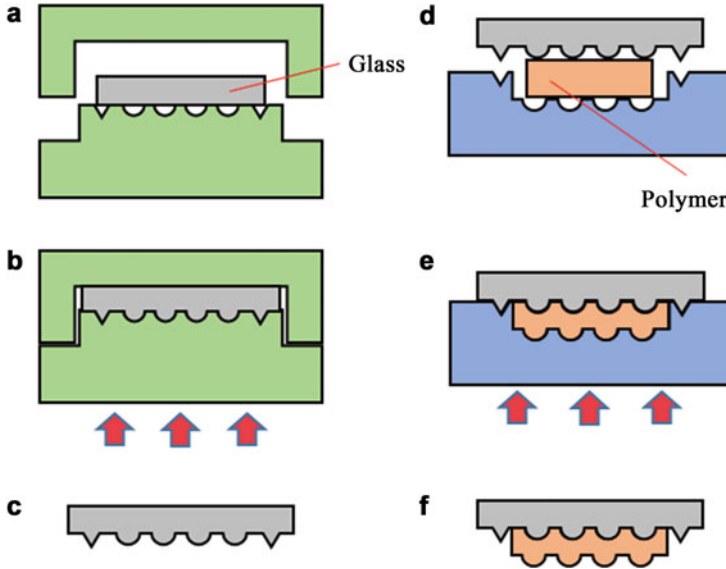


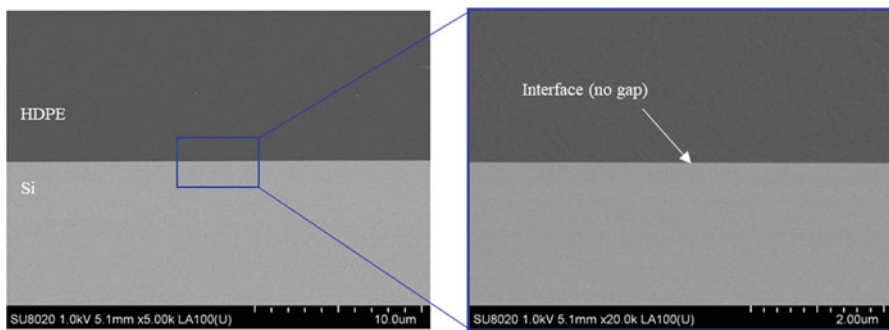
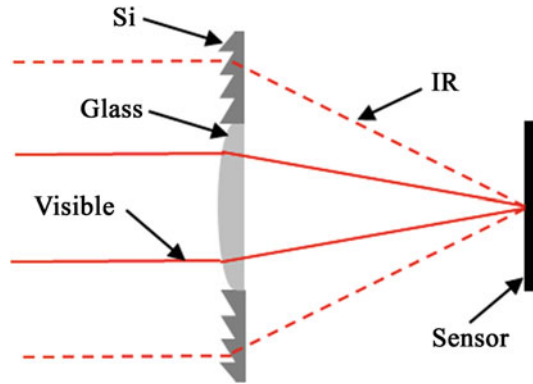
Fig. 3 Fabrication of glass-polymer hybrid lens utilizing the compression molding process: (a–c) glass molding process, and (d–f) hybrid glass-polymer hot embossing

glue between the two substrates (Li et al. 2011). In general, the compression molding process is similar to the glass press molding process. It enhances the efficiency of molding the optical lenses.

A combination of glass and Si for simultaneous visible and infrared imaging has also been performed, whereby the glass is placed at the centre of a Si lens without any adhesion (Takahata et al. 2013). The combination of the Si and the glass for this application is shown in Fig. 4. Undeniably, the fabricating process is challenging. This is mainly due to the time-consuming etching process utilized to fabricate the Fresnel lens, which are made of Si. Nevertheless, the quality of the surface finish produced through this method is considered poor as compared to other lens-forming methods.

21.2.3 Si-HDPE Hybrid Lens

As the solution, the Si-HDPE hybrid substrate/lens is proposed. It combines high stiffness, thermal stability and IR transmittance of Si, and high formability of HDPE. Moreover, both materials have different refractive index; 1.5 for HDPE and 3.5 for Si. For Si-HDPE hybrid lens/substrate design, only one side of the Si is laminated with an extremely thin HDPE layer. This is due to the properties of HDPE that possesses high IR absorbance. Previous researchers used a ~320 micron-thick layer of polymer to laminate a plano-convex shaped silicon lens with adhesive, followed

Fig. 4 A Si-glass hybrid lens**Fig. 5** Si-HDPE interface bonding

by cutting the Fresnel structures on the polymer via diamond turning (Vicker 2003; Vicker and LeBlanc 2001). However, an extra precaution is required for the adhesive selection, as it will affect the IR transmittance.

The present authors formed an ultrathin Si-HDPE hybrid substrate through press molding for IR microlens arrays in previous research. In the study, an extremely thin (~80 micron-thick) HDPE film was press molded onto a thin and flat Si wafer without adhesives and found its transmittance improved for some IR region (Abdul Manaf and Yan 2016). The HDPE layer on Si surface also acts as anti-reflective coating due to its lower refractive index compared to Si. The interface gap between the Si-HDPE substrates is also eliminated by using the press molding process, whereby the interface adhesion is improved with the use of a mechanical lock. The interface gap needs to be eliminated as it will result in light diversion according to Snell's law. The Si-HDPE interface is depicted in Fig. 5, by which the interface bonding is done by the silane-crosslinking HDPE resin.

In fabricating the lens, a two-side polished Si wafer was cut into 15×15 mm squares to be used for the Si-HDPE hybrid Fresnel design. A polished Si is utilized to prevent scattering of light on the surface. The Si thickness was set to $755 \mu\text{m}$ to ensure the IR absorbance at a minimum. Only one side of the Si is laminated with

Table 1 Si material properties

Material properties	Value
Type	P
Doping element	Boron
Resistance, Ω .cm	27
Thickness, μm	755
Refractive index	3.5
Surface roughness (Ra), nm	3.5

Table 2 HDPE material properties

Material properties	Value
Density, g/cm^3	0.955
Melting point, $^{\circ}\text{C}$	133
Softening temperature, $^{\circ}\text{C}$	125
Melt flow rate (190 $^{\circ}\text{C}$, 21.2 N), $\text{g}/10$ min	9
Refractive index	1.5

80- μm -thick HDPE to reduce the IR absorbance, making the total thickness of the hybrid substrate equals 835 μm . The material properties of both materials, i.e., Si and HDPE, are tabulated in Tables 1 and 2, respectively.

21.3 Hybrid Fresnel Lens Design

To realize the application of the hybrid lens in the IR field, the Si-HDPE hybrid Fresnel lens was designed by means of Zemax Optical Design software. During the lens design, the refractive index is an important factor that is required to be defined for different IR wavelength. The Si refractive index was obtained from the Zemax software library, while the HDPE refractive index was obtained from the literature (Horwitz 2011). A Conrady fitting tool and default dispersion data of Zemax software were used to determine the HDPE refractive index (n) for the IR region of 8–13 μm , as follows:

$$n = n_0 + \frac{a}{\lambda + b} / (\lambda^{3.5}) \quad (1)$$

where $n_0 = 1.20048915$, $a = 4.52708247$, $b = -387.18421$, and λ is the wavelength. The results of the calculated refractive index of HDPE for different wavelengths are illustrated in Fig. 6, which shows a good agreement between the calculated and the reference. The refractive index data was then entered into the Zemax software for lens design and performance analysis.

A double lens system for the angle of view of 30° was designed using a Si-HDPE hybrid substrate with a combination of a spherical (Lens 1) and an aspherical (Lens2) Fresnel lens. For the best optical performance, Lens 1 curvature radius was set to

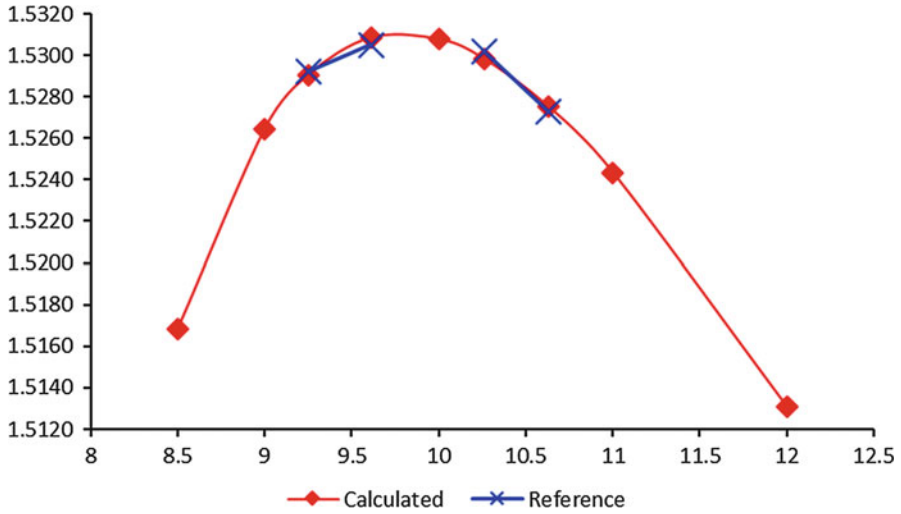


Fig. 6 HDPE refractive index for different wavelength

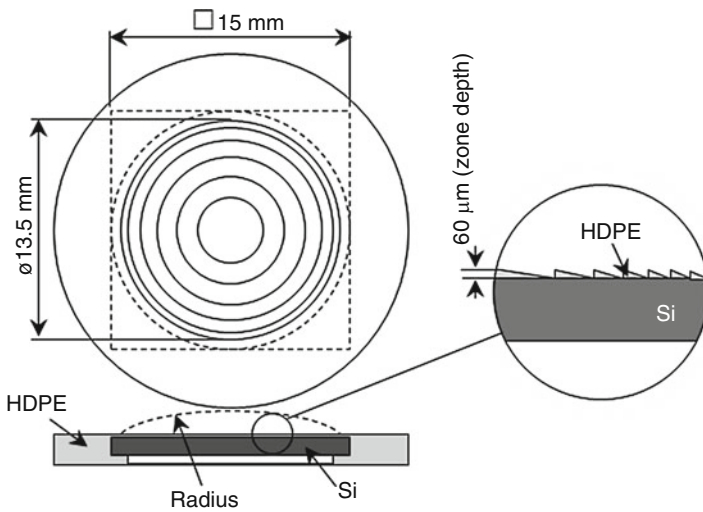


Fig. 7 Schematic diagrams of Si-HDPE hybrid Fresnel lens design

11.636 mm, while Lens 2 with a radius of 11.034 mm. Both planoconvex lenses with the Fresnel structure were formed on an 80-μm-thick HDPE layer of the Si-HDPE hybrid substrate. The Si-HDPE hybrid lens with the diameter of 13.5 mm Fresnel structure design is shown schematically in Fig. 7, and its parameters are summarized in Table 3.

Table 3 Double Si-HDPE hybrid lens design parameters

Parameters	Value
Lens radius (R):	
Lens 1 (spherical) (mm)	11.636
Lens 2 (aspherical) (mm)	11.034
Lens 2 conic constant (k)	-2.813
Lens diameter (D) (mm)	13.5
Fresnel zone depth (h) (μm)	60
HDPE thickness (μm)	80
Si thickness (μm)	755

As the Si-HDPE hybrid Fresnel lens composed of an extremely thin polymer layer and thin Si, a thin lens maker's formula was used (Eq. 2) to calculate the focal distance (f) of the lens. In the calculation, only the refractive index of HDPE is considered. This is due to Si used is flat, and hence it is considered negligible. In calculating the focal distance, the lens material refractive index (n_{lens}), and the radius curvature (r) of the lens is considered. Different materials have different refractive index, and it will vary for each wavelength (Li et al. 2011). The wavelengths selected were between 8.5 and 12 μm of IR region due to the accuracy of the fitted data as represented in Fig. 6.

$$\frac{1}{f} = (n_{\text{lens}} - 1) \left(\frac{1}{r} \right) \quad (2)$$

Meanwhile, the focal length (f_T) of the combined lens can be calculated using the following equation, Eq. 3, whereby the focal length of Lens 1 is represented by f_1 and the focal length of Lens 2 is represented by f_2 . In addition, the air gap between the two lenses is represented by d , which was set to 0.95 mm. The resulting focal length obtained by the Zemax software was 10.982 mm.

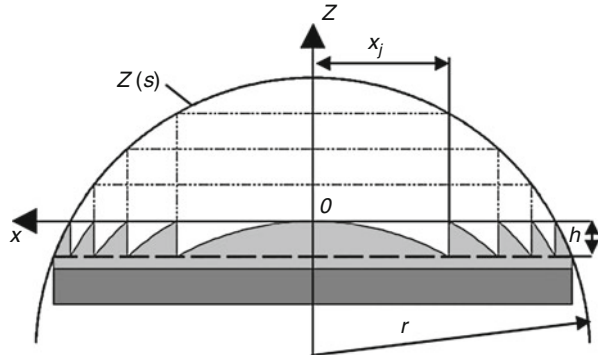
$$f_T = \left(\frac{f_1 f_2}{f_1 + f_2 - d} \right) \quad (3)$$

Figure 8 shows schematically the diffractive surface geometry of the Fresnel lens. As Lens 2 is an even aspherical lens, the lens curvature can be calculated using the aspheric lens equation, Eq. 4, to define the profile, as follows:

$$Z(s) = \frac{C_s^2}{1 + \sqrt{1 - (1 + k)C_2 s^2}} \quad (4)$$

where Z is sag of the surface parallel to the Z axis, s is a radial distance from the optical axis, C is lens curvature (inverse of radius), and k is the conic constant. In this lens design, the conic constant (k) for Lens 2 was set to 2.813.

Fig. 8 Fresnel structure surface geometry



As the Fresnel lens is composed of diffractive surfaces, the surface is divided into concentric rings by cylindrical surfaces at the zone steps whereby the zone depth (h) of each ring is set to $60\ \mu\text{m}$. Each of the ring radial coordinate (x_j) can be calculated using the following equation, Eq. 5:

$$x_j = \sqrt{j \cdot h \left(\frac{2}{c} - j \cdot h \right)} \tag{5}$$

where j is the Fresnel zone sequential number counted from the center of the lens axis (z) and h is the zone depth. Meanwhile, as the Fresnel lens is unpopular to be used as optical lenses due to the light reflection at the zone side wall, no draft angle was designed to reduce the reflection.

The lens parameters were entered into Zemax software for design analysis and performance optimization. Figure 9 shows the lens structure design by the software whereby the stop pupil diameter was set to 9 mm. The stop pupil diameter was set to improve the lens performance, as well as to reduce the light reflection at the Fresnel side wall. The ratio of the lens focal length to the diameter of the stop pupil diameter (F -number) of the lens can be determined by using the following equation, Eq. 6:

$$F = \frac{f}{D} \tag{6}$$

where f is for the focal length and the entrance/stop pupil diameter is represented by D . The back focal length (BFL) obtained by the Zemax software for infinite object distance was 10.115 mm, while for the 400 mm, distance was 10.422 mm. The total track from the entrance pupil to image surface was 16.3 mm. The final lens systems final design parameters are summarized in Table 4.

The ray trace of the lens design at the pupil diameter of 9 mm was also obtained via the Zemax software and showed in Fig. 10a. The incident angles of 0° , 7.5° , 10.5° , and 15° are indicated by the blue, green, red, and yellow lines, respectively. From the ray trace observation, the lens design would suffer some aberration at the angle of

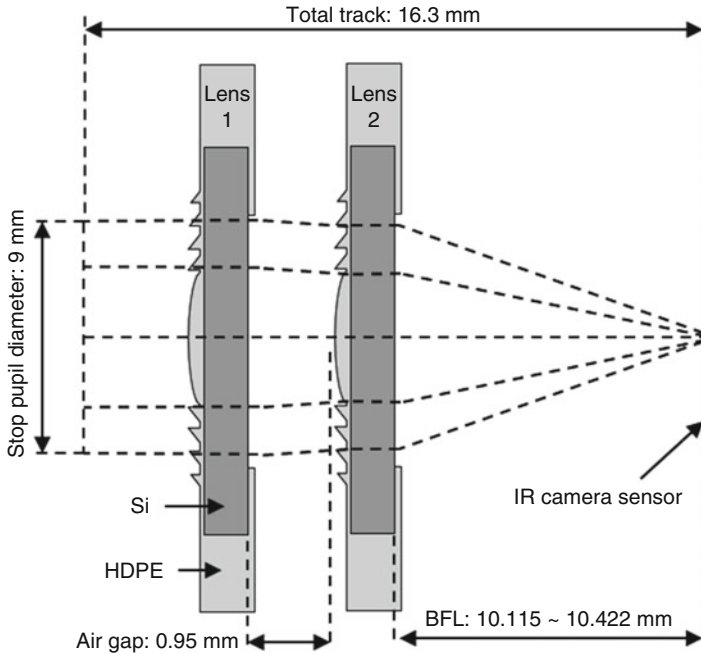


Fig. 9 Schematic diagram of a double Si-HDPE hybrid Fresnel lens system

Table 4 Design results of the lens unit

Parameters	Value
Wavelength range (μm)	8.5–12
Principal wavelength (μm)	10
Effective focal length (mm)	10.98
Back focal length for ∞ (mm)	10.11
Entrance pupil diameter (mm)	9
F-number	1.29
Field of view (FOV) (degrees)	30
Total track (mm)	16.3

10.5 and 15° as compared to lower angles. This can be seen more clearly in Fig. 10b, which shows a slightly bigger coma aberration of the aforementioned angles.

Figure 11 shows ray aberration of tangential (P_y) and sagittal (P_x) as a function of the pupil coordinate on different object wavelength and angles. All lines at P_y and P_x axis are zero in the case of an ideal lens system, in which the paraxial model is functioning. However, the ray fan for the P_y axis incident angle of 7.5° began to become off-axis at the wavelength of 8.5, 10, and 12 μm . This off-axis phenomenon will lead to some image distortion. Larger image distortion was found as the angle is increased to 10.5 and 15°, whereby the off-axis of the ray is also increased. Meanwhile, at the angle of 15°, off-axis of the ray aberration is only apparent at

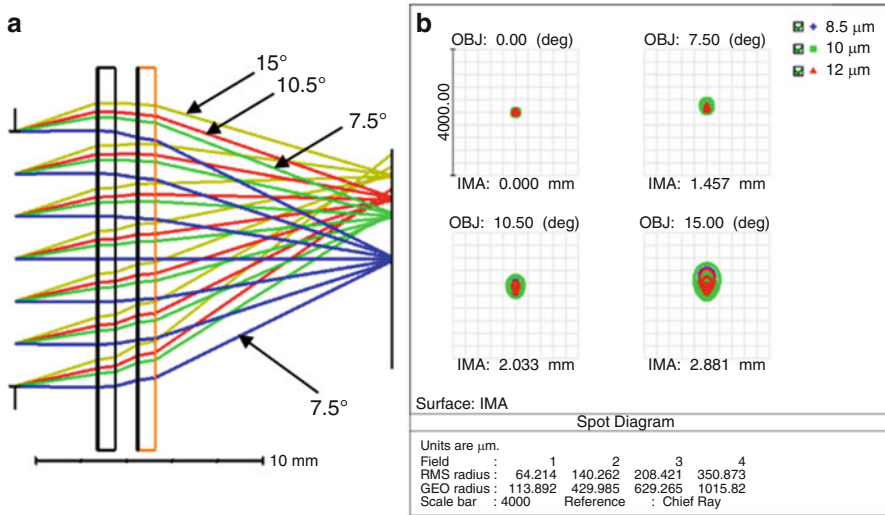


Fig. 10 Zemax lens design data: (a) ray trace of the lens system and (b) spot diagram at lens focal point

the P_x axis. Considering the thickness of the HDPE is extremely thin thus limits the lens design, the distortion resulting from the lens system design is neglected.

21.4 Mold Fabrication

The material selected for the Fresnel mold insert is aluminum as it has enough strength during the press molding of the polymer. Owing to its good machinability characteristics, the Fresnel lens structures were machined using NanoForm-X ultra-precision diamond lathe (Ametech Inc., USA), which is equipped with an air bearing spindle. Moreover, to ensure that the sharp corners of the diffractive surfaces are able to be machined, a sharply pointed 60° V-shaped angle single crystalline diamond tool was selected for the cutting process. A constant spindle speed of 2700 rpm during rough cut was selected during roughing the diffractive surface of the Fresnel mold insert, whereby the depth of cut was 10 μm . A feed rate of 2.7 mm/min was set, in which six roughing tool passes were used.

Meanwhile, for the semifinishing process, the spindle speed and feed rate were unchanged; however, the depth of cut was reduced to 4 μm , while for finishing, the feed rate was then reduced to 0.15 mm/min. The same cutting parameters were used for cutting both the spherical and an aspherical Fresnel mold inserts. A photograph of fabricated mold inserts is shown in Fig. 12, in which the final surface roughness was 4.82 nm Ra.

The cross sections for lens mold are provided in Fig. 12b, which is replicated by using UV curable resin. From the cross-sectional observation, the zone depth of 60 μm of the Fresnel structures was precisely fabricated using an ultraprecision diamond lathe.

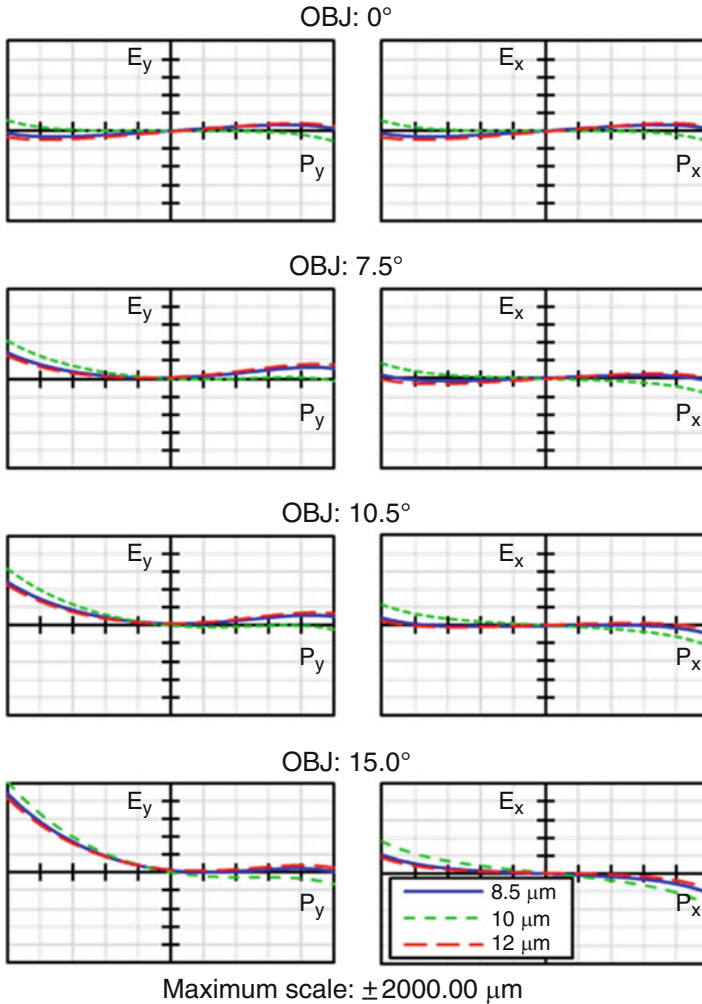


Fig. 11 Transverse ray fan plot

21.5 Press Molding for Hybrid Lenses

In the research, the Fresnel structures are directly press molded onto an extremely thin polymer layer of a Si-HDPE hybrid substrate. To realize the form accuracy and to achieve the high aspect ratio of the Fresnel lens structures, a press molding is considered as the best method to be used. It has been demonstrated to be an effective process for forming microstructures onto glass or polymers (Yan et al. 2009; Worgull et al. 2010; Zhou et al. 2011; Peng et al. 2014), by which the Fresnel lenses could be attained at a higher precision and lower cost. It can significantly reduce the higher cost and time-

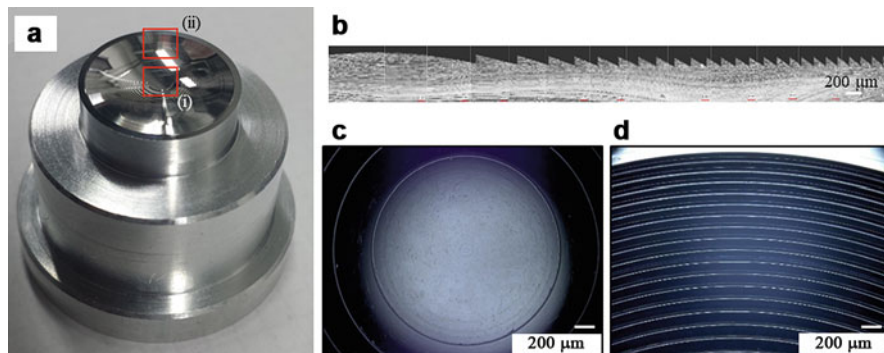


Fig. 12 (a) Photograph of an aluminum mold insert with Fresnel structure, (b) mold insert cross section of a Fresnel structure obtained by UV curing, (c) magnified view of rectangle (i) showing Fresnel structure center area, and (d) magnified view of rectangle (ii) showing Fresnel structure outer area

consuming diamond turning process. However, to ensure the form accuracy of the Fresnel lens, it is essential to precisely control the press molding condition. Instead of lens design, the image quality also depends on the form accuracy of the pressed lenses. Optimum press molding conditions should also be determined to realize the crosslink binding between the HDPE and the Si (Abdul Manaf and Yan 2016).

In fabricating the Si-HDPE hybrid lenses, a press molding machine (GMP211, Toshiba Machine Co. Ltd., Japan) was used. The maximum molding temperature was 800 °C with the temperature accuracy of ± 1 °C which monitored by the thermocouple sensors. The nitrogen gas was purged into a transparent silica glass tube chamber during molding to prolong the mold life and also to prevent oxidation of the mold when it is operated at high temperatures. With a 0.98-N resolution, the machine is capable of operating at a minimum force of 0.2 kN and a maximum force of 20 kN. Two mold half was required during the press molding, in which the upper mold is fixed without any movement. During molding, the lower mold moved toward the stationary upper, whereby an AC servomotor will control the movement of the mold at a resolution of 0.1 μm.

In forming the Si-HDPE hybrid Fresnel lens, two sets of mold were used, in which two steps of the press molding process were utilized. Both of the steps employed the isothermal molding process in which the molds and sample heated at the same temperature (He et al. 2007). During the first step (Step 1), a flat Si-HDPE hybrid substrate was formed by using the same method as the authors' previous research (Abdul Manaf and Yan 2016), as illustrated in Fig. 13. In this first step, the Si was placed inside the lower mold cavity, followed by HDPE resin. The resin is heated slightly above HDPE melting temperature (140 °C) and pressed at the minimum pressing force (0.2 kN). The mechanical lock also can be formed in this step, which is used to improve Si-HDPE adhesion. The HDPE thickness can be controlled up to ~80 μm during this step. The different sides of the press-molded Si-HDPE substrate that were formed during Step 1 is illustrated in Fig. 14.

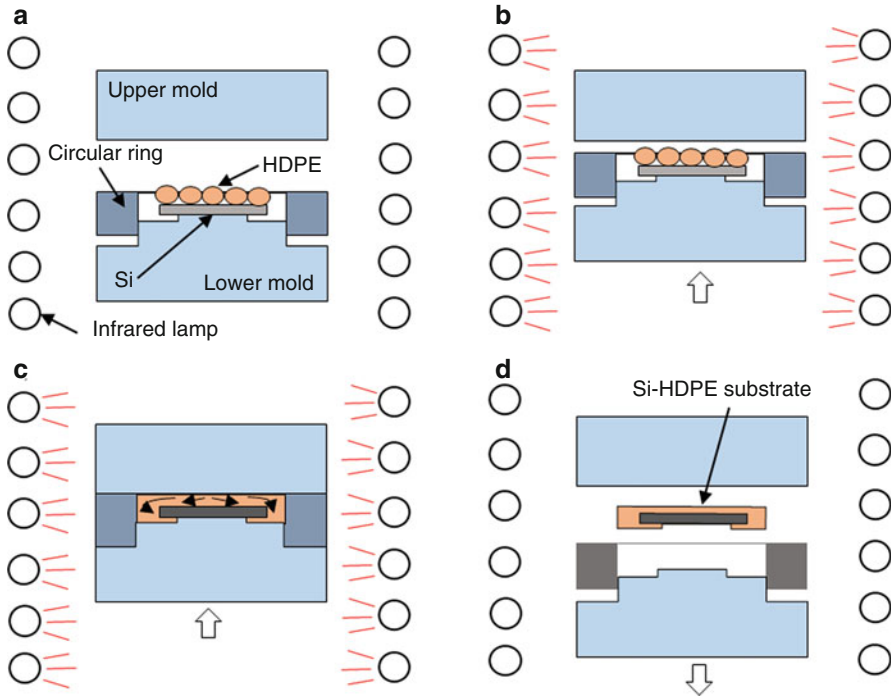


Fig. 13 Step 1 – press molding process of a Si-HDPE hybrid substrate: (a) material setup, (b) heating, (c) pressing, and (d) cooling and Si-HDPE substrate removal

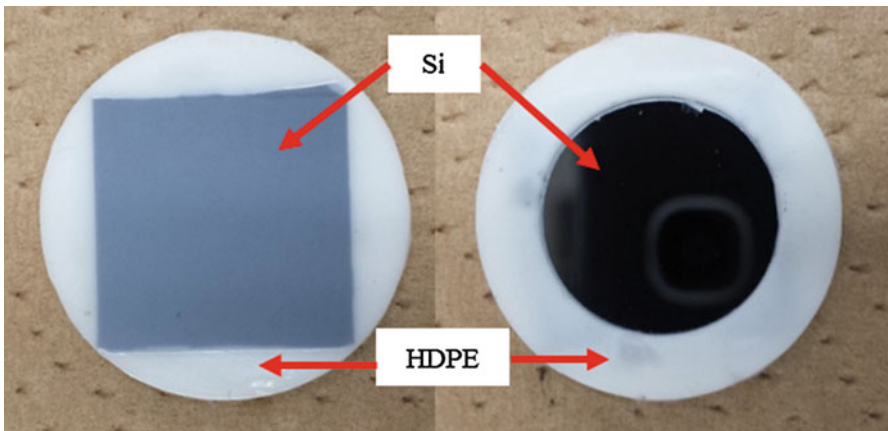


Fig. 14 Photograph of press-molded Si-HDPE hybrid substrate, showing different sides

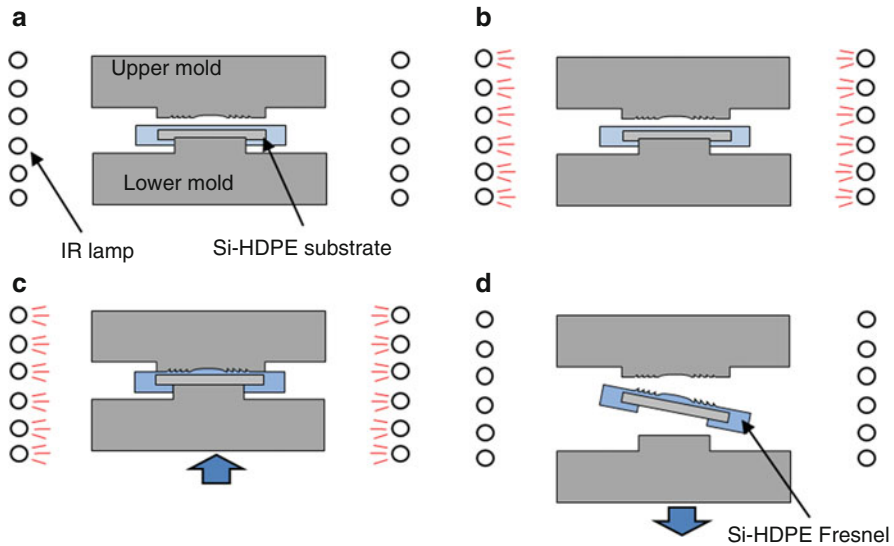


Fig. 15 Step 2 – press molding process of a Si-HDPE hybrid lens: (a) hybrid substrate setup, (b) heating, (c) pressing, and (d) cooling and Si-HDPE hybrid Fresnel lens removal

In the second step (Step 2) of the press molding, the preformed Si-HDPE hybrid substrate that was fabricated in Step 1 is heated above the glass transition (T_g) of HDPE, and the pressing process will take place. The processes are illustrated in Fig. 15. As the press molding was carried out in a none vacuum condition, the lens is exposed to the air trapping that in turn affects the surface integrity (Abdul Manaf and Yan 2017). Air pockets were generated at the boundaries between the HDPE resin and the Si substrate when the HDPE resin was used in press molding. Thus, the use of flat-shaped HDPE is preferred to minimize the air trapping phenomenon.

In Step 2, the best pressing temperature is required to be defined to achieve the lens form accuracy before the other pressing parameters are decided. The Si-HDPE hybrid substrate is pressed with 0.2 kN pressing force at three different pressing temperatures, i.e., 125 °C, 128 °C, and 130 °C. The pressing force was increased between 0.4 and 1.2 kN once the temperature was decided and the Fresnel zone depth was evaluated for the best molding parameters. The molding steps are summarized as follows:

- (a) The press-molded Si-HDPE hybrid substrate is placed into the mold cavity followed by the closure of the molding chamber.
- (b) The lower mold is elevated closer to the stationary upper mold and the movement stop when a 2-mm gap between the upper mold and hybrid substrate is achieved. The gap is to improve the heating process. The nitrogen gas is purged into the chamber for 20 s to prevent mold oxidation during heating.

- (c) The molds and specimen are heated from room temperature to the molding temperature at a heating rate of approximately $0.6\text{ }^{\circ}\text{C/s}$ by using IR lamp.
- (d) The temperature is then maintained for 100 s when the molds and specimen reach the required temperature, followed by the pressing until the mold is completely closed. The pressing force is set between 0.4 and 1.2 kN.
- (e) The pressing force is maintained while the chamber is purged with a nitrogen gas again for cooling down both molds and specimen at a rate of approximately $0.3\text{ }^{\circ}\text{C/s}$ until the temperature was $90\text{ }^{\circ}\text{C}$.
- (f) Lastly, the molded Si-HDPE hybrid Fresnel lens is demolded from the molds after the mold opening and cooled down naturally to room temperature. The complete cycle time of the press molding process is approximately 420 s.

21.6 Fresnel Lens Form Accuracy

The Si-HDPE hybrid Fresnel lens was formed by using press molding under different pressing temperatures. To evaluate the form accuracy of the lens, the lens structure was replicated by using UV curing process, and the cross-sectional cut was made to the replicated sample. The Fresnel zone depth molded at the pressing force of 0.2 kN and pressing temperatures of $125\text{ }^{\circ}\text{C}$, $128\text{ }^{\circ}\text{C}$, and $130\text{ }^{\circ}\text{C}$ is illustrated in Fig. 16. It could be seen that the increase of the pressing temperature resulted in a higher Fresnel zone depth. The zone depth was measured at 10 and $16\text{ }\mu\text{m}$ at the temperature of $125\text{ }^{\circ}\text{C}$ and $128\text{ }^{\circ}\text{C}$, respectively. As the temperature is increased to $130\text{ }^{\circ}\text{C}$, the zone depth is increased to $20\text{ }\mu\text{m}$. This observation suggests that the pressing temperature is nontrivial as it will lower down the HDPE viscosity, and hence, a higher Fresnel zone can be achieved (Peng et al. 2014). From the results, a temperature of $130\text{ }^{\circ}\text{C}$ was selected for further experimentation with different press molding parameters.

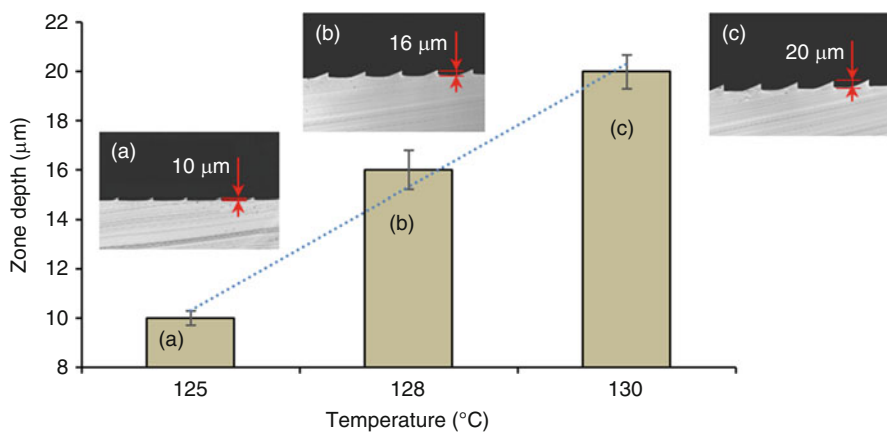


Fig. 16 Zone depth change of the Fresnel structure for different temperatures under the pressing force of 0.2 kN

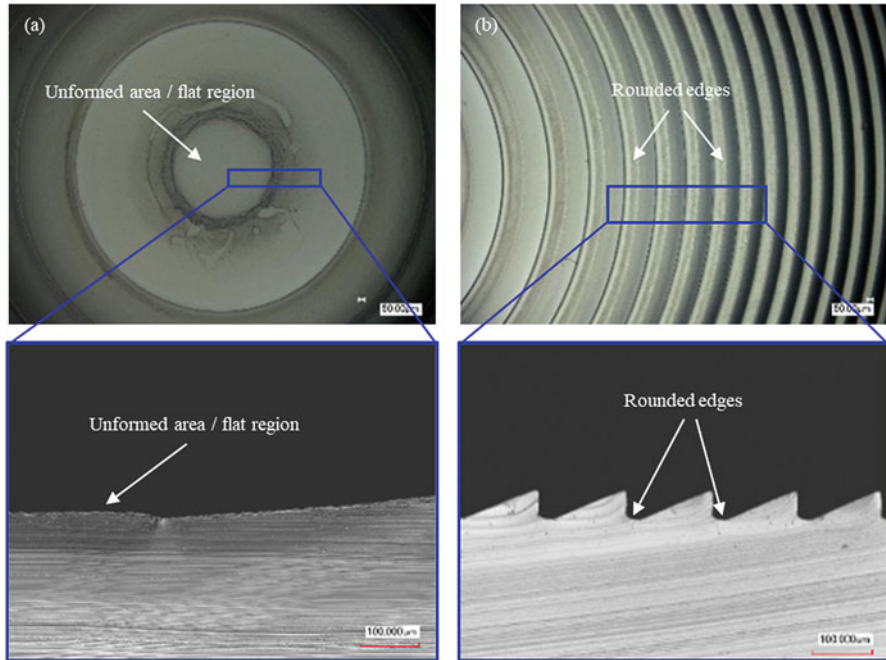


Fig. 17 Microscope images of formed Fresnel lens under pressing temperature of 130 °C

A series of press molding experiments with different pressing force was performed at the temperature of 130 °C. The microscope images of the formed Fresnel are depicted in Fig. 17. From the figures, it could be observed that the Fresnel structures are not entirely formed at the center area of the lens, leaving a flat area/region, as shown in Fig. 17a. This phenomenon is found to happen for all the pressing forces used in the press molding. The increase in the pressing force did not eliminate completely the flat area; however, the flat area became smaller with the increase in the pressing force. Meanwhile, it is also discovered that the rounded Fresnel ridges occur at the lower pressing force, as shown in Fig. 17b. Insufficient pressing force and polymer recovery might be the reason of rounded Fresnel ridges at the outer lens area (Liu et al. 2010). However, the rounded edges phenomenon was completely eliminated when the pressing force increased to 1.0 and 1.2 kN. Further increase in the pressing force at this temperature may cause the Si breakage due to the relatively thin Si used for the hybrid lens.

For further investigation, the Fresnel zone depth was measured to evaluate the dimensional accuracy of the press molded lens under 130 °C. From the cross-sectional measurement, the zone depth was measured at 22 and 46 μm when it is formed at a pressing force of 0.6 and 0.8 kN, respectively, as depicted in Fig. 18. The zone depth is increased to 53 and 54 μm, respectively, with the increase in the pressing temperature to 1.0 and 1.2 kN. However, the target zone depth of 60 μm was not achieved. Further increase in the pressing force might expose the Si to breakage.

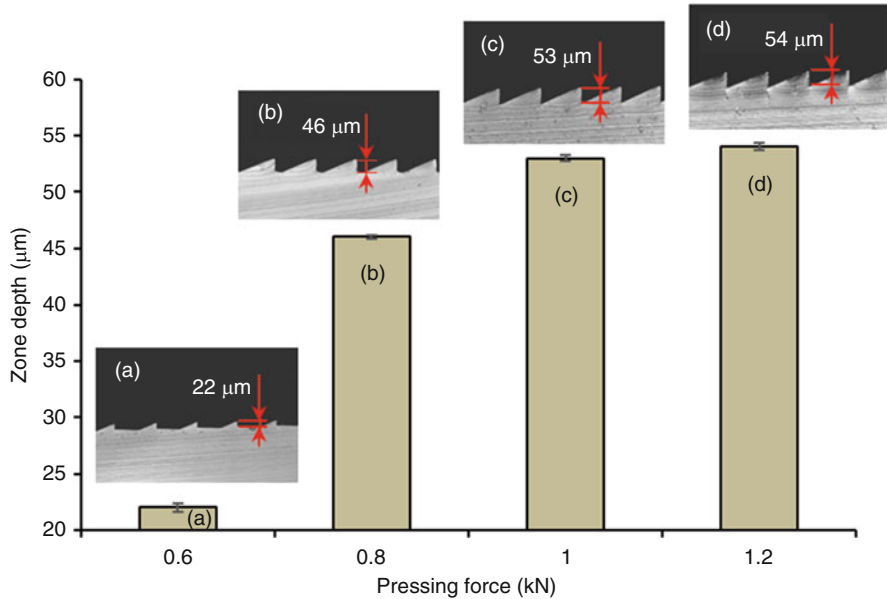


Fig. 18 Zone height of the Fresnel under different pressing forces at a temperature of 130 °C

From the findings, it could be deduced that further increase in the pressing temperature should be considered to improve the form accuracy as the temperature of 130 °C is found to be unsuitable.

For the Fresnel zone depth improvement, the pressing temperature was slightly increased to 131 °C, and a press molding experiment was performed. The pressing temperature is kept at a minimum as a higher temperature will lead to a higher polymer shrinkage, and consequently, it will affect the form accuracy (Zhu et al. 2011). However, due to the low viscosity of the polymer at higher temperature, the initial pressing force in the experiment is reduced to 0.4 kN, while the maximum pressing force is set to 1.0 kN. The microscope images of the formed Fresnel are shown in Fig. 19. Interestingly, the rounded edges were significantly reduced for all pressing forces as compared to the previous experiments (see Fig. 17). This phenomenon is due to the low viscosity of the polymer, which makes the polymer flow smoothly inside the cavity (Zhu et al. 2011). Meanwhile, an unformed area persisted at a lower pressing force and is reduced by gradually increasing the pressing force to 0.6 and 0.8 kN. The unformed area was completely eliminated when 1.0 kN of pressing force was utilized, as shown in Fig. 19a. This was also confirmed by the cross-sectional observation, where the Fresnel curvature was obtained, and the flat area was eliminated.

For further Fresnel zone depth observation, a cross section of the diffractive surface of the lens was obtained for measurement and illustrated in Fig. 20. It is found that the zone depth of 57 and 57.6 μm was obtained with the pressing force of 0.4 and 0.6 kN. As expected, due to further increase in the pressing force to 0.8 kN, the zone depth increased to 58.3 μm. The Fresnel zone depth of 60 μm was accurately formed at the

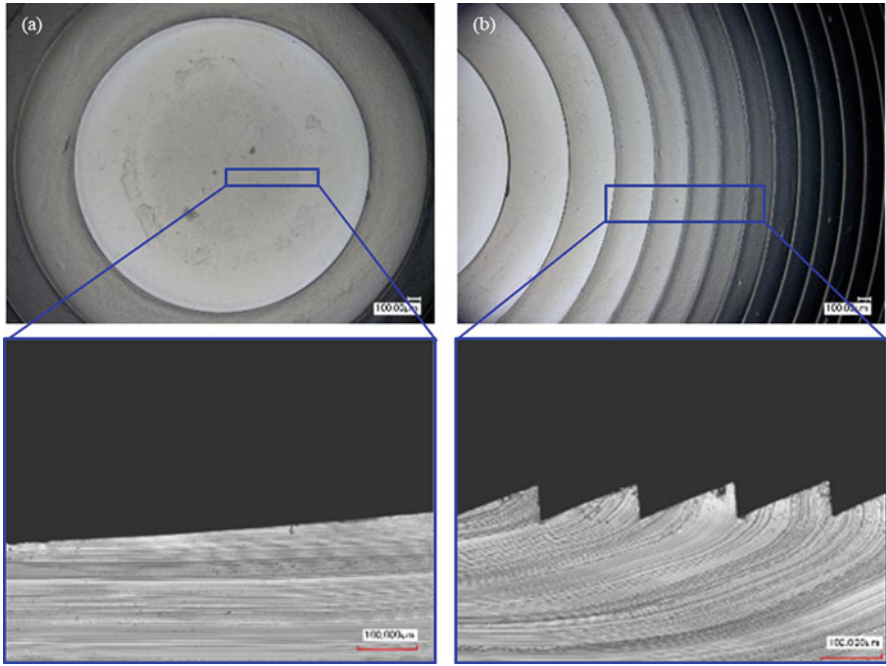


Fig. 19 Microscope images of formed Fresnel lens under different pressing forces at a temperature of 131 °C

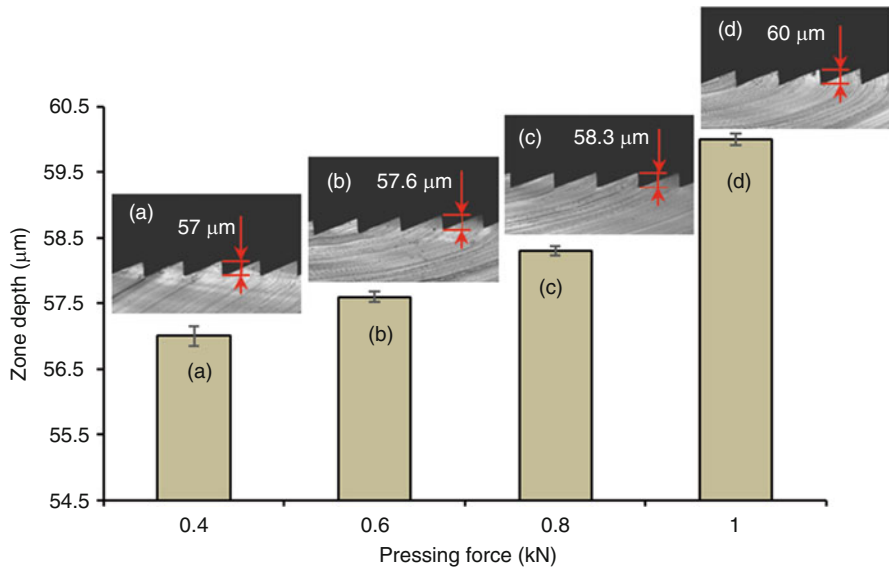


Fig. 20 Zone height of the Fresnel under different pressing forces at a temperature of 131 °C

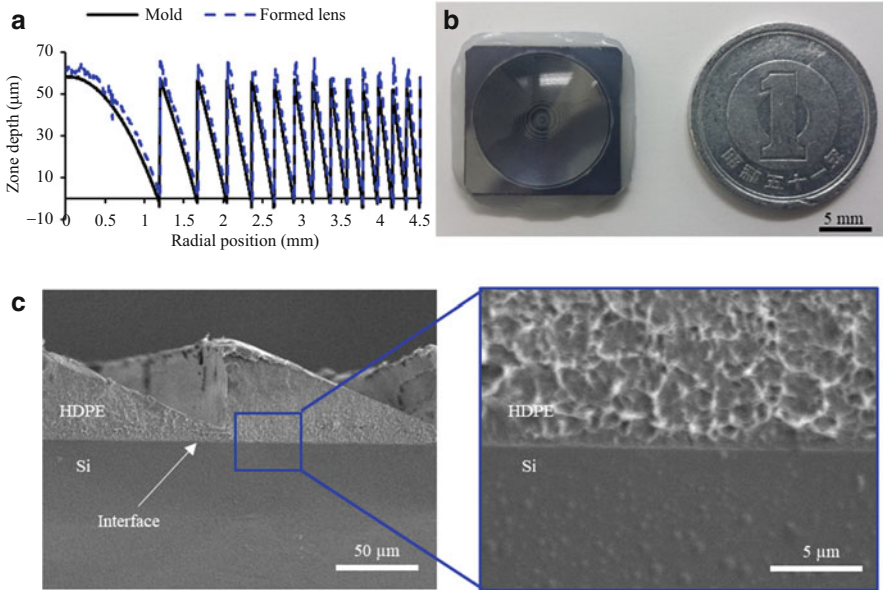


Fig. 21 (a) Cross-sectional profile of lens geometry, (b) a press molded Si-HDPE hybrid Fresnel lens and a Japanese coin, and (c) cross-sectional SEM images of a Si-HDPE hybrid Fresnel lens. (Reprinted with permission from ref. (Abdul Manaf et al. 2017), [Optics Express])

pressing force of 1.0 kN along the elimination of the flat zone as illustrated in Fig. 19. These findings clearly show that the form accuracy depends on the pressing temperature and also the pressing force, similar to hot embossing (Peng et al. 2014). For the lateral dimensional observation, it is also found that it was accurately replicated, as shown in Fig. 21a. Under the pressing force of 1.0 kN and pressing temperature of 131 °C, the surface roughness of 6.78 nm Ra was also obtained. Figure 21b is a photograph of a formed Si-HDPE hybrid Fresnel lens and a coin for comparison of the size. Meanwhile, the cross section of the Si-HDPE hybrid Fresnel lens is also observed by a scanning electron microscope (SEM) and shown in Fig. 21c. The diffractive wall of the Fresnel was properly duplicated by using press molding, while no gap was found at the interface between the Si and HDPE, showing that the Step 2 of the press molding does not affect the bonding.

21.7 Lens Performance Evaluation

21.7.1 Modulation Transfer Function

To evaluate the actual lens performance, the modulation transfer function (MTF) is carried out. In addition, the effective focal length (EFL) measurements also performed where both of the measurements were done by using ImageMaster HR

Table 5 MTF measurement parameters

Measurement conditions	Value
Spatial frequency and pitch (lp/mm)	1 ~ 10/1
Angle of view (max. image height) / division pitch	15°/5°
Collimator (mm)	50
AF frequency (lp/mm)	5
Total angle of view	30°
Object distance (m)	Infinite
Light source orientation	Sagittal/tangential
Center wavelength (μm)	10
Wavelength range (μm)	8.2–12.8

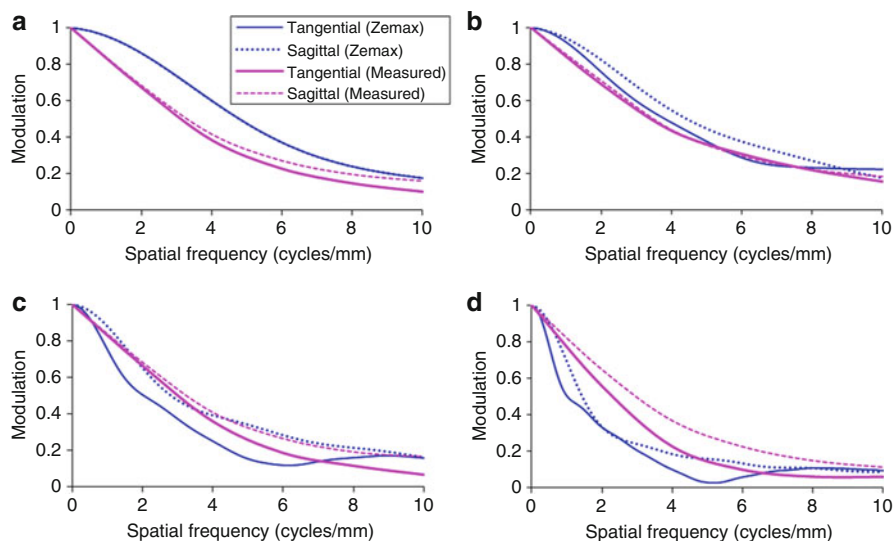
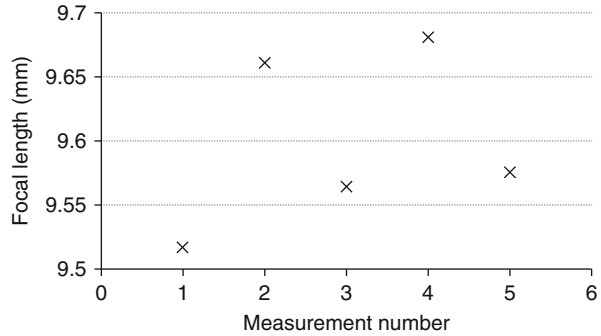


Fig. 22 Comparison of geometric MTF calculated by Zemax and measured results for different field angles: (a) $\theta = 0^\circ$, (b) $\theta = 5^\circ$, (c) $\theta = 10^\circ$, and (d) $\theta = 15^\circ$. (Reprinted with permission from ref. (Abdul Manaf et al. 2017), [Optics Express])

test station (Trioptics Japan Co., Ltd., Japan) at different field angles. The machine is capable of achieving the MTF measurement accuracy and repeatability (on-axis and off-axis) at ± 0.03 MTF and ± 0.02 MTF, respectively. The details of the measurement parameters are listed in Table 5. The actual lens performance result obtained was then compared with the simulated MTF data of Zemax optical design software.

As illustrated in Fig. 22, the experimental MTF data and Zemax data show good agreement. A slight difference in the MTF curve could be observed in Fig. 22a in which the experimental curve stands below the simulated MTF at the field angle of 0° due to poor line image density or line spread function (LSF) during MTF measurement.

Fig. 23 Focal length measurement results at a wavelength of $10\ \mu\text{m}$



However, similar curves were noticed as the field angle increased to 5° and 10° as shown in Fig. 22b and c, respectively, for both the tangential and sagittal orientation. Though, a higher contrast was noticed at the measured tangential frequency of 10° field angle at a lower frequency. The lens demonstrated a better performance at a lower frequency compared to Zemax curve as illustrated in Fig. 22d as the field angle is increased to 15° ; however, a slightly lower contrast is noticed as the frequency is increased for the tangential curve. This phenomenon is due to the variances of the light passing through the Fresnel diffractive surface. To conclude, the overall MTF performance of the lens is 0.1 above the modulation, resulting in a low contrast of the images.

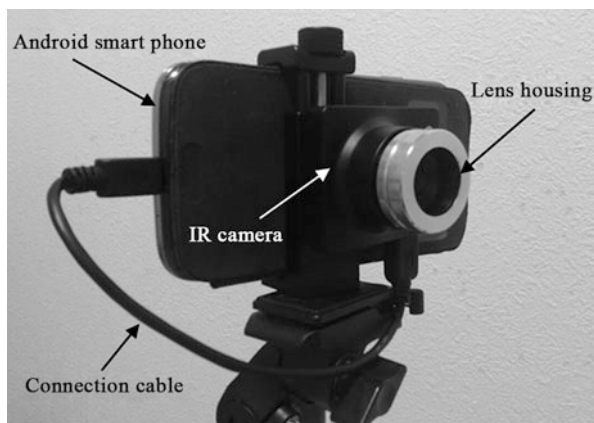
In order to obtain a better image during imaging, a series of EFL measurements at the wavelength of $10\ \mu\text{m}$ was also carried out and illustrated in Fig. 23. From the measurement, the average measured focal length was at 9.6 mm, and is still within the range $\pm 1.5\ \text{mm}$ of designed focal length (10.982 mm).

21.7.2 Night Mode Imaging

An imaging test was performed in the night mode using the Therm-App (Opgal Optronic Industries Ltd.) 384×288 pixels IR thermal camera, which is operating on an Android-based smartphone. The camera IR spectrum is for long-wave IR region ($7\text{--}14\ \mu\text{m}$) with an image sensor sensitivity of $17\ \mu\text{m}$ pixels pitch. The formed Fresnel lenses were attached to a custom built aluminum camera housing with an adjustable mechanism for back focal length setting as shown in Fig. 24. At the distance of 400 mm and 2 m, a human object is captured, and therefore, the images can be used to define the Si-HDPE hybrid Fresnel lens capability and performance.

The spherical and aspherical lenses were assembled to the aluminum lens housing, and the white-hot imaging mode was selected for the camera setting. The object images were captured for both short and long distance of 400 mm and

Fig. 24 Camera setup for night imaging performance evaluation



2 m, respectively, and are illustrated in Fig. 25 along with the visible light images for comparison. The bad pixels of the camera were corrected to suit the lenses. From the imaging, it is noticed that the object was identified with an acceptable image quality at a shorter imaging distance (400 mm). Some of the object details were also able to be recognized. However, due to the chromatic aberration phenomenon, the image sharpness is lower when the image is captured at the distance of 2 m. Though, both images showed dark images due to the low contrast of the designed lens.

Meanwhile, the images captured with the lenses also suffer some chromatic aberration, which caused blurred object image. It can be seen in Fig. 25d in rectangle (i). The phenomenon is due to the scattering of the light on the diffractive surfaces of the Fresnel lens, and therefore stray light occurred (Fujii et al. 2015). In addition, it is worth to note that this phenomenon is also due to the reflection of the Si itself. The stray light and reflection generation can be seen in Fig. 26. Meanwhile, the effective lens design wavelength is set in between 8.5 and 12 μm , while image sensor sensitivity wavelength is in between 7 and 14 μm . This wavelength difference caused the degradation of the image quality, in turn producing the blurred image.

The Si-HDPE hybrid Fresnel lens also works with other IR lens material for higher-precision IR imaging application. In the trial, a spherical hybrid Fresnel lens (Lens 1) is combined with the convex-concave lens of Ge, as shown in the schematic diagram illustrated in Fig. 27a. As shown in Fig. 27b and c, a more clearer image was captured with a lower chromatic aberration as shown in Fig. 27c in rectangle (i). This lens combination promotes a better image due to the lower stray light generation as no diffractive surface on the Ge lens, along with the better IR transmittance of Ge. By using ImageJ software, the image was compared with the image that is captured from the double hybrid Fresnel and the comparison is illustrated in Fig. 28. From the comparison, it could be seen that higher gray value is recorded when a combination of hybrid Fresnel and Ge convex-concave lens was used.

Fig. 25 Visible light and night vision images at different distances; (a and b) 400 mm and (c and d) 2 m, and rectangle (i) showing image aberration. (Reprinted with permission from ref. (Abdul Manaf et al. 2017), [Optics Express])

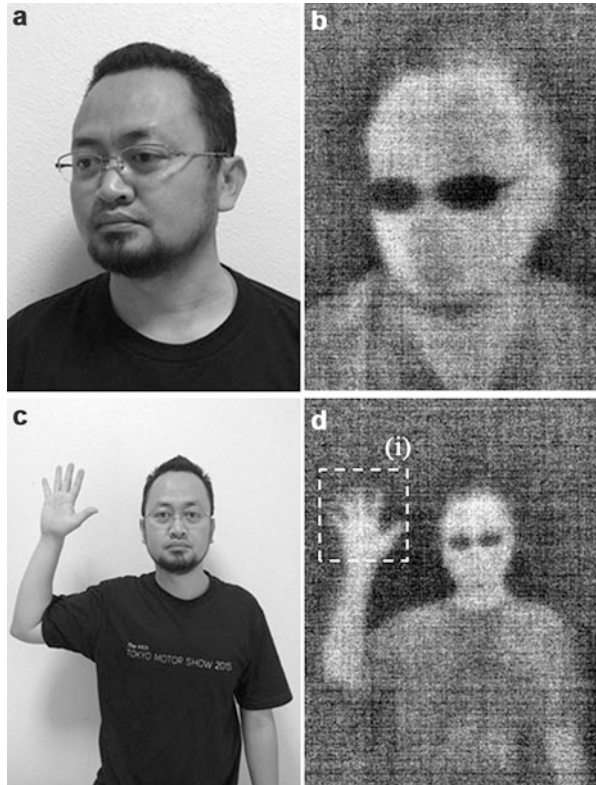
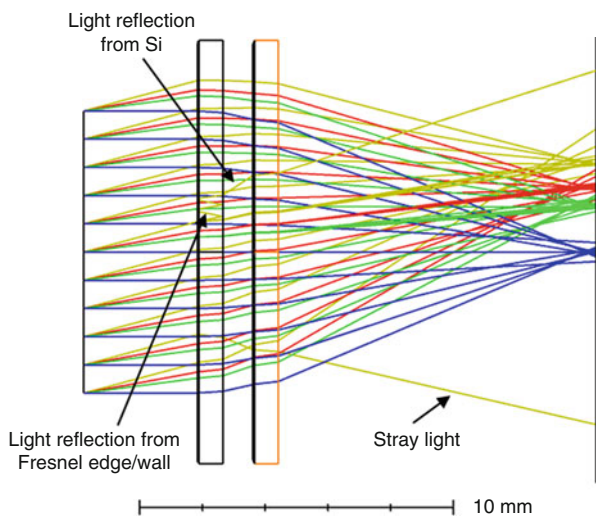


Fig. 26 Schematic diagram of stray light formation from the lens system



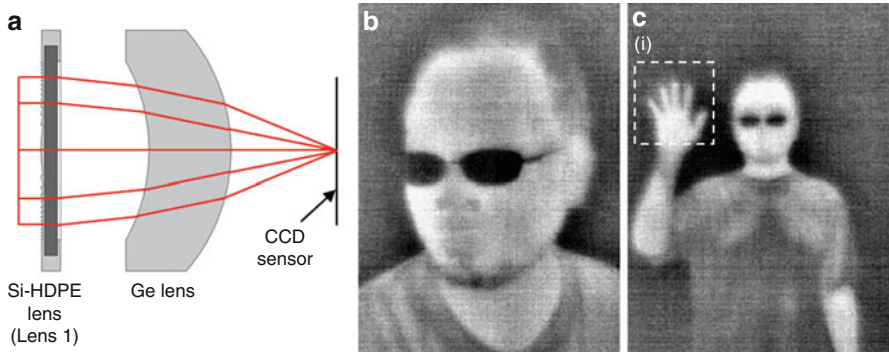


Fig. 27 (a) Schematic diagram of combining a Si-HDPE hybrid lens and germanium lens, (b) and (c) night vision images captured by combining a Si-HDPE hybrid lens and a germanium lens at different distances; (b) 400 mm and (c) 2 m, and rectangle (i) showing image aberration. (Reprinted with permission from ref. (Abdul Manaf et al. 2017), [Optics Express])

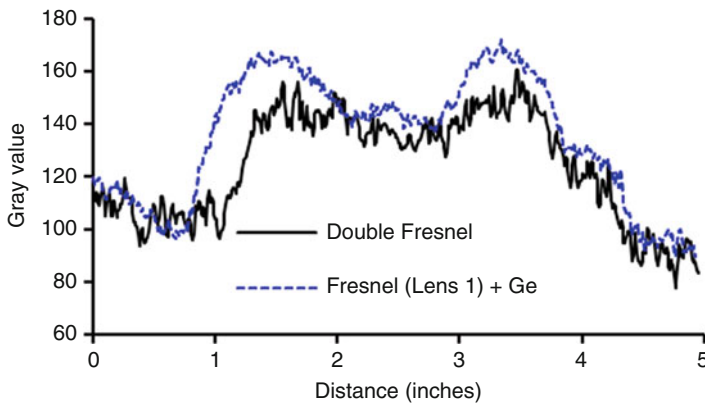


Fig. 28 Image sharpness evaluation between double Si-HDPE hybrid Fresnel lens and a combination of a spherical Si-HDPE hybrid Fresnel (Lens 1) + Ge lens. (Reprinted with permission from ref. (Abdul Manaf et al. 2017), [Optics Express])

21.7.3 Thermography Imaging

Finally, the developed Si-HDPE hybrid lenses could also be used for thermography imaging, in which the temperature of the object can be measured. It can be seen from Fig. 29, the temperature distribution of the mug filled with hot water is recognized and measured. The image is also compared with the image captured by Therm-App 19 mm Ge lens, and it is evident that no significant difference is observed. However, the temperature value and accuracy need to be calibrated in the event that the hybrid lenses are to be used for thermography applications.

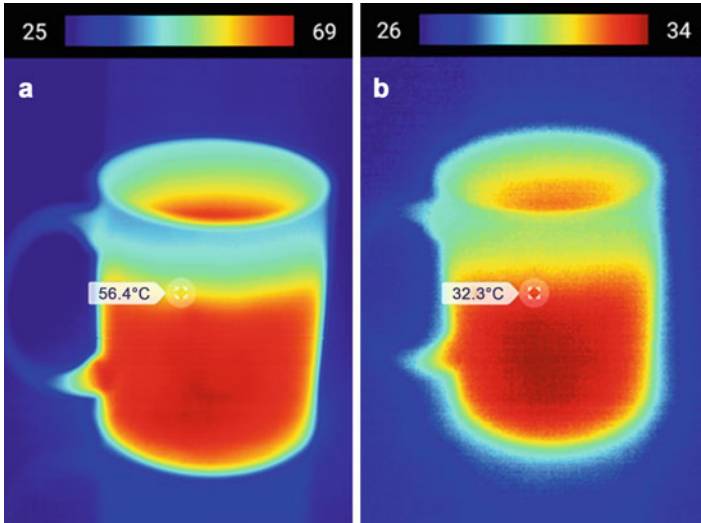


Fig. 29 Thermography images of different lens systems: (a) standard germanium lens and (b) uncalibrated double Si-HDPE hybrid Fresnel lens. (Reprinted with permission from ref. (Abdul Manaf et al. 2017), [Optics Express])

21.8 Summary and Outlook

Press molding has become a field of research interest in the IR optical systems, along with the development of the IR substrate. In this chapter, the press molding of Si-HDPE hybrid Fresnel lens has been introduced and discussed based on recent research outcomes of the author's research. A cost-effective method for fabricating ultrathin Si-HDPE hybrid Fresnel lens and IR optical components by using a press molding were presented in this chapter. The development of these lenses might open the potential for the lenses to be used in applications in future IR optical technologies such as search and rescue, night security surveillance, night driving assistance, as well as engineering thermography. The hybrid lens capabilities for night mode imaging as well as for thermography are also discussed in this chapter. However, it is noteworthy to mention that the development of the hybrid lenses is still ongoing. A variety of other high-precision forming methods that has yet been investigated could also be utilized in fabricating such hybrid lenses. The room for future research and development in this area is indeed endless.

References

- Abdul Manaf AR, Yan J (2016) Press molding of a Si-HDPE hybrid lens substrate and evaluation of its infrared optical properties. *Precis Eng* 43:429
- Abdul Manaf AR, Yan J (2017) Improvement of form accuracy and surface integrity of Si-HDPE hybrid micro-lens arrays in press molding. *Precis Eng* 47:469

- Abdul Manaf AR, Sugiyama T, Yan J (2017) Design and fabrication of Si-HDPE hybrid Fresnel lenses for infrared imaging systems. *Opt Express* 25(2):1202–1220
- Askins S, Victoria M, Hererro R, Domínguez C, Anton I, Sala G (2011) Effects of temperature on hybrid lens performance. *AIP Conf Proc* 1407:57–60
- Claytor RN, Claytor NE (2003) Low-cost polymer infrared imaging lens. *Proc SPIE* 5074:855–866
- Deegan J, Walsh K, Lindberg G, Benson R, Gibson D, Bayya S, Sanghera J, Stover E (2015) Index change of chalcogenide materials from precision glass molding processes. *Proc SPIE* 9451, *Infrared Technology and Applications XLI*, 94511R
- Fujii T, Gaulet A, Hattori K, Konno K, Tanaka A, Bosmans R, Sawada M, Yazawa H (2015) Fresnel lens sidewall design for imaging optics. *J Eur Opt Soc vol. 10:90702H-9070-7*
- Goss B (2002) Bonding glass and other substrates with UV curing adhesives. *Int J Adhes Adhes* 22:405–408
- Grulois T, Druart G, Guérineau N, Crastes A, Sauer H, Chavel P (2014) Extra-thin infrared camera for low-cost surveillance applications. *Opt Lett* 39(11):3169–3172
- Grulois T, Druart G, Sauer H, Chambon M, Guérineau N, Magli S, Lasfargues G, Chavel P (2015) Reduction of material mass of optical component in cryogenic camera by using high-order Fresnel lens on a thin germanium substrate. *Appl Opt* 54(20):6313–6320
- He Y, Fu J-Z, Chen Z-C (2007) Optimization of control parameters in micro hot embossing. *Microsyst Technol* 14(3):325–329
- Horwitz JW (2011) Infrared refractive index of polyethylene and a polyethylene-based material. *Opt Eng* 50(9):093603
- Huang CY, Chen CC, Chang KS, Chou HY, Hsu WY, Lee TX (2013a) Fabrication of a hybrid optical micro-component with a thermosetting polymer and glass. *Proc SPIE* 8769, *International Conference on Optics in Precision Engineering and Nanotechnology*, 87693O
- Huang CY, Chen YK, Huang SH, Shye DC (2013b) Fabrication of a hybrid aspheric lens using glass and thermosetting polymer molding technique. *Mater Sci Forum* 773–774:525–533
- Kulakova NA, Nasyrov AR, Nesselova IM (2010) Current trends in creating optical systems for the IR region. *J Opt Technol* 77:324–330
- Li L, Yi AY (2013) An affordable injection-molded precision hybrid glass–polymer achromatic lens. *Int J Adv Manuf Technol* 69(5–8):1461–1467
- Li L, He P, Wang F, Georgiadis K, Dambon O, Klocke F, Yi AY (2011) A hybrid polymer–glass achromatic microlens array fabricated by compression molding. *J Opt* 13(5):55407
- Liu C, Li JM, Liu JS, Wang LD (2010) Deformation behavior of solid polymer during hot embossing process. *Microelectron Eng* 87(2):200–207. Elsevier B.V
- Namnabat S, Gabriel JJ, Pyun J, Norwood AR, Dereniak EL, Laan J (2014) Sulfur copolymers for infrared optical imaging. *Proc SPIE* 9070, *Infrared Technology and Applications XL*, 90702H
- Peng L, Deng Y, Yi P, Lai X (2014) Micro hot embossing of thermoplastic polymers: a review. *J Micromech Microeng* 24(1):13001
- Takahata T, Matsumoto K, Shimoyama I (2013) A silicon-glass hybrid lens for simultaneous color-and-thermal imaging. 2013 *Transducers & Eurosensors XXVII: The 17th International Conference on Solid-State Sensors, Actuators and Microsystems*, Barcelona pp 1408–1411
- Vicker D (2003) Molded and laminated infrared imager Laminated Kino/Asphere. *SPIE* 5074:814–817. (Figure 4)
- Vicker D, LeBlanc R (2001) Midwave infrared imager with plastic laminated diffractive/aspheric surfaces. *SPIE* 4369:642–648
- Worgull M, Schneider M, Heilig M, Kolew A, Dingreiter H, Mohr J (2010) Replication of optical components by hot embossing. *SPIE*. Thienpont H et al (eds) vol. 7716, pp 771604–771614
- Yan J, Yoshino M, Kuriagawa T, Shirakashi T, Syoji K, Komanduri R (2001) On the ductile machining of silicon for micro electro-mechanical systems (MEMS), opto-electronic and optical applications. *Mater Sci Eng A* 297(1–2):230–234
- Yan J, Syoji K, Tamaki J (2003) Some observations on the wear of diamond tools in ultra-precision cutting of single-crystal silicon. *Wear* 255(7–12):1380–1387
- Yan J, Maekawa K, Tamaki J, Kuriyagawa T (2005) Micro grooving on single-crystal germanium for infrared Fresnel lenses. *J Micromech Microeng* 15(10):1925–1931

- Yan J, Zhou T, Yoshihara N, Kuriyagawa T (2009) Shape transferability and microscopic deformation of molding dies in aspherical glass lens molding press. *J Manuf Technol Res* 1(1–2):85–102
- Yang A, Zhang M, Li L, Wang Y, Zhang B, Yang Z, Tang D (2016) Ga-Sb-S chalcogenide glasses for mid-infrared applications. *J Am Ceram Soc* 99(1):12–15
- Zhou T, Yan J, Masuda J, Oowada T, Kuriyagawa T (2011) Investigation on shape transferability in ultraprecision glass molding press for microgrooves. *Precis Eng* 35:214–220
- Zhu X, Simon TW, Cui T (2011) Hot embossing at viscous state to enhance filling process for complex polymer structures. *Microsyst Technol* 18(3):257–265
- Zwiers RJ, Dortant GC (1985) Aspherical lenses produced by a fast high-precision replication process using UV-curable coatings. *Appl Opt* 24(24):4483



Microspring Fabrication by Anisotropic Gelation

22

Hiroaki Onoe and Koki Yoshida

Contents

22.1	Introduction	692
22.2	Fabrication Methods for Hydrogel Microsprings	693
22.2.1	Self-Folding	693
22.2.2	Liquid Rope-Coiling Effect	693
22.2.3	Stereolithography and Template	696
22.3	Microspring Fabrication by Anisotropic Gelation	696
22.3.1	Hydrogel Microspring Formation by Using Bevel-Tip Capillary	696
22.3.2	Mechanism of Spring Formation	697
22.3.3	Configurations of Formed Hydrogel Microsprings	701
22.3.4	Encapsulation of Functional Materials in Hydrogel Microsprings	704
22.4	Summary and Outlook	708
	References	709

Abstract

Springs are fundamental mechanical parts that can store mechanical energies by their deformation. Although metals are generally used as materials for springs, hydrogel-based microscale springs have recently been reported with inspiration from micro-/nanoscale biological structures and functions in living organisms. In this chapter, firstly, recent hydrogel microspring formation methods, including self-folding, liquid rope-coiling, stereolithography and templating, are introduced. After overviewing those technologies, a formation method of hydrogel microsprings by using anisotropic gelation with bevel tip capillaries is mainly

H. Onoe (✉) · K. Yoshida
Department of Mechanical Engineering, Faculty of Science and Technology, Keio University,
Kanagawa, Japan
e-mail: onoe@mech.keio.ac.jp

discussed. Sodium alginate solution is ejected into calcium chloride solution via a bevel-tip capillary. The ejected sodium alginate rapidly gels with reaction to calcium ions in the calcium chloride solution around the bevel tip, which results in continuous formation of microscale spring-shaped calcium alginate structures. Analysis of its formation principle reveals that the anisotropic gelation depends on the flow velocity of the calcium alginate solution and the tip angle of the capillary. By controlling the flow patterns in the bevel-tip capillary, variations of formed hydrogel microsprints, such as tubular, bilayer and core-shell springs, can be fabricated. Finally, those hydrogel microsprints are applied to stimuli-responsive soft actuators and three-dimensional tissue culture as possible applications. Hydrogel microsprints will be applicable to various fields including biochemical sensors, soft actuators, and scaffolds for tissue culture.

Keywords

Hydrogel · Spring · Microfluidics · Laminar flow · Soft matter

22.1 Introduction

A spring is an old-established basic element of mechanical parts used in widespread industrial products. Springs use elasticity of materials for their deformation by external force, and the deformation recovers when the force is removed. This characteristic of springs plays broad range of roles in industrial products for absorbing motions, storing mechanical energies, measuring weights, etc. Furthermore, uses of springs have not been limited in such engineered mechanical products: Living organisms in nature also have adopted “spring-shaped” organs and tissues as their biological parts. For example, Spirochetes, which has microscale spring-shaped flagella, achieves efficient movements in liquid by rotating their flagella (Charon and Goldstein 2002; Harman et al. 2013). Vorticella moves quickly by the deformation of their spring-shaped stalk that is driven by thin muscle tissues inside (Sareh and Rossiter 2013; Upadhyaya et al. 2008). In a human body, Meissner’s corpuscles that include microspring-shaped tissues in their structure work as soft tactile sensors (Guinard et al. 2000). Even in nanoscale biological macromolecules, springs and coil structures are frequently observed, such as DNA, proteins, and their structures and functions have been fascinating scientists and engineers both in analytical and synthetic aspects (Marsden and Kros 2010).

From an engineering point of view, mimicking those structures and functions shown in nature is effective for elements of autonomous mechanical systems driven by chemical or biological reactions that could be expected for biomedical applications or energy-efficient nature-friendly systems (Zhang et al. 2016; Kim et al. 2013). As a material for creating such microsprints, hydrogel is one of possible candidates. Hydrogel is a material containing a high proportion of water in its macromolecules network and has been studied for long time and extensively used in food industries and medical applications in our daily lives (Ahmed 2015). By

using hydrogels as a material for the microsprings, microsprings interacting to chemicals, biomolecules, cells, and tissues could be realized. In this chapter, recent fabrication technologies and expected applications of hydrogel microsprings will be introduced and discussed. Especially, in the latter part of the chapter, an anisotropic gelation method for forming hydrogel microspring will be focused.

22.2 Fabrication Methods for Hydrogel Microsprings

22.2.1 Self-Folding

Self-folding is a spontaneous deformation process of foldable thin layer of materials. Basically, bilayer plates or fibers composed of two materials having different coefficient of expansion are used to self-folding materials (Gracias 2013; Ionov 2013). By stimulating the bilayer plates or fibers, these structures deformed three dimensionally because the one material expands/shrinks larger than the other material to the stimulus (Chen et al. 2016; Jeon et al. 2017). The materials for self-folding structures can be formed into such plate or fiber shapes by using common two-dimensional lithography or spinning technologies. By using this self-folding approach, hydrogel microsprings were formed with wide variety of materials in various ranges in the scale.

Li et al. demonstrated self-folding of rectangular microscale cantilevers composed of a bilayer structure of polyvinyl alcohol (PVA)-poly(acrylic acid) (PAA) and chromium (Cr) on a silicon (Si) substrate (Li et al. 2012). The bilayer microcantilever was fabricated by photolithography and released by sacrificial etching. Due to isotropic strain/stress at the interface of the PVA-PAA layer (~150 nm in thickness) and the Cr layer (~50 nm in thickness), the microscale bilayer cantilevers subsequently curled up and formed hydrogel/metal hybrid microspring structures by self-folding. Zhang et al. fabricated spring-shaped “helical microgel ribbons” composed of a gold (Au) layer and a poly(*N*-isopropylacrylamide)(pNIPAAm) hydrogel layer (Zhang et al. 2017) (Fig. 1). The pNIPAAm hydrogel was molded on a patterned substrate, followed by sputtering of Au layer on the molded pNIPAAm hydrogel. By releasing the bilayered pNIPAAm/Au ribbon-like structures in water, swell of pNIPAAm hydrogel caused the folding of the ribbon. Adjusting the dimensions of the ribbon, spring-shape helical ribbon was self-folded. Those self-assembled hydrogel springs above could be used for fluidic sensors that can measure the surrounding flow velocity by the deformation of the spring (Li et al. 2012), and could work as components in actuators or micromotors (Zhang et al. 2017).

22.2.2 Liquid Rope-Coiling Effect

When viscous liquid stream is dragged down in the air by gravity and touched to a ground substrate, the liquid forms a continuous helical pattern by buckling of the

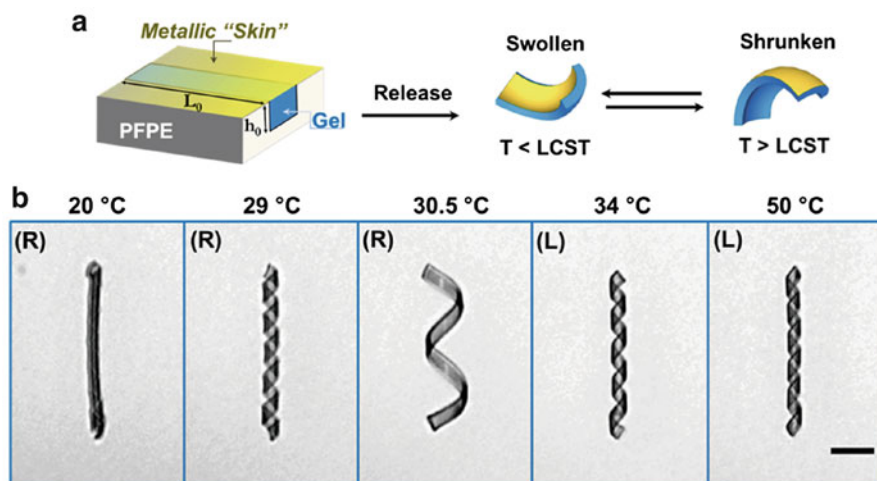


Fig. 1 Bilayer hydrogel/metal microsprings by self-folding (Zhang et al. 2017). (a) Conceptual self-folding processes for the microspring. (b) Microscopic images of the microsprings. A scale bar: 10 μm

liquid stream. This phenomenon is known as “liquid rope-coiling effect,” which has been of interest in fluid physics (Barnes and Woodcock 1958; Ryu and Samuel 1998). Recently, several groups have reported the formation of hydrogel microsprings using this phenomenon.

Tottori et al. reported calcium alginate hydrogel microcoils (microsprings) fabricated by using a co-axial microfluidic device (Tottori and Takeuchi 2015). A fast core stream of viscous sodium alginate solution supplemented with sodium citrate was bent and coiled in a slow sheath stream of poly(ethylene glycol) solution containing calcium chloride. The coiled sodium alginate solution gradually gelled with reacting to diffused calcium ions, resulting in the formation of calcium alginate hydrogel microcoils (microsprings). Using the same system, supercoil structures (coiled coil structures) were demonstrated by combining first-order coiling at a merge point of two viscous liquids around a microfluidic nozzle and second-order coiling caused by fluid buckling near a ground substrate (Nie and Takeuchi 2017) (Fig. 2). Zhu et al. showed dextran-based hydrogel microsprings by using liquid rope-coiling effect in a microfluidic device (Zhu and Guo 2016). Polymerizable dextran (GMA-dex) viscous stream was coiled in poly(ethylene glycol) (PEG) stream and polymerized with dehydration or ultraviolet (UV) light irradiation. This polymerized hydrogel microsring exhibited a water-responsive shape memory behavior that can recover its spring shape after stretched. This unique characteristic could potentially be expected to use in biomedical tools.

Not only in microfluidic devices, but in electric field, liquid rope-coiling effect was observed and utilized to form polymer springs. Kong et al. demonstrated the formation of poly(caprolactone) microcoils (microsprings) by applying voltage

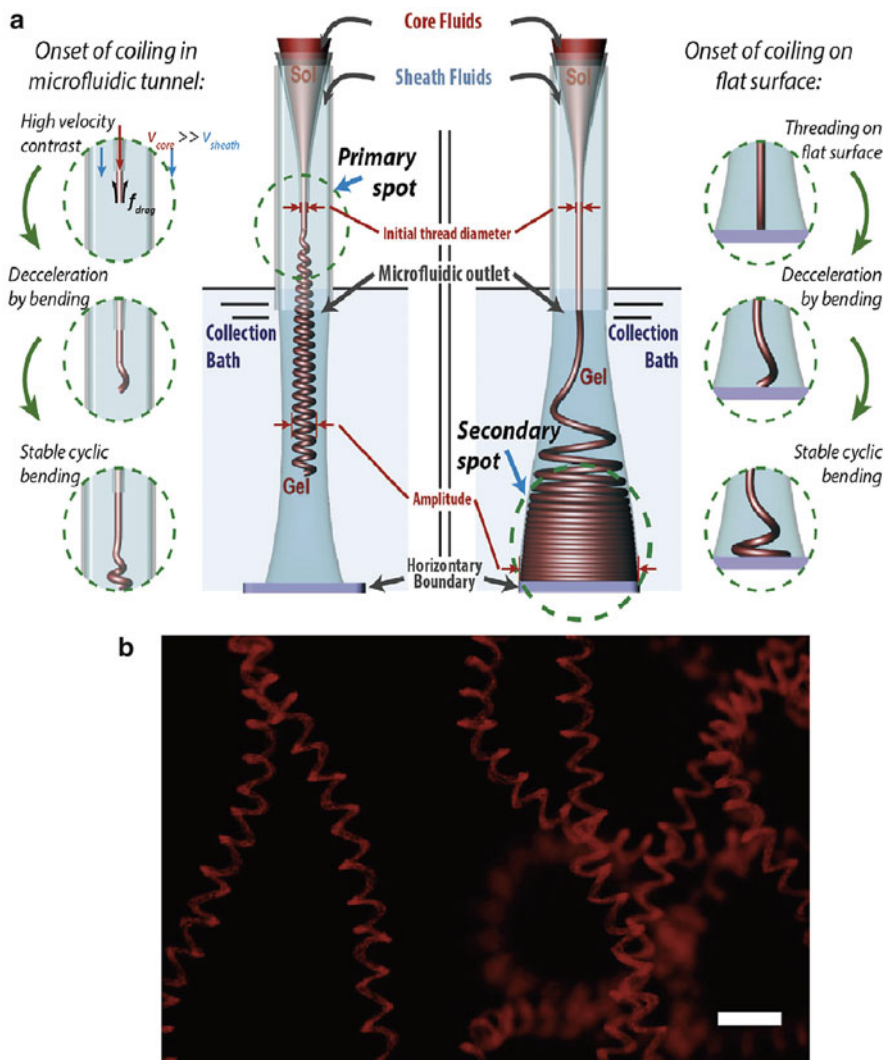


Fig. 2 Hydrogel microsprints formed by liquid rope-coiling effect (Nie and Takeuchi 2017). (a) Conceptual illustration of hydrogel microsprint formation by liquid rope-coiling effect. (b) Microscopic images of the formed microsprints. Scale bar: 1.5 mm

between fluidic nozzle and a collecting substrate (Kong et al. 2016). The diameter of the coil was controlled by changing the applied voltage (0–6.5 kV).

Those reports of hydrogel microsprints formed by liquid rope-coiling effect were basically focusing on their formation mechanism and variations of structures. One of the possible applications is to construct 3D helical microfluidic channels reported in the following literatures: Yang et al. demonstrated helical microfluidic channels fabricated by dissolving PVA microsprints embedded in poly(dimethylsiloxane)

(PDMS) (Yang et al. 2017). The PVA microsprings were fabricated by gravity-driven liquid rope-coiling effect in air. Thanks to the water-soluble characteristics of PVA, embedded PVA microsprings in a PDMS block were easily dissolved by hot water. Xu et al. reported the formation of helical microchannel in calcium alginate hydrogel by using “heterogeneous rope-coiling effect” (Xu et al. 2017). In their method, spring-shaped void structure was directly and continuously formed by creating co-axial laminar flow of nonviscous calcium chloride solution (core) and viscous calcium alginate solution (sheath). This helical microchannel could mimic the structure of in vivo spiral artery in endometrium, and perfusion and permeability tests were demonstrated by using this helical microchannel.

22.2.3 Stereolithography and Template

In addition to the self-folding and liquid rope-coiling effect, a couple of different methods have been reported for forming hydrogel microsprings. Sochol et al. proposed hydrogel microspring arrays fabricated by using direct-write laser lithography (Sochol et al. 2013). Photo-polymerizable PEG were serially solidified along to the 3D trajectory of the focused laser spot. Using this lithography approach, microscale PEG hydrogel spring array was formed on a substrate. The microspring array was designed to analyze traction force generated by cells three dimensionally. Cell culture on the microspring array was performed to test the feasibility of the concept. Sun et al. showed magnetized hydrogel microsprings for culturing smooth muscle cells (Sun et al. 2017). The alginate microfibers encapsulating magnetic nanoparticles were fabricated by using microfluidic device and reeled to a template rod by robotic magnetic tweezers. Although both two approaches are basically serial processes and need specialized apparatuses to form hydrogel microsprings, high preciseness and design flexibilities could be achieved.

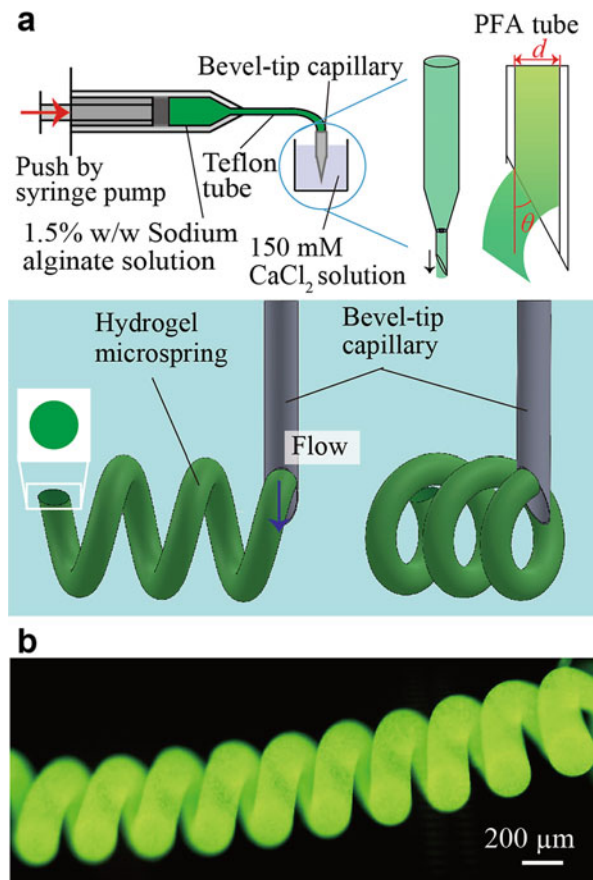
22.3 Microspring Fabrication by Anisotropic Gelation

22.3.1 Hydrogel Microspring Formation by Using Bevel-Tip Capillary

Other method for forming microscale hydrogel springs has recently been reported by Yoshida et al. (Yoshida and Onoe 2017). This method utilizes anisotropic gelation of the flow of pregel solution created by a bevel-tip capillary for continuous hydrogel microspring formation. As shown in Fig. 3, sodium alginate solution is injected into a calcium chloride solution with the bevel-tip capillary. Sodium alginate rapidly gels with reaction to calcium ions in the calcium chloride solution around the bevel tip, which results in the formation of microscale spring-shaped calcium alginate structures.

Typical setup for forming hydrogel spring is shown in Fig. 3. The setup comprises a pumping system (e.g., syringe pump) that can send solution at constant flow speed, a bevel-tip capillary, and a tube for connection. As the bevel-tip capillary, Teflon tubes

Fig. 3 Formation of hydrogel microsprings by anisotropic gelation via a bevel-tip capillary (Yoshida and Onoe 2017). (a) Conceptual illustration of the setup for forming hydrogel microspring. (b) Microscopic images of the formed microsprings



(typical inner diameters: 100–300 μm), where the tip was cut to be tapered (tip angle: 20–40°) by a razor blade (Yoshida and Onoe 2017), as well as a ground glass tube or commercially available injection needles (Yoshida and Onoe 2015) can be used. This method has advantages on its simple setup and does not require any expensive apparatuses and special skills. Using this setup, sodium alginate solution (approximately 1.0–3.0 wt%) is ejected into calcium chloride solution (approximately 50–1000 mM) at constant flow rate. When the flow rate is an appropriate value, a calcium alginate hydrogel microspring can be continuously formed.

22.3.2 Mechanism of Spring Formation

The principle of this hydrogel microspring formation is different from those of the previously mentioned methods above including self-folding using volume shrinkage difference of bilayer structures or liquid rope-coiling effect of viscous fluid stream.

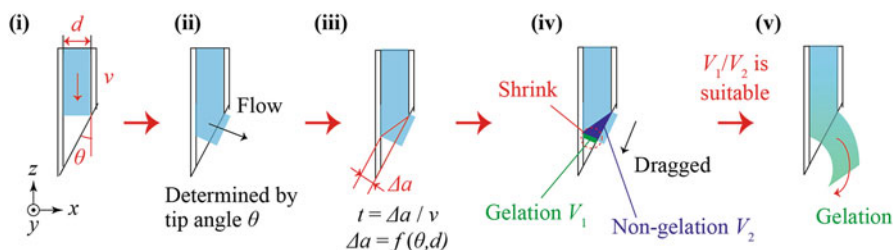


Fig. 4 Principle for forming hydrogel microsprings by anisotropic gelation (Yoshida and Onoe 2017)

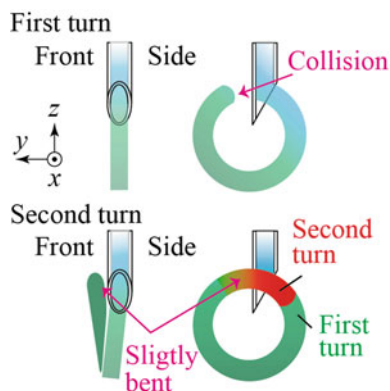
This phenomenon has not been fully understood yet, but could be explained as the complex phenomenon comprising fluid mechanics around the bevel tip and volume shrinkage at the gelation.

Hypothetic mechanism of the spring formation using anisotropic gelation is as follows: sodium alginate solution is ejected from a bevel-tip capillary as a flow velocity of v , where the diameter and tip angle of the capillary are d and θ , respectively (Fig. 4 (i)). The geometry of the tip angle determines the ejected angle of the sodium alginate flow into calcium chloride solution (Fig. 4 (ii)). As a result, only one side of the sodium alginate flow contacts to calcium chloride solution, shown as Δx (Fig. 4 (iii)) where the flow passes the region, Δx , for a certain time, $t = \Delta x/v$. During the time, t , gelation of alginate gradually occurs from the outside to inside of the alginate flow anisotropically by reaction of diffused Ca^{2+} ions (Fig. 4 (iv)) (this spatial anisotropy of gelation around the bevel tip is named as “anisotropic gelation”). Generally, volume of the gelated calcium alginate decreases after the gelation process. This volume reduction drags the flow of the sodium alginate solution, causing the formation of curved hydrogel structures continuously (Fig. 4 (v)).

The formed hydrogel structure symmetrically turns along the x plane in Fig. 5. Thus, the turned hydrogel structure collides to the capillary at its first turn. After the collision, the hydrogel structure randomly shifts to positive or negative y direction by avoiding the capillary and starts to form second turns. As a result, spring-shaped hydrogel structure is fabricated.

This spring formation phenomenon involves many physical and chemical parameters such as (i) fluidic parameters including flow velocity (v), densities and viscosities of sodium alginate solution and calcium chloride solution, and interfacial energies between the both solution, (ii) geometric parameters of a bevel-tip capillary including diameter (d), tip angle (θ), and surface wettability of the capillary, and (iii) gelation parameters including concentration of both sodium alginate and calcium chloride solutions, temperature. In addition to these parameters regarding anisotropic gelation around the bevel tip, kinetic parameters of hydrogel spring during the formation, such as rotational moment of the formed spring, fluidic resistance between the spring and the calcium chloride solution, gravity, and buoyancy forces should be considered. Most of those parameters are not independent to each other.

Fig. 5 First and second turns at the microspring formation process (Yoshida and Onoe 2017)



This complexity makes it difficult to identify the dominant parameters in this spring formation phenomenon to reveal its mechanisms clearly.

Among the parameters, the flow velocity, v , the diameter of the capillary, d , and tip angle of capillary, θ , as shown in Fig. 6, do not affect the gelation reaction itself between sodium alginate and calcium chloride solution. Thus, use of these parameters is effective to analyze the phenomenon as a first step.

The phase diagram of spring formation under varied flow velocities and tip angles for 100 μm of the capillary diameter is shown in Fig. 6 (results for other capillary diameters were in (Yoshida and Onoe 2017)). Depending on the flow velocity, v , formed hydrogel structures can be categorized into three different shapes: (i) fibers, (ii) springs, and (iii) unstable structures (Fig. 6). Which shape is formed is strongly related to the flow velocity, v , at a certain tip angle: for example, at 30° of the tip angle, formed structures is “unstable structures” in slow flow velocity range, $v = \sim 0.01\text{--}0.03$ m/s (yellow region in Fig. 6). However, if the flow velocity goes up around $\sim 0.03\text{--}0.1$ m/s, “springs” is formed at high possibilities (red marked region in Fig. 6). When the flow velocity is too fast, over ~ 0.1 m/s, straight “fibers” are formed even if the bevel-tip capillary is used.

These shape transitions from “unstable structures” to “springs,” and from “springs” to “fibers” along the increase of the flow velocity occur for all tip angles between 20° and 40° (Fig. 6), indicating that appropriate balance between the flow velocity and gelation caused by Ca^{2+} ion diffusion is necessary for spring formation by anisotropic gelation. This experimental result is well match to the hypothetic mechanisms mentioned above: Increase of v shortens the time, t , which represents only one side of the alginate flow contacted to the calcium solution, resulting in the formation of “fibers.” Of course, the tip angle over 50° does not make a sufficient duration of t , causing the formation of “fibers” for all the varied velocities.

In this spring formation method, the anisotropic volume shrinkage of sodium alginate solution at the gelation explains the drag of the alginate flow to form the spring. One question arises in this process: what does the required thickness of gelled calcium alginate for spring formation? To examine this, thin tube-like sodium alginate flow, which can be created by co-axial capillary system

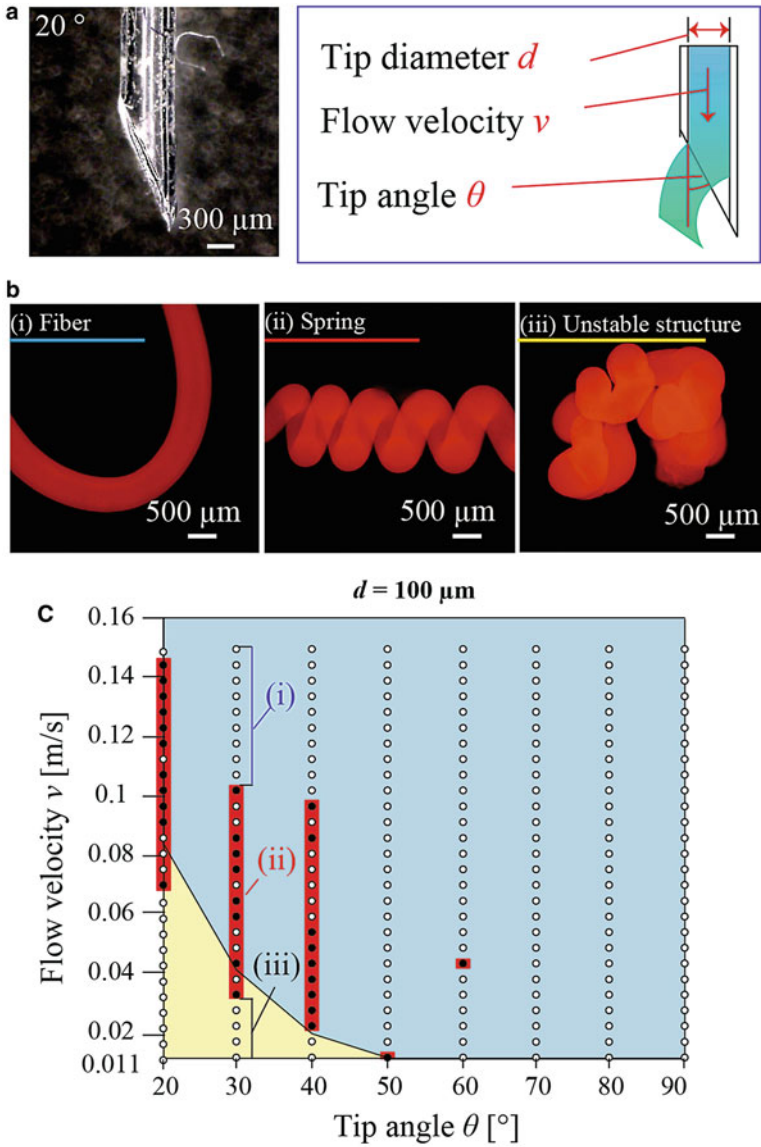


Fig. 6 Effects of flow velocity and tip angle on the formation of hydrogel microsprings. **(a)** Image of a bevel-tip capillary and definition of parameters. **(b)** Fluorescent microscopic images of formed hydrogel structures. **(c)** Diagram of formed structures by varying flow velocity and tip angle (Yoshida and Onoe 2017)

(Onoe et al. 2013), was tested for spring formation using the same setup (Fig. 7). The tube-like flow was made by co-centric laminar flow composed of propylene alginate solution (nongelating alginate) as an inner flow and sodium alginate solution as an outer flow. The thickness of the sodium alginate flow can be tuned

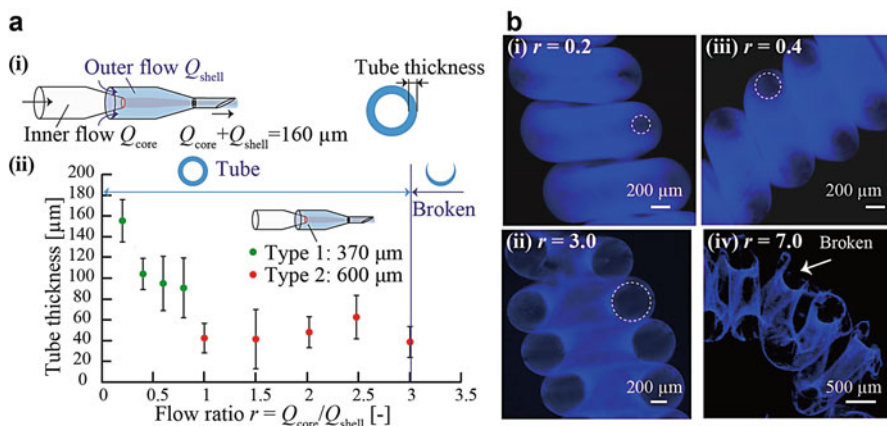


Fig. 7 Formation of tubular hydrogel microsprings. **(a)** Relationship between tube thickness and flow ratio for tubular microspring formation. **(b)** Fluorescent microscopic images of formed tubular springs (Yoshida and Onoe 2017)

precisely by controlling the flow ratio, R , between inner flow, Q_{core} , and outer flow, Q_{shell} (Fig. 7). Interestingly, tube-like sodium alginate flow can form hollow calcium alginate microsprings up to $r \approx 0.7$ (Fig. 7), which is equivalent to the tube thickness of only $\sim 40 \mu\text{m}$ for $\sim 520 \mu\text{m}$ inner diameter of the hollow hydrogel spring.

This result indicates that thin peripheral layer of sodium alginate flow mainly works for forming hydrogel microsprings. That is, the most peripheral layer of flow is required to be sodium alginate, but the inner part of the flow cannot be limited to sodium alginate because the inner part does not affect much for the spring formation. This is a unique and preferable characteristic of this method, because other materials can be encapsulated inside the hydrogel microsprings easily. Considering applications of hydrogel microsprings, this is the advantage to other spring formation methods because of its versatility of encapsulation ability.

22.3.3 Configurations of Formed Hydrogel Microsprings

Configurations of the microsprings are affected by various parameters including fluidic parameters, capillary parameters, gelation parameters, and kinetic parameters. For example, capillary diameter, d , clearly affected by the size of the fabricated springs: Fig. 8a shows the three different hydrogel springs fabricated by bevel-tip capillaries having different diameters. Spring index, R , is utilized to describe the configuration of springs, which is defined by $R = (D_{spring} - D_{wire})/D_{wire}$, where D_{spring} is the outer diameter of spring and D_{wire} is the wire diameter of the spring (Fig. 8b). Among the various parameters above, influence on spring configurations by fluid velocity and tip angle are summarized in Fig. 8c and d. The spring index, R , tends to increase slightly in the range of ~ 2.0 – 4.0 with the increase of flow velocity, v , for $\theta = 30^\circ$ capillaries having 100 – $300 \mu\text{m}$ of diameters; however, there is no

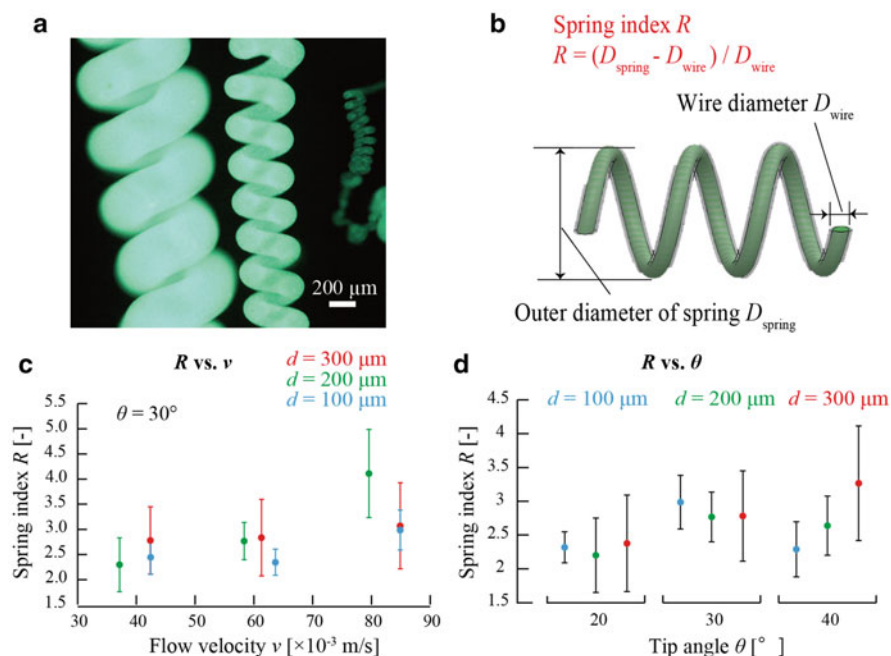


Fig. 8 Configurations of formed hydrogel microsprings. **(a)** Images of hydrogel microsprings formed by different capillary diameters. **(b)** Definitions of the parameters. **(c)** Relationship between spring index and flow velocity. **(d)** Relationship between spring index and tip angle (Yoshida and Onoe 2017)

significant difference in the values of R . As the increase of tip angle θ , R similarly tends to increase in the same R range but with no significant difference. Thus, these results conclude that flow velocity and tip angle of the capillary do not influence the configurations of springs, and the fabricated springs have a certain range of spring index $R \sim 2.0$ – 4.0 in this method.

In addition to the spring index, R , pitch of the spring, distance between each turn, is an important characteristic in configuration. In principle, as described above, fabricated microsprings by this anisotropic gelation method are densely packed. To change the pitch of the microsprings, external dragged force to the y axis direction in Fig. 5 has to act to the spring during the formation.

Figure 9 shows an example of pitch control by using buoyancy force (Yoshida et al. 2017). By setting the bevel-tip capillary horizontally in CaCl_2 solution, the fabricated hydrogel microspring is dragged upward by buoyancy force created by the difference of densities between the sodium alginate solution and the CaCl_2 solution (Fig. 9a). When the volume of the fabricated spring is small, the buoyancy force is not sufficient to expand the pitch of the spring by dragging (Fig. 9b). As the spring formation continuing, the buoyancy force becomes larger and the pitch gradually increases. As a result, a microspring having a densely packed region and

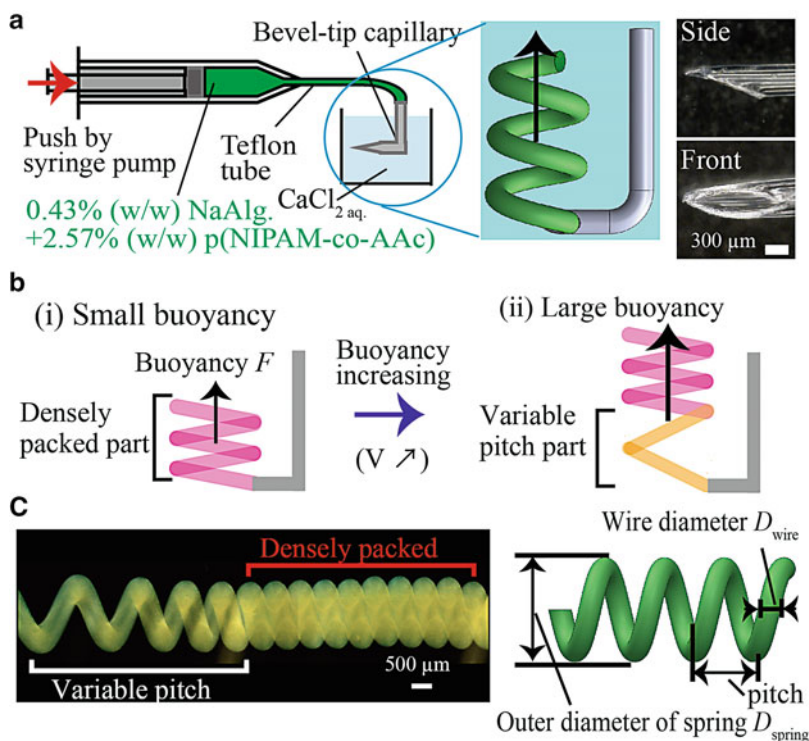


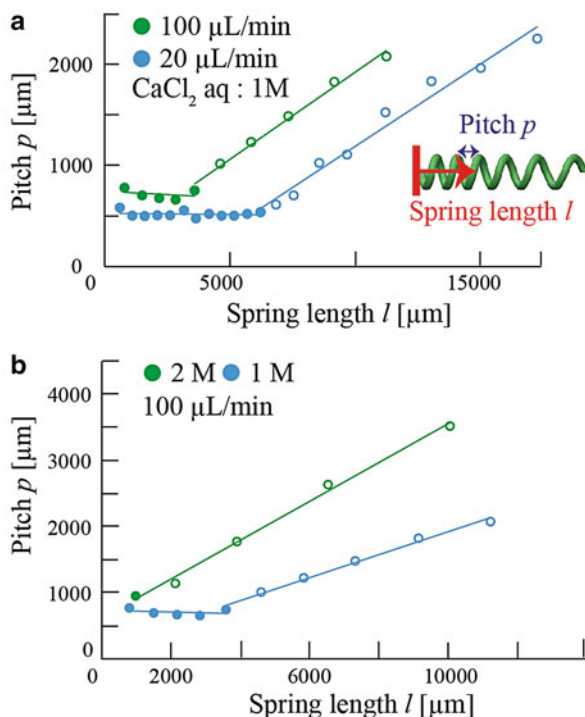
Fig. 9 Pitch control of hydrogel microsprings by using buoyancy force. (a) Conceptual illustration of the setup for controlling pitches of the hydrogel microsprings. (b) Mechanism of dragging a spring during the formation process. (c) Fluorescent microscopic image of the formed hydrogel microspring with variable pitch (Yoshida et al. 2017)

a variable pitch region is created (Fig. 9c). As shown in Fig. 10, the pitch of the spring was initially constant in the densely packed region ($z < \sim 3000 \mu\text{m}$ for $v = 100 \mu\text{L}/\text{min}$), but the pitch gradually increased at $l > 3000 \mu\text{m}$ in proportion to the length, l . The length of the densely packed region depends on flow velocities, since the larger the volume of the spring becomes, the larger the buoyancy force acts on the spring during the formation (Fig. 10a). Similarly, the higher the concentration of CaCl_2 solution, the larger the buoyancy force acts to the spring, resulting in the shorter length of densely packed region (Fig. 10b).

Pitch control by using buoyancy force is just a one way to apply an external force to the spring during the spring formation. Due to the characteristics of the buoyancy force, it is difficult to fabricate a spring having desired pitch with constant width. To control the pitch arbitrarily, other external force could be used: For example, by generating fluid flow around the bevel tip, the flow could work as an external dragged force to control the pitch.

In addition to the pitch of the spring, chirality of the spring is of interest in the formation process. Without an external drag force mentioned above, the chirality of

Fig. 10 Relationship between pitch and spring length for varying flow velocity and concentration of calcium chloride solution (Yoshida et al. 2017)



the spring (helix) is basically random, because initial pitch shift at the spring formation process is caused by the collision of the formed hydrogel and the capillary (Fig. 5). However, by determining the direction of the initial pitch shift by an external drag force to the spring, the chirality of the formed spring can be controlled. Figure 11 shows the chirality control of the formed springs by buoyancy force during the formation process. By changing the direction of the bevel tip capillary, hydrogel microsprints having left-handed helix or right-handed helix can be selectively formed (Fig. 11). Considering applications of the microsprint, the Chirality plays an important role, for example, determining swimming directions of spring-shaped rotational actuators (Tottori et al. 2012) or selective resonance of polarized electromagnetic waves of helix-shaped antennas (Kan et al. 2015).

22.3.4 Encapsulation of Functional Materials in Hydrogel Microsprints

Encapsulation of functional materials into hydrogel microsprint is one of the important characteristics for functionalization. There are two major ways to encapsulate functional materials into the hydrogel microsprints: (i) dispersing/mixing materials directly into hydrogel or (ii) encapsulating materials into a core part of core-shell type hydrogel microsprints.

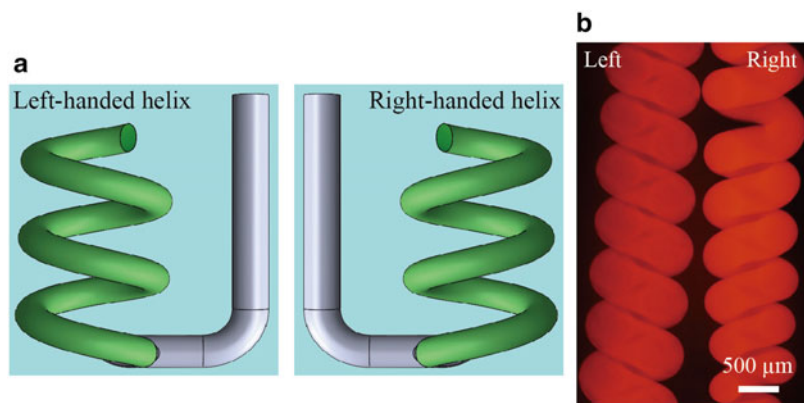


Fig. 11 Chirality control of hydrogel microsprints. (a) Conceptual illustration of chirality control. (b) Images of fabricated hydrogel microsprints with chirality control

Micro- or nanoscale functional beads are often mixed and dispersed in hydrogel pregel solution to label or to functionalize the hydrogel microsprints. Typical pore size of calcium alginate is approximately few nanometers, indicating that micro-/nano-beads having diameters more than the pore size can be retained inside the calcium alginate hydrogel. Fluorescent and magnetic micro-/nano-beads are used for visualizing and magnetizing the microsprints, respectively. By combining laminar flow patterns inside the bevel-tip capillary before gelation, wide variations of cross-sectional patterns of encapsulation can be achieved, for example, core-shell patterns (Fig. 12).

Other than micro-/nano-beads, functional polymers can be mixed into alginate hydrogel network to form blended polymer networks (Onoe et al. 2013; Nakajima et al. 2017; Wen et al. 2014; Ju et al. 2001). Stimuli-responsive hydrogel actuators have generally been expected to realize autonomous soft actuators and microrobots driven by physical and chemical energy sources distributed in environments (Maeda et al. 2007). Figure 13 shows the spring-shaped hydrogel soft actuators composed of blended alginate and poly-(*N*-isopropylacrylamide-*co*-acrylic acid) (p(NIPAAm-*co*-AAc) hydrogel. Both sodium alginate and p(NIPAAm-*co*-AAc) are ionically cross-linked with Ca^{2+} ions in the calcium chloride solution, which forms temperature and pH responsive gel layer in the spring-shaped actuator. The other layer includes sodium alginate solution supplemented with propylene glycol alginate for adjusting the viscosity of the solution. This bilayer stimuli-responsive hydrogel microsprint can compress its structure along the direction of the long axis by responding to the increase of temperature (Fig. 13). By using this bilayer spring structure, the degrees of compression and expansion can be magnified compared to those of bulk-state stimuli-responsive hydrogel.

Core-shell type hydrogel microsprint can encapsulate functional materials without mixing or dispersing to calcium alginate hydrogel. By creating co-axial laminar flow comprising target functional material as a core stream and sodium alginate as a

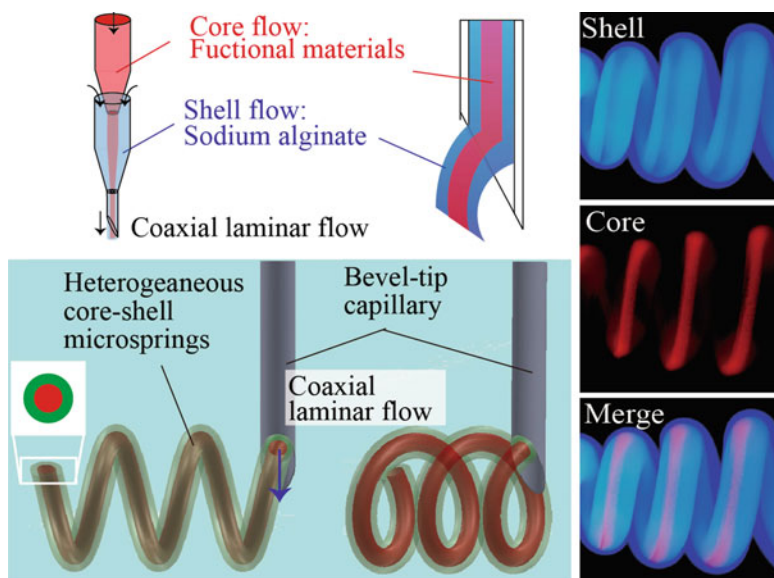


Fig. 12 Core-shell hydrogel microsprings by creating co-axial laminar flow in a bevel-tip capillary (Yoshida and Onoe 2017)

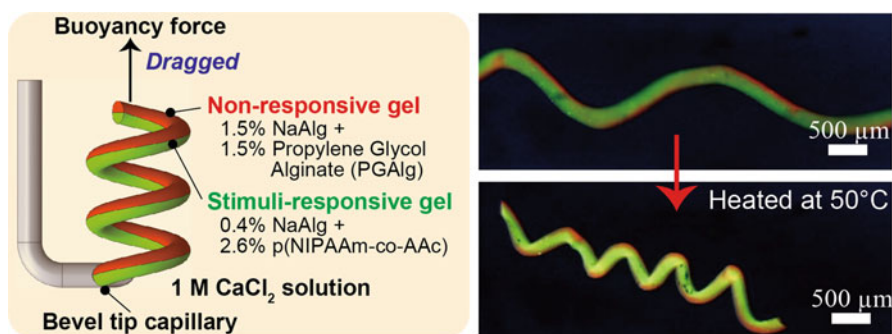


Fig. 13 Double-layer temperature-responsive hydrogel microsprings for soft actuators (Yoshida et al. 2017)

shell stream in the bevel-tip capillary, a core-shell type hydrogel microspring can be formed in the calcium chloride solution (Fig. 12). Figure 14 shows an example of agarose/alginate core-shell hydrogel microspring. After forming its spring structure by extruding the core-shell flow into the calcium chloride solution, sol-state agarose was solidified by decreasing temperature from 37 °C to 4 °C. Fluorescent microscopic observation clearly shows that core agarose structure was created in the shell of calcium alginate hydrogel. Enzymatic removal of the calcium alginate shell by alginate lyase treatment reveals that the core agarose was certainly solidified inside

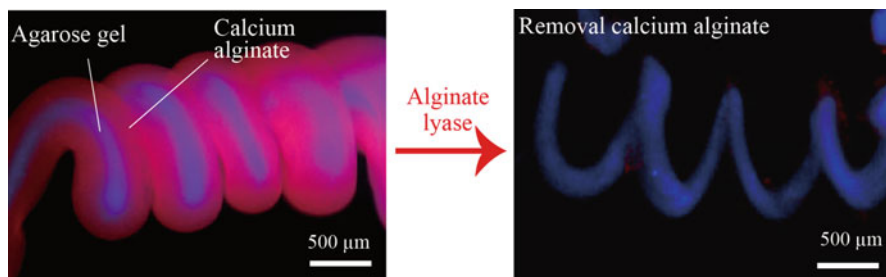


Fig. 14 Agarose/alginate core-shell hydrogel microsprings (Yoshida and Onoe 2017)

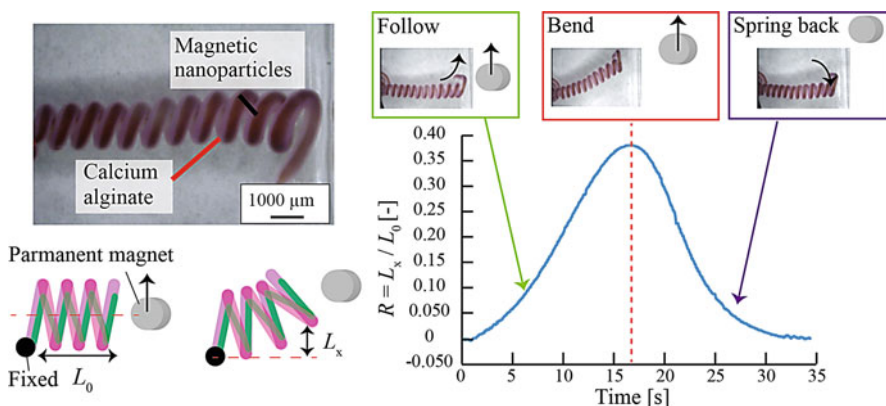


Fig. 15 Agarose/alginate core-shell hydrogel microsprings (Yoshida and Onoe 2017).

the shell (Fig. 14). This result means that the calcium alginate spring structure formed by this anisotropic gelation method can be replaced to other materials with this core-shell encapsulation if the encapsulated materials can be retained inside the calcium alginate shell. This encapsulation of materials in the core could expand the possibility of microsprings to various applications including biomimetic actuators, biochemical sensors, and 3D scaffold for in vitro tissue culture.

Among various functionalities, magnetic responsiveness has been frequently used to an application for magnetic-field-driven actuators (Li et al. 2013; Fuhrer et al. 2009). Encapsulation of magnetic nanoparticles in the core-shell hydrogel spring is demonstrated in Fig. 15. The microspring bent by responding to magnetic field created by a permanent magnet and sprang back to its original shapes after removal of the magnetic field (Figs. 3, 4, 5, 6, 7, 8, 9, 10, 11, 12, 13, 14, and 15). This demonstration shows the magnetic responsiveness of the microspring as well as its mechanical characteristics.

Finally, encapsulation of living cells in the core-shell hydrogel microsprings shows the possible uses of hydrogel microsprings for tools in tissue engineering and mechano biology. Microfabricated biocompatible scaffolds for three-

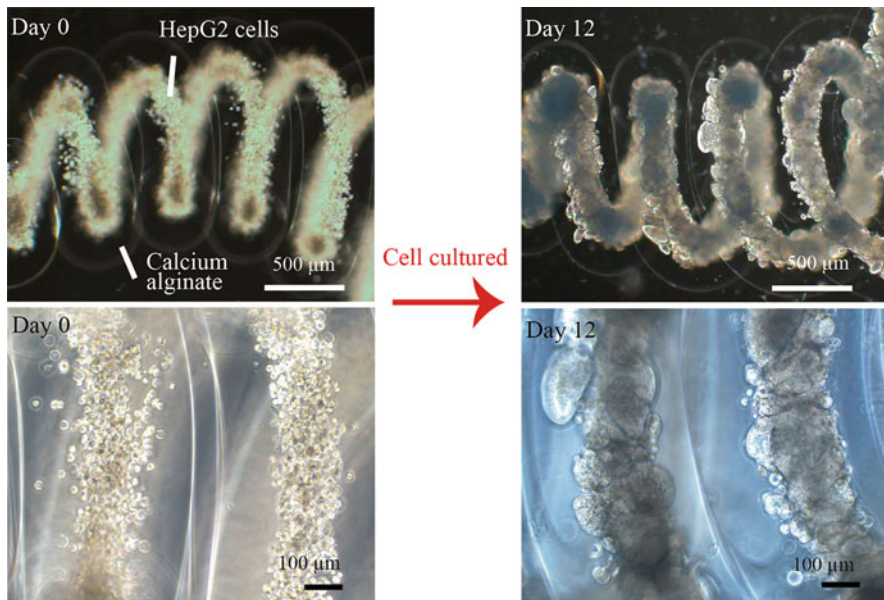


Fig. 16 HepG2 cells cultured in collagen/alginate core-shell hydrogel microsprings (Yoshida and Onoe 2017)

dimensional (3D) tissue culture *in vitro* have garnered attentions in tissue engineering fields for mimicking tissues *in vitro*. By encapsulating mammalian cells with collagen hydrogel into the core of the hydrogel microspring, spring-shaped tissues can be organized *in vitro*. Figure 16 shows that HepG2 (human hepatoma cell line) cells were encapsulated with collagen hydrogel in a calcium alginate hydrogel microspring. After culturing 12 days in a culture medium, the encapsulated HepG2 cells proliferated and formed a spring-shaped tissue inside the shell. This result shows that the hydrogel microspring can be used as a 3D cell culture scaffold. Interestingly, the cell-cultured microspring can be expanded by manipulation of tweezers, resulting in applying mechanical stretch to the HepG2 tissue. Although the response of the spring-shaped tissue to the mechanical stimuli has not been reported yet, the spring-shaped scaffold thus could be effective to analyze mechano-responses of the encapsulated tissues.

22.4 Summary and Outlook

Formation methods for hydrogel microsprings have been overviewed. Especially, the anisotropic gelation method, including its principle, variations, and applications, was introduced in detail. This method has an advantage on its simplicity of the formation setup using simple bevel-tip capillaries and on its wide variation of applications. To control the size and shape of hydrogel microsprings precisely, the

formation mechanism mentioned should be analyzed not only by fluidic and capillary parameters, but also by parameters regarding chemical reactions such as concentration and temperature effects.

Inspired from micro-/nanoscale biological structures and functions in living organisms, hydrogel microsprints will be expected for biochemical sensors, soft actuators, and scaffolds for tissue culture. For those applications, variation of materials that can be used for hydrogel microsprints could be important for further developments. In addition, hybrid microsprints composed of organic hydrogel materials and inorganic materials could open possible applications for not only chemical and biological systems but also fascinating optical or electromagnetic active meta-materials.

References

- Ahmed EM (2015) Hydrogel: preparation, characterization, and applications: a review. *J Adv Res* 6(2):105–121
- Barnes G, Woodcock R (1958) Liquid rope-coil effect. *Am J Phys* 26(4):205
- Charon NW, Goldstein SF (2002) Genetics of motility and chemotaxis of a fascinating group of bacteria: the spirochetes. *Annu Rev Genet* 36:47–73
- Chen Z, Huang G, Trase I, Han X, Mei Y (2016) Mechanical self-assembly of a strain-engineered flexible layer: wrinkling, rolling, and twisting. *Phys Rev Appl* 5(1):1–33
- Fuhrer R, Athanassiou EK, Luechinger NA, Stark WJ (2009) Crosslinking metal nanoparticles into the polymer backbone of hydrogels enables preparation of soft, magnetic field-driven actuators with muscle-like flexibility. *Small* 5(3):383–388
- Gracias DH (2013) Stimuli responsive self-folding using thin polymer films. *Curr Opin Chem Eng* 2(1):112–119
- Guinard D, Usson Y, Guillermet C, Saxod R (2000) PS-100 and NF 70-200 double immunolabeling for human digital skin meissner corpuscle 3D imaging. *J Histochem Cytochem* 48(2):295–302
- Harman M, Vig DK, Radolf JD, Wolgemuth CW (2013) Viscous dynamics of lyme disease and syphilis spirochetes reveal flagellar torque and drag. *Biophys J* 105(10):2273–2280
- Ionov L (2013) Bioinspired microorigami by self-folding polymer films. *Macromol Chem Phys* 214(11):1178–1183
- Jeon SJ, Hauser AW, Hayward RC (2017) Shape-morphing materials from stimuli-responsive hydrogel hybrids. *Acc Chem Res* 50(2):161–169
- Ju HK, Kim SY, Lee YM (2001) pH/temperature-responsive behaviors of semi-IPN and comb-type graft hydrogels composed of alginate and poly(*N*-isopropylacrylamide). *Polymer (Guildf)* 42(16):6851–6857
- Kan T et al (2015) Enantiomeric switching of chiral metamaterial for terahertz polarization modulation employing vertically deformable MEMS spirals. *Nat Commun* 6:8422
- Kim S, Laschi C, Trimmer B (2013) Soft robotics: a bioinspired evolution in robotics. *Trends Biotechnol* 31(5):287–294
- Kong T et al (2016) Rapid mixing of viscous liquids by electrical coiling. *Sci Rep* 6:1–8
- Li W et al (2012) Superelastic metal microsprints as fluidic sensors and actuators. *Lab Chip* 12(13):2322
- Li Y et al (2013) Magnetic hydrogels and their potential biomedical applications. *Adv Funct Mater* 23(6):660–672
- Maeda S, Hara Y, Sakai T, Yoshida R, Hashimoto S (2007) Self-walking gel. *Adv Mater* 19(21):3480–3484
- Marsden HR, Kros A (2010) Self-assembly of coiled coils in synthetic biology: inspiration and progress. *Angew Chem* 49(17):2988–3005

- Nakajima S, Kawano R, Onoe H (2017) Stimuli-responsive hydrogel microfibers with controlled anisotropic shrinkage and cross-sectional geometries. *Soft Matter* 13(20):3710–3719
- Nie M, Takeuchi S (2017) Microfluidics based synthesis of coiled hydrogel microfibers with flexible shape and dimension control. *Sensors Actuators B Chem* 246:358–362
- Onoe H et al (2013) Metre-long cell-laden microfibres exhibit tissue morphologies and functions. *Nat Mater* 12(6):584–590
- Ryu WS, Samuel ADT (1998) Fluid ‘rope trick’ investigated. *Nature* 392(6672):140
- Sareh S, Rossiter J (2013) Kirigami artificial muscles with complex biologically inspired morphologies. *Smart Mater Struct* 22(1):14004
- Sochol RD et al (2013) Cells on arrays of microsprings: an approach to achieve triaxial control of substrate stiffness. In: *Proceedings of the IEEE International Conference on Micro Electro Mechanical Systems*, pp 90–93
- Sun T et al (2017) Robotics-based micro-reeling of magnetic microfibers to fabricate helical structure for smooth muscle cells culture. In: *Proceedings of the IEEE International Conference on Robotic Automation*, pp 5983–5988
- Tottori S, Takeuchi S (2015) Formation of liquid rope coils in a coaxial microfluidic device. *RSC Adv* 5(42):33691–33695
- Tottori S, Zhang L, Qiu F, Krawczyk KK, Franco-Obregón A, Nelson BJ (2012) Magnetic helical micromachines: fabrication, controlled swimming, and cargo transport. *Adv Mater* 24(6):811–816
- Upadhyaya A, Baraban M, Wong J, Matsudaira P, van Oudenaarden A, Mahadevan L (2008) Power-limited contraction dynamics of *Vorticella convallaria*: an ultrafast biological spring. *Biophys J* 94(1):265–272
- Wen C, Lu L, Li X (2014) Mechanically robust gelatin-alginate IPN hydrogels by a combination of enzymatic and ionic crosslinking approaches. *Macromol Mater Eng* 299(4):504–513
- Xu P, Xie R, Liu Y, Luo G, Ding M, Liang Q (2017) Bioinspired microfibers with embedded perfusable helical channels. *Adv Mater* 29(34):1–7
- Yang W-m, Zhu T-k, Jin Y-a, Fu J-z (2017) Facile fabrication of helical microfluidic channel based on rope coiling effect. *Microsyst Technol* 23(7):2957–2964
- Yoshida K, Onoe H (2015) Self-assembled hydrogel microspring for soft actuator. In: *Proceedings of the IEEE international conference on micro electro mechanical systems (MEMS)*, pp 26–28
- Yoshida K, Onoe H (2017) Functionalized core-shell hydrogel microsprings by anisotropic gelation with bevel-tip capillary. *Sci Rep* 7:45987
- Yoshida K, Nakajima S, Kawano R, Onoe H (2017) Stimuli-responsive hydrogel microsprings for multiple and complex actuation. In: *Proceedings of the IEEE international conference on micro electro mechanical systems (MEMS)*, pp 837–840
- Zhang C, Mcadams DA, Grunlan JC (2016) Nano/micro-manufacturing of bioinspired materials: a review of methods to mimic natural structures. *Adv Mater* 28(39):8566
- Zhang H, Mourran A, Möller M (2017) Dynamic switching of helical microgel ribbons. *Nano Lett* 17(3):2010–2014
- Zhu A, Guo M (2016) Microfluidic controlled mass-transfer and buckling for easy fabrication of polymeric helical fibers. *Macromol Rapid Commun* 37(5):426–432



Masahiko Yoshino and Motoki Terano

Contents

23.1	Introduction	712
23.2	Fabrication Process of a Metal Nanodot Array by Thermal Dewetting	714
23.2.1	Experimental Studies	714
23.2.2	Theoretical Study of the Thermal Dewetting Mechanism	717
23.2.3	Minimum Nanodot Size	721
23.3	Fabrication Process of a Metal Nanodot Array of Uniform Dot Size Based on the Combination of Nano-plastic Forming and Thermal Dewetting	724
23.3.1	Experimental Studies	724
23.3.2	Theoretical Study	729
23.4	Fabrication Process of a Metal Nanodot Array Using Patterned Substrates	732
23.4.1	Experimental Studies	732
23.4.2	Theoretical Study on the Dot Transfer Mechanism	738
23.5	Summary and Outlook	742
	References	743

Abstract

Metal nanodot arrays exhibit unique optical characteristics, and they are expected to find widespread applications in biosensors and various optical devices. In this section, simple and efficient manufacturing processes are introduced for metal nanodot arrays. These processes are based on the combination of thin metal film coatings deposited on substrates and thermal dewetting. The first process discussed herein is a conventional thermal dewetting method. With this method, it is shown that the average dot diameter can be controlled based on the chosen

M. Yoshino (✉)

Department of Mechanical Engineering, Tokyo Institute of Technology, Tokyo, Japan
e-mail: myoshino@mes.titech.ac.jp

M. Terano

Department of Mechanical Systems Engineering, Okayama University of Science, Okayama, Japan
e-mail: m_terano@mech.ous.ac.jp

process conditions. The second process is based on the use of grid patterning on coated metal films. This process can allow fabrication of nanodot arrays with uniform dot diameters and achieve highly ordered alignment of dots. The third process generates a metal nanodot array based on a self-organization manner on a nanogrid-patterned substrate. It constitutes a high-productivity process based on the transfer of the metal nanodot array to an adhesive film. The basic mechanisms underlying these processes are discussed herein.

Keywords

Metal nanoparticles · Optical characteristics · Biosensors · Metal coating · Thermal dewetting · Nano plastic forming · Grid patterning · Self-organization · Productivity · Agglomeration · Surface energy · Dot transfer

23.1 Introduction

It is known that a collective oscillation of free electrons is induced in a metal surface when visible or infrared light is projected to this surface, whereby light of a specific wavelength is strongly absorbed or reflected. This phenomenon is called surface plasmon resonance (SPR). Since SPR is very sensitive to surface conditions, such as molecular adsorption to metal surfaces, it is used in various optical devices, including biosensors. However, SPR occurs only when the incident light and the metal surface are arranged in specific geometric positions, and a precise apparatus design is necessary to use SPR for biosensors.

While SPR occurs on the metal surface, localized surface plasmon resonance (LSPR) occurs on the surface of metal nanoparticles (Mortazavi et al. 2012). When light is projected to metal nanoparticles, the collective oscillation of free electrons induces polarization in the nanoparticles, and plasmons are localized on the surface. LSPR depends on the refractive index of the medium around the metal nanoparticles. Plasmonic sensors utilizing this phenomenon have been studied previously (Hong et al. 2012; Raphael et al. 2012; Sepulveda et al. 2009; Kajiura et al. 2009). Furthermore, a strong electric field is generated in the vicinity of the surface of the nanoparticles owing to the occurrence of LSPR, and a particularly strong electric field is induced in the narrow gap between adjacent nanoparticles. This phenomenon is useful for increasing the sensitivity of Raman spectroscopy. In this way, application of fine metal particles to various sensor devices is expected.

In the case of Au nanoparticles or Ag nanoparticles, LSPR is induced by visible light or infrared light. Since infrared light often interact with molecules, LSPR can be combined with spectroscopic analyses of fluorescence, or Raman scattering. Thus, applications of gold or silver nanoparticles have been attracting increasing attention (Zeng et al. 2011). Many applications are expected for these nanoparticles owing to these optical properties that can control light behavior at the nanoscale, and they are envisaged to serve an important role in combination with photonics and electronics. For example, studies on plasmonic biosensors (Dmitriev et al. 2008; Saito et al. 2012; Otte et al. 2011), surface-enhanced Raman scattering

(SERS) (Oh and Jeong 2012; Agapov et al. 2013), surface-enhanced fluorescence (SEF) (Zhang et al. 2012; Kandziolka et al. 2013), photodetector (Senanayake et al. 2011), applications to electromotive force devices (Tsai et al. 2010), etc. have already been reported.

These phenomena depend on the size and morphology of nanoparticles, and highly ordered nanoparticles exhibit higher performances than random ones. Since nanoparticles fixed on a solid material are easier to handle than powder or liquid solutions of nanoparticles, uniform nanoparticles aligned on a substrate with a regulated layout are useful. We refer to these ordered metal nanoparticles that are aligned on a transparent substrate as metal nanodot array.

To allow the translation of the metal nanoparticles to these practical applications, it is necessary to develop an efficient fabrication process for metal nanoparticles. Various nanofabrication techniques have been studied to produce metal nanodot arrays with reproducible and controllable morphologies.

Such metallic nanostructures can be implemented using conventional lithographic methods, such as the ultraviolet lithography process (UVL) or the electron beam lithography process (EBL). Although these processes are advantageous for mass production of complex and fine nanostructures, like integrated circuits in semiconductors, large and expensive facilities are needed in which stringent process control is required. Additionally, focused ion beam (FIB) systems are utilized for machining various nano-sized structures in many laboratories since they can etch various materials with an ion beam according to computer-controlled patterns. However, this technology is not suitable for mass production of nanostructured devices because of its low-machining rates and high facility costs.

Nanoimprint lithography (NIL) was developed as an efficient method for nanopatterning (Chou et al. 1996; Lucas et al. 2008). The lithographic processes, such as resist coating, etching, and lift-off processes, are used in the same way as in conventional lithographic methods. No-resist nanoimprinting in metal was also reported to fabricate plasmonic nanostructures with high resolution and low cost (Varghese et al. 2013). However, the nanostructure mold used in the NIL process was made based on EBL and etching processes. Hence, NIL depends on conventional lithographic procedures.

Meanwhile, in order to reduce the facility cost and increase productivity, self-organization processes are attracting increasing attention. To this date, researchers have developed nanosphere lithography (Knoben et al. 2011; Cheung et al. 2006) and porous anodic alumina (PAA) (Saito et al. 2012; Huang et al. 2010). These methods are able to fabricate periodic metal dot patterns on a substrate using comparably simple experimental procedures and do not need accurate control of equipment. However, they have limitations in terms of the geometric specifications of the constructed nanostructures. Another process for high-throughput and low-cost fabrication of a metal nanodot array is the thermal dewetting method (Tan et al. 2012; Agapov et al. 2013; Lee et al. 2009; Leem et al. 2012). This process consists of spatter coating and thermal dewetting subprocesses and is much simpler than other nanofabrication processes. However, it also has limitations in terms of controlling the size and morphology of nanodots.

The authors have been developing a high-throughput fabrication process of metal nanodot arrays in which Au or Ag particles with several hundred nanometers in diameter are regularly arranged on a substrate, such as glass (Yoshino et al. 2011; Yoshino et al. 2012). In order to address problems of conventional processes, the authors employed combinations of precision machining and self-organization methods. Three self-organization processes of nanodot arrays are introduced in this chapter.

23.2 Fabrication Process of a Metal Nanodot Array by Thermal Dewetting

23.2.1 Experimental Studies

Figure 1 illustrates a conventional self-organization process of a metal nanodot array by means of the thermal dewetting method. In this process, a substrate is cleaned in an ultrasonic acetone bath and then dried. The substrate should be constructed using a high-melting-point material, and the interface energy between the metal of the nanodots and the substrate should be moderately low. A metal film is deposited on a substrate by using a sputter coater. The coated substrate is then annealed in an electric furnace. Based on the thermal dewetting mechanism, the coated metal film is separated into many small pieces and agglomerated into small semispherical dots. As a result, many random metal nanodots are generated on the substrate.

Figure 2 shows field emission scanning electron microscope (FE-SEM) micrographs of Au nanodots generated using this process on various types of substrates, i.e., (a) quartz glass, (b) single crystal quartz, (c) (1 0 0) silicon wafer, and (d) sapphire wafer. In this experiment, an Au thin film was deposited on these substrates in argon gas atmosphere using a direct current (DC) sputter coater. The pressure was 10 Pa, the ionization current was 5 mA, the distance between the substrate and the target was 35 mm, and the sputtering time was adjusted so that the thickness of the Au thin film was 10 nm. These coated specimens were then inserted into an electric furnace preheated to annealing temperatures (700 °C.). After they were annealed in the furnace for 10 min, the substrates were taken out from the

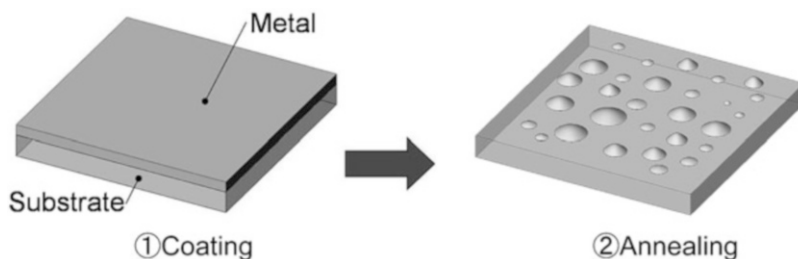


Fig. 1 Schematic illustration of the examined processes for nanodot array fabrication

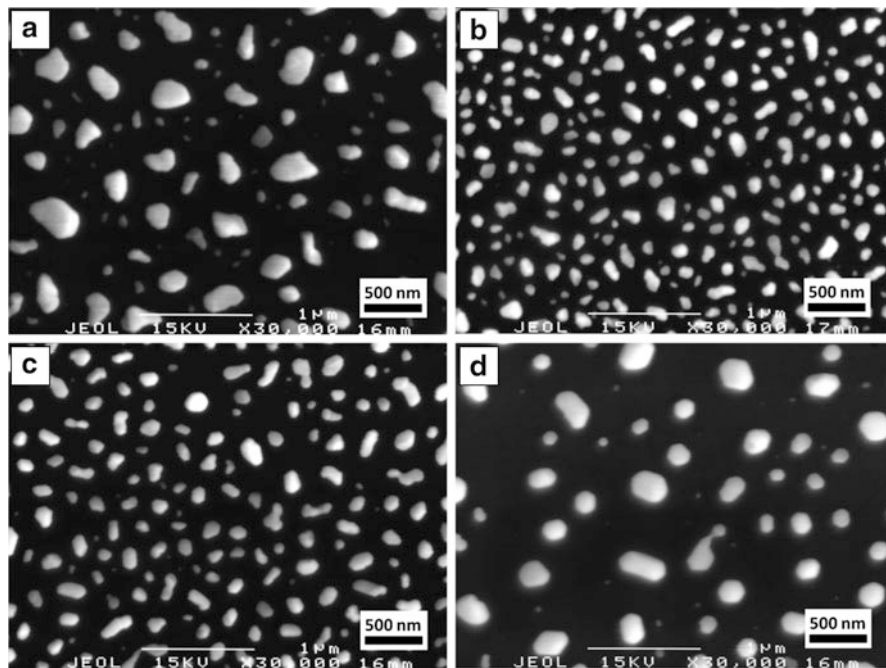


Fig. 2 Au nanodots generated on various substrates using the thermal dewetting method: (a) quartz glass plate, (b) quartz wafer, (c) silicon wafer, and (d) sapphire wafer. Annealing condition: $700\text{ }^{\circ}\text{C} \times 10\text{ min}$

furnace and cooled down in air. Although annealing was conducted in air atmosphere, the effect of the oxidization on Au film and substrates was negligible.

These results indicate that the size and arrangements of generated dots are random, but the dot size depends on the material of the substrate. It is apparent that the dot sizes on (a) the quartz glass substrate and on (d) the sapphire wafer substrate are large, whereas the corresponding sizes on (b) the single crystal quartz substrate and on (c) the silicon wafer substrate are relatively small.

Figure 3 shows results of similar experiments using a platinum (Pt) film on these substrates. The thickness of the Pt thin film was 10 nm, and the annealing condition was $900\text{ }^{\circ}\text{C}$ for 10 min in atmospheric air. Similar to the Au dots in Fig. 2, the sizes and arrangement of generated dots are random. Dots in Fig. 3 are apparently smaller than those in Fig. 2.

Figure 4a compares the average dot diameter (column) and the standard deviation (error bar) of Au nanodots and Pt nanodots observed in Figs. 2 and 3. Apparently, the average diameter and the standard deviation of Au nanodots are larger than those of the Pt nanodots. In addition, it is found that the influence of the substrate material on the average dot diameter is significant for Au nanodots, but it is less pronounced for Pt nanodots. Figure 4b compares the relative standard deviations of dot diameters. The standard deviation of Au nanodots on the quartz glass substrate exceeds 50%,

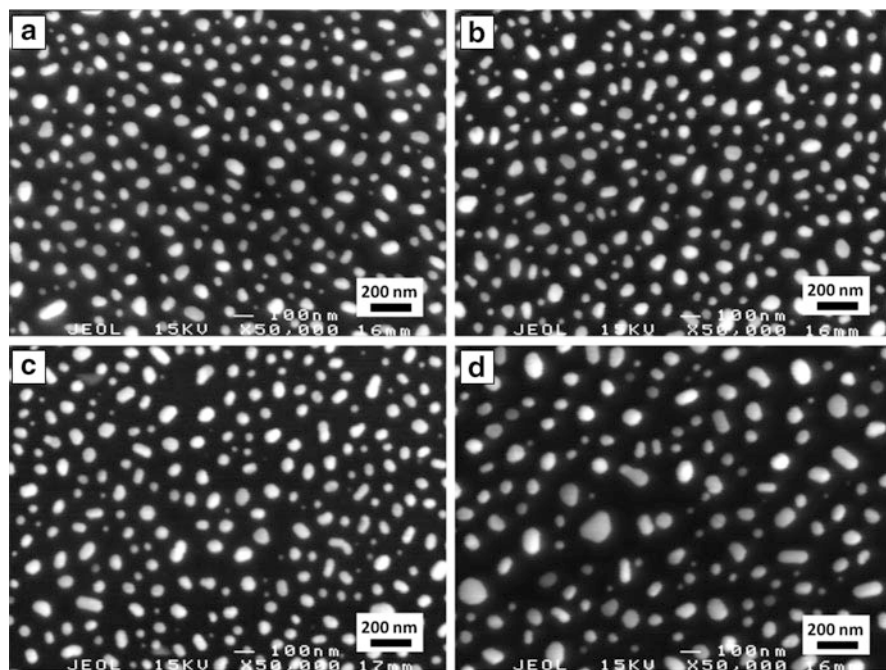


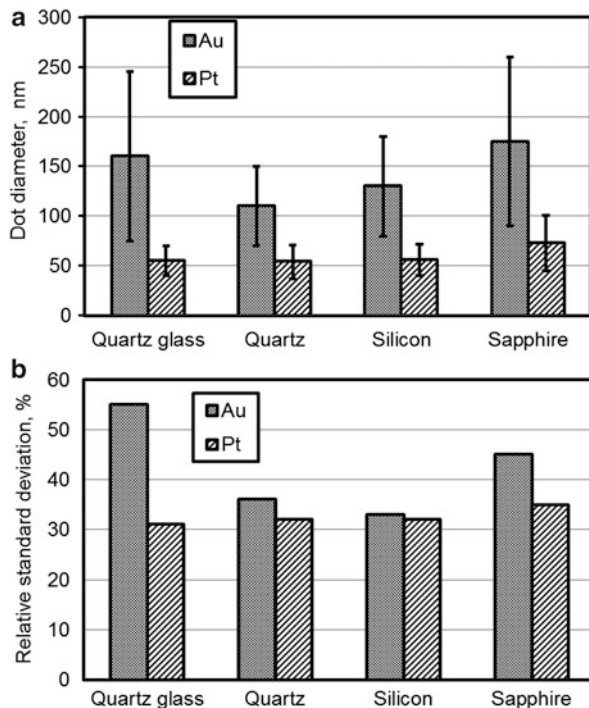
Fig. 3 Pt nanodots generated on various substrates using the thermal dewetting method: (a) quartz glass plate, (b) quartz wafer, (c) silicon wafer, and (d) sapphire wafer. Annealing condition: $900\text{ }^{\circ}\text{C} \times 10\text{ min}$

and these dots are fairly larger than those on the quartz and silicon substrates. Meanwhile, the relative standard deviation of Pt nanodots is approximately 30% for all tested substrates. These characteristics are attributed to interface energy differences between the metal film and the substrate.

Figure 5 shows the change of morphology of agglomerating Au nanodots as a function of annealing temperature in the in situ SEM observation of annealing. In this experiment, thin Au films were coated on quartz glass substrates with a thickness of 10 nm. These substrates were then annealed in the SEM. Temperature was increased gradually to $700\text{ }^{\circ}\text{C}$, and change of morphology was observed continuously. When the temperature became (a) $550\text{ }^{\circ}\text{C}$, voids and pileups appear on the coated film. When the temperature became $600\text{ }^{\circ}\text{C}$, voids connected each other, due to growth of the voids, and the coated film was separated into many pieces of complicated island shapes, as indicated in Fig. 5b. When the temperature became $650\text{ }^{\circ}\text{C}$, these pieces were further separated into smaller particles (Fig. 5c). When the temperature reached $700\text{ }^{\circ}\text{C}$, these particles were agglomerated into round dots, as indicated in Fig. 5d.

These experimental results confirmed that the thermal dewetting process depends on the combination of substrate material, metal, and annealing time. Although experimental data are not shown herein, it was also confirmed that the film thickness and annealing temperature also influenced the thermal dewetting process.

Fig. 4 Comparison of (a) the average dot diameter (column) and the standard deviation (error bar) of the Au nanodots and Pt nanodots and (b) the relative standard deviations estimated from Figs. 2 and 3



23.2.2 Theoretical Study of the Thermal Dewetting Mechanism

Many researchers have studied mathematical models describing the thermal dewetting of a metal film coated on a substrate in order to reveal the effects of the processing conditions on thermal dewetting (Cheynis et al. 2011; Danielson et al. 2006; Rayleigh 1879). However, to this date, the effects exerted by the surface energies and the contact angle between the metal layer and substrate on the size of the subsequently formed dots have not been clarified.

The authors considered a mathematical model of thermal dewetting where a deposited metal film agglomerated into a hemispherical metal dot (Yoshino et al. 2015). Figure 6 illustrates the assumed thermal dewetting process. Firstly, a metal film is deposited on the surface of a substrate with a high melting temperature, such as silicon wafer or quartz glass. The specimen is then annealed in a furnace at a lower temperature compared to the melting temperature of the metal film, and metal atoms migrate to stable positions based on diffusion. (1) Defects existing in the deposited metal film (Zhigal'skii and Jones 2003) are widened to form voids based on diffusion, and many voids appear on the metal film at the beginning of the thermal dewetting process. (2) As the voids grow, they start to become connected to adjacent voids. (3) These voids separate the metal film into many islands. (4) Each isolated metal island agglomerates into a hemispherical dot. Throughout this process, the free energy of the metal and substrate system is reduced.

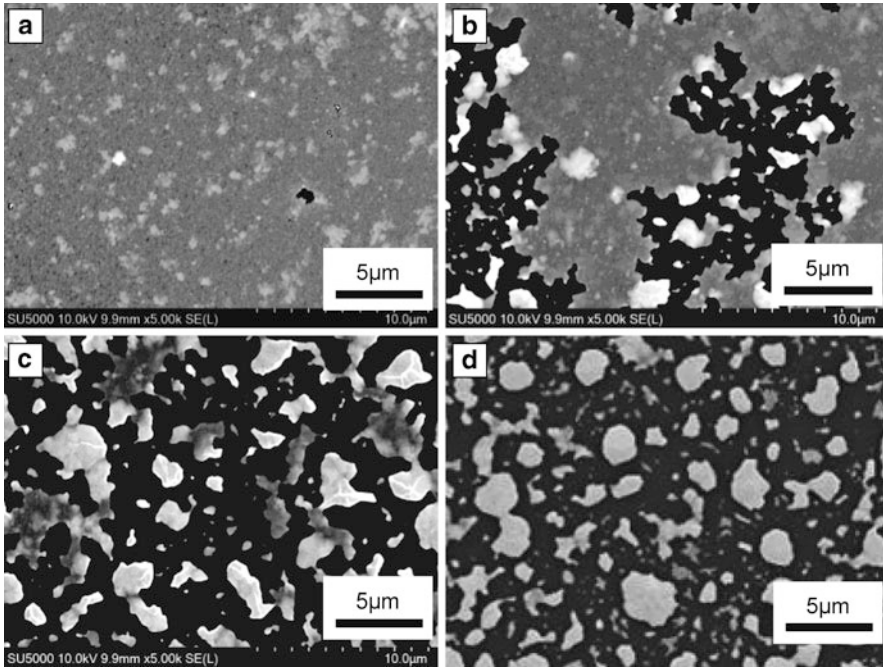


Fig. 5 Change of morphology of Au nanodots as a function of the annealing temperature in the in situ SEM observation of annealing: (a) 550 °C, (b) 600 °C, (c) 650 °C, and (d) 700 °C, when the annealing temperature was increased gradually

We consider herein a simplified model of this thermal dewetting process where a plane metal film agglomerates into a hemispherical dot, as shown in Fig. 7. This constitutes an axisymmetric model around the centerline of the dot, where D_0 is the average diameter of a circular substrate that agglomerates into a single hemispherical dot. In this model, the dot shape is maintained hemispherical throughout the agglomeration process, D is the temporal dot diameter during agglomeration, and D_c is the final dot diameter at the stable state. The dot's height gradually increases as the dewetting time increases, when the angle θ between the dot surface and the substrate at the dot's periphery also increases. Hereafter, θ is referred to as the temporal contact angle. The temporal contact angle θ corresponds to the contact angle θ_c at the end of the agglomeration when the dot attains a stable state. It is known that the contact angle θ_c is related to the surface energies based on Young's equation (Young 1805):

$$\gamma_I - \gamma_S = -\gamma_M \cos \theta_c \quad (1)$$

where γ_M is the surface energy per unit area of the metal, γ_S is that of the substrate, and γ_I is the interfacial energy between the metal and the substrate.

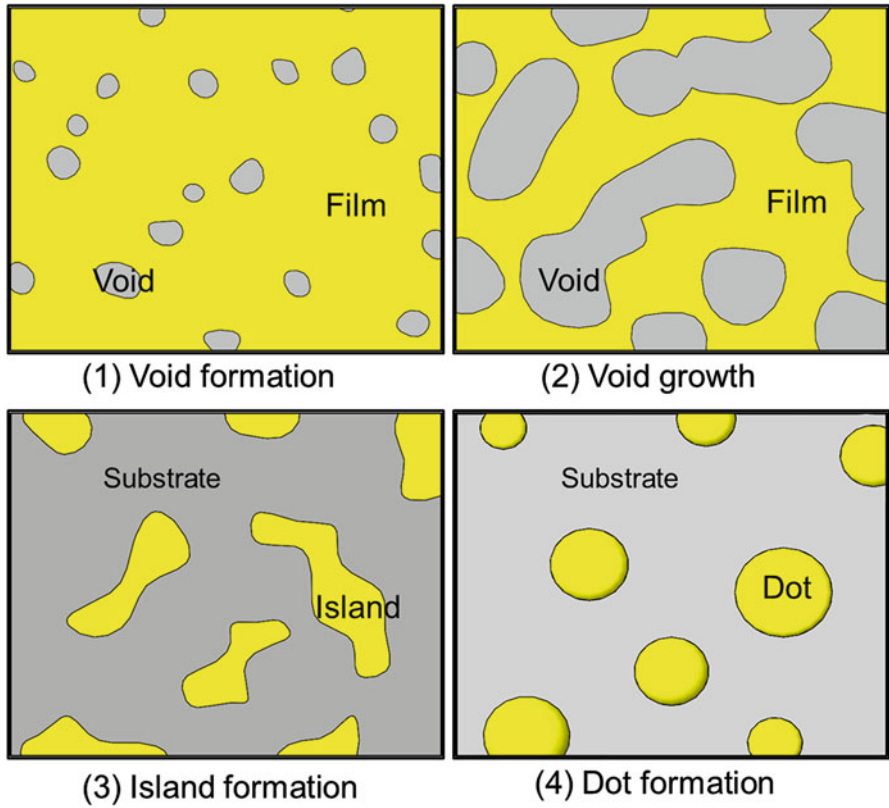
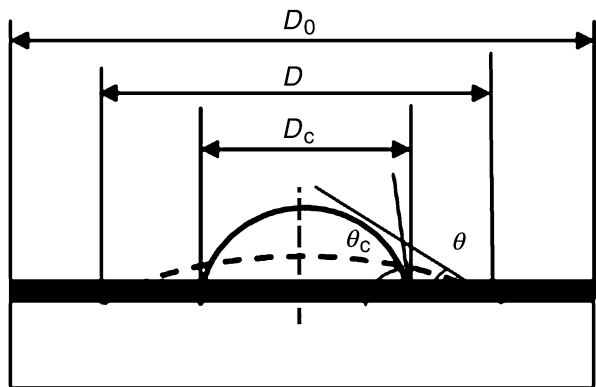


Fig. 6 Thermal dewetting process of a metal film deposited on a substrate

Fig. 7 Geometrical model of a metal and substrate system during the agglomeration



Using these energies, the total free energy of the substrate and metal system before annealing G_1 can be calculated by,

$$G_1 = A\gamma_M + A\gamma_I = A(\gamma_M + \gamma_I) \quad (2)$$

where A is the area of the substrate and is calculated by

$$A = \pi D_0^2/4 \quad (3)$$

Substituting Eq. 3 into Eq. 2, we obtain

$$G_1 = \frac{\pi D_0^2}{4}(\gamma_M + \gamma_I) \quad (4)$$

Since the total free energy of the system G_2 during agglomeration is the sum of the surface energy of a dot, the surface energy of the exposed substrate and the interfacial energy G_2 is calculated by

$$G_2 = S_M\gamma_M + S_I\gamma_I + (A - S_I)\gamma_S \quad (5)$$

where S_M is the area of the surface of the hemispherical metal dot and S_I is the area of interface between the metal dot and substrate.

When the temporal contact angle θ is smaller than 90° , S_M and S_I are calculated by

$$S_M = \frac{\pi D^2}{2} \frac{1 - \cos \theta}{\sin^2 \theta} \quad (6)$$

$$S_I = \frac{\pi D^2}{4} \quad (7)$$

Using Eqs. 5, 6, and 7, and Young's Eq. 1, we obtain

$$G_2 = \frac{\pi D^2}{4} \frac{\gamma_M}{1 + \cos \theta} \{2 - (1 + \cos \theta) \cos \theta_c\} + \frac{\pi D_0^2}{4} \gamma_S \quad (8)$$

Thus, reduction of the total free energy by agglomeration is obtained as

$$\Delta G = G_1 - G_2 = \frac{\pi \gamma_M}{4} \left\{ D_0^2 (1 - \cos \theta_c) - D^2 \frac{2 - \cos \theta_c - \cos \theta \cos \theta_c}{1 + \cos \theta} \right\} \quad (9)$$

When the temporal contact angle θ is greater than 90° , S_M and S_I are calculated by

$$S_M = \frac{\pi D^2}{2} (1 - \cos \theta) \quad (10)$$

$$S_I = \frac{\pi D^2}{4} \sin^2 \theta \quad (11)$$

Using Eqs. 5, 10, and 11, and the Young's Eq. 1, we obtain

$$G_2 = \frac{\pi D^2}{4} \gamma_M \{2 - 2 \cos \theta - \sin^2 \theta \cos \theta_c\} + \frac{\pi D_0^2}{4} \gamma_S \quad (12)$$

In this case, reduction of the total free energy by agglomeration is

$$\begin{aligned} \Delta G &= G_1 - G_2 \\ &= \frac{\pi \gamma_M}{4} \{D_0^2(1 - \cos \theta_c) - D^2(2 - \cos \theta - \sin^2 \theta \cos \theta_c)\} \end{aligned} \quad (13)$$

Herein, we define the nondimensional energies of G_1 , G_2 , and ΔG as follows:

$$\Gamma_1 = \frac{G_1}{t^2 \gamma_M} = \frac{\pi}{4} \xi_0^2 \left(1 + \frac{\gamma_I}{\gamma_M}\right) \quad (14)$$

$$\Gamma_2 = \frac{G_2}{t^2 \gamma_M} = \frac{\pi \Xi_0^2}{4} \left\{ \frac{2 - \cos \theta_c - \cos \theta \cos \theta_c}{1 + \cos \theta} \frac{\xi^2}{\Xi_0^2} + \frac{\gamma_S}{\gamma_M} \right\} \quad \theta < 90^\circ \quad (15)$$

$$\Gamma_2 = \frac{G_2}{t^2 \gamma_M} = \frac{\pi \Xi_0^2}{4} \left\{ (2 - 2 \cos \theta - \sin^2 \theta \cos \theta_c) \frac{\xi^2}{\Xi_0^2} + \frac{\gamma_S}{\gamma_M} \right\} \quad \theta > 90^\circ \quad (16)$$

$$\Delta \Gamma = \frac{\Delta G}{t^2 \gamma_M} = \frac{\pi \Xi_0^2}{4} \left\{ (1 - \cos \theta_c) - \frac{\xi^2}{\Xi_0^2} \frac{2 - \cos \theta_c - \cos \theta \cos \theta_c}{1 + \cos \theta} \right\} \quad \theta < 90^\circ \quad (17)$$

$$\Delta \Gamma = \frac{\Delta G}{t^2 \gamma_M} = \frac{\pi \Xi_0^2}{4} \left\{ (1 - \cos \theta_c) - \frac{\xi^2}{\Xi_0^2} (2 - \cos \theta - \sin^2 \theta \cos \theta_c) \right\} \quad \theta > 90^\circ \quad (18)$$

where ξ and ξ_0 are normalized diameters defined by

$$\xi = \frac{D}{t} \quad (19)$$

$$\Xi_0 = \frac{D_0}{t} \quad (20)$$

23.2.3 Minimum Nanodot Size

It is also assumed that the metal volume is conserved throughout a dewetting process because the annealing temperature is much lower than the melting temperature of the deposited metal. When the temporal contact angle θ is smaller than 90° , the volume of a hemispherical dot V is calculated as

$$V = \frac{\pi}{24} \frac{D^3}{\sin^3 \theta} (2 - 3 \cos \theta + \cos^3 \theta) \quad (21)$$

Because the volume of a dot is equivalent to the volume of a metal film deposited on the substrate, the following equation is obtained:

$$V = \frac{\pi}{24} \frac{D^3}{\sin^3\theta} (2 - 3 \cos\theta + \cos^3\theta) = At = \frac{\pi}{4} D_0^2 t \quad (22)$$

Thus, the dot diameter is calculated as

$$D = \left(\frac{6 \sin^3\theta D_0^2 t}{2 - 3 \cos\theta + \cos^3\theta} \right)^{1/3} \quad (23)$$

This is rewritten as follows using the nondimensional diameters,

$$\xi = \frac{D}{t} = \left(\frac{6 \Xi_0^2}{2 - 3 \cos\theta + \cos^3\theta} \right)^{1/3} \sin\theta \quad (24)$$

When the temporal contact angle θ is greater than 90° , we obtain

$$\xi = \frac{D}{t} = \left(\frac{6 \Xi_0^2}{2 - 3 \cos\theta + \cos^3\theta} \right)^{1/3} \quad (25)$$

Figure 8 shows an example of calculated variations of Γ_1 , Γ_2 , and $\Delta\Gamma$ as a function of ξ using Eqs. 14, 18, 24, and 25. The parameters used in this calculation were

$$\begin{aligned} \theta_c = 90^\circ, \quad \gamma_M = 1, \quad \gamma_S = 1, \quad \gamma_I = 1, \quad \Xi_0 \\ = 50, \quad (D_0 = 500 \text{ nm}, \quad A = 1.96 \times 10^5 \text{ nm}^2, \quad t = 10 \text{ nm}) \end{aligned}$$

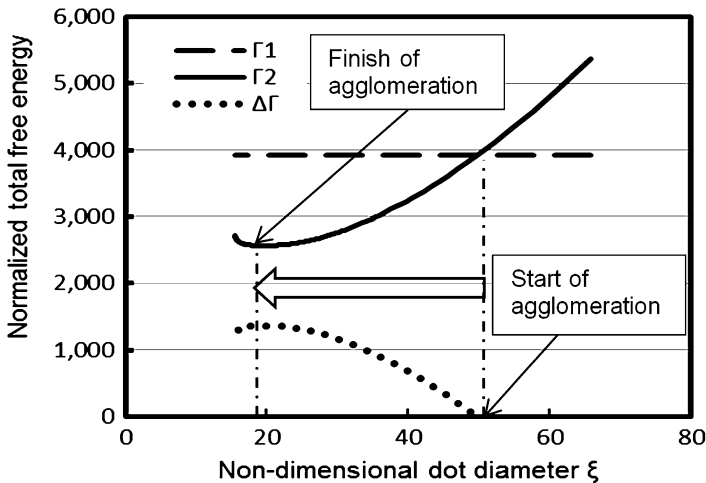


Fig. 8 Variation of the free energies as a function of the dot diameter ξ . Simulation parameters are $\theta_c = 90^\circ$, $\gamma_M = 1$, $\gamma_S = 1$, $\gamma_I = 1$, $\xi_0 = 50$, $(D_0 = 500 \text{ nm}, A = 1.96 \times 10^5 \text{ nm}^2, t = 10 \text{ nm})$

In this graph, agglomeration starts from $\xi = 50$ and finishes at $\xi = 20$. Γ_2 decreases when ξ decreases, and Γ_2 reaches its minimum value, and the contact angle attains θ_c when ξ becomes minimum. The final nondimensional dot diameter ξ_c is calculated by

$$\xi_c = \begin{cases} \left(\frac{6 \Xi_0^2}{2-3 \cos \theta_c + \cos^3 \theta_c} \right)^{1/3} \sin \theta_c, & \text{when } \theta_c < 90^\circ \\ \left(\frac{6 \Xi_0^2}{2-3 \cos \theta_c + \cos^3 \theta_c} \right)^{1/3}, & \text{when } \theta_c \geq 90^\circ \end{cases} \quad (26)$$

In addition, Eqs. 17 and 18 indicate that $\Delta\Gamma$ depends on Ξ_0 and that the driving force of agglomeration is weakened when ξ_0 becomes smaller. Because $\Delta\Gamma$ must be positive to initiate the dot agglomeration process,

$$\Delta\Gamma = \frac{\pi}{4} \Xi_0^2 \left\{ (1 - \cos \theta_c) - \frac{\xi^2}{\Xi_0^2} \frac{2 - \cos \theta_c - \cos \theta \cos \theta_c}{1 + \cos \theta} \right\} > 0 \quad \theta < 90^\circ \quad (27)$$

$$\Delta\Gamma = \frac{\pi}{4} \Xi_0^2 \left\{ (1 - \cos \theta_c) - \frac{\xi^2}{\Xi_0^2} (2 - \cos \theta - \sin^2 \theta \cos \theta_c) \right\} > 0 \quad \theta > 90^\circ \quad (28)$$

By substituting Eqs. 24 and 25, the minimum substrate diameter $\Xi_{0\min}$ is determined as

$$\Xi_{0\min} = 6 \sqrt{\frac{2 + \cos \theta_c}{1 - \cos \theta_c}} \quad (\text{for } \theta < 90^\circ \text{ and } \theta > 90^\circ) \quad (29)$$

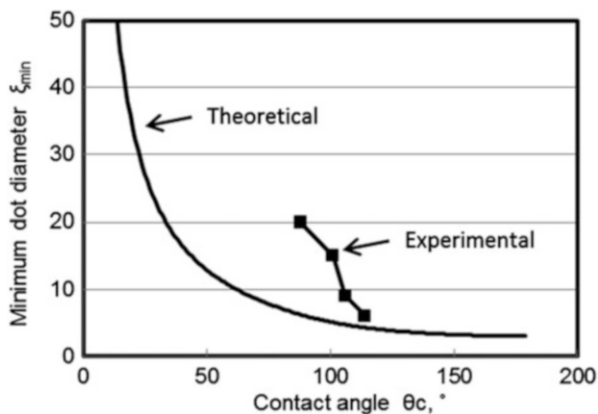
If the diameter of the substrate per dot is smaller than $\Xi_{0\min}$, the metal film cannot become a hemispherical dot but remains as a metal film on the substrate. Thus, the minimum dot diameter ξ_{\min} generated from the minimum substrate diameter $\Xi_{0\min}$ is obtained as follows:

$$\xi_{\min} = \begin{cases} \frac{6 \sin \theta_c}{1 - \cos \theta_c} & \theta_c < 90^\circ \\ \frac{6}{1 - \cos \theta_c} & \theta_c > 90^\circ \end{cases} \quad (30)$$

The dot size generated by thermal dewetting cannot be smaller than the minimum dot diameter ξ_{\min} . Figure 9 shows the relationship between the dot diameter and the contact angle. The solid curve represents the variation of the minimum dot diameter ξ_{\min} . The solid symbols denote experimental data of the normalized average dot diameter of Au nanodots generated on substrates of various materials. It is found from this figure that both experimental and theoretical values elicit similar trends, whereby the dot diameter decreases as a function of the contact angle θ_c .

It is also found that the experimental dot diameter is larger than the theoretical dot diameter. This is because the dot diameter depends on the size of the islands that were separated by growing voids in the early stage of dewetting, as explained in Fig. 6. Since the number of the voids depends on the density of the initial defects in the deposited

Fig. 9 The relationship between the dot diameter and the contact angle



metal film, and the growth rate relies on the chosen annealing conditions, the dot diameter is influenced by the spattering and annealing conditions. The experimentally measured dot diameter will agree with the theoretically estimated dot diameter when the density of the initial defects in the deposited metal film is sufficiently high and annealing conditions are appropriate. Meanwhile, if there is no defect in the metal film, all of metal film aggregates into a dot. Correspondingly, very large metal dots are generated.

Accordingly, the average nanodot diameter depends on the contact angle, the defect density in the coated metal film, and the thickness of the coated film. Since the contact angle is dependent on the surface energies of the dot material and the substrate, it is not a controllable parameter when the combination of these materials is considered. The defect density in a coated metal depends on the spattering conditions, such as the spatter gas pressure, temperature of material, ionization voltage, and spattering current. Although these are controllable parameters, it is difficult to control the defect density in the coated metal film by adjusting these parameters. However, the thickness of the coated film is easy to control accurately, and its effect on the average nanodot size is apparent. Additionally, the annealing condition is an effective parameter that controls the nanodot diameter. Once the materials of the nanodot and substrate are determined, the average nanodot size can be controlled by adjusting the spattering condition, thickness of the metal film, and the annealing condition.

23.3 Fabrication Process of a Metal Nanodot Array of Uniform Dot Size Based on the Combination of Nano-plastic Forming and Thermal Dewetting

23.3.1 Experimental Studies

As discussed in the previous section, the average nanodot size can be controlled by the thickness of the coated metal film in the conventional thermal dewetting process. However, the sizes of individual nanodots depend on the size of separated metal film

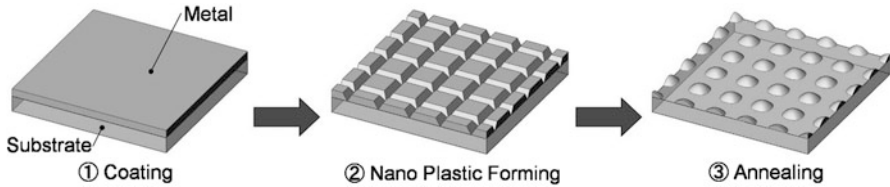


Fig. 10 Proposed fabrication process for the construction of a nanodot array

islands, which in turn is attributed to the statistical distribution of defects in the metal film. Therefore, the dispersion of nanodot sizes cannot be controlled. In order to address this problem, the authors developed a new fabrication process of a metal nanodot array with a uniform dot size.

Figure 10 shows a new manufacturing process of a nanodot array. Firstly, the substrate is cleaned by ultrasound in an acetone bath, and a thin metal film is then deposited on the substrate using a sputter coater. A square nanogroove grid is then machined on the coated film using the nano-plastic forming (NPF) method. The details of NPF are explained below. Finally, the substrate is annealed in an electric furnace so that the thin metal film is aggregated into nanodots using the thermal dewetting mechanism.

In this section, experimental results are shown using quartz glass as the substrate. The thickness of the quartz glass substrate was a 1 mm, and its surface was finished by polishing. The quartz substrate was cleaned by ultrasound in an acetone bath and then dried. Thereafter, a thin Au film was deposited on the substrate using a DC sputter coater. The sputtering gas was Ar, and its pressure was 10 Pa. The thickness of the coated gold layer was set to 5 or 10 nm by controlling the sputtering time. After a square nanogroove grid was fabricated on the coated Au film using NPF, the substrate was annealed in an electric furnace in atmospheric air. The annealing temperature was 700 °C, and the annealing time was 10 min.

NPF is a metal-forming method applicable at the nano-/microscales. It can produce minute structures that are smaller than 1 μm only by indenting a specially designed tool directly on the work material. Figure 11 shows a NPF tester developed for the experiment. It consists of high-precision XY and Z stages. The feed resolution of the X stage is 1 nm, and those of the Y and Z stages are 10 nm. A specimen is set on the XY stage. A diamond tool and a load cell are mounted on the Z stage. The indentation load measured by the load cell is acquired by the computer and fed back to control the motion of the Z stage to control the indentation load. The diamond tool is impressed on the specimen by moving the Z stage downward. All stage motions implemented during the NPF procedure are controlled by the computer. NPF is executed in a clean chamber so that the influence of dust is avoided.

Figure 12 shows an optical micrograph of a knife-edge tool used by the NPF for nanogroove grid patterning. It is made of a single crystal diamond. Its length is 1 mm, and its edge angle is 60°. Its ground edge was very sharp, and the edge radius was smaller than 50 nm.

Fig. 11 Nano-plastic-forming tester

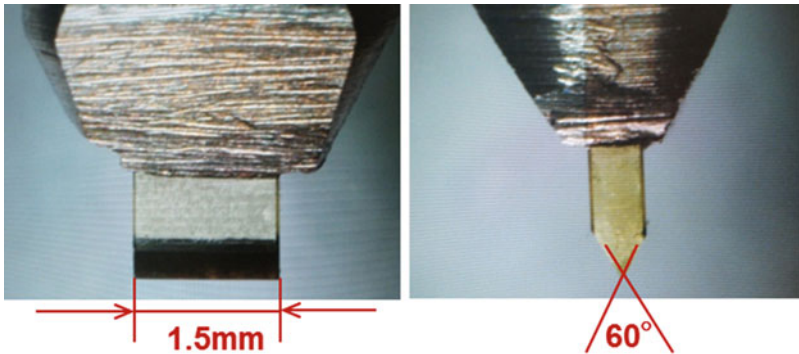
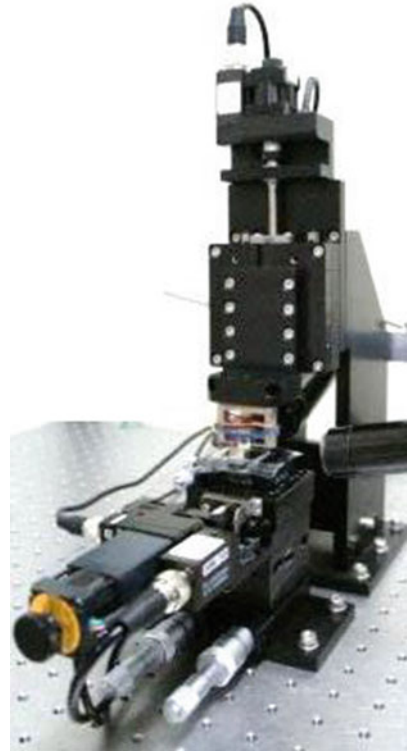
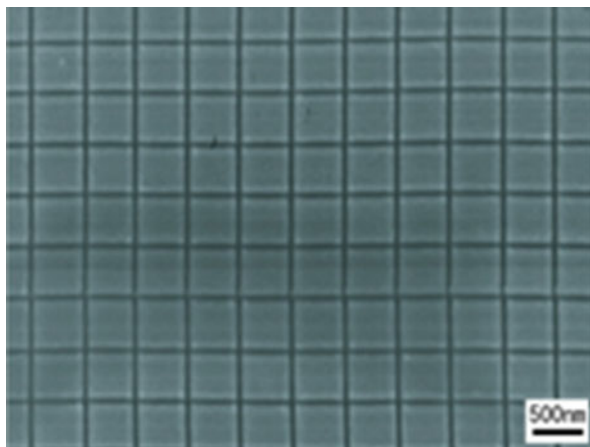


Fig. 12 Knife-edge tool used for nanogroove grid patterning using NPF

Figure 13 shows an SEM image of a nanogroove grid formed on the gold thin film coated on the quartz glass substrate. This image is an example of a groove grid with a 500 nm interval. The thickness of the gold film was 10 nm. The indentation load was 0.5 N. It is confirmed that very thin grooves can be fabricated by simple indentation

Fig. 13 FE-SEM micrographs of nanogroove grids on the coated gold layer. The thickness of the gold film is 10 nm, and the indentation load is 0.5 N



of the knife-edge tool. In spite of the plastic deformation of the gold layer induced by NPF, the gold layer was maintained attached on the substrate.

Figure 14 shows the nanodot arrays generated on the quartz glass substrate based on annealing. Metal films were agglomerated into small dots by the thermal dewetting mechanism.

Dots are approximately located at the centers of each of the grid squares except in (a). In Fig. 5a, the thickness of the coated film and grid size of (a) were 10 and 1000 nm, respectively. The Au film was separated into several dots in each grid and was agglomerated into random nanodots. The average diameter of the agglomerated nanodots was 235 nm with a relative standard deviation of 22%. In contrast, in Fig. 5b, the thickness of the coated film and grid size were, respectively, equal to 10 and 500 nm, and a dot was agglomerated at the center of each grid. The dot size was almost uniform, and dots were aligned in a regular grid pattern. The average diameter of the nanodots was 187 nm with a relative standard deviation of 7%. In Fig. 5c, the thickness of the coated film was 5 nm, and the grid size was 175 nm. The Au nanodots were aligned in a regular grid pattern, and the dot sizes were uniform. The average diameter of the nanodots was 125 nm, and the standard deviation was 2%. Additionally, in Fig. 5d, when the thickness of the coated film was 5 nm and the grid size was 100 nm, many dots were aligned in the grid pattern. The average diameter of the nanodots was 93 nm, and the standard deviation was 2%.

Figure 15 shows an FE-SEM micrograph of the Au nanodot array where the thickness of the metal film is 5 nm and the grid size is 75 nm. It is found that many dots were aligned within the grid pattern, but many dots were bonded with neighboring dots. The average diameter of the nanodots was 79 nm, but the standard deviation was 19%, values that are fairly larger than those corresponding to the results of Fig. 14.

These results indicate that the size and distance of the nanodots are determined by the size of the groove grids. Since the metal film is separated into uniform square shapes using NPF, dots are agglomerated in a regular lattice pattern with uniform dot distances, as seen in Fig. 14b–d. However, when the grid size is too large, as shown in Fig. 14a, the

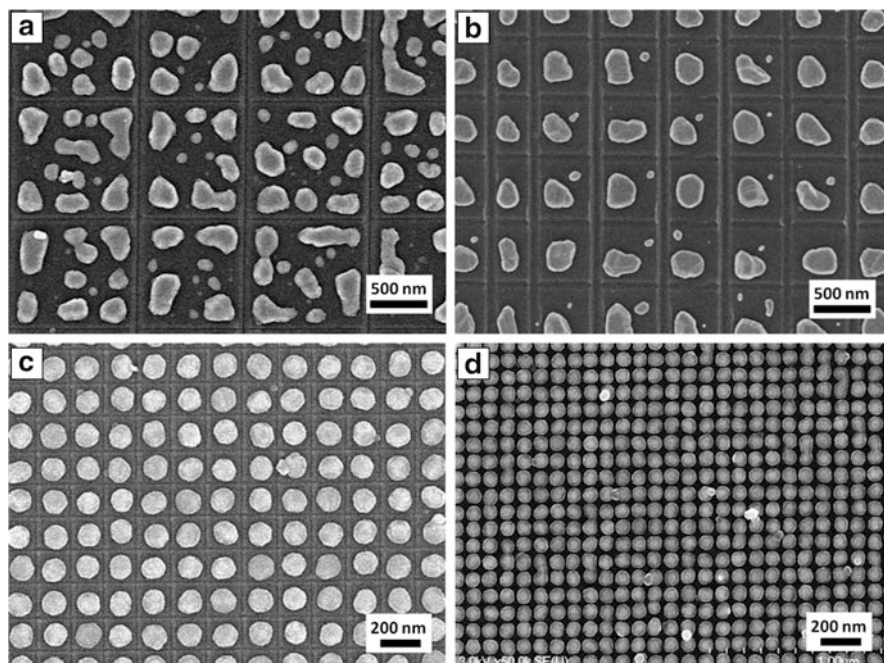
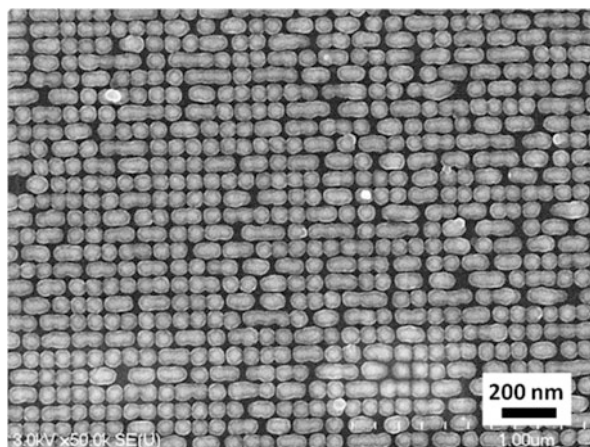


Fig. 14 FE-SEM micrographs of Au nanodot arrays. The thicknesses of the metal films and the grid sizes were (a) 10 nm and 1000 nm, (b) 10 nm and 500 nm, (c) 5 nm and 175 nm, and (d) 5 nm and 100 nm. Annealing conditions were $700\text{ }^{\circ}\text{C} \times 10\text{ min}$

Fig. 15 FE-SEM micrographs of the Au nanodot array, whereby the thickness of the metal film is 5 nm and the grid size is 75 nm. The annealing conditions were $700\text{ }^{\circ}\text{C} \times 10\text{ min}$



metal films in each grid was separated into multiple dots. This is because the grid size was larger than the minimum dot diameter. In contrast, when the grid size is too small, as seen in Fig. 15, dots are not separated by the groove grids because the grid size was smaller than the minimum dot diameter. These problems can be solved by controlling

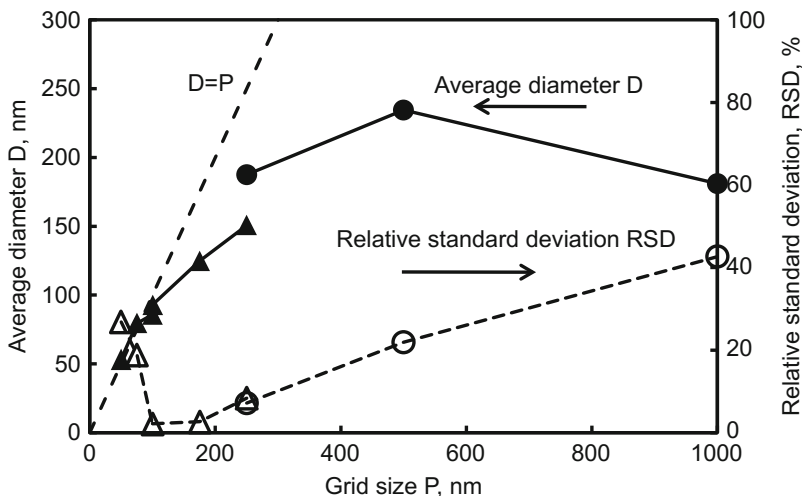


Fig. 16 Variation of the average nanodot sizes and relative standard deviations as a function of the grid size

the thickness of the coated metal film. It has also been confirmed that nanodot arrays with arbitrary sizes in the range of several tens to several hundreds of nm can be fabricated using the proposed process.

Figure 16 shows the variation of the average diameter of nanodots (solid symbols), and their standard deviations (open symbols), as a function of grid size. Circles denote data of Au-coated films with 10 nm in thickness, while triangles denote corresponding data for films with 5 nm in thickness. The broken line indicates the limit of the nanodot's diameter that effectively equals the grid's size. It is confirmed from the figure that the average dot diameter increases when the grid size increases in instances when the grid size is smaller than 500 nm. However, the average diameter decreases when the grid size is 1000 nm. This is attributed to the separation of the dots within the grid squares, as shown in Fig. 14a. The relative standard deviation also decreases with decreases of the grid size. However, the relative standard deviation increases when the grid size becomes smaller than 100 nm. This is owing to the bonding of the nanodots, as observed in Fig. 15.

It should be noted that the relative standard deviations of these nanodots are much smaller than those of Fig. 4b, with the exception of the 1000 nm grid. This indicates that the uniformity of the dot size is much better than the conventional dewetting process. In addition, the layout of the nanodots is regulated very well, and the regularity of the dot alignment is apparently high. This new process is advantageous in terms of the uniformity and controllability of the dot's size and alignment.

23.3.2 Theoretical Study

Figure 17 illustrates the agglomeration process of nanodots by thermal dewetting. The coated metal film is separated into square grids by the groove grid. P is the distance of grooves, which corresponds to the groove grid size. It is the thickness of

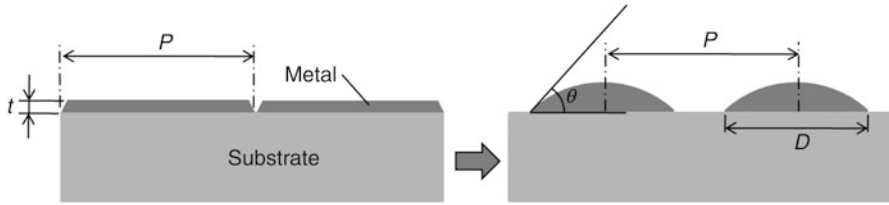


Fig. 17 Geometrical changes of nanodots incurred from the use of thermal dewetting

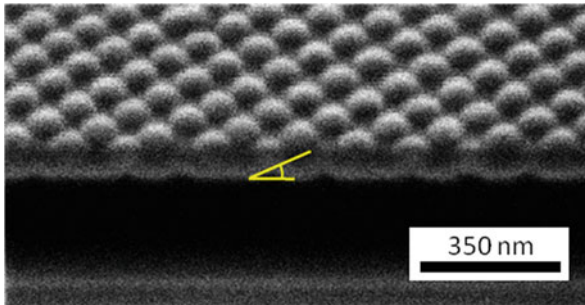


Fig. 18 Scanning ion microscopy (SIM) image of a cross section of a nanodot array. The thickness of the gold layer was 5 nm, patterned grid size was 100 nm, annealing temperature was 700 °C, and the annealing time was 10 min. The cross section was machined by an FIB and was observed at an angle of 45° defined in an anticlockwise direction with respect to the specimen's surface

the coated film. A coated metal film in each grid square agglomerates into hemispherical dots by thermal dewetting, as shown on the right subplot in Fig. 17. In this case, D is the diameter of the dot, and θ_c is the contact angle of a nanodot. By assuming that the volume conservation of the metal film occurs throughout the thermal dewetting process, the following equations are obtained:

$$D = \left\{ \frac{24P^2t \sin^3\theta_c}{\pi(2 - 3\cos\theta_c + \cos^3\theta_c)} \right\}^{\frac{1}{3}} \quad (0^\circ < \theta_c \leq 90^\circ) \quad (31)$$

$$D = \left\{ \frac{24P^2t}{\pi(2 - 3\cos\theta_c + \cos^3\theta_c)} \right\}^{\frac{1}{3}} \quad (90^\circ \leq \theta_c \leq 180^\circ) \quad (32)$$

The contact angle was measured from the cross section of nanodots in Fig. 18. Figure 18 shows a scanning ion microscopy (SIM) image of a cross section of a nanodot array, where dots were sectioned by FIB etching. In the figure, the cross section was observed obliquely at an angle of 45° defined in an anticlockwise direction with respect to the substrate's surface. By compensating the inclined angle of observation, we estimated that the contact angle was almost 41°.

Fig. 19 Relationship between the diameter of the nanodots and the grid size. Symbols are experimental data. The thickness of the gold layer was 5 nm. The solid curve is the theoretical value calculated using Eq. 3 where the contact angle is 41°

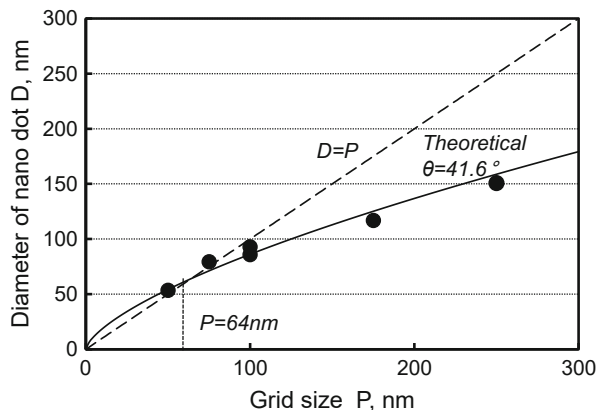


Fig. 20 Theoretical variation of the diameter of nanodots as a function of the grid size. The contact angle is 41° . The thicknesses of the gold layers are 1, 2, and 2.5 nm

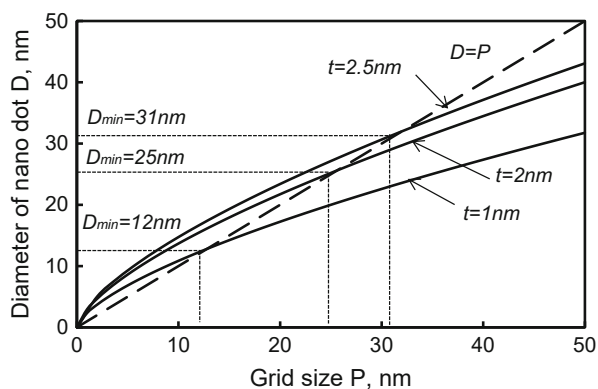
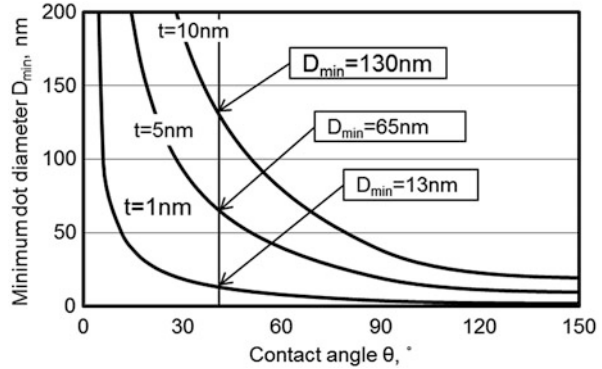


Figure 19 shows the relationship between the nanodot diameter D and the grid size P . Symbols denote the average diameter of the nanodots obtained by experiments where the thickness of the gold layer was 5 nm. The solid curve indicates the variation of the dot diameter of Eq. 3, where the contact angle θ is 41° . It is confirmed that the experimental data agree well with the theoretical values. The broken line represents the condition at which $D=P$, where dots are connected to neighboring dots. It is found from the figure that the solid line crosses the dashed line at $P = 64$ nm and exceeds the dashed line when the grid size is smaller than P_c . Therefore, 64 nm represents the minimum diameter of nanodots that can be fabricated under present condition.

Figure 20 shows the variation of the diameter of the nanodots calculated based on Eq. 31. Three levels of coating thicknesses are shown in the graph. The broken line indicates that $D=P$, and the cross point of the curve and dashed line indicate the minimum dot diameter. The minimum dot diameter equations are obtained from Eqs. 31 and 32 assuming validity of the condition whereby $D=P$.

Fig. 21 Calculated variation of minimum diameter D_{\min} against the contact angle θ



$$D_{\min} = \frac{24t \sin^3 \theta_c}{\pi (2 - 3 \cos \theta_c + \cos^3 \theta_c)} \quad (0^\circ < \theta_c \leq 90^\circ) \quad (33)$$

$$D_{\min} = \frac{24t}{\pi (2 - 3 \cos \theta_c + \cos^3 \theta_c)} \quad (90^\circ \leq \theta_c \leq 180^\circ) \quad (34)$$

Figure 21 shows the calculated variation of the minimum dot diameter D_{\min} as a function of the contact angle θ for three levels of the metal film thickness, i.e., 1, 5, and 10 nm. It is found that D_{\min} decreases with the increase of the contact angle θ . The vertical line in the graph indicates that $\theta = 41^\circ$ and that the D_{\min} values in the graph present the minimum dot diameter when $\theta = 41^\circ$. The data of $D_{\min} = 65$ nm on $t = 5$ nm agree with the experimental data shown in Fig. 19. This graph indicates that a very small nanodot array with a diameter of 13 nm can be fabricated when the coating thickness is 1 nm.

Accordingly, the dot diameter can be controlled by controlling the metal film thickness and the grid size, even when the combination of the substrate and nanodot material is determined.

23.4 Fabrication Process of a Metal Nanodot Array Using Patterned Substrates

23.4.1 Experimental Studies

Although the aforementioned method is effective for fabrication of metal nanodot arrays, there is a problem since a nanogroove grid has to be formed on each coated specimen. Since the NPF's operation time increases with the area of the nanodot array, this process is not suitable for mass production of large-area nanodot arrays. In order to overcome this disadvantage, authors are developing another manufacturing process for nanodot arrays (Truong et al. 2012).

Figure 22 illustrates the basic steps of this process. Specifically, a quartz glass plate on which a nanogroove grid was fabricated a priori is utilized as the substrate for the nanodot array. Subsequently, a thin Au film is coated on the substrate, and the substrate is annealed. The metal thin film naturally separates on the nanogrooves and self-organizes into a nanodot array. Thereafter, an adhesive polymer is pasted on the nanodot array and then peeled off. The nanodot array is transferred to the polymer film. This polymer film is used as a nanodot array. Since the substrate can be used repeatedly, the fabrication process of the nanogroove grid does not to be conducted for every nanodot array. Accordingly, high productivity can be achieved by the repetition of the Au film-coating process, self-organization using annealing, and transfer to polymer films.

Figure 23 shows an FE-SEM micrograph of a quartz glass substrate on which a nanogroove grid of 500 nm square is fabricated using the EB lithographic method. The groove grid was fabricated on the substrate using the NPF method. The width and depth of the grooves were less than 100 nm. Many hard brittle materials, such as quartz glass, can be formed by plastic deformation without generating cracks when the depth of deformation is smaller than the critical depth. Since the critical depth of

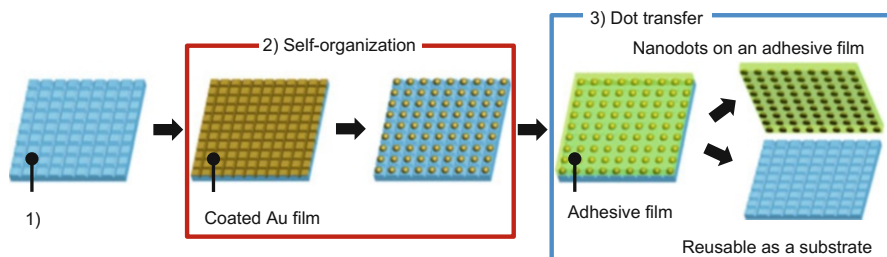
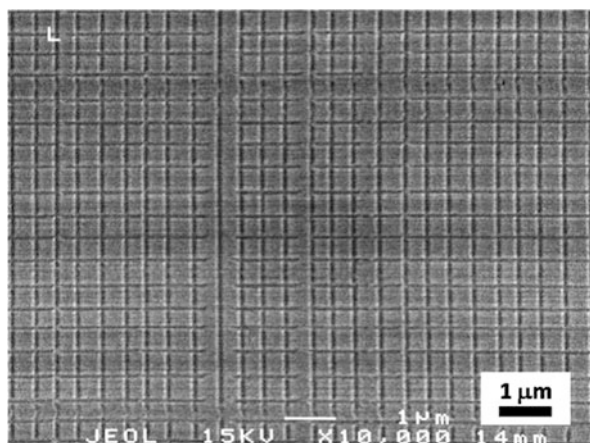


Fig. 22 Efficient fabrication process of nanodot arrays using a patterned substrate and dot transfer

Fig. 23 FE-SEM micrograph of a prepatterned quartz glass substrate coated with Au



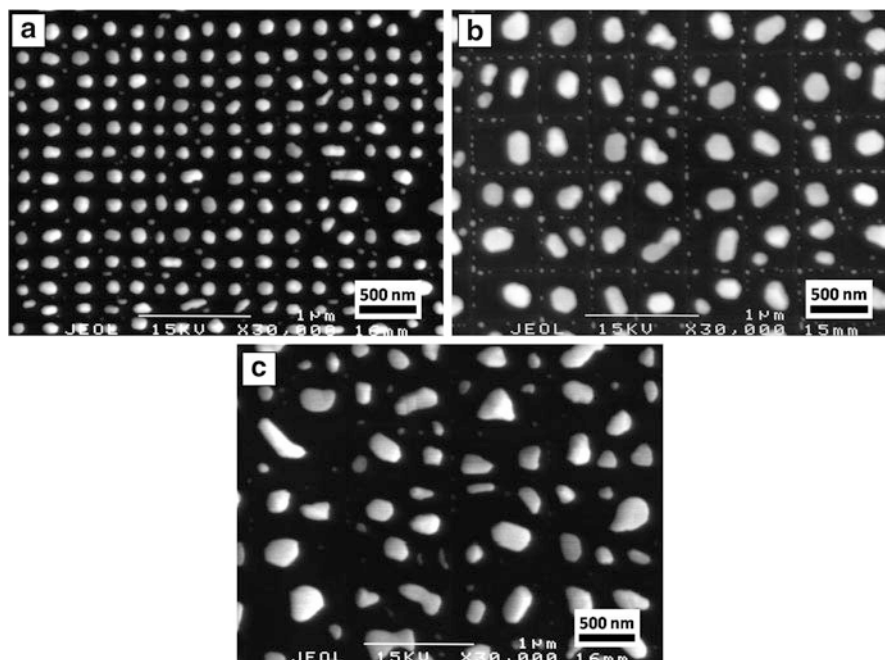


Fig. 24 Nanodot array generated on the patterned substrate. Groove grid size: (a) 250 nm, (b) 500 nm, and (c) 1000 nm

quartz glass is approximately 200 nm for a 60° knife-edge tool, nanogroove grids can be fabricated by nano-indentation of the knife-edge tool without generating cracks in the quartz substrate. In Fig. 23, although a thin Au film with a thickness of 10 nm is coated on the substrate, a nanogroove grid is observed.

Figure 24 shows FE-SEM images of nanodot arrays generated on the patterned substrates using annealing. The sizes of the groove grid that was preliminarily fabricated on the quartz glass substrate were (a) 250 nm, (b) 500 nm, and (c) 1000 nm. The thickness of the coated Au film was 10 nm, and the annealing condition was 700 °C × 10 min. In the case of (a) and (b), the Au nanodots are almost aligned in the center of each grid. Although the regularity is lower than that exhibited by the nanodots in the previous section, this is because the annealing conditions were not appropriate for this nanodot array. Small dots are found arranged in a lattice pattern between large nanodots. These are the Au dots that remained on the bottom of the groove grids of the quartz substrate. The Au thin film was separated on the grooves, and a separated film agglomerated into a large nanodot that was located at the center of the lattice. Most of the Au atoms were aggregated at the large nanodots based on diffusion, but some of the gold remained on the bottom of the groove, and formed small dots aligned along the grooves. In addition, plural dots were found in some of the grids. They were separated during the agglomeration process because the heat treatment conditions and sputtering conditions were not appropriate for this grid size

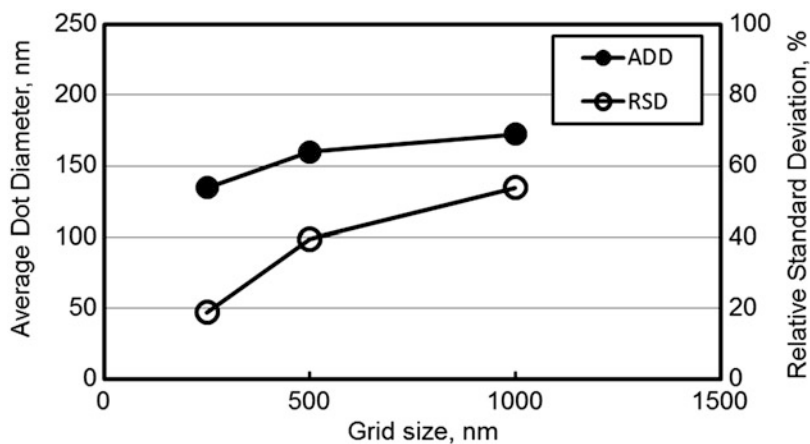


Fig. 25 Variation of the average nanodot size and the relative standard deviation as a function of the grid size

and film thickness. By adjusting these conditions, the separation of dots in a groove grid can be prevented. In (c), random and nonuniformly distributed dots were generated even though a groove grid was fabricated. This is because the grid size was too large and film separation occurred in a groove grid.

Figure 25 shows the variation of the average diameter of nanodots (solid symbols) and their standard deviation (open symbols) as a function of the grid size. The average dot diameter does not increase linearly with the grid size. This is because the average dot diameter of the 500 nm grid includes diameters of smaller dots that remained on the grooves. Thus, the relative standard deviation is also large as compared to that of the nanodot array described in the previous section (see Fig. 14). By eliminating the data pertaining to the small dots on the grooves, the average dot diameter for a grid of 500 nm becomes much larger, and the relative standard deviation much smaller. In the case of the 1000 nm grid, the average nanodot diameter becomes equal to approximately 160 nm, which is almost the same as that of the nanodot array described in the previous section (see Fig. 14), and with the random dot pattern in Fig. 4a. Controlling the size using the groove grid was not effective at this experimental condition.

Figure 26 shows FE-SEM micrographs of nanodots agglomerated on the patterned quartz glass substrates after annealing. The groove grid was fabricated by NPF, and the grid size was 100 nm. These substrates were coated with Au films with the thicknesses of 6, 8, 10, 12, 14, and 16 nm. These substrates were then annealed at 600 °C for 10 min. When the gold-coating layer was 6 nm, small randomly distributed dots were generated both on the grid square and on the grooves, and the regularity of the nanodots was poor. When the thickness was 8 nm, the uniformity and regularity of the nanodot array were improved. Some dots aligned approximately at the center of the grid square, but many small dots were located randomly both on the grid square and on the grooves. When the gold film thickness was 10 nm,

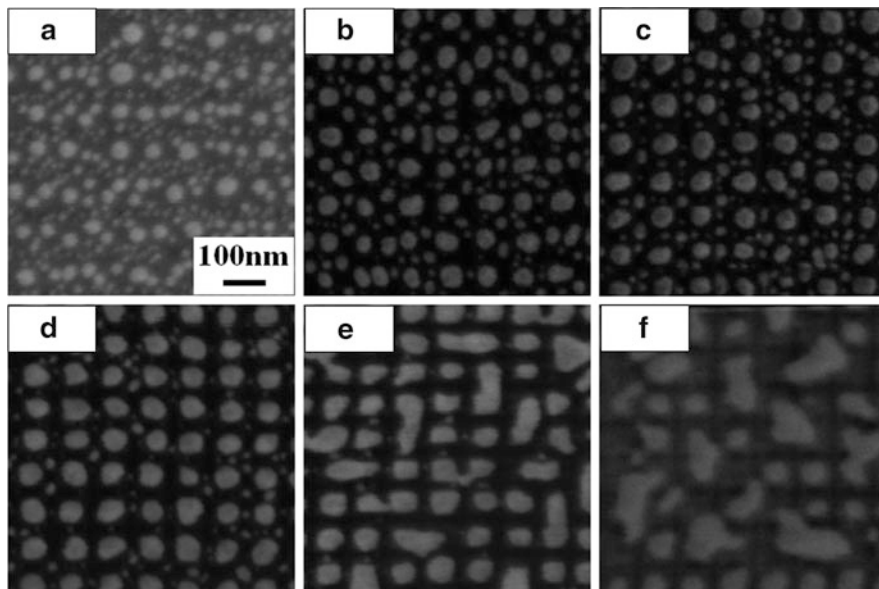


Fig. 26 FE-SEM micrographs of nanodot arrays aggregated on patterned quartz glass substrates after annealing at 600 °C for 10 min. Thickness of the coated film: (a) 6 nm, (b) 8 nm, (c) 10 nm, (d) 12 nm, (e) 14 nm, and (f) 16 nm

the uniformity and regularity of the nanodot array were further improved. The dots almost aligned on a grid pattern, and the regularity was apparent. However, only a few small dots remained that were randomly distributed. When the thickness was 12 nm, good nanodot array uniformity and regularity were achieved. The dots aligned at the center of each groove grid. When the thickness was 14 nm, the uniformity and regularity of the nanodot array became worse because some dots were connected to the adjacent dots. When the gold film thickness was 16 nm, the dots were randomly agglomerated on the substrate.

Figure 27 illustrates three types of dot agglomeration patterns observed in the experiments (Truong et al. 2014). When the coated film is very thin, the film is agglomerated into many small dots, as shown in Fig. 27a. These small dots are randomly distributed on the substrate. When the gold film has a proper thickness, as shown in Fig. 27b, the metal film is separated at the grooves, and the metal film on the grid square agglomerates into a dot. As a result, dots of uniform size are aligned in accordance with a grid pattern. When the metal film is too thick, as shown in Fig. 27c, the depth of the grid pattern of the grooves on the gold film surface is too shallow when compared to the thickness of the metal film, and the metal film is not separated at the groove grid perfectly. As a result, some dots are connected with the adjacent dots, and uniformity and regularity of the nanodot array become poor. The control of the thickness of the metal film and the annealing condition is important in order to obtain a nanodot array with good regularity.

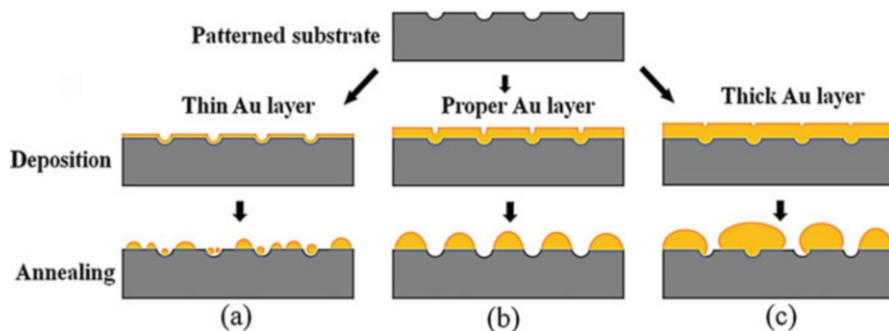


Fig. 27 Schematic illustration of three types of dot aggregation patterns: (a) thin gold film, (b) proper gold film thickness, and (c) thick gold film

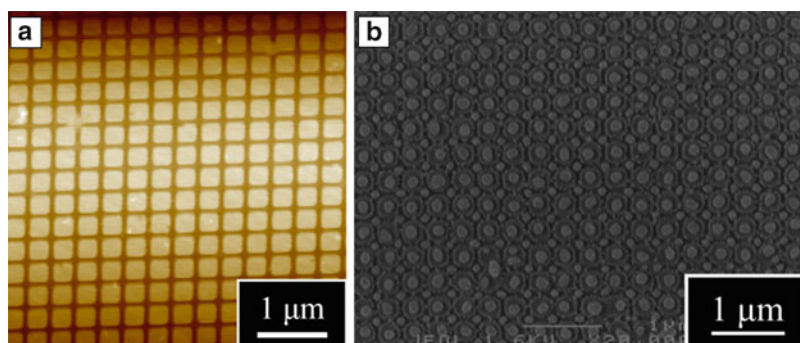


Fig. 28 (a) Grid patterned substrate used for dot transfer experiment, and (b) Au nanodots generated using coating and annealing

Figure 28 shows an example of a grid-patterned substrate and Au nanodots used for a dot transfer experiment. Specifically, Fig. 28a shows an AFM image of the nano-groove grid on the quartz glass substrate. The size of the patterned area of the groove grid was $5 \times 5 \text{ mm}^2$. The grid size was 300 nm, and the width of the groove was 50 nm. Correspondingly, Fig. 28b is the FE-SEM image of the nanodots agglomerated on the substrate using thermal dewetting. The thickness of the coated Au film was 10 nm. The coated substrate was annealed at 800 °C for 10 min. It is found that uniform Au nanodots were agglomerated at the center of each grid square area. These dots were aligned in a lattice pattern, and they formed a nanodot array. The average dot diameter was approximately 140 nm. Small dots were also agglomerated at the cross points of the grid. These are Au dots that originated at the bottom of the grooves.

Vinyl chloride adhesive was pasted on the Au nanodot array and cured at 50 °C for 30 min to achieve complete dehydration. The cured resin film was then peeled off from the substrate manually. Figure 29 shows an FE-SEM micrograph of (a) the surface of the substrate and (b) the surface of vinyl chloride adhesive after the peeling operation. It was found that most of all the Au nanodots on the substrate

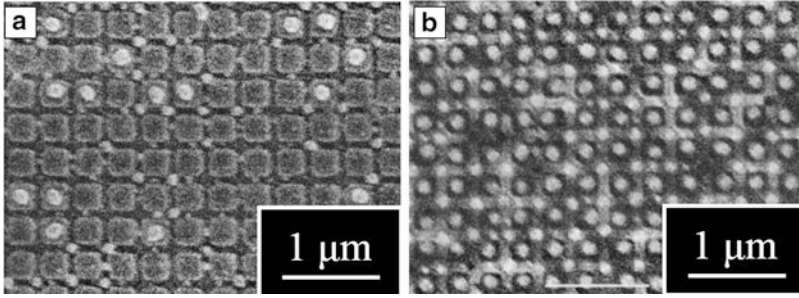


Fig. 29 SEM photographs of surface of (a) the substrate and (b) vinyl chloride adhesive film after the peeling operation

were transferred to the adhesive. However, some dots still remained on the substrate, and the dot transfer ratio was not 100%. It is necessary to improve the dot transfer ratio to apply this process to practical industrial production.

23.4.2 Theoretical Study on the Dot Transfer Mechanism

Figure 30 illustrates two cases that occur in relation to a nanodot in the dot transfer operation:

- (a) Case I: a dot is not transferred to the adhesive film but remains on the substrate.
- (b) Case II: a dot is transferred to the adhesive film by assuming that the dot shape is semispherical and the shape of the dot does not change through the transfer process.

The total free energy of the system in each case is calculated based on the following equations:

$$W_I = S_s\gamma_s + S_d\gamma_d + S_i\gamma_i + S_s\gamma_p + S_d\gamma_p \quad (\text{case I}) \quad (35)$$

$$W_{II} = S_s\gamma_s + S_i\gamma_s + S_s\gamma_p + S_i\gamma_d + S_d\gamma_{p'} \quad (\text{case II}) \quad (36)$$

where S_s is the area of substrate surface, S_d is the area of the surface of the dot, and S_i is the interface area between the dot and the substrate. Additionally, γ_s is the surface energy of the substrate, γ_d is the surface energy of the dot, γ_i is the interfacial energy between the dot and the substrate, γ_p is the surface energy of the adhesive, and $\gamma_{p'}$ is the interfacial energy between the dot and the adhesive.

The difference ΔW of the total free energy between cases I and II is calculated as follows:

$$\begin{aligned} \Delta W &= W_I - W_{II} \\ &= (S_s\gamma_s + S_d\gamma_d + S_i\gamma_i + S_s\gamma_p + S_d\gamma_p) - (S_s\gamma_s + S_i\gamma_s + S_s\gamma_p + S_i\gamma_d + S_d\gamma_{p'}) \\ &= S_d(\gamma_d + \gamma_p - \gamma_{p'}) + S_i(\gamma_i - \gamma_s - \gamma_d) \end{aligned} \quad (37)$$

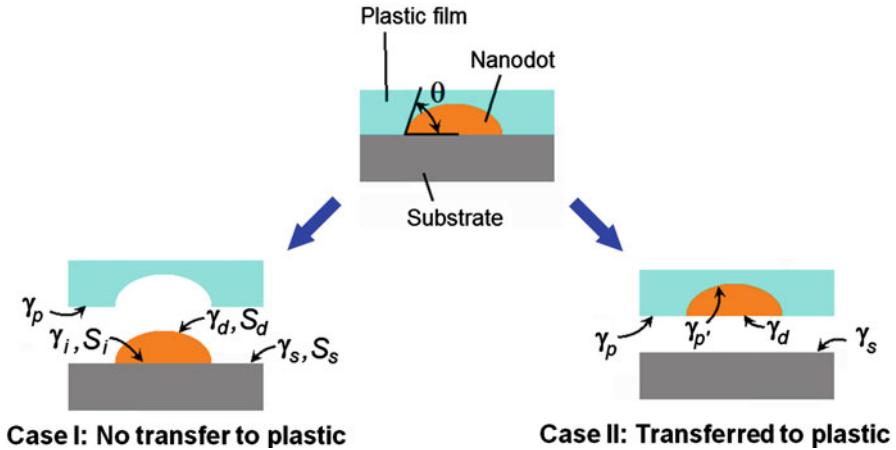


Fig. 30 Model of dot transfer from a substrate to an adhesive film

Correspondingly, the Young's equation is expressed as follows:

$$\gamma_s - \gamma_i = \gamma_d \cos \theta_c \quad (38)$$

where θ_c is the contact angle between the dot and the substrate. By substituting Eq. 38 into Eq. 37, we obtain

$$\Delta W = S_d(\gamma_d + \gamma_p - \gamma_{p'}) - S_i \gamma_d (1 + \cos \theta_c) \quad (39)$$

The surface area S_d of a dot is calculated using the dot diameter D as follows:

$$S_d = \frac{\pi D^2}{2} \frac{1}{1 + \cos \theta_c} \quad \text{for } \theta_c < 90^\circ \quad (40)$$

$$S_d = \frac{\pi D^2}{2} (1 - \cos \theta_c) \quad \text{for } \theta_c \geq 90^\circ \quad (41)$$

The interfacial area S_i between the dot and the substrate is then calculated as

$$S_i = \frac{\pi D^2}{4} \quad \text{for } \theta_c < 90^\circ \quad (42)$$

$$S_i = \frac{\pi D^2}{4} \sin^2 \theta_c \quad \text{for } \theta_c \geq 90^\circ \quad (43)$$

By substituting Eqs. 40, 41, 42, and 43 into Eq. 39, we obtain

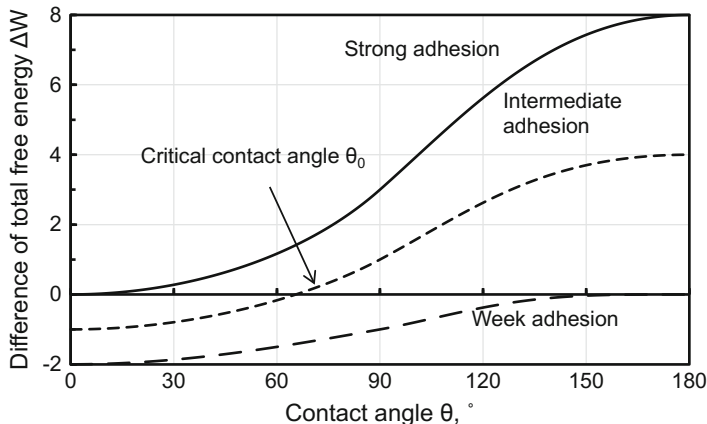


Fig. 31 Variation of ΔW as a function of θ_c

$$\begin{aligned} \Delta W &= W_I - W_{II} \\ &= \begin{cases} \frac{\pi D^2}{4} \frac{\gamma_d}{1 + \cos \theta_c} \left\{ 2 \left(1 + \frac{\gamma_p - \gamma_{p'}}{\gamma_d} \right) - (\cos \theta_c + 1)^2 \right\} & \theta_c < 90^\circ \\ \frac{\pi D^2}{4} \gamma_d (1 - \cos \theta_c) \left\{ 2 \left(1 + \frac{\gamma_p - \gamma_{p'}}{\gamma_d} \right) - (\cos \theta_c + 1)^2 \right\} & \theta_c \geq 90^\circ \end{cases} \end{aligned} \tag{44}$$

When $\Delta W < 0$, the dot remains on the substrate (case I), while when $\Delta W > 0$, the dot is transferred to the adhesive film (case II).

Figure 31 shows the calculated variation of ΔW as a function of the contact angle θ_c . In this figure, three cases are presented according to balance of surface energies, i.e., $(\gamma_p - \gamma_{p'})/\gamma_d = -1, 0$, and 1 , which represent the weak adhesion, intermediate adhesion, and strong adhesion cases, respectively.

It is found from Fig. 31 that ΔW increases as a function of θ_c . In this graph, the three curves represent three levels of adhesion strengths for the adhesive film. The continuous curve represents the adhesive film in the strong adhesion case. In this case, a nanodot is transferred to the film regardless of its contact angle. The dotted curve represents the adhesive in the weak adhesion case. The nanodot is not transferred to this plastic regardless of its contact angle. The dashed curve (the center curve) represents the adhesive in the intermediate adhesion case. The nanodot is transferred to the film when the contact angle is large.

In order to calculate the transfer rate, it is necessary to consider variations in the contact angle. Denote the average contact angle as θ_m . The contact angle at which $\Delta W = 0$ is defined as the critical contact angle θ_0 . According to the dot transfer theory discussed above, all of the nanodots are transferred when the contact angle θ_c exceeds θ_0 , while none of the nanodots are transferred when the contact angle θ is

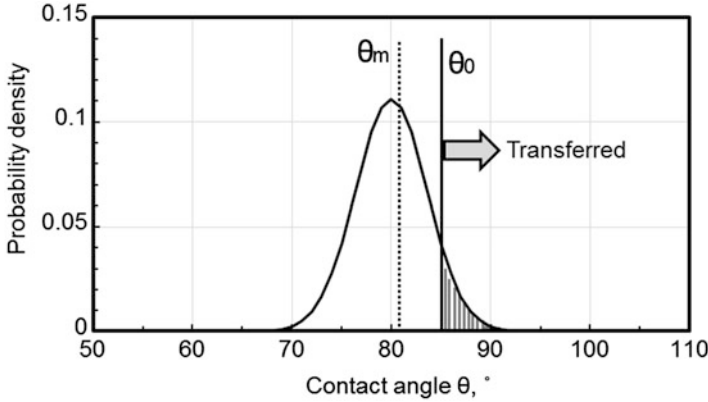


Fig. 32 Normal distribution of contact angles when $\theta_m = 80^\circ$ and $\sigma = 3.6^\circ$

smaller than θ_0 . Since there are dispersions in the shapes of the actual nanodots, it is assumed that the contact angle also disperses in accordance with the normal distribution. Assuming that the standard deviation of the contact angle is σ , the probability density function $p(\theta)$ of the contact angle θ is expressed by the following equation:

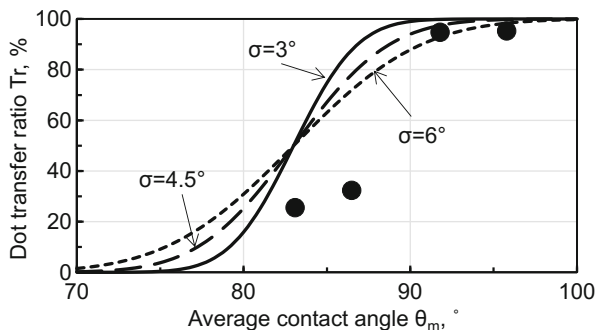
$$p(\theta) = \frac{1}{\sqrt{2\pi}\sigma} \exp\left\{-\frac{(\theta - \theta_m)^2}{2\sigma^2}\right\} \quad (45)$$

Figure 32 shows an example of the normal distribution of the contact angles when $\theta_m = 80^\circ$ and $\sigma = 3.6^\circ$. Nanodots whose contact angles are larger than the critical contact angle θ_0 are transferred to the adhesive film. Since the fraction of transferred nanodots is represented by the area highlighted in blue in the graph, the transfer ratio is obtained by dividing this area by total area of the probability density function $p(\theta)$ ($=1$). Therefore, the transfer ratio T_r is calculated as

$$T_r = \int_{\theta_0}^{\infty} p(\theta)d\theta = \int_{\theta_0}^{\infty} \frac{1}{\sqrt{2\pi}\sigma} \exp\left\{-\frac{(\theta - \theta_m)^2}{2\sigma^2}\right\} d\theta = \frac{1}{2} + \frac{1}{2} \operatorname{erf}\left(\frac{\theta_m - \theta_0}{\sqrt{2}\sigma}\right) \quad (46)$$

Accordingly, the dot transfer ratio is determined by the error function of the average contact angle θ_m , the critical contact angle θ_0 , and the standard deviation σ of the contact angle. Figure 33 shows the variation of the dot transfer ratio as a function of the average contact angle θ_m . The solid line is the theoretical dot transfer ratio calculated by Eq. 46, and the plotted symbols denote the experimental data. The calculated transfer ratio increases smoothly as a function of the average contact angle θ_m . The variation of the theoretical values agrees with the trend of the experimental data. In addition, as the standard deviation σ of the contact angle becomes large, the change of the dot transfer ratio becomes more gradual.

Fig. 33 Variation of the dot transfer ratio as a function of the average contact angle θ_m



Based on the discussion arguments listed above, it is understood that the dot transfer ratio can be increased by increasing the average contact angle θ_m , and by decreasing the dispersion of the contact angle σ . The adhesion strength $(\gamma_p - \gamma_p')/\gamma_d$ of the adhesive film is also factor that affects the dot transfer ratio. The increase of the surface energy of the adhesive, γ_p , and the decrease of the interfacial energy between the dot and the adhesive, γ_p' , increase the dot transfer ratio.

23.5 Summary and Outlook

A metal nanodot array exhibits unique optical properties. For this reason, it is expected to be used in biosensors and various optical devices. Additionally, a metal nanodot array has a comparably simple structure. As a result, it can be manufactured by conventional lithographic methods. However, the latter involve complicated processes and are associated with high production costs.

In this section, efficient fabrication processes of metal nanodot arrays were introduced using thermal dewetting. The characteristics of the conventional thermal dewetting process were first discussed based on experimental data, and on a physical model of dot agglomeration owing to free energy reduction. A new fabrication process based on grid patterning using NPF and thermal dewetting was then explained. It is useful to manufacture a nanodot array comprising uniform and highly ordered nanodots that could control the dot diameter from several tens to several hundreds of nm. Finally, a manufacturing process was presented for a nanodot array using thermal dewetting on a grid-patterned substrate, and the dot transfer technique was explained. High-throughput production of a nanodot array is expected using this process.

Although there are still many issues that need to be solved, it will be possible to further increase the area size of the nanodot array, increase its productivity, and reduce the production cost in combination with other technologies, such as the nanoimprinting method. It is expected that high-performance sensors and optical devices can be realized using metal nanodot arrays.

References

- Agapov RL, Srijanto B, Fowler C, Briggs D, Lavrik NV, Sepaniak MJ (2013). Lithography-free approach to highly efficient, scalable SERS substrates based on disordered clusters of disc-on-pillar structures. *Nanotechnology* 24:505302
- Cheung CL, Nikolic RJ, Reinhardt CE, Wang TF (2006). Fabrication of nanopillars by nanosphere lithography. *Nanotechnology* 17:1339–1343
- Cheyne F, Bussmann E, Leroy F, Passanante T, Müller P (2011). Dewetting dynamics of silicon-on-insulator thin films. *Phys Rev B* 84:245439
- Chou SY, Krauss PR, Renstrom PJ (1996). Imprint Lithography with 25-Nanometer Resolution. *Science* 272:85–87
- Danielson DT, Sparacin DK, Michel J, Kimerling LC (2006). Surface-energy-driven dewetting theory of silicon-on-insulator agglomeration. *J Appl Phys* 100:083507
- Dmitriev A, Hägglund C, Chen S, Fredriksson H, Pakizeh T, Käll M, Sutherland DS (2008). Enhanced Nanoplasmonic Optical Sensors with Reduced Substrate Effect. *Nano Lett* 8:3893–3898
- Hong Y, Huh YM, Yoon DS, Yang J (2012). Nanobiosensors Based on Localized Surface Plasmon Resonance for Biomarker Detection. *J Nanomater* 2012:759830
- Huang Z, Meng G, Huang Q, Yang Y, Zhu C, Tang C (2010). Improved SERS Performance from Au Nanopillar Arrays by Abridging the Pillar Tip Spacing by Ag Sputtering. *Adv Mater* 22:4136–4139
- Kajiura M, Nakanishi T, Iida H, Takada H, Osaka T (2009). Biosensing by optical waveguide spectroscopy based on localized surface plasmon resonance of gold nanoparticles used as a probe or as a label. *J Colloid Interface Sci* 335:140–145
- Kandziolka M, Charlton JJ, Kravchenko II, Bradshaw JA, Merkulov IA, Sepaniak MJ, Lavrik NV (2013). Silicon Nanopillars As a Platform for Enhanced Fluorescence Analysis. *Anal Chem* 85:9031–9038
- Knoben W, Brongersma SH, Crego-Calama M (2011). Plasmonic Au islands on polymer nanopillars. *Nanotechnology* 22:295303
- Lee Y, Koh K, Na H, Kim K, Kang JJ, Kim J (2009). Lithography-Free Fabrication of Large Area Subwavelength Antireflection Structures Using Thermally Dewetted Pt/Pd Alloy Etch Mask. *Nanoscale Res Lett* 4:364–370
- Leem JW, Yeh Y, Yu JS (2012). Enhanced transmittance and hydrophilicity of nanostructured glass substrates with antireflective properties using disordered gold nanopatterns. *Opt Express* 20:4056–4066
- Lucas BD, Kim JS, Chin C, Guo LJ (2008). Nanoimprint Lithography Based Approach for the Fabrication of Large-Area, Uniformly-Oriented Plasmonic Arrays†. *Adv Mater* 20:1129–1134
- Mortazavi D, Kouzani AZ, Kaynak A, Duan W (2012). Developing lspr design guidelines. *Prog Electromagn Res* 126:203–235
- Oh YJ, Jeong KH (2012). Glass Nanopillar Arrays with Nanogap-Rich Silver Nanoislands for Highly Intense Surface Enhanced Raman Scattering. *Adv Mater* 24:2234–2237
- Otte MA, Estevez M-C, Carrascosa LG, Gonzalez-Guerrero AB, Lechuga LM, Sepulveda B (2011). Improved Biosensing Capability with Novel Suspended Nanodisks. *J Phys Chem C* 115:5344–5351
- Raphael MP, Christodoulides JA, Mulvaney SM, Miller MM, Long JP, Byers JM (2012). A New Methodology for Quantitative LSPR Biosensing and Imaging. *Anal Chem* 84:1367–1373
- Rayleigh L (1879). On the instability of Jets. *Proc Lond Math Soc* S1-10(1):4–12
- Saito M, Kitamura A, Murahashi M, Yamanaka K, Hoa LQ, Yamaguchi Y, Tamiya E (2012). Novel Gold-Capped Nanopillars Imprinted on a Polymer Film for Highly Sensitive Plasmonic Biosensing. *Anal Chem* 84:5494–5500
- Senanayake P, Hung C-H, Shapiro J, Lin A, Liang B, Williams BS, Huffaker DL (2011). Surface Plasmon-Enhanced Nanopillar Photodetectors. *Nano Lett* 11:5279–5283

- Sepulveda B, Angelome PC, Lechuga LM, Liz-Marzan LM (2009). LSPR-based nanobiosensors. *NanoToday* 4:244–251
- Tan CL, Jang SJ, Lee YT (2012). Localized surface plasmon resonance with broadband ultralow reflectivity from metal nanoparticles on glass and silicon subwavelength structures. *Opt Express* 20:17448–17455
- Truong DP, Yamanaka A, Yoshino M (2012). High Throughput Method to Fabricate Ordered Nano Dot Array on Various Plastic Films. *Key Eng Mater* 523–524:633–638
- Truong DP, Terano M, Yoshino M (2014). Fabrication of an ordered nanodot array by thermal dewetting on a patterned substrate. *Manuf Lett* 2(2):60–63. <https://doi.org/10.1016/j.mfglet.2014.02.004>
- Tsai SJ, Ballarotto M, Romero DB, Herman WN, Kan HC, Phaneuf RJ (2010). Effect of gold nanopillar arrays on the absorption spectrum of a bulk heterojunction organic solar cell. *Opt Express* 18:A528–A535
- Varghese LT, Fan L, Xuan Y, Tansarawiput C, Kim S, Qi M (2013). Resistless Nanoimprinting in Metal for Plasmonic Nanostructures. *Small* 9:3778–3783
- Yoshino M, Ohsawa H, Yamanaka A (2011). Rapid fabrication of an ordered nano-dot array by the combination of nano-plastic forming and annealing methods. *J Micromech Microeng* 21:125017
- Yoshino M, Osawa H, Yamanaka A (2012). Effects of process conditions on nano-dot array formation by thermal dewetting. *J Manuf Process* 14:478–486
- Yoshino M, Li Z, Terano M (2015). Theoretical and Experimental Study of Metallic Dot Agglomeration Induced by Thermal Dewetting. *J Micro Nano-Manuf* 3(2):021004
- Young T (1805). An essay on the cohesion of fluids. *Phil Trans R Soc London* 95:65–87
- Zeng S, Yong K, Roy I, Dinh X, Yu X, Luan F (2011). A Review on Functionalized Gold Nanoparticles for Biosensing Applications. *Plasmonics* 6(3):491–506. <https://doi.org/10.1007/s11468-011-9228-1>
- Zhang W, Ding F, Li WD, Wang Y, Hu J, Chou SY (2012). Giant and uniform fluorescence enhancement over large areas using plasmonic nanodots in 3D resonant cavity nanoantenna by nanoimprinting. *Nanotechnology* 23:225301
- Zhigal'skii GP, Jones BK (2003) Taylor & Francis, London. The physical properties of thin metal films. Chap. 4, ISBN:0-415-28390-6



Surface Micro-/Nanostructuring Using Self-Assembly of Fine Particles

24

Arata Kaneko

Contents

24.1	Introduction	746
24.2	Basics of Self-Assembly Using Suspension	746
24.3	Micro-/Nanopatterning Based on Self-Assembly	751
24.3.1	Top-Down Approaches for Spatially Controlled Self-Assembly	751
24.3.2	Templates for Self-Assembly	752
24.3.3	Self-Assembly on Hydrophilic/Hydrophobic Patterns	754
24.3.4	Self-Assembly on Micro-geometry Templates	757
24.3.5	Complex Structures of Different Particles, Obtained by Multiple Drawing	759
24.4	Applications of Self-Assembled Particles	760
24.4.1	Transferring of Particles	760
24.4.2	Surface Modification of Particles with Functional Thin Film	761
24.4.3	Surface Modification of Particles with Proteins	762
24.4.4	Optical Applications of Self-Assembled Particles	764
24.4.5	Self-Patterning of Cultured Cells on Particles	766
24.5	Summary	769
	References	769

Abstract

This chapter describes the self-assembly of fine particles for micro-/nanostructuring and its applications. The self-assembly technique is based on aggregation, which is induced by a lateral capillary force (meniscus force) among particles in an evaporating suspension. Autonomously aggregated particles form a close-packed hexagonal arrangement. A specified template restricts the assembling particles to the desired pattern, producing microstructures of self-assembled particles on a substrate. Both spatially controlled wettability and microscale geometry are

A. Kaneko (✉)

Faculty of System Design, Tokyo Metropolitan University, Tokyo, Japan

e-mail: kaneko-arata@tmu.ac.jp

© Springer Nature Singapore Pte Ltd. 2018

J. Yan (ed.), *Micro and Nano Fabrication Technology*, Micro/Nano Technologies,

https://doi.org/10.1007/978-981-13-0098-1_24

745

important candidates to be used in templates for the self-assembly of particles. These templates are fabricated by either micro-contact printing (μ CP) of self-assembled monolayers (SAMs) or conventional lithography and etching; e.g., sub-micrometer silica and polystyrene particles can be structured in an array of linear or circular dot patterns of an order of tens of micrometers. The self-assembly of particles previously coated with functional materials can produce specific surface structures to be utilized in microdevices such as chemical sensors or biochips. Also, the surface asperities of arranged particles may increase the specific surface area to enhance the chemical reactions and improve the adhesion of cultured cells.

Keywords

Self-assembly · Particle · Surface · Micro-/nanosstructure

24.1 Introduction

Presently, various fine particles are commercially available and are changing every year regarding material (metals, semiconductors, polymers, and biomaterials), size (nanometers to millimeters), shape (spheres, rods, polytopes, wires, tubes, etc.), and function (optical, chemical, electrical, mechanical, biological, etc.). Using such fine particles, it is possible to develop novel devices with innovative design, structure, fabrication process, and function; e.g., the fabrication of an opal structure of hexagonally packed spherical particles has been attempted for a photonic crystal over the years. Many studies have reported that some nanoparticles, such as Au, have unique catalytic effects and surface plasmon resonance properties. For practical devices fabricated using fine particles, it is necessary that those particles are structured in the desired location, geometry, density, thickness, and arrangement on an arbitrary substrate. Except for the direct synthesis of particles, e.g., by chemical vapor deposition (CVD) on a substrate, micromanipulation using micro-tweezers and laser trapping (optical tweezers) is the most promising technique for structuring fine particles (Baur et al. 1998; Junno and Deppert 1995; Applegate et al. 2004). The micromanipulation techniques enable to realize high accurate assembling for single or aggregated particles. It, however, involves an array of micromanipulators automatically and independently controlled, which requires complicated and expensive systems, to enhance its manufacturing efficiency for microstructure of particles. Meanwhile, the self-assembly of particles, which belongs to the bottom-up technologies, is an important candidate for practical device fabrication using simplified equipment and processes. This chapter focuses on the self-assembly of spherical particles and describes its basics as well as the examples of fabricated structures and some applications.

24.2 Basics of Self-Assembly Using Suspension

This section describes the basics of particle self-assembly using a suspension. The particles are previously dispersed in a specific solvent to achieve self-assembly because the process requires the characteristics of a liquid (solvent), with the help

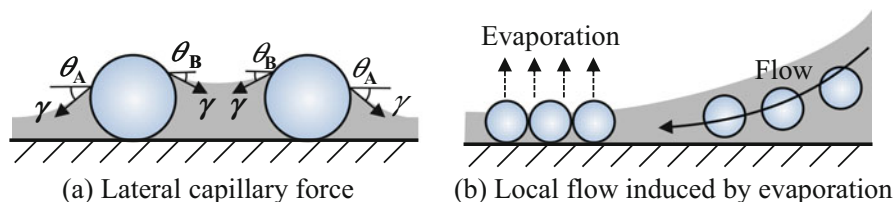


Fig. 1 Mechanism of the self-assembly of particles using a lateral capillary force (meniscus force) on a solid substrate. A lateral capillary force, induced by surface tension, makes neighboring particles aggregate to form an assembly. Local evaporation and flow generate a continuous self-assembly around the contact line of the suspension

of transportation, assembly, and location of particles, while avoiding the undesired aggregation of particles as a dry powder. Self-assembly utilizes an important and interesting mechanism, which involves evaporating a suspension on a solid surface as follows: a method based on lateral capillary force is effective for structuralizing fine particles by self-assembly without manipulation. This section describes self-assembly techniques for structuralizing spherical micro-/nanoparticles on a solid substrate. This process is simplified but can be applied to various particle materials. Figure 1 depicts a schematic of the two-dimensional model of self-assembly using a lateral capillary force. Let us assume that a suspension of particles evaporates on a solid surface. Generally, the solvent mainly evaporates from the fringe of the wetting film, which is called triple contact line of liquid, solid, and vapor phases. When the thickness of the wetting solvent film reaches a value below the diameter of the spherical particles, a lateral capillary force, also called liquid bridge force or meniscus force, generates between the neighboring spherical particles as illustrated in Fig. 1a (Paunov et al. 1993). The lateral capillary force is induced by a difference in direction of surface tension acting on the particle. It is expressed by Eq. 1 (Kralchevski and Nagayama 1994), where θ_A and θ_B are local contact angles of the solvent on the particle surface and γ is surface tension of the solvent. The surface tension acts in a tangential direction to the liquid surface. When these contact angles, θ_A and θ_B , satisfy Eq. 2, the lateral capillary force acts as an attractive force between the neighboring particles in the thinning wetting solvent film. This attractive force makes neighboring particles autonomously aggregate, forming a two-dimensional structure, and is larger than some repulsive forces such as electrostatic, friction, and viscous forces (Nishikawa et al. 2003). This interaction induces the self-assembly of the particles at the fringe of the suspension around the triple contact line. Furthermore, the evaporating solvent induces a local flow of the suspension from inside to the triple contact line, as depicted in Fig. 1b. The local flow of the suspension involves the transportation of particles to the evaporating region so that it continuously supplies them to the self-assembling region. Repeating the process results in the continuous self-assembly of particles so that the spherical particles are naturally structured in a hexagonal package. Spherical particle is

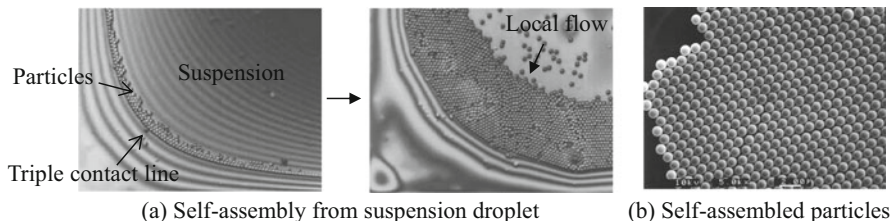


Fig. 2 Simple self-assembly of particles in a dropped suspension: **(a)** Snapshots of assembling particles in the thinner wetting film of a suspension around the triple contact line. The particles are aggregated in a two-dimensional layer by lateral capillary forces among them. Evaporation of the solvent induces a local flow, transporting particles to the self-assembling region around the triple contact line. This autonomous aggregation results in a closed-packed hexagonal arrangement **(b)**, i.e., in the self-assembly of particles

preferable for self-assembly because it produces stable and uniform arrangements, but the method can also be applied to other shapes of particles.

$$F = \gamma \cos \theta_A - \gamma \cos \theta_B \quad (1)$$

$$\theta_B > \theta_A > 0 \quad (2)$$

Simple self-assembly is easily achieved in a dropped suspension. Figure 2 shows snapshots of self-assembling spherical polystyrene particles with a diameter of 1 μm on a Si substrate (observed using a digital microscope). The polystyrene particles are previously dispersed (1 vol%) in water using a dispersant. Some interference stripes of black lines are observed around the triple contact line, and since these interference stripes are related to the thickness of the solvent wetting film, it is estimated to be in the order of hundreds of nanometers. A local flow of the suspension is also confirmed by transportation of the particles. The polystyrene particles are aggregated and structured along the triple contact line of the suspension, which mainly results in a two-dimensional hexagonal package (opal structure) of arranged particles, depicted in Fig. 2b. This type of opal structure is also called a two-dimensional colloidal crystal. The self-assembly is easily achieved on a hydrophilic surface to produce a thinner wetting film around the suspension fringe. However, in the case of a hydrophobic surface, the particles are likely to aggregate in a three-dimensional structure due to the higher contact angle of the suspension. This is because the thickness of the solvent wetting film is not smaller than the particle diameter around the fringe of the suspension. As mentioned in Eq. 1, it is noted that the surface tension of the solvent determines the lateral capillary force, which dominates particle aggregation. Water has the highest surface tension (72 mN/m) to generate a large capillary force in typical solvents, although lower surface tension of organic solvents, such as ethanol (22 mN/m) and toluene (28 mN/m), offer a better dispersibility for most particles as compared to water. In the case of self-assembly using a suspension of an organic solvent, it should make effort to decrease repulsive forces such as electrostatic and friction forces to cover low surface tension. It might be achieved by use of smaller particle or lower

adhesive surface of substrate. Although self-assembly using a suspension droplet is readily available, without requiring specific equipment, the geometry and layer number of structured particles cannot be desirably controlled. We should employ additional techniques and specified templates for self-assembly to obtain the desired geometry, as described in the following section. This is required for practical devices using self-assembled particles.

The Langmuir–Blodgett technique is a well-known method for fabricating monolayer thin films. This technique transfers fine objects to a substrate from an interface between liquid and vapor and can produce monolayered structures on that substrate, as amphiphatic molecules to be monolayer on the solvent surface. The technique can also be applied to fine particles so that a particle monolayer is fabricated on a substrate surface (Fulda and Tieke 1994). It should be noted that this technique requires the particle surface to be two-dimensionally aggregated at the interface of solvent and vapor.

Spin coating is a popular method of thin-film fabrication using a solution. This technique can also produce a thin film of self-assembled particles using a suspension (Mihi et al. 2006; Colson et al. 2011), although it is generally utilized for polymer solutions such as a photoresist. Most research facilities have an equipment for spin coating, while it has applicability to various materials of particles. In the case of spin coating, self-assembly does not generate around the triple contact line unlike the case of the dropped suspension shown in Fig. 2, as the suspension widely spreads in advance of self-assembly. Spin coating is also likely to vary the thickness (coverage) of particles between the center and the outside of substrate. Both of rotational speed and particle concentration might be appropriately adjusted to obtain uniformly assembled particles. It is reasonable that spin coating allows us to easily fabricate a thin film of particles.

The continuous convective method is yet another technique for producing thickness-controlled thin films of self-assembled particles (Dimitrov and Nagayama 1996). This procedure can keep a constant thickness of the suspension around the contact line, which results in a stable assembling of particles. The continuous convective method is implemented by applying dip coating or bar coating to the self-assembly, as illustrated in Fig. 3. These techniques provide a relatively linear motion of the suspension so that it readily coats the particles over the hydrophilic substrate. The relative velocity (drawing speed) determines the particle assembling rate as well as the evaporation rate. The coverage of self-assembled particles is a function of the drawing speed, as expressed by Eq. 3:

$$\varepsilon = \beta \frac{j\varphi}{hV(1 - \varphi)} \quad (3)$$

where j is the evaporation rate, φ is the particle concentration, h is the layer number of particles, V is the drawing speed, and β is a constant coefficient. The drawing speed must be appropriately adjusted in accordance with humidity, substrate hydrophobicity, and particle concentration to obtain a desired layer number and coverage of self-assembled particles. Figure 3c depicts an example of the dip coating system

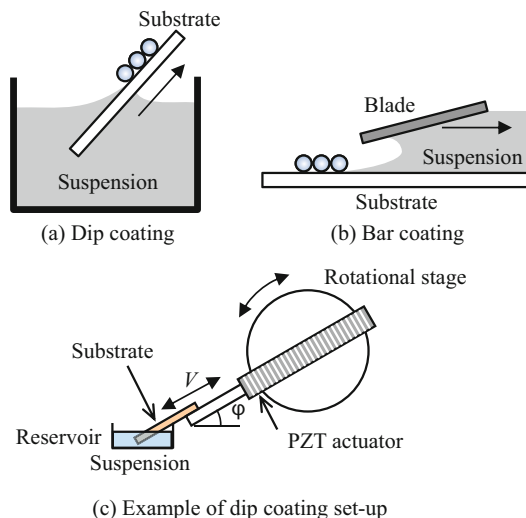


Fig. 3 The convective continuous method for achieving uniform self-assembly over a substrate. A triple contact line is constantly shifted to continuously expand the area of assembling particles. Conventional (a) dip coating or (b) bar coating easily achieves self-assembly based on the mechanism. (c) An accurate motion stage, such as a PZT actuator, is recommended for suspension concentrations below 1 vol% because the drawing speed of the substrate should be controlled in the order of $\mu\text{m/s}$ to obtain a higher coverage of monolayered particles

(Kanamori et al. 2008). As described in Eq. 3, the coverage of assembled particles is inversely proportional to drawing speed. The evaporation rate, which is strictly evaluated and controlled, is strongly related with environmental conditions (temperature and humidity). If a particle suspension with concentration below 1 vol% is utilized under normal environmental conditions (e.g., temperature 300 K and humidity 50%), a drawing speed of less than 0.1 mm/s is adequate for obtaining a higher coverage structure of self-assembled particles in our experiments. The setup requires a velocity-controllable precision motion stage, such as a piezo actuator, to achieve a motion speed in the order of $\mu\text{m/s}$. An environmentally controlled chamber is also recommended to control the evaporation rate of the solvent.

Figure 4 depicts typical examples of self-assembled polystyrene particles obtained by the continuous convective method. A monolayer of polystyrene particles is fabricated on a hydrophilic SiO_2 substrate at an appropriate drawing speed. The particles are arranged in a hexagonally packed opal structure, which is readily fabricated in the order of square centimeters (“wafer scale”) so that it can be utilized as a photonic crystal (Velikov et al. 2002). This kind of self-assembled particles is hardly formed on hydrophobic substrates with contact angle larger than 90° , because the surface tension acts to keep the particles in the suspension around its fringe just like a self-cleaning effect of surface. The receding contact angle of solvent decreases with drawing speed. Indeed a hydrophobic substrate apparently behaves like hydrophilic with the higher drawing speed, but too high drawing speed causes to decrease

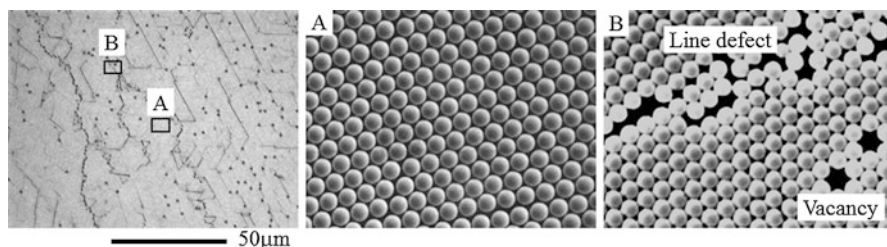


Fig. 4 Self-assembled particles obtained by the convective continuous method

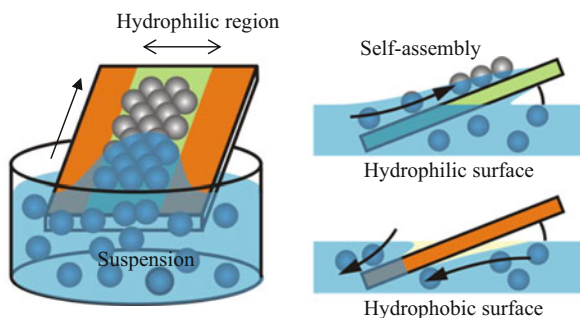
the coverage of particles. Therefore, hydrophilic substrates are preferable for self-assembly of particles. Some line defects and vacancies can be also observed in the arranged particles. These defects seem to be due to inhomogeneous wetting and evaporation, fluctuations in temperature and humidity, variations in particle diameter, surface roughness, and contamination. Especially, monodisperse particles are essentially required to fabricate accurate arrangements. Currently, SiO_2 and polystyrene (latex) are commercially available as monodisperse particles with diameters in the range of hundreds of nanometers to several micrometers. This process is known as thin-film coating and also requires a template to restrict the region of self-assembly for a designed particle microstructure.

24.3 Micro-/Nanopatterning Based on Self-Assembly

24.3.1 Top-Down Approaches for Spatially Controlled Self-Assembly

Dip-pen nanolithography is an effective top-down process, which can be combined with a bottom-up self-assembly method to obtain the desired particle structure (Demers and Mirkin 2001). This technique draws self-assembled particles using a microprobe (an AFM cantilever is typically used), of which the apex is constantly wet with a nanoparticle suspension. Furthermore, the microprobe is also able to scratch to locally remove a thin film such as self-assembled monolayer previously coated on a substrate, so that self-assembly can be achieved on the scratched region because of larger adhesion force for the suspension and/or the particles (Garno et al. 2003). Dip-pen nanolithography can produce highly spatially controlled particle structures using the accurate motion stage of a PZT control, although its productivity is considerably low as well as a micromanipulation technique. Thus, for large-area manufacturing, it is necessary to use a specified system with a multi-microprobe array. The ink-jet process is also a great technique for fabricating particle structures (Smith et al. 2006; Perelaer et al. 2008). Since this technique has been practically used as a wiring technology in printed electronics, it is more convenient for producing patterns of highly dense aggregated nanoparticles rather than accurately arranged structures. Also, this method should be utilized on a specified template, described in the following sections, to obtain two-dimensional patterns of arranged particles.

Fig. 5 Spatially designed self-assembly of particles by the convective continuous method on a hydrophilic-patterned substrate. The suspension of particles selectively spreads and evaporates on the hydrophilic regions. The self-assembly of particles is restricted only to the hydrophilic regions



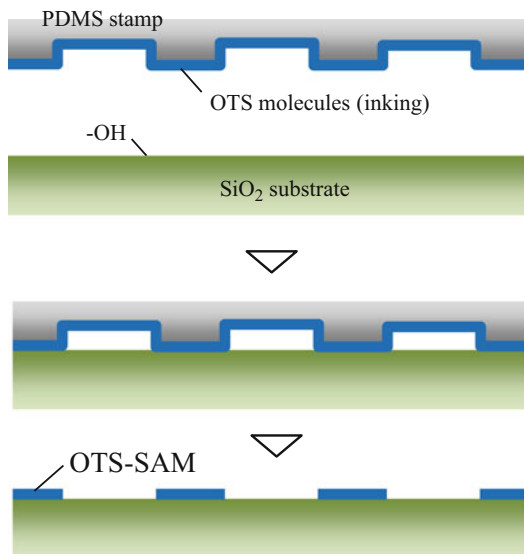
24.3.2 Templates for Self-Assembly

To obtain spatially designed particle microstructures, the self-assembly process is performed on a specified template to have a selective affinity to the particles and/or the suspension. The particles are selectively structured on the patterned region with enhanced adhesion using physical, chemical, or biochemical bonding. Magnetic particles are easily located on a pattern of magnetic material (Yellen and Friedman 2004). Au particles are specifically adsorbed on thiol series of molecules coated on a substrate because of chemical bonding (Masuda et al. 2000, 2002). As avidin–biotin interactions generate a great affinity in the biochemical bonding of proteins, avidin-coated substrates and biotin-coated particles allow a selective adsorption of particles (McNally et al. 2003). A pattern of DNA also works as a template for self-assembly through the use of electrostatic adsorption (Yonezawa et al. 2002). However, this type of selective adsorption inevitably restricts the applicable (surface) materials of the particles.

It is reasonable that a specific template for various particle materials can spatially control the wetting (spreading) of suspensions (Fustin et al. 2004). A combination of template types with the convective continuous method produces microstructures of self-assembled particles on desired positions. We can prepare two kinds of templates as follows: one is a pattern with locally controlled wettability, and the other is a pattern of surface geometry. The pattern with spatially designed wettability is produced by a micro-/nanoscale patterning of hydrophilic and/or hydrophobic material, which is also called “hydrophilic/hydrophobic pattern” (Kaneko et al. 2005). Figure 5 depicts a schematic of self-assembly on an array of hydrophilic material by the continuous convective method. A locally placed hydrophilic region leads to the selective spreading and evaporation of a water-based suspension, while the template of the substrate is drawn up from the suspension. This enables inducing the self-assembly of particles on only the hydrophilic regions. This template is applicable to various particle materials dispersed in water.

Some hydrophobic polymers, such as polytetrafluoroethylene (PTFE), are good candidates for constituent materials of the templates. They are easily coated by physical vapor deposition (PVD) and CVD and can be patterned by liftoff process or dry etching. Self-assembled monolayers (SAMs) are effective materials for fabricating hydrophobic or hydrophilic thin films when glass or silicon is utilized as templates for the substrate. Since silane series of molecules are chemically bonded

Fig. 6 Basic procedure for the micro-contact printing (μ CP) of an octadecyl-trichloro-silane self-assembled monolayer. The simplified process includes stamping a micro-ridged PDMS, inked with OTS molecules, to a Si and SiO_2 surface. The OTS molecules form a self-assembled monolayer by chemical bonding via hydroxy groups



by siloxane linkages to form SAMs onto glass and Si surfaces by wet or dry processes, many silane-based materials for SAMs are commercially available. Octadecyl-trichloro-silane (OTS) is a typical hydrophobic SAM material. Immersing a glass (SiO_2) or a Si substrate in a solvent (toluene, cyclohexane) solution of OTS coats the substrate surface with an OTS-SAM. The micro-/nanoscale patterning of this OTS-SAM is achieved by UV, laser, or electron-beam lithography, plasma processing, and micro-contact printing (μ CP) (Xia and Whitesides 1997); e.g., an OTS-SAM was completely dissolved by an electron beam with a dose of $3000 \mu\text{C}/\text{cm}^2$ in our study (Kaneko et al. 2005). However, these lithography-based processes do not only take several hours per cm^2 to fabricate a pattern, or also require considerably expensive equipment and specific masks. Meanwhile, μ CP enables the direct drawing of a pattern of OTS-SAMs using a simplified system and with high throughput.

Figure 6 depicts a schematic of the μ CP of an OTS-SAM. A micro-ridged polydimethylsilane (PDMS) stamp is prepared by casting a prepolymer to a master mold. A photoresist structure or an etched Si wafer is utilized as master molds. The PDMS stamp with micro-ridge is inked with OTS molecules. A Si or glass substrate should be previously treated to have enough hydroxy groups by chemical oxidation, UV irradiation, plasma irradiation, or ozonation. Contacting the PDMS stamp transfers the OTS molecules to be formed in a designed two-dimensional pattern according to the stamp geometry on the SiO_2 and Si surface. μ CP should be processed in an environmentally controlled chamber (globe box) with a humidity below 10% because most silane series of molecules are likely to react with water to be undesirably polymerized. Figure 7 illustrates an example of an OTS-patterned SiO_2 surface. An OTS-SAM with a thickness of about 1.4 nm is formed in a line-and-space pattern (Fig. 7a). The surface of the OTS-SAM and the exposed SiO_2 have contact angles of

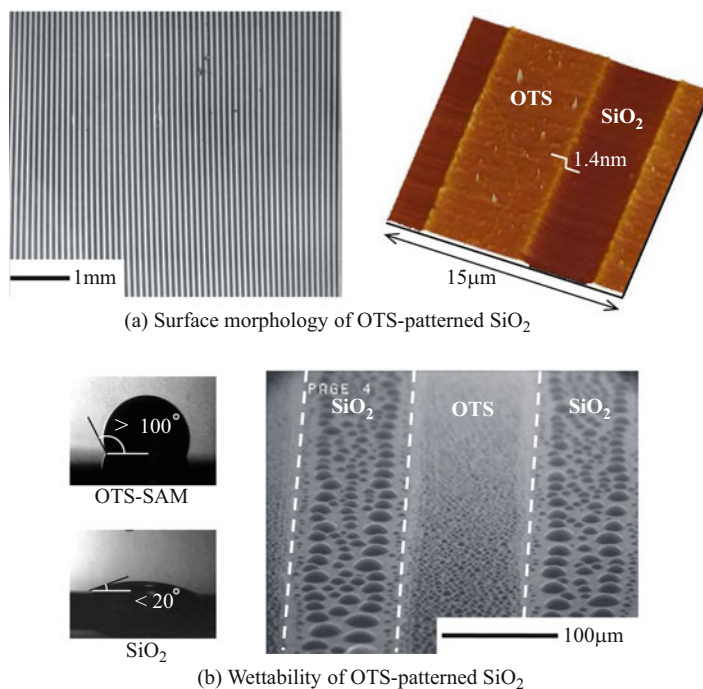


Fig. 7 Example of an OTS-patterned SiO_2 surface fabricated by μCP as a template of spatially controlled wettability. An OTS-SAM is accurately formed in a line-and-space pattern according to the design of the PDMS stamp. The surface has a specific hydrophobicity and hydrophilicity design

more than 100° and less than 10° , respectively (Fig. 7b). The spatial difference in wettability is also confirmed in the range of micrometers by an environmentally controlled scanning electron microscope, depicted in the right image of Fig. 7b. The shape of the microdroplets generated by the condensation of water vapor differs between the area of the OTS-SAM and the SiO_2 . As described above, the spatially controlled wettability can be designed to make a hydrophobic/hydrophilic pattern in the order of tens of micrometers by μCP . The hydrophobicity of the OTS-SAM can be kept for more than 1000 h under atmospheric conditions. Several types of monomer molecules for other SAMs are commercially available. Thiol series of SAMs, which are often utilized for similar purposes as the silane series, can be formed on Au surfaces.

24.3.3 Self-Assembly on Hydrophilic/Hydrophobic Patterns

This section describes examples of line-and-space structures of self-assembled particles on templates of patterned substrates. An OTS-patterned substrate, which is described above, was drawn up from a suspension of polystyrene spherical

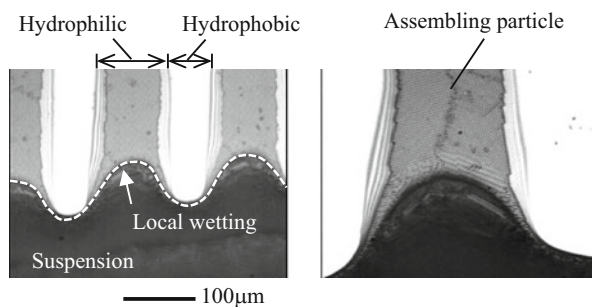


Fig. 8 In situ observation of the self-assembly of particles on a template of line-and-space pattern of the hydrophilic and hydrophobic regions, where the OTS-SAM is locally coated on the SiO_2 surface. The suspension is spatially selectively spread to induce self-assemblies of particles on the hydrophilic SiO_2 lines, while it is repelled on the OTS-SAM region

particles with a diameter of $1 \mu\text{m}$. Figure 8 illustrates a snapshot of the self-assembly processed by the setup shown in Fig. 3 (Kanamori et al. 2008). The suspension was locally spread in the hydrophilic region, where the dashed white line indicates the contact line of the suspension to produce the self-assembled particles. Polystyrene particles were locally formed in a monolayer thin film on the hydrophilic patterns. This self-assembly moved synchronously by drawing the substrate. The assembled width of the particles was slightly narrower than the hydrophilic width. Particles did not assemble and remain in the hydrophobic region. These characteristics were maintained throughout the dip coating.

Figure 9 depicts that applying self-assembly to a specified template easily produces microstructures of fine particles. The substrate was processed by the above-described self-assembly process. A line-and-space pattern of self-assembled particles was fabricated on the whole area of the substrate ($10 \times 10 \text{ mm}$). The particles had a regular hexagonally packed arrangement in the hydrophilic pattern, as is the case of a hydrophilic substrate without OTS-SAM patterns, depicted in Fig. 4. Although some variations and fluctuations in the thickness and lateral profile of the assembled particles can be attributed to an imperfectly controlled wettability for the suspension, they can be improved by a more careful fabrication of the templates to achieve a uniform wettability.

As described above, the drawing speed is a dominant factor in self-assembly processes based on convective continuous methods (Kaneko et al. 2005). The line width of self-assembled particles, i.e., the coverage to the hydrophilic area, can be changed by varying the drawing speed of the substrate. Figure 9c depicts an example of a narrower width of self-assembled particles processed at a drawing speed of $400 \mu\text{m/s}$ on the same substrate as that of Fig. 9a, which was drawn up at $0.7 \mu\text{m/s}$. The line width of the self-assembled particles varies as a function of the drawing speed, as illustrated in Fig. 9d. It linearly decreases at drawing speeds higher than $5 \mu\text{m/s}$ and remains almost constant at drawing speeds below this value. The critical drawing speed is given by the concentration of particles and the hydrophilic width of

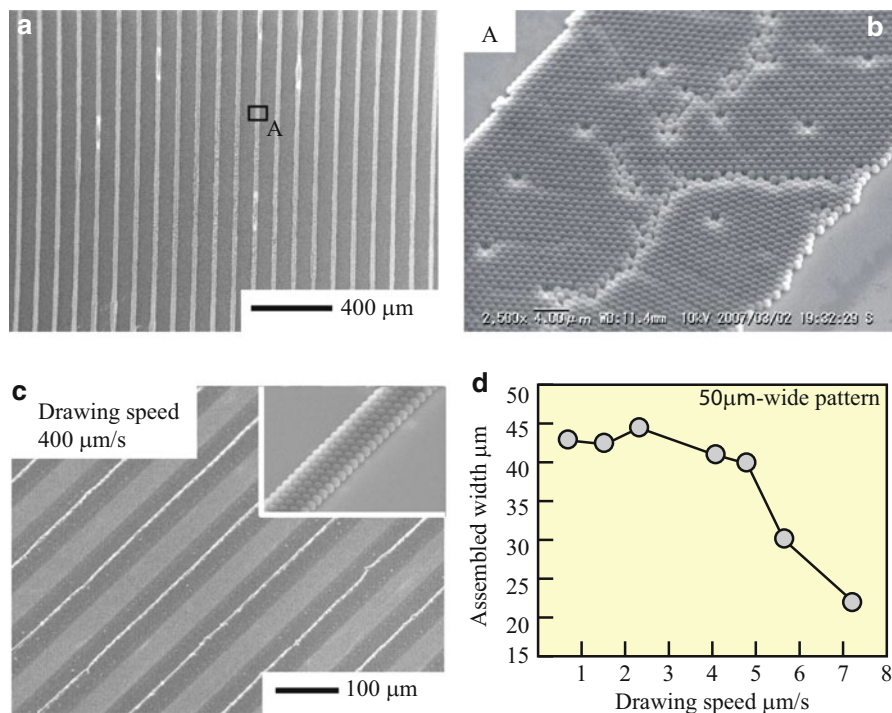


Fig. 9 Examples of self-assembled particles on a template on which the line patterns of a hydrophobic OTS-SAM are located on the hydrophilic SiO_2 surface. The particles are spatially selectively structured on the hydrophilic regions. The line width of the self-assembled particles linearly decreases with increasing drawing speed of the substrate

the template. Microstructures of assembled particles also contain line defects, vacancies, and fluctuations, which are attributed to variations in suspension spreading, assembly direction, and particle size as well as to contamination. To avoid line defects and domain formation, an effective approach is to prepare a template with geometries such as grooves and holes. Side walls function as seed crystals to align the orientations of assembling particles.

To assemble particles with a diameter smaller than 100 nm, one must consider factors such as surfactant concentration, variation in particle size, and Brownian movement. These factors affect the distance between particles, causing disorders in the particle arrangement. As shown in Fig. 10a, b, disorders and gaps are markedly formed during the self-assembly of 100 nm particles as compared to the assembly of 400 nm and 1 μm particles. Especially, higher concentration of surfactant makes vacant defects, although membranous coating of surfactant is also utilized to form particles not in completely closed-pack but in slightly separated arrangement. Self-assembly based on the convective continuous method was applied not only to a template consisting of straight line patterns but also to one containing curved lines and isolated islands, as depicted in Fig. 10c, d. In the case of such templates with

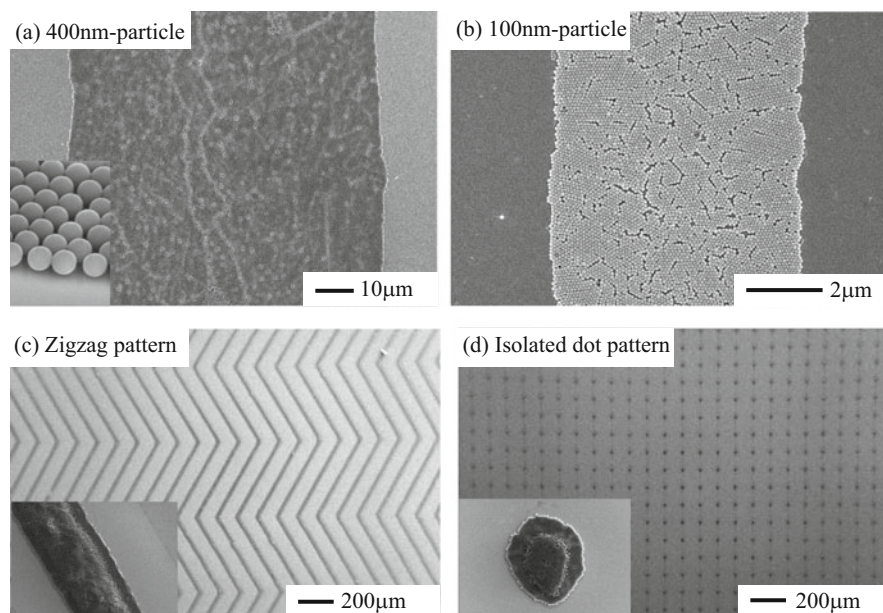
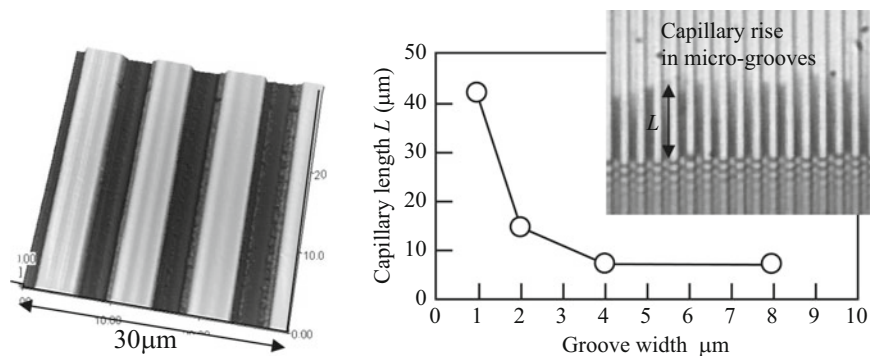


Fig. 10 Examples of the self-assembly of nanoparticles and applications to various patterns. The self-assembly of finer particles (diameter <100 nm) (or on complex geometrical patterns) requires some considerations regarding surface tension and the surfactant concentration of the suspension, variations in particles size, and Brownian movement

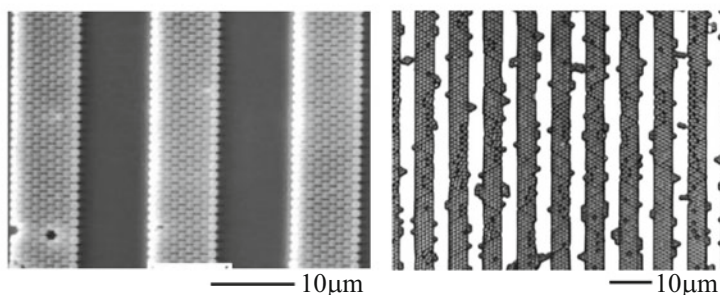
complex geometrical patterns, the higher surface tension of the suspension makes it more difficult to fit its spreading profile in the hydrophilic pattern and control the layer number of assembled particles (Kanamori et al. 2008). Therefore, a suspension containing an organic solvent with a low surface tension is preferable to achieve a high shape accuracy of the self-assembled particles.

24.3.4 Self-Assembly on Micro-geometry Templates

Surface micro-/nano-geometries also work as a template. For example, micro-holes of a photoresist pattern can be accurately filled with spherical particles (Yin et al. 2001). Some templates of surface geometries fill concave structures with particles by simple casting of suspension unlike the case of continuous convective method (dip coating) (Ye et al. 2001; Li et al. 2005). Figure 11a shows a microgrooved Si surface as a template for self-assembly, fabricated by reactive ion etching. The microgrooves induce a capillary rise, provoking a local spreading of the suspension, as the Si surface has a uniform wettability after chemical treatment. The length of the capillary rise is inversely proportional to the groove depth so that it functions like the hydrophilicity shown in Fig. 8. The capillary rise also allows the solvent in the suspension to locally evaporate and results in self-assembly based on the convective



(a) Micro-grooved template and local capillary rise of water in the micro-grooves.



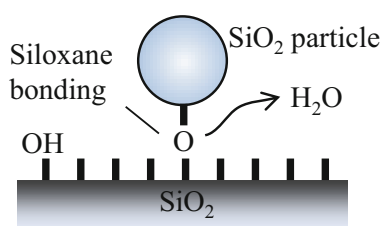
(b) Self-assembled particles in micro-grooves

Fig. 11 Examples of microgrooved templates for self-assembly. Microgrooves with a depth of 120 nm induce a local capillary rise of suspension. These particles are arranged with few line defects because of geometrical restriction of the side walls

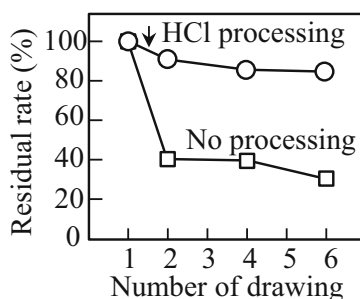
continuous method in the microgrooves (Kaneko et al. 2006). Figure 11b shows an example of self-assembled particles (1 μm diameter) in microgrooves. In the case of 1 μm depth template, these particles exhibit fewer disorders and line defects (domains) in their arrangement compared to the particles obtained using a hydrophilic pattern because the side walls of the microgrooves function as a geometric restriction that aligns the assembling directions shown in the left image of Fig. 11b. Particles can be assembled on shallower microgrooves, as illustrated in the right image of Fig. 11b where the groove depth is 120 nm. However, these shallower template grooves also make the particles locate at undesired regions on the micro-ridges. Coating hydrophobic material on top of the micro-ridges is a reasonable approach to improve the spatial selectivity in the self-assembly of particles. These geometrical templates also have another feature regarding the productivity because they can be easily replicated from a master fabricated by lithography techniques or dry etching. This technique can also be applied to a film, as well as to a Si or a glass substrate, so that it possesses an adaptability to a roll-to-roll process with high manufacturing efficiency.

24.3.5 Complex Structures of Different Particles, Obtained by Multiple Drawing

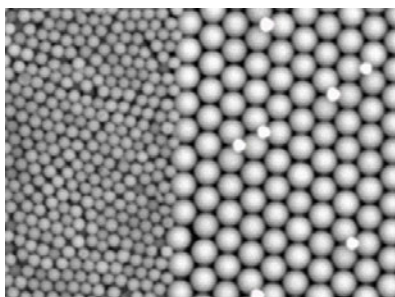
Further complex structures, composed of several kinds of particles, which are effective for various applications in bio-/microdevices, can be also fabricated by self-assembly with multiple drawing through the convective continuous method. Figure 12 shows examples of complex structures of particles obtained by multiple drawing and the related technique. Multiple drawing requires the fixation (bonding) of particles firstly assembled on a template. It has been reported that SiO_2 particles can be simply fixed by a chemical reaction in acid, as depicted in Fig. 12a (Masuda et al. 2000, 2002). The chemical reaction is to make a dehydration condensation of two hydroxy groups, which exist on the surface of the SiO_2 particles and the glass substrate. Upon immersing the substrate in an acid, such as HCl or H_2SO_4 , the dehydration condensation of both hydroxy groups creates a siloxane bonding



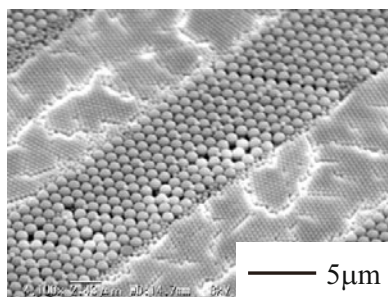
(a) Siloxane bonding of particle induced by acid



(b) Residual rate of particles



(c) Alternate arrangement using repetitive self-assembly and acid bonding



(d) Alternate arrangement using repetitive self-assembly and thermal bonding

Fig. 12 Chemical bonding of SiO_2 particles on a glass substrate and alternate structures of different particles obtained by repetitive self-assembly through the convective continuous method. The groove depth is 120 nm. An acid solution (HCl or H_2SO_4) causes dehydration condensation at the hydroxy groups, thus inducing siloxane bonding between the particles and the substrate. A second drawing process makes particles that are structured between the lines of the firstly self-assembled particles

between the particles and the substrate. Figure 12b depicts the residual rate of SiO₂ particles, which were assembled and chemically bonded to a substrate by hydrochloric acid processing, plotted against the frequency of drawing from water. The SiO₂ particles maintained their initial geometry, with little detachment after hydrochloric acid processing for 15 min (Nishio et al. 2009). Figure 12c shows an example of alternate arrangements of two types of particles by repetitive drawings (self-assembly) and particle bonding with hydrochloric acid. A microgroove template and a hydrophobic pattern were utilized for the first self-assembly drawing. A Si substrate was etched to form an array of microgrooves, and then the top surfaces of the micro-ridges were coated with a hydrophobic OTS-SAM by μ CP. The first drawing (convective continuous method) filled the microgrooves with 1 μ m SiO₂ particles. The second drawing process (using another suspension of particles) took place after the chemical bonding of the firstly structured particles, followed by a surface modification, which was carried out to make the micro-ridges of the template substrate hydrophilic by plasma treatment. In the second drawing, the particles were assembled in the “microgrooves” between the firstly self-assembled particles. This process allows different functions of particles to be located on the same substrate. In the case of polymer particles, the assembled particles can be thermally bonded to the substrate, instead of by chemical reactions, because of their low glass transition and melting points. Figure 12d illustrates another alternate structure composed of different sizes of polystyrene particles. Smaller particles (with a diameter of 400 nm) were filled with larger particles (with 1 μ m diameter), which were firstly self-assembled and subsequently thermally bonded. Some other approaches have been proposed and demonstrate to bind a particle to another particle and/or a substrate, as specific adhesives such as ultraviolet curable resin are previously dispersed in suspension. It is noted that an appropriate technique is employed to fit for the purpose of structure and application.

24.4 Applications of Self-Assembled Particles

24.4.1 Transferring of Particles

A microstructure of self-assembled particles can be transferred from a template substrate to another plate by a transfer printing technique. Figure 13 shows an example of a contact printing process for a microstructure of particles (Takeda et al. 2016). The particles are previously structured on a transparent substrate with any template. Meanwhile, a photopolymer, typically a UV-curable resin, which is frequently utilized in photo-nanoimprint, is coated on another plate. The thickness of the photopolymer is adjusted to be less than the diameter of the particles. The transparent substrate is pressed to the photopolymer-coated plate to embed the lower half of the particles. The photopolymer is cured by UV irradiation from the back side of the substrate. Softly releasing the substrate transfers the microstructure of particles to the photopolymer-coated plate. In the case of transparent spherical particle, this type of microstructures can be utilized as a micro-lens array. As this process does not require any adhesives in

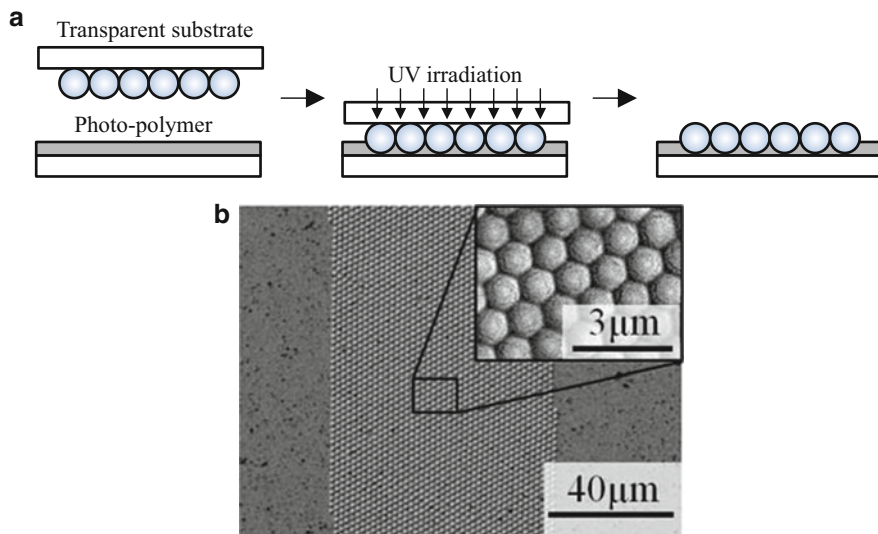


Fig. 13 (a) Schematic of the fabrication flow of infilled particles. A transparent substrate with previously self-assembled particles is contacted and pressed on a spin-cast photopolymer thin film. The photopolymer is subsequently cured by UV irradiation. The self-assembled particles are transferred to the photopolymer. (b) Example of a transferred microstructure of particles

the particle suspension, the particles can be transferred and fixed without an undesired coating of adhesive material. These types of transferring particles enable microstructures of particles to be applied in various substrates and films as well as for template substrates to be recycled.

24.4.2 Surface Modification of Particles with Functional Thin Film

Functionalization based on surface modification is effective for the fabrication of microdevices using particles, as reported in previous studies. A wet process is preferable for surface modification of particle, although vapor deposition can coat dry particle with metal and polymer thin film as well as that of a substrate (Behrend et al. 2005). Self-assembled monolayer coating and physical adsorption are important candidates for surface modification, which is used to functionalize particles. Typical examples of this process are described in this section. SAMs, including alkanethiol or silane coupling, can improve the wettability, tribological properties, and chemical stability of solid surfaces. Certain SAMs have important potential industrial applications. Silica particles can be covered into silane series of SAMs, such as octadecyl-trichloro-silane (OTS) or 3-aminopropyltriethoxysilane (APTES) (Arslan et al. 2006). These coatings provide organic groups to particles made of inorganic material, thus enhancing their affinity to organic materials including

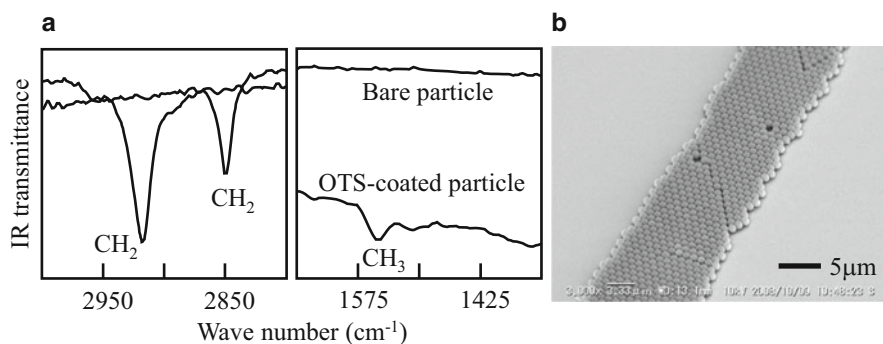


Fig. 14 Example of self-assembled OTS-coated particles. The peaks of CH₂ and CH₃ derived from the OTS molecule are clearly found in the IR transmittance of particles. The particles can be also assembled on the hydrophilic pattern

biomaterials; e.g., APTES forms a hydrophilic SAM on a silica surface because it consists of an amino group and ethyl group. It is estimated that APTES-coated particles are slightly hydrophobic as compared to bare silica particles because the water contact angle is about 50° on the flat surface of the APTES-SAM. Besides, OTS-SAMs are hydrophobic.

A dry powder of silica particles was dipped into a toluene solution of OTS or APTES to grow each SAM. Then, it was naturally dried on silicon wafers, after rinsing in another toluene solution, and finally dispersed in pure water containing a small amount of surfactant to form the suspension. Figure 14a depicts the IR transmittance of silica particles after the OTS-SAM process. Specific peaks induced by CH₃ and CH₂ indicate the successful coating of OTS. Similar specific peaks were also observed in another sample coated with APTES-SAM. There is also a major difference in the water contact angles between an agglutinate of coated particles and bare particles. A hydrophilic-/hydrophobic-patterned substrate was drawn up from the suspensions of the OTS-coated particles at 80 μm/s. Figure 14b illustrates an SEM image of the patterned substrates after the process. These OTS-coated particles were also assembled only on the hydrophilic region as well as that of bare silica particles. This result demonstrates that the water meniscus force (lateral capillary force) also induces the aggregation of hydrophobic particles. Contrary to the case of bare particles, the line width of OTS-coated particles increases with the drawing speed (the line width at 80 μm/s is larger than that at 4 μm/s).

24.4.3 Surface Modification of Particles with Proteins

Biomaterial coating and microstructuring of particles are important techniques for biochemical applications, such as protein chips. For example, they have great interests in biosensing application using surface plasmon resonance

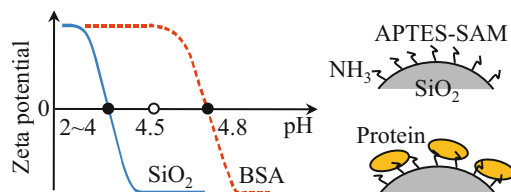


Fig. 15 Mechanisms of protein coating to particle based on electrostatic adsorption. The pH-controlled solution generates attractive electrostatic force by the difference in isoelectric point between BSA and SiO_2 , so that the surface of SiO_2 particles is gradually coated with BSA. When the SiO_2 particles are previously coated with APTES-SAM, the adsorbed BSA can be tightly bonded to the amino groups of APTES

(Tsukagoshi et al. 2007; Dahint et al. 2007). An expected effect is to increase specific surface area to be a field for chemical reaction in biosensing, especially a biosensing with antigen–antibody reaction detection of labeled elements to be bonded to a surface of reaction field. The antigen (or antibody) differs from one element to be detected to another. Therefore, a key technology is how to make a structured surface with larger specific area and to coat specific protein (antigen, antibody, etc.) on the structured surface. Self-assembly of protein-coated particles is an important candidate technique for the above-described purpose. Protein coating is achieved by physical and chemical adsorption in some wet processes. Figure 15 depicts a schematic of the electrostatic adsorption mechanism for bovine serum albumin (BSA) to silica particles. BSA is a typical protein that is generally used as a standard protein in the biochemical analysis using the antigen–antibody reaction. BSA molecules and silica particles are, respectively, positively and negatively charged in a solution of pH 4.5, as the APTES-coated particles are mixed with the solution of BSA. Due to the difference in surface potential, the BSA molecules adsorb onto the surface of the silica particles by electrostatic forces. If the particles are previously coated with APTES-SAMs containing amino groups, as explained in the previous section (Fig. 14), most protein molecules (including BSA) can bind to the particles more strongly because of biochemical connections to the amino groups. These protein-coated particles are filtered and re-dispersed in deionized water for subsequent self-assembly (Alkan et al. 2005; Duran et al. 2007; Bouafsoun et al. 2007; Paul 1984). Electrostatic adsorption can be also applied to coating of nanoparticles onto microparticles (Gu et al. 2004).

The authors demonstrated both the BSA (protein) coating of SiO_2 particles and their self-assembly on the hydrophilic/hydrophobic pattern. Figure 16 depicts SEM and fluorescence images of a patterned substrate after the self-assembly process (Kaneko et al. 2009). The hydrophilic-/hydrophobic-patterned substrate was drawn up from a suspension of BSA-adsorbed particles at a speed of $4 \mu\text{m/s}$. The geometry of the assembled particles is similar to that of the bare silica particles. The seven bright regions in the fluorescence image demonstrate that BSA molecules were successfully supported on the particles throughout the process. It is reasonable that the particles could play the role of a protein carrier, so they could be used in

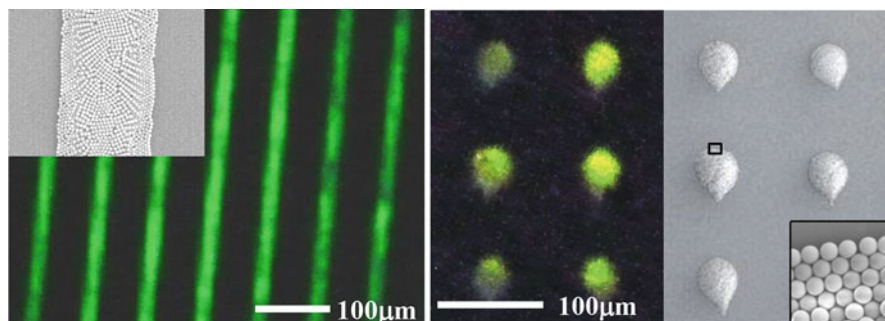


Fig. 16 SEM and fluorescence microscopy image of the self-assembly of protein-coated particles. The particles can be selectively structured on the hydrophilic pattern. The BSA molecules (proteins) can be tightly supported to the surface of particles after the self-assembly process

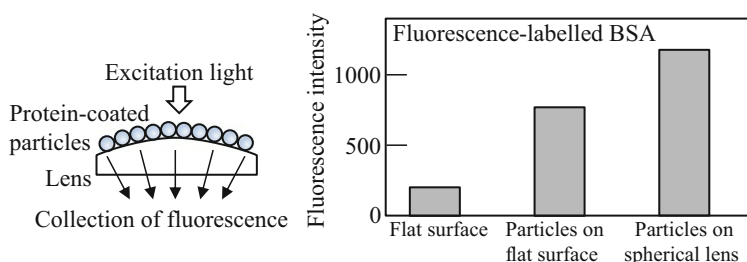


Fig. 17 Improvements of fluorescence collection by self-assembled particles. Self-assembled particles increase specific surface area to be a field for antigen–antibody reaction. The intensity of fluorescence corresponds to the sensitivity in the chemical reaction. The highest intensity of fluorescence is obtained with a spherical lens covered with self-assembled particles

micro-/bio-devices, such as protein chips. As described above, the surface asperities of self-assembled particles have a beneficial effect on biochemical sensing based on antigen–antibody reactions owing to an increase in specific surface area. Especially, a lens covered with particles supporting antigen (or antibody) is much effective in collection of fluorescence. Figure 17 shows an example of enhanced fluorescence intensity with self-assembled particles and spherical lens (Nshio et al. 2012). The intensity of fluorescence corresponds to the sensitivity in the chemical reaction, so that the technique can improve the sensitivity in biosensing as well as the productivity of device.

24.4.4 Optical Applications of Self-Assembled Particles

Nanostructured substrate surfaces are suitable for applications involving optically functional surfaces, such as antireflective layers for flat or flexible displays, although

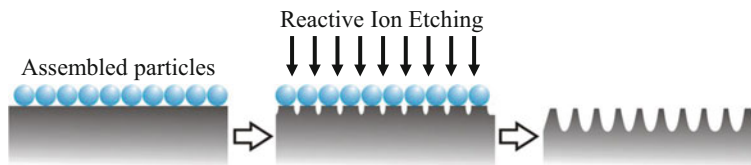


Fig. 18 Colloidal lithography for fabricating a micro-/nanotextured surface. A substrate is locally etched via the interfaces among self-assembled particles

a layered structure of self-assembled particles can also enhance the surface optical properties. Antireflective surfaces can be achieved using nanostructures with a spatial frequency comparable to the optical wavelength. This nanostructured surface is fabricated on a glass substrate by dry etching with a specific mask of resist, oxide, or nitride film generally prepared by lithography and deposition. It essentially involves high cost and complicated processes. Self-assembled particles can work as a mask for dry etching (Han et al. 2005; Cheung et al. 2006), so that they are used as a replacement for conventional mask materials. Figure 18 depicts a schematic of this process, which is also called colloidal lithography or nanosphere lithography. A substrate is locally etched via micro-/nanoscale interspaces between close-packed particles. It should be noted that this process easily produces a micro-/nanotextured surface without requiring expensive equipment or a photomask (unlike conventional electron-beam lithography and photolithography methods). They are also sputtered and etched to become reduced in size by ions and radicals, although SiO_2 or polystyrene particles have certain etching resistance characteristics. The reduction in size affects the geometry of nanotextured surface. Etching conditions should be adjusted with consideration in etching rate of particle as well as that of conventional materials of mask.

This section explains an application of the above-described etching technique to make a low-reflection surface. Figure 19 illustrates an example of a nanotextured Si surface fabricated by self-assembled SiO_2 particles (300 nm) and reactive ion etching (RIE) (Kobayashi et al. 2008). To have a higher coverage of particles, a Si wafer was repetitively drawn from a suspension containing a small amount of binder. Figure 19a depicts a Si surface etched by SF_6 using parallel-plate-type RIE. The surface was also ultrasonically cleaned in toluene to completely remove the particles from the mask. The etched Si surface was covered with an array of nano-pillars with a conical shape. The height of the nano-pillar was approximately 500 nm with an interval of 300 nm. The optical properties of the etched Si surface were greatly different from those of the original Si wafer, as depicted in Fig. 19b. The etched Si substrate with nano-pillars appears black to indicate its low reflectivity, while the original Si wafer is mirror-finished with high reflectivity. Figure 19c depicts the typical reflectance of the etched Si wafer with nano-pillars, where it has a reflectance lower than 3% for wavelengths in the range 400–700 nm. It is reasonable that the nanostructure can be also replicated on a polymer surface using the Si wafer as a master mold. As described above, the three-dimensional profile of the nanostructures

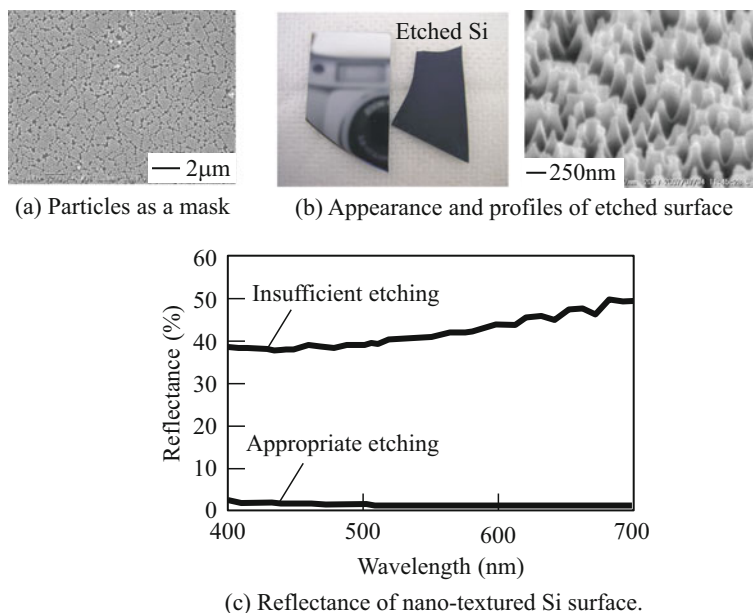


Fig. 19 Examples of nanostructured surfaces prepared by reactive ion etching with self-assembled SiO_2 particles as a mask. A Si wafer is etched via the interfaces among the particles. The etched Si surface has an array of nano-pillars with a specific arrangement according to the hexagonal package of particles. The nanostructure decreases the optical reflectance of the Si surface

is determined by the particle diameter, particle material, and etching conditions (electric power, pressure, etching time, etc.). The etching conditions should be appropriately adjusted to obtain the desired nanostructure profile. Nevertheless, colloidal lithography and etching are suitable techniques for producing functional nanostructured surfaces with specific wettability and particular optical, tribological, adhesive, chemical, and biological properties.

24.4.5 Self-Patterning of Cultured Cells on Particles

The surface asperities of self-assembled particles can be applied to a scaffold to achieve specified cell adhesion and growth. It has been reported that nanostructured scaffold surfaces can produce an *in vivo*-like environment for cultured cells (Leclerc et al. 2003). Both the adhesion and growth of cells are affected by the surface geometry as well as by biochemical properties. A specified nanostructure pattern induces the cultured cells to adhere spatially selectively and also to migrate and grow in controlled directions (Ranella et al. 2010; Ahn et al. 2013). The surface asperities of self-assembled particles function as specified scaffolds instead of nanostructures fabricated by highly expensive and complicated semiconductor processes. Figure 20 depicts the

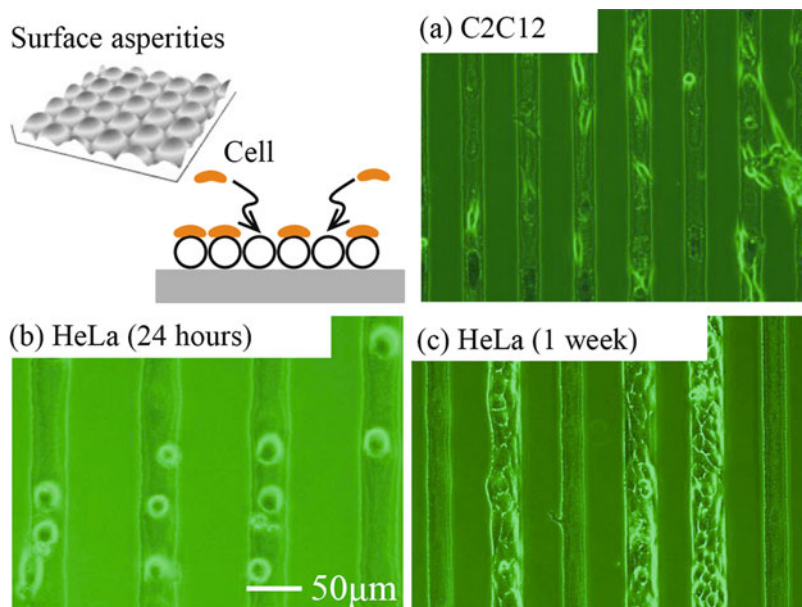


Fig. 20 Self-patterning of cultured cells on self-assembled particles. The adhered cells are autonomously located on the line structure of self-assembled particles (a and b). The cells also spatially selectively grow in the line structure (c). The surface asperities of the particles enhance the cell adhesiveness to selectively locate cells on the line structures

examples of cell adhesion and growth on line-space-line patterns of particles (Kaneko and Takeda 2016; Takeda et al. 2015), which were previously fabricated on a glass substrate by the procedure described in Sect. 3. In these experiments, HeLa cells (human cervix cells) or C2C12 cells (mouse myoblast cells) were cultured on a glass substrate containing the self-assembled particles, after being irradiated by ultraviolet radiation for sterilization and decomposition (removal) of the OTS-SAM. The cultured cells were preferentially located on the line structures of the particles, resulting in the autonomous patterning of cells. Figure 20c shows a microscope image obtained 1 week after cell seeding. Since the HeLa cells were densely grown to be confluent on the line microstructures of the particles, these line structures exhibited a spatially limited growth of cells. The surface asperities of the particle arrangement enhanced the adhesiveness of the cells as compared to the bare glass surface.

The cells do not directly adhere to the particle microstructures. They reach the structure by extension and migration. Figure 21a depicts snapshots of adhered HeLa cells on the substrate. A cell got expanded to the neighboring line structure of assembled particles, and it finally migrated from the glass region to the line structure. There is no difference in material to change cell adhesiveness between the particles and the substrate. Therefore, the cells preferentially adhere to the surface asperities (morphologies) of the arranged particles rather than to the flat surface. This aligning process of PC12 cells is similar to the case of neurite

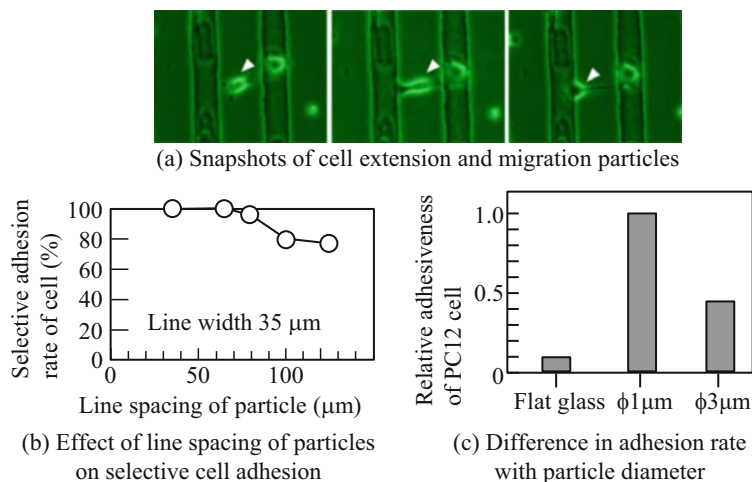


Fig. 21 Adhesion of PC12 cells on self-assembled fibronectin-coated particles. (a) The adhered cell extends and migrates to reach the neighboring structure of particles and then keeps the location stably. (b) Selective adhesions of cells are achieved with line spacing below specific distance. (c) Cell adhesiveness is affected by surface asperities determined by particle diameter

extension of microgrooved surfaces (Hirono et al. 1988; Torimitsu and Kawana 1990). Both the particle diameter and the line spacing of assembled particles strongly affect cell adhesion, as shown in Fig. 21b, c, because they determine geometrical features related to the surface asperity. In the case of PC12 cells, complete cell patterning on assembled particles is achieved on line spacings below 70 μm (Kaneko et al. 2012). Although the self-patterning of cells requires an appropriate particle-surface-geometry matching for each cell, the design of microstructured particles can be easily changed by adjusting the particle diameter and the template pattern. This is an advantage compared to other structures fabricated by conventional machining and etching.

Microstructures of protein-coated particles have a specific function in cell adhesion by the synergetic effect of surface asperities and biochemical properties (Sugihara and Kaneko 2013). Although SiO₂ surfaces generally have a poor cell adhesiveness, this can be improved by coating them with a cell-adhesive protein, such as fibronectin. Self-assembly of fibronectin/APTES-coated SiO₂ particles was achieved by the process described in Sect. 3 and Figs. 15 and 16. Figure 22 depicts typical results of PC12 cell adhesion on a linear structure of fibronectin-coated particles. In addition to the self-patterning of cells, these adhered cells were isolated from each other without any aggregation, unlike the case of bare SiO₂ particles. Little aggregation suggests that cell adhesiveness can be greatly improved by fibronectin coating to achieve a highly arranged cell patterning. These PC12 cells can differentiate into neuron-like cells on the linear particle structures upon adding nerve growth factor (NGF) to the culture medium. The differentiated cells extend their neurites to grow in a longitudinal direction of the

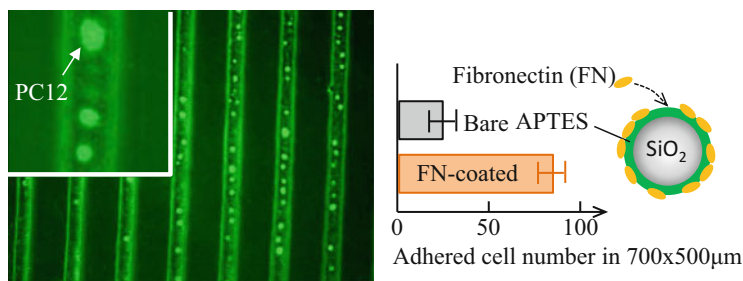


Fig. 22 Adhesion of PC12 cells on self-assembled fibronectin-coated particles. The cells are highly aligned on the center of line structure of fibronectin-coated particles as compared to that of bare particles. The number of adhered cells on fibronectin-coated particles is also much larger than that of bare particles. Surface modification of proteins is effective in application of self-assembled particles to a bio-microdevice using cultured cells

line structure of particles (Takeda et al. 2012). The surface geometry of self-assembled particles has an ability to induce directional guidance of neurites just like microgrooves do (Xuefeng et al. 2008; Tsuruma et al. 2006).

24.5 Summary

Self-assembly techniques can be successfully applied to obtain micro-/nanostructured surfaces (instead of the conventional top-down processes such as precision machining, laser machining, and semiconductor processes). Thus, these methods could have promising applications in novel microdevice fabrication.

References

- Ahn J, Son SJ, Min J (2013) The control of cell adhesion on a PMMA polymer surface consisting of nanopillar arrays. *J Biotechnol* 164:543–548
- Alkan M, Tekin G, Namli H (2005) FTIR and zeta potential measurements of sepiolite treated with some organosilanes. *Microporous Mesoporous Mater* 84:75–83
- Applegate R, Squier J, Vestad T (2004) Optical trapping, manipulation, and sorting of cells and colloids in microfluidic systems with diode laser bars. *Opt Express* 12(19):4390–4398
- Arslan G, Özmen M, Gündüz B, Zhang X, Ersöz M (2006) Surface modification of glass beads with an aminosilane monolayer. *Turk J Chem* 30:203–210
- Baur C, Bugacov A, Koel B (1998) Nanoparticle manipulation by mechanical pushing: underlying phenomena and real-time monitoring. *Nanotechnology* 9:360–364
- Behrend CJ, Anker JN, McNaughton BH, Kopelman R (2005) Microrheology with modulated optical nanoprobe (MOONs). *J Magn Magn Mater* 293:663–670
- Bouafsoun A, Helali S, Mebarek S, Zeiller C, Prigent AF, Othmane A, Kerkeni A, Jaffrézic-Renault N, Ponsoinet L (2007) Electrical probing of endothelial cell behavior on a fibronectin/polystyrene/thiol/gold electrode by Faradaic electrochemical impedance spectroscopy (EIS). *Bioelectrochemistry* 70:401–407

- Cheung CL, Nikolic RJ, Reinhardt CE, Wang TF (2006) Fabrication of nanopillars by nanosphere lithography. *Nanotechnology* 17(5):1339–1343
- Colson P, Cloots R, Henrist C (2011) Experimental design applied to spin coating of 2D colloidal crystal masks: a relevant method? *Langmuir* 27(21):12800–12806
- Dahint R, Trileva E, Acunmana H, Konrad U, Zimmera M, Stadler V, Himmelhaus M (2007) Optically responsive nanoparticle layers for the label-free analysis of biospecific interactions in array format. *Biosens Bioelectron* 22:3174–3181
- Demers LM, Mirkin CA (2001) Combinatorial templates generated by dip-pen nanolithography for the formation of two-dimensional particle arrays. *Angew Chem Int Ed* 40:3069–3071
- Dimitrov A, Nagayama K (1996) Continuous convective assembling of fine particles into two-dimensional arrays on solid surfaces. *Langmuir* 12(5):1303–1311
- Duran C, Sato K, Hotta K, Watari K (2007) Covalently connected particles in green bodies fabricated by tape casting. *J Am Ceram Soc* 90(1):279–282
- Fulda KU, Tieke B (1994) Langmuir films of monodisperse 0.5 μm spherical particles with hydrophobic core and a hydrophilic shell. *Adv Mater* 6(4):288–290
- Fustin CA, Glasser G, Spiess HW, Jonas U (2004) Parameters influencing the templated growth of colloidal crystals on chemically patterned surfaces. *Langmuir* 20(21):9114–9123
- Garno JC, Yang Y, Amro NA, Cruchon-Dupeyrat S, Chen S, Liu GY (2003) Precise positioning of nanoparticles on surfaces using scanning probe lithography. *Nano Lett* 3:389–395
- Gu S, Kondo T, Konno M (2004) Preparation of silica-polystyrene core-shell particles up to micron sizes. *J Colloid Interface Sci* 272:314–320
- Han S, Hao Z, Wang J, Luo Y (2005) Controllable two dimensional photonic crystal patterns fabricated by nanosphere lithography. *J Vac Sci Technol* 23(4):1585–1588
- Hirono T, Torimitsu K, Kawana A, Fukuda J (1988) Recognition of artificial microstructures by sensory nerve fibers in culture. *Brain Res* 446:189–194
- Junno T, Deppert K (1995) Controlled manipulation of nanoparticles with an atomic force microscope. *Appl Phys Lett* 66(26):3627–3629
- Kanamori Y, Kaneko A, Moronuki N, Kubo T (2008) Self-assembly of fine particles on patterned wettability in dip coating and its scale extension with contact printing. *J Adv Mech Des Syst Manuf* 2:783–791
- Kaneko A, Takeda I (2016) Textured surface of self-assembled particles as a scaffold for selective cell adhesion and growth. *Int J Autom Technol* 10(1):62–68
- Kaneko A, Moronuki N, Shibata T, Kogiso J, Uchida K, Kubo T (2006) An application of dip-coating technique to fabrication of self-assembled microstructure on hydrophilic/hydrophobic-patterned substrate. In: 6th international conference of euspen, vol 2, pp 288–291, Baden bei Wien, Austria
- Kaneko A, Mogi M, Yamamura Y, Moronuki N (2006) Fabrication of self-assembled microstructure on using controlled liquid spreading on textured surface. *JSPE publication series*, vol 5, Springer, London, pp 191–196
- Kaneko A, Aruga D, Moronuki N, Kanamori Y (2009) Self-assembly of surface-modified fine particles on patterned substrate. In: 9th international conference of euspen, vol 2, pp 414–417, San Sebastian, Spain
- Kaneko A, Sugihara T, Murakami H, Takeda I, Tanaka Y, Moronuki N (2012) Fabrication of spatially-patterned cells using selective adhesion on pre-structured fine particles. *Key Eng Mater* 523–524:615–620
- Kobayashi H, Moronuki N, Kaneko A (2008) Self-assembly of fine particles applied to the production of antireflective surfaces. *J Korean Soc Precis Eng* 9(1):25–29
- Kralchevski PA, Nagayama K (1994) Capillary forces between colloidal particles. *Langmuir* 10:23–36
- Leclerc E, Sakai Y, Fujii T (2003) Cell culture in 3-dimensional microfluidic structure of PDMS (polydimethylsiloxane). *Biomed Microdevices* 5:109–114
- Li J, Xing R, Huang W, Han Y (2005) A self-assembly approach to fabricate the patterned colloidal crystals with a tunable structure. *Colloids Surf A Physicochem Eng Asp* 269:22–27
- Masuda Y, Seo W, Koumoto K (2000) Arrangement of nanosized ceramic particles on self-assembled monolayers. *Jpn J Appl Phys* 39:4596–4600
- Masuda Y, Itoh M, Yonezawa T, Koumoto K (2002) Low-dimensional arrangement of SiO_2 particles. *Langmuir* 18(10):4155–4159

- McNally H, Pingle M, Lee SW, Guo D, Bergstrom DE, Bashir R (2003) Self-assembly of micro- and nano-scale particles using bio-inspired events. *Appl Surf Sci* 214:109–119
- Mihi A, Ocaña M, Míguez H (2006) Oriented colloidal-crystal thin films by spin-coating microspheres dispersed in volatile media. *Adv Mater* 18(17):2244–2249
- Nishikawa H, Maenosono S, Yamaguchi Y, Okubo T (2003) Self-assembling process of colloidal particles into two-dimensional arrays induced by capillary immersion force: a simulation study with discrete element method. *J Nanopart Res* 5:103–110
- Nishio M, Kaneko A, Moronuki N (2009) Complex assembly of fine particles by repeated dip-coating process. In: The 3rd international conference of asian society for precision engineering and nanotechnology, Kitakyushu, Japan
- Nshio M, Moronuki N, Tanaka Y, Kaneko A (2012) Self-assembly of functional particles on optical element for sensitivity improvement of bio-chemical sensor. *Key Eng Mater* 516:60–65
- Paul JI (1984) Multiple fibronectin subunits and their post-translational modifications. *J Biol Chem* 259(21):13477–13487
- Paunov VN, Kralchevsky PA, Denkov ND, Nagayama K (1993) Lateral capillary forces between floating submillimeter particles. *J Colloid Interface Sci* 157(1):100–112
- Perelaer J, Laat AWM, Hendriks CE, Schubert US (2008) Inkjet-printed silver tracks: low temperature curing and thermal stability investigation. *J Mater Chem* 18:3209–3215
- Ranella A, Barberoglou M, Bakogianni S, Fotakis C, Stratakis E (2010) Tuning cell adhesion by controlling the roughness and wettability of 3D micro/nano silicon structures. *Acta Biomater* 6:2711–2720
- Smith PJ, Shin DY, Stringer JE, Derby B, Reiset N (2006) Direct ink-jet printing and low temperature conversion of conductive silver patterns. *J Mater Sci* 41:4153–4158
- Sugihara T, Kaneko A (2013) Self-patterning of PC12 cells on micro-structures of protein-modified particles. *J Solid Mech Mater Eng* 7(2):142–154
- Takeda I, Kaneko A, Tanaka Y, Moronuki N (2012) Selective cell-adhesion on micro-structured fine particles. *Key Eng Mater* 516:130–135
- Takeda I, Kawanabe M, Kaneko A (2015) Autonomous patterning of cells on microstructured fine particles. *Mater Sci Eng C* 50:173–178
- Takeda I, Kawanabe M, Kaneko A (2016) An investigation of cell adhesion and growth on micro/nano-scale structured surface -self-assembled micro particles as a scaffold. *Precis Eng* 43:294–298
- Torimitsu K, Kawana A (1990) Selective growth of sensory nerve fibers on metal oxide pattern in culture. *Dev Brain Res* 51(1):128–131
- Tsukagoshi T, Kondo Y, Yoshino N (2007) Protein adsorption on polymer-modified silica particle surface. *Colloids Surf B Biointerfaces* 54:101–107
- Tsuruma A, Tanaka M, Yamamoto S, Fukushima N, Yabu H, Shimomura M (2006) Topographical control of neurite extension on stripe-patterned polymer films. *Colloids Surf A* 284–285: 470–474
- Velikov KP, Moroz A, Blaaderen A (2002) Photonic crystals of core-shell colloidal particles. *Appl Phys Lett* 80:49–51
- Xia Y, Whitesides GM (1997) Extending microcontact printing as a microlithographic technique. *Langmuir* 13(7):2059–2067
- Xuefeng W, Christian AO, Qinghua L, Jun H (2008) Cell directional migration and oriented division on three-dimensional laser-induced periodic surface structures on polystyrene. *Biomaterials* 29(13):2049–2059
- Ye YH, Badilescu S, Truong VV (2001) Self-assembly of colloidal spheres on patterned substrates. *Appl Phys Lett* 79:872–874
- Yellen BB, Friedman G (2004) Programmable assembly of colloidal particles using magnetic microwell templates. *Langmuir* 20:2553–2559
- Yin Y, Lu Y, Gates B, Xia Y (2001) Template-assisted self-assembly: a practical route to complex aggregates of monodispersed colloids with well-defined sizes, shapes, and structures. *J Am Chem Soc* 123(36):8718–8729
- Yonezawa T, Genda H, Koumoto K (2002) Cationic silver nanoparticles dispersed in water prepared from insoluble salts. *Chem Lett* 32(2):1172–1173

Part V

Physical/Chemical Machining Technology



Micro-electrical Discharge Machining of Hard Brittle Materials

25

Pay Jun Liew and Jiwang Yan

Contents

25.1	Overview of Electrical Discharge Machining	776
25.1.1	Principle of EDM	777
25.1.2	Micro-EDM and Its Types	778
25.1.3	Micro-EDM of Hard and Brittle Materials	779
25.2	Carbon Additive Assisted Micro-EDM of RB-SiC	785
25.2.1	Machining Equipment and Conditions	785
25.2.2	Result and Discussion	785
25.3	Ultrasonic Cavitation Assisted Micro-EDM	787
25.3.1	Machining Equipment and Condition	788
25.3.2	Results and Discussion	789
25.4	Hybrid Tool for EDM and Grinding	798
25.4.1	Experimental Methods	799
25.4.2	Results of Micro-EDM	800
25.4.3	Results of Micro-grinding	801
25.5	Summary and Outlook	802
	References	804

Abstract

In recent years, the use of single crystals and ceramic materials such as silicon carbide (SiC), alumina, and silicon nitride has received intensive attention in mechanical and manufacturing engineering. However, due to their high

P. J. Liew (✉)

Manufacturing Process Department, Faculty of Manufacturing Engineering, Universiti Teknikal Malaysia Melaka, Hang Tuah Jaya, Melaka, Malaysia
e-mail: payjun@utem.edu.my

J. Yan

Department of Mechanical Engineering, Keio University, Yokohama, Japan
e-mail: yan@mech.keio.ac.jp

© Springer Nature Singapore Pte Ltd. 2018

J. Yan (ed.), *Micro and Nano Fabrication Technology*, Micro/Nano Technologies,
https://doi.org/10.1007/978-981-13-0098-1_25

775

hardness, these materials are typically difficult to machine by mechanical machining methods. In particular, the fabrication of microstructures and high aspect ratio micro hole on these hard and brittle materials by using cutting and abrasive machining is very difficult and involves high production cost. As an alternative approach, micro-electrical discharge machining (micro-EDM) is effective. In this chapter, three major approaches that have been used by previous researchers to improve the EDM machinability of low conductivity and insulating ceramic materials such as powder mixed EDM, assisting electrode EDM and electrical discharge milling and grinding, will be overviewed. Then some newly developed technologies for machining hard and brittle materials by using micro-EDM will be introduced. One is hybrid micro-EDM by combining ultrasonic cavitation and carbon nanofibers. The effect of carbon nanofiber concentration and ultrasonic vibration on micro hole geometry, surface topography, and surface roughness will be described. By using the hybrid EDM process, high aspect ratio micro holes and micro dimples were successfully fabricated on RB-SiC. Another example is a hybrid tooling technology using polycrystalline diamond (PCD) for micro-EDM and grinding of single-crystal SiC. This enabled achieving extremely smooth surfaces in nanometer level after EDM.

Keywords

Micro-electrical discharge machining · Hard and brittle materials · Carbon nanofibers · Hybrid tool · Micro-structures

25.1 Overview of Electrical Discharge Machining

Electrical discharge machining (EDM), also known as spark machining, is an electrothermal machining process, whereby a desired shape is obtained using electrical discharges (sparks). In EDM, both electrode and workpiece are submerged in a dielectric fluid, which is generally kerosene or deionized water. During the process, there is no mechanical contact between the electrode and the workpiece. The electrical sparks are generated in a dielectric fluid by electrical energy and act as a cutting tool, to remove the workpiece material by melting and evaporation. The volume removed by a single spark is small, in the range of 10^{-6} – 10^{-4} mm³; however the sparks occur at a high frequency, typically 10,000 times per second (Descoedres 2006).

The dielectric fluid plays an important role in the EDM process. According to Kalpakjian and Schmid (2001), the dielectric fluid acts as an insulator and flushing medium to carry away the debris and provide the cooling medium to the tool and the workpiece. The machining performance of EDM depends on many factors, such as electrode material, workpiece material, non-electrical machining parameters, and electrical machining parameters. Figure 1 shows the Ishikawa cause-effect diagram for EDM process.

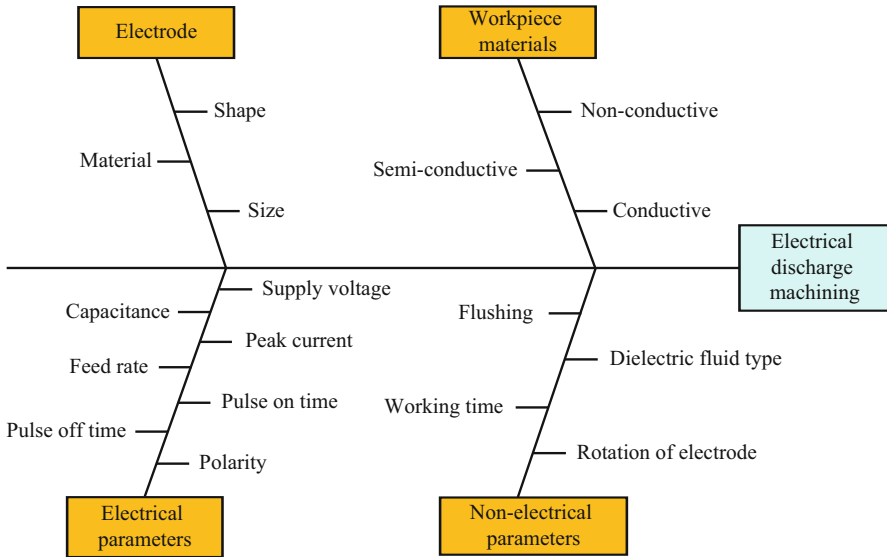


Fig. 1 Ishikawa cause-effect diagram of EDM process

25.1.1 Principle of EDM

According to Schumacher (2004), the sparking phenomena or electrical discharge during EDM can be separated into three important phases, namely, preparation phase for ignition, phase of discharge, and interval phase between discharges. Figure 2 gives an overview of the erosion process due to a single EDM discharge. The phenomena of sparking are briefly explained, as below:

- (a) Voltage is applied between the electrode and the workpiece. At low electric current, electrons pass through the dielectric fluid from the negative electrode toward the positive workpiece and vice versa. An electric field or energy column is created.
- (b) At the closest point between the electrode and workpiece, the breakdown of the dielectric fluid is initiated. When the breakdown occurs, the voltage falls and a current rises abruptly. A plasma channel (ionized, electrically conductive gas with high temperature) is created between the electrode and the workpiece.
- (c) During the discharging phase, the discharge current is maintained to assure a continuous bombardment of ions and electrons on the electrodes. This will cause strong heating of the workpiece material and electrode material. As a result, small molten metal pool at the surface is created. A small quantity of metal can be directly vaporized due to the heating. The plasma channel expands and the vapor bubble grows. Therefore, the radius of the molten metal pool increases with time.
- (d) At the end of the discharge, the current and the voltage are shut down. When the plasma is put off, the heat generation stops, and the pressure falls rapidly, but the

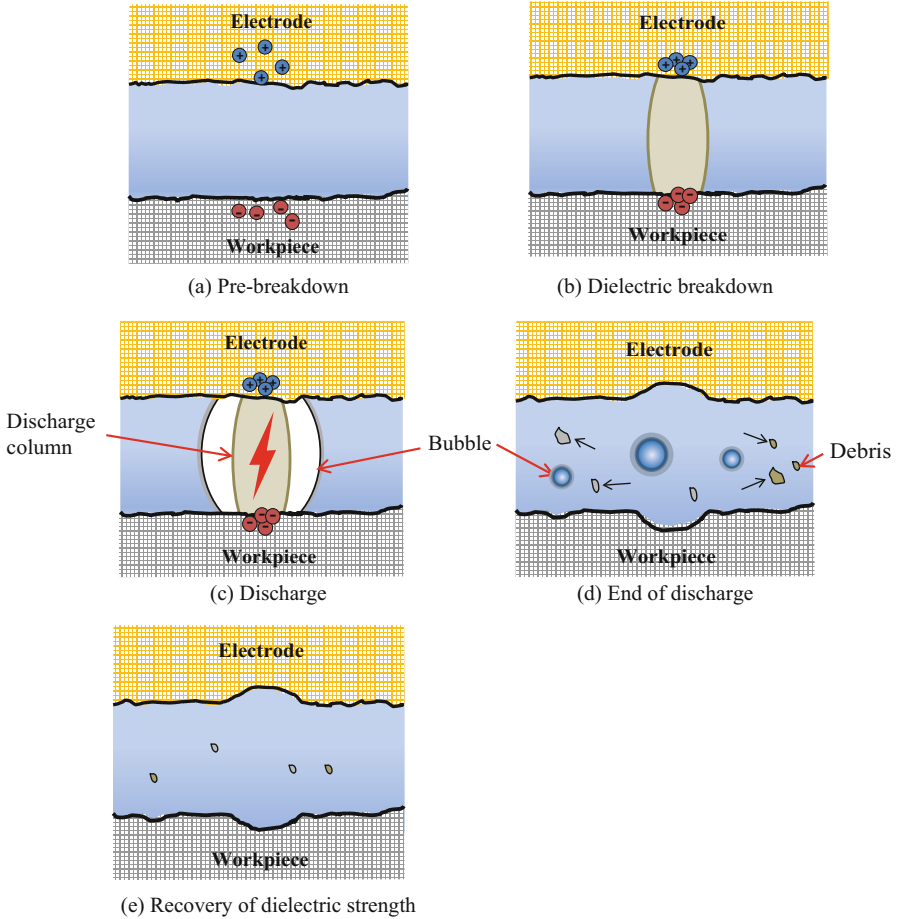


Fig. 2 Erosion process due to a single EDM discharge (Schumacher 2004, with permission from Elsevier)

vapor bubble continues to grow until it collapses to smaller bubbles. The plasma implodes under the pressure imposed by the surrounding dielectric. Consequently, the molten metals are evaporated and ejected into the dielectric, leaving a small crater at the workpiece surface (typically 1–500 μm in diameter, depending on the current).

(e) After the end of discharge, ions and electrons are recombined, and the dielectric breakdown strength is recovered.

25.1.2 Micro-EDM and Its Types

In principle, the mechanism of the micro-EDM process and macro-EDM process is similar. The main differences between these two processes are in the size of the tool

used, the power supply of discharge energy, and the resolution of the X-, Y-, and Z-axis movements (Masuzawa 2000). Zahiruddin and Kunieda (2012) reported that the significant difference between micro-EDM and macro-EDM was the power density. It was found that the power density of micro-EDM was approximately 30 times greater than that of macro-EDM. Consequently, energy efficiency and removal efficiency in micro-EDM were significantly greater than those of macro-EDM.

There are four different types of micro-EDM technologies which are used for manufacturing micro-features, namely, die-sinking micro-EDM (an electrode with micro-features is employed to produce its mirror image in the workpiece), micro-wire EDM (a wire is used to cut through a conductive workpiece), micro-EDM drilling (micro-electrodes are used to “drill” micro holes in the workpiece), and micro-EDM milling (micro-electrodes are employed to produce three-dimensional cavities by adopting a movement strategy similar to that in conventional milling) (Pham et al. 2004).

In the micro-EDM machine that was used in this chapter, two main types of machining can be distinguished, namely, die-sinking micro-EDM and wire electro-discharge grinding (WEDG). In die-sinking EDM, the workpiece is formed either by replication of the shaped tool electrode or by three-dimensional movement of a simple electrode. Normally, negative electrode polarity is used when performing a test using die-sinking EDM. Tungsten rod, which is shaped by WEDG, is normally used as an electrode and fed in the z direction, toward the workpiece that immersed in the dielectric fluid. Die-sinking EDM is mainly used to produce injection molds. WEDG, which was developed by Masuzawa et al. (1985), uses a brass wire to erode away material from a rotating workpiece to produce a cylindrical shaft. The workpiece (anode) is held vertically in a mandrel that rotates at 3000 rpm, and its position is slowly fed in the z direction. A $\phi 100 \mu\text{m}$ brass wire (cathode) is supported on a wire guide, and its position is controlled in the x- and y-directions. The electrical discharges, which are produced by resistor-capacitor (RC), erode the material from the workpiece and the brass wire, within a small gap ($\sim 2 \mu\text{m}$) filled with dielectric oil (Morgan 2004). WEDG has been widely adopted to fabricate micro-tool electrode for micro-EDM as well as other processes. Compared to serial machining with single tool electrode, machining by micro-tool electrode array has become an important topic in micromachining to improve throughput and precision (Chung et al. 2011). For example, Yi et al. (2008) successfully machined square hole by micro-EDM using 4×4 copper electrode array that fabricated by reserve EDM, as shown in Fig. 3. The results show that the productivity was improved to five times of that in the case using a single electrode.

25.1.3 Micro-EDM of Hard and Brittle Materials

Recently, micro-EDM has become popular to machine hard ceramic material. The growing popularity of micro-EDM can be attributed to its advantages, such as low installation cost and its ability to machine complex three-dimensional shapes easily regardless of material hardness (Reynaerts et al. 1998). Furthermore, during machining with micro-EDM, there is no direct contact between the electrode and

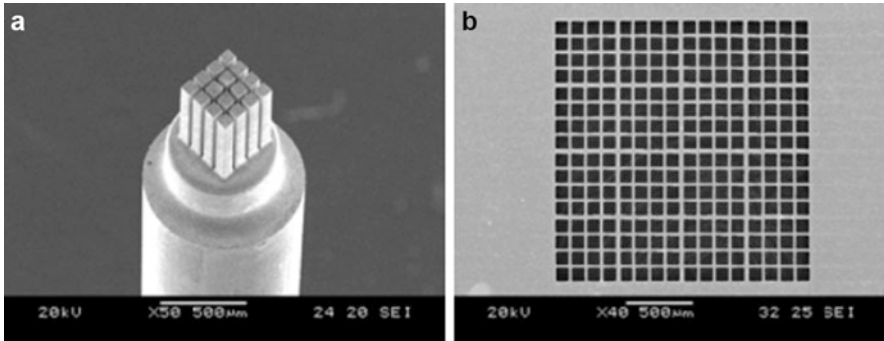


Fig. 3 (a) A 4×4 Cu electrode array fabricated by reverse EDM, (b) square holes by micro-EDM using the 4×4 Cu electrode array (Yi et al. 2008, with permission from Springer)

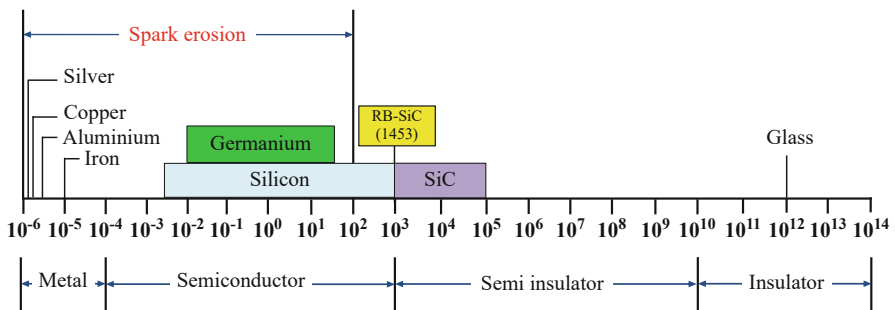
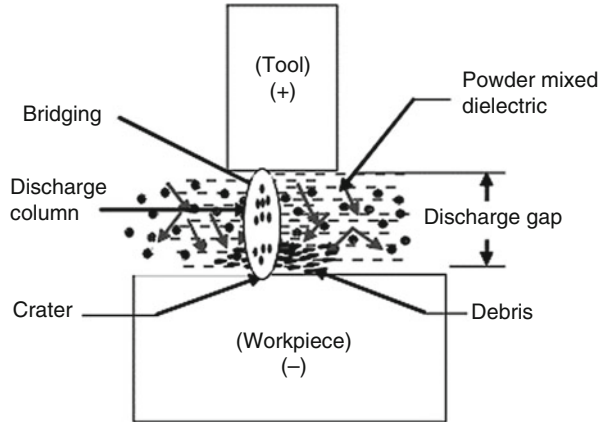


Fig. 4 Resistivity of various materials (Ωcm) (Lee et al. 2013, with permission from Elsevier)

workpiece, thus eliminating mechanical stress, chatter, and vibration problems (Ho and Newman 2003). EDM has been used extensively for machining various ceramic materials. For example, a comparative study of the die-sinking EDM of three different ceramic materials was carried out by Puertas and Luis (2004). Clijsters et al. (2010) also manufactured complex parts on SiSiC materials using EDM. When machining hard and brittle ceramic materials by EDM, information about the workpiece conductivity/resistivity is therefore an absolute prior requirement. The resistivity of the workpiece is a limiting factor for the discharge current, which directly affects the material removal rate (Lee et al. 2013). Various materials with their resistivity are shown in Fig. 4. As mentioned earlier, $100 \Omega\text{cm}$ is the upper limit of electrical resistivity for a ceramic workpiece to be machined by EDM (Konig et al. 1988). However, most ceramics are not sufficiently conductive, which is a major problem when applying EDM to ceramic materials. For example, the reaction bonded silicon carbide (RB-SiC) ceramic material that was used in this chapter possesses a very high electrical resistivity, which is around $1453 \Omega\text{cm}$.

Fig. 5 Principle of powder mixed EDM (Kansal et al. 2007, with permission from Elsevier)



It is typically difficult to be machined directly by EDM. Hence, the method for increasing the EDM machinability of materials is crucial. From the past researches, several methods have been used, as summarized in the following subsections.

25.1.3.1 Powders Mixed EDM

The mechanism of powder mixed EDM (PMEDM) is different from the conventional EDM with the pure dielectric fluid. In powder mixed EDM, suitable conductive materials in the form of powders are mixed into the dielectric fluid, as schematically shown in Fig. 5. Under the influence of high potential intensity, the particles are charged and accelerated, move in the zigzag fashion, and may act as conductors. At the sparking gap between electrode and workpiece, the particles arrange themselves in the form of chain-like structures and interlock to each other in the direction of flow of current. The chain formation helps in bridging the discharge gap, and subsequently, the insulating strength of the dielectric fluid decreases due to the bridging effect. Thus, discharge column is easily formed, and short circuit is easy to take place, leading to early explosion in the gap (Kansal et al. 2007). A smaller crater size is created due to the gap enlargement and high frequency of discharge. The flowing powder additive creates another bridging effect, discharge column, and lastly explosion. The discharging processes repeat continuously until the final shape is obtained.

Powder mixed EDM proved to be an effective process to improve the machining efficiency and surface finish of materials. For example, Yeo et al. (2007) added 45–55-nm-sized SiC powders into dielectric, and they found that the surface craters became smaller than those produced in powder-free dielectric fluid. Chow et al. (2008) added SiC powders into pure water as dielectric fluid in the EDM of titanium alloy and confirmed the improvement in surface quality and material removal rate. Gunawan et al. (2009) added molybdenum disulfide (MoS_2)

powders and improved the material removal rate and surface roughness of Cu, brass, and Cu-W workpiece materials. Gunawan et al. (2011) also tried suspending nano graphite powders in dielectric fluid with the combination of ultrasonic vibration. They found that the machining time was reduced up to 35%.

Powder mixed EDM was also applied to the EDM of ceramic materials. Jahan et al. (2010a, b) studied the effect of adding graphite, aluminum, and nonconductive alumina powders in EDM of tungsten carbide ceramics. They found that the graphite powders provided a smooth surface and the aluminum powders resulted in higher spark gap and higher material removal rate, whereas the alumina powders had little effect on the EDM performance. Nevertheless, for low conductivity or insulating ceramic materials, it was difficult to obtain good machining performance by powder addition. For example, Tani et al. (2002) used Al, Gr, Si, Ni, and ZrB₂ powders to assist the EDM of insulating Si₃N₄ ceramics and found that even though the removal rate was increased, the surface roughness was barely improved. This was due to the generation of long pulse discharge in the EDM process.

25.1.3.2 Assisting Electrode EDM

Pioneer work can be traced to Mohri et al. (1996), who developed a new method of machining insulating ceramic material by EDM. It is called assisting electrode method. In this method, a metal plate or metal mesh is arranged on the surface of ceramic insulator as an assisting electrode. The machining process is shown in Fig. 6. In the early stage, discharges are generated between the metal plate and tool electrode. When the metal plate is eroded, the dielectric oil is thermally decomposed. Cracked carbon from the working oil and other electrical conductive compounds from the metal plate are deposited on the surface of ceramics. It keeps electrical conductivity on the surface of the workpiece during the machining. Hence, discharge continues to occur over the ceramics.

Figure 7 shows the machining apparatus for the assisting electrode method by WEDM. By using this method, insulating ceramics such as alumina and Si₃N₄ have been machined by sinking EDM (Muttamara et al. 2003; Fukuzawa et al. 2004; Muttamara et al. 2009). In addition, Tani et al. (2004) and Fukuzawa et al. (2009) fabricated three-dimensional complex shape successfully on the insulating Si₃N₄ and ZrO₂ with this assisting electrode method by WEDM. Sabur et al. (2013) also machined nonconductive ceramic ZrO₂ using assisting electrode by EDM. The experimental results show that the material is removed in EDM of nonconductive ZrO₂ ceramic mostly by spalling, and it increases with the increase of input power. Recently, Gotoh et al. (2016) also used the long pulse discharge in WED-milling to machine insulating ceramic Si₃N₄. With this long pulse discharge, an electrical conductive layer is formed on the surface of the insulating ceramic, which maintains stable machining.

25.1.3.3 Electrical Discharge Milling and Mechanical Grinding

In order to improve the EDM machinability of high resistivity of ceramic material, a new compound machining process that integrates electrical discharge (ED) milling and mechanical grinding is proposed (Liu et al. 2008). The principle for ED milling

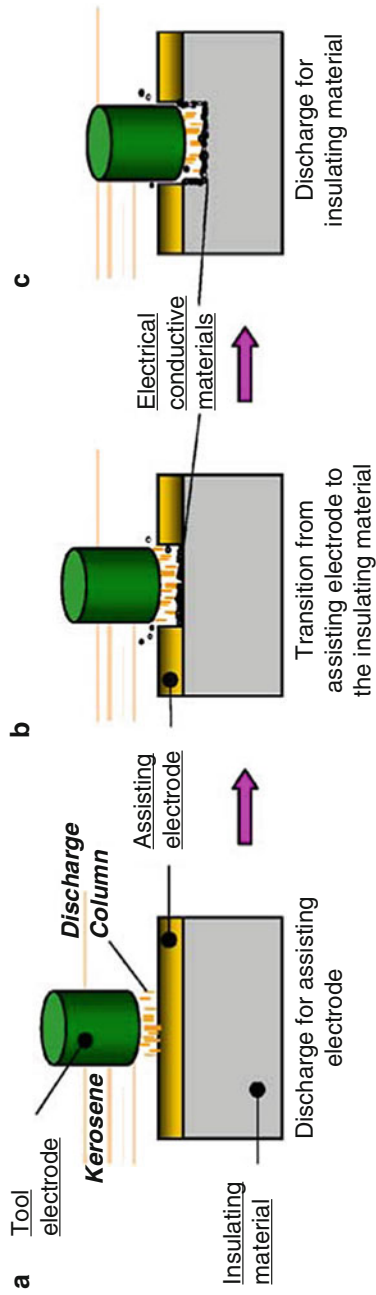


Fig. 6 Machining process of insulating materials using assisting electrode (Fukuzawa et al. 2004, with permission from Elsevier)

Fig. 7 WEDM of insulating ceramics (Fukuzawa et al. 2009, with permission from Elsevier)

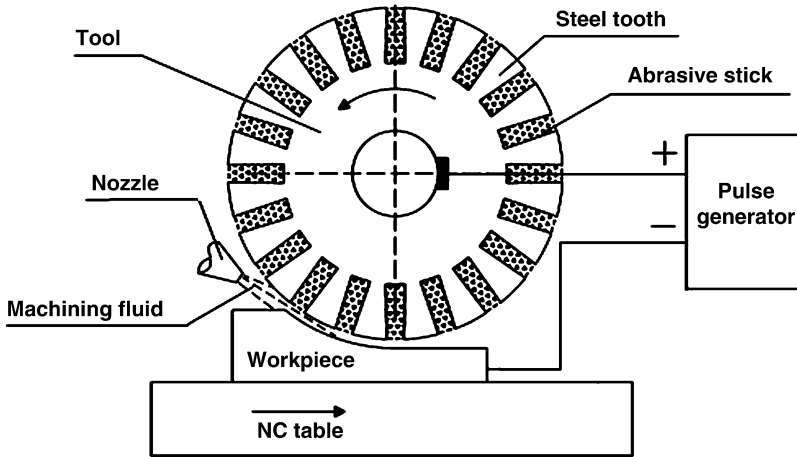
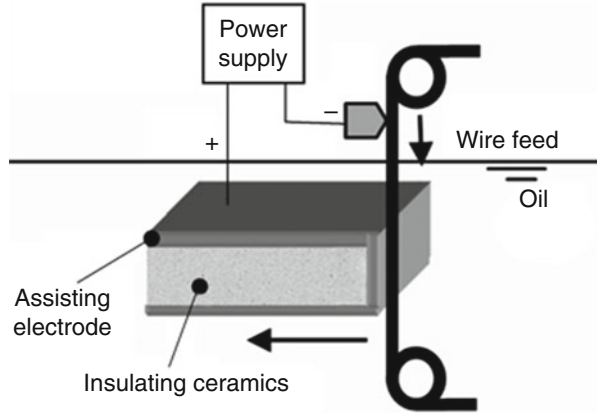


Fig. 8 ED milling and mechanical grinding (Ji et al. 2010, with permission from Sage Publications)

and mechanical grinding is shown in Fig. 8. In this hybrid process, the tool and the workpiece are connected to the positive and the negative poles of the pulse generator, respectively. Steel wheel with teeth is used as a tool. During machining, the tool rotates at a high speed on a rotary spindle which is driven by an AC motor. The water-based emulsion machining fluid is flushed into the gap with a nozzle, and the ceramic workpiece is fed toward the tool with an NC table. Electrical discharges are produced when the distance between the workpiece and the steel tooth reaches the discharge gap and caused the ceramic to be removed by ED milling. With a steel toothed wheel as the tool electrode, high resistivity SiC ceramic can be easily machined by ED milling (Liu et al. 2009; Ji et al. 2010, 2011).

The aforementioned methods are the three major approaches that have been used by the previous researchers to improve the EDM machinability of low conductivity and insulating ceramic materials. In this chapter, new machining method will be developed for increasing the machining efficiency of RB-SiC by using micro-EDM while maintaining the surface integrity and dimensional accuracy of machined microstructures.

25.2 Carbon Additive Assisted Micro-EDM of RB-SiC

For improving the machining efficiency of RB-SiC, carbon additive assisted micro-EDM of RB-SiC was proposed (Liew et al. 2013a). In this experiment, two different types of additives, namely, spherical carbon powders and cylindrical carbon nanofibers, were added into the dielectric fluid, respectively. The spherical carbon was in 150 nm cluster size, while the carbon nanofiber was 150 nm in diameter and 6–8 μm in length. The effect of these additives on the spark gap and material removal rates was investigated experimentally.

25.2.1 Machining Equipment and Conditions

Micro-EDM test was performed on the sample using a micro-EDM machine Panasonic MG-ED82W. Tungsten rods with 300 μm diameters were used as tool electrodes. Each test was run on the sample for a duration of 5 min, and average of three tests for each parameter setting was taken. The dielectric fluid used was hydrocarbon dielectric oil CASTY-LUBE EDS, which has a high flash point. Before the experiment, the required amounts of additives and dielectric fluid were measured separately before being mixed together and homogenized in a mixer for 20 min. This is to ensure that the carbon nanofibers are dispersed uniformly in the dielectric fluid. Table 1 summarizes the experimental conditions.

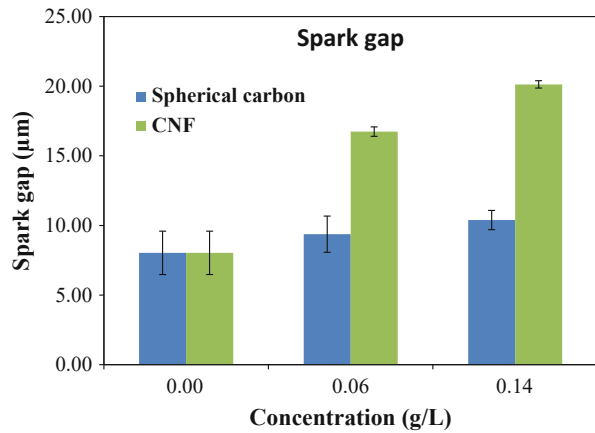
25.2.2 Result and Discussion

25.2.2.1 Spark Gap

Figure 9 shows the effect of carbon additives on spark gap. It indicates that the spark gap increases with the increase of spherical carbon powders and carbon nanofiber concentrations. Moreover, it is worth noting that carbon nanofiber could produce bigger spark gap compared to the one obtained with addition of spherical carbon powders. Presumably, when carbon nanofibers were added into the dielectric fluid, long and thin carbon nanofibers might be able to bridge the gap between the electrode and workpiece more significantly by interlocking to each other if compared to round-shaped carbon powders. Furthermore, the high electrical conductivity of

Table 1 Experimental conditions

Rotational speed	3000 rpm
Voltage	110 V
Condenser capacitance	3300 pF
Feed rate	3 $\mu\text{m/s}$
Dielectric fluid	EDM oil CASTY-LUBE EDS
Additive	Carbon nanofibers (CNFs) Carbon powder
Concentrations	0, 0.06, 0.14 g/L
Machining time	5 min

Fig. 9 Effect of spherical carbon powders and carbon nanofibers on spark gap

carbon nanofiber might help to reduce the insulating strength of the dielectric fluid, resulting in bigger sparking gap compared to the one obtained with spherical carbon powders.

25.2.2.2 Material Removal Rate

Figure 10 shows the effect of spherical carbon powders and carbon nanofibers on material removal rates (MRR). Clearly, with the addition of carbon nanofibers, the material removal rate is six to ten times higher than the one obtained with spherical carbon powders, especially at high concentration of additive. This result demonstrated that the frequency of discharge might be increased by the addition of carbon nanofibers. In addition, the sparking gap that is induced by the spherical carbon powders as mentioned in previous paragraph is typically lower than that of carbon nanofibers; thus, the debris may not be removed easily from the machining gap and cause an unstable machining which leads to the reduction of material removal rates.

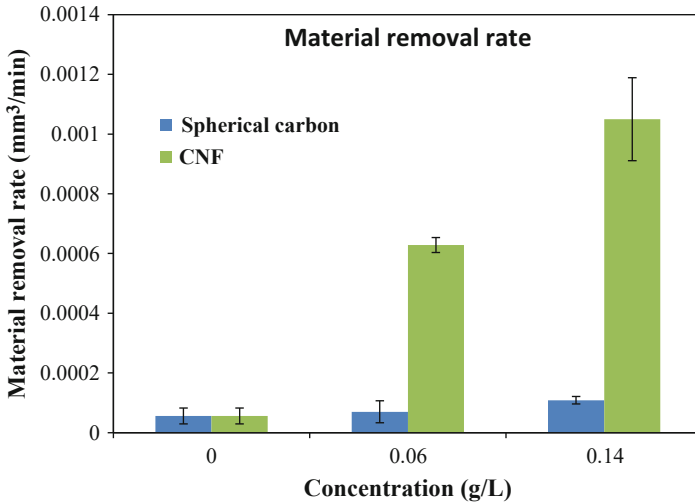


Fig. 10 Effect of spherical carbon powders and carbon nanofibers on material removal rate

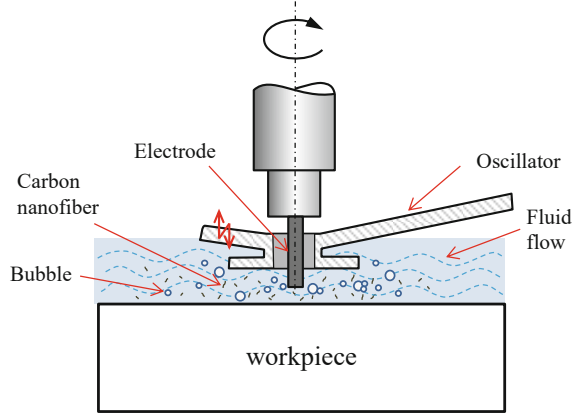
Based on the aforementioned results, it is proved that carbon nanofiber additives are more effective in increasing the spark gap than the spherical powders. Subsequently, the debris can be removed easily, and material removal rates can be improved to a significant degree.

25.3 Ultrasonic Cavitation Assisted Micro-EDM

In recent years, the industrial demand for microstructural surface such as micro-groove, microlens array, micropyramid arrays, and microprism array has been steadily increasing. Due to the wide applications of these functional microstructured surfaces in optical and biomedical engineering and microelectromechanical systems (MEMS), precision manufacturing process becomes essential to produce these microstructured surfaces, not only in terms of dimension and shape but also in the roughness quality of the machined surface (Hung et al. 2006).

Micro-EDM has gained an interest from many researchers as a precision machining tool for producing micro-features, such as fabrication micromolds for plastic lenses and glass, micro holes, microgrooves, and micro dimples. The growing popularity of micro-EDM can be attributed to its advantages, such as low installation cost (Reynaerts et al. 1998) and it can machine complex three-dimensional shapes easily regardless of material hardness. Furthermore, during machining with micro-EDM, there is no direct contact between the electrode and workpiece, thus eliminating mechanical stress, chatter, and vibration problems (Ho and Newman 2003).

Fig. 11 Schematic diagram of cavitation assisted micro-EDM



However, due to the narrow sparking gap in micro-EDM, the removal of debris remains a challenging issue, especially in deep hole machining and fine finishing with lower discharge energy. In this chapter, a hybrid EDM process by combining ultrasonic cavitation and carbon nanofiber addition is proposed to improve machining efficiency, surface quality, and form accuracy of deep micro holes in RB-SiC ceramic material (Liew et al. 2014). Ultrasonic vibration was directly applied to the dielectric fluid in the machining region by using a probe-type vibrator (instead of vibrating the dielectric tank) to generate cavitation to assist micro-EDM of deep micro holes in RB-SiC. The effect of ultrasonic vibration was investigated in combination with the addition of carbon nanofibers into dielectric fluid.

Figure 11 shows the schematic diagram of cavitation assisted micro-EDM. In this method, a suitable amount of carbon nanofibers is added and mixed in the dielectric fluid, and then a probe-type oscillator horn is placed into the dielectric fluid over the workpiece. When ultrasonic vibration is applied to the dielectric fluid, intense ultrasonic waves travel through the liquid, generating small cavities that enlarge and collapse. This phenomenon is called as cavitation (Suslick 1989). Normally, in micro-EDM, the debris is removed by the gaseous bubbles escaping from the working area through the narrow discharge gap (Yu et al. 2009; Wang et al. 2012). In this chapter, instead of gaseous bubbles, the ultrasonic cavitation will dominate the removal of discharge-induced debris. Thus, stable machining performance might be obtained. Moreover, the ultrasonic vibration of dielectric fluid might prevent the carbon nanofibers from accumulating, so that the carbon nanofibers will disperse evenly in the dielectric fluid. As a result, frequency of electro discharge in the EDM of RB-SiC might be improved.

25.3.1 Machining Equipment and Condition

As the ultrasonic vibration device, SC-450 cavitation generator (Taga Electric Co., Ltd, Japan) with a power output of 50 W was used in this experiment. It has vibration

Table 2 Experimental conditions

Rotational speed	3000 rpm
Voltage	80 V, 100 V
Condenser capacitance	Stray capacitance (~ 1 pF), 3300 pF
Feed rate	3 $\mu\text{m/s}$
Vibration frequency	20 ± 1.5 kHz
Vibration amplitude	0~14 μm
Working distance	1~4 mm
Dielectric fluid	EDM oil CASTY-LUBE EDS
Additive	Carbon nanofibers (CNFs)
CNFs size	Diameter = 0.15 μm
Concentration	Length = 6~8 μm 0.06 g/L
Machining time	30~150 s

frequency of 20 kHz and maximum amplitude of 14 μm . The electrode was inserted through the hole at the end of the oscillator horn of a cavitation generator during the EDM process. The ultrasonic vibration was applied to the dielectric fluid by the oscillator horn, to cause the cavitation effect. The oscillator horn was placed approximately 2–3 mm from the workpiece.

With the roughing parameters, the changes in the micro hole geometry, surface topography, and surface roughness were investigated experimentally. For comparison, three types of micro-EDM tests were then carried out, namely, (1) carbon nanofibers addition in EDM oil only, (2) ultrasonic cavitation in pure EDM oil, and (3) combination of ultrasonic cavitation with addition of carbon nanofibers in EDM oil. Micro hole machining was performed on the sample for duration of specified time, and each parameter setting was repeated for three times. After each EDM cycle, electrode dressing was performed by using wire electro-discharge grinding (WEDG) in order to improve their form accuracy. Table 2 shows the experimental conditions.

25.3.2 Results and Discussion

25.3.2.1 Micro Hole Geometry

Micro hole geometry after EDM was investigated. Figure 12 presents SEM micrographs of machined micro hole obtained under various machining conditions. Figure 13a–c shows three typical cross-sectional profiles corresponding to the micro hole shown in Fig. 12a–c, respectively. The profiles were measured by laser probe profilometer NH-3SP. It is clear that with addition of carbon nanofibers but without ultrasonic cavitation (Fig. 12a), a cone-shape protrusion was formed in the center of the micro hole. In the sparking gap, the stagnation of debris occurs intensively around the center of the micro-cavity, where the debris particles interact with the tool electrode (Ekmekci and Sayar 2013), causing concavity at the center

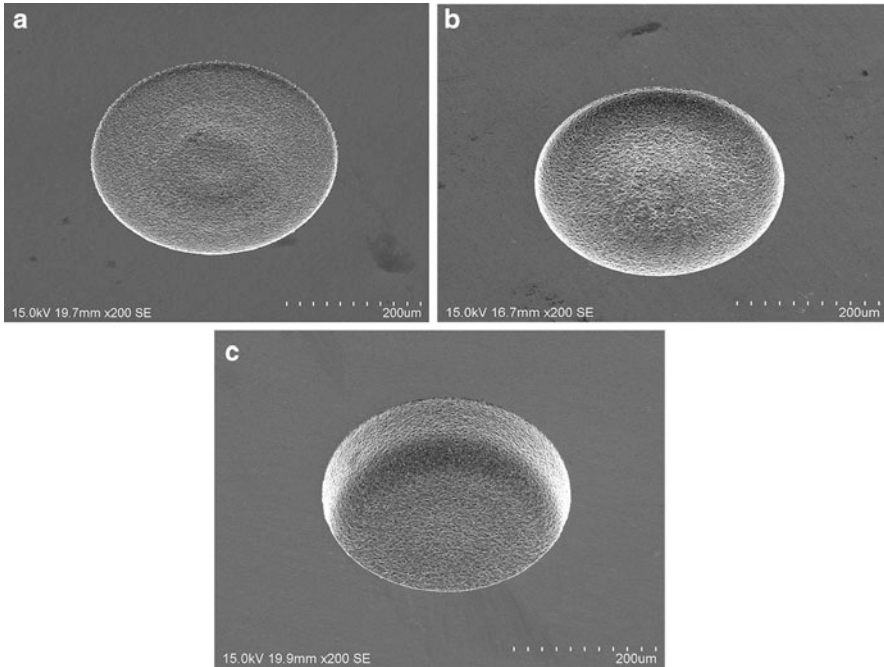


Fig. 12 SEM micrograph of micro hole after machining time of 2 min: (a) with 0.06 g/L carbon nanofibers only, (b) with ultrasonic cavitation in pure EDM oil, and (c) with ultrasonic cavitation and carbon nanofibers

of tool tip, and in turn, a cone-shape protrusion was formed at the bottom of the micro hole. The cone-shape protrusion was formed also when the ultrasonic cavitation was applied to the pure EDM oil (Fig. 12b). However, as shown in Fig. 12c, the cone-shape protrusion was insignificant, that is the bottom of micro hole became flat, when combination of ultrasonic cavitation and carbon nanofibers was used. At the same time, the depth of micro hole is deeper, as shown in Fig. 13. Carbon nanofibers addition in the dielectric fluid reduces the insulating strength of the dielectric fluid, causing a bigger discharge gap between the tool electrode and the workpiece. Thus, debris will be flushed out effectively with the help of cavitation bubble, and piled debris density in the center of micro hole will be prevented. This indicates that combination of ultrasonic cavitation and addition of carbon nanofibers in the dielectric fluid is more helpful for improving the form accuracy of the micro hole than EDM with the aid of either one exclusively.

25.3.2.2 Surface Topography

Figure 14 shows SEM micrographs of the machined surface obtained under various machining conditions. It is seen that with ultrasonic cavitation in pure EDM oil

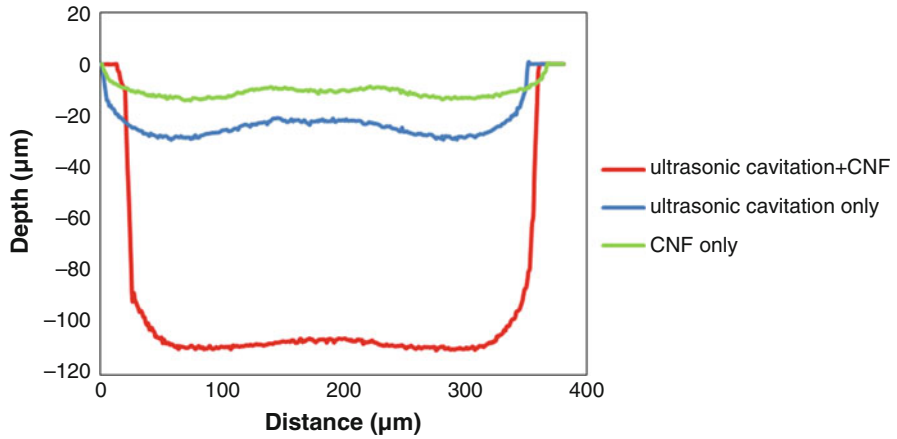


Fig. 13 Comparison of cross-sectional profiles of machined micro hole under various conditions

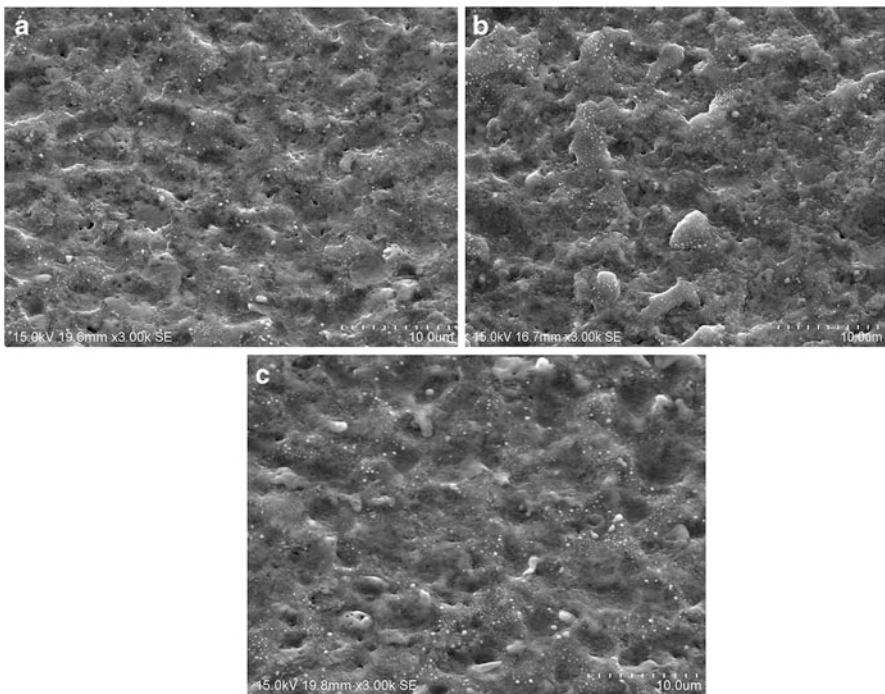


Fig. 14 Comparison of machined surface after machining time of 2 min: (a) with 0.06 g/L carbon nanofibers only, (b) with ultrasonic cavitation in pure EDM oil, and (c) with ultrasonic cavitation and carbon nanofibers

(without the carbon nanofiber addition), the surface of the micro hole was very rough and covered with resolidified material (Fig. 14b). In contrast, the machined surface in Fig. 14a and b were smoother, and surface craters became remarkably smaller. In this case, the material removal mechanism of RB-SiC involves spalling of large flakes, which is different from the other conductive materials. For this reason, we can say that the effect of ultrasonic cavitation only is insignificant for improving the surface topography of RB-SiC.

Next, laser probe profiling system was used to measure the surface roughness of the machined surface. Figure 15a–c shows three typical surface roughness profiles with the same scale corresponding to the micro hole shown in Fig. 12a–c, respectively. The minimum surface roughness is 0.2002 nmRa, which was obtained under the conditions of combination of ultrasonic cavitation and carbon nanofibers addition (Fig. 15c).

The vibration of dielectric fluid avoids the settling of carbon nanofibers at the bottom of the tank and induces multiple fine discharge, resulting better surface topography. At the same time, vibration-induced cavitation bubbles help to reduce the adhesion of resolidified debris on the machined surface. The surface roughness obtained with addition carbon nanofibers (Fig. 15a) was slightly higher (0.2173 nmRa). The roughest surface is 0.2814 nmRa obtained under the machining condition of ultrasonic cavitation in pure dielectric fluid. From these results, it can be easily elucidated that the hybrid process of ultrasonic cavitation and carbon nanofibers addition in the dielectric fluid is helpful for improving the surface finish of RB-SiC.

25.3.2.3 Process Mechanism

Figure 16 shows the schematic model for debris removal through the cavitation assisted micro-EDM with carbon nanofibers' addition in the dielectric fluid. Due to the pressure fluctuation in dielectric fluid which is induced by low-intensity ultrasonic waves, the generated cloud cavitation tends to oscillate at the working area. In a cloud cavitation, the nonlinear bubble dynamics produce nonlinear interactive effects which cause cascading of fluctuation energy (Kumar and Brennen 1991; Brennen 1995). Due to this fluctuating energy in the dielectric fluid, the debris might be flushed out from the gap easily. In some circumstances, as shown in Fig. 16, the cavitation bubbles might be initiated at the sparking gap between the electrode and workpiece during discharging phase, due to the pressure wave that propagates in the dielectric fluid. In this way, the debris will be ejected easily through the fluctuating cavitation bubbles, and instead, improving the machining efficiency of RB-SiC. In addition, the vibration of dielectric fluid uniformly disperses the carbon nanofibers and helps to activate the discharges, leading to a better surface finish and high material removal rate.

25.3.2.4 Fabrication of High Aspect Ratio Micro Hole

Next, hybrid EDM of ultrasonic cavitation and carbon nanofiber addition in dielectric fluid was applied to fabricate high aspect ratio micro holes on RB-SiC. Tungsten

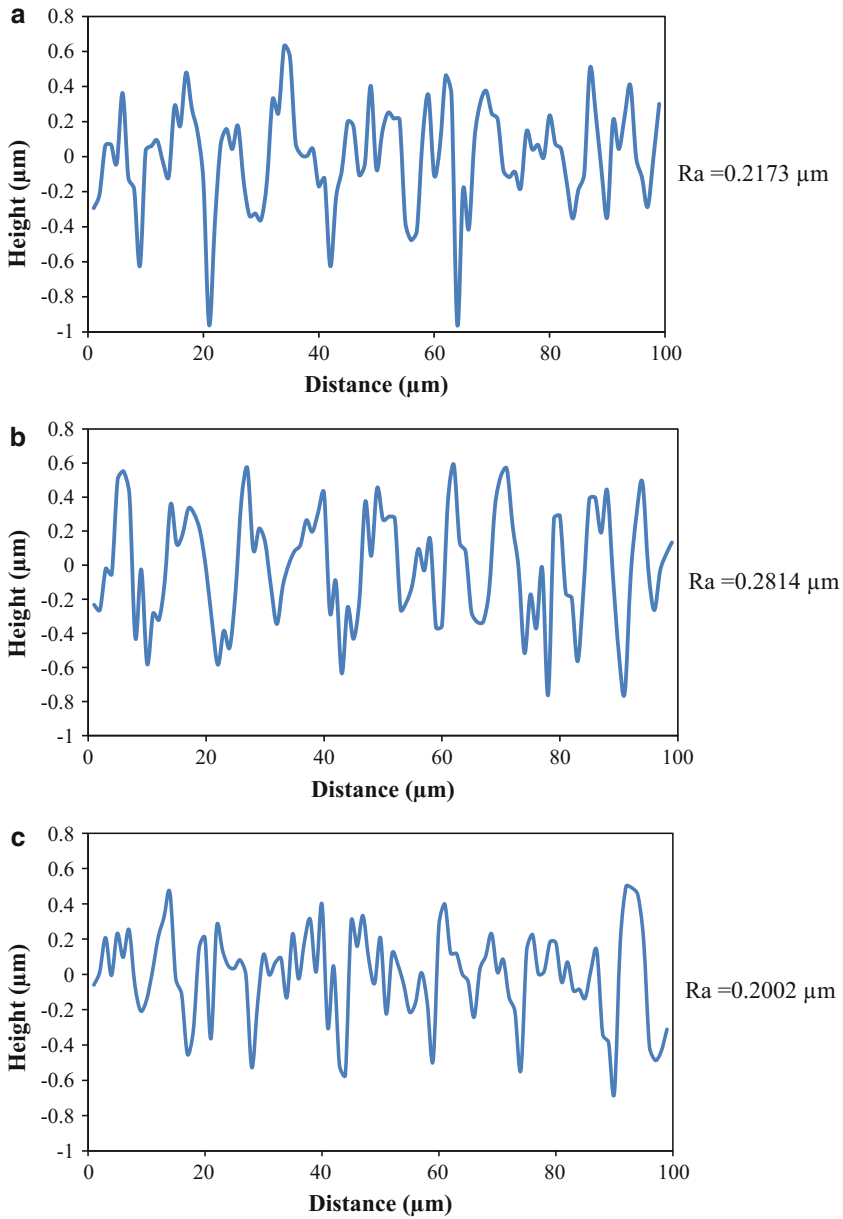


Fig. 15 Surface roughness profile: (a) with 0.06 g/L carbon nanofibers only, (b) with ultrasonic cavitation in pure EDM oil, and (c) with ultrasonic cavitation and carbon nanofibers

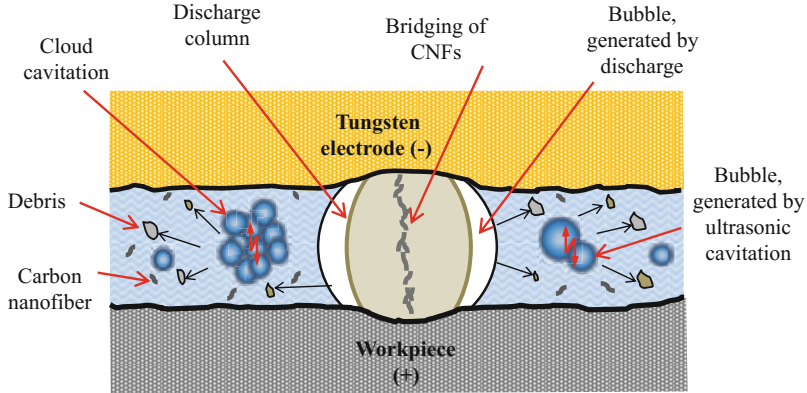


Fig. 16 Schematic model of debris removal with ultrasonic cavitation and addition of carbon nanofibers, through oscillation of cloud cavitation and cavitation bubbles that initiated during discharging phase

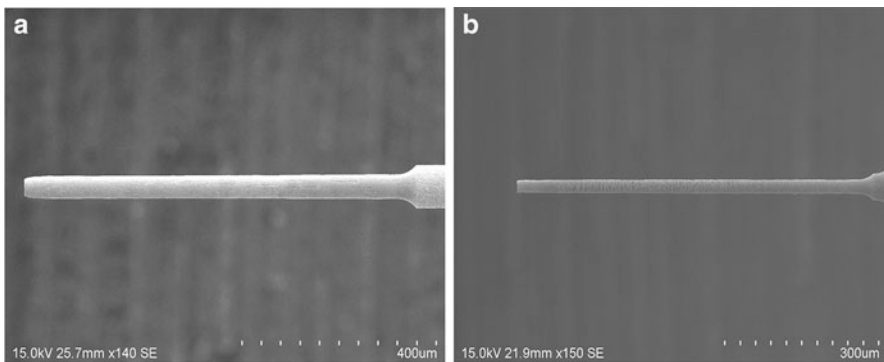


Fig. 17 Microelectrodes: (a) 50 μm diameter, (b) 23 μm diameter

rods with 300 μm diameters were used as tool electrodes. The electrodes were formed into approximately 50 μm and 23 μm diameters by the WEDG unit equipped in the experimental setup. The fabricated electrodes are shown in Fig. 17. Machining tests of high aspect ratio micro hole were then performed on RB-SiC using die-sinking EDM.

SEM micrographs of the high aspect ratio micro holes are shown in Fig. 18. An aspect ratio of 11.5 was achieved within 10 min by using 50 μm diameter tool electrode, and an aspect ratio of 21.7 micro hole was also successfully machined with the 23 μm electrode in 4 min machining time.

In order to examine the bottom surface and side wall surface integrity of high aspect ratio micro hole, the machined micro hole in Fig. 18a was dissected by a diamond cutter. Then, the sample was polished using the diamond slurry and

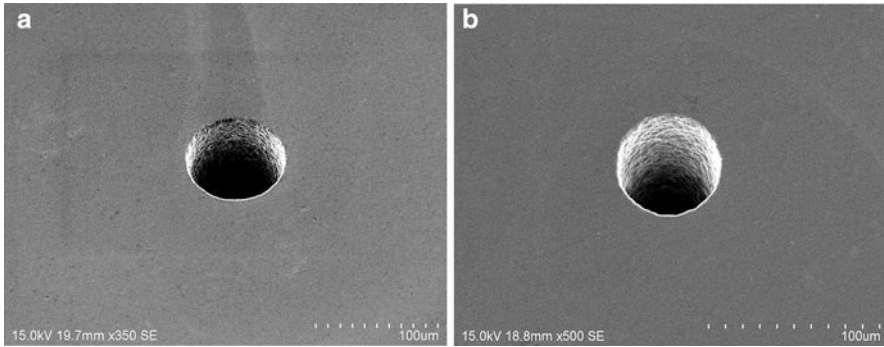


Fig. 18 High aspect ratio micro holes obtained with (a) 50 μm diameter tool electrode and (b) 23 μm diameter tool electrode

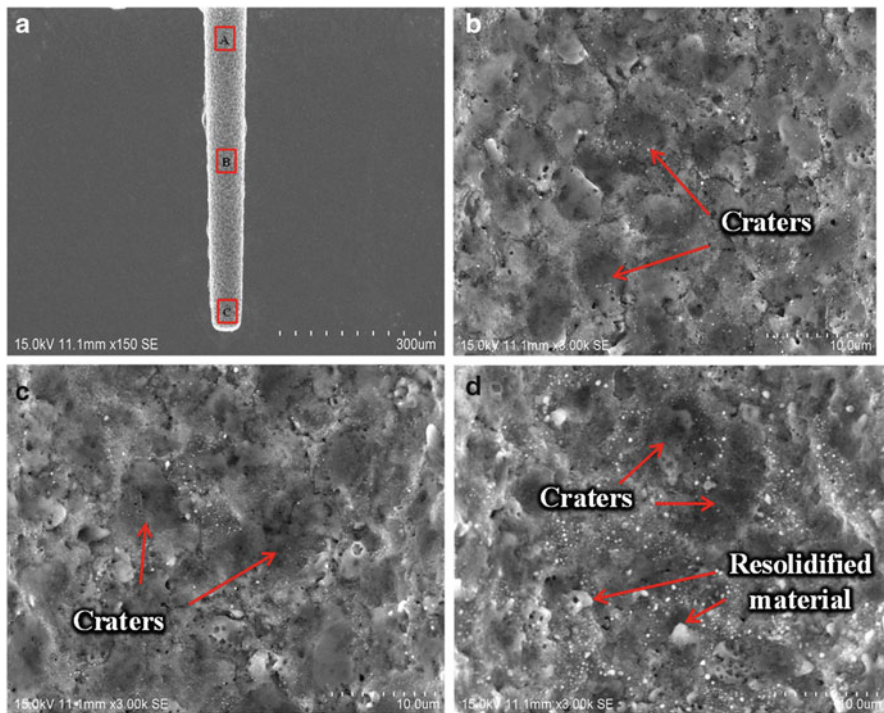


Fig. 19 SEM micrographs of (a) cross section of micro hole, (b) machined surface at zone A, (c) machined surface at zone B, (d) machined surface at zone C

subsequently observed by SEM. Figure 19a shows SEM micrograph of the cross-sectioned micro hole. It is worth noting that the bottom surface of the micro hole was flat without cone-shape protrusion even though the hole was very small and deep. Subsequently, the microstructures of the side wall of micro hole were also examined,

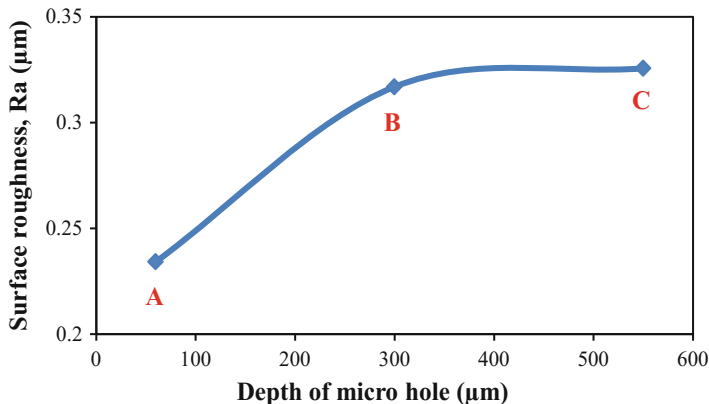


Fig. 20 Surface roughness at three locations in Fig. 19a

as shown in Fig. 19b–d. It can be seen that the side walls of micro hole were covered with overlap discharge craters and micropores which are induced by high electro-discharge energy. In addition, careful examination on the microstructures revealed that the crater sizes are increasing with the depth of the micro hole (from zone A to zone C), although this micro hole was fabricated with one parameter setting. The wall surface, especially the one in Fig. 19d, is even covered with resolidified material.

The surface roughness of hole side walls was then measured using the laser probe profilometer. The measurements were performed along the longitudinal direction at three locations as shown in Fig. 19a. Figure 20 is a plot of the change of surface roughness. It is seen that the surface roughness of the side wall increases with the depth of micro hole and the trend of which is similar to that in Fig. 19b–d. It is presumable that as the depth of micro hole increases, the debris is difficult to be flushed out, resulting in short circuit more frequently. This effect ended up with the increase of the surface roughness. On the other hand, when the hole is shallow, the debris is easily to be removed by the cavitation bubbles, leading to a better surface finish.

25.3.2.5 Fabrication of Micro Dimple Array

With the slight incline of workpiece and short fine finishing time, micro dimple array was also fabricated on RB-SiC ceramic material with the fine finishing conditions of 80 V and stray capacitance (Liew et al. 2013b). Figure 21a shows SEM micrograph of a single dimple. Figure 21b is a magnified view of the dimple surface. Clearly, the adherence of tungsten particles from electrode could be significantly suppressed by means of combination of ultrasonic cavitation and carbon nanofibers, where the amount of deposited tungsten microparticles was minimal. Good cross-sectional profile without cone-shape protrusion also can be obtained, as depicted in Fig. 21c. A measurement of surface roughness was performed across the center of the micro

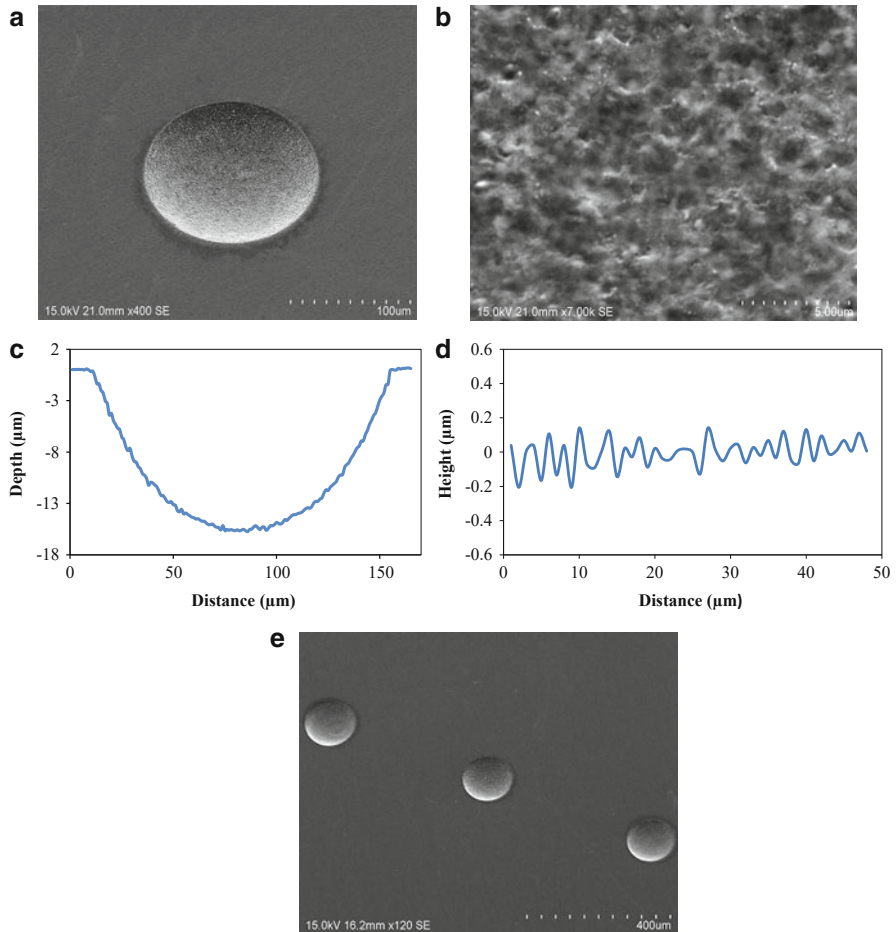


Fig. 21 Machined micro dimples obtained with hybrid process: (a) a single dimple, (b) magnified view of dimple surface, (c) cross-sectional profile of dimple, (d) surface roughness profile of dimple, and (e) dimple array (3×1)

dimple, and the evaluation length was 50 μm. The surface profile is depicted in Fig. 21d. It should be pointed out that the surface roughness of the micro dimple improved significantly, where nanometer level surface roughness (78.1 nmRa) could be obtained. Figure 21e shows SEM micrograph of a fabricated micro dimple array. These surfaces were far smoother than the one obtained without ultrasonic cavitation, as shown in Fig. 22. Without ultrasonic cavitation, tungsten electrode material was deposited on the machined surface, as depicted in Fig. 22b. The finished surface was quite rough, with a surface roughness of 0.1410 nmRa (Fig. 22c).

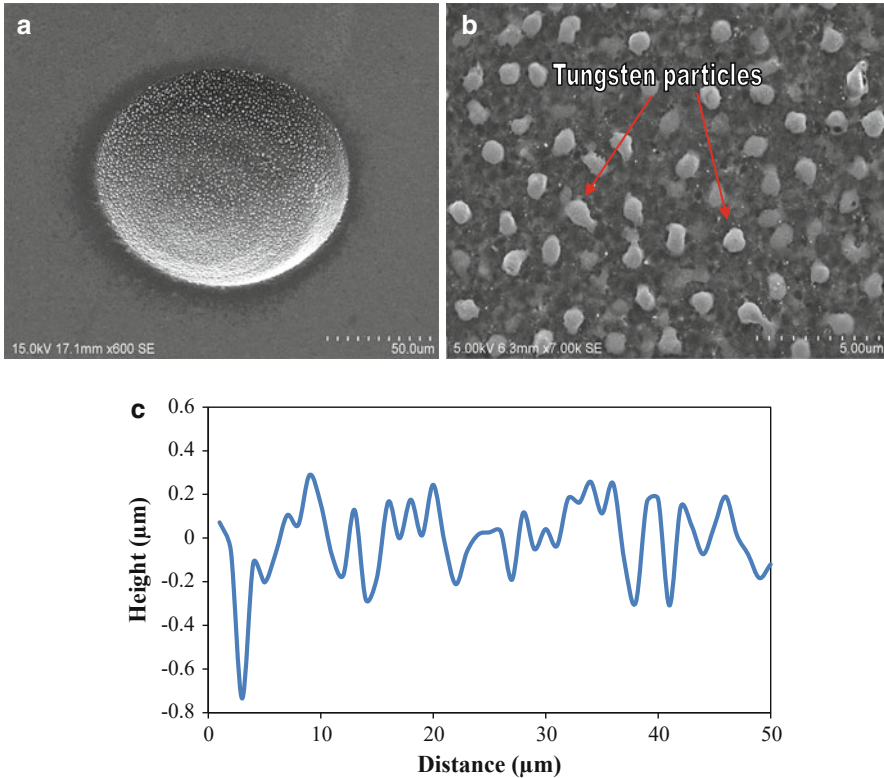


Fig. 22 Machined micro dimple without ultrasonic cavitation: (a) a single dimple, (b) magnified view of dimple surface, and (c) surface roughness profile of dimple

The proposed hybrid EDM process has been demonstrated to be useful for fabricating microstructures on hard brittle ceramic materials.

25.4 Hybrid Tool for EDM and Grinding

Single-crystal silicon carbide (SiC) is an excellent material for high-temperature and high-power electronic devices and microelectromechanical systems (MEMS). Compared to Si, SiC has higher thermal conductivity, current density, and breakdown electric field strength, as well as a broader band gap. However, owing to its hardness and brittleness, SiC is very difficult to machine (Tanaka and Shimada 2013). In this chapter, Yan and Tan (2015) attempted the EDM of SiC using sintered diamond (polycrystalline diamond, PCD) as a tool electrode. PCD is a composite of diamond grains sintered with a metallic binder such as Co. PCD is not only excellent for cutting and milling (Zhang et al. 2013; Katahira et al. 2014) but also useable as an electrode for EDM.

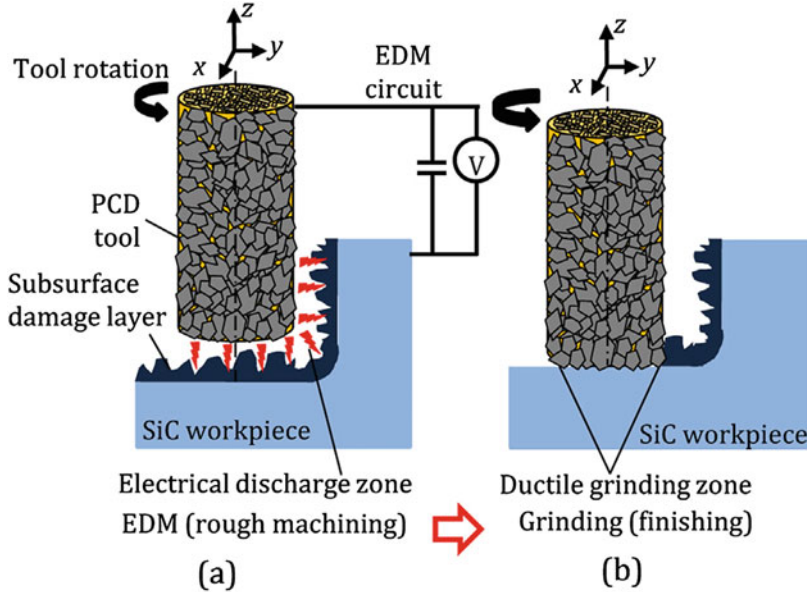


Fig. 23 Models for micromachining of SiC using a PCD hybrid tool

EDM typically creates high surface roughness and severe subsurface damage (SSD) including micro-cracks and material phase changes, as illustrated in Fig. 23a. Although the SSD layer can be removed by special polishing processes, such as plasma-assisted polishing (Yamamura et al. 2011), such polishing is very time-consuming and cannot finish three-dimensional structures or curved surfaces. Therefore, in this chapter, after EDM, the PCD electrode was used directly as a grinding wheel for finishing the EDMed surface and removing the SSD layer. Because the metallic binder in PCD is preferentially removed by electrical discharges during EDM, diamond grains protrude out of the PCD surface and act as fixed abrasive cutting edges, which remove the SSD layers efficiently through ductile mode grinding, as shown in Fig. 23b. The proposed machining process uses a single tool on a single machine and takes advantage of both the high MRR of EDM and the high surface integrity of grinding. In addition, it enables the flexible machining of three-dimensional and curved structures.

25.4.1 Experimental Methods

PCD rods with diameters of 1 mm were used as tools. It contains diamond grains with a mean size of 0.5 μm at a concentration of 90% in a Co binder. The thermal conductivity of PCD is 290 W/(m K). An n-type single-crystal 4H-SiC wafer with a surface orientation of (0 0 0 1) was used as the workpiece. The wafer was 50 mm in diameter and 0.36 mm in thickness, with a CMP finish. A micro-EDM machine (Panasonic MG-ED82 W) was used in the experiments. EDM experiments were performed at voltages of

70 and 110 V, using PCD as anode and SiC as cathode. The tool electrode's rotation rate was 3000 rpm. Both plunge grinding and mill grinding were performed using the same EDM machine and the same PCD tool. In plunge grinding, the tool feed rate in the z direction was 0.1 mm/s. In mill grinding, the depth of cut in the z direction per tool pass was 1 mm, and the tool feed rate in the y direction was set between 2.5 and 25 mm/s. The total depth of grinding was 10 mm.

25.4.2 Results of Micro-EDM

25.4.2.1 Subsurface Material Structure

Figure 24 shows cross-sectional SEM images of the EDMed surfaces. At the top of each surface, thick recast layers are clearly seen. As voltage increases from 70 to 110 V, the thickness of the recast layer increases from ~2 to ~3 μm . The results strongly demonstrate that 4H-SiC undergoes melting and resolidification during EDM, and that the local temperature in the electrical discharge zone rises above 2730 °C, the melting point of 4H-SiC.

Figure 25a shows a schematic of material removal in EDM. The high temperature generated in the electrical discharge zone (Hinduja and Kunieda 2013) causes melting and vaporization of the worked material, leaving craters on the workpiece surface. Figure 25b shows topographical changes of PCD and structural changes in SiC after EDM. Owing to the material decomposition of SiC, the workpiece undergoes surface softening. Meanwhile, the Co binder on the PCD tool surface is preferentially removed during EDM, creating chip pockets and permitting diamond grains to protrude out of the tool's surface, similar to the electrical discharge dressing of grinding wheels. These two aspects, namely, workpiece surface softening and diamond grain protrusion, are essential for the subsequent ductile mode grinding process.

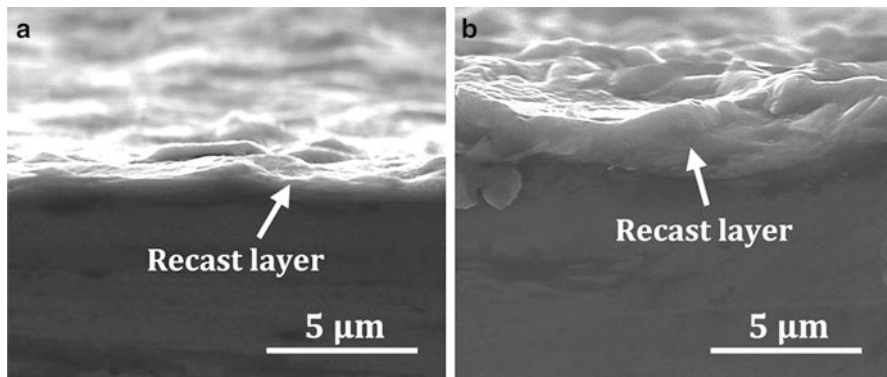
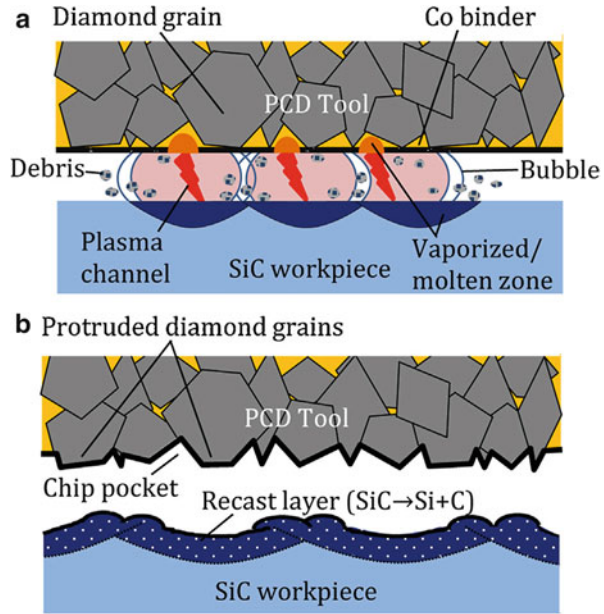


Fig. 24 Cross-sectional SEM images of EDMed surfaces at (a) 70 V and (b) 110 V, showing an increase in recast layer thickness with voltage

Fig. 25 Schematics of (a) material removal in EDM and (b) topographical and structural changes in both PCD and SiC



25.4.3 Results of Micro-grinding

25.4.3.1 Surface Topography Change

With the EDM power source switched off, the same PCD tool was used directly for plunge grinding tests in the SiC sample. A cut depth of 10 mm was defined in the z direction with no tool feed in the y direction. Figure 26 shows SEM images of the bottoms (a, c) and fringes (b, d) of two EDMed cavities. For the cavity EDMed at a voltage of 110 V (a, b), discharge craters were not completely removed by grinding, indicating that the SSD was deeper than 10 mm. For the cavity EDMed at 70 V (c, d), however, craters are barely visible, with only grinding marks evident on the surface.

25.4.3.2 Effects of Transverse Tool Feed

To eliminate the grinding marks formed via plunge grinding, as shown in Fig. 26, mill grinding was performed by traverse feeding the PCD tool in the y direction. Figure 27a is a micrograph of an EDMed micro-cavity. The surface is rough with dense discharge craters. Figure 27b shows an EDMed and then mill-ground micro-cavity at a traverse tool feed rate of 25 mm/s. The surface appears as smooth as the surrounding area finished by CMP. The time for EDM was 8.1 min and that for grinding was 7.3 min, respectively.

25.4.3.3 Comparison of Surface Roughness

Figure 28 shows a plot of surface roughness after different process steps. The surface roughness of an as-received 4H-SiC wafer with a CMP finish is also shown for

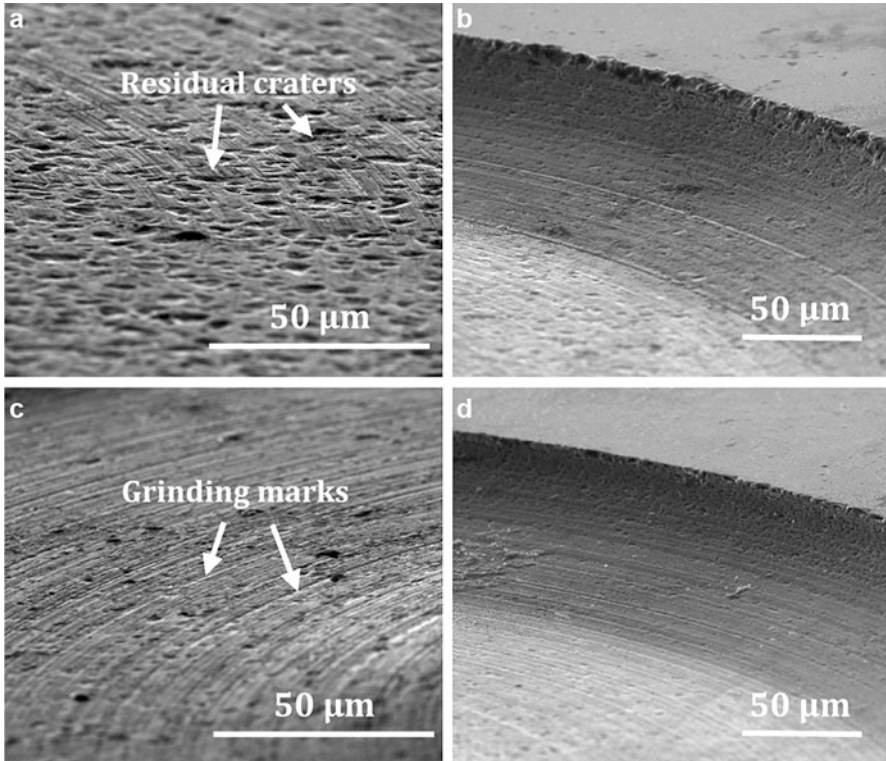


Fig. 26 SEM images of the bottoms (a, c) and fringes (b, d) of EDMed cavities after plunge grinding. The voltages used in EDM were (a, b) 110 V and (c, d) 70 V

comparison. The surface roughness R_a after EDM was 417 nm ($S_a = 439$ nm). After mill grinding, however, R_a decreased to 1.85 nm ($S_a = 2.60$ nm), a factor of 200 less than that of the EDMed surface. The surface quality resulting from the proposed process approaches is achieved by CMP, while the processing time is distinctly shorter than that of CMP.

25.5 Summary and Outlook

In this chapter, a comprehensive review on the micro-EDM of hard and brittle ceramic materials was presented. Three main methods that are commonly used to improve the machining efficiency of hard and brittle ceramic materials were powder mixed EDM, assisting electrode EDM and electrical discharge milling and mechanical grinding. Following the review, a few recently developed technologies in this area were introduced. For example, adding carbon nanofibers into the dielectric fluid can significantly improve the spark gap and material removal rate compared to that

Fig. 27 Micrographs of (a) an EDMed cavity and (b) an EDMed and then mill-ground cavity by introducing a traverse tool feed

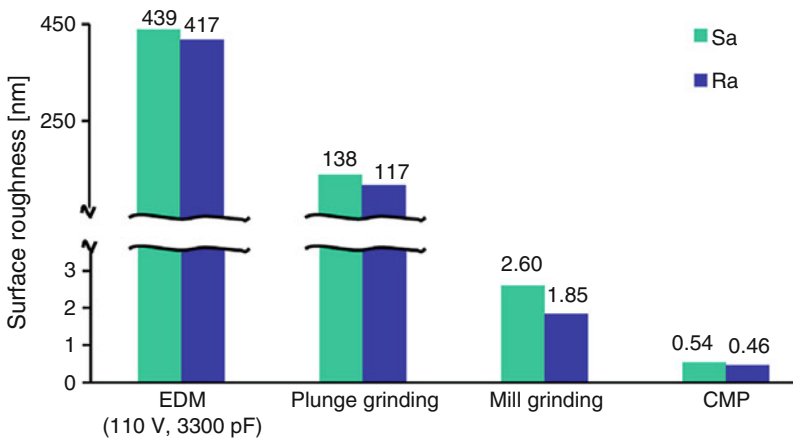
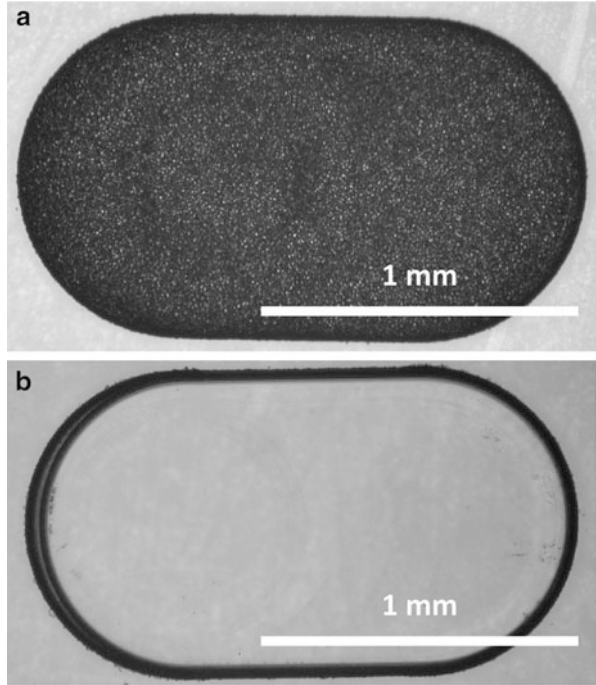


Fig. 28 Comparison of surface roughness resulting from different process steps using the PCD hybrid tool versus CMP

of spherical carbon powder. Ultrasonic cavitation assisted micro-EDM with carbon nanofibers addition in the dielectric fluid can distinctly improve the form accuracy, depth, and surface finish of the micro hole. The hybrid micro-EDM process can be applied to machine high aspect ratio micro holes and micro dimple array on hard

brittle RB-SiC ceramic material. Finally, a novel hybrid tooling technology was introduced by using sintered diamond (polycrystalline diamond, PCD) as a hybrid tool for EDM and grinding. An extremely smooth surface ($R_a = 1.85 \text{ nm}$) was obtained on single-crystal SiC after EDM using the same tool.

Micro-EDM is a promising technology that can cater to the growing demands for miniaturization in various industrial sectors. Compared to other traditional machining technologies, micro-EDM requires a low installation cost, and it can machine complex or 3D micro shapes easily. Furthermore, micro-EDM is very flexible and suitable for prototypes with high added value. Future developments in the area of micro-EDM of hard and brittle materials would be focused on the development of control algorithms and power supply, analysis of energy consumption, surface alloying/coating on complicated shapes, predictive modeling of the process, and so on. Intensive studies on these aspects would help to overcome the difficulties associated with shaping the single crystals and ceramics parts.

References

- Brennen CE (1995) Cavitation and bubble dynamics. Oxford University Press, New York
- Chow HM, Yang LD, Lin CT et al (2008) The use of SiC powder in water as dielectric for micro-slit EDM machining. *J Mater Process Technol* 195:160–170
- Chung DK, Shin HS, Park MS et al (2011) Recent researches in micro electrical machining. *Int J Precis Eng Manuf* 12(2):371–380
- Clijsters S, Liu K, Reynaerts D et al (2010) EDM technology and strategy development for the manufacturing of complex parts in SiSiC. *J Mater Process Technol* 210:631–641
- Descocudres A (2006) Characterization of electrical discharge machining plasmas. Ecole Polytechnique Federale De Lausanne PhD's Thesis
- Ekmekci B, Sayar A (2013) Debris and consequences in micro electric discharge machining of micro-holes. *Int J Mach Tool Manu* 65:58–67
- Fukuzawa Y, Mohri N, Tani T et al (2004) Electrical discharge machining properties of noble crystals. *J Mater Process Technol* 149:393–397
- Fukuzawa Y, Mohri N, Gotoh H et al (2009) Three-dimensional machining of insulating ceramics materials with electrical discharge machining. *Trans Nonferrous Met Soc China* 19:s150–s156
- Gotoh H, Tani T, Mohri N (2016) EDM of insulating ceramics by electrical conductive surface layer control. *Procedia CIRP* 42:201–205
- Gunawan SP, Mahardika M, Hamdi M et al (2009) Effect of micro-powder suspension and ultrasonic vibration of dielectric fluid in micro-EDM processes-Taguchi approach. *Int J Mach Tool Manu* 49:1035–1041
- Gunawan SP, Muslim M, Hamdi M et al (2011) Accuracy improvement in nanographite powder-suspension dielectric fluid for micro-electrical discharge machining process. *Int J Adv Manuf Technol* 56:143–149
- Hinduja S, Kunieda M (2013) Modelling of ECM and EDM processes. *CIRP Ann* 62(2):775–797
- Ho KH, Newman ST (2003) State of the art electrical discharge machining (EDM). *Int J Mach Tool Manu* 43:1287–1300
- Hung JC, Lin JK, Yan BH et al (2006) Using a helical micro-tool in micro-EDM combined with ultrasonic vibration for micro-hole machining. *J Micromech Microeng* 16:2705–2713
- Jahan M, Rahman M, Wong YS (2010a) Modelling and experimental investigation on the effect of nanopowder-mixed dielectric in micro-electrodischarge machining of tungsten carbide. *Proc Inst Mech Eng B* 224(11):1725–1739

- Jahan M, Rahman M, Wong YS (2010b) Study on the nano-powder-mixed sinking and milling micro-EDM of WC-Co. *Int J Adv Manuf Technol* 53:167–180
- Ji R, Liu Y, Zhang Y et al (2010) Machining performance and surface integrity of SiC ceramic machined using electrical discharge milling and the mechanical grinding compound process. *Proc Inst Mech Eng B* 224:1511–1518
- Ji R, Liu Y, Zhang Y et al (2011) Machining performance of silicon carbide ceramic in end electric discharge milling. *Int J Refract Met Hard Mater* 29:117–122
- Kalpakjian S, Schmid SR (2001) *Manufacturing engineering and technology*, 4th edn. Prentice-Hall, Upper Saddle River, Pearson Publisher, New Jersey
- Kansal HK, Singh S, Kumar P (2007) Effect of silicon powder mixed EDM on machining rate of AISI D2 die steel. *J Manuf Process* 9(1):13–22
- Katahira K, Takesue S, Komotori J et al (2014) Micromilling characteristics and electrochemically assisted reconditioning of polycrystalline diamond tool surfaces for ultra-precision machining of high-purity SiC. *CIRP Ann* 63(1):329–332
- Konig W, Dauw DF, Levy G et al (1988) EDM-future steps towards the machining of ceramics. *CIRP Ann* 37(2):623–631
- Kumar S, Brennen CE (1991) Nonlinear effects in the dynamics of clouds of bubbles. *J Acoust Soc Am* 89:707–714
- Lee S, Scarpulla MA, Bamberg E (2013) Effect of metal coating on machining of high purity germanium using wire electrical discharge machining. *J Mater Process Technol* 213:811–817
- Liew PJ, Yan J, Kuriyagawa T (2013a) Carbon nanofiber assisted micro electro discharge machining of reaction-bonded silicon carbide. *J Mater Process Technol* 213(7):1076–1087
- Liew PJ, Shimada K, Mizutani M et al (2013b) Fabrication of microstructures on RB-SiC by ultrasonic cavitation assisted micro-electrical discharge machining. *Int J Automot Technol* 7(6):621–629
- Liew PJ, Yan J, Kuriyagawa T (2014) Fabrication of deep micro-holes in reaction-bonded SiC by ultrasonic cavitation assisted micro-EDM. *Int J Mach Tool Manu* 76:13–20
- Liu Y, Ji R, Li Q et al (2008) Electrical discharge milling of silicon carbide ceramic with high electrical resistivity. *Int J Mach Tools Manuf* 48:1504–1508
- Liu Y, Ji R, Li Q et al (2009) An experimental investigation for electric discharge milling of SiC ceramics with high electrical resistivity. *J Alloys Compd* 472:406–410
- Masuzawa T (2000) State of the art of micromachining. *CIRP Ann* 49:473–488
- Masuzawa T, Fujino M, Kobayashi K et al (1985) Wire electro-discharge grinding for micro-machining. *CIRP Ann* 34(1):431–434
- Mohri N, Fukuzawa Y, Tani T et al (1996) Assisting electrode method for machining insulating ceramics. *CIRP Ann* 45(1):201–204
- Morgan CJ (2004) *Micro electro-discharge machining: techniques and procedures for micro fabrication*. Master's thesis, University of Kentucky
- Muttamara A, Fukuzawa Y, Mohri N et al (2003) Probability of precision micro-machining of insulating Si₃N₄ ceramics by EDM. *J Mater Process Technol* 140:243–247
- Muttamara A, Fukuzawa Y, Mohri N et al (2009) Effect of electrode material on electrical discharge machining of alumina. *J Mater Process Technol* 209:2545–2552
- Pham DT, Dimov SS, Bigot S et al (2004) Micro-EDM-recent developments and research issues. *J Mater Process Technol* 149:50–57
- Puertas I, Luis CJ (2004) A study on the electrical discharge machining of conductive ceramics. *J Mater Process Technol* 153-154:1033–1038
- Reynaerts D, Meeusen W, Brussel HV (1998) Machining of three-dimensional microstructures in silicon by electro-discharge machining. *Sensor Actuator A* 67:159–165
- Sabur A, Ali MY, Maleque MA et al (2013) Investigation of material removal characteristics in EDM of nonconductive ZrO₂ ceramic. *Procedia Eng* 56:696–701
- Schumacher BM (2004) After 60 years of EDM the discharge process remains still disputed. *J Mater Process Technol* 149:376–381
- Suslick KS (1989) The chemical effects of ultrasound. *Sci Am* 260:80–86
- Tanaka H, Shimada S (2013) Damage-free machining of monocrystalline silicon carbide. *CIRP Ann* 62(1):55–58

- Tani T, Fukuzawa Y, Nanbu K, Mohri N (2002) Machining phenomena in EDM of insulating ceramics with powder mixed oil. *J Jpn Soc Elec Mach Eng* 36(81):39–46
- Tani T, Fukuzawa Y, Mohri N, Saito N, Okada M (2004) Machining phenomena in WEDM of insulating ceramics. *J Mater Process Technol* 149(1–3):124–128
- Wang J, Han F, Cheng G, Zhao F (2012) Debris and bubble movements during electrical discharge machining. *Int J Mach Tools Manuf* 58:11–18
- Yamamura K, Takiguchi T, Ueda M et al (2011) Plasma assisted polishing of single crystal SiC for obtaining atomically flat strain-free surface. *CIRP Ann* 60(1):571–574
- Yan J, Tan TH (2015) Sintered diamond as a hybrid EDM and grinding tool for the micromachining of single-crystal SiC. *CIRP Ann Manuf Technol* 64:221–224
- Yeo SH, Tan PC, Kurnia W (2007) Effects of powder additives suspended in dielectric on crater characteristics for micro electrical discharge machining. *J Micromech Microeng* 17:N91–N98
- Yi SM, Park MS, Lee YS et al (2008) Fabrication of a stainless steel shadow mask using batch mode micro-EDM. *Microsyst Technol* 14(3):411–417
- Yu ZY, Zhang Y, Li J et al (2009) High aspect ratio micro-hole drilling aided with ultrasonic vibration and planetary movement of electrode by micro-EDM. *CIRP Ann Manuf Technol* 58:213–216
- Zahiruddin M, Kunieda M (2012) Comparison of energy and removal efficiencies between micro and macro EDM. *CIRP Ann – Manuf Technol* 61:187–190
- Zhang Z, Peng H, Yan J (2013) Micro-cutting characteristics of EDM fabricated high-precision polycrystalline diamond tools. *Int J Mach Tools Manuf* 65:99–106



Wataru Natsu

Contents

26.1	Introduction	808
26.2	Outline and Features of Electrochemical Machining	809
26.2.1	Outline of Electrochemical Machining	809
26.2.2	Feature of Electrochemical Machining	810
26.3	Mechanism of Anodic Dissolution and Simplified ECM Physical Model	812
26.3.1	Formation of Electrical Double Layer and Mechanism of Anodic Dissolution	812
26.3.2	Simplified ECM Physical Model and the Machining Rate	813
26.4	Micro ECM with Ultrashort Pulse	815
26.4.1	Principle of Micro ECM with Ultrashort Pulse (Schuster et al. 2000)	815
26.4.2	Examples of Micro ECM with Ultrashort Pulse	817
26.4.3	Micro ECM Using Electrostatic Induction Feeding Method	821
26.5	Micro Wire ECM	823
26.5.1	Surface Finishing with Bipolar Pulse	823
26.5.2	Multi-Wire ECM	824
26.5.3	Enhancement of Mass Transport in Wire ECM	825
26.5.4	Measures to Eliminate Tool Wear in Wire ECM	828
26.6	Electrolyte Jet Machining	828
26.6.1	Principle and Machining System of Electrolyte Jet Machining	828
26.6.2	Applications	831
26.6.3	Characteristics of Pit and Groove Machining	834
26.7	Generating Complicated Shapes by Superimposing Simple Patterns with Electrolyte Jet Machining	837
26.7.1	Calculating Shape of Elemental Curved Groove	839
26.7.2	Shape Generation by Superimposing Elemental Curved Grooves	844
26.7.3	Generation of Spherical Surface	847
26.8	Summary and Outlook	852
	References	853

W. Natsu (✉)

Tokyo University of Agriculture and Technology, Koganei City, Tokyo, Japan

e-mail: summer@cc.tuat.ac.jp

Abstract

Electrochemical machining (ECM) is a machining method with a long history, especially applied in parts manufacturing in airplane and automobile industries. Although the advantages of ECM are very clear and attractive compared to other machining methods, its lower machining accuracy and bad environmental impact hindered the expansion of its application. Due to realization of micro ECM by using ultrashort voltage pulse with a width of several tens of nanoseconds, reported in 2000, electrochemical machining came to be noted again. In addition, other new technologies such as ECM by vibrating tool electrode and detoxification of electrolytic waste were developed for industrial application. In this chapter, after the outline and features of electrochemical machining is explained, the mechanism of anodic dissolution and ECM model are briefly introduced. Then, some up-to-date ECM researches and technologies, especially in micro ECM with ultrashort pulse and wire ECM, and electrolyte jet machining are introduced. After the explanation of the principle and method to generate complicated shapes by superimposing simple patterns with electrolyte jet machining, the outlook and vision of ECM technologies in future are described.

Keywords

Electrochemical machining · ECM · Micro machining · Anodic dissolution · Electrolyte

26.1 Introduction

Electrochemical machining (ECM) is a machining method which applies the principle of electrochemistry to the industrial application with a long history. ECM is mainly aimed at obtaining desired shapes and sizes by concentrating and limiting the electrochemical dissolution on a desired portion of the anode workpiece. Besides removal process with electrochemical machining, electroplating, electroforming, and electrolytic polishing are other main applications.

As will be explained in this chapter, both the advantages and drawbacks of ECM are very obvious. The most attractive feature of ECM which differs from other methods is that a high machining rate and superfine surface quality can be realized at the same time, without tool wear. Meanwhile, the poor machining accuracy and unstable machining process are the main drawbacks which hinder its application expansion in industries. The poor machining accuracy and unstable process are mainly caused by the large inter-electrode distance and the change in the current density spatially and temporally over the workpiece surface due to the flow of heat, bubbles, and other by-products with the electrolyte. Therefore, the machining conditions for specific parts are usually obtained from a large amount of trial and error and difficult to apply to other parts. If high machining accuracy and stable process can be easily realized, the ECM will be surely utilized more.

In order to understand the features and up-to-date technologies of electrochemical machining, especially in the micromachining area, the outline and features of

electrochemical machining, the mechanism of anodic dissolution, and ECM model will be briefly introduced. Then, some up-to-date ECM researches and technologies, especially micro ECM with ultrashort pulse and wire ECM, and electrolyte jet machining are introduced. At last, the principle and method to generate complicated shapes by superimposing simple patterns with electrolyte jet machining is explained.

26.2 Outline and Features of Electrochemical Machining

26.2.1 Outline of Electrochemical Machining

In ECM, two pieces of metal are immersed separately in the electrolyte and connected to a power supply as shown in Fig. 1. If the voltage is high enough, the valence electrons shared by all of the atoms of anode will detach from their original atomic owners and flow toward the positive pole of power supply, and the metal atoms become positive ions. The dissolution of positive ions into the electrolyte realizes the anode material removal. Also, various chemical reactions such as generation of hydrogen gas occur on the surface of the cathode surface.

A typical configuration of the system is shown in Fig. 2. Electrochemical machining possesses an attractive feature different from other machining methods that the higher the current density is, the higher the machining speed and the machining accuracy, the smoother and finer surface will be. Therefore, the following processing conditions (Sato 1970; Wilson 1971) are generally used to increase the productivity of shape forming, as well as other machining characteristics. The applied voltage is set to 5–20 V, to ensure a corresponding current density of 30–200 A/cm². The inter-electrode distance between the tool electrode (cathode) and the workpiece (anode) is set to 0.02–0.7 mm. In order to remove the large amount of machined by-products including heat, and gas generated in the

Fig. 1 Schematic of electrochemical machining

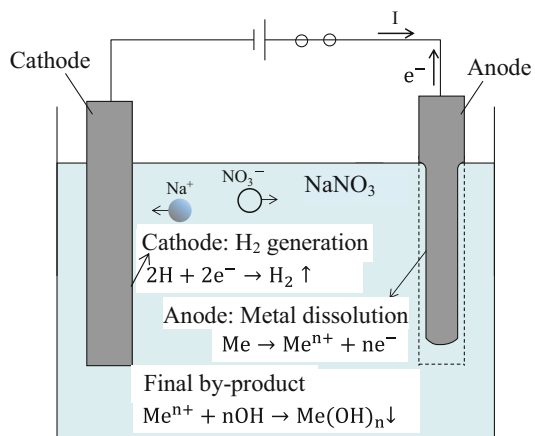


Fig. 2 Typical ECM machining system

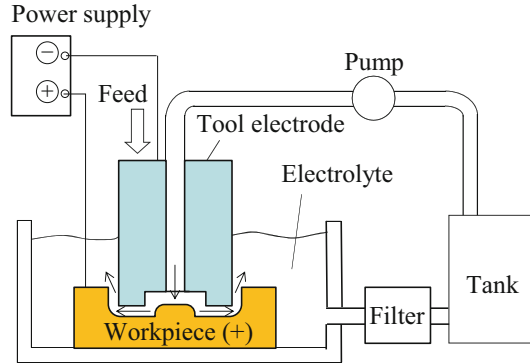
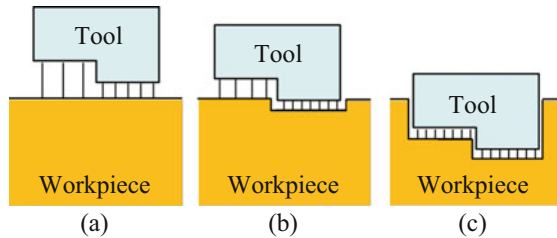


Fig. 3 Process of shape transfer in ECM



The vertical line in the gap is the image of the machining current, and the magnitude of the current density is represented by the density of vertical lines.

inter-electrode area, electrolyte flows at a flow rate of 6–60 m/s through the gap area under a high pressure.

Figure 3 shows the shape transfer process in ECM. Although the machining current flows over the entire surface of the workpiece facing the tool electrode, the current density is higher at the portion where the inter-electrode distance is shorter. Therefore, the removal amount at that portion becomes larger. By feeding the tool electrode with the progress of machining, the current density finally becomes uniform over the entire machined surface, and the shape of the tool is thus transferred to the workpiece.

26.2.2 Feature of Electrochemical Machining

The advantages of electrochemical machining are extremely attractive, although the weak points and limitation of the machining method are also very obvious. The features of ECM are listed in Table 1. The high productivity and excellent surface quality without tool wear are its most attractive features. Meanwhile, there is another nontraditional machining method, electrical discharge machining (EDM), which is usually compared with ECM. Although ECM and EDM have the same features at the viewpoints of non-contact between the tool and the workpiece, and machinability for difficult-to-cut materials, their machining principles are totally different. The

Table 1 Advantages and disadvantages of electrochemical machining

Advantages of ECM	Disadvantages of ECM
<ul style="list-style-type: none"> • Extremely high material removal rate compared to electrical discharge machining, since the removal rate is determined by the applied current which flows over the whole workpiece surface • Excellent surface quality, especially under high current and high machining rate, which is quite different from other machining methods • Suitable for difficult-to-cut materials, because the workpiece is removed by the anodic dissolution regardless of the mechanical property of the metallic material • Potential for micro- and nanomachining, because the removal of material is in an atom unit • No tool wear, since there is no dissolution that occurs on the cathode (tool electrode) surface • No heat-affected zone on the workpiece surface, as seen in thermal machining methods like electrical discharge machining and laser beam machining, because electrochemical machining is a chemical machining method • No residual stresses and cracks on the surface which are typically generated by mechanical machining, because there is no force exerting to the surface due to non-contact between tool and workpiece 	<ul style="list-style-type: none"> • Poor machining accuracy • Unstable machining process • Difficult to detect and control the inter-electrode distance • Only metallic materials can be machined • Possible environmental hazards caused by the used electrolyte containing electrolytic by-products • Corrosion resistance measures of the surrounding machine are necessary

Table 2 Main differences in electrochemical machining and electrical discharge machining

	ECM	EDM
Removal mechanism	Electrochemical machining (dissolution from anode surface due to electrochemical reaction)	Thermal machining (melt and evaporation of material by heat caused by discharges)
Working fluid	Electrolyte with ion conductive property (solution such as NaCl and NaNO ₃)	Superhigh isolating fluid or gas (oil, deionized water, and air)
Processing power supply	Direct current or pulse	Pulse
Area where machining current flows	The machining current flows through all area touched with electrolyte, and anodic dissolution occurs. The machining energy is dispersed	The dielectric breakdown takes at one location; the discharging current concentrates flow in the arc column with a very small diameter. The machining energy is concentrated

main differences in the mechanism and machining characteristics between these two methods are summarized in Tables 2 and 3 for comparison.

For detailed and systematic ECM theories, the following references are recommended: *Electrochemical Machining and Chemical Machining*, written by

Table 3 Machining characteristics of ECM and EDM

	Electrochemical machining	Electrical discharge machining
Productivity	High	Low
Machining accuracy	Low	High
Surface quality	Super fine	Fine
Tool electrode wear	No wear	Wear
Stability of machining process	Unstable	Stable
Machinable material	Metal materials	Conductive materials and some insulating materials
Electrode design	Time-consuming	Simple
Waste treatment	Complicated and costly	Easy

K. Sato and published by Asakura Publishing Co., Ltd. in 1970 (in Japanese); *Practice and Theory of Electrochemical Machining*, written by J.F. Wilson and published by John Wiley & Sons, Inc. in 1971; *Principles of Electrochemical Machining*, written by J.A. McGeough and published by Chapman & Hall, London, in 1974; and *Electrochemical Systems*, Third edition, written by J. Newman and K.E. Thomas-Alyea and published by John Wiley & Sons, Inc. in 2004.

Due to its high productivity and excellent surface quality, electrochemical machining cannot only be applied in die and mold manufacturing but also in mass production of parts manufacturing in all industrial fields such as the aircraft, automobile, and medical equipment. ECM is especially suitable for manufacturing parts made of difficult-to-cut materials and with complex shape and high surface quality, like turbine blades for aircraft engines.

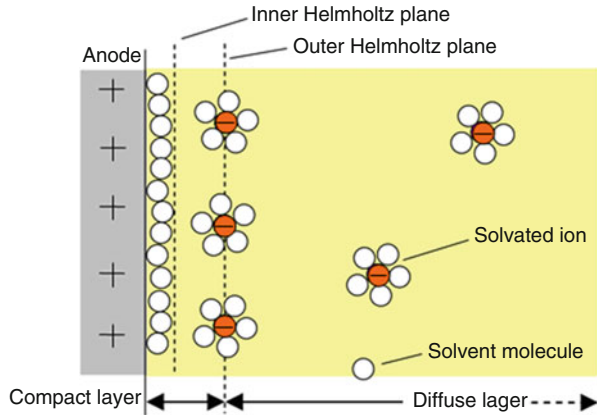
Because of the above weak points, electrochemical machining is conventionally considered not suitable for micromachining, because the machining current follows and dissolution occurs even in the area where the inter-electrode distance is larger than 0.5 mm. However, these years' innovative methods have been proposed to control the inter-electrode distance can be controlled smaller than 1 μm with ultrashort voltage pulses. Thus, the micro ECM becomes possible, and the advantages of ECM of excellent surface quality with no tool wear can be utilized in the field of micromachining.

26.3 Mechanism of Anodic Dissolution and Simplified ECM Physical Model

26.3.1 Formation of Electrical Double Layer and Mechanism of Anodic Dissolution

The electrical double layer formed at the electrode/electrolyte interface plays the key role in the anodic dissolution of electrochemical machining. When a voltage is applied between the cathode (tool electrode) and the anode (workpiece) which are

Fig. 4 Electrical double layer on electrode/electrolyte interface



immersed in the electrolyte, an electrical double layer consisting of the compact layer and the diffuse layer forms on the anode/electrolyte and cathode/electrolyte interfaces (see Fig. 4). Since the thickness of the Helmholtz layer is as thin as about several times the diameter of solvent molecules, a very strong electric field forms on the interface. If the electric field intensity is sufficiently strong, electrons are extracted from the metal atoms on the surface of the anode, and the positive ion dissolves into electrolyte. Thus, the anodic dissolution and material removal occur.

Since the time period of formation of the electrical double layer is ultrashort at the order of ns, in the conventional ECM with a direct current power source which supplies a constant voltage, or a pulse power source which supplies a pulsed voltage with the width in millisecond order, the machining phenomenon is almost carried out under the condition of complete formation of the electrical double layer. That is to say, the influence of the transient state of the electrical double layer is negligible and no need to take it into consideration.

26.3.2 Simplified ECM Physical Model and the Machining Rate

The basis of electrochemical machining is Faraday's laws of electrolysis which are quantitative relationships based on the electrochemical researches published by Michael Faraday in 1834. Since electrolysis is a phenomenon caused by the exchange of electrons, the amount of substances dissolving from the anode surface and the amount of substances depositing, or the amount of gas generating on the cathode surface, are determined by the valence of ions related to the transfer of electrons and the supplied electricity quantity. The ECM removal rate is directly influenced by the current density over the anode surface, because the dissolution occurs on the anode surface.

After the electrical double layer completely forms, that means the transient non-Faraday current flowing for charging the electrical double layer can be ignored, the ECM removal rate is directly determined by the density of electrolytic current

(Faraday current) on the anode surface. The way to calculate the current density and the removal rate is as follows.

It is believed that the current in a solution relates to the net flux of the charged species. Therefore, the current density i in the electrolyte can be calculated as (Newman and Thomas-Alyea 2004):

$$i = F \sum_i z_i N_i \quad (1)$$

where F is Faraday's constant, z_i is the charge number of the i th species, and N_i is the flux density of the i th species.

Since the ion movement in the electrolyte is the sum of the migration, diffusion, and convection effects, N_i can be defined as (Newman and Thomas-Alyea 2004):

$$N_i = -D_i \nabla c_i + c_i u - z_i m_i F c_i \nabla \varphi_l \quad (2)$$

where D_i is the diffusion coefficient of the i th species, c_i is the concentration of the i th species, u is the velocity vector of the electrolyte, m_i is the mobility of the i th species, and φ_l is the electric potential. In Equation (2), $-D_i \nabla c_i$ indicates the ion movement in response to the concentration gradients, i.e., the diffusion effect; $c_i u$ indicates the ion movement in response to the bulk fluid motion, i.e., the convection effect; and $-z_i m_i F c_i \nabla \varphi_l$ indicates the ion movement in response to the electric field, i.e., the migration effect.

Also, the equation for the electroneutrality condition is given by (Hinduja and Kunieda 2013):

$$\sum_i z_i c_i = 0 \quad (3)$$

In the case that the electrolyte in the machining area is continuously refreshed with the electrolyte flow, the concentration gradient term can be ignored and the above equations reduce to Laplace's equation (Hinduja and Kunieda 2013):

$$i = - \left(F^2 \sum_i (z_i)^2 m_i c_i \right) \nabla \varphi_l = -K_e \nabla \varphi_l \quad (4)$$

where K_e is the electrical conductivity.

It is generally known that the driving force for the chemical reaction on the workpiece electrode is the surface overpotential η_s , which is the difference between the electrode potential φ_s and the electrolyte potential φ_l near the electrode (Low et al. 2007):

$$\eta_s = \varphi_s - \varphi_l \quad (5)$$

The rate of reaction, i.e., the local current density on the surface of the electrode, can be adequately expressed by the surface overpotential with Butler-Volmer equation (Vijayasekaran and Basha 2005; Scott 1991):

$$i = i_0 \left(\exp\left(\frac{\alpha_a F}{RT} \eta_s\right) - \exp\left(-\frac{\alpha_c F}{RT} \eta_s\right) \right) \quad (6)$$

where i_0 is the exchange current density, α_a and α_c are the apparent transfer coefficients, T is the temperature, and R is the universal gas constant.

Once the local current density distribution is determined, the machining rate V_d on the workpiece surface can be derived using Faraday's law:

$$V_d = -Mi/zF\rho \quad (7)$$

where M is the molar mass, z is the charge number, and ρ is the density of the workpiece material.

26.4 Micro ECM with Ultrashort Pulse

Microstructures of metal play a very important role in the industrial field because of its desirable properties. For 3D micromachining of hard metals, various manufacturing processes have been developed, such as milling, laser machining, electrical discharge machining (EDM), electrochemical machining (ECM), and so on. Although micro mechanical milling can be used to machine microstructures at a high speed and low cost, the micro cutting tool is easily broken during the tool preparing process and the milling process. Moreover, post-processes are required to remove burrs. Micro EDM can machine micro-holes and 3D microstructures made of conductive materials, regardless of their mechanical properties. However, the amount of electrode wear should be predicted and compensated for (Yu et al. 1998) because of tool wear. In addition, heat-affected zone is formed on the machined surface and degrades the surface qualities in the case of heat processes like EDM and laser machining. On the other hand, electrochemical machining can be used to generate high quality and complicated surface of the metallic workpiece without mechanical stress, heat-affected zone, and tool wear. However, ECM is conventionally considered not suitable for micromachining due to its inter-electrode distance in the order of millimeter, until Schuster et al. (2000) reported that the inter-electrode distance can be limited to a few micrometers by applying ultrashort pulses of nanosecond duration.

26.4.1 Principle of Micro ECM with Ultrashort Pulse (Schuster et al. 2000)

As explained in Sect. 3.1 that the electrical double layer (EDL, or DL) in the electrode/electrolyte interface forms as a voltage step is applied between the electrodes immersed in electrolyte. This electrical double layer can be handled as a capacitor that accumulates electric charges, and its capacity is called electrical

Fig. 5 Equivalent circuit of electrochemical machining. (Bard and Faulkner 2001)

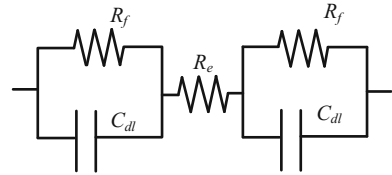
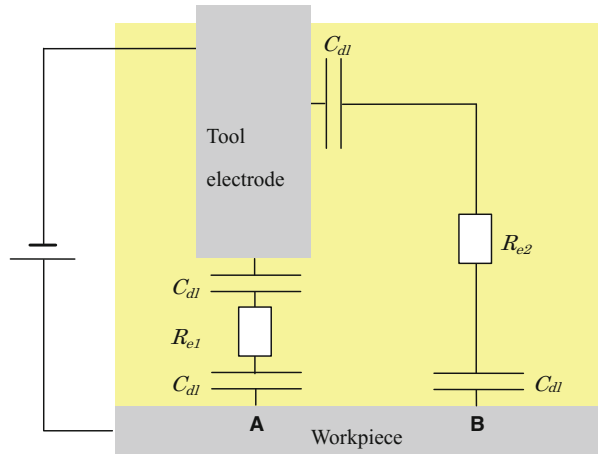


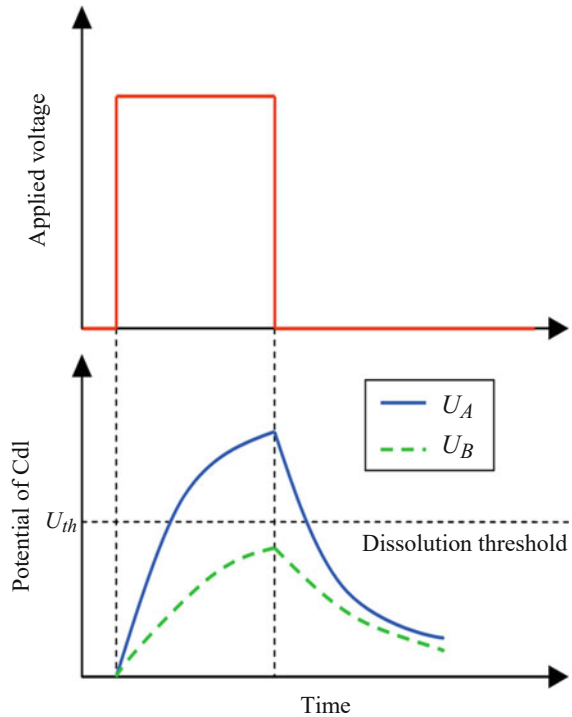
Fig. 6 Simplified ECM equivalent circuit. (Schuster et al. 2000)



double-layer capacity. The electrochemical machining phenomenon including the charging of the double layer and the machining can be represented by an equivalent circuit (Bard and Faulkner 2001) shown in Fig. 5. When considering the influence of the double-layer formation, a simplified ECM equivalent circuit can be illustrated in Fig. 6 (Schuster et al. 2000). In the circuits, C_{dl} represents the double-layer capacity, and R_e represents electrolyte resistance. When a voltage step is applied, charge of double-layer capacity takes place. The charging current has to flow through the electrolyte, whose resistance R_e is proportional to the length of the current path, that is, the inter-electrode distance. In Fig. 6, point A represents the machining position with a shorter distance to the tool electrode, while point B represents the machining position with a longer distance. The temporal change in voltage across the double layer can be expressed with Eq. (8) and Fig. 7. It can be found from Eq. (8) and Fig. 7 that the potential U_A increases faster than the potential U_B , due to different electrolyte paths. In ECM, the dissolution phenomenon on the anode surface occurs after the potential on the double layer reaches a threshold U_{th} . If the application of voltage is shut down in a very short period, like several ns, the potential on the point B will not reach the threshold U_{th} ; thus no material will dissolve at location B, and controlling the dissolution in a narrow inter-electrode distance is realized.

$$U(t) = \frac{1}{2} U_0 \left(1 - e^{-\frac{t}{R_e C_{dl}}} \right) \tag{8}$$

Fig. 7 Temporal change in voltage across the electric double layer



26.4.2 Examples of Micro ECM with Ultrashort Pulse

3D micro ECM milling of microstructures was firstly proposed and achieved by Schuster et al. (2000) from Fritz-Haber Institute of Germany. Figure 8 shows two typical microstructures fabricated in Cu. By using a Pt cylinder tool with 10 μm in diameter, the delicate Cu prism was machined by the following steps: Firstly, the tool was etched vertically, 12 μm deep into the workpiece. Then, after “drilling” this vertical hole, the tool was moved laterally along a rectangular path in the Cu sheet like a miniature milling cutter. Then the outer rectangular trough was etched with a total depth of 22 μm (Fig. 8a). The fabrication of a very thin Cu tongue (2.5 $\mu\text{m} \times 10 \mu\text{m} \times 15 \mu\text{m}$) was realized in a similar manner (Fig. 8b) (Schuster et al. 2000). Figure 9 shows another two examples of microstructures etched into a stainless steel sheet using micro ECM milling, in which the electrolyte of 3 M HCl/6 M HF was utilized (Cagnon et al. 2003).

Researchers from Seoul National University developed a micro ECM milling process for machining microstructures in stainless steel utilizing a dilute and less toxic electrolyte of 0.1 M H_2SO_4 (Kim et al. 2005a, b; Park et al. 2006; Park et al. 2004). The formation of a passive layer was successfully prevented by applying the balance electrode to control the potential drop between the electrodes and the electrolyte (Kim et al. 2005a, b), and the bubble generation and boiling were also minimized to avoid the possible vibration of micro tool electrode. The effects of tool

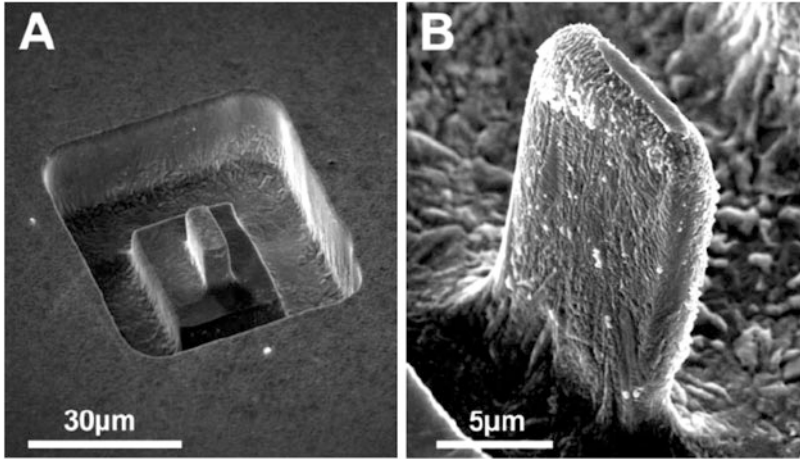


Fig. 8 (a) Cu small prism (5 μm by 10 μm by 12 μm) and (b) Cu tongue with a thickness of 2.5 μm machined with 2 MHz, 50 ns, -1.6 V pulses in 0.01 M HClO_4 and 0.1 M CuSO_4 . (Schuster et al. 2000)

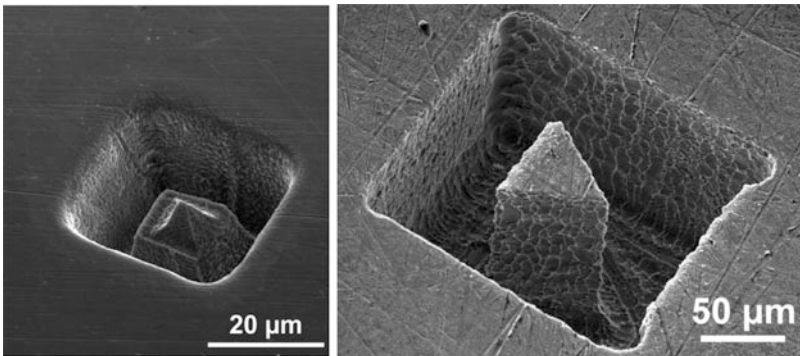


Fig. 9 Microstructures of pyramid and prism etched into a stainless steel sheet with micro ECM milling. (Cagnon et al. 2003)

electrode size on characteristics of micro ECM were investigated. It was found that as the tool area increases, the electrical double-layer capacitance increases and the electrolyte resistance decreases. As a result, the rising time of the double-layer potential increases, and it is more difficult to obtain effective machining potential within the ultrashort pulse duration. Therefore, the tool electrode size and insulation are very important for machining high aspect ratio structures (Park et al. 2006). Various microstructures, including microgrooves, micro hemisphere on the top of a cylinder, micro cylinder, etc., with very smooth surface on 304SS, were fabricated in their work, as shown in Fig. 10.

To reduce the taper of the side wall of microstructures, the disk-type electrode was introduced. Figure 11 depicts the principle of this measure. The disk-type

Fig. 10 Micro hemisphere with 60 μm (304 SS, 6 V, 60 ns pulse on-time, 1 μs period) (Kim et al. 2005b)

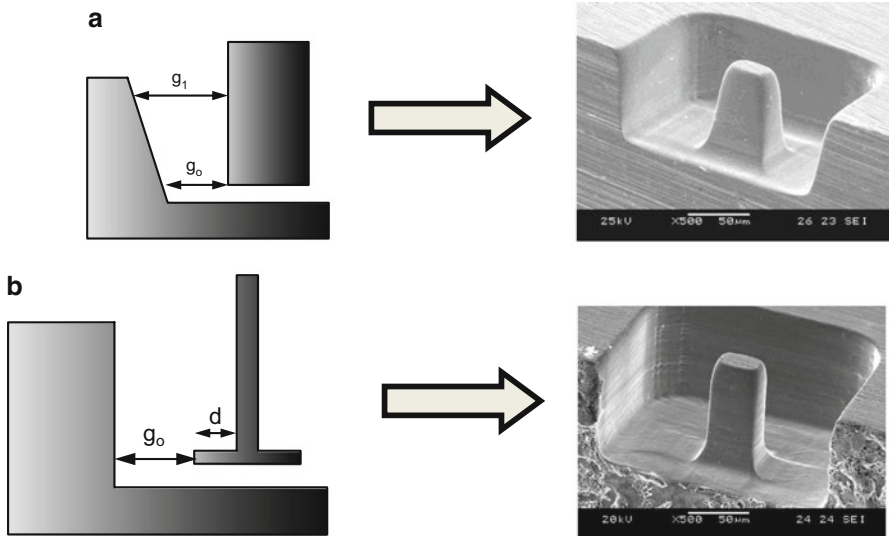
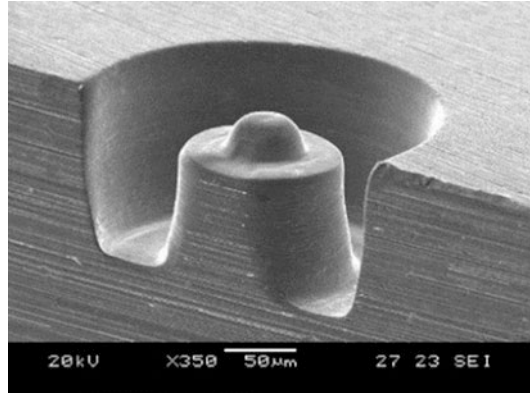


Fig. 11 Schematic of the effect of electrode shape on the side wall profile (Kim et al. 2005b). (a) cylindrical electrode; (b) disk-type electrode

electrodes used in machining and micro columns with negligible taper are shown in Fig. 12 (Kim et al. 2005b).

Plenty of researches on micro ECM milling have been carried out soon afterward worldwide. The famous research affiliations include Nanjing University of Aeronautics and Astronautics, Harbin Institute of Technology, Tsinghua University from China, etc. (Zhu 2012; Yong Liu 2010). Researchers from Nanjing University of Aeronautics and Astronautics presented a micro ECM milling by layer process using the micrometer-scale in situ-fabricated cylindrical tungsten electrode as the tool, and

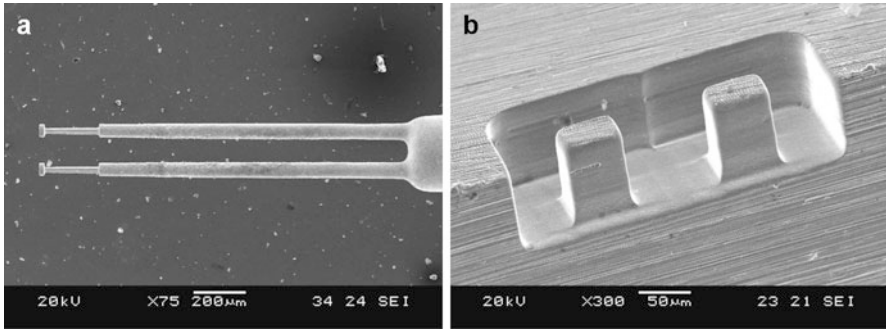


Fig. 12 Dual disk-type electrodes and dual columns fabricated with micro ECM milling. (Kim et al. 2005b). (a) dual disk-type electrodes; (b) dual columns machined with dual disk-type electrodes

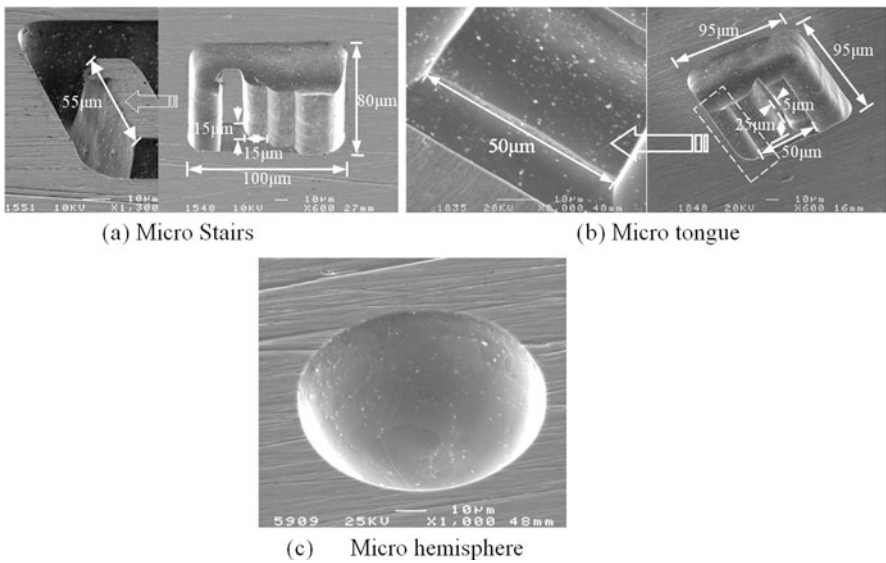


Fig. 13 Micro features of GH3030. (Zhu 2012; Yong Liu 2010)

3D complex microstructures with physical dimension of several 10 µm on GH3030 have been obtained, as shown in Fig. 13 (Zhu 2012; Yong Liu 2010).

Instead of a cylindrical rod, a tensioned micro wire is used as the cathode tool in micro wire ECM with ultrashort pulse. Kim et al. (2005b) reported that various microgrooves were machined by using a platinum wire electrode with 10 µm in diameter. Optimal pulse conditions for stable machining were obtained experimentally, which were 6 to 7 V voltage amplitude, 60 to 100 ns pulse width, and 6 to 9 µs period. Under the optimized machining conditions, microgrooves with 20 µm width were machined (Fig. 14). In the process, 0.1 M/l H₂SO₄ was preferred because the

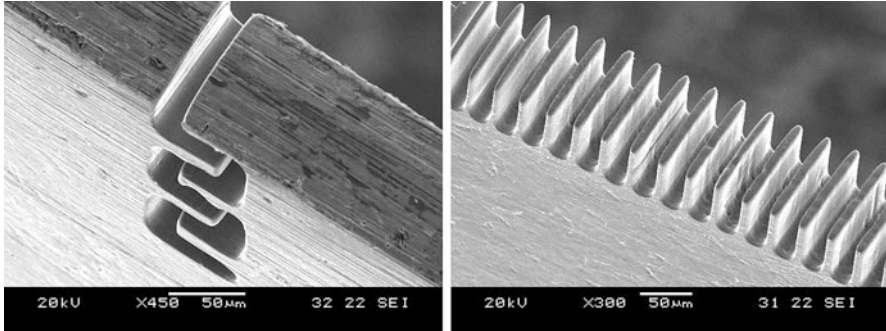


Fig. 14 Microgrooves by ultrashort pulse micro wire ECM (304 SS, 6.5 V, 75 ns pulse on time, 6.5 μ s period). (Kim et al. 2005b)

acid electrolyte usually produces much less by-products than common salt electrolytes, which is important for a steady machining process in micro wire ECM (Kim et al. 2005b).

In micro electrochemical machining utilizing ultrashort voltage pulses, since a long pulse off time is required for discharge of electric charges accumulating on the double layer, the machining speed becomes extremely slow. Besides, as the size of tool electrode increases, the time period which needs for the potential of the electrical double layer to rise to the potential required for dissolution becomes longer. Therefore, a time-consuming scanning method with a micro tool to generate complicated shape is the main method in micro ECM.

26.4.3 Micro ECM Using Electrostatic Induction Feeding Method

As described in the above section that a pulse generator with very high frequency characteristics is required in ECM with ultrashort pulse, since the pulse width is smaller than 100 ns. Even with a high-performance pulse generator, ultrashort pulses may not be realized depending on the wiring method of the ECM equipment. In order to easily obtain such an ultrashort pulse in ECM without using an expensive ultrashort pulse generator, Koyano and Kunieda (2013) proposed a micro ECM method by using the electrostatic induction feeding circuit, which had been originally developed for micro EDM (Kunieda et al. 2007). The pulse generator and equivalent circuit for electrostatic induction feeding ECM is shown in Fig. 15, and the waveforms of pulse voltage and current are shown in Fig. 16. When a pulse voltage is supplied across the inter-electrode gap, the electrical double layer is formed on the surface of electrodes. Since the pulse voltage with a constant pulse duration is coupled to the tool electrode by a feeding capacitance C_1 , current only flows at the instance when the pulse voltage changes to high or low as shown in Fig. 16. Hence, the current pulse duration is nearly equal to the rise and fall time regardless of the pulse on time of the pulse voltage. With this method, a pulse

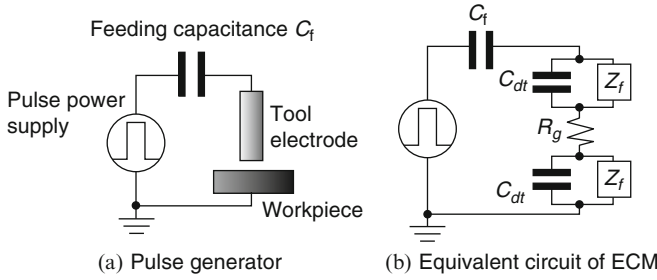
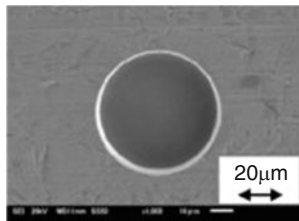
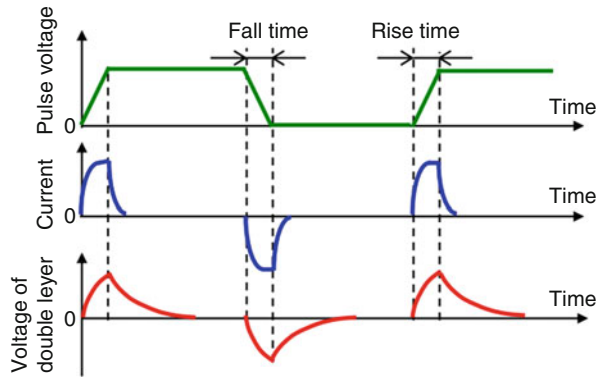
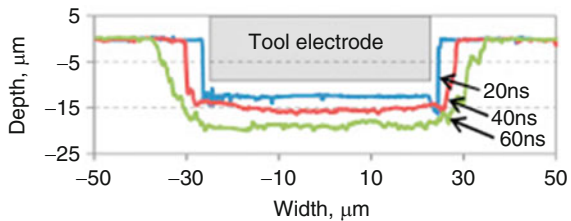


Fig. 15 ECM with electrostatic induction feeding method. (Koyano and Kunieda 2013)

Fig. 16 Waveform of pulse voltage and current and voltage of double layer. (Koyano and Kunieda 2013)



(a) Machined micro-hole with a rise and fall time of 20ns



(b) Cross-sectional shapes of machined micro-holes with various rise/fall time

Fig. 17 ECM of micro-hole with electrostatic induction feeding method. (Koyano and Kunieda 2013)

duration shorter than several tens ns was easily obtained and micro-hole machining was realized (Fig. 17). Meanwhile, since the pulse current generated with this electrostatic induction feeding method is bipolar, it is convenient to machine tungsten or tungsten carbide with a neutral electrolyte (Maeda et al. 1967; Natsu and Kurahata 2013). Han et al. (Han and Kunieda 2017) fabricated tungsten micro-rods successfully with the bipolar current pulse generated by the electrostatic induction feeding method and with a neutral electrolyte, NaNO_3 aqueous solution (Fig. 18).

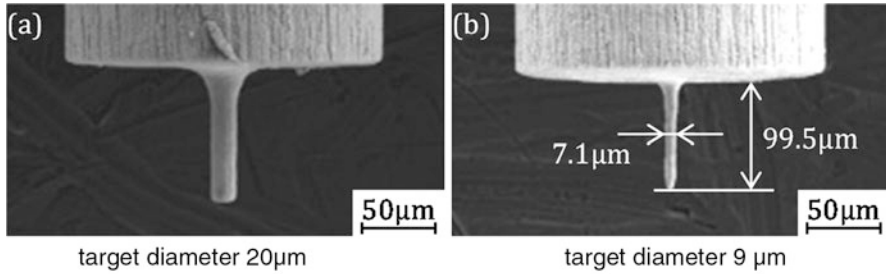


Fig. 18 Micro-rods machined with different target diameters. (Han and Kunieda 2017)

26.5 Micro Wire ECM

Since there is no tool wear theoretically in ECM, the breakage of micro wire will not happen due to tool wear. Therefore, the machining equipment, especially the wire feed system, becomes simple compared to wire EDM.

Figure 19 shows the wire ECM system. The pulsed voltage is applied between anode workpiece and cathode wire electrode in an electrolyte cell. The workpiece is electrochemically removed, and a narrow slit is produced as the cathode wire moves toward the anode workpiece.

At present, researches on improving the machining accuracy, surface quality, and machining efficiency of wire ECM are focused on the following aspects: ultrashort pulse micro wire ECM, bipolar pulse micro wire ECM, multi-wire ECM, and enhancement of mass transport in wire ECM. The ultrashort pulse micro wire ECM was explained in Sect. 4.2. In this section, other researches are introduced.

26.5.1 Surface Finishing with Bipolar Pulse

It is well known that good surface quality can be achieved by ECM under a high current density. However, when the wire electrode moves across the workpiece surface, the final machined surface is affected by the low current density region as shown in Fig. 20, which leads to a poor and nonlustrous surface. In order to improve the surface quality, it is necessary to limit the effect of the low current density area on the machined surface. As mentioned in Sect. 4.1, when a sufficiently short pulse voltage is applied, electrochemical dissolution occurs only at the high current density area, while at the low current density area charging of the electrical double layer instead of dissolution takes place. Therefore, the machining area can be limited in high current density area. In order to improve the machining rate and surface quality in wire ECM, Furuyama et al. (Furuyama et al. 2016) proposed a surface finishing method by supplying a reversed pulse current to accelerate the discharge of the electrical double layer and shorten the period of recovery of the inter-electrode area environment. They found that the machined surface quality is poor with unipolar pulse voltage, while a glossy surface with low surface roughness could be

Fig. 19 Schematic of wire electrochemical machining

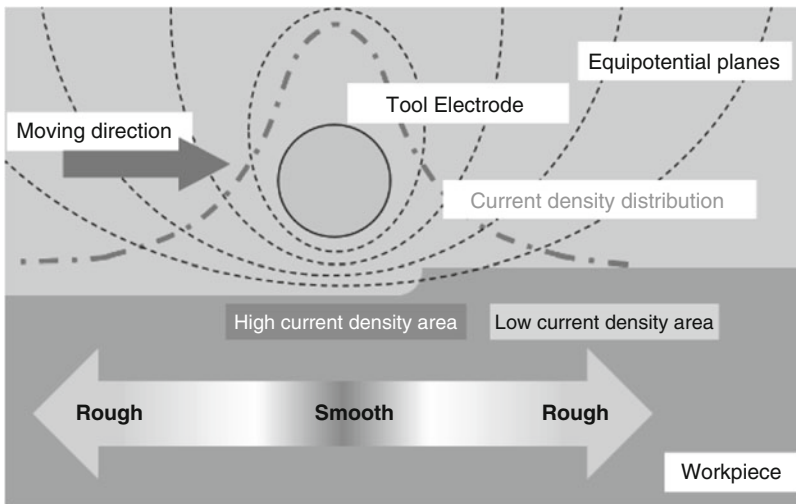
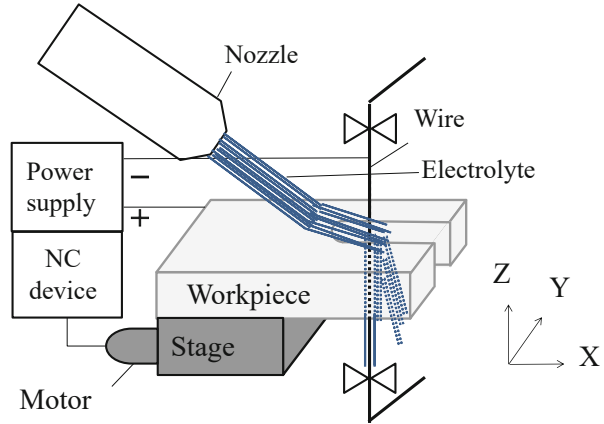


Fig. 20 Problems of surface finishing in the wire ECM. (Furuyama et al. 2016)

obtained at duty factors 10% to 40% (see Fig. 21). As shown in Fig. 22, by using a bipolar pulse voltage of duty factor 40%, with the voltage 15 V and the subpulse voltage -4 V, the initial surface roughness of $R_a 2.0 \mu\text{m}$ was successfully reduced to $0.39 \mu\text{m}$ in a short machining time.

26.5.2 Multi-Wire ECM

Array microstructures, such as comb structures in micro-actuators and multiple slits in X-ray phase-contrast imaging systems, are usually used in high-precision devices for their specific functions. The main problem in machining array microstructures with

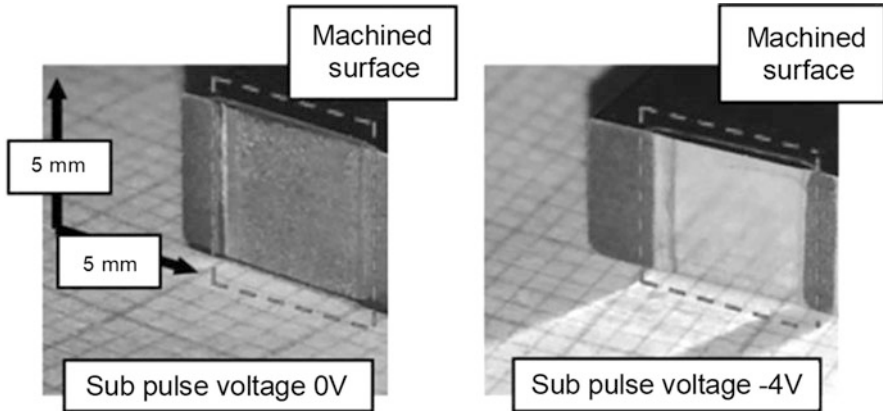


Fig. 21 Comparison of machined surfaces at subpulse voltage 0 V and -4 V. (Furuyama et al. 2016)

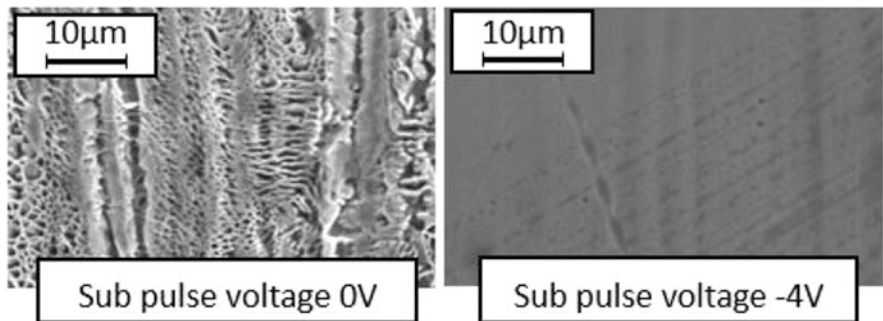


Fig. 22 Comparison of ECM surfaces at subpulse voltage 0 V and -4 V. (Furuyama et al. 2016)

wire ECM is that the machining efficiency is too low owing to the slow feed speed of wire electrode. In order to solve this problem and improve the machining efficiency, multi-wire ECM was proposed to fabricate array microstructure. He et al. (He et al. 2017) reported that micro ECM with 15 wire electrodes at a maximum feed rate of $5.0 \mu\text{m/s}$ was realized. With experimentally obtained optimal pulse conditions for stable machining, 18 V pulse voltage, $7 \mu\text{s}$ pulse on time, and $20 \mu\text{s}$ period, a multiple-slit microstructure with high aspect ratio of 20 was fabricated by using 15 wire electrodes, and X-shaped micro-parts with high surface quality (R_a 128.0 nm, R_q 162.0 nm, and R_{max} $1.72 \mu\text{m}$) were produced by using 7 wire electrodes (He et al. 2017) (Fig. 23).

26.5.3 Enhancement of Mass Transport in Wire ECM

In micro wire ECM, in order to achieve higher machining accuracy, the inter-electrode distance is controlled in several micrometers or even sub-micrometer.

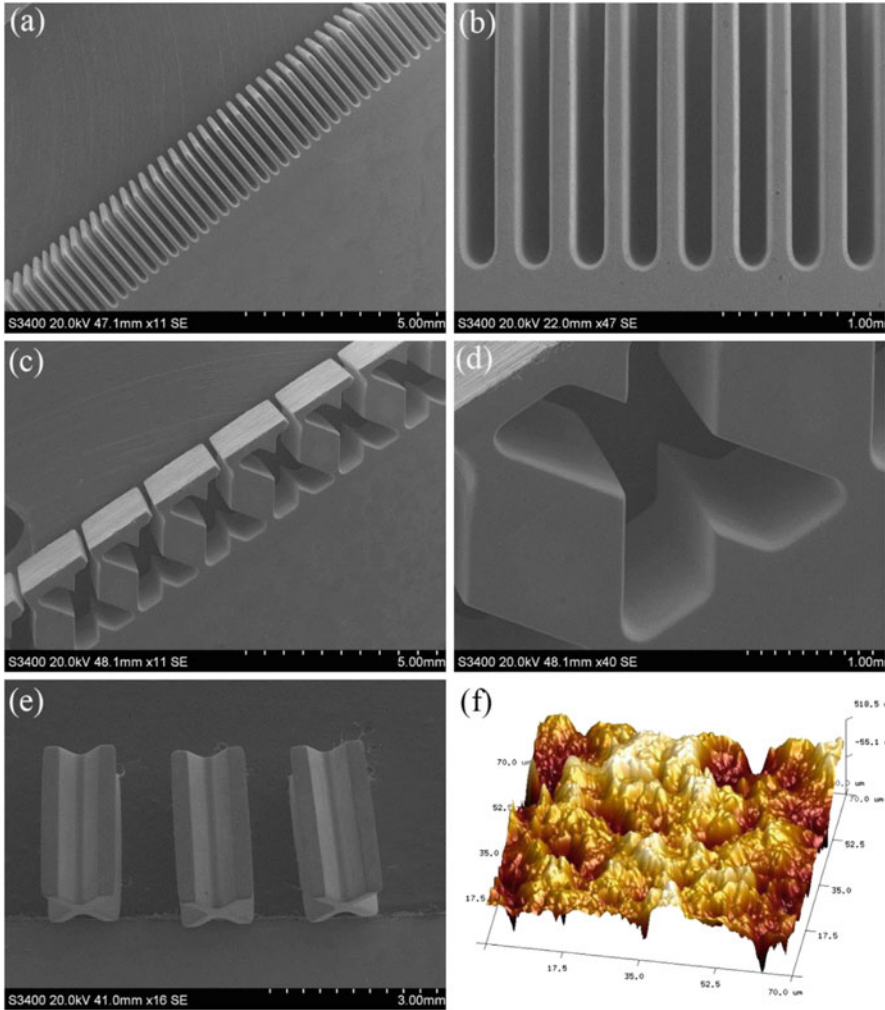


Fig. 23 Microstructures machined by multi-wire ECM. (He et al. 2017)

Especially in the case of machining deep and narrow grooves, the removal of by-products, such as hydroxide, hydrogen, and oxygen gas, from the inter-electrode gap area and supply of fresh electrolyte become very difficult, which leads to unstable machining process. In order to enhance the mass transport in the gap area, Zeng et al. (2012) proposed the following approaches: (a) electrolyte flushing along the wire, (b) ring wire traveling in one direction, and (c) micro-vibration of cathode wire for renewing the electrolyte in the machining gap. With the electrolyte flushing along the wire with a flow rate of 0.75 m/s and a wire feed rate of 0.5 $\mu\text{m/s}$, micro spline and microbeam on 5 mm-thick stainless steel 304 were fabricated as shown in Fig. 24. By traveling a ring wire with wire diameter of 200 μm at a

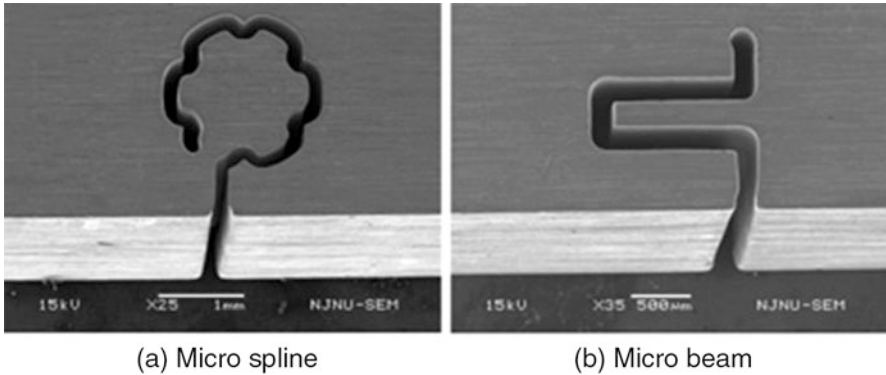


Fig. 24 Microstructures on stainless steel with electrolyte flushing. (Zeng et al. 2012)

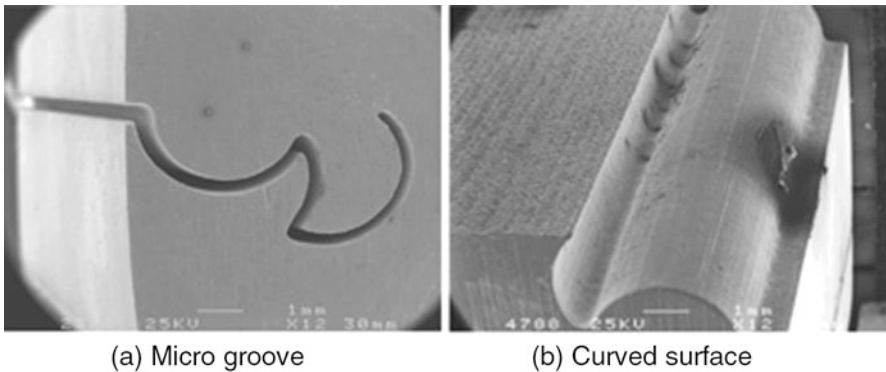


Fig. 25 Microstructures with high aspect ratio fabricated with traveling wire. (Zeng et al. 2012)

traveling speed of 0.015 m/s in the gravity direction, the by-products were efficiently removed from the gap area, and the microstructures of high aspect ratio as shown in Fig. 25 were fabricated. Since the width of machined groove width of 350 μm was cut in a 20 mm-thick stainless steel 304 plate, the aspect ratio was reached about 57 (Zeng et al. 2012).

He et al. (2017) proposed to use a wire electrode with surface microstructures to enhance the mass transport in wire ECM, by utilizing the increased adhesion energy between the liquid and wire surface. Spikelike microstructures with various sizes were successfully fabricated on a 50 μm diameter tungsten wire electrode by adjusting the laser fluence of nanosecond laser machining (Fig. 26). The comparative experiments of wire ECM using a smooth wire electrode and proposed wire with surface microstructures showed that the wire electrode processed by laser process with tool axial vibration can effectively improve the electrolyte mass transport efficiency, resulting in improved machining efficiency and homogeneity of machined slit (He et al. 2017).

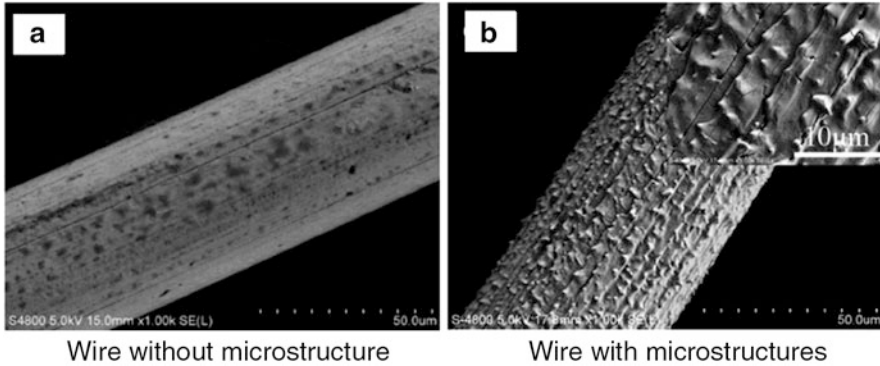


Fig. 26 SEM images of tungsten wire surfaces. (He et al. 2017)

26.5.4 Measures to Eliminate Tool Wear in Wire ECM

One of the most attractive features is that there is no tool wear in ECM with the direct voltage power supply, regardless of the kind of material. However, tool electrode wear occurs depending on the tool material when a pulse power supply is used (Abe et al. 2006; Endo and Natsu 2012). Because the desired shape is difficult to obtain, or the wire breakage occurs during machining due to wire wear, it is necessary to reduce or eliminate the tool electrode wear in order to obtain a higher machining accuracy and stable machining process.

The reason of tool wear in pulse ECM is thought to be caused by the undershoot of the total current flowing through the circuit as the pulse falls, as shown in Fig. 27. In ECM with pulse power supply, the electric charge accumulated on the electrical double layer during the pulse on time will discharge during the pulse off time. As a result, the current flows in the reverse direction, which means that the tool electrode changes from being a cathode to an anode during that period. This reverse current generated during the pulse off time causes the tool wear. Endo et al. (Endo and Natsu 2012) reported that the use of a low-level voltage higher than 0 V shown in Fig. 28 is effective for preventing wear to a tungsten tool electrode. Yamaguchi et al. (Yamaguchi and Natsu 2017) applied this anti-wear measures in pulse wire ECM and successfully eliminate the wire wear (see Fig. 29). Also the influence of the low-level voltage on the machining characteristics was investigated experimentally and analyzed theoretically.

26.6 Electrolyte Jet Machining

26.6.1 Principle and Machining System of Electrolyte Jet Machining

Electrolyte jet machining (Chase et al. 1972; Datta et al. 1989; Kozak 1989; Kunieda et al. 1993) is carried out by jetting electrolyte from a nozzle toward the workpiece while applying voltage between the nozzle and workpiece as shown in Fig. 30. When

Fig. 27 Current waveform with applied pulse voltage

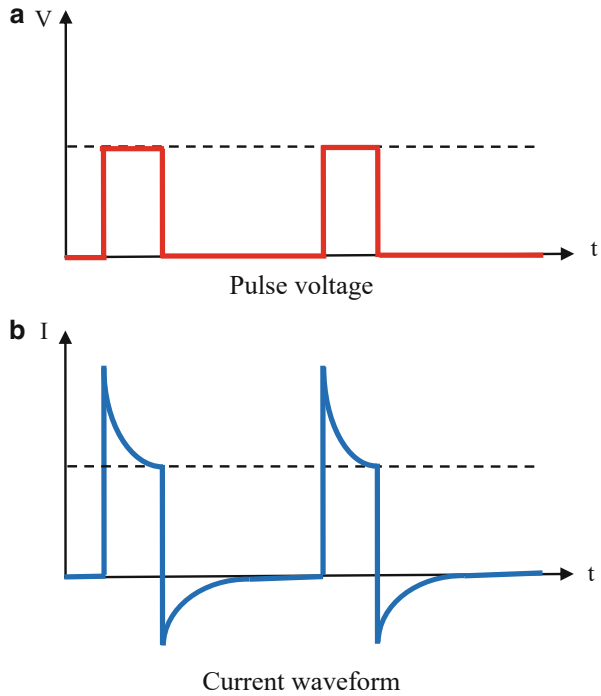
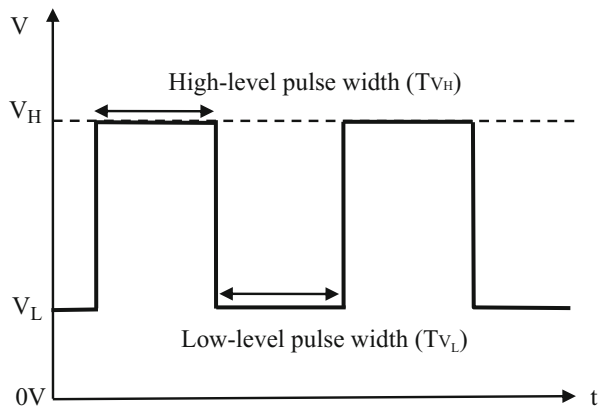


Fig. 28 Waveform of pulse with a raised low-level voltage. (Endo and Natsu 2012)



the electrolyte is supplied at a sufficient flow rate, a sudden change in thickness of the radial electrolyte occurs in areas far away from the nozzle due to the hydraulic jump phenomenon (Bryson 1972). In this case, the electric potential distribution of the electrolyte flow and the current density distribution over the workpiece surface (see Fig. 31), calculated by Yoneda et al. (Yoneda and Kunieda 1996), show that the current density peaks at the center of the jet and decreases rapidly from the center. Therefore,

Fig. 29 Observations of tool electrode before and after machining for 10 min. (Yamaguchi and Natsu 2017)

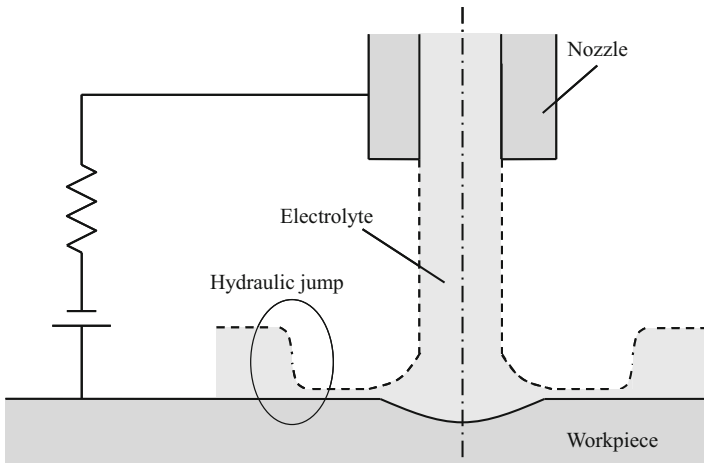
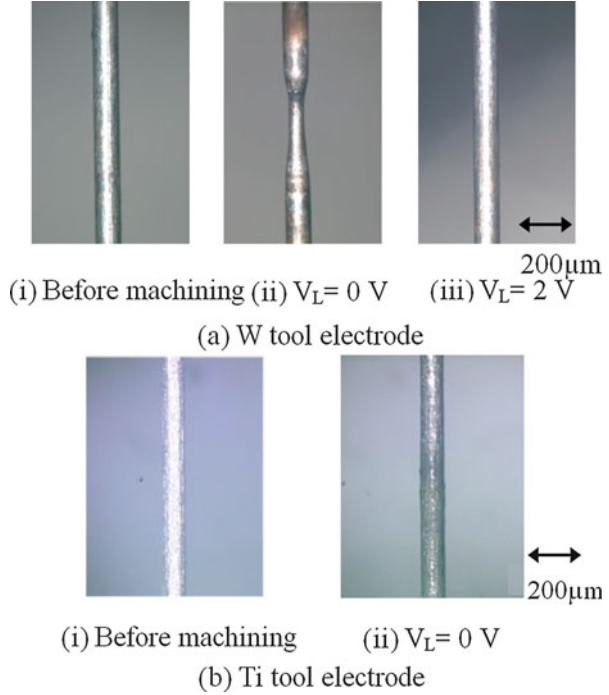


Fig. 30 Schematic of electrolyte jet machining

only the workpiece material exposed to the jet is removed by anodic dissolution, because the current is restricted to the area limited by the jet.

The removal amount and machining position can easily be controlled by controlling the current and nozzle position. Furthermore, since the removal amount is

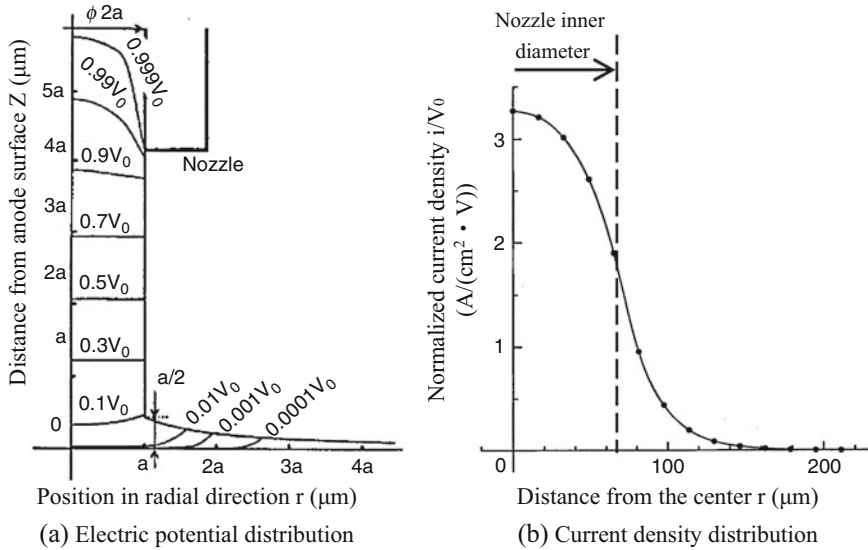


Fig. 31 Electric potential distribution and current density distribution. (Yoneda and Kunieda 1996)

determined by the quantity of electricity, it is independent of the inter-electrode distance as long as constant current is supplied. Rigid gap width control is therefore not needed even for micromachining. Using these features, microfabrication of complicated shapes such as grooves on hydrodynamic bearings and molds for micro lens arrays can be efficiently achieved by scanning the versatile minute nozzle instead of using complicated and less flexible masks.

Figure 32 shows an example of the experimental setup. The workpiece is installed on the machining table which can be positioned horizontally by an X-Y stage. The nozzle is installed on the slide table which can be moved in the Z direction to adjust the gap width between the workpiece and nozzle. The electrolyte is pressurized by an air compressor in the pressure tank and jetted from the nozzle toward the workpiece.

The removal rate of the workpiece material is generally determined by the current density in electrolyte jet machining. However, the generation of the oxide film becomes dominant in the area where the current density is lower than the threshold, when a passivation-type electrolyte is used. Since the generated passive film prevents machining of the material, material removal is limited to a narrower area, thus improving machining precision. For this reason, a sodium nitrate aqueous solution, which is a passivation-type electrolyte, is suitable to realize precision machining.

26.6.2 Applications

Although electrolyte jet machining is mostly applied in removing process by dissolution from the anode surface, adding process (Bocking et al. 1995; Kunieda et al. 1998)

Fig. 32 Experimental equipment for electrolyte jet machining

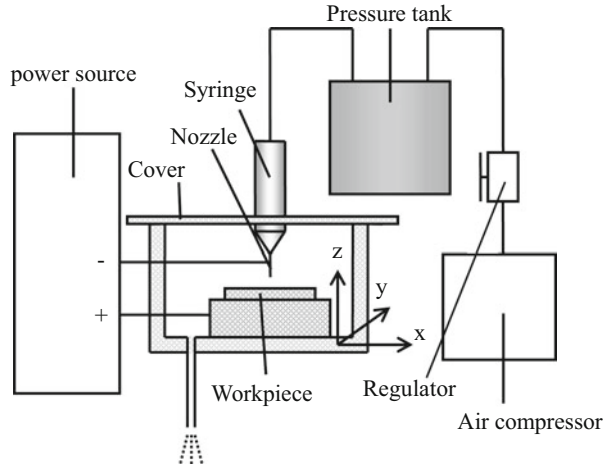
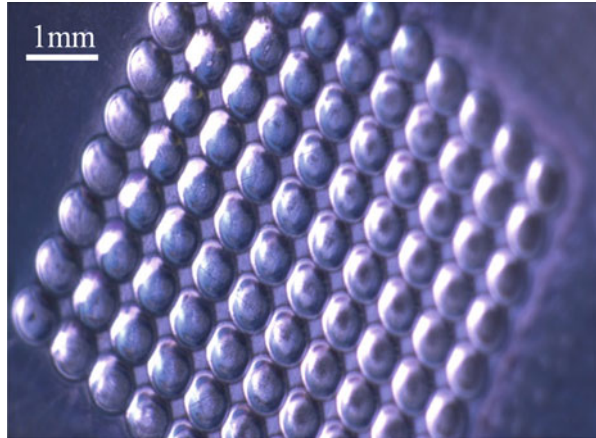


Fig. 33 Additive process of pit array on a copper plate (Natsu et al. 2006) (20 wt% $\text{Cu}(\text{NO}_3)_2$ electrolyte, 25 mA, 6 s/pit)



by metallic ion deposition on the cathode and coloring process (Mori and Kunieda 1997) by anodic oxidation film formation were also reported. Figure 33 shows an example of additive machining of a pit array on a copper plate (Natsu et al. 2006), while Fig. 34 shows an example of coloring process on a titanium plate (Mori and Kunieda 1997). Kawanaka et al. (Kawanaka and Kunieda 2015) proposed a mirrorlike finishing technique by electrolyte jet machining. In order to solve the problem of the decrease in the surface quality of the machined surface by the low current density area, they suggested to reciprocate the jet at a high translating speed or use pulsed current and bipolar pulse even at low translating speeds (see Fig. 35).

As an application of electrolyte jet machining, the influence of micro patterns on the sliding surface was investigated (Kunieda et al. 1993). Walker et al. (2017) successfully used the electrolyte jet machining to create textured dimple features in a hypereutectic Al-Si alloy and found that under boundary and mixed lubrication

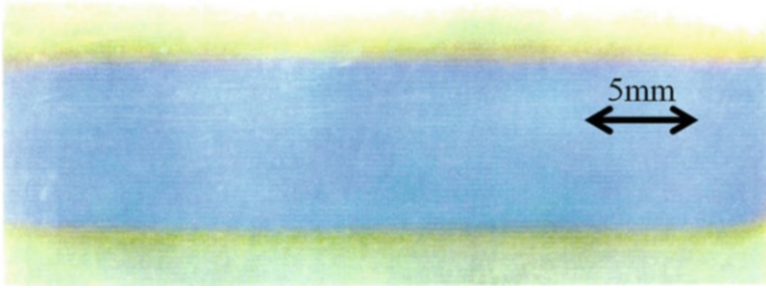
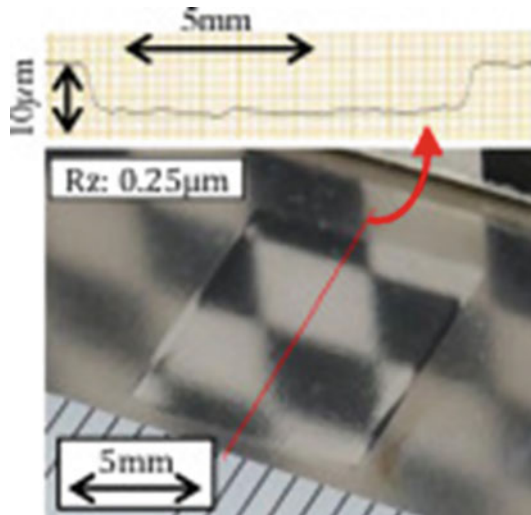


Fig. 34 Coloring process on a titanium plate. (Mori and Kunieda 1997)

Fig. 35 Examples of mirrorlike finishing using slit nozzle (v , 0.5 mm/s; i , 157 A/cm²; on time, 100 μ s; duty factor, 67%). (Kawanaka and Kunieda 2015)



regimes, textured Al-Si surfaces all exhibited a reduction in average coefficient of friction values.

In order to accelerate practical application, laser-assisted jet electrochemical machining was attempted to improve machining precision and efficiency (Datta et al. 1989; Rajurkar and Kozak 2001; Pajak et al. 2006). In addition, high machining efficiency by using multiple nozzles (Ikeda et al. 2006) and micromachining by adopting filter and vacuuming devices (Ooshiro et al. 2007) were successfully achieved.

Electrolyte jet machining techniques have conventionally been considered to be limited to planar interactions with the electrolyte jet being maintained normal to the workpiece surface. In order to enable a step change in the viability of electrolyte jet machining as an efficient micro-milling technology capable of producing complex 3D shapes, Mitchell-Smith et al. (Mitchell-Smith and Speidel 2018) investigated the viability and resultant effects of articulating the nozzle relative to the workpiece and showed that through variation of the angle of jet address an extra level of flexibility and performance is possible.

26.6.3 Characteristics of Pit and Groove Machining

Since complicated shapes and patterns are superimposed by pits and grooves in electrolyte jet machining (Natsu et al. 2007), the characteristics of pit and groove machining are explained in this section.

In order to examine the effects of current density and machining time on surface roughness, pit machining was carried out fixing the workpiece at one position while supplying the electrolytic current between the nozzle and workpiece. Figure 36 shows the photograph of the machined pits when the machining time was adjusted for different current densities in order to obtain a 25 μm deep pit for every condition. The machined surface is not glossy when the current density is lower than $50\text{A}/\text{cm}^2$, but becomes glossy with the increase of the current density. Figure 37 shows the measured surface roughness at the center of the pit using a laser microscope. The machined surface is considerably rougher at the lower current density, and the value of the surface roughness decreases rapidly with increased current density and finally plateaus at about R_z 0.1 μm . Next, to examine how the surface roughness changes

Fig. 36 Photos of machined pit

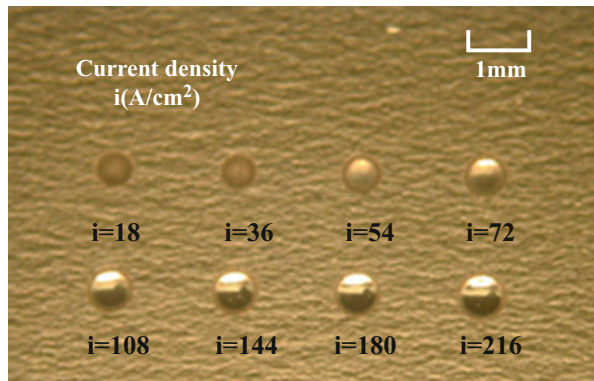
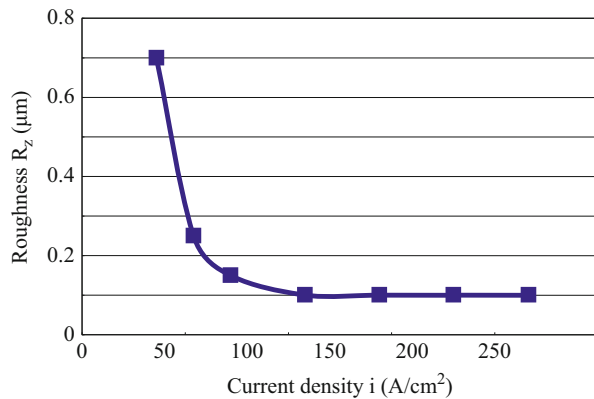


Fig. 37 Relationship between surface roughness and current density



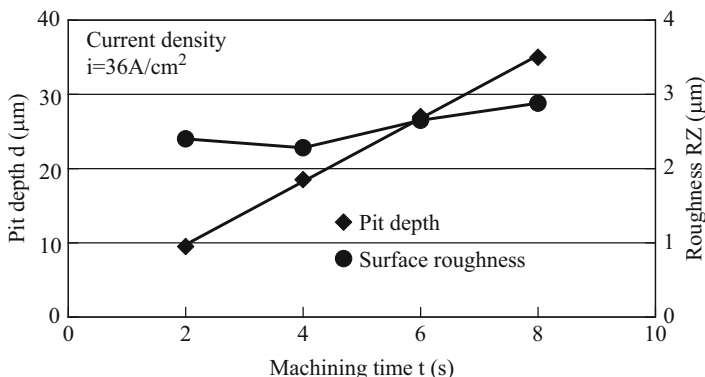


Fig. 38 Influence of machining time on pit depth and surface roughness with current density of $36A/cm^2$

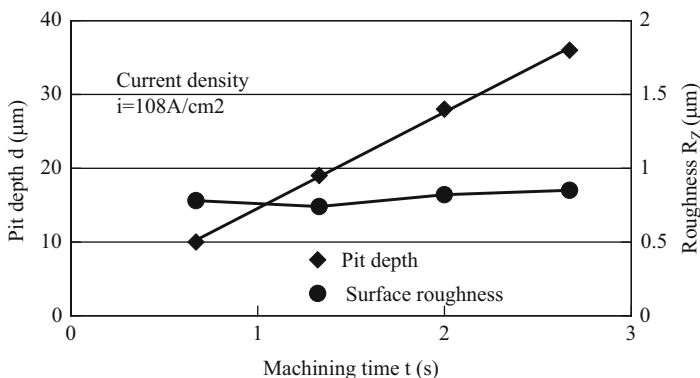
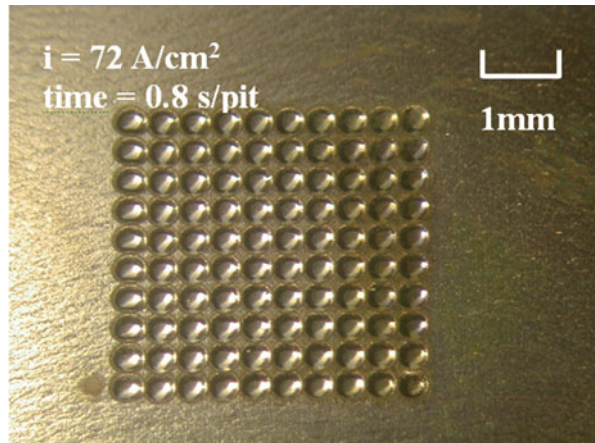


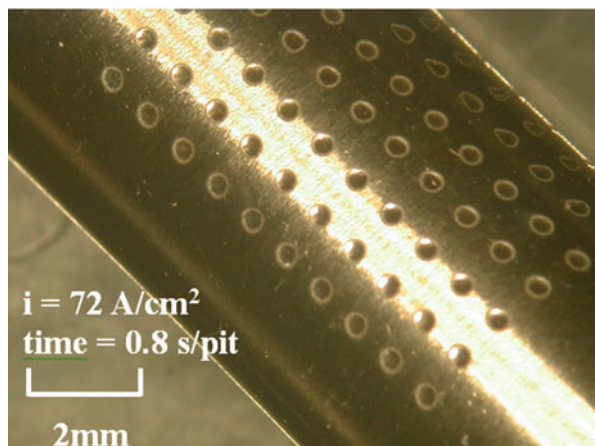
Fig. 39 Influence of machining time on pit depth and surface roughness with current density of $108A/cm^2$

with machining time, pit machining was carried out under the same current density. Figures 38 and 39 show the change in pit depth and surface roughness with the machining time at current densities of $36A/cm^2$ and $108A/cm^2$, respectively. These figures prove that the surface roughness is more or less determined by the current density and is not influenced by the machining time, though the pit depth increases in proportion to the machining time. It is clear from the above results that the current density greatly influences the surface roughness of the machined pit surface in electrolyte jet machining and that selecting higher current density improves not only the machining speed but also the surface roughness when machining stainless steel. Figure 40 shows pit arrays on a plate and a cylindrical surface was produced with a nozzle of 0.26 mm in inner diameter. After the workpiece was stopped at one position, the electrolytic current was supplied for 0.8 seconds. Then the nozzle was relocated, and this process was repeated. The rotating stage was used for machining

Fig. 40 Example of array machining



(a) Machined pit array on plate

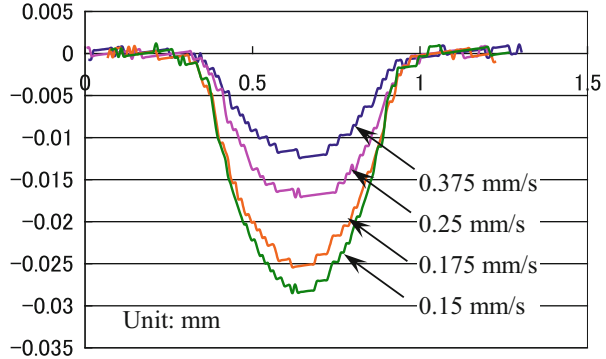


(b) Machined pit array on cylinder

patterns on the cylindrical surface. It is found that a glossy pit of about $20\ \mu\text{m}$ in depth can be obtained within a very short time of 0.8 seconds.

Grooves can be obtained if the nozzle is moved over the workpiece surface while the electrolytic current is supplied. Figure 41 shows the measured cross-sectional shape of a machined groove. The result shows that the groove width remains the same even if the depth changes with the scanning speed. Figure 42 shows the results of investigating the relationship between the groove depth and nozzle scanning speed for fixed current densities. It can be seen that the groove depth is inversely proportional to the scanning speed, which means that grooves of different depth can be easily obtained by controlling the scanning speed of the nozzle.

Grooves with the same depth can be obtained by one scan at a slower speed or by several scans at a faster speed. The change in surface roughness with the

Fig. 41 Shape of machined groove

superimposing times is shown in Figs. 43 and 44, which indicates that for grooves with the same depth, surface roughness is improved by superimposition, and the more the number of superimposing times, the smoother will the machined surface be. The reason why using a high scanning speed provides a smooth surface may be as follows: When the nozzle is moved to machine a groove, the already machined groove surface is inevitably exposed to the peripheral part of the electrolyte jet where the current density is much lower. As discussed above that low current densities result in poor surface roughness, the excellent surface produced by high current density around the center of the jet is therefore roughened by the low density part of the electrolyte jet due to nozzle movement. However, the high quality surface will not damage greatly if the exposure period of the surface to the jet area of low current density is short. This is why surface roughness improves at higher scanning speeds.

Figure 45 shows grooving examples by a nozzle of 0.26 mm in inner diameter. The pattern on the plate (photo (a)) is assumed to be that on a thrust hydrodynamic bearing surface. The groove depth is about 30 μm , and the machining time is about 150 seconds. The pattern on the cylindrical surface is assumed to be that on a radial hydrodynamic bearing surface and the machining time for every groove is about 6 seconds. These results show that complicated patterns can be efficiently machined by controlling the nozzle movement.

26.7 Generating Complicated Shapes by Superimposing Simple Patterns with Electrolyte Jet Machining

The characteristics of electrolyte jet machining for simple pits and grooves have been described in Sect. 6.3. However, the machining of more complicated shapes is usually required in practical use. Since it has been confirmed that the superimposition principle works in electrolyte jet machining (Natsu et al. 2007; Schubert et al. 2016), scanning the nozzle will therefore make it possible to generate complicated shapes. In this chapter, the generating method to obtain three-dimensional surfaces by superimposing elemental curved grooves will be explained.

Fig. 42 Relationship between groove depth and nozzle scanning speed

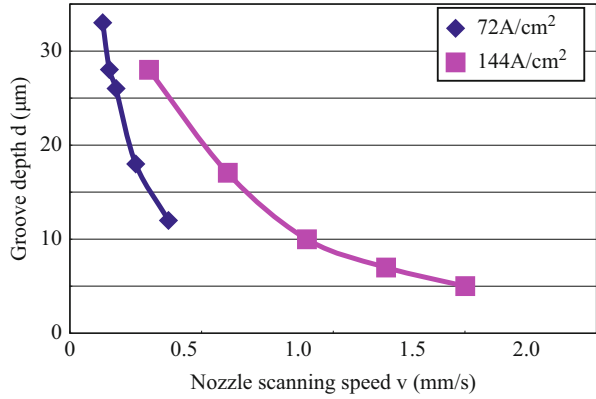


Fig. 43 Influence of scanning number on surface roughness

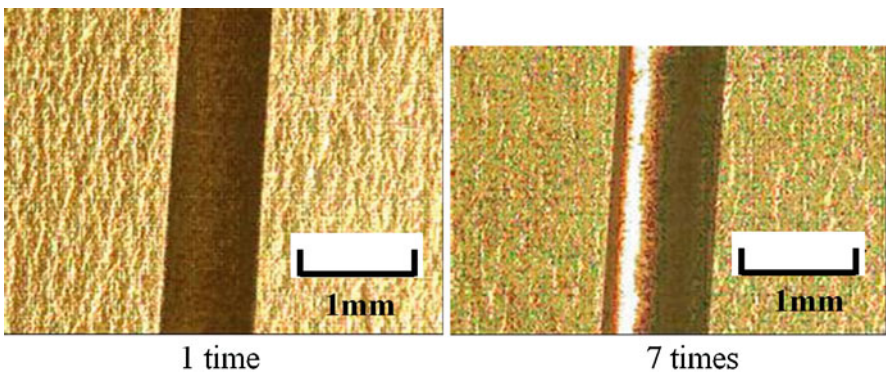
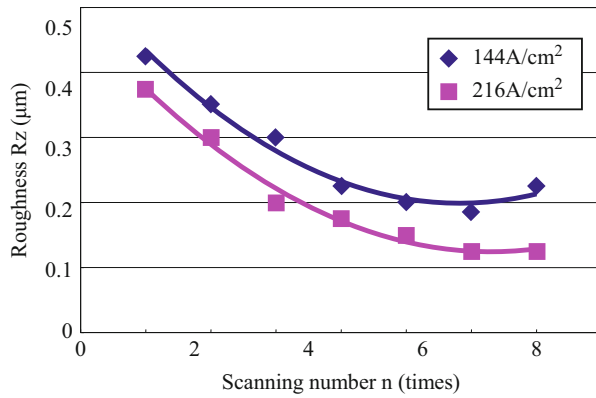
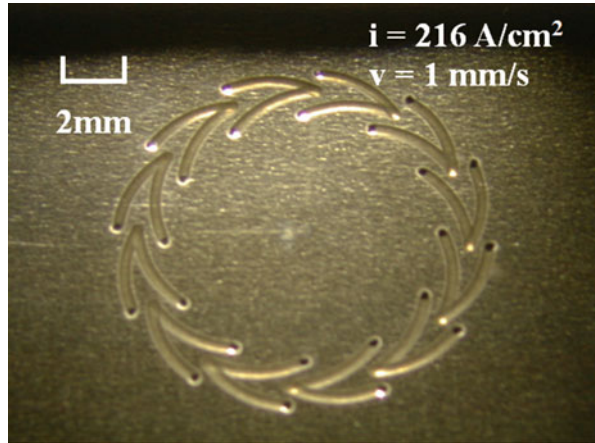
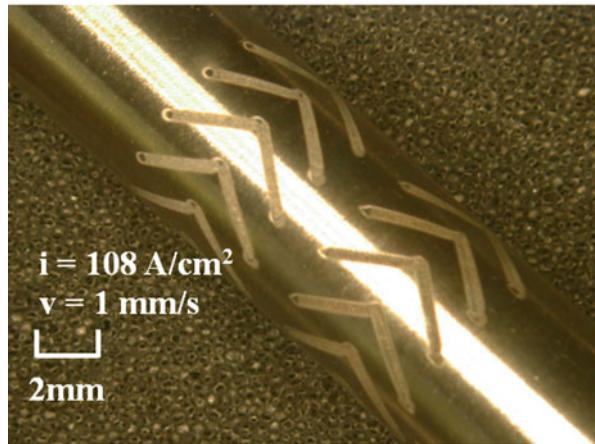


Fig. 44 Improvement of surface roughness by n -times scanning with n -times higher feed speed

Fig. 45 Example of groove machining



(a) Machined groove on plate



(b) Machined groove on cylinder

26.7.1 Calculating Shape of Elemental Curved Groove

26.7.1.1 Difference between Linear Groove and Curved Groove

The removal amount per unit area of the workpiece is proportional to the current density and the time period that the jet stays at that area. In the case that the nozzle is moved in a straight line, the current density and staying period of the jet is the same at the right and left sides of the nozzle center trajectory, as long as the distance from the nozzle center is equal. Hence, the machining amount on both sides is equal and the cross-sectional shape shows a line symmetry (Natsu et al. 2007). However, when the nozzle is moved circularly as shown in Fig. 46, the shape of the arched path along which a certain point on the workpiece follows in the jet differs between the right and left sides of the nozzle center trajectory, even if the distance from the nozzle center is equal. Hence, the current density is not equivalent. In addition, the central angle of

Fig. 46 Nozzle path for machining curved groove

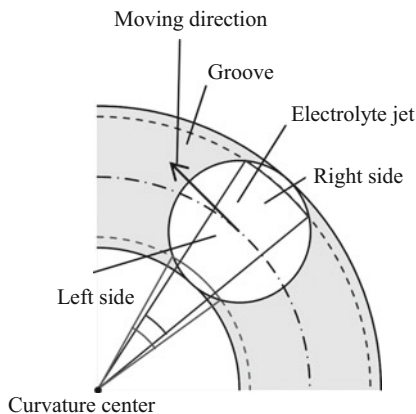


Table 4 Conditions for pit machining

Nozzle inner diameter [μm]	50
Electrolyte	NaNO_3
Electrolyte concentration [wt %]	20
Tank pressure [MPa]	0.5
Gap width [mm]	0.3
Machining current [mA]	3
Machining time [s]	0.5
Workpiece	Stainless steel

the arc differs between the right and left sides of the nozzle center. Thus the staying time of the jet differs according to the right or left side of the trajectory, which means that the cross-sectional shape will not be symmetrical in this case, and the shape changes with the radius of center trajectory.

26.7.1.2 Calculation of Cross-Sectional Shape of Elemental Curved Groove

This section describes the calculation method of the cross-sectional shape of an elemental curved groove from a pit shape which is produced by a stationary jet. Since the material in the area with low current density is not removed when sodium nitrate electrolyte is used, the produced shape differs from the current density distribution which can be obtained from analysis. Hence, the shape of the curved groove is calculated based on the pit shape obtained experimentally using a stationary jet. When other kinds of electrolyte, such as sodium chloride, are used in experiments, the shape of curved groove will be calculated based on the corresponding pit shape obtained experimentally.

The cross-sectional shape of a pit obtained under the conditions shown in Table 4 is shown in Fig. 47. The radius of the obtained pit R_0 is $37.5 \mu\text{m}$. From this experimental result, the depth of the standard pit machined by a stationary jet per unit time, 1 s, is expressed as a function of the distance from the pit center, R mm:

Fig. 47 Cross-sectional shape of machined pit

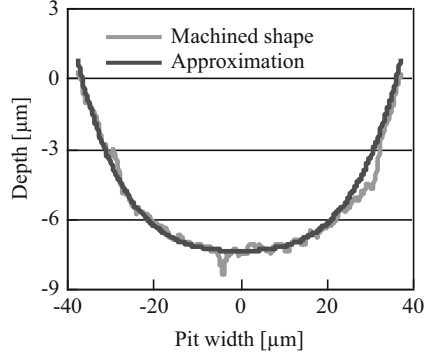
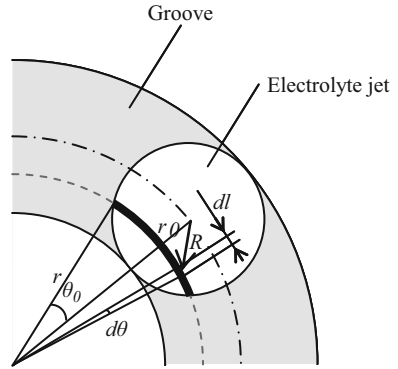


Fig. 48 Method to calculate depth of curved groove



$$D(R) = (6.0 \times 10^{-6})R^4 + (3.2 \times 10^{-3})R^2 - 14.8 [\mu m] \tag{9}$$

Then the cross-sectional shape of the curved groove obtained by scanning the nozzle circularly is calculated as follows. Figure 48 shows the relation between the generated groove and trajectory of the electrolyte jet. To calculate the groove depth at a location with a distance r from the curvature center, the arched path in the jet shown with the bold line in Fig. 48 is considered. Suppose that the nozzle scanning speed at the nozzle center is v_0 and the distance between the curvature center and nozzle center is r_0 , then the passing speed v of the electrolyte jet at the location distanced r from the curvature center can be expressed as:

$$v = \frac{r}{r_0} v_0 \tag{10}$$

The time dt needed for the jet to pass the infinitesimal length dl on the path can be expressed as:

$$dt = \frac{r_0}{rv_0} dl = \frac{r_0}{rv_0} rd\theta = \frac{r_0}{v_0} d\theta \tag{11}$$

Here, since the depth of the standard pit, $D(R)$, is expressed with Eq. (9), the calculated depth of the curved groove can be expressed by Eq. (12) by integrating the machining depth of the standard pit with the time dt :

$$d(r) = \int_{-t_0}^{t_0} D(R)dt = \int_{-\theta_0}^{\theta_0} D(R) \frac{r_0}{v_0} d\theta \tag{12}$$

Here, R is the function of θ and can be expressed as:

$$R = \sqrt{r^2 + r_0^2 - 2rr_0 \cos \theta} \tag{13}$$

In the case that the radius of nozzle center trajectory r_0 is equal or smaller than the pit radius R_0 , a circle area whose radius is $r_0 + R_0$ as shown in Fig. 49a will be produced. The depth at position r is obtained by integral from $-\theta_0$ to θ_0 as shown in Eq. (12), where θ_0 is expressed by Eq. (14):

$$\begin{aligned} \theta_0 &= \pi && (r_0 \leq R_0 \text{ and } r \leq R_0 - r_0) \\ \theta_0 &= \cos^{-1} \frac{r^2 + r_0^2 - R_0^2}{2rr_0} && (r_0 \leq R_0 \text{ and } r > R_0 - r_0) \end{aligned} \tag{14}$$

When r_0 is larger than R_0 , a ring area between the circles where radii are $r_0 - R_0$ and $r_0 + R_0$, respectively, will be produced as shown in Fig. 49b. The depth of the groove at r position is obtained by integrating from $-\theta_0$ to θ_0 , where θ_0 is expressed by:

$$\theta_0 = \cos^{-1} \frac{r^2 + r_0^2 - R_0^2}{2rr_0} \quad (r_0 > R_0) \tag{15}$$

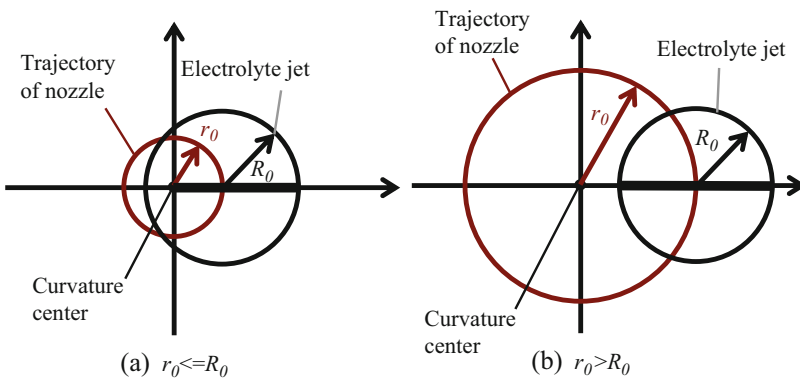


Fig. 49 Machined area

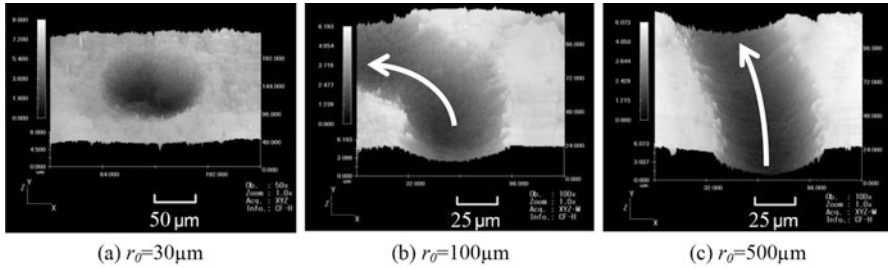


Fig. 50 Curved grooves machined using micro nozzle grooves

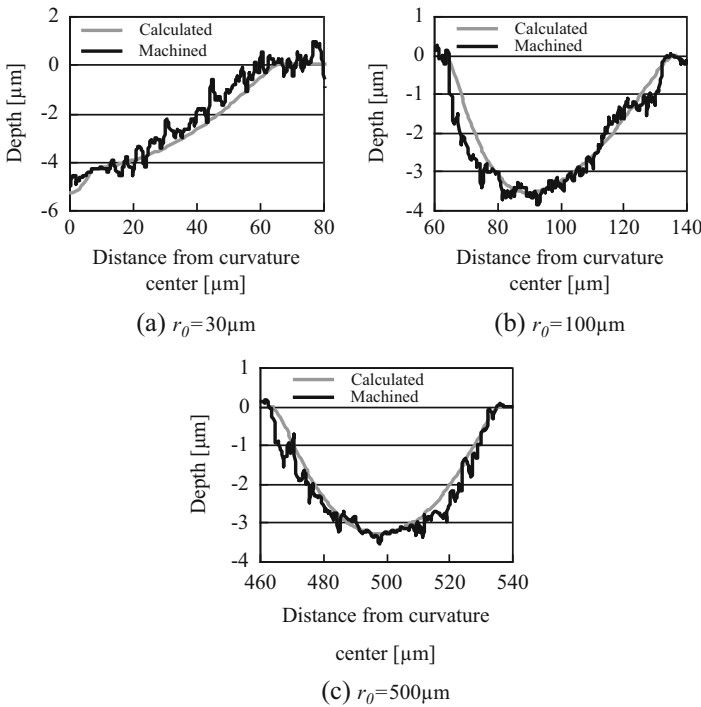


Fig. 51 Cross-sectional shape of elemental curved grooves

26.7.1.3 Confirmation of Calculated Result

In order to compare calculated groove depths with experimental ones, three curved grooves whose radius of nozzle trajectory r_0 was 30 μm , 100 μm , and 500 μm were machined. The nozzle scanning speed was set to 0.25 mm/s, and the machining conditions shown in Table 4 were used. Figure 50 shows the machined shapes of the curved grooves, and Fig. 51 shows their cross-sectional shapes. The calculated results are also shown in the same figure for comparison. Since all calculated results are similar to the machined shapes, the reliability of the calculation method is

confirmed. In addition, from Fig. 51b and c it can be found that the cross-sectional shape is not line symmetry. The reason is that the staying time of the jet at a unit area on the left side of the nozzle center trajectory is longer than that on the right side. As a result, the deepest position of the groove shifted to the left side of the nozzle center. For a curved groove with a radius of curvature of 100 μm and 500 μm , the deepest position shifted to the left by 12.7% and 2.7% of the groove width, respectively.

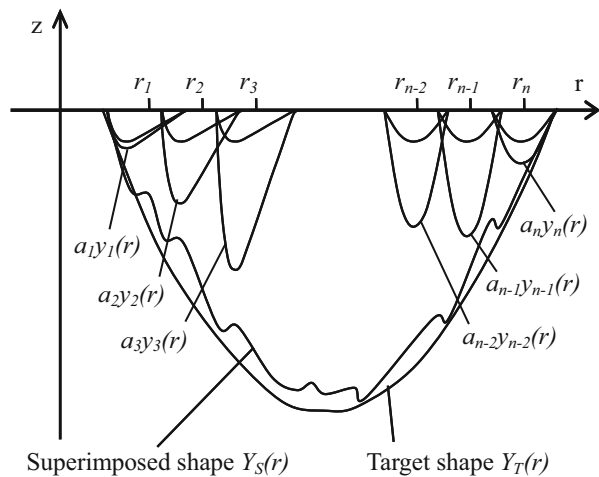
26.7.2 Shape Generation by Superimposing Elemental Curved Grooves

Two-dimensional complicated surface can be generated by superimposing linear grooves (Natsu et al. 2007). However, to obtain a three-dimensional surface such as spherical surface, superimposition of curved grooves is necessary.

26.7.2.1 Theory for 3D Surface Generation by Superimposing Elemental Curved Grooves

There are different ways to generate a 3D surface shape by superimposing curved grooves. Here, it is carried out by controlling the path and scanning speed of the nozzle. The cross-sectional shape of the i th elemental curved groove with the nozzle scanning speed of v_0 is obtained by the method explained in Sect. 7.1 and expressed as $y_i(r)$. Then, the cross-sectional shape of the i th curved groove with the nozzle scanning speed of $\frac{v_0}{a_i}$ and the same trajectory as the i th elemental curved groove is $a_i y_i(r)$. Suppose the target shape Y_T is approximated by superimposition of n elemental curved grooves (see Fig. 52), the superimposed groove shape Y_S can then be expressed by summation of i th curved groove $a_i y_i(r)$ as:

Fig. 52 Shape generation by superimposing elemental curved grooves



$$Y_s(r) = \sum_1^n a_i y_i(r) \quad (16)$$

To evaluate the difference between the target and superimposed shapes, an evaluation function Φ is adopted as follows:

$$\phi = \sum_1^n [Y_T(r_j) - Y_s(r_j)]^2 \quad (17)$$

Here, r_j represents the r coordinate value of the evaluated point, where the difference between the target and superimposed shape is evaluated. Since the difference was evaluated on the trajectory of the nozzle center, the total number of evaluated points was n . It is clear that other variables except a_i in the evaluation function are known. Therefore in order to obtain the superimposed shape which best fits the target one, there is only a need to find out a set of superimposed coefficients a_i ($i = 1$ to n) which minimizes the evaluating function. This means that the optimized superimposed coefficients can be obtained by solving the n simultaneous equations derived by equating the derivative of the evaluation function with respect to a_i to 0 as follows:

$$\frac{\partial \phi}{\partial a_i} = 0 \quad (i = 1, 2, \dots, n) \quad (18)$$

Since a curved groove k times deeper than that of the elemental groove can be obtained by reducing the scanning speed to $1/k$ of v_0 which was used to obtain the elemental curved groove, the scanning speed to obtain the depth $a_i y_i(r)$ is expressed by:

$$v_i = \frac{v_0}{a_i} \quad (19)$$

26.7.2.2 Example of Groove Generation

In order to confirm the validity of the above method, a target curved groove whose cross-sectional shape is $375 \mu\text{m}$ wide and $20 \mu\text{m}$ deep, parabolic curve, expressed by the following equation, was generated:

$$Y_T(r) = (5.68 \times 10^4)(r - 350)^2 - 20 \quad [\mu\text{m}] \quad (20)$$

Twenty-five elemental curved grooves whose radius of curvature ranges from 200 to $500 \mu\text{m}$ were superimposed at a radial interval of $12.5 \mu\text{m}$, which is one-quarter of the nozzle inner diameter.

Figure 53a shows the cross-sectional shape of the superimposed groove obtained by the calculation and the target shape, while Fig. 53b shows the difference between the results of the superimposed and target shapes. The difference between the superimposed and target shapes is called superimposing error, while the difference

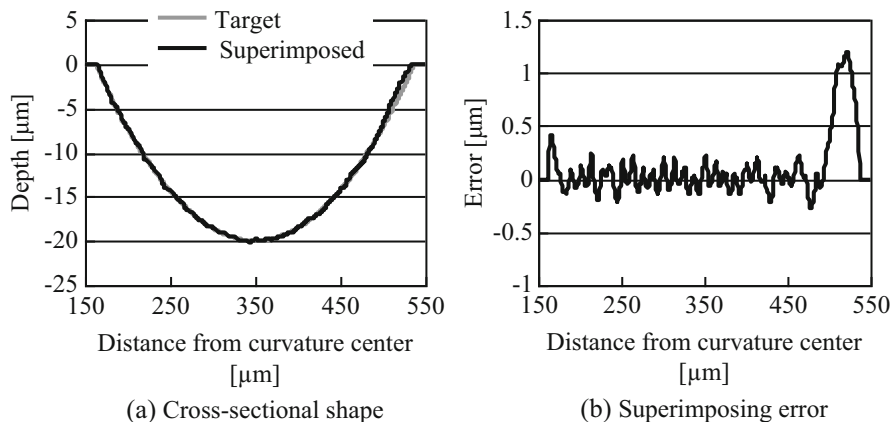
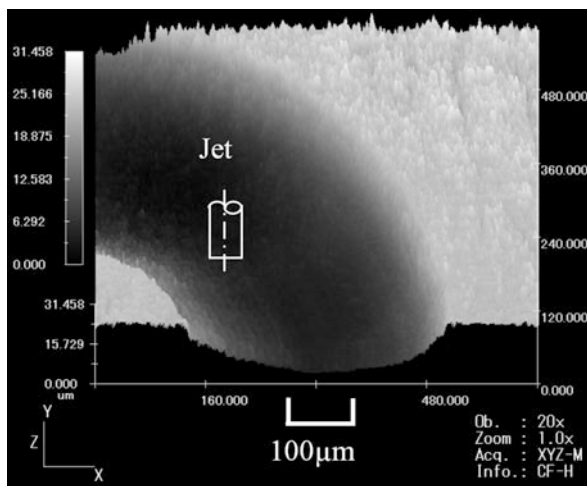


Fig. 53 Comparison of superimposed and target shapes

Fig. 54 Groove shape machined by superimposing elemental curved grooves



between the machined and target shapes is called machining error. Figure 53 shows that the shape of the superimposed groove is nearly the same as that of the target curved groove, although there is some error on the edge area of the groove.

The superimposed curved groove was machined using the nozzle scanning speeds obtained from the above method. Other machining conditions were the same as those in Table 4. Figure 54 shows the three-dimensional shape measured using a laser confocal microscope. Furthermore, Fig. 55a shows the target, calculated, and measured cross-sectional shape, while Fig. 55b shows the superimposing and machining errors. It can be seen from Fig. 55 that the machined shape more or less corresponds

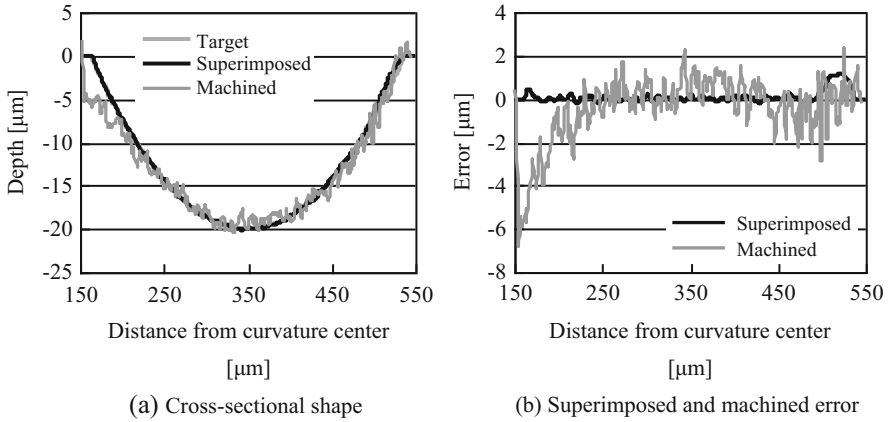


Fig. 55 Comparison of target, superimposed, and machined shapes

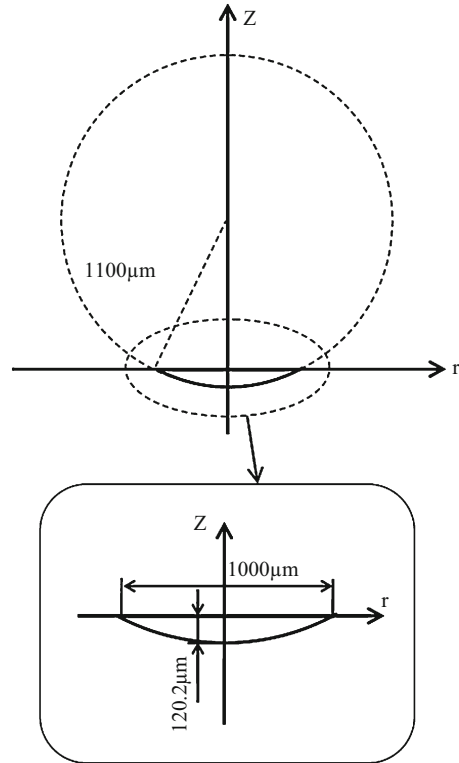
with the target one except at the edge area of the groove. This fact proves that complicated shapes can be generated by superimposing the elemental curved grooves.

26.7.3 Generation of Spherical Surface

In the above section, a parabolic shaped groove was generated by superimposing the elemental curved grooves whose curvature radii were larger than the pit radius. However, in order to obtain an arbitrary surface, superimposing the elemental curved grooves whose radii of curvature of the nozzle center trajectory are smaller than the pit radius is necessary. In this section, a spherical surface which needs superimposition of these two kinds of elemental grooves is generated and the results are discussed. Also described are superimposing errors which occur in three kinds of superimposing methods, namely, one-step superimposing, layer-by-layer superimposing, and layer-by-layer superimposing with interval optimization. Here, one-step superimposing means to reach the target depth by superimposing each elemental curved groove only once. In the case of layer-by-layer superimposing, the target depth is obtained by multiple steps of superimposition in order to reduce the accumulated error and increase superimposing precision. The target surface is a portion of spherical surface shown in Fig. 56. The radius of the spherical surface is 1100 μm and the depth is 120.2 μm .

26.7.3.1 One-Step Superimposing

In the case of one-step superimposing, 1 pit and 37 elemental curved grooves are used to generate the spherical surface. The pit was produced at the center first. Then, 37 concentric curved grooves were superimposed with a uniform radial interval of 12.5 μm . Under this condition, the superimposed coefficients for the pit and each

Fig. 56 Target shape

elemental groove were obtained with Eq. (18), and the superimposed result was calculated with Eq. (16). The target and calculated cross-sectional shapes are shown in Fig. 57. The results show that there exists considerable superimposing error around the center of the spherical cave, although the error is insignificant at other locations.

26.7.3.2 Layer-By-Layer Superimposing

If the target spherical surface is generated by several steps, the superimposing error caused by the former step may be compensated by the following steps to some degree. Therefore, the layer-by-layer superimposing is attempted.

A spherical cave of $120.2\mu\text{m}$ in depth was generated with three layers and six layers. In the case of three layers, the target depth for each layer is $40\mu\text{m}$, $40\mu\text{m}$, and $40.2\mu\text{m}$, respectively. While in the case of six layers, the target depth for the first five layer is $20\mu\text{m}$ and for the last layer $20.2\mu\text{m}$. The superimposing method for each layer is the same as that used in one-step superimposing. That is, a pit was produced at the center first, and then 37 concentric curved grooves were superimposed with a uniform interval of $12.5\mu\text{m}$. The superimposed coefficients for the pit and each elemental groove were obtained from Eq. (18). The target and calculated cross-sectional shapes in the case of six-layer superimposing are shown in Fig. 58. The

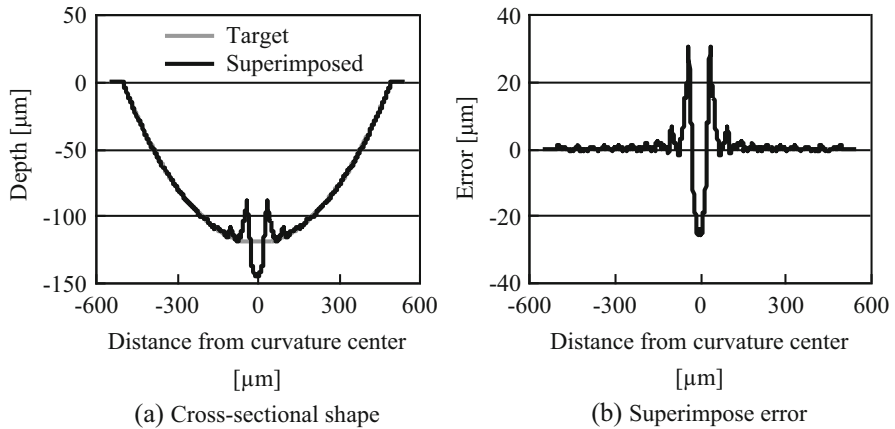


Fig. 57 Cross-sectional shape and superimposed error in the case of one-step superimposing

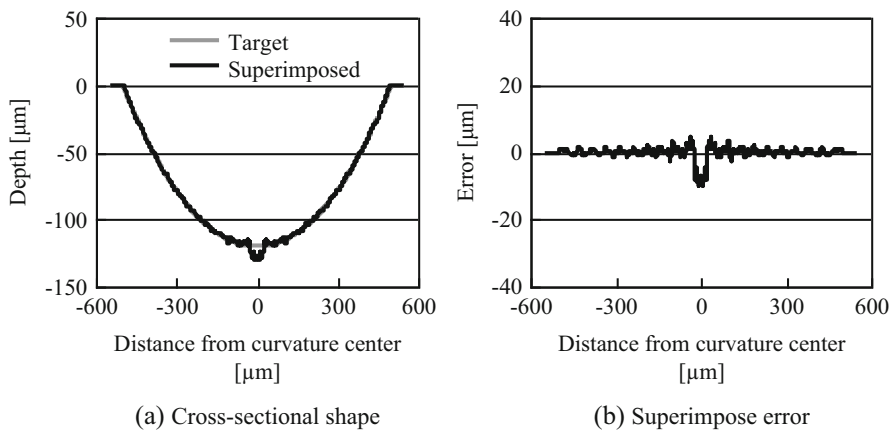


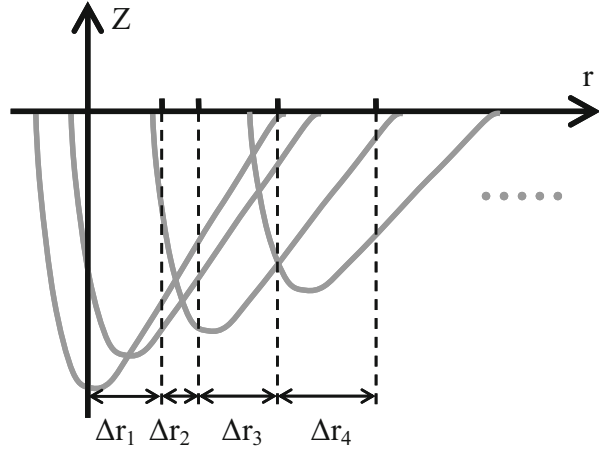
Fig. 58 Cross-sectional shape and superimposed error in the case of layer-by-layer superimposing

peak-to-valley value of the error for one-step superimposing is $57\ \mu\text{m}$ (see Fig. 57b) while that for the three-layer superimposing is $27\ \mu\text{m}$ and that for the six-layer superimposing is about $14\ \mu\text{m}$. From these results, it can be concluded that the layer-by-layer superimposing is an effective way to reduce the superimposing error. Although further increase in the number of layers may decrease superimposing error, excessive number will result in an increased machining time because the scanning speed of the nozzle has a limit.

26.7.3.3 Layer-By-Layer Superimposing with Interval Optimization

Although it is found that layer-by-layer superimposing could reduce the superimposing error greatly, there still remains some superimposing error at the bottom.

Fig. 59 Optimization of radial interval of elemental curved grooves



Hence, the influence of radial interval on superimposing error is investigated. A six-layer superimposing was carried out. Since the depth of the superimposed surface is excessive, deeper than the target shape at the center, the pit at the center is not produced as shown in Fig. 58. Thus, the spherical surface was machined by superimposing 38 concentric elemental curved grooves. Besides, since the superimposing error near the center was remarkable, the interval of the path was optimized at the center area only. As shown in Fig. 59, the radial interval for the first four curved grooves are changed from 1 to 35 μm , while the total of them are fixed as expressed by the following equation:

$$\Delta r_1 + \Delta r_2 + \Delta r_3 + \Delta r_4 = 37.5 [\mu\text{m}] \quad (21)$$

For the other 34 grooves, the interval was fixed at 12.5 μm . The optimal superimposed coefficients for the 38 circular grooves were obtained from Eq. (18), under the different combinations for Δr_1 to Δr_4 . The superimposed cross sections for different combinations are then compared, and the cross-sectional shape with the smallest superimposing error is shown in Fig. 60. Comparing Fig. 58 with Fig. 60, it can be seen that optimizing the radial interval reduces the superimposing error not only at the center area but also in the peripheral area.

26.7.3.4 Comparison of Machined and Calculated Results

Using the optimized interval and scanning speed obtained in Sect. 5.3, the layer-by-layer machining was carried out. The measured three-dimensional shape and the cross-sectional shape are shown in Figs. 61 and 62, respectively. From Fig. 62, it can be seen that by superimposing elemental circular grooves, a spherical shape could be generated. However, the machining error of 30 μm in maximum was generated. The reason for this machining error is considered to be due to the change in the gap width during machining.

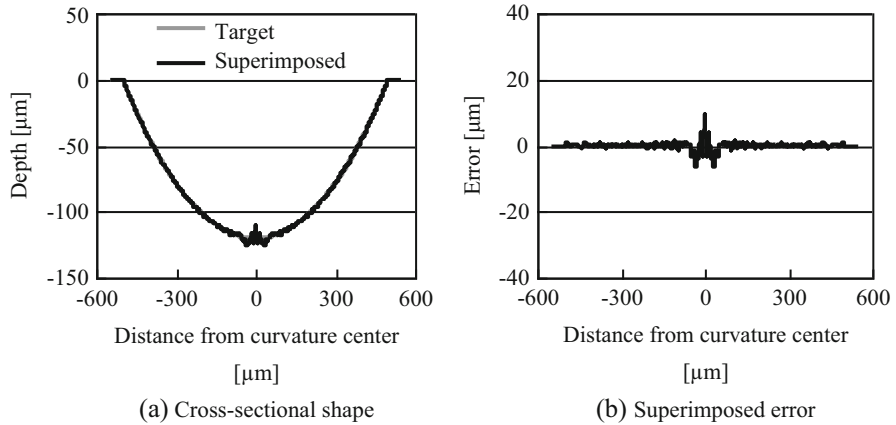


Fig. 60 Cross-sectional shape and superimposed error in the case of layer-by-layer superimposing with interval optimization

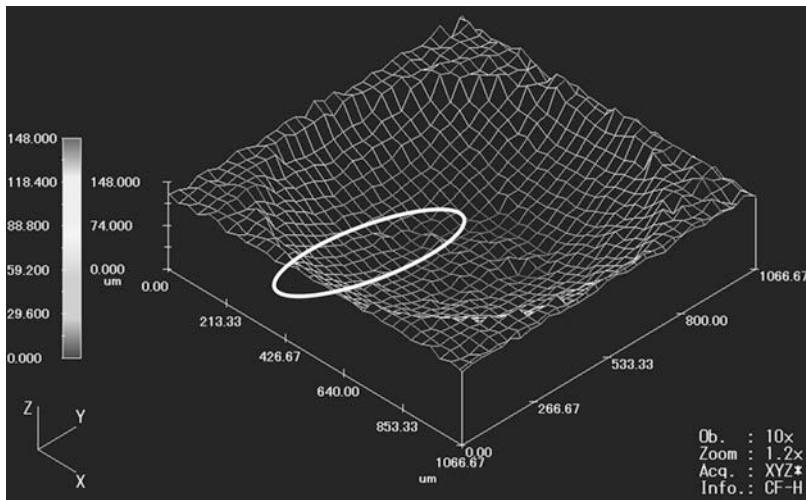


Fig. 61 Machined spherical surface

In order to investigate the influence of the gap width, two grooves were machined at the gap width 0.3 mm and 0.42 mm, which were the same as the gap width before and after the spherical surface generation. The scanning speed for the two grooves is 0.25 mm/s. The cross-sectional shapes of the obtained grooves are shown in Fig. 63. It is found from the results that the machined area broadened with the increase of the gap width. Hence, for precision machining, the change in the gap width should be taken into consideration.

Fig. 62 Cross-sectional shape of machined spherical surface

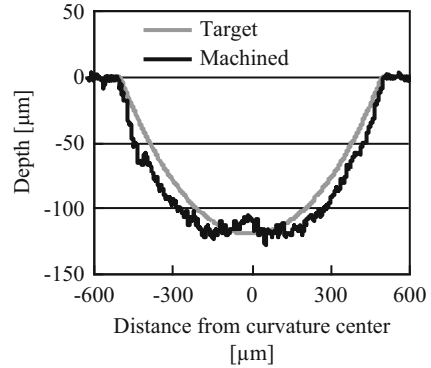
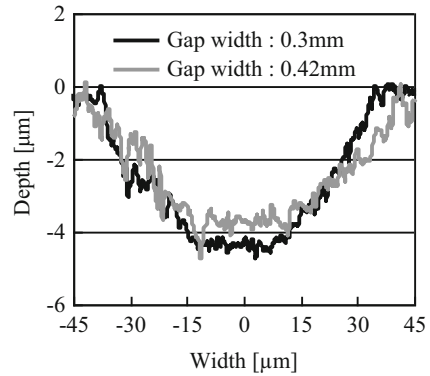


Fig. 63 Influence of change in gap width



26.8 Summary and Outlook

Electrochemical machining should be utilized more and more for industrial applications, because of its unique feature that both higher productivity and finer surface quality are realized at the same time for parts made of difficult-to-cut metals and with complicated shape. Moreover, features of no heat-affected zone, no mechanical damage, and no burrs on the machined surface are especially attractive for functional parts of medical equipment and semiconductor manufacturing equipment. In addition, the cost of tool manufacture and preparation is greatly reduced, and usage of the complicated tool becomes possible due to the feature of no tool wear. However, low machining accuracy due to the large inter-electrode distance, unstable and difficult-to-control machining process due to the complicated inter-electrode phenomenon, and the bad environmental impact due to its waste hinder the expansion of ECM application. Recently, active researches and development activities are being conducted to solve those problems. From now on, we can expect a drastic expansion of ECM application in the near future by further clarifying electrochemical machining phenomenon, realization of stabilization of machining process, breakthrough of

detoxification treatment of waste, establishment of technology to detect and control inter-electrode distance and processing state, establishment of machining technology for hard-to-process material, and so on.

One of the noteworthy innovation technologies in these years is the micro ECM machining with ultrashort voltage pulse, with which microstructures with superfine surface are obtained because the inter-electrode distance is controlled smaller than several micrometers. However, the machining speed becomes extremely slow in micro ECM with ultrashort voltage pulse, since a very long off-time is required to discharge the electric charges on the double layer. Also, the tool wear occurs due to pulse power supply. New breakthrough technologies are expected to increase the attractiveness and application of micro ECM, for example, application of reverse pulse to accelerate the discharge process of electric charges on the double layer, usage of specific pulse waveforms or tool electrode materials to eliminate the tool electrode wear, and combination of micro ECM with EDM or other methods to shorten total machining time.

With the constant efforts of researchers in academic fields and engineers in applied fields, the future of conventional ECM and micro ECM will become brighter and brighter.

References

- Abe T, Masaki T, Wada T, Masuzawa T (2006) Study on micro-ECM with short pulses. *J Jpn Soc Elect Machin Eng* 40(93):29–35. (in Japanese)
- Bard AJ, Faulkner LR (2001) *Electrochemical methods: fundamentals and applications*, 2nd edn. Wiley, New York, p 376
- Bocking CE, Dover SJ, Bennet GR (1995) An investigation into the suitability of high speed selective jet electrodeposition for rapid tooling. *First National Conference on Rapid Prototyping and Tooling Research*, pp 157–173
- Bryson AE (1972) *Waves in Fluids, Illustrated Experiments in Fluid Mechanics*, pp 105–112
- Cagnon L, Kirchner V, Kock M, Schuster R, Ertl G, Gmelin WT, Kück H (2003) Electrochemical micromachining of stainless steel by ultrashort voltage pulses. *Z Phys Chem* 217:299–313
- Chase BD, Holt DB, Unvala BA (1972) Jet polishing of semiconductors. *J Electrochem Soc* 119(3):310–313
- Datta M, Romankiw LT, Vigliotti DR, von Gutfeld RJ (1989) Jet and laser-jet electrochemical micromachining of nickel and steel. *J Electrochem Soc* 136(8):2251–2256
- Endo K, Natsu W (2012) Influence of low-level voltage in pulse ECM on electrode wear and machining accuracy. *Appl Mech Mater* 217-219:2388–2392
- Furuyama K, Kunieda M, Hashimoto T, Yuzawa T (2016) Surface finishing achieved by ECM with a moving wire electrode. *Int J Elect Mach* 21:18–24
- Han W, Kunieda M (2017) Fabrication of tungsten micro-rods by ECM using ultra-short-pulse bipolar current. *CIRP Annals Manuf Technol* 66(1):193–196
- He HD, Qu NS, Zeng YB, Yao YY (2017) Enhancement of mass transport in wire electrochemical micro-machining by using a micro-wire with surface microstructures. *Int J Adv Manuf Technol* 89:3177–3186
- He HD, Zeng YY, Yao YS, Qu NS (2017) Improving machining efficiency in wire electrochemical micromachining of array microstructures using axial vibration-assisted multi-wire electrodes. *J Manuf Process* 25:452–460

- Hinduja S, Kunieda M (2013) Modelling of ECM and EDM processes. *CIRP annals – manufacturing Technology* 62:775–797
- Ikeda T, Natsu W, Kunieda M (2006) Electrolyte jet machining using multiple nozzles. *Int J Elect Machin* 11:25–31
- Kawanaka T, Kunieda M (2015) Mirror-like finishing by electrolyte jet machining. *CIRP Ann Manuf Technol* 64(1):237–240
- Kim BH, Ryu SH, Choi DK, Chu CN (2005a) Micro electrochemical milling. *J Micromech Microeng* 15/1:124–129
- Kim BH, Na CW, Lee YS, Choi DK, Chu CN (2005b) Micro electrochemical machining of 3D micro structure using dilute sulfuric acid. *Annal CIRP* 54(1):191–194
- Koyano T, Kunieda M (2013) Micro electrochemical machining using electrostatic induction feeding method. *CIRP Annal Manufact Technol* 62(1):175–178
- Kozak J (1989) Some aspects of electro jet drilling. *Developments in production engineering design & control*, 363–369
- Kunieda M, Yoshida M, Yoshida H, Akamatsu Y (1993) Influence of micro indents formed by electro-chemical jet machining on rolling bearing fatigue life, *ASME, PED-Vol64*, 693–699
- Kunieda M, Katoh R, Mori Y (1998) Rapid prototyping by selective electro deposition using electrolyte jet. *Annal CIRP* 47(1):161–164
- Kunieda M, Hayasaka A, Yang XD, Sano S, Arae I (2007) Study on Nano EDM using capacity coupled pulse generator. *Annal CIRP* 56(1):213–216
- Low CTJ, Roberts EPL, Walsh FC (2007) Numerical simulation of the current, potential and concentration distributions along the cathode of a rotating cylinder hull cell. *Electrochim Acta* 52:3831–3840
- Maeda S, Saito N, Haishi Y (1967) Principle and characteristics of electro-chemical machining. *Technical Report of Mitsubishi Electric* 41(10):1267–1279. (in Japanese)
- Mitchell-Smith J, Speidel A (2018) A.T.Clare, advancing electrochemical jet methods through manipulation of the angle of address. *J Mater Process Technol* 255:364–372
- Mori Y, Kunieda M (1997) Maskless Coloring of Titanium Alloy Using Electrolyte Jet. *Proc. of JSEME Annual Meeting*, pp 13–16 (In Japanese)
- Natsu W, Kurahata D (2013) Influence of ECM pulse conditions on WC alloy micro-pin fabrication. *Proceedings of the 17th International Symposium on Electromachining*, pp 675–679
- Natsu W, Ikeda T, Kunieda M (2006) Study on characteristics of high speed electrolyte jet machining. *Proceedings of the 7th International Conference on Frontiers of Design and Manufacturing*, pp 333–338
- Natsu W, Ikeda T, Kunieda M (2007) Generating complicated surface with electrolyte jet machining. *Precis Eng* 31(1):33–39
- Newman J, Thomas-Alyea KE (2004) *Electrochemical systems*, 3rd edn. Wiley, New Jersey
- Ooshiro S, Kunieda M, Natsu W (2007) Study on micro electrolyte jet machining. *Proc. of the 15th ISEM*, pp 387–392
- Pajak PT, Desilva AKM, Harrison DK, Mcgeough JA (2006) Precision and efficiency of laser assisted jet electrochemical machining. *Precis Eng* 30:288–298
- Park BJ, Chu CN (2004) Microfabrication by electrochemical machining and deposition. Presentation slide, September 9, 2004, From: <https://zh.scribd.com/presentation/39159630/Micro-Fabrication-by-ECM-and-Deposition>
- Park BJ, Kim BH, Chu CN (2006) The effects of tool electrode size on characteristics of micro electrochemical machining. *Annal CIRP* 55(1):197–200
- Rajurkar KP, Kozak J (2001) Laser assisted electrochemical machining. *Trans of NAMRI* 29:421–427
- Sato K (1970) *Electrochemical machining and chemical machining*, Asakura Publishing Co., Ltd. (In Japanese)
- Schubert A, Hackert-Oschätzchen M, Martin A, Winkler S, Kuhn D, Meichsner G, Zeidler H, Edelmann J (2016) Generation of complex surfaces by superimposed multi-dimensional motion in electrochemical machining. *Proced CIRP* 42:384–389

- Schuster R, Kirchner V, Allongue P, Ertl G (2000) Electrochemical micromachining. *Science* 289:98–101
- Scott K (1991) *Electrochemical reaction engineering*. Academic Press, London
- Vijayasekaran B, Basha CA (2005) Modeling in electrochemical engineering—a critical review. *Trans SAEST* 40:1–13
- Walker JC, Kamps TJ, Lam JW, Mitchell-Smith J, Clare AT (2017) Tribological behaviour of an electrochemical jet machined textured al-Si automotive cylinder liner material. *Wear* 376–377 (Part B):1611–1621
- Wilson JF (1971) *Practice and theory of electrochemical machining*. Wiley, New York
- Yamaguchi K, Natsu W (2017) Investigation of influence of low-level voltage on machining characteristics in pulse wire ECM. *Int J Elect Machin* 22:14–19
- Yoneda K, Kunieda M (1996) Numerical analysis of cross sectional shape of micro-indentations formed by the electrochemical jet machining. *J JSEME* 29(62):1–8. (In Japanese)
- Yong Liu (2010) *Fundamental research on micro electrochemical milling*. PhD thesis, Nanjing University of Aeronautics and Astronautics (in Chinese)
- Yu ZY, Masuzawa T, Fujino M (1998) Micro-EDM for three-dimensional cavities – development of uniform wear method. *Annal of the CIRP* 47/1:169–172
- Yong Liu, Di Zhu, Linsen Zhu. 2012, Micro electrochemical milling of complex structures by using in situ fabricated cylindrical electrode, *Int J Adv Manuf Technol* 60:977–984
- Zeng YB, Yu Q, Wang SH, Zhu D (2012) Enhancement of mass transport in micro wire electrochemical machining. *CIRP Ann Manuf Technol* 61:195–198



Takayuki Shibata, Junji Sasano, and Moeto Nagai

Contents

27.1	Introduction	858
27.2	Localized Modification of Self-Assembled Monolayers (SAMs)	859
27.2.1	Transition Metal Catalysts	859
27.2.2	Organometallic Catalysts	863
27.2.3	Organocatalysts	863
27.2.4	Enzyme Catalysts	864
27.2.5	Photocatalysts	865
27.3	Localized Chemical Dissolution of Inorganic Materials	866
27.3.1	Germanium	866
27.3.2	Silicon	867
27.3.3	Zinc Oxide	871
27.4	Localized Photocatalytic Degradation of Biological Cells	876
27.5	Summary and Outlook	878
	References	879

Abstract

Atomic force microscopy (AFM)-based nanolithography and nanostructure fabrication have attracted much attention in recent years in nanoscience and nanotechnology. The AFM-based technique has unique abilities such as precise positioning on the patterned surface to be modified, surface measurements (such as topography, friction force, and phase imaging) after the fabrication process, and localized surface characterization (mechanical, electrical, magnetic, and thermal properties) at the nanometer scale. The approaches developed to date can be divided into subtractive processes (such as direct mechanical modification and thermomechanical writing) and additive ones (such as local anodic oxidation

T. Shibata (✉) · J. Sasano · M. Nagai
Department of Mechanical Engineering, Toyohashi University of Technology,
Toyohashi, Japan
e-mail: shibata@me.tut.ac.jp

and dip pen nanolithography). Employing a catalytically active AFM probe, a novel nanofabrication strategy has also been used to carry out highly localized catalytic chemical reactions to enable the direct and resistless nanoscale patterning and structuring of various organic/inorganic materials. This chapter focuses on the principles and methods of catalytic AFM-based nanofabrication, challenges in its developments, and the possible solutions.

Keywords

Atomic force microscopy (AFM) · AFM-based nanolithography · AFM-based nanofabrication · Catalyst-functionalized AFM probe · Catalytic chemical reaction · Localized chemical etching · Localized electrochemical etching · Photocatalytic oxidation · Cell membrane perforation

27.1 Introduction

Strategies for manufacturing nanoscale devices can generally be categorized into top-down and bottom-up approaches (Tseng 2008) that could also be integrated with each other. In the top-down approaches, a large piece of material is deconstructed to form nanoscale patterns down to a few tens of nanometers. Common examples include photolithography, electron beam lithography, X-ray lithography, nanoimprint lithography (NIL), and soft lithography. The bottom-up approaches utilize the self-assembly of molecules or colloids, atomic layer deposition (ALD), focused ion beam (FIB)-assisted deposition, etc. to assemble small building blocks (atoms, molecules, and nanoparticles) into larger designed structures driven by the thermodynamics.

The atomic force microscopy (AFM)-based technique enables both top-down and bottom-up strategies, further combining the advantages of the two approaches to fabricate complex nanostructures. Thus, the AFM-based technique has emerged as a powerful tool for nanolithography and nanostructure fabrication. The direct driving force in this technique can be based on mechanical, thermal, electrical, chemical interactions, or their combinations (Garcia et al. 2014). The AFM-based nanofabrication features a high spatial resolution at the nanoscale and flexibility in both two-dimensional (2D) pattern and three-dimensional (3D) structure generation. Additionally, the equipment is relatively easy to operate and potentially low in cost. Most importantly, this technique allows reliable process control in precise positioning on the patterned surface to be modified, surface measurements (such as topography, friction force, and phase imaging) after the fabrication process, and localized surface characterization (mechanical, electrical, magnetic, and thermal properties) at the nanometer scale. To date, several methods have been developed for subtractive processes such as direct mechanical modification (Tseng 2011) and thermomechanical writing (King et al. 2013) and additive processes such as local anodic oxidation (LAO) (Ryu and Garcia 2017) and dip pen nanolithography (DPN) (Brown et al. 2014).

Mechanical modification is the most straightforward approach to remove material at the nanoscale level. It can be carried out by mechanical scratching of solid surfaces

of soft materials (polymers, resists, and biomaterials) or hard materials (metals, ceramics, and semiconductors). However, this process suffers from the intrinsic problems of tip wear and scratch-induced surface damage. Meanwhile, thermo-mechanical writing has been developed to perform fast, reliable nanoindentation on polymer surfaces. In particular, it may be applied to high-density data storage, by using a heated AFM tip for both writing and reading data bits on a polymer surface. The bit size is 30–40 nm, and the array chip size is a few millimeters. The LAO, also referred to as oxidation scanning probe lithography (o-SPL), enables the direct and resistless nanoscale patterning of a large variety of materials: metals, semiconductors, and organic materials such as self-assembled monolayers (SAMs) and biomolecules. This technique is based on controlling the oxidation in selective surface areas by applying a voltage between the AFM tip (negative) and the sample surface (positive) in the presence of oxyanionic species (mostly hydroxide ions (OH^-) provided by the electrolysis of water). In the DPN method, molecules or materials of interest can be coated onto an AFM tip as a “nanopen,” and directly deposited onto a substrate surface with sub-50 nm resolution. In this process, the “ink” can be transferred to the solid surface by diffusion through a water meniscus at the tip-surface interface to build the desired nanostructures. Finally, another nanofabrication strategy can enable highly localized catalytic chemical reactions on a substrate surface by employing catalyst-functionalized AFM probes. This chapter will focus on the principles and methods of this catalytic AFM-based nanofabrication technology, which is relatively new and still being developed.

27.2 Localized Modification of Self-Assembled Monolayers (SAMs)

The catalytic AFM-based nanofabrication technology is generally applied to chemically modify the terminal functional groups of preformed SAMs in a spatially defined fashion, by using AFM probes coated with catalysts such as transition metals, transition metal oxides (as photocatalysts), organometallics, or organic polymers. Similarly, enzymes can be used in either the destructive nanolithography of polypeptide chains, or the constructive nanolithography of materials (Carnally and Wong 2014). These techniques are collectively known as catalytic scanning probe lithography (cSPL). A number of useful modified cSPL techniques have been developed over the past two decades, and their applications now include the direct production of solid surfaces with specific chemical functionalities at nanoscale spatial resolution. Various techniques based on the different types of catalytic chemical reactions are summarized in Table 1.

27.2.1 Transition Metal Catalysts

In 1995, the first attempt was made to catalytically hydrogenate azide-terminated SAMs on a glass substrate in hydrogen (H_2)-saturated isopropanol [$(\text{CH}_3)_2\text{CHOH}$]

Table 1 An overview of catalytic scanning probe lithography (cSPL) approaches based on the different types of catalyst-induced chemical reactions

Catalyst	Material	Environment	Chemical reaction scheme	Critical dimension	Normal load and scan speed	References
Transition metal catalyst						
Pt	Modification of azide-terminated SAM (on glass)	Isopropanol saturated with H ₂	Hydrogenation Reduction of terminal azide to amine	10 × 10 μm ²	~400 nN 1 μm/s	Müller et al. 1995
Pd	Modification of azide-terminated SAM (on glass)	Buffered formic acid (HCO ₂ H/HCO ₂ Na)	Hydrogenation Reduction of terminal azide to amine	200 nm	3.6–4.6 μN ~5 μm/s	Blackledge et al. 2000
Pd	Modification of CBZ-amino-terminated SAM (on glass)	Buffered formic acid (HCO ₂ H/HCO ₂ Na)	Hydrogenation Conversion of CBZ to amine	30–40 nm	3.1 μN ~1.5 μm/s	Blackledge et al. 2000
Pd	Modification of vinyl-terminated SAM (on glass)	ASiH in decane (C ₁₀ H ₂₂)	Alkene hydrosilylation Addition of ASiH on terminal alkene	40–60 nm	3.0 μN ~5 μm/s	Blackledge et al. 2000
Cu	Modification of azide-terminated SAM (on Si)	Terminal alkynes in C ₂ H ₅ OH	Cu(I)-catalyzed azide-alkyne cycloaddition (CuAAC)	50 nm	200–350 nN ~2 μm/s	Paxton et al. 2009
Mn-TACN complexes	Modification of alkene-terminated SAM (on Si)	H ₂ O ₂ in acetonitrile (CH ₃ CN)	Alkene epoxidation	150–200 nm	200–600 nN ~4.8 μm/s	Valyaev et al. 2013
Organometallic catalyst						
PVP-PdNPs	Modification of aryl bromide- or aryl iodide-terminated SAM (on Au)	3-aminophenylboronic acid in CH ₃ CO ₂ Na/CH ₃ OH	Suzuki coupling (C-C bonding formation)	12–15 nm	15–25 nN ~1 μm/s	Davis et al. 2006
PVP-PdNPs	Modification of styrene-terminated SAM (on Au)	4-iodo benzoic acid in NaHCO ₃ /DMF	Heck coupling (C-C bonding formation)	13 nm	25–40 nN ~2 μm/s	Davis et al. 2006

Organocatalyst						
MBS-H ⁺	Modification of TBDMS SAM (on Au/glass)	In air	Silyl ether hydrolysis	25 nm	<10 nN ~6 μm/s	Péter et al. 2004
Enzyme catalyst						
V8 proteinase	Cleavage of peptide (on mica)	Phosphate buffer (pH 7.8)	Peptide hydrolysis (Cleavage at glutamic acid)	4 × 6 μm ²	<50 pN ~0.05 μm/s	Takeda et al. 2003
V8 proteinase	Cleavage of peptide (on glass)	Phosphate buffer (pH 7.8)	Peptide hydrolysis (Cleavage at glutamic acid)	~5 μm	1.2 nN ~0.05 μm/s	Nakamura et al. 2007
Alkaline phosphatase	Deposition of NBT formazan (on mica)	BCIP/NBT in buffer solution	Dephosphorylation of BCIP and subsequent oxidation of NBT	150–170 nm	— ~0.01 μm/s	Riemenschneider et al. 2005
Horseshoe peroxidase	Deposition of PANI nanostructures (on mica)	Aniline monomer/ H ₂ O ₂ in HCl	Polymerization of aniline	~350 nm	— ~0.3 μm/s	Luo et al. 2009
Photocatalyst						
TiO ₂ -NPs	Degradation of textile azo dye (on glass)	In air	Photochemical oxidation (UV irradiation at 254 nm)	30 × 30 μm ²	10–100 nN ~100 μm/s	Zorbas et al. 2005
TiO ₂	Degradation of OEG-terminated SAM (on glass)	In air	Photochemical oxidation (UV irradiation at 325 nm)	50–70 nm	— 1.8–2.5 μm/ s	Ul-Haq et al. 2013

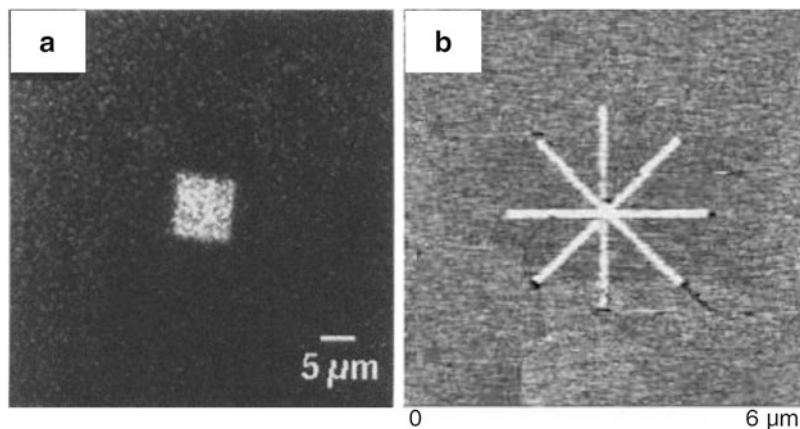


Fig. 1 Typical examples showing the chemical modification of the terminal functional group of preformed SAMs in a spatially defined fashion using catalytically active AFM probes. **(a)** A fluorescence microscopy image of a square pattern (over a $10 \times 10 \mu\text{m}^2$ area) modified by the reduction of the azide groups to amino groups with a Pt-coated AFM probe, followed by derivatizing the amine surfaces with a fluorogenic reagent (ATTO-TAG). **(b)** A lateral force microscopy image of a line pattern with a width of ca. 100 nm fabricated by the hydrolysis of the silyl ether moieties of TBDMS SAMs with an Au-coated AFM probe functionalized with MBS- H^+ as a catalyst (Reprinted from Müller et al. 1995 with kind permission from American Association for the Advancement of Science (AAAS) and Péter et al. 2004 with kind permission from American Chemical Society (ACS))

by scanning with a platinum (Pt)-coated AFM probe over the SAM surface. This caused the reduction of the azide group ($-\text{N}_3$) to amino group ($-\text{NH}_2$) (Müller et al. 1995). A $10 \times 10 \mu\text{m}^2$ square area was successfully modified with patterns in the contact mode with a normal load of 400 nN at a scan speed of $1 \mu\text{m}/\text{s}$, and a patterning resolution of ~ 40 nm can be achieved, as shown in Fig. 1a.

Using the same basic concept, a catalytically active palladium (Pd)-coated AFM probe was used to carry out the catalytic transfer hydrogenation of the end functional groups of SAMs formed on a glass substrate to convert $-\text{N}_3$ to $-\text{NH}_2$ (Blackledge et al. 2000). Line patterns with a minimum width of approximately 200 nm were obtained, by using a normal load of 3.6–4.6 μN at a scan speed of $5 \mu\text{m}/\text{s}$ in a formic acid buffer ($\text{HCO}_2\text{H}/\text{HCO}_2\text{Na}$). The Pd-catalyzed transfer hydrogenation of the benzyloxycarbonyl (CBZ) protecting functional group ($-\text{COOCH}_2\text{C}_6\text{H}_5$) of aminosiloxane SAMs was similarly demonstrated. A normal load of 3.1 μN at a scan speed of $1.5 \mu\text{m}/\text{s}$ was used to create lines as narrow as 30–40 nm in a buffered formic acid solution. Using another reaction scheme, the Pd-catalyzed addition of solvated aminobutyldimethylsilane (ASiH) [$\text{HSi}(\text{CH}_3)_2(\text{CH}_2)_4\text{NH}_2$] on the terminal alkene groups of siloxane SAMs was achieved with a normal load of 3.0 μN at a scan speed of $5 \mu\text{m}/\text{s}$ in a decane ($\text{C}_{10}\text{H}_{22}$) solution containing ASiH. The widths of the formed lines were in the range of 40–60 nm. In these processes, the normal load required for the catalytic chemical reaction was estimated to be greater than 2.5 μN .

A different approach toward the constructive patterning of SAMs is based on the copper(I)-catalyzed azide-alkyne cycloaddition (CuAAC) click reaction by employing a Cu-coated AFM probe (Paxton et al. 2009). The patterning of alkynes onto azide-terminated SAMs formed on a Si substrate was made possible by using an ethanolic solution (C_2H_5OH) of a terminal alkyne containing either 4-pentynoic acid, propargylamine, or 2,5,8,11-tetraoxatetradec-13-yne. A minimal line width of 50 nm can be achieved with a normal load of 200–350 nN at a scan speed of 2 $\mu m/s$, while the SAMs were mechanically deformed when the normal load was greater than 400 nN.

In another example, the local epoxidation of an alkene-terminated SAMs was performed, by using an AFM probe with an immobilized homogeneous transition metal catalyst in acetonitrile (CH_3CN) containing hydrogen peroxide (H_2O_2) as oxidant (Valyaev et al. 2013). Manganese (Mn) complexes with 1,3,7-triazacyclononane (TACN)-type ligands were immobilized on the surface of the Si-based AFM probe. Features having a line width of 150–200 nm were formed at a scan speed up to 4.8 $\mu m/s$. The reaction efficiency was similar when the normal load was varied in the range of 200–600 nN. But when the load exceeded 700–800 nN, mechanical degradation of the SAMs and the Mn-TACN complex catalyst at the surface of the AFM tip was observed.

27.2.2 Organometallic Catalysts

In a first report, an organometallic catalyst was used to initiate selective carbon-carbon (C-C) bond formation via the Suzuki coupling reaction (Davis et al. 2006). Si_3N_4 -based AFM probes coated with polyvinyl-pyrrolidone-modified Pd nanoparticles (PVP-PdNP) were used to spatially control surface-confined C-C catalytic coupling reactions of aryl bromide- or iodide-terminated SAMs on Au in a methanol (CH_3OH) solution of sodium acetate (CH_3CO_2Na) containing 3-aminophenylboronic acid [$H_2NC_6H_4B(OH)_2$], which can be reliably coupled to the terminal aryl halide or styrene moiety of the underlying SAMs. Patterns with line widths as thin as 12–15 nm can be formed with a normal load of 15–25 nN at a scan speed of 1 $\mu m/s$. Similarly, the Heck coupling reaction was successfully employed to modify styrene-terminated SAMs on Au in an *N,N*-dimethylformamide (DMF) [$(CH_3)_2NCHO$] solution of sodium bicarbonate ($NaHCO_3$) containing 4-iodo benzoic acid ($IC_6H_4CO_2H$). $IC_6H_4CO_2H$ was used as a reagent to couple to the terminal styrene moiety of the underlying SAMs. Features with a minimum line width of 13 nm were formed with a normal load of 25–40 nN at a scan speed of 2 $\mu m/s$.

27.2.3 Organocatalysts

An organocatalyst was employed to induce local hydrolysis of the silyl ether moieties of bis(*o-tert*-butyldimethyl-siloxyundecyl)disulfide (TBDMS) SAMs on

Au (Péter et al. 2004). In this process, gold (Au)-coated AFM probes were functionalized with 2-mercapto-5-benzimidazole sulfonic acid (MBS- H^+) as a catalyst. As shown in Fig. 1b, a well-defined line pattern with a width of ca. 100 nm can be fabricated. In this work, the smallest line width obtained was 25 nm (comparable to the size of the contact between the tip and substrate) by scanning the catalytic probe in air at a speed of 6 $\mu\text{m/s}$ with a minimized normal load kept below 10 nN to avoid physical damage of the SAMs.

27.2.4 Enzyme Catalysts

The enzyme-assisted (enzymatic) nanolithography by using biocatalytic AFM probes was first demonstrated in 2003 (Takeda et al. 2003). In this method, an AFM probe was covalently functionalized via amide bonds with *Staphylococcal* serine V8 protease that recognizes glutamic or aspartic acid residues in the peptide and digests the peptide's carboxyl acid terminus. A rectangular pattern ($4 \times 6 \mu\text{m}^2$) was formed by scanning over the surface of the peptide layer composed of A(AEAAKA)₆C covalently immobilized on a mica substrate in a phosphate buffer (pH 7.8). This result indicated that the protease immobilized to the AFM tip specifically hydrolyzed peptide bonds at the C-terminal of glutamic acid (E). It is noted that a slow scan speed of 0.05 $\mu\text{m/s}$ and a small normal load of less than 50 pN should be maintained during the lithography process to allow sufficient reaction time and suppress the mechanical scratching of the peptide layer, respectively.

The same research group also designed fluorescence resonance energy transfer (FRET) peptides as reporter peptides to estimate the enzymatic activity of the *Staphylococcal* serine V8 protease-functionalized AFM probe (Nakamura et al. 2007). The designed 9-mer peptide, FK(TAMRA)KAAEACK(FAM)G, was labeled with carboxyfluorescein (FAM) as a reporter fluorophore and tetramethylrhodamine (TAMRA) as a quencher molecule. The peptide was covalently immobilized on a glass substrate previously silanized with 3-aminopropyltrimethoxysilane (APTMS). In this approach, when the FRET peptide was hydrolyzed at the C-terminal of glutamic acid (E) by the protease on the AFM tip, the fluorescence of FAM can be observed owing to the release of the quencher molecule (TAMRA) from the peptide. A line pattern with a width of 5 μm can be formed with a normal load of 1.2 nN at a scan speed of 0.05 $\mu\text{m/s}$ in a phosphate buffer. The 5- μm line width corresponds to the apex of the pyramidal AFM tip pre-flattened by FIB etching, because the amount of enzyme immobilized on the normal sharp tip was not enough to show clear fluorescence.

An alternative approach to realize constructive nanolithography (instead of the destructive nanolithography described above) has also been proposed (Riemenschneider et al. 2005). In this concept, the enzyme alkaline phosphatase (AP) conjugated with streptavidin was immobilized onto the tip of Si_3N_4 -based AFM probes (with the tip previously functionalized with biotin) via specific biotin-streptavidin interaction. The AP-functionalized AFM probe was slowly moved across the surface of a mica substrate in contact mode at a scan speed of 0.01 $\mu\text{m/s}$

in a solution containing the substrate 5-bromo-4-chloro-3-indolyl-phosphate ($C_8H_6BrClNO_4P$, BCIP) and the cofactor nitro blue tetrazolium (NBT). In this process, the dephosphorylation of BCIP reduces NBT, and as a result insoluble NBT diformazan precipitates are deposited on the mica surface. A line pattern with a width of 150–170 nm and a height of 10 nm was successfully fabricated.

Another study used horseradish peroxidase (HRP)-functionalized Si_3N_4 -based AFM probes in a hydrochloric acid (HCl) solution (pH 4.5) containing aniline monomer and hydrogen peroxide (H_2O_2) (Luo et al. 2009). HRP catalyzed the oxidative polymerization of aniline in the presence of H_2O_2 to produce polyaniline (PANI), which is a conducting polymer (CP) that has attracted great interests in biosensors, nanoelectronics, electrochromic energy storage devices, and so on. The PANI nanostructure with a length of 3 μm , a width of 350 nm, and an average height of 5 nm was formed on a mica substrate at a scan speed of 0.3 $\mu m/s$.

27.2.5 Photocatalysts

Titanium dioxide (TiO_2) exhibits outstanding photocatalytic activity and photoinduced superhydrophilicity, significantly high physical and chemical stability, non-toxicity, relatively low cost, ready availability, and biocompatibility (Hashimoto et al. 2005). Therefore, it is useful in many engineering applications for antifogging, self-cleaning, self-sterilizing, air and water purification, hydrogen evolution, and solar energy conversion functions. Its superior photocatalytic oxidative power to degrade most organic compounds and some inorganic ones has also attracted attention with regard to nanofabrication.

The first successful attempt of AFM-based lithography featuring the photocatalytic activity of TiO_2 was made in 2005, where TiO_2 -functionalized AFM probes were used to carry out the spatially confined photocatalytic oxidation on a thin film of synthetic textile azo dye (Procion Red MX-5B) in air under UV irradiation at 254 nm (Zorbas et al. 2005). In this approach, TiO_2 nanoparticles (120 nm-sized chunks of anatase TiO_2) were attached to the Si-based AFM tip by UV-curable glue. Localized photocatalytic degradation of the azo dye was observed after repeated raster scanning over a $30 \times 30 \mu m^2$ area with the TiO_2 -coated AFM probe in a tapping mode with a normal load of 10–100 nN and a scan speed of $\sim 100 \mu m/s$. After 8 h of scanning, the surface roughness decreased by nearly 70%. However, in this early study, the photochemical oxidation reaction was very slow.

As a further refinement of this basic concept, the selective degradation of protein-resistant oligo(ethylene glycol) (OEG)-terminated silane SAMs on a glass substrate was successfully conducted by localized photocatalytic oxidation using a TiO_2 -coated AFM probe. The apex of the probe tip was illuminated by the light from a 325-nm HeCd laser in close proximity to the silane SAMs (UI-Haq et al. 2013). Standard contact mode AFM probes with spring constants of 0.12–0.35 N/m were coated with a 15–20 nm thick Ti layer by thermal evaporation and then annealed in air at 450 °C for 30 min to produce the photocatalytically active anatase phase. As shown in Fig. 2a, the OEG-terminated silane SAMs were patterned by elimination of

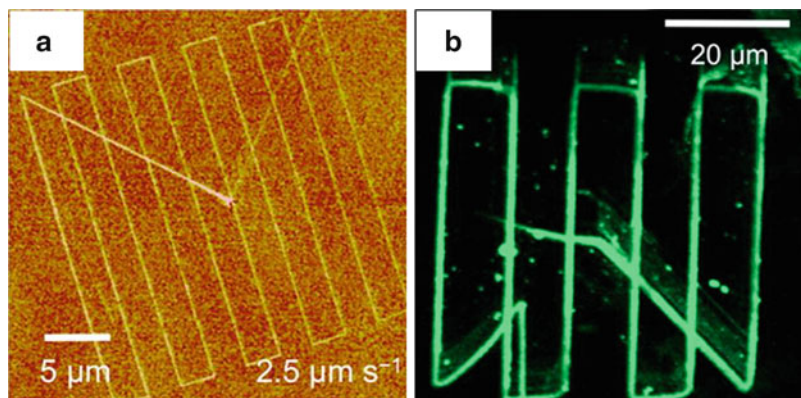


Fig. 2 (a) A lateral force microscopy image of the selective degradation of protein-resistant OEG-terminated silane SAMs by using a TiO₂-coated AFM probe. (b) A confocal fluorescence microscopy image of the patterned sample obtained after the conjugation with His-tagged GFP (Reprinted from Ul-Haq et al. 2013 with kind permission from American Chemical Society (ACS))

ethylene glycol groups [-(OC₂H₄)₆₋₉OCH₃] to form aldehyde functional groups (-CHO) that bind nitrilotriacetic acid via an amine linker. Subsequently, the patterned substrate was immersed in a solution of His-tagged green fluorescent protein (GFP). Features having a line width of 50–70 nm were formed reproducibly, as shown in Fig. 2b. It is noteworthy that continuous lines were obtained at scan speeds ranging of 1.8–2.5 μm/s, while the formed line patterns became discontinuous at the higher scan speed of 4.0 μm/s.

27.3 Localized Chemical Dissolution of Inorganic Materials

27.3.1 Germanium

In recent years, metal-assisted chemical etching (MACE) has been considered as another promising nanofabrication method to prepare Si nanostructures with a high aspect ratio (e.g., nanowires and nanopores), due to its simplicity and relatively low cost (Han et al. 2014). In this process, the catalytic activity of noble metals (e.g., Ag, Au, or Pt) patterned on the Si surface promotes the selective etching of Si. The MACE technique is based on a local galvanic cell mechanism. In a widely accepted model, the local cathodic reduction of the oxidizing agents (such as H₂O₂ or dissolved oxygen) is enhanced on the noble metal. The generated holes (h⁺) lead to the etching of Si via local anode oxidation by the injection of holes into the valence band of Si. However, the strongly corrosive and highly toxic solution of hydrofluoric acid (HF) was required here as an etchant for the direct dissolution of Si and/or formed silicon dioxide (SiO₂).

Using the same principle, AFM-based nanofabrication of Ge (100) was reported by using a Pt-coated AFM probe (Kawase et al. 2013). In this process, a Ge surface is

oxidized by the O₂ molecules dissolved in water to form the water-soluble GeO₂. Therefore, the metal-induced chemical etching of Ge surfaces can be controlled in a small region near the contact point between the probe tip apex and Ge surface. After 10 scans over a 1 × 1 μm² area at a normal force of 3 nN for 45 min, a narrow square-shaped recess with a depth of ca. 4 nm was successfully fabricated in just water saturated with dissolved oxygen.

27.3.2 Silicon

The most straightforward approach of AFM-based material removal is the mechanical scratching of Si surfaces with diamond AFM tip, diamond-coated Si tip, or diamond-like carbon (DLC)-coated Si tip. However, due to the hardness of the Si surface, this approach has been generally limited to the fabrication of shallow grooves (with a depth of a few nanometers) at a relatively high normal load of ~10 μN (Ogino et al. 2008). Moreover, there remain the intrinsic problems of tip wear and scratch-induced surface damage.

AFM-based nanofabrication was used as a chemical etching strategy for the direct removal of Si by using a catalytically active Pt-coated AFM probe (Yamamoto et al. 2017). The nanofabrication was carried out with a commercially available AFM system (Asylum Research MFP-3D-BIO) that was placed on an inverted microscope (Nikon Ti-U). Si-based AFM probes (Olympus AC200TN; nominal spring constant: 9 N/m; nominal tip radius: ~7 nm) were thermally oxidized to obtain a protective layer (thickness: 80 nm) and then coated with a 10-nm Ti adhesive layer and a 100-nm Pt thin film using a sputtering method. After the film deposition, the radius of the AFM tip apex was increased to ~80 nm. The reciprocating AFM tip motion on the Si surfaces was repeated 25 times in each direction for 4 μm, at a normal load of 2 μN and scan speed of 1 μm/s in deionized (DI) water saturated with O₂ (~8.2 mg/L) at room temperature. After the nanofabrication processing, AFM images (10 × 10 μm²) were obtained at a scan speed of 25 μm/s in the tapping mode with the same probe that was used for nanofabrication.

Figure 3 shows typical nanostructures fabricated on single-crystal Si (100) surfaces by using two types of AFM probes. With the uncoated Si probe, unexpected protuberances (height: 2–5 nm; width: ca. 600 nm) were formed on the Si surface (Fig. 3a). The line width was defined by the full width at half maximum (FWHM). These protuberances are most likely due to the formation of a friction-induced oxide layer that is often observed in AFM-based mechanical scratching of Si surfaces (Miyake et al. 2014). In contrast, narrow grooves with a depth of ca. 0.8 nm and a width of ca. 170 nm were successfully fabricated by using a Pt-coated AFM probe (Fig. 3b). It is important to note that shallower grooves with a depth of less than 0.1 nm were obtained by using an AFM probe coated with an Au thin film (thickness: 100 nm) instead of the Pt thin film. These results reveal that Si can be removed by the Pt-assisted catalytic chemical etching process in water at room temperature, without using harsh chemicals such as HF or mechanical scratching. Figure 4 shows an example of the etched letters “TUT MEMS Lab” (with a depth of

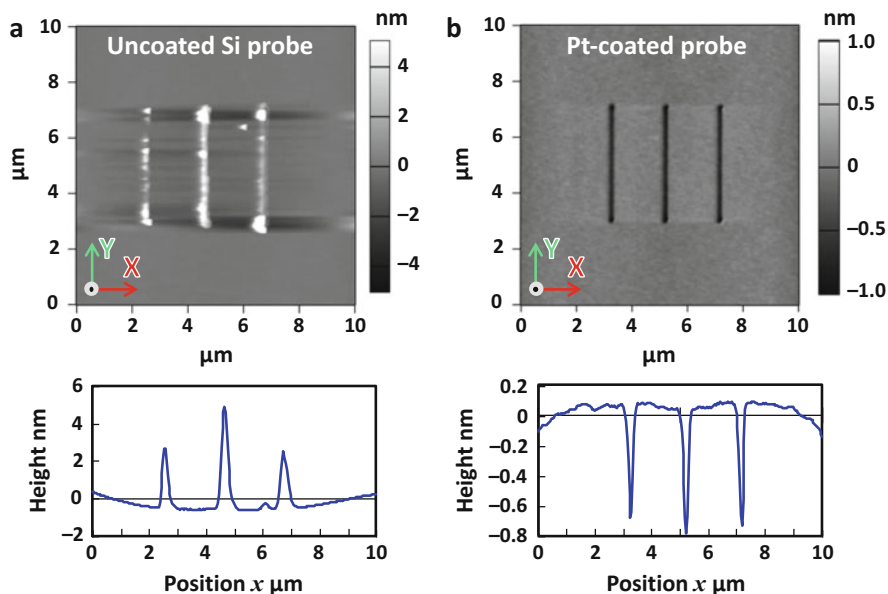
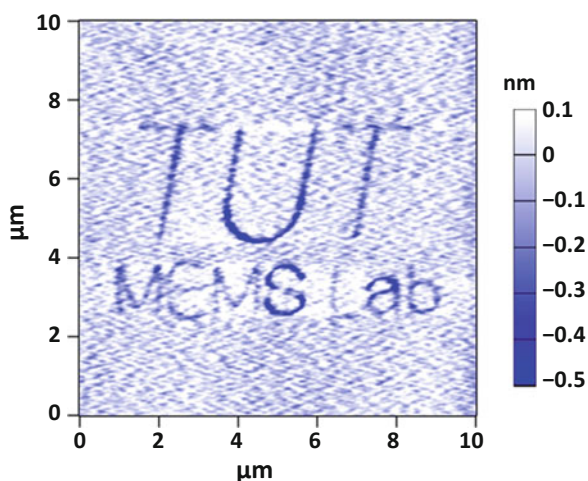


Fig. 3 Typical examples of nanofabrication of Si surfaces in water by using two types of AFM probes operated in the contact mode with a normal load of $2 \mu\text{N}$ at a scan speed of $1 \mu\text{m/s}$. (a) An uncoated Si probe and (b) Pt-coated AFM probe. The cross-sectional profiles of the fabricated grooves are also shown (Reprinted from Yamamoto et al. 2017 with kind permission from Elsevier)

Fig. 4 AFM topography image of the letters “TUT MEMS Lab,” written on the Si surface by using a Pt-coated AFM probe with a normal load of $1 \mu\text{N}$ at a scan speed of $0.1 \mu\text{m/s}$. Each groove was made by traversing the tip over the Si surface only once (a single scan) (Reprinted from Yamamoto et al. 2017 with kind permission from Elsevier)



$\sim 0.2 \text{ nm}$ and a width of $\sim 380 \text{ nm}$) written on the Si surface with only a single scan at a normal load of $1 \mu\text{N}$ and a scan speed of $0.1 \mu\text{m/s}$.

In the same work, in order to enhance the material removal rate, an applied potential was tested in the nanofabrication process with the expectation that an

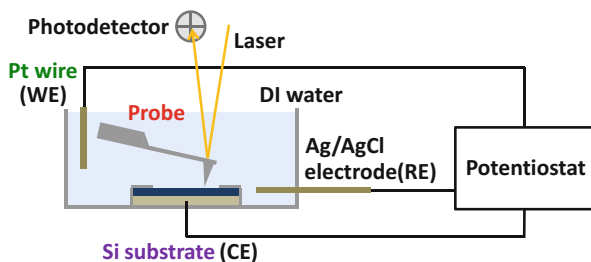
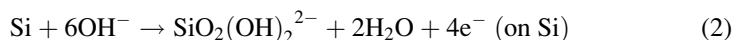


Fig. 5 Schematics of the experimental setup for electrochemically assisted catalytic etching of Si in water by applying an anodic potential to an additional Pt-wire electrode, which was used as the working electrode (WE) in a three-electrode configuration. The Si substrate and Ag/AgCl wire were used as the counter electrode (CE) and reference electrode (RE), respectively (Reprinted from Yamamoto et al. 2017 with kind permission from Elsevier)

electrochemical driving force should assist the removal of Si. A three-electrode configuration was used in the experimental setup shown in Fig. 5. Here, a Pt wire (diameter: 0.3 mm) was immersed in the liquid cell and used as the working electrode (WE), whereas the Si substrate and Ag/AgCl wire were used as the counter electrode (CE) and reference electrode (RE), respectively. It is important to note that although the Pt-coated AFM probe was not directly connected to the electrical circuit, it could be at almost the same potential as the Si substrate (CE) during nanofabrication because they were in physical contact with each other.

Figure 6 shows the effect of the anodic potential applied to the Pt-wire electrode on grooves fabricated using a Pt-coated AFM probe. As expected, the depth of the groove increased up to 43.9 nm at an applied anodic potential of +2.0 V versus Ag/AgCl. The removal rate of Si showed a dramatic 50-fold increase without significantly increasing the line width (ca. 160 nm at FWHM) compared to those obtained without any applied potential (depth: 0.8 nm; width: 170 nm at FWHM, Fig. 3b).

The entire reaction in the Pt-assisted catalytic chemical etching of Si in water without an applied potential can be described as follows and summarized in Fig. 7a.



In Eq. 1, the dissolved O_2 molecules are reduced to OH^- ions by reacting with water (H_2O) on the surface of the Pt-coated AFM tip. In the second step, Si atoms are oxidized by the OH^- ions to form water-soluble silicates according to Eq. 2. In this manner, dissolved oxygen plays a key role in this nanofabrication method. Overall, Si is dissolved via a direct four-electron pathway based on a local galvanic cell mechanism. It is also noteworthy that using an oscillating cantilever of the Pt-coated AFM probe (at a vibrational amplitude of 300–500 nm and a frequency of 0.3–1.3 kHz) to stir the water effectively enhances the Si removal rate by

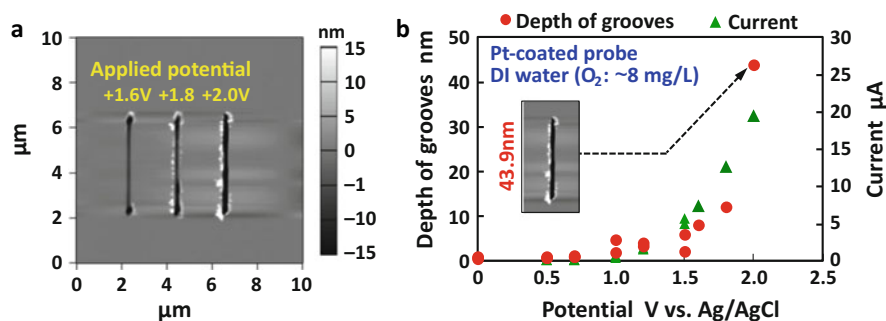


Fig. 6 Effect of the applied anodic potential of the Pt-wire electrode (WE) with the experimental setup in Fig. 5. (a) AFM image of the grooves fabricated by using a Pt-coated AFM probe at a normal load of 2 μN and scan speed of 1 $\mu\text{m/s}$ in water saturated with dissolved oxygen. (b) Depth of the grooves (marked with \bullet) and the electric current (marked with \blacktriangle) as a function of the anodic potential applied to the Pt-wire electrode (Reprinted from Yamamoto et al. 2017 with kind permission from Elsevier)

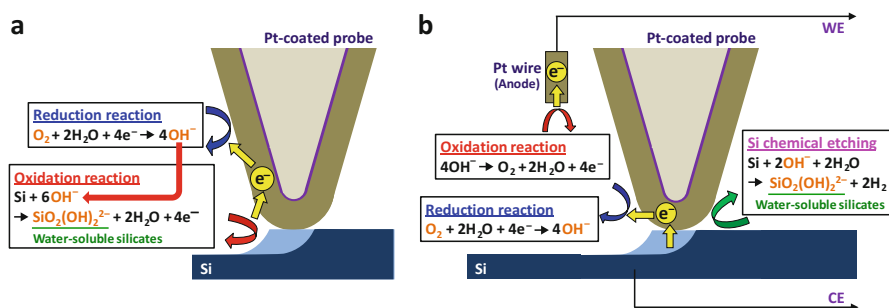
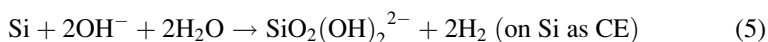
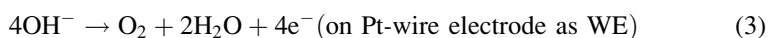


Fig. 7 (a) Mechanism of the Pt-assisted catalytic chemical etching of Si in water containing dissolved O_2 and (b) the electrochemically assisted catalytic etching of Si by the application of an anodic potential to an additional Pt-wire electrode (Reprinted from Yamamoto et al. 2017 with kind permission from Elsevier)

overcoming the oxygen mass transfer limitations during the nanofabrication process. These chemical reactions occur in the immediate vicinity of the Pt-coated tip apex, and the reduction reaction of dissolved O_2 molecules is significantly enhanced by the catalytic activity of Pt. As a result, localized Si removal can be achieved.

On the other hand, the electrochemically assisted catalytic etching of Si with an anodic potential applied to an additional Pt-wire electrode can be described as follows, summarized in Fig. 7b.



In Eq. 3, following the electrolysis of water, the oxidation reaction occurs as an anodic reaction to generate four electrons on the surface of the Pt-wire electrode, with an anodic potential of more than +1.0 V versus Ag/AgCl. In the second step, a four-electron reduction reaction of the dissolved O₂ molecules occurs simultaneously with a cathodic reaction on the surface of the catalytic Pt-coated tip according to Eq. 4, resulting in the generation of OH⁻ ions. In this electrochemical reaction, the number of generated OH⁻ ions can be increased by applying a higher anodic potential to the Pt-wire electrode. In the third step, the formed OH⁻ ions react with Si atoms to form water-soluble silicates [SiO₂(OH)₂²⁻] according to a purely chemical reaction in Eq. 5. Therefore, the chemical etching of Si proceeds in the same way as in an alkaline solution, in contrast to the electrochemical reaction of Eq. 2 that takes place without any applied potential (Fig. 7a). Note that in the second step, the Si substrate is a candidate for the cathodic electrode as well as the Pt-coated probe. However, this reduction reaction would occur preferentially on the Pt catalyst rather than the Si surface. Therefore, the etching of Si can be successfully controlled in a region highly localized in the vicinity of the Pt-coated tip apex.

27.3.3 Zinc Oxide

The selective etching of ZnO based on scanning electrochemical microscopy (SECM) has been proposed (Tang et al. 2012). ZnO thin films were electrodeposited on the surface of an indium-tin oxide (ITO)-coated glass substrate. Micrometer-scale ZnO patterns (etched hole diameter: ~80 μm) can be formed in an electrolyte containing sodium nitrite (NaNO₂) and potassium hydroxide (KCl) at a constant potential of 1.2 V versus SCE. The reaction was carried out for 200 s in a three-electrode configuration using a Pt ultramicroelectrode (UME) with a tip diameter of ca. 26 μm, and the distance between the UME and substrate was kept at ~500 nm during the etching process. In this process, ZnO can be dissolved by the reaction of protons (H⁺) generated on the surface of the UME tip via the reaction of ZnO + 2H⁺ → Zn²⁺ + H₂O. Adding tris(hydroxymethyl)aminomethane as a scavenger to the electrolyte reduced the diameter of the etched hole by ~30 μm, because Tris effectively consumes the etchant (H⁺) so that the latter could not diffuse far from the UME tip.

In another study, the direct patterning of ZnO in water was successfully performed through a material removal process based on highly localized catalytic chemical etching with a Pt-coated AFM probe (Shibata et al. 2017b). The AFM probe laterally traversed the ZnO surface along the same line (25 times in each direction) over a scan length of 4 μm. The AFM was operated in the contact mode with a normal load of 2 μN at a scan speed of 1 μm/s in DI water that was nearly saturated with dissolved O₂ (~8.2 mg/L) at room temperature, in the same way as the catalytic AFM-based nanofabrication of Si described previously.

Figure 8 shows nanoscale grooves fabricated on the surface of polished ZnO (000 $\bar{1}$) single crystals using either an uncoated Si probe or a Pt-coated probe without

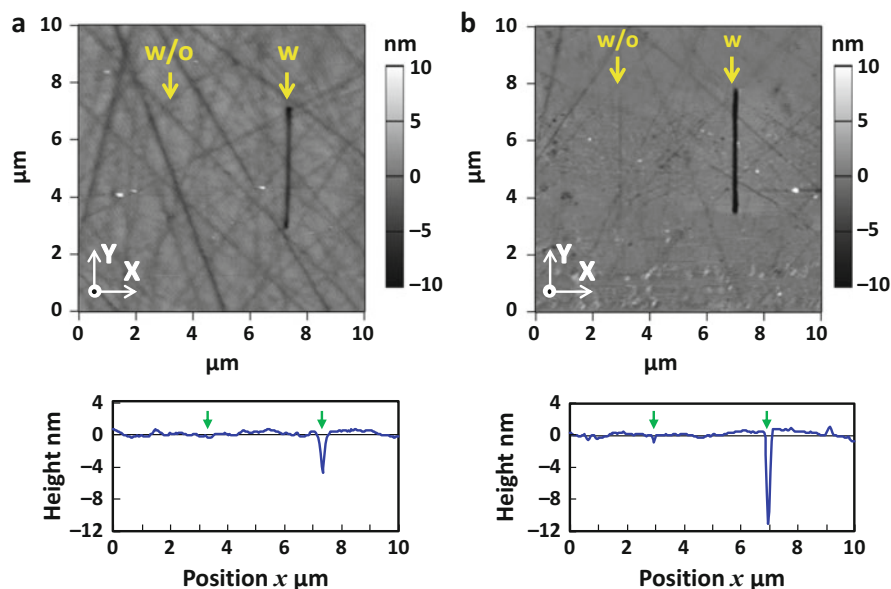


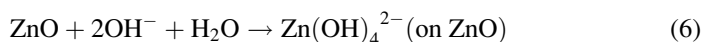
Fig. 8 Nanoscale grooves fabricated on ZnO surfaces in water using two types of AFM probes operated in the contact mode with a normal load of $2 \mu\text{N}$ at a scan speed of $1 \mu\text{m/s}$. **(a)** An uncoated Si probe without oscillation of the Si cantilever (left-hand side) and with oscillation of the cantilever (right-hand side). **(b)** A Pt-coated AFM probe without oscillation (left-hand side) and with oscillation of the cantilever (right-hand side) (Reprinted from Shibata et al. 2017b licensed under the Creative Commons Attribution (CC BY) license)

any applied potential, where the AFM probe and the ZnO substrate were not electrically connected to each other. In the case of the uncoated Si probe (Fig. 8a), a narrow groove with a depth of 5 nm and a width of 200 nm (FWHM) was fabricated with an oscillating Si cantilever at a vibrational amplitude of 360 nm at 630 Hz, although no groove was observed without oscillation of the cantilever. This is because if the fabrication process subjected to mechanical scratching, the normal load between the tip and the sample surface substantially increases with the vibrational amplitude, resulting in a deeper groove (Hyon et al. 1999). For the Pt-coated probe (Fig. 8b), only a very shallow groove (<1 nm deep) was obtained without an oscillating cantilever, while a narrow groove with a depth of 12 nm and a width of 160 nm (FWHM) was fabricated at a vibrational amplitude of 310 nm at 430 Hz. This behavior is similar to that for the uncoated Si probe.

However, the depth of the groove fabricated by the Pt-coated probe even with a blunt tip (radius: 115 nm) was twice of that fabricated by the uncoated Si probe with a sharp tip (radius: 7 nm), although the estimated mean stress at the tip apex in the former (ca. 6 GPa) was much smaller than that in the latter (ca. 36 GPa), according to the Hertzian contact stress theory. Thus, the results suggest that the surface of ZnO could be fabricated via Pt-assisted catalytic chemical etching in water by using the

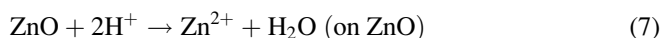
Pt-coated probe with a blunt tip, as in the case of the etching of Si. Meanwhile, by using the uncoated Si probe with a sharp tip, the grooves were fabricated via only mechanical scratching instead of a chemical etching pathway.

In Eq. 1, the concentration of generated OH^- ions increases in the immediate vicinity of the Pt-coated tip, by a mechanism similar to that in the AFM-based Pt-assisted catalytic chemical etching of Si in water mentioned previously (Yamamoto et al. 2017). Thus, it was possible to conclude that ZnO dissolves in water as soluble hydroxyl complexes such as $\text{Zn}(\text{OH})_4^{2-}$ via the following chemical reaction, which is the most widely accepted mechanism for the chemical dissolution of ZnO in an alkaline environment:



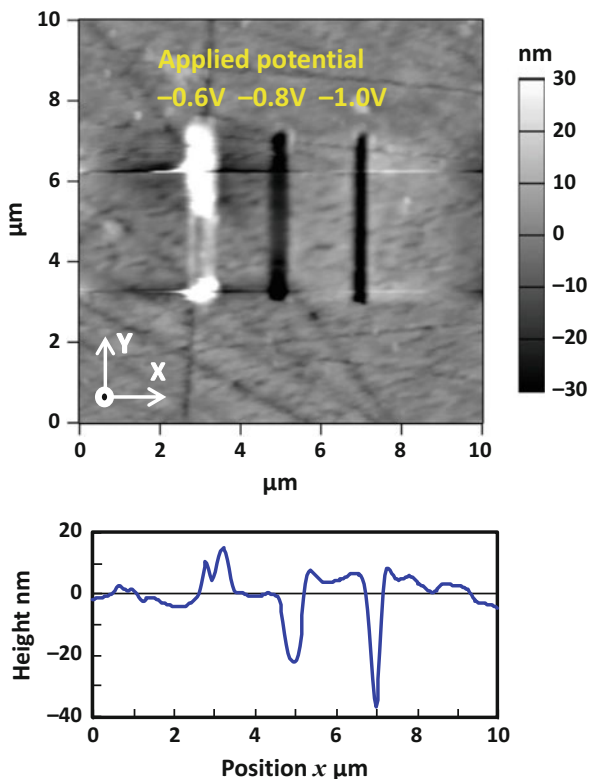
In this reaction, the OH^- ions preferentially react with surface defects on ZnO. Additionally, there was hardly any electron flow from the ZnO substrate to the Pt-coated tip owing to the presence of a reverse-biased Schottky barrier. This suggests that the reduction reaction in Eq. 1 will take place on the surface of the Pt-coated tip when electrons flow across their contact points via defect levels mechanically induced in the ZnO surface. Thus, it is reasonable to conclude that the oscillating cantilever effectively enhances the ZnO removal rate by mechanically inducing defects on the ZnO surface.

Previous studies asserted that the etching rate of ZnO in basic solutions (Eq. 6) is much slower than that in acidic solutions, although the amphoteric oxide ZnO can react in many acidic solutions such as HCl and HF and basic solutions such as NaOH and KOH. In order to increase the material removal rate, ZnO must be fabricated in an acidic environment via the reaction pathway described as follows:



Based on the above etching behavior of ZnO, electrochemically assisted and localized etching of ZnO in water was also investigated in a three-electrode configuration. Figure 9 shows the nanoscale grooves fabricated on the surface of ZnO by applying a cathodic potential to the Pt-wire electrode (WE) using an oscillating Pt-coated AFM probe (vibrational amplitude: 320 nm; frequency: 1.5 kHz) using the same experimental setup shown in Fig. 5, except replacing the Si substrate with ZnO. Note that although the Pt-coated AFM probe was not directly connected to the electrical circuit, it had the same polarity as that of the ZnO substrate used as the counter electrode (CE) during nanofabrication because they were in physical contact with each other. As a result, the depth of the groove increased up to 45 nm at an applied potential of -1.0 V versus Ag/AgCl. The removal rate of ZnO was increased by fourfold compared to that obtained without any applied potential (Fig. 8b). However, at an applied potential of -0.6 V versus Ag/AgCl, unexpected protuberances with a height of ~ 15 nm were formed on the ZnO surface, which may be due to the formation of $\text{Zn}(\text{OH})_2$ via the following reaction pathway:

Fig. 9 Nanoscale grooves fabricated on the ZnO surface in water by applying a cathodic potential to an additional Pt-wire electrode used as the working electrode (WE) in a three-electrode configuration by using a Pt-coated AFM probe. The cross-sectional profile of fabricated grooves is also shown (see diagram below) (Reprinted from Shibata et al. 2017b licensed under the Creative Commons Attribution (CC BY) license)



As shown in Fig. 10a, in the anodic region, OH^- ions are generated on the surface of the cathodically polarized Pt-coated AFM tip by the cathodic reduction of dissolved O_2 (Eq. 1). The depths of the fabricated grooves (less than 15 nm) did not change significantly. Therefore, the grooves may have been fabricated by mechanical scratching rather than a chemical etching pathway. In contrast, the depths of the fabricated grooves increased dramatically in the cathodic region at applied potentials lower than -0.8 V versus Ag/AgCl without a significant increase in the line width (Fig. 10b).

The electrochemically assisted catalytic etching of ZnO with a cathodic potential applied to an additional Pt-wire electrode is summarized in Fig. 11, being subjected to a chemical reaction with H^+ ions according to Eq. 7. The most important step is to control the formation of H^+ ions on the surface of the catalytic Pt-coated tip. Thus, the anodic oxidation of water according to the following reaction would be enhanced on the surface of the Pt-coated tip:

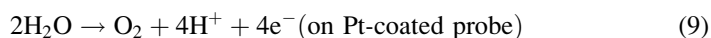
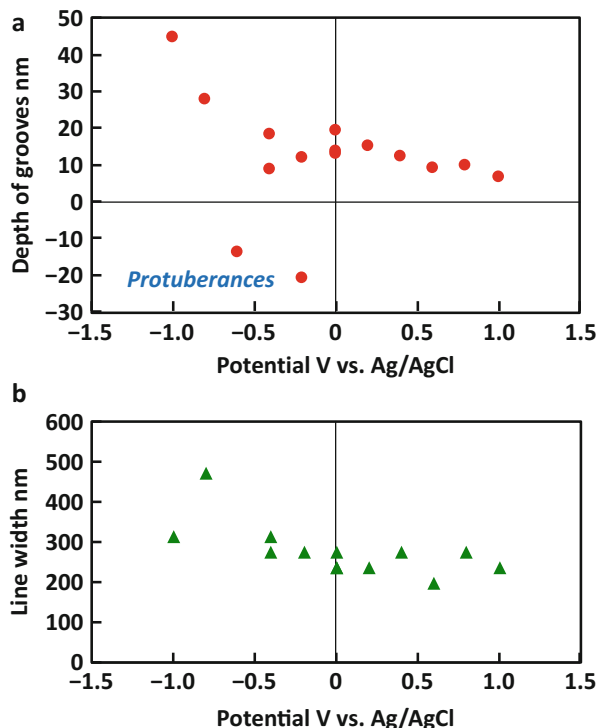
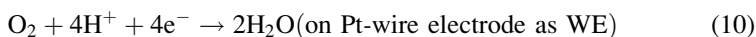


Fig. 10 Effect of potential applied to a Pt-wire electrode on the ZnO etching process. (a) Depth of fabricated grooves and (b) their line widths (FWHM) as a function of the applied potential (Reprinted from Shibata et al. 2017b licensed under the Creative Commons Attribution (CC BY) license)



In order to enhance this oxidation reaction, the reverse chemical reaction, i.e., the reduction reaction, can be controlled by applying a cathodic potential to an additional Pt-wire electrode used as the working electrode (WE), because the oxidation reaction is always present in conjunction with the reduction reaction. The following reduction reaction is expected to take place on the surface of the additional Pt-wire electrode:



The dissolved O_2 in water is the key in promoting the above reaction. The chemical dissolution of ZnO takes place by reaction with H^+ ions (Eq. 7) generated at the surface of the anodically polarized Pt-coated tip via the anodic oxidation of H_2O (Eq. 9). Furthermore, although the ZnO substrate is also a candidate for the anodic electrode as well as the Pt-coated probe, this oxidation reaction would occur preferentially on the Pt catalyst. Therefore, the etching of ZnO can be controlled in a highly localized region in the immediate vicinity of the Pt-coated tip apex. It is concluded that the AFM-based nanofabrication technique utilizing Pt-mediated electrochemical reactions has the ability to chemically etch other materials that can react with H^+ or OH^- ions to form a water-soluble complex, by controlling the cathodic or anodic polarity of the additional Pt-wire electrode, respectively.

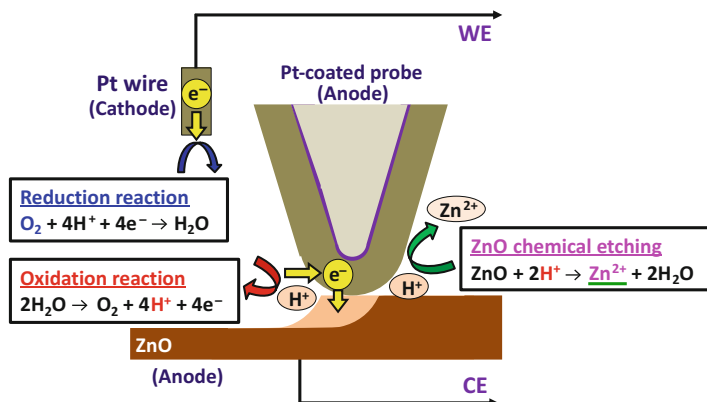


Fig. 11 Mechanism of electrochemically assisted and localized etching of ZnO in water containing dissolved O₂ using a catalytically active Pt-coated AFM probe, when a cathodic potential is applied to an additional Pt-wire working electrode (Reprinted from Shibata et al. 2017b licensed under the Creative Commons Attribution (CC BY) license)

27.4 Localized Photocatalytic Degradation of Biological Cells

As described previously, TiO₂-functionalized AFM probes could enable highly localized photocatalytic oxidation of organic compounds (Zorbas et al. 2005; Ul-Haq et al. 2013). To apply the AFM-based nanofabrication technique in bioscience and biotechnology, the penetration of the membranes of living cells by photocatalytic TiO₂-coated AFM probes was demonstrated, based on a highly localized photochemical oxidation reaction under UV irradiation in a physiological saline solution (Shibata et al. 2017a). In this work, single-phase TiO₂ thin films with anatase structures were obtained by anodic oxidation of Ti thin films (100 nm thickness) sputtered on a Si-based AFM probe (Olympus AC200TN; nominal spring constant: 9 N/m; nominal tip radius: ~7 nm) that was previously thermally oxidized to a thickness of approximately 80 nm. Note that the tip radius of TiO₂-coated AFM probes was increased up to ~50 nm, compared with a nominal tip radius of ~7 nm for uncoated AFM probes.

Cell membrane perforation tests with the TiO₂-coated AFM probes were conducted on a commercially available AFM system (Asylum Research MFP-3D-BIO), which was placed on an inverted microscope (Nikon Ti-U). As shown in Fig. 12a, a UV light (330–380 nm, ~1.25 mW/cm²) was carefully aligned and focused on the initial contact point between the surface of the cell membrane and the tip apex of the AFM probe with a microscope objective lens (60×, NA = 0.7) in insertion tests. Figure 12b shows a typical optical microscopy image of the insertion with a living HeLa cell adhered to a glass coverslip at an indentation speed of 300 nm/s. In Fig. 13, the insertion was confirmed by the cell's red fluorescence, which came from a popular red fluorescent dye, propidium iodide (PI), entering the living cell. Since PI cannot permeate through the membranes of living cells,

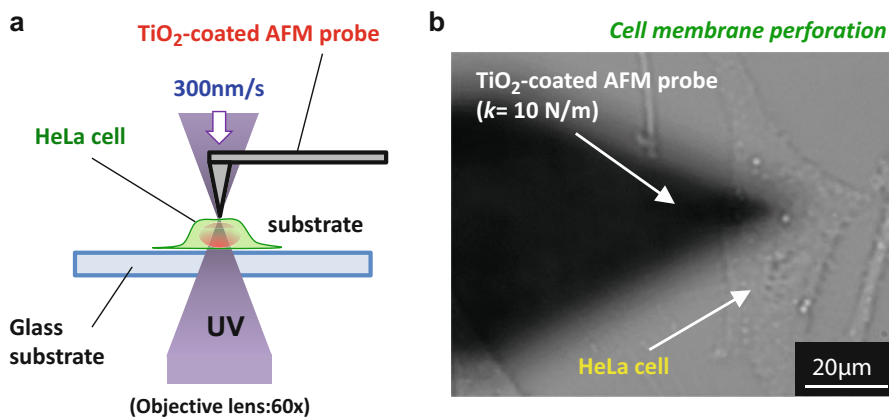


Fig. 12 (a) Experimental setup and (b) an optical microscopy image showing insertion tests with living HeLa cells, conducted on the AFM system at an indentation speed of 300 nm/s using TiO₂-coated AFM probes under UV irradiation (Reprinted from Shibata et al. 2017a with kind permission from the American Institute of Physics (AIP))

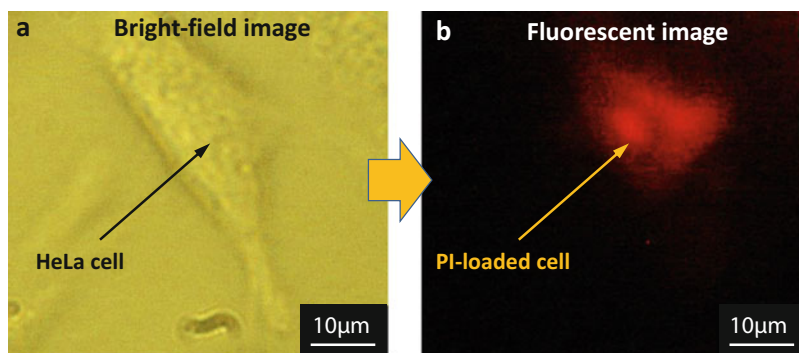


Fig. 13 (a) A bright-field microscopy image and (b) a fluorescence microscopy image of a living HeLa cell, which was loaded and stained with propidium iodide (PI) after the penetration of its cell membrane by the TiO₂-coated AFM probe under UV irradiation (Reprinted from Shibata et al. 2017a with kind permission from the American Institute of Physics (AIP))

physically formed pores (such as those created by the perforation of the cell membrane) are the only route for the dye to enter the cell and stain the nuclei.

The penetration force and the probability of cell membrane perforation, obtained using uncoated or TiO₂-coated AFM probes with or without UV irradiation, are summarized in Table 2. With an uncoated AFM probe and no UV irradiation, the probability of cell membrane perforation was estimated to be 46% ($n = 24$), which is similar to that obtained using an uncoated AFM probe under UV irradiation [46%, ($n = 44$)]. The resulting penetration force, 120 ± 40 nN ($n = 20$), was also nearly identical. Therefore, the UV light had no effect on cell membrane penetration

Table 2 Probability of the cell membrane perforation and the penetration force obtained with uncoated and TiO₂-coated AFM probes with or without UV irradiation (Reprinted from Shibata et al. 2017a with kind permission from the American Institute of Physics (AIP))

	Uncoated probe		TiO ₂ -coated probe	
	w/o UV	w/ UV	w/o UV	w/ UV
Probability (%)	46 (<i>n</i> = 24)	46 (<i>n</i> = 44)	0 (<i>n</i> = 18)	78 (<i>n</i> = 23)
Penetration force (nN)	150 ± 70 (<i>n</i> = 11)	120 ± 40 (<i>n</i> = 20)	N/A	110 ± 30 (<i>n</i> = 18)

N/A data not available

at least under our experimental conditions. Conversely, no cell membrane penetration was observed (0% for 18 insertion tests) with the TiO₂-coated AFM probe and no UV light. This is likely because that an increased tip radius (up to 50 nm, compared to 7 nm for uncoated AFM probes) reduces the mean stress at the tip apex on the cell membrane by one to two orders of magnitude. In contrast, the probability of cell membrane perforation was improved to 78% (*n* = 23) even when using the blunt-tipped probe compared to the uncoated probe. The mean penetration force was estimated to be 110 ± 30 nN (*n* = 18) for all insertion tests, suggesting that the degradation of cell membrane was clearly accelerated by the TiO₂ photocatalyst. Remarkably, the cell viability after the membrane perforation was estimated as 100% (*n* = 8). As a result, such direct nanoscale modification of living cells under near physiological conditions can be carried out using highly localized photochemical oxidation with a catalytic TiO₂-coated AFM probe. This technique can be used for minimally invasive intracellular delivery.

27.5 Summary and Outlook

This chapter presents an overview of catalytic AFM-based nanofabrication mediated by a highly localized chemical reaction by employing suitable catalytically active AFM probes. An important feature of this strategy is the combination of the AFM and catalyst. The AFM can provide spatial resolution and alignment accuracy at the nanometric level during nanofabrication processing. On the other hand, the catalyst allows a chemical reaction to proceed at a lower temperature, increases the reaction rate by lowering the activation energy, and/or controls the chemical reaction pathway. There have been many reports about modifying the terminal functional group of preformed SAMs with a spatial resolution on the order of 10 nm using catalyst-functionalized AFM probes (e.g., coated with transition metals, transition metal oxides, organometallics, or organic polymers as catalyst). These approaches are generally referred to as catalytic scanning probe lithography (cSPL). Enzyme-assisted nanolithography by using biocatalytic AFM probes (enzymatic nanolithography) has also been developed to enable the distractive nanolithography of polypeptide chains or the constructive nanolithography of materials of interest. Recently, inorganic materials (Ge, Si, and ZnO) have been successfully subjected

to highly localized catalytic chemical etching at room temperature by using Pt-coated AFM probes. Instead of harsh chemicals, this approach uses just water saturated with dissolved oxygen that can act as an oxidizer. Therefore, it provides a platform for nanofabrication technologies with low environmental impact. In another unique approach, membranes of living cells were penetrated by using a photocatalytic TiO₂-coated AFM probe. Under UV irradiation in a physiological saline solution, the material was removed by a highly localized photochemical oxidation reaction. This technique may enable the minimally invasive delivery of biomolecules, including DNA, RNA, peptides, proteins, and various other small molecules, into almost any type of cells.

In general, however, the low throughput is the main limitation for the wide industrial adoption of AFM-based nanofabrication techniques, even though these technologies possess extremely high resolution, alignment accuracy, and reliability, together with the advantages of relatively easy operation at a potentially low cost. Therefore, a general challenge for all AFM-based techniques is to improve the throughput while maintaining the nanometric feature size. The most straightforward solution is to use an array structure consisting of multiple AFM probes. In this parallel system, the throughput is proportional to the number of probes in the array, making it possible to perform nanofabrication at a considerably faster rate and also to dramatically improve the speed of in situ sample inspection. If this problem can be solved in the near future, there will be no doubt that AFM-based nanofabrication is a promising technology to provide nanoscale devices and systems necessary for the sustained evolution of electronic, photonic, biomedical, and nanosystems.

References

- Blackledge C, Engebretson DA, McDonald JD (2000) Nanoscale site-selective catalysis of surface assemblies by palladium-coated atomic force microscopy tips: chemical lithography without electrical current. *Langmuir* 16(22):8317–8323
- Brown KA, Eichelsdoerfer DJ, Liao X, He S, Mirkin CA (2014) Material transport in dip-pen nanolithography. *Front Phys* 9(3):385–397
- Carnally SAM, Wong LS (2014) Harnessing catalysis to enhance scanning probe nanolithography. *Nanoscale* 6(10):4998–5007
- Davis JJ, Bagshaw CB, Busuttill KL, Hanyu Y, Coleman KS (2006) Spatially controlled Suzuki and Heck catalytic molecular coupling. *J Am Chem Soc* 128(43):14135–14141
- Garcia R, Knoll AW, Riedo E (2014) Advanced scanning probe lithography. *Nat Nanotechnol* 9(8):577–587
- Han H, Huang Z, Lee W (2014) Metal-assisted chemical etching of silicon and nanotechnology applications. *Nano Today* 9(3):271–304
- Hashimoto K, Irie H, Fujishima A (2005) TiO₂ photocatalysis: a historical overview and future prospects. *Jpn J Appl Phys* 44(12):8269–8285
- Hyon CK, Choi SC, Hwan SW, Ahn D, Kim Y, Kim EK (1999) Direct nanometer-scale patterning by the cantilever oscillation of an atomic force microscope. *Appl Phys Lett* 75(2):292–294
- Kawase T, Mura A, Dei K, Nishitani K, Kawai K, Uchikoshi J, Morita J, Arima K (2013) Metal-assisted chemical etching of Ge(100) surfaces in water toward nanoscale patterning. *Nanoscale Res Lett* 8(1):151

- King WP, Bhatia B, Felts JR, Kim HJ, Kwon B, Lee B, Somnath S, Rosenberger M (2013) Heated atomic force microscope cantilevers and their applications. *Annu Rev Heat Transf* 16:287–326
- Luo X, Pedrosa VA, Wang J (2009) Enzymatic nanolithography of polyaniline nanopatterns by using peroxidase-modified atomic force microscopy tips. *Chem Eur J* 15(21):5191–5194
- Miyake S, Wang M, Kim J (2014) Silicon nanofabrication by atomic force microscopy-based mechanical processing. *J Nanotechnol* 2014:102404
- Müller WT, Klein DL, Lee T, Clarke J, McEuen PL, Schultz PG (1995) A strategy for the chemical synthesis of nanostructures. *Science* 268(5208):272–273
- Nakamura C, Miyamoto C, Obataya Takeda S, Yabuta M, Miyake J (2007) Enzymatic nanolithography of FRET peptide layer using V8 protease-immobilized AFM probe. *Biosens Bioelectron* 22(9–10):2308–2314
- Ogino T, Nishimura S, Shirakashi J (2008) Scratch nanolithography on Si surface using scanning probe microscopy: influence of scanning parameters on groove size. *Jpn J Appl Phys* 47(1):712–714
- Paxton WF, Spruell JM, Stoddart JF (2009) Heterogeneous catalysis of a copper-coated atomic force microscopy tip for direct-write click chemistry. *J Am Chem Soc* 131(19):6692–6694
- Péter M, Li X-M, Huskens J, Reinhoudt DN (2004) Catalytic probe lithography: catalyst-functionalized scanning probes as nanopens for nanofabrication on self-assembled monolayers. *J Am Chem Soc* 126(37):11684–11690
- Riemenschneider L, Blank S, Radmacher M (2005) Enzyme-assisted nanolithography. *Nano Lett* 5(9):1643–1646
- Ryu YK, Garcia R (2017) Advanced oxidation scanning probe lithography. *Nanotechnology* 28(14):142003
- Shibata T, Iio N, Furukawa H, Nagai M (2017a) Nanofabrication technique based on localized photocatalytic reactions using a TiO₂-coated atomic force microscopy probe. *Appl Phys Lett* 110(6):063701
- Shibata T, Yamamoto K, Sasano J, Nagai M (2017b) Electrochemically assisted localized etching of ZnO single crystals in water using a catalytically active Pt-coated atomic force microscopy probe. *AIP Adv* 7(9):095012
- Takeda S, Nakamura C, Miyamoto C, Nakamura N, Kageshima M, Tokumoto H, Miyake J (2003) Lithographing of biomolecules on a substrate surface using an enzyme-immobilized AFM tip. *Nano Lett* 3(11):1471–1474
- Tang J, Zheng J-J, Yu Y-T, Chen L, Zhang N, Tian Z (2012) Selective etching of ZnO films on an ITO substrate using a scanning electrochemical microscope. *Electrochim Acta* 83:247–252
- Tseng AA (ed) (2008) *Nanofabrication: fundamentals and applications*. World Scientific, Singapore
- Tseng AA (2011) Removing material using atomic force microscopy with single- and multiple-tip sources. *Small* 7(24):3409–3427
- Ul-Haq E, Patole S, Moxey M, Amstad E, Vasilev C, Hunter CN, Leggett GJ, Spencer ND, Williams NH (2013) Photocatalytic nanolithography of self-assembled monolayers and proteins. *ACS Nano* 7(9):7610–7618
- Valyaev DA, Clair S, Patrone L, Abel M, Porte L, Chuzel O, Parrain J-L (2013) Grafting a homogeneous transition metal catalyst onto a silicon AFM probe: a promising strategy for chemically constructive nanolithography. *Chem Sci* 4(7):2815–2821
- Yamamoto K, Sato K, Sasano J, Nagai M, Shibata T (2017) Localized etching of silicon in water using a catalytically active platinum-coated atomic force microscopy probe. *Precis Eng* 50:344–353
- Zorbas V, Kanungo M, Bains SA, Mao Y, Hemraj-Benny T, Misewich JA, Wong SS (2005) Current-less photoreactivity catalyzed by functionalized AFM tips. *Chem Commun* 36:4598–4600



3D Microfabrication Using Photocatalytic Reaction

28

Satoru Takahashi

Contents

28.1	Introduction	882
28.2	Concept of 3D Microfabrication Using Photocatalytic Reaction	883
28.2.1	2D Microfabrication Using Photocatalyst Substrate	883
28.2.2	3D Microfabrication Using Photocatalyst Nanoparticles	884
28.3	Realization of 3D Microfabrication Using Photocatalytic Reaction	885
28.3.1	Basic Experiment for 3D Microfabrication	885
28.3.2	Evaluation of Material Property of Deposited Microstructures	891
28.3.3	Evaluation of Fabrication Characteristics	893
28.4	Automatic 3D Microfabrication Using Photocatalytic Reaction	895
28.4.1	Automatic 3D Microfabrication System	895
28.4.2	Automatic 3D Microfabrication Experiments	896
28.4.3	Various Developments of 3D Microfabricated Structures	898
28.5	Summary and Outlook	899
	References	901

Abstract

This chapter describes a new type of laser additive manufacturing processing based on photocatalytic reaction, which provides a three-dimensional (3D) complex microstructure fabrication with a process resolution of a few tens of micrometers. This 3D microfabrication technique is based on the following unique fabrication principle. In metal ion solution, excited titanium dioxide (TiO_2) photocatalyst nanoparticles dispersed in 3D space in liquid phase deposit the metal only at the beam waist of a converging laser beam under proper optical and chemical condition. Therefore, by sweeping the beam waist within the solution, any shape of 3D microstructure can be fabricated. Evaluation of material property

S. Takahashi (✉)

Research Center for Advanced Science and Technology (RCAST), The University of Tokyo, Tokyo, Japan

e-mail: takahashi@nanolab.t.u-tokyo.ac.jp

© Springer Nature Singapore Pte Ltd. 2018

J. Yan (ed.), *Micro and Nano Fabrication Technology*, Micro/Nano Technologies,

https://doi.org/10.1007/978-981-13-0098-1_28

881

of deposited microstructures by a scanning electron microscopy (SEM), an energy-dispersive X-ray spectroscopy (EDX), and an X-ray diffraction spectroscopy (XRD) analyses confirmed its unique processing principle. Several demonstrational fabrication experiments suggest its high feasibility for fabricating 3D complex microstructures.

Keywords

Microfabrication · 3D microstructures · Photocatalyst · Additive manufacturing · Micromachines · Photocatalyst nanoparticles · TiO₂ nanoparticles · Photocatalytic reaction

28.1 Introduction

This chapter describes a new type of three-dimensional (3D) complex microstructure fabrication technique based on photocatalytic reaction. This technique is performed by precisely controlling the local reduction position of metal ions caused by photocatalytic reaction in the three-dimensional liquid phase. Since photocatalytic reaction can be directly used as processing energy of micro-additional processing, this technique is characterized by being able to realize 3D microfabrication even with a low-power continuous wave laser source, not an ultrashort pulse laser like multiphoton processing technique. In this microfabrication technique, titanium dioxide (TiO₂) photocatalyst is mainly employed, which is well known as one of the most active photocatalytic materials with which an existence of photon causes a photoelectrochemical reaction.

Scientific studies on TiO₂ photocatalyst started in about 1970 (Fujishima et al. 1969). After emerging as an excellent photocatalyst material not only for photoelectrochemical solar energy conversion but also for environmental purification, TiO₂ photocatalyst has been practically applied to various fields including solar cell, air purification, sterilization and cancer therapy, and so on (Fujishima et al. 2000). There exist two types of photo-induced effects on TiO₂ surface as shown in Fig. 1. One is the photocatalytic reaction (Fig. 1a) and the other is photo-induced highly hydrophilic conversion (Fig. 1b), proceeding on the TiO₂ surface irradiated with UV. The photo-induced highly hydrophilic conversion is generated by increasing the amount of hydroxyl groups on its surface irradiated with UV light (Hashimoto and Irie 2004; Wang et al. 1997).

For the 3D microfabrication described in this chapter, the former photo-induced effect, photocatalytic reaction, by TiO₂ is used (Fig. 2). When a TiO₂ photocatalyst absorbs light having energy greater than its bandgap energy (TiO₂ absorbs light with wavelength that is shorter than about 400 nm), it generates pairs of holes and electrons, and the electrons in the valance band are transferred to the conduction band. These electron–hole pairs cause oxidation–reduction reactions. The holes are so oxidative that they can break apart the water molecules to form hydrogen gas and hydroxyl radicals. And the electrons can reduce oxygen molecules to form superoxide anions (Fujishima and Honda 1972). If excitation of TiO₂ occurs in ionic solution of noble metal whose ionicity is lower than H⁺, reduction of the metal ions is possible. Actually, it was reported that under illumination with UV light, TiO₂

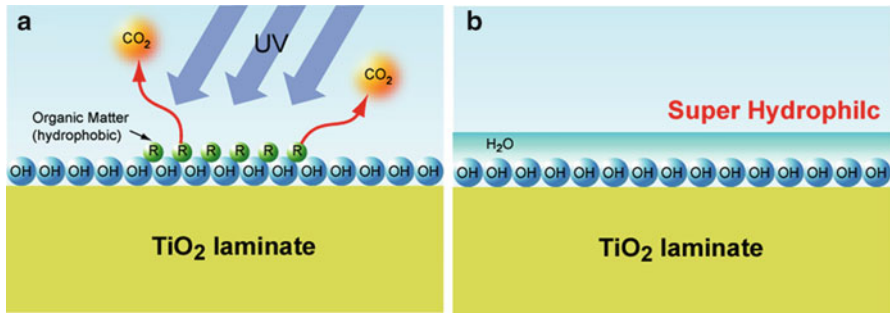
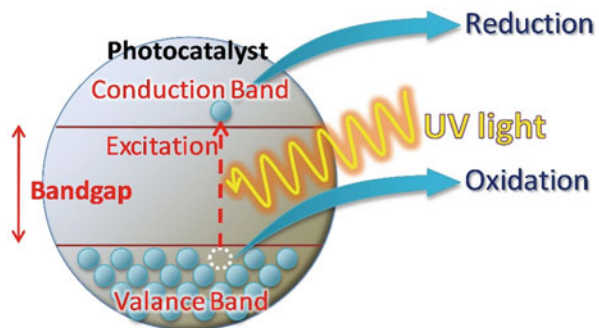


Fig. 1 Photo-induced effects on TiO_2 surface. (a) Photocatalytic reaction. (b) Photo-induced highly hydrophilic conversion

Fig. 2 Excitation of photocatalyst



caused reduction of metal ions and deposition of metals such as silver (Herrmann et al. 1988) and platinum (Ishii et al. 1998).

28.2 Concept of 3D Microfabrication Using Photocatalytic Reaction

28.2.1 2D Microfabrication Using Photocatalyst Substrate

Ishii et al. reported that 2D patterns of Pt were fabricated along focal point traces of 380 nm wavelength excitation laser beam on the surface of rutile TiO_2 substrates (Ishii et al. 1998). It was also reported that silver can be deposited on the other powered semiconductors, such as CdS , Fe_2O_3 , and WO_3 , using wavelengths in the visible spectral region (Herrmann et al. 1988). Tatsuma et al. realized 2D micro-patterning induced by photocatalytic reaction of TiO_2 with photomask (Tatsuma et al. 2002). Ohko reported that absorbed Ag ion of AgNO_3 can be reduced to Ag nanoparticle by using commercial black fluorescent lamp for dried AgNO_3 aqueous solution on TiO_2 film from anatase sol (Ohko et al. 2003).

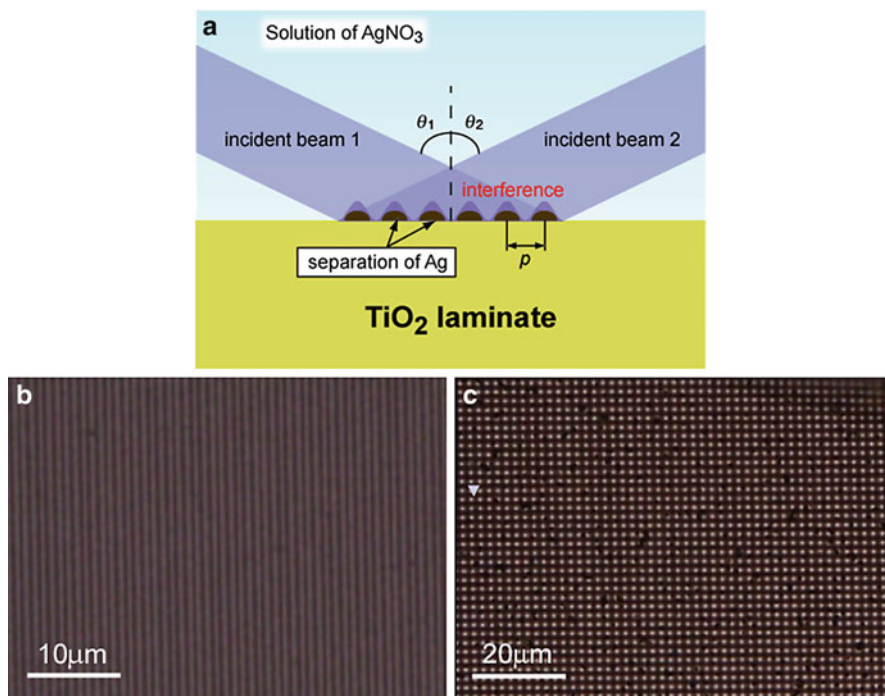


Fig. 3 Examples of 2D structure microfabrication on TiO_2 photocatalyst film using interference pattern (Okuno 2005). (a) Fabrication condition. (b) Optical microphotograph image of silver grating by a standing wave of counter propagating laser beams. (c) Optical microphotograph image of silver 2D grating by two standing waves having a vertical relationship

Figure 3 shows one of typical experiments for 2D microstructure fabrication using TiO_2 photocatalyst film (Folium, Kawasaki Heavy Industries Ltd.). In this experiment, the excited region on TiO_2 photocatalyst film is controlled by the interference pattern, which can be easily generated by using the counter-propagating laser beams (He-Cd Laser, wavelength = 325 nm, power 10 mW). Ag ions of AgNO_3 aqueous solution located near the excited region are reduced, and silver is deposited, corresponding to the interference pattern (Fig. 3a). Thus 1D grating (Fig. 3b) by using a set of counter-propagating laser beams and 2D grating (Fig. 3c) by using two sets of counter-propagating laser beams having a vertical relationship can be fabricated (Okuno et al. 2005).

28.2.2 3D Microfabrication Using Photocatalyst Nanoparticles

In 2006, Aso et al. proposed a 3D microfabrication principle using photocatalytic reaction by photocatalyst nanoparticles (Aso et al. 2006). While a TiO_2 substrate-like film is employed for 2D microfabrication, a suspension of TiO_2 photocatalyst nanoparticles in an aqueous solution of metal ion is employed in order to achieve

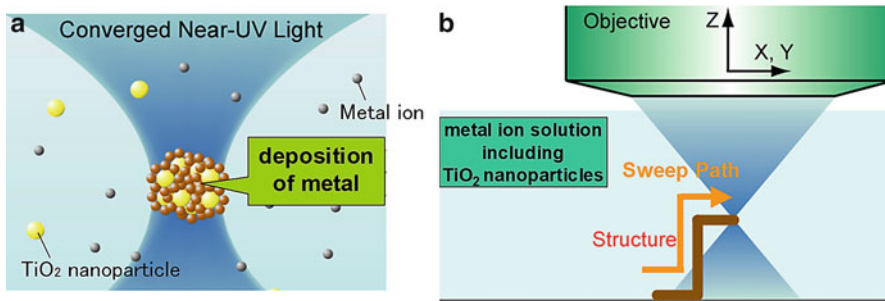


Fig. 4 3D microfabrication principle using a suspension of TiO_2 photocatalyst nanoparticles in metal ion solution (Aso 2006). (a) 3D space deposition of metal using converged near-UV light. (b) 3D microstructuring by three-dimensionally sweeping the beam waist of the converging laser beam

3D microfabrication (Fig. 4). If a converging laser beam illuminates the TiO_2 nanoparticles in the 3D solution, a cluster of metal will appear at the beam waist by the photocatalytic redox reaction (Fig. 4a). Therefore, by sweeping the beam waist, a three-dimensional structure would be formed along the path of it (Fig. 4b).

Figure 5 shows results of a fundamental exposing experiment for studying influence of a wavelength of light source on processing phenomena by the photocatalytic reaction. TiO_2 nanoparticles (NTB-1, Showa Titanium Co. Ltd., primary particle size: 10–20 nm, phase formation: brookite) were dispersed in an ammonium aqueous solution of AgNO_3 . In the case of 325-nm-wavelength, meaning that energy of its photon is greater than bandgap energy of TiO_2 , TiO_2 nanoparticles locating in the entire laser propagating area can be excited. As a result, silver ions cannot be reduced at only 3D point of the beam waist but be reduced at almost the entire laser irradiation area by the TiO_2 nanoparticles dispersed in the 3D liquid phase (Fig. 5a).

On the other hand, in the case of 405 nm-wavelength, Aso et al. found that silver ions can be reduced at only the 3D point of the beam waist of the converging laser beam (Fig. 5b). Although absorption in TiO_2 is limited to the UV region and visible light is hardly absorbed, these experiments revealed that by using a converging laser beam with a wavelength of 405 nm, it is possible to locally excite TiO_2 nanoparticles and reduce silver at the beam waist. Therefore, by scanning the beam waist in the solution, arbitrary 3D silver structures can be expected to be fabricated.

28.3 Realization of 3D Microfabrication Using Photocatalytic Reaction

28.3.1 Basic Experiment for 3D Microfabrication

Figure 6 shows a typical experimental setup (Okuno et al. 2006) to realize the concept of the 3D microfabrication. The light source of the system is a wavelength 405 nm laser diode whose maximum output is 55 mW (LDM Series Blue, Omicron

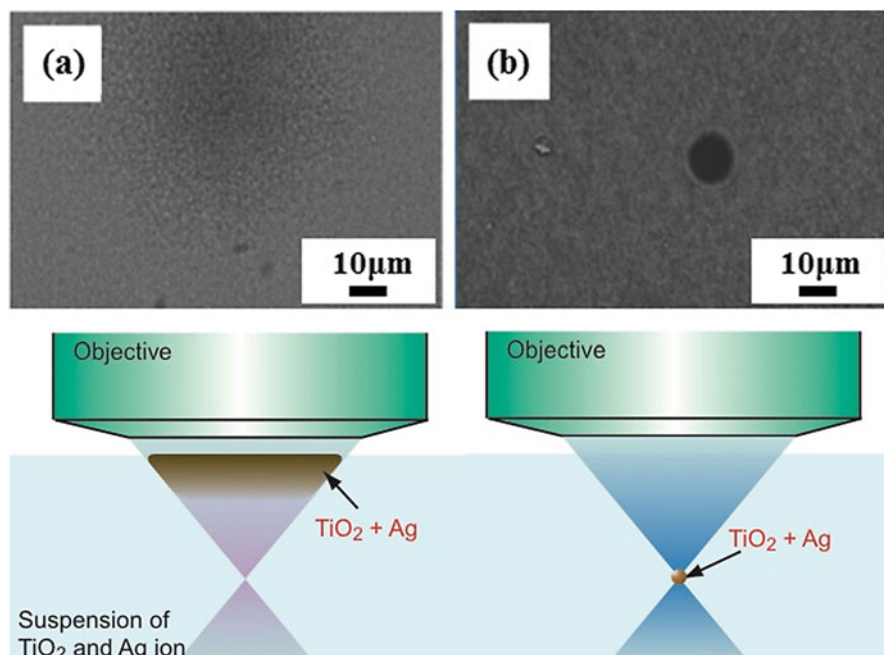


Fig. 5 Fundamental exposing experiment on the wavelength dependence by converging laser beam in sample solution; wavelength of laser is (a) 325 nm, (b) 405 nm (Aso 2006)

Laserage). Its exit aperture is connected with a single-mode optical fiber with a 3.3 μm diameter (LDM-405 FAS, Omicron Laserage). The end point of the fiber can be positioned by a motorized linear stage under computer control (LINEAR-BALL GUIDE, SURUGA SEIKI Ltd.). With this stage, it is possible to position the fiber end by 2 μm resolution. After going through the fiber, the light is gathered together to a parallel beam by a collimating lens with a focal length 48 mm and an 8 mm effective diameter (06GLC205, MELLES GRIOT). Via a beam splitter, the laser beam enters a 40x objective with a 0.9 numerical aperture (CFI S Fluor 40x, NIKON). By the objective, the laser beam is converged at a point on the sample stage. And a CCD camera enables observation of the fabrication process in real time. To avoid CCD saturation, a dichroic mirror is inserted in front of the CCD imaging lens.

In order to fabricate continuous structures following the beam waist scan, the deposition should start on the cover slip or on the substrate. Matsuda et al. experimentally analyzed the effect of substrate to get continuous structures under the condition shown in Table 1. Firstly, to analyze the effect of the substrate, the deposition process was observed when the beam waist was set about 50 μm above the substrate. A typical in-process microscopic image obtained from the side is shown in Fig. 7. It was not observed that a continuous structure was fabricated, i.e., below the beam waist, silver grains appeared in a discontinuous manner and flew downward. Next, the deposition processes for different distances between the beam

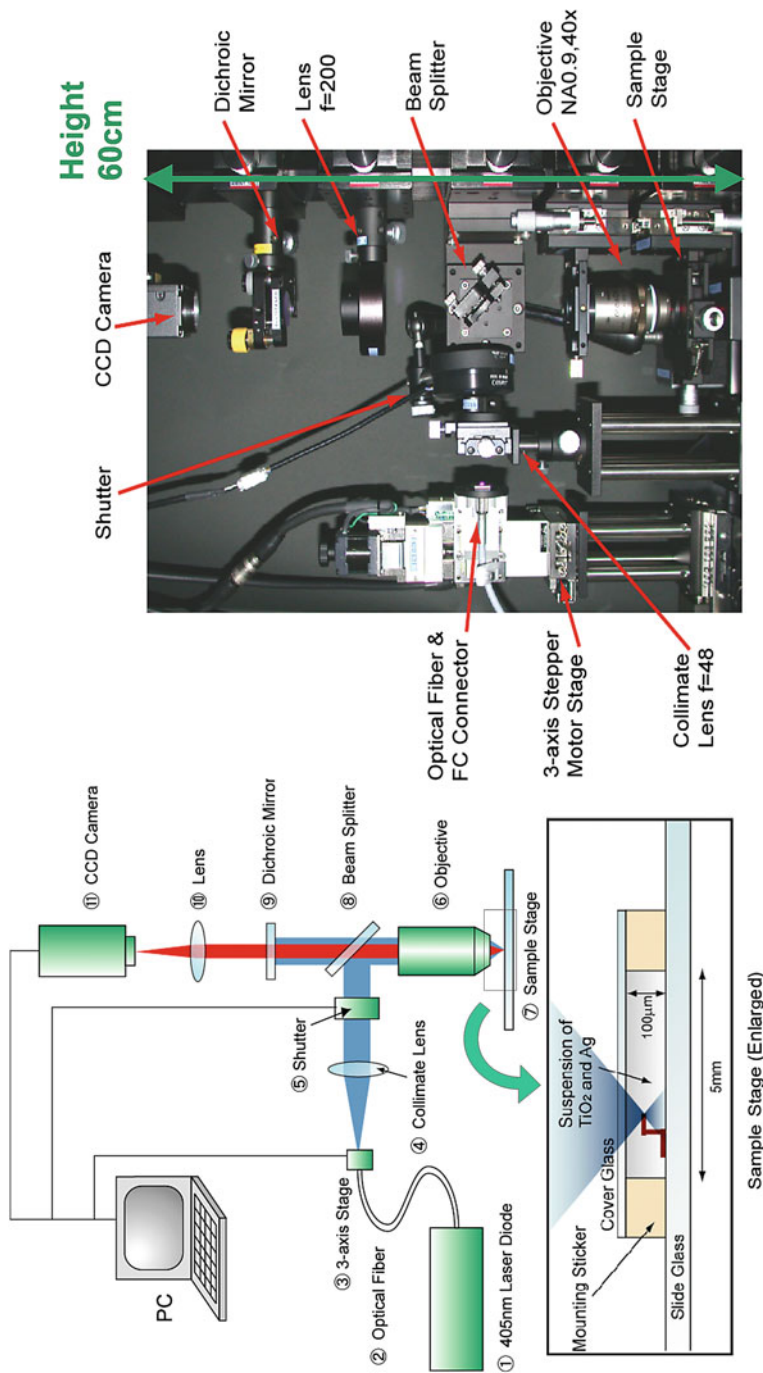
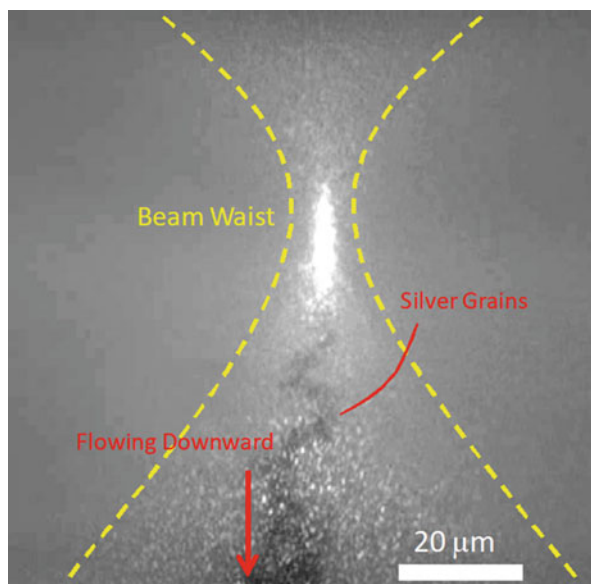


Fig. 6 Typical experimental setup. The laser diode on the left side of the diagram provides a wavelength 405 nm laser beam. Via an optical fiber, a collimating lens, a beam splitter, and an objective, the laser is converged at a point on the sample stage on the right side of the diagram. The fiber end can be positioned by a computer-control stage so that it is possible to manipulate the beam waist with the computer (Okuno 2006)

Table 1 Fabrication condition (Matsuda et al. 2010)

Sample solution	TiO ₂ particle size 10–20 nm	0.7 wt%
	AgNO ₃	0.01 mol/l
	NH ₃	9 wt%
Fabrication beam power (measured before objective lens)		2 mW
Scan velocity	Z-direction	1.5 μm/s
	X-direction	1.0 μm/s

Fig. 7 In-process observation of deposition at the beam waist (Matsuda et al. 2010)

waist and the substrate were compared. These visualization experiments showed that the deposition condition depended on a considerable extent on the distance between the beam waist and the substrate. Three important cases are shown in Fig. 8. When the distance was less than about 20 μm, continuous deposition on the substrate was observed (Fig. 8a, b). When the distance was greater than about 20 μm, continuous deposition was not observed, but many grains of silver were found (Fig. 8c).

These results show that the substrate considerably affects the deposition condition and that the deposition condition depends on the distance between the beam waist and the substrate. For continuous deposition, in particular, the distance must be lesser than a certain value. This suggests that some fixed substance such as the substrate or a deposited structure is necessary near the beam waist to ensure continuous deposition. This phenomenon seems relevant to the thermal conditions, fluid dynamical conditions, or optical conditions around the beam waist.

Figure 9 shows the in-process observation of 3D microfabrication under the continuous deposition condition. The structures were found to be growing and

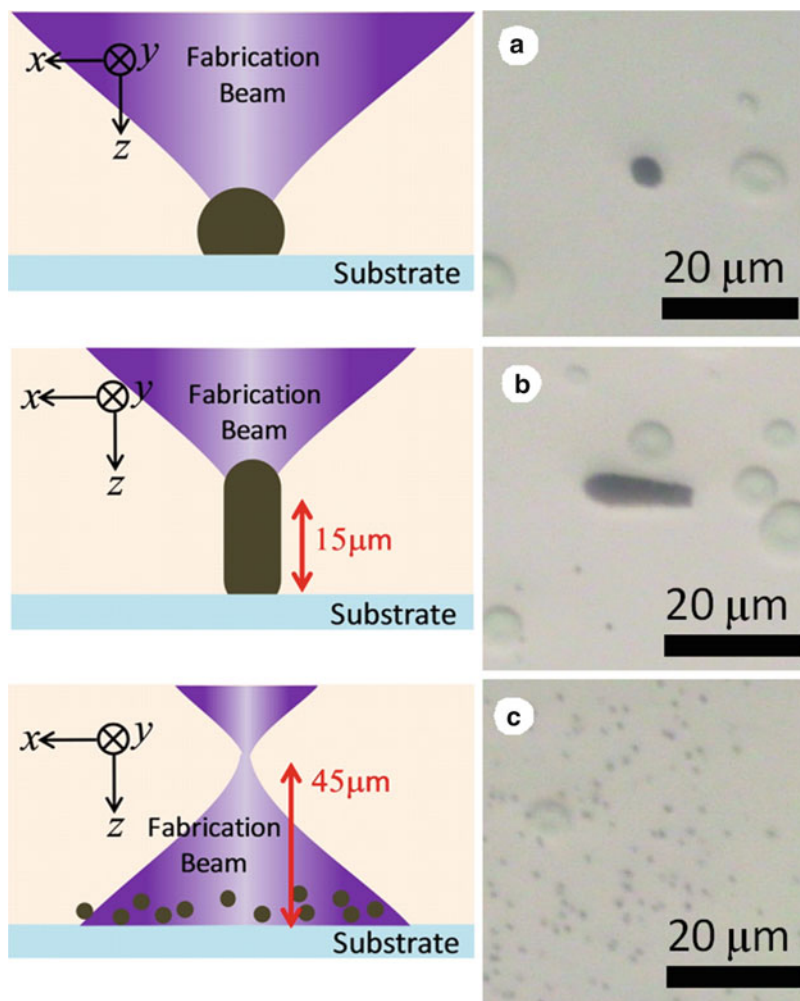


Fig. 8 Effect of substrate on deposition condition. The distances between the beam waist and the substrate are 0, 15, and 45 μm in (a), (b), and (c), respectively. The exposure times are 10, 10, and 100s in (a), (b), and (c), respectively. The images on the right side are taken using the top view unit. In (b), the image was taken after the structure was laid down (Matsuda et al. 2010)

scattering light at their growth point. From this observation, it was confirmed that the deposition of silver was localized in 3D and that the microscale structure underwent 3D growth following the beam waist scan. The deposition region was relatively longer in the z-direction than in the x- and y-directions (Fig. 9B). This may correspond to the light intensity distribution of 3D profile of beam waist (Matsuda et al. 2010).

Figure 10B shows an example of microstructures, fabrication of which includes cross-linking structures (Fig. 10A). This result suggests that the 3D microfabrication method based on the continuous deposition by TiO_2 nanoparticles dispersed in the

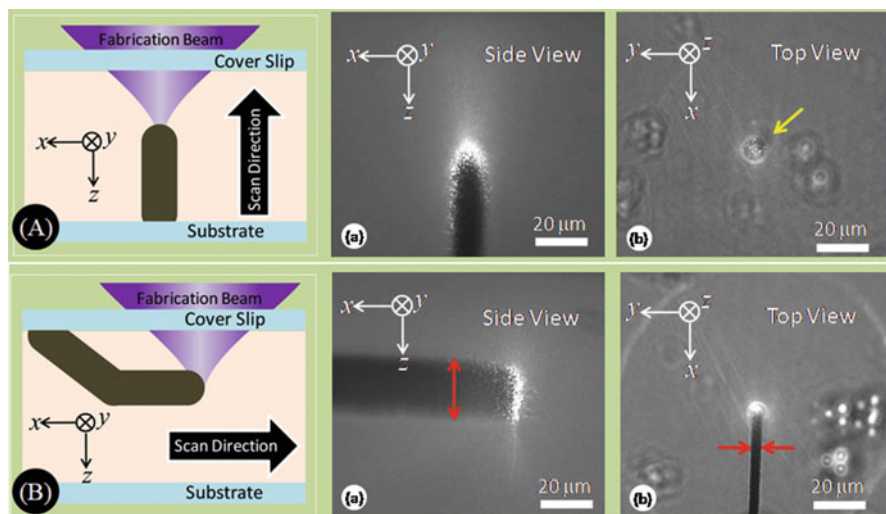


Fig. 9 In-process observation of 3D microfabrication based on continuous deposition. (A) Z-direction scan. (B) X-direction scan. (a) Side view and (b) top view (Matsuda et al. 2010)

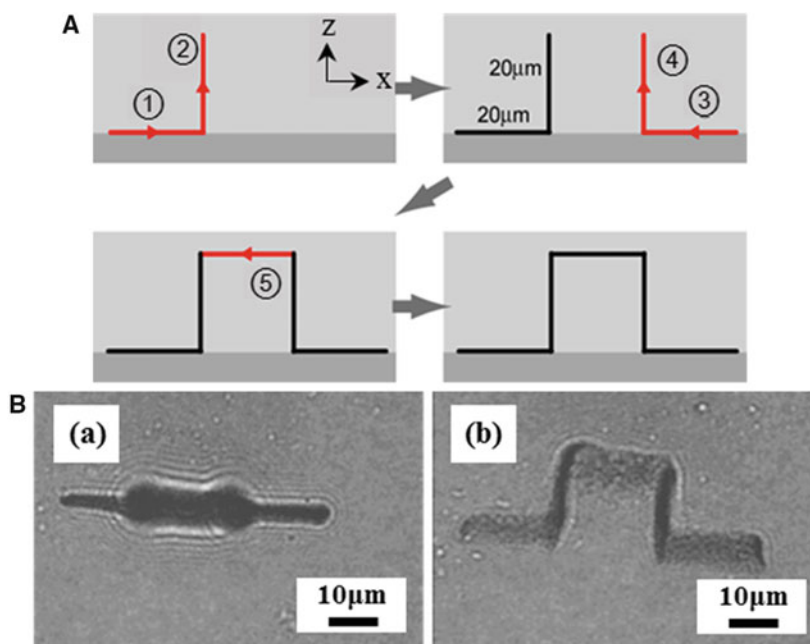


Fig. 10 (A) Process of fabricating three-dimensional cross-linking structure. (B) Observation of cross-linking structure. (a) Top view and (b) side view (Horita 2015)

three-dimensional liquid phase can fabricate a variety of 3D micro-wire frame structures that are not limited to a technique of writing figures with a single stroke of the brush (Horita et al. 2015).

28.3.2 Evaluation of Material Property of Deposited Microstructures

In this section, some analyses of material property of microstructures deposited with the 3D microfabrication using a suspension of TiO_2 photocatalyst nanoparticles in Ag ion solution are discussed.

Figure 11 shows the typical result of an energy-dispersive X-ray spectroscopy (EDX) analysis for fabricated material. Figure 11a shows a scanning electron microscopy (SEM) image and Fig. 11b–d mean EDX results of the following objective elements: the presence of the Ti (b), the presence of the Ag (c), and the presence of both the Ti and the Ag (d), respectively (Horita et al. 2015). Figure 12 shows a result of an X-ray diffraction (XRD) spectroscopy analysis, which provides composition of the deposited substance. This analysis was performed with XRD spectroscopy apparatus (EX-350M, Horiba, Ltd.). The diffraction angles at which the spectrum peaks appear match those of silver metal and TiO_2 (Okuno et al. 2006). Figure 13 shows a set of scanning electron microscope (SEM) images for observing

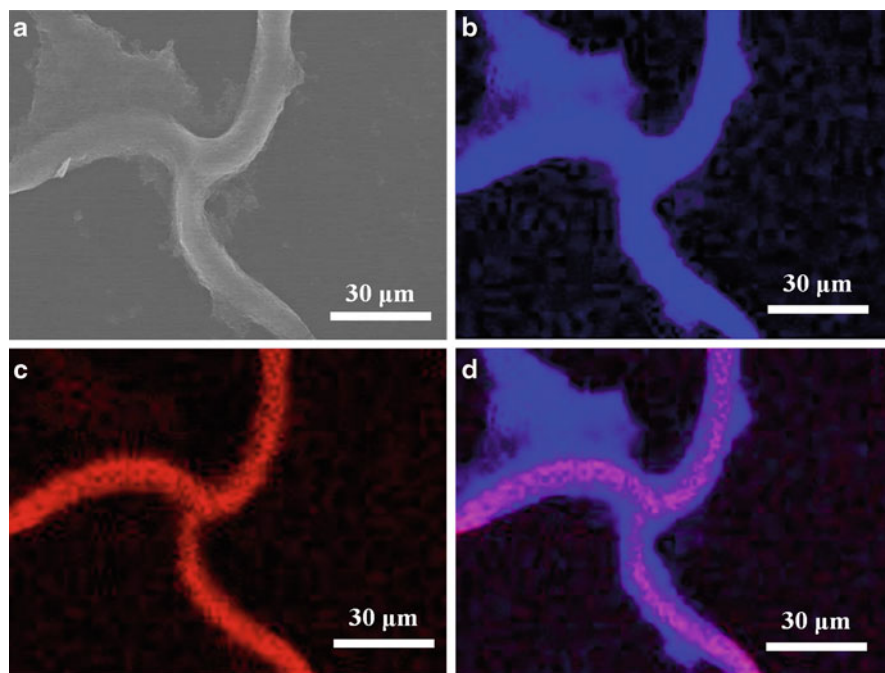


Fig. 11 (a) SEM image and EDX analysis results. (b) Distribution of Ti. (c) Distribution of Ag. (d) Distribution of Ti and Ag (Superimposition of (b) and (c) (Horita 2015)

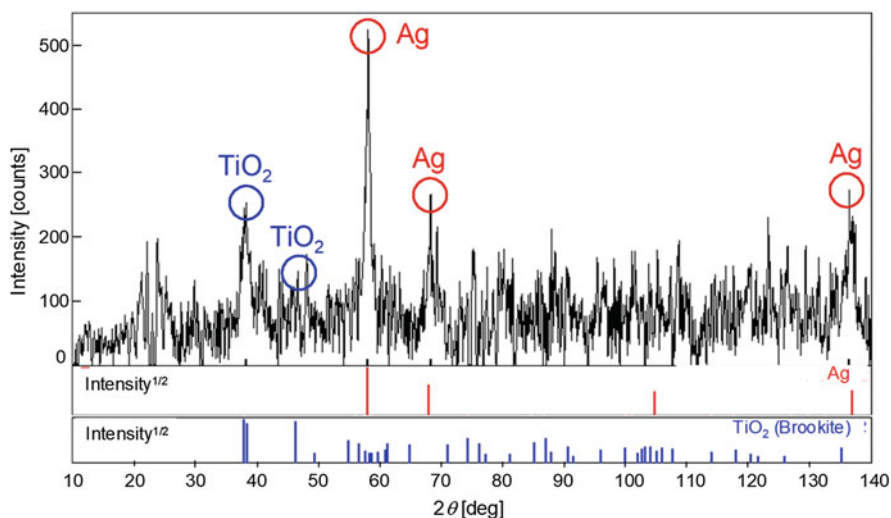


Fig. 12 XRD analysis of the deposited substance. XRD patterns of Ag metal and TiO₂ (Brookite) are attached at the foot of the obtained pattern. The diffraction angle 2θ at which a spectrum peak appears matches that of Ag metal and TiO₂ (Okuno 2006)

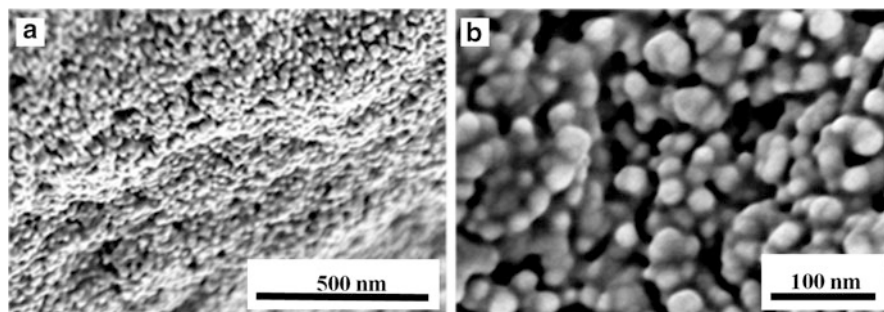


Fig. 13 High-magnification SEM image of sample surface: (a) $\times 100k$ magnification, (b) $\times 300k$ magnification (Horita 2015)

detailed textures of the deposit substance with high resolution, which was performed with a field-emission SEM (FE-SEM, S-5500, Hitachi High-Technologies Corp.).

From the fact that the distribution of Ti is a little bit larger than that of Ag in Fig. 11d and the fact that the diameter of the agglomerated particles is about roughly 20 nm corresponding to the diameter of the employed TiO₂ nanoparticles in Fig. 13, generated structures by beam waist scan seem to be covered with TiO₂ nanoparticles (Fig. 14). Although detailed understanding of structuring mechanism of the method still needs a variety of further analyses, the basic concept of 3D microfabrication principle based on photocatalytic oxidation–reduction (redox)

Fig. 14 Estimation of 3D structure generation mechanism by beam waist sweep (Horita 2015)

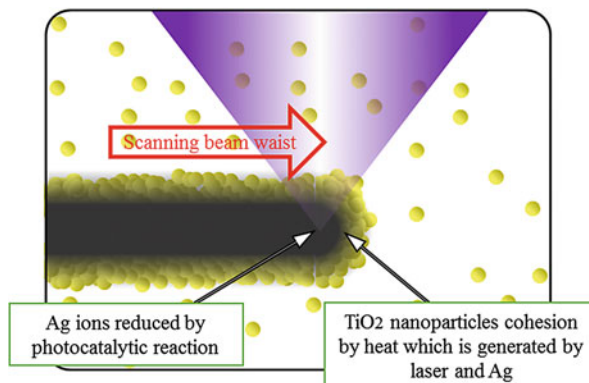
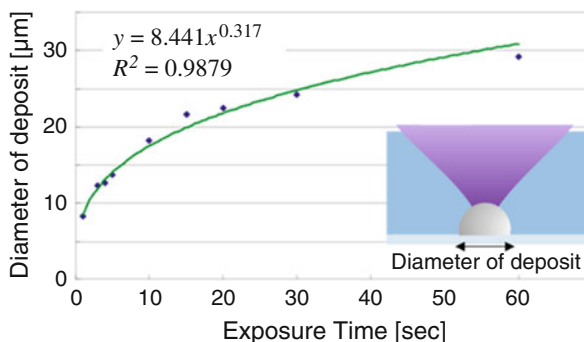


Fig. 15 Relation of diameter of deposits and exposure time under static condition keeping beam waist on surface of substrate with laser power of 7 mW (Horita 2015)



reaction is confirmed from the fact that Ag metal is clearly detected as a main substance from the generated structures in Fig. 12 (Horita et al. 2015).

28.3.3 Evaluation of Fabrication Characteristics

In this section, the processing characteristics of the 3D microfabrication are experimentally discussed. Figure 15 shows the relationship between the diameter of deposits and exposure time under a static condition that beam waist is not swept but is kept on a surface of substrate with laser power of 7 mW (Horita et al. 2015). It was found that the diameter of the deposits was proportional to approximately 1/3 power of the exposure time, which means the volume of the deposits has a linear relationship with the light energy. This fact is consistent with the processing principle that electrons are generated by the input of photons to precipitate and reduce silver ions. Figure 16 shows the relationship between the diameter of deposits and laser power for exposure time of 5 and 10 s. It was found that when the total exposure amount consisting of the product of the laser output and the exposure time is equal, the processing line width is roughly equal.

Fig. 16 Correlation of diameter of deposit and laser power under the static condition. At the equal point of diameter, total energy is the same because total energy is the product of laser power and exposure time (Horita 2015)

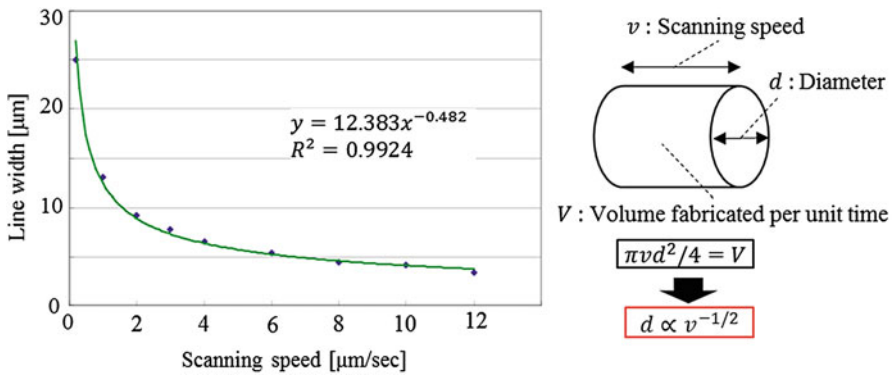
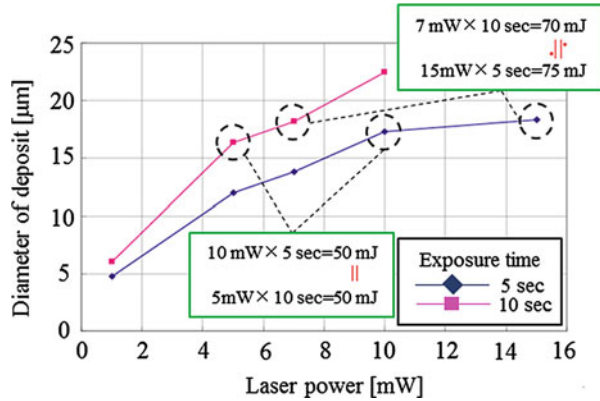


Fig. 17 Relation of line width and scanning speed of beam waist which are laterally swept along surface of substrate (Okuno 2006)

Next, the processing characteristics under a dynamic condition sweeping the beam waist laterally along the surface of the substrate are discussed. Figure 17 shows how sweeping velocity v (scanning speed) would influence the line width of deposited Ag d at a certain light intensity (Okuno et al. 2006). As a result, it was observed that d monotonously decreased with increasing v . Then it turned out that d was approximately proportional to $1/2$ power of the sweeping velocity v . This can be explained with the hypothesis that deposited metal grows with geometric similarity, and its amount is linear with exposure. If deposited Ag grows similarly, the cross-section area of the line is proportional to $1/2$ power of the diameter d . And if amount of deposited Ag has linearity with exposure, the cross-section area is proportional to -1 power of v because the time period in which a certain cross section can receive exposure energy is proportional to -1 power of v . Therefore d is proportional to $-1/2$ power of v , which suggest that it is possible to control line width from several μm to several tens of μm by adjusting the sweeping velocity.

28.4 Automatic 3D Microfabrication Using Photocatalytic Reaction

28.4.1 Automatic 3D Microfabrication System

Figure 18 shows the other typical type of 3D microfabrication system, with which the 3D position of beam waist can be numerically controlled by computer over a longer range (Takahashi et al. 2010). This microfabrication system mainly consists of a microfabrication unit (1), a top view in-process visualization unit (2), and a side view in-process visualization unit (3) as shown in Fig. 3. The microfabrication unit (1) is mainly consisting of a laser diode with 405 nm wavelength as a light source with output of 55 mW (LDM Series Blue, Omicron Laserage), high-power objective lens with a numerical aperture of 1.20 (UPLSAPO60XW, Olympus Corp.), and an automatic motorized three-axis stage with a resolution of 25 nm and with a travel range of $4 \times 4 \times 4$ mm (NanoMax Stage MAX341/M, Thorlab Japan Inc.). This unit was designed so that laser spot, which causes photocatalytic reduction locally inside the TiO_2 nanoparticles suspension, could be automatically manipulated in all three directions covering a several mm cubic area under computer control. By sharing the high-power objective lens, the top view in-process visualization unit (2) allows us to observe the fabricated structures with the magnification of 40 times from above. On the other hand, the side view in-process visualization unit (3), by using a long working distance objective lens and a tube lens with the focal length of 400 mm, allows us to observe the fabricated structures with also 40 times from side. By both in-process

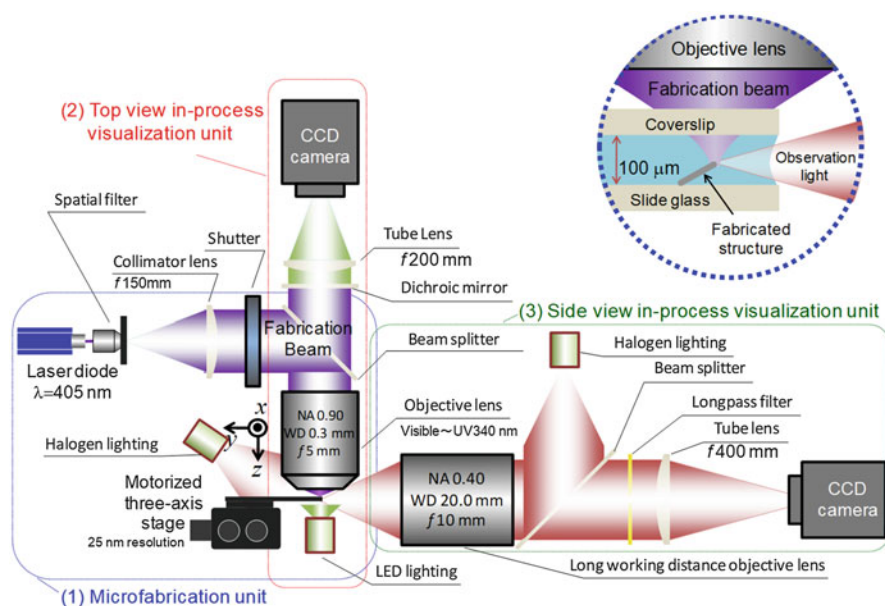


Fig. 18 Automatic 3D microfabrication system (Takahashi 2010)

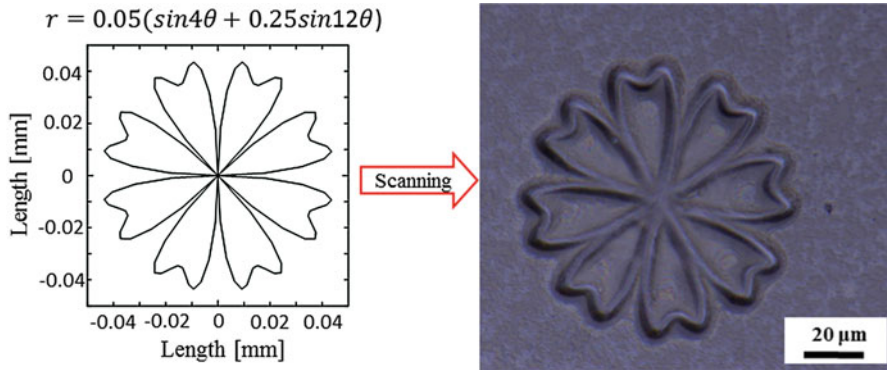


Fig. 19 An example of 2D microstructure. Petaloid shape fabricated on substrate, which is described by mathematical polar equations, under computer numerical control (Horita 2015)

visualization units, the microfabrication process can be microscopically observed. The fabrication region was set between a glass substrate and a cover slip with a gap of about 100 μm , in which the metal ion solution including TiO_2 nanoparticles is maintained by surface tension (upper right, Fig. 18). The sample solution is mounted on a motorized three-axis stage, and it can undergo 3D translational motion relative to the beam waist. The whole system is located on a vibration isolation table.

28.4.2 Automatic 3D Microfabrication Experiments

Figure 19 shows typical 2D microstructures automatically fabricated on a surface of a substrate by a beam-waist-position computer numerical control system like Fig. 18, where a petaloid shape described by mathematical equations such as polar equations was fabricated (laser power, 1.8 mW; scanning speed, 2 $\mu\text{m/s}$; fabrication time, 7 min) (Horita et al. 2015).

Figure 20 shows an example of fundamental 3D wire-flame microstructures, a microbox, which means a cuboid with sides of 60, 60, and 30 μm and a decoration circle suspended in the squares (Okuno et al. 2006). The numerically controlled 3D beam waist sweeping path shown in Fig. 20A means that the fabrication process includes a cross-linking process. Figure 20B was gotten under processing condition of laser power, 7 mW, and scanning speed, 3 $\mu\text{m/s}$ @z-direction and 2 $\mu\text{m/s}$ @x,y-direction. An optical microscopic observation for the fabricated structure, focal plane of which is adjusted on a substrate surface (a) and a top surface of the fabricated structure (b), suggests that microstructure can be fabricated completely along the 3D sweep path as designed. The microbox wasn't too weak to collapse immediately. It was seen that when the microbox came off the slide glass, it turned over in the solution with its shape kept, which means the parts of the microbox were combined with some strength.

Figure 21b shows a microcoil demonstrated as an example of the most versatile 3D free-form curve structure (Takahashi et al. 2007), which was fabricated by

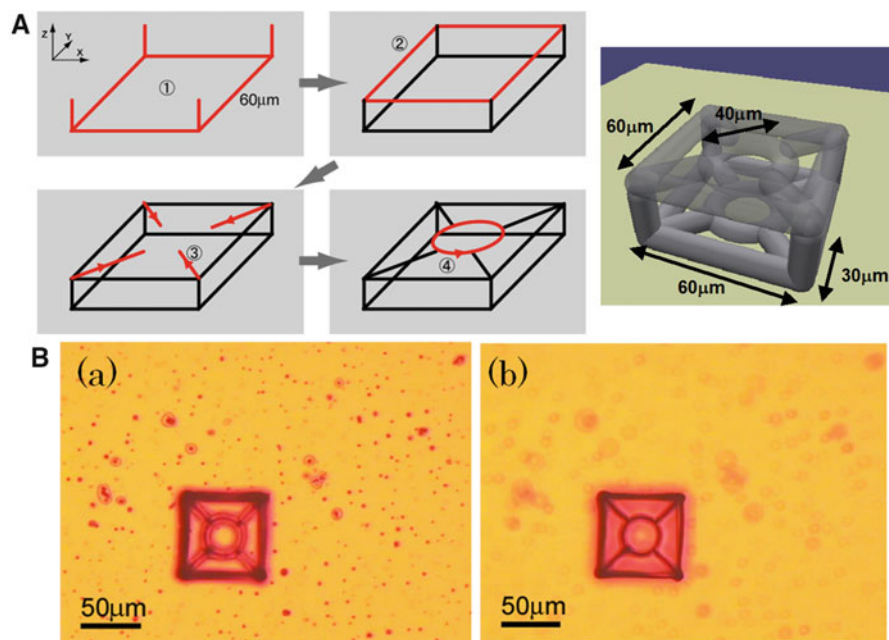


Fig. 20 An example of 3D wire-frame microstructures. A microbox with sides of 60, 60, and 30 μm . (A) Numerically controlled 3D beam waist sweeping path. (B) Fabricated structure observed with optical microscope, focal plane of which is adjusted on a substrate surface, (a) and a top surface of the fabricated structure (b) (Okuno 2006)

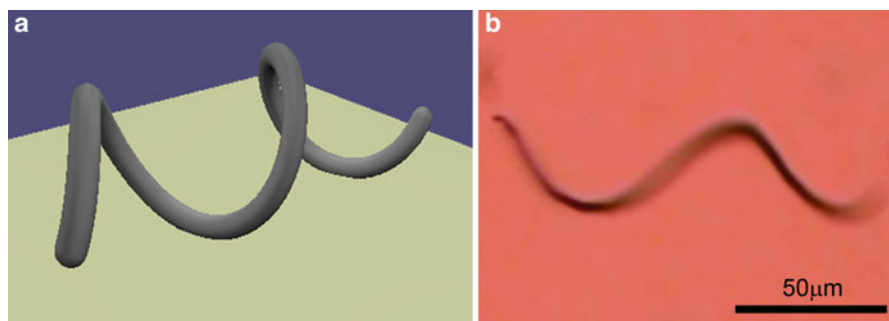


Fig. 21 An example of 3D free-form microstructures. A microcoil with a 60 μm diameter (Takahashi 2007)

sweeping the beam waist in a spiral with a 60 μm diameter (Fig. 21a). Because this 3D microfabrication method using photocatalyst nanoparticles is based on 3D direct writing corresponding to beam waist scanning in 3D space, this method provides method provides flexible processing capability applicable to various microstructures.

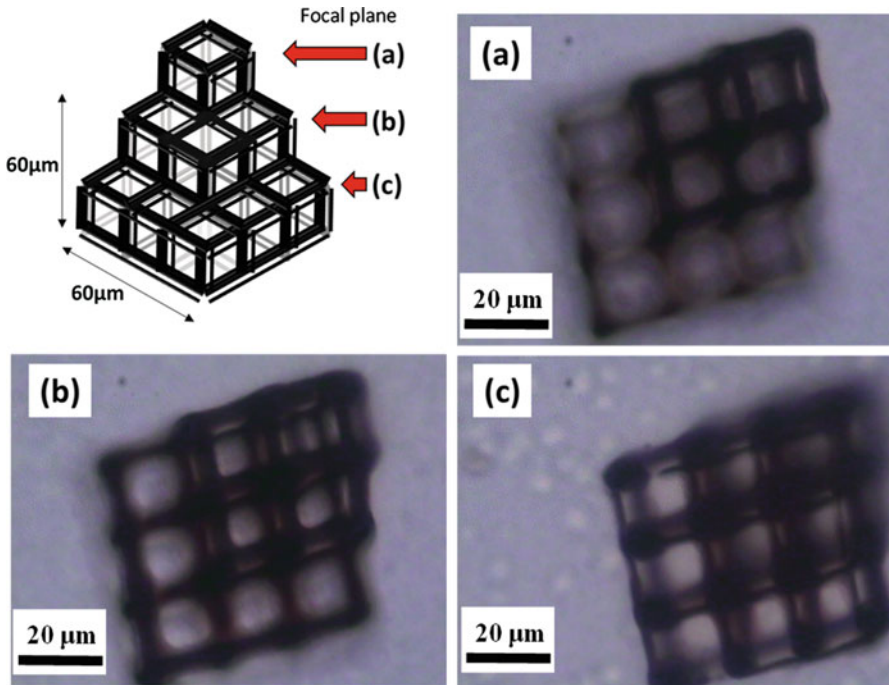


Fig. 22 The schematic of three-dimensional lattice structure and the fabricated object observed at each focal plane with optical microscopic, (a) top, (b) middle, and (c) bottom (Horita 2015)

28.4.3 Various Developments of 3D Microfabricated Structures

Here, some cases of processing with a more complicated 3D structure will be shown. Figure 22 shows a micro 3D lattice structure consisting of combinations of unit wire frame structures (laser power, 1.8 mW; scanning speed, 2 $\mu\text{m/s}$; fabrication time, 11 min.). The optical microscopic observation with focal plane shift obviously suggests that the unit wire frame structures are three-dimensionally configured as designed (Horita et al. 2015).

Figures 23 and 24 show microstructures having free movable parts, which is one of the most interesting processing characteristics of this method obtained by its direct drawing fashion (Takahashi et al. 2007). Figure 23 shows a chain-like structure, fabricated as an example of complex 3D microstructures, which is difficult to fabricate with a material removal processing. This chain-like structure consists of two triangle elements (each side, 100 μm) and two rectangular elements (long side, 100 μm ; short side, 40 μm) as shown in Fig. 23A. In this experiment, it takes about 30 min to fabricate the whole microstructure. Figure 23B(a) and B(b) show the fabricated chain-like structure, rolling over in the suspension flow. From this result, a three-dimensionally complex chain-like structure, each part of which is freely movable, can be also fabricated, and the fabricated structures have a certain level of strength with which the structures keep their shape in the suspension flow.

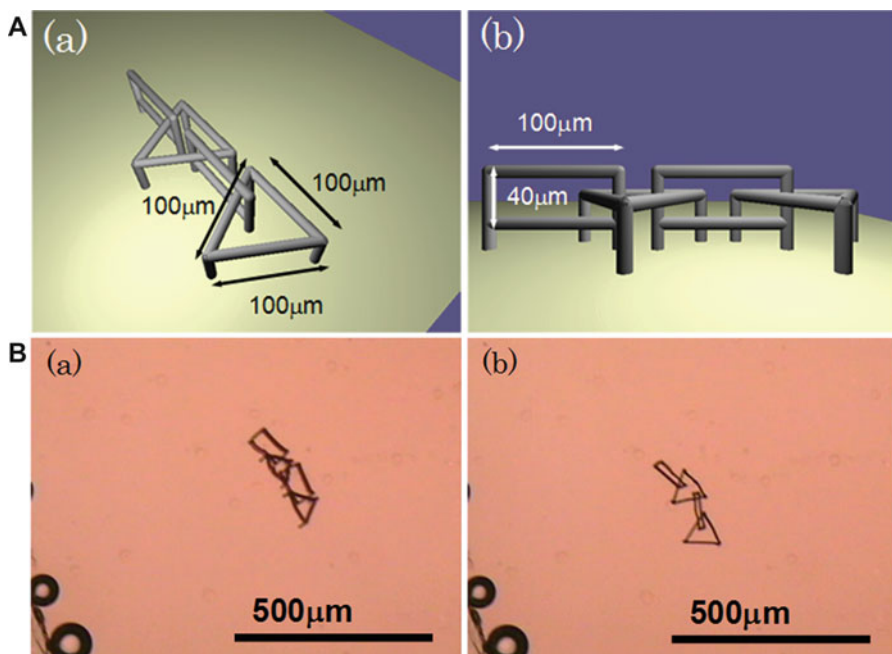


Fig. 23 Fabrication of complex 3D microstructures having free movable parts (Takahashi 2007). (a) Chain-like structure. (b) Fabricated structure, rolling over in the suspension flow

Figure 24 shows a micro-rotor structure, which was fabricated for demonstration as an example of functional 3D microstructures. This micro-rotor structure consists of a ring rotor with a diameter of 50 μm having two fins and a center shaft with a diameter of 12 μm as shown in Fig. 24A. In this experiment, the center shaft was fabricated by laminating the deposited clusters. The fabrication time is also about 30 min. Figure 24B means that the fabricated rotor can rotate around the center shaft, which was caused by inducing vibration. This result suggests that the proposed method allows us to fabricate functional 3D microstructures.

28.5 Summary and Outlook

In this chapter a new type of laser additive manufacturing processing based on photocatalytic reaction was described, which provides a 3D complex microstructure fabrication with a process resolution of a few tens of micrometers. This technique is performed by precisely controlling the local reduction position of metal ions caused by using photoelectrochemical reactions of TiO₂ nanoparticles dispersed in 3D space in liquid phase. It is true that this technique can be treated as a kind of 3D laser direct writing, but this doesn't need an ultrashort pulse laser-like multiphoton processing technique because its processing principle is based on a unique fashion that reduction

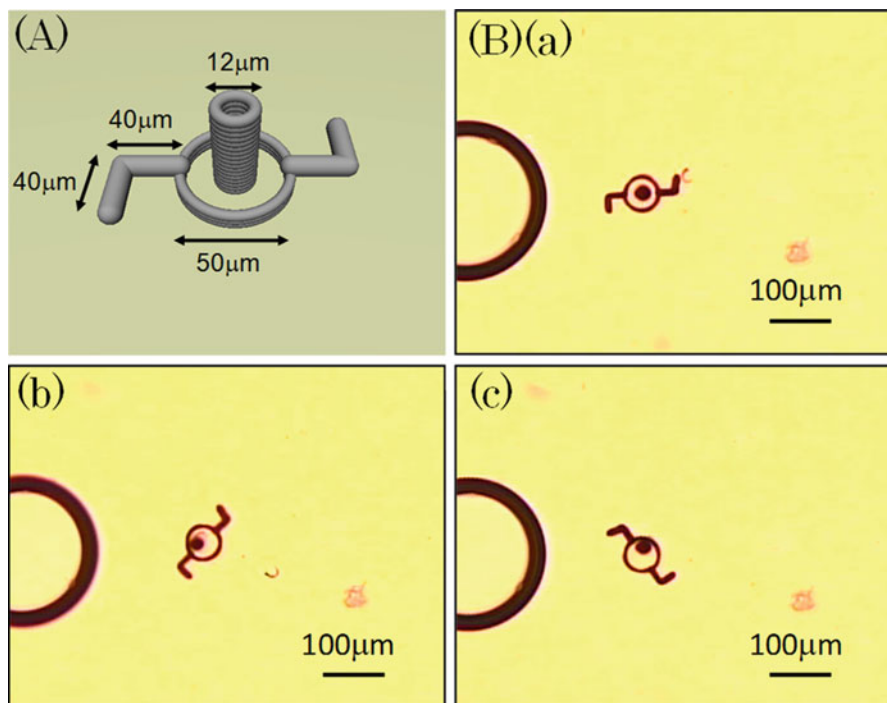


Fig. 24 Fabrication of functional 3D microstructures (Takahashi 2007). (A) Micro-rotor structure. (B) Fabricated structure, which can rotate around the shaft

of metal ions via the photocatalysis of TiO_2 nanoparticles excited at the laser beam waist can be directly used as processing energy of micro-additional processing.

The in-process microscopic visualization of the fabrication process and the component analyses for the photochemically generated material such as SEM-EDX, XRD, and so on revealed that photocatalytic deposition of silver can be performed only at the position of the beam waist of the converging laser beam with the wavelength of 405 nm in silver nitrate solution and that when the beam waist was swept, the silver structure grew in 3D following its path.

Experimental study showed that the 3D microfabrication method based on the continuous deposition can fabricate a variety of 3D micro-wire frame structures that is not limited to a technique of writing figures with a single stroke of the brush but has cross-linking structures.

An automatic microfabrication system, with which a 3D position of a beam waist can be precisely controlled by automatic stages with computer, allows us to fabricate complex 3D microstructures including 3D free-form structures, mechanical functional structures having movable parts, which are difficult to fabricate with a material removal processing.

This unique fabrication method is expected to be applied not only to fabrication of dynamic functional microelements such as micro-three-dimensional parts of microrobot

and complicated three-dimensional micromechanical elements but also to fabrication of advanced electromagnetic wave control functions typified by metamaterials (Tanaka et al. 2006) by positively utilizing high dielectric constant characteristics of titanium oxide as well as high electrical conductivity characteristics of silver.

References

- Aso T, Okuno M, Takahashi S, Takamasu K (2006) Fundamental study on metal micromachining technique by photocatalysis (3rd report) – development of 3-dimensional micromachining equipment. In: 2006 JSPE spring meeting, Tokyo, pp 1193–1194
- Fujishima A, Honda K (1972) Electrochemical photolysis of water at a semiconductor electrode. *Nature* 238:37–38
- Fujishima A, Honda K, Kikuchi S (1969) Photosensitized electrolytic oxidation on semiconducting n-type TiO₂ electrode. *Kogyo Kagaku Zasshi* 72:108–113
- Fujishima A, Rao TN, Tryk DA (2000) Titanium dioxide photocatalysis. *J Photochem Photobiol C1*:1–21
- Hashimoto K, Irie H (2004) Photo-induced hydrophilic conversion of TiO₂ surface. *Surf Sci* 25 (5):252–259
- Herrmann J, Disdier J, Pichat P (1988) Photocatalytic deposition of silver on powder titania: consequences for the recovery of silver. *J Catal* 113:72–81
- Horita Y, Yoshigoe H, Matsuda K, Michihata M, Takamasu K, Takahashi S (2015) Research on three-dimensional microfabrication using photocatalytic reaction at the vicinity of beam waist. *Trans JSME* 81(832):1–13
- Ishii H, Juodkazis S, Matuo S, Misawa H (1998) Photoelectrochemical fabrication of sub-micrometer platinum pattern on titanium dioxide single crystal surface. *Chem Lett* 27 (7):655–656
- Matsuda K, Takahashi S, Takamasu K (2010) Development of in-process visualization system for laser-assisted three-dimensional microfabrication using photocatalyst nanoparticles. *Int J Precis Eng Manuf* 11(6):811–815
- Ohko Y, Tatsuma T, Fujii T, Naoi K, Niwa C, Kubota Y, Fujishima A (2003) Multicolour photochromism of TiO₂ films loaded with silver nanoparticles. *Nat Mater* 2:29–31
- Okuno M, Aso T, Takahashi S, Takamasu K (2005) Fundamental study on metal micromachining technique by photocatalysis (2nd report) – fabrication of submicrometer periodic structure. In: 2005 JSPE autumn meeting, Kyoto, pp 941–942
- Okuno M, Aso T, Takahashi S, Takamasu K (2006) A novel microfabrication technique for three-dimensional metal structures by photocatalysis. In: Proceedings of the 21st annual meeting of the American Society for Precision Engineering, Monterey, pp 301–304
- Takahashi S, Okuno M, Takamasu K (2007) Metal 3D micro structures fabrication using photocatalyst nanoparticles – direct writing of 3D micro structures by 3D beam scanning. *Opt Alliance* 18 (5):70–73
- Takahashi S, Matsuda K, Yoshigoe H, Takamasu K (2010) Laser direct fabrication of three-dimensional microstructures using photocatalyst nanoparticles. In: Proceedings of 4th CIRP international conference of high performance cutting, Gifu, pp 381–384
- Tanaka T, Ishikawa A, Kawata S (2006) Two-photon-induced reduction of metal ions for fabricating three-dimensional electrically conductive metallic microstructure. *Appl Phys Lett* 88 (081107):1–3
- Tatsuma T, Kubo W, Fujishima A (2002) Patterning of solid surfaces by photocatalytic lithography based on the remote oxidation effect of TiO₂. *Langmuir* 18(25):9632–9634
- Wang R, Hashimoto K, Fujishima F, Chikuni M, Kojima E, Kitamura A, Shimohigoshi M, Watanabe T (1997) Light-induced amphiphilic surfaces. *Nature* 388:431–432



Silicon Etching for Multiple-Height Microstructures

29

Minoru Sasaki

Contents

29.1	Introduction	904
29.2	Motivation of Use of Si Material	904
29.3	Si Etching Using Bosch Process	905
29.4	Scallop	907
29.5	Etching Rate Distribution	909
29.6	Black Silicon	911
29.7	3D Structures Realized Using RIE	912
29.8	Multiple Masks for Digital Steps	912
29.9	Example of 3-Stepped Trench	913
29.10	Reducing Scallop	914
29.11	Application of the Superconducting Coil	919
29.12	Summary and Outlook	922
	References	922

Abstract

Techniques of Si etching for realizing multiple-height microstructures are described. Up to now, the lithography-based techniques have grown from the planer structures to the three-dimensional structures especially in MEMS field. The characteristic advantage is processing many points at the same time with the high throughput. On the other hand, the shape accuracy has to depend on the uniformity of the active species which generate the reaction. In this chapter, the relating techniques are described. One application example of fabricating the coil trench for the superconducting magnetic energy storage (SMES) is picked up.

M. Sasaki (✉)
Toyota Technological Institute, Nagoya, Japan
e-mail: mnr-sasaki@toyota-ti.ac.jp

KeywordsSilicon etching · Multiple-height microstructures · Smoothing sidewall scallop

29.1 Introduction

The typical technique progressed in the Si micromachining will be the deep reactive ion etching (deep RIE) (Laermer et al. 2015). Especially in the MEMS field, the required structure tends to be three-dimensional (3D) for utilizing the mechanical function which relates to the structure shape. In many cases, the shape in its depth direction is determined by the projection of a top mask pattern. When the target shape becomes 3D having the size of around 100 μm , it sometimes seems to be near to that prepared by the precision machining using the drill, end mill, and so on. Of course, the shape accuracy becomes one important issue. The precision machining can control the shape directly, since the machining center has the sensors for controlling the displacement of the stage for scanning the sample or the processing point. On the other hand, the Si micromachining bases on the lithography technique. The processing reaction occurs at many points at the same time. This will give the high-throughput advantage even when the pattern size becomes smaller. However, this advantage does not guarantee the same processing speed at different points but depends on the uniformity. Due to this background, the technique glows much differently from that in the precision machining. The effort for the higher etching rate is paid with the balance of the uniformity, which will relate to the shape accuracy. In this chapter, the fabrication techniques are described adopting the topic of the multiple-height microstructures, which are sometimes required in the MEMS devices.

29.2 Motivation of Use of Si Material

Table 1 lists the material properties of the single crystal Si and the steel. The single crystal Si can be obtained at the reasonable price, since the semiconductor industry develops well. The single crystal material can give the fine structure without suffering the nonuniformity of the material grain. Compared to this, the steel has the grain. Its size is typically 10–30 μm , which cannot be ignored for realizing the microstructures. The crystal Si has the relatively lower Young's and torsional moduli. The ratio is about 20% lower compared to those of the steel. As for the yield stress, the crystal Si has the similar value compared to that of the steel. The big difference is the lower density of the crystal Si. Its value is only 30% of that of the steel, smaller than that of Al of 2800 kg/m^3 . So, when the mechanical structure is fabricated, Si can provide the light-weighted element having the similar mechanical strength. This is attractive meaning that the Si micro-actuators have the faster response (Urey 2002). As for the thermal performance, Si has the similar melting point. Si has the relatively larger specific heat. However, this is not so serious

Table 1 Material properties for Si and the carbon steel

		Silicon	Steel
Matrix		Single crystal is possible	Typical grain size is 10–30 μm
Young's modulus	[GPa]	130–188	203–210 Seika (2006)
Torsional modulus	[GPa]	58–80	82–84 Seika (2006)
Yield stress	[MPa]	1000–3500 Tsuchiya (2005)	200–1300 Seika (2006)
Density	[kg/m^3]	2330	7800
Melting point	[$^{\circ}\text{C}$]	1414	1200–1500
Specific heat Hakko Electric Co., Ltd (n.d.)	[$\text{J}/\text{kg } ^{\circ}\text{C}$]	678	461–502
Thermal conductivity Hakko Electric Co., Ltd (n.d.)	[W/mK]	83.7	10–60
Coefficient of thermal expansion	[$\text{ppm}/^{\circ}\text{C}$]	2.8	9–12

counting the smaller density. The heat capacitance of the Si element will be smaller than that of the steel having the same shape and volume. The thermal conductivity of Si is larger. The Si element is easier to stabilize its temperature.

29.3 Si Etching Using Bosch Process

It was 1990 when the project starts in the company Robert Bosch GmbH for developing a new plasma Si etching technique (Laermer and Urban 2005). Until that, KOH wet etching is popular for fabricating the deep trenches or cavities. This uses the Si crystal orientation dependence restricting the realizable shapes. In principle, the plasma etching has the larger freedom without the crystal orientation dependence. In addition to this advantage, the other performances are required to exceed those of KOH wet etching. This is because the equipment is much expensive, since the vacuum pumps or RF power sources are inevitably necessary. The aimed performances are the etching speed $>2 \mu\text{m}/\text{min}$, realization of the vertical sidewall, and the etching selectivity against the mask material larger than 50:1. The frequency of the etching reaction depends on the density of the active gases. In a natural sense, the etching rate is lower than that of the liquid (Williams and Muller 1996). For realizing the higher etching rate, the higher plasma density is required. At that date, the inductively coupled plasma (ICP)-RIE starts to appear in the market. In 1992, the Bosch process is invented (Laermer and Schilp 1992). After that, it becomes the core of the technology to grow. Latter of 1993, Bosch company aborts the equipment development by themselves and licensed with the company Surface Technology Systems (STS) developing the equipment and the process technique (Bhardwaj et al. 1997). At 1995, three etchers are firstly shipped to the USA, Europe, and Japan. STS is invested under the control of the company Sumitomo precision products. The total number of the shipped etcher grows >50 at 1997 and >100 at 1998. Table 2 lists the

Table 2 Performances of the etcher from STS at 1997

Etching rate	1.5–3.0 μm/min
Selectivity to resist mask	50–100: 1
Selectivity to SiO ₂ mask	120–200: 1
Sidewall profile	90 ± 2°
Uniformity in wafer	+/- 2.5–5%
Aspect ratio	Up to 30

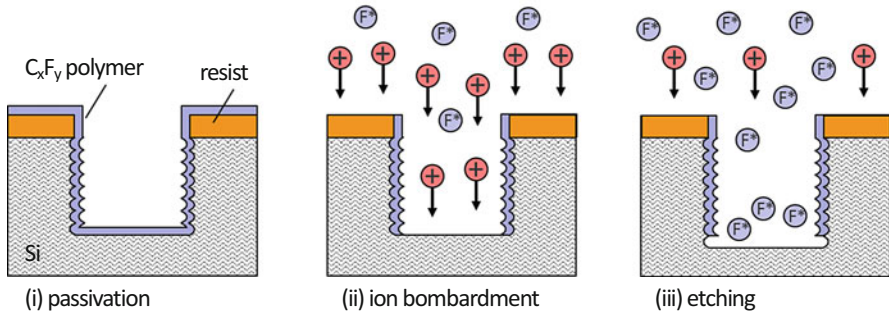
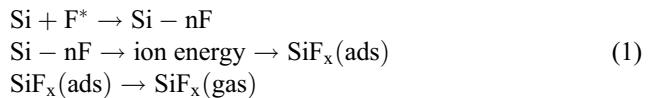


Fig. 1 One cycle of the Bosch process

etcher performances at 1997. The etching rate realized is higher than that of KOH etching (about 1 μm/min) in the usual condition. At 2004, the share reaches >80% in the MEMS field. Main data in the following are obtained by the standard etcher (MUC-21, ASE-SRE) from Sumitomo precision products.

Figure 1 shows the schematic drawing for explaining the Bosch process. This bases on the cycle process repeating the gas exchange for the passivation and the etching in sequence, not introducing these gases at the same time. The plasma condition can be tuned at each step. Usually, the gases used for the passivation and the etching are C₄F₈ and SF₆, respectively. SF₆ gas is popular in the plasma Si etching for many other etchers, since SF₆ gas generates many fluorine radical F* giving the larger etching rate. The chemical reaction used is as follows (Bhardwaj et al. 1997).



F* is small in its size and can enter in the Si crystal matrix. Since F* has the large electric negative degree, F* strongly ionizes Si atom positively. The reaction proceeds spontaneously, although the ion bombardment is used as the additional assistance. The chemical reaction makes the etching isotropic. The characteristic point in the Bosch process is the existence of the passivation step. The performances required in the passivation film are (i) the generated polymer should enter the etched

Table 3 Typical recipe parameters. The platen power is supplied at the low frequency (380 kHz) compared to that of the coil (13.56 MHz). This is for suppressing the notching

	Gas	Flow	Time	RF power		Pressure
		[sccm]	[s]	Coil [W]	Platen [W]	[Pa]
Passivation	C ₄ F ₈	85	8	600	0	2
Etching	SF ₆	130	14	600	10	4

trench/hole inside well, (ii) the passivation ability should be obtained against F* incidence, and (iii) the deposited film should be removed soon in the etching plasma. Many gases are tested considering the candidates such as CHF₃, C₂H₂F₂, C₃F₆, C₄F₆, C₄F₈, C₄F₁₀, and so on. Eventually, C₄F₈ is selected. Figure 1(i) shows the passivation step. The fluorocarbon C_xF_y film deposits on the top surface and the trench inside over the substrate. Figure 1(ii) shows the transition step before the etching starts. Here, the main players are the ions having the kinetic energy and the normal incident angle being attracted by the bias voltage. They physically attack the passivation film on the planer surfaces (top and bottom surfaces) removing the passivation film. The top planer surface is protected by the mask material. The bottom planer surface is exposed to the etching plasma with F*. The sidewall surface is protected by the fluorocarbon film, since the ion bombardment is not incident on the sidewall. So, the etching proceeds directionally to the bottom not to the sidewall. Figure 1(iii) shows the etching step. Now, the main player is changed to F* from the ions. This etching step is controlled to be a short period. During this step, the isotropic etching proceeds. This is essential for suppressing the black Si, which is described later. And the cycle returns to (i) the passivation step. Repeating the cycle, the Si etching proceeds protecting the trench sidewall.

The advantage of the cycle process is that the plasma condition can be optimized for the passivation and the etching, respectively. The Bosch process takes the balance to realize the nearly vertical etching as the total. If the passivation and the etching gases are introduced at the same time, the realizable profile is different. Table 3 lists the parameters for one typical recipe. This recipe realizes the etching rate of 1.2 μm/cycle. The sidewall angle is 90.1° for the trench having the etching depth of 80 μm and the width of 3 μm.

29.4 Scallop

Figure 2a shows one cross-sectional view of the etched trench. This trench depth is 7.7 μm. The aspect ratio is about 1. The number of the etching cycle is 10, and the same number of corrugation is observed. This is called as the scallop. The first etching is relatively shallow compared to others. This may relate to the natural oxide layer, grown in air at room temperature on Si surface. This natural oxide layer has to be removed before starting the Si etching. This first etching depth or the profile can be the issue when the sub-μm level shape accuracy is required. The following corrugation is much regular. In this case, the etching rate is about 820 nm/cycle, and the corrugation

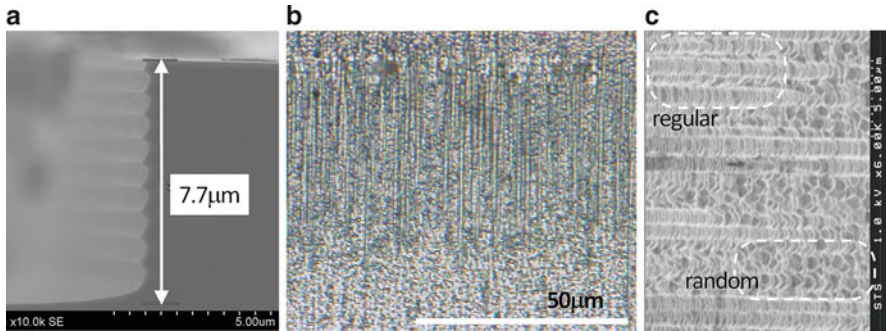
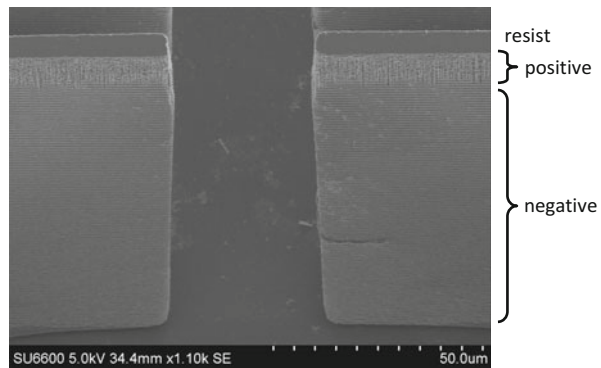


Fig. 2 (a) Typical etched sidewall with the scallop. (b) Optical micrograph of another sidewall observed at the lower magnification. The scale bar is 50 μm . (c) A region having regular scallop and random corrugation

Fig. 3 Controlled sidewall profile from positive to negative



of the scallop depth is about 180 nm. The bottom shows the rounded profile over the larger area. Figure 2b is the optical micrograph with the lower magnification observing another deeper trench. When the trench becomes deeper, the regular scallop tends to be random. The etching rate is about 1.1 $\mu\text{m}/\text{cycle}$. The recipes are different between Fig. 2a, b. Figure 2c shows one magnified image. The regular corrugation starts to mix with the random one. With the depth, the ratio of the random region increases. Such tendency of the etched surface is reported from the initial stage. Marxer et al. (1997) report the etched surface roughness $R_{\text{rms}} = 36 \text{ nm}$ for top-30 μm , the vertical stripes start to appear for 30–45 μm , and $R_{\text{rms}} = 1000 \text{ nm}$ for 45–75 μm depth (Marxer et al. 1997). Since their application is the optical switch which reflects the light beam at the sidewall, the sidewall roughness is important. With the process, the etching chamber accumulates the passivation polymer material. There is also the tendency that the etching rate decreases gradually with time.

Figure 3 shows the trench controlling the sidewall profile from positive (15 μm depth from the top) to negative (down to bottom). Table 4 shows the recipe for getting the positive profile. The passivation factor is enhanced, and the etching factor is

Table 4 A set of parameters for obtaining the positive profile

	Gas	Flow	Time	RF power		Pressure
		[sccm]	[s]	Coil [W]	Platen [W]	[Pa]
Passivation	C ₄ F ₈	85	9	600	3	2.13
Etching	SF ₆	130	10	600	15	3.47

Table 5 A set of parameters for obtaining the larger negative profile

	Gas	Flow	Time	RF power		Pressure
		[sccm]	[s]	Coil [W]	Platen [W]	[Pa]
Passivation	C ₄ F ₈	85	8	600	0	2
Etching	SF ₆	130	16	600	10	4

reduced compared with those of Table 3. The platen power is increased, since more ion bombardment becomes necessary for removing the passivation film. Although the increase is only 3 or 5 W, this gives the significant physical impact on the material. As shown in Fig. 3, the sidewall profile is quite different. The top positive sidewall has the random corrugation. Under that, the negative sidewall recovers the regular scallop. Bosch process works stable more with the negative profile (Table 5).

29.5 Etching Rate Distribution

The uniformity is important for the micromachining, since the reaction occurs at many points at the same time. The etching rate is decided not only by the equipment performance but also by other factors. The RIE lag is the well-known phenomenon. When the trench width is narrower, the etching speed becomes lower, since the passing of the active plasma species through the narrower trench becomes more difficult. For obtaining the uniform etching rate, the pattern should have the same trench width over the wafer. This is the issue of the device design.

Another pattern effect is the etching area ratio against the wafer area. Equation (1) indicates that the etching rate is decided by the number of the incident F*. When the plasma generation condition is the same, the number of F* is the same and limited even when the etching area of the sample changes. F* has the relatively long lifetime and can migrate in the process chamber. So, when the etching area is larger, F* density which can arrive on the trench bottom decreases. This decreases the etching rate. Figure 4 shows one example, whose application is explained later. Almost all 4-in. wafer area is filled by the spiral trench pattern for making three steps. The bottom, middle, and top trenches are 18, 34 (+89% compared to the bottom), and 50 (+178% compared to the bottom) μm wide, respectively. One spiral pitch is 72 μm . When the process is carried out by 35 cycles using the same recipe, the average etching depths are 8.9, 7.8 (−13%), and 6.6 (−25%) μm for bottom, middle, and top trenches, respectively. For making these three etching depth the same, the number of cycle should be tuned. Figure 4 also shows the spatial distribution of the etching rate. The

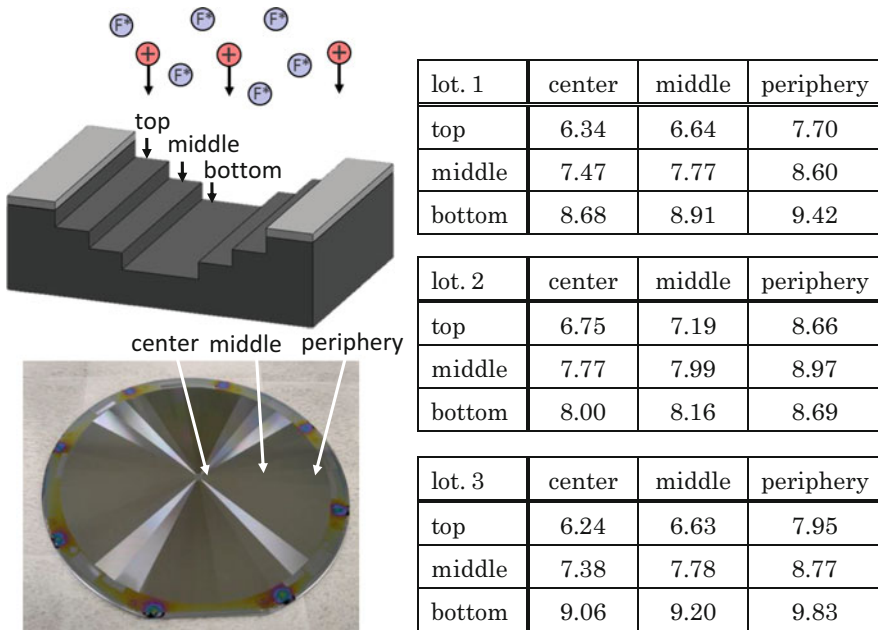
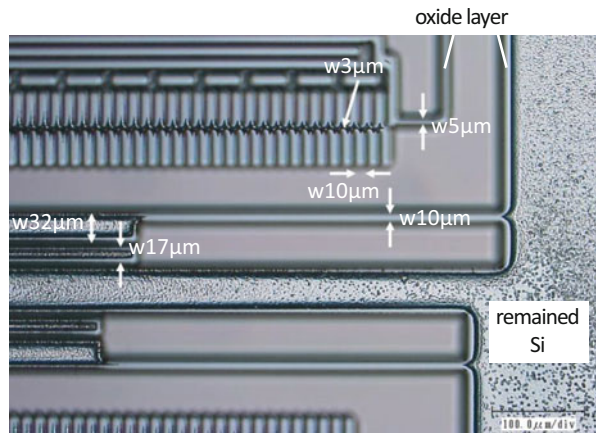


Fig. 4 Etching depth distribution of 3-stepped trenches on 4-in. wafer

Fig. 5 Si trench pattern having some width



etching rate is larger at the wafer periphery. Since ICP is used, the plasma density is relatively higher at around the ICP coil. The ICP coil is placed over the wafer in the etcher. The uniformity relies on the diffusion of the plasma active species.

The spatial distribution of the etching ratio becomes clearer when the device layer in the Si-on-insulator (SOI) wafer is etched to the buried oxide. The oxide layer has smooth surface showing the clear interference color. Figure 5 is the SOI wafer just before the trench etching reaches to the buried oxide. The device Si layer is 15 µm

thick. The trench widths in this region are 5, 10, 17, and 32 μm . As for 5- and 10- μm -width trenches, the clear oxide layer appears. This indicates the faster etching rate. In the small area between the up and the down combs, Si remains. Here, the trench width is locally 3 μm . This can be explained by the normal RIE lag. As for 17- and 32- μm -width trenches, their center area remains Si, but their trench edges show the buried oxide indicating the removing of Si. The local etching rate is larger near to the sidewall, because F^* migrates from the neighbor where F^* is not consumed being blocked by the mask.

29.6 Black Silicon

Figure 6 shows one example of the black Si. When such needle array is generated, the incident light reflection decreases, and the area seems to be black by the naked eye. This is known not only in the deep RIE but also in the general RIE. Usually, the vertical etching means the use of the accelerated ions which are normally incident on the substrate accelerated by the bias voltage. Such ion bombardment tends to generate the problem of the micro-mask, which are the small sputtered mask material or the nonvolatile reaction products, for example. Since the ions are well-collimated with the bias voltage, once the micro-mask adheres on the Si surface, the vertical etching is difficult to remove that remaining the shadow region of the Si structure. The resultant is called as the black Si or the grass. In the Bosch process, the etching step shown in Fig. 1(iii) is isotropic. Notice the etching profile at the sidewall is rounded for each cycle. The Si etching enters beneath the micro-mask, and the macro-mask can be removed. The inset of Fig. 6 shows the micro-masks with different sizes. The allowable size of the micro-mask, which does not grow the black Si, corresponds to the corrugation depth of the scallop. In principle, the Bosch process can suppress the growth of the black Si. The etching profile tends to have the negative sidewall, since the trench should be free from the black Si. Even in the Bosch process, the black Si is generated when the passivation effect is too strong compared to the etching effect. Notice that the recipe shown in Table 4 for the

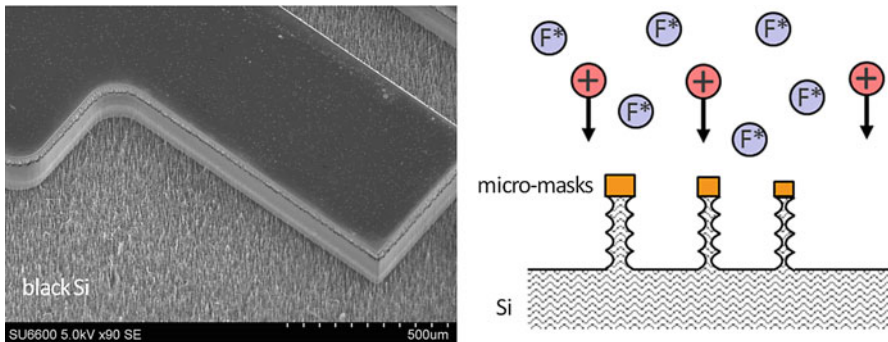


Fig. 6 An example of black Si

positive profile has the larger platen power. The increased ion bombardment generates more micro-masks. In the delicate situation, the black Si is locally generated depending on the trench structure. For another example, when the wafer size increases from 3 to 4 in., the black Si can occur using the same recipe. This is because 4-in. wafer usually exposes the larger Si area to the etching plasma; the average etching rate decreases. So, the recipe has to be tuned to strengthen the etching effect.

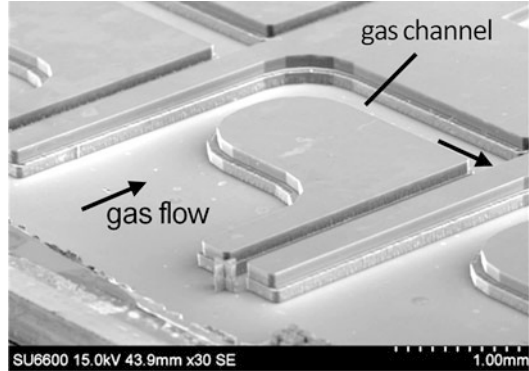
29.7 3D Structures Realized Using RIE

The mask pattern for the deep RIE is prepared on the top surface, since the photolithography patterning is effective only on the planar surface. The challenge toward 3D means controlling the depth profile. A gray scale mask can give 3D resist structure (Gimkiewicz et al. 1999), which can be transferred to Si substrate. Since the deep RIE has the selectivity of $>80:1$ between Si and the resist, the deep Si structure can be obtained from the resist mask (Mehra et al. 2000). The patterned resist shape especially at the outline becomes important, since it is magnified to Si material. One example is the microneedle array fabricated with the consecutive control of the plasma etching conditions to anisotropic or isotropic giving the center cavity (Griss and Stemme 2003). By controlling the aperture size of the mask pattern, RIE lag and its envelope can make a rounded 3D profile (Rao et al. 2004; Marty et al. 2005). The rounded resist profile also can be transferred to Si (Takahashi et al. 2007). A blade shape for a compressor has been demonstrated (Waits et al. 2005). Etching using high ion energies means the physical attack to the sample materials. This decreases the selectivity, since Si is the hard material compared to the soft material of the photoresist. When the sample temperature is high, the photoresist material is easily damaged. The profile of AZ1500 photoresist profile changes at a noticeable level over 120 °C (Kumagai et al. 2012). The cooling becomes important. The thermal contact becomes important between the sample and the stage which is cooled in the system. Since the analogue shape control is influenced by the delicate conditions, the shape accuracy over the wafer requires the tight control.

29.8 Multiple Masks for Digital Steps

Multiple-height structures having digital steps are approximated 3D structure allowing the process margin, and they can be realized using the delay masking. These structures usually consist of masks of photoresist and other materials (e.g., SiO₂, SiN, Al). To prepare SiO₂ (Sasaki et al. 2006; Milanovic et al. 2004) or SiN (Mita et al. 2006) films, the growth temperature must be high. They are clean materials, although the high-temperature process is sometimes avoided when the device has the underlying IC structure for maintaining its doping profile. When the metal mask is used (Mita et al. 2000), there is a risk making the micro-mask problem bigger. The photoresist mask can be cleaned with O₂ plasma. UV-cured photoresist can be used

Fig. 7 Fabricated gas channel chip with 2-stepped sidewall



as one embedded mask. UV curing is the treatment realized by heating the photoresist in vacuum with UV irradiation. UV curing makes the resist molecules link together to form larger ones. UV-cured photoresist becomes stable against thinner and UV exposure. In case of AZ1500 resist having the thicknesses of about 3 μm , UV curing is at 100 $^{\circ}\text{C}$, about 3 kPa for 40 min. The light (main wavelength 240–380 nm, $\sim 1 \text{ W/cm}^2$) of a high-pressure mercury lamp is irradiated. On the UV-cured photoresist mask, the normal photoresist pattern can be prepared (Kumagai et al. 2012). Figure 7 shows the example of the stepped gas channel, which enhances the ignition of the micro-plasma (Sato et al. 2014). After RIE, the top positive photoresist can be removed by UV exposing and developing. Since there is the remained passivation film on the top surface, being deposited during the previous Si etching, ashing before flush exposure and developing will give the better result of the selective removal of the top normal resist (Sato et al. 2014). Then, the underlying UV-cured resist mask will appear.

29.9 Example of 3-Stepped Trench

Figure 8 shows the fabrication sequence of the 3-stepped trench using three masks. The trenches are defined by SiO_2 and photoresist masks having three different widths. The buffered HF etchings of SiO_2 layer are carried out for getting the embedded masks. (1) The starting Si wafer has 1- μm -thick oxide layer. (2) The first mask pattern is transferred on the photoresist. (3) The oxide layer is half-etched. (4) The second mask pattern with the narrower trench width is transferred. (5) The oxide layer open at the bottom is removed. (6) The third mask pattern is transferred to the photoresist. Since the underlying oxide thickness is thinner than the photoresist thickness, the patterning does not suffer from the non-planer substrate disturbance. (7) The first Si etching is carried out. (8) The resist film is removed appearing the underlying oxide mask. (9) The second Si etching is carried out. (10) The SiO_2 mask with wider trench appears after SiO_2 etching. (11) After the third Si etching is carried out, (12) all SiO_2 layer is removed realizing the 3-stepped trench.

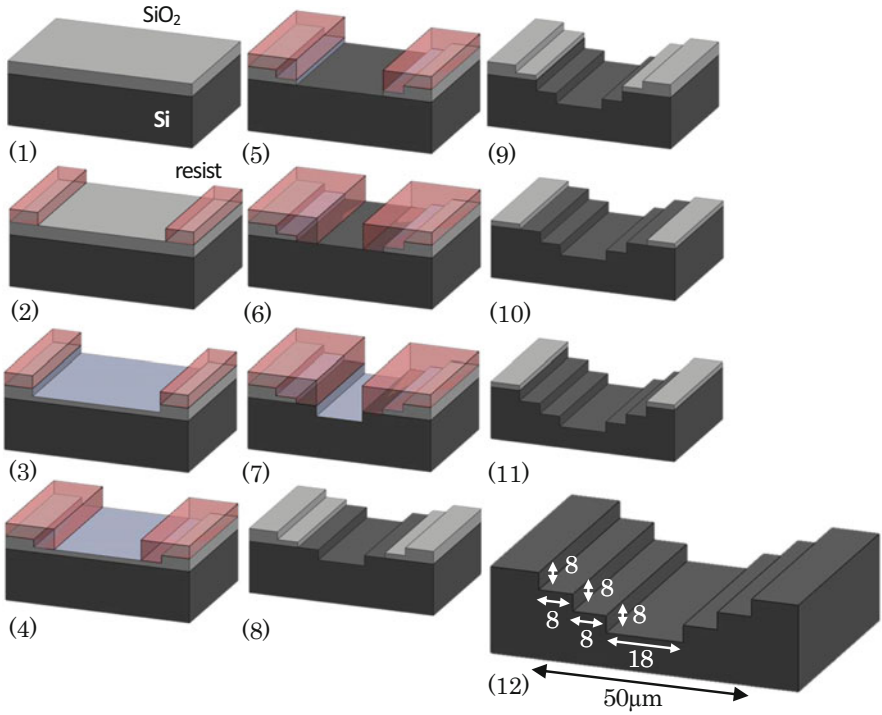


Fig. 8 Fabrication sequence of 3-stepped trench

Figure 9a shows the spiral trench. This is the center region of 3-in. wafer. Figure 9b shows 3-stepped bank for constructing the trench. Figure 9c shows the magnified sidewall. The scallop is clear. The white line indicates the sharpness of the scallop edge. The step corner is etched additionally. This may relate to the focused ion bombardment gathered by the electron minus charging at the corner.

29.10 Reducing Scallop

There are efforts for reducing the scallop. The basic policy of the recipe tuning for reducing the scallop is reducing the etching depth per cycle. As for the tunable range of the time in the recipe, there are limitations from the etcher hardware. The usual mass flow controller for supplying the process gas needs the response time. There are reports of the ultrafast gas switching (Laermer and Urban 2002) using the specially designed hardware. There is another time constant decided by the balance between the chamber volume and the evacuation speed. When the period is too short to

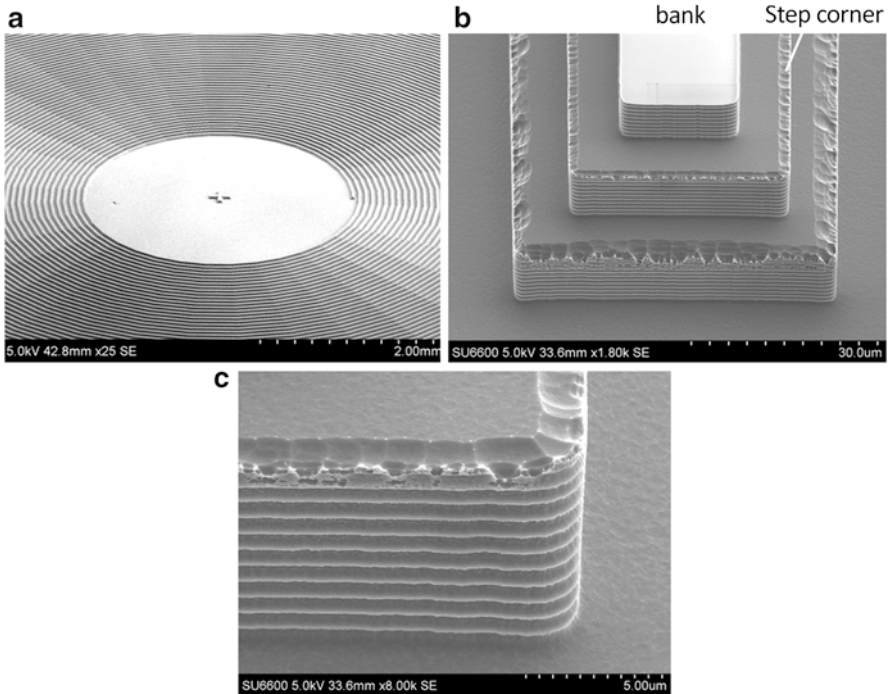


Fig. 9 (a) SEM image of the spiral trench. (b) three-stepped structure. (c) Scallop on the sidewall. The tilt angle of the stage is 55°

exchange the gases, the gas mixture simply occurs. The smaller process chamber with the higher speed evacuation pump is advantageous (Tanaka et al. 2016).

Table 6 shows one recipe example. Its design policy is as follows. (1) Decreasing the times for passivation and etching. This is the straightforward method and effective. (2) The next method is adding passivation gas at etching step for reducing the etching speed. Even when the passivation gas is mixed somewhat, the etching effect overcomes. However, this increases the risk of generation of micro-masks and the black Si. (3) One countermeasure is introducing O_2 gas at a few %. The flow rate of 2sccm is the minimum value of the etcher hardware used. The chamber cleaning proceeds stabilizing the etching condition. Furthermore, adding small amount of O_2 in SF_6 plasma has the effect to increase the etching rate (d'Agostino and Flamm 1981; Syau et al. 1991). SO_2F_2 and SO_2F_2 are reported to be generated. (4) Since O_2 gas will make the passivation film thinner, the platen power for attacking the passivation film is decreased to 5 W. The mask selectivity is maintained. 5 W is enough for 4-in. wafer. (5) Times for the passivation and the etching steps are further tuned for avoiding the black Si all over the wafer. The detail condition can change

Table 6 A set of parameters for obtaining the reduced scallop

	Gas [sccm]			Time	RF power		Pressure
	C ₄ F ₈	SF ₆	O ₂	[s]	Coil [W]	Platen [W]	[Pa]
Passivation	79	0	2	5	500	0	2
Etching	9	90	2	8	500	5	2

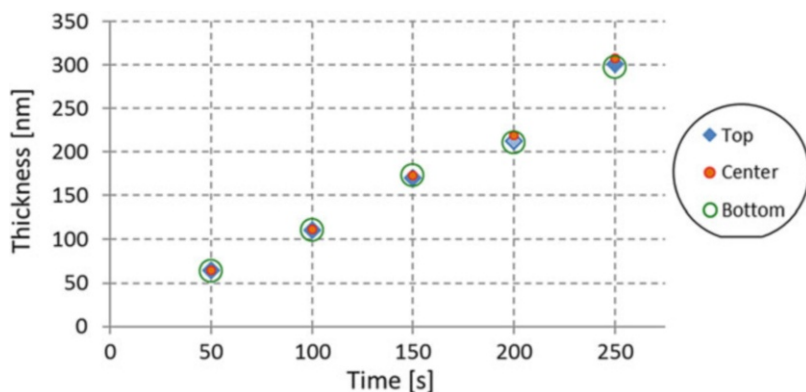


Fig. 10 The thickness of the passivation film grown by the recipe in Table 6. The ellipsometer at the wavelength of 632.8 nm is used. The refractive index of the film is estimated to be 1.37, which is reasonable compared to the bulk fluorocarbon resin

depending on the pattern. The etching rate is about 190 nm/cycle. The selectivity against the resist mask is about 50.

Figure 10 shows the C_xF_y film thickness against time. The plasma condition is the same with the passivation step in Table 6. The measurement is carried out at three points on 4-in. wafer. The linear relation is obtained. The deposition rate is 1.1–1.2 nm/s. So, the passivation film thickness for protecting the sidewall is about 6 nm in the recipe shown in Table 6.

Figure 11a shows the trench after the deep RIE using the recipe shown in Table 6. Figure 11b shows the magnified 3-stepped bank. The bank terrace is flat, and the step corner becomes sharp compared to that in Fig. 9b. This may relate to the decrease of the platen power. Figure 11c shows the magnified sidewall. Compared to Fig. 9c, the scallop becomes finer. The scallop depth is estimated to be about 40 nm.

Figure 12 shows the oxidation process after Si etching for smoothing the sidewall. (1) Starting is the wafer after the deep RIE. (2) The oxidation generates the oxygen diffusion inside Si material. The interface between the oxide and Si is rounded. Since the oxidation speed is influenced by the stress especially at the lower temperature, the higher temperature is better. The following results are obtained at 1100 °C growing the oxide thickness of 1 μm. This consumes Si by about 400 nm, which is larger than the scallop depth. (3) The sidewall smoothing is obtained when SiO₂ layer is etched out.

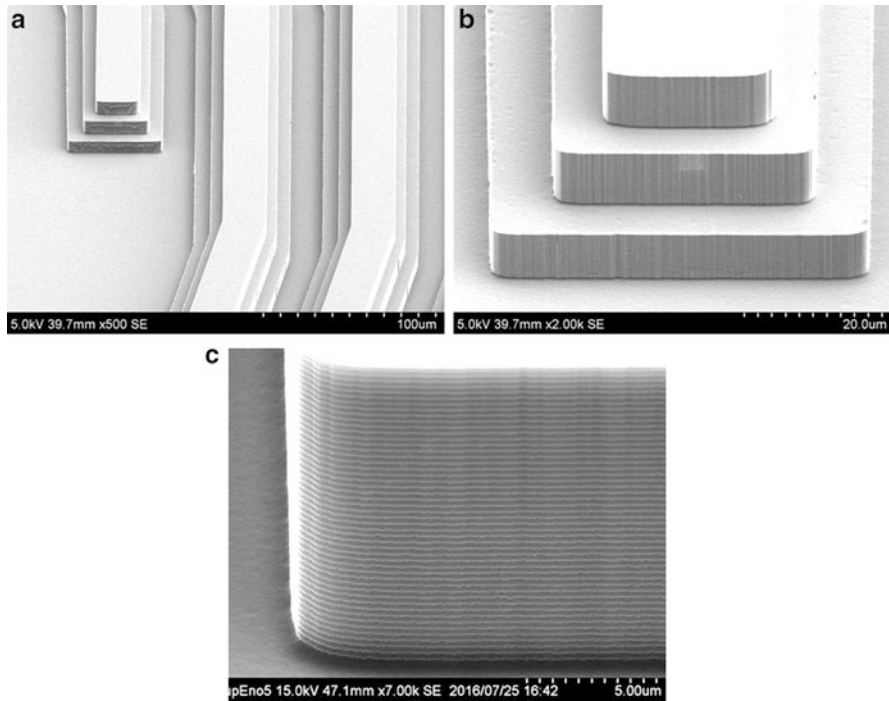


Fig. 11 (a, b) Three-stepped trench. (c) Scallop on the sidewall. The tilt angle of the stage is 60°

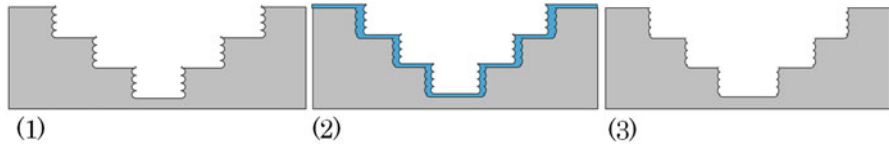


Fig. 12 Sequence for smoothing the sidewall scallop using the high-temperature oxidation and the subsequent oxide etching

Figure 13 shows the sidewall profile after the oxidation. Figure 13a is obtained starting from the sidewall shown in Fig. 9. The shape is rounded, but the initial scallop is recognizable. Figure 13b is obtained starting from the sidewall shown in Fig. 11. The lateral ripple of the scallop disappears. On the sidewall, the surface has little contrast (which is difficult to find the focus position) indicating the smooth surface. The trench corner is also rounded. The vertical stripes are rather outstanding. They are considered to occur by the mask pattern. Another smoothing method is H_2 annealing (Hajika et al. 2014). In that, the structure Si atom migrates under H_2 environment at the high temperature. This technique does not change the structural

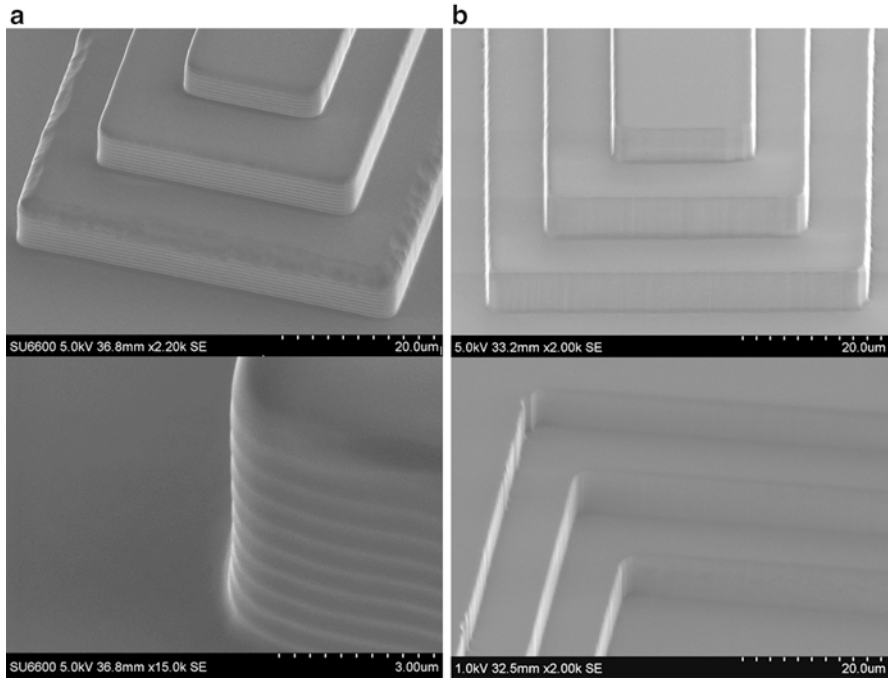


Fig. 13 Sidewalls after the smoothing process shown in Fig. 12. Sample prepared from the trenches shown in Figs. (a) 9 and (b) 11

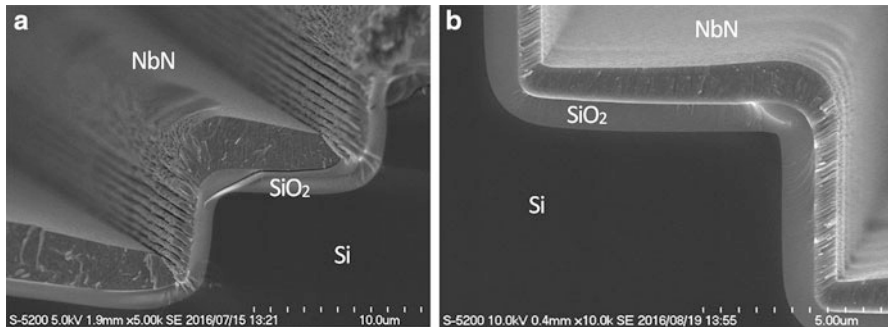


Fig. 14 Sputter-deposited NbN films inside the trenches. The starting trenches are shown in Figs. (a) 9 and (b) 11. (Courtesy of Y. Suzuki and T. Motohiro (Nagoya University))

Si volume, although the specific equipment becomes necessary. In case of the high-temperature oxidation, the rather normal equipment contributes the fabrication quality combining with the deep RIE etcher.

Figure 14 shows the cross-section of the trench with the sputter-deposited NbN film after the smoothing process. Figure 14a is obtained when the starting trench is

as shown in Fig. 9. The periodic stripe is clearly seen on the sidewall. There are separation gaps between the stripes. When the material is deposited in the trench, the scallop can be a serious problem. The self-shadowing against the incident atom exaggerates the corrugation causing the interfaces or the voids. Figure 14b is obtained when the starting trench is as shown in Fig. 11. The film becomes continuous without the periodic stripe on the vertical sidewall. The better material quality is expected.

29.11 Application of the Superconducting Coil

As an application example, the superconducting magnetic energy storage (SMES) is picked up (Ali et al. 2010). Figure 15 shows the conceptual drawing of the compact SMES proposed. The spiral trench is prepared on the Si wafer. The superconducting coil is made by the material deposition inside the trench. Here, the material is NbN, which is good for the feasibility study. Figure 15b shows the cross-sectional drawing of 3-stepped trench filled with NbN and Cu. In contrast to the single rectangular trench (Sugimoto and Motohiro 2013; Sugimoto et al. 2017), this trench opens to the upside allowing the wide incident angle ($\pm 45^\circ$) for NbN sputter deposition. Cu metal is for safety preparing the current path when the superconducting condition is broken. The hoop force will be applied to the current path of the coil. For the mechanical support, the hard Si material is suitable. From the center of one electrode, the spiral trench runs to the outside electrode.

The spiral trench is the single coil which covers almost all area of 3-in. wafer. The total trench length is 45 m. For SMES application, the disconnection of the spiral is

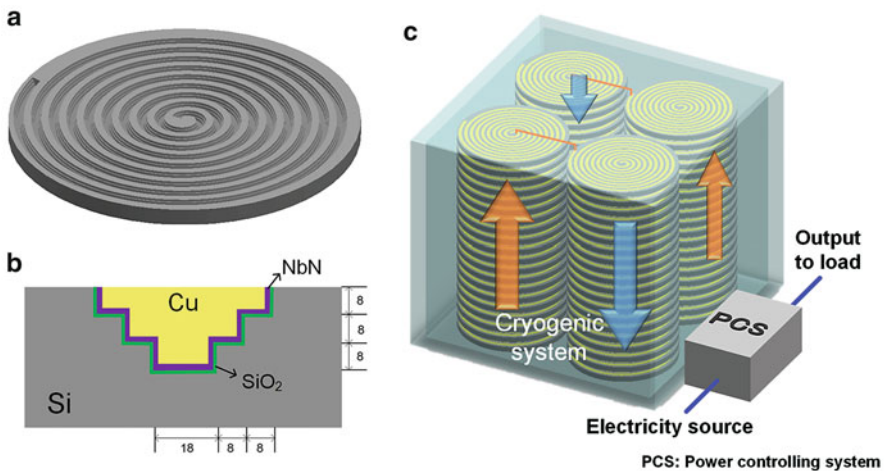


Fig. 15 Schematic of the compact SMES system. (a) Spiral trench in one wafer. (b) Cross-sectional view of the multisteped trench filled with NbN and Cu. (c) Connecting superconducting coils in the cryo-chamber. The supposed volume including the cryo-pump is $0.3 \times 0.3 \times 0.6 \text{ m}^3$

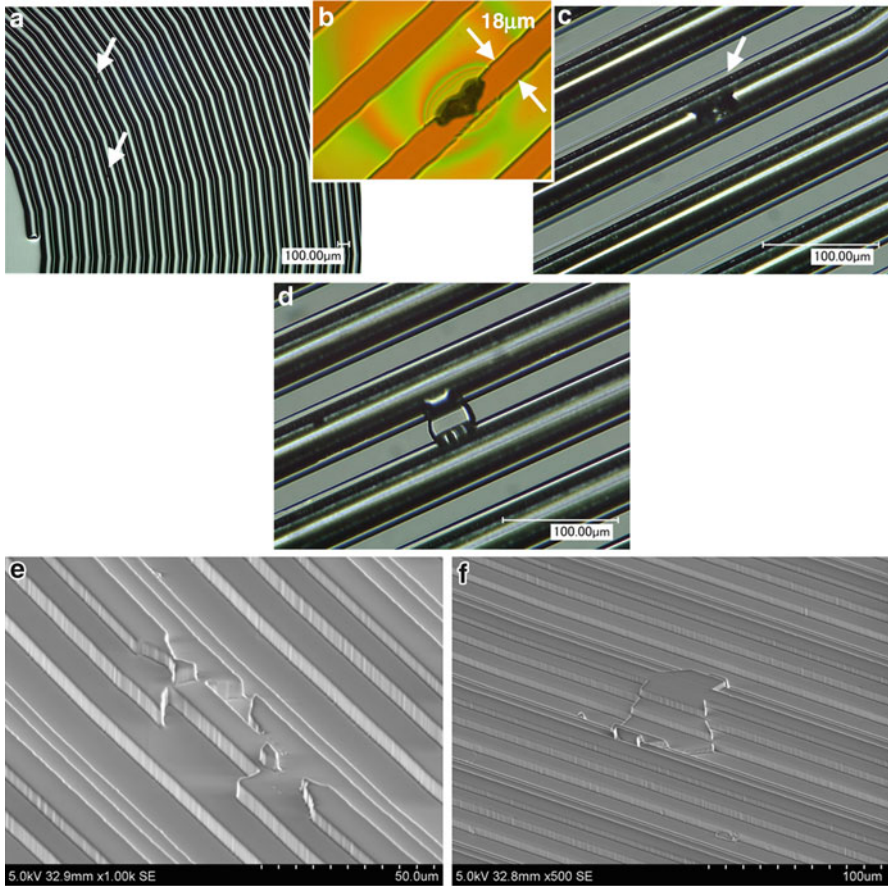


Fig. 16 (a) Low-magnification optical micrograph with two defects indicated by the white arrows. (b) The dust mixed in the photoresist film during the patterning process. (c, d) Magnified image of the smaller defects. (e, f) Magnified image of the larger defects

fatal and should be avoided. Figure 16a is the optical micrograph of the trench with lower magnification. Two defects are seen as indicated by the white arrows. The current path can be blocked there. Figure 16b shows one defect mixed in the resist processing. Figure 16c shows the defect which makes the etching depth shallower by one step. The trench remains for two steps. Figure 16d is the case when the trench bank is locally etched. This causes the shortage of one turn route not the disconnection. So, this is again fail-safe. Figure 16e, f are cases influenced by the bigger dusts. The multistep design is valid even for such cases. In the multistep design, the disconnection only occurs when the defects are at the same position in all patterning. Such possibility is very low.

On the oxidized wafer, the sputter NbN of the superconducting material and the electroplated Cu are deposited. After the wafer polishing, the superconducting coil as

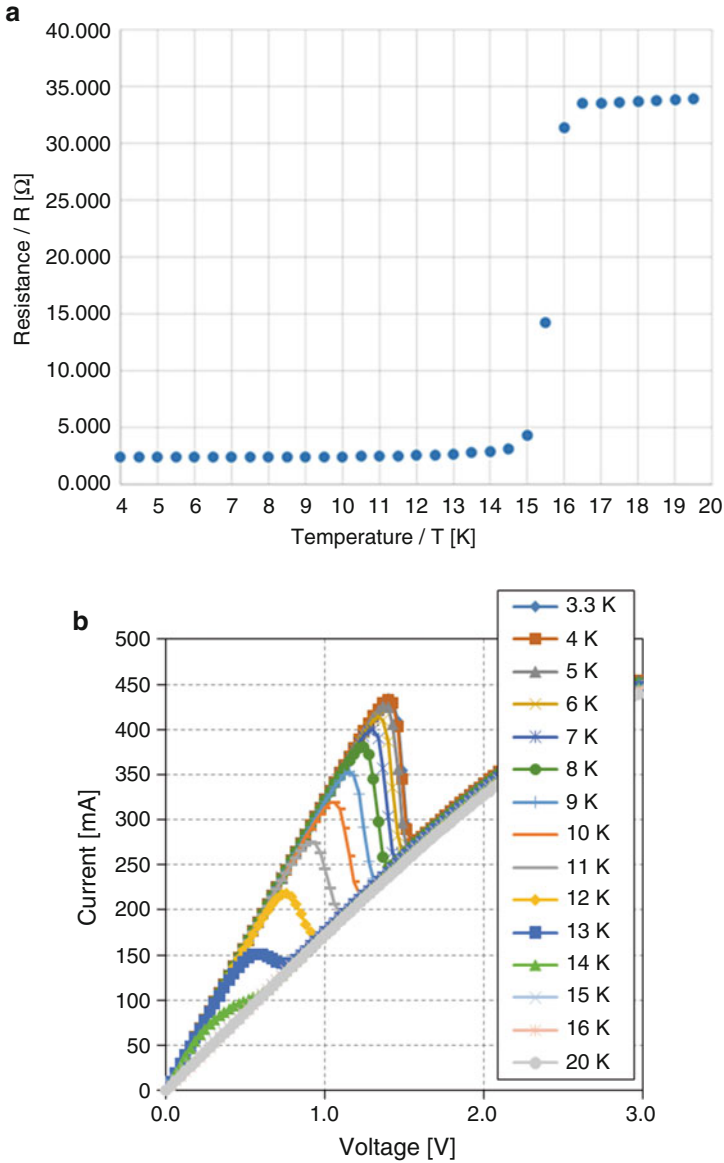


Fig. 17 Results of the superconducting electrical characteristics for one coil wafer. **(a)** Temperature dependence of the series resistance. **(b)** Current-voltage curves at different temperatures. (Courtesy of Y. Suzuki and T. Motohiro (Nagoya University))

shown in Fig. 15b is obtained. The electrical performance between ends is measured in the cryo-chamber. Figure 17a shows the resistance-temperature curve. The series resistance quickly decreases below 15.5 K. This is the transition to the superconducting. The remained resistance is the contact resistance. Figure 17b shows the current-voltage

curves at different temperatures. The curves show the steeper increase of the current at the smaller voltage indicating the superconducting. At the larger voltage, the current drops to another linear line with the larger resistance. This is the normal conduction. At 7 K, the current reaches 400 mA keeping the superconducting condition.

29.12 Summary and Outlook

Techniques for realizing the multiple-height Si microstructures are described relating to the Bosch process and the lithography-based micromachining. Detailed understanding of the micromachining characteristics will enable to realize the new applications. The multiple-height microstructure is the approximated shape of the analogue 3D one, which can be designed with the reasonable process margin. As an example, a 45-m-long spiral trench covering 3-in. wafer is shown for preparing the coil of the compact SMES. The 3-stepped structure is fabricated by three-time patterning and the subsequent Si etchings, which can reduce the disconnection risk caused by the random defects which are included inevitably. The scallop can be decreased by tuning recipe to give 200-nm level etching rate per cycle and can be removed by the thermal oxidization and the etching of the grown SiO₂. This improves the NbN film quality deposited later. The fabricated coil is confirmed to show the clear superconducting. The microstructure with more heights will be a simple future direction of the technique described. The etching quality (e.g., uniformity, shape accuracy, reproducibility) will relate to the condition control of the process chamber. At present, the temperature is controlled from the outside. As the characteristics of the lithography-based technique, the new material (e.g., mask material, eco-friendly gas) or the processing technique can combine with the described etching and patterning techniques.

References

- d'Agostino R, Flamm DL (1981) Plasma etching of Si and SiO₂ in SF₆-O₂ mixtures. *J Appl Phys* 52(1):162–167
- Ali MH, Wu B, Dougal RA (2010) An overview of SMES applications in power and energy systems. *IEEE Tras Sustain Energ* 1(1):38–47
- Bhardwaj J, Ashraf H, McQuarrie A (1997) Dry silicon etching for MEMS. In: Proceedings of symposium on microstructures and microfabricated systems at the annual meeting of the electrochemical society, May 4–9
- Gimkiewicz C, Hagedorn D, Jahns J, Kley EB, Thoma F (1999) Fabrication of microprisms for planar optical interconnections by use of analog gray-scale lithography with high-energy-beam-sensitive glass. *Appl Opt* 38(14):2986–2990
- Griss P, Stemme G (2003) Side-opened out-of-plane microneedles for microfluidic transdermal liquid transfer. *J Microelectromech Syst* 12(3):296–301
- Hajika R, Yoshida S, Kanamori Y, Esashi M, Tanaka S (2014) An investigation of the mechanical strengthening effect of hydrogen anneal for silicon torsion bar. *J Micromech Microeng* 24(10):105014
- Hakko Electric Co., Ltd (n.d.) home page <http://www.hakko.co.jp/qa/qakit/html/h01020.htm>

- Kumagai S, Hikita A, Iwamoto T, Tomikawa T, Hori M, Sasaki M (2012) Multiple-height microstructure fabricated by deep reactive ion etching and selective ashing of resist layer combined with UV curing. *Jpn J Appl Phys* 51:01AB04
- Laermer F, Schilp A (1992) Method for anisotropically etching silicon. German Patent DE-4241045, US Patent 5,501,893
- Laermer F, Urban A (2005) Milestones in deep reactive ion etching. Digest of technical papers of the 13th international conference on solid-state sensors, actuators and microsystems 3B1.1, pp 1118–1121
- Laermer F, Urban A (2002) Plasma system and method for anisotropically etching structures into a substrate. European Patent 1,554,747 B1
- Laermer F, Franssila S, Sainiemi L, Kolari K (2015) “Deep reactive ion etching” handbook of silicon based MEMS materials and technologies, Chap. 21, 2nd edn. Elsevier, Oxford, pp 444–469
- Marty F, Rousseau L, Saadany B, Mercier B, Francais O, Mita Y, Bourouina T (2005) Advanced etching of silicon based on deep reactive ion etching for silicon high aspect ratio microstructures and three-dimensional micro- and nanostructures. *Microelectron J* 36:673–677
- Marxer C, Thio C, Gretillat M-A, de Rooij NF, Battig R, Anthamatten O, Valk B, Vogel P (1997) Vertical mirrors fabricated by deep reactive ion etching for fiber-optic switching applications. *J Microelectromech Syst* 6(3):277–285
- Mehra A, Zhang X, Ayón AA, Waitz IA, Schmidt MA, Spadaccini CM (2000) A six-wafer combustion system for a silicon micro gas turbine engine. *J Microelectromech Syst* 9(4):517–527
- Milanovic V, Matus GA, McCormick DT (2004) Gimbal-less monolithic silicon actuators for tip-tilt-piston micromirror applications. *IEEE J Sel Top Quantum Electron* 10(3):462–471
- Mita Y, Tixier A, Oshima S, Mita M, Gouy J-P, Fujita H (2000) A silicon shadow mask with unlimited patterns and a mechanical alignment structure by Al-Delay masking process. *IEEJ Trans Sens Micromachines* E120(7):357–362
- Mita Y, Kubota M, Harada T, Marty F, Saadany B, Bourouina T, Shibata T (2006) Contour lithography methods for DRIE fabrication of nanometre–millimetre-scale coexisting microsystems. *J Micromech Microeng* 16(6):S135
- Rao MP, Aimi MF, MacDonald NC (2004) Single-mask, three-dimensional microfabrication of high-aspect-ratio structures in bulk silicon using reactive ion etching lag and sacrificial oxidation. *Appl Phys Lett* 85(25):6281–6283
- Sasaki M, Nakai F, Hane K, Yokomizo K, Hori K (2006) Absolute micro-encoder using image obtained by ball lens assembled inside wafer. *J Opt A* 8(7):S391
- Sato R, Sawada T, Kumagai S, Sasaki M (2014) Multiple-height microstructure fabricated by deep reactive ion etching and soft resist masks combined with UV curing. *J Phys Conf Series* 518:012012
- Seika M (2006) Strength of materials, Chap. 14. Kyoritsu Shuppan Co., Ltd., Tokyo. [in Japanese]
- Sugimoto N, Motohiro T (2013) Anisotropic I-V characteristics of spontaneously emerged periodic stripes of superconducting NbN thin films on Si trench sidewall by RF magnetron sputtering. *Vacuum* 93(7):13–21
- Sugimoto N, Iguchi N, Kusano Y, Fukano T, Hioki T, Ichiki A, Bessho T, Motohiro T (2017) Compact SMES with a superconducting film in a spiral groove on a Si wafer formed by MEMS technology with possible high-energy storage volume density comparable to that of rechargeable batteries. *Supercond Sci Technol* 30(1):015014
- Suzuki Y, Iguchi N, Adachi K, Ichiki A, Hioki T, Hsu C.-W, Sato R, Kumagai S, Sasaki M, Noh J.-H, Sakurahara Y, Okabe K, Takai O, Honma H, Watanabe H, Sakoda H, Sasagawa H, Doy H, Zhou S, Hori H, Nishikawa S, Nozaki T, Sugimoto N, Motohiro T (2017) “Complete Fabrication of a Traversable 3 μm Thick NbN Film Superconducting Coil with Cu plated layer of 42m in Length in a Spiral Three-Storeyed Trench Engraved in a Si Wafer of 76.2 mm in Diameter Formed by MEMS Technology for a Compact SMES with High Energy Storage Volume Density”, IOP Conf. Series: Journal of Physics: Conf. Series 897:012019.
- Syau T, Baliga BJ, Hamaker RW (1991) Reactive ion etching of silicon trenches using SF₆/O₂ gas mixtures. *J Electrochem Soc* 138(10):3076–3081

- Takahashi K, Kwon HN, Mita M, Saruta K, Lee J-H, Fujita H, Toshiyoshi H (2007) A silicon micromachined f- θ microlens scanner array by double-deck device design technique. *IEEE J Sel Top Quantum Electron* 13(2):277–282
- Tanaka H, Ogiso H, Nakano S, Hayami T, Miyazaki T, Khumpuang S, Hara S (2016) Scallop reduction in Bosch process using a small chamber and rapid gas switching rate. *IEEJ Trans Sens Micromachines* 136(12):499–504. [in Japanese]
- Tsuchiya T (2005) Reliability characterization of MEMS materials. *IEEJ Trans Sensors Micro-machines* 125(7):289–293. [in Japanese]
- Urey H (2002) Torsional MEMS scanner design for high-resolution display systems. *Proc SPIE* 4773:27–37
- Waits CM, Morgan B, Kastantin M, Ghodssi R (2005) Microfabrication of 3D silicon MEMS structures using gray-scale lithography and deep reactive ion etching. *Sens Actuators A* 119:245–253
- Williams KR, Muller RS (1996) Etch rates for micromachining processing. *J Microelectromech Syst* 5(4):256–269



Local Wettability Modification and Its Micro-Fluidic System Application

30

Yuko Aono and Atsushi Hirata

Contents

30.1	Introduction	926
30.2	Wettability Modification	929
30.3	Materials and Laser Modification Systems	933
30.3.1	Materials	933
30.3.2	Laser Modification Systems	933
30.3.3	Contact Angle Measurement	935
30.4	Modification of Non-treated Silicon and Glass	935
30.4.1	Silicon	935
30.4.2	Borosilicate Glass	938
30.4.3	Problems	941
30.5	Modification of Pretreated Silica Glass with Hydrophobic Terminal Group	942
30.5.1	Properties of Coupled Terminal Groups	942
30.5.2	Wettability Modification	943
30.5.3	Surface Geometry and Transparency	946
30.6	Micro-Fluidic Applications	947
30.6.1	Surface Flow Channel	947
30.6.2	Self-Transportation Channel	950
30.7	Summary and Outlook	952
	References	954

Abstract

Micro-fluidic systems function as promising devices in many fields such as biochemistry and conventionally consist of packaged groove-type micro-channels. In this chapter, surface flow channels independent of geometric formation such as grooves are introduced. The surface flow channels are based on wettability modulation. Liquid preferentially flows toward more wettable surface;

Y. Aono · A. Hirata (✉)

Department of Mechanical Engineering, Tokyo Institute of Technology, Tokyo, Japan

e-mail: aono.y.aa@m.titech.ac.jp; hirata.a.aa@m.titech.ac.jp

© Springer Nature Singapore Pte Ltd. 2018

925

J. Yan (ed.), *Micro and Nano Fabrication Technology*, Micro/Nano Technologies,

https://doi.org/10.1007/978-981-13-0098-1_30

therefore a locally modified surface with higher wettability can function as a surface flow channel even if the modified surface is entirely flat and an invisible line. Furthermore, a surface channel with gradient of wettability demonstrates self-transportation ability for micro-droplets. This chapter especially focuses on the local modifications and modulations of wettability on silicon and glass substrates using laser irradiation, which change surface chemical composition or nanoscale roughness by laser thermal effect. The laser modification results in wide range of contact angles from 40 to 110° on silica glass of which surface is pretreated with hydrophobic terminal groups (-CF₃). The variation of wettability is caused by thermal decomposition of the terminal groups depending on laser irradiation conditions. The correlation between the remaining surface hydrophobic group and contact angle is confirmed by quantitative analysis of fluorine on the surface. In addition, this chemical modification preserves surface geometry and transparency of the substrate. The local wettability modification by laser irradiation is then applied to form micro-fluidic systems and achieves invisible surface flow channel with self-transportation ability by spatial wettability control.

Keywords

Laser modification · Wettability modulation · Micro-fluidic system · Surface channel · Self-transportation

30.1 Introduction

In general, micro-fluidic system is an integration of micro-channels, reactors, and sensors on a chip, which is often called lab-on-a-chip or micro-total-analysis-system (μ TAS) (Erickson and Li 2004). The concept of these integrated fluidic systems was introduced by Manz et al. (1990), while several micro-fluidic systems had already been developed for gas chromatography (Terry et al. 1979) or ink-jet printing nozzle (Bassous et al. 1977). Currently, micro-fluidic systems have widely been adopted in the wide realm of science and engineering. One of the representative examples is biochemical applications such as a DNA analysis, immunological reaction, and blood monitoring (Jakeway et al. 2000; Chován and Guttman 2002; Erickson and Li 2004). In this field, miniaturizing has great advantages in analyzing in vivo or at bedside with reduction of usage of biological or scarce sample and rapid mixing and reaction time. Furthermore, it can precisely control volume and concentration of each micro-droplet by its geometrical design (Tan et al. 2004).

Micro-channel is the fundamental component of the micro-fluidic systems. It links reactors and delivers droplets throughout the system. Conventional micro-channels consist of thin grooves packaged with cover plate in 3D geometry. Micro-fabrication methods for the channels or grooves have been reported for a variety of materials ranging from silicon and glasses to various polymers such as polydimethylsiloxane (PDMS). Until the 1990s, many micro-fabrication processes such as lithography and etching had been developed in the silicon microprocessor industry, and then the processes were applied to the micro-channel fabrication in the

same manner as microelectromechanical systems (MEMS) (Woolley et al. 1996; Schwesinger et al. 1996; Tanaka et al. 2004). In addition to the MEMS processing, a mechanical processing by micro-end-milling using submillimeter tools was developed (Vázquez et al. 2010; Yun et al. 2008). This method is versatile and effective for metallic materials, although it has difficulty to machine ductile materials. Laser processing (Bellouard et al. 2004; Kim et al. 2005; Malek 2006) and electrical discharge machining (Doan et al. 2009) were also applied to micro-channel formation. In particular, femtosecond laser is a powerful tool for micromachining, and there are a number of reports about micro-channel formation after the 2000s. The adoption of femtosecond laser achieves less thermal damage as well as high-aspect ratio groove on silicon (Tull et al. 2006), silica glass (Marcinkevičius et al. 2001; Bellouard et al. 2004), and polymers (Suriano et al. 2011).

As other approaches, rapid prototyping and printing techniques have been adopted for the micro-channel fabrication process. Rapid prototyping using stereolithography with photosensitive polymer was reported by Ikuta et al. (1994). After that, various 3D-printed micro-fluidic devices have been reported (Bhattacharjee et al. 2016). Not only direct printing, an idea of using 3D-printed template and imprinting on polymers were also introduced (Duffy et al. 1998; Comina et al. 2014), which have advantages in productive efficiency. Although conventional materials for the 3D-printed devices are centered on polymer, a method for high-quality glass 3D printing has recently been proposed (Kotz et al. 2017), and it is expected to achieve printed micro-fluidic systems with higher physical and chemical durability.

Another type of micro-channel dealing with fluids or droplets not in capillaries and grooves but exactly on virtually flat surface of the substrates has been proposed. The concept of this surface flow channel was applied to digital micro-fluidic (DMF) systems which manipulate liquids in discrete droplets on the surface of micro-fluidic devices called as “one-plate” or “open” DMF (Choi et al. 2012). The early open-type micro-fluidic systems were operated by electrostatic force on shallow guiding grooves (Washizu 1998). Although the surface flow channel with electrostatic actuation was able to achieve more controllable operation of the droplets by selecting a voltage-applied electrode with suitable timing, the fabrication process was complicated like the production of the packaged groove type that had been common micro-fluidic systems.

More simple and efficient fabrication methods for surface flow or open-type micro-channel are direct printing or drawing of channels on the surface of substrates. The methods can define channels on the basis of the difference of surface wettability. One of wettability-based micro-channels was demonstrated on a paper substrate (Martinez et al. 2010; Dungchai et al. 2011). Wax or photoresist was printed and impregnated on the paper substrate, and then the impregnated area turned hydrophobic which played a role as a barrier of fluids, as shown in Fig. 1. Consequently, liquid preferentially flows on hydrophilic area without any grooves. This technique has been applied to various applications such as blood sensors (Songjaroen et al. 2012), reviewed by Cate et al. (2015).

Surface wettability on inorganic materials is controlled by deposition, texturing, or surface modification. These techniques for wettability modulation are described in

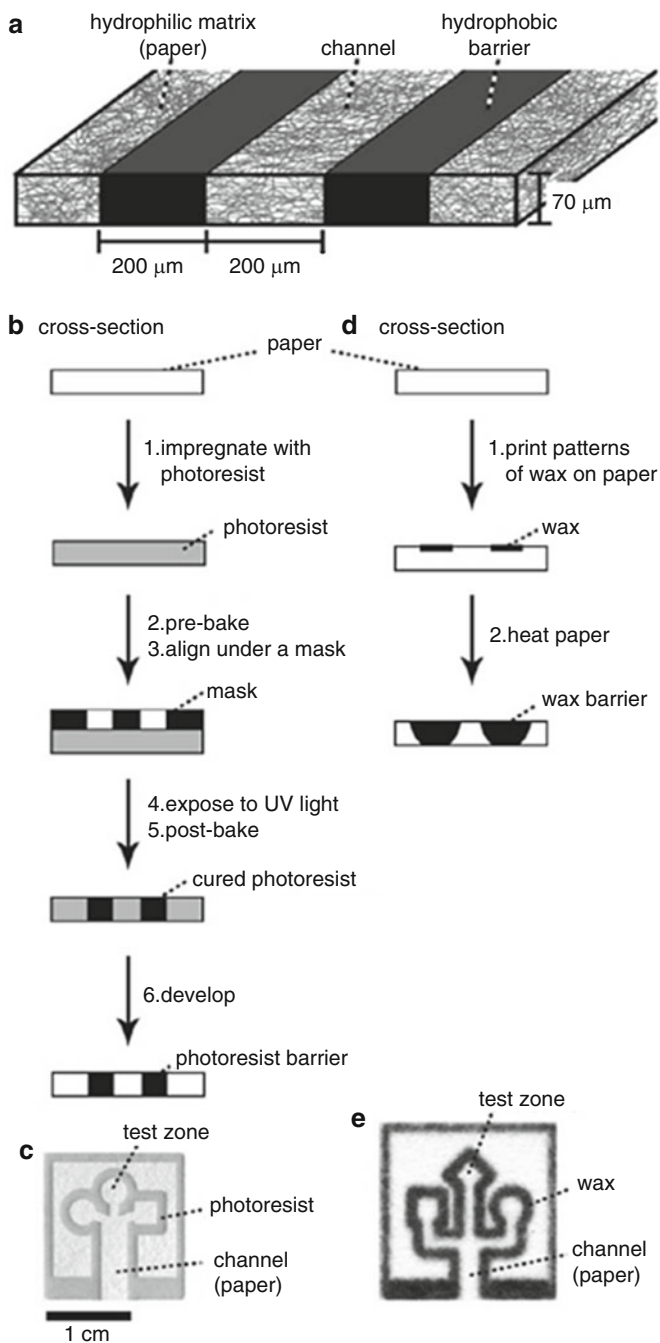


Fig. 1 Fabrication process of paper-based micro-fluidic devices by patterned immersion of hydrophobic photoresist or wax into paper. (Reprinted with permission from Martinez et al. 2010, copyright 2018 American Chemical Society)

Sect. 2. An example of drawing of wettability-based micro-channel by laser irradiation is introduced in this chapter. This is based on a local wettability modification by laser treatment, which can control the wettability from hydrophilic to hydrophobic in continuity on silicon and glass substrates (Aono et al. 2015, 2016). Firstly, principles of wettability modulation by laser-induced surface modification are introduced for silicon and glass. Secondly, an effective pretreatment for glass is adopted, and wide-range modulation of the surface wettability is demonstrated from hydrophobic to hydrophilic. Finally, the laser modification method is applied to form surface flow channels and then provide more functional channels that exhibit self-transportation ability.

30.2 Wettability Modification

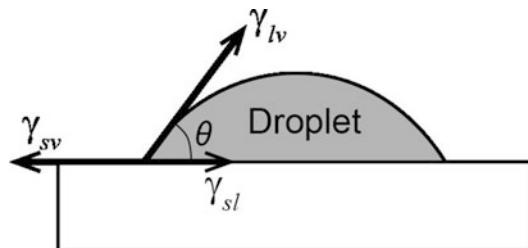
Wettability is an important property for a number of surface applications including the micro-fluidic systems. An index of surface wettability is contact angle θ which is an angle of tangent line of liquid droplet on the solid surface as shown in Fig. 2 (Kwok and Neumann 1999). Young introduced that contact angle has relation with three interfacial tensions (Young 1805). The contact angle is determined by Young's equation:

$$\gamma_{lv} \cos \theta = \gamma_{sv} - \gamma_{sl} \quad (1)$$

where γ_{lv} , γ_{sv} , and γ_{sl} are interfacial tensions between liquid-vapor, solid-vapor, and solid-liquid, respectively. The interfacial tensions of solid surface, often called surface free energy, is determined by chemical factors such as material composition and surface functional groups. In particular, γ_{sl} easily changes with the surface conditions and thus greatly influences the wettability. In addition, surface roughness also affects the contact angle. The relation between surface texture and wettability was introduced by Wenzel (1949) and Cassie (Cassie and Baxter 1944). Each model suggested that the higher surface roughness brings the higher contact angle on hydrophobic surface. The lotus effect which is a well-known superhydrophobic phenomenon is also based on these models; the leaves of lotus have numerous micro-bumps (Sun et al. 2005).

Wettability control has been a key technological issue for many applications such as windows, analytical glass instruments, wet process of semiconductor

Fig. 2 Contact angle and surface tensions among liquid droplet, solid surface, and surrounding atmosphere



manufacturing, or medical instruments. An approach to obtain hydrophobic and superhydrophobic ($\theta > 150^\circ$) surface is micro-texturing on the basis of Cassie's theories. Zorba et al. (2006) demonstrated silicon surface processed by femtosecond laser irradiation. The process fabricated the surface having micro-order spikes which exhibited hydrophobicity with higher contact angle of 128° comparing to around 65° before the process. This texturing process using femtosecond lasers was also applied to metallic surfaces (Kietzig et al. 2009; Wu et al. 2009; Fadeeva et al. 2011), glasses (Zhou et al. 2009; Tang et al. 2010; Ahsan et al. 2013), and polymers (De Marco et al. 2010; Cardoso et al. 2011). As other texturing processes to produce superhydrophobic surface, for example, 3D diffuser lithography (Im et al. 2010) and deep reactive ion etching (Tropmann et al. 2012) were also developed.

In a different approach from the physical micro-texturing, chemical surface modifications were also in common use. Monolayer of molecules bonded on surface can drastically change surface wettability, and this layer is less likely to effect on surface geometry of substrate than the micro-texturing method; the technique is therefore attractive for some optical applications or molds for micro- or nano-patterns (Kim et al. 2007). The typical hydrophobic terminal groups are $-\text{CF}_3$ and related fluorocarbons (Nishino et al. 1999) which are practically used as water-repellent coating film for windows (Akamatsu et al. 2001). Ogawa et al. (1993) reported a transparent and superhydrophobic glass modified by $\text{CF}_3(\text{CF}_2)_7(\text{CH}_2)_2\text{SiCl}_3$. The glass surface exhibited the contact angle of 155° and the unaltered transparency in wavelength range of between 400 and 700 nm. Furthermore, Baldacchini et al. (2006) combined the chemical modification with the physical micro-texturing by femtosecond laser irradiation and achieved the high contact angle of 160° on silicon surface as shown in Fig. 3. Givenchy et al. (2009) proposed the combination process for PDMS surface and achieved superhydrophobic polymer with the contact angle of exceeding 160° .

The chemical modification has also been used to obtain hydrophilic or superhydrophilic surfaces on which contact angle is less than 5° . Those highly wettable surfaces play an important role as hydrophobic surfaces do in such applications as

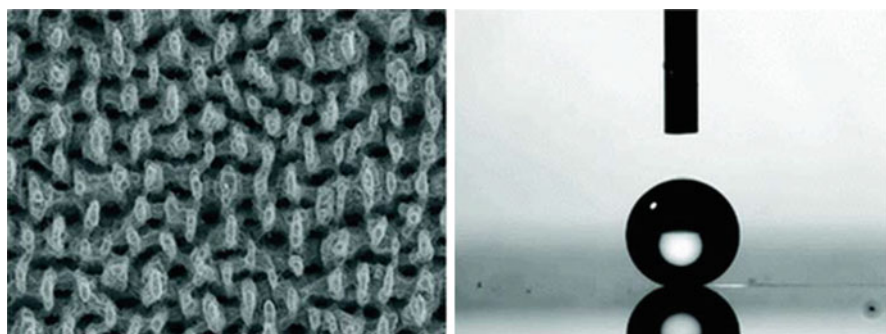


Fig. 3 Superhydrophobic silicon surface modified by both chemical and femtosecond laser irradiation processes. (Reprinted with permission from Baldacchini et al. 2006, copyright 2018 American Chemical Society)

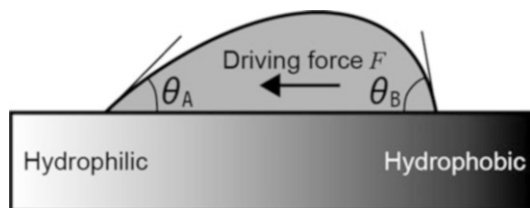
biological surface treating living tissues (Wichterle and Lim 1960) and self-cleaning coatings (Parkin and Palgrave 2005). Silanol group (-SiOH) is a common hydrophilic group for silicon compounds. The group can be activated by simultaneous UV exposure under moisture and oxygen plasma treatment on silicon and glass surfaces (Sun et al. 2002; De Rosa et al. 2003). On PDMS which is a kind of silicon rubbers, the similar oxidation or oxygen plasma treatment is an effective procedure for hydrophilic modification (Bhattacharya et al. 2005), although the hydrophilicity gradually diminishes (Hillborg and Gedde 1999). In addition, superhydrophilic photocatalyst has gathered much attention (Wang et al. 1997). Titanium oxide photocatalyst is excited by UV irradiation and exhibits superhydrophilicity during the irradiation, which is based on partial elimination of hydrocarbons by the photocatalytic decomposition (Takeuchi et al. 2005).

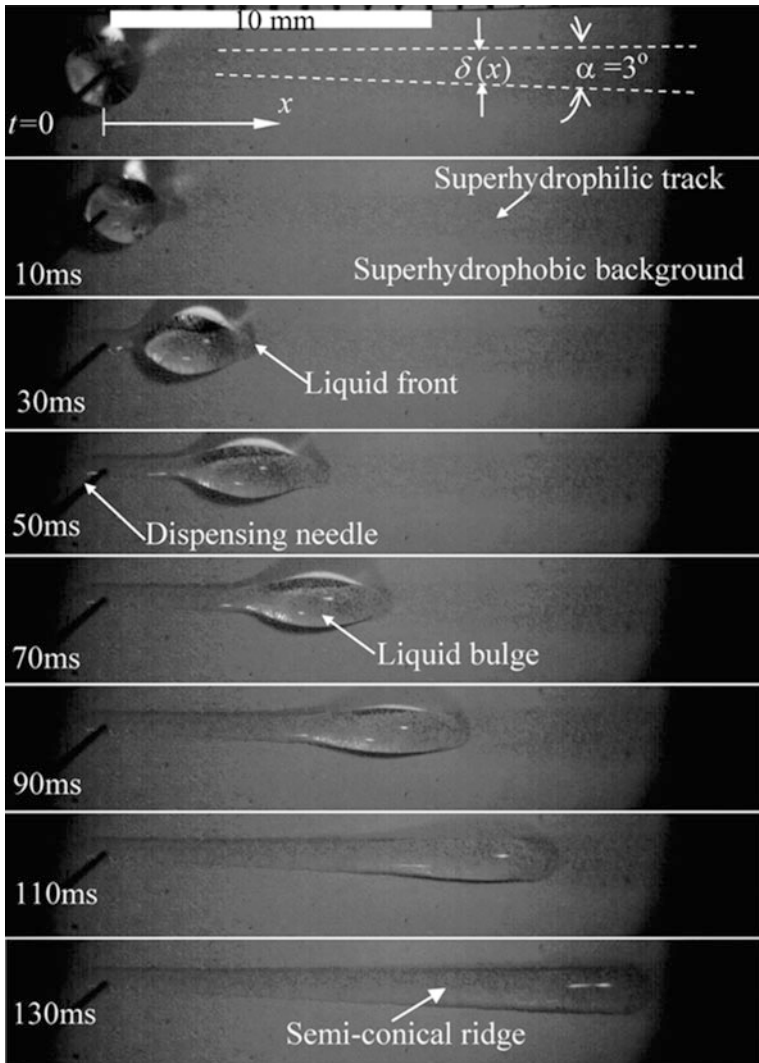
Wettability has an important role not only statically but dynamically. For the operation of discrete micro-droplets of liquid on the open or surface flow channel without grooves and covers, droplet transportation methods are key technology because conventional pressure-based driving mechanisms for inner channels cannot work well. The pumpless driving has been achieved by non-contact force such as gravity, electrostatic (Chaudhury and Whitesides 1992; Mertaniemi et al. 2011) magnetic force (Long et al. 2009), as well as capillary action (Mertaniemi et al. 2011). Wettability modulation is another candidate for the operation of droplets. A droplet on a surface with wettability gradient is subject to driving force F given by

$$dF = \gamma_{lv}(\cos \theta_A - \cos \theta_B)dx \quad (2)$$

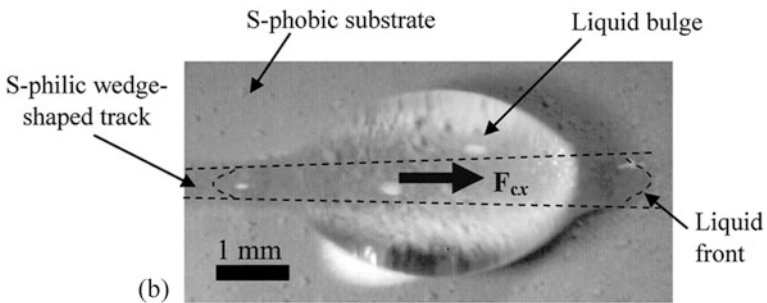
where γ_{lv} is the interfacial tension between liquid and vapor, dx is the sectional height of the droplet, and θ_A and θ_B are local contact angles at the front and back edge of the droplet, respectively, as shown in Fig. 4 (Chaudhury and Whitesides 1992). Ghosh et al. (2014) introduced the wettability-based self-transformation on open micro-fluidic channel by wedge-shaped superhydrophilic track formed on a superhydrophobic substrate. The wettability on the micro-fluidic system consists of only two phases of superhydrophilic and superhydrophobic, using photocatalytic effect of TiO_2 , but the spatial ratio of these two phases continuously varies and generates the driving force for self-transportation (Fig. 5). Nakashima et al. (2015) further developed this two-phase wettability self-transportation by series of wedge-shaped patterns. In their research, hydrophilic SiO_2 film was deposited and patterned by photolithography on hydrophobic cyclo-olefin polymer substrate.

Fig. 4 Driving force of droplet on wettability gradient surface





(a)



(b)

Fig. 5 (continued)

In the following section, continuous wettability control and laser drawing are introduced. The mechanism for this wettability modulation is on both geometric and chemical modification. The two-phase wettability systems harnessed only two types of areas (i.e., their surface consisted of only two contact angles). In contrast, the continuous wettability control method can design arbitrary contact angles within wide allowable range. This is achieved by gradual change of degree of roughness or quantity of surface groups.

30.3 Materials and Laser Modification Systems

30.3.1 Materials

Materials used for the local wettability modification were silicon, borosilicate glass, and silica glass without or with pretreatment by terminal modification. Both of silicon and glass have high stability and durability for the micro-fluidic applications. Glass has high transparency as well, which is suitable for optical monitoring and sensing of fluids.

The silicon substrate was diced into $20 \times 20 \text{ mm}^2$ from CMP-polished (100) silicon wafers $500 \mu\text{m}$ thick. The substrates of borosilicate glass (Pyrex) and synthetic silica glass (ES100, TOSOH) were also 20 mm square with the thicknesses of 10 and 0.7 mm , respectively. Both sides of the glasses were mirror polished. All substrates were at first ultrasonically cleaned in acetone, ethanol, and deionized water for a total of 30 min .

The ultrasonic cleaning of silica glass for pretreated substrate was followed by an UV-ozone cleaning for 30 min and silane coupling treatment for terminal modification with hydrophobic groups. Two types of groups were coupled, one is $-\text{CF}_3$ (Durasurf 5210-S, Harves) and the other is $-(\text{CH}_3)_2$ (Syron-CT, Aldrich). After the UV-ozone cleaning, the silica glass substrate was dipped into each agent solution. The substrate treated with $-\text{CF}_3$ was then annealed at $100 \text{ }^\circ\text{C}$ for 1 h and rinsed with hydrofluoroether (Novtec7100, 3 M). On the other hand, the substrate treated with $-(\text{CH}_3)_2$ was rinsed with toluene and isopropyl alcohol without annealing.

30.3.2 Laser Modification Systems

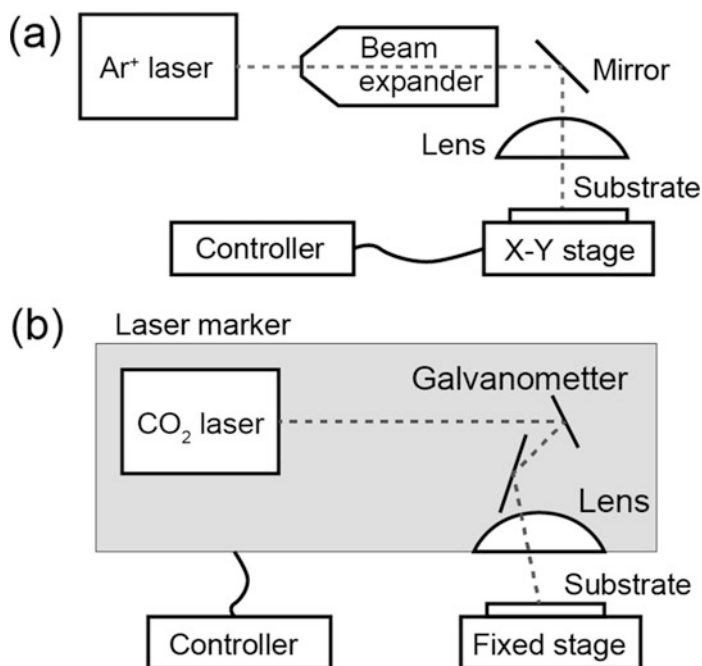
Laser sources were selected for each material. The basis of the laser wettability modification is thermal treatment; therefore sources which are continuous wave (CW) with absorption-efficient wavelength were adopted. For the silicon surface



Fig. 5 Self-transportation of droplet on wedge-shaped superhydrophilic track (a) time-lapsed images of droplet and (b) liquid bulge. (Reprinted with permission from Ghosh et al. 2014, copyright 2018 Royal Society of Chemistry)

Table 1 Specifications of laser devices

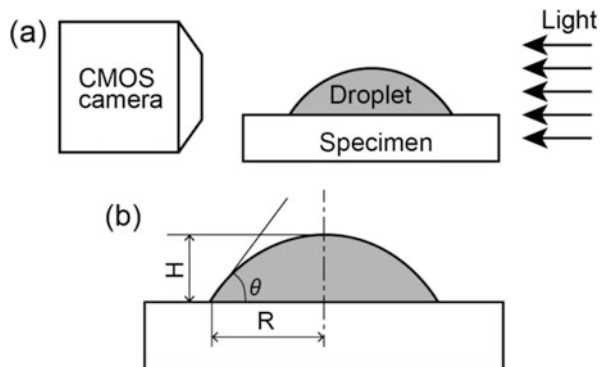
Laser source	Argon ion	CO ₂
Wavelength (nm)	514.5	9300
Power (W)	2.5–8.0	0.1–1.8
Spot diameter (μm)	2.6	160
Scan speed (mm/s)	10	10–240
Scan interval (μm)	10	50

**Fig. 6** Schematics of laser irradiation systems: (a) continuous argon ion laser for silicon substrate modification and (b) laser marker with continuous CO₂ laser source for borosilicate and silica glass substrate modification

modification, CW-Ar ion laser was selected. The laser includes multi-wavelength line but representative value is 514.5 nm, green laser beam. On the other hand, borosilicate and silica glass were modified with CW-CO₂ laser of which wavelength is 9.3 μm, infrared laser, because glass has high transparency in visible light range. This laser is a commercial laser marker (LP4200, Panasonic). The specifications of both laser beams are summarized in Table 1.

Optical systems for the modification are shown in Fig. 6. In the Ar ion laser irradiation system, the silicon substrate was set on an X-Y automatic stage. The laser beam of 2.6 μm in spot diameter was focused on the substrate through a beam expander and lens. The focused point was fixed and the substrates moved during the

Fig. 7 Schematics of contact angle measurement (a) setup and (b) feature size of droplet



modification, whereas the CO₂ laser system scanned the laser beam over the fixed substrate with an installed galvanometer mirror. The spot diameter of the CO₂ laser beam was 160 μm. The modification was conducted with scanning of the substrate or laser beam at constant laser power, stage driving or laser scanning speed (both called as scan speed), and scan interval which is width between each scanning line.

30.3.3 Contact Angle Measurement

Contact angles were measured with a CMOS camera and a micropipet as shown in Fig. 7a. A substrate was horizontally placed, and a 0.2 ml of deionized water droplet was gently dropped on the surface. A shadowgraph of the droplet was observed with the camera from a lateral view. The contact angle θ was then calculated using a half-angle method (Chinnam et al. 2015):

$$\frac{\theta}{2} = \tan^{-1} \frac{H}{R} \quad (3)$$

where H and R are the height and radius of the base of the droplet on the test surface, respectively, as shown in Fig. 7b.

30.4 Modification of Non-treated Silicon and Glass

30.4.1 Silicon

The CW-Ar ion laser beam was scanned one line on the silicon substrate. The laser power was 2.5 and 4 W, and the scan speed was 10 mm/s. After the irradiation, the surfaces were observed with an optical microscope and a scanning probe microscope (SPM: Nanocute, Hitachi), the images taken with which are shown in Fig. 8. The bottom row of Fig. 8 shows optical microscopic images of the dew condensed surfaces. At 2.5 W, it is difficult to identify the laser-scanned line from the

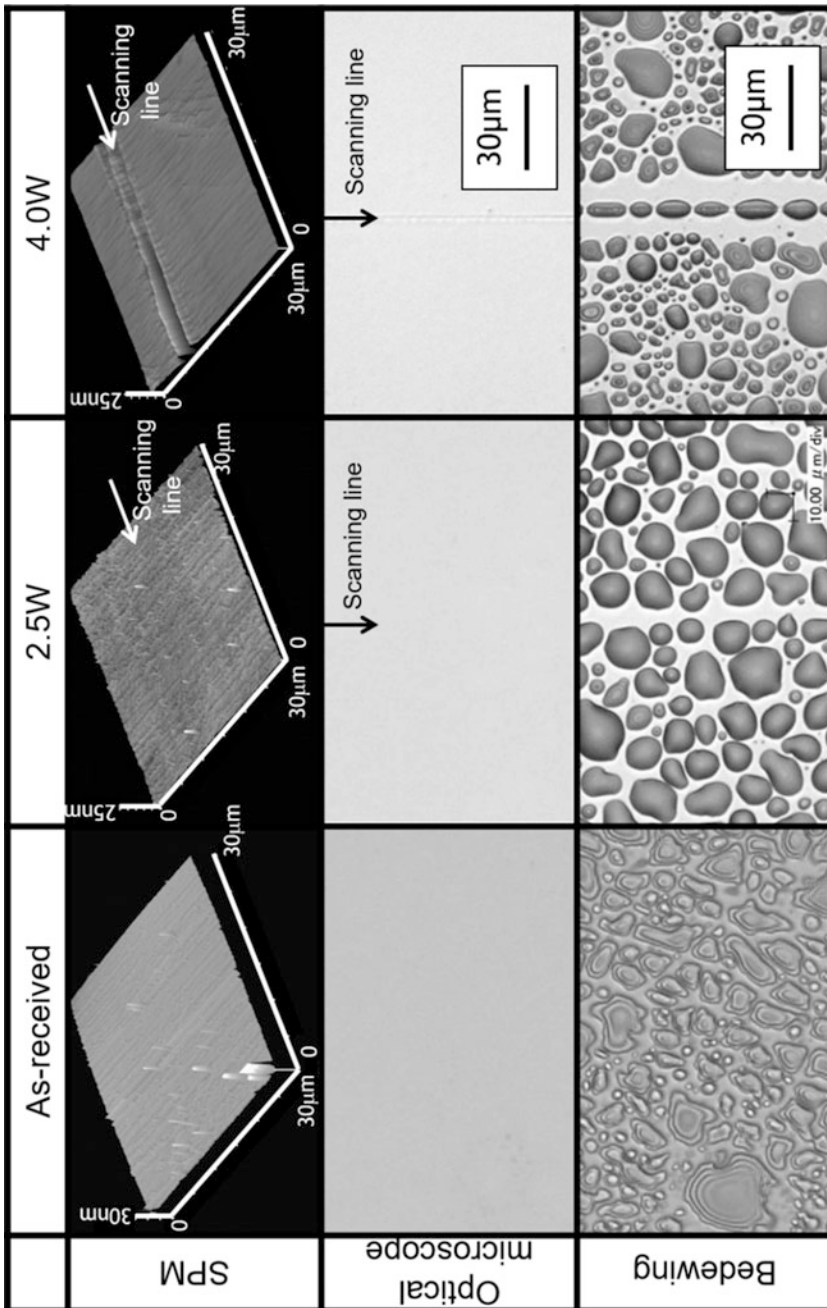


Fig. 8 Modified lines on silicon substrate and dew condensed surface observed by optical microscope and SPM

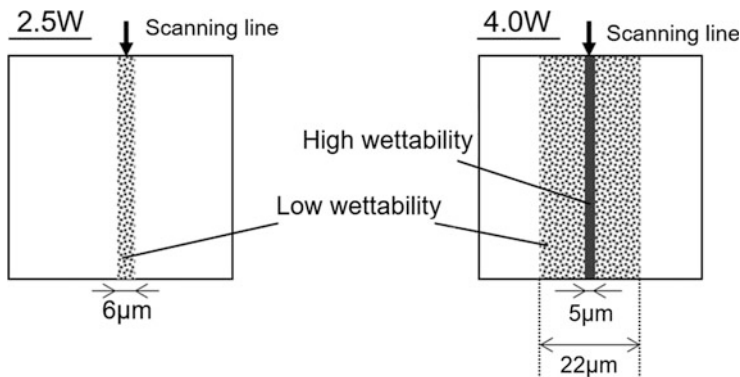


Fig. 9 Illustrations of wettability change after line laser modification on silicon substrate

microscopic image. The SPM image reveals two thin lines on both sides of the scanned area of which the depth is less than 1 nm. After the dew condensation, the scanned area becomes clear; the dew is unformed around on the laser-scanned line, although the dew forms at random on the whole as-prepared surface. The results indicate that the laser-irradiated area was modified and turned into hydrophobic surface at 2.5 W. The irradiated line at 4 W is clearly observed in the optical microscopic image. The dew formed on the center of the laser-scanned line, while the dew formation is undeveloped around both sides of the scanned line. Qualitative changes of wettability after laser irradiation can be summarized as depicted in Fig. 9. The hydrophilic area at 4 W coincides with the geometric change area observed with the SPM. It is assumed that thermal effect for the silicon substrate is the main cause of the reduction of wettability unless morphological change happens.

Contact angles were measured on the modified surfaces which were prepared by laser scanning at 10 μm scan interval. Figure 10 shows the change of contact angle by the laser irradiation. A trend of wettability depends on whether the irradiation causes geometric change or not, although as-prepared surface indicated unstable contact angle. At 2.5 W, without the geometric change, the contact angle increases; however, quantitative repeatability and control of the contact angle are not achieved. The modification is expected to involve native oxidation layer, surface functional groups, and remaining organic contamination, but it is difficult to condition their existence and quantity.

The geometric change which appeared over 4 W is a stable and reproducible phenomenon, contrary to the instability of the surface chemical conditions. The surface modified at 4 W becomes hydrophilic, and this contact angle shift increases with increase in laser power from 4 to 5 W because the geometric change also increases. It can be explained by the Wenzel equation (Wolansky and Marmur 1999):

$$\cos \theta' = r \cos \theta \quad (4)$$

Fig. 10 Contact angle change of silicon substrate, 10 mm/s scan speed and 10 μm scan interval

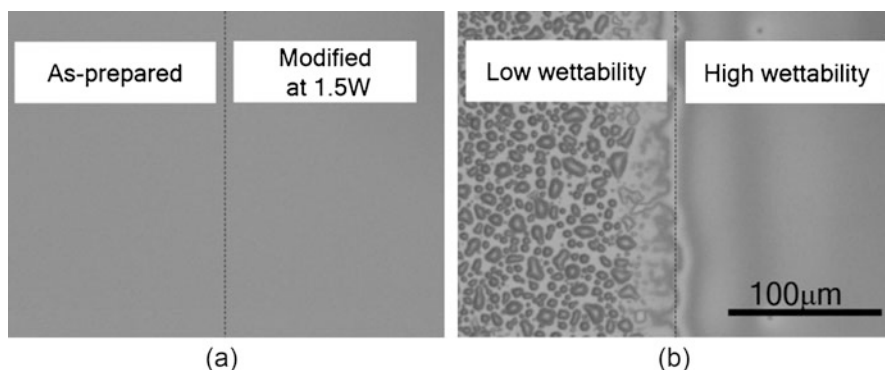
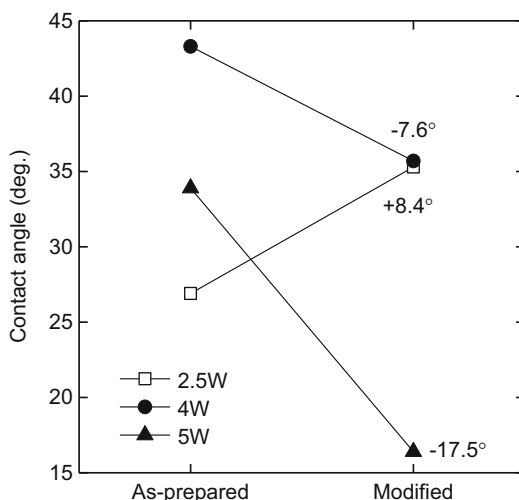


Fig. 11 Optical microscopic images of as-prepared and modified hydrophilic borosilicate glass

where θ' , θ , and r are the contact angle of a practical rough surface, the contact angle of an ideal (i.e., perfectly flat and homogeneous) surface, and the ratio of surface area of the practical surface to that of the ideal surface ($r > 1$), respectively. The equation means the increase of the surface roughness brings the lower contact angle when the contact angle is less than 90° .

30.4.2 Borosilicate Glass

The prepared borosilicate glass was modified with the CO_2 laser marker at 1.2 and 1.5 W. Laser scan speed and scan interval were fixed at 50 mm/s and 50 μm , respectively. Figure 11 shows optical microscopic images of the modified glass

Fig. 12 Contact angle of modified borosilicate glass, 50 mm/s scan speed and 50 μm scan interval. (Reprinted with permission from Aono et al. 2015)

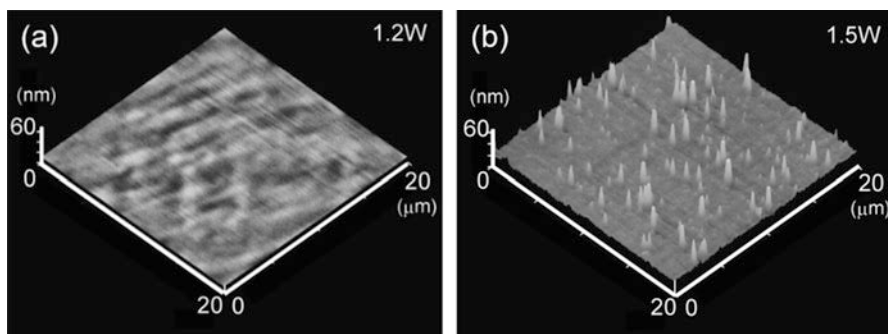
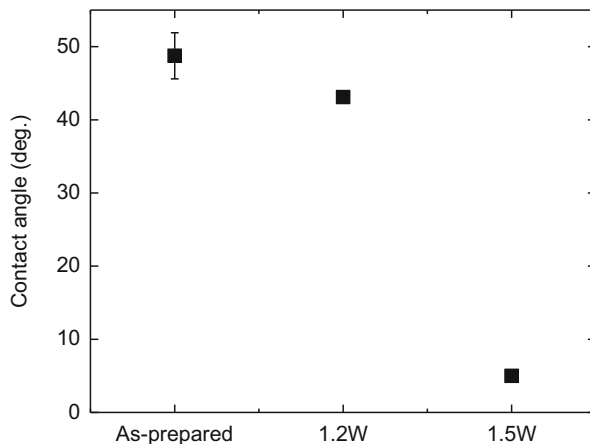
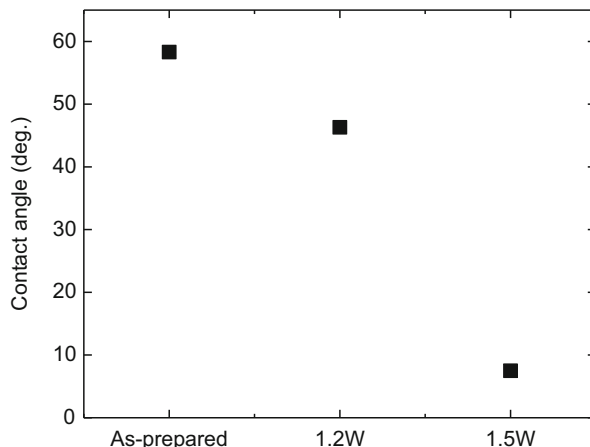


Fig. 13 SPM images of modified borosilicate glasses at (a) 1.2 W and (b) 1.5 W

surface. The right half of the surface was modified at 1.5 W, while the left surface remained as-prepared. Although geometric and optical change cannot be observed on the image taken in dry atmosphere, there appears an obvious difference after dew condensation on the surface. A lot of independent droplets were formed on the as-prepared surface, and this indicates that glass surface apparently became opaque. On the other hand, the condensed dew on the modified surface exhibits formation of thin and continuous water film, which is an extremely different behavior from that on the as-prepared surface.

The contact angles of the modified surface are shown in Fig. 12. The modification at 1.5 W reduced the contact angle from 48 to 5°. The contact angle also decreases at 1.2 W, but the reduction is limited. Morphology of the modified surfaces is shown in Fig. 13. A number of small bumps in nanometers high are generated on the modified surface at 1.5 W. According to the Wenzel equation (Eq. 1), the increase of roughness leads to the decrease of contact angle when the contact angle is less than 90°. Surface area ratio r was then calculated to confirm the effect of the

Fig. 14 Contact angle of modified silica glass, 50 mm/s scan speed and 50 μm scan interval

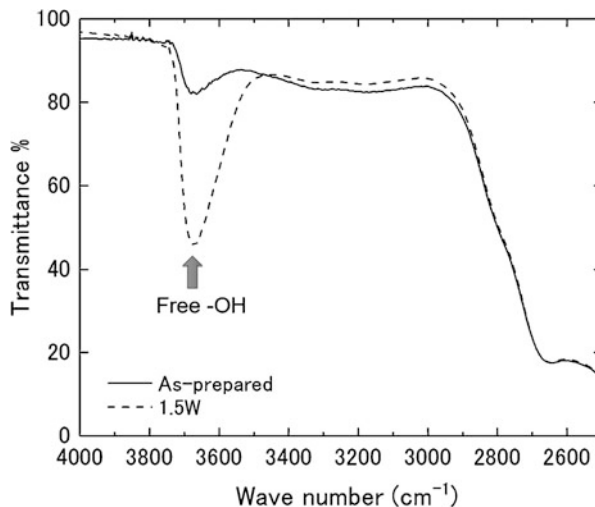


geometric change. From the SPM profile, the surface area ratio of the surface modified at 1.5 W is only 1.002, which is not so large as to describe the drastic reduction of the contact angle. Therefore, it is expected that there is any other effect of the laser irradiation except for geometric change.

Another possible cause for the wettability modification is chemical changes of surface. This change was confirmed by Fourier transform infrared spectroscopy (FT-IR: IR-Prestige21, Shimadzu). This measurement was conducted in the transmission mode. The silica glass without the pretreatment of terminal modification (i.e., only cleaned by solvents and deionized water) was used as specimen instead of the borosilicate glass because of its high transparency in infrared range and high purity. Modification conditions were the same as the borosilicate glass modification, 50 mm/s scan speed, 50 μm scan interval, and 1.2, 1.5 W laser power. After the laser irradiation, the contact angle of the silica glass reduces from 59 to 8° (see Fig. 14) without detectable geometric change as with the borosilicate glass modification. The results of FT-IR on as-prepared and the modified at 1.5 W are shown in Fig. 15. An obvious change was detected at around 3700 cm^{-1} that derives from free -OH group, which means the increase of surface silanol (-SiOH) group. This terminal group exhibits hydrophilicity, i.e., low contact angle, and exists on the ultra-clean raw surface of the glass.

According to the results mentioned above, the wettability change on the glass surface was caused by removal or decomposition of native organic substances covering the silanol group, which is the thermal effect of the laser irradiation. After the elimination of the organic substances, the glass surface is covered with silanol groups and exhibits its original superhydrophilic property. As another evidence of this speculation, there is a fact that the modified hydrophilic property cannot keep a long time in the atmosphere. Shortly after the laser irradiation or organic substance elimination, absorption of contaminants from circumstances would begin and gradually increase the contact angle. After only a few days of the modification, the effect dissipates, and there is little wettability difference between as-prepared and laser-irradiated surfaces.

Fig. 15 FT-IR spectra of silica glass, free -OH group peak at 3700 cm^{-1}



30.4.3 Problems

In this section, non-treated substrates except for standard cleaning were modified. This modification is based on two types of surface reaction caused by laser irradiation; one is geometric or morphological change which increases surface roughness and leads to wettability change, and the other is chemical change including surface terminal group condition such as silanol group.

The geometric change brings permanent and stable wettability change; however, this modification often accompanies excess surface deformation leading to apparent change in terms of surface geometry as shown in Fig. 8. This cannot be ignored when this surface deals with micro- or pico-litter small droplets because this geometric change behaves in a similar way to groove channel.

A problem of the native surface terminal group modification is instability of modified property. The initial surface wettability depends on material conditions such as how to be fabricated, processed, stored, and cleaned, and it is impossible to manage these conditions homogeneously. Therefore, the terminal surface group and its concentration, native oxidation, and attached organic substance are unstable, which results in varied initial wettability. Furthermore, the surface easily reverts to the similar condition as the native surface after modification. For example, the silanol group is liable to combine with organic substance in atmosphere, and it loses its high hydrophilic property. In addition, the initial contact angles of the native silicon and glass surface are around $40\text{--}60^\circ$, and thermal effect of the laser irradiation could reduce this contact angle without the geometric change, but the initial value was not so high. Thus, the contrast between modified and unmodified area is limited in hydrophilic range, and margin of wettability control is narrow.

30.5 Modification of Pretreated Silica Glass with Hydrophobic Terminal Group

30.5.1 Properties of Coupled Terminal Groups

To realize more stable and flexible surface wettability modification by laser, pretreatment to modify terminal group on the surface of the silica glass was adopted. Some of the functional group exhibits high contact angles relating to hydrophobic property, so that the range of wettability modulation can be expanded. In this section, two types of hydrophobic functional groups were selected and tried to produce continuous wettability modulation by control of the concentration of the functional groups by laser irradiation.

The pretreated silica glass substrates were prepared by the procedure described in Sect. 3.1. Before the terminal group modification processes, the contact angle of the silica glass was around 10° owing to the UV-ozone cleaning. After the pretreatment, $-\text{CF}_3$ and $-(\text{CH}_3)_2$ surfaces indicate around 110° and 90° , respectively. The shadow-graph of the droplets on the $-\text{CF}_3$ surface is shown in Fig. 16.

The proposed modification is based on control of the concentration of the surface hydrophobic group by laser thermal effect as shown in Fig. 17; therefore thermal effect on the pretreated surface wettability was confirmed in advance. The pretreated substrates were annealed in an electric furnace in the air. Annealing temperature was varied by 50°C from 100 to 550°C and kept for 5 min at each temperature. Contact angles after annealing at each temperature were measured at room temperature. The results are shown in Fig. 18. The contact angles of the $-\text{CF}_3$ and $-(\text{CH}_3)_2$ surfaces gradually drop to less than 20° above around 300 and 400°C , respectively. The contact angles can have intermediate value between as-terminated hydrophobic surfaces and initial hydrophilic surfaces during the reduction. It suggests that the local wettability modification over a wide range of contact angle can be realized by appropriate laser irradiation conditions.

In addition, the surface geometry and transparency remained unaltered by both terminal group treatments. These properties are shown and discussed in the following sections.

Fig. 16 Water droplet on hydrophobic silica glass surface terminated with $-\text{CF}_3$ group

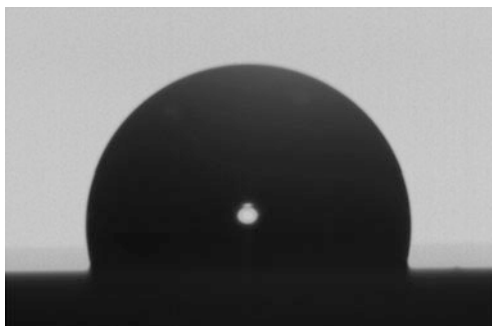


Fig. 17 Concept of continuous wettability modulation by control of concentration of hydrophobic terminal group

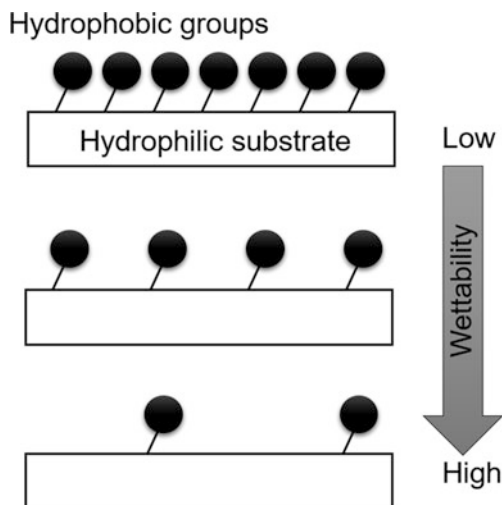
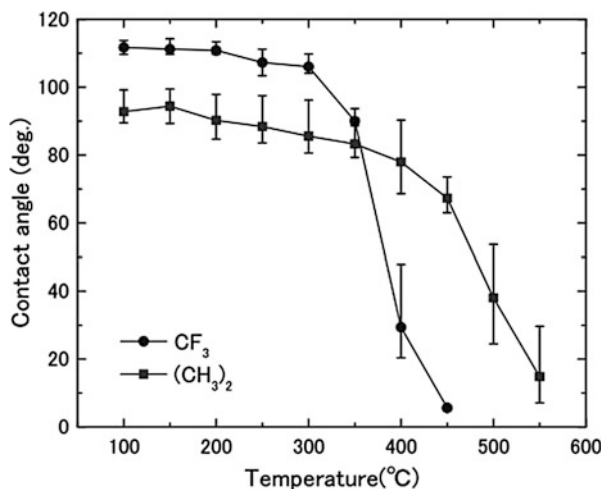


Fig. 18 Contact angles of annealed silica glass surface terminated with $-\text{CF}_3$ and $-(\text{CH}_3)_2$ groups. (Reprinted with permission from Aono et al. 2016, copyright 2018 Applied Surface Science)



30.5.2 Wettability Modification

Both terminated surfaces were modified with the CO_2 laser marker under various laser powers and scan speeds. The laser power and the scan speed were in the range of 0.1–1.8 W and 10–240 mm/s, respectively. Scan interval was fixed to 50 μm . After the laser irradiation, contact angles were immediately measured with a 0.2 ml droplet of deionized water.

The modified surface wettability is shown in Fig. 19. The contact angles decrease with higher laser power or slower scan speed under which the input energy increases. The contact angle on the $-\text{CF}_3$ -terminated surface is especially well-controlled with high

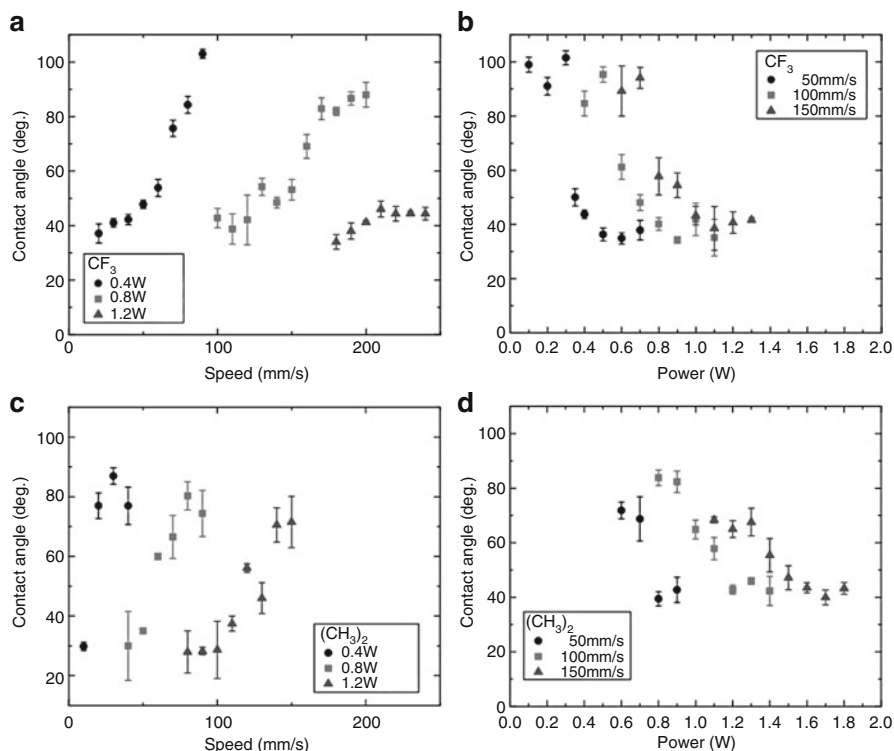


Fig. 19 Contact angles of laser-modified silica glass terminated with hydrophobic groups, (a, b) dependence on scan speed and laser power of $-\text{CF}_3$ -terminated surface and (c, d) same dependence of $-(\text{CH}_3)_2$ -terminated surface. (Reprinted with permission from Aono et al. 2016, copyright 2018 Applied Surface Science)

reproducibility by tuning of the scan speed. Compared with the $-(\text{CH}_3)_2$ -terminated surface, the $-\text{CF}_3$ -terminated surface changes into hydrophilic at lower laser power or faster scan speed. This result corresponds with the results of the annealing experiment mentioned in previous section where $-\text{CF}_3$ group was decomposed at lower temperature than $-(\text{CH}_3)_2$ group (see Fig. 18). In addition, the contact angles for $-(\text{CH}_3)_2$ exhibit wider range of the error bars in both results of the laser modification and the annealing experiment.

The changes of the modified contact angle are saturated at around $30\text{--}40^\circ$, although the angle on UV-ozone cleaned surface showed less than 10° before the $-\text{CF}_3$ - or $-(\text{CH}_3)_2$ -terminated treatment. It suggests imperfect decomposition of the groups or redeposition of decomposed organic substance.

Surface elemental analysis was conducted after the laser modification of the $-\text{CF}_3$ -terminated surface to evaluate remaining $-\text{CF}_3$ group quantitatively using X-ray photoelectron spectroscopy (XPS: ESC5500, ULVAC). Results of the XPS evaluation are shown in Fig. 20. The modification conditions were selected from Fig. 19 to obtain a linear change of the contact angle; $-\text{CF}_3$ -terminated surface

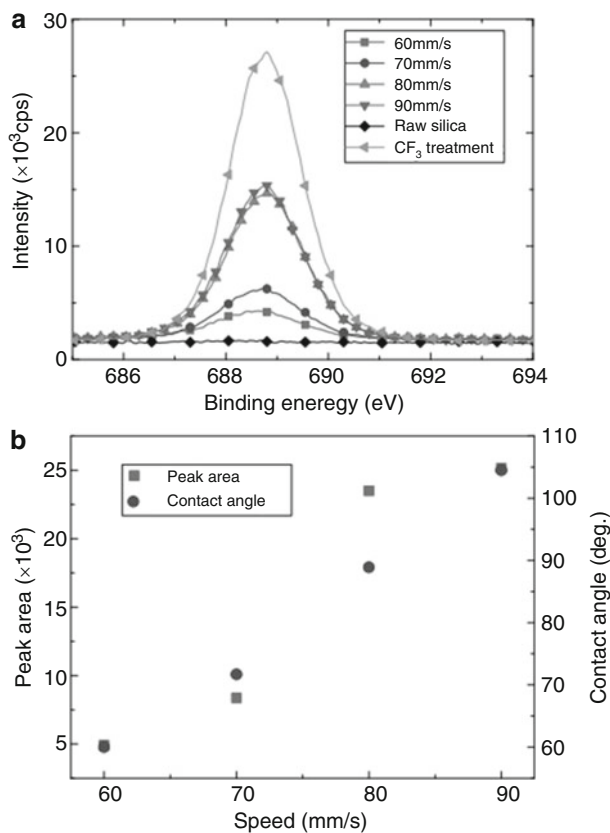
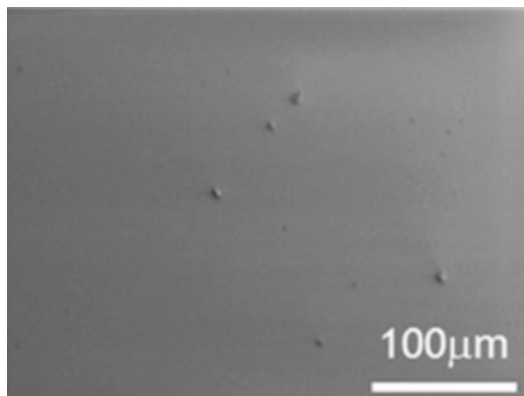


Fig. 20 XPS analyses of $-\text{CF}_3$ -terminated silica glass surface modified at 0.4 W laser power: (a) spectra of fluorene peak and (b) peak area of fluorene peak of XPS spectra and corresponding contact angles. (Reprinted with permission from Aono et al. 2016, copyright 2018 Applied Surface Science)

modified at a fixed power of 0.4 W and scanning speed of 60, 70, 80, and 90 mm/s. In addition, a raw silica glass after the UV-ozone cleaning and a $-\text{CF}_3$ -terminated glass before the laser irradiation were also analyzed. Figure 20a is the measured F1 s peaks around 689 eV which correspond to the amount of surface fluorine. The raw silica surface exhibits no peaks around this binding energy. It indicates that the silica glass and its surface include no fluorine and its compound, and all detected fluorine by XPS is derived from pretreated $-\text{CF}_3$ group. The intensity becomes the highest on the $-\text{CF}_3$ -terminated surface without laser irradiation. The amount of fluorine then decreases depending on the laser irradiation conditions. The F1 s peak areas of the laser-irradiated surface are plotted with the corresponding contact angles in Fig. 20b. The peak area gradually decreases with decrease of the scan speed, which is a similar trend to that of the contact angle. From the results, it is suggested that the wettability of silica surface is controlled by quantitative control of hydrophobic groups on its surface, and this control can be achieved by laser irradiation within selected local area.

Fig. 21 SEM image of $-\text{CF}_3$ -terminated silica glass surface modified at 1.2 W laser power and 100 mm/s scan speed. (Reprinted with permission from Aono et al. 2016, copyright 2018 Applied Surface Science)



Furthermore, the proposed modification process in this section achieves highly stable wettability control. The repeatability of the modification is high as suggested in Fig. 19. The modified state is also temporally stable. The contact angles before and after the modification were preserved for more than 2 weeks.

30.5.3 Surface Geometry and Transparency

Under all irradiation conditions shown in Fig. 19, no crack or damage was observed on the modified surface using an optical microscope. A typical SEM image is shown in Fig. 21, the $-\text{CF}_3$ -terminated surface on which was modified at a laser power of 1.2 W and scanning speed of 100 mm/s. The contact angle of the surface was around 40° , and this was enough angle to modify the surface to be hydrophilic. There is no crack or groove caused by the laser irradiation except for small bumps. Since these bumps were unobserved before the irradiation, the cause of the bump formation is the laser irradiation. They were probably produced by laser beam absorption of small dust on the glass surface. This absorption was visible as intermittent light emission during laser irradiation, although no light emission was detected during regular modification.

For more detailed observation, the silica surfaces were scanned with the SPM, and surface roughness was evaluated. Obtained SPM images are shown in Fig. 22a–c. These are (a) a raw silica glass, (b) a modified $-\text{CF}_3$ terminated glass (1.2 W, 100 mm/s), and (c) a modified $-(\text{CH}_3)_2$ -terminated glass (1.5 W, 100 mm/s). Both of the modified surfaces turned hydrophilic at contact angle of around 40° . On these detailed surface images, no obvious differences are found after the modification. Surface roughness R_a and R_z are calculated from the SPM images as shown in Fig. 23. Both the pretreatment for $-\text{CF}_3$ or $-(\text{CH}_3)_2$ termination and the laser modification had little or no effect on the surface morphology. Their surface roughness remains as low as that of a raw silica surface.

One of advantages of using glass for micro-fluidic systems is its high transparency which enables monitoring, observation, and sensing. The optical property is easily affected by surface morphology and coating layer. The transparencies of the pretreated and laser-modified silica glass were measured with a UV-VIS

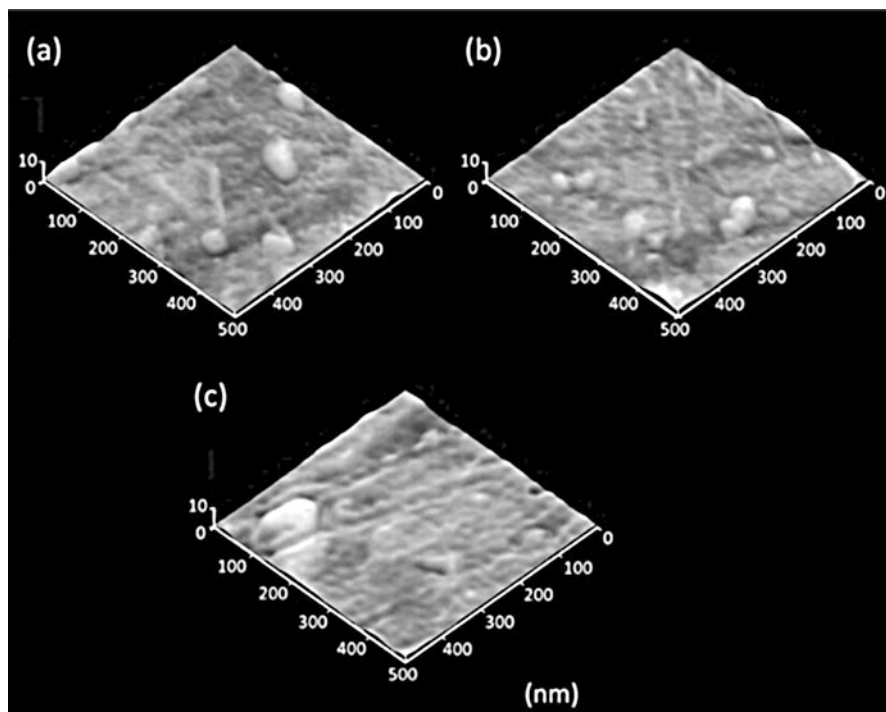


Fig. 22 SPM images of (a) raw silica glass, (b) $-\text{CF}_3$ -terminated surface modified at 1.2 W laser power and 100 mm/s scan speed, and (c) $-(\text{CH}_3)_2$ -terminated surface modified at 1.5 W, 100 mm/s. (Reprinted with permission from Aono et al. 2016, copyright 2018 Applied Surface Science)

spectrophotometer (V550, JASCO). The samples were a raw silica glass, a pretreated glass with $-\text{CF}_3$ and $-(\text{CH}_3)_2$ groups, and the laser modified under the same conditions of the modification for the previous SPM surface observation: 1.2 W, 100 mm/s for $-\text{CF}_3$, and 1.5 W, 100 mm/s for $-(\text{CH}_3)_2$. The pretreatment and the laser irradiation were conducted on both surfaces of raw silica glasses. The measured spectral transmittances are shown in Fig. 24. Within the wavelength ranging from 400 to 900 nm, the transmittances of all specimens are around 93%, and there is less difference depending on the surface conditions. The demonstrated modification was achieved without degrading the glass transparency.

30.6 Micro-Fluidic Applications

30.6.1 Surface Flow Channel

Non-textured flow channels were then drawn on a flat glass surface. This surface flow channels are based on the locally different wettability. On the boundary between hydrophobic and hydrophilic area, water droplet prefers to move toward

Fig. 23 Surface roughness of raw silica, terminated surfaces with hydrophobic groups, and modified hydrophilic surfaces (same laser conditions as Fig. 22). (Reprinted with permission from Aono et al. 2016, copyright 2018 Applied Surface Science)

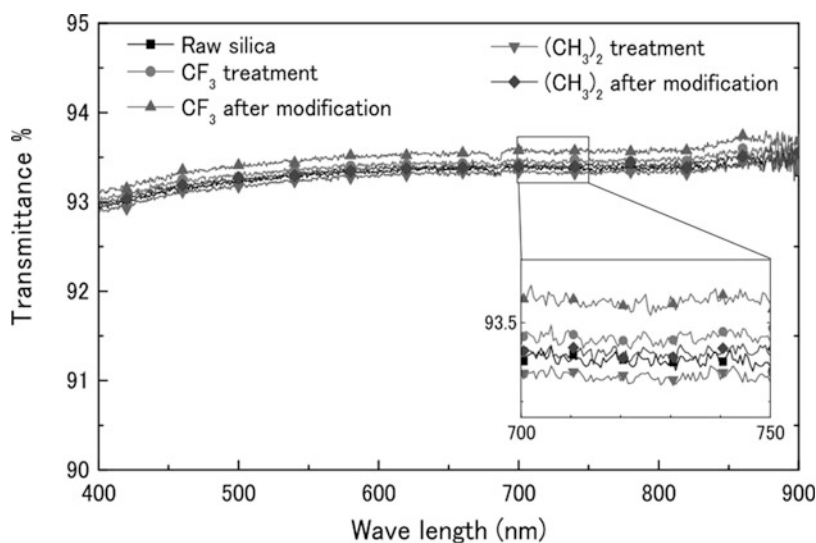
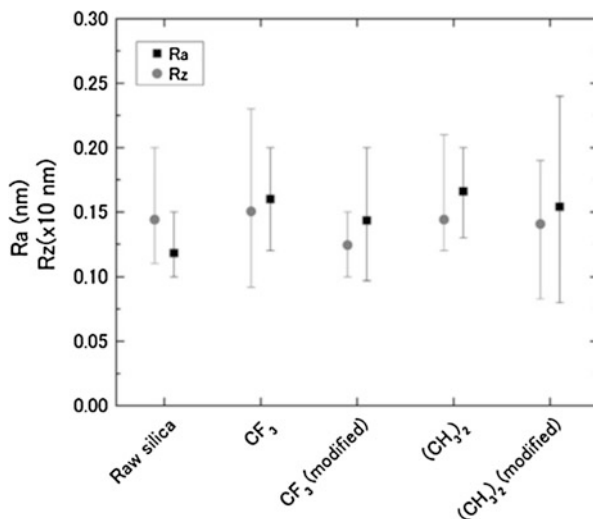


Fig. 24 UV-VIS transmission spectra of raw silica, terminated surfaces with hydrophobic groups, and modified hydrophilic surfaces (same laser conditions as Fig. 22). (Reprinted with permission from Aono et al. 2016, copyright 2018 Applied Surface Science)

hydrophilic area by contact angle hysteresis. Consequently, the boundary can act as channel barrier for water droplet on the hydrophilic area. The proposed surface flow channels were fabricated on the surfaces of borosilicate glass and a -CF₃-terminated silica glass. Modification conditions were selected from Figs. 12 and 19 to obtain more hydrophilic area than non-modified area.

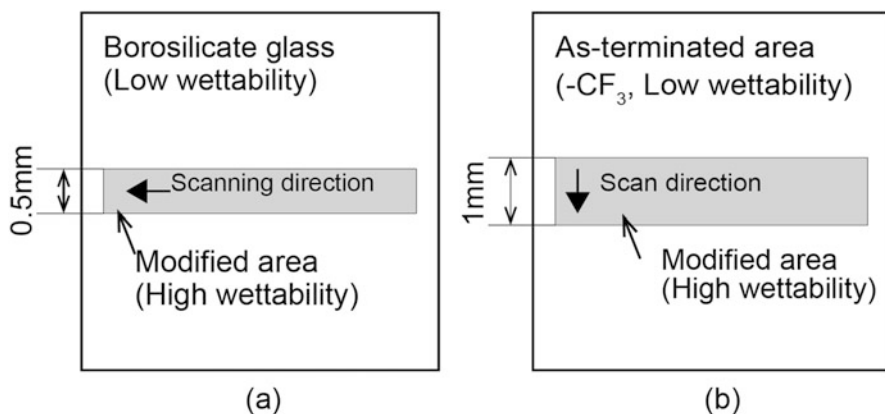


Fig. 25 Schematics of laser modification for plane surface flow channel on (a) borosilicate glass and (b) -CF₃-terminated silica glass

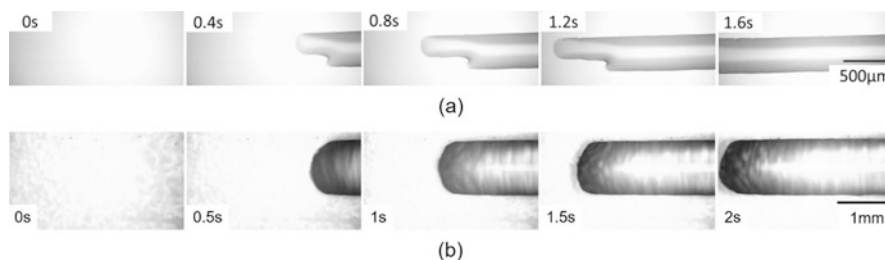


Fig. 26 Top view of plane surface flow channels on (a) borosilicate glass and (b) -CF₃-terminated silica glass

On the raw borosilicate glass, the CO₂ laser beam was irradiated in a line with 0.5 mm width as shown in Fig. 25a. Laser power, scan speed, and scan interval were 1.5 W, 50 mm/s, and 50 μm, respectively. Scanning direction was the same as a channel direction. Contact angle on the modified channel area was expected around 5° from Fig. 13. Another surface flow channel was drawn on the -CF₃-terminated silica glass as illustrated in Fig. 25b. The width of the channel was 1 mm, and the scanning direction was in a perpendicular direction to the channel direction. Laser irradiation conditions were 0.6 W of laser power, 50 mm/s of scan speed, and 50 μm of scan interval. Expected contact angle of the modified area is around 40°, which is higher than that of the modified borosilicate glass, but unmodified area has much higher contact angle (perfectly hydrophobic, around 100°); thereby enough contrast of contact angle can be realized.

After the modification, the borosilicate and silica glasses were horizontally placed and then deionized water was continuously dropped on a side of the drawn modified areas under monitoring with an optical microscope from above. Series of the microscopic images are shown in Fig. 26. Before water droplet was loaded, the modified area cannot be distinguished from unmodified area by any cracks, damages, or grooves on the both

substrates. In contrast to the uniform surface appearance, the dropped water spread or flowed along the invisible channels drawn by laser irradiation with clear boundary. The widths of the water flows are about 0.5 and 1 mm, respectively, which correspond to the modified widths. The water flows finally reached the opposite side ends without overflows. The laser scanning direction had no influence on the water flow even if not along with the channel direction.

The surface flow channels were successfully demonstrated on both borosilicate and silica glasses. However, the wettability of the borosilicate glass without any terminated treatment is so unstable that the functionality as the surface flow channel continued only a few days, while the channel drawn on the pretreated silica glass functioned for more than 2 weeks.

30.6.2 Self-Transportation Channel

The proposed open-type surface flow channel requires some sort of liquid transportation mechanism except for pump system. In this section, micro-channels with the ability of self-transportation are developed by the laser local modification, which is based on the contact angle hysteresis mentioned in Sect. 2.

Micro-channels with self-transportation ability are fabricated by the two types of laser modification; with/without geometric change of surface on a silicon and a $-CF_3$ -terminated silica glass. Silicon surface becomes more hydrophilic and has lower contact angles with increasing laser power higher than 4 W as it results in geometric change (Fig. 8). A design of the self-transportation channel on the silicon surface is shown in Fig. 27a. The irradiated laser power was increased by 0.5 W from 4 to 8.5 W. The width of irradiation area for each power condition was 0.5 mm, and the width of channel was 2 mm. Scanning direction was perpendicular to the channel direction.

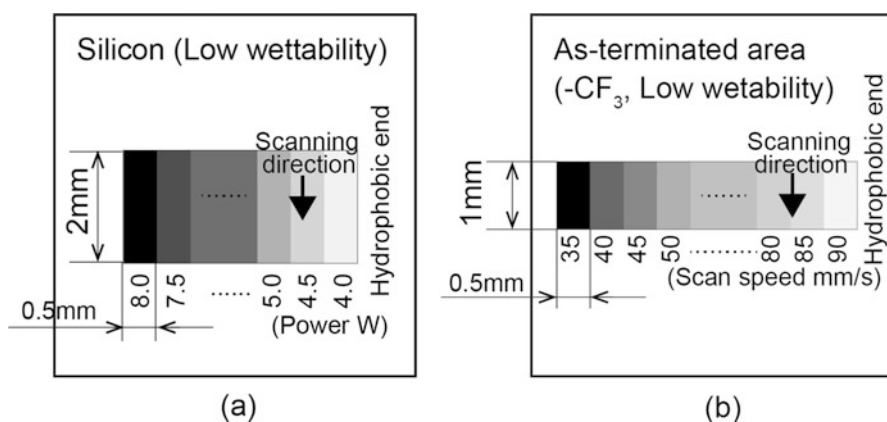


Fig. 27 Schematics of laser modification for channels with gradient wettability on (a) silicon and (b) $-CF_3$ -terminated silica glass

On the $-\text{CF}_3$ -terminated silica glass surface, another channel with self-transportation ability was drawn as illustrated in Fig. 27b. Concerned with Fig. 19, the scan speed rather than laser power was selected as controlled parameter because it was expected to achieve more gradual and continuous modulation of contact angle. The scan speed was decreased by 5 mm/s from 90 to 35 mm/s at the constant laser power of 0.4 W. Under these conditions, maximum and minimum contact angles were estimated as 100 and 40°, respectively. The section for each scan speed was 0.5 mm in width, and the channel width was 1 mm. The scanning direction was normal to the channel direction.

After the modification of both spatially graduated channels, a drop of deionized water was placed on the edge of each channel with higher contact angle. On the silicon surface, the droplet did not move toward more hydrophilic sections. This result indicates that the force produced by the unbalance of surface free energy was not enough for the droplet to start to move because the highest contact angle of this hydrophilic channel was as low as 35° estimated from Fig. 10. Then the assistant force produced by the upward current of vaporized alcohol was employed to initiate the droplet to flow. A cotton sheet impregnated with ethanol was placed under the silica glass and then deionized water was dropped again. The ethanol subsequently vaporized at room temperature, and its vapor current made the droplet unstable, and consequently the droplet easily moved on the channel owing to this effect.

The self-transportation on the silicon substrate was monitored with an optical microscope as shown in Fig. 28a. The droplet moves toward higher laser power section or more hydrophilic area without any external force. The problems of this self-transportation channel are the following; although the modification is based on microscopic geometric change, apparent scanning lines are formed at areas modified by higher laser power as shown in the left side of Fig. 28a. Such a severe damage in an optical microscopic scale restricts applications of the self-transportation channel because of lack of transparency, scattered debris, and trapping of micro-sized liquid droplet into the laser-machined groove on the surface channel. At lower laser power sections, shown in the right side of Fig. 28a, only the side of the channel was damaged with apparent lines. The damages are caused by the XY stage acceleration and deceleration when it turned back at the channel edge. The scan speed became slow, and the silicon surface was damaged by excess laser energy. Another problem is the obvious lack of the driving force. The assistance of upward current of alcohol is not suitable for many chemical or biological applications.

On the other hand, the gradual wettability channel on the $-\text{CF}_3$ -terminated silica glass successfully brings the droplet from higher to lower contact angle sections without the upward current and any external force as shown in Fig. 28b. The spherical droplet immediately spreads toward the hydrophilic side elongating its shape. In addition, the modification produced no damages or geometric change of the substrate. These advantages come from the basis of the quantity control of hydrophobic terminal groups on hydrophilic surface of the substrate, which brings non-damaged wide-range modulation of surface wettability from hydrophobia to hydrophilia.

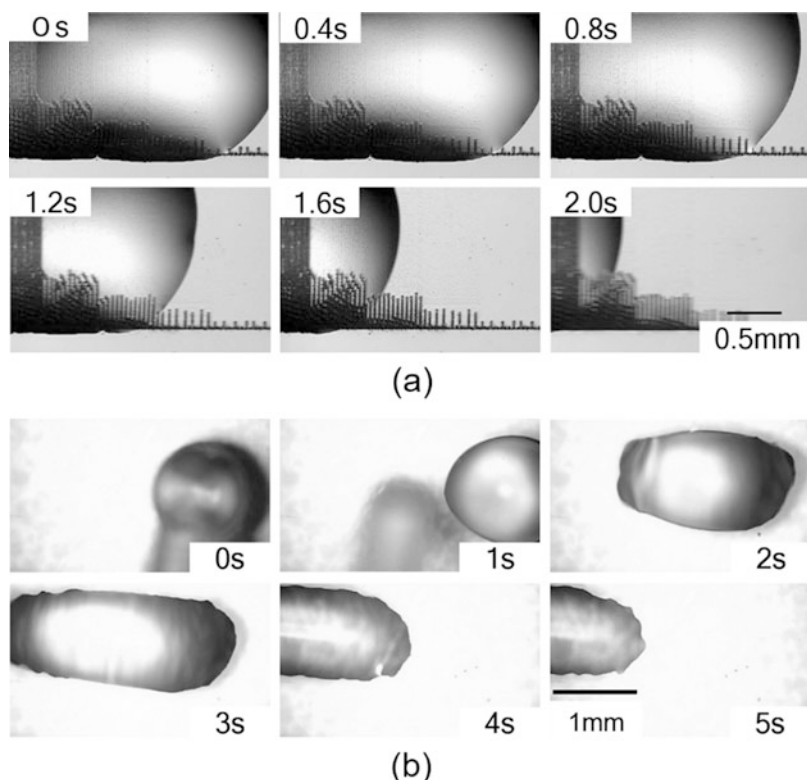


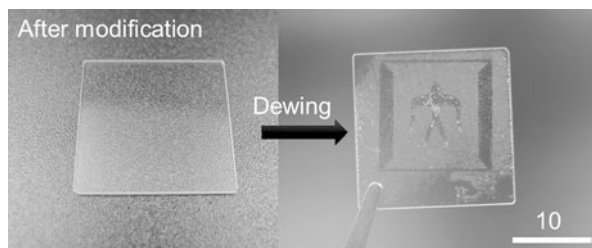
Fig. 28 Top views of self-transportation of deionized water droplet on (a) silicon and (b) $-\text{CF}_3$ -terminated silica glass

30.7 Summary and Outlook

Local wettability modification by laser irradiation was demonstrated on silicon and glass substrates. The wettability modification is based on morphological or chemical change of surface. On silicon substrate, contact angles decreased with morphological change, which was explained by the Wenzel equation. On raw borosilicate and silica glasses, laser irradiation also reduced contact angles but unaccompanied by noticeable morphological change. The reduction would be induced by increasing of a surface hydrophilic group, and it is probably caused by thermal decomposition of surface organic substances. This chemical modification was superior in terms of non-damaged, although the modified higher wettability surface could maintain only for 2 days because of natural redeposition of the organic substances.

To achieve more stable wettability modulation, pretreatment of termination with hydrophobic group was introduced on silica glass substrate. After the pretreatment with $-\text{CF}_3$, the surface exhibited hydrophobicity of which contact angle was around 110° . After the laser irradiation, the contact angle gradually decreased to 40° depending on

Fig. 29 Laser drawing by local wettability modification on $-CF_3$ -terminated silica glass



irradiated laser power or scan speed; higher power or slower speed irradiation led to more hydrophilic surface. The remaining quantity of fluorine coming from surface $-CF_3$ corresponded to the contact angle. The results indicated that the wettability change was caused by partial thermal decomposition of the $-CF_3$ groups. The modification did not degrade surface roughness and transparency of the glass substrate. Furthermore, the modified wettability could be preserved over 2 weeks.

The laser local modification was applied to draw open-type surface flow channel without grooves and packaging. At first, surface flow channels consisting of two-phase (i.e., consisting of hydrophobic and hydrophilic area) plane were fabricated on raw borosilicate glass and $-CF_3$ -terminated silica glass. The hydrophilic line successfully acted as channel on both substrates, although non-treated borosilicate glass could maintain its modified wettability in a short while. Next, channels with self-transportation ability were achieved by continuous wettability modulation. Liquid droplets were subject to driving force from surface wettability gradation and transported toward more hydrophilic area. On $-CF_3$ -terminated silica glass, deionized water droplet was self-transported without any assistant external force, and there is no damage or degradation.

The advantages of this laser modification for micro-fluidic systems are the following:

- It is a simple fabrication process using a commercial laser marker, water-repellent agent for windows, and glass. No special fabrication process including micro-mechanical machining and micro-patterning such as photolithography, deposition, and bonding is required. Furthermore, the self-transportation channel suggests possibility of operation without any pumps or actuators.
- It is easy to design systems for each unique requirement because the process is a simple drawing using laser beam similar to laser printing as shown in Fig. 29. In this figure, the mark was drawn on the $-CF_3$ -terminated silica glass in several tens of seconds without any mask and cleaning process.
- This modification causes no degradation of glass properties when it is based on chemical surface group control. The modified surface is free from contamination and allows optical monitoring and sensing through the glass substrate.

These advantages will enable on-demand designing and printing of micro-fluidic system on-site where it is used and by someone who use the system.

For more functional and complicated micro-fluidic system on surface, further studies are awaited. Ghosh et al. show droplet merging and splitting channels on surface (Ghosh et al. 2014). The laser drawing method can be expected to achieve similar function. Another challenge is to transfer the laser wettability modification to polymer materials because polymer has different advantages to silica glass: lightweight, affordable price, and easy to combine with on-site geometric formation such as 3D printing.

References

- Ahsan MS, Dewanda F, Lee MS et al (2013) Formation of superhydrophobic soda-lime glass surface using femtosecond laser pulses. *Appl Surf Sci* 265:784–789. <https://doi.org/10.1016/j.apsusc.2012.11.112>
- Akamatsu Y, Makita K, Inaba H, Minami T (2001) Water-repellent coating films on glass prepared from hydrolysis and polycondensation reactions of fluoroalkyltrialkoxysilane. *Thin Solid Films* 389:138–145. [https://doi.org/10.1016/s0040-6090\(01\)00901-4](https://doi.org/10.1016/s0040-6090(01)00901-4)
- Aono Y, Shinohara W, Tokura H (2015) Laser modification of silicon and borosilicate glass wettability for micro-fluidic systems. *Int J Autom Technol* 9:668–673
- Aono Y, Hirata A, Tokura H (2016) Non-textured laser modification of silica glass surface: wettability control and flow channel formation. *Appl Surf Sci* 371:530–537. <https://doi.org/10.1016/j.apsusc.2016.03.040>
- Baldacchini T, Carey JE, Zhou M, Mazur E (2006) Superhydrophobic surfaces prepared by microstructuring of silicon using a femtosecond laser. *Langmuir* 22:4917–4919. <https://doi.org/10.1021/la053374k>
- Bassous E, Taub HH, Kuhn L (1977) Ink jet printing nozzle arrays etched in silicon. *Appl Phys Lett* 31:135–137. <https://doi.org/10.1063/1.89587>
- Bellouard Y, Said A, Dugan M et al (2004) Fabrication of high-aspect ratio, micro-fluidic channels and tunnels using femtosecond laser pulses and chemical etching. *Opt Express* 12:2120–2129. <https://doi.org/10.1364/opex.12.002120>
- Bhattacharjee N, Urrios A, Kang S, Folch A (2016) The upcoming 3D-printing revolution in microfluidics. *Lab Chip* 16:1720–1742. <https://doi.org/10.1039/c6lc00163g>
- Bhattacharya S, Datta A, Berg JM, Gangopadhyay S (2005) Studies on surface wettability of poly(dimethyl) siloxane (PDMS) and glass under oxygen-plasma treatment and correlation with bond strength. *J Microelectromech Syst* 14:590–597. <https://doi.org/10.1109/jmems.2005.844746>
- Cardoso MR, Tribuzi V, Balogh DT et al (2011) Laser microstructuring for fabricating superhydrophobic polymeric surfaces. *Appl Surf Sci* 257:3281–3284. <https://doi.org/10.1016/j.apsusc.2010.10.156>
- Cassie ABD, Baxter S (1944) Wettability of porous surfaces. *Trans Faraday Soc* 40:546. <https://doi.org/10.1039/tf9444000546>
- Cate DM, Adkins JA, Mettakoonpitak J, Henry CS (2015) Recent developments in paper-based microfluidic devices. *Anal Chem* 87:19–41. <https://doi.org/10.1021/ac503968p>
- Chaudhury MK, Whitesides GM (1992) How to make water run uphill. *Science* 256:1539–1541. <https://doi.org/10.1126/science.256.5063.1539>
- Chinnam J, Das D, Vajjha R, Satti J (2015) Measurements of the contact angle of nanofluids and development of a new correlation. *Int Commun Heat Mass Transfer* 62:1–12. <https://doi.org/10.1016/j.icheatmasstransfer.2014.12.009>
- Choi K, Ng AHC, Fobel R, Wheeler AR (2012) Digital microfluidics. *Annu Rev Anal Chem* 5:413–440. <https://doi.org/10.1146/annurev-anchem-062011-143028>

- Chován T, Guttman A (2002) Microfabricated devices in biotechnology and biochemical processing. *Trends Biotechnol* 20:116–122. [https://doi.org/10.1016/S0167-7799\(02\)01905-4](https://doi.org/10.1016/S0167-7799(02)01905-4)
- Comina G, Suska A, Filippini D (2014) PDMS lab-on-a-chip fabrication using 3D printed templates. *Lab Chip* 14:424–430. <https://doi.org/10.1039/c3lc50956g>
- De Givenchy ET, Amigoni S, Martin C et al (2009) Fabrication of superhydrophobic PDMS surfaces by combining acidic treatment and perfluorinated monolayers. *Langmuir* 25: 6448–6453. <https://doi.org/10.1021/la900064m>
- De Marco C, Eaton SM, Suriano R et al (2010) Surface properties of femtosecond laser ablated PMMA. *ACS Appl Mater Interfaces* 2:2377–2384. <https://doi.org/10.1021/am100393e>
- De Rosa RL, Schader PA, Shelby JE (2003) Hydrophilic nature of silicate glass surfaces as a function of exposure condition. *J Non-Cryst Solids* 331:32–40. <https://doi.org/10.1016/j.Jnoncrystol.2003.08.078>
- Doan CX, Kim BH, Chu CN (2009) Micro-structuring of glass with features less than 100 μm by electrochemical discharge machining. *Precis Eng* 33:459–465. <https://doi.org/10.1016/j.precisioneng.2009.01.001>
- Duffy DC, Medonald JC, Schueller OJA, Whitesides GM (1998) Rapid prototyping of microfluidic systems in poly(dimethylsiloxane). *Anal Chem* 70:4974–4984. <https://doi.org/10.1021/ac980656z>
- Dungchai W, Chailapakul O, Henry CS (2011) A low-cost, simple, and rapid fabrication method for paper-based microfluidics using wax screen-printing. *Analyst* 136:77–82. <https://doi.org/10.1039/c0an00406e>
- Erickson D, Li D (2004) Integrated microfluidic devices. *Anal Chim Acta* 507:11–26. <https://doi.org/10.1016/j.aca.2003.09.019>
- Fadeeva E, Truong VK, Stiesch M et al (2011) Bacterial retention on superhydrophobic titanium surfaces fabricated by femtosecond laser ablation. *Langmuir* 27:3012–3019. <https://doi.org/10.1021/la104607g>
- Ghosh A, Ganguly R, Schutzius TM, Megaridis CM (2014) Wettability patterning for high-rate, pumpless fluid transport on open, non-planar microfluidic platforms. *Lab Chip* 14:1538–1550. <https://doi.org/10.1039/c3lc51406d>
- Hillborg H, Gedde UW (1999) Hydrophobicity changes in silicone rubbers. *IEEE Trans Dielectr Electr Insul* 6:703–717. <https://doi.org/10.1109/94.798127>
- Ikuta K, Hirowatari K, Ogata T (1994) Three dimensional micro integrated fluid systems (MIFS) fabricated by stereo lithography. In: *Proceedings IEEE micro electro mechanical systems an investigation of micro structures, sensors, actuators, machines and robotic systems*. IEEE, pp 1–6. <https://doi.org/10.1109/MEMSYS.1994.555588>
- Im M, Im H, Lee J-H et al (2010) A robust superhydrophobic and superoleophobic surface with inverse-trapezoidal microstructures on a large transparent flexible substrate. *Soft Matter* 6:1401. <https://doi.org/10.1039/b925970h>
- Jakeway SC, De Mello AJ, Russell EL (2000) Miniaturized total analysis systems for biological analysis. *Fresenius J Anal Chem* 366:525–539. <https://doi.org/10.1007/s002160051548>
- Kietzig AM, Hatzikiriakos SG, Englezos P (2009) Patterned superhydrophobic metallic surfaces. *Langmuir* 25:4821–4827. <https://doi.org/10.1021/la8037582>
- Kim TN, Campbell K, Groisman A et al (2005) Femtosecond laser-drilled capillary integrated into a microfluidic device. *Appl Phys Lett* 86:201106. <https://doi.org/10.1063/1.1926423>
- Kim M, Kim K, Lee NY et al (2007) A simple fabrication route to a highly transparent superhydrophobic surface with a poly(dimethylsiloxane) coated flexible mold. *Chem Commun* 22:2237–2239. <https://doi.org/10.1039/b618123f>
- Kotz F, Arnold K, Bauer W et al (2017) Three-dimensional printing of transparent fused silica glass. *Nature* 544:337–339. <https://doi.org/10.1038/nature22061>
- Kwok DY, Neumann AW (1999) Contact angle measurement and contact angle interpretation. *Adv Colloid Interf Sci* 81:167–249. [https://doi.org/10.1016/s0001-8686\(98\)00087-6](https://doi.org/10.1016/s0001-8686(98)00087-6)
- Long Z, Shetty AM, Solomon MJ, Larson RG (2009) Fundamentals of magnet-actuated droplet manipulation on an open hydrophobic surface. *Lab Chip* 9:1567. <https://doi.org/10.1039/b819818g>

- Malek CGK (2006) Laser processing for bio-microfluidics applications (part II). *Anal Bioanal Chem* 385:1362–1136. <https://doi.org/10.1007/s00216-006-0517-z>
- Manz A, Graber N, Widmer HM (1990) Miniaturized total chemical analysis systems: a novel concept for chemical sensing. *Sensors Actuators B* 1:244–248. [https://doi.org/10.1016/0925-4005\(90\)80209-1](https://doi.org/10.1016/0925-4005(90)80209-1)
- Marcinkevičius A, Juodkakis S, Watanabe M et al (2001) Femtosecond laser-assisted three-dimensional microfabrication in silica. *Opt Lett* 26:277–279. <https://doi.org/10.1364/ol.26.000277>
- Martinez AW, Phillips ST, Whitesides GM, Carrilho E (2010) Diagnostics for the developing world: microfluidic paper-based analytical devices. *Anal Chem* 82:3–10. <https://doi.org/10.1021/ac9013989>
- Mertaniemi H, Jokinen V, Sainiemi L et al (2011) Superhydrophobic tracks for low-friction, guided transport of water droplets. *Adv Mater* 23:2911–2914. <https://doi.org/10.1002/adma.201100461>
- Nakashima Y, Nakanishi Y, Yasuda T (2015) Automatic droplet transportation on a plastic microfluidic device having wettability gradient surface. *Cit Rev Sci Instrum* 86:015001. <https://doi.org/10.1063/1.4905530>
- Nishino T, Meguro M, Nakamae K et al (1999) The lowest surface free energy based on $-CF_3$ alignment. *Langmuir* 15:4321–4323. <https://doi.org/10.1021/la981727s>
- Ogawa K, Soga M, Takada Y, Nakayama I (1993) Development of a transparent and ultra-hydrophobic glass plate. *Jpn J Appl Phys* 32:L614–L615. <https://doi.org/10.1143/jjap.32.L614>
- Parkin IP, Palgrave RG (2005) Self-cleaning coatings. *J Mater Chem* 15:1689. <https://doi.org/10.1039/b412803f>
- Schwesinger N, Frank T, Wurmus H (1996) A modular microfluid system with an integrated micromixer. *J Micromech Microeng* 6:99–102. <https://doi.org/10.1088/0960-1317/6/1/023>
- Songjaroen T, Dungchai W, Chailapakul O et al (2012) Blood separation on microfluidic paper-based analytical devices. *Lab Chip* 12:3392. <https://doi.org/10.1039/c2lc21299d>
- Sun T, Feng L, Gao X, Jiang L (2005) Bioinspired surfaces with special wettability. *Acc Chem Res* 38:644–652. <https://doi.org/10.1021/ar040224c>
- Suni T, Henttinen K, Suni I, Mäkinen J (2002) Effects of plasma activation on hydrophilic bonding of Si and SiO_2 . *J Electrochem Soc* 149:348–351. <https://doi.org/10.1149/1.1477209>
- Suriano R, Kuznetsov A, Eaton SM et al (2011) Femtosecond laser ablation of polymeric substrates for the fabrication of microfluidic channels. *Appl Surf Sci* 257:6243–6250. <https://doi.org/10.1016/j.apsusc.2011.02.053>
- Takeuchi M, Sakamoto K, Martra G et al (2005) Mechanism of photoinduced superhydrophilicity on the TiO_2 photocatalyst surface. *J Phys Chem* 109:15422–15428. <https://doi.org/10.1021/jp058075i>
- Tan Y-C, Fisher JS, Lee AI et al (2004) Design of microfluidic channel geometries for the control of droplet volume, chemical concentration, and sorting. *Lab Chip* 4:292–298. <https://doi.org/10.1039/b403280m>
- Tanaka S, Chang K-S, Min K-B et al (2004) MEMS-based components of a miniature fuel cell/fuel reformer system. *Chem Eng J* 101:143–149. <https://doi.org/10.1016/j.cej.2004.01.017>
- Tang M, Hong MH, Choo YS et al (2010) Super-hydrophobic transparent surface by femtosecond laser micro-patterned catalyst thin film for carbon nanotube cluster growth. *Appl Phys A Mater Sci Process* 101:503–508. <https://doi.org/10.1007/s00339-010-5887-6>
- Terry SC, Jerman JH, Angell JB (1979) A gas chromatographic air analyzer fabricated on a silicon wafer. *IEEE Trans Electron Devices* 26:1880–1886. <https://doi.org/10.1109/t-ed.1979.19791>
- Tropmann A, Tanguy L, Koltay P et al (2012) Completely superhydrophobic PDMS surfaces for microfluidics. *Langmuir* 28:8292–8295. <https://doi.org/10.1021/la301283m>
- Tull BR, Carey JE, Mazur E et al (2006) Silicon surface morphologies after femtosecond laser irradiation. *MRS Bull* 31:626–633. <https://doi.org/10.1557/mrs2006.160>
- Vázquez E, Rodríguez CA, Elías-Zúñiga A, Cuirana J (2010) An experimental analysis of process parameters to manufacture metallic micro-channels by micro-milling. *Int J Adv Manuf Technol* 51:945–955. <https://doi.org/10.1007/s00170-010-2685-4>

- Wang R, Hashimoto K, Fujishima A et al (1997) Light-induced amphiphilic surfaces. *Nature* 388:431–432. <https://doi.org/10.1038/41233>
- Washizu M (1998) Electrostatic actuation of liquid droplets for micro-reactor applications. *IEEE Trans Ind Appl* 34:732–737. <https://doi.org/10.1109/28.703965>
- Wenzel RN (1949) Surface roughness and contact angle. *J Phys Colloid Chem* 53:1466–1467. <https://doi.org/10.1021/j150474a015>
- Wichterle O, Lim D (1960) Hydrophilic gels for biological use. *Nature* 185:117–118. <https://doi.org/10.1038/185117a0>
- Wolansky G, Marmur A (1999) Apparent contact angles on rough surfaces: the Wenzel equation revisited. *Colloids Surf A* 156:381–388. [https://doi.org/10.1016/S0927-7757\(99\)00098-9](https://doi.org/10.1016/S0927-7757(99)00098-9)
- Woolley AT, Hadley D, Landre P et al (1996) Functional integration of PCR amplification and capillary electrophoresis in a microfabricated DNA analysis device. *Anal Chem* 68:4081–4086. <https://doi.org/10.1021/ac960718q>
- Wu B, Zhou M, Li J et al (2009) Superhydrophobic surfaces fabricated by microstructuring of stainless steel using a femtosecond laser. *Appl Surf Sci* 256:61–66. <https://doi.org/10.1016/j.apsusc.2009.07.061>
- Young T (1805) An essay on the cohesion of fluids. *Philos Trans R Soc Lond* 95:65–87. <https://doi.org/10.1098/rstl.1805.0005>
- Yun DJ, Seo TI, Park DS (2008) Fabrication of biochips with micro fluidic channels by micro end-milling and powder blasting. *Sensors* 8:1308–1320. <https://doi.org/10.3390/s8021308>
- Zhou M, Yang HF, Li BJ et al (2009) Forming mechanisms and wettability of double-scale structures fabricated by femtosecond laser. *Appl Phys A Mater Sci Process* 94:571–576. <https://doi.org/10.1007/s00339-008-4920-5>
- Zorba V, Persano L, Pisignano D et al (2006) Making silicon hydrophobic: wettability control by two-lengthscale simultaneous patterning with femtosecond laser irradiation. *Nanotechnology* 17:3234–3238. <https://doi.org/10.1088/0957-4484/17/13/026>